BauSIM 2024 in Wien
23. September – 26. September

BauSIM 2024

10te Konferenz von IBPSA-DACH, TU Wien, Österreich

Proceedings

ISBN: 978-3-200-10068-8

www.tuwien.at

BauSIM 2024
Vorwort / Preface

Thomas Bednar[1], Sabine Sint[1]
1 Forschungsbereich Bauphysik, TU Wien

Die BauSIM 2024, unter der Schirmherrschaft der International Building Performance Simulation Association Deutschland Österreich Schweiz (IBPSA-DACH), fand vom 23. bis 26. September in Wien statt und bot eine herausragende Gelegenheit für den wissenschaftlichen Austausch über die neuesten Entwicklungen im Bereich der Gebäude- und Quartiersimulation. Im Zentrum dieser Veranstaltung standen innovative Forschungsergebnisse, die nicht nur zur Optimierung des Energieverbrauchs von Gebäuden beitragen, sondern auch entscheidende Impulse für die nachhaltige Stadtentwicklung und den Klimaschutz liefern. Ein zentrales Thema war, wie Simulationsmethoden zur Bewältigung der Herausforderungen von Klimaneutralität und Energieeffizienz beitragen können. Die präsentierten Beiträge liefern wichtige Erkenntnisse zur Reduktion des Energieverbrauchs, der Optimierung erneuerbarer Energien und der Sicherstellung thermischer Behaglichkeit in Gebäuden und Quartieren. Sie verdeutlichen die enge Verzahnung von Bauphysik, Technischer Gebäudeausrüstung und Simulationstechniken als Schlüssel zur Lösung komplexer Probleme.

Dieser Band umfasst 59 Full-Paper-Beiträge, die nach einem strengen Peer-Review-Verfahren ausgewählt wurden. Die Beiträge decken ein breites Spektrum ab, das sowohl grundlegende Forschung als auch angewandte Lösungen umfasst. Sie beschäftigen sich mit hochaktuellen Themen wie der energetischen Gebäude- und Quartiersmodellierung, der Verbesserung des thermischen und akustischen Komforts sowie der Nutzung maschinellen Lernens und künstlicher Intelligenz zur Modellierung des Nutzerverhaltens. Auch die Rolle von Building Information Modeling (BIM) und digitalen Zwillingen im Kontext von Planung, Ausführung und Betrieb von Gebäuden wird in mehreren Beiträgen behandelt.

Die Beiträge leisten einen wichtigen Beitrag zum internationalen Diskurs über nachhaltiges Bauen und bieten wertvolle wissenschaftliche Ressourcen für Forschende, Planer und Entscheidungsträger. Wir danken den Autorinnen und Autoren für ihre innovativen Arbeiten, die sowohl neue Forschungsimpulse liefern als auch praktische Lösungen für die Zukunft der gebauten Umwelt bieten.

BauSIM 2024, under the auspices of the International Building Performance Simulation Association Germany Austria Switzerland (IBPSA-DACH), took place in Vienna from September 23 to 26 and offered an outstanding opportunity for scientific exchange on the latest developments in the field of building and district simulation. This event focused on innovative research results that contribute to optimizing the energy consumption of buildings and provide the decisive impetus for sustainable urban development and climate protection. A central topic was how simulation methods can contribute to overcoming the challenges of climate neutrality and energy efficiency. The papers presented provide essential insights into reducing energy consumption, optimizing renewable energies, and ensuring thermal comfort in buildings and districts. They illustrate the close interlinking of building physics, technical building services, and simulation techniques as the key to solving complex problems.

This volume comprises 59 full-paper contributions selected through a rigorous peer-review process. The contributions cover a broad spectrum, including fundamental research and applied solutions. They deal with cutting-edge topics such as energy-efficient building and neighborhood modeling, improving thermal and acoustic comfort, and using machine learning and artificial intelligence to model user behavior. The role of Building Information Modeling (BIM) and digital twins in the context of planning, construction, and operation of buildings is also covered in several articles.

The articles contribute to the international discourse on sustainable building and offer valuable scientific resources for researchers, planners, and decision-makers. We want to thank the authors for their innovative work, which provides both new research impulses and practical solutions for the future of the built environment.

BauSIM 2024 in Wien
23. September – 26. September

10 Jahre simulationsgestützte Entwicklung von Fenstern mit Vakuumglas für neue und Bestandsfensterkonstruktionen

Ulrich Pont[1], Magdalena Wölzl[1], Peter Schober[2], Matthias Schuss[1]

1 TU Wien, Inst. f. Architekturwissenschaften, Austria, E-Mail: {ulrich.pont|magdalena.woelzl|Matthias.schuss}@tuwien.ac.at

2 Holzforschung Austria, Wien, Österreich, E-Mail: peter.schober@outlook.at

Kurzfassung

Die AutorInnen haben im Jahr 2014 begonnen die Integration von damals vergleichsweise neuen Vakuumgläsern (VG) für verschiedene Fensterkonstruktionen zu untersuchen. Dabei spielte numerische Wärmebrückensimulation eine wesentliche Rolle, da im Vergleich zu aufwendiger Mock-Up-Erstellung und Differenzklimakammertest mit der Simulation rasch und vergleichsweise zuverlässig die thermische Performance kritischer Bereiche (Randverbund, Abstandhalter) beurteilt werden konnte. Namhafte Unternehmen von Fenster- und Zulieferindustrie sowie des Fensterbauhandwerks konnten für kooperative Forschungsprojekte gewonnen werden, in welchen die auf Simulation basierenden Entwicklungsstände unterschiedlicher technologischer Integrationsvarianten in iterativen Prozessen unter Berücksichtigung mannigfaltiger Spezifika weiterentwickelt werden konnten, bis Funktionsprototypen bzw. Realisierungen in Realbauwerken erreicht wurden. Die Verwendung von numerischer Wärmebrücken-simulation war hier auf der einen Seite weiterhin ein wesentliches Werkzeug, auf der anderen Seite konnten die Ergebnisse mit Realmessdaten abgeglichen und hinsichtlich Ihrer Genauigkeit bewertet (und bestätigt) werden. Der Beitrag zieht nach 4 Projekten und 10 Jahren intensiver Bemühungen Bilanz über die erreichten Ergebnisse und diskutiert die Vorteile und Herausforderungen, die sich mit der Verwendung von Simulationswerkzeugen ergeben haben.

Abstract

In 2014, the authors started to investigate the integration of then comparatively new vacuum glass products for different window constructions. Numerical thermal bridge simulation played a key role here, as the thermal performance of critical areas (edge seal and distance pillars) could be assessed quickly and comparatively reliably using the simulation, compared to complex mock-up creation and testing in differential climate chambers. Building on two exploratory projects, cooperative research projects were started and carried out with well-known representatives of the window and supplier industry and the window construction trade, in which the simulation-based development statuses of different technological integration variants could be further developed in iterative processes, considering many different specifics, until functional prototypes or realizations in real buildings were achieved. The use of numerical thermal bridge simulation continued to be an essential tool here on the one hand, while on the other hand the results could be compared with real measurement data and evaluated (and confirmed) with regard to their accuracy. After 4 projects and 10 years of intensive efforts, the article takes stock of the results achieved and discusses the advantages and challenges that have arisen with the use of simulation tools.

Einleitung

Die Kulturgeschichte des Fensters kann als reichhaltig und interessant betrachtet werden, jedoch galten Fenster schon immer als Schwachstelle in der Gebäudehülle im Hinblick auf Statik und die verschiedenen Schutzfunktionen der Hülle. Diese Funktionen betreffen die Wärme- und Schalldämmung, die Wasser- und Winddichtigkeit sowie Verschattung und den Schutz vor (sommerlicher) Überhitzung in der heißen Jahreszeit. In Mitteleuropa hat der technologische Fortschritt der Fenster-technologien in den letzten 250 Jahren vielleicht die technisch fortschrittlichsten Fenster der Welt hervorgebracht, allerdings ist die Geschichte verschiedener Entwicklungsmeilensteine eine vergleichsweise lineare: Iterative Verbesser-ungen umfassten das Hinzufügen einer zusätzlichen Ebene mit Fensterflügeln (Kastenfenster), die Einführung von Dichtungen in Fugen und Stulp, die Vervielfachung der Glasscheiben pro Fensterflügel inklusive

ruhender Gaszwischenräume (Zweifach- und Dreifachverglasung), die Einführung von auf den Scheiben angebrachten Folien, die den Strahlungswärmedurchgang durch die Gläser beeinflussen, die Verwendung verschiedener Gase (anders als trockene Luft) als Füllgase für Zwischenräume, die Entwicklung dichter Randabschlüsse und die standardmäßige Anwendung von Dreh-Kipp-Beschlägen. Es kann davon ausgegangen werden, dass diese linearen Verbesserungen sich ihrer maximalen Effizienz annähern. Es muss an dieser Stelle aber betont werden, dass solche Fenster heute in der Regel oft schwere Konstruktionen mit Dreifach-verglasungen sind, die auch zum Teil stark dimensionierte und damit manchmal klobig wirkende Rahmenkonstruktionen erfordern.

Die Idee von Gläsern mit evakuiertem Innenraum („Vakuumglas“ / VG) existiert schon lange, die persistierenden technischen Probleme eine Dauerhaftigkeit des Vakuums sicherzustellen, können aber erst sein einigen Jahren (10 – 20 Jahre, vergleiche dazu Pont et al. 2018a) als gelöst betrachtet werden. Unter einem Vakuumglas versteht man in der Regel zwei parallele Glasscheiben, die einen kleinen, evakuierten Zwischenraum von oft weniger als einem Millimeter aufweisen. Zur Aufrecht-erhaltung der Parallelität der Scheiben sowie des Vakuums ist in der Regel ein Gitter aus winzigen Abstandhaltern („Pillar“) integriert, sowie besteht ein dichter Randverbund entlang der Kanten. Darüber hinaus verfügen die meisten Vakuumverglasungen über eine sogenannte Getterfläche, die Restpartikel aus dem evakuierten Raum filtern soll, sowie oft auch über eine Evakuierungsöffnung. Da die Wärmeübertragungsprozesse Wärmekonvektion und -leitung jeweils ein Medium erfordern, das im evakuierten Zwischenraum nicht vorhanden ist, weisen solche Gläser typischerweise sehr gute Wärmedämmleistungen bei vergleichsweise geringer Systemstärke auf. Der Randverbund (in den meisten Fällen aus Glas oder Metall gefertigt) und die Pillar stellen jedoch lineare und punktuelle Wärmebrücken dar und müssen bei der Planung und Konstruktion von Fenstern berücksichtigt werden. Neuere Entwicklungen scheinen die Problematik der linearen Wärmebrücke entlang des „kalten“ Randverbundes durch technologischen Fortschritt und zielgerichtete Konstruktion zu adressieren und nennen dies "Vakuumglas der nächsten Generation", im Gegensatz zum älteren "Vakuumglas der 1. Generation" (VGLASS, 2024). Abb. 1 veranschaulicht die wichtigsten Begriffe und Bestandteile typischer VG-Produkte (1. Generation) und ihre Umsetzung in Rahmenkonstruktionen. Angesichts der wärmetechnischen Eigenschaften von Vakuumglas - hohe Wärmedämmfähigkeit bei eher geringer Systemstärke - erschien und erscheint eine Anwendung sowohl im Fensterneubau als auch als Option zur energieeffizienzsteigernden Nachrüstung historisch bedeutsamer Bausubstanz sinnvoll: Zu Beginn der Forschungs- und Entwicklungsarbeiten der Autoren im Jahr 2014 war dieses Potenzial angesichts der wenigen Veröffentlichungen, die sich mit der Integration von VG in neue/zeitgemäße und historische Fenster beschäftigten, noch nicht ausgeschöpft. Mit anderen Worten: Während sich die Forschung und Entwicklung stark auf die Technologie von VG konzentrierte, wurde die Anwendungs-forschung im Bereich der (europäischen) Fenstertechnik nicht in zufriedenstellender Weise eingesetzt. Ziel dieses Beitrages ist es, die eingesetzten Methoden und abgeleiteten Ergebnisse von 10 Jahren Forschung an Fenstern mit implementierten VGs darzustellen. Dabei werden die damit verbundenen Herausforderungen und Voraus-setzungen, die diese Anstrengungen ermöglicht haben, aus einer ex-post Perspektive beschrieben. Darüber hinaus wird ein Ausblick auf die jüngsten Forschungs- und Entwicklungsarbeiten gegeben.

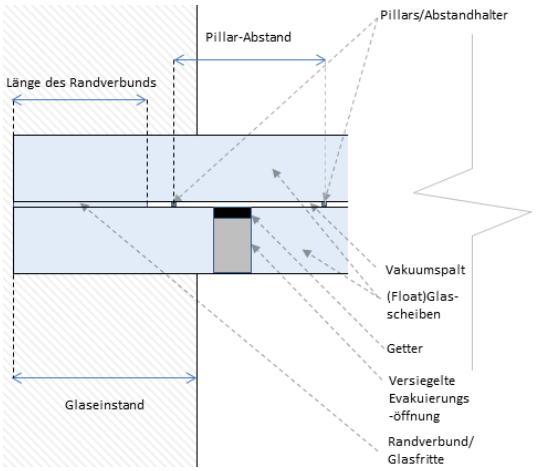

Abbildung 1: Typische Elemente & Terminologie von VG der 1. Generation (Abb.: AutorInnen)

Anwendungsfälle, Voraussetzungen & Beobachtungen

Die hochwärmedämmenden VG erscheinen sowohl für neue Fensterkonstruktionen als auch für die Nachrüstung von bestehenden, historisch bedeutsamen Fensterkonstruktionen, wie z.B. Wiener Kastenfenstern, gut geeignet zu sein. Dabei haben die Zielsetzungen für beide Anwendungsfälle Gemeinsamkeiten, aber auch große Unterschiede: Neue Fenster können und sollten auf ein optimales thermisches Verhalten

hin optimiert werden und dabei sollen dem heutigen gestalterischen Zeitgeist entsprechen. Dementsprechend ist die Integration anderer zeitgemäßer Technologien (z.B. Anbindung an Gebäudeautomation, Motorisierung zwecks hochwertiger und autonomer hygienischer Lüftung, etc.) wünschenswert Darüber hinaus können für solche Fenster auch nicht-konventionelle Bedienungs- und Öffnungsschemata in Betracht gezogen werden, z.B. ungewöhnliche Öffnungsarten und -richtungen. Historisch bedeutsame Fenster sollen dagegen möglichst unter Erhalt der bestehenden Erscheinungsform thermisch verbessert werden. Daher muss jeder Eingriff mit den in der Regel zarten (Holz-)Konstruktionen kompatibel sein, aber gleichzeitig eine sorgfältige Berücksichtigung der linearen Wärmebrücke entlang des Vakuumglas-Randverbundes sicherstellen. Abb. 2 fasst die Gemeinsamkeiten und Unterschiede zusammen. Aus einer Ex-post-Perspektive lassen sich Beobachtungen (B) und Voraussetzungen (V) benennen, die zum Erfolg der Forschung in den vergangenen 10 Jahren beigetragen haben (Tab. 1).

Abbildung 2: Unterschiede zwischen den F&E-Ansätzen für neue und bestehende Fensterkonstruktionen (eigene Abbildung AutorInnen)

Tabelle 1: Beobachtungen (B) und Vorrausetzungen (V) für erfolgreiche VG-Fenster-F&E-Projekte

Typ	Beschreibung
B1	Die Forschung an VGs selbst datiert bis zurück ins Jahr 1913 (oder früher, vgl. Zoller 1913), es gab jedoch vor unseren Forschungsbemühungen wenige Publikationen zum Thema VG-Integration in (europäische) Fenster.
B2	Die zentraleuropäischen Fensterhersteller haben das große Potential von VG stets anerkannt, waren aber zögerlich solitäre Pionierforschungsarbeit als Einzelunternehmen durchzuführen, v.a. aufgrund von Vorbehalten gegen VGs (Dauerhaftigkeit, rasche Verfügbarkeit bei Glasbruch)
B3	Für die Glasindustrie würde das Umschwenken von Dreischeibenverglasungen auf VGs betriebswirtschaftliche Herausforderungen bedeuten: Es wird eine Scheibe weniger benötigt, große Investitionen in Produktionstechnik, sowie Lizenzgebühren an Patenthalter wären erforderlich.
B4	Grundsätzlich werden Fenster im gesamten Wertschöpfungsprozess von „Planen, Bauen, Sanieren“ als thermisch/energetische Schwachpunkte betrachtet.
V1	Aufgrund der Vorbehalte gegenüber dem VG waren extensive Testserien mit VG-Produkten erforderlich um Verhalten und Charakteristiken kennenzulernen
V2	In der F&E-Arbeit waren klar definierte Entwickungsziele zu definieren (wie auch „Nicht-Ziele“) um für neue und Bestandsfenster zu Ergebnissen zu kommen.
V3	Für die F&E-Arbeiten war ein Konsortium aus Stakeholdern unterschiedlicher Hintergründe erforderlich (Wissenschaft und Wirtschaft/Industrie) um multiperspektivisch arbeiten zu können. Außerdem war es wesentlich eine vertrauensvolle, zielgerichtete, konstruktive Arbeitsatmosphäre sicherzustellen und Partikularinteressen einzelner Stakeholder zu berücksichtigen, aber gegenüber den generellen Entwicklungszielen hintanzuhalten.

Überblick über die VG-F&E-Projekte

Mit dem Sondierungsprojekt VIG-SYS-RENO (2014-2015) wurde ein erster Grundstein für Integration von Vakuumglas in historisch relevante Bestandsfenster gelegt. Dieser Startpunkt hatte mehrere Gründe: Zum einen hat in China eine Firma in großem Maßstab die VG-Produktion gestartet, zum anderen äußerten facheinschlägige, öffentliche Forschungs-förderungsprogrammen Interesse an Projekten, die Bestandsgebäude durch Einzelmaßnahmen zu ertüchtigen im Stande wären. Es wurden prinzipielle Eigenschaften verschiedener VGs im Labor vermessen und simulations- und laborbasierte Nachrüstmöglichkeiten für Flügelfenster mit VG verifiziert. Anschließend wurde ein weiteres Sondierungsprojekt namens MOTIVE (2016-2017) durchgeführt. In diesem Projekt wurden disruptive neue Ansätze für neue Fenster mit VG in einer hohen Anzahl angedacht und einer prinzipiellen Simulation und einem kleinmaßstäblichen Mock-Up-Test unterzogen. Da die österreichische Fensterindustrie sowie die Beschlag- und Dichtungsindustrie ihr Interesse in diese Richtung bekundeten, starteten wir ein Verbundprojekt mit dem Namen FIVA (2018 - 2020), um neue Fenster mit VG weiterzuentwickeln. Als Ergebnis erhielten wir vier funktionale Prototypen von hochisolierenden Fenstern mit VG, die es in dieser Form nicht von der Stange gab. Um auch dem Forschungstrack im Gebäudebestand weiter zu folgen, wurde das Projekt VAMOS (2019-2021) gestartet, in welchem – gemeinsam mit Fensterbau-Tischlereien - sechs bestehende Bauwerke mit Kastenfenstern ausgewählt wurden und eine Reihe von Fenstern mit Vakuumglas ertüchtigt und dann einem rigorosen Langzeitmonitoring unterzogen wurden. Aktuell wird einer der Fensterprototypen aus dem FIVA-projekt (ein Abstell-Schiebefenster) im Rahmen von Auftragsforschung gemeinsam mit einem

namhaften Industriepartner weiterentwickelt (Projekte SLIDE und MOVISTA, laufend seit 2021).

Methoden

Die multiperspektivischen und iterativen Arbeitsabläufe, die für die Entwicklung und Prüfung von mit VG ausgestatteten Fenstern erforderlich sind, erfordern unterschiedliche Ansätze, Methoden und Hintergrundwissen aus verschiedenen Bereichen, einschließlich Tischlerei, Industrietechnik, Bauphysik, normative Prüfung, Monitoring und Diagnostik sowie Marketing-und Kommunikations-fähigkeiten. Abb. 3 veranschaulicht den Arbeitsablauf bzw. die Verteilung der Arbeitspakete im Projekt FIVA, das sich auf die Entwicklung neuer Fenster mit Vakuumglas zusammen mit wichtigen Akteuren der österreichischen Fensterbauindustrie konzentrierte. Dabei bildete der iterative Ansatz zur Verbesserung der Konstruktion, der thermischen sowie der akustischen Leistung der Fensterprototypen ein Schlüsselelement bei der Entwicklung von vier Fensterprototypen. In späteren Phasen des Projekts wurden die eher endgültigen Funktionsprototypen typischen Prüfroutinen wie Luftdichtheit, Dichtheit gegen Wind-Driven Rain usw. unterzogen. Darüber hinaus wurden (end-)nutzerbezogene Aspekte bearbeitet, da neue Fenstertypologien eine gewisse Akzeptanz bei den Verbrauchern voraussetzen, da sie sich sonst aus industrieplanerischer und wirtschaftlicher Sicht nicht als erfolgreiches Bauteil durchsetzen können.

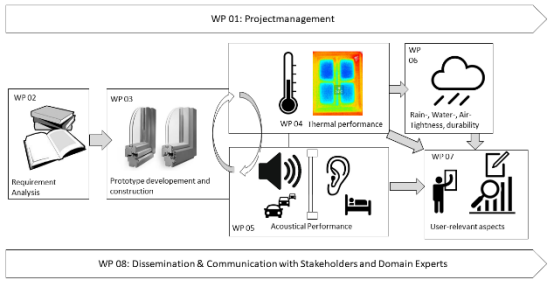

Abbildung 3: Arbeitspakete und Projektablauf des Projektes FIVA (eigene Abbildung AutorInnen)

In unserer Forschungs- und Entwicklungsarbeit setzten wir in der Regel die folgenden Methoden ein: **(i) Skizzenbasiertes Design** als Grundlage für iterative Konstruktionsverbesserungen: Anhand von technischen Zeichnungen von VGs und (bestehenden) Fenstertechnologien (2D-Schnittentwürfen, 3D-Skizzen), wurde die Integration der VG-Produkte in bestehende (Kasten-)Fensterrahmen erarbeitet sowie die Kompatibilität mit bestehenden Rahmen zeitgenössischer Fensterprodukte geprüft. Während bei ersterem die Änderung der Rahmengeometrie keine Option war, wurde bei letzterem schnell klar, dass bestehende Fensterrahmenkonstruktionen aufgrund fehlender Randverbundabdeckung und damit einhergehender Probleme mit perimetralen Wärmebrückeneffekten (und damit verbundener Kondensation) nicht ohne weiteres für VG geeignet waren. Noch vor den Simulationsbemühungen wurde beschlossen, neue Fenster mit Vakuumglas eher mit disruptiven neuen Ansätzen anzugehen als bestehende linearen Entwicklungsbemühungen fortzusetzen. **(ii) Simulation** (und Berechnung): Simulationen ermöglichen einen schnellen und einfachen Einblick in die Leistungsfähigkeit unterschiedlicher Fensterkonstruktionen. Numerische Wärmebrückensimulation wurde verwendet, um wichtige Leistungsindikatoren für die Details der Fensterkonstruktion zu erhalten (sowohl in 2D- als auch in 3D-Simulationen). Diese Indikatoren umfassten den f_{Rsi}-Wert, die mind. Oberflächentemperaturen sowie die Temperaturen innerhalb der Konstruktion an bestimmten kritischen Stellen (z.B. Kondensationsrisiko hinter Gummidichtungen). Neben thermischen Simulationen wurden in den letzten Jahren auch numerische Methoden für das mechanische Verhalten von festen und beweglichen Teilen von Rahmenentwicklungen eingesetzt. Es versteht sich von selbst, dass an bestimmten Punkten des Entwicklungsprozesses sowohl die angenommenen Eingangsdaten in der Modellierung (z.B. "Ersatzleitfähigkeit des Vakuumspalts") als auch die "relativen" Ergebnisinformationen aus den Simulationen (z.B. Vergleich der Oberflächentemperaturen verschiedener Konstruktionsvarianten) kritisch bewertet und validiert/verifiziert werden mussten. Ein wesentlicher Punkt war auch die Frage, ob man – durch die Pillars – stets 3D-Simulationen anwenden sollte oder nicht? In Pont und Mahdavi (2017) konnte gezeigt werden, dass die Abweichung in Ergebnissen bei 2D-Simulationen bei entsprechender Modellierung kaum ins Gewicht fallen. **(iii) Labortests und Monitoring:** Eine der Hauptanstrengungen in den ersten Jahren der beschriebenen Bemühungen war die Prüfung von VG-Produkten im Hinblick auf ihre thermischen, akustischen, mechanischen und dauerhaften Eigenschaften. Während vor zehn Jahren in Europa keine industrielle VG-Produktion lief, bedeutete der Kauf von VG-Scheiben vergleichsweise lange Lieferzeiten, da die Scheiben aus den Vereinigten Staaten oder Fernostasien zu unseren Prüfeinrichtungen kamen. Natürlich wurde die Haltbarkeit der Glasprodukte in dieser Situation der Lieferzeiten zu einem noch wichtigeren Thema: Eine typische

Frage der Tischler lautete: "Was soll ich tun, wenn eine der Scheiben bricht? Wie lange wird es dauern, bis ich Ersatz bekomme?" Diese Frage wurde einerseits durch globale Ereignisse wie COVID-19 oder den Containerschiffsstau im Suezkanal verschärft, verlor aber auch dadurch an Relevanz, dass 2020 eine europäische Produktionslinie anlief. In späteren Phasen wurde Monitoring insbesondere für die Kastenfenster mit VG durchgeführt. Hier konnten wir nachweisen, dass unsere Simulationen, die von vergleichsweise extremen Randbedingungen ausgingen, als solide Grundlage für eine Leistungsvorhersage der mit VG ausgestatteten Fenster dienen können. In der Realität stellte sich jedoch heraus, wie wichtig eine sorgfältige handwerkliche Ausführung beim Einbau und bei der Montage von Fenstern mit VG ist, da z.B. Lücken in der Gummidichtung die Leistung des Fensters negativ beeinflussen und die thermische Verbesserung durch die VG-Scheibe bei weitem wett machen können. **(iv) Aspekte des Handwerks und der Industrietechnik:** In den kollaborativen F&E-projekten zu neuen Fenstern und ertüchtigen Kastenfenstern wurden Aspekte der effektiven Montage, der Statik der Bauteile, der Vorfertigung im Werk, des Transports, der Montage, des Anschlusses an die umgebenden Wandsysteme, der Feinabstimmung der beweglichen Teile und der Wartung zu einer wichtigen und zu berücksichtigenden Perspektive, die vor allem von den Industriepartnern eingebracht wurde. Dies geschah in iterativen Entwicklungsschritten in einem Ping-Pong-Austausch mit Simulationsbemühungen. Die Industriepartner stellten auch Funktionsprototypen und Mock-ups für Labor- und Praxistests her. Ein sehr wichtiger Aspekt in diesem methodischen Ansatz war auch die Reduzierung der Komplexität der Entwürfe im Hinblick auf das "KISS"-Prinzip (keep it super simple), da wir oft mögliche, aber schwer zu realisierende Lösungen identifiziert haben, die wir in weiteren Entwicklungsschritten weggelassen haben, da ihre Chance, gebaute Realität zu werden, vergleichsweise gering war. **(v) Peer Review:** Wie bereits erwähnt, war eine offene und konstruktive Atmosphäre in den F&E-Projekten, an denen mehrere Firmen beteiligt waren, eine entscheidende Voraussetzung für schnelle Fortschritte. Der Arbeitsfortschritt wurde in diesem Sinne einer ständigen internen Begutachtung unterzogen. In späteren Phasen wurden die verschiedenen Projekte auch von externen Fachleuten begutachtet: Vier Prototypen ungewöhnlicher neuer Fenster, die VG wurden beim Fenster-Türen-Treff 2020 ausgestellt. Dort wurden Fachkollegen gebeten, diese Prototypen anhand eines strukturierten Bewertungsbogens kritisch zu beurteilen. Bei den Kastenfenstern, die einem umfangreichen Monitoring der wichtigsten Leistungsindikatoren unterzogen wurden, wurden Personen, die sich oft in unmittelbarer Nähe dieser Demonstrationsfenster aufhielten (z.B. bei Büronutzung jene, deren Arbeitsplatz an das Fenster angrenzte), um zusätzliches, subjektives Feedback gebeten.

Ergebnisse

Nachstehend wird ein Einblick in die erzielten Ergebnisse gegeben: Aufgrund der Platzbeschränkungen eines Papers sei an dieser Stelle auf die vom Fördergeber betriebene Ergebnisberichtplattform verwiesen, wo die umfassenden Endberichte frei zugänglich sind (via www.nachhaltigwirtschaften.at; Pont et al. 2018a, Pont et al. 2018b, Pont et al. 2020, Pont et al. 2023b)

Kastenfensterertüchtigung

Im Rahmen des VIG-SYS-RENO-Projekts wurde die Verbindungsstelle zwischen Vakuumglas und Holzrahmen von Kastenfenstern als kritische Zone identifiziert (Kondensation oder Vereisung an kürzlich nachgerüsteten Fenstern ist nicht akzeptabel). Die Simulationen ergaben jedoch, dass ohne eine grundlegende Änderung der Geometrie und/oder des Materials der Holzfensterprofile ein immanentes Kondensationsrisiko bestehen bleiben würde. Interessant war auch, wie sich die Verwendung von VG im äußeren oder inneren Flügel auswirkt. Die alte Faustregel, dass hochdämmende Schichten möglichst auf der Außenseite von Konstruktionen angeordnet werden sollten, während Schichten mit hohem Diffusionswiderstand möglichst auf der Innenseite von Konstruktionen angeordnet werden sollten, ist nur schwer anwendbar, da VGs in der Regel sowohl einen hohen Diffusions- als auch einen hohen Wärmedurchlasswiderstand aufweisen. Abb. 4 zeigt die Temperaturkonturen entlang der Innenoberfläche von beiden Flügeln von Kastenfenstern für verschiedene Fälle (Float/Float, Vakuum/Float, Float/Vakuum). Es ist deutlich zu erkennen, dass die Verwendung von VG auf der Innenseite zu einem kälteren Zwischenraum und einer niedrigeren Oberflächentemperatur auf dem äußeren Flügel führt, während eine Verwendung auf der Außenseite die Temperaturen des anderen Flügels nicht wesentlich beeinflusst. Da diese Ergebnisse von einem Wärmebrücken-simulationsprogramm stammen, sind konvektive Effekte in dieser Analyse nur rudimentär berücksichtigt. Abb. 5 zeigt eine schematische

Darstellung des Wärmestroms bei der Verwendung von VG in Innen- und Außenflügeln von Kastenfenstern. In Anbetracht dieser (und anderer) Ergebnisse wurde deutlich, dass eine Umsetzung und Realmonitoring erforderlich sind, um die Leistung von mit VG ausgestatteten Fenstern beurteilen zu können. Abb. 6 zeigt eines der Demobauwerke und die Messausstattung. Tab. 2 bietet einen Überblick über die Demonstrationsstandorte und die verschiedenen Eigenschaften der entsprechenden Fenster.

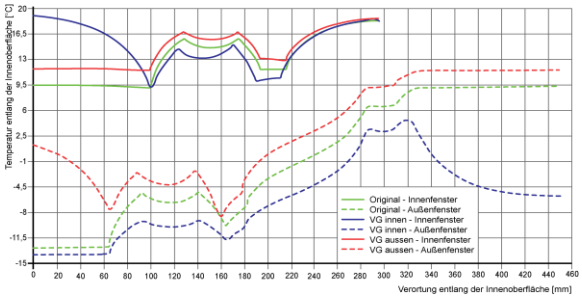

Abbildung 4: Temperaturverlauf entlang der Flügel von Kastenfenstern unterschiedlicher Konfiguration (Abbildung: AutorInnen)

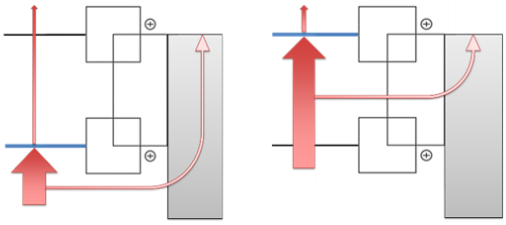

Abbildung 5: Konzeptuelle Darstellung des Wärmestromverlauf bei Anwendung von VG im Innen- (l.) & Außenflügel (r.) (Abb: AutorInnen)

Abbildung 6: Testgebäude (l.) und mit Monitoring-Equipment ausgestattetes Kastenfenster (Abb: AutorInnen)

Wir konnten nachweisen, dass sich die U-Werte der Fenster deutlich verbessert haben und dass - bei entsprechenden Begleitmaßnahmen (wie Heizkörper in den Räumen/unter den Fenstern, Anbringen von Dichtungen usw.) - bei normalen (nicht extremen) Winterbedingungen kein Kondensationsrisiko besteht. Sowohl aus Messungen als auch aus Berechnungen/ Simulationen wurde festgestellt, dass die Flügelfenster erheblich verbessert werden können (Rückgang von 2,5-3,5 $W.m^{-2}.K^{-1}$ auf 0,5-1,5 $W.m^{-2}.K^{-1}$). Für ein typisches Wiener Gründerzeitgebäude würde die VG-Verbesserung Kastenfenstern zu einer Verringerung des Heizbedarfs um etwa 10 % führen, abhängig vom Fenster-Wand-Verhältnis des entsprechenden Gebäudes.

Tabelle 2: Testsites für VG in Kastenfenstern

Bild	Beschreibung
	Schloss in Wels | Rahmenstockfenster in der Leibung | Innen öffnend, 2flg. + Oberlicht | Wohnraum | Maßnahme: Glastausch
	Villa in Wien | Pfostenstockfenster außenbündig | außenöffnend, 2flg. + Oberlicht | Wohnraum/Wohnung | Maßnahme: Außenfenster neu
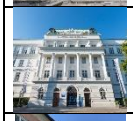	Universitätsgebäude Wien | Pfostenstock außenbündig | Außen-öffnend, 2flg. | Büroraum | Maßnahme: Flügel neu
	Stift Wilhering | Doppelrahmen außenbündig | Innen-öffnend, 2 flg. | Leerraum (keine Nutzung) | Neufenster im Steingewände
	Architekturbüro in Salzburg | Pfostenstock außenbündig | außen-öffnend | 2flg. | Büroraum | Neufenster
	Büroräumlichkeiten Innsbruck | Rahmenstock in der Leibung | innen-öffnend | 2flg. | Büroraum | Neufenster.

Neufenster mit Vakuumglas

Im Rahmen der Projekte MOTIVE und FIVA konnten verschiedene VG-Fenster entwickelt werden, welche zum Teil recht exotische Bedienungs-/Öffnungsschemata bieten. Im Rahmen des FIVA-Projekts konnten vier verschiedene Funktionsprototypen entwickelt, getestet und als Mock-Ups realisiert werden. Tabelle 3 zeigt diese Funktionsprototypen A - D und einige Schlüsseleigenschaften, die aus Simulationen abgeleitet wurden. Durch die Verwendung eines High-End-VG mit einem U_g-Wert von 0,4 $W.m^{-2}.K^{-1}$ (Systemdicke weniger als 1 cm) konnten sehr gute U_{Win}-Werte erzielen werden (alle unter 0,8 $W.m^{-2}.K^{-1}$). Die in der Tabelle angegebene Mindesttemperatur unterstellt stationäre Innen- und Außentemperaturen von 20 °C bzw. -10 °C. Die U-Werte dieser Funktionsprototypen wurden anhand der EN ISO 10077 (2018, 2020) berechnet (zum Zeitpunkt der Durchführung kannte diese Norm keine VGs). Diese Funktionsprototypen wurden im Rahmen des Fenster-Türen-Treffs 2020 in Salzburg einem Peer Review unterzogen. Abbildung 7 zeigt die Ausstellung mit den Mock-Ups. Die Bewertung verschiedener Merkmale des Funktionsprototyps erfolgte im österreichischen Schulnotensystem (1... ausgezeichnet, 5 nicht zufriedenstellend). Während alle Prototypen grundlegend

wohlwollend bewertet wurden, wurden die Prototypen A und D aufgrund ihrer Innovation (D) und der Aspekte Kundenakzeptanz, Montage und Bedienung (A) favorisiert. Diese Prototypen und die Ausstellung veranschaulichten das Potenzial neuer, innovativer Fenster mit VG, Motorisierung/ Automatisierung und Integration innovativer Technologien. Dabei ist eine zentrale Botschaft des Projektergebnisses, dass einige disruptive Innovationen in jeden kommenden Entwicklungsschritt neuer Fenstertechnologien integriert werden sollten.

Tabelle 3: Funktionsprototypen aus FIVA

Darstellung	Spezifika
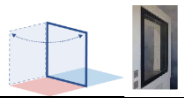	Type A- Drehfenster innen öffnend f_{Rsi}: 0.74 | $\theta_{si,min}$: 12,23 °C | U_{Win}:0.78 W.m^{-2}.K^{-1}
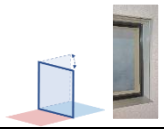	Type B- Drehfenster außen öffnend f_{Rsi}: 0.77 | $\theta_{si,min}$: 13,05 °C | U_{Win}:0.72 W.m^{-2}.K^{-1}
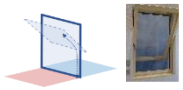	Type C- Kippfenster f_{Rsi}: 0.75 | $\theta_{si,min}$: 12,55 °C | U_{Win}:0.68 W.m^{-2}.K^{-1}
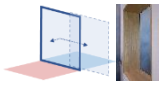	Type D- Abstell-Schiebefenster f_{Rsi}: 0.74 | $\theta_{si,min}$: 12,07 °C | U_{Win}:0.64 W.m^{-2}.K^{-1}

Abbildung 7: Ausgestellte VG-Fenster-Funktionsprototypen (Abb: AutorInnen)

Prototyp D hat zu einer Folgeentwicklung geführt: Während das Original mit handelsüblichen Teleskopauszügen, die man aus dem Automobilbau kennt, ausgestattet wurde und vergleichsweise aufwändige Beschläge und Motorisierung beinhaltete, hat die Weiterentwicklung im Rahmen des SLIDE/MOVISTA – Projektes von Grund auf neue Beschläge adressiert (KDM-INNO, 2024). Nach zwei Jahren intensiver Entwicklungsarbeit wurde das MOVISTA-Fenster auf der weltgrößten Messe für Bauelemente, der Bau 2023 in München, Deutschland, ausgestellt. Es wurde von Fachleuten und Endkunden gut aufgenommen, und obwohl der gezeigte Prototyp noch nicht auf dem Markt erhältlich war, deuteten mehrere Besucher an, dass sie aufgrund seiner Integrationsmöglichkeiten in die Gebäudeautomation, seiner Ästhetik, des platzsparenden Bedienkonzepts und der Robustheit der integrierten Technologien sofort eine große Anzahl dieser Fenster kaufen würden. Abbildung 8 veranschaulicht schematisch das Bedienungs-/Öffnungsschema des Fensterprototyps sowie den ausgestellten Fensterprototyp zeigt.

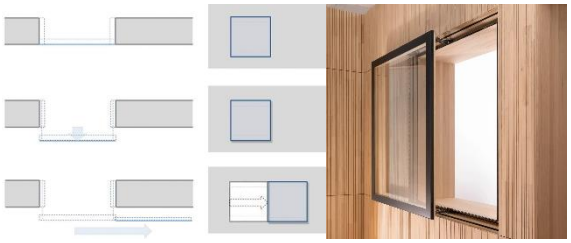

Abbildung 8: Prinzipieller Bewegungsablauf von Prototyp D bzw. dem MOVISTA Fenster (l. Abb: AutorInnen); MOVISTA-Mock-Up wie auf der Bau 2023 gezeigt (r., Image Source: KDM-INNO.com)

Schlussfolgerung und Ausblick

Der gegenständliche Beitrag zeigte die Ansätze, applizierten Methoden (insbesondere die numerische Wärmebrückensimulation) und in Auszügen die Ergebnisse von Forschungs- und Entwicklungsbemühungen in Richtung der Integration von VG in zeitgenössische und historisch wertvolle Fenster. Die Integration von VG in bestehende Kastenfensterkonstruktionen kann einen wertvollen Beitrag zur Reduktion von Energiekonsum und Emissionen des Gebäudebestands beitragen, ohne die üblichen destruktiven Auswirkungen auf die Bauwerke zu haben, die ein Fenstertausch zu neuen Fenstern mit einer Ebene und gröberen Stockmaßen verursacht. Bei der Genese von neuen Fenstern hat sich gezeigt, dass übliche Denkmuster und das Verfolgen des üblichen linear-iterativen Entwicklungspfades der vergangenen Dekaden nicht wirklich sinnvoll ist, da die VGs (zumindest die der ersten Generation) ganz andere Konstruktionsprinzipien benötigen: Tatsächlich sollte der Fensterflügel anhand der Erfordernisse des eingesetzten VG konstruiert werden, während Stock und feststehende Elemente als Einhausung von Motorisierung, Verschlüssen und auch Dichtungen dienen sollten. Solche Fenster können auch die Transformation von reinen Hüllelementen zu haustechnischen Systemen durch die Einbindung in Gebäudeautomation leisten (z.B. automatisiertes Lüften). Gleichwohl die gezeigten Forschungen über 10 Jahre passierten, ist ein Ende der Entwicklungen bei weitem nicht erreicht. Neben der weiteren Verfeinerung der technischen Aspekte der gezeigten Fensterprototypen hinsichtlich heutiger Notwendigkeiten (Stichwort: Verschattung), ist auch die Kommunikation über die Technologie an interessierte Stakeholder ein großes Thema, um beispielsweise das weitere

Verlustiggehen von Kastenfenstern zu verhindern. Das bezieht auch Sanierungsfördergeber mit ein, in deren Förderungsprogrammen beim Fenster in der Regel nur der Fenstertausch gefördert wird, nicht aber die Sanierung. Aspekte wie Einbettung in die Kreislaufwirtschaft sind aber gerade beim Bestand ein großes Thema, während Vorfertigung, rasche und einfache Montage, sowie Aspekte der Bedienbarkeit ebenfalls wichtige weitere Entwicklungspunkte darstellen. Gebäudesimulation und Bauteilsimulation spielen bei all diesen Aspekten eine große Rolle, im gezeigten hat sich vor allem die numerische Wärmebrückensimulation als ausgezeichnetes Arbeitsvehikel zur raschen performativen Einordnung der Auswirkung von Konstruktionsentscheidungen und -varianten bewährt.

Disclaimer & Danksagung

Da das gegenständliche Paper Projekte, Methoden und Resultate zwecks fundierten Überblicks zusammenfasst, wurden Teile davon bereits in früheren Publikationen gezeigt. In Pont et al. 2023 werden darüber hinaus ein Großteil der gezeigten Inhalte detailliert diskutiert. Die beschrieben F%E-Bemühungen wären ohne die generöse Förderung der österr. Forschungsförderungsgesellschaft nicht möglich gewesen (Projects VIG-SYS-RENO No: 845225, Motive No: 854690, FIVA No: 867352, VAMOS No: 878272). Die F&E-Bemühungen in den Projekten SLIDE/MOVISTA wurden durch die Fa. KDM/Blum gefördert. An den gezeigten F&E-Bemühungen haben folgende Institutionen neben den AutorInnen beigetragen: Fa. AGC Interpane, Fa Blum, Fa. Gaulhofer, Fa. IEB Eisele, Fa. Katzbeck, Fa. MaCo, Fa. Prohaska, Fa. Schaden, Fa. Svoboda, Fa. Wick-Norm, Fa. Winkler und Fa. Zoller-Prantl

Literatur

EN-ISO 10077. 2018: ÖNORM EN ISO 10077-2 Wärmetechnisches Verhalten von Fenstern, Türen und Abschlüssen - Berechnung des Wärmedurchgangskoeffizienten - Teil 2: Numerisches Verfahren für Rahmen (ISO 10077-2:2017)

EN-ISO 10077. 2020: ÖNORM EN ISO 10077-1 Wärmetechnisches Verhalten von Fenstern, Türen und Abschlüssen - Berechnung des Wärmedurchgangskoeffizienten - Teil 1: Allgemeines (ISO 10077-1:2017, korrigierte Fassung 2020-02).

KDM-INNO. 2024. KDM-Innovation; available via https://www.kdm-inno.com/de (checked in December 2023)

Pont, U., Heiduk, E., Schober, P., Romirer, H., Dolezal, F., Proskurnina, O., Schuss, M., Sustr, C., Hohenstein, H., Mahdavi, A. 2018a. Sondierung von Fenstersystemen mit innovativen Gläsern, speziell Vakuum-Isoliergläsern, zur Gebäudesanierung. Berichte aus Energie- und Umweltforschung 33/2018; available via https://nachhaltigwirtschaften.at/resources/sdz_pdf/berichte/schriftenreihe-2018-33-vigsysreno.pdf (checked in Dec. 2023)

Pont, U., Mahdavi, A. 2017. "A comparison of the performance of two- and three-dimensional thermal bridge assessment for typical construction joints";in: "Building Simulation Applications Proceedings", M Baratieri, V. Corrado, A. Gasparella, F. Patuzzi (Hrg.); bu.press (publisher of the Free University of Bozen-Bolzano), 3. (2017), ISSN: 2531-6702; Paper-Nr. 75, 8 S.

Pont, U., Schuss, M., Mahdavi, A., Schober, P., Hauer, K., Lux, C. 2018b. Modellierung, Optimierung, und technische Integration von Vakuumglas-Elementen; Berichte aus Energie- und Umweltforschung 24/2018; available via https://nachhaltigwirtschaften.at/resources/sdz_pdf/berichte/schriftenreihe-2018-24-motive.pdf (checked in Dec.2023)

Pont, U., Wölzl, M., Schuss, M., Mahdavi, A., Schober, P., Haberl, J., Lux, C. 2020. Fensterprototypen mit integriertem Vakuumglas (FIVA); Berichte aus Energie- und Umweltforschung 47/2020; available via https://nachhaltigwirtschaften.at/resources/sdz_pdf/schriftenreihe-2020-47-fiva.pdf (checked in Dec.2023)

Pont, U., Schober, K. P., Wölzl, M., Schuß, M. W., & Haberl, J. 2023a. A Review on the FIVA-Project: Simulation-Assisted Development of Highly-Insulating Vacuum Glass Windows. In G. Pernigotto, F. Patuzzi, A. Prada, V. Corrado, & A. Gasparella (Eds.), Building Simulation Applications BSA 2022. 5th IBPSA Italy Conference, Bozen-Bolzano, 29th June - 1st July 2022. Konferenzbeiträge/Atti/Proceedings (pp. 69–76). bu, press - Bozen-Bolzano University Press. https://doi.org/10.34726/3864

Pont, U., Schuss, M., Wölzl, M., Schober, P., Hauer, K., Haberl, J., Lux, Ch. 2023b. Vakuumglas-Kastenfenster: Performance-Monitoring in Sanierungsprojekten; Berichte aus Energie- und Umweltforschung 29/2023; available via https://nachhaltigwirtschaften.at/resources/sdz_pdf/schriftenreihe-2023-29-vamos.pdf (checked in December 2023)

Pont, U., Schober, K. P., Wölzl, M., & Schuß, M. W. 2023c). Vakuumglasintegration in Bestands- und Neufenster. In Nabil. A. Fouad (Ed.), Bauphysik-Kalender 2023. Ernst & Sohn,

VGLASS. 2024. V-Glass – Vacuum Insulating Glass; available via https://www.vg12.com/ (checked in December 2023)

Zoller, A. 1913. Hohle Glasscheibe. Patent-Nummer: No 387655

BauSIM 2024 in Wien
23. September – 26. September

A transient simulation-based approach for in-situ estimation of U-values using artificial neural networks

Alexander Benz[1], Kay Smarsly[2] und Conrad Voelker[1]

[1]*Bauhaus-Universität Weimar, Germany, alexander.benz@uni-weimar.de, conrad.voelker@uni-weimar.de*

[2]*Hamburg University of Technology, Germany, kay.smarsly@tuhh.de*

Abstract

The U-value is the most important criterion for evaluating the quality of thermal envelopes. However, reliable estimations of in-situ U-values are still subject to current research activities. This paper presents the application of artificial neural networks (ANNs) for estimating U-values using synthetic input data derived from transient building element simulations. Building elements, represented in established building typologies, are modeled using finite volume methods. The boundary conditions as well as the thermal impacts induced by internal and external climate are modeled with a transient behavior. The results of the aforementioned simulations, in particular internal and external surface temperatures as well as heat flux density, serve as inputs for the ANNs. The authors study different ANNs, including the hyperparameters and training strategies, focusing on the performance of predicting U-values. Finally, the proposed method is applied to in-situ measurements.

Introduction

The state of the art for in-situ measurement of U-values is comprehensively described in *ISO 9869-1* (2014) referencing to the heat flow meter method (HFM-method). However, the HFM-method requires a stationary state of the investigated component as a basic prerequisite. Due to transient environmental influences and occupant behaviors such stationary conditions are rarely met during in-situ measurements. The average method, proposed within *ISO 9869-1* (2014), assumes that despite these influences a reliable estimation of the U-value can be obtained by averaging over a long period of time. In reality this period of data acquisition and analysis may vary based on the type of wall (light constructions with a specific heat capacity of $< 20\,\mathrm{kJ/(m^2K)}$ or heavy constructions with $> 20\,\mathrm{kJ/(m^2K)}$) and should cover a minimum period of 72 hours (*ISO 9869-1* (2014)). Significantly longer measurement periods of up to two weeks are reported by Rasooli et al. (2016). In addition to these long periods of averaging, results are usually connected with significant deviations, ranging up to 20 % (Gaspar et al. (2016), An-Heleen & Staf (2016)). Additional impacts, such as moisture or degradation of materials, are documented to further influence the U-value obtained from in-situ measurements (Litti et al. (2015)). To reduce the period of testing and to improve the result of in-situ investigations, alternative methods should be applied. With the ability to conduct non-linear regressions, ANNs can quantify the transient behavior of building elements during in-situ investigations. Hence, significant improvement is expected when applying ANNs for the analyzes of in-situ measurements.

Previous studies, working on the application of ANNs in the context of in-situ measurements, primarily focused on using measured data originating from previous in-situ investigations (Bienvenido-Huertas, Moyano, Rodríguez-Jiménez & Marín (2019)). Relying on this type of input data requires cumbersome measurements over long periods of time, leading to a significant workload. Hence, Bienvenido-Huertas, Rubio-Bellido, Pérez-Ordóñez & Moyano (2019) used simulated training and test data to predict U-values. However, in both approaches the trained Multi-Layer Perceptrons (MLPs) directly refer to the U-value thus not only accounting on the transient heat storage effects but also at transient heat transfer (occurring at the external as well as on the internal surface). Hence, the U-value predicted using these proposed methods contain a systematical error when compared to tabulated U-values or standardized computation methods, as both rely on standardized and con-

stant heat transfer coefficients. Furthermore, the method published in Bienvenido-Huertas, Rubio-Bellido, Pérez-Ordóñez & Moyano (2019) was not validated against in-situ measurements, thus the performance of this method remains unclear. This paper is addressing the previously described inaccuracies, incorporated in the predictions, by predicting an intermediate value which is subsequently used for computing the U-value. Therefore synthetic training data are used. In contrast to previous work of other authors, this paper includes a test on real world measurement data, showing the potentials and limitations of current research activities.

Methodology

Within this study MLPs are trained following a supervised training process. MLPs consist of a sequence of layers (input- and output-layer and at least one hidden-layer), each containing at least one neuron. The inter-neuronal connections between two layers can be quantified by so called weights. Finding the optimal weights is the central aspect during the training procedure. As shown in Figure 1, the methodological approach of this study is a supervised learning process.

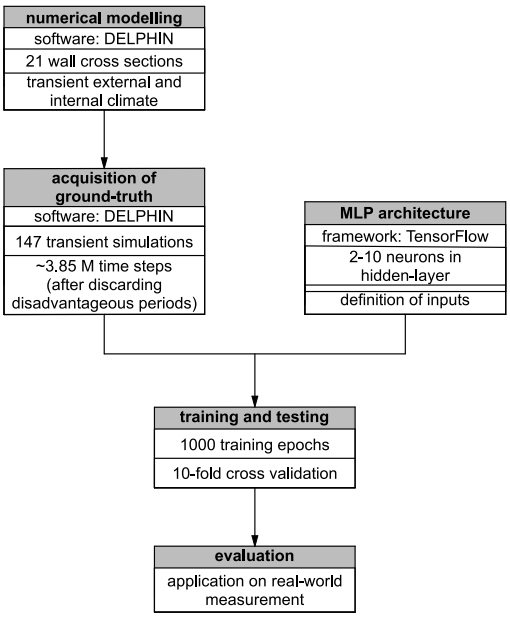

Figure 1: Workflow for modeling and simulating of building elements and subsequent optimization and testing of MLPs

Modeling of building elements and designing the general architecture of MLPs define the initial steps of the workflow. Transient simulations (two year simulations within the software DELPHIN Grunewald & Nicolai (2024)) are linked to the modeled building elements. DELPHIN is a software for the calculation of the transient hygro-thermal behavior of constructions, using finite volume method. The software was developed at TU Dresden and allows for the computation of 2d as well as 3d constructions using efficient computational algorithms Grunewald & Nicolai (2024). The outputs of DELPHIN (e.g., temperatures and heat fluxes) are used as training inputs for the MLPs. Hence, the proposed methodology can be applied on alternative simulation software which compute the required training inputs. For simulations, all constructions are cross-combined with seven climate datasets, resulting in 147 different time series. Forwarding only the second year of the two year simulations to the training datasets ensures an independence from the initial temperature state. Therefore, each time series contains 52,560 time steps with a temporal resolution of 10 minutes (8760 h with 6 increments per simulated hour). For enhancing the quality of input-data, i.e. focusing on favorable time series in the context of U-value estimation (high temperature gradients), each time series is filtered. Filtering consists of discarding potentially disadvantageous conditions and focusing on potentially cold external climates. Hence, the first three and the last three months of each time series for creating the ground truth are used for further investigations. A ground truth with a total amount of approximately 3.85 million different states (26,208 time steps per simulation) is obtained. Each transient state is described by the external and internal surface temperature (Θ_{se} and Θ_{si}) as well as the heat flux density on the internal surface (q_{si}). Feature engineering is applied to enhance the available input data, this includes computing mean values in the intervals of 24 hours and 12 hours for each time series. This concludes the acquisition of a ground-truth in the range of $R_{target,MLP} = 0.27 - 7.52\,(m^2K)/W$ (respectively $U_{target,MLP} = 0.13 - 2.27\,W/(m^2K)$). Training, validation and testing are subsequently conducted on the designed MLPs. The supervised training routine in this study consists of a validation process, implemented as a 10-fold cross validation. Hence, approximately 3.5 million transient states are used during each training loop whereas the remaining 0.35 million states are used during validation. The optimal MLP-configuration is used for further evaluation on real-world measurement data.

Transient simulations

The ground truth required for training and testing the MLPs is created by conducting transient simulations of external wall models. Respective wall geometries are modeled as cross-sections according to descriptions of typical elements given in Loga et al. (2015), Böhmer et al. (2010). Corresponding material properties, documented in IBP (2024), are assigned to the corresponding layers in the model (material density ρ, thermal conductivity λ, heat storage capacity c_p). The overall heat transfer is separated into a convective and radiative heat transfer. The external convective heat transfer h_{ce}, given as $h_{ce} = 4 + 4v$, is modeled using the wind speed v (in $\frac{m}{s}$) present at the investigated structure. The external radiation heat transfer considers the long and short wave radiation. Within the long wave radiation a constant emissivity of $\epsilon = 0.9$ is implemented for all surfaces in order for the simulation to take into account the atmospheric reflection (given by the corresponding climate file). The short wave radiation is computed using an absorption coefficient of $\alpha = 0.6$. Further parameters required to compute the heat transfer are taken from the respective climate file (German Test Reference Year (TRY)). The climate data in the TRY are given in steps of one hour. To meet the interval of 10 minutes applied for in-situ measurements and to enhance the quantity of training data obtained from simulations, the hourly values are applied as boundary conditions in a 10 minute resolution using linear interpolation. This interval of 10 minutes is commonly used for obtaining in-situ data during measurements Bienvenido-Huertas, Moyano, Rodríguez-Jiménez & Marín (2019).
The internal heat transfer is modeled based on *DIN 6946* (2018) as a combination of radiation and convection being $h_i = 7.69 W/(m^2K)$.

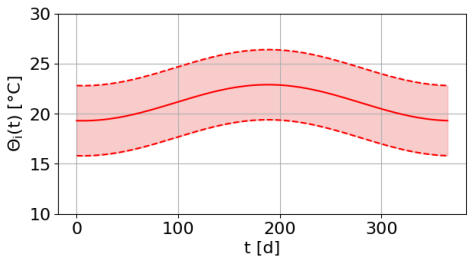

Figure 2: Interior air temperature ($\Theta_i(t)$) for the use case of a living room with respective variation boundaries (dashed lines), based on Hofmann et al. (2022)

$\Theta_i(t)$ is implemented, using a regression model developed by Hofmann et al. (2022) based on empirical measurements. To enhance the variance for the simulations and eventually the input combinations for the MLPs, values for Θ_i are randomly chosen within the variation boundaries, given by Hofmann et al. (2022) and displayed in Figure 2. The simulation outputs (Θ_{si}, Θ_{se} and q_{si}) were obtained in 10 minute intervals, following the resolution of the boundary conditions. A subsequent filter yields 26,208 different states per simulation as input data for the MLPs.

In-situ measurements

A final evaluation of the proposed methodology is conducted using real input data obtained during in-situ measurements. These measurements were conducted at a north-facing facade (with two measurement positions, shown in Figure 3) during 22.12.2016-03.02.2017 at the campus of Bauhaus-Universität Weimar. The investigated structure is a monolithic wall with a thickness of $d_{P1} = 0.45\,m$ at P1 and $d_{P2} = 0.35\,m$ at P2 respectively.

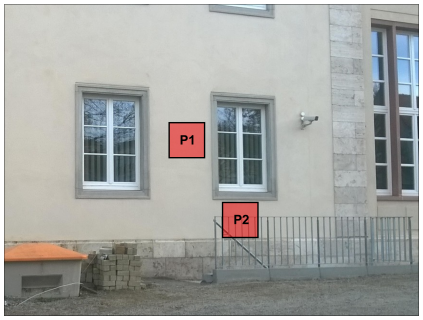

Figure 3: Positions P1 and P2 for in-situ measurements

Based on documents and tabulated material properties, the corresponding U-values (computed following *DIN 6946* (2018)) can be given as intervals of $U_{P1,DIN6946} = 1.01 - 1.45\,W/(m^2K)$ and $U_{P2,DIN6946} = 1.20 - 1.79\,W/(m^2K)$. To compute the R-value based on measured data, the average method for heat flux measurements, as described in *ISO 9869-1* (2014), was chosen (Equation 1). Hence, a heat flux sensor in combination with two temperature sensors (external and internal surface) were installed on the surfaces of the investigated structure. The R-value is subsequently used for calculating a standardized U-value following Equation 2 applying the values of $R_{si} = 0,13\,W/(m^2K)$ and $R_{se} = 0,04\,W/(m^2K)$ respectively.

$$R = \frac{\sum_{j=1}^{n} q_j}{\sum_{j=1}^{n} (\Theta_{si,j} - \Theta_{se,j})} \quad (1)$$

$$U = \frac{1}{R_{si} + R + R_{se}} \quad (2)$$

The accuracy ranges of the applied sensors are given in Table 1. The data acquisition interval was one minute. All measured values were subsequently averaged over a period of 10 minutes. A convective heater in the room was constantly active during the measurement, favoring a constant indoor air temperature and heat flux through the investigated walls. Potential influences imposed in the form of radiation or convection from this heating devices are reduced by a styrofoam shield next to the sensors.

Table 1: Accuracy ranges of the applied sensors

Sensor	**Accuracy**
temperature sensor	$\pm 2.5K$
heat flux sensor	$\pm 0.05 \cdot c(\Theta)$
with $c(\Theta) = 12.13\frac{W}{m^2K} - 14.19 \cdot 10^{-3}\frac{W}{m^2K^2}(\Theta - 23°C)$	

Parameter study

The MLPs within this parameter study consist of three layers (one hidden-layer), investigates the performance of the MLPs depending on the number of neurons in the hidden-layer. The TensorFlow library (Abadi & et al. (2016)) is used for designing the MLP-configuration and implementing the training routine. The optimal MLP-configuration is found by conducting a parameter study, in which the number of neurons in the hidden-layer is varied. The mean squared error (MSE) is used as a loss-function. For a full validation during the training, a 10-fold cross validation is applied, from which the mean values (over all folds) of MSE, MAE (mean absolute error), RMSE (root mean squared error) as well as R^2 are computed as evaluation metrics. For comparison, U-values ($U_{ISO9869}$) using the average method are calculated along with the predictions made by MLPs. This method is standardized and well documented in *ISO 9869-1* (2014).

The conducted parameter study investigates the performance of the MLPs depending on the number of neurons in the hidden-layer. Based on pre-studies, the following hyperparameters were chosen: learning rate of 0.01, stochastic gradient descent as optimizer, momentum = 0.1, L2-regularization = $2 \cdot 10^{-5}$. MLP01 is designed with an input-layer of seven neurons, whereas MLP02 contains 10 neurons in the input-layer. The three additional neurons in MLP02 are a result of feature engineering, which further computes a 12 hours mean values (see Table 2). The output is fixed to one single value (target), representing the predicted thermal resistance (R_{MLP}).

Table 2: Inputs for the MLPs

Variable	**Definition**
d	Thickness of the external wall [m]
Θ_{si}	Internal surface temperature [°C]
Θ_{se}	External surface temperature [°C]
q_{si}	Internal heat flux density [W/(m^2)]
$\overline{\Theta}_{si,24}$	Mean internal surface temperature over a period of 24 h [°C]
$\overline{\Theta}_{se,24}$	Mean external surface temperature over a period of 24 h [°C]
$\overline{q}_{si,24}$	Mean heat flux density at internal surface over a period of 24 h $[W/(m^2)]$
$\overline{\Theta}_{si,12}$	Mean internal surface temperature over a period of 12 h [°C]
$\overline{\Theta}_{se,12}$	Mean external surface temperature over a period of 12 h [°C]
$\overline{q}_{si,12}$	Mean heat flux density at internal surface over a period of 12 h [W/(m^2)]

Figures 4 and 5 visualize the training and validation performance after 100 epochs of training as mean values of R^2 and MSE depending on the number of neurons in the hidden-layer. Whereas MSE is intended to be minimized during the training process, R^2 represents the goodness of fit and should be close to 1. A more interpretable metric is given by MAE which uniformly weights the error and can be directly understood as the under- or overestimation of the R-value. In contrast to this metric, MSE has a higher sensitivity for values further off the correct target value.

Figure 4 (a) refers to MSE and R^2 of MLP01. The results proof, that already a small MLP of three neurons is able to perform a similar regression as models with six to eight neurons in the hidden-layer. The MSE slightly peaks at four neurons and starts to increase after reaching a minimum between six

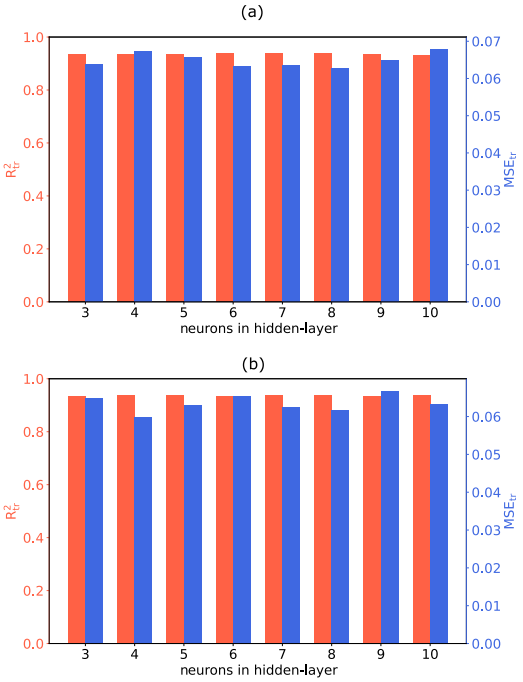

Figure 4: Performance of MLP01 (a) and MLP02 (b) depending on the number of neurons in the hidden-layer

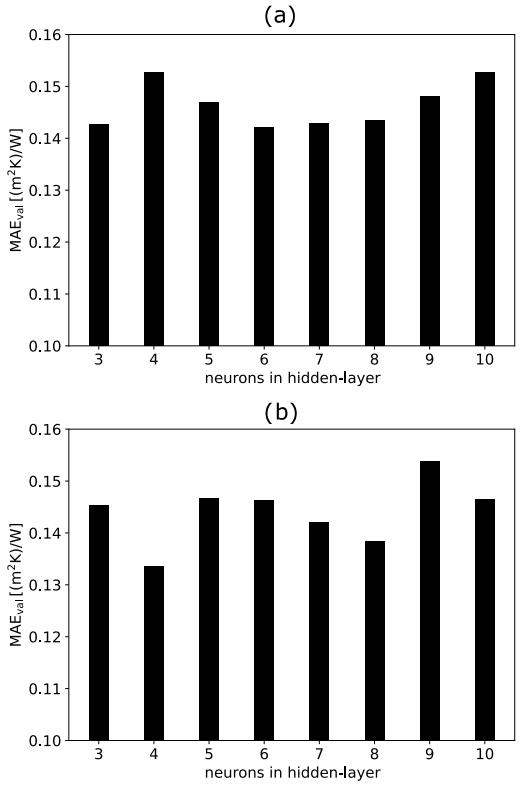

Figure 5: MAE of MLP01 for validation (a) and MAE for MLP02 for validation (b), depending on the number of neurons in the hidden-layer

to eight neurons in the hidden-layer. In contrast, R^2 tends to remain constant throughout the parameter study. A more interpretable metric is given by MAE on the validation dataset in Figure 5 (a). This metric can directly be translated into the absolute error made in the prediction by the MLPs. The minimum MAE is obtained for six neurons. Hence, a configuration of 7-6-1 is chosen as the optimized MLP01. Figure 4 (b) refers to MSE and R^2 of MLP02. The results show, a minimal MSE is obtained for four neurons. An increase of MSE can be observed for six and nine neurons, whereas R^2 remains practically constant for the investigated configurations. Similar to MLP01, the MAE on the validation dataset is given in Figure 5 (b). The minimum MAE is obtained with four neurons. Hence, a configuration of 10-4-1 is chosen as the optimized MLP02.

Results

Based on the previous parameter study, the MLP-configurations with the best average performance are chosen for a more comprehensive analysis (MLP01 with 7-6-1 configuration and MLP02 with 10-4-1 configuration). Therefore, the performance during training and validation is investigated. Subsequently, the results on the three independent test datasets as well as on the in-situ measured data are presented. For a full understanding of the MLP, the initially introduced metrics (MSE, MAE, RMSE, R^2) are utilized for describing the performance.

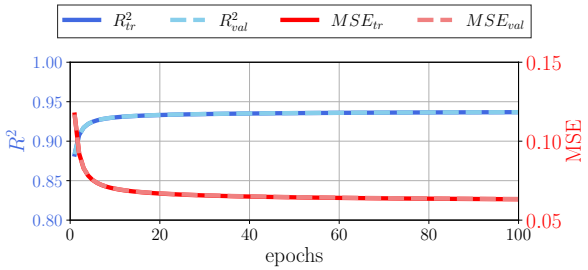

Figure 6: Evolution of regression performance during training of MLP01

For both MLP-configurations (MLP01 and MLP02), R^2 and MSE show a convergence tows a common threshold for training and validation performance (approximately 0.94 for R^2 and 0.065 for MSE respectively). Hence, an overfitting on the training data is minimized. One sign of a potential overfitting would be a divergence of the training and validation performance.

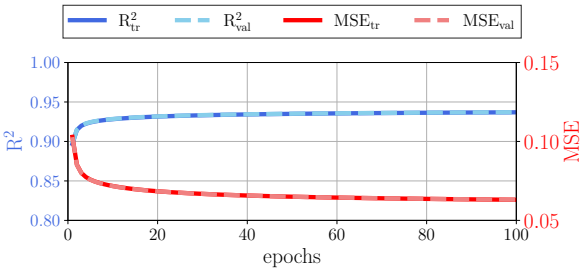

Figure 7: Evolution of regression performance during training of MLP02

Visualizing the MLP-predictions on a fully independent test dataset (Figures 8 to 10) presents a comprehensive insight on the evolution of the performances. U_{MLP01} is computed utilizing the predictions for R_{MLP01}, using the tabulated heat transfer coefficients for a vertical wall given in *DIN 6946* (2018). U_{MLP02} is computed accordingly based on R_{MLP02}. For reference, the results obtained by the standardized average method ($U_{ISO9869}$), are also shown in these Figures. As the standardized computation of $R_{ISO9869}$ is comprehensively described in *ISO 9869-1* (2014), no further information regarding this calculation is given. Referring to the single predictions, shown in Figures 8(a) to 10(a), MLPs present a significantly lower oscillation around the target values than the reference method. This indicates a well developed ability to make predictions close to the true value for given input values. As a consequence of these minimal oscillations, the mean values over time (Figures 8(b) to 10(b)) present a convergence to the reference values $U_{target,MLP}$. In contrast to the predicted U-values, the conventionally computed U-values show a stronger oscillation in the single values (Figures 8(a) to 10(a). For test cases 1 and 2, these oscillations result in a relatively long period for convergence with an offset of approximately $0.2\,W/(m^2K)$ after three days measurement. For test case 3, no convergences was observed, as the mean value steadily steadily declines after the first day of measurement. To summarize the performance on the test cases, the MLP predictions converge faster to the reference values and show no significant deviation after three days of measurement. In test cases 1 and 2, the convergence is practically present within the first day of measurement. However, in test case 3, the mean value over time shows a significant decline during this first day of measurement. A potential explanation could be, that the MLPs are specialized on higher U-values ($> 1.00\,W/(m^2K)$). Thus, making predictions on lower U-values more inaccurate. An enhanced ground truth can be beneficial for more accurate predictions for these lower U-values.

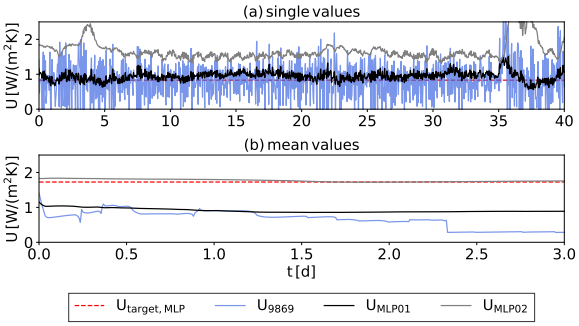

Figure 8: Performance of MLPs on test case 1

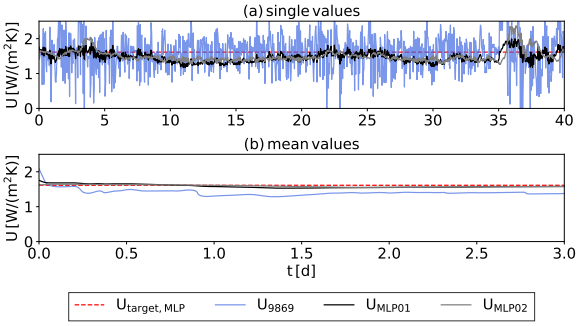

Figure 9: Performance of MLPs on test case 2

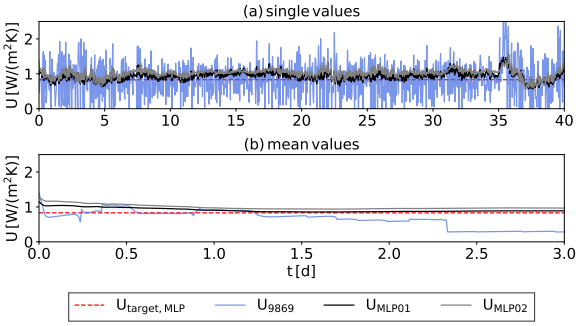

Figure 10: Performance of MLPs on test case 3

A final test of the proposed methodology is performed by applying the MLPs on a dataset obtained through in-situ measurements (the measurement setup is briefly described in the methodology of this paper). Figures 11 and 12 show the U-values predicted by MLP01 and MLP02 as single values (Fig-

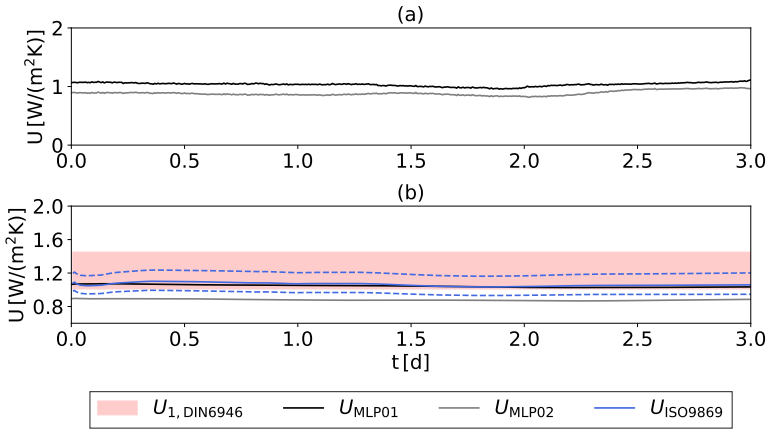

Figure 11: Performance on evaluation data of MLP01

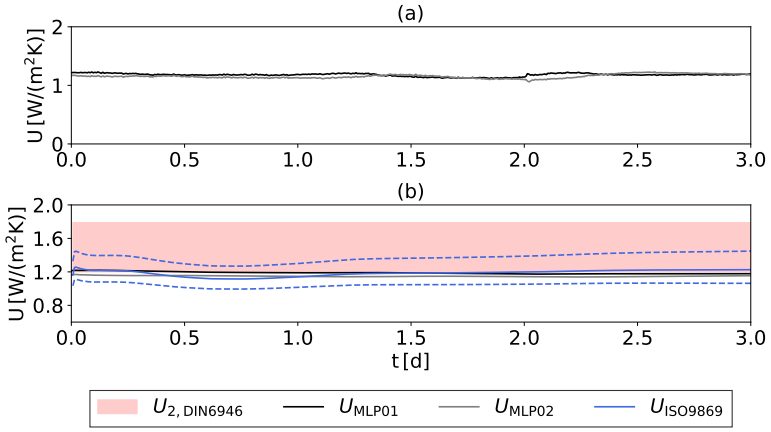

Figure 12: Performance on evaluation data of MLP02

ures 11(a) and 12(a)) and as mean values (Figures 11(b) and 12(b)). For minimizing effects from sensor installation and heating of the room, the first three days of measurement are discarded and a period of the three subsequent days is presented. This minimal measurement period is required by *ISO 9869-1* (2014). The mean values computed by the average method in *ISO 9869-1* (2014) are given with the margins of error. These margins are obtained from the inaccuracies of the measurement devices (given in Table 1 and computed using the propagation of error. The intervals of the theoretical U-values ($U_{1,DIN6946}$ and $U_{2,DIN6946}$), obtained from documents, are also presented in Figures 11 and 12. For both positions, the single MLP-predictions (Figures 11(a) and 12(a)) show stable predictions with a relatively low oscillation. At P1, the prediction of MLP01 is inside the range of $U_{1,DIN6946}$ throughout the entire period. Additionally the MLP01 predictions are confirmed by the long term mean value of $U_{ISO9869}$. MLP02 however, seems to underestimate the U-value at P1. At P2, the predictions by the MLPs are almost similar to the long term mean value of $U_{ISO9869}$. Both MLP predictions show again a very stable prediction. However, all values are at the minimal value of the theoretical range of $U_{2,DIN6946}$.

Conclusions

The paper explores the effectiveness of ANNs in estimating U-values, utilizing MLPs with various configurations for implementation. The empirical foundation of this has been a relatively limited dataset comprising 147 time series, derived from transient thermal simulations of 21 constructions

under 7 climate scenarios, and conducted using DELPHIN software. The analysis has revealed that even MLPs with modest configurations, specifically those with a single hidden layer and a few neurons, can accurately predict the R-values of external walls. Validation tests on a dataset have displayed an MAE of roughly 0.14 $(m^2K)/W$. This level of accuracy, although promising, indicates a significant risk of incorrect predictions due to the MAE influence on the U-value computations. Applying the the models to in-situ measurements, the predictions from MLP01, utilizing 24-hour mean values, has aligned with theoretical values derived from documentation. Further evaluation with real-world data collected from in-situ measurements has presented encouraging outcomes. The MLP predictions have remained consistent throughout the measurement period and aligned with the long-term mean values calculated using the *ISO 9869-1* (2014) average method. It is worth mentioning, however, that the in-situ measurements have been performed under optimal conditions, without room usage, with constant heating, and on a north-facing wall, which may not fully challenge the capabilities of the MLP, as corroborated by minor discrepancies observed between the average method and MLP predictions. Given aforementioned constraints, along with potential inaccuracies stemming from unknown material properties and environmental impacts, further laboratory measurements may be devised, aiming to cover a broader range of conditions to validate the effectiveness of the MLPs comprehensively. The insights gained in this study will also guide the enhancement of the dataset used for training and encourage exploration of alternative ANN models, such as recurrent neural networks, to potentially improve prediction accuracy and reliability.

Acknowledgments

We gratefully thank Technical University Dresden for providing us a test license of the software DELPHIN.

References

Abadi, M. & et al. (2016), 'Tensorflow: A system for large-scale machine learning', *Proceedings of the 12th USENIX Symposium on Operating Systems Design and Implementation* p. 265–283.

An-Heleen, D. & Staf, R. (2016), 'Comparison of characterisation methods determining the thermal resistance of building components from onsite measurements', *Energy and Buildings* **130**, 309–320.

Bienvenido-Huertas, D., Moyano, J., Rodríguez-Jiménez, C. E. & Marín, D. (2019), 'Applying an artificial neural network to assess thermal transmittance in walls by means of the thermometric method', *Energy and Buildings* **233–234**, 1–14.

Bienvenido-Huertas, D., Rubio-Bellido, C., Pérez-Ordóñez, J. L. & Moyano, J. (2019), 'Optimizing the evaluation of thermal transmittance with the thermometric method using multilayer perceptrons', *Energy and Buildings* **198**, 395–411.

Böhmer, H., Fanslau-Görlitz, D. & Zedler, J. (2010), U-Werte alter Bauteile, Technical report, Institut für Bauforschung e.V., Stuttgart Deutschland.

DIN 6946 (2018), Technical report, Deutsches Institut für Normung, Berlin, Deutschland.

Gaspar, K., Casals, M. & Gangolells, M. (2016), 'A comparison of standardized calculation methods for in situ measurements of façades u-value', *Energy and Buildings* **130**, 592–599.

Grunewald, J. & Nicolai, A. (2024), DELPHIN 6.1.6, Technische Universität Dresden, Technical report, Technische Universität Dresden, Germany.

Hofmann, M., Geyer, C. & Kornadt, O. (2022), 'Dependencies of the indoor climate on the course of the seasons and derivation of regressions from long-term measurements', *Indoor Air* **32**, e13058.

IBP (2024), MASEA - Materialdatensammlung für die energetische Altbausanierung, Technical report, Fraunhofer-Institut für Bauphysik IBP.

ISO 9869-1 (2014), Technical report, International Organization for Standardization, Geneva, Switzerland.

Litti, G., Khoshdel, S., Audenaert, A. & Braet, J. (2015), 'Hygrothermal performance evaluation of traditional brick masonry in historic buildings', *Energy and Buildings* **105**, 393–411.

Loga, T., Stein, B., Diefenbach, N. & Born, R. (2015), Deutsche Wohngebäudetypologie, Technical report, Institut Wohnen und Umwelt, Darmstadt Deutschland.

Rasooli, A., Itard, L. & Ferreira, C. I. (2016), 'A response factor-based method for the rapid in-situ determination of wall's thermal resistance in existing buildings', *Energy and Buildings* **119**, 51–61.

BauSIM 2024 in Wien
23. September – 26. September

Comparison of detailed large-scale Thermal Energy Storage simulation models

Alice Tosatto[1], Fabian Ochs[1]
1 Unit of Energy Efficient Building, Universität Innsbruck, Austria, E-Mail:
alice.tosatto@uibk.ac.at
fabian.ochs@uibk.ac.at

Abstract

Numerical modelling of large-scale thermal energy storage (TES) systems plays a fundamental role in their planning, design and integration into energy systems, i.e., district heating networks. This work presents a comparison of the implementation of numerical models of buried TES in Matlab and Comsol. Both tools allow the modelling of the surrounding ground with the finite-element method, while the water domain is modelled one-dimensionally. The Comsol model allows a high level of detail and flexibility and is recommended for TES optimization in a system context. The Matlab model, on the other hand, is more simplified with a focus on fast system simulations. The models are compared in terms of energy flows, temperature stratification and simulation performance. Different TES geometries are investigated, i.e., tank and pit with various slopes, different envelope qualities (i.e., insulation) are considered. In terms of energy flows, the two models are in good agreement, however, deviations in the thermal stratification are found between the two modelling approaches.

Introduction

In order to increase the penetration of renewables in the energy system, energy storage systems are a key element to bridge the energy gap between supply and demand, both on the short- and on the long-term period. In district heating (DH) systems, large-scale thermal energy storage (TES) is an emerging technology, which has seen a significant expansion in the last years (Bolton et al., 2023). The high investment costs and their key role in increasing the flexibility, redundancy and stability of the energy system require reliable tools that are able to depict their operation, both on a system level and on a detailed component level.

As mentioned by Ochs et al. (2022), given the complexity of the TES, both on an individual and a system level, quite a number of different numerical models and simulation tools have been implemented to study and optimize the characteristics of TES and DH systems with TES. These tools can be categorized into energy system simulation tools, and detailed tools enabling detailed heat and also mass transfer modelling. Both categories are fundamental in the design phases of the TES system. An overview of different tools is presented in Table 1. There is some overlap in the tools, e.g., in TRNSYS and Modelica more detailed TES models have been implemented recently (Gauthier, 2020; Reisenbichler et al., 2022) and simplified system simulations have been proven in Comsol (Tosatto et al., 2023).

Table 1 Categorisation of TES models.

Software / Tool	Modelling Target
Energy system level	
Modelica/Dymola[1], TRNSYS[2], MATLAB/Simulink[3]	• System modelling • Interactions between TES and DH system components
Detailed component level	
COMSOL Multiphysics[4], CFD softwares[5]	• Design of TES geometry and envelope elements • Details of injection /extraction elements • Stratification • Ground water flow

[1](Reisenbichler et al., 2022), [2](Gauthier, 2020), [3](Ochs, 2014), [4](Dahash et al., 2020), [5] (Xiang, Xie, et al., 2022)

Within the TRNSYS simulation environment there exist several models widely employed in the praxis. In these coarse structure models, the flow inside the TES is considered as 1D (finite difference (FD) or plug flow).

For modelling of large-scale TES two so-called non-standard types have been available in TRNSYS already since more than 20 years: the

XST-model (type 342) (Mazzarella, 1994) and the ICEPIT-model (type 343) (Hornberger, 1998). The XST-model allows to simulate cylindrical water tanks. In contrast, the ICEPIT model was developed for gravel-water pit TES but it is possible to consider water as storage medium, too. The ICEPIT-model allows simulating cylindrical geometries and truncated cones, which is one of the advantages compared to the XST-model. Both models use the FD approach for modelling the heat conduction in the ground. The models have been validated against measured data and compared against each other. They deliver comparable results (Ochs, 2009), but are both not flexible enough with respect to geometry.

A very flexible model is the multiport-store-model (MST, type 340). However, it can only be applied for free-standing cylindrical thermal energy stores. In (Steinweg et al., 2011) the type 340 has been coupled with a FD model to account for heat conduction in the surrounding ground.

More recently, a 3D model for TES (type 1322) in TRNSYS has been developed by TESS and is able to model the pyramid stump shape. In case of truncated cone shapes, type 1300 (coupled with type 1301, that models the surrounding soil and the insulation layer above the TES) can be employed (Gauthier, 2020). More recently, type 1535 was implemented from type 1300 and it includes an immersed heat exchanger in the interior (Gao et al., 2024).

In Matlab/Simulink environment, a TES model has been implemented by Ochs (2015). This model is versatile in terms of geometry, allowing to change the TES slope (between cylindrical tank and shallow pit) and to couple a 2D finite element (FE) model of the surrounding soil.

In Modelica/Dymola, several TES models are available in Modelica-based libraries. A TES model developed upon the existing storage model from the Modelica Buildings library was used to simulate seasonal TES and compared against measured data from the pit TES in Dronninglund (Reisenbichler et al., 2022).

In Comsol Multiphysics environment, Dahash et al. (2020) implemented a detailed FE model of the TES and the surrounding ground validated against measured data of the Dronninglund TES. The FE discretisation enables a flexible definition of the TES geometry both in 2D and 3D, and allows the modelling of hybrid (cylinder-cone) TES shapes. Moreover, the possibility to include and couple multiphysics equations allows to include in the analysis the groundwater (Dahash, Ochs, Giuliani, et al., 2021). System-level aspects can be included with equation-based models of other components (e.g., heat pumps), as implemented by Tosatto et al. (2023).

The previously mentioned models were cross-validated against each-other considering their energy flows, temperatures and stratification within the gigaTES project (Ochs et al., 2022). Further work within the IEA ES Task 39 extended the model comparison to establish a clear methodology for new models (IEA, 2024).

Additionally, Luo et al. (2023) implemented a semi-analytical model of a buried TES coupled with the surrounding ground using Python language, which was cross-validated against the COMSOL-based TES model.

A detailed CFD model of the water domain of a pit TES including the surrounding soil was developed and validated against measured data of the Dronninglund TES by Xiang, Gao, et al. (2022). Aim of the study was the investigation of the thermal stratification characteristics, but due to the required computational effort, water and solid domain were validated separately and for the water domain four representative cases within the operational period were selected.

Scope of the work

Scope of this paper is the detailed comparison of two different numerical models of buried large-scale water-based TES. The two models are implemented in the Matlab and Comsol Multiphysics environments: both tools allow the modelling of the surrounding ground with the FE method, while the water domain is modelled one-dimensionally using partial differential equations (PDE). The Comsol model allows a very detailed depiction of the TES (in terms of geometry) with a simplified consideration of the energy system, while the Matlab model is simplified in terms of geometry with a focus on a fast modelling of a complex energy system (also in Matlab/Simulink). In the next section an overview of the implementation of the two models is presented and differences in the numerical methods are highlighted. The influence of TES aspect ratio (ratio between height and diameter) and slope of the sidewalls on the energy balance and thermal stratification has been highlighted by many authors (Dahash, Ochs, & Tosatto, 2021), and will therefore be part of the analysis.

Different TES geometries (cylindrical tanks with different heights and pits with different slopes) are modelled in both environments and compared. Through the analysis of the energy flows (charging, discharging, thermal losses) and of the thermal stratification, the difference between the two models is investigated and discussed. The aim is to compare the ability of

the two models to depict the TES operation and to highlight deviations between the two models also in terms of simulation time.

Simulation

MATLAB

Fluid domain

The fluid domain is represented by a one-dimensional FD approach with N elements (Ochs, 2015). Exemplarily the differential equation is shown for element i (applies for *1< i <N)* (Fig. 1)*:*

$$V\rho c_p \frac{\partial \vartheta}{\partial t} = \dot{m} c_p (\vartheta_{i-1} - \vartheta_i) + U_i A_{S,i} (\vartheta_{s,i} - \vartheta_i) + \frac{\lambda_{eff,top}}{h_{top}} A_{i-1} (\vartheta_{i-1} - \vartheta_i) + \frac{\lambda_{eff,bottom}}{h_{bottom}} A_{i+1} (\vartheta_{i+1} - \vartheta_i) \quad (1)$$

Here ϑ is the temperature and V is the volume of the segment *i*, ρ the density and c_p the specific heat capacity of the fluid, $\dot{m}$ the (dis-) charging mass flow, *U* the (overall) heat transfer coefficient of the envelope, A_s the mantle area of the segment *i*, *h* the segment height and *A* the segment cross section area. In case of cones the segments are divided such that they possess equal volume (hence the height of the segments is increasing with depth). λ_{eff} is the effective thermal conductivity of the storage medium which is enhanced in case of inverse thermocline.

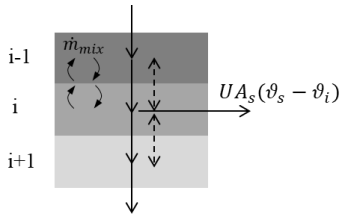

Figure 1 *Schematic representation of three storage segments (i-1, i. i+1) with energy fluxes* (Ochs, 2014)*.*

In standard operation of the TES (charging/discharging) a thermocline will develop in the TES. The combined effect of thermal diffusion, heat loss via the TES cover, walls and bottom and inlet flow induced mixing leads to degradation of the thermocline over time. An inversed thermocline will not occur in reality if the TES is operated appropriately (i.e., charged from top to bottom and discharged from bottom to top) due to buoyancy. In the simulation, in case of standstill (i.e., no charging/discharging) without mixing algorithms an inversed thermocline would occur in particular due to the relatively high heat losses of the top segment (to the top and to the wall).

There are several approaches to model the mixing of the storage water to avoid the occurrence of an inversed thermocline. Simple approaches consider mixing of adjacent elements with inverse thermocline. More complex approaches include buoyancy driven flow. However, these can be quite simulation time consuming.

In this model, the effective thermal conductivity of the storage medium is increased in case of inversed thermoclines acc. to Eq. 2.

$$\lambda_{eff,top} = \lambda_{eff,0} + \lambda_{eff,mix,top} \cdot \left((\vartheta_{i-1} - \vartheta_i) < 0\right) \quad (2)$$

$$\lambda_{eff,bottom} = \lambda_{eff,0} + \lambda_{eff,mix,bottom} \cdot ((\vartheta_{i+1} - \vartheta_i) > 0)$$

The mixing effective thermal conductivity is calculated using a power law approach:

$$\lambda_{eff,mix,top/bottom} = C \cdot \Delta\vartheta^n \quad (3)$$

Solid domain

For complex geometries the FE method is chosen. Matlab provides functions and interactive tools, such as the PDETOOL, to solve these problems. Parabolic PDEs can be solved with the PDETOOL using the form

$$d \cdot \frac{\partial u}{\partial t} - div(c \cdot grad(u)) + a \cdot u = f \quad (4)$$

where the coefficients *d*, *c* and *f* are a function of the position *x* and time *t* and are independent from the variable *u*. Applied to heat transfer, Eq. 4 forms to:

$$\rho \cdot c_p \cdot \frac{\partial \vartheta}{\partial t} - div(\lambda \cdot grad(\vartheta)) + a \cdot \vartheta = \dot{q} \quad (5)$$

The temperature ϑ is a function of time t, the spatial coordinates (x, y), and the heat source ($\dot{q}$ or $a \cdot \vartheta$). The required properties of the ground (λ, ρ, c_p) can be a function of the position (x, y). In cylindrical coordinates in 2D the solid domain around a cylindrical or conical storage can be represented by

$$r\rho c_p \frac{\partial \vartheta}{\partial t} - \frac{\partial}{\partial r}\left(r\lambda \frac{\partial}{\partial r}\vartheta\right) - \frac{\partial}{\partial z}\left(\lambda \frac{\partial}{\partial z}\vartheta\right) = \dot{q}r \quad (6)$$

Method of Lines

Using the Method of Lines, (see also (Ochs, 2015)) the PDE can be transformed in an ordinary differential equation (ODE) that can be solved using Matlab or Matlab/Simulink.

$$\frac{d}{dt} = M^{-1}(F + G + R + KU + QU + HU) \quad (7)$$

Here, U is the dependent variable, K is the stiffness matrix, M is the mass matrix, F is the right side vector, Q is for the system matrix and G is the u related term. H and R are zero in case of Neumann BC and nonzero in case of Dirichlet BC.

The system of ODEs resulting from the method of lines (Eq. 7) can be coupled with the system of ODEs for the fluid domain (FD approach, Eq. 1)

and be solved by Matlab (closed system of ODEs). The PDE parameters are updated with time, the integration is performed by a Matlab ODE solver (e.g., ode45 or ode23).

In case of Simulink a Level-2 S-function can be used. In the Block Initialization the states of the PDE are initialized (one state for each node). The update of the derivatives (Method of Lines) is performed in the Derivatives Block. The outputs are the temperatures at the nodes, the fluid outlet temperature (with given inlet temperature and mass flow) or the heat flow (Ochs, 2015).

COMSOL

In COMSOL, both solid and fluid domain are modelled in FE (Dahash, Ochs, & Tosatto, 2021). Comsol offers significant advantages in the meshing: the software allows the user to refine the mesh in specific regions (e.g., the border between the soil and the TES, or the envelope element itself) in order to allow a better resolution where the temperature gradients leading to the heat transfer phenomena are larger, while a coarser mesh can be arranged on the soil layers further from the TES (Fig. 2).

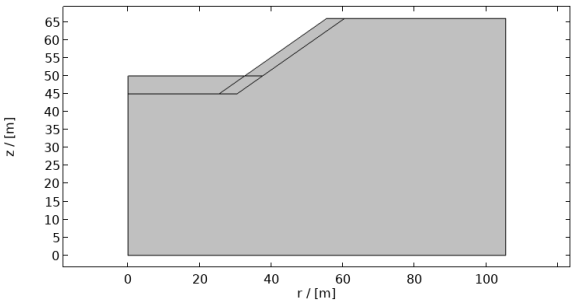

Figure 2 Example of shallow pit TES geometry implementation in COMSOL environment with mesh refinement layers close to the TES.

The fluid domain is modelled as a line source with the coefficient form boundary PDE, and the coupling with the soil can be solved with a closed PDE system, according to Eq. 8.

$$\rho A_i c_p \frac{d\vartheta_i}{dt} = \rho \dot{V} c_p \frac{d\vartheta_i}{dz_i} + A_i \frac{d}{dz_i}\left(\lambda_{eff,mix} \frac{d\vartheta_i}{dz_i}\right) - \dot{q}_{loss,i} \quad (8)$$

A buoyancy sub-model is implemented to increase the local fluid thermal conductivity in presence of inverse thermocline, following Eq. 9.

$$\lambda_{eff,mix} = C \cdot \left(\frac{d\vartheta}{dt}\right)^{0.5} \cdot \left(\frac{d\vartheta}{dz} < 0\right) \quad (9)$$

Neumann boundary conditions to describe the charging/discharging flow (mass flow and temperature) are applied in the inlet/outlet port position, while the thermal losses from the cover and the bottom elements are applied in in the very top and bottom nodes and coupled to the solid domain. The side wall thermal losses to the ground are implemented in the source term (Eq. 8), which enables the direct coupling with the surrounding ground.

The MUMPS solver is used to run the simulations.

TES Model case study

The two TES models are compared considering different geometries based on the case study suggested in IEA ES Annex 39. The geometry characteristics of the different cases are presented in Table 2. In all configurations the TES is fully buried. In all the cases, the cover is assumed insulated with an overall heat transfer coefficient (HTC) of 0.1 W/(m^2·K). Two envelope configurations are investigated for the side and bottom elements: non-insulated (i.e., HTC = 90 W/(m^2·K)) and insulated (i.e., overall HTC = 0.2 W/(m^2·K)). The ground surrounding the TES is also considered in the model with the following properties: thermal conductivity 1.8 W/(m·K), density 2100 kg/m^3, specific heat capacity 1333.3 J/(kg·K).

The different TES geometries are analysed under the same operation conditions (presented in Table 3). The protocol developed within the IEA Task 39 (IEA, 2024) is followed: 5 years of TES operation are simulated, in order to reach a steady state operation after the ground pre-heating in the first years. The results for the last year are then considered for the model comparison in the Results section.

Table 2 Geometry characteristics of the analysed cases (pit and cylindrical tank).

Slope / [°]	H / [m]	D_{top} / [m]	D_{bottom} / [m]	Volume / [m^3]
26.6	16	119.00	55.10	99494.5
30	16	115.24	59.82	99494.5
35	16	110.85	65.15	99494.5
45	16	104.50	72.50	99494.5
60	16	98.06	79.58	99494.5
75	16	93.23	84.66	99494.5
90	16	88.98	88.98	99494.5
90	27	69	69	100960

Table 3 TES operation for one year: inlet/outlet volumetric flow, inlet temperatures during charging and discharging phase (IEA, 2024).

Time start:end / [h]	Phase	$\dot{V}$ / [m^3/h]	T_{in} / [°C]
0:2919	Charge	-30	90
2920:3649	Storage	0	0
3650:6569	Discharge	30	30
3570:8760	Idle	0	0

In both models the water domain is discretized in 50 nodes. The injection and extraction points are located 0.5 m from the top and bottom of the TES. In the COMSOL model, a further refinement closer to the injection and extraction elements is used to improve the numerical resolution.

Several temperature probes are considered in the ground surrounding the storage, both on the side and on the bottom of the TES, see Figure 3.

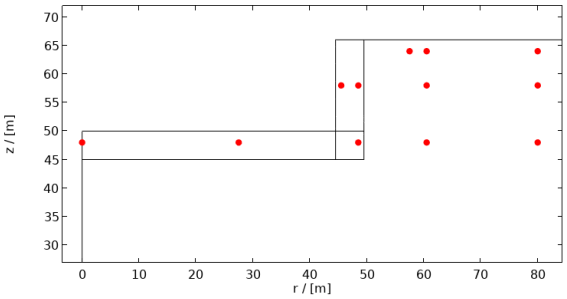

Figure 3 Ground temperature probes (for the example of the 16 m high cylindrical tank TES, Comsol).

Results

The impact of TES slope is investigated in the two models (Matlab and Comsol), which are compared from the point of view of the simulation performance (i.e., closing error, simulation time), charging/discharging energy, thermal losses and temperature stratification.

Figure 4 presents the yearly temperature profile for the last year of operation for the non-insulated and insulated 27 m high cylindrical tank TES. The two models show a good agreement, with divergencies mostly in the charging and discharging phases, in the bottom layers temperatures during the storage phase and in the top layers temperature in the idle phase (standstill).

Figure 5 shows the development of the ground temperatures during the investigated period for the non-insulated pit with 26° slope. Both Matlab and Comsol model present a similar trend but with deviations in the range of few Kelvins in particular in the soil below (Fig. 5, bottom) and next to the bottom of the TES (Fig. 5, top): this is in line with the different water temperatures on the bottom of the TES observed in the two models. The ground discretisation has been investigated (mesh independence test) and it can be concluded that it has no relevant influence on the results (neither on the temperatures nor on the heat flux).

The difference in water temperature between the two models has a direct impact on the charged energy. Figure 6 presents the energy charged, discharged and lost during the fifth year of operation, for the case without insulation.

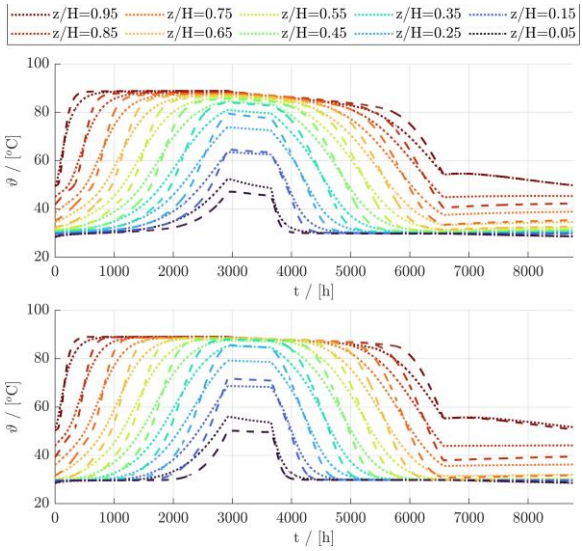

Figure 4 Water temperature profile during the 5th year of operation for the non-insulated (top figure) and insulated (bottom figure) 27 m tank TES. Dotted lines: Matlab. Dashed lines: Comsol.

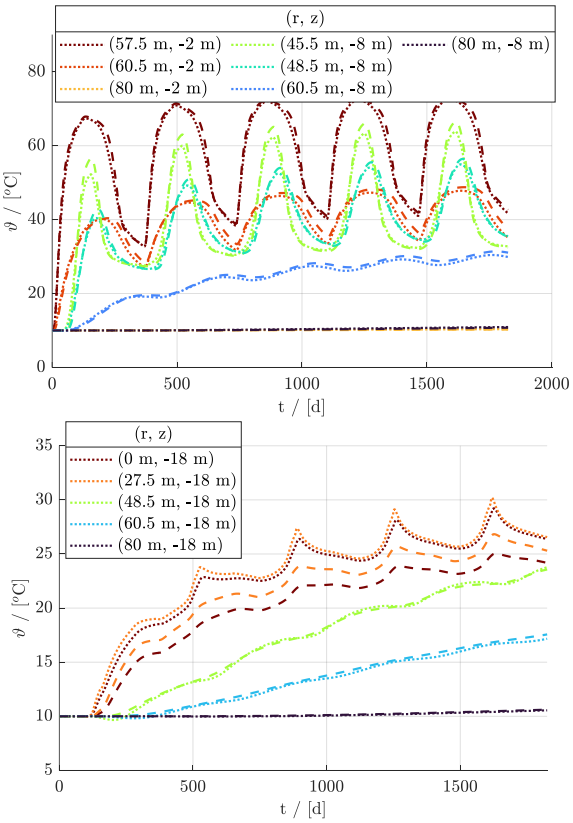

Figure 5 Ground Temperatures for the non-insulated pit (26°) TES, the ground level is the reference for the z axis coordinates. The dotted curves are the ground temperatures from Matlab, the dashed from Comsol. Lateral temperatures (top figure). Bottom temperatures (bottom figure).

Both models show a good agreement and predict the same trend with respect to the slope, with respect to the tank depth and with respect to the side wall and bottom insulation. The average deviation between the two models is 3 % for the charging energy and 4.7 % for the discharged energy. The thermal losses show a good agreement, with minimal deviations confirming the independence of the soil discretization. In both models, the better performance of the TES with increasing slope can be seen. In both models, the variation of enthalpy with respect to the TES capacity between the 1st and last day of the year is below 1 %.

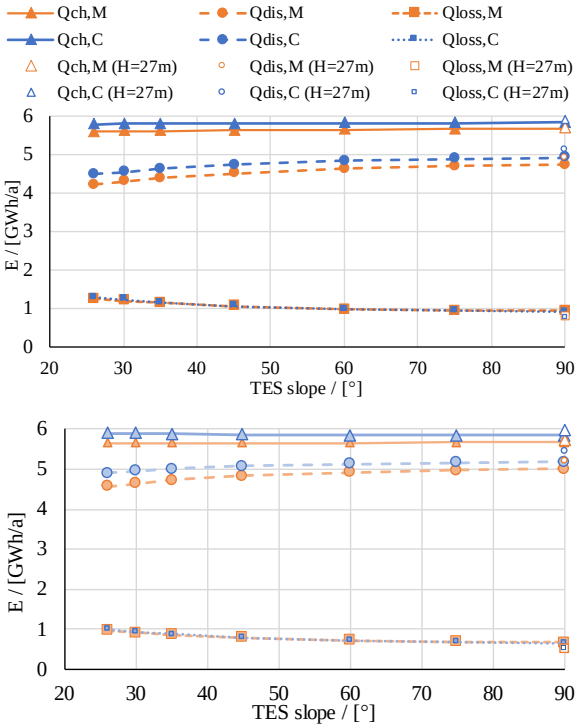

Figure 6 Energy flows in the 5th year of operation as a function of the TES slope for the non-insulated case (top figure) and insulated case (bottom figure). Qch: charged energy. Qdis: discharged energy. Qloss: thermal losses. M: Matlab. C: Comsol.

With respect to the closing error (numerical error) both tools present a very low error for the cylindrical TES, but the Matlab model shows a deviation transitioning from a cylinder (slope 90°) to a shallow pit TES (slope 26°) of up to 2 %. Figure 7 shows the error (relative to the charged energy) on the energy balance for the Matlab model.

Figure 8 presents the water temperature profiles for six specific time steps in the 5th year of TES operation for the non-insulated shallow pit (slope 26°) and the 27 m high non-insulated as well as insulated tank, in order to be able to analyse the thermal stratification of the two models.

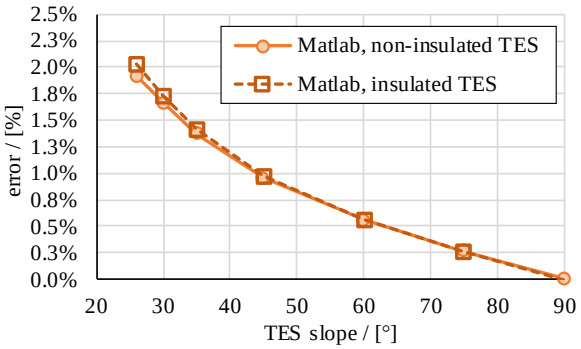

Figure 7 Closing error of the MATLAB model in the investigated non-insulated TES cases.

The differences between the two models are visible in both the cylindrical tank and in the shallow pit and are independent of the wall and bottom insulation. Overall, both models show good agreement in the temperature trend and in the ability to capture the impact of the TES shape on the temperature profile, but the thermocline thickness resulting from the Matlab model is larger than the one resulting from the Comsol model. This can be observed through the entire operation, in both dynamic operation phases (i.e., charging and discharging) and static ones (i.e., storage, idle) in both investigated TES shapes. Both models are able to capture the impact of the thermal insulation on the thermal stratification. Both Comsol and Matlab show in the non-insulated cylindrical tank TES (Fig. 8b) lower temperatures and larger thermocline thickness than in the insulated tank TES (Fig. 8c), albeit with the difference already mentioned in the previous paragraph.

Discussion and Conclusion

This work presents a comparison of two detailed numerical TES models, implemented in Matlab and Comsol environment. This work extends the comparison of different models done in the framework of the IEA ES Annex 39 project. Both models use the FE method for the soil domain. Comsol presents a higher flexibility in terms of meshing. Matlab uses a FD (discretized) approach for the modelling of the fluid domain, while in Comsol the fluid domain is modelled as line source using PDE (differential FE approach). Through the differential approach, the Comsol model allows greater flexibility with respect to the position of the inlet and outlet, while in Matlab with the discrete number of fluid elements this is not the case.

Overall, the two models provide a good agreement, however in terms of stratification and in particular TES bottom fluid and ground temperature there is a relevant deviation, leading also to a difference of up to 4 % in the annual

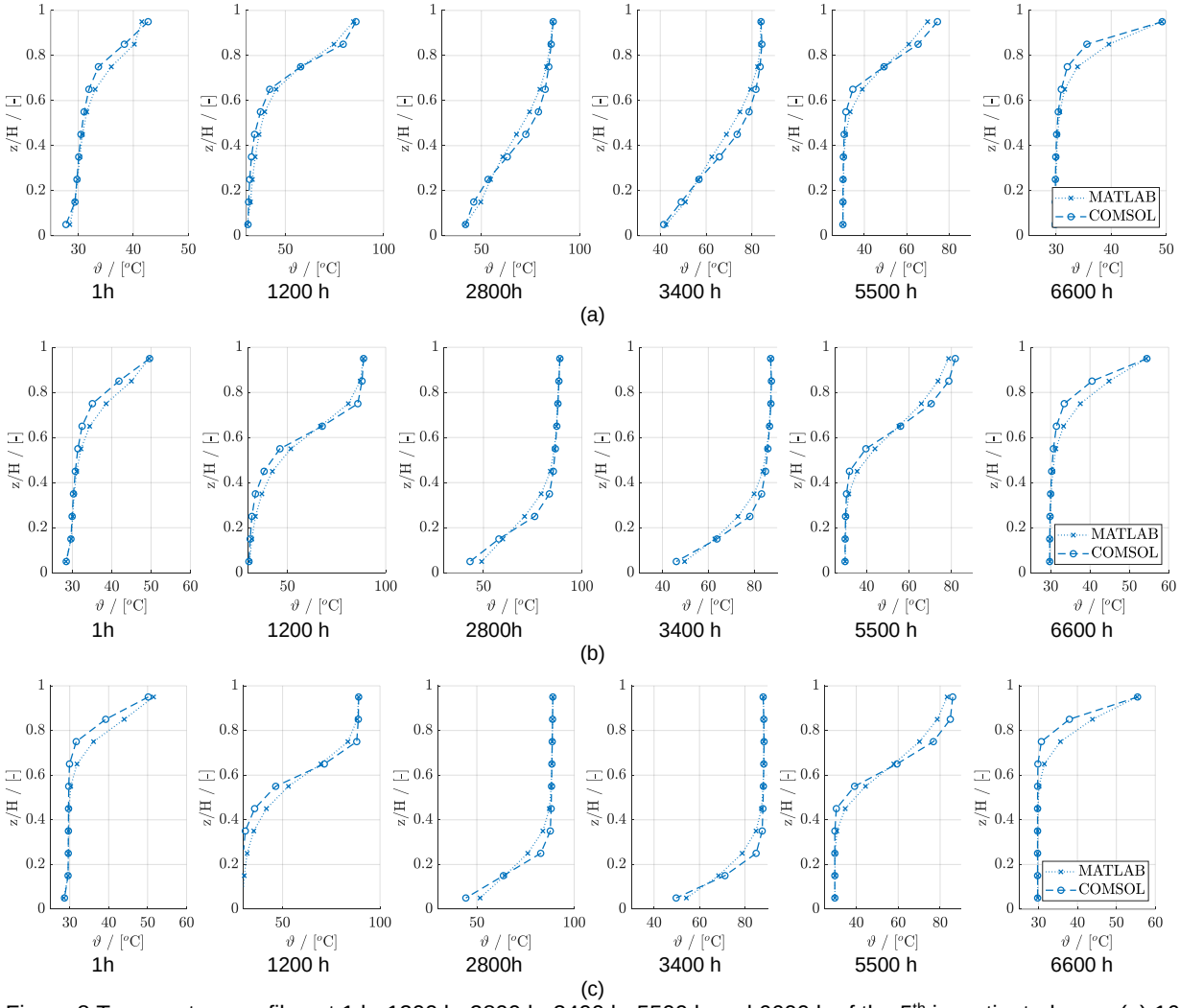

Figure 8 Temperature profiles at 1 h, 1200 h, 2800 h, 3400 h, 5500 h and 6600 h of the 5th investigated year. (a) 16 m pit with 26° slope (without insulation). (b) 27 m high cylindrical tank TES (without insulation). (c) 27 m high cylindrical tank TES (with insulation).

charging and discharging energies (while the deviation in thermal losses is negligible). Although both models are able to predict the effect of geometry (height, slope) and envelope quality, there is a relevant deviation in the thermocline thickness, which is larger in Matlab with the discrete (FD) fluid domain than in Comsol with the differential FE approach for the fluid domain.

Beyond numerical aspects, a relevant difference can be highlighted between the two models: the simulation time for the example of the pit TES with 26° slope is around 6 min in Matlab, and around 40 min in Comsol.

Overall, for pre-design purposes, the presented models show good agreement, but further analysis to understand the reason for the deviations are required and studies will be continued within the IEA collaboration.

Acknowledgement

This research was carried within the framework of IEA ES Annex 39 (Large thermal energy storage for District Heating, Project Nr.: 883015) and of the new IEA ES Task 45 and the authors are grateful for the international collaboration withing these activities and the financial support by Austrian FFG/BMK for this work.

References

Bolton, R., Cameron, L., Kerr, N., Winskel, M., & Desguers, T. (2023). Seasonal thermal energy storage as a complementary technology: Case study insights from Denmark and The Netherlands. *Journal of Energy Storage*, *73*, 109249. https://doi.org/10.1016/J.EST.2023.109249

Dahash, A., Ochs, F., Giuliani, G., & Tosatto, A. (2021). Understanding the interaction between groundwater and large-scale

underground hot-water tanks and pits. *Sustainable Cities and Society*, *71*, 102928. https://doi.org/10.1016/j.scs.2021.102928

Dahash, A., Ochs, F., & Tosatto, A. (2021). Techno-economic and exergy analysis of tank and pit thermal energy storage for renewables district heating systems. *Renewable Energy*, *180*, 1358–1379. https://doi.org/10.1016/J.RENENE.2021.08.106

Dahash, A., Ochs, F., Tosatto, A., & Streicher, W. (2020). Toward efficient numerical modeling and analysis of large-scale thermal energy storage for renewable district heating. *Applied Energy*, *279*. https://doi.org/10.1016/j.apenergy.2020.115840

Gao, M., Fan, J., & Furbo, S. (2024). Numerical Investigation of a Large-Scale Water Pit Heat Storage. *EuroSun2022 Proceedings*, 1–11. https://doi.org/10.18086/eurosun.2022.13.10

Gauthier, G. (2020). *Benchmarking, and improving models of subsurface heat storage dynamics Comparison of Danish PTES and BTES installation measurements with their corresponding TRNSYS models. GEOTHERMICA – ERA NET Cofund Geothermal*. www.heatstore.eu

Hornberger, M. (1998). *Solar unterstützte Heizung und Kühlung von Gebäuden, Forschungsberichte des Deutschen Kälte- und Klimatechnischen Vereins, Nr. 47* [Diss.]. ITW, University of Stuttgart.

IEA. (2024). *IEA ES Task 39 - Large Thermal Energy Storages for District Heating*. https://iea-es.org/task-39/

Luo, Y., Cui, D., Hu, L., Ochs, F., Tosatto, A., Xu, G., Tian, Z., Dahash, A., Yu, J., Yuan, G., Chen, Y., Wang, D., Liu, Y., & Fan, J. (2023). Semi-analytical modeling of large-scale water tank for seasonal thermal storage applications. *Energy and Buildings*, *278*, 112620. https://doi.org/10.1016/J.ENBUILD.2022.112620

Mazzarella, L. (1994). *Multi-flow stratified thermal storage model with full mixed layers. Pdm-XST*. ITW, University of Stuttgart, and Dipartimento Energetica, Politecnico di Milano.

Ochs, F. (2009). *Modelling Large-Scale Thermal Energy Stores* [Univ. Diss.]. University of Stuttgart.

Ochs, F. (2014). Large-Scale Thermal Energy Stores in District Heating Systems – Simulation Based Optimization. *EuroSun 2014: International Conference on Solar Energy and Buildings, Aix-Les-Bains, France, 16-19 September*, 1–8. https://doi.org/10.18086/eurosun.2014.19.09

Ochs, F. (2015). Simulation Based Optimization of Pit and Tank Thermal Energy Storage for Solar District Heating Systems. *3rd International Solar District Heating Conference (SDH 2015)*.

Ochs, F., Dahash, A., Tosatto, A., Reisenbichler, M., O'Donovan, K., Gauthier, G., Kok Skov, C., & Schmidt, T. (2022). Comprehensive Comparison of Different Models for Large-Scale Thermal Energy Storage. *Proceedings of the International Renewable Energy Storage Conference 2021 (IRES 2021)*, 36–51. https://doi.org/10.2991/ahe.k.220301.005

Reisenbichler, M., O'Donovan, K., Tugores, C. R., van Helden, W., & Wotawa, F. (2022). Towards More Efficient Modeling and Simulation of Large-scale Thermal Energy Storages in Future Local and District Energy Systems. *Building Simulation Conference Proceedings*, 2155–2162. https://doi.org/10.26868/25222708.2021.30911

Tosatto, A., Dahash, A., & Ochs, F. (2023). Simulation-based performance evaluation of large-scale thermal energy storage coupled with heat pump in district heating systems. *Journal of Energy Storage*, *61*, 106721. https://doi.org/10.1016/J.EST.2023.106721

Xiang, Y., Gao, M., Furbo, S., Wang, D., Tian, Z., & Fan, J. (2022). Heat transfer of a large-scale water pit heat storage under transient operations. *Journal of Energy Storage*, *55*, 105455. https://doi.org/10.1016/J.EST.2022.105455

Xiang, Y., Xie, Z., Furbo, S., Wang, D., Gao, M., & Fan, J. (2022). A comprehensive review on pit thermal energy storage: Technical elements, numerical approaches and recent applications. *Journal of Energy Storage*, *55*, 105716. https://doi.org/10.1016/J.EST.2022.105716

BauSIM 2024 in Wien
23. September – 26. September

Development and Validation of a Finite Element Pyrolysis Model for Simulating Fire Resistance Tests of Wood Building Elements

Boris Sandor[1], Peter Kitzmüller[2], Andreas Cziegler[3], Sylvia Polleres[1] and Günther Schwabegger[2]

[1]*Holzforschung Austria, Franz-Grill-Straße 7, 1220 Vienna, Austria*

[2]*Institut für Brandschutztechnik und Sicherheitsforschung, Petzoldstraße 45, 4020 Linz, Austria*

[3]*Österreichisches Gießerei-Institut, Parkstraße 21, 8700 Leoben, Austria*

Abstract

Modern wood buildings have to meet high standards with regard to fire resistance. This is in stark contrast to the nature of wood as a flammable material. Therefore, wooden building elements have to undergo real fire resistance tests in order to prove their performance under high thermal loads. Those tests are expensive, time consuming and are only a snapshot of a single component made of an inhomogeneous and anisotropic medium. Simulations are a way to get a better understanding of the physical processes occurring during fire resistance tests and could provide deeper insight into the importance of hard to control variables such as density variations, water content and fiber deviations.

In this paper we develop a multiphase model of wood pyrolysis in which five species interact together with three different irreversible reactions. The underlying reaction mechanism is derived from previous work and complemented by supplementary physical mechanisms such as solid phase expansion and transport mechanisms of water and pyrolysis gases.

Laboratory scale methods such as dilatometry and small scale fire tests in an oven with a sample size of up to 0.25 m^2 were used to validate the proposed model. The laboratory experiments were performed to gather thermophysical parameters and to validate the kinetic parameters of the reactions between the phases of the multiphase model while the main purpose of the fire tests was to demonstrate the applicability of the model to those tests.

Both kinds of real world tests show good agreement between them and the numerical simulations.

Introduction

Wood is a ubiquitous material with a wide array of applications ranging from construction to furniture making. Especially in the former, modern building codes expect high performant timber structures that are resilient against fire. Utilizing numerical methods in the design phase of new timber solutions can lead to improved components with regards to fire safety without the need for expensive real world testing Giraldo et al. (2012). Furthermore, simulations can provide deeper insight into the physical processes occurring during pyrolysis and their relative importance to fire resistance. With this information new approaches to the design of timber structures can be developed Hens et al. (2022).

There have already been many different methods to model the pyrolysis of wood and wood derivatives as discussed in Moghtaderi (2006) and Nyazika et al. (2019). Pyrolysis models are usually classified into thermal and comprehensive models depending on whether or not a kinetic reaction scheme is utilized to obtain the fuel conversion. In all models the internal variables such as composition of the fuel, density, additives and moisture content are as important to consider as external factors like oxygen concentration and heat load.

Description of the pyrolysis model

In this paper we develop a comprehensive numerical model for the pyrolysis of wood by expanding on the model presented by Shen et al. (2007). It is a multiphase model consisting of five species and three reactions as shown in fig. 1. The species are denoted in the subsequent equations with the sub-

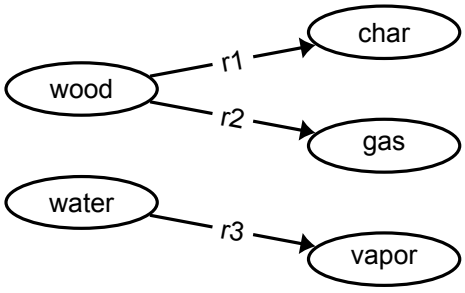

Figure 1: Reaction mechanism of the pyrolysis model according to Shen et al.

scripts w, c, g, a, v respectively. The subscript a (for aqua) is chosen for the species water instead of l in the original. The system of equations in eq. (1) describes the model mathematically.

$$\frac{\partial \rho_w}{\partial t} = (-k_1 - k_2)\,\rho_w \tag{1a}$$
$$\frac{\partial \rho_c}{\partial t} = k_1 \rho_w \tag{1b}$$
$$\frac{\partial \rho_g}{\partial t} = k_2 \rho_w \tag{1c}$$
$$\frac{\partial \rho_a}{\partial t} = -k_3 \rho_a \tag{1d}$$
$$\frac{\partial \rho_v}{\partial t} = k_3 \rho_a \tag{1e}$$

The multiphase reaction scheme is coupled with a heat transfer equation

$$\frac{\partial T}{\partial t} s_{\text{eff}} = \nabla\left(\lambda_{\text{eff}} \nabla T\right) + Q \tag{2}$$

where s_{eff} is the effective volumetric heat capacity

$$s_{\text{eff}} = \rho_w c_w + \rho_c c_c + \rho_a c_a \tag{3}$$

and λ_{eff} is the effective thermal conductivity

$$\lambda_{\text{eff}} = \frac{\lambda_w \rho_w + \lambda_c \rho_c}{\rho_w + \rho_c} \tag{4}$$

The term Q includes all further thermal contributions such as the heat of the reactions and the change in enthalpy of the phases.

The three reactions are global, single step Arrhenius type and described by

$$k_i = A_i \exp\left(\frac{-E_i}{RT}\right) \tag{5}$$

While this model delivers accurate numerical results when applied to relatively simple scenarios its basic assumptions make it inadequate for simulating fire resistance tests. To remedy those shortfalls, we improve upon the model in four major ways.

1. the model is expanded into three dimensions
2. temperature dependent material data for species wood and char are included
3. the fluid phases are given explicit transport mechanisms
4. the model is coupled with a linear, elastomechanical model in which the thermal and hygroscopic expansions of the solid phases are taken into account

Three-dimensional pyrolysis

Wood is an anisotropic medium and it's important to model it as such because the material properties change drastically with respect to the orientation of the fibers. Most mathematical descriptions of wood use a cylindrical coordinate system, where the three principal directions are longitudinal along the grain, radially outward from the pith and transverse, which is orthogonal to the previous two.

In this paper we employ a transversely isotropic material model of wood because it accounts for its anisotropic nature, improving the representation of material properties that vary with fiber orientation thus providing a more realistic simulation of pyrolysis. It combines the radial and transverse principal axes into a single plane of symmetry. This simplifies the acquisition of material data and the calculations for the thermal and hygroscopic expansions as shown in a later section. Furthermore the material properties do not change as much between radial and transverse directions Boutelje (1962). The two directions longitudinal and transverse are denoted by the subscripts l and t respectively.

Temperature dependent material data

In addition to its anisotropy most material properties of wood are also temperature dependent which introduces inherent non-linearities that have been omitted in the original model Pečenko et al. (2015). For the solid species wood and char temperature dependent material data was taken from Cziegler & Kaschnitz (2023). This includes the thermal conductivity, heat capacity and thermal expansion coefficients.

Transport mechanisms for fluid phases

Wood, as a porous material, allows for fluids to move through it. These movements can have a significant impact to the behavior of wood during

a fire. Water by far has the largest contribution to the behavior because it removes a large amount of heat when it evaporates, thus cooling the surrounding material. Instead of modelling fluid flow directly by coupling a full CFD simulation, we added diffusion processes, which are commonly used to model these transports in building material simulations.

Diffusion for pyrolysis gases and water vapor

The movement of gases within porous materials is largely caused by pressure differences which can be described by diffusion equations. Such an equation was taken from Autengruber et al. (2021) and combined with the reactions mechanism to replace equations eq. (1c) and eq. (1e).

$$\frac{\partial \rho_g}{\partial t} = \nabla \left(\boldsymbol{D_v} \nabla \rho_g \right) + k_2 \rho_w \tag{6a}$$

$$\frac{\partial \rho_v}{\partial t} = \nabla \left(\boldsymbol{D_v} \nabla \rho_v \right) + k_3 \rho_a \tag{6b}$$

The diffusion tensor $\boldsymbol{D_v}$ is highly temperature dependent and given by

$$\boldsymbol{D_v} = \boldsymbol{\xi} \times 2.31 \times 10^{-5} \frac{p_{atm}}{p_{atm} + p_{gas}} \left(\frac{T}{273\,\mathrm{K}} \right)^{1.81} \tag{7}$$

where $\boldsymbol{\xi}$ is a tensor to account for different diffusion coefficients among the principal axes. Both phases are gases and ideally, they each contribute pressure partially to the total pressure. We model them separately because the numerical implementation is more stable and efficient. Since they occupy different temperature ranges, they are not influencing each other too much. By the time pyrolysis starts and wood is converted to produce gas most of the water has evaporated already.

Diffusion and thermophoresis of water

Both are transport phenomena of condensed water which play a crucial role within the microstructure of wood. Diffusion refers to the movement of water molecules within the porous structure of wood. It is driven by concentration gradients. While it is a slow process with large time constants that are not typical for fire resistance tests it is included in the model for completeness.

Thermophoresis, on the other hand, is the movement of water driven by temperature gradients. When such a gradient develops within wood, it can induce a flow of water molecules from regions of higher temperature to lower temperature. This phenomenon becomes significant during processes involving steep temperature gradients, such as drying, thermal treatment of wood or fire resistance tests.

Both of these effects are included in the model by replacing eq. (1d) with the following equation

$$\frac{\partial \rho_a}{\partial t} = \nabla \left(\boldsymbol{D_a} \nabla \rho_a \right) + \nabla \left(\boldsymbol{D_{aT}} \nabla T \right) - k_3 \rho_a \tag{8}$$

The equation as well as the numerical values for the diffusion tensor $\boldsymbol{D_a}$ and the thermophoresis tensor $\boldsymbol{D_{aT}}$ are taken from Frandsen (2007).

Thermal and hygroscopic expansion

Like most materials wood expands with increased temperature which can have significant implications for its dimensional stability and structural integrity. Since the contributions to the thermal expansion from both wood and char have to be considered their sum is referenced to the total density.

In addition to thermal effects wood is also a hygroscopic medium. It absorbs water from the surrounding air and stores it in the cells of the microstructure. The water molecules excerpt a pressure that expands the cells and therefore the macroscopic structure as well. The hygroscopic strains are only relevant before pyrolysis starts since by then the liquid water has been evaporated. Note that both longitudinal and transverse strains have to be calculated since they are different. The total strain in one direction throughout the domain is given by eq. (9).

$$\frac{\partial \varepsilon}{\partial t} = \frac{\alpha_w \rho_w + \alpha_c \rho_c}{\rho_w + \rho_c} \frac{\partial T}{\partial t} + \frac{\beta}{\rho_w} \frac{\partial \rho_a}{\partial t} \tag{9}$$

The symbols α and β denote the coefficients of thermal and hygroscopic expansion respectively. From the strain field the displacement field $\boldsymbol{u}$ can be obtained by the linear strain-displacement relation.

$$\varepsilon_{ij} = \frac{1}{2} \left(\frac{\partial u_i}{\partial x_j} + \frac{\partial u_j}{\partial x_i} \right) \tag{10}$$

Since the expansion directly influences the densities of the species solved for this change has to be taken into account. It is compensated by adding the time derivative of the volumetric ratio J between the deformed and reference configuration to the right hand side each of the equations in eq. (1). It is defined as

$$J = \det \left(\boldsymbol{I} + \frac{\partial \boldsymbol{u}}{\partial \boldsymbol{x}} \right) \tag{11}$$

Experimental Setup

Temperature dependent density

An experiment performed in Cziegler & Kaschnitz (2023) was used to validate the kinetic parameters of the reaction mechanism for the proposed model and the chosen wood species of spruce. With a pushrod-dilatometer the temperature dependent density of spruce wood and charred spruce was measured. The samples with the dimensions of 25 mm x 5 mm x 5 mm were subject to a heat rate of 2 K min^{-1} under an inert argon atmosphere. The slow heat rate and small sample size ensures that the temperature within the specimen is relatively uniform. From the measured expansion in both longitudinal Δl_l and transversal directions Δl_t the temperature dependent density was obtained

$$\rho\left(T\right) = \frac{\rho_{\text{ref}}}{\left(1+\frac{\Delta l_l(T)}{l_{l,\text{ref}}}\right)\left(1+\frac{\Delta l_t(T)}{l_{t,\text{ref}}}\right)^2} \tag{12}$$

Since the dilatometer does not consider mass change during the measurement the density change during the transition between virgin wood and char cannot be captured adequately by dilatometry alone and the results are supplemented with a thermogravimetric analysis from the same publication.

Fire resistance tests

To demonstrate the applicability of the model to fire resistance tests small scale tests have been performed. Two specimens of solid spruce timber have been cut to a size of 520 mm x 520 mm x 160 mm. Because of the size it was not possible to construct the specimen from a single piece of timber and has had to be glued together. The fiber orientation as well as the glue surfaces were chosen to be perpendicular to the direction of the thermal load. Type K thermocouples have been installed in each sample at depths of 1 cm, 2 cm, 4 cm, 6 cm (measured from the fire exposed side). They were inserted into a 4mm hole drilled parallel to the fire exposed surface from the side for a length of at least 8 cm. This was to ensure the thermocouples do not conduct heat away from the measurement tip due to its high thermal conductivity compared to wood Beck (1962). Each layer was probed four times to decrease statistical noise in the resultant data. A detailed setup of the probes is shown in fig. 2. Four specimens were mounted to a concrete frame with two of them being cross laminated timber elements which are unrelated to this work.

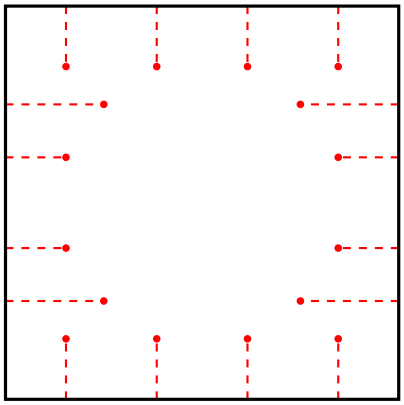

Figure 2: Layout of the thermocouples within a specimen.

The assembly was mounted on top of the oven in a ceiling configuration. The contact surfaces between the specimens and concrete were insulated with stone wool to prevent heat and gases from the oven to escape. A fire resistance test according to 13501-2 (2023) was carried out for approximately 90min.

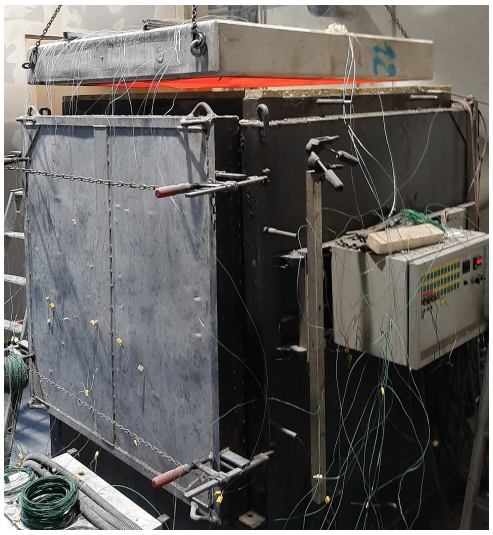

Figure 3: Fire resistance test of the spruce samples.

Numerical analysis

The developed model was implemented in the commercial finite element software COMSOL (2024). A custom environment was created with the relevant equations and material data since there is no pyrolysis model included by default. Some boundary conditions are assumed to be the same for all stud-

ies. The values of ρ_g and ρ_v were set to zero at all boundaries. Similarly, if not stated otherwise the flux of bound water at the boundaries was assumed to be zero.

Simulation of temperature dependent density

The small samples for the dilatometry experiments were modeled by exploiting the three planes of symmetry. An octant of the sample was modeled with symmetry conditions on three sides. The thermal conditions of the remaining sides were

$$q = h_{conv} \left(T - T_{2K}\left(t\right)\right) \tag{13}$$

where T_{2K} is a linear rise in temperature of 2 K min^{-1}. For the numerical mesh hexahedral elements with side length of 0.1 mm and quadratic shape functions for all equations were chosen.

Simulation of fire resistance test

The thermal boundary conditions on the fire exposed side $(x = 0)$ of the specimen considered convective and radiative heat transfer. The heat flux q is given by

$$q = \sigma\epsilon \left(T^4 - T_{ETK}^4\left(t\right)\right) + h_{conv} \left(T - T_{ETK}\left(t\right)\right) \tag{14}$$

where $T_{ETK}\left(t\right)$ is the uniform temperature curve according to 13501-2 (2023). On the side that is not exposed to fire T_{ETK} is substituted with the ambient temperature T_0. All other sides were assumed to be perfectly insulated $(q = 0)$. To ensure a unique solution for the elastomechanical part rigid body motion was suppressed. As in the numerical dilatometry experiment hexahedral elements with quadratic shape functions were used. However, due to the larger specimen size and the fact that the thermal load is uniform parallel to the surface an element size of 2 mm x 2 mm x 0.5 mm was chosen.

Results

As shown in fig. 4 the numerical analysis shows good agreement with the dilatometry experiment. The evaporation of water around 100 °C and the resulting increase of density of the species wood due to shrinking is captured well both in magnitude and timing. Starting at around 200 °C pyrolysis converts wood to char with equally accurate results.

Comparing the new approach with the original model by Shen et al highlights the importance of

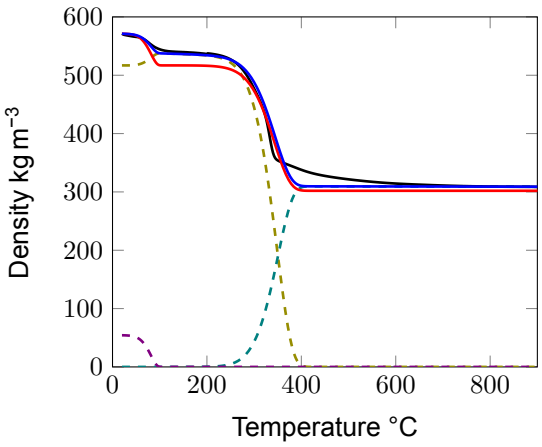

Figure 4: Comparison between the experiment and the numerical simulation of the temperature dependent density. The solid black and blue lines are the empirical and simulated densities respectively while the red line depicts the results from the model of Shen et al. The dashed lines represent the individual phases. Brown: wood, cyan: char, violet: water.

incorporating the deformation into the model. Especially the hygroscopic shrinking due to the evaporation of bound water is necessary to predict the densities accurately. It's important to note that the density profile is a result of the numerical simulation. The values after the evaporation of water and after pyrolysis has converted wood to char is not set explicitly. They are determined by the kinetic parameters of eq. (5) and the boundary/initial conditions. Because the simulated resultant density matches the expected value from the experiment the model adequately describes the pyrolysis.

The fire resistance simulations perform equally well as shown in fig. 5. The curves show the expected change in temperature rise at around 100 °C and difference in slope between the different measurement depths. However, at higher temperatures there are noticeable deviations.

The biggest contribution to the deviation at high temperatures is the buildup of an insulating char layer. In the real test the accumulating char layer is either burned off or delaminates from the sample. The delamination in solid timber happens mainly because of cracks resulting from internal stresses due to thermal expansion. In timber elements such as cross laminated timber the glue lines are also prone to delamination because of thermal degradation of the glue. These effects are not considered in the presented model, thus the observed deviation in the results.

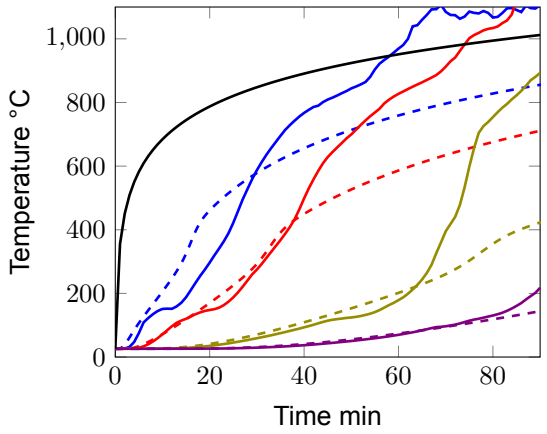

Figure 5: Comparison between the fire resistance test and the numerical simulation. Blue: 1 cm, red: 2 cm, brown: 4 cm, violet: 6 cm. The empirical data is represented by solid lines while the simulated data is visualized by dashed lines. The solid black line is the uniform temperature curve T_{ETK}.

Conclusion

The developed model shows good agreement between real world fire tests and the numerical analysis. Future work could possibly include more sophisticated reaction pathways, conversion or delamination of char, coupled CFD, external loads or additional materials found in wooden constructions such as wood derivatives and gypsum. There is great potential for this kind of more comprehensive pyrolysis models especially considering the comparably simple reaction mechanism used in this work. With these modifications the model would be a great asset for civil engineers, architects and governing entities.

References

13501-2, □. E. (2023), Fire classification of construction products and building elements Part 2: Classification using data from fire resistance and/or smoke control tests, excluding ventilation services, Standard, European Committee for Standardization, Brusseles, BG.

Autengruber, M., Lukacevic, M., Gröstlinger, C. & Füssl, J. (2021), 'Finite-element-based prediction of moisture-induced crack patterns for cross sections of solid wood and glued laminated timber exposed to a realistic climate condition', *Construction and Building Materials* **271**(11), 121775.

Beck, J. V. (1962), 'Thermocouple Temperature Disturbances in Low Conductivity Materials', *Journal of Heat Transfer* **84**(2), 124–131.

Boutelje, J. B. (1962), 'The relationship of structure to transverse anisotropy in wood with reference to shrinkage and elasticity', *Holzforschung* **16**(2), 33–46.

COMSOL (2024), 'Comsol multiphysics® v6.2'.

Cziegler, A. & Kaschnitz, E. (2023), 'High temperature thermophysical properties for the numerical simulation of construction materials exposed to fire load', *Thermal Conductivity 35/Thermal Expansion 23, Proceedings of the 35th International Thermal Conductivity Conference and the 23th International Thermal Expansion Symposium* .

Frandsen, H. L. (2007), 'Selected constitutive models for simulating the hygromechanical response of wood', *Ph.D. Thesis* (Aalborg University).

Giraldo, M., Rodríguez-Trujillo, V. & Burgos, C. (2012), 'Computer-simulation research on building-façade geometry for fire-spread control in buildings with wood claddings', *The 2012 World Conference on Timber Engineering* **2**.

Hens, I., Solnosky, R. & Brown, N. (2022), 'Parametric framework for early evaluation of prescriptive fire design and structural feasibility in tall timber', *Journal of Architectural Engineering* **29**.

Moghtaderi, B. (2006), 'The state-of-the-art in pyrolysis modelling of lignocellulosic solid fuels', *Fire and Materials* **30**(1), 1–34.

Nyazika, T., Jimenez, M., Samyn, F. & Bourbigot, S. (2019), 'Pyrolysis modeling, sensitivity analysis, and optimization techniques for combustible materials: A review', *Journal of Fire Sciences* **37**(4-6), 377–433.

Pečenko, R., Svensson, S. & Hozjan, T. (2015), 'Modelling heat and moisture transfer in timber exposed to fire', *International Journal of Heat and Mass Transfer* **87**, 598–605.

Shen, D. K., Fang, M. X., Luo, Z. Y. & Cen, K. (2007), 'Modeling pyrolysis of wet wood under external heat flux', *Fire Safety Journal* **42**(3), 210–217.

BauSIM 2024 in Wien
23. September – 26. September

Hygrothermal performance of internal insulation systems with moisture-adaptive vapour retarders

Marianna Muchorowska[1], Michele Bianchi Janetti[1], Albert Rössler[2]
1 Universität Innsbruck, Österreich, E-Mail: Marianna.Muchorowska@uibk.ac.at
2 ADLER-Werk Lackfabrik, Österreich

Abstract

In this study, the hygrothermal performances of a moisture-adaptive vapour retarder in form of a paint coating is investigated via numerical simulation with the software *Delphin*. The vapour retarder is combined with an exemplary internal insulation system by analysing the temperature and moisture distribution in the construction under different boundary conditions. Simulations are performed to determine the limits of the system in relation to the risk of moisture damages due to mould growth and to optimize the water vapour diffusion resistance factor of the vapour retarder (s_d-value) as a function of the relative humidity. The impact of different construction parameters (thicknesses of the wall and insulation layer), employed materials and boundary conditions (driving rain, solar radiation, internal and external temperature/relative humidity) are investigated. The numerical results reported in this study serve as pre-dimensioning of the vapour retarder and support future development of applicative solutions.

Introduction

The application of internal insulation is often the only way to significantly reduce transmission heat losses and improve thermal comfort of listed and historical buildings. The insulation system, however, must be carefully planned and implemented in order to avoid moisture related damages and health hazards caused by mould growth. Moisture-adaptive vapour retarders represent a promising solution in this context, as they inhibit vapour penetration from the indoor air into the construction during winter, without preventing the wall from drying out during summer (Künzel, 1999; Vereecken et al., 2015; Knarud et al., 2021). Existing products consist of polyamide membranes whose vapour transmittance increases with the water content (Picard et al., 2008). Scientific works show, though, that despite the advantages of such moisture-adaptive vapour retarders, improvements are required to achieve better adaptation of their properties to the environmental conditions and construction-specific requirements.

Moisture-adaptive vapour retarders in form of paint coating are rarely applied so far, they promise however major advantages compared to the well-established membrane-based solutions. While commercially available membranes present predefined properties and crucial limits regarding the s_d-value variability, a vapour retarder based on paint coating can be flexibly adapted to specific building physics and environment-related requirements. The adaptation can be performed by using suitable binders and varying the layer thickness. The coating can be applied to products for internal finishing such as timber boards, oriented strand boards (OSB), clay or gypsum boards, directly in the factory on a large industrial scale.

To bring this promising solution to its full potential however, further development is required since existing paint coatings do not present yet the required characteristics in terms of moisture adaptive vapour transmittance. This development process is undertaken in an ongoing research project through three essential stages, for which interdisciplinary cooperation in the fields of building physics and chemical engineering is required. In a first stage, the optimal vapour diffusion resistance factor of the vapour retarder (s_d-value) is defined via hygrothermal simulation for expected environmental conditions and construction-specific characteristics. In a second stage, a paint coating with the required characteristics is developed by suitable chemical-engineering methods. In the final stage the functionality of the developed solution is demonstrated via lab tests and on-site monitoring.

This paper address results on the first project stage, i.e., related to the definition of the targeted moisture dependent s_d-value of the paint coating. The results obtained by numerical simulation with the software *Delphin* serve as pre-dimensioning

of the vapour retarder and support the development planned in next project stages.

Model and simulation

Wall model

The investigated construction (Figure 1) represents a historical brick wall refurbished by means of internal insulation. This exemplary case study is applied in all simulation variants reported below.

Existing brick wall	30.0 cm
Existing plaster	1.5 cm
Cellulose	5.0 cm
Vapour retarder	
Loam-cork board	3.0 cm

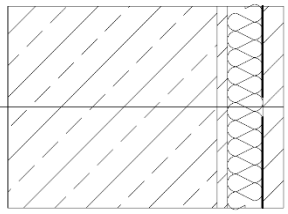

Figure 1: Wall model used for simulation

The considered construction is common in European buildings of the last centuries and has been chosen for this study since internal insulation systems are typically used for renovation of listed buildings. It is composed by 30 cm load bearing wall made of historic bricks and an inside historic plaster with thickness of 1.5 cm. The internal insulation system applied to refurbish the building envelope is composed by 5 cm thick blown cellulose insulation combined with a loam-cork composite board on the internal side. The moisture adaptive vapour retarder is applied on the back side of this loam-cork board. The material properties are presented in Table 1.

Table 1: Material properties, ρ – density; μ – vapour diffusion resistance factor; λ – thermal conductivity; c_p – specific heat capacity

Material	**ρ [kg/m³]**	**μ [-]**	**λ [W/mK]**	**c_p [J/kgK]**
Brick	1 773.1	43.10	0.838	862
Historic Plaster	1 800.0	12.00	0.820	850
Blown Cellulose	92.8	2.42	0.052	2 005
Loam Cork board	460.4	19.79	0.085	803

Boundary and initial conditions

As a preliminary stage, the indoor climate is characterized by a constant air temperature of 20°C and a relative air humidity of 50%. The outdoor air temperature throughout the year is approximated by a sinusoidal curve within a range of -5°C to 25°C. Additionally, the outdoor relative humidity is presumed to remain constant at 80% throughout the year. In subsequent stages, the effect of varying indoor relative humidity, external temperature and including realistic weather conditions (solar radiation, wind-driven rain) is investigated. These variations of boundary conditions are specified later on in dedicated sections. As initial conditions of the construction, T=20°C and RH=50% are applied. It was observed that periodic boundary conditions are established in the wall after two years, therefore the third simulation year is considered to evaluate the hygrothermal construction behaviour.

Moisture adaptive vapour retarder

The moisture transport behaviour of vapour retarders, is typically described by the correlation between the s_d-value and relative humidity on the retarder, termed the s_d-curve. For simplicity, the s_d-curve of the moisture-adaptive vapour retarder is represented in this study by a rump function with s_d-values of 20 m and 0.1 m at low and high relative humidity, respectively. The transition from the low relative humidity to the high relative humidity region is characterized by a linear decrease of the s_d-value. Accordingly, the moisture adaptive vapour retarder is characterized by two sole parameters: parameter A represents the relative humidity at which the average s_d-value is reached, i.e., the ramp location along the horizontal axis of the diagram, while parameter B denotes the width of the transition range. An exemplary s_d-curve with highlighted parameters A and B, is illustrated in Figure 2.

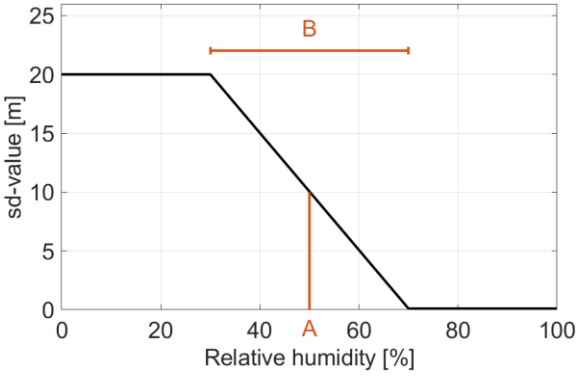

Figure 2: s_d-curve of the moisture adaptive vapour retarder. Parameter A represents the ramp location along the horizontal axis of the diagram, while parameter B denotes the width of the transition range.

Selection of the optimal s_d-curve

The selection of the optimal s_d-curve involves two steps, as delineated in Table 2. Initially, simulations are performed by varying parameter A only, while B=8 and the above-mentioned boundary conditions are applied. The minimum relative humidity value between the wall

and insulation is obtained for A=60%. This value is then applied in the subsequent stage, in which the impact of parameter B, ranging from 1 to 32, is investigated. It can be observed that reducing parameter B leads to lower relative humidity behind the insulation. However, no significant improvement is obtained for B<8. Therefore, B=8 is selected as reference value for further simulation stages.

Table 2: List of s_d-curves evaluated by means of numerical simulation. The corresponding maximal relative humidity behind insulation (max. RH) is reported.

Moisture-depended vapour retarder	**A [%]**	**B [%]**	**max. RH [%]**
Step A: selection of parameter A			
A.1.	45	8	93.80
A.2.	50	8	93.71
A.3.	55	8	81.28
A.4.	60	8	80.00
A.5.	65	8	80.83
Step B: selection of parameter B			
B.1.	60	1	79.64
B.2.	60	2	79.73
B.3.	60	4	79.81
B.4.	60	8	80.00
B.5.	60	16	80.67
B.6.	60	32	81.54

Simulation stages and variants

The primary objective of the simulations is to evaluate the influence of a moisture-dependent vapour retarder on the relative humidity distribution within the wall under diverse boundary conditions and wall configurations. In particular, the relative humidity between wall and insulation is investigated, which shall remain below 80% to avoid mould germination (Hens, 2007). The impacts of various parameters on the relative humidity behind the insulation are systematically investigated in five separate stages to assess their individual effects on the the hygrothermal construction behaviour. In each iteration, only one parameter is altered, while the remaining parameters are held constant as previously delineated.

In the first stage, the influence of the indoor humidity on the relative humidity behind the insulation is investigated. The second stage, concerns investigation of the impact of the external temperature. In the third and fourth stage, the effects of varying the insulation and load-bearing wall thicknesses are assessed, respectively. Lastly, the effect of applying realistic external conditions (temperature, relative humidity, solar radiation, and wind-driven rain) is investigated.

Results analysis and discussion

Influence of the internal relative humidity

Simulations are performed by varying the indoor relative humidity between 40% and 60%. Five different system variants are investigated. Variant 1 represents the baseline scenario without any vapour retarder, variant 2 incorporates a vapour retarder with a constant s_d-value of 20m and variant 3 includes a moisture-dependent vapour retarder (B.4. from Table 2). Due to fluctuations in indoor relative humidity, adjustments to the s_d-curve are considered to obtain lower relative humidity behind the insulation. The applied s_d-curves are reported in Figure 3, where Curve 1 represents the previously selected variant B.4 (A=60; B=8), Curve 2 is characterized by a shift of the ramp toward higher relative humidity while Curve 3 presents a wider transition range of the s_d-value.

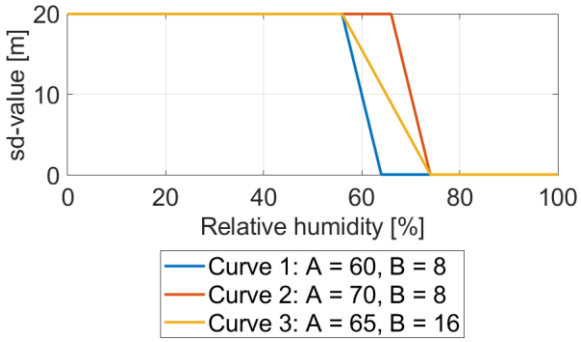

Figure 3: s_d-curves applied in the first simulation stage

Obviously, any increase of the indoor relative humidity leads to higher relative humidity levels behind the insulation (Figure 4). Adjustments to the vapour retarder curve are necessitated by changes of internal relative humidity. While Curve 1 is suitable for RH_i=40% and RH_i=50%, the vapour retarder remains open for RH_i=60%, leading to relative humidity levels behind the insulation akin to those obtained in the absence of any vapour retarder (Variant 1, Figure 4). The critical threshold of 80% is overtaken in all investigated variants for RH_i=60%, however it can be observed that Curve 2 and Curve 3

perform significantly better than Curve 1 in this case.

On the other hand, Curve 2 (Variant 4, Figure 4), tailored for RH_i=60%, yields values of relative humidity behind the insulation slightly above 80% also for RH_i=40. Curve 3 (Variant 5) represents a favourable compromise for scenarios characterized by high uncertainty in indoor relative humidity. It ensures at dry indoor conditions relative humidity levels behind the insulation below 80%, by equally avoiding extreme peaks in case of increased indoor humidity.

Influence of the external temperature

In the second stage, the influence of the external temperature on the relative humidity behind the insulation is evaluated, while internal conditions and external relative humidity remain constant as specified above. The simulation investigates five diverse time evolutions of the external temperature T_e described by sinus curves of yearly period and representing five exemplary climates:

- Climate 1, temperature range: -20°C to 30°C, representing very cold winters and very warm summers.
- Climate 2, temperature range: -10°C to 15°C, representing cold winters and fresh summers.
- Climate 3, temperature range: -5°C to 25°C, representing mild-cold winters and mild-warm summers.
- Climate 4, temperature range: 0°C to 20°C, representing mild winters and mild summers.
- Climate 5, temperature range: 0°C to 30°C, representing mild winters and very warm summers.

For each climate, three variants are investigated: no vapour retarder, vapour retarder with constant s_d-value of 20 m, and variable vapour retarder (Curve 1, Figure 3). The outcomes are reported in Figure 5.

For all considered external temperatures, the implementation of any vapour retarder proves being advantageous relative to the diffusion-open system (Variant 1). Moreover, the moisture-

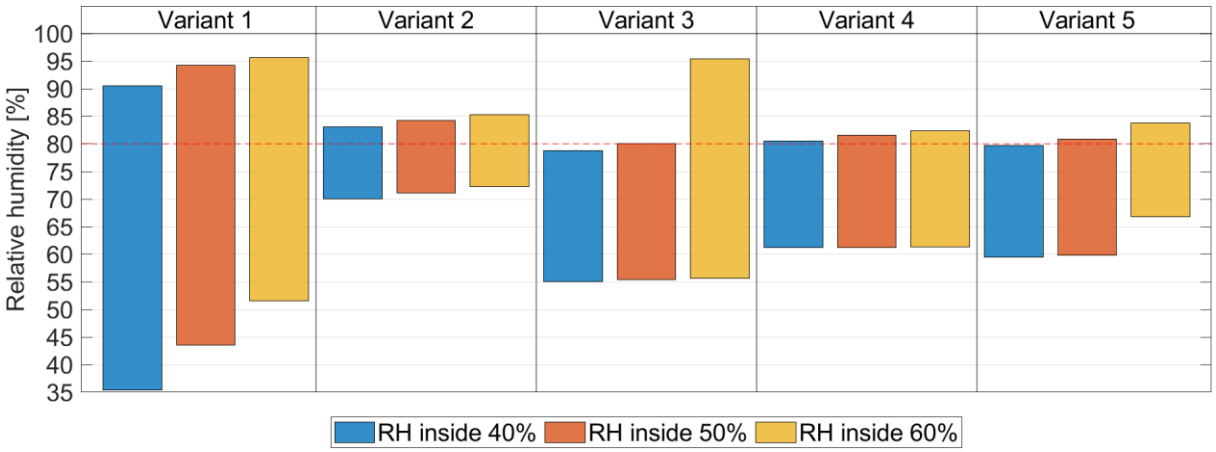

Figure 4: Influence of the internal humidity, relative humidity range behind the insulation for different variants: Variant 1 (no vapour retarder), Variant 2 (constant s_d-value), Variant 3 (variable s_d-value, Curve 1), Variant 4 (variable s_d-value, Curve 2), Variant 5 (variable s_d-value, Curve 3)

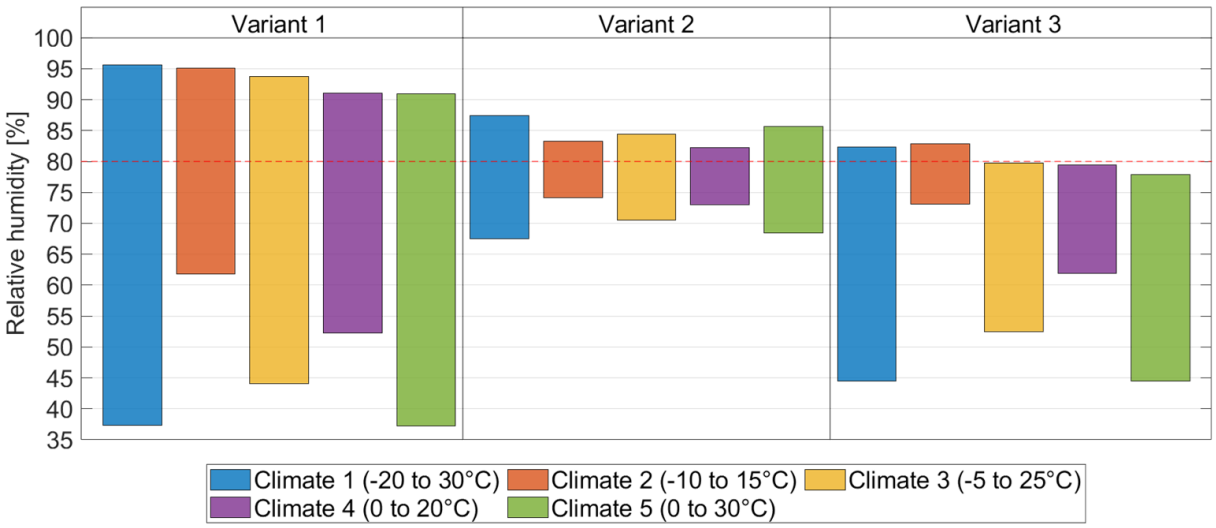

Figure 5: Influence of the external temperature, relative humidity range behind the insulation for different variants: Variant 1 (no vapour retarder), Variant 2 (constant s_d-value), Variant 3 (variable s_d-value)

adaptive vapour retarder (Variant 3) performs generally better relative to the constant-s_d-solution (Variant 2). In Climate 1 (characterized by cold winters), the strong moisture diffusion from the internal side during the cold season leads however to maximal relative humidity behind the insulation exceeding 80% even with the application of a variable vapour retarder. Moreover, in certain climates, the duration of the drying period may be insufficient for holding the relative humidity below the threshold value of 80%. This is the case of Climate 2, where the summer temperature remains below 15°C with little drying potential toward the indoor air. As a consequence, critical values of relative humidity behind the insulation are reached.

The results underscore the significance of a prolonged summer period in mitigating relative humidity within the wall. Climates 3, 4, and 5 experience temperatures above 0°C for over 250 days annually, ensuring adequate drying duration, thereby preventing maximal relative humidity behind the insulation from reaching the critical 80% threshold. Although the drying potential in Climate 3 and 4 is smaller than in Climate 1, in the former cases lower relative humidity behind the insulation is reached due to the reduced moisture diffusion from the indoor air during the cold season. Uncritical conditions are observed in climates characterized by mild winters and warm summers (Climate 5), which is consistent with theoretical expectations.

Influence of the insulation thickness

The relative humidity behind the insulation is clearly influenced by the temperature distribution within the wall, which in turn is impacted by the insulation thickness. A thicker insulation results in lower wall temperatures, consequently increasing the relative humidity behind the insulation. To investigate the impact of the insulation thickness, this parameter is varied between 2.5 cm and 10 cm. For each thickness, the former three variants are investigated: no vapour retarder, vapour retarder with constant s_d-value of 20 m, and variable vapour retarder (Curve 1, Figure 3).

As illustrated in Figure 6, increasing the insulation thickness leads to higher relative humidity behind it. Under the considered boundary conditions, with insulation thickness of 7.5 cm or more, the maximal relative humidity behind the insulation remains above 80%, even with variable vapour retarders. Equally, thicker insulation results in lower temperatures behind the insulation, potentially inducing freeze-thaw cycles which are a major cause of damage for construction materials.

For walls with 2.5 cm insulation, the internal surface temperature drops to 17.5°C, with thermal comfort related issues. Furthermore, the U-value of the wall with 2.5 cm insulation is twice higher as the one obtained with 10 cm insulation, leading to consequently higher thermal losses. To strike a balance between thermal comfort, energy efficiency, construction durability and moisture related issued, the system featuring 5 cm insulation is selected as the optimal option.

Influence of the wall thickness

In this stage, the influence of the bearing wall thickness on the relative humidity behind the insulation is investigated. Different wall thicknesses between 20 cm and 50 cm are examined.

Increasing the thickness of the brick wall leads to a reduction of the maximum relative humidity behind the insulation (Figure 7). This reduction demonstrates a linear trend within the

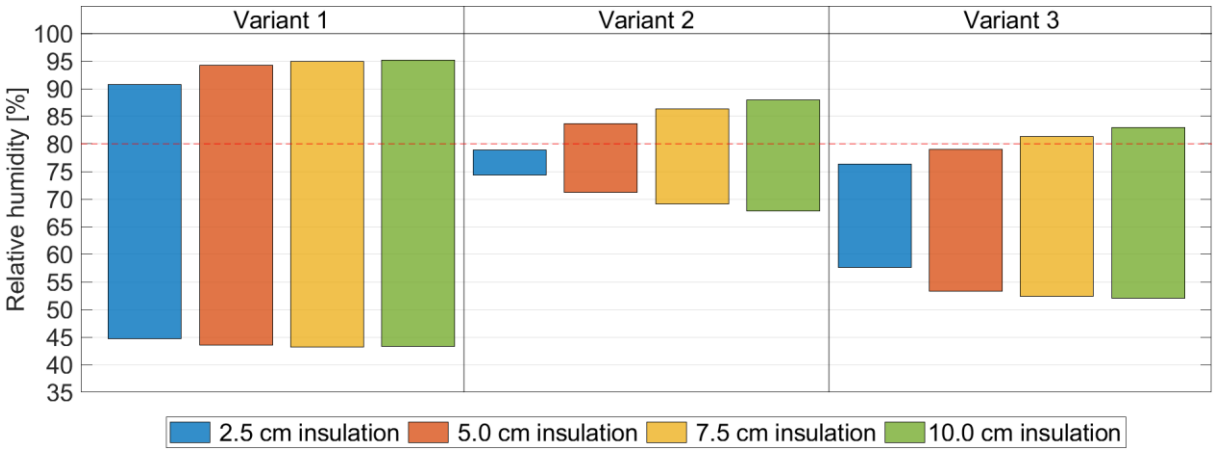

Figure 6: Influence of the insulation thickness, relative humidity range behind the insulation for different variants: Variant 1 (no vapour retarder), Variant 2 (constant sd-value), Variant 3 (variable sd-value)

investigated range of wall thicknesses (20 cm to 50 cm) and is more pronounced in models featuring a vapour retarder, particularly in case of a moisture-variable s_d-value. Comparing the thickest and thinnest walls, the variation in maximum relative humidity behind the insulation amounts to 2% for the model lacking a vapour retarder, 3% in the model with a constant vapour retarder, and 8% in the model with a variable vapour retarder.

In constructions designed to enhance internal drying processes (e.g., those without a vapour retarder or incorporating a moisture-adaptive vapour retarder), an increase in wall thickness correlates with decreased fluctuations in relative humidity behind the insulation across seasons. This phenomenon is associated with reduced annual temperature variations.

Comparison between simplified and realistic weather data

In the previous stages, outside boundary conditions were simplified to a sinusoidal temperature function and constant relative humidity. Real weather conditions, involving daily variations in temperature and humidity, as well as solar radiation, and wind-driven rain, represent a more complex scenario which require further investigation. Real-world weather dynamics can either increase or reduce relative humidity within the wall, contingent upon seasonal variations and wall orientation. Initially, the simulation considers realistic external temperatures while maintaining a constant external relative humidity of 80%. Next, both external temperature and relative humidity are adjusted based on the realistic weather data. In the subsequent iteration, realistic boundary conditions are extended by solar radiation on a north oriented and a south oriented wall, representing a worst-case and a best-case scenario, respectively. Finally, the

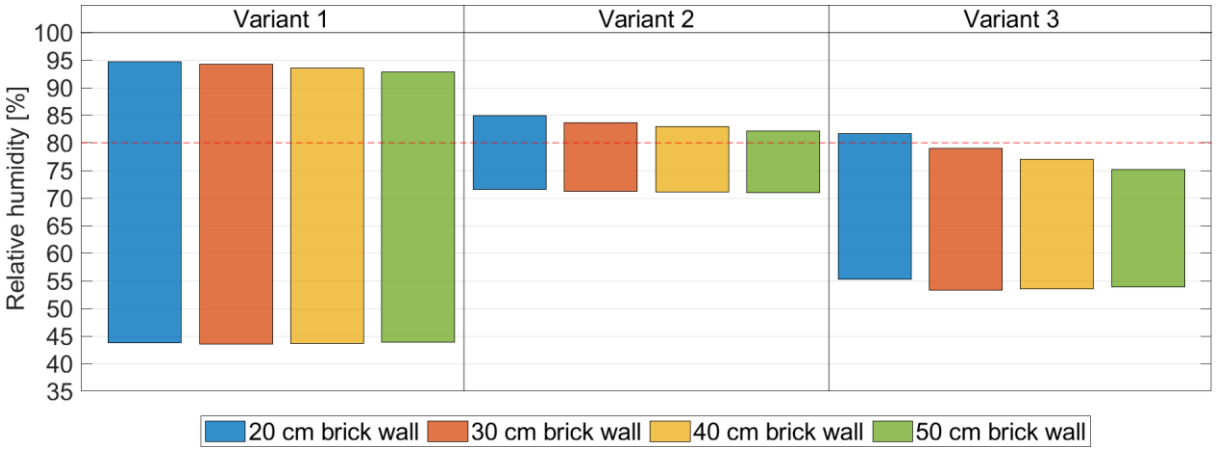

Figure 7: Influence of the wall thickness, relative humidity range behind the insulation for different variants: Variant 1 (no vapour retarder), Variant 2 (constant sd-value), Variant 3 (variable sd-value)

Figure 8: Realistic weather data, relative humidity range behind the insulation for different variants: Variant 1 (no vapour retarder), Variant 2 (constant s_d-value), Variant 3 (variable s_d-value)

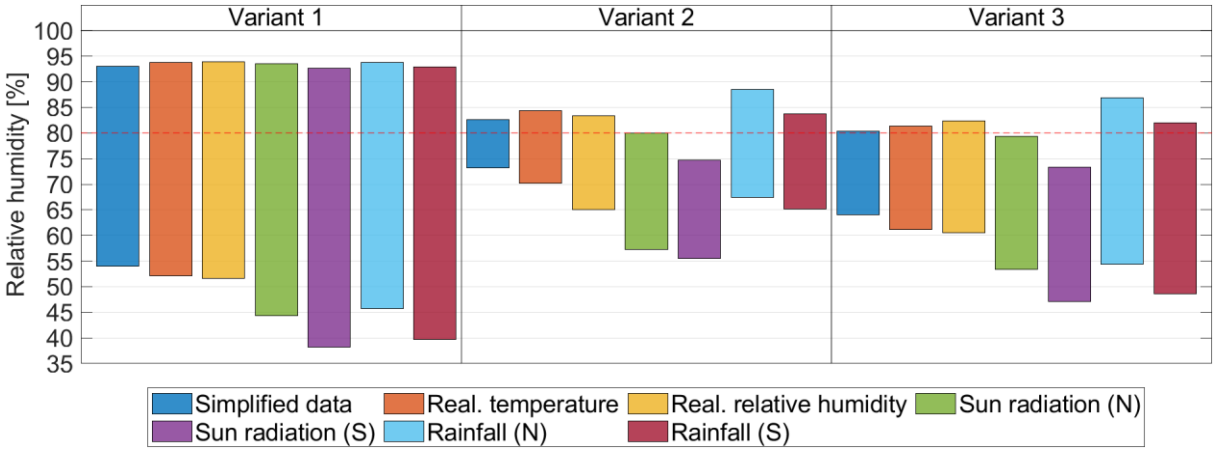

aforementioned climate dataset is completed to incorporate wind-driven rain, again considering both north and south wall orientation. The climate data used for simulation are sourced from the *Delphin* database (location: Munich, Germany).

As shown in Figure 8, real outside temperatures, characterized by high fluctuations, return higher relative humidity values compared to those obtained under simplified boundary conditions. The discrepancy between results is more pronounced for models featuring vapour retarders, particularly those with constant s_d-values. Likewise, fluctuations in outside humidity throughout the year worsen humidity levels. In models without a vapour retarder or featuring a moisture-dependent one, relative humidity within the insulation exhibits a broader range between minimum and maximum values.

Results from models incorporating solar radiation demonstrate a noteworthy reduction in humidity levels in both north- and south-facing walls. Solar radiation alone facilitates more robust drying, yet fails to block moisture accumulation during winter. Consequently, optimal outcomes are attained in models integrating both solar radiation and a vapour retarder. For instance, relative humidity in south-facing walls can be decreased by up to 21% with the application of a vapour retarder featuring a variable s_d-value. While reductions in north-facing walls are comparatively smaller, they remain significant (at the level of 15%). Given that solar radiation diminishes moisture within the wall, results from these simulations consistently yield lower values of relative humidity than those under simplified boundary conditions.

Wind-driven rain boosts moisture access from the exterior of the wall. As constant vapour retarders (Variant 2, Figure 8) inhibit inward drying, walls featuring them exhibit higher humidity levels than those observed for moisture adaptive vapour retarders (Variant 3, Figure 8). Results suggest however, that absence of rain protection invariably results in wall dampness and relative humidity exceeding 80%. Proper rain protection measures, as application of external plaster or hydrophobic coatings are therefore essential when applying internal insulation.

Conclusion

This study shows that in the investigated internal insulation system vapour retarders contribute at consistently reducing the relative humidity behind the insulation, relative to the values observed for the diffusion open system. Moisture adaptive vapour retarders perform generally better than constant vapour retarders, underscoring the importance of further developing this solution.

The selection of the s_d-curve significantly influences relative humidity behind the insulation and must be carefully tailored to specific boundary conditions. In this respect, the application of paint-coating based vapour retarders can be advantageous relative to standard membrane-based vapour retarders, due to an expected better adaptability of the s_d-curve.

Of utmost importance in designing moisture adaptive vapour retarders is the expected magnitude and variability of the indoor relative humidity. Results suggest that for an expected constant internal relative humidity, an s_d-curve characterized by a steep transition from the low to the high relative humidity region offers optimal performance. Conversely, in scenarios with significant relative humidity fluctuations, a less steep s_d-curve is preferable to avoid extreme peaks of relative humidity behind the insulation.

Irrespective of the external temperature fluctuation, vapour retarders play a crucial role, with moisture-dependent variants yielding superior outcomes. Relative humidity behind the insulation is influenced not only by wetting but also by drying periods, presenting challenges in climates with fresh/mild summers or very cold winters.

Insulation layers exceeding 5 cm pose a risk of elevated relative humidity behind the insulation and subsequent condensation. In such cases, a moisture-dependent vapour retarder visibly reduces maximum relative humidity behind the insulation, effectively preventing mould growth.

While the insulation thickness remains the primary impact factor, wall thickness also plays a significant role on the vapour retarder performance. Thicker walls mitigate relative humidity fluctuations within insulation throughout the year, and can thus be considered less critical as thinner walls.

Realistic whether data, as wind-driven rain and solar radiation, as well as the wall orientation must be taken into account to properly design the insulation system and the vapour retarder. In particular it is extremely important to ensure adequate protection from wind-driven rain, which can induce relevant moisture absorption from the external surface of the wall. Therefore, in the further course of the research, the impact of applying external rain protection solutions (external plastering, hydrophobic treatments) will be investigated.

Future research will moreover address the design of airtight connections (e.g., connections with windows and doors) and impact of possible discontinuities or damages in the vapour retarder (e.g., if holes are drilled into the wall).

Acknowledgement

The authors wish to acknowledge the financial support from the Austrian Research Promotion Agency (FFG), project: Thesis, FO999901743.

Die Ausschreibung „Technologien und Innovationen für die klimaneutrale Stadt“ ist Teil des FTI-Schwerpunkts „Klimaneutrale Stadt“ des Bundesministeriums für Klimaschutz, Umwelt, Energie, Mobilität Innovation und Technologie (BMK). Die Abwicklung erfolgt im Auftrag des BMK durch die Österreichische Forschungsförderungsgesellschaft (FFG) gemeinsam mit der Austria Wirtschaftsservice Gesellschaft mbH (AWS).

References

Delphin. (2024). Simulation program for the calculation of coupled heat, moisture, air, pollutant, and salt transport. https://bauklimatik-dresden.de/delphin/

Knarud JI, Geving S, Kvande T. (2021). Moisture performance of interior insulated brick wall segments subjected to wet ting and drying – A laboratory investigation. Building and Environment. 188:107488.

Künzel HM. (1999). Flexible vapour control solves moisture problems of building assemblies - smart retarder to replace the conventional PE-film. J. Therm. Envelope Build. Sci. 23(1):95–102.

Picard E, Gerard JF, Espuche E. (2008). Water transport properties of polyamide 6 based nanocomposites prepared by melt blending: On the importance of the clay dispersion state on the water transport properties at high water activity. J. Memb. Sci. 313:284–295.

Vereecken E, Van Gelder L, Janssen H, Roels S. (2015) Interior insulation for wall retrofitting - A probabilistic analysis of energy savings and hygrothermal risks. Energy Build. 89:231–244.

Hens H. (2007). Building Physis - Heat, Air and Moisture. Fundamentals and Engineering Methods with Examples and Exercises. Ernst & Sohn, Berlin, Germany

BauSIM 2024 in Wien
23. September – 26. September

Combined web-based and BIM tool plugin toolchain to support data exchange during BIM2SIM workflows

Josef Miller[1], Alexandra Jäger[2], Georg Fröch[1], Rainer Pfluger[1], Philipp Zech[2], Martin Hauer[1,3]

[1]University of Innsbruck, Unit of Material Technology

[2]University of Innsbruck, Department of Computer Science

[3]Bartenbach GmbH

Abstract

Early optimization minimizes the energy loads and thus reduces the buildings energy demand. However, model-driven simulation and optimization in the early planning phases poses several challenges, like responsibility for parameter values, exchange format and exchange requirements. In a BIM2BEM (Building Information Modelling to Building Energy Modeling) workflow, the simulation tool sets the requirements for the exchange. Properties must be defined, mapped between different tools, and then imported in such a way that they can be used on both sides. However, mostly there is a lack of information for a simulation workflow, because of missing data and problems with interoperability. Furthermore, the question of the responsibility of simulations, i.e. the input data used for the simulation, has not been clarified. As part of BIM2BEM-Flow a combined “web-based and BIM tool plugin” toolchain was developed to support all involved stakeholders in the organization and management of exchange requirements between BIM and external simulation tools. The tools are designed to define and manage parameters, coordinate exchange requirements between BIM and simulation tools and facilitate full implementation in BIM. The parameters are already defined in such a way that they contain all the necessary information for a BIM2BEM workflow. The results of the BIM2BEM-Flow project are presented in the following article.

Introduction

Based on the data of the Global Alliance for Buildings and Construction (GlobalABC), the construction sector demands 36% of the global energy and is responsible for 39% of the global CO_2 emissions. Compared to the planning and construction phase, the building operation is responsible for up to 78% of the life cycle costs, which can be attributed to the energy demand and the CO_2 emissions during the operation. For buildings with a high CO_2 footprint the emissions over the life cycle can be up to 30% for the operation phase and for buildings with a low CO_2 footprint even up to 50% (DGNB, 2021).

As is known from the MacLeamy curve, early changes in a construction project have a high impact, while costs are low, where during the progress of the project changes become more cost-intensive and complicated. Already within the early design stage, building shape, orientation, location, and window-wall-ratio (WWR) can be optimized, and by that the necessary demand for technical regulation (heating, cooling, air conditioning, artificial light and shading systems, controlling) can be reduced to a minimum (Porsani et al., 2021). Consequently, the costs and CO2 emissions during operation can be minimized (Figure 1).

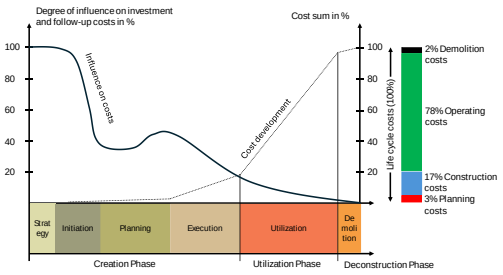

Figure 1: m.o.o.con Lifecycle Costs (Herzog, 2018)

The Architecture, Engineering, Construction and Operating (AECO) industry is still struggling to implement a continuous integral approach. Beside the just mentioned shortcomings, further challenges can be mentioned:

Giel & Issa, 2016; Alfred Olatunji & Alfred, 2011

- The fragmented contract structures of the AECO industry complicate the digital process
- Varying BIM expertise between the project participants
- Lack of BIM expertise among building operators and owners

Ullah et al., 2019:

- BIM benefits are not outweighing the implementation costs
- Legal issues
- Data ownership issues
- Complexity of the BIM Model
- Interoperability between software tools
- Lack of standardized tools and protocols

Gao et al., 2019; Barlish & Sullivan, 2012; Azhar & Asce, 2011; Habibi, 2017; Pereira et al., 2021:

- Reliable data during early design stage
- Question of responsibility for simulation
- Time pressure within the project
- Investment driven motivation instead of ecological

have to be considered in near future to overcome current obstacles.

With Building Information Modelling (BIM), a concept was introduced to ease an integral project approach. But the idea of all project information in a digital model, usable by every stakeholder of the project, has encountered some challenges and limitations. BIM tools are providing mostly all the necessary capabilities of enriching the 3D model with all necessary metadata. But first, required data must be compiled, based on the requirements of exchange, this information must be enriched within the BIM tool and then be exported without losing information, in a way that it is usable in other tools (e.g. energy simulation). Although gbXML and IFC are the most established open BIM formats for building data exchange with building energy tools, they still do not sufficiency meet the requirements of the complexity of AECO elements, like curved geometry (gbXML) or lack of depth in the representation of HVAC systems (IFC). While the IFC can be enriched with additional information and definitions, the risk of incompatibility with other tools rises. Also, most of the building energy simulation tools do not support IFC, which is another challenge to solve (Porsani et al., 2021). An additional issue is the definition of the level of detail for the parameter exchange (e.g. heat transfer coefficient), depending on the planning phase and thus the requirement for result accuracy. This kind of information is probably unknown within the early design stage, but early design optimization is crucial for later building energy performance. So, who takes the responsibility for early design calculation assumptions? Gathering all this exchange requirements and transferring them into the BIM tool is complex and time consuming.

Methodology

Semantics, crucial in linguistics and logic, focuses on the meaning of language and symbols, ensuring consistent interpretation (Ciccozzi et al., 2023). In the context of BIM and BEM, semantics plays a vital role in data exchange interoperability. It helps in correctly interpreting data across different systems, enhancing efficiency and accuracy, promoting a unified interpretation of meaning for improved interoperability in BIM and BEM. ClosedBIM API-based simulations, such as Revit - Sefaira or a web-based platform (Biblus, BIMServer.center, BIMcollab), are more consistent and less error-prone, while in the openBIM approach the use of the models and the associated information for further simulations is problematic. Although a closedBIM approach has the advantage of solving some interoperability problems through a standardized development environment, it is stiff and inflexible and forces project participants to work with a specific software. Also, it excludes companies if the software or know-how is not available, which is why the openBIM approach is being pursued in project XY. Although Revit is used as a BIM tool, the focus is on the correct mapping and transfer of information using IFC.

To support openBIM data exchange and enable BIM2BEM workflows as well as tackle the challenges presented in the previous section, the following requirements have to be fulfilled:

R1. Central management of parameters, which are part of exchange requirements. Enabling the definition of mapping information for different BIM and SIM tools for those parameters. Enabling the definition of default values for parameters, to facilitate meaningful simulations even in the early planning stages.

R2. A simplified interface to these parameters that makes it possible to coordinate the parameters required for a specific BIM2BEM workflow.

R3. Offering BIM tool support to enhance a model with the parameters necessary for a certain BIM2SIM workflow and offer mapping-empowered export capability.

R4. The ability to compare different simulation results in a standardized view to support a comparison of variants

With BIMQ (BIMQ, 2024), there is a solution for organizing the exchange of requirements and transferring them to the BIM tool, but there is no link for mapping this information from the requirements database to the BIM tool and to the simulation tool. With the freeBIM Merkmalserver (freeBIM, 2024), a database was developed to

provide component information in a standardized way. However, there is no functional connection to tools from the AECO industry.

To fulfill R1-R4, a combined web-based and BIM tool plugin toolchain has been developed in the research project BIM2BEM-Flow (Figure 2). It consists of two web-based applications as well as a BIM tool plugin. For this project, we've decided to focus on the BIM tool Revit, since it is one of the most widely used tools in the industry and, most importantly, used by our project partner. The first application, a web-based UI to create and coordinate parameters on a database, fulfills R1. Parameters can be defined in so-called libraries, by the usual attributes name, id, unit and description. Additionally, mapping information for specific simulation and BIM tools can be defined. Currently, this encapsulates different names for the same parameter in different tools but will be extended in future versions to include conversion logic for different units. Different sets of default values for parameters can be created and managed. This work is based on the preliminary work of the freeBIM Merkmalserver (Fröch et al., 2019)

To tackle R2, the Parameter Workflow Manager (PWM) application has been created. Workflows as a concept of defining specific exchange scenarios and responsibilities can be managed. By defining which BIM and which SIM tool is used in a workflow, relevant parameters on the database can be inferred. To enrich a BIM model with these relevant parameters and support the actual mapping to a format that can be usable with the chosen simulation tool (R3), a BIM tool plugin, called Revit Workflow Manager (RWM), has been created. With this information all necessary exchange requirements, based on a specific exchange scenario (workflow), can be created, including already all necessary information for the exchange. As an open exchange format, IFC was used for data exchange between BIM and SIM tool.

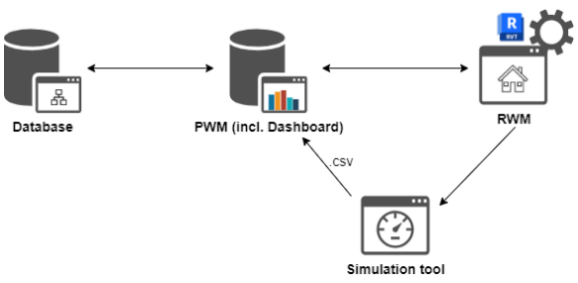

Figure 2: BIM2BEM-Flow software components and relations between them

Parameter database application (R1)

The core of the concept lies in the correct definition of the properties and the mapping of those to BIM and SIM tools. Parameters as well as necessary adjacent entities (named groups of parameters, associations of groups to construction components) can be created and managed in a library. In general, a parameter is described by its name, id, description, unit, value type (list or single), data type, phase and use case (Fröch et al., 2019). Furthermore, it is possible to create default value sets to define default values for parameters. Most importantly, however, flexible mapping functionality is offered for all core entities. Properties and sets can be mapped to any target tool in any version. Naturally, mapping capability is also offered for construction components, to enable the match of construction components on the database to whatever structure and terminology is supported within a BIM tool (Figure 3). Whether there exists a mapping for a certain BIM and SIM tool, as well as parameter meta data, builds the base for the parameter inference mechanism of a workflow.

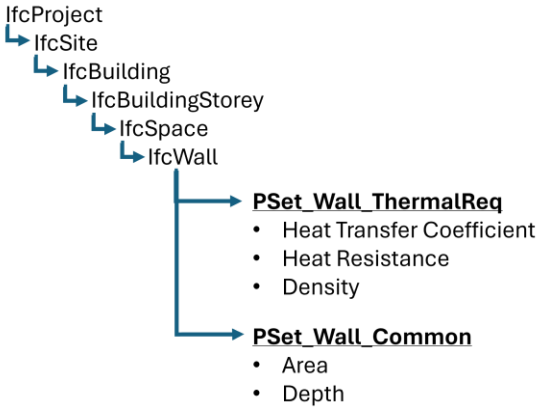

Figure 3: Example of an IFC based construction component hierarchy, where the parameter group 'PSet_Wall_ThermalReq' is associated with the construction component 'IfcWall'. The group contains three parameters

PWM – Project Workflow Manager (R2)

The PWM helps to define, document, and encapsulate the necessary BIM process information. It represents the collaborative nature of BIM by allowing the definition of projects where multiple stakeholder companies cooperate in. The respective project manager of each company determines which employees of the company are working on the project. For every project, multiple workflows can be defined, as multiple different kinds of simulations are likely to occur (e.g. energy, day, and artificial light, etc.). Workflows are a key concept in our approach to enable a BIM2SIM process: they model the exchange requirements within a project.

A workflow contains the following data:

- Which company and employee are responsible on the BIM side, which tool is used
- Which company and employee are responsible on the SIM side, which tool is used
- Meta data: phase, use case (e.g. artificial light simulation, heating energy demand, etc.), parameter library and optional an initial default set on the database

This data is used to determine what parameters on the database are relevant for which workflow, using inference. This algorithm works the following way: parameters of the chosen parameter library are relevant, if:

1. They contain a mapping to the simulation tool,
2. They are relevant for the chosen use case.

RWM – Revit Workflow Manager (R3)

The RWM is a Revit plugin, and it implements three main features:

- Coordination of workflows and import of parameters from the database associated with those workflows
- Special support for editing those parameters
- Export a valid IFC file for a workflow, containing all relevant parameters, mapping the parameters from their BIM form to their SIM form

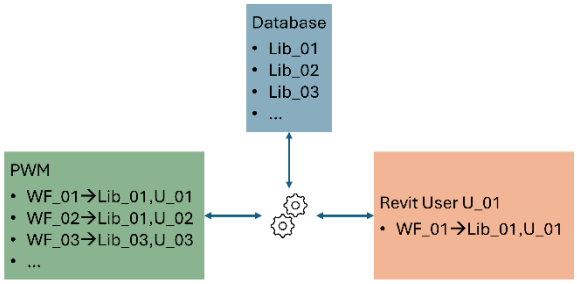

Figure 4: Schematic example of workflow and library coordination between database, PWM and RWM

The RWM plugin is connected to the PWM, which is in turn connected to the database. To import a workflow into a model, the user must be authenticated first, and is then only able to edit workflows that they are responsible for as defined on the PWM. Considering the possibility that one or more workflows may have already been imported, each containing overlapping information, such as the shared usage of an exemplary window parameter PSI_WindowWall, the RWM consistently conducts check-ups and seeks user confirmation prior to any overwriting action (Figure 4).

After a workflow has been imported, the values of its associated parameters can be set. This is currently implemented by a user choosing a workflow and a certain construction component, which will then display a list of parameters that are associated with this workflow and the chosen construction component. All values can either be set manually, or a default value set, which must be part of the library chosen for the workflow, can be used. This choice of value is stored in the background and can later be exported as a documentation IFC file of the model. Responsibility is clearly defined and documented by assigning workflows and the associated data to the logged-in user and change documentation. The user can choose to store the changes either simply for the chosen construction component, or, in order to increase usability, apply the made changes to a subset or all other construction components of the same type.

Once all parameters associated with a workflow have been set, it is possible to export the model in the context of a workflow. This export triggers the mapping logic and exports the workflow parameters in a way that the chosen SIM tool can understand them. To help the user determine whether all parameters necessary for a workflow have been set, a simple version of a model checker has been implemented. Even though buildingSMART is offering a new validation format with the Information Delivery Specifications (IDS) (buildingSMART, 2024), it was decided to check the completeness of information within the Revit plugin, besides ensuring the correct export of the IFC, it also ensures the completeness of the BIM model itself.

Mapping

The BIM2BEM-Flow Project is focusing on energy simulations (heating, cooling, day- and artificial light). In this kind of BIM2BEM scenario, the exchange requirements, in this case represented by the necessary parameters, are determined by the simulation tool. Revit2DALEC (Miller et al., 2020) for example has an IFC import, for geometrical and alphanumerical information. To import the IFC, the parameters must be arranged within the IFC, as expected by the importer of Revit2DALEC. Revit2DALEC for example works with IFC entities (IfcProject, IfcBuilding, IfcSpace, IfcWindow, IfcCurtainWall, IfcWall, IfcRoof and IfcSlab). Within these entities parameters are arranged in property sets. Property name and property set name, and the unit must be correct.

Oftentimes, the parameters needed for a SIM tool are slightly different from their form in the BIM tool. These differences can be as simple as a different name (e.g "Frame_PSI" in the BIM tool to "F_PSI" in the SIM tool), or a bit more complex like a different unit. In order to run a valid BIM2BEM workflow, it is necessary to map parameters from their BIM form to their BEM form.

This mapping information is stored centrally with all other parameter data within the database application. For every parameter, parameter group or even construction component, it is possible to define a mapping for certain parameter attributes like name in a certain tool (e.g. Database – HeatTransferCoefficient → Revit Wall – ThermalTransmissionCoefficient → IFC IfcWall – U-Value).

Revit-specific mapping process

The creation of parameters, mapping those parameters into Revit and the IFC export, several steps are necessary and depending on the requirements of Revit and the IFC. Within the database, parameters are assigned to parameter groups which are assigned to building elements. To ensure the import of parameters into Revit and the correct export into IFC, these building elements are connected to an IFC entity within the database. While importing the workflow and creating the parameters, the Revit IFC import options are queried (Figure 5). Within these options IFC entities are assigned to Revit building elements (*BuiltInCategories).* From the IFC entity assignment on the database and the Revit IFC import options, the import mapping is generated.

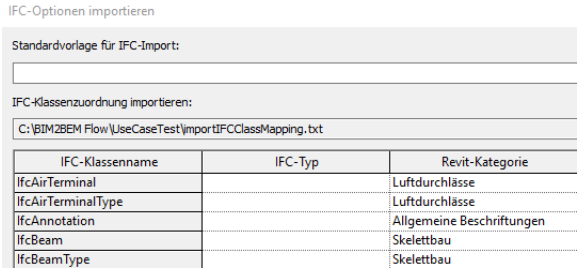

Figure 5: Revit Import Options

The correct export of the IFC is ensured by two parts. The first part is the Revit IFC export options, where the Revit building elements (*BuiltInCategories)* are assigned to IFC entities. The second part is the automatic creation of an IFC *export user defined property sets* text file, which is used for the definition of a specific IFC export (Figure 6). Inside this file property sets are named and assigned to IFC entities - as described before, IFC entities are connected to Revit *BuildInCategories* by the Revit IFC export options. This property sets are defined by mapping the Revit parameters to the export parameters and the definition of a data type.

```
# User Defined PropertySet Definition File
#
# Format:
#    PropertySet:      <Pset Name>     I[nstance]/T[ype]       <element list separated by ','>
#       <Property Name 1>       <Data type>     <[opt] Revit parameter name, if different from IFC>
#       <Property Name 2>       <Data type>     <[opt] Revit parameter name, if different from IFC>
#       ...
#
# Data types supported: Area, Boolean, ClassificationReference, ColorTemperature, Count, Currency,
#       ElectricalCurrent, ElectricalEfficacy, ElectricalVoltage, Force, Frequency, Identifier,
#       Illuminance, Integer, Label, Length, Logical, LuminousFlux, LuminousIntensity,
#       NormalisedRatio, PlaneAngle, PositiveLength, PositivePlaneAngle, PositiveRatio, Power,
#       Pressure, Ratio, Real, Text, ThermalTransmittance, ThermodynamicTemperature, Volume,
#       VolumetricFlowRate
#
#PropertySet:   PSet_Wall       T       IfcWall
#       NominalLength   Real    Revit.NominalLength
#       NominalWidth    Real    Revit.NominalWidth
#       NominalHeight   Real    Revit.Type.NominalHeight
```

Figure 6: Revit IFC Export mapping definition file

The procedure explained above, ensures a correct mapping from Revit parameter import to IFC export. The correct creation of parameters within Revit is secured by the definition of a measurement unit and the parameter type (type or instance) within the database. Also, if an existing Revit parameter should be used, the mapping must be registered on the database as well.

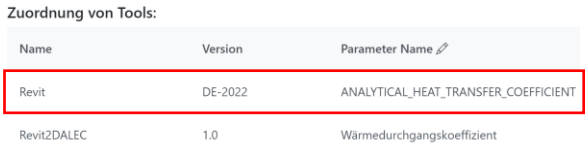

Figure 7: database parameter: U-Wert

The measurement unit is connected to the Revit API *ParameterType.* Using the Revit API, the database parameter can now be created within Revit. First, if a Revit parameter mapping exists (as shown in Figure 7, red box), there is no need for a new creation. Secondly, each parameter is tested if it already does exist from an earlier implementation. Thirdly, if the parameter does not exist, it is implemented as a new parameter. A parameter can be created as an instance or type parameter being an attribute of the *BindingMap* class. Also, the *BuildInParameterGroup* must be instantiated. Instantiation of the *Definition* attribute creates a *SharedParameter* (Figure 8), which is defined by *Name, ParameterGroup* and *ParameterType* (Figure 9). *ParameterType* is connected to the measurement unit of the database, and the parameter type of the database is connected to the *BindingMap* Instantiation as Instance or Type.

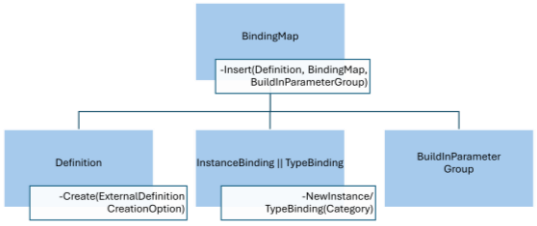

Figure 8: Revit API BindingMap Class

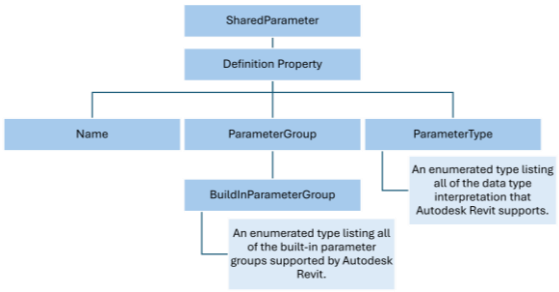

Figure 9: Revit API SharedParameter Class

Layer, roles and workflow

One big challenge for a consistent digital planning process is the question of responsibility in the planning process. During the early design process, parameter values for energy simulations must be assigned based on an assumption. During this phase, it would be important to provide the architects with simple results from thermal simulations for a comparison of variants. Because of unclear responsibility, early design optimizations are not performed. BIM2BEM-Flow has several layers to clarify and document responsibilities (Figure 10).

Each of this layer has a clear assignment of a role and will be introduced in the following sections. It is not intended to define new roles or change existing roles in BIM projects. Role names can be seen as a suggestion.

PWM Layer

At the beginning of a project, a *BIM Project Manager* (BPM) must define all stakeholders or participating companies of the project. These specifications can also be adapted during the course of the project. A company is assigned with a *Project Manager* (PM). The PM lists all employees (E) involved in the project. Within the next steps a workflow must be defined. A workflow within this project is a clear definition of a use case scenario. A workflow defines the used BIM tool and the used simulation tool, as also the responsible company and person on both sites. Furthermore, the phase of a workflow must be set (e.g. concept design, detail design, final design) and the use case as well (e.g. artificial light simulation, heating energy demand). The parameter library must also be assigned; assigning a default value set is optional. New workflows are created by the requirements of the exchange. Each workflow is assigned with a PM. The PM than has the responsibility of defining those workflows.

Database Layer

Since a workflow is a definition of an exchange between BIM and simulation, it is dependent on a defined mapping from the database. For this reason, a *database Manager* (YM) is indispensable. There can be several YM, since a lot of workflows with different demands can be required. The YM creates new parameter libraries, which contain all information for an exchange from BIM to simulation. Also default value sets can be created and assigned to the mapping parameters. All this information is managed by the YM. Created libraries can be reused in another project, as this work is the most time consuming and the function of a workflow deeply relies on a correct mapping.

RWM Layer

As described, within a workflow a BIM and a simulation responsibility are ensured. The BIM person is responsible for the digital model and can only access workflows, which he/she has rights to. Importing those workflows into the BIM tool, parameters and defined default values are authorized by the database.

IFC Layer

Values not taken from default sets are documented during export, through a parameter documentation IFC file. With this concept, responsibilities are clearly defined and documented. This approach should encourage architects to run early design optimizations, since model enrichment and default parameter values are defined within the database.

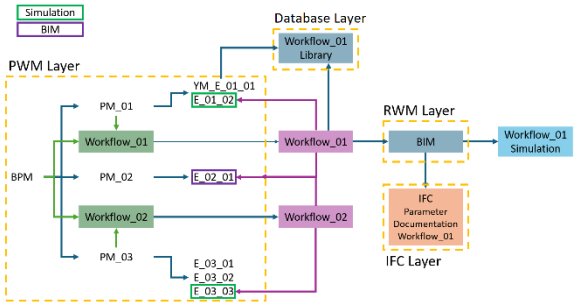

Figure 10: Layers and roles

Simulation

With the given workflow concept a specific IFC is exported. It contains all the necessary information to run the simulation for a specific use case. Within the BIM2BEM-Flow project two proof of concepts with Revit2DALEC (Werner et al., 2017), (Miller et al., 2020) and PHPP have been performed. The Revit2DALEC tool has a direct IFC import. PHPP works with an IFC converter bim2PH, converting the IFC into a PHPP readable format (*.ppp). Other tools like IDA ICE, EnergyPlus, DesignBuilder do not support a complete IFC import. Converting to IDF is essential for EnergyPlus compatibility. IDA ICE has an IFC import, but only for geometrical information (Porsani et al., 2021). Most import

options basically focus on geometrical information, not parameter data.

Dashboard (R4)

Mapping and the associated clean transfer of information from the BIM model to the simulation are the basis for running reliable simulations. However, complicated simulation tools and the associated complex presentation and interpretation of results pose fundamental challenges for architects, especially in the early planning phase, and prevent an early comparison of variants. As part of the BIM2BEM-Flow project, an energy dashboard is being developed that assigns the results to predefined result parameters on the basis of a CSV file and simplifies a comparison of variants by simply displaying the excess or shortfall. However, the energy target corridor dashboard is still under development and will not be completed until the end of the project in October 2024.

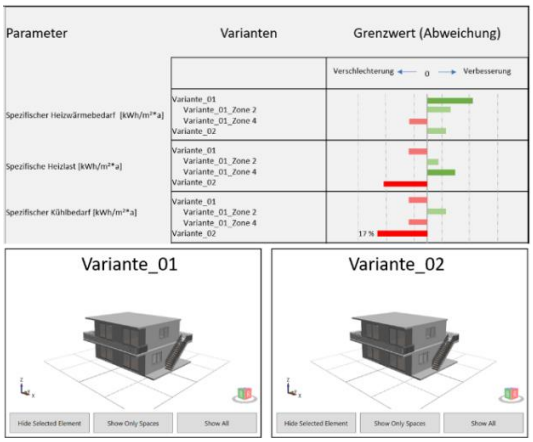

Figure 11: Conceptual design of the dashboard

Discussion and Summary

With the given 4-layer concept of database, PWM, RWM and IFC, a tool chain has been developed to organize and structure exchange parameters from the project beginning to the design phase. Due to the nature of the tool chain, roles are assigned and create a clear hierarchy of responsibilities. The tool structure supports these roles and responsibilities with automation where possible, as well as a consistent documentation of information. At every stage of the project workflow, it is possible to trace the origin of information and identify the creator. Creating a library for the first time can be time consuming and challenging. To facilitate this process, a CSV import has been implemented. Additionally, architects don't need to be concerned about model enrichment and parameter values, since it is all organized on the database before, and relevant parameters can be inferred via the PWM. With this approach various challenges identified in BIM literature (Gao et al., 2019), (Sattler et al., 2019), (Kamel & Memari, 2019), (Farzaneh et al., 2019) are addressed. The biggest shortcoming on parameter servers or parameter standardization efforts lies in the usability of the information. Often, parameter servers end up as unused information storages. Even if the server can import its data into BIM, no clear benefit for an openBIM simulation workflow is given, since no mapping information is defined. In the end, the digital model ends up as a data storage with a lot of unusable information. With a consistent definition of parameter mappings from server parameter to BIM parameter and further on to simulation parameter and the definition of all essential information during this process, a source is created, which is of benefit during the entire process. The project is still at an early stage of development and requires further testing and development. Further investigation is required to determine how information can be transformed during changing project phases without losing data and, at the same time, maintaining consistency. Although the tool chain is supporting and encouraging project stakeholders to aim for early design optimization, the challenges from the simulation tool side are still hard to overcome. Since it cannot be expected in near future, that software developers adapt to open standards as an import format, converting mechanisms must be developed to connect BIM and simulation tools in an openBIM approach.

Acknowledgement

The work presented is based on the project results of BIM2BEM-Flow funded by Austrian Research Promotion Agency (FFG) started on November 2021, ongoing.

References

Alfred Olatunji, O., & Alfred, O. (2011). A preliminary review on the legal implications of BIM and model ownership. In *www.itcon.org-Journal of Information Technology in Construction* (Vol. 16). http://www.itcon.org/2011/40

Azhar, S., & Asce, A. M. (2011). Building Information Modeling (BIM): Trends, Benefits, Risks, and Challenges for the AEC Industry. In *Leadership Manage. Eng* (Vol. 11, Issue 3).

Barlish, K., & Sullivan, K. (2012). How to measure the benefits of BIM - A case study approach. *Automation in Construction*, *24*, 149–159. https://doi.org/10.1016/j.autcon.2012.02.008

BIMQ. (2024). *BIMQ*. https://www.bimq.de/en/

buildingSMART. (2024). *IDS - Information Delivery Specification*. https://www.buildingsmart.org/what-is-information-delivery-specification-ids/

Ciccozzi, A., de Rubeis, T., Paoletti, D., & Ambrosini, D. (2023). BIM to BEM for Building Energy Analysis: A Review of Interoperability Strategies. *Energies*, *16*(23), 1–45. https://doi.org/10.3390/en16237845

DGNB. (2021). *BENCHMARKS FÜR DIE TREIBHAUSGASEMISSIONEN DER GEBÄUDEKONSTRUKTION Ergebnisse einer Studie mit 50 Gebäuden*. https://www.bundesregierung.de/breg-de/themen/klimaschutz/klimaschutzgesetz-2021-1913672

Farzaneh, A., Monfet, D., & Forgues, D. (2019). Review of using Building Information Modeling for building energy modeling during the design process. In *Journal of Building Engineering* (Vol. 23, pp. 127–135). Elsevier Ltd. https://doi.org/10.1016/j.jobe.2019.01.029

freeBIM. (2024). *freeBIM Merkmalserver*. Https://Db.Freebim.at/#/Login.

Fröch, G., Gächter, W., Tautschnig, A., & Al., E. (2019). Merkmalserver im Open-BIM-Prozess. *Bautechnik*, *96*, 338–347.

Gao, H., Koch, C., & Wu, Y. (2019). Building information modelling based building energy modelling: A review. In *Applied Energy* (Vol. 238, pp. 320–343). Elsevier Ltd. https://doi.org/10.1016/j.apenergy.2019.01.032

Giel, B., & Issa, R. R. A. (2013). Quality and maturity of BIM implementation in the AECO industry. *Applied Mechanics and Materials*, *438–439*, 1621–1627. https://doi.org/10.4028/www.scientific.net/AMM.438-439.1621

Giel, B., & Issa, R. R. A. (2016). Framework for Evaluating the BIM Competencies of Facility Owners. *Journal of Management in Engineering*, *32*(1). https://doi.org/10.1061/(asce)me.1943-5479.0000378

Habibi, S. (2017). The promise of BIM for improving building performance. *Energy and Buildings*, *153*, 525–548. https://doi.org/10.1016/j.enbuild.2017.08.009

Herzog, B. (2018). *Den Lebenszyklus im Blick Nachhaltiges und vorausschauendes Handeln als Managemententscheidung zur Steigerung der Wertschöpfung und der Kostensicherheit. Lebenszyklus Themendossier*. www.moo-con.com

Kamel, E., & Memari, A. M. (2019). Review of BIM's application in energy simulation: Tools, issues, and solutions. In *Automation in Construction* (Vol. 97, pp. 164–180). Elsevier B.V. https://doi.org/10.1016/j.autcon.2018.11.008

Miller, J., Moser, F., Stumpf, J. P., & Pfluger, R. (2020). REVIT2DALEC : A BIM2BEM COMBINED THERMAL AND DAY- AND ARTIFICIAL LIGHT ENERGY CALCULATION WITH DALEC USING THE MVD. *BauSIM 2020*.

Pereira, V., Santos, J., Leite, F., & Escórcio, P. (2021). Using BIM to improve building energy efficiency – A scientometric and systematic review. *Energy and Buildings*, *250*. https://doi.org/10.1016/j.enbuild.2021.111292

Porsani, G. B., Del Valle De Lersundi, K., Sánchez-Ostiz Gutiérrez, A., & Fernández Bandera, C. (2021). *Interoperability between Building Information Modelling (BIM) and Building Energy Model (BEM)*. https://doi.org/10.3390/app11052167/Academic

Sattler, L., Lamouri, S., Pellerin, R., & Maigne, T. (2019). Interoperability aims in building information modeling exchanges: A literature review. *IFAC-PapersOnLine*, *52*(13), 271–276. https://doi.org/10.1016/j.ifacol.2019.11.180

Ullah, K., Lill, I., & Witt, E. (2019). An overview of BIM adoption in the construction industry: Benefits and barriers. In *Emerald Reach Proceedings Series* (Vol. 2, pp. 297–303). Emerald Group Holdings Ltd. https://doi.org/10.1108/S2516-285320190000002052

Werner, M., Geisler-Moroder, D., Junghans, B., Ebert, O., & Feist, W. (2017). DALEC–a novel web tool for integrated day- and artificial light and energy calculation. In *Journal of Building Performance Simulation* (Vol. 10, Issue 3). https://doi.org/10.1080/19401493.2016.1259352

BauSIM 2024 in Wien
23. September – 26. September

Konzepte zur BIM-basierten Konfiguration und Parametrisierung von Beleuchtungssteuerungen abgeleitet aus Literatur- und Marktrecherchen

Sascha Hammes[1], Philipp Zech[2], David Geisler-Moroder[1], Emanuele Goldin[2], Rainer Pfluger[1]

1 Universität Innsbruck, Arbeitsbereich Energieeffizientes Bauen, Österreich, sascha.hammes@uibk.ac.at, david.geisler-moroder@uibk.ac.at, rainer.pfluger@uibk.ac.at

2 Universität Innsbruck, Institut für Informatik, Österreich, philipp.zech@uibk.ac.at, emanuele.goldin@uibk.ac.at

Kurzfassung

Building Information Modeling (BIM) nimmt eine immer wichtigere Rolle bei der Planung und Umsetzung von Beleuchtungssystemen ein. Steuerungen haben einen großen Einfluss auf die lichttechnischen Leistungsindikatoren Komfort, Energie und Gesundheit und erfordern eine Zusammenführung von BIM-Methoden mit den technischen Planungsverfahren. Aktuell sind jedoch Modellierungsaspekte von Steuerungen nur unvollständig in BIM abgedeckt. Basierend auf einer umfassenden Literatur- und Marktrecherche erfolgte eine Bedarfsermittlung notwendiger Anforderungen an unterstützende Werkzeuge für die BIM-basierte Planung und Umsetzung von Beleuchtungssteuerungen. In diesem Beitrag werden die wichtigsten Ergebnisse aus der Anforderungsermittlung vorgestellt sowie des daraus entwickelten BIM-Modellierungsrahmen, welcher als Revit Plug-in konzipiert ist. Ergebnisse einer Prototypbewertung unter Verwendung des Technologieakzeptanzmodells zeigen, dass die geschaffenen Vorteile einer BIM-basierten Konfiguration und Parametrisierung von Steuerungen bauseitige Aufwände reduzieren und die Systemperformanz verbessern können.

Abstract

Building Information Modelling (BIM) is playing an increasingly key role in the planning and implementation of lighting systems. Controls have a major influence on the lighting performance indicators of comfort, energy and health and require the integration of BIM methods with technical planning processes. Currently, however, modelling aspects of controls are only incompletely covered in BIM. Based on comprehensive literature and market research, the requirements for support tools for the BIM-based planning and implementation of lighting control systems were determined. This article presents the most important results from the requirements analysis and the BIM modelling framework developed from it, which is designed as a Revit plug-in. The results of a prototype evaluation using the technology acceptance model show that the advantages created by BIM-based configuration and parameterisation of control systems reduce on-site effort and improve system performance.

Einleitung

Limitierungen durch derzeitige Bauabläufe

Leistungsindikatoren von Beleuchtungssystemen umfassen insbesondere Aspekte des Komforts (visuell wie thermisch), des elektrischen Energiebedarfs und der biologischen Wirksamkeit (Bellia et al., 2020; Dubois & Blomsterberg, 2011; Haq et al., 2014; Webb, 2006). Mit dem Gewerk Beleuchtung sind zudem starke Wechselwirkungen mit anderen Gewerken verbunden. So ist der Kunstlichteinsatz direkt mit der Kühllast verbunden (Ryckaert et al., 2010). Der Tageslichteintrag ist gekoppelt mit thermischen Energieeinflüssen (Ouf, Park & Gunay, 2021), die sich wiederum auf Planung und Betrieb der Gewerke Heizung und Kühlung auswirken. Das Gewerk Beleuchtung stellt somit ein interdisziplinäres Feld mit Schnittstellen zu verschiedenen Gewerken dar.

Die Steuerung erweist sich dabei sowohl im gewerkspezifischen als auch im integralen Kontext als wesentlich für die Erzielung gewünschter Systemperformanzen (Aghemo et al., 2013; Dubois & Blomsterberg, 2011; Chew et al., 2017; Haq et al., 2014). Lösungsansätze zum Design von Beleuchtungssystemen können zwischen angedachten Konzepten der frühen Planungsphase und der tatsächlichen Umsetzung stark differieren, da die Beteiligten der Gebäudeplanung oftmals über ein tieferes Hintergrundwissen zum

Gebäudegesamtkonzept verfügen, während der Handlungs- und Entscheidungsraum für ausführende Unternehmen primär aus den verfügbaren Informationen der Ausschreibung resultiert.

Während der Gebäudeentwurfsphase sind zudem meist kaum bis keine Informationen über das energetisch relevante Nutzerverhalten verfügbar, sodass pauschalisierte Annahmen über nutzerbezogene Steuerungsparameter erfolgen. Steuerungen, die auf nicht auf realistische Nutzungsszenarien hin optimiert und getestet werden, münden oftmals in einem energetisch ineffizienten Betrieb. Das Resultat dessen sind Abweichungen zwischen Planung und Betrieb, sogenannte Energy Performance Gaps (EPG), mit der Unbestimmtheit des Nutzerverhaltens als Ursache (van Dronkelaar et al., 2016; Yoshino, Hong & Nord, 2017). Post-Occupancy Evaluations (POE) stellen für das Facility Management (FM) eine Plattform dar, um nach Inbetriebnahme Verbesserungsmaßnahmen abzuleiten und die Performanz von technischen Gebäudeanlagen zu verbessern (Preiser, 1995). POE bieten zudem für die Planung die Möglichkeit, Erfahrungen aus umgesetzten Projekten in künftigen Projekten zu berücksichtigen.

Mit der Gebäudeinbetriebnahme und vor allem mit Ablauf der Gewährleistungsfrist verringern sich die Möglichkeiten ausführende Unternehmen ohne hohen Kosteneinsatz für nachträgliche Steuerungsadaptionen heranzuziehen. Ein breites Portfolio an proprietären Systemen mit verschiedenen Entwicklungsumgebungen, wie es derzeit am Markt verfügbar ist, kann kaum vollumfänglich durch das FM bedient werden. Aufgrund der verschiedenen mitwirkenden Parteien fehlt zudem oftmals die Transparenz hinsichtlich der Zuordnung von Verantwortlichkeiten und deren Rückverfolgung bei etwaigem Fehlverhalten. Nachträgliche Steuerungsanpassungen zur Verbesserung der Systemperformanzen oder um Änderungen der Raumnutzung zu berücksichtigen, münden daher meist in kostenintensive Adaptionstätigkeiten durch das FM oder werden in vielen Fällen aufgrund des hohen Aufwandes gänzlich unterlassen. Unzureichende Transparenz und begrenzte Möglichkeiten des kollaborativen Steuerungsdesigns können zudem zu Fehlern und eingeschränkter Funktionalität führen, wodurch in weiterer Folge energetische Potentiale und auch der Nutzerkomfort beschränkt werden (Fedoruk et al., 2015). So zählt nach Fedoruk et al. (2015) auch der Informationsverlust mit zu den wesentlichen Ursachen des EPGs. Um Einschränkungen hinsichtlich Transparenz, Systeminteroperabilität und Funktionalität zu vermeiden und den Erfolg lichttechnischer Leistungsindikatoren sicherzustellen, bedarf es geeigneter Werkzeuge und Methoden, welche die unterschiedlichen Interessen der einzelnen Beteiligten im Steuerungsdesignprozess zusammenführen.

Potentiale für das Steuerungsdesign mit BIM

Building Information Modelling (BIM) bietet die Möglichkeit eines effizienten und gemeinsamen Informationsmanagements zwischen den einzelnen Interessensgruppen und über die einzelnen Phasen des Lebenszyklus eines Gebäudes hinweg (Andriamamonjy et al., 2019). Aus der Projektierung in BIM resultieren digitale Abbildungen der Bauobjekte, welche durch geometrische, topologische und technisch-funktionale Informationen und weitere Metadaten angereichert sind und als Datengrundlage dienen (Alonso et al., 2019; Andriamamonjy et al., 2019). BIM bietet somit grundsätzlich die Plattform für das kollaborative Steuerungsdesign.

Digitale Zwillinge beschreiben ein aufsteigendes Konzept für die Echtzeit-Überwachung, -Steuerung und -Optimierung von cyberphysikalischen Anlagen. Speziell im Steuerungsbereich und damit verbundenen Logikimplementierungen, Erfolgskontrollen und nachträglichen Systemadaptierungen bieten Digitale Zwillinge enormes Potential zur Steigerung der Energieeffizienz und des Komforts. BIM als Kollaborationsplattform kann somit den erforderlichen modellbasierten Informationsaustausch zwischen den Projektbeteiligten schaffen und die Grundlage für den Digitalen Zwilling liefern. Aktuell sind Modellierungsaspekte der Gebäudesteuerungen nur unvollständig in BIM abgedeckt und spiegeln sich daher im Digitalen Zwilling nicht wider.

Aufbau und Zielsetzung

In dieser Studie wird daher ein erweiterter BIM-Modellierungsrahmen für die Erfassung statischer und dynamischer Informationen der Gebäudeautomation am Beispiel der Gewerke Tages- und Kunstlicht eingeführt. Die resultierende Verankerung der Steuerung im BIM (und damit dem Digitalen Zwilling) eröffnet die Möglichkeit gewerkeübergreifende Konzepte zu verfolgen und die Steuerung vorab zu konfigurieren, zu parametrisieren und zu testen. Die Akzeptanz und damit der Erfolg von solch stark anwendungsbezogenen Werkzeugen ist maßgeblich davon abhängig, wie gut die Anforderungen der einzelnen Beteiligten der Baubranche in der Funktionalität abgebildet werden. Aus diesem Grund setzt die Entwicklung des vorgestellten BIM-Modellierungsrahmen auf umfangreiche Literatur- und Marktrecherchen, um notwendige Anforderungen zu identifizieren. Die Ergebnisse werden im nachfolgenden Kapitel beschrieben sowie die darauf aufbauende Ausgestaltung der Werkzeuge zur Steuerungsentwicklung in BIM.

Die Ergebnisanalyse einer Prototypbewertung unter Verwendung des Technologieakzeptanzmodells (TAM) zeigt, dass das entwickelte Lösungskonzept den Gebäudebetrieb verbessert und bauseitige Aufwände reduzieren kann. BIM-basiertes Datenmanagement, Modell-Repositories, eine Loslösung von Steuerungssoftware und Steuerungshardware durch Middleware sowie domänenspezifische Sprachen (DSL) bilden das Rückgrat des Konzepts und werden durch Elemente der Simulation und Datenanalyse erweitert, um ein Framework für alle Projektbeteiligten zu schaffen. Neben einer abschließenden Zusammenfassung der Ergebnisse, wird der vorgestellte Modellierungsrahmen für die Steuerungskonfiguration in den Kontext aktueller Forschungstrends gesetzt.

Methodik

Literaturrecherche

Eine systematische Literaturrecherche wurde genutzt, um einen Überblick zur BIM-Integration von Beleuchtungssteuerungen zu schaffen und Ansätze und Herausforderungen zu identifizieren, die bei der Ausarbeitung des Modellierungsrahmens berücksichtigt werden sollen (Hauer, et al., 2024). Nach mehrfacher Filterung auf thematische Relevanz wurden 57 Publikationen im Kontext BIM-basiertes Steuerungsdesign bewertet, synthetisiert und daraus Evidenzen abgeleitet. Gestützt wurde dies durch ergänzende bibliometrische Analysen. Die Ergebnisse führen auf, dass Beleuchtungssteuerungen in BIM und Anwendungen Digitaler Zwillinge derzeit stark unterrepräsentiert sind (Hauer, et al., 2024). Trotz derzeitiger Standardisierungsansätze sind wesentliche Herausforderungen in Inkonsistenzen und semantischen Lücken proprietärer Informationsmodelle zu identifizieren, die u.a. einen erforderlichen Informationsaustausch zwischen den einzelnen Disziplinen limitieren (Andriamamonjy et al., 2019). Bestehende Forschungsaktivitäten zur Steuerungsintegration in BIM konzentrieren sich primär auf die Gewerke Heizung, Lüftung und Klima (HLK). Hierzu zählen bspw. die Arbeiten von Sporr et al., die HLK-Steuerungen in BIM implementieren, basierend auf Gebäude- und Komponentendaten, die aus IFC-Daten (Industry Foundation Classes) abgeleitet wurden (Sporr, Zucker & Hofmann, 2019; Sporr, Zucker & Hofmann, 2020). Nytsch-Geusen et al. (2019) bieten eine simulationsbasierte Methode zur Gestaltung und Bewertung von HLK-Steuerungsstrategien, welche auf einer bidirektionalen Kopplung von Modelica und dem openHAB aufbauen. Dies erlaubt in der Entwurfsphase Gebäudesteuerungen unter Einbezug dynamischen Systemverhaltens zu testen, zu verbessern und bei Erfolg auf das reale Gebäude zu übertragen. Adaptierungen für andere Gewerke bestehen derzeit nicht.

Marktbefragung

Ergänzend zur Literaturrecherche erfolgte eine umfangreiche Marktbefragung zu den Themen BIM und Arbeitsprozesse in der Planung und Entwicklung von Steuerungen jeweils mit Fokus Beleuchtung. Da Anforderungen an einen BIM-Modellierungsrahmen für Beleuchtungssteuerungen zwischen den einzelnen Beteiligten abweichen können, wurden die Fragen auf involvierte Zielgruppen zugeschnitten und getrennt bewertet. Zu den Gruppen zählen das produzierende Gewerbe, der Handel, die Fachplanung, ausführende Unternehmen, Forschung und Entwicklung (F&E), GebäudeeigentümerInnen sowie das Facility Management (FM). Die Umfrage erfolgte online auf freiwilliger Basis, ohne Erhebung persönlicher Daten und ohne Vergütung. Umgesetzt wurde die Befragung mit der Online-Applikation LimeSurvey (Version 3.22.4+200212). Verbreitet wurde die Umfrage insbesondere über Newsletter und Mailing-Listen von branchenspezifischen nationalen und internationalen Kanälen. Hierzu zählen u.a. die lichttechnischen Gesellschaften LiTG/LTG und CIE, die Internationale Energie Agentur (IEA, Tasks 70 – Low Carbon, High Comfort Integrated Lighting) sowie verschiedene FM-Verbände. Durchführungszeitraum war März bis September 2023. 272 Rückläufe sind insgesamt eingegangen (8 davon aus korrespondieren Workshops). Davon wurden 165 als verwertbar eingestuft, da diese mindestens drei der acht Fragegruppen vollständig beantwortet haben (2 inhaltliche und den demografischen Themenbereich). Abbildung 1 zeigt eine Aufteilung der Rückmeldungen nach Zielgruppen. Die Zielgruppen F&E, Fachplanung, produzierendes Gewerbe und FM sind am stärksten vertreten. Teilnahmen aus den Bereichen Handel, ausführende Unternehmen und BaueigentümerInnen sind nicht ausreichend vertreten und werden daher für Fragestellungen, die nicht unabhängig der Zielgruppe sind, vernachlässigt. Eine geografische Verortung der Rückläufe zeigt, dass Teilnehmende hauptsächlich im Arbeitsstandort Österreich tätig sind (50,91%, Abb. 2).

Die Umfrage führt auf, dass die Relevanz von BIM mit der Reichweite des Tätigkeitsbereichs steigt, d.h. für international operierende Unternehmen hat BIM eine höhere Relevanz als für regional agierende Unternehmen (Abb. 3), was sich mit aktueller Literatur deckt, die eine breite BIM-Nutzung insbesondere in Großunternehmen verortet (Hong et al., 2018). Die Ergebnisse zeigen weiter bei Kleinst- und Kleinunternehmen einen umgedrehten Effekt, d.h. eine hohe Relevanz bei regionalen Tätigkeiten. Zu

berücksichtigen bei den Umfrageergebnissen ist, dass in manchen Ländern rechtliche Vorgaben zur BIM-Nutzung bestehen.

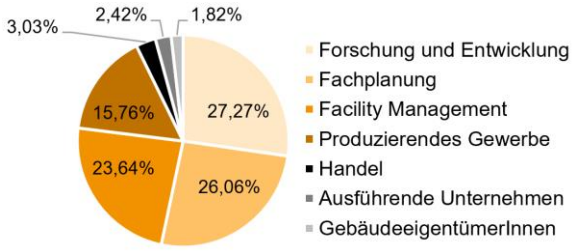

Abbildung 1: Verteilung der 165 verwertbaren Rückläufe der Marktbefragung nach Zielgruppe.

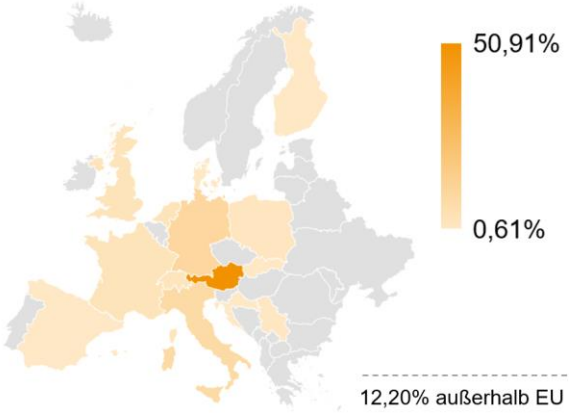

Abbildung 2: Übersicht zur geografischen Verteilung der Rückmeldungen, dargestellt über die Farbskala, mit Bezug zu Minimal- und Maximalwerten.

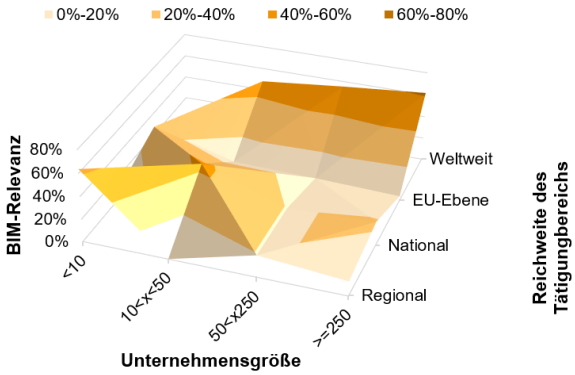

Abbildung 3: Relevanz von BIM im Arbeitsalltag in Abhängigkeit von Reichweite des Tätigungsbereichs und Unternehmensgröße.

Bei Teilnehmenden, in denen BIM von Relevanz ist (71,79% aller Teilnehmenden), werden die Gründe bessere Transparenz im Bauprozess (25,29%), effizientere Planung, bzw. Aspekte einer bauphasenübergreifenden Produktüberwachung für das produzierende Gewerbe (25,29%), Wettbewerbsrelevanz (20,11%) und Qualitätssicherung (20,11%) als Gründe der BIM-Nutzung genannt. 5,75% konnten dies nicht beurteilen und 3,45% nannten andere Gründe.

Die im Studienkontext angestrebte BIM-basierte Vorkonfiguration von Steuerungen wird von 46,81% der Teilnehmenden als relevant eingestuft, 23,40% sehen hierin keine Relevanz und 29,79% konnten das Thema nicht zuordnen. Nach Inbetriebnahme werden von den Gruppen F&E und Fachplanung insbesondere Nachhaltigkeitsaspekte, Fehlersuche und Energiemanagement sowie Datenmonitoring als relevante Aspekte genannt (Abb. 4). Dies ist wesentlich für die Transformation des Systemabbilds hin zum Digitalen Zwilling.

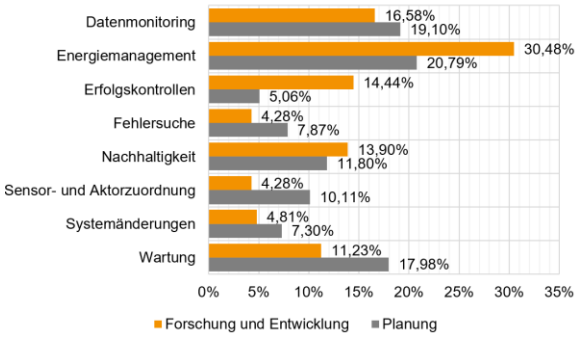

Abbildung 4: Verteilung relevanter Aspekte nach Inbetriebnahme, erhoben über die Marktumfrage (Frage nur für aufgeführten Zielgruppen verfügbar; Art der Frage: Ranking, max. 3 Antworten).

Herausforderungen, die im Zusammenhang einer breiten BIM-Nutzung stehen und damit Anforderungen darstellen, die der angestrebte Entwicklungsrahmen sicherstellen muss, sind insbesondere Zeitaufwände und mangelndes Fachpersonal. Zudem können unzureichende Schnittstellen als Herausforderung einer breiten BIM-Nutzung herausgestellt werden (vgl. Tab. 1).

Das FM übernimmt nach Inbetriebnahme die Rolle der Ansprechperson für NutzerInnen hinsichtlich der Sicherstellung von Komfortansprüchen und stellt im Weiteren durch Wartung und Verbesserung technischer Gebäudekomponenten einen effizienten und stabilen Gebäudebetrieb sicher. Die Steuerung stellt dabei eine Schlüsselkomponente dar, um diese Ziele sicherzustellen. Es ergibt sich jedoch, dass nur 18,75% der Teilnehmenden aus der Gruppe FM tatsächlich bei aufkommendem Bedarf und außerhalb von Gewährleistungsfristen Steuerungen eigenständig adaptieren. 71,88% führen keine Änderungen durch (9,37% konnten dies nicht beurteilen), obwohl etwa die Hälfte dies gerne würde (47,82% der Befragten, 8,7% konnten dies nicht beurteilen und 43,48% haben nicht den Wunsch zur eigenständigen Anpassung von Steuerungen). Als Ursachen werden insbesondere technische Herausforderungen und unzureichendes technisches Hintergrundwissen gleichermaßen identifiziert (Abb. 5).

Tabelle 1: Herausforderungen einer BIM-Nutzung in Abhängigkeit der Zielgruppen, erhoben über die Marktumfrage (Frage nur für aufgeführte Zielgruppen verfügbar; Art der Frage: Ranking, max. 3 Antworten).

	Planung	Industrie	F&E
Einschränkungen der Funktionalität	7,62%	9,65%	8,51%
Fehlende Schnittstellen	17,14%	14,04%	12,77%
Keine Nachfrage	0,48%	6,14%	6,38%
Kostenaufwände	13,81%	14,91%	9,04%
Lücken im Systemablauf	10,95%	7,89%	12,23%
Unzureichendes Fachpersonal	20,00%	21,93%	23,41%
Komponenten-abbildung	9,05%	8,77%	13,83%
Zeitaufwände	20,95%	16,67%	13,83%

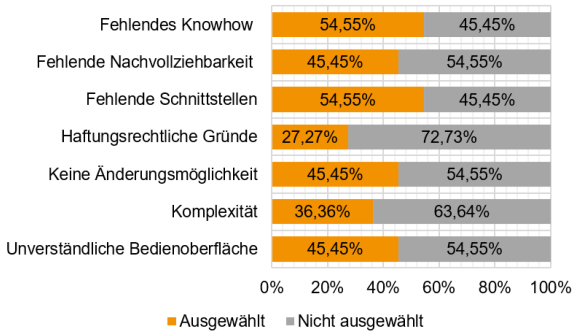

Abbildung 5: Verteilung der Ursachen, warum eigenständige Steuerungsanpassungen nicht erfolgen (Art der Frage: Mehrfachauswahl).

Erstellung von Steuerungstopologien in BIM

Als BIM-Software und als Ausgangslage für die Entwicklungen wird Revit von Autodesk herangezogen. Um darin Steuerungstypologien zu erstellen und Steuerungen zu konfigurieren, wurden zunächst geeignete Familienvorlagen für relevante Komponenten modelliert. Zu den Steuerungskomponenten zählen die physische Hardware der Steuerung sowie die Sensorik und Aktorik. Die Familienvorlagen definieren ihrerseits die Anforderungen an Entitäten, dass diese im geschaffenen Revit-Zusatzmodul als Steuerungskomponenten erfasst werden (DIN CEN/TS 17623, 2021 wurde berücksichtigt). Neben spezifischer Parameterdefinitionen einzelner Gerätetypen wurde eine allgemeingültige geometrische Vorlage für eine jede Steuerungskomponente geschaffen, um eine Konsistenz in der Syntax zu einer übergeordneten DSL (domain specific language) sicherzustellen. Die grafische DSL für Revit dient der Erweiterung von BIM um relevante Daten des Gewerks Steuerung. In einem ersten Schritt wurden runde Symbole für Sensoren, rechteckige Symbole für Aktoren und Rauten für die Steuerungshardware verwendet (vgl. Abb. 6 und Abb. 7). Diese können langfristig pro spezifische Instanz einer Familie durch technische Symbole ersetzt werden. Jede Komponente verfügt über eine einmalige Identifikationsnummer (ID). Zudem können die formulierten Familiendateien, analog zu anderen Familiendateien in BIM, um zusätzliche Eigenschaften erweitert werden, dass jede Steuerungskomponente über einen spezifischen Parametersatz verfügt. Hierzu zählen bspw. Versorgungsspannung, Protokoll, Leitungsanforderungen (u.a. Kabeltyp- und Querschnittsinformationen).

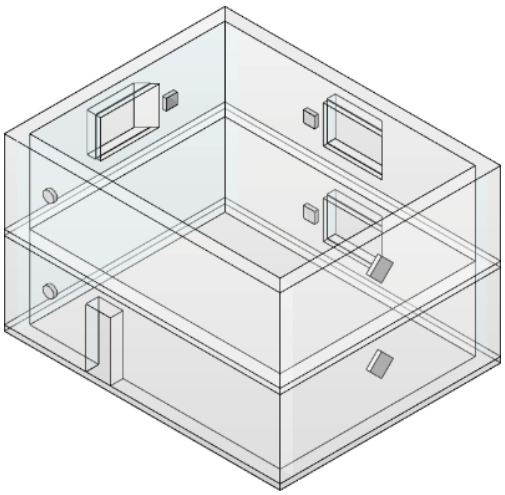

Abbildung 6: Darstellung eines nichtrealen Gebäudes erweitert um Steuerungshardware (Raute), Sensorik (kreisförmiges Symbol) sowie Aktorik (Quadrat).

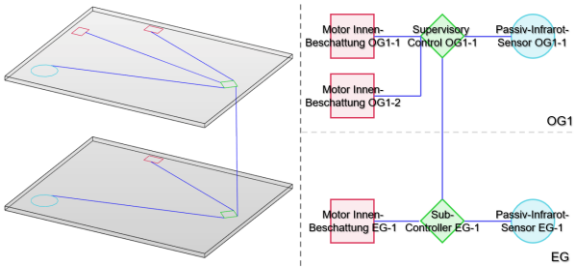

Abbildung 7: Darstellung der Verbindungen zwischen Sensorik, Aktorik und Steuerungsknoten im Gebäude mit ausgeblendeten Wänden (links) und als exemplarischer Topologie-Export (rechts).

Die Interaktionsmöglichkeiten des Revit Add-Ins sind gekoppelt an hinterlegte Eigenschaften der Unterkategorien der Steuerungskomponenten. Um die Steuerungstopologie im digitalen Gebäudemodell zu verankern, wurden im Add-In eine Reihe von Funktionen und Befehlen vorgesehen. Über die Option Komponenten importieren, soll der prinzipielle Produktaufruf erfolgen, die den Spezifika der Familienvorlagen folgen.

Anschließend werden die einzelnen Entitäten im digitalen Gebäudemodell entsprechend dem vorgesehenen Montageort platziert (Abb. 6). Über Aufruf des Befehls zur Erstellung der Topologie, können die einzelnen Komponenten miteinander verbunden werden, d.h. die Sensoren und Aktoren (bspw. Passiv-Infrarot-Sensor und Leuchte) werden einer Steuerung zugewiesen (Abb. 7). Der Einsatz von Sub-Controllern im Kontext einer Supervisory Control (übergeordneten Steuerlogik) ist mit dem Add-In möglich. Einzelne Topologie-Ansichten ermöglichen das Arbeiten auf Raum-, Etagen- oder Gebäudeebene, letzteres mit oder ohne Außenanlagen. Erstellte Topologien können als .dot-Datei exportiert werden. Exportierte Topologien ohne Gebäudemodell können mit GraphViz visualisiert werden (GraphViz, 2024). Um Darstellungen lesbar zu halten, können vor Export Verbindungen einzelner Steuerungsknoten in Gebäudeeinsichten ein- oder ausgeblendet werden (auf Raum-, Etagen- oder Gebäudeebene). So kann bspw. die Verbindungsstruktur zwischen den Steuerknoten für das gesamte Gebäude ausgegeben werden ohne Sensoren und Aktoren und für einzelne Raumbereiche die Verknüpfung der Sensoren und Aktoren mit der jeweiligen Steuerung. Für jede erstellte Verbindung werden Informationen über Quell- und Zielgerät in erweiterten Speichern hinterlegt, um die Erzeugung redundanter Verbindung zu unterbinden. Im Weiteren unterbinden integrierte Grundlogiken im Add-In die Verknüpfungen zwischen einzelnen Sensoren und Aktoren ohne Steuerungsbaustein, was Fehlern vorbeugen soll. Bestehen Steuerungen als Edge-Computing, bspw. integriert in der Aktorik (auch wenn dies nur die Erstellung einfacher Regelkreise umfasst), bedarf es der Platzierung eines weiteren Steuerungsknotens im Gebäudemodell. Dadurch soll ein Abbild der genutzten Steuerlogik im BIM gewährleistet werden. Ergänzende Aktualisierungsprogramme stellen die ordnungsgemäße Verwaltung von Geräten und Verbindungen sicher, was wiederum eine vollwertige Integration der entwickelten DSL im Revit-Ökosystem gewährleistet.

Die Steuerungslogik wird als Teil des BIM mit der textuellen DSL modelliert. Ausgehend davon werden Laufzeitartefakte erzeugt (Programmcode in Skriptsprache Lua und vergleichbare). Diese werden in Laufzeitumgebungen übertragen, welche je nach System und Protokoll entweder Inhalt der Middleware sind oder mit dieser kommunizieren. Die Middleware agiert als Kommunikationsschnittstelle zwischen Gebäudemodell mit Steuerungssoftware (und Logik) und der bauseitig vorhanden Steuerungshardware. Der Modellaustausch zwischen den Beteiligten im Bauprozess und im Betrieb folgt dem Herstellerneutralen IFC-Standard. Eine Übertragbarkeit des vorgestellten Konzepts auf die Steuerung anderer Gewerke ist möglich. Weitere Details zum Modellierungsrahmen in Zech et al. (2024).

Akzeptanzbewertung

Um den vorgestellten BIM-Modellierungsrahmen für Steuerungen auf Anwendbarkeit zu überprüfen und damit auch zu evaluieren, ob erhobene Anforderungen aus Markt- und Literaturrecherche sichergestellt sind, erfolgte die Durchführung eines Technologieakzeptanzmodells (TAM) nach Riemenschneider und Hardgrave (2001). Bewertet wurden 19 Rückmeldungen aus Planung (15) und F&E (4) insbesondere hinsichtlich subjektiver Empfindung zum Nutzen und zum Einarbeitungsaufwand sowie zur wahrgenommenen Benutzerfreundlichkeit und Nützlichkeit (Zech, et al., 2024).

Ergebnisanalyse und Diskussion

Die Relevanz des Informationsmanagements

Während bislang für die Gewerke Tages- und Kunstlicht meist nur Geometriedaten und Bauteileigenschaften in BIM verwaltet wurden, zielt die vorgestellte Entwicklung auf eine Erweiterung der BIM-Struktur, um eine ganzheitliche Spezifikation der Steuerung und deren Anwendbarkeit über alle Gebäudephasen sicherzustellen. Mit der Abbildung des Gewerks Steuerung und damit verbundener Betriebsdaten in BIM, wird die Transformation hin zum Digitalen Zwilling komplementiert. Erst dieser Schritt erlaubt eine umfängliche Evaluierung der Realsituation. Betriebsdaten können so vor dem Hintergrund der Steuerlogik bewertet werden. Dies stellt einen notwendigen Schritt dar, um Performance Gaps zu reduzieren, die aus oftmals unzureichenden Annahmen über das Nutzerverhalten im Zuge der Entwurfsphase resultieren. Die bauphasenübergreifende Abbildung von Energie- und Prozessdaten bietet in Kombination mit POE die Möglichkeit Potentiale zur Energiereduktion zu identifizieren (über die Markbefragung als relevant herausgestellt, vgl. Abb. 4). Darauf aufbauend können Maßnahmen abgeleitet werden, um Systemperformanzen technischer Anlagen zu verbessern und energetische Lücken zwischen Planung und Betrieb zu schließen. Dem FM bietet die Kopplung von Digitalem Zwilling und POE zudem Unterstützung in den Aufgabenfeldern Wartung und Instandhaltung. Gewonnene Erkenntnisse aus POEs können in die Planungsebene rückgeführt werden, um in künftigen Projekten das Risiko von EPGs zu reduzieren.

Die Überführung der Steuerungskonfiguration in die BIM-Ebene erlaubt zusätzliche Aspekte aus dem Gebäudemodell beim Steuerungsdesign zu

berücksichtigen, bspw. die Position von Arbeitsplätzen, was bessere Systemperformanzen verspricht. Mit der Trennung von Steuerungssoftware und -hardware durch Middleware und über Nutzung von APIs sowie Softwareanbindung an den Digitalen Zwilling soll zudem die Inbetriebnahme der Steuerung vor Ort automatisiert werden, was mit einer Reduktion bauseitiger Aufwände einhergehen kann. Auch Arbeitsaufwände für Planende im Kontext der Erstellung von Steuerungstopologien können durch das geschaffene Revit Add-In reduziert und vereinfacht werden, wodurch die wesentlich identifizierten Herausforderungen einer breiten BIM-Nutzung – fehlendes Fachpersonal und Zeitaufwände – angegangen werden. Auch nachträgliche Nutzungsänderungen können durch die zentrale Verwaltung von Steuerungsdaten ressourceneffizient berücksichtigt werden.

Integrale Systeme und IKT-Technologien

Gewerkeübergreifende Systeme können Vorteile für Energie und Komfort bieten. Deren Umsetzung geht jedoch auch mit höherer Systemkomplexität und damit Fehleranfälligkeit einher. Zudem scheitern integrale Systeme derzeit meist an unzureichender Interoperabilität und bestehenden Gewährleistungsgrenzen, dass deren Abbildung in BIM aktuell unvollständig ist. Erweiterungen der BIM-Struktur setzen daher auf eine ganzheitliche Spezifikation der Gebäudetechnik und Anwendbarkeit über alle Gebäudephasen. Die vorgestellte Lösung wurde generisch entwickelt, um eine Integration weiterer Gewerke sicherzustellen. Der vorgestellte Modellierungsrahmen soll einen Beitrag liefern, um bisherige technische Schranken zur Planung und Umsetzung integraler Systeme zu lösen und deren Potentiale abrufbar machen.

Proprietäre Systeme beschränken oftmals die Umsetzbarkeit von innovativen Konzepten aus der Informations- und Kommunikationstechnologie (IKT), bspw. von Anwendungen künstlicher Intelligenzen (Rocha et al., 2016). Durch die Trennung proprietärer Hardware und Ausgestaltung von Steuerungskonzepten sollen die Potentiale von IKT-Lösungen leichteren Einzug in die Praxis erhalten.

Transparenz und Akzeptanz

Als besonders wertvoll erweist sich die gemeinsame Anwenderschnittstelle in BIM zum Gewerk Steuerung und die damit verbundene Transparenz zwischen allen Beteiligten. Die Ergebnisse des TAMs führen eine starke Akzeptanz für den entwickelten BIM-basierten Modellierungsrahmen auf (Zech, et al. 2024).

Zusammenfassung

Die Übertragung des Gewerks Steuerung in das digitale Gebäudemodell schafft Transparenz zwischen den einzelnen Zielgruppen über alle Phasen des Lebenszyklus eines Bauprojekts hinweg. Zudem verspricht der entwickelte Modellierungsrahmen die Planung und Umsetzung von Beleuchtungssteuerungen zeit- und kosteneffizienter zu gestalten. Durch die Kopplung Digitaler Zwillinge mit POE wird die Möglichkeit eröffnet, um Steuerungen im Nachgang zu optimieren und somit nutzerbezogene Effekte des Lichts bestmöglich abzurufen. Eine Übertragbarkeit auf andere Gewerke ist über generische Ausgestaltungen gegeben. Durch die gemeinsame Anwenderschnittstelle kann die Umsetzung integraler Konzepte erleichtert werden, was Vorteile für Komfort und Energie verspricht.

Ausblick

Building Energy Performance Simulations (BEPS) bieten die Möglichkeit Gebäudesysteme vor und nach Inbetriebnahme energetisch und hinsichtlich von Komfortkriterien zu testen und zu bewerten. Es bestehen bereits Methoden zur Zusammenführung von BIM und BEPS (vgl. Andriamamonjy et al., 2019). Ungelöst ist dabei jedoch meist die Berücksichtigung der Steuerlogik, welche einen großen Einfluss auf die Zielgrößen ausübt. Mit der vorgestellten Überführung der Steuerung ins digitale Gebäudemodell wird ein wesentlicher Beitrag geleistet, um Systeme samt deren Logik in Simulationsumgebungen zu testen und evaluieren und Systeme iterativ zu verbessern. In künftigen Forschungstätigkeiten gilt es jedoch geeignete Workflows auszubilden, die Arbeitsaufwände geringhalten (Anforderung nach Marktumfrage, Tab. 1).

Danksagung

Diese Arbeit wurde im Rahmen des Forschungsprojekts „TwinLight – BIM-basierte Umsetzung von Tages- und Kunstlichtsteuerungen“ umgesetzt (Beiter, 2022), welches von der Österreichischen Forschungsförderungsgesellschaft (FFG) unter der FFG-Fördervertragsnummer 898708 im Programm „Stadt der Zukunft“ finanziell gefördert wird. „Stadt der Zukunft" ist ein Forschungs- und Technologieprogramm des Bundesministeriums für Klimaschutz, Umwelt, Energie, Mobilität Innovation und Technologie (BMK). Es wird im Auftrag des BMK von der Österreichischen Forschungsförderungsgesellschaft (FFG) gemeinsam mit der Austria Wirtschaftsservice Gesellschaft mbH (AWS) und der Österreichischen Gesellschaft für Umwelt und Technik (ÖGUT) abgewickelt.

Literatur

Aghemo, C., et al. 2013. Management and monitoring of public buildings through ICT based systems: Control rules for energy saving with lighting and HVAC services, Frontiers of Architectural Research 2(2), 147-161.

Alonso, R., et al. 2019. SPHERE: BIM Digital Twin Platform, Proceedings 20(1), 9.

Andriamamonjy, A., et al. 2019. A combined scientometric and conventional literature review to grasp the entire BIM knowledge and its integration with energy simulation, Journal of Building Engineering 22, 513-527.

Beiter, J. 2022. TwinLight - BIM-basierte Umsetzung von Tages- und Kunstlichtsteuerungen, Nachhaltig Wirtschaften, https://nachhaltigwirtschaften.at/de/sdz/projekte/twinlight.php, Aufruf 21.02.2024.

Bellia, L., et al. 2020. Impact of daylight saving time on lighting energy consumption and on the biological clock for occupants in office buildings, Solar Energy 211, 1347-1364.

Chew, I., et al. 2017. Smart lighting: The way forward? Reviewing the past to shape the future, Energy and Buildings 149, 180-191.

DIN CEN/TS 17623:2021-08. 2021. BIM-Merkmale für die Beleuchtung - Leuchten und Sensoren, Beuth-Verlag.

Dubois, M.-C., Blomsterberg, Å. 2011. Energy saving potential and strategies for electric lighting in future North European, low energy office buildings: A literature review, Energy and Buildings 43(10), 2572–2582.

van Dronkelaar, C., et al. 2016. A Review of the Energy Performance Gap and Its Underlying Causes in Non-Domestic Buildings, Frontiers in Mechanical Engineering 1(17).

GraphViz, 2024. Online: https://graphviz.org, letzter Aufruf: März 2024.

Fedoruk, L. E., et al. 2015. Learning from failure: understanding the anticipated–achieved building energy performance gap, Building Research & Information 43(6), 750-763.

Haq, M. A. U., et al. 2014. A review on lighting control technologies in commercial buildings, their performance and affecting factors, Renewable and Sustainable Energy Reviews 33, 268-279.

Hauer, M., et al. 2024. Integrating Digital Twins with BIM for Enhanced Building Control Strategies: A Systematic Literature Review Focusing on Daylight and Artificial Lighting Systems, Buildings, 14(3), 805.

Hong, Y., et al. 2018. BIM adoption model for small and medium construction organisations in Australia, Engineering, Construction and Architectural Management 26(2), 154-183.

Nytsch-Geusen, C., et al. 2019. The Digital Twin as a Base for the Design of Building Control Strategies, Proceedings of the 16th IBPSA Conference, Rome, Italy, Sept. 2-4, 2019, 4141-4148.

Ouf, M. M., Park, J. Y., Gunay, H. B. 2021. A simulation-based method to investigate occupant-centric controls, Building Simulation 14, 1017-1030.

Preiser, W. F. E. 1995. Post-occupancy evaluation: how to make buildings work better, Facilities 13(11), 19-28.

Riemenschneider, C. K., Hardgrave, B. C. 2016. Explaining Software Development tool Use with the Technology Acceptance Model, Journal of Computer Information Systems 41(4), 1-8.

Rocha, H., et al. 2016. Exterior lighting computer-automated design based on multi-criteria parallel evolutionary algorithm: optimized designs for illumination quality and energy efficiency, Expert Systems with Applications 45, 208-222.

Ryckaert, W., et al. 2010. Criteria for energy efficient lighting in buildings, Energy and Buildings 42(3), 341-347.

Sporr, A., Zucker, G., Hofmann, R. 2019. Automated HVAC Control Creation Based on Building Information Modeling (BIM): Ventilation System, IEEE Access 7, 74747-74758.

Sporr, A., Zucker, G., Hofmann, R. 2020. Automatically Creating HVAC Control Strategies Based on Building Information Modeling (BIM): Heat Provisioning and Distribution, Energies 13(17), 4403.

Webb, A. R. 2006. Considerations for lighting in the built environment: Non-visual effects of light, Energy and Buildings 38(7), 721-727.

Yoshino, H., Hong, T., Nord, N. 2017. IEA EBC annex 53: Total energy use in buildings—Analysis and evaluation methods, Energy and Buildings 152, 124-136.

Zech, P., et al. 2024, Model-Based Auto-Commissioning of Building Control Systems, Proceedings of the 26th International Conference on Enterprise Information Systems, Angers, France: SCITEPRESS - Science and Technology Publications, 121-128.

BauSIM 2024 in Wien
23. September – 26. September

BIMReason - Validating BIM Model Correctness

Philipp Zech[1], Peter Burger[1], Sascha Hammes[2], David Geisler-Moroder[2] und Ruth Breu[1]

[1]*Department of Computer Science, University of Innsbruck, Tyrol, Austria*

[2]*Unit of Energy Efficient Building, University of Innsbruck, Tyrol, Austria*

Abstract

Inspections for compliance and building analysis are critical to the success of any construction endeavor. At present, such assessments are primarily conducted manually by experts in the Architecture, Engineering, and Construction (AEC) sector resulting in a tedious, labor-intensive, and generally ineffective undertaking. Yet, with the gradual adoption of Building Information Modeling (BIM), automated building analysis and compliance checking become feasible. The Industry Foundation Classes (IFC), in particular, has received a lot of traction in the AEC industry as a vendor-neutral data model. Its well-defined semantics can be exploited by reasoning engines that allow for semantic reasoning on building models, the core mechanism required for automated compliance checking and building analysis. In this paper, a general-purpose model-checking framework for IFC building models, as well as an appropriate specification layout are introduced. Model-checking via semantic reasoning is realized using various technologies from the Semantic Web. To showcase and evaluate our implementation, a sample specification is developed and tested on two IFC building models.

Introduction

The advent of digitization in the Architecture, Engineering and Construction (AEC) industry and the increased requirements for collaboration among stakeholders has led to a progressive adoption of Building Information Modeling (BIM) (Boje et al. 2020, Charef et al. 2019) over recent years. Before BIM, 2D/3D drawings, floor plans, and formal paperwork were the most common techniques in planning and implementing building projects. BIM on the other hand aims to represent a building project as a *shared digital representation of physical and functional characteristics of any built object […] which forms a reliable basis for decisions* (Kalinichuk 2015). Ideally, the resulting BIM model then comprises the 3D geometry of the building, cost information, information about energy usage, and information on more specific subjects such as Mechanical, Electrical, and Plumbing (MEP), and Heating, Ventilation, and Air Conditioning (HVAC) systems. At its core, BIM attempts to assign semantic meaning to building elements and makes this information available and interpretable by computers.

By far the most prevalent standard in the BIM environment is the Industry Foundation Classes (IFC) (Pauwels et al. 2017) which defines an open data exchange and file format for BIM, and allows for a common, vendor-neutral way to represent building data in the AEC domain. This vendor neutrality allows for the development of vendor-neutral automation tools, e.g., for the model-checking of BIM models. Currently, model-checking of BIM models that surpass clash and collision detection is generally done manually using human judgment (Amor & Dimyadi 2021). This process is inefficient and highly error-prone (Xue & Zhang 2022, Zhang & El-Gohary 2017, Lee et al. 2020). Therefore, the automation of BIM model-checking is highly relevant.

Commensurate with current issues in BIM-based model-checking, this paper introduces a general-purpose model-checking framework for BIM model analysis and compliance. Our contribution is developed as a plugin for the Eclipse framework (Eclipse Foundation 2023). The resulting framework allows IFC-based building models to be checked against various specifications. To achieve this, a checking pipeline, together with a corresponding specification language, was developed. The reasoning part was implemented using technologies from the Semantic Web, specifically through the use of Apache Jena (Apache Foundation 2023).

Our contribution is outlined as Design Science Research (DSR) (Wieringa 2014) and produces a tool as an artifact. The development of our artifact follows a systematic process, starting with gathering requirements and ending with creating prototypes and conducting experiments. The artifact is implemented as a solution to the following design science problem, outlined using the DSR template (Wieringa 2014):

Improve *BIM model quality* (context)
by designing *a vendor-neutral tool* (artifact)
that satisfies *reasoning on BIM models* (requirement)
to deliver *automated BIM model-checking*. (goal)

DSR usually refers to an *artifact* as a prototype at Technology Readiness Level 3 (TRL3), representing a conceptual solution at an early stage of technology development. Using a cyber demonstrator, our proposal achieves a TRL5 (cf. Sec. *Artifact Implementation*). The next section outlines the background of our work and state-of-the-art, followed by Sec. *Solution Proposal*, which introduces our contribution. Before we conclude in Sec. *Conclusion* we evaluate our proposal in Sec. *Results and Discussion* on two BIM models by evaluating them against an exemplary specification as developed throughout Sec. *Solution Proposal*.

Background and Related Work

Reasoning in the context of building models can be defined as the act of deducing logical conclusions from an existing building model in order to get valuable information that can be utilized for subsequent interpretation. The most common applications of reasoning in the AEC industry are compliance checking and building performance analysis.

Compliance checking is the procedure of verifying that a building model is consistent with a certain law, specification, or regulation. The normative texts for compliance checking generally specify a set of rules, that produce *true, false, unknown* or *warn* as a result (Eastman et al. 2009). Common examples of compliance checking are the assessment of fire codes, accessibility, or general codes that ensure the safety of the building. Building performance analysis on the other hand is used to evaluate how well a building operates in terms of specific criteria. This includes the analysis of energy efficiency, the computation of green building scores, evaluation of indoor air quality and acoustics (Tian et al. 2021). Building performance analysis relies on complex computations and simulations and produces a variety of different, most often numerical results. It is also not uncommon for compliance checking to enforce certain requirements on the building's performance, such as a minimum level of energy efficiency.

Compliance checking and building performance analysis is complex, and to this day, it is most often carried out manually, by domain experts. In some cases, computer software is used to assist this manual reasoning. Still, this is known to be repetitive, error-prone, inefficient, and a contributing factor to declining productivity in projects (Amor & Dimyadi 2021, Zhang & El-Gohary 2017, Gade et al. 2021). Therefore, automating this reasoning process is highly desired (Gade & Svidt 2021). With the advent of BIM and IFC, the first promising implementations for automated compliance checking and building analysis started to appear (Lee et al. 2020, Sacks et al. 2019, Sydora & Stroulia 2019). Notable stable and available implementations are the Solibri Model Checker, DesignCheck, or Fornax' ePlanCheck. Although these provide solid approaches to (semi-)automated compliance checking, they are (i) restricted in the range of specifications, i.e., checks that can be executed, (ii) implemented as a black-box, and (iii) generally do not support custom rule definition (Gade et al. 2021, Gade & Svidt 2021, Issa & Olbina 2015, Lee et al. 2020).

The specifications for compliance checking and building performance analysis are most often written in natural language. The translation of these normative texts to machine-interpretable checks is extremely complex (Amor & Dimyadi 2021). The most common reason for this is the mismatch between the information required in the specification and the information provided by the building model. As an example, many fire codes define concepts such as emergency exit routes, fire scores of building elements, and the flammability of certain materials. Therefore, mechanisms are required that help with aligning concepts from the specification to concepts in the building model (Amor & Dimyadi 2021).

To enable reasoning on BIM models, the semantics have to be understood by a reasoning engine (Hitzler & Van Harmelen 2010). Even though IFC is computer-readable, it is not directly suited for inference. To mitigate this, we employ the ifcOWL (Pauwels & Terkaj 2016), the RDF-based ontology counterpart of the IFC. The resulting representation of the BIM then can be fed as input to a reasoning engine which implement the formal inference system defined by Web Ontology Language (OWL) (Antoniou & Harmelen 2009), and by using the concepts defined in the ifcOWL ontology, additional knowledge can be derived from the underlying BIM model. However, even though reasoning on BIM models solely using the OWL semantics and ifcOWL is a powerful way to infer new information from it, supplying the reasoning procedure with additional semantics is often required (Jiang et al. 2022). For that, the Semantic Web provides the Semantic Web Rule Language (SWRL) (Horrocks et al. 2004). SWRL can be used to implement custom semantics in the form of inference rules. An inference rule consists of an *antecedent* and a *consequent* part. If in a reasoning procedure, the *antecedent* of a rule can be derived from the existing data, then the *consequent* is inferred and added for further inference. This process is repeated until no more inferences can be concluded. Rule-based reasoning is thus useful to implement recursive computations. In the context of reasoning on BIM models, it also helps with the alignment

between specification implementation and the BIM model.

In addition to rule-based reasoning, the Semantic Web also provides the Semantic Web Protocol and RDF Query Language (SPARQL) (Arenas & Pérez 2011) to extract information from RDF-based ontologies by pattern matching. However, SPARQL also specifies special `CONSTRUCT`-queries, where the results from query execution are stored back to the model on which the query was executed. This allows for query-based reasoning on RDF data. Query-based reasoning is especially useful for existential quantification, aggregation, and complex mathematical computations.

Solution Proposal

Our proposal requires two inputs: (i) an IFC-based BIM model to check, and (ii) rule specifications against which the BIM model will be evaluated. The checking engine should have the capability to check BIM models against multiple specifications. The result of the checking procedure is a list of check results. The reasoning part of the checking engine is implemented using existing technologies from the Semantic Web. The final checking engine is then packaged and deployed as a plugin for the Eclipse IDE.

Since the conditions for the desired implementations allow for different solution proposals, a requirements analysis was conducted at the beginning of the project and further reevaluated and enhanced throughout the implementation. This was crucial to narrow down the possible solution candidates. The requirements analysis was driven by our DSR problem (cf. Sec. *Introduction*), existing research in the field of automation in the AEC industry, research on the adoption of Semantic Web Technologies in the AEC industry, research on the nature and structure of normative texts, and solutions to practical problems and needs discovered during development. The following list outlines the most important requirements as determined during our analysis (in no particular order):

R1: Range of supported building models. A variety of building models supported by the verification technique is desired and a top priority. The checking engine uses BIM models as inputs, hence at least IFC models should be supported. IFC is the most advanced BIM standard and is supported by most BIM applications. The suggested verification framework only accepts single-file IFC models, although the Semantic Web can integrate multi-file and multi-standard models. As IFC data format versions (mainly IFC2x3 and IFC4) are not backward compatible, version alignment is needed. Additionally, version alignment establishes an *n:m* link between building models and specifications, enabling model verification across several specifications.

R2: Range of specifications that can be implemented. According to legal text research and building analysis research, compliance checking and building performance analysis are the most common forms of building analysis. These two analyses differ largely in calculation and findings. Building performance analysis involves computation and numerical results, while compliance verification checks specific requirements. In addition to flexible check outputs, checks should convey complicated computations and inferences. Specifications often include existential quantification, mathematical formula implementation, aggregations, and recursions. Thus, the checking engine should support complex specifications with a flexible, expressive specification layout.

R3: Simple distribution and management of specifications. Specification implementation, distribution, and maintenance should be straightforward. A specification should be a single artifact provided to the checking engine. This streamlines the import logic and improves distribution. Keeping the complete specification in one place simplifies management. Besides dissemination and maintenance, specification implementations should be transparent and verifiable by third parties.

R4: Extensible execution model. The entire verification process should be adaptable. Therefore, the checking engine implementation is simple and extendable as the BIM environment may evolve. New standards and exchange formats may make using a single IFC file as input insufficient.

R5: Performance. Time should be reasonable for checking. Performance and other needs are difficult to balance as checking huge models requires several sacrifices. First off, models need to be converted into ifcOWL. At this, caching and reducing the overall model size are not feasible as this would impede specification expressiveness and flexibility (Jiang et al. 2022). Inference is another performance-affecting step that is time-consuming on big models. In addition, support for SPARQL `CONSTRUCT`-queries is essential, as rule-based reasoning struggles with complex mathematical formulas and aggregations (Jiang et al. 2022) which we mitigate by these very SPARQL `CONSTRUCT`-queries (cf. Sec. *Specification Layout*).

Solution Overview

Our solution implements a pipeline architecture as outlined in Fig. 1. The BIM model and the specification implementation on which to check the BIM model are the two inputs to the pipeline. These are then passed through a series of steps, viz. import, inference, checking, and results extraction. The final component, viz. *Results Extractor*, produces a list of check results as output. To enable semantic reasoning, the IFC building model is translated to ifcOWL by the *Model Importer*.

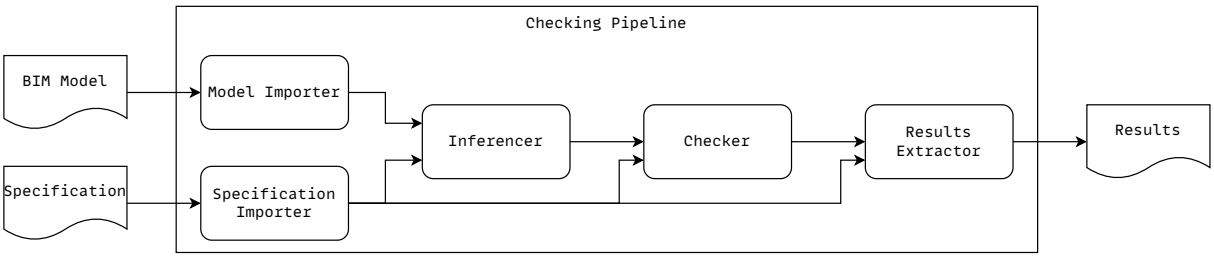

Figure 1: Pipeline of the checking procedure.

Specification Layout

As mentioned earlier, a wide range of specifications should be supported by the checking engine. To solve this, an opinionated specification layout was developed. By design, the specification implementation supplies most of the logic required for the check execution. The sole purpose of the *Checker* is then to apply this logic to the BIM model in a sensible sequence of steps. Only a few assumptions are made on how checks are implemented, and no assumptions are made on the check results. This allows for very expressive and flexible specification implementations and simplifies the checking procedure as a whole. Essentially, specification implementations are defined to be ZIP archives (.zip) compliant with the following, well-defined directory layout (cf. Fig. 4):

checks/{check}.jr The `checks/` directory contains a list of check implementations in the form of Jena Rules (.jr). There can be arbitrarily many rule files in this directory. These rules are used to implement the concrete checks (rules from normative texts), which generate the final check results. The naming of the files is open to the implementer of the specification, yet it is advised to name them according to the actual checks they implement. There can be multiple check implementations per file. The checking rules themselves are definite Horn clauses in implication form (Giordano et al. 1992) and composed of an antecedent and a consequent. The antecedent is used to define the objects to be tested, whereas the consequent defines the check result that is applied to the object. Fig. 2 shows an example of such a check implementation. In this specific case, the antecedent of the rule defines a pattern that matches every element `?s` of type `myspec:door`, where `?s` has a property `myspec:hasWidth` with a corresponding value `?w` that is less than `"813"`. The task of a rule-based reasoning engine is then to find all possible assignments of `?s` and `?w` that satisfy this pattern. For each solution, the consequent of the rule is evaluated and added to the model. In this case, the consequent assigns `myspec:FAIL` to the tested door (`?s`) on the check `myspec:check_IBC_2015_Section_1010_b`. Conceptually, this rule describes, that every door that is less than 813mm wide fails the check defined in the IBC 2015, Section 1010b. For more details, see Sec. *Checker*.

```
[someCheck:
    (?s rdf:type myspec:Door)
    (?s myspec:hasWidth ?w)
    lessThan(?w, "813"^^xsd:double)
        -> (?s myspec:check_IBC_2015_Section_1010_b
     myspec:FAIL)]
```

Figure 2: An excerpt of an exemplary .jr file used for check implementation.

inference/ontologies/{graph}.ttl The `ontologies/` sub-directory within the `inference/` directory contains an arbitrary number of RDF graphs stored as Turtle (.ttl) files. There can be arbitrary many of these files, and the naming of them is open to the specification implementer. Also, there is no restriction to the content of the Turtle files. They are imported during the inference step and appended to the building model. This could be used to import external schemata and ontologies for providing additional semantics on top of the ifcOWL. For more details, see Sec. *Inferencer*.

inference/rules/{rule}.jr The `inference/rules/` directory contains an arbitrary number of rule files (.jr), which in turn contain the rules used for rule inference. Similar to the rules in the `checks/` directory, the naming of them is open to the implementer. These rules are used to enrich the building model with additional information, including the implementation of the OWL semantics and IFC version alignment. A concrete example of IFC version alignment is shown in Fig. 3. Here, two rules are used to map different *IfcDoor* implementations (IFC2x3 and IFC4) to a common `myspec:Door`. For more details, see Sec. *Inferencer*.

```
[(?x rdf:type ifc2_3:IfcDoor) -> (?x rdf:type myspec:
    Door)]
[(?x rdf:type ifc4:IfcDoor) -> (?x rdf:type myspec:
    Door)]
```

Figure 3: Implementation of IFC version alignment using rule files from the `inference/rules/` directory.

inference/queries/{query}.sparql The `inference/queries/` directory contains an arbitrary number of SPARQL-queries used for query inference. The naming of the queries is open to the implementer. The content of the SPARQL files has to be a valid SPARQL `CONSTRUCT`-query. Other than that, there are no restrictions on the concrete implementation of the queries. The queries in this directory are used to implement inferences that cannot be realized using rule-based inference, such as complex, mathematical computations, existential quantification, and aggregations. For more details, see Sec. *Inferencer*.

extraction/extraction.sparql The `extraction/` directory contains a mandatory `extraction.sparql` file. Once check execution is completed, this query is used to extract the final check results from the model. Other than being a valid SPARQL `SELECT`-query, the exact implementation is open to the implementer of the specification. However, it is common to implement the extraction query in such a way, that each element of the result list contains information about the object that was tested, an additional identified for the object, the check on which the object was tested, and the final check result. The results from the extraction query form the output of the checking procedure. For more detail, see Sec. *Results Extractor*.

Fig. 4 shows the layout of a possible specification implementation. For an actual specification implementation, see Sec. *Results and Discussion*.

Artifact Implementation

Many software libraries provide support for technologies from the Semantic Web. In our implementation, Apache Jena was used, as it provides a general platform for many Semantic Web technologies including reading, writing, and manipulating RDF data, support for rule-based reasoning, a custom rule language similar to SWRL, an implementation of the OWL semantics through rule-based reasoning, and query-based reasoning using SPARQL `CONSTRUCT`-queries.

```
specification.zip
    checks/
        check1.jr
        check2.jr
    inference/
        ontologies/
            rdf1.ttl
            rdf2.ttl
        rules/
            rules1.jr
            rules2.jr
            rules3.jr
        queries/
            query1.sparql
            query2.sparql
    extraction/
        extraction.sparql
```

Figure 4: Directory structure and corresponding files of a specification implementation.

Specification Importer

Importing a specification, together with model import, forms the first stage in our pipeline. Theoretically, specification import and model import could be executed in parallel. However, importing the specification first results in better *fail fast* performance in case of an erroneous specification. Specifically, the *Specification Importer* reads and parses the specification thereby parsing the supplied rules, queries, and RDF graphs to their respective objects in Apache Jena. If the supplied specification file does not conform to the layout defined in Fig. 4, it is rejected. The final result of specification import is an in-memory representation of the supplied specification as required in later steps.

Model Importer

After specification import is completed, the IFC-based BIM model is imported. As no assumptions are made on the BIM model, any valid IFC file is considered a valid input. The IFC-based BIM model is then converted into ifcOWL and forwarded to Apache Jena for in-memory storage. The final result of this step is a single RDF graph, containing the BIM model as used in later steps of the pipeline.

Inferencer

Once specification and model are imported, semantic enrichment is performed on the BIM model by using the inference section (`inference/`) from the imported specification. The idea behind the inference step is to enrich the BIM model with additional information, that can then be used in the check execution. Generally, inference is divided into three steps, each dedicated to a different type of inference, viz. additional ontology import, rule inference, and query inference. These steps are ex-

ecuted in sequence, whereby the order is crucial as the inference results of previous steps can be used in subsequent steps. In the proposed implementation, execution is ordered by *generality*: (i) additional ontology import, (ii) rule inference, and (iii) query inference, whereby ontology import is the most general, and query inference is the most specific.

Checker

Checks are implemented as Jena rules and provided in the imported specification (`checks/{check}.jr`). The antecedent of a checking rule defines the pattern of objects that are subject to a specific check. The consequent is then implemented in such a way, that the inference thereof represents the result of applying the check on the object. This is achieved by defining the consequent of a checking rule as a `(?object, ?check, ?result)` triple. The `?object` represents the object that is checked, `?check` is an identifier for the concrete check that is applied to the object, and the check result is captured by `?result`. Using the `GenericRuleReasoner` from Jena, these rules are executed on the enriched model (cf. Sec. *Inferencer*). The inferred statements are then considered the check results. Although checks could also be implemented directly in the inference step, outsourcing check execution into a different step ensures that all the model enrichment is performed before the checking rules are applied.

Results Extractor

The *Result Extractor* extracts the final results after check execution using the SPARQL extraction query provided in the specification (`extraction/extraction.sparql`). The exact implementation of how and what results are extracted is open to the implementer of the specification. For example, for our evaluation in Sec. *Results and Discussion*, each check was specifically declared to be of type `spec:Check`. The extraction query then simply selects all the triples from the model, wherein the `?predicate` in `(x, ?predicate, y)` is of type `spec:Check`. It is also worth mentioning, that the final check results no longer have to be RDF triples. For example, it might be useful to append the IFC-ID of tested objects to their respective check results, making it a query solution with 4 fields (the RDF identifier of the tested object, the IFC identifier of the tested object, the RDF identifier of the check, and the check result). As check result extraction is the last step in the pipeline, its results are considered to be the output of the entire checking procedure.

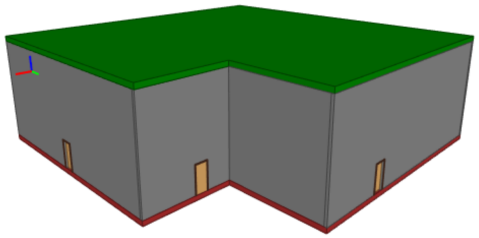

Figure 5: The simple model used for testing.

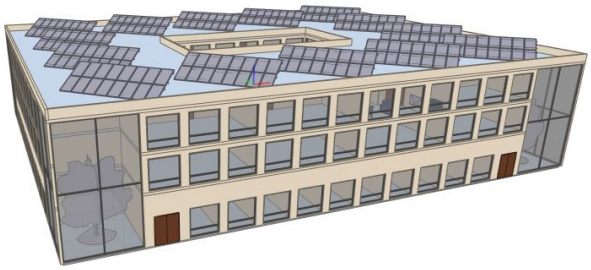

Figure 6: The complex model used for testing.

Results and Discussion

To evaluate our proposal, a sample specification was developed and tested on two different IFC building models. The models were obtained from an open repository[1]. The first building model shown in Fig. 5 is a simple, single-story building that lacks any interior walls. The IFC version of this model is IFC4. The second building model shown in Fig. 6 is a large, multi-story office building. The IFC version used for this building model is IFC2x3. Different IFC versions were chosen to enforce version alignment within the specification implementation. The used models, specifications and implementation are available for download at https://www.github.com/phizech/modelchecker. In the following, we report on the performance of our proposal. All experiments were conducted on a Windows 10 x64 machine running on an Intel(R) Core(TM) i7-4790 CPU@3.60GHz with 16GB DDR3 RAM. It is expected, that the time for checking increases with model size.

Tbl. 1 shows the detailed performance evaluation of the checking procedure on both the small and the large building model. In summary, the checking procedure on the smaller building model took a total of 5.035 secs, whereas the checking on the larger building model took a total of 124.018 secs. In both cases, the model enrichment step takes the longest, with 3.432 secs for the smaller and 87.002 secs for the larger model. Considering the actual size of the models (small: 0.269MB, large: 13.625MB), the correlation between model

[1] http://smartlab1.elis.ugent.be:8889/IFC-repo/

size and time taken for enrichment appears to be super-linear. This is also reflected in the size of the RDF graph before and after enrichment. For the small model, the size of the RDF graph approximately doubled from 37831 statements to 73619 statements after enrichment, whereas for the large model, the RDF graph increased by a factor of four, from 1796200 statements to 7715966 statements.

The time for specification import is independent of the model used, with 0.593 secs for the smaller model, and 0.735 secs for the large model. The time required for model import is expected to be linearly proportional to the model size. However, since this step downloads the ifcOwl ontology and several other transitive dependencies from the internet, the import of small building models could also require several secs. In both cases, the model import was the most expensive step after enrichment and took 3.432 secs for the small model and 30.975 secs for the large model.

Check execution took 0.017 secs for the small model and 1.401 secs for the large model. The time taken for result extraction is almost negligible, with 0.010 secs for the small model and 0.034 secs for the large model. The checking process resulted in a total of 23 final check results for the small model and 637 for the large model. Fig. 7 shows a screenshot of the current report layout. Admittedly, the result presentation merits improvement, yet it already provides crucial information regarding which BIM model elements do not fulfill the earlier specified check (cf. Fig. 2).

Table 1: Performance measurements.

	Simple model	Complex model
IFC version	IFC4	IFC2x3
model size (MB)	0.269	13.625
specification import (secs)	0.593	0.735
model import (secs)	3.432	30.975
enrichment duration (secs)	0.934	87.002
checking (s)	0.017	1.401
result extraction (s)	0.010	0.034
logging and misc (s)	0.049	3.871
total duration (s)	5.035	124.018
RDF triples after import	37831	1796200
RDF triples after enrichment	73619	7715966
RDF triples after checking	73642	7716336
number of check results	23	637

In synopsis, our proposal delivers advances to existing work by introducing a generic, open-source platform for model checking of BIM models that (i) allows for the definition of custom rules, (ii) provides full transparency regarding which rules are implemented how, and (iii), supports checking BIM models of considerable size (cf. Fig. 6) in a reasonable time. Currently, the specification needs to be developed manually, yet, as suggested by Zhang & El-Gohary (2017) and Zhou & El-Gohary (2021), Natural Language Processing (NLP) provides an avenue for the automated generation of specifications from regulation bodies.

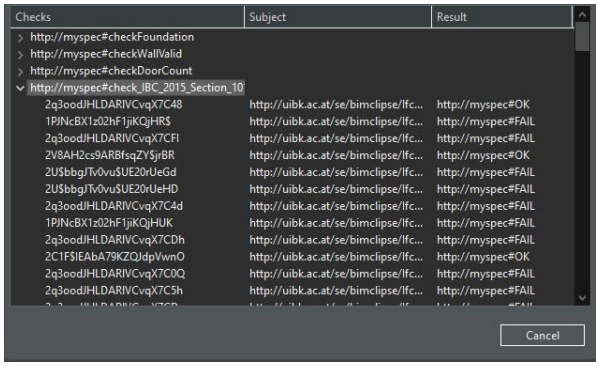

Figure 7: Results of evaluating the sample check from Fig. 2 against the BIM model from Fig. 6.

Conclusion

In this paper, a general-purpose checking framework for the analysis of IFC-based BIM models was introduced. Alongside the checking engine, an opinionated layout for specification implementations was developed. The checking engine receives an IFC building model and a specification implementation as input. The specification is then tested on the imported building model using semantic reasoning. The output of the checking procedure is a list of check results. To showcase the functionality, a sample specification was developed and tested on two BIM models with different IFC versions. The evaluation of the checking procedure on both building models shows, that the proposed implementation can successfully test specifications on different building models in a reasonable amount of time. In future work we plan to improve our solution's performance and reporting facilities and investigate the application of NLP for the automated generation of specifications from building standards.

Acknowledgment

The research leading to these results has received funding from the Austrian Research Promotion Agency (FFG) under Grant Agreement No.: 898708, TwinLight.

References

Amor, R. & Dimyadi, J. (2021), 'The promise of automated compliance checking', *Developments in the Built Environment* **5**, 100039.

Antoniou, G. & Harmelen, F. v. (2009), 'Web ontology language: OWL', *Handbook on ontologies* pp. 91–110.

Apache Foundation (2023), 'Apache Jena'. **URL:** *https://jena.apache.org/*

Arenas, M. & Pérez, J. (2011), Querying semantic web data with SPARQL, *in* 'Proceedings of the thirtieth ACM SIGMOD-SIGACT-SIGART symposium on Principles of database systems', pp. 305–316.

Boje, C., Guerriero, A., Kubicki, S. & Rezgui, Y. (2020), 'Towards a semantic Construction Digital Twin: Directions for future research', *Automation in Construction* **114**, 103179.

Charef, R., Emmitt, S., Alaka, H. & Fouchal, F. (2019), 'Building Information Modelling adoption in the European Union: An overview', *Journal of Building Engineering* **25**, 100777.

Eastman, C., min Lee, J., suk Jeong, Y. & kook Lee, J. (2009), 'Automatic rule-based checking of building designs', *Automation in Construction* **18**(8), 1011–1033.

Eclipse Foundation (2023), 'Eclipse IDE'. **URL:** *https://www.eclipse.org/ide/*

Gade, P. N., Jensen, R. L. & Svidt, K. (2021), Practitioner experiences and requirements for rule translation used for building information model-based model checking, *in* 'Cooperative Design, Visualization, and Engineering: 18th International Conference, CDVE 2021, Virtual Event, October 24–27, 2021, Proceedings 18', pp. 84–96.

Gade, P. N. & Svidt, K. (2021), 'Exploration of practitioner experiences of flexibility and transparency to improve BIM-based model checking systems', *Journal of Information Technology in Construction* **26**, 1041–1060.

Giordano, L., Martelli, A. & Rossi, G. (1992), 'Extending Horn clause logic with implication goals', *Theoretical Computer Science* **95**(1), 43–74.

Hitzler, P. & Van Harmelen, F. (2010), 'A reasonable semantic web', *Semantic Web* **1**(1-2), 39–44.

Horrocks, I., Patel-Schneider, P. F., Boley, H., Tabet, S., Grosof, B., Dean, M. et al. (2004), 'SWRL: A semantic web rule language combining OWL and RuleML', *W3C Member submission* **21**(79), 1–31.

Issa, R. R. A. & Olbina, S., eds (2015), *Building Information Modeling: Applications and Practices*.

Jiang, L., Shi, J. & Wang, C. (2022), 'Multi-ontology fusion and rule development to facilitate automated code compliance checking using BIM and rule-based reasoning', *Advanced Engineering Informatics* **51**, 101449.

Kalinichuk, S. (2015), 'Building information modeling comprehensive overview', *Journal of Systems Integration* **6**(3), 25.

Lee, Y.-C., Ghannad, P., Dimyadi, J., Lee, J.-K., Solihin, W. & Zhang, J. (2020), A comparative analysis of five rule-based model checking platforms, *in* 'Construction Research Congress 2020', pp. 1127–1136.

Pauwels, P. & Terkaj, W. (2016), 'EXPRESS to OWL for construction industry: Towards a recommendable and usable ifcOWL ontology', *Automation in construction* **63**, 100–133.

Pauwels, P., Zhang, S. & Lee, Y.-C. (2017), 'Semantic web technologies in AEC industry: A literature overview', *Automation in Construction* **73**, 145–165.

Sacks, R., Bloch, T., Katz, M. & Yosef, R. (2019), Automating design review with artificial intelligence and BIM: State of the art and research framework, *in* 'ASCE International Conference on Computing in Civil Engineering 2019', pp. 353–360.

Sydora, C. & Stroulia, E. (2019), Towards rule-based model checking of building information models, *in* 'ISARC. Proceedings of the International Symposium on Automation and Robotics in Construction', Vol. 36, pp. 1327–1333.

Tian, Z., Zhang, X., Wei, S., Du, S. & Shi, X. (2021), 'A review of data-driven building performance analysis and design on big on-site building performance data', *Journal of Building Engineering* **41**, 102706.

Wieringa, R. (2014), *Design Science Methodology for Information Systems and Software Engineering*, Springer Berlin Heidelberg.

Xue, X. & Zhang, J. (2022), 'Regulatory information transformation ruleset expansion to support automated building code compliance checking', *Automation in Construction* **138**, 104230.

Zhang, J. & El-Gohary, N. M. (2017), 'Integrating semantic NLP and logic reasoning into a unified system for fully-automated code checking', *Automation in Construction* **73**, 45–57.

Zhou, P. & El-Gohary, N. (2021), 'Semantic information alignment of BIMs to computer-interpretable regulations using ontologies and deep learning', *Advanced Engineering Informatics* **48**, 101239.

BauSIM 2024 in Wien
23. September – 26. September

CityDPC: A Python Library for handling 3D City Model Datasets

Maxim Shamovich[1], Simon Raming[1], Avichal Malhotra[2], Christoph van Treeck[1] und Jérôme Frisch[1]

[1] *Institute of Energy Efficiency and Sustainable Building (E3D), RWTH Aachen University,Germany*

[2] *ITK Engineering GmbH, Germany*

Abstract

This study presents CityDPC, a Python library for geometric computations on CityGML and CityJSON datasets, merging features from tools such as CityATB. It supports loading, analyzing, validating, and manipulating 3D city model datasets, aiming to enhance Python applications for urban building stock analyses. It introduces a shared building class to expedite new data formats integration and improve software development and interoperability among urban-scope applications. A novel feature is the calculation of party or shared walls, showcased in a UBEM (Urban Building Energy Modeling) context through TEASER+ integration. This demonstrates the library's utility in urban energy modeling, calculating shared walls to advance existing tools' functionality and foster innovative urban-scale building analysis applications.

Introduction

Urban-scale energy quantification and performance-related simulation often help stakeholders predict the energetic requirements of buildings in an urban context. Generally used in an urban area's design, operations, and commissioning phases, the method allows urban planners and simulation scientists to predict energy trends across cities and city quarters efficiently (Malhotra 2023). However, due to the rapidity of climate change and increasing Greenhouse Gas (GHG) emissions, a detailed energy modeling of the buildings at an individual level is currently not feasible (Deng et al. 2023). Therefore, a potential UBEM approach enables the virtual modeling of urban areas quantitatively by defining the geo-referenced building-related data and energy-specific attributes for computing, identifying, and optimizing a building's energy performance characteristics. It is a method employed for computing, evaluating, and optimizing the energy performance of the buildings and is used for applications including energy demand calculations, identification of retrofitting requirements, and energy-saving potentials (Reinhart & Davila 2016).

UBEM utilizes various modeling techniques and standardized formats to create virtual representations of city-wide, building-specific data through data models. These models differ in their geometric and semantic definitions, enabling simulation scientists and energy modelers to choose the best format for their needs. CityGML (Gröger & Plümer 2012), an official OGC standard, is a prevalent data format offering semantic and topological information in 3D city models. Built on the Geographic Markup Language (GML) standard, CityGML includes thematic modules for detailed urban modeling, now in its third iteration (version 3.0.0) (Kutzner et al. 2020). The Building Module is particularly useful for simulation purposes.

CityJSON (Ledoux et al. 2019), an alternative format, complements CityGML by emphasizing compact file sizes and web compatibility, retaining CityGML's comprehensive urban modeling features while enhancing data processing efficiency and usability. It supports urban spatial data integration with web technologies, facilitating efficient urban environment visualization and analysis. CityJSON meets the modern demand for a format that marries CityGML's detailed urban element representation with the needs of web-based applications and tools.

Both formats provide valuable explicit information in the context of UBEM for geometric and semantic building attributes, and implicit information, such as the number of shared walls, which must be computed from building surface intersections. The CityDPC Python library extracts both explicit and implicit building data from popular 3D city model formats and facilitates managing multiple datasets.

Related Work

This section explores the landscape of tools designed for the editing, generation, examination, and manipulation of CityGML and CityJSON datasets, which are instrumental in the processing, analysis, and visualization of urban geospatial information.

Besides commercial tools, such as FME[1], the last couple of years have seen a plethora of open-source tools and APIs for handling the two city models.

On the CityJSON side, a variety of open-source software solutions have been developed to interact with CityJSON files, a collection of which can be found on the official CityJSON website[2]. For parsing CityJSON files, the tool cjio[3] can be used. Utilizing a Python CLI, users can engage in the processing and manipulation of CityJSON files by sequentially chaining different operators, facilitating the execution of numerous processing operations simultaneously. Throughout this pipeline, it is possible to save intermediate versions of the CityJSON model as distinct files. It is used as the backbone for multiple tools that build upon the functionality. For Example, the cjval[4] or cjdb (Powałka et al. 2024). The first is a CityJSON validation tool, and the latter is a postgres database for CityJSON files.

citygml4j[5] is an open-source Java API that simplifies working with CityGML by enabling easy parsing, processing, and output of CityGML data. It features core modules for handling CityGML 3.0 data and extensions, with serialization capabilities for various formats, including GML/XML and CityJSON across multiple versions. This library abstracts the XML schema definitions into a Java object model and handles the file parsing. Additionally, citygml-tools[6] provides a command-line utility for comprehensive file processing.

The GML-Toolbox[7] stands as a comprehensive suite designed for the adept management of spatial data, accommodating a broad spectrum of standardized formats, including CityGML (encompassing every version along with its Application Domain Extensions). It is programmed in C++. The toolbox is equipped with an extensive array of functionalities for each supported format. Users can perform both reading and writing operations on file-based data, ensuring data integrity through geometrical and syntactical verification via schema validation. Furthermore, it offers tools for the assessment and modification of attribute values, facilitating transformations across different reference systems. Additionally, the GML Toolbox enhances data interaction through its support for visualization in conjunction with external viewers. Moreover, Geiger et al. showed a coupling of the toolbox with two building performance simulation (BPS) tools (Geiger et al. 2019).

DESCity (Malhotra 2023), a platform proposing possible solutions to limited data availability and inconsistency of CityGML models, incorporates open-access standalone tools (mentioned in the later sections) for searching, transforming, interpolating, generating, validating, and simulating CityGML datasets. Developed as a stand-alone platform, DESCity is available as a web-based platform alongside an open-source Python-based module. Its development envisions to manifest CityGML's full potential by enhancing the format's usability within the UBEM-based energy-related applications. Each tool within DESCity serves an individual purpose and supports the development, validation and usage of CityGML models for energy demand simulation workflows.

As one specific focus point of this paper, the impact of shared, common, or party walls on UBEM will be examined. Therefore, it follows a brief literature review of various studies that have explored this aspect.

Geiger et al. (2018) developed a framework to enhance CityGML data for energy simulation purposes. This process includes a step for geometrical verification, which not only checks for geometrical inconsistencies but also identifies overlapping surfaces between buildings. When a building part is next to another building, the overlapping area is categorized as either a shared or a virtual wall based on its association. Adjacent buildings' overlapping areas are defined as shared surfaces. However, this study does not delve into how the incorporation of shared walls affects the outcomes of the simulations specifically.

Braun et al. (2018) introduce a similar process within the SimStadt UBEM framework, highlighting the issue of unacknowledged shared walls in city-scale simulations, particularly when utilizing CityGML data. In many cases, terraced houses are modeled as separate entities in the dataset, lacking a semantic link between adjacent buildings within the GML file. When shared walls are accurately recognized and incorporated into the model, the discrepancy between the simulated and actual heating demands for buildings significantly de-

[1] https://fme.safe.com/
[2] https://www.cityjson.org/software/
[3] https://github.com/cityjson/cjio
[4] https://github.com/cityjson/cjval
[5] https://github.com/citygml4j/citygml4j
[6] https://github.com/citygml4j/citygml-tools
[7] https://github.com/KIT-IAI/GMLToolbox

creases, aligning more closely with real-world measurements. The oversight of shared walls impacts not only the calculation of the building's total external surface area but also influences the estimation of the total window area, which in many models is derived using a window-to-wall ratio and applied to all exterior walls.

Agugiaro et al. (2022) compared two approaches for shared wall identification. The hybrid approach makes use of 3D data to compute the areas of all the surfaces, while a 2D representation of the building footprint is used to determine adjacent buildings. The second approach, fully 3D geometry-based, makes use of the 3DCityDB (Yao et al. 2018), and the method entails identifying a wall surface adjacent to another building and subsequently conducting a 3D geometrical intersection. The hybrid and fully 3D approaches showed minor differences in surface area estimates and similar energy demands in the steady-state energy model, with discrepancies more pronounced in terraced, corner, and semi-detached houses due to a limitation in accounting for party wall areas.

The landscape of tools for editing, generating, examining, and manipulating CityGML and CityJSON datasets has significantly expanded, featuring both commercial and open-source options. However, there remains a gap for a comprehensive tool that operates in Python and offers an object-oriented structure, which could streamline interactions with other tools while providing a multifunctional base for further developments. Moreover, this study aims to address the need to evaluate the influence of common walls and more precise volume calculations on dynamic urban energy simulations.

Library/Package Architecture

The library adopts an object-oriented architecture, aligning with the hierarchical structure of objects found in file formats and their potential applications, as illustrated in Figure 1. At its core, the *AbstractBuilding* class encapsulates the majority of semantic data typical to CityGML and CityJSON files, with building geometries managed by dedicated classes, Surface and Geometry.

The *Surface* class is responsible for computing values such as area or vector normals for GML surfaces and includes a function to clean surfaces that are overly complex due to an excessive number of points — a common issue in real-world datasets. This cleaning function simplifies surfaces by eliminating superfluous points along a line, retaining only the essential corner points.

The *Geometry* class is responsible for all solid representations found in CityGML and CityJSON. It is mostly used for the Level of Detail (LoD)1.

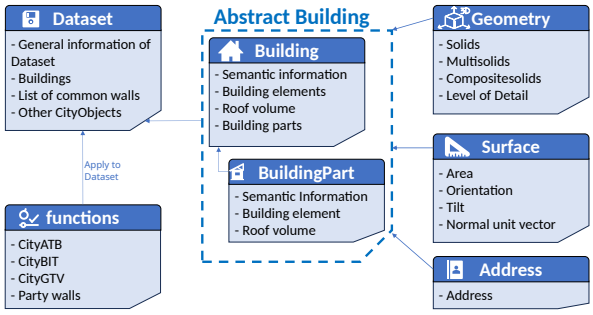

Figure 1: Library Class Structure

The *Dataset* class functions as a container for storing all buildings within a Python dictionary. It serves as the framework for both inputting and outputting buildings in CityGML and CityJSON formats. These sets represent the largest operational unit within the library. Initially, a 3D city model file is loaded into a dataset. Of course, multiple datasets can be loaded and worked with at the same time. Currently, operations between different datasets are limited to merging and joining functionalities; however, more complex inter-dataset procedures are envisioned in future.

Input and Output

As of this writing, the library is capable of importing and managing CityGML data across versions 1.0, 2.0, and 3.0. However, it's important to note that currently, the support for CityGML 3.0 is restricted to geometries and semantic details that are also present in earlier versions, excluding the new geometry and feature types unique to version 3.0. Regarding CityJSON, the library can handle all versions up to 2.0 as input. For both CityGML and CityJSON formats, the library supports building data up to LoD2.

In terms of output, it can generate files in the same versions of CityGML that it supports for input, whereas for CityJSON, only the most recent version, 2.0, is available for output.

Functions

In addition to the specialized functions tailored for class-specific operations, this package offers a suite of feature functions designed for application across the entire dataset. The CityATB function,

grounded in the study by Malhotra et al. (2020), empowers users to conduct thorough analyses of the dataset's content. This includes but is not limited to, performing queries to ascertain the diversity of building types present or determining the version of the file standard utilized. Moreover, the dataset's scope can be precisely defined to include only buildings located within a specific area, as designated by polygon coordinates, or those that match a particular address.

The CityBIT function, as described by Malhotra, Raming, Frisch & van Treeck (2021), addresses the issue of missing data within the buildings represented in the dataset. This functionality not only facilitates the interpretation of incomplete data but also supports the generation of building models from the ground up, a process that will be illustrated in a forthcoming use case. As of the latest update, the tool supports the creation of buildings at LoD 0, 1, and 2, offering users a choice among six distinct roof types for their models.

The CityGTV function, as outlined by Malhotra, Pan, Frisch & van Treeck, C. (2021), streamlines the process of transforming building model coordinates in regions with scarce geometrical data. Furthermore, the function set is also capable of validating the 3D city models for geometrical and modeling correctness.

Merging previously independent tools into a single framework facilitates seamless transitioning between processes that were once separate. This integration enables users to rely on a unified library as the backbone for existing Graphical User Interfaces (GUIs). Consequently, enhancements in input or output capabilities automatically extend across the entire suite of tools.

Shared Wall Calculations

The newest feature of the toolset is the computation of shared walls between neighboring buildings and their components within a dataset. Initially, buildings that might share a wall are identified by considering their footprint along with a slight buffer. This approach streamlines the process by eliminating the need to analyze every surface in the dataset.

For each building identified as having potential shared walls, the surface areas of the walls and their normal vectors are computed.

Then, a preliminary filtering step determines which wall surfaces could be in contact. This involves identifying adjacent building surfaces with opposing normal vectors, which are then selected for further analysis.

Firstly, the surfaces are aligned with the X-Z plane. This alignment simplifies the computational processes involved and facilitates the accurate determination of the mean distance between the two given surfaces. Should this average distance be found to be less than 0.15 meters, an intersection analysis is conducted utilizing the shapely library.

This is then employed to ascertain the area of intersection between these surfaces. If the area resulting from this intersection exceeds a predefined threshold, the surfaces in question are classified as common walls.

The selection of the initial buffer of 0.15 meters as average distance and the intersection criteria are based on practical experience with real-world datasets. This approach accounts for the common imperfections in modeling, even when the geometries are technically valid.

Finally, the results are stored in a Python list, which includes the IDs of the adjacent buildings or building parts, the IDs of the intersecting polygons, and the coordinates and area of the intersected surfaces.

Use Case Workflow Demonstration

The TEASER framework (Remmen et al. 2016), streamlines the process of UBEM by automating the generation of simulation models with minimal input through an archetype approach based on the TABULA typology[8]. This methodology significantly simplifies energy assessments by using predefined building archetypes that require only the building's net leased area, usage type, and construction year for categorization. The framework supports the construction of reduced-order models in the Modelica language and enables automatic simulations via Dymola with the BuildingsPy library. TEASER+ is a fork of the open-source software package, expanding on its CityGML input and export capabilities (Malhotra et al. 2019).

Modifications were necessary to integrate the novel library into TEASER+ to enhance its functionality. This included introducing new input options to accommodate CityDPC datasets and streamlining the codebase by externalizing the handling of various file formats. Such adjustments facilitate the incorporation of additional input sources, including CityGML version 3.0 and CityJSON, with minimal changes to the software. Adjustments were also required for the process of generating buildings, which previously relied solely on CityGML files. A significant addition was the implementation of a

[8] https://webtool.building-typology.eu/

common wall class, which functions similarly to the existing inner wall class by serving as an adiabatic heat storage component. It is assumed that the materials and construction elements used for these common walls mirror those of the outer walls.

Use Case 1

The district is located in Essen, Germany, and comprises 117 residential buildings. Due to data privacy policies in Germany and on the European level, the authors refrain from mentioning the addresses and coordinates of the selected area. The multi-family housing units have varying numbers of floors, ranging from two to four, and contain three to eight dwelling units. The construction was completed in the 1950s and early 1960s. All buildings underwent some retrofitting measures, although it is unknown to the authors which exact refurbishment efforts were performed. The freely available CityGML model in LoD2 was obtained from the cadastral office[2].

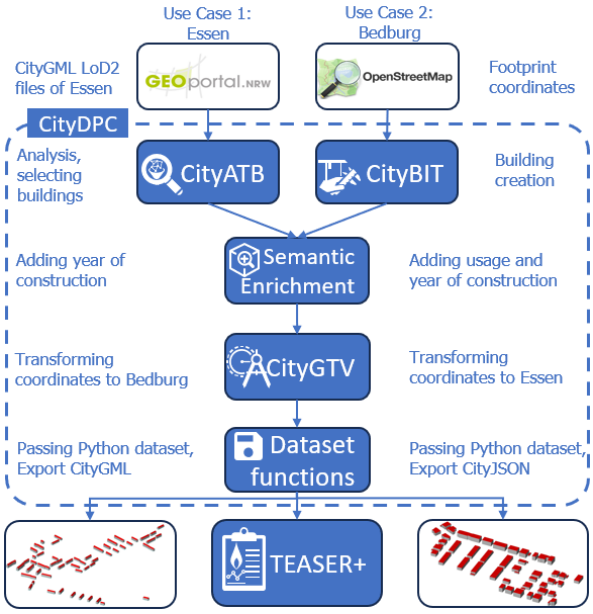

Figure 2: Use case processing steps

All pre-processing is conducted using the CityPDC library. The CityATB function assists in identifying the relevant buildings within the downloaded tiles. To achieve this, the search function is utilized based on the address name. Buildings that have a known year of construction through a project are then selected. Subsequently, these selected buildings are examined for discrepancies, such as duplicate entries. After loading the desired buildings into the specific class, the dataset is enriched with supplementary details about the buildings' ages.

Use Case 2

The second district is situated in Bedburg, Germany, and is a newly constructed area that is still under development. This district predominantly features single-family homes ranging from one to three stories. Out of 91 buildings, 23 of which have a garage modeled as a building part. In a bid to promote environmental sustainability, all structures adhere to the KfW 55 Standard[9], a benchmark for energy efficiency in building construction.

The second scenario depicts the development of a district that has yet to be fully realized. Although construction has commenced, there are no existing CityGML or building models for the area. To compensate, alternative resources such as Open Street Map can be utilized to generate 3D city models. This process involves extruding the building's footprint to create a LoD2 model, choosing a roof type from predefined options as outlined by the CityBIT function, and defining the building's height. The resulting city model is saved in CityJSON format.

To showcase this capability, the districts initially mapped in Essen and Bedburg are converted to switch the locations of both districts. This mimics the scenario faced by urban planners, who evaluate various possibilities for city expansion, for instance. Once the datasets are complete, they are joined and used as input for the UBEM simulation using TEASER+. TRY weather data for Essen was used for both districts.

The procedural steps for both scenarios are illustrated in Figure 2.

Results

In use case 1, Essen, the shared walls are depicted in green in Figure 3. Buildings within the red circle are not classified as adjacent. This scenario illustrates the importance of the previously mentioned threshold settings. A buffer distance of 0.15 meters is inadequate for the algorithm to recognize the walls as adjacent. Adjusting the buffer to 0.25 meters, however, is sufficient for the algorithm to identify the walls as neighboring. Without an in-situ inspection, determining from the data alone whether

[2] https://www.geoportal.nrw/

[9] https://www.kfw.de/inlandsfoerderung/Privatpersonen/Bestehende-Immobilie/Energieeffizient-sanieren/Das-Effizienzhaus/

the buildings are truly adjacent or if this is a modeling discrepancy is challenging.

Among the 117 buildings analyzed, 93 are semi-detached, indicating they adjoin only one neighboring building, leading to a single shared wall. Nevertheless, it is common in modeling practices to represent wall surfaces using several polygons. As a result, a building with a single common wall might be composed out of various GML surfaces, which applies to the majority of Essen's buildings. Additionally, 16 buildings are identified as fully terraced, while a mere seven stand as detached. Importing 117 buildings into the dataset class and executing the necessary computations to complete all additional required attributes takes 0.64246 seconds. The execution of the party-wall algorithm, which is applied to the pre-initialized dataset, takes 0.84899 seconds to finish. All the measurements have been done on a standard commodity laptop.

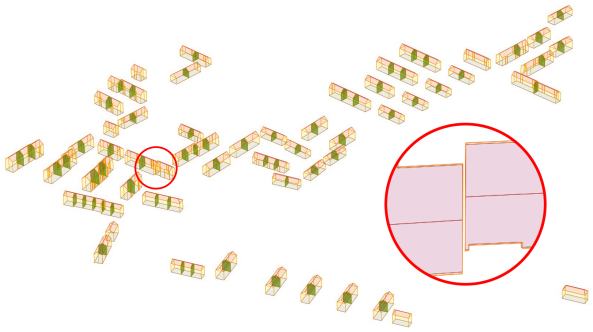

Figure 3: Essen district, shared walls found in green. Detached building pair in red circle

Table 1: Percentage Change in Heating Load

district	total	semi-detached	terraced
Essen	-31%	-30.6%	-34.6%
Essen (retrofit)	-8.1%	-7.42%	-17.07%
Bedburg	-17.9%	-14.87%	-28.86%
Bedburg (retrofit)	-19.4%	-16.05%	-31.33%

The impact of incorporating shared walls into the simulations for heating load estimations is depicted in Table 1. When shared walls are included, the cumulative heating load across all buildings is reduced by 31% compared to the simulations that omit them. Moreover, this reduction can reach up to 38% for the heating load in individual buildings.

This can be explained by the reduction in outer wall surfaces exposed to the ambient temperature. On average, 20.43% of the exterior wall surface is directly adjacent to another building. As a result of the enrichment processes employed by TEASER+, there is also a corresponding reduction in window area by approximately the same percentage. The highest percentage of shared walls is 48.7%. The mean for semi-detached and terraced houses is 19.61% and 39.23%, respectively.

Applying retrofit strategies to the district results in a substantial reduction in the percentage change of heating load. This reduction is largely attributed to the increased U-value of the external walls, which lowers the overall thermal loss across the building envelope. Remarkably, the shared walls model reveals an increased heating load for seven buildings, with the maximum observed change being 3.43%.

The outcomes of the estimation for shared walls in the second use case are depicted in Figure 4. Among the 113 building structures analyzed, 87 are identified as single-family homes, with the remainder comprising garages. A detailed breakdown reveals that 39 buildings are semi-detached, and 37 are terraced houses, encompassing both the adjoining garages and the neighboring residential buildings. Additionally, there are 11 houses that are detached and stand independently.

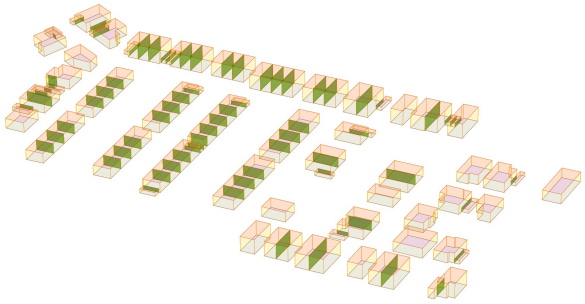

Figure 4: Bedburg district, shared walls illustrated in green

Across all examined buildings, around 30% of the exterior wall surface is identified as shared. In semi-detached buildings, this figure stands at 24.5%, while for terraced buildings, it reaches close to 50%, with some structures showing up to 66% of their wall area as shared.

Table 1 details the heating load percentage change for a second scenario, showing less contrast between standard and retrofit conditions compared to the Essen case. Nonetheless, the range of percentage changes in heating load for individual buildings is broader, spanning from -48.52% to

12.26% in the standard scenario and from -50.28% to 11.14% in the retrofit scenario.

Contrary to the Essen case, where retrofitting led to a decrease in heating load percentage, the Bedburg model shows an increase. This discrepancy is likely due to several factors. First, the initial U-value of the Bedburg case's building envelope was significantly higher than that of the Essen standard scenario. Second, the adjustment in the U-value from standard to retrofit in Bedburg was less pronounced. Additionally, the comparison involves different housing types, with one scenario focusing on multi-family homes and the other on single-family houses, affecting the outer-wall-to-volume ratio.

Discussion

The library we've developed, with its object-oriented design and focus on building structures, is exceptionally well-suited for UBEM applications. Its integration into the TEASER+ framework proved to be straightforward, demonstrating the library's compatibility and ease of use within existing systems.

However, there are some limitations to address. Currently, the library supports CityGML version 2.0 LoD3 and 4 but lacks additional classes for windows and doors, which would refine its modeling capabilities. Furthermore, the latest CityGML standards, which include detailed representations of interior units like voluminous storeys and rooms, are not fully supported with dedicated classes. While other city elements and furniture are currently grouped in a list rather than individual object classes, it's under consideration whether these items should be modeled with the same level of detail as buildings, given their relevance to most applications may vary. However, the library should remain solely focused on the geometric features and semantic information included in the CityGML standard.

In the implementation in TEASER+, there is an assumption that designates all areas of a party wall as adiabatic. This approach is somewhat oversimplified because, ideally, only the portions of the wall that overlap with adjacent buildings should be treated as adiabatic, and only if the set point temperatures of the adjacent thermal zones do not deviate considerably. As all buildings are modeled as a single homogeneous thermal zone with the same use conditions, this simplification did not significantly impact the outcomes in the demonstrated use cases. Nonetheless, it is an area that warrants further attention and refinement in future studies.

The practical application emphasized the importance of integrating shared walls into UBEM frameworks. Comparing standard versus retrofit scenarios highlights the significant impact shared walls can have on building performance simulations. However, the simulation results are not yet validated against real-life measurements, nor were the simulation models calibrated for the two specific use cases at this moment. Nonetheless, the complex dynamics between thermal loss through the building envelope and thermal gains from solar radiation on external walls and through windows introduce considerable variability in heating load estimates across different modeling strategies, often in unpredictable ways. This variability, as evidenced by the contrasting outcomes of the two case studies, is significantly influenced by the ratio of envelope surface area to building volume.

Conclusion and Future Work

This study introduces CityDPC, a Python library that enhances 3D city modeling by integrating and improving upon existing tools. It offers efficient analysis and manipulation of CityGML and CityJSON data, incorporating new features like shared wall calculations to streamline urban building analysis and ensure compatibility across urban-scale applications. The library is open-source and accessible via [https://github.com/RWTH-E3D/CityDPC], encompassing the demonstrated test cases along with all necessary scripts and data. Future development will focus on the interface to expand CityDPC's use in tools and GUIs, integrate solar simulations for enhancing urban energy models, and broaden its application to other Python-based UBEM tools, boosting comparability and consistency in urban modeling.

Expanding TEASER+ to fully utilize CityDPC's capabilities presents an exciting avenue for innovation. Approaches such as clustering buildings into blocks with shared thermal zones or modeling building clusters with multiple zones for coupled simulations could greatly enhance simulation efficiency and, in the case of coupled thermal zones, accuracy. Moreover, applying CityDPC and TEASER+ to specific test cases, such as the extensively enriched Rijssen-Holten area (Tufan et al. 2022), will validate the library's effectiveness and comparability to other simulations.

Acknowledgment

We gratefully acknowledge the financial support by BMWK, promotional reference 03EWR010B.

References

Agugiaro, G., Zwamborn, A., Tigchelaar, C., Matthijssen, E., León-Sánchez, C., van der Molen, F. & Stoter, J. (2022), 'On the influence of party walls for urban energy modelling', *The International Archives of the Photogrammetry, Remote Sensing and Spatial Information Sciences* **XLVIII-4/W5-2022**, 9–16.

Braun, R., Weiler, V., Zirak, M., Dobisch, L., Coors, V. & Eicker, U. (2018), Using 3D CityGML Models for Building Simulation Applications at District Level, *in* '2018 IEEE International Conference on Engineering, Technology and Innovation (ICE/ITMC)', IEEE, Stuttgart, pp. 1–8.

Deng, Z., Javanroodi, K., Nik, V. & Chen, Y. (2023), Using urban building energy modeling to quantify the energy performance of residential buildings under climate change, *in* 'Building Simulation', Springer, pp. 1–15.

Geiger, A., Benner, J., Häfele, K.-H. & Hagenmeyer, V. (2018), Thermal energy simulation of buildings based on the CityGML energy application domain extension, *in* 'BauSIM2018 - 7. DACH IBPSA-Konferenz', KIT, pp. 295–302.

Geiger, A., Benner, J., Häfele, K.-H. & Hagenmeyer, V. (2019), Building Energy Simulations at Urban Scale Based on Standardized Data Models Using a Transparent Enrichment Process, *in* 'Building Simulation 2019', Rome, Italy, pp. 3202–3208.

Gröger, G. & Plümer, L. (2012), 'CityGML - Interoperable semantic 3D city models'.

Kutzner, T., Chaturvedi, K. & Kolbe, T. H. (2020), 'CityGML 3.0: New Functions Open Up New Applications', *PFG – Journal of Photogrammetry, Remote Sensing and Geoinformation Science* **88**(1), 43–61.

Ledoux, H., Arroyo Ohori, K., Kumar, K., Dukai, B., Labetski, A. & Vitalis, S. (2019), 'CityJSON: A compact and easy-to-use encoding of the CityGML data model', *Open Geospatial Data, Software and Standards* **4**(1), 4.

Malhotra, A. (2023), DESCity: District Energy Simulations using CityGML models, PhD thesis, RWTH Aachen University.

Malhotra, A., Pan, Y., Frisch, J. & van Treeck, C. (2021), Geometrical interoperability of 3D CityGML building models for urban energy use cases, *in* '2021 Building Simulation Conference'.

Malhotra, A., Raming, S., Frisch, J. & van Treeck, C. (2020), CityATB: CityGML analysis toolbox for energy performance simulations, *in* '8th Conference of IBPSA Germany and Austria', Verlag der Technischen Universität Graz, Graz, Austria.

Malhotra, A., Raming, S., Frisch, J. & van Treeck, C. (2021), CITYBIT: CityGML Building Interpolation Tool for Energy Performance Simulations, *in* '2021 European Conference on Computing in Construction', pp. 245–252.

Malhotra, A., Shamovich, M., Frisch, J. & van Treeck, C. (2019), Parametric Study of the Different Level of Detail of CityGML and Energy-ADE Information for Energy Performance Simulations, *in* 'Building Simulation 2019', Rome, Italy, pp. 3429–3436.

Powałka, L., Poon, C., Xia, Y., Meines, S., Yan, L., Cai, Y., Stavropoulou, G., Dukai, B. & Ledoux, H. (2024), Cjdb: A Simple, Fast, and Lean Database Solution for the CityGML Data Model, *in* T. H. Kolbe, A. Donaubauer & C. Beil, eds, 'Recent Advances in 3D Geoinformation Science', Springer Nature Switzerland, pp. 781–796.

Reinhart, C. F. & Davila, C. C. (2016), 'Urban building energy modeling - A review of a nascent field', *Building and Environment* **97**, 196–202.

Remmen, P., Lauster, M., Mans, M., Fuchs, M., Osterhage, T. & Müller, D. (2016), 'TEASER: An open tool for urban energy modelling of building stocks.', *Journal of Building Performance Simulation* **11**(1), 84–98.

Tufan, Ö., Arroyo Ohori, K., León-Sánchez, C., Agugiaro, G. & Stoter, J. (2022), 'Development and testing of the CityJSON energy extension for space heating demand calculation', *ISPRS Archives* **XLVIII-4/W4-2022**, 169–176.

Yao, Z., Nagel, C., Kunde, F., Hudra, G., Willkomm, P., Donaubauer, A., Adolphi, T. & Kolbe, T. H. (2018), '3DCityDB - a 3D geodatabase solution for the management, analysis, and visualization of semantic 3D city models based on CityGML', *Open Geospatial Data, Software and Standards* **3**(1), 5.

BauSIM 2024 in Wien
23. September – 26. September

Extending an IFC-based Framework to include an Automated CFD-Setup using Pre-Computed Boundary Conditions

Veronika Richter[1], Christoph van Treeck[1] and Jérôme Frisch[1]

[1] *Institute of Energy Efficiency and Sustainable Building (E3D), RWTH Aachen University, Germany*

Abstract

Computational Fluid Dynamic (CFD) simulations are used in building design, including design and performance optimization, as well as thermal comfort, fire, and evacuation simulations. However, even if CAD models of the building are available, setting up the CFD model and preprocessing the data require geometric simplification to reduce computational time and model healing. These preprocessing steps require high manual effort, which is, together with the computational cost, one of the main reasons why CFD is rarely applied in building design processes outside of research. Aiming to automize the CFD model setup, this paper describes the development of an IFC-based framework enabling the extraction of geometric data required for OpenFOAM CFD simulations. Our framework is based on the IFC Space Boundary geometry. This CFD-based setup is linked to IFC-based Building Performance Simulation (BPS) results that are used as boundary conditions for the CFD model setup. These BPS results are obtained from the open-source bim2sim tool, which generates IFC-based BPS models using EnergyPlus. Our preprocessed CFD models can be exported for OpenFOAM CFD simulations. Also, our proposed framework reduces the manual effort for CFD preprocessing via geometric generation and meshing. Through the open-source CFD-Kernel OpenFOAM, our framework fully integrates into the open-source bim2sim process. In further research, the resulting CFD models are then used for detailed IFC-based thermal comfort analysis.

Introduction

Within the field of Building Information Modeling (BIM), Computational Fluid Dynamic (CFD) simulation is used in building operation, design and performance optimization, as well as in thermal comfort, fire, and evacuation simulations. (Kang et al. 2022).

As setting up CFD models may require high manual effort, the openBIM standard Industry Foundation Classes (IFC) can be used to simplify the setup process (Nytsch-Geusen et al. 2003). More specifically, the so-called Space Boundaries (SB), represented in IFC by the *IfcRelSpaceBoundary* entities, are a suitable representation for the setup of CFD models (Fichter et al. 2021).

On the basis of a survey (Müller et al. 2022) conducted with participants from 14 construction companies performing CFD analysis, model preparation was cited as the most time-consuming factor in the CFD process. Other cited time-consuming factors were the meshing and setup of boundary conditions. The survey also showed that when an IFC model was provided, the following major issues occurred: (1) the geometry was too complex, thus requiring high manual effort in model reduction; or (2) the geometry was not watertight and thus not fully enclosed by building parts but has gaps.

Therefore, from industry and related research we observe a gap in the interoperable use of IFC models to improve the accessibility of CFD simulations within the building design process. Our presented approach integrates into the open-source IFC-based multi-domain simulation tool called bim2sim[1]. This tool combines IFC-based simulation approaches for Building Performance Simulation (BPS), Heating, Ventilation, Air Conditioning (HVAC), and Thermal Comfort in a modular plugin structure (Richter, Syndicus, Frisch & van Treeck 2023). The bim2sim tool has already demonstrated that IFC-based construction surface geometry is feasible in proprietary data preprocessing for CFD purposes in ANSYS Fluent (Müller et al. 2022).

In the present study, we further automate this

[1] bim2sim tool: https://github.com/BIM2SIM/bim2sim, accessed on 26 February 2024

process to an open-source CFD setup with OpenFOAM, and we integrate this approach as a new plugin into the bim2sim tool, called *PluginOpenFOAM*. Our new approach includes geometric processing and enrichment of HVAC equipment (here: space heaters and air terminals), automatic surface type-based mesh refinement, and mapping of precomputed BPS boundary conditions. These precomputed boundary conditions (i.e., heat flux and temperatures of the boundary surfaces of the selected timestep) are generated from the bim2sim *PluginEnergyPlus*, which uses EnergyPlus as computational kernel for BPS. The presented approach reduces the manual effort for setting up CFD models and paves the way for fully integrated open-source CFD simulations within an IFC-based multi-domain simulation environment. In future research, the presented CFD approach can be further extended for use in fire safety and thermal comfort simulations.

Related Research

This section focuses on BIM-based approaches for setting up CFD simulations and provides an overview of IFC-based CFD applications in related research and industry.

There are reviews of the BIM-CFD transformation process in related research, but they consider only proprietary data exchange and fail to mention open data exchange (Zheng et al. 2023, Kang et al. 2022). In Germany, especially in public construction projects, the software landscape of project participants is diverse and cannot be limited to specific proprietary software. Standardized data exchange formats (mainly IFC as the data exchange format for BIM processes) are required for data exchange between project participants. Therefore, this paper focuses on IFC-based model generation for CFD purposes.

Related research has developed different methods for the IFC-based setup of CFD models. Nytsch-Geusen et al. (2003) introduce an early IFC-based (IFC Versions 1.5.1 and 2x) approach to setting up CFD models using results of multi-zone thermal building simulations as boundary conditions. Other studies present IFC-based CFD setups creating the CFD geometry based on *IfcProducts* (Lan et al. 2021, Lee et al. 2021, Park et al. 2020). However, these studies disregard the use of *IfcRelSpaceBoundary* entities. In their studies on IFC-based CFD model setups with OpenFOAM, Lee et al. (2021) and Park et al. (2020) focused on geometric simplification, as well as optimization and validation of grids.

IfcRelSpaceBoundary geometry has been used within the BIM2SIM Project (Müller et al. 2022) to set up indoor airflow CFD models for ANSYS Fluent. In addition, the meshing for OpenFOAM has been exemplary evaluated for building surroundings.

The application scenarios for IFC-based CFD in related research focussed on indoor airflow, thermal comfort, and fire simulations. Lan et al. (2021), Lee et al. (2021) tested their approaches on the simulation of indoor airflow (i.e., temperature distribution and velocities). Müller et al. (2022) applied the IFC-based CFD setup to prove a pressure differential system and the scenario of smoke removal in a staircase. Richter, Lorenz, Syndicus, Frisch & van Treeck (2023) analyzed the required IFC entities for thermal comfort on different simulation scales, and they named the CFD simulation as the approach with the highest requirements on IFC data availability.

Methodology

The methodology section starts with a description of the IFC data requirements for the setup, followed by the basic required OpenFOAM input data structure for indoor CFD simulations. Based on this OpenFOAM file structure, the data mapping of geometric and semantic IFC-based data is defined. This section concludes with an introduction to the IFC-based OpenFOAM Input file generation, which includes the underlying algorithms of the geometric preprocessing of the data mapping. Our methods are currently developed and tested for the case of a single office but can easily be extrapolated for larger room settings.

IFC requirements for CFD setup

For setting up an IFC-based CFD model, the space surrounding *IfcRelSpaceBoundary* must form a watertight model (Müller et al. 2022), which should be validated prior to CFD setup using applicable validation tools (e.g., Richter et al. (2022)). The bim2sim tool integrates an algorithm to heal geometric inconsistencies within a given set of space boundaries (Müller et al. 2022).

Additionally to the IFC quality requirement, Richter, Lorenz, Syndicus, Frisch & van Treeck (2023) introduced a mapping of IFC entities to design stages and simulation granularities for the simulation objective of indoor thermal comfort. As

a minimum requirement for IFC-based CFD simulations in the building design stage, they listed, among others, data on *IfcRelSpaceBoundary* entities of space surrounding objects (wall, floor, ceiling), as well as on the positions of HVAC devices. They identified furniture positions as optional, but these would improve the representation of reality within the CFD model.

OpenFOAM structure for building indoor simulations

CFD simulations for building indoor environments that use the open-source CFD kernel OpenFOAM require a specific structure of input data files. These can be broadly categorized into the categories of *constant* data (i.e., mainly mesh data), *system* data (i.e., simulation control and solver settings), and *time series* data (i.e., initial or boundary conditions)[2]. This file structure of the OpenFOAM input files is visualized in Figure 1 (right).

For automated IFC-based CFD setup, we can distinguish between files that can be obtained (1) based on standardized values from templates such as suitable solvers for the use case (dark gray), (2) based on standardized values requiring IFC-specific geometric information such as surface names (blue), and (3) highly customized files (not highlighted) that require a high number of parameters, such as boundary conditions (e.g., heat fluxes, temperatures) or parameters calculated from IFC-geometry (e.g., refinement boxes).

IFC-OpenFOAM input data mapping

While the solver settings can be chosen according to the simulation objective (here: indoor airflow) and only require minor modifications across CFD simulations on similar scenarios, the building geometry and boundary conditions can be obtained from the input IFC data. The process of mapping IFC-based data to OpenFOAM input files (Fig. 1, right) is visualized in Figure 1 (left).

Based on the available building and equipment data in IFC, we further distinguish geometric and semantic data in this process. The geometric data mapping process starts with generating suitable geometry for CFD, resulting in triangulated shapes. The geometric data can be uniquely identified using the corresponding semantic information, holding information on the surface type (wall, window, ceiling, floors, air terminals, heaters), each uniquely identifiable using the corresponding *GlobalId* from the IFC file. For the geometric data mapping, in a first step, the geometry has to be exported to the *triSurface*-directory in the STL file-format. If the position and/or shapes of the HVAC equipment is not available, several IFC-based enrichment options apply. For the setup of space heating, (1), surface floor heating can be applied, or (2), radiator shapes can be automatically generated based on setup of the *IfcSpace*. In case the parameters for air inlets/outlets are not available, (1) an appropriate inlet/outlet type can be chosen based on the *IfcSpace*-dependent volumetric flow rate, or (2) a simplified inlet/outlet geometry can be created automatically.

Once the geometric data is generated and exported in the STL format, it is used as input for further pre-computation of OpenFOAM input data. The complete set of geometric data is fit into a bounding box that forms the basis of the blockMesh boundaries. The refinement surfaces and regions are defined based on the generated geometries and the semantic information on the surface types. The refinement levels are set according to the surface types and complexity of the geometry. For defining the other OpenFOAM input data, mainly the names of the STL files (geometry names) and the surface types are essential. For defining the initial boundary conditions (temperature and heat flux), the surface types and the BPS results from the PluginEnergyPlus are considered.

The outlined data mapping is only a rough overview of the OpenFOAM setup's IFC-based data mapping, distinguishing geometric and semantic information. The complete IFC-based OpenFOAM process is described in the following section.

Process of IFC-based CFD Setup

For setting up the IFC-based CFD model using OpenFOAM, several steps are required to (1) select the geometric elements, (2) apply settings for the meshing process, and (3) set boundary conditions. For the meshing setup, we use OpenFOAMs blockMesh and snappyHexMesh. We initialize the boundary conditions based on the pre-computed BPS results from the IFC-based BIM2SIM process. The implementation of the IFC-based CFD setup is visualized in Figure 2.

We implemented the PluginOpenFOAM using a modified version of the open-source butterfly

[2]OpenFOAM Documentation: https://www.openfoam.com/documentation/user-guide/2-openfoam-cases/2.1-file-structure-of-openfoam-cases, accessed on 13 January 2024

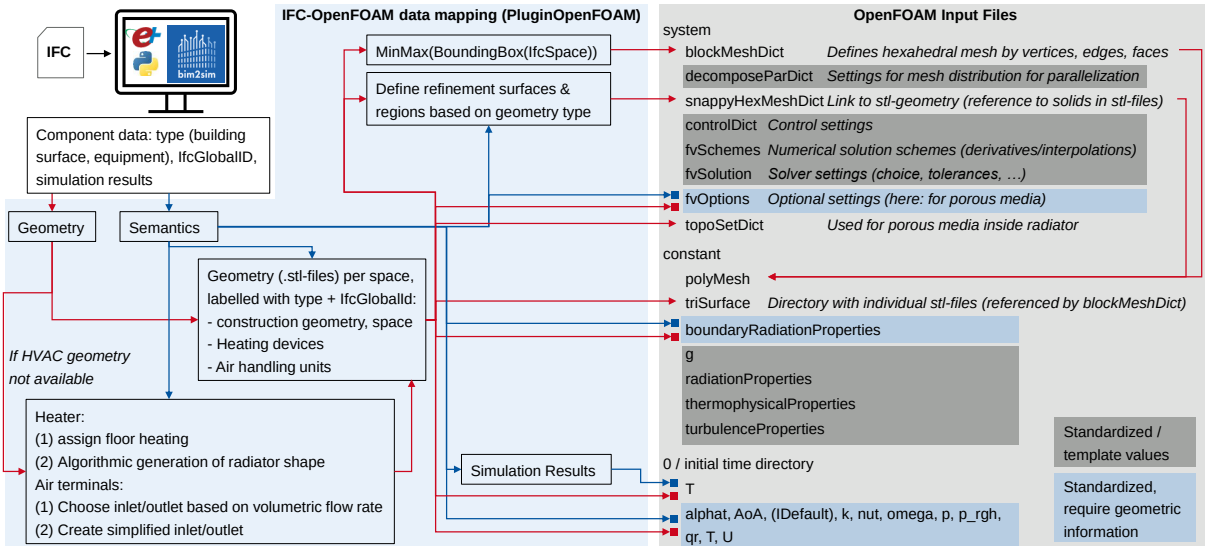

Figure 1: Data mapping process: Mapping geometric and semantic IFC-based data to OpenFOAM structure in PluginOpenFOAM (left) to the resulting OpenFOAM input files (right). The data mapping splits into geometric data processing (red lines) and semantic data processing (blue lines).

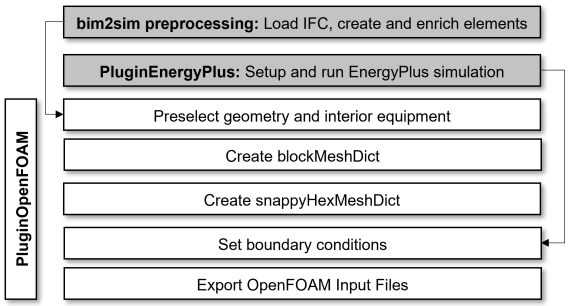

Figure 2: Structure of the PluginOpenFOAM.

plugin[3] for Grasshopper, which we updated from Python 2.7 for use in Python 3 and further modified for stand-alone use without Grasshopper. We decided to use butterfly, as it assists with the parametric setup of OpenFOAM use cases.

Pre-select geometry and interior equipment: CFD simulations require high computing resources due to high-resolution computations, as opposed to BPS, where having only a single node per zone is common. For the setup of a CFD simulation, it is therefore crucial to limit the computation to the desired space and to only include objects and surfaces in the mesh that are relevant to the simulation objective. Depending on the use case, suitable algorithms could be used to, e.g., identify thermal zones that require a detailed analysis of thermal comfort.

[3]butterfly plugin by ladybug-tools: https://github.com/ladybug-tools/butterfly, accessed on 22 February 2024

While second-level space boundaries have an explicit relation to an *IfcSpace* and, thus, can be easily selected for the CFD setup, HVAC equipment and furniture do not have such a relation to the space. Therefore, a prerequisite for an automated IFC-based CFD setup of interior spaces is a mapping process of the equipment to the spaces. To map the equipment to a space, we evaluate if the center of mass of an equipment shape is inside of the shape of this space. The efficiency of this process can be increased by the pre-selection of equipment entities per storey or a larger group of spaces.

All shapes are exported into STL files as triangulated shapes. The building construction is exported in a single file (name: 'space_IfcGlobalId') using the respective *GlobalId* in the IFC file as a general identifier. Within this STL file, the space boundaries are represented by individual solids, each uniquely identifiable by a unique key of surface type and *GlobalId*. The triangulated shapes of the HVAC equipment are exported similarly but may require further modification and/or replacement by appropriate STL shapes based on their equipment types and sizes.

If no IFC-based data on the HVAC equipment is available, an assumption for the position and parametrization can be applied. For missing space heaters, the simplest option is the parametrization of floor heating. Another option is to automatically place a radiator underneath a window (unless it is a window that reaches the floor). For this option,

a radiator shape is created that has, e.g., a distance of 12 cm to the floor and ends 5 cm below the lower surface of the window. The heater has a given depth of 8 cm and was placed in the center below the window with a wall distance of 5 cm. The heater shape consists of four vertical plates with zero thickness. A similar construction of a radiator has been applied by Risberg et al. (2017). The constructed heater shape is exported as a triangulated STL file.

For missing air terminals, the inlet/outlet type can be selected according to the space type and the expected volumetric flow rate, and an appropriate air terminal STL file can be selected for this use case. A simpler option is to use a simple gap in the ceiling as an air outlet and add a single surface below the ceiling as an inlet. In both cases, the inlet and outlet can be automatically positioned at the longer axis of the ceiling (Fig. 3), where we placed the inlet and outlet at 25 % and 75 % of the longer wall axis. These constructions are also exported to STL files with appropriate naming relating to the surface type.

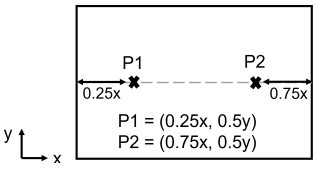

Figure 3: Top view of the inlet and outlet position in a small room.

blockMesh: The *blockMeshDict* is created as a bounding box around the shape of the *IfcSpace*. If HVAC equipment, e.g., air terminals, exceed the surrounding of the space shape (if they are installed above a suspended ceiling and the space itself is delimited by this ceiling), the air terminals are included in this bounding box. The boundaries of the blockMesh are chosen to be slightly larger than the bounding box itself to prevent computational errors in the meshing process. The block mesh cell number is computed based on the length of the space and a grid size of 0.08 m (Risberg et al. (2017): 0.10 m may also be small enough).

snappyHexMesh: The meshing instructions for a meshing setup using snappyHexMesh are represented by the *snappyHexMeshDict* in OpenFOAM. The previously exported STL files are referenced within this dictionary. The *locationInMesh* that identifies the inner part of the mesh is set to the center of the related *IfcSpace*.

Refinement regions and surfaces are defined according to the type of the (related) *IfcProduct*. As visualized in Figure 4, the exterior coordinates of

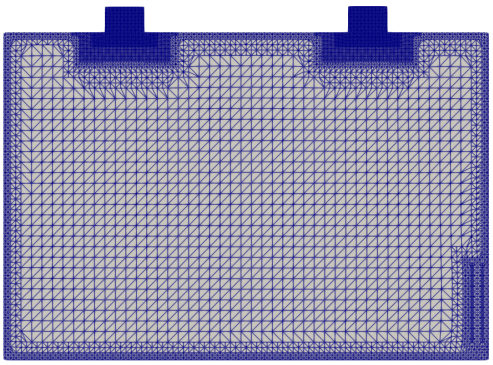

Figure 4: Automatic object-dependent mesh refinement around the space heater and the air terminals.

the refinement regions are defined by increased bounding boxes around the shapes. Within this region, the mesh is refined. For radiators and air terminals, we define two different levels of refinement to obtain more accurate results, where the smaller region has a higher granularity than the larger region that surrounds the respective object. Highly granular surfaces, such as the surface of the air terminal, are automatically assigned a high surface refinement level.

Set Boundary Conditions: The initial conditions are set according to the selected date and time within the EnergyPlus result files for the selected space (Fig. 5). For initializing the temperature boundary conditions, we match the *Surface Inside Face Temperature* from PluginEnergyPlus with the corresponding surface in the PluginOpenFOAM based on their *GlobalIds*. Similarly, the *Surface Inside Face Conduction Heat Transfer Rate per Area* is mapped as the initial condition for the surface heat transfer.

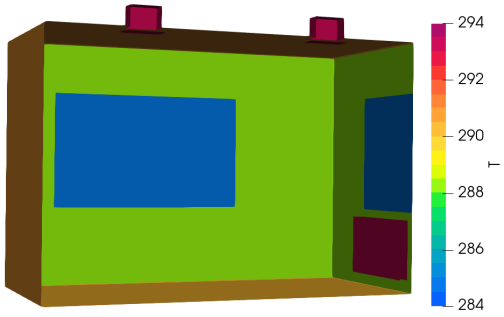

Figure 5: Initial conditions (surface temperatures) of the space, assigned based on results from the bim2sim PluginEnergyPlus.

For the radiator, we calculate the total heating power based on the energy balance of the surface heat transfer, as we currently neglect additional internal loads and solar radiation through the win-

dows. Thus, we cannot take the total heating load from the EnergyPlus results as parametrization for the heating power. We split the heating power of the radiator into 30% radiative and 70% convective power (cf. EN 442-2[4]). The convective power is implemented using a porous medium that is placed within the vertical boundaries of the radiator, which has been validated for automotive radiators with convection plates (Kang et al. 2014, Aydın et al. 2021). As our radiator does not have convection plates but uses the porous media approach, validation of this setup is required in further research.

The volumetric flow rate of the air inlet should be defined based on the data provided by the IFC file. If this is not available, it should be selected according to the room size and expected people within the room.

Simulation

We tested the setup on a single office room based on an IFC4 building (FZK-Haus)[5]. As this file does not provide any data on HVAC systems, the geometry of space heaters and air terminals is derived from the available IFC geometry. The EnergyPlus simulations that are the basis for the OpenFOAM boundary conditions are generated using the bim2sim PluginEnergyPlus using the winter design day, 21.12., 11 am, and the TMYx Weather file of Aachen, Germany. The selected room has two neighboring exterior walls with a window each and a door in one of the interior walls. The zone mean air temperature is $20\,^{\circ}$C, and the operative temperature calculated from the PluginEnergyPlus is $18.28\,^{\circ}$C.

The *buoyantSimpleFoam* solver includes radiation and natural convection within the computation for steady-state analysis of the space. P1[6] is used as the radiation model. The constructed mesh is validated the OpenFOAM mesh validation tool *checkMesh*. We performed 25000 iterations for each of the use cases. However, the residuals have shown that 5000-6000 iterations would have been sufficient to reach a quasi-steady state. For each use case, we display the temperature distribution as well as the direction of air flow, which is represented by unscaled arrows.

[4]DIN EN 442-2:2015-03: Radiators and convectors – Part 2: Test methods and rating; German version EN 442-2:2014

[5]FZK-Haus, provided by KIT, Institute for Automation and Applied Informatics (IAI).

[6]OpenFOAM Documentation - Radiation Model P1: https://www.openfoam.com/documentation/guides/latest/api/classFoam_1_1radiation_1_1P1.html, accessed on 26 February 2024

Case 1: Floor heating

In the first use case, the heating load is introduced via floor heating. Figure 6 displays the surface temperatures and the natural convection fields caused by the heated floor and exterior windows in a slice at same position as applied in Figure 5. Although

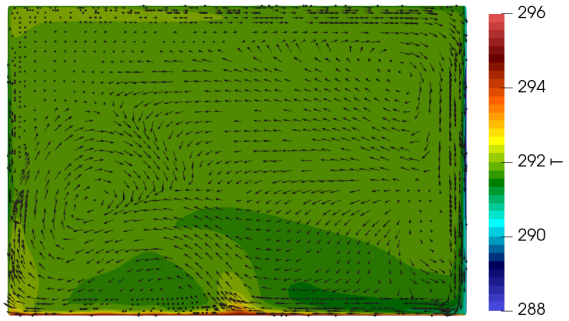

Figure 6: Air temperature and airflow for floor heating, $u_{max} = 0.258\,\mathrm{m\,s^{-1}}$, $u_{mean} = 0.066\,\mathrm{m\,s^{-1}}$.

the magnitude of the air velocity u is minimal, we see a distinct convective flow pattern downwards at the exterior window (right), across the heated flow towards the inner wall, and upwards at the inner wall (left). The surface temperature of the heated floor is $23.5\,^{\circ}$C and, thus, in the acceptable range for heated surface temperatures.

Case 2: Radiator

The second case replaces the floor heating with a single radiator automatically placed underneath one of the windows. The radiator has a radiative power of $165.56\,$W ($30\,\%$ of total heating power), which is set on the surface geometry of the radiator, and a convective power of $386.31\,$W, which is set in the porous medium within the radiator shape.

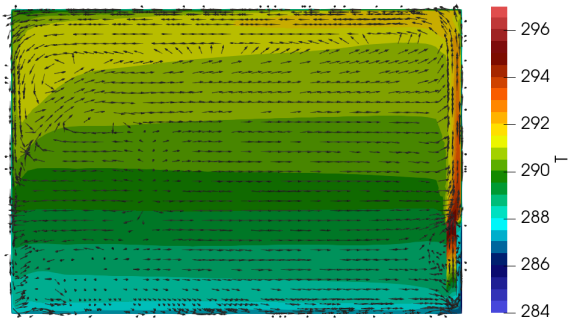

Figure 7: Air temperature and airflow in the room slicing through the radiator, $u_{max} = 0.509\,\mathrm{m\,s^{-1}}$, $u_{mean} = 0.082\,\mathrm{m\,s^{-1}}$.

Figure 7 shows the temperature distribution and the velocity field in the slice through the radiator.

The convective stream within the radiator can be clearly seen in the temperature distribution within and above the radiator and in the velocity fields. The maximum velocity of the natural convection caused by the radiator is about twice the velocity than in case of natural convection of the heated floor, which is reasonable due to the convective forces inside the radiator.

Case 3: Radiator and simple air terminals

Figure 8 displays the setup of the radiator case automatically enriched by a simplified air terminal as an air inlet and outlet. The incoming air is inserted at the top of the inlet box and deflected by a plate located 2 cm below the ceiling, 5 cm wider than the inlet box on each side. The same setup is applied to the outlet. The volumetric flow rate is set to be $90\,\mathrm{m^3\,h^{-1}}$, relating to a volumetric flow of $30\,\mathrm{m^3\,h^{-1}}$/person.

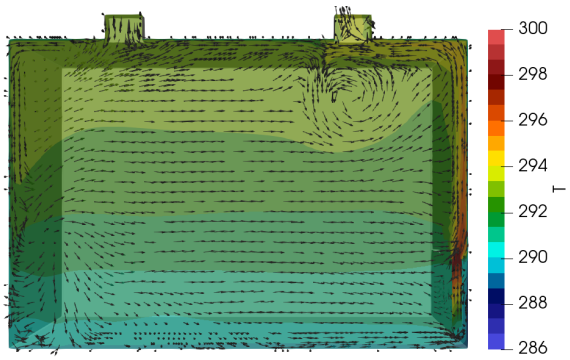

Figure 8: Use case setup with radiator and simplified inlet (left) and outlet (right) geometry. Air temperature and airflow, $u_{max} = 1.046\,\mathrm{m\,s^{-1}}$, $u_{mean} = 0.169\,\mathrm{m\,s^{-1}}$.

The velocity field in Figure 8 shows the airflow along the ceiling from the inlet, and to the outlet. Due to buoyancy forces, a swirl is created below the outlet. However, this is a very simplified setup for inlet and outlet. The air velocities from the inlet are low (about $1.0\,\mathrm{m\,s^{-1}}$) for mechanical ventilation purposes due to the relatively large inlet and outlet geometry related to a small volumetric flow rate.

Discussion and Limitations

The use case results regarding the observed velocities, velocity fields, and air temperatures are reasonable. However, both the simulation results itself, but also the automated IFC-based workflow to setup geometry and boundary conditions need further verification and validation. This can be obtained by own measurements in real buildings for which a validated IFC representation exists, by reconstructing use cases from related research as IFC scenarios, by comparing the IFC and CFD model geometry (similar to Richter et al. (2022)), or by comparing the IFC-based CFD models to the CFD models created by an expert. We simulated the cases using steady-state approaches. To better detect variations in turbulences around the air outlets, the use cases should be evaluated in transient approaches in further research.

Further research is required in a variety of fields. The approach must be extrapolated for larger room settings with multiple space heaters and air inlets and outlets, which should be extracted from available IFC files. To overcome the issue of air terminal shapes causing troubles in the meshing process, a library with suitable replacement STL files for air terminals should be set up, including different types and sizes to match the individual use cases. These air terminals could be easily mapped to the positions given in the IFC. Another option for reducing the computational cost of meshing and CFD simulation would be mapping the air terminal's turbulence profile to a surface. Therefore, we would avoid the complex meshing of multiple air inlets even in a larger room setting. In the presented setup, we manually selected the room that should be simulated. Here, an algorithm should be developed to automatically select rooms based on precomputed BPS results (i.e., identify critical rooms based on the simulation objective: e.g., evaluate surface temperature differences in a room to detect radiation asymmetry for further evaluation in CFD-based thermal comfort scenarios).

Generally, the presented approach should be tested and improved regarding mesh quality, computational efficiency, and scalability.

Our study only considered air temperatures and velocity fields, so the application domain should be extended to indoor air quality evaluation scenarios and thermal comfort applications. The approach could even be adapted for other IFC-based CFD applications, e.g., fire simulations.

Conclusion

We presented an extension to the IFC-based bim2sim framework that automatically generates CFD input files for OpenFOAM. This implementation is integrated into the bim2sim tool as the new PluginOpenFOAM. The presented setup uses the pre-computed boundary conditions (surface tem-

peratures and heat fluxes) from the BPS simulation performed within the bim2sim PluginEnergyPlus. An appropriate HVAC setup has been derived from the available IFC-based construction and simulation results due to missing HVAC IFC data. The approach has been tested and evaluated for plausibility for the room setup of a single office. In further research, the Plugin should be extended to larger room setups and IFC files providing HVAC data. The extended plugin will be published within the open-source bim2sim tool.

Acknowledgment

This research was funded by the Federal Ministry for Economic Affairs and Climate Action within the project “BIM2Praxis” (grant number 3EN1050A). Simulations were performed with computing resources granted by RWTH Aachen University under project rwth1588.

References

Aydın, A., Engin, T., Yasar, H., Yeter, A. & Perut, A. H. (2021), ‘Computational Fluid Dynamics Analysis of a Vehicle Radiator Using Porous Media Approach’, *Heat Transfer Engineering* **42**(11), 904–916.

Fichter, E., Richter, V., Frisch, J. & van Treeck, C. (2021), Automatic generation of second level space boundary geometry from IFC models, *in* ‘Proceedings of Building Simulation 2021: 17th Conference of IBPSA’, Building Simulation Conference Proceedings, KU Leuven.

Kang, K.-Y., Wang, X., Wang, J., Xu, S., Shou, W. & Sun, Y. (2022), ‘Utility of BIM-CFD Integration in the Design and Performance Analysis for Buildings and Infrastructures of Architecture, Engineering and Construction Industry’, *Buildings* **12**(5), 651.

Kang, N., Mo, N. K. & Zheng, W. Q. (2014), ‘Three Dimensional Simulation of the Heat Dissipation of an Automotive Radiator Based on Porous Media Method’, *Applied Mechanics and Materials* **543–547**, 207–210.

Lan, X., Cao, J., Lv, G. & Zhou, L. (2021), ‘Simulation method for indoor airflow based on the Industry Foundation Classes model’, *Journal of Building Engineering* **39**, 102251.

Lee, M., Park, G., Jang, H. & Kim, C. (2021), ‘Development of Building CFD Model Design Process Based on BIM’, *Applied Sciences* **11**(3), 1252.

Müller, D., Jansen, D., van Treeck, C., Fichter, E., Richter, V., Lüdemann, B., Jahangiri, P., Brunkhorst, J., Dahnke, M. & Warnecke, C. (2022), BIM2SIM - Methodenentwicklung zur Erstellung von Simulationsmodellen aus Daten des Building Information Modeling: Gemeinsamer Endbericht, Technical report, Aachen.

Nytsch-Geusen, C., Klempin, C., Nuñez v. Voigt, J. & Rädler, J. (2003), INTEGRATION OF CAAD, THERMAL BUILDING SIMULATION AND CFD BY USING THE IFC DATA EXCHANGE FORMAT, *in* ‘Proceedings of Building Simulation 2003: 8th Conference of IBPSA’, Eindhoven, Netherlands.

Park, G., Kim, C., Lee, M. & Choi, C. (2020), ‘Building Geometry Simplification for Improving Mesh Quality of Numerical Analysis Model’, *Applied Sciences* **10**(16), 5425.

Richter, V. E., Syndicus, M., Frisch, J. & van Treeck, C. (2023), ‘Extending the IFC-Based bim2sim Framework to Improve the Accessibility of Thermal Comfort Analysis Considering Future Climate Scenarios’, *Applied Sciences* **13**(22), 12478.

Richter, V., Lorenz, C.-L., Syndicus, M., Frisch, J. & van Treeck, C. (2023), Framework for automated IFC-based thermal comfort analysis based on IFC model maturity, *in* IBPSA, ed., ‘Proceedings of Building Simulation 2023: 18th Conference of IBPSA’, Building Simulation Conference Proceedings.

Richter, V., Malhotra, A., Fichter, E., Hochberger, A., Frisch, J. & van Treeck, C. (2022), Validation of IFC-based Geometric Input for Building Energy Performance Simulation, *in* I. USA, ed., ‘Proceedings of 2022 Building Performance Modeling Conference and SimBuild Co-Organized by ASHRAE and IBPSA-USA’.

Risberg, D., Westerlund, L. & Hellström, G. (2017), ‘Computational fluid dynamics simulation of indoor climate in low energy buildings: Computational set up’, *Thermal Science* **21**(5), 1985–1998.

Zheng, L., Lu, W., Wu, L. & Zhou, Q. (2023), ‘A review of integration between BIM and CFD for building outdoor environment simulation’, *Building and Environment* **228**, 109862.

BauSIM 2024 in Wien
23. September – 26. September

PEExcel: A fast one-stop-shop Assessment and Simulation framework for Positive Energy Districts

Simon Schneider[1], Raphael Drexel[1], Thomas Zelger[1], José Baptista[2]

1 Department of Industrial Engineering, University of Applied Sciences Technikum Wien, Austria, E-Mail: simon.schneider@technikum-wien.at

2 Department of Engineering, School of Science and Technology, University of Trás-os-Montes and Alto Douro, Portugal

Abstract

We present a simulation and assessment framework *PEExcel* that allows researchers and practitioners to quickly model and assess the primary energy and emission balance of operation, use and mobility of a district beginning in an early planning phase as a decision support system (DSS) for the Austrian klima**aktiv** label "climate neutral Positive-Energy-District-" (ger. "klimaneutrales Plus-Energie-Quartier").

The framework provides a one-stop-shop spreadsheet-based tool for input gathering, simulation, analysis, and assessment. It provides a quick and comprehensive overview on user-specified scenarios that achieve the required balances targets by the standard and features simulation times below ten seconds per district scenario on regular laptop machines.

It implements an hourly thermoelectric simulation model and a built-in energy-flexible DSM controller for thermally activated building systems (TABS), hot water buffer tanks, electrochemical and EV batteries as well as offsite flexibility signals.

It also serves as a common receiver and merger for most common assessment results: Timestep data for onsite renewable heat and electricity generation from generic sources, load and occupancy profiles, weather and climate data, conversion factors, etc. The framework combines this data in a ready-made analysis and assessment toolbox that includes a dashboard, interactive views of input and simulation timestep data (loads, States-of-charge, etc.), and formatted results pages featuring energy balances, load profiles, energy flows and assessment results.

Introduction

Positive Energy Districts (PED) represent large and complex systems, their implementation requires integrated planning in a holistic manner across multiple disciplines and domains ("Ten questions concerning positive energy districts | Elsevier Enhanced Reader," n.d.). City planners believe that addressing PED implementation challenges in the early conceptual phase through a broad stakeholder commitment approach can help prevent many problems by incorporating these intentions into the master planning directives (Nielsen et al., 2019).

However, it is apparent that for a PED definition focusing on a holistic and integrated energy assessment, including building operation and use, mobility and embodied energy, current dynamic models are unfeasible to deploy in early planning phases (Hedman et al., 2021).

The lack of early integration of energy planning in the district development is mostly due to the lack of data to feed more intricate energy simulation frameworks (Koutra et al., 2018): Even if sufficient data is available and modelling possible, using district simulation models is typically too resource-intensive to deploy early, as the planning will inevitably change in the process, rendering detailed simulation results invalid. On the other hand, simpler decision support systems (DSS) employing stationary methods can lack resolution of key flexibility features of PEDs or lack coverage of all required energy flows.

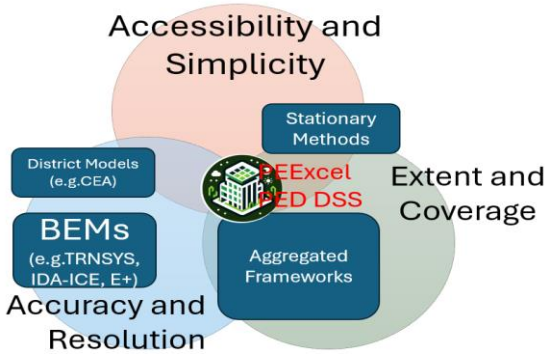

Figure 1 District energy models (DEMs) trade-off between accessibility & simplicity of modeling, accuracy, resolution and speed of simulation results, and coverage of energy services (from HVAC, DHW, plug-loads, mobility to embodied energy)

Aims and Design principles

The framework design is based on district implementation observations: PED feasibility is investigated in early district planning with many project data still unknown, and building mass and geometries can be subject to frequent change. This work aims to provide a simulation and assessment framework that is **simple to use**, **highly iterable** and **covers all aspects** of the klima**aktiv** "Positive-Energy-District Standard" of district operation and use, mobility and embodied energy and emissions with sufficient temporal and spatial resolution to serve as a DSS in an early planning stage. The theoretical framework of the underlying PED definition is based on (Schneider et al., 2023).

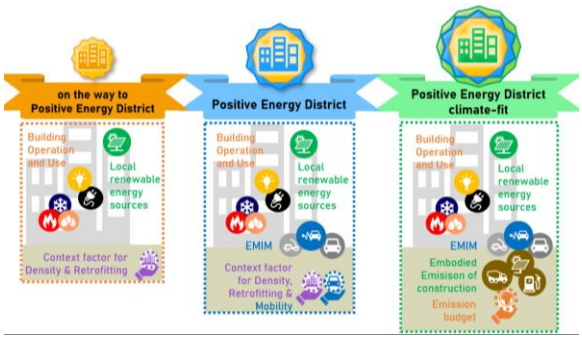

Figure 2 Available klima**aktiv** certifications for three system boundaries from operation and use (left) to individual motorized mobility (center) to embodied emissions (right)

This PED assessment necessitates hourly modelling of energy flows including e-mobility to resolve effects of sector-coupling and flexible operation and integration of electrical (batteries and EVs) and thermal storage (TABS and DHW tanks).

In addition to these requirements, the design of the framework pursues the following goals: 1) **Reduce cost of model creation**: "Default first, input later": Reduction of required input data by extensive provisioning of defaults from Austrian building code and scientific literature (Institute for Housing and Environment, 2017; Österreichisches Institut für Bautechnik, 2019). 2) **Reduce cost of data transformation**: Provision of copy-paste interfaces for data from Energy Performance Certificates (EPC) and Passive House Planning Packages (PHPP). 3) Simple creation and fast iteration through different district **scenarios**. 4) Simple **iterability** within the planning process. 5) **Accessibility and transparency**: No use of proprietary tools and software. Open access of the algorithms and data, transparency of calculations for practitioners without skills or experience in programming or scripting. 7) Simple **extensibility** and **customizability** of the simulation model for practitioners. 8) One-Stop-Shop for planning, evaluating, quality assurance and verification, reduction of data transfer requirements to a minimum.

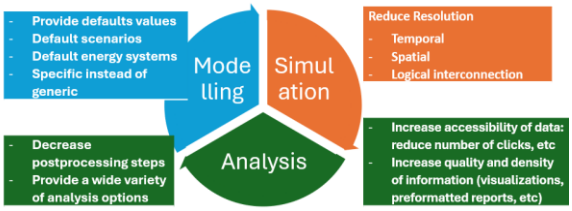

Figure 3 Design goals of the framework for three key activities of PED planning

Approach and Structure

Due to the design goals, the framework is implemented as an Excel Spreadsheet, and the simulation model is exclusively implemented in cell formulas, allowing for immediate tracing of errors, as well as edits and additions without resorting to VBA macros, or other types of scripting (i.e. with Python or MATLAB). This also ensures that virtually all stakeholders can receive, open, use, change and send the framework by themselves. The framework presentation is structured in the following three sections:

1. Model input structure and interfaces
2. Simulation model
3. Analysis and Assessment

Model input structure and interfaces

The implementation as a spreadsheet tool realizes numerical inputs in two ways:

1. Independent, atomic parameters are input in cells.
2. Semantically connected parameters (e.g. timeseries data or catalogue components) are grouped into catalogues stored in 1d or 2d cell ranges and selected by selector cell inputs.

More complex interfaces supported by Excel such as links to local or remote files or databases were foregone for the sake of accessibility and reduced external points of failure.

All model inputs can be categorized as mandatory or optional. Mandatory inputs have been reduced as much as possible and provisioned with default parameters and catalogues drawn from Austrian legal code and best-practice examples (Passive house components, etc.). The following table overviews the number and type of parameters for district modelling, requiring at a minimum nine numeric values, five catalogue selections and five

Boolean selections, which specify reference areas and usage mix, type of hull, HVAC system and flexibility strategy. In addition, 153 numeric values, 15 catalogue and 7 Boolean selections are provisioned with default values but can be specified if known by the user. Although the framework provides default timeseries data for both weather data and PV yields of a handful of locations in Austria that can be used as a starting point, TSD are typically required to be provided from other sources. But all required timeseries such as weather, usage profiles and onsite renewable production through PV can also be used from default settings. The following table shows mandatory and optional inputs per model category.

Table 1 Types of input parameters: **Mandatory** inputs are bolded, +optional inputs with defaults are preceded by a +, (N) Numeric Values, (B) Boolean, (C) Catalogue Selections, Annual Timestep Data (TSD),

Model input category	**Mandatory** +optional inputs
Reference Areas: Gross floor areas per usage	**6N**+2N
Thermal Hull	**4N1C** +31N
HVAC system	+11C,35N,6B
Space Use	+11N,66TSD
Local Renewables	**1B**+2N,1B,2TSD
Mobility	**1B**+1C,48N
Flexible Control, DSM	**3B,3C**+12N,1TSD
Weather	**1C**+6TSD
Embodied GWP	+11N
Balance Assessment	**1N**+1N,2C,3TSD
Total mandatory and +optional model inputs	**9N,5C,5B** +153N,15C,7B, +76TSD

Input and Output serialization

All non-timeseries, atomic input data (numeric, Boolean and catalogue selections), both mandatory and optional is serialized into an input vector with 194 values, representing a district scenario that together with a 295d vector of annual outputs can be represented by a single row of tabular data. Such scenario rows can subsequently be easily created, copied, compared, and reloaded for later analysis and refinement. This also facilitates the unsupervised serial simulation of batches of dozens to hundreds of scenarios configuration without additional user input.

Multiple Input layers

The serialization of model inputs also facilitates the separation of concerns within the same excel spreadsheet: Separate, user specific sheets can expose certain inputs and outputs selectively, including interfaces that the users are familiar with (e.g. PHPP, EPC forms, for architects, for bachelor and masters students), filling in the rest according to user group specific assumptions. Researchers also have access to the simulation model for verification and modification purposes and maintainers actively manage these views with permission management.

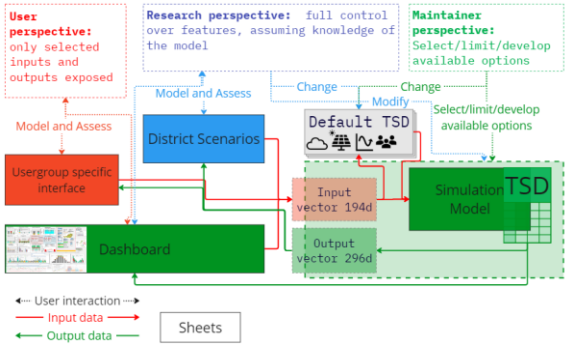

Figure 4 Model inputs and data interface structure of the PEExcel PED DSS framework.

User interface

In addition to relying on Excel's own application interface, the framework implements a custom UI ribbon offering shortcuts for menu and sheet navigation, selecting and editing scenarios.

Figure 5 Custom UI ribbon of the PEExcel PED DSS framework.

Simulation Model

The simulation model is designed to assess district scenarios in regard to their achievement of the positive energy balance targets of the klima**aktiv** PED certification standards, which necessitate the following requirements: 1) Dynamic simulation of energy flows on an hourly basis, 2) Representation of all energy services and flows for operation, use of the district's buildings, then individual motorized mobility and scope 3 embodied energy and emissions and 3)

Use of standardized defaults for space use profiles and primary energy conversion factors (Österreichisches Institut für Bautechnik, 2019). To achieve this, the simulation model is designed to trade low spatial resolution for high temporal resolution (hourly) and functional coverage over an entire year. It implements a simple single thermal zone with an RC-model for the entire district.

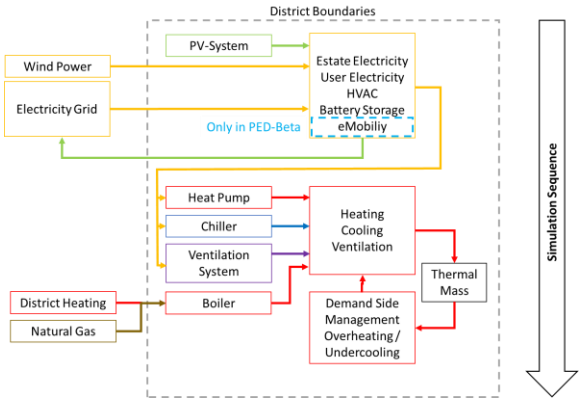

Figure 6 Model energy flows and nodes.

As can be seen in Figure 6, the model can include a boiler and a heat pump system. For comparison reasons, districts are simulated by default with four common heating systems shown in Table 2, main difference being the conversion efficiencies, transmission losses and PE- and emission conversion factors for the balance assessment.

Table 2 Default energy supply options

Energy Supply	Heating, DHW	Cooling
Natural gas	Combi boiler	VCR
District heating	DH station	VCR
Heat pump without DSM	Heat pump	Heat pump
Heat pump with DSM	Heat pump	Heat pump

Flexibility

Flexible district operation through demand side management (DSM) is modelled by using TSD of a standardized signal to control the charging and discharging of district storages, that include both thermal and electric options: TABS, DHW buffer tanks, EVs and electric batteries. Key element of the usage of building thermal mass as storage is for users to consent to a potential overachievement of their temperature setpoints, e.g. 24°C instead of 22°C, but never a reduction of setpoints. Similarly, EV, Electric battery and DHW buffer tank state-of-charge (SoC) are controlled between a minimum and maximum setpoint storing local and regional renewable surpluses whenever a corresponding signal is present.

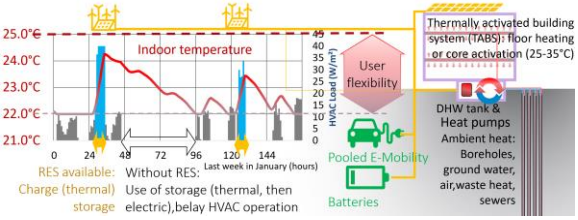

Figure 7 Flexible operation of district thermal and electric energy storages.

The DSM signal governing times of opportune grid consumption can be user defined but is representing offsite wind peak events in Austria 2015 by default for certification purposes.

One drawback of spreadsheet-based models is that dynamic and branching logical structures are hard to implement, debug and compute thanks to the required linearization into a calculation chain. This prohibits an arbitrary configuration of energy dispatch between sources and sinks. Instead, a fixed dispatching order is implemented, whose individual flows can be calibrated or turned off, but not reordered or redirected. In this linear chain, the first energy supply dispatched is from local renewables, followed by battery discharge, then from volatile regional sources (e.g. wind peak shaving) and only then regular grid electricity is used. On the demand side, user plug loads are covered first, followed by HVAC and E-mobility demand for regular operation reaching minimum specified requirements (i.e. room and DHW temperatures, aggregated EV SoC). At this point any available local or regional renewable surpluses are used for DSM, i.e. to charge the available thermal and electric storages (TABS, DHW buffer tank, EV and other batteries.

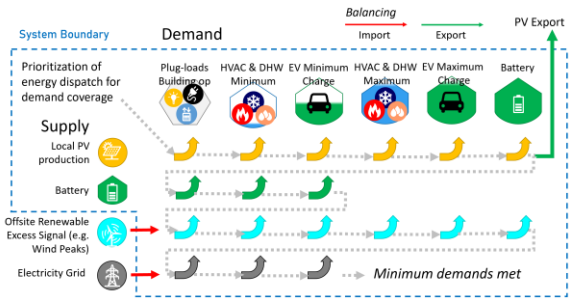

Figure 8 Model system boundary and energy flow dispatch strategy between model components for each hourly timestep.

Mobility

Key feature of the PEExcel DSS framework is the quantitative model for energy and emissions associated with everyday motorized individual

mobility (EMIM) from the district. It uses annual statistical mileage per modal split and regional location based on the Austrian Mobility (Tomschy et al., 2016).

The association of personal EMIM mileage to the district reference areas is achieved by a top-down allocation approach for all usages, allocating the statistical EMIM mileage with a certain usage destination (home, work, shopping) evenly across all floor areas in Austria of that type (residential, office, etc.) As described in (Schneider et al., 2023), this virtual balancing approach only considers energy demands from destination travel. Actual charging and fuel demand can be modelled by increasing the ratio of source travel also taken into the energy balance. It also includes a virtual sectoral mobility energy budget derived from national decarbonization scenarios.

This allows the assessment of changes in the energy and emission balance based on 1) Share of EVs of total district EMIM, 2) Temporal EV charging profile, 3) EV battery parameters and SOC thresholds, 4) bidirectional loading but also other effects such as reduced EMIM mileage due to alternative mobility measures such as cargo-bike and bike sharing, reduced parking space, and similar measures.

Analysis and Assessment

The *PEExcel* framework gathers the simulation data in a ready-made analysis and assessment toolbox that includes a dashboard, interactive views of input and simulation timestep data (loads, States-of-charge, etc.), and formatted results pages featuring energy balances, load profiles, energy flows and assessment results.

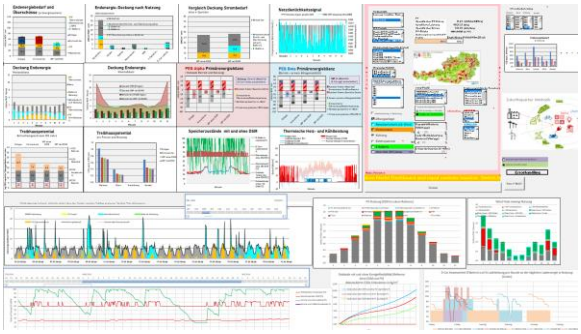

Figure 9 Screenshot of the PEExcel DSS framework Dashboard indicating main scenario selections and results.

Here, the following results are compared for 4 supply scenarios: Natural Gas, District Heating, and Heatpumps with and without flexible operation:

- Annual Energy end use balance
- Annual primary energy balance with and without mobility
- GHG Emission balance over the lifecycle including embodied emissions

Additionally, for the currently investigated scenario, the following results are displayed:

- Annual demand coverage distribution for each energy service
- Monthly Energy End Use
- Monthly Primary Energy demand, renewable and non-renewable
- Hourly Flexibility use
- Hourly storage SOC (electric, e-cars, thermal TABS and DHW tank)
- Hourly heating and cooling loads
-

The main assessment metric for positive energy districts is a positive annual total primary energy balance of energy imports and exports over the system boundary. One key element to achieve this is the inclusion of virtual context factors (Schneider et al., 2023), which depend on the district's density and the surrounding energy system for mobility and which are automatically included in the assessment balance:

The effects of flexible DSM effects can be analysed by a dynamic view of the hourly timeseries that can be panned and zoomed to a specific timeframe. Here, the effects of available local renewable surpluses and regionally available excess wind power and other external grid signals on the district storage SOC of TABS, DHW Buffer tanks, Electric Batteries and EV can be analysed. This flexible operation and its effect on the balance through dynamic weighting of the primary energy conversion factor is described in (Schneider et al., 2023), and its effect on the resulting balance can be assessed in an hourly and monthly view

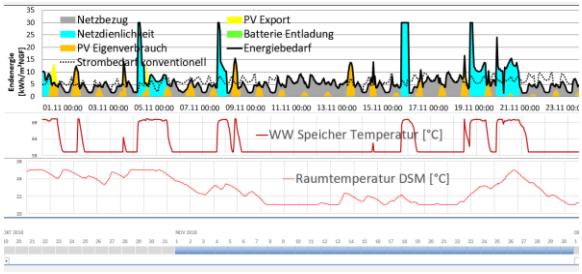

Figure 10 Interactive view of flexible load and storage SOC TSD

Scenario comparison

One major goal of the PEExcel DSS framework is to cover a large area of the PED solution space quickly and facilitate modelling, assessment, and comparison of many scenarios. This is achieved by dynamic diagrams for the energy end use

balance, and the primary energy balance with and without mobility that can display selected simulated district scenarios, as shown below.

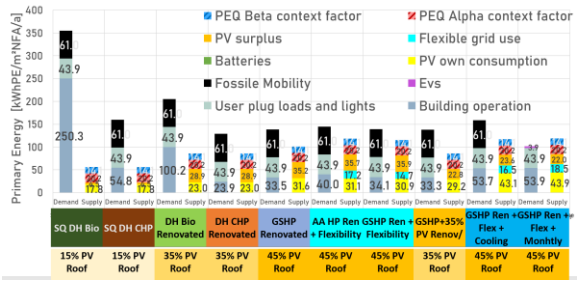

Figure 11 Example comparison of ten different scenarios in primary energy balance for operation and mobility.

Comparison to other DEMs: City Energy Analyst (Fonseca et al., 2016)

A comparison of simulated heating demands for 68 buildings in a historic Viennese district with 90% residential, a wide range of building types and a 20% renovation rate yielded the following results:

Table 3 Example district “Alliiertenviertel” in Vienna

Construction period	Buildings <Original / Renovated>		Gross Floor area [m²]
until 1918	32	11	90 554
1919-1944	2	1	8 466
1945-1960	4	2	16 669
1961-1970	6	1	21 768
1981-1990	3	0	9 846
1991-2000	1	0	3 947
2001-2010	3	0	12 230
Total	**53**	**15**	**180 492**

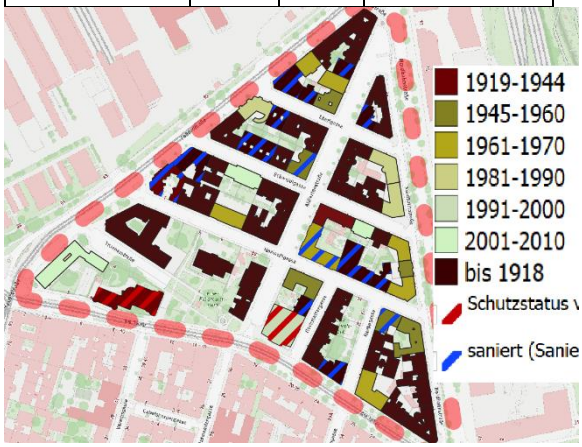

The assessment framework was compared in two scenarios: As-is (“stock”) and with all buildings renovated to current building code. The results in the following figure show both models with identical building geometry and building specific properties (U-Values, etc) and have an overall good correlation between the excel tool and CEA, especially for the existing building stock. Here, the red line indicates statistically typical heat demands for buildings of that age, renovation and usage. For the renovated cases, our tool results are higher and closer to Austrian renovation benchmarks (Richard Büchele et al., 2021), CEA results were too low in most instances (heating demands below 20 for regular Gründerzeit renovations), which is mostly attributed to default values of occupancy and internal loads not matching Austrian

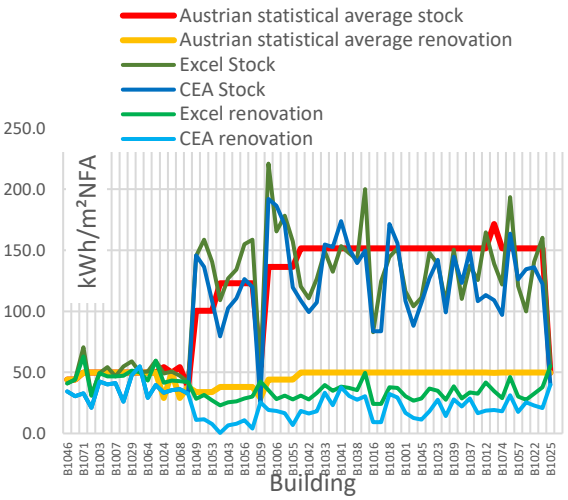

Figure 12 Heat demand for 68 buildings for scenario “stock” (current situation) and “renovation” for our simulation framework “Excel” and the City Energy Analst (CEA) compared to Austrian building type benchmarks

Discussion

This section discusses the advantages and disadvantages of the spreadsheet-based model.

Model Limits

The model design imposes the following that can be differentiated in soft limits, which can be overcome by minor changes in input data or calculation logic, and hard limits that are imposed by the model structure and cannot be circumvented in the current framework. Hard limits are:

- **Usage mix**: The number of different uses (governing load profiles, occupancy, air exchange rates, etc.) can not exceed the 6 predefined uses, however defaults of existing uses can be altered to reflect a different use type altogether.
- **Thermal LOD**: Indoor temperature in the entire district is equally distributed, no

zonal differences can be resolved. Also at any given time, the entire district uses the same temperature setpoint.
- The dispatch sequence cannot be changed or added on to simulate different controls or energy flows, only the existing steps representing individual predefined energy flows in Figure 6 can be enabled and calibrated.
- **Geometry LOD**: Geometric information is merged into eight aggregated will areas facing in eight cardinal directions, and two areas for roofs and ground floors and cellars. Detailed geometric effects such as orientation-based insolation and shading cannot be modelled.
- **Fixed hourly temporal resolution**

Additionally in the default framework the following "soft" limits exist, that can be circumvented if necessary:

- **Monovalent energy system**: Although 4 different systems are simulated simultaneously by default (gas, DH, HP w/&w/o DSM), it is not immediately possible to mix energy systems to rely on two or more energy systems at the same time (excl. PV).
- **Multiple different construction and hull types** in the district cannot be modelled directly but need to be merged by taking averages weighted by the corresponding reference areas. E.g. for thermal transmittances, thermally activated building mass, etc.)

Simulation Speed and Coverage

Simulation speeds of BEMs are heavily dependent on model LOD and size and can reach from seconds to hours and days for large district models. One approach to limiting run time is to limit such simulations to a smaller timeframe such as typical days or weeks. By contrast, the simulation times of our model is independent of district size and is reliably below 10s on regular laptop machines. This cheapness enables the heavy use of variational analysis iterating through 600 district scenarios per hour.

Accessibility: Model creation

The cost of model creation is critical to its accessibility, determined by the extent of manual steps and the availability and quality of default data. Our framework restricts the potential to model any kind of district energy system (DES) to a high LOD and instead aims to make modelling of typical decarbonized DES as cheap as possible with suitable default parameters and catalogue options. It trades a lack of customizability, flexibility and LOD in the solution space for quicker model creation and iteration.

Accessibility: Deployment

The tool is designed as a DSS in the early planning phases for district development stakeholders such as city planners, architects and engineers that are not necessarily familiar with expensive BEMs and DEMs.

Accessibility: Open source

The spreadsheet and supplementary material is publicly available as open source[1]. Furthermore, all calculations and algorithms are directly accessible as cell formulas and can be inspected and changed at will.

Functional Coverage

Although it may be possible in principle, modifying existing frameworks to cover additional energy services, such as user plug-loads, and in particular EMIM and embodied energy, typically also incurs additional modelling costs to supply required data and processing models to the framework. Compared to simple stationary methods, the tool provides higher temporal resolution and accuracy for critical KPIs such as energy self-sufficiency, ratio of own-consumption, and temporally weighted primary energy and emission conversions.

Algorithm programming with VBA

MS Excel files can be modified programmatically with Visual Basic for Applications (VBA). The framework makes use of this, but only for convenience functions such as navigation, loading and saving of scenario configurations and results and other utility functions for development, maintenance, and debugging. In contrast, the calculation logic was deliberately implemented in sheet formulas exclusively to ensure that users can trace calculations and potential errors with readily available excel functions.

Version control

Although limited options exist, a major disadvantage of spreadsheets is their inherent inaccessibility of a kind of version control commonly found in software development (Macedo et al., 2019). The combined structure of data, algorithms and user interface in a single file severely hinders any form of parallel activities, in particular collaborative development of features and version control. As such, structural integrity and validity of the framework implementation is

[1] at https://github.com/simonschaluppe/peexcel

naturally low and development cycles need to be carefully orchestrated.

Testing and Validation

Ensuring the validity of the simulation model is a main concern of the DSS framework. This is typically done by both unit tests and integration tests, testing individual functional units and the integration into the whole system respectively. For a spreadsheet-based solution, unit tests can hardly be realized, because the control flow of the calculations is hardcoded and cannot be changed dynamically. Instead, the framework is forced to rely on integration tests only, which are realized as hundreds of district scenario test cases with known results.

Managing file size

The entire spreadsheet tool of the PED DSS framework consists of 25 sheets. The hourly simulation consists of 375 energy flows, calculated for 8760 timesteps each. When dealing with this amount of structured data in an unstructured data format such as Excel, it is very important to carefully manage cross references between cells and sheets: If done incorrectly, files can gain orders of magnitude in size due to redundant and lengthy links. In general, calculation on any given sheet should only reference previous ones to the left and then to the top, avoiding references to the bottom and right and especially cross-sheet lookups as much as possible. With these optimizations, the file size is 75 MB for regular .xlsm and 48 MB when stored in a binary .xlsb format.

Conclusion

This paper presents a simulation and assessment framework for the Austrian klima**aktiv** certification of climate neutral Positive Energy Districts. It allows researchers and practitioners to quickly model and assess the primary energy and emission balance of operation and mobility of a district and provides a quick yet detailed overview on user-specified scenario configurations that achieve the energy and emission balances required by the certification standard. The framework provides a one-stop-shop spreadsheet-based tool for input gathering, simulation, analysis, and assessment. It serves as a common receiver and merger for most common assessment results: Timestep data for onsite renewable heat and electricity generation from generic sources, stationary load profiles, weather and climate data, conversion factors, etc.

The hourly thermoelectric simulation enables dynamic assessment of energy flexibility operation but due to the limitations of spreadsheets the flexibility strategy itself is fixed.

Its strengths lie in its fast deployment and low cost of model creation, quick iterability and high number of investigable scenarios due to its fast simulation times of five to twenty seconds per run on regular laptop machines.

However, these capabilities come at the expense of the spatial resolution and the flexibility of the energy model itself, limiting the application of the tool to its designed use cases.

Acknowledgements

This research was partly funded by the Austrian Research Promotion Agency (FFG) research project “Zukunftsquartier Österreich” (Schöfmann et al., 2020) and the federal ministry for climate.

Data and Tool Availability Statement

The PEExcel PED DSS framework is publicly available at https://github.com/simonschaluppe/peexcel.

References

Fonseca, J.A., Thomas, D., Willmann, A., Elesawy, A., Schlueter, A., 2016. The City Energy Analyst Toolbox V0.1 7 p. https://doi.org/10.3929/ETHZ-A-010690828

Hedman, Å., Rehman, H.U., Gabaldón, A., Bisello, A., Albert-Seifried, V., Zhang, X., Guarino, F., Grynning, S., Eicker, U., Neumann, H.-M., Tuominen, P., Reda, F., 2021. IEA EBC Annex83 Positive Energy Districts. Buildings 11, 130. https://doi.org/10.3390/buildings11030130

Institute for Housing and Environment, 2017. TABULA - Typology Approach for Building Stock Energy Assessment [WWW Document]. TABULA WebTool. URL https://webtool.building-typology.eu/#bm (accessed 5.8.22).

Koutra, S., Becue, V., Gallas, M.-A., Ioakimidis, C.S., 2018. Towards the development of a net-zero energy district evaluation approach: A review of sustainable approaches and assessment tools. Sustainable Cities and Society 39, 784–800. https://doi.org/10.1016/j.scs.2018.03.011

Macedo, J., De Sousa Saraiva, J., Cunha, J., Moreira, R., 2019. Get Your Spreadsheets Under (Version) Control. Presented at the Conferencia Iberoamericana de Software Engineering, pp. 100–113.

Nielsen, B.F., Baer, D., Lindkvist, C., 2019. Identifying and supporting exploratory and exploitative models of innovation in municipal urban planning; key challenges from seven Norwegian energy ambitious neighborhood

pilots. Technological Forecasting and Social Change 142, 142–153. https://doi.org/10.1016/j.techfore.2018.11.007

Österreichisches Institut für Bautechnik, 2019. OIB RL6 -Energieeinsparung und Wärmeschutz, OIB-330.6-026/19.

Richard Büchele, Lukas Götzlich, Richard Heimrath, Thomas Mach, Franz Mauthner, Ingrid Schardinger, 2021. Spatial Energy Planning for Heat Transition D4.2 RECOMMENDATIONS FOR HARMONISED STANDARD METHODS FOR Spatial Energy Planning.

Schneider, S., Zelger, T., Sengl, D., Baptista, J., 2023. A Quantitative Positive Energy District Definition with Contextual Targets. Buildings 13, 1210. https://doi.org/10.3390/buildings13051210

Schöfmann, P., Zelger, T., Bartlmä, N., Schneider, S., Leibold, J., Bell, D., 2020. Zukunftsquartier - Weg zum Plus-Energie-Quartier in Wien (No. 11/2020), Berichte aus Energie- und Umweltforschung. Austrian Research Promotion Agency, Vienna.

Ten questions concerning positive energy districts | Elsevier Enhanced Reader, n.d. https://doi.org/10.1016/j.buildenv.2022.109017

Tomschy, R., Josef, F., Follmer, R., Sammer, G., Klementschitz, R., 2016. Österreich unterwegs 2013/2014. BMFIT, Wien.

BauSIM 2024 in Wien
23. September – 26. September

Artificial neural networks use for the design of geothermal probe fields

Tobias Blanke[1,3], Felix Pfeiffer[1,3], Joachim Göttsche[1] und Bernd Döring[3]

[1] *Solar-Institute Jülich (SIJ), FH Aachen, Deutschland*

[3] *Institute of Smart Building Engineering (ISBE), FH Aachen, Deutschland*

Abstract

The utilization of geothermal energy is crucial for achieving sustainable heating solutions during the transition to renewable energy sources. Geothermal probes, also known as borehole heat exchangers, are used to extract heat from the ground. These probes can operate individually or be combined into probe fields to meet larger heating demands. The design of these fields must account for potential undercooling or overheating over extended periods. G-functions are typically employed to calculate the thermal behavior of the ground with interconnected borehole heat exchangers. However, calculating numerical solutions for these functions can be very time-consuming.

This study involves training artificial neural networks (ANN) using pre-calculated g-functions. The accuracies and calculation times of the trained ANN were then compared. The study created a dataset with over 819 000 g-functions for a rectangular probe field. Two different ANNs were trained using 80 % of the dataset. The study then determined the accuracy of the g-functions generated by the ANN and the calculation speed.

The results indicate that the mean absolute percentage error was below 2.3 %. On average, the calculation time was less than 0.1 % of the original time. Large probe fields performed better than average in terms of calculation time. The reduced calculation time enables the computation of complex tasks within a reasonable timeframe, including depth sizing and borefield design optimizations.

Introduction

Progressing the implementation of the heat transition requires innovative approaches to harness renewable energy, with geothermal energy emerging as a promising source of sustainable heat (CIUCCI 2023, Anderson & Rezaie 2019, Rybach 2022). The scalability of ground-source heat pumps, which can be utilized not only individually but also combined to form probe fields, is gaining significance (Rybach 2022). In the planning and designing of such fields, the long-term thermal development, particularly the avoidance of undercooling or overheating over several decades, plays a central role in achieving successful and sustainable energy production (Peere et al. 2021).

The dimensioning of geothermal fields poses a challenging task, requiring a comprehensive approach due to its complexity and numerous influencing factors (Cimmino & Cook 2022, Raos et al. 2022). Various methods for sizing such fields can be found in the relevant literature, differing in terms of their complexity and accuracy (Peere et al. 2021). Studies, as documented in Peere et al. (2021), have shown that simplified methods are not universally applicable, as the calculation of geothermal fields depends on a multitude of factors. Particularly noteworthy is the semi-analytical solution proposed by Cimmino (Cimmino 2019), which is based on the use of g-functions. This solution allows for the calculation of the effective temperature at the borehole wall and is based on the dimensionless inlet fluid temperature and a newly introduced effective thermal resistance of the borefield (Peere et al. 2021). This innovative approach opens up new avenues for more precise and differentiated analyses in the dimensioning of geothermal fields. However, this method comes with a significant time commitment, making the calculation time-consuming (Spitler et al. 2020).

One option to improve the calculation time is the use of artificial neural networks (ANNs) (Dusseault & Pasquier 2019, Pasquier et al. 2018, Shoji et al. 2022). They have also been used in the studies by Dusseault & Pasquier (2019), Pasquier et al. (2018) and Shoji et al. (2022). Shoji et al. (2022) used an ANN on an infinite cylindrical source model for the ground response calculation. This ANN leads

to calculation times of more than 5 seconds for a 20 year horizon, which is slower than the calculation time of a g-function in Cimmino & Cook (2022). Dusseault & Pasquier (2019) and Pasquier et al. (2018) used g-functions for the ANN training. Pasquier et al. (2018) focused on short-term g-functions, resulting in accurate results and calculation times below 10 ms. This short-term g-function are assumed to be independent of the geothermal probe field. Dusseault & Pasquier (2019) focused on combining short and long-term effects on a geothermal field within a 30 m x 30 m area. This paper considers a flexible placement of the geothermal probes within this area. This ANN requires about 11 ms to calculate 40 g-function values representing a 100 year simulation. ANNs are reasonable for borefield design algorithms which require a high amount of g-functions. An Example could be the determination of the number of boreholes to cover a certain demand.

This publication examines the impact of applying ANNs on the calculation of rectangular geothermal fields since rectangular shapes are assumed to be the most commonly used shape. This rectangular shape is a key difference from Dusseault & Pasquier (2019) and the assembled area is also not limited to an area of 30 m x 30 m. In this case, ANNs are also trained to work with previously calculated g-functions to predict the thermal development in the ground. In the course of this investigation, not only are the accuracies of ANN-based designs compared to untrained data, but also the associated calculation times are thoroughly examined. This approach allows for a comprehensive evaluation of the effectiveness and efficiency of ANNs as a potential alternative in the design of geothermal fields. To achieve this goal, an extensive dataset with over 819 000 g-functions for a rectangular probe field was created. Using 80 % of this dataset, two different ANNs were trained. The first creates multiple outputs for all time steps simultaneously, and the second creates one output per time step, which is an additional input here. The study focuses on accuracy concerning untrained data as well as calculation speed. The results of this study provide insights not only into the precision of artificial neural networks but also into their potential for reducing calculation time.

Methodology / Simulation

Table 1 presents the different variants for the input of g-function examples used for ANN training and verification. It is worth noting that all borefields are rectangular in shape. The number of boreholes given represents the number in one of the two directions of the borefield, and all possible combinations with that number of boreholes are covered. For example, the number of boreholes could be 2 in width direction and 3 in length direction, or 20 in width direction and 7 in length direction. The maximum number of boreholes in the borefield is set to 30 in each direction, resulting in a maximum of 900 boreholes in total. Similarly to the number of boreholes, the spacing between boreholes varies in both directions. For instance, in one variant, the spacing could be 2 meters in width direction and 6 meters in length direction. In contrast, the parameters depth, burial depth, borehole radius, and thermal diffusivity are not direction-dependent and apply to each borehole in the respective variant. These parameter variations lead to more than 819 000 g-functions, a substantial dataset. According to a rule of thumb, this is 1000 times the number of outputs and 100 times the number of features (8) (Alwosheel et al. 2018), ensuring robust training and verification of the ANN.

All g-functions have been calculated using pygfunction (Cimmino 2023). The g-functions are calculated for 100 years with a one-hour time steps using the Claesson-Javed function to simplify the time steps (Claesson & Javed 2012). This function yields to 87 values for each g-function.

Table 1: Input parameter variations

input	unit	values
number of boreholes in width direction	-	1, 2, 3, 4, 7, 10, 20, 30
number of boreholes in length direction	-	1, 2, 3, 4, 7, 10, 20, 30
borehole spacing in width direction	-	2, 4, 6, 9
borehole spacing in length direction	-	2, 4, 6, 9
depth	m	50, 100, 150, 200, 300, 400, 500, 1000
burial depth	m	1, 5, 10, 100
borehole radius	m	0.05, 0.1, 0.15, 0.2, 0.4
thermal diffusivity	mm^2/s	10, 5, 1, 0.5, 0.1

The g-functions are utilized for training and testing the neural network, which is implemented using TensorFlow (Google 2023). 80 % of the calculated g-functions are used for ANN training, while the remaining 20 % are reserved for validation purposes. Two neural networks are utilized - the first reproduces 87 values at once, while the second gets the time step as input and creates these 1 g-function values. The number of layers and nodes is limited

to the weighting factor and training data size, which should be linked by a factor of 50 (Alwosheel et al. 2018), resulting in a maximum number of weights of approximately 13025.

The first ANN uses three dense layers with varying numbers of neurons. The first dense layer has various neurons from 4 to 1032 with a step of 4. The second layer fills up until the maximal number of weights for the sample data set is reached, while the last dense layer has 87 neurons. The time step difference between the g-function and the first value is used for both training and validation. Additionally, the input data is normalized by dividing it by the maximal value of each input category.

The second ANN also uses three layers but produces only one output; hence, the last layer has only one neuron. The same rules as for the previously explained ANN are also applied to this one.

In order to determine the optimal configuration for two ANNs, their layers have varying potential numbers of neurons. So, these different numbers of neurons are fit for 50 epochs using Adam as optimizer (Keskar & Socher 2017, Kingma & Ba 2014). Different accuracy indicators, such as the mean absolute error (MAE) and mean square error (RMSE) (Willmott & Matsuura 2005), are then calculated. The best configuration for each ANN is chosen based on these indicators and used for performance calculation and validation. Before this validation, they will get a detailed fitting using stochastic gradient descent with momentum optimizer Robbins & Monro (1951), Keskar & Socher (2017)

These best neural networks are used for an example implementation in GHEtool (Peere & Blanke 2022). With this implementation a time comparison will be performed to investigate the time benefits. Furthermore, the accuracy in depth sizing and temperature calculation will be presented. The new implementation will be compared to the current pygfunction implementation for borehole depth sizing in the four validation cases of Peere et al. (2021). These four cases differ in their limiting temperature appearance and are visualizied in Figure 1. The first case leads to an overheating of the borefield in the first year and the second case in the last year. The third case leads to undercooling in the first year and the last case in the last year. The borefield has a width of 9 probes, a length of 12, and a spacing of 6.5 m in width direction and 5.5 m in length direction. The Borehole depth is 110 m and starts at 4 m below ground with a radius of 75 mm. 0.2 m K/W is the thermal resistance of the probe. The ground temperature is assumed to be 10 °C and the soil has a conductivity of 3 W/(m K) as well as a heat capacity of 2.4 MJ/m^3. This is close to being the parameters of Peere et al. (2021). Only the number of boreholes in width, the depth and the spacing have been slightly changed to deviate from the sample data.

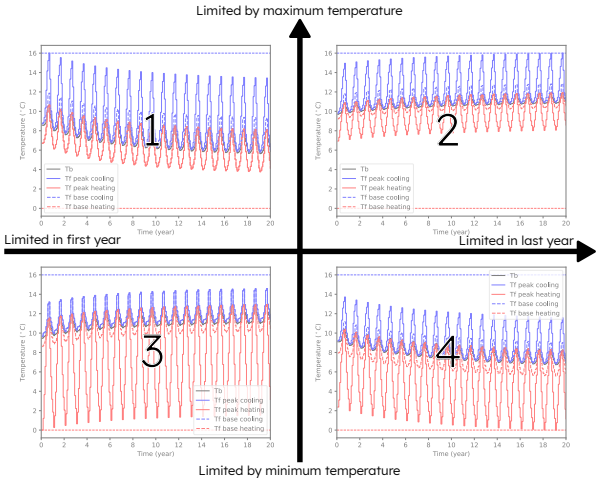

Figure 1: Visualization of the four validation cases

For all four cases two different depth sizing algorithms are performed. The first one is based on Peere et al. (2021) called L2, using only the three most important months of the year for heating and cooling design. L3 utilizes data from all months.

Results analysis and discussion

Figure 2 shows the MAE and RMSE for the two ANNs. Both networks lead to different numbers of neurons for the minimal value area. The 87-neuron design leads to a minimal MAEs and RMSEs around 256 neurons. So, here, 256 neurons for the first layer and 32 neurons for the second layer are chosen and considered for detailed training. The 1-neuron design leads to a minimal MAEs and RMSEs around 400 neurons. So, here, 400 neurons for the first and 23 neurons for the second layer are chosen and considered for detailed training.

Table 2 displays the global accuracy indicators for the detailed ANN training. The MAE for both ANNs is around 0.2, which is small compared to the mean value of the data, which is around 15.9 and the median value around 4.5. The median absolute error (DAE) is 0.13 for the 87-neuron design and 0.06 for the 1-neuron design, which is also tiny. Both absolute errors are lower for the 1-neuron design than for the 87-neuron design. The RMSE shows the opposite trend. The error is 0.38 and 0.59, which is still relatively small. The mean ab-

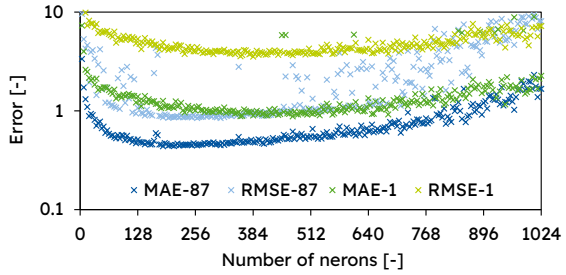

Figure 2: Error for both neural network layouts of different number of neurons

solute percentage error (MAPE) for all layouts is around 2.3 %. So, the ANN training worked well.

Table 2: Accuracy indicators for the neural network training

Neurons	data	MAE [-]	DAE [-]	RMSE [-]	MAPE [%]
87	trian	0.2142	0.1256	0.3800	2.28
	test	0.2155	0.1257	0.3825	2.29
1	trian	0.1878	0.0560	0.5951	2.29
	test	0.1872	0.0559	0.5947	2.29

Figure 3 shows the error and calculation time for the 87-output design. The figure displays the absolute error, the relative absolute error to sample data, and the calculation time for both the sample data and the ANN data. The absolute error and the relative error are low. The maximal absolute error is about 60, while the majority of the errors are between 0.2 and 0.003. The maximal relative absolute error is about 100 %, while the majority of the errors are between 0.8 % and 6 %. Between the test data and the training data, there is no big difference in the error calculation. So, it can be concluded, that the ANN has been trained successfully. The calculation time is significantly lower for the ANN compared to the sample data. The calculation time for the median is less than 0.01 % of the original sample data calculation time.

Figure 4 shows the error and calculation time for the 1-output design. The figure shows the absolute error, the relative absolute error to sample data and the calculation time for the sample data and the ANN data. The absolute error and the relative error are low. The maximal absolute error is about 100, while the majority of the errors are between 0.02 and 0.002. The maximal relative absolute error is about 110 %, while the majority of the errors are between 0.7 % and 3 %. Between the test data and the training data, there is no big difference for the error calculation. So, it can be concluded, that the ANN has been trained successfully. The calculation time is significantly lower for the ANN compared to the sample data. The calculation time for the median is less than 0.005 % of the original sample data calculation time.

Figure 5 illustrates the outcomes of the validation process conducted on the four cases outlined in Peere et al. (2021). The initial plot delineates the computation time, demonstrating a remarkable reduction achieved through the integration of ANNs. The employment of ANNs has expedited the calculations by a factor of 100 compared to the conventional approach.

Subsequently, the following graph depicts the absolute discrepancy in depth between the original calculation and those conducted utilizing ANNs. The depth variance remains below 2 % and 2.8 meters across all cases, albeit exhibiting slightly higher deviations in cases 2 and 4. This discrepancy can be attributed to the intricate nature of these cases, which are tailored for the preceding year, necessitating precise g-function values for accurate modeling. Nonetheless, an error margin below 2.5 m generally appears acceptable (Peere et al. 2023).

Lastly, the third graph presents the absolute temperature divergence across the four cases, calculated based on depths derived from the conventional algorithm. The discrepancies observed are below 0.3 K, indicating a satisfactory level of accuracy (Peere et al. 2023).

Conclusion

In this publication two different ANNs have been introduced aiming to approximate g-function values of a rectangular borefield. Therefore, a sample data set of 819 000 g-functions has been created. This set has been used to train different layer designs of the two ANNs. The best two have been considered for extensive training and the resulting trained ANNs have been used for validation. The validation shows, that the simulation time can be decreased for the pure g-function calculation as well as for the depth sizing algorithm by a factor of 100. The mean absolute error and the mean squared error stay below 1 %. So, the ANN approach is appropriate for the g-function calculation.

As future work, an approach could involve using ANNs for algorithms with extensive g-function calculation, such as designing the borefield probe number in a certain area to fit specific demand requirements. Furthermore, a more general approach, similar to the one in Dusseault & Pasquier

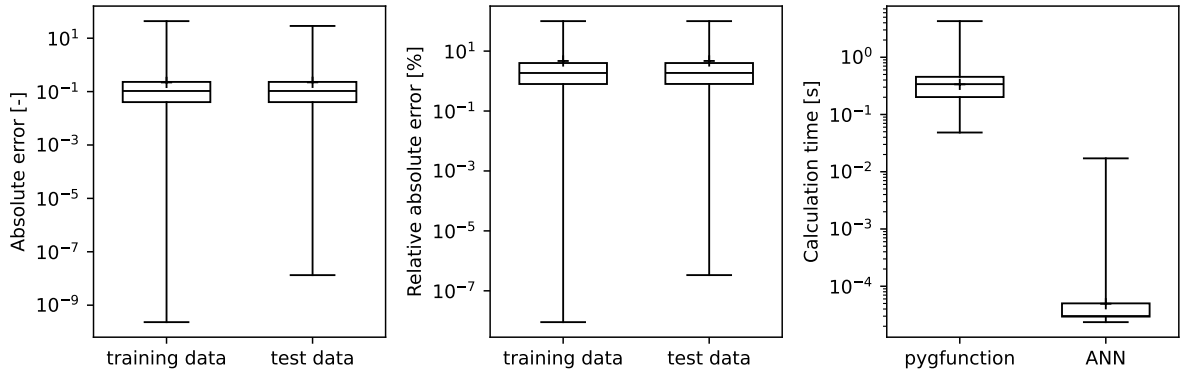

Figure 3: Results for the calculation time, depth error and temperature error of the 87 neurons output-layout

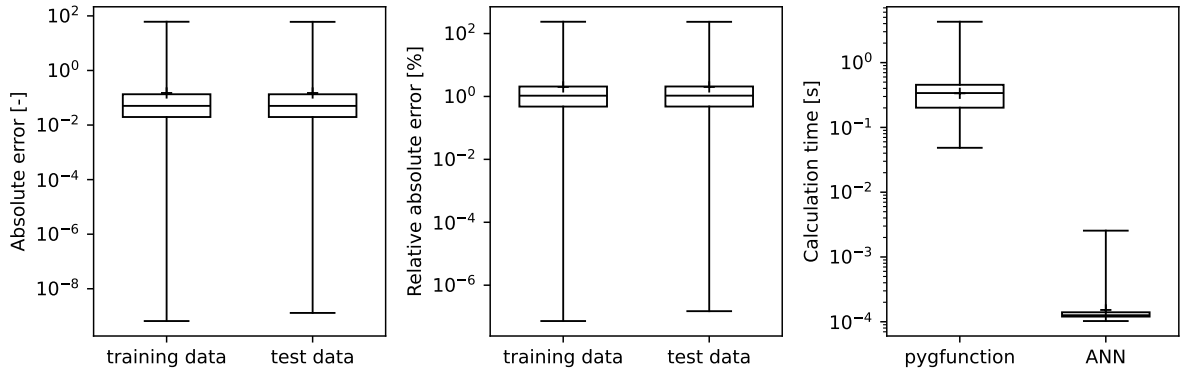

Figure 4: Results for the calculation time, depth error and temperature error of the 1 neuron output-layout

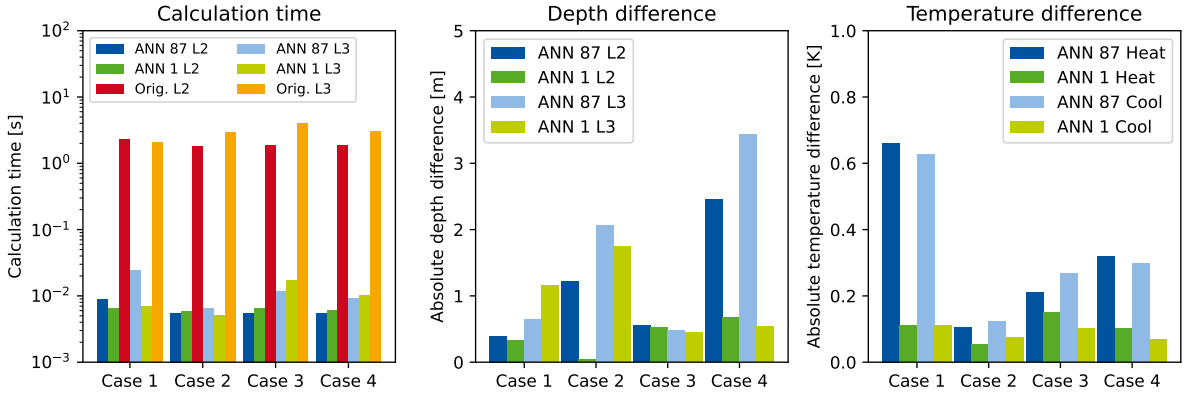

Figure 5: Validation for the different cases of Peere et al. (2021)

(2019), which takes a non-rectangular borefield as input, should be investigated over a larger area than in Dusseault & Pasquier (2019). Additionally, new data sets for different borefield shapes can be created and ANNs can be trained.

Abbreviations

ANN Artificial neural network

DAE Median absolute error

MAE Mean absolute error

MAPE Mean absolute percentage error

RMSE Root mean square error

References

Alwosheel, A., van Cranenburgh, S. & Chorus, C. G. (2018), 'Is your dataset big enough? sample size requirements when using artificial neural networks for discrete choice analysis', *Journal of Choice Modelling* **28**, 167–182. DOI: 10.1016/j.jocm.2018.07.002.

Anderson, A. & Rezaie, B. (2019), 'Geothermal technology: Trends and potential role in a sustainable future', *Applied Energy* **248**, 18–34. DOI: 10.1016/j.apenergy.2019.04.102.

Cimmino, M. (2019), 'Semi-Analytical Method for g -Function Calculation of bore fields with series- and parallel-connected boreholes', *Science and Technology for the Built Environment* **25**(8), 1007–1022. DOI: 10.1080/23744731.2019.1622937.

Cimmino, M. (2023), 'pygfunction (2.2.2)'. DOI: 10.5281/zenodo.7517471.

Cimmino, M. & Cook, J. (2022), 'pygfunction 2.2: New features and improvements in accuracy and computational efficiency', *IGSHPA Research Track 2022* . DOI: 10.22488/okstate.22.000015.

CIUCCI, M. (2023), *Innovative technologies in the development of geothermal energy in Europe*, Publications Office. DOI: 10.2861/68832.

Claesson, J. & Javed, S. (2012), 'A Load-Aggregation Method to Calculate Extraction Temperatures of Borehole Heat Exchangers', *Ashrae Transactions* **118**, 530–539.
URL: *https://api.semanticscholar.org/CorpusID:108003926*

Dusseault, B. & Pasquier, P. (2019), 'Efficient g-function approximation with artificial neural networks for a varying number of boreholes on a regular or irregular layout', *Science and Technology for the Built Environment* **25**(8), 1023–1035. DOI: 10.1080/23744731.2019.1634932.

Google (2023), 'TensorFlow (2.15.0)'.
URL: *https://www.tensorflow.org/*

Keskar, N. S. & Socher, R. (2017), 'Improving Generalization Performance by Switching from Adam to SGD', *Computer Science* . DOI: 10.48550/arXiv.1712.07628.

Kingma, D. P. & Ba, J. (2014), 'Adam: A Method for Stochastic Optimization', *International Conference on Learning Representations* . DOI: 10.48550/arXiv.1412.6980.

Pasquier, P., Zarrella, A. & Labib, R. (2018), 'Application of artificial neural networks to near-instant construction of short-term g-functions', *Applied Thermal Engineering* **143**, 910–921. DOI: 10.1016/j.applthermaleng.2018.07.137.

Peere, W. & Blanke, T. (2022), 'GHEtool: An open-source tool for borefield sizing in Python', *Journal of Open Source Software* **7**(76), 4406. DOI: 10.21105/joss.04406.

Peere, W., Hermans, L., Boydens, W. & Helsen, L. (2023), Evaluation of the oversizing and computational speed of different open-source borefield sizing methods, *in* 'Proceedings of Building Simulation 2023: 18th Conference of IBPSA', BS 2023, IBPSA. DOI: 10.26868/25222708.2023.1287.

Peere, W., Picard, D., Cupeiro Figueroa, I., Boydens, W. & Helsen, L. (2021), 'Validated combined first and last year borefield sizing methodology.'. DOI: 10.26868/25222708.2021.30180.

Raos, S., Hranić, J., Rajšl, I. & Bär, K. (2022), 'An extended methodology for multi-criteria decision-making process focused on enhanced geothermal systems', *Energy Conversion and Management* **258**, 115253. DOI: 10.1016/j.enconman.2022.115253.

Robbins, H. & Monro, S. (1951), 'A Stochastic Approximation Method', *The Annals of Mathematical Statistics* **22**(3), 400–407. DOI: 10.1214/aoms/1177729586.

Rybach, L. (2022), 'Geothermal Heat Pump Production Sustainability—The Basis of the Swiss

GHP Success Story', *Energies* **15**(21), 7870. DOI: 10.3390/en15217870.

Shoji, Y., Katsura, T. & Nagano, K. (2022), 'MICS-ANN model: An artificial neural network model for fast computation of G-function in moving infinite cylindrical source model', *Geothermics* **100**, 102315. DOI: 10.1016/j.geothermics.2021.102315.

Spitler, J., Cook, J. & Liu, X. (2020), 'Recent Experiences Calculating g-functions for Use in Simulation of Ground Heat Exchangers', *Geothermal Resources Council Transactions* .
URL: *https://hdl.handle.net/11244/335285*

Willmott, C. J. & Matsuura, K. (2005), 'Advantages of the mean absolute error (MAE) over the root mean square error (RMSE) in assessing average model performance', *Climate Research* **30**, 79–82. DOI: 10.3354/cr030079.

BauSIM 2024 in Wien
23. September – 26. September

Begleitende Simulationsanalysen zur Unterstützung der energetischen Sanierung des Hochschulcampus Berlin-Charlottenburg

Helena Burchard, Werner Kaul-Gothe, Christoph Nytsch-Geusen, Lucas Westermann

Universität der Künste Berlin, Deutschland, E-Mail: nytsch@udk-berlin.de

Kurzfassung

Auf dem Hochschulcampus Berlin-Charlottenburg (HCBC) befinden sich über 40 Gebäude der Technischen Universität Berlin (TUB) und der Universität der Künste Berlin (UdKB), die sich mehrheitlich in einem energetisch nicht sanierten Zustand befinden und zu einem erheblichen Anteil unter Denkmalschutz stehen. Neben der Behebung altersbedingter Bauschäden sind an den Gebäudehüllen und der Gebäudetechnik dringend energetische Sanierungsmaßnahmen erforderlich, da beide Universitäten mit der Stadt Berlin Klimaschutzvereinbarungen abgeschlossen haben, um die CO_2-Emissionen des Gebäudebestands auf dem Campus in den nächsten Dekaden nachhaltig zu reduzieren.

Vor diesem Hintergrund werden in der zweiten Phase des Verbundprojekts HCBC in Kooperation mit den Bauabteilungen beider Universitäten eine Vielzahl begleitender Simulationsanalysen mit unterschiedlichen Zielsetzungen durchgeführt. Dies reicht von der überschlägigen Ertragsermittlung dachintegrierter Fotovoltaikanlagen, der Kühllastberechnung eines größeren Gebäudekomplexes im Rahmen einer Kälteanlagen-Sanierung, über Studien zur Gebäudekühlung über passive Nachtlüftung für eine Fassadensanierung eines denkmalgeschützten Gebäudes bis hin zur Energie- und Raumklimaanalyse für ein neu geplantes Laborgebäude.

Der Beitrag beschreibt anhand von acht Beispielen aus den Projekten HCBC und InMoB (Inside insulation based on layer composites with moisture buffers), in welchem Maß begleitende Simulationsanalysen die Konzeptentwicklung, die Mittelakquise, die Planung und die Umsetzung von Sanierungsmaßnahmen und Neubauvorhaben in energetischer Hinsicht unterstützen und effizienter gestalten können.

Im Weiteren wird auf die Herausforderungen eingegangen, die sich aus dem hohen Handlungsdruck und der Zielstellung der höchstmöglichen Wirksamkeit dieser Maßnahmen ergeben.

Abstract

The university campus Berlin-Charlottenburg is home to over 40 buildings of the Technische Universität Berlin (TUB) and the Berlin University of the Arts (UdKB). The majority of which are in an unrenovated state in terms of energy efficiency and a significant portion are heritage-listed. Apart from repairing age-related structural damage, the building envelopes and building services urgently require energy-efficient refurbishment measures as both universities have signed climate protection agreements with the city of Berlin in order to sustainably reduce the CO_2 emissions of the building stock on campus over the next decades.

In this context, a large number of accompanying simulation analyses with different objectives are being carried out as part of the HCBC research project in cooperation with both universities' building departments.

The type of simulation analyses ranges from the rough determination of the yield of roof-integrated photovoltaic systems, the cooling load calculation of a larger building complex as part of a cooling system renovation, studies on building cooling via passive night ventilation for a facade renovation of a listed building to the energy and indoor climate analysis for a newly planned laboratory building.

Using eight examples from the HCBC and InMoB (Inside insulation based on layer composites with moisture buffers) projects, the article describes the extent to which the use of accompanying simulation analyses can support the development of concepts, the acquisition of funds, and the planning and implementation of urgently required energy-efficient refurbishment measures and new construction projects and make them more efficient.

The challenges arising from the high pressure to act and the objective of maximizing the effectiveness of these measures are also discussed.

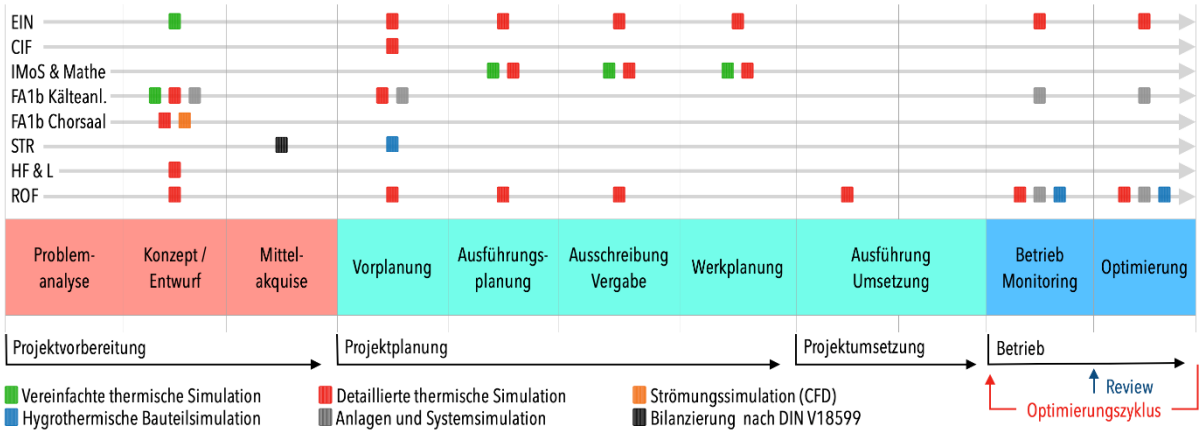

Abbildung 1: Simulative Untersuchungen des Fachgebiets VPT zu verschiedenen Gebäuden (Kürzel, s. „Anwendungsbeispiele“) im Rahmen der Projekte HCBC und InMoB von der Problemanalyse bis zum Betrieb

Simulation im Gebäudebereich

Die Anwendung von Simulationswerkzeugen im Gebäudebereich blickt inzwischen auf eine fast 50-jährige Geschichte (z.B. TRNSYS 1975) zurück. Dem unbestreitbaren Nutzen zuverlässiger Bedarfs- und Betriebsprognosen stand und steht jedoch stets der zu betreibende Aufwand für die Ermittlung der Randbedingungen und die Erstellung geeigneter Modelle gegenüber. Mit steigender Rechenleistung und immer komfortableren grafischen Bedieneroberflächen hat sich das Verhältnis zwischen Aufwand und Nutzen jedoch deutlich verschoben, so dass sich für die Gebäude- und Anlagensimulation immer breitere Anwendungsfelder ergeben.

Das Verbundprojekt HCBC (HCBC I 2018) der TUB und der UdKB hatte aufgezeigt, wie durch zielgerichtete Gebäude- und Anlagen-Sanierung auf möglichst ökonomischem Wege bereichsübergreifend ein Höchstmaß an energetischer Effizienz für den Gebäudebestand des Hochschul-Campus Berlin Charlottenburg erreicht werden könnte. Dabei wurden die durch die Sanierung erzielbaren energetischen Einsparpotentiale anhand gemessener Verbräuche und mit Modellen in Modelica (Modelica 1997) simulativ ermittelter zukünftiger Bedarfe identifiziert und quantifiziert. Zusätzlich wurde der Investitionsbedarf für die jeweiligen Maßnahmen berechnet und die Maßnahmen nach ökonomisch-energetischer Effizienz priorisiert.

Im laufenden Nachfolgeprojekt (HCBC II 2019) liegt der Schwerpunkt neben der Weiterentwicklung der Methoden auf der wissenschaftlichen Unterstützung bei der praktischen Umsetzung der Ergebnisse aus HCBC I, umfasst aber inzwischen auch Aspekte der Neubauplanung der TUB. Die beteiligten Fachgebiete und Institute sind dazu in unterschiedlichem Maße in den Planungs- und Bauprozess begleitend eingebunden. Die energetische Gebäude- und Anlagen-Simulation gewinnt dabei als Prognosewerkzeug und Entscheidungshilfe kontinuierlich an Bedeutung.

Unbekanntes Terrain für die Planer

Der Planungs- und Bauprozess an sich ist stets von erheblichem organisatorischem und administrativem Aufwand geprägt. Insofern ist nachvollziehbar, warum die Planungsbeteiligten bei der Nutzung der gemessen an der Entwicklung des Bauens nach wie vor noch jungen Simulationsverfahren als Hilfsmittel und Werkzeug zögern und eher auf altbewährte Methoden zurückgreifen. Ist doch der Aufwand für die Vorbereitung und Erstellung der notwendigen Modelle wie auch die Auswertung der Ergebnisse selbst für erfahrene Anwender nicht immer im Vorwege zutreffend abzuschätzen.

Umso mehr scheint es von Bedeutung, die Simulation im Rahmen von Forschungsprojekten in den Planungs- und Bauprozess von Neubauten und Sanierungen einzubinden. Die dabei gewonnenen Erfahrungen hinsichtlich der zweckorientierten Wahl der Werkzeuge und der Beschränkung auf das notwendige Maß der Detaillierung können nach Auffassung der Autoren dabei helfen, die Akzeptanz der Simulation als selbstverständlichen Teil des Bauens bei allen Planungsbeteiligten deutlich zu erhöhen.

Anwendungsbeispiele

Abbildung 1 zeigt die Bandbreite der vom Fachgebiet Versorgungsplanung und Versorgungstechnik (FG VPT) mit simulativen Methoden durchgeführten Untersuchungen für acht Beispielgebäude über den jeweiligen Planungsverlauf von der Problemanalyse bis zum Betrieb. Projektübergreifend wurden von den Projektpartnern verschiedene Themen bearbeitet:

- Ertragsprognosen (Neubau Fotovoltaik, Solarthermie und Geothermie)

- Leistungs- und Mengenabschätzung für die Investitionskostenprognose (Sanierung gebäudetechnischer Anlagen/ Fotovoltaik/Solarthermie/Geothermie)
- Einsparungsprognosen (Strom/Wärme/Kälte/CO_2)
- Bedarfsprognosen (Strom/Wärme/Kälte)
- Raumklimaprognosen (Aufenthaltsqualität, Temperatur, Luftströmung)
- Machbarkeitsstudien (Gebäudetechnologie, Betriebsstrategien)
- Vergleichsanalysen (Gebäudetechnologie, Betriebsstrategien)
- Bauphysikalische Untersuchungen (Bauschadensvermeidung/Kostenreduktion

Je nach Anforderung wurde eine entsprechende Simulationsmethode und ein geeignetes Werkzeug gewählt. Dabei wurde angestrebt, die Detailierung der Modelle mit Blick auf das Aufwand-Nutzen-Verhältnis auf das für den jeweiligen Zweck notwendige Maß zu beschränken:

- Detaillierte thermische Gebäudesimulation (IDA ICE 2024)
- Stark vereinfachte thermische Gebäudesimulation (IDA ICE 2024)
- Detaillierte Einzelraumsimulation (IDA ICE 2024) und Strömungssimulation (CFD, OpenFOAM 2024/ IDA ICE 2024)
- Stark vereinfachte thermische Einzelraumsimulation mit IDA ICE 2024
- Detaillierte Anlagensimulation (PolySun 2024 bzw. Modelica 1997)
- Detaillierte Systemsimulation (Modelica 1997)
- Detaillierte Bauteilsimulationen (DELPHIN 2024)
- Vereinfachte Bilanzierung nach (DIN V 18599 2018)

Der folgende Überblick einer Reihe von durch das FG VPT im Rahmen der Forschungsprojekte HCBC und InMoB durchgeführten Untersuchungen zeigt die unterschiedlichen Vorgehensweisen im Zusammenhang mit dem jeweiligen Einsatzzweck.

Einsteinufer 43 (EIN)

Abbildung 2: Verwaltungsgebäude am Einsteinufer 43

Problemstellung: Bauschäden, winterlicher und sommerlicher Wärmeschutz, Luftqualität

Maßnahmen: Sanierung Fassade, Fenster, Haustechnik

Status: Sanierung begonnen

Simulationsthemen:

- Sommerliche Überhitzung
- Heizenergiebedarf
- Verschattungsstudie
- Machbarkeitsstudie mechanische und natürliche Nachtlüftung
- Automatisierter Sonnenschutz
- Verglasungsqualität

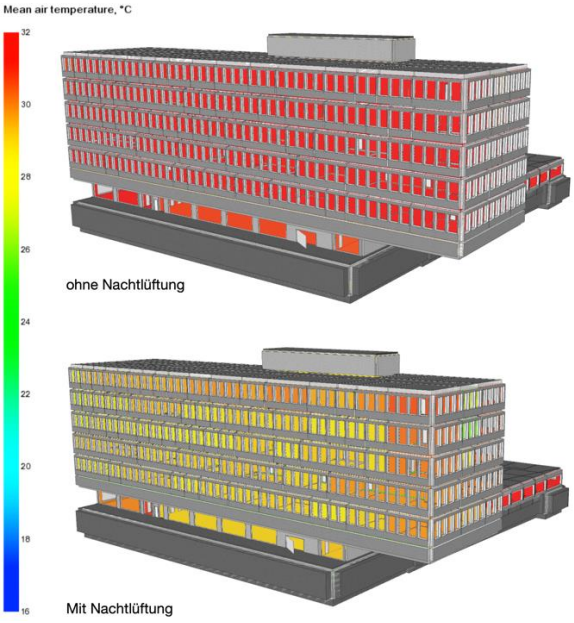

Abbildung 3: Vergleichssimulationen mit und ohne Nachtlüftung für das Gebäude EIN in IDA ICE

Fazit: Das energetische Verhalten des Gebäudes am Einsteinufer 43 wurde bereits zur Problemanalyse und Konzeptfindung mit einem vereinfachten IDA ICE-Modell simuliert, um den Überhitzungsgrad in bestimmten Räumen zu ermitteln und nachhaltige Lösungsmöglichkeiten zu finden. In detaillierteren Simulationen mit einem raumscharfen 191-Zonen-Modell wurden anschließend die mechanische und natürliche Nachtlüftung und deren Auswirkungen auf den Heiz- und Kühlenergiebedarf in einer Machbarkeitsstudie mit IDA ICE verglichen.

Die Ergebnisse führten zur Realisierung der natürlichen Nachtlüftung mit motorischer Fensteröffnung. Das Konzept wurde von der Vorplanung bis in die Ausschreibung und Vergabe immer wieder konkretisiert und simulativ abgebildet.

Der Schlüssel für den erfolgreichen Einsatz der Simulation bei der Konzeption und Planung der

Sanierungsmaßnahmen findet sich hier in erster Linie in der engen und vertrauensvollen Zusammenarbeit zwischen dem FG VPT, der Abteilung Bau und Liegenschaften (BL) der UdKB und den beauftragten Planern.

Chemical Invention Factory (CIF)

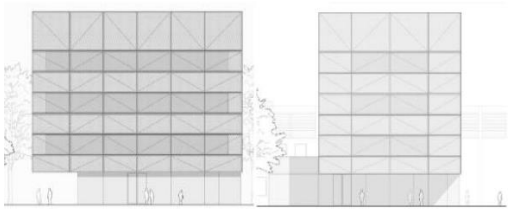

Abbildung 4: Siegerentwurf für das Chemical Invention Factory (CIF), Quelle: TUB

Kurzbeschreibung: Neubau des *John Warner Center for Start-Ups in Green Chemistry*, kurz der *Chemical Invention Factory (CIF)* auf dem Hochschul-Campus Berlin Charlottenburg Technischen Universität Berlin (TUB)

Problemstellung: Zu erwartender Heiz- und Kühlbedarf, Fensterqualitäten, Unklare Auswirkungen des halbtransparenten Fassadenvorhangs aus Drahtgeflecht

Maßnahmen: Neubau

Status: vermutlich weiterhin Vorplanung

Simulationsthemen:

- Verschattungsstudien
- Heizenergiebedarf
- Kühlenergiebedarf
- Sommerliche Überhitzung

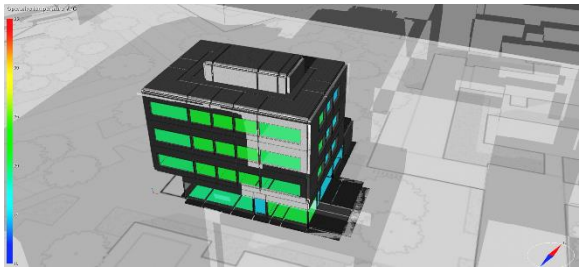

Abbildung 5: Verschattungsstudie für das Chemical Invention Factory (CIF) der TUB in IDA ICE

Fazit: Die Untersuchungen zum Neubau der *Chemical Invention Factory (CIF)* der TUB wurden in einem sehr frühen Stadium der Planung vorgenommen. Die Randbedingungen waren mit Ausnahme der zu erwartenden Nutzungsprofile unscharf, so dass die Ergebnisse nur einen groben Hinweis auf die energetischen Auswirkungen der zu treffenden Entwurfsentscheidungen ermöglichten. Insbesondere die nicht geklärte Materialität und Transparenz des Fassadenvorhangs machte eine seriöse simulative Abbildung der zu erwartenden Bedarfe schwierig. Da eine direkte Kommunikation mit den Planern nicht möglich war, konnte der Einfluss auf die weitere Planung nicht abgeschätzt werden. Derzeit erscheint es unklar, ob das Bauvorhaben seitens der TUB weiterverfolgt wird.

Interdisziplinäres Zentrum für Modellierung und Simulation (IMoS) & Neubau Mathematik-Gebäude (beide TUB)

Abbildung 6: Visualisierung IMoS & Mathematik (Quelle: TUB)

Kurzbeschreibung: Neubauten der TUB an der Fasanenstraße in Berlin

Problemstellung: Ertragspotential der Fotovoltaik (PV) unter Berücksichtigung der geplanten Dachaufbauten, Einfluss der Eigenverschattung, Ausrichtung der PV-Module

Maßnahmen: Neubau

Status: In Bau

Simulationsthemen:

- Verschattungsanalysen
- Ertragsanalyse Fotovoltaik (PV)
- Variantenuntersuchung Ausrichtung

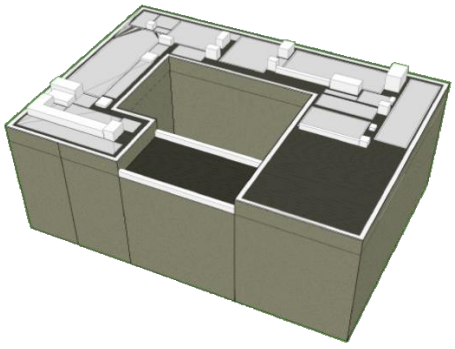

Abbildung 7: Simulationsmodell zur PV-Ertragsprognose IMoS

Fazit: Haustechnische Aggregate, Leitungen und sonstige Aufbauten nehmen auf den Dächern der beiden direkt aneinandergrenzenden Neubauvorhaben der TUB erheblichen Raum ein. Im Rahmen der Ausschreibung und Vergabe und der anschließenden Ausführungsplanung wurde die solare Einstrahlung für die verbleibenden Dachflächen unter Einbeziehung der Eigenverschattung in IDA ICE simulativ untersucht. Die Ergebnisse dienten als Eingangsdaten für das

Programm Polysun Designer. Hier wurden abschließend die potenziellen Erträge der Fotovoltaik unter verschiedenen Neigungswinkeln ermittelt.

Die Ergebnisse wurden - soweit dies im Baufortschritt erkennbar ist – für die weitere Planung herangezogen und in der Ausführung auch berücksichtigt. Ein weiterer Austausch mit der Bauabteilung der TUB erfolgte nicht.

Kälteanlage: Fasanenstraße 1b (KS, Uni.T, Fa1b)

Abbildung 8: Gebäudekomplex Fasanenstraße 1b mit Konzertsaal (links unten), Altbau und Theater (rechts oben) (Quelle: Google Maps)

Kurzbeschreibung: Gebäudekomplexe in der Fasanenstraße 1b der UdKB bestehend aus Universitätstheater (Uni.T), Konzertsaal (KS) und zentraler Altbau (Fa1b), alle denkmalgeschützt

Problemstellung: Analyse der Kältebedarfe in Bezug auf Gleichzeitigkeit der Nutzung in Uni.T und KS, nachträgliche Anlagenoptimierung

Maßnahmen: Erneuerung und Erweiterung der bestehenden Kälteanlage aus den 1970er Jahren

Status: Maßnahme abgeschlossen

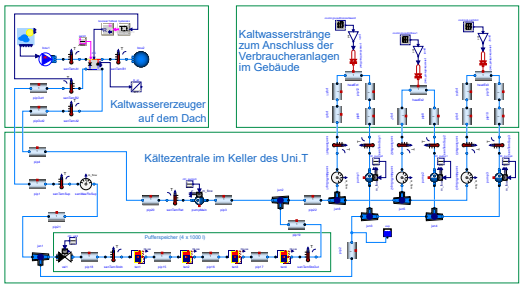

Abbildung 9: Modelica-Modell der Kälteanlage zur Validierung und Optimierung der Anlage

Simulationsthemen:

- Bedarfsprognose Kälte
- Leistungsabschätzung
- Einsparungsprognosen
- Optimierung/Validierung

Fazit: Im Vorfeld des Austauschs der alten Kälteanlage (ca. 1975) wurden mit mehrzonigen thermischen Gebäudesimulationen (IDA ICE) der einzelnen Gebäudeteile (KS, Altbau, Uni.T) Lastkurven des Kältebedarfs erstellt, welche sowohl die an das System angeschlossenen Kälteabnehmer als auch potenziell Erweiterungen der Kälteversorgung mit einbezieht.

Aufbauend auf diesen Lastkurven wurde mit Hilfe einer Anlagensimulation in Modelica eine anfängliche Leistungsabschätzung der zu planenden Anlage und eine darauf basierende Einsparungsprognose vorgenommen, um Planer und Bauabteilung der UdKB in der Vorplanung und Ausschreibung zu unterstützen.

Nach Installation der neuen Kälteanlage wurde das vorhandene Anlagenmodell auf Basis der Ausführungsplanung angepasst und in der Kälteverteilung detailliert erweitert. Dieses Modell soll durch umfangreiches Monitoring validiert werden, um als Grundlage für simulative Versuche zur Anlagenoptimierung zu dienen.

Chorsaal: Fasanenstraße 1b

Abbildung 10: Konzertsaal mit Chorsaal (rot Markiert) mit alter dezentraler Lüftung

Kurzbeschreibung: Chorprobensaal innerhalb des Konzertsaal Gebäudes im Gebäudekomplex der Fasanenstraße 1b

Problemstellung: Machbarkeitsstudie einseitiger Quelllüftung unter Betrachtung der Raumbelegung mit Chorgruppen

Maßnahmen: Fenstersanierung, Austausch der Lüftung

Status: Fenstersanierung abgeschlossen, Einbau zentraler Lüftung in Bau

Simulationsthemen:

- Raumluftströmungsanalyse

Fazit: In der Beratung der Bauabteilung der UdKB im Zusammenhang mit der Sanierung der Fenster im Chorsaal des Gebäudekomplexes in der Fasanenstraße 1b wurde ein Ersatz für die alte dezentrale Belüftung konzipiert. Dabei wurde zugunsten des Schutzes vor Straßenlärm und des sommerlichen Wärmeschutzes eine zentrale Lüftungsanlage mit Wärmerückgewinnung und Anschluss an die erwähnte Kälteanlage empfohlen. Aufgrund der musikalischen Nutzung des Raums wurde zudem eine Belüftung über ein Quellluftsystem geprüft, um Zugerscheinungen

und Strömungsgeräusche zu minimieren. Der Vorschlag wurde mittels Gebäudesimulation und CFD in IDA ICE geprüft und es konnte gezeigt werden, dass das Konzept eine gleichmäßige Luftversorgung ermöglichen kann. Aufgrund einer komplexeren Einbausituation wurde von Seiten des Planers und der Bauabteilung jedoch eine Belüftung über ein Mischlüftungssystem vorgezogen.

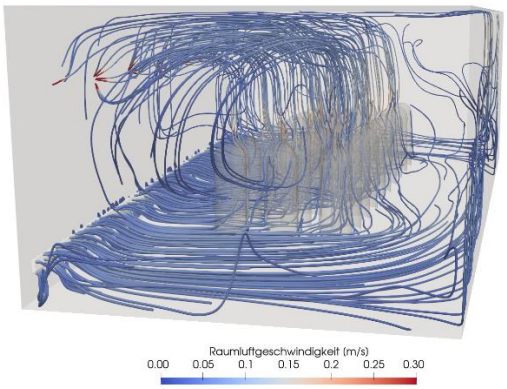

Abbildung 11: Simulierte Raumluftströmung der Quelllüftung im Chorsaal in der Fasanenstraße 1b

Straße des 17. Juni 118 (STR)

Abbildung 12: Gebäude der UdKB an der Straße des 17. Juni 118

Kurzbeschreibung: ehemaliges Gerichtsgebäude von 1910, Westflügel nach Kriegsschäden 1954 als einfacher Zweckbau erneuert, teilweise denkmalgeschützt, heute genutzt von der UdKB

Problemstellung: fehlende Kennzahlen zur Beantragung von Fördermitten

Maßnahmen: Innendämmung Altbau, Dämmung West und Nordfassade, Fensteraustausch, Austausch bzw. Substitution Glasbausteinflächen

Status: Mittelakquisition

Simulationsthemen:

- Einsparungspotentiale Wärme/CO_2

Fazit: Für die Akquisition von Fördermitteln für Sanierungsmaßnahmen an diesem Gebäude, welche aus energetischer Sicht dringend notwendig sind, wurden Kennzahlen zur potenziellen Energie- bzw. CO_2- Einsparung benötigt. Dazu wurden Bilanzvergleiche im vereinfachten Ein-Zonen Verfahren nach DIN 18599 (DIN V 18599, 2018) unabhängig von den Bedingungen des §32-1 mit der Software ZUB Helena Ultra (ZUB Helena 2024) durchgeführt.

Die Ergebnisse wurden von der Abteilung BL der UdKB für die Antragstellung genutzt.

Im Rückblick wäre eine entsprechend vereinfachte Gebäude-Simulation z.B. mit IDA ICE vom Aufwand her vergleichbar gewesen.

Zudem wird eine Innendämmung des Altbaus im Rahmen des Forschungsprojektes InMoB (InMoB, 2024) an einer Innenwand eines ausgewählten Raumes angebracht und ausgewertet.

In dem Projekt werden Materialkombinationen als kostengünstige, ökologische und feuchteregulierende Innendämmung untersucht, mit denen die Energieeffizienz von Gebäuden mit erhaltenswerten Sichtfassaden verbessert werden kann. Die Auswahl der Materialien und Schichtdicken erfolgte durch zuvor durchgeführte Simulationen mit dem Simulationsprogramm DELPHIN.

Hermann-Föttinger-Institut & Lebensmittelchemie (HF & L, beide TUB)

Abbildung 13: Luftaufnahme Gebäude HF (Quelle: Apple Maps)

Kurzbeschreibung: als Gebäude für die Forschung in den 50er und 60er Jahren errichtet, heute Institute für Fluid-Dynamik, Technische Akustik und Lebensmittelchemie der TUB.

Problemstellung: Fehlende Lastgangprofile für Wärme und Kälte, Sinnhaftigkeit der Einbindung in ein Wärme-/Kältenetz

Maßnahmen: -

Status: Problemanalyse, Konzeptentwicklung

Simulationsthemen:

- Bedarfsprognose Wärme
- Bedarfsprognose Kälte

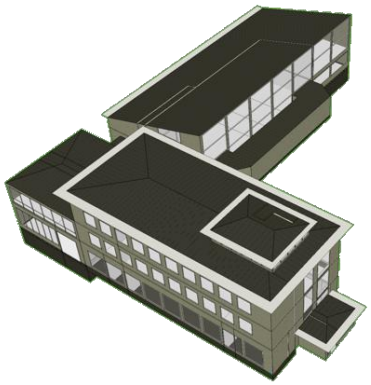

Abbildung 14: IDA ICE-Modell Gebäude HF

Fazit: Die Untersuchungen an den beiden Gebäuden HF und L wurden vorgenommen, um im Rahmen einer Machbarkeitsstudie für balancierter Wärme- und Kältenetze auf den Campus Berlin-Charlottenburg entsprechende Lastprofile zu erzeugen. Mit Hilfe von Simulationen in IDA ICE in mittlerer Detaillierung konnten zwar die entsprechenden Bedarfe gut abbildet werden, allerdings bleiben erhebliche Unsicherheiten, da insbesondere im Gebäude HF durch die wechselnde Nutzung der Experimentalanlagen (z.B. Windkanal) stark volatile Bedarfe entstehen.

Die erzeugten Lastprofile flossen in die Netzsimulationen der HCBC-Projektpartnern ein.

Rooftop Experimentalgebäude (ROF)

Abbildung 15: Rooftop Experimentalgebäude

Kurzbeschreibung: als Wettbewerbsbeitrag zum Solar Decathlon Europe 2014, Wiederaufbau als Experimentalgebäude 2017

Problemstellung: Prototypische Anwendung verschiedener Simulationsmethoden

Maßnahmen: Wiederaufbau und Betrieb als Experimentalgebäude

Status: Wiederaufbau abgeschlossen, Forschungsbetrieb andauernd

Simulationsthemen:

- Verschattungsstudie
- thermische Gebäudesimulation.
- digitalen Zwilling (Anlage und Gebäude)
- VR-Gebäudemodell
- detaillierte Einzelraumsimulation
- hygrothermische Bauteilsimulation

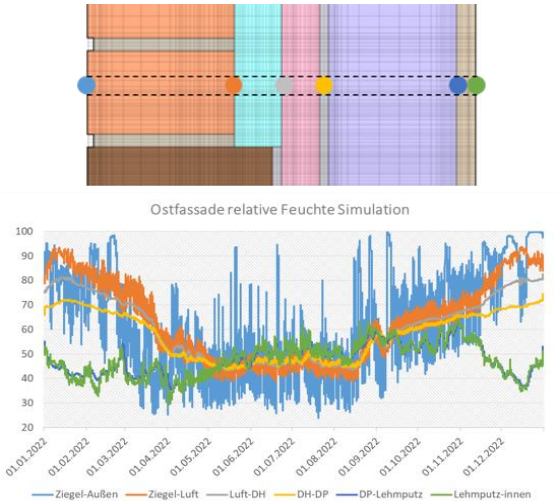

Abbildung 16: Simulationsmodell und Simulationsergebnis (relative Feuchte)

Fazit: Das Rooftop-Gebäude (ROF) wurde für den internationalen Wettbewerb Solar Decathlon Europe 2014 in Versailles (F) von einem Team von Studierenden der UdKB und der TUB geplant und gebaut. Im Jahr 2017 wurde es als Experimentalgebäude auf dem Hochschulcampus Berlin-Charlottenburg wieder aufgebaut und wird seitdem neben dem Seminar- und Laborbetrieb vor allem im Rahmen der Forschungsprojekte HCBC und InMoB genutzt (Rooftop, 2023).

Im Rahmen des Wiederaufbaus und dem Experimentalbetrieb wurde eine Vielzahl an unterschiedlichen begleitenden Simulationen durchgeführt (siehe Simulationsthemen).

Für das Projekt InMoB werden seit dem Jahr 2021 Messungen an zwei Testfassaden am Rooftop-Experimentalgebäude durchgeführt, die mit einer Materialkombination aus hygrisch aktivem Dämmstoff, einer Holzfaserdämmung und Lehminnenputz gedämmt sind.

Um möglichst viele Materialkombinationen und verschiedene Schichtdicken untersuchen zu können, wurden zusätzlich zu den Messungen hygrothermische Simulationsanalysen mit dem Simulationsprogramm DELPHIN durchgeführt. Dadurch kann für jede Fassade die bauphysikalisch optimale Materialkombination und Dämmstärke ermittelt werden.

Die mit DELPHIN erstellten Simulationsmodelle wurden anhand der Messergebnisse des Testfassadenprüfstandes validiert.

Diskussion

Im Rückblick haben sich Gebäude-, Bauteil- und Anlagensimulationen im Verlauf der Projekte HCBC und InMoB als wertvolle Unterstützung des gesamten Projektierungs-, Planungs- und Bauprozesses bewährt.

Wie insbesondere das Beispiel Einsteinufer 43 (EIN) zeigt, kann der frühzeitige Einsatz von Werkzeugen wie IDA ICE und/ oder Polysun bei der Lösungsfindung für bestehende bauliche bzw. gebäudetechnische Problemstellungen im Bestand zu kostengünstigeren und nachhaltigeren Lösungen führen. Gleiches gilt auch für den Neubau. Allerdings zeigt das Beispiel Chemical Invention Factory (CIF), dass für eine korrekte Parametrisierung und damit zuverlässige Simulationsergebnisse bereits grundlegende Entwurfsentscheidungen getroffen sein bzw. im direkten Austausch mit den Projektbeteiligten diskutiert werden müssen.

Auch wenn die potenziellen Kosten für begleitende Simulationen im Verhältnis zu den Gesamtkosten eines Sanierungs- oder Neubauprojekts eher gering ausfallen, bleibt das Verhältnis von Aufwand und Nutzen kritisch zu bewerten. Die beschriebenen Erfahrungen belegen zwar, dass der Arbeitsaufwand für Modellierung, Simulation und Bewertung durch die zweckmäßige Wahl von Werkzeugen und angepasster Detailtiefe sinnvoll begrenzt werden kann, allerdings werden die Ergebnisse nur dann wirklich wertvoll, wenn:

- der Simulationszweck klar definiert ist,
- die Bauteil- bzw. Gebäudegeometrie,
- die notwendigen Wetterdaten,
- die Materialdaten,
- die Anlagenstruktur und die grundlegenden Betriebsdaten sowie,
- die Nutzungsarten und -intensitäten

zur Verfügung stehen oder leicht approximiert bzw. abgeschätzt werden können. Die Beschaffung dieser Informationen kann ohne eine enge Kooperation zwischen den Projektbeteiligten schnell zu einem zeitaufwändigen und damit außerhalb eines Forschungsprojektes teuren Unterfangen werden. Darüber hinaus sind auch die Aufbereitung und Kommunikation der Ergebnisse mit einem nicht zu unterschätzenden Arbeitsaufwand verbunden.

Zusammenfassung

Der beispielhafte Einsatz begleitender Simulationen im Rahmen von Forschungsprojekten wie HCBC oder auch InMoB macht deutlich, in welchem Maße die Einbeziehung dieser Technologien den Planungs- und Bauprozess wirksam unterstützen können sowie welche Voraussetzungen und Vorarbeiten hierfür erfüllt bzw. geleistet werden müssen. Diese Erkenntnisse können – geeignete Vermittlung vorausgesetzt – die Akzeptanz bei Bauherren und Planern nach Auffassung der Autoren deutlich erhöhen.

Danksagung

Die vorgestellten Forschungsergebnisse basieren auf den Projekten „EnEff:Stadt: EnEff HCBC 1. Umsetzungsphase Hochschulcampus Berlin-Charlottenburg“ (Förderkennzeichen: 03ET1632B, gefördert vom BMWK) und „InMoB – Grundlagenuntersuchungen zum hygrothermischen Verhalten hygrisch aktiver und nicht aktiver Schichtverbünde als Grundlage für kostengünstige und energieeffiziente Innendämmung“ (gefördert im Innovationprogramm Zukunft Bau des BBSR).

Literatur

HCBC I 2018. Münch, B. et al., Schlussbericht Eneff: HCBC I Hochschul Campus Berlin-Charlottenburg,: TUB/UdKB, 2018

HCBC II 2019. Webseite Projekt EnEff:Stadt: HCBC 1. Umsetzungsphase Hochschul-Campus Berlin-Charlottenburg: https://blogs.tu-berlin.de/hri_hcbc/projekt/

InMoB 2024. Burchard, H., Nytsch-Geusen, C., & Kaul-Gothe, W. InMoB-Grundlagenuntersuchungen zum hygrothermischen Verhalten hygrisch aktiver und nicht aktiver Schichtverbünde. Bauphysiktage Weimar 2024: Bauphysik in Forschung und Praxis.

TRNSYS 1975. Wikipedia-Seite zu TRNSYS: https://de.wikipedia.org/wiki/TRNSYS

Modelica 1997. Webseite Modelica Association: https://modelica.org/

IDA ICE 2024. Webseite IDA ICE, EQUA Simulation AB: https://www.equa.se/de/ida-ice

PolySun 2024. Website Polysun, Vela Solaris AG: https://www.velasolaris.com/software

OpenFOAM 2024 Website OpenFOAM, OpenCFD Ltd: https://www.openfoam.com

DELPHIN 2024. Website DELPHIN, Institut für Bauklimatik Technische Universität Dresden: https://www.bauklimatik-dresden.de/delphin

Rooftop, 2024. Website Rooftop-Gebäude, Universität der Künste Berlin FG VPT: http://www.solar-rooftop.de

DIN V 18599 2018: Deutsches Institut für Normung e.V. Berlin Germany: Energetische Bewertung von Gebäuden-Berechnung des Nutz-, End-und Primärenergiebedarfs für Heizung, Kühlung, Lüftung, Trinkwarmwasser und Beleuchtung, 2024

ZUB Helena 2024. Website ZUB Helena, ZUB Systems GmbH: https://www.zub-systems.de/de/produkte/helena

BauSIM 2024 in Wien
23. September – 26. September

CityGML Data Preparation for Thermal Building Simulation at District Level

Andreas Geiger[1], Yingcong Zhong[1], Steffen Hempel[1],
Karl-Heinz Häfele[1], Veit Hagenmeyer[1]

[1] *Institute for Automation and Applied Informatics, Karlsruhe Institute of Technology, Germany*

Abstract

More and more cities and countries around the world are providing CityGML LoD2 (**L**evel **o**f **D**etail) building models, either commercially or as open data. Although these models divide the outer shell of buildings into walls, roofs and floor areas, most of the input parameters required for thermal simulation are missing. In addition, CityGML allows different modeling approaches, so that the geometry of the models must also be checked, the neighborhood relationships analyzed and the models modified if necessary.

The present article describes the analysis of CityGML models regarding the model structure and geometry. This includes checking the buildings geometry to be a closed volume, considering neighboring buildings as shading objects, and enriching building physics parameters depending on the year of construction. The geometry processing for buildings with several building parts, the calculation of shared surfaces in the case of closed constructions and the determination of neighboring buildings are described in detail. The enrichment of the building models with building physics and building usage parameters is introduced. All concepts are implemented in software and tested with the EnergyPlus simulation kernel. The software, which can be used to convert basic CityGML models into comprehensive CityGML Energy ADE models, will be available to the community as freeware.

1. Introduction

Urban **B**uilding **E**nergy **M**odeling (UBEM) broadens the **B**uilding **E**nergy **M**odeling (BEM) approach from the single building scale to the city, regional or national level. UBEM is much more than the simple aggregation of individual building energy models, as it takes into account the design of the building stock, the microclimate and the mutual influence of energy loads (Malhotra et al., 2022a).

There are basically two approaches to UBEM: top-down and bottom-up. While the top-down approach works mainly with historical time series at a high aggregation level, the bottom-up approach operates at a disaggregated level and requires a lot of information to describe individual components. The building physics based bottom-up approach requires the most detailed information possible about the building stock (Kavgic et al., 2010).

CityGML (Gröger et al., 2012) as a comprehensive semantic city model provides a standardized data model for buildings in an urban context. The data model allows buildings to be represented at different levels of detail and facilitates a decomposition of buildings into individual boundary surfaces (e.g. wall, roof, and ground). The extensive availability of CityGML building models in many countries around the world provides a good basis for building physics based thermal simulations. Although CityGML as a general semantic city model does not provide energy and simulation relevant features and properties, it offers a mechanism for schema extensions (**A**pplication **D**omain **E**xtension - ADE) (Biljecki et al., 2018). The CityGML Energy ADE is one such schema extension, defined by an international working group to meet the requirements of UBEM (physics based bottom-up approach).

Several tools are available for using public available CityGML data for thermal simulation. SimStadt (Coors et al., 2021) is designed to simulate and analyze the energy performance of buildings at the district or city level. It supports CityGML and EnergyADE as the data format for input of the simulation. Enrichment of CityGML data and the generation of an EnergyADE dataset is not supported. Another energy urban modelling and simulation tool is CitySIM (Rosser et al., 2019). A simulation based on CityGML and EnergyADE data is also possible here. However, it is unclear to what extent this information can also be stored in EnergyADE and whether geometric adjustments are supported.

However, apart from the tool presented here, only CityEnrich (Malhotra et al., 2022b) is currently available for an enrichment of CityGML datasets with energy relevant parameters. CityEnrich allows the manual assignment of parameters per element type and usage profile, but it is not possible to assign them automatically on the basis of a building age class and building function. None of the tools mentioned above seem to check the input data both structurally and geometrically and adapt the structure, semantics and geometry if necessary.

The present paper introduces a process for enriching differently structured CityGML building models with features and properties necessary for thermal simulation. Although CityGML provides a standardized building model, it allows different geometric and semantic variations, so that the model has to be analyzed in a first process step. Depending on the results of the analysis, building parts are merged into a single zone model in a further process step. In the following process step, neighborhood relationships are then established between the individual buildings in order to identify and process a closed construction and to determine buildings for shading assessment. In the final process steps, the building model is then completed with information on building usage (e.g. user behavior) and building physics (e.g. thermal conductivity) using CityGML Energy ADE features and properties.

The resulting building models can be exported as a CityGML EnergyADE dataset and shared with other applications. In the in-house application KITModelExplorer, the CityGML EnergyADE models can be converted into EnergyPlus (EnergyPlus, 2024) input data and simulated.

2. CityGML and CityGML Energy ADE

CityGML as a comprehensive city model represents many aspects of a city, such as buildings, vegetation and transportation infrastructure. The data model is therefore subdivided into individual thematic modules. As the work described in the following relates to thermal building simulation, the focus is on the building module (Gröger et al., 2012).

CityGML and the CityGML extension Energy ADE have often been described comprehensively in several publications, so that only special modeling aspects are addressed here. The latest CityGML version 3.0 (Kolbe et al., 2021) offers few relevant innovations with regard to the requirements of thermal building simulations, meaning that the work described here relates to CityGML version 2.0. In addition, in practice only a few data sets are available in CityGML version 3.0. Although CityGML can provide several levels of detail, the description here focuses on Level of Detail 2 (LoD2), as most of the datasets are available at this level of detail (Geiger et al., 2022). In principle, the considerations listed in the present article also apply to LoD3 building models.

2.1. CityGML

A CityGML building model can have several levels of detail and can be composed in different ways. The subdivision of a building into building parts is based on various aspects (e.g. roof shape or building function) and is therefore not standardized. The use of building installations (e.g. winter gardens and dormers) is also not clearly defined. The building, building part and building installation feature can be represented optionally as a surface model and as a volume model. Additionally, these features can also be semantically subdivided into boundary surfaces such as wall, roof and ground surfaces (SIG3D 2017). This variety of possible combinations requires a structural and geometric analysis of the CityGML building models in order to be able to use the model for thermal building simulations. In most cases, the models have to be modified semantically (e.g. creation of shared walls) and geometrically (e.g. merging of building parts) after the analysis.

The outer boundary surfaces usually form the building envelope. Simulation kernels for a thermal simulation require certain construction properties (e.g. layer thickness, thermal conductivity), which are assigned to the boundary surfaces. Since CityGML does not define any standardized attributes for boundary surfaces and the CityGML material concept only contains visualization properties, material constructions, e.g. for walls, are difficult to implement without a CityGML extension.

Since the CityGML is a general-purpose model but provides a schema extension mechanism (ADE) for domain-specific applications, features for modeling energy-relevant information are not included in the CityGML schema and must be defined in an ADE.

2.2. CityGML Energy Application Domain Extension (ADE)

As mentioned in the previous chapter, domain-specific CityGML features must be specified in a schema extension. In 2015, an international group of urban energy simulation developers was established to define a common CityGML Energy ADE. The aim was to close the gap between the general use of city models and urban energy modeling by extending the schema with

additional features and attributes. For thermal building simulation, the CityGML Energy ADE can extend a CityGML building model without interfering with the original CityGML model structure. This has the advantage that a relationship between the CityGML building model and the CityGML Energy ADE building model exists only on a common building feature level.

For thermal building simulation, the extensions for describing the thermal zones and their usage are particularly relevant. The thermal zone is bounded by LoD-independent thermal boundaries and owns further energy-relevant attributes. The thermal boundaries can be described with geometry as well as with alpha-numerical properties and are further classified into outer wall, interior wall, shared wall, ground slab, roof, floor and ceiling. Furthermore, thermal boundaries can refer to openings. The physical building parameters that are particularly important for a thermal simulation, such as composition, thermal conductivity and heat capacity, can be specified in detail with the construction, layer and material features (Nouvel et al., 2015).

A thermal zone can contain several so-called usage zones. The usage zone defines the user behavior and the characteristics of other energy-related factors, such as heating and cooling profiles, air change rates and internal heat loads. In order to model these behaviors, new features have been introduced that support schedules and time series (Benner et al., 2016).

The CityGML Energy ADE has other modules, but these are not relevant to the process described here and will therefore not be discussed further.

3. Data Preparation

In more and more countries, CityGML building data is provided by official bodies. In Germany, the federal states provide CityGML LoD2 data mostly as open data or commercially (CityGML Wiki, 2024). However, the available LoD2 CityGML building data provided is not uniform (Geiger et al., 2022). For this reason, it is necessary to analyze and harmonize the building geometry. In principle, the checking and analysis of semantic data can be classified into three categories: consistency, correctness and completeness (Geiger, et al., 2021). Consistency means the syntactic and semantic correctness of the data, in this case a validation against the corresponding CityGML schema. If this is not fulfilled, there are already errors when reading and interpreting the data. The checking process takes into account the correctness and completeness of the building data. Checking for correctness is currently restricted to geometrical analysis like checking for closed volume or surface planarity. This is essential for buildings and building parts where the geometry can be represented by a volume geometry or by a volume resulting from the individual boundary surfaces. During the completeness check, the required features and attributes are analyzed and with the correctness check, specified values are checked to ensure the used values are within a valid range.

3.1. Building and Building Parts

For the thermal analysis of buildings at city or district level, the workflow presented here is based on a single thermal zone per building. The calculation of buildings with multiple zones - if building parts are present - is possible in principle, but is not discussed in this article. If building parts are present, it is assumed that the building parts are connected to each other and form a single building envelope, although this is not explicitly required by the CityGML specification. The main requirement is to check and ensure that the building represents a closed volume and that the external thermal surfaces can be derived from this closed volume.

According to the CityGML specification, buildings can be modeled as single buildings or as buildings with one or more building parts. In most cases, the buildings and building parts are available in LoD2. However, it occasionally happens that a LoD1 building or building part without boundary surfaces is provided. A combination of LoD1 and LoD2 building parts is also possible (Figure 1).

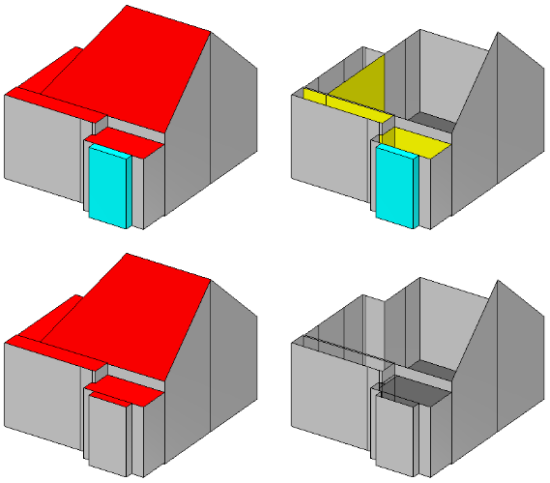

Figure 1: Building consisting of LoD1 and LoD2 building parts (upper row – original CityGML building; lower row the newly generate building envelope; roof surfaces are hidden on the right side)

Firstly, a closed volume is ensured for each part of the building and then the thermal surfaces for the LoD1 components are determined based on the surface orientation and semantically classified as wall, roof and ground surfaces. Vertical surfaces with a maximum slope of 10° are classified as *WallSurface*. Surfaces oriented in a positive Z direction and with an angle between 0° and 80° are classified as *RoofSurface* while all surfaces oriented in a negative Z direction with an angle between 0° and -80° are classified as *GroundSurface*. If building parts are present, they are geometrically united by Boolean operations to form a thermally homogeneous envelope. The contact surfaces between the building parts are calculated and classified as *ClosureSurface* if necessary. In some cases, the original CityGML data already contain *ClosureSurface* between the building parts.

When analyzing the geometry, it also revealed that some of the existing geometries of type GML *Solid* do not meet the requirements of a closed volume. This is due to an incorrect assignment of the LoD2 faces to the faces of a GML *Solid*. In these cases, collinear points that would be required for an edge check are missing. In this case, it is checked whether the collinear points can be supplemented by an edge analysis and thus a closed volume can be generated.

3.2. Neighborhood Relations

In addition to a closed single zone, the relationship to neighboring buildings is of particular importance for the thermal analysis of buildings. With CityGML it is possible to describe a building, but there are no relationships between the buildings. This means that this information must be derived geometrically. For this purpose, a respective Voronoi diagram is used.

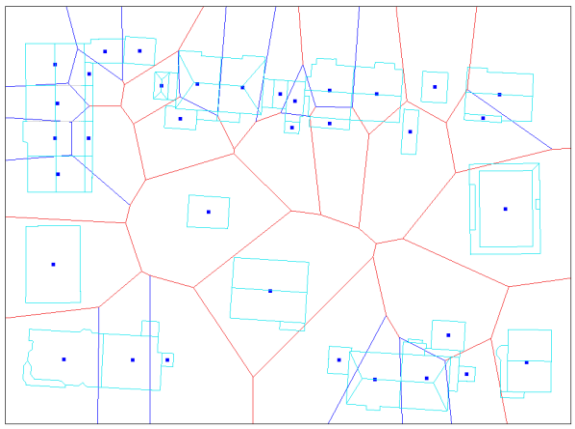

Figure 2: Voronoi diagram showing the neighborhood relations of the buildings (edges to touching buildings are colored blue; all other edges are colored red)

A Voronoi diagram is a mathematical concept that divides an area into regions based on the distance to a set of points (Burrough et al., 2015). The implementation is based on the Euclidian distance. In this case, the Voronoi diagram is used to determine the direct neighbors for each building (Figure 2). This is undertaken by first calculating the geometric center of gravity for each building and using it as the center point for calculating the Voronoi diagram. From the direct neighboring buildings identified in this way, the surfaces are then checked geometrically for connections. A subsequent step analyzes the list of direct neighbors to determine whether buildings intersect within a tolerance (e.g. 5 cm). Intersections between two buildings that consist exclusively of a point or an edge are ignored. For all other intersections, the actual intersection area is calculated using 2D Boolean operations and assigned to the respective neighboring buildings as shared walls (Figure 3).

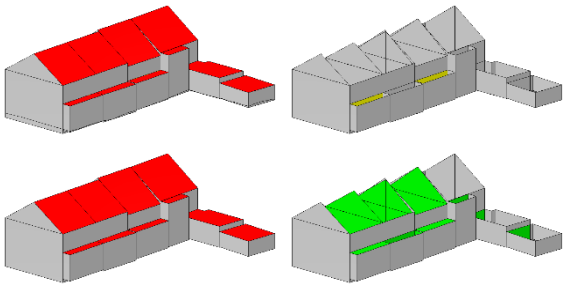

Figure 3: Closed construction (upper row: original CityGML model with outer walls (grey) between the buildings; lower row thermal boundaries with shared walls (green) between the buildings

3.3. Openings

The heat loss and solar gain through windows is a significant influencing factor (Geiger et al., 2020) in the thermal simulation of buildings. However, the CityGML building models in LoD2 do not have windows. For this reason, there is an option in the enrichment process to specify a wall-window or a roof-window ratio. These window areas are calculated geometrically and assigned as a *ThermalOpening* to the corresponding wall respectively roof surface. For the window calculation process, some boundary conditions are defined. These include that the dimensions of the target surface must have least a length of one meter and the area must be larger than two square meters. This prevents openings being created in small surfaces (Figure 4).

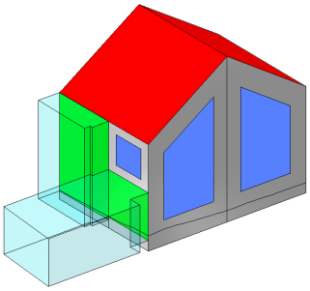

Figure 4: LoD2 building with calculated opening geometries (blue) (Shared walls (green) and small wall surface (below shared walls) are ignored)

3.4. Neighboring Buildings as Shading Objects

As already mentioned, UBEM considers not only the individual building but also the mutual influence of the buildings. Solar gains, for example, also depend on the mutual shading of the buildings. EnergyPlus therefore offers the option of defining shading objects in the building simulation. As the time performance of the simulation depends on the number of shading objects, only selected neighboring buildings should be considered as shading objects.

As previously described in Chapter 3.2, a respective Voronoi diagram provides the direct neighbors of a building. In the current implementation of shading objects, not only the direct neighbors are taken into account, but also their respective neighbors. Figure 5 shows the direct neighbors (dark grey) and their neighbors (light grey) for the selected green building.

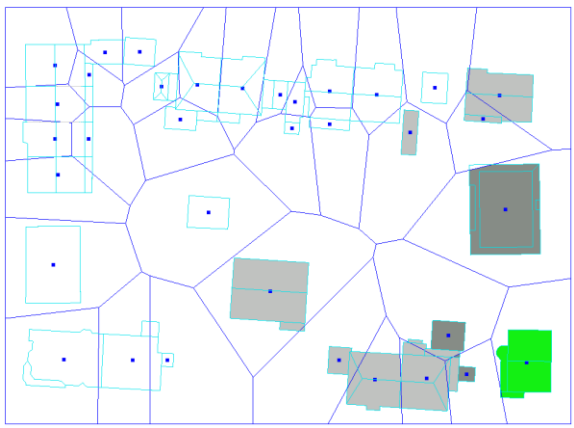

Figure 5: Voronoi diagram showing the neighborhood relations of buildings for shading

For each building in a district, a set of neighbors is determined and assigned to the building as shading objects. In order to keep the geometric complexity of these shading objects low, the original CityGML model with possible building parts is not used, but the newly calculated reduced thermal envelope of the buildings. The information regarding shading objects cannot yet be mapped in the CityGML Energy ADE and must therefore be redetermined if required.

3.5. Building Usage

Beside a correct building geometry, a thermal simulation requires usage profiles that describe the behavior of various influencing factors on a thermal zone in the form of time series (Geiger et al., 2020). These are profiles for the use of heating and cooling, profiles for additional heat sources within a thermal zone such as technical devices, lighting, but also the users and finally ventilation and shading devices. In Germany, the DIN 18599-10 standard describes a total of 44 space usage profiles. However, there is no direct link between CityGML building functions and DIN 18599-10 space usage profiles. As a replacement, a mapping between the CityGML building function codes and DIN 18599-10 has been created. The mapping uses an experience-based relative ratio to estimate the proportion of space use profiles within a building. One building usage profile was calculated for each ALKIS building function from a maximum of eight DIN 18599-10 room use profiles (Geiger et al., 2022). If no building function is available, the usage profiles must be selected manually.

3.6. Building physics

Finally, the material information is missing to perform a thermal simulation. In this last task, the automatic assignment is based on the building attribute *yearOfConstruction*. If this attribute is not available, a suitable construction must be selected manually. In order to obtain suitable material information for a year of construction, the data from TABULA, which was created as part of the Intelligent Energy Europe project, is used (TABULA, 2024). The data contains building typologies for the energy assessment of residential buildings that provides statistical building physics. These building typologies are based on a set of reference buildings representing certain size and age classes of the building stock within a country and data are provided for 21 European countries. Four building types are considered and eleven building age classes are covered for each building type. The data set contains typical component information for walls, floor slabs, roofs and windows. Unfortunately, the data is not stored in the form of a database; instead, EXCEL tables are offered for download. Therefore, the data had to be extracted and mapped in a separate data structure. Based on this new data structure, the material information can now be queried with the attribute *yearOfConstruction* by searching for the corresponding period in the construction age classes. As non-residential buildings are not

included in TABULA, it is planned to use data from the Institute for Housing and Environment – Institut Wohnen und Umwelt GmbH (IWU) – for this in future, although this will only take into account the German building stock (Hörner et al., 2022).

4. Implementation

The enrichment process for CityGML building models described above is realized as a plugin (KITModelViewer PlugIns, 2024) for the KITModelViewer application (KITModelViewer, 2024), formerly FZKViewer. The plugin will be available as part of the freeware version. Although all the process steps mentioned are already developed, the module is still in a prototype state and the results of the enrichment process still depend strongly on the quality (mainly the geometric quality) of the input data.

The requirements for the automated enrichment process and the possible user interactions are explained in more detail below.

After loading a CityGML dataset either as a file or via an OGC-compliant Web Feature Service (WFS), the enrichment plugin can be started. In the first step, all buildings to be processed are displayed and outlined on a 2D map in order to visually check their completeness and geographical location. In a second step, model statistics are generated to provide the user with an overview of the model structure, the model geometry, the correctness of the geometry, the presence of relevant properties and the number of thermal zones generated. If the model statistics meet the user's requirements, the building physics and building usage can be assigned.

Regardless of whether a building or a district is being processed, the module primarily attempts to interpret the GML standard attributes *function* and *yearOfConstruction* in order to perform automatic enrichment. The following requirements apply to automatic enrichment:

- The assignment of usage profiles relies on the ALKIS building code provided in the attribute *function*.
- The assignment of the material definitions results from the attribute *yearOfConstruction* and is obtained from the TABULA data.

Based on the parameters provided by the buildings, the enrichment process automatically assigns usage profiles and the material information. If this automatic assignment is not possible for one or more buildings, manual assignment to a corresponding ALKIS code or a corresponding building age class is also possible.

The total number of buildings and the number of buildings to be enriched are automatically derived from the completeness of the parameter sets and presented to the user.

In addition to assigning the material structure of the building elements and the profiles for the building usage, the percentage ratio of window area to wall or roof area can be defined.

All information generated during the enrichment process is added only to the CityGML Energy ADE features *ThermalZone* and *UsageZone*. The original data and the geometry of the buildings remain unchanged.

Once all operations and checks have been made, the generated CityGML Energy ADE model can either be exported and made available to other applications or converted into EnergyPlus input data using our internal version.

5. Example

The KIT/IAI Institute has stored CityGML building models that are freely available from the German state offices (approx. 41 million buildings) in a GIS database and retrieves the CityGML data via a Web Feature Service (WFS). The implemented functions introduced in this paper were tested by selecting a small building block in Cologne, which contains both buildings with building parts (LoD1 and LoD2) and a closed construction (Figure 6). The test model consists of 35 building models, of which 10 building models are subdivided into building parts (28 building parts in total).

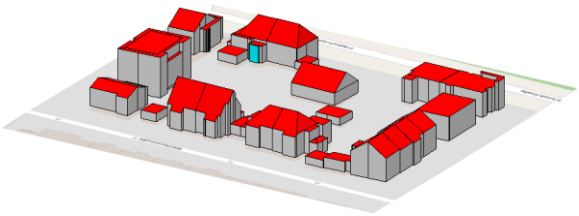

Figure 6: The selected building stock in Cologne retrieved from the CityGML database

The building parts are connected to each other by the *ClosureSurface* feature (see Figure 7) and are all classified by the attribute *function*: 21 x "residential building", 1 x "residential building with trade and services", 3 x "building for business or industry", 6 x "garage", 1 x "shed" and 3 x "roof". None of the building models have the year of construction attribute.

Figure 7: The *ClosureSurface* features (yellow surfaces) which separate the building part

In the first step, buildings that are not to be taken into account (e.g. garages, sheds and roofings) are ignored and the building parts are merged into a single zone (Figure 8).

Figure 8: The building stock after merging the building parts and removing the buildings which are not simulated (e.g. garages, sheds and roofings)

Then the neighborhood relationships are established, a closed construction method is detected and corresponding shared walls are created (Figure 9).

Figure 9: The calculated *SharedWall* featured for building in a closed construction

In the final step of the geometric generation of the single zone models, window elements are generated for a preset wall-window ratio (Figure 10).

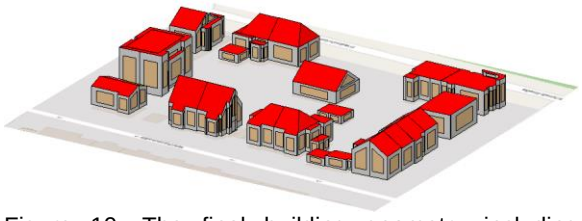

Figure 10: The final building geometry including windows generated according to the preset wall-window ratio

In addition to the correct geometric calculation of the thermal zone, attributes for building volume and base area are derived from the generated building envelope. If the CityGML attribute *storeysAboveGround* is available, it is used together with the base area to determine the heated area. Otherwise, the number of storeys is determined using a predefined average storey height and the building height. Depending on the building usage, schedules are generated in a further step, which describe the usage behavior in general terms. Specifically, schedules are generated for the set point temperatures (heating, cooling), presence of people, lighting and internal loads. And finally the material parameters are assigned based of the attribute *yearOfConstruction* and TABULA.

Conclusion and Outlook

The method introduced in the present paper allows a CityGML building model to be enriched in several subsequent steps for thermal building simulations. To ensure maximum transparency and interoperability, the enrichment is performed according to the model specifications of the CityGML Energy ADE. Both geometric and semantic modifications to the original CityGML building model may be necessary to generate the thermal building envelope. Enrichment with information for building usage and building physics is achieved with the use of customized libraries based on DIN 18599-10 and TABULA. The data derived from this is converted into CityGML Energy ADE time series and component structures and is therefore transparent for all subsequent processes. The method enables the widespread CityGML building models to be used for thermal building simulation and, the enriched CityGML Energy ADE building models to be shared with other applications in an open data model.

The enrichment process is prototypically integrated into the KITModelViewer software. The results of the geometric operations on the model are heavily dependent on the structure and quality of the input data and must be tested with additional different data sets and adapted if necessary. The libraries for assigning data for building usage and for component structures are implemented in a rudimentary way. Both the content and the use of these libraries must be easily and flexibly expandable in the future.

The functionality to enrich CityGML building models with energy-relevant information and the export to CityGML Energy ADE will be part of future versions of the freeware KITModelViewer.

References

Benner, J.; Geiger, A.; Häfele, K.-H., 2016. Virtual 3D City Model Support for Energy Demand Simulations on City Level – The CityGML. REAL CORP 2016. 22-24 June 2016. ISBN 978-3-9504173-1-9.

Biljecki, F.; Kumar, K.; Nagel, C., 2018. CityGML Application Domain Extension (ADE): overview of developments. Open geospatial data, softw. stand. 3, 13 (2018). https://doi.org/10.1186/s40965-018-0055-6.

Burrough, P. A.; McDonnell, R.; Lloyd, C. D., 2015. "8.11 Nearest neighbours: Thiessen (Dirichlet/Voroni) polygons". Principles of Geographical Information Systems. Oxford University Press. pp. 160–. ISBN 978-0-19-874284-5.

CityGML Wiki: Open Data Initiatives in Germany. https://www.citygmlwiki.org/index.php?title=Open_Data_Initiatives_in_Germany. last access 23.02.2024.

Coors, V.; Rodrigues, P.; Weiler, V.; Duminil, E.; Klöber, A.; Holweg, D.; Brüggemann, T.; Bohn, K.; Groll, L.; Balbach, B., 2021. EnEff:Stadt - SimStadt 2.0: Schlussbericht : Laufzeit des Vorhabens: 01.07.2017-31.12.2020, Berichtszeitraum: 01.07.2017-31.12.2020, Hochschule für Technik Stuttgart.

EnergyPlus: Building energy simulation program. https://energyplus.net/. last access 23.02.2024.

Geiger, A.; Nichersu, A.; Häfele, K.-H.; Hagenmeyer, V., 2022. Usage Profile Enrichment of CityGML Models for Urban Building Energy Modeling. Proceedings of BauSim Conference 2022: 9th Conference of IBPSA-Germany and Austria, International Building Performance Simulation Association (IBPSA). doi:10.26868/29761662.2022.28.

Geiger, A., Häfele, K.-H. and Hagenmeyer, V., 2021. Quality Check of openBIM Input Data for Thermal Building Simulation based on mvdXML, 17th International IBPSA Building Simulation Conference. - Bruges, Belgium, 2021.

Geiger, A.; Nichersu, A.; Hagenmeyer, V., 2020. Sensitivity of input data in building heating energy demand simulation. BauSIM 2020. 23. - 25. September 2020, Graz.

Gröger G. [et al.], 2012. OGC City Geography Markup Language (CityGML) En-coding Standard, Version: 2.0.0. - OGC 12-019. Open Geospatial Consortium, 2012.

Hörner, M.; Bischof, J., 2022. Building typology of the non-residential building stock in Germany - methodology and first results. Conference: eceee 2022 Summer study. European Council for an Energy Efficient Economy.

KITModelViewer: Softwaretool for for reading, exploring and editing of semantic data models. https://www.iai.kit.edu/ifc. last access 21.02.2024.

KITModelViewer PlugIns: PlugIn Repository for KITModelViewer. https://github.com/KIT-IAI/SDM_Plugin_General. last access 21.02.2024.

Kavgic M. [et al.], 2010. A review of bottom-up building stock models for energy consumption in the residential sector, Building and Environment, Volume 45, Issue 7, (2010) page 1683-1697, ISSN 0360-1323, https://doi.org/10.1016/j.buildenv.2010.01.021.

Kolbe T. H. [et al.], 2021. OGC City Geography Markup Language (CityGML) Part 1: Conceptual Model Standard. - https://docs.ogc.org/is/20-010/20-010.pdf: Open Geospatial Consortium, 2021.

Malhotra Avichal [et al.], 2022a. Information modelling for urban building energy simulation - A taxonomic review. Building and Environment. 2022.

Malhotra Avichal [et al.], 2022b. An Open-Source CityGML Enrichment Tool (CityEnrich). Proceedings of BauSim Conference 2022: 9th Conference of IBPSA-Germany and Austria, International Building Performance Simulation Association (IBPSA). Weimar. doi:10.26868/29761662.2022.56.

Nouvel, R.; Kaden, R.; Bahu, J-M.; Kaempf, J.; Cipriano, P.; Lauster, M.; Benner, J., 2015. Genesis of the CityGML Energy ADE; Future Buildings and Districts - Sustainability form Nano to Urban Scale. International Conference CISBAT 2015, Lausanne, CH, September 9-11, 2015.

Rosser, J. F.; Long, G.; Zakhary, S.; Boyd, D. S.; Mao, Y.; Robinson, D., 2019. Modelling Urban Housing Stocks for Building Energy Simulation using CityGML EnergyADE. isprs International Journal of Geo-Information 2019, 8, 163, doi:10.3390/ijgi8040163.

SIG3D 2017: Modeling Guide for 3D Objects - Part 2: Modeling of Buildings (LoD1, LoD2, LoD3). https://en.wiki.quality.sig3d.org/index.php?title=Modeling_Guide_for_3D_Objects_-_Part_2:_Modeling_of_Buildings_(LoD1,_LoD2,_LoD3). last access 07.02.2024.

TABULA: National Building Typologies. https://episcope.eu/building-typology/. last access 23.02.2024.

BauSIM 2024 in Wien
23. September – 26. September

Component-based machine learning modeling for predicting building energy performance – An overview

Philipp Geyer[1], Xia Chen[1], and Seyed Azad Nabavi[1]

1 Sustainable Building Systems Group, Institute for Design and Construction, Faculty of Architecture and Landscape, Leibniz University Hannover, Germany, E-Mail: Azad.nabavi@iek.uni-hannover.de

Introduction

In addition to the use of building simulation, in recent years data-driven methods using machine learning (ML) have been developed that have the ability to act as surrogate for building energy prediction (Amasyali and El-Gohary, 2018; Westermann and Evins, 2019). Such data-driven models have high potential by reducing modelling and computation effort drastically and thus allowing extension of examined configurations by two to three magnitudes to consider variety of designs as well as uncertainties. However, there are two major drawbacks of such models: (1) First, they form a black box, i.e. they do not use physics when predicting which excludes the possibility to check and understand the calculations; (2) The prediction relies on the data that has been used to train the models, which causes problems for cases that "extrapolate" outside the training data.

For this context, we have developed a method aligned with systems engineering that we call component-based machine learning (CBML) (Geyer and Singaravel, 2018). This method does not train a model for the whole building, as it is the case for most state-of-the-art energy predictions, which we call monolithic. CBML creates data-driven models for the components of a building, i.e. walls, windows, etc. Due to its object-oriented modelling paradigm as typical feature of building information model (BIM) (Borrmann et al., 2018), this approach allows for a close integration with the model structures of digital design and planning in BIM. One the one hand, the close integration with the structures of design and planning is superior generalization and reusability of the data-driven models created by machine learning; On the other hand, CBML uses exclusively engineering quantities to connect data-driven components leading to built-in interior interpretability and explainability (Geyer et al., 2023).

This paper provides an overview of the current development of CBML. First, it introduces the method of CBML; experiments on the build envelope and building systems show its accuracy and the generalization of CBML predictions compared to predictions of monolithic models. The next section extends static predictions of one value to time series predictions. A further step in the combination of data-driven components with building simulation; this leaves strict limitation to building components and includes process components. Finally, we will discuss interpretability and explainability of CBML.

The CBML Method

Key element of the method is the data-driven component that represents dynamic physics that is usually determined by coupled differential equations (Clarke, 2001). By using training data that represent the dynamic behavior within the components, it is possible to capture this complex behavior by ML depending on the features of the component. Figure 1 shows on the left selected components with features and exemplary training data for the thermal behavior of the building envelope. The training data are derived by building simulation (Energy Plus); however, the use of real-world data acquired by sensors is possible. A process of supervised machine learning applied at component level yields the data-driven model of the component. The composition of these pre-trained components, as represented by the test cases in Figure 1 (right), allows for prediction in new designs—a key capability for design and planning activities of buildings with their unique character.

Building envelope experiments

A systematic empirical examination using typical test cases reveals the prediction and generalization capabilities of the method. A set of parametric models of typical office buildings has been defined and simulated to serve as a dataset of energy use intensity (EUI) dependent on typical design variables, which are building geometry, u-values, g-value, heat capacities, permeability,

internal mass, operating hours, internal loads, and system efficiencies (for details please see Geyer et al., 2023). Data of a box building (Fig. 1a) serve to predict design cases significantly vary in shape, shown at the top left in Figures 2a and 2c. These variations form typical use cases of building design, as they frequently happen in architecture. For the first dataset in Figure 2 left, which contains a group of prism-like building shapes, the coefficient of determination R^2 is improved from 0.94 for a best-practice monolithic approach to 0.99. The results of a more complex case including zones with ceilings against indoor and outdoor climate, which is not included training data of the box building, is shown in Figure 2 right; in this case, an bad R^2 of 0.71 for the monolithic case is improved to 0.94—an sufficient level for design of buildings. This demonstrates the superior generalization capabilities of the component-based approach for typical design ranges.

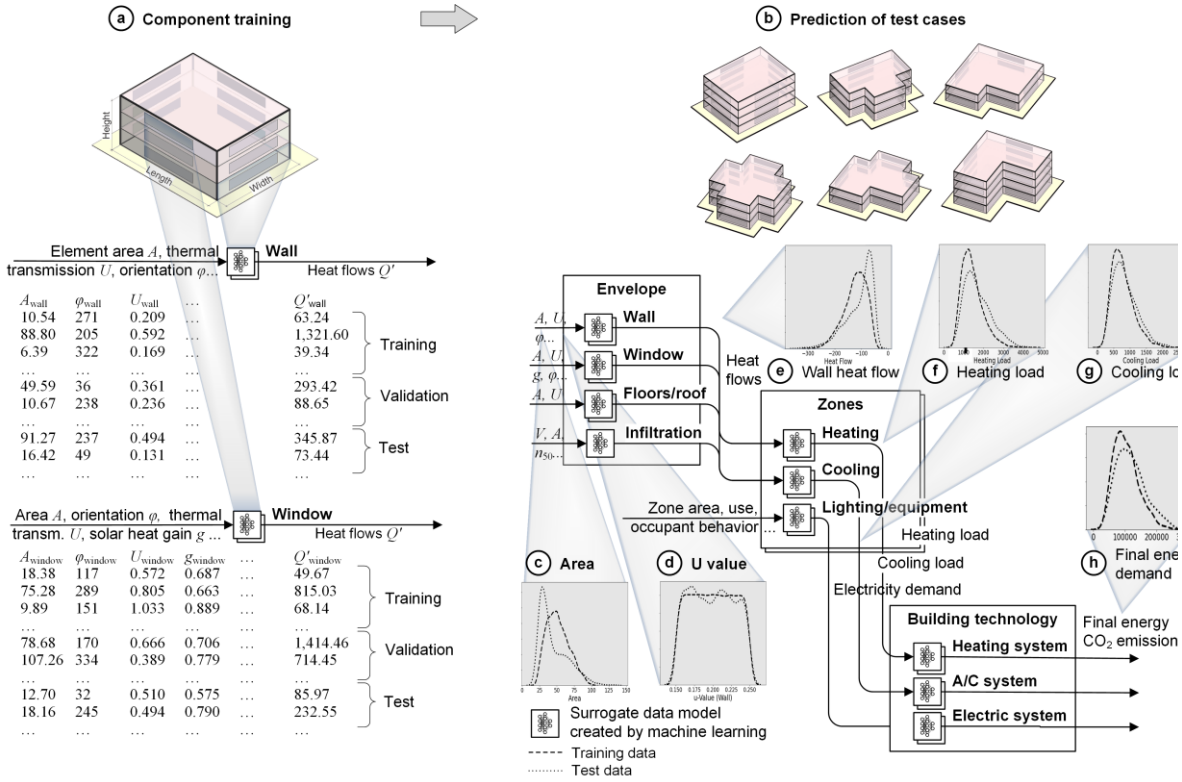

Figure 1: Component-based ML components with training data and systems for prediction of test cases with statistical distributions (grey boxes).

Building systems experiments

Early prediction of HVAC energy usage is crucial for energy efficiency and user comfort but is traditionally complex and relies on building simulations. Modelling the HVAC system in buildings as a major contributor to the building energy consumption is the next step in application of CBML approach. This step represents insofar further complexity as it includes circular dependencies which form a challenge for a hierarchical system organization. For this reason, we have test applicability of the hierarchical approach in a study (Nabavi et al., 2023). The study focuses on developing CBML approach for building components to investigate the importance of building components' hierarchy on prediction performance machine learning techniques. Two hierarchical structures are explored: The first one is based on energy flow Zone–Secondary HVAC–Primary HVAC (Z-S-P) and the second one on design logic Zone–Primary HVAC–Secondary (Z-P-S). The structure of the proposed hierarchies is presented in Figure 3a and Figure 3b, respectively. A random forest regression algorithm is applied to the CBML model achieves high R^2 values (0.98 to 0.99) for zone, primary HVAC, and secondary HVAC components, particularly in the Z-P-S hierarchy. Notably, the hierarchy based on design logic exhibits superior accuracy in predicting secondary HVAC components, emphasizing the importance of design dependencies in defining predictive hierarchies. This highlights the significant role of primary HVAC configurations in modeling secondary components, showcasing the effectiveness of CBML in forecasting HVAC system performance.

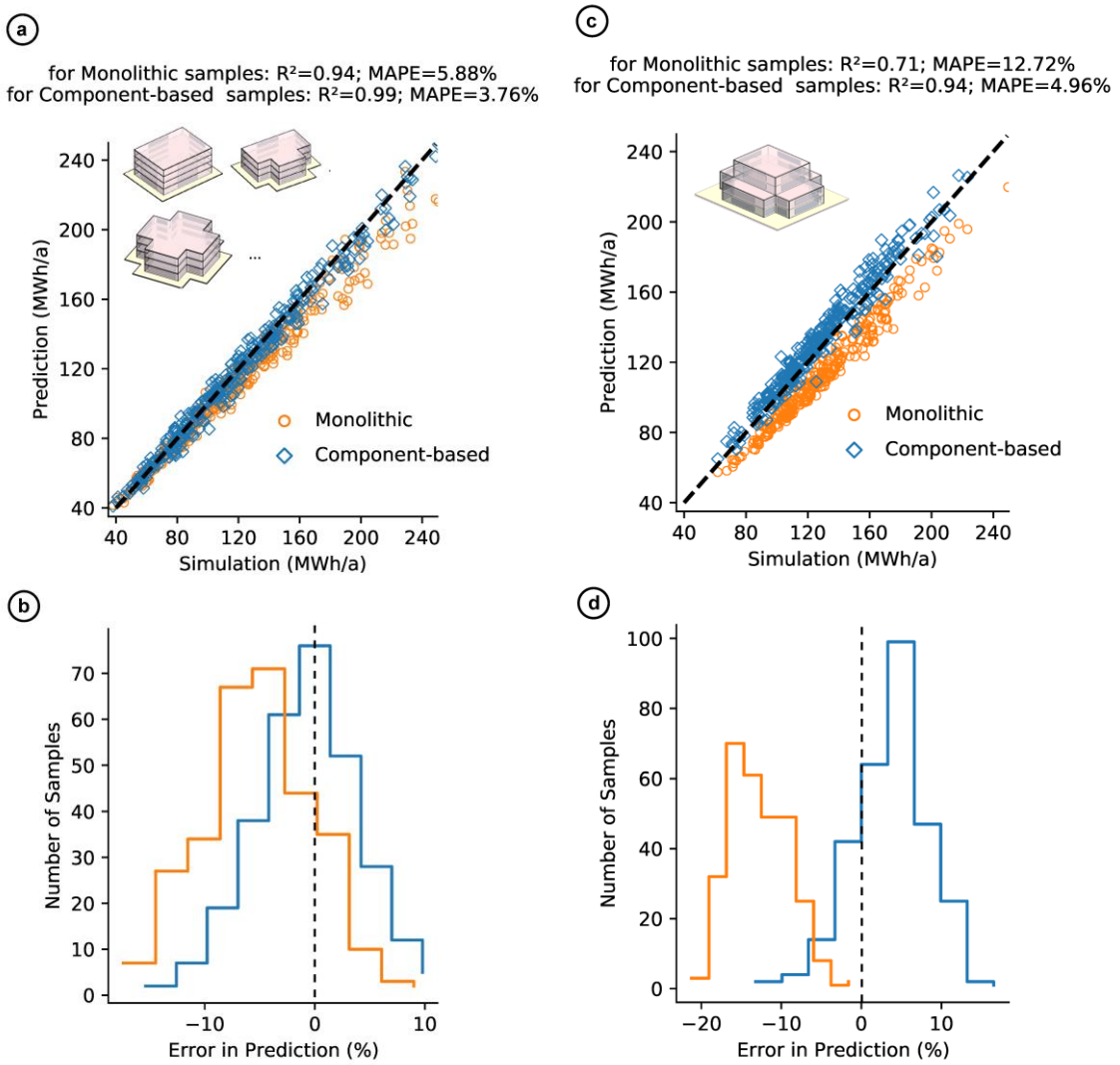

Figure 3: Comparison of the energy use intensity (EUI) for results of component- based ML prediction versus traditional monolithic ML prediction (Geyer et al., 2023)

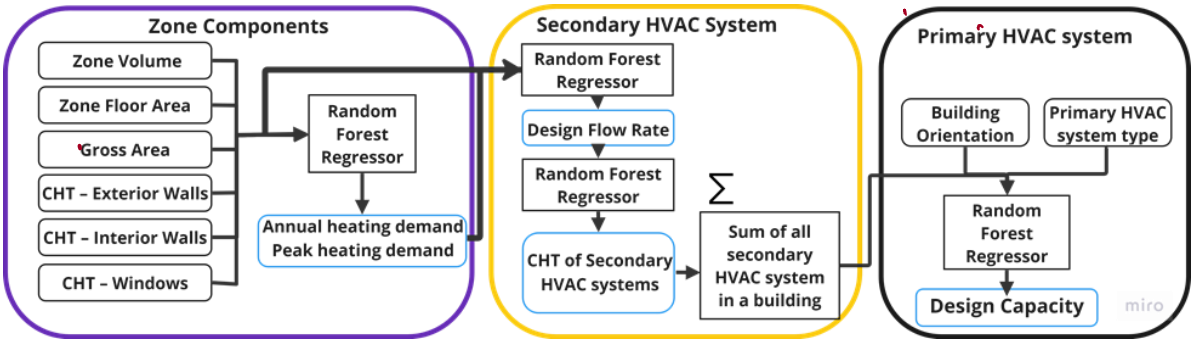

Figure 2a: Zone-Secondary HVAC-Primary HVAC hierarchy.

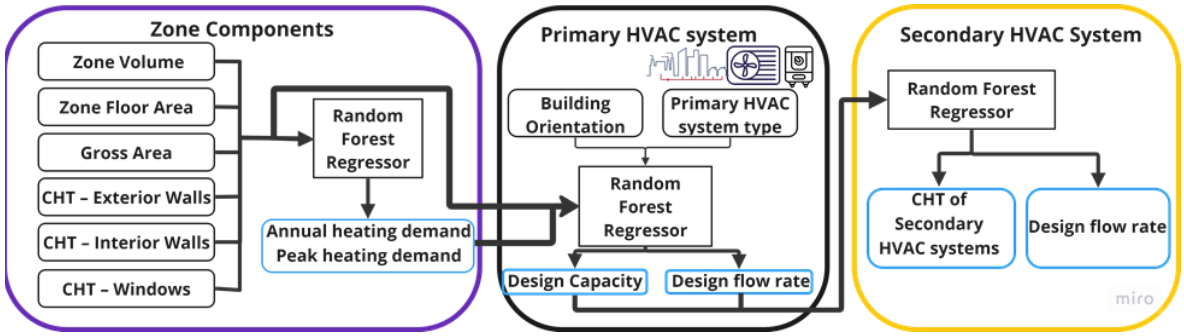

Figure 3b: Zone- Primary HVAC- Secondary HVAC hierarchy (Nabavi et al., 2023).

Time-series predictions

Besides yearly totals, accurate predictions of hourly energy consumption assists in evaluating several design alternatives and operation strategies (Deb et al., 2017). Especially, the integration of buildings into energy networks exploiting renewable energy and storage capacities requires the prediction of their time-series energy demand. Too address this challenge, one previous study (Chen et al., 2021) proves that the CBML is able to predict dynamic time-series energy performance for new design cases by deriving a set of reusable data-driven model components. The ability of the ML model to generalize via different decomposition levels has been demonstrated. The resulting hourly energy predictions during the design phase are useful for equipment sizing, controlling peak energy demands, and leveling the load in the networks. To better capture the dynamic of the time-series data, the category of Gradient Boosting Decision Tree (GBDT) (Friedman, 2001) has been applied in this study and excelled in practice the Light Gradient Boosting Machine (LightGBM) algorithm (Guolin Ke et al., 2017). A model structure comparison between the monolithic and the CBML approaches for time-series prediction is presented in Figure 4.

In conclusion, the CBML approach is capable of capturing the peak load and usage patterns for non-existent buildings, achieving comparable performance as the monolithic ML approach in time-series prediction. Therefore, the method allows for the quick and accurate prediction of time-series with peaks and patterns, the integration in

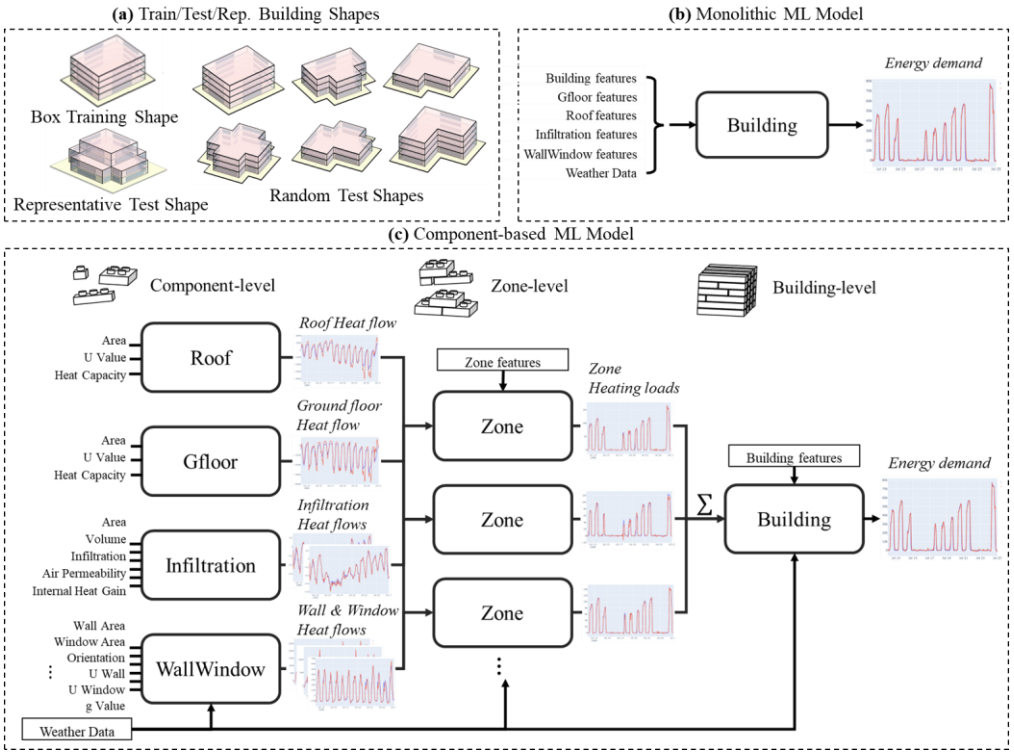

Figure 4: Time series prediction: (a) building shapes for training and test; (b) monolithic ML modelling scheme; (c) component-based ML model scheme (Chen et al., 2023).

digital design and modeling of buildings, and the explainability by inter-component information form important benefits in early design phases.

Robustness against sparse data

The deployment of ML applications often requires large datasets—a requirement that can pose a major challenge in fields where data is sparse or inconsistent. By spatially and semantically decomposing the building design into components, the CBML approach is essentially a concept of rebalancing the integration of prior knowledge into data-driven processes, more specifically, the model organization, and mitigating the learning costs of ML models. A further study (Chen et al., 2023) discussed its two-fold advantages: First, by disentangling compositionality of building design, CBML transfers the extrapolation problem at a building level, into the interpolative behavior among building components (Figure 5).

Second, we conclusively proved that, when CBML is trained on datasets that are sparse, inconsistent, and small, it demonstrates a robust predictive capability. Importantly, this advantageous characteristic is independent of the specific ML model used and carries huge benefits for real-world applications offering better performance if the amount of data is limited. To simulate sparse, inconsistent data scenarios, which are challenging for traditional data-driven ML approaches, we applied a high masking ratio to the training set and validated the performance comparison result of CBML and monolithic approach within various ML approaches on the test/representative dataset; the different building shapes in datasets are presented in Figure 5. Specifically, we randomly sampled the training set at rates of 1%, 0.1%, 0.05%, 0.025%, and 0.0125%. At the building level, the smallest training set only contains 195 inconsistent time-series hourly data points out of a possible 5000 different building

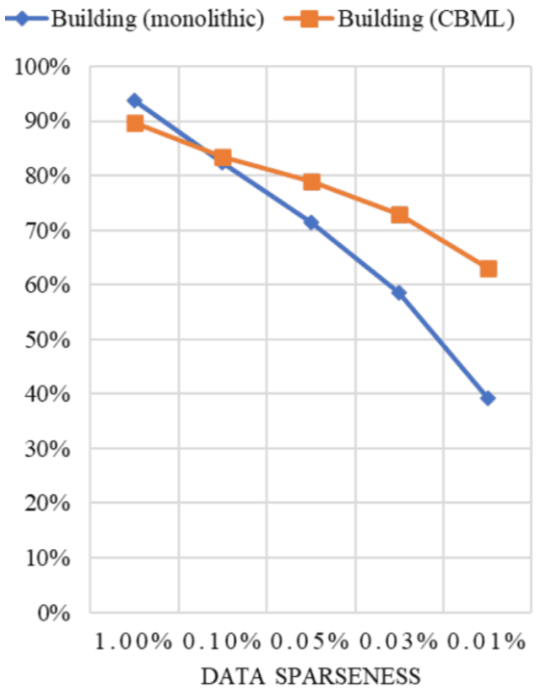

Figure 5: Drop of accuracy with increasing data sparseness.

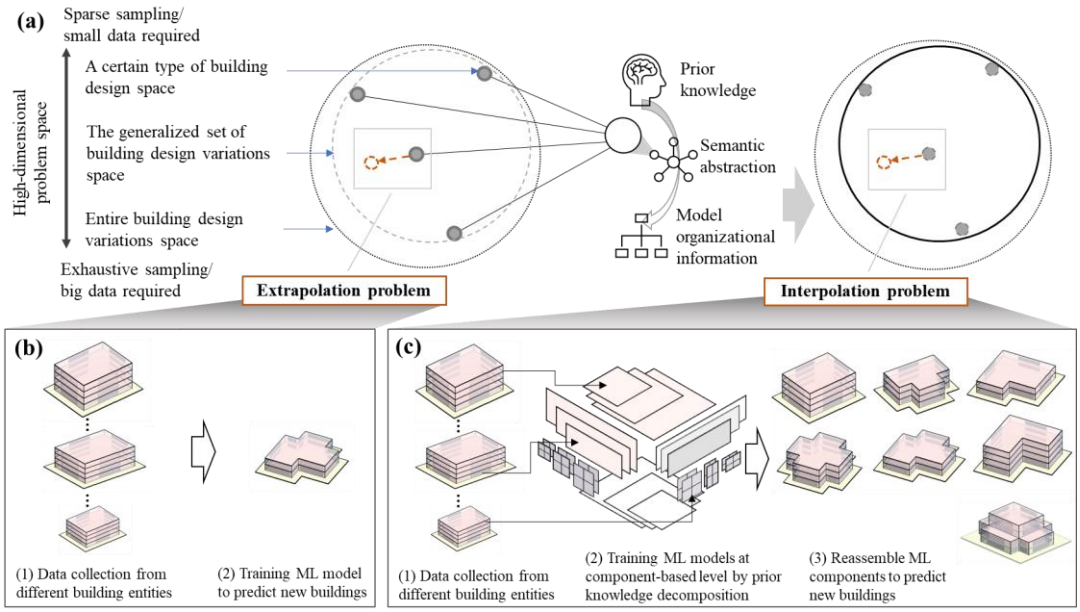

Figure 6 Generalization via prior knowledge encoding: (a) Applying domain-related decomposition knowledge transfers the ML prediction problem from extrapolation to interpolation and covers a larger problem space; (b) Monolithic modeling: extrapolation problem; (c) Component-based machine learning: interpolation problem (Chen et al., 2023).

samples, creating an extreme case of data sparseness. Figure 6 shows the drop of accuracy with data sparseness. The results demonstrate better accuracy of CBML in case of data sparseness. We summarize that the generalization and robustness of ML models benefit from the knowledge integration incorporated by the component structure of CBML.

Hybridization with building simulation

To address the data-reliance issue of training the ML model, especially for the CBML approach, data augmentation is one vital supplemental approach. In this context, a hybrid approach (Chen et al., 2022) is proposed to boost prediction accuracy and ease this barrier from both application perspectives: the data acquisition effort and the detailed simulation effort. This idea is inspired by the mindset of Seasonal and Trend decomposition using Loess (STL) decomposition (Cleveland et al., 1990), an essential abstraction mindset to distinguish data into periodic and steady patterns, which both can be separately predicted by different fit-for-purpose approaches. This mindset also implies the theory of uncertainty decomposition, which refers to two distinct types of uncertainties (Kiureghian and Ditlevsen, 2009): *aleatory* and *epistemic*. Epistemic uncertainties are risen due to limited data or understanding, which is possible to be reduced by gathering more information or by refining models. Epistemic uncertainties are further decomposable into two sub-types: *parametric* and *structural* (Liu et al., 2019). Both, ML and first principles are complementary approaches to address periodic and steady features, which provides the foundation of the hybrid-model approach. Inherent from the previous section, the ensemble, tree-based ML algorithm, LightGBM is used in the study. The hybrid approach process illustration is demonstrated in Figure 8.

The output conducted by the first-principles model carries periodic patterns: encoded domain knowledge regarding thermodynamic behaviors, building characteristics, and component decomposition information in time-series format.

As Figure 8 shows, the target building static features are firstly used in the first-principle model, combined with domain knowledge, and encoded into the simulation result. The result is then aligned with the historical records and weather data, fed into the ensemble tree-based model, the right box illustrated the process of mixture input data with the ensemble learning detail. This representation aligns with the format of historical records, which enables the knowledge mentioned earlier to feed into ML models for further integration. The ML model then learns the difference between historical records and simulation output - the unsystematic patterns or parametric uncertainties caused by implicit factors in reality.

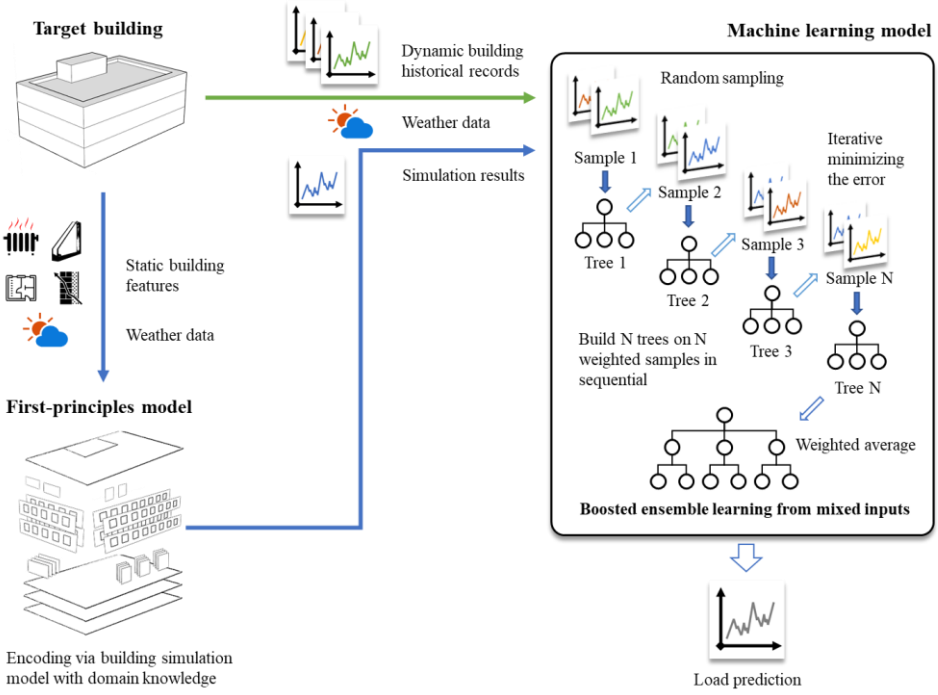

Figure 7 Demonstration of the hybrid modelling approach (Chen et al., 2022).

The overall hybrid approach contributes to accuracy enhancement and model interpretation.

Interpretability and explainability

An important feature of CBML is that all interfaces of the data-driven component models use engineering quantities and units. From an perspective of ML, the prediction thus forms a deep neural network (DNN) whose activations however are at defined interfaces directly interpretable by engineering expertise. Furthermore, the reuse of components is a case of transfer learning (Pan and Yang, 2010) using pre-trained data-driven models in new contexts. This combined reusability with interpretability at component interfaces allows for network-internal explanations. Figure 8 provides an overview of explainability methods derived for CBML from the scheme presented by Arrieta et al. (2020). First, we have direct interpretability activations of the network at the component interfaces as physical quantities as yearly average predictions (Fig. 8a, e, h) and time-series predictions (Fig. 8b, f, i). The calculation of sensitivities with respect to design variables (Fig. 8c, g) furthermore allows to achieve understanding of the design space and thus provides explainability of selected design solutions. Finally, decision trees (Fig. 8d) as data-driven models producible by ML allow for direct understanding of ML predictions as human can read the split points understanding why a model predicts a specific physical quantity. These different ways of infiltrating the data-driven model by physical quantities and considerations allows for explainability linking the non-physical black-box world of machine learning with domain knowledge and the human expertise.

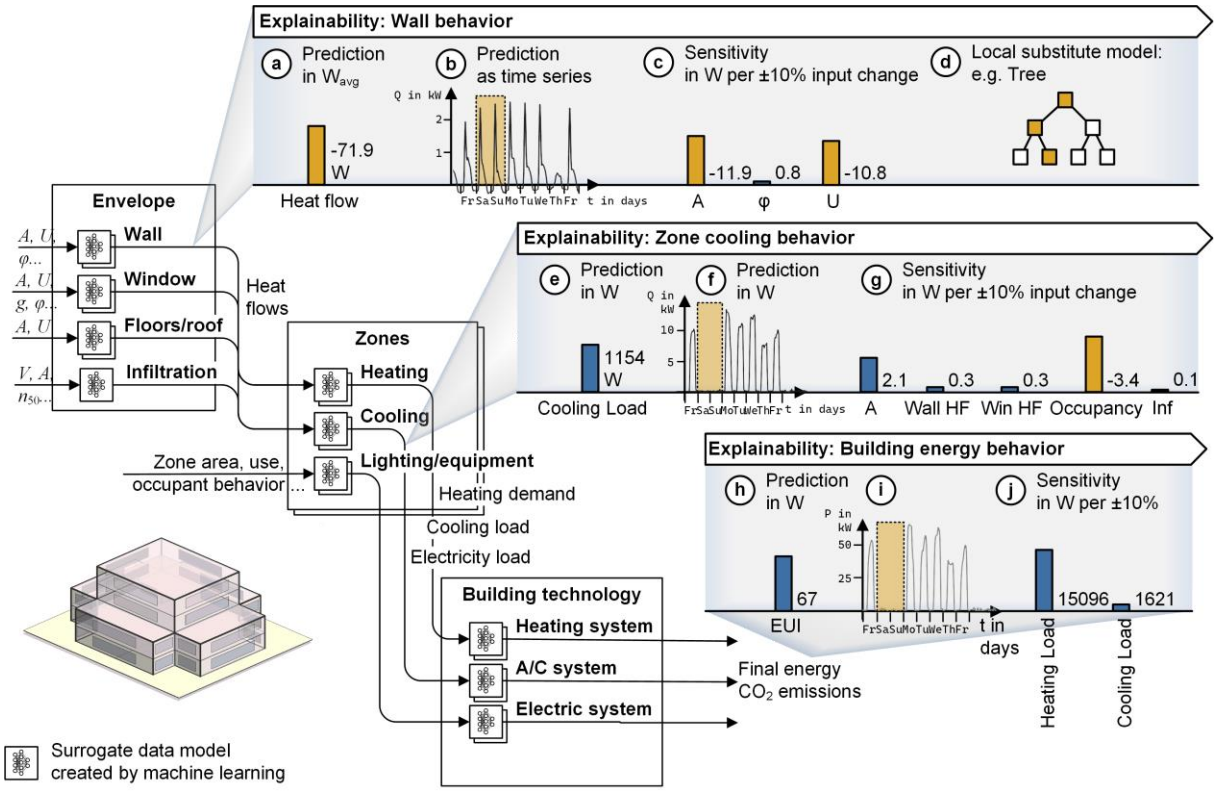

Figure 8: Methods of explainability using component-based ML (Geyer et al., 2023).

Conclusions

The organization of data-driven models created by component-based machine learning following in a systems engineering paradigm demonstrated better generalization as this method is able to transfer trained models between cases and configurations, which is a key capability for design support. By capturing the dynamic thermal behavior of buildings the method proved capabilities in complex system prediction. Furthermore, the interfaces using engineering quantities form allow for direct interpretability and explainability, which forms a basis of trustworthy AI in engineering. We have demonstrated these capabilities for building energy performance including the prediction of yearly totals as well as time series data for the building envelope as well as the building systems. Furthermore, the knowledge integration by the domain-specific systems decomposition generates superior robustness in case of sparse data. Finally, not only because of its generalization and explainability capabilities but also be

cause of its seamless integration with digital design and planning, we consider the CBML approach ideal for data-driven design and planning of energy efficient and sustainable buildings.

Acknowledgement

The authors acknowledge the support of Deutsche Forschungsgemeinschaft (DFG) in form of funding the research through the grant GE1652/3-1/2 within the researcher unit FOR 2363 EarlyBIM and through the Heisenberg grant GE1652/4-1.

References

Amasyali K, El-Gohary N (2018): A review of data-driven building energy consumption prediction studies. *Renewable and Sustainable Energy Reviews*, *81*, 1192–1205, https://doi.org/10.1016/J.RSER.2017.04.095

Arrieta AB, Díaz-Rodríguez N, Ser JD, Bennetot A, Tabik S, Barbado A, … Herrera F (2020): Explainable Artificial Intelligence (XAI): Concepts, taxonomies, opportunities and challenges toward responsible AI. *Information Fusion*, *58*, 82–115, https://doi.org/10.1016/j.inffus.2019.12.012

Borrmann A, König M, Koch C, Beetz J (2018): *Building information modeling*. Springer

Chen X, Guo T, Kriegel M, Geyer P (2022): A hybrid-model forecasting framework for reducing the building energy performance gap. *Advanced Engineering Informatics*, *52*, 101627, https://doi.org/10.1016/j.aei.2022.101627

Chen X, Singh MM, Geyer P (2021): Component-based machine learning for predicting representative time-series of energy performance in building design. 28th International Workshop on Intelligent Computing in Engineering, Berlin

Chen X, Singh MM, Geyer P (2023): Utilizing Domain Knowledge: Robust Machine Learning for Building Energy Prediction with Small, Inconsistent Datasets. arXiv https://doi.org/10.48550/arXiv.2302.10784

Clarke J (2001): *Energy Simulation in Building Design*. Oxford: Butterworth-Heinemann Retrieved from http://www.sciencedirect.com/science/article/pii/B9780750650823500012

Cleveland RB, Cleveland WS, McRae JE, Terpenning I (1990): STL: A seasonal-trend decomposition. *J. Off. Stat*, *6*(1), 3–73,

Deb C, Zhang F, Yang J, Lee SE, Shah KW (2017): A review on time series forecasting techniques for building energy consumption. *Renewable and Sustainable Energy Reviews*, *74*, 902–924, https://doi.org/10.1016/j.rser.2017.02.085

Friedman JH (2001): Greedy Function Approximation: A Gradient Boosting Machine. *The Annals of Statistics*, *29*(5), 1189–1232,

Geyer P, Singaravel S (2018): Component-based machine learning for performance prediction in building design. *Applied Energy*, *228*, 1439–1453, https://doi.org/10.1016/j.apenergy.2018.07.011

Geyer P, Singh MM, Chen X (2023): Explainable AI for engineering design: A unified approach of systems engineering and component-based deep learning. arXiv https://doi.org/10.48550/arXiv.2108.13836

Guolin Ke, Meng Q, Finley T, Wang T, Chen W, Ma W, … Liu T-Y (2017): Lightgbm: A highly efficient gradient boosting decision tree. *Advances in Neural Information Processing Systems*, *30*, 3146–3154,

Kiureghian AD, Ditlevsen O (2009): Aleatory or epistemic? Does it matter? *Structural Safety*, *31*(2), 105–112, https://doi.org/10.1016/j.strusafe.2008.06.020

Liu J, Paisley J, Kioumourtzoglou M-A, Coull B (2019): Accurate Uncertainty Estimation and Decomposition in Ensemble Learning. In: *Advances in Neural Information Processing Systems*Vol. 32, , Curran Associates, Inc. Retrieved from https://proceedings.neurips.cc/paper/2019/hash/1cc8a8ea51cd0adddf5dab504a285915-Abstract.html

Pan SJ, Yang Q (2010): A Survey on Transfer Learning. *IEEE Transactions on Knowledge and Data Engineering*, *22*(10), 1345–1359, https://doi.org/10.1109/TKDE.2009.191

Westermann P, Evins R (2019): Surrogate modelling for sustainable building design – A review. *Energy and Buildings*, *198*, 170–186, https://doi.org/10.1016/j.enbuild.2019.05.057

BauSIM 2024 in Wien
23. September – 26. September

Effect of Dew Point Temperature and Sky Patch Discretization on Annual Daylight Simulations

David Geisler-Moroder[1], Lukas Prost[2], Nicolas Roy[3]
1 University of Innsbruck, Austria, david.geisler-moroder@uibk.ac.at
2 Keyshot A/S, Denmark, lukas.prost@keyshot.com
3 VELUX A/S, Denmark, nicolas.roy@velux.com

Abstract

Climate-based daylight modeling is now the established state of the art in daylight planning practice. The validated matrix-based methods such as the three-phase or five-phase method as extensions to the daylight coefficient approach, enable time-efficient annual daylight simulations and form the basis in most common software tools. In addition to the room, the façade system and the external situation, the description of the sky model is an essential input variable for these methods. Common practice is to use the Perez sky model, which predicts a sky distribution from direct and diffuse irradiance values. The continuous model is then discretized into sky regions to satisfy the based matrix approach.

In this paper we first investigate the influence of the consideration of the dew point temperature in the Perez model both on the sky model itself and on the resulting daylight performance metrics in an example building. Based on a study for 3130 locations worldwide, we show for which climates a correct mapping is of major importance. Secondly, we analyze the effects of the different distribution of skylight and sunlight on discrete sky patches and discuss the differences with regard to resulting interior daylight values as well as the challenges for daylight simulation methods.

Introduction

Dynamic building performance simulations are using climate data mimicking representative weather conditions at the investigated location for design purposes. In the field of daylight, climate-based daylight simulations (CBDM) [Mardaljevic, 2006] are generally based on the daylight coefficient (DC) approach in order be able to carry out the computationally demanding simulations in a reasonable amount of time. From the presumably first approaches of Tregenza and Waters [Tregenza and Waters, 1983] via the generalized model by Bourgeois et al. [Bourgeois, Reinhart and Ward, 2008] to advanced approaches such as the three-phase or the five-phase methods [McNeil, 2014] [Lee, Geisler-Moroder and Ward, 2018], these DC approaches are all based on a subdivision of the sky hemisphere into discrete solid angle areas (so-called patches). In annual CBDM simulations, relative contributions to the daylighting in the interior from each of these patches are calculated and then multiplied by the brightness of the sky for each time step. Almost all methods rely on the Perez model for the conversion of hourly, direct and diffuse irradiance data to the sky's luminance distribution [Brembilla and Mardaljevic, 2019]. It should also be noted that according to Brembilla [Brembilla, 2021] the absolute values in this weather data, especially the direct components, should be taken with caution.

Perez et al. [Perez et al. 1990] developed models "to predict short time-step solar energy and daylight availability". All presented models are following the same structure, i.e.

$$Y = X * F(insolation\ condition,\ receptor/sun\ geometry) \quad (1)$$

where

Y is the modelled quantity, X is the quantity depending on the three basic inputs (i) direct irradiance, (ii) global irradiance, and (iii) three-hourly dew point temperature, and F is a transfer function given as

$$F(\epsilon, \Delta, Z, W) = a_i(\epsilon) + b_i(\epsilon) f(W) + c_i(\epsilon) g(Z) + d_i(\epsilon) h(\Delta). \quad (2)$$

F in turn depends on discrete functions a_i, b_i, c_i, and d_i, each with eight possible values defined for eight bins of sky clearness ϵ (see [Perez et al. 1990]). Further, the sky brightness Δ, the solar zenith angle Z, and the atmospheric precipitable water content W. The latter is calculated as

$$W = exp(0.07 * Td - 0.075)\ [cm] \quad (3)$$

where $Td\ [°C]$ denotes the three-hourly surface dew point temperature (see Figure 1).

The dew point temperature (DPT) is the temperature at which the air is saturated with water vapor and moisture condenses on surfaces to form dew. It is thus a direct measure of moisture content in the air. More moisture in the air means more scattering and more absorption of the sunlight penetrating the atmosphere. The DPT therefore also influences the resulting sky luminance distribution.

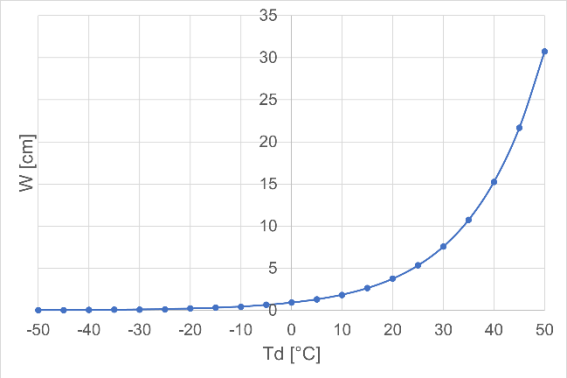

Figure 1: The precipitable water content W $[cm]$ used in the luminous efficacy model as function of the three-hourly surface dew point temperature Td $[°C]$.

As one of the models, a luminous efficacy model is set up in [Perez et al., 1990]. This makes it possible to convert radiometric to photometric values, i.e., to enable illuminance calculations based on global and diffuse irradiation inputs.

Based on the luminous efficacy model, Perez et al. [Perez, Seals and Michalsky, 1993a,b] further developed an "all-weather model for sky luminance distribution", which allows to define a reasonable sky representation for an arbitrary location based on standard irradiance time series. With such data being widely available in standardized weather data files (e.g. [EnergyPlus Weather Data, 2024], or [Climate.OneBuilding.org, 2024], this model (the so-called Perez model) can be used to perform climate data-based annual building performance simulations, such as CBDM.

In Radiance [Ward and Shakespeare, 1998], the de-facto standard software for daylight simulations, the Perez sky model is implemented in the tools *gendaylit* [gendaylit.c, 2024] and *gendaymtx* [gendaymtx.c, 2024]. The former allows to generate a continuous sky distribution for a specific situation defined through its location, date and time, and direct and diffuse irradiance, the latter to generate an annual Perez sky matrix already discretized into Tregenza or Reinhart sky patches. For each time step, it reads the direct normal radiation and the diffuse horizontal radiation from a weather tape in the Daysim weather file (WEA) format, which can be converted from an EnergyPlus weather (EPW) file using the *epw2wea* [epw2wea.c, 2024] tool.

In both methods, in their current version, a fixed DPT is used and initialized at 10.97 °C in *gendaylit* and at 11.0 °C in *gendaymtx*, respectively. While the "-d" option allows the user to define a temperature in *gendaylit*, for annual simulations based on *gendaymtx* the fixed temperature is used. While 11 °C is an adequate average value for some climates (e.g. Copenhagen, Figure 2), for others this DPT does not occur the entire year (e.g. Accra, Figure 3).

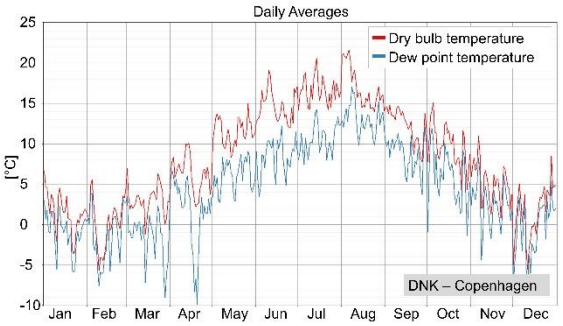

Figure 2: Annual daily average dry bulb and dew point temperatures in Copenhagen, Denmark, as per EPW weather file DNK_Copenhagen.061800_IWEC.epw.

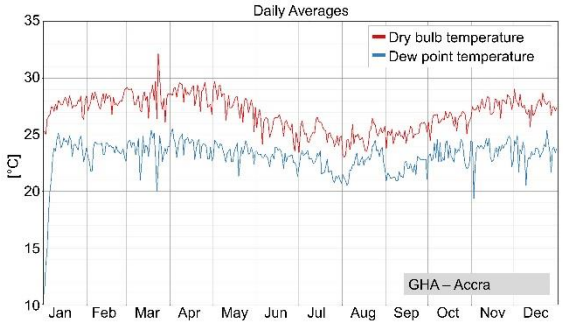

Figure 3: Annual daily average dry bulb and dew point temperatures in Accra, Ghana, as per EPW weather file GHA_Accra.654720_SWERA.epw.

In a comparison study of Radiance and the VELUX Daylight Visualizer [VELUX, 2024], where the three-hourly moving average DPT is used, this difference in the implemented methods was raised as a possible reason for variations in the results [Geisler-Moroder, 2023]. This raised the question of how relevant the DPT is for daylight calculations and for which climate zones it must be taken into account in CBDM simulations. The issue has been previously discussed at the 21st International Radiance Workshop 2023 ([Wienold, 2023] and [Geisler-Moroder, 2023]). Building on these initial findings, we carried out a comprehensive analysis for worldwide locations.

The aforementioned discretization of the sky distribution into patches is another challenge.

Depending on the implemented daylight simulation method (e.g. backward ray tracing or photon mapping), the representation is better suited either as a solid angle covering the full patch or a small light source the size of the sun. We also show that the respective selection can influence the daylight results in the interior.

Method

To be able to analyze the effect of the DPT in the Perez sky model on the resulting sky luminance distribution we adapted the *epw2wea* tool to additionally extract the DPT for each hour from the EPW file into an extended WEA file. We further adapted the *gendaymtx* tool to use the three-hourly DPT which we calculate as moving average from the weather tape instead of the fixed value.

We defined a simple reference office space with a double pane window (τ_v = 80%) in one façade, typical surface properties for floor, walls, and ceiling (30%, 50% and 80%, respectively), and a regular sensor grid on workplane height 0.85m (see Figure 4). Additionally, we evaluated the unobstructed exterior horizontal illuminance and the vertical illuminance in the four cardinal directions.

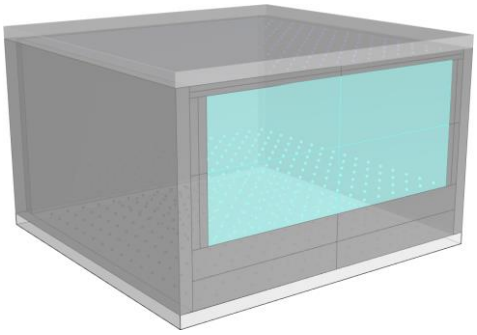

Figure 4: Simple reference office room.

The simulations were done using the two-phase method (i.e., classical DC-method), where relative contributions for the 145 Tregenza sky patches are pre-calculated. With *gendaymtx* the annual Perez sky matrix discretized into the Tregenza patches was generated for the "default" version (i.e., fixed 11 °C DPT) and for the "epwDP" version, using the three-hourly DPT from the EPW file.

The DPT is essentially dependent on the temperature and humidity and differs significantly in the various climate zones (see Figure 5). For our analysis we chose all 3130 locations worldwide, which are available in the online software DALEC [Werner et al., 2017].

For the comparisons of different sky patch sizes, we again modified the *gendaymtx* tool. In addition to the built-in sky discretizations Tregenza and its Reinhart subdivisions, we implemented the possibility to assign the luminous flux of each of these patches to a cone with specified opening angle. We examined two common angles in daylighting applications: 0.5° for the sun and 11°, which is used in instruments that measure sky luminances discretized in Tregenza patches [Diakite-Kortlever, 2021].

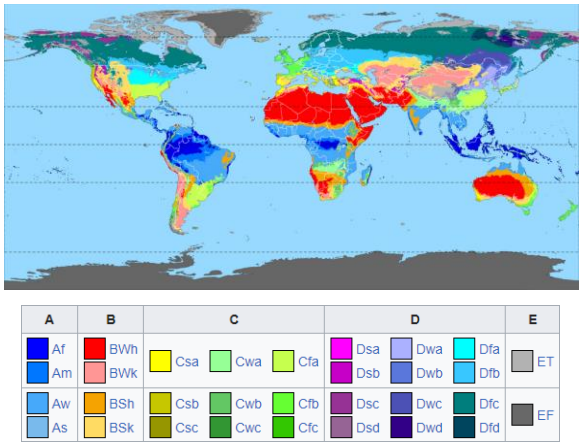

Figure 5: Updated Köppen-Geiger climate classification map [Beck et al., 2018]. Main groups: tropical (A), arid (B), temperate (C), continental (D), and polar (E). (Image: [Wikimedia Commons, 2024]).

Results

We first evaluated a cumulative annual sky to see the relative differences in the sky luminance distribution and absolute values. For the two locations Copenhagen, Denmark, and Accra, Ghana, the sky distributions and relative differences are shown in Figure 6 and Figure 8, respectively. While for Copenhagen the difference between a fixed DPT of 11 °C and the three-hourly moving average from the weather data is marginal, significant differences occur for Accra. This is especially prominent for areas of the sky hemisphere outside the sun paths.

Figure 7 and Figure 9 show the annual results for the average illuminance on the sensor grid at workplane height for the reference office room with the window oriented to the South for Copenhagen and Accra, respectively. Similar as for the cumulative sky, the results for Copenhagen show very little differences, while in Accra relative differences of 10% and more occur. This is especially pronounced during the times when no direct sunlight hits the south façade, i.e. between March and October.

For Copenhagen, the mean of all non-zero reported average illuminances is 2561 lx when using 11 °C as fixed DPT, and 2564 lx when using the three-hourly average. The mean biased relative deviation is +0.1%, with a minimum of -5.8% and a maximum of +4.0%.

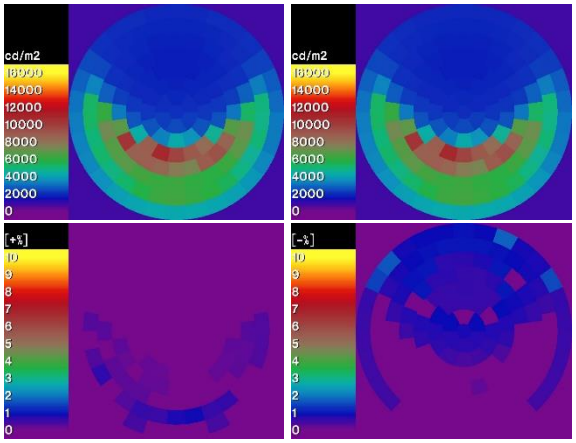

Figure 6: Cumulative, annual sky distribution for Copenhagen, Denmark. Top row: Perez sky model using a constant dew point temperature of 11 °C (left), and using three-hourly moving average from weather file (right). Bottom row: Relative differences where moving average yields higher results (left) and lower results (right), respectively.

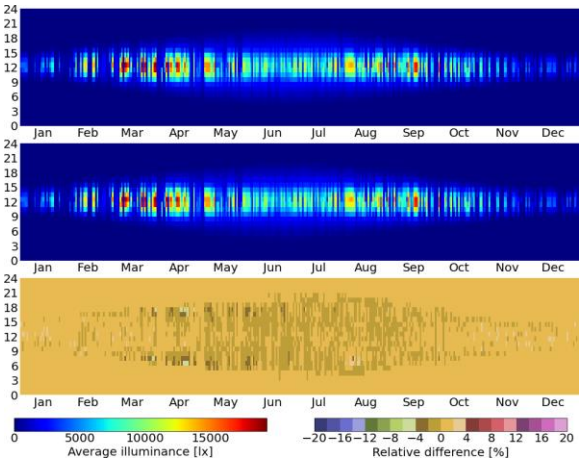

Figure 7: Annual average illuminance values for the reference room with south-facing window for Copenhagen, Denmark, using a constant dew point temperature of 11 °C (top), the three-hourly moving average from the weather file (center), and relative difference (bottom).

For Accra, the mean value is 2351 lx for 11 °C, and 2451 lx using the temperature from the weather data, with a mean biased relative deviation of +3.9%, a minimum of -2.7%, and a maximum of +15.1%.

We then looked at the effect that the DPT has on the reported daylighting results for different locations worldwide. We used the 3130 selected weather data files to calculate exterior, unobstructed illuminance values, as well as interior workplane illuminances for the reference office room. In Figure 10 we report the relative differences between using the default 11 °C DPT and using the epwDP, i.e., three-hourly average DPT from the EPW files.

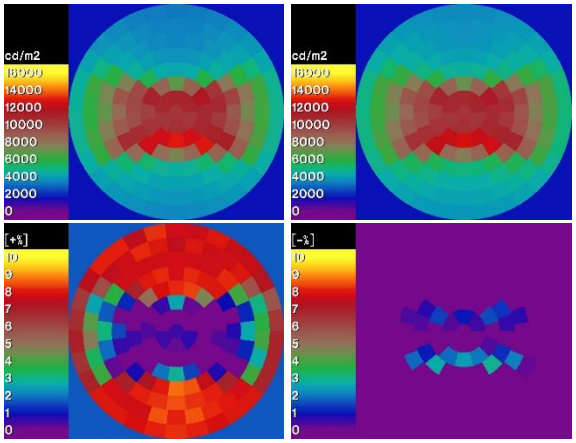

Figure 8: Cumulative, annual sky distribution for Accra, Ghana. Top row: Perez sky model using a constant dew point temperature of 11 °C (left), and using three-hourly moving average from weather file (right). Bottom row: Relative differences where moving average yields higher results (left) and lower results (right), respectively.

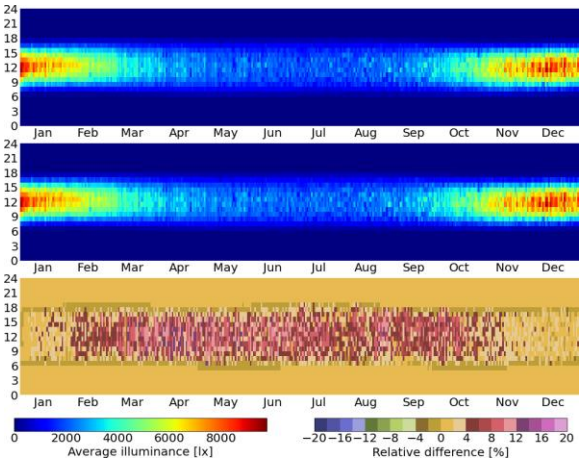

Figure 9: Annual average illuminance values for the reference room with south-facing window for Accra, Ghana, using a constant dew point temperature of 11 °C (top), the three-hourly moving average from the weather file (center), and relative difference (bottom).

With epwDP, the sky component yields higher results in equatorial areas and slightly lower results in continental / polar areas, and exactly vice versa for the sun component. The reported global horizontal illuminance, however, matches very well. Table 1 summarizes the results from Figure 10 and indicates the 5% and 95% percentiles as proxy for minimum and maximum values. This first result means that the consideration of the DPT is particularly relevant for applications in which sunlight is used specifically for daylighting.

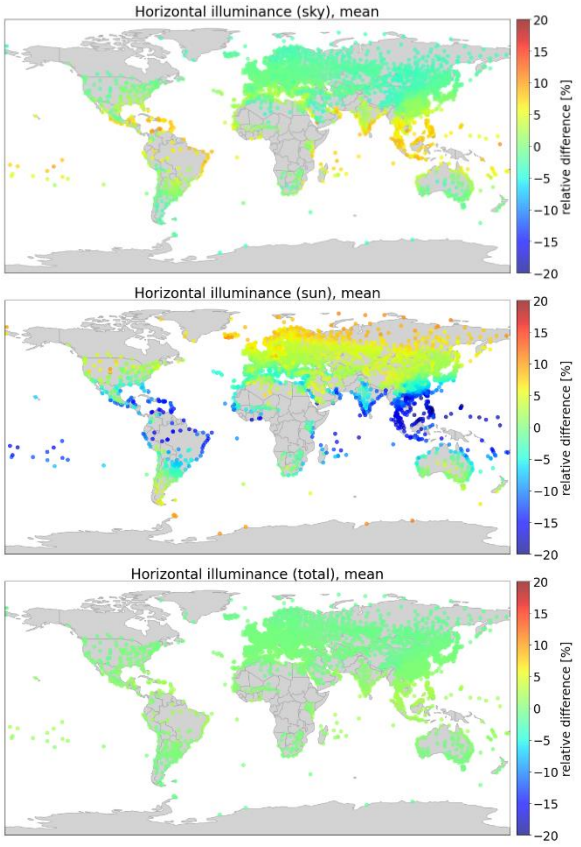

Figure 10: Relative differences for annual mean values of exterior horizontal illuminance at worldwide locations between fixed (11 °C) and EPW based dew point temperature. From top to bottom: diffuse (sky), direct (sun), and global (total) horizontal illuminance.

Table 1: Evaluation of worldwide results for exterior horizontal illuminance (Eh) from Figure 10.

Eh	Mean	Median	PC5	PC95
Sky	0.0%	-0.8%	-3.0%	6.5%
Sun	0.2%	2.4%	-14.2%	6.9%
Total	-0.1%	-0.2%	-1.0%	1.7%

Next, we analyzed how the differences in the Perez sky model based on the DPT affects the daylight availability in an interior space with a south-facing window. For this, we used the two-phase method (DC-approach) and simulated the annual average illuminances on the sensor grid in the reference office. Figure 11 shows the worldwide distribution of differences between using the fixed 11 °C DPT and the epwDP for the diffuse component (sky), the direct component (sun), and the total, respectively. Table 2 summarizes the results that indicate, that there is a slight bias towards higher results when using the epwDP. Again, the relative differences are predominant for the direct sun contribution.

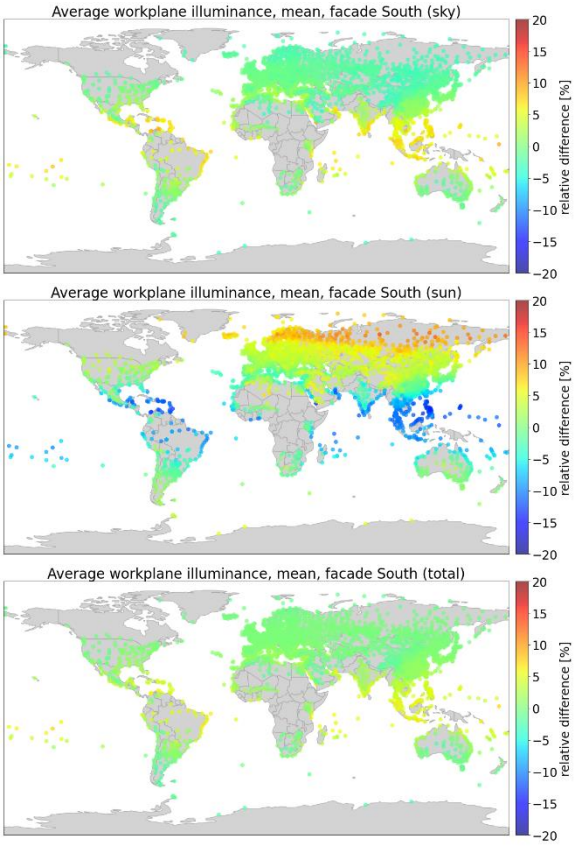

Figure 11: Relative differences for annual mean values of average workplane illuminances for the reference office with south-facing window between fixed (11 °C) and EPW based dew point temperature. From top to bottom: differences for diffuse (sky), direct (sun), and global (total) contribution.

Table 2: Evaluation of worldwide results for average workplane illuminance in reference office room with south-oriented façade (Em, faç.S) from Figure 11.

Em, faç.S	Mean	Median	PC5	PC95
Sky	-0.1%	-0.7%	-2.8%	5.6%
Sun	1.3%	2.6%	-9.4%	7.9%
Total	0.6%	0.1%	0.8%	4.2%

To check whether the orientation of the daylight opening of the investigated room has a major impact on the reported differences, we further simulated the same setup now with a north-facing window. Figure 12 shows the resulting relative differences for the sky and sun components as well as the aggregated (total) results. The trend is the same, but somewhat less pronounced than for the south-facing variant, as can be seen from the summarized numbers in Table 3. The differences are however mainly due to the fact that 89% of the sites included (2780/3130) are located in the northern hemisphere and are therefore more sensitive to the effects of the direct sun with a south-facing window.

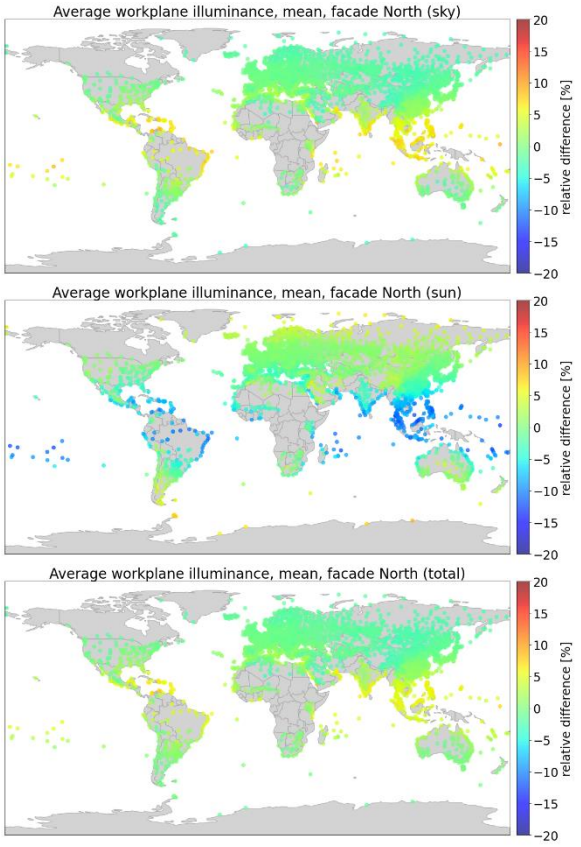

Figure 12: Relative differences for annual mean values of average workplane illuminances for the reference office with south- facing window at worldwide locations between fixed (11 °C) and EPW based dew point temperature. From top to bottom: differences for diffuse (sky), direct (sun), and global (total) contribution.

Table 3: Evaluation of worldwide results for average workplane illuminance in reference office room with north-oriented façade (Em, faç.N) from Figure 12.

Em, faç.N	Mean	Median	PC5	PC95
Sky	0.0%	-0.7%	-2.6%	5.6%
Sun	-1.1%	-0.1%	-8.6%	2.7%
Total	-0.1%	-0.6%	-2.4%	4.6%

Finally, we evaluate how the spatial daylight availability is affected by the DPT in the Perez sky model. To do this, we evaluate the spatial daylight autonomy sDA500lx,80% (i.e., the fraction of the area for which the daylight autonomy at level 500lx exceeds 80%) for the reference room with a north-facing window. To better illustrate the relative influence, we chose rather high thresholds of 500 lux and 80%, which do not lead to results that are not suitable for comparison for the majority of global locations (sDA 0% or 100%) for our test case without any shading system.

Figure 13 shows the sDA500lx,80% results for the two approaches “default” (11 °C) and “epwDP” (moving average DPT), together with the difference in the reported sDA values. The summary in Table 4 indicates that while the worldwide average is small (-0.5%), there are 5% of locations that predict -2.7% or more deviation downwards and another 5% of locations that predict 1.9% or more upwards in sDA500lx,80% when using epwDP.

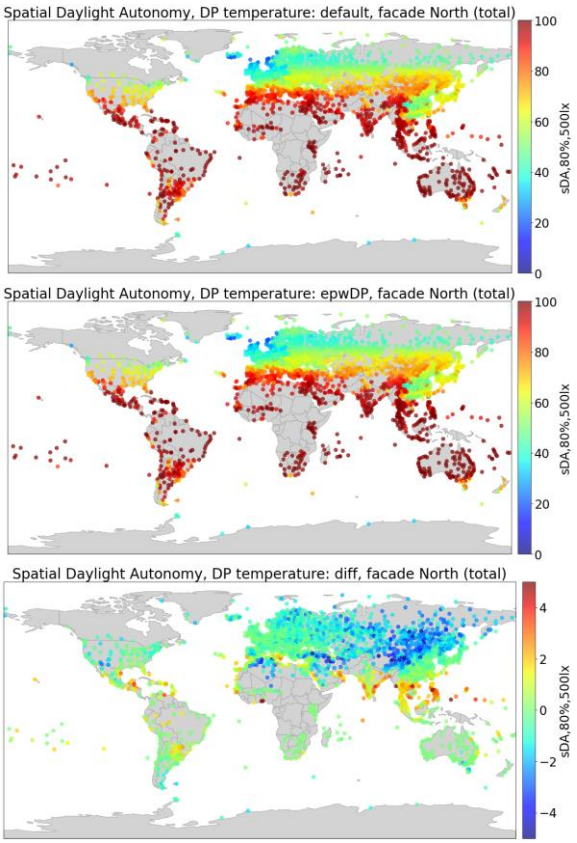

Figure 13: Spatial Daylight Autonomy sDA500,80% results for the reference office with window facing North at worldwide locations for Perez sky based on fixed (11 °C) dew point temperature (top), three-hourly average temperature from EPW file (center) and absolute differences (bottom).

Table 4: Evaluation of differences in worldwide results for Spatial Daylight Autonomy sDA500,80% for the reference office with window facing North in Figure 13.

sDA500,80%	Mean	Median	PC5	PC95
Total	-0.5%	-0.4%	-2.7%	1.9%

To evaluate how the patch size of the sky discretization influences the simulated interior daylight availability, we performed simulations for the reference office with a south-oriented façade. We compare the default Tregenza subdivision, that covers the entire hemisphere subdivided into 145 patches, as reference, against conical solid angles centered around the Tregenza directions and with opening angles 11° (used for Tregenza sky measurements) and 0.5° (mimicking the

sun). While the 11° cone solid angles cover very similar areas of the hemisphere as the reference Tregenza patches, the 0.5° cones only cover a small part of it in 145 specific directions.

Figure 14 shows the annual average illuminances for the reference office with a south-oriented façade when using the Tregenza sky patches (top) and when using the adapted 11° cone patches (center). The bottom image shows the relative differences. Figure 15 shows the comparison for 0.5° cone patches.

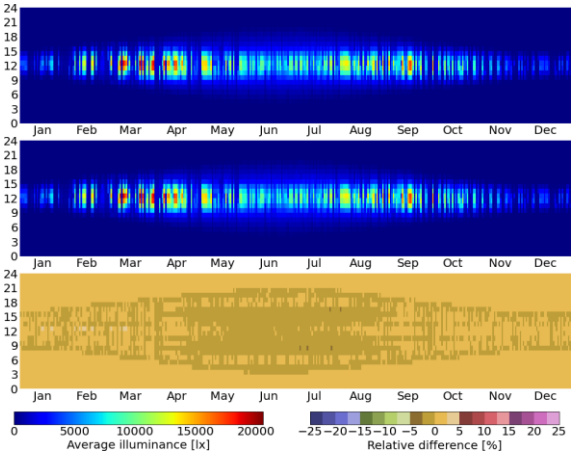

Figure 14: Annual average illuminances for south-oriented office. Tregenza sky patches (top), 11° cones (center), relative differences (bottom).

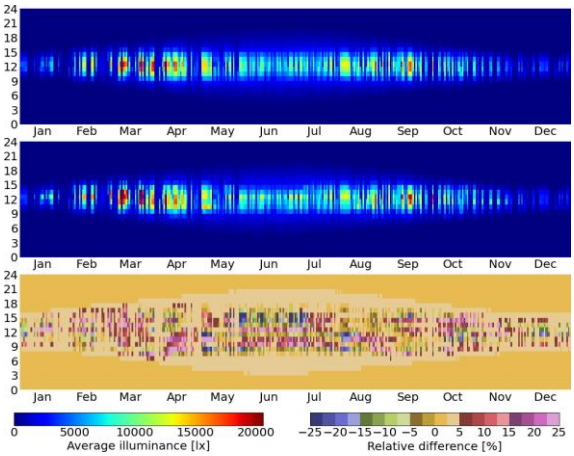

Figure 15: Annual average illuminances for south-oriented office. Tregenza sky patches (top), 0.5° cones (center), relative differences (bottom).

Table 5 summarizes the results from Figure 14 and Figure 15. Expectedly, the 11° cone solid angle reports similar results as the reference Tregenza patches. The 0.5° cones, however, report large deviations for selected hours (minimum and maximum average illuminance values Em and relative deviations rD), as well as a general higher average reported value (mean biased relative deviation, MBrD).

Table 5: Evaluation of average illuminance results for south-oriented office from Figure 14 and Figure 15.

Sky Patches	Tregenza	11°	0.5°
Mean Em	2393 lx	2395 lx	2477 lx
Max Em	18864 lx	19252 lx	20609 lx
MBrD	-	-0.02 %	+3.16 %
min rD	-	-2.70 %	-39.4 %
max rD	-	+3.95 %	+55.5 %

The renderings in Figure 16 shed some light on the reason for these deviations. For three selected sensor points the hemispherical views show that the sky patches are partly covered by the wall surrounding the window. This in turn means that parts of the luminous flux is or is not transmitted into the space.

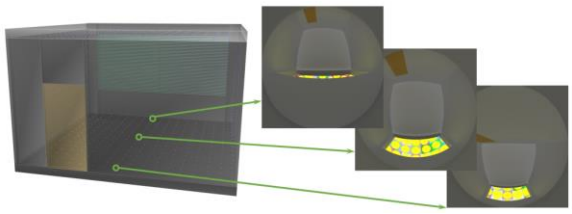

Figure 16: Hemispherical fisheye renderings showing the views to the different sky patches (Tregenza: colored, rectangular patches; 11°: yellow disks; 0.5°: red dots at centers of yellow disks).

Conclusion

We analyzed the effect of the dew point temperature on the Perez sky model and its relevance for daylighting simulations. Based on a simulation study for a simple reference room at worldwide locations we could show that using the three-hourly average value from a weather file the sky component yields higher results in equatorial areas and slightly lower results in continental / polar areas, and exactly vice versa for the sun component. If skylight and sunlight similarly contribute to interior daylighting, the difference is not very pronounced and the practical implications are limited. Since the relative differences are higher for the sun component, in real-world applications particular attention should be paid if the architectural design and daylight planning are primarily designed for sunlight utilization.

The second investigation on the effect of the used sky patch size showed that the interplay of geometry and sky patch discretization can lead to differences in the reported interior daylight results. Whether the sun with its small solid angle (cone with opening angle of about 0.5°) is depicted as such or via a larger sky patch must be decided as a compromise between the possibilities of the implemented daylight simulation method and the required accuracy.

Acknowledgement

David Geisler-Moroder received funding through the project “see-it - Camera based, user centric daylight control system for optimized working conditions” under FFG funding contract number 893523 from the BMK (Federal Ministry Republic of Austria Climate Action, Environment, Energy, Mobility, Innovation and Technology) within the "City of the Future" programme managed by the Austrian Research Promotion Agency FFG.

References

Beck H.E., Zimmermann N.E., McVicar T.R., et al. 2018. *Present and future Köppen-Geiger climate classification maps at 1-km resolution.* Scientific Data 5, 180214.

Bourgeois D., Reinhart C.F. and Ward G. 2008. *Standard Daylight Coefficient Model for Dynamic Daylight Simulations.* Building Research and Information, 36 (1), 68–82.

Brembilla E. 2021. *Opinion: Should you trust the sun?* Lighting Research & Technology, Volume 53, Issue 7.

Brembilla E. and Mardaljevic J., 2019. *Climate-Based Daylight Modelling for compliance verification: Benchmarking multiple state-of-the-art methods.* Building and Environment 158, pp. 151-164.

Climate.OneBuilding.Org. 2024. https://climate.onebuilding.org/, accessed 05 March 2024.

Diakite-Kortlever A. (ed.). 2021. *Spectral sky models for advanced daylight simulations.* A Technical Report of IEA SHC Task 61 / EBC Annex 77 Subtask C3. DOI: 10.18777/ieashc-task61-2021-0005.

EnergyPlus Weather Data. 2024. https://energyplus.net/weather, accessed 05 March 2024.

epw2wea.c, v.2.3, 2024. https://www.radiance-online.org/cgi-bin/viewcvs.cgi/ray/src/cv/epw2wea.c?revision=2.3, accessed 06 March 2024.

Geisler-Moroder D., Prost L., Roy N. 2023. *Validation of DVIZ simulations with BSDFs against Radiance.* 21st International Radiance Workshop 2023, Innsbruck, Austria.

gendaylit.c, v.2.21. 2024. https://www.radiance-online.org/cgi-bin/viewcvs.cgi/ray/src/gen/gendaylit.c?revision=2.21, accessed 05 March 2024.

gendaymtx.c, v.2.39. 2024.https://www.radiance-online.org/cgi-bin/viewcvs.cgi/ray/src/gen/gendaymtx.c?revision=2.39, accessed 05 March, 2024.

Lee E.S., Geisler-Moroder D. and Ward G. 2018. *Modeling the direct sun component in buildings using matrix algebraic approaches: methods and validation*. Solar Energy 160, 380-395.

Mardaljevic J. 2006. *Examples of climate-based daylight modelling.* CIBSE National Conference 2006, Engineering the Future.

McNeil A. 2014. *BSDFs, Matrices and Phases.* 13th International Radiance Workshop 2014, London, UK.

Perez R., Ineichen P., Seals R., Michalsky J. and Stewart R. 1990. *Modeling Daylight Availability and Irradiance Components from Direct and Global Irradiance.* Solar Energy, Vol. 44, pp. 271-289.

Perez R., Seals R. and Michalsky J. 1993. *All weather model for sky luminance distribution Preliminary configuration and validation.* Solar Energy, Vol. 50, Issue 3, pp. 235-245.

Perez R., Seals R. and Michalsky J. 1993. *Erratum to All Weather Model for Sky Luminance Distribution.* Solar Energy, Vol. 51, Issue 5, p. 423.

Tregenza P.R. and Waters I.M.M. 1983. *Daylight coefficients*. Lighting Research & Technology, Volume 15, Issue 2.

VELUX. 2024. VELUX Daylight Visualizer https://www.velux.com/what-we-do/digital-tools/daylight-visualizer, accessed 08 March 2024.

Ward, G. and Shakespeare R.A. 1998. *Rendering with Radiance. The Art and Science of Lighting Visualization.* Morgan Kaufmann Publishers.

Werner M., Geisler-Moroder D., Junghans B., Ebert O. and Feist W. 2017. *DALEC – a novel web tool for integrated day- and artificial light and energy calculation*. Journal of Building Performance Simulation, 10:3, 344-363.

Wienold J. 2023. *The “forgotten” influence of atmospheric humidity on sky modeling with gendaylit.* 21st International Radiance Workshop 2023, Innsbruck, Austria.

Wikimedia Commons. 2024. License CC BY 4.0. https://commons.wikimedia.org/wiki/File:K%C3%B6ppen-Geiger_Climate_Classification_Map.png, accessed 07 March 2024.

BauSIM 2024 in Wien
23. September – 26. September

Energetische Gebäude- und Anlagensimulation als Werkzeug bei der Ausbildung von Architekturstudierenden

Christoph Nytsch-Geusen, Werner Kaul-Gothe
Universität der Künste Berlin, Germany, Institut für Architektur und Städtebau
E-Mail: nytsch@udk-berlin.de und we.kaul@udk-berlin.de

Kurzfassung

An der UdK Berlin wird im Masterstudiengang Architektur seit ca. 10 Jahren das Pflichtseminar „Klimadesign und Energieeffizienz“ mit ca. 20 Studierenden pro Semester durchgeführt. Inhalt der Lehrveranstaltung ist ein architektonischer Entwurf zu wechselnden Themen, bei dem seine raumklimatische und energetische Optimierung im Mittelpunkt steht. Hierfür erlernen die Teilnehmer die Methode der energetischen Gebäude- und Anlagensimulation und ihre Anwendung im Entwurfsprozess.

Die Studierenden bearbeiten dazu in 4er Teams ein Projekt zum jeweiligen Semesterthema, z.B. den Entwurf einer Plusenergieschule. Der architektonische Entwurf wird von ihnen mit dem Simulationswerkzeug IDA ICE abgebildet, die im Energiekonzept beschriebene energetische Anlagentechnik mit dem Simulationswerkzeug Polysun Designer. Mit diesen Simulationswerkzeugen erstellen die Studierenden für ihre Entwürfe sowohl Analysen zur thermischen Behaglichkeit als auch Energiebilanzierungen für die Gebäudehülle und die im Energiekonzept festgelegte Anlagentechnik. Hierbei werden die Simulationsanalysen im Entwurfsprozess wiederholt ausgeführt, um bestmögliche Kompromisse einer guten thermischen Behaglichkeit bei einem minimalen Einsatz nichterneuerbarer Energien aufzuzeigen. Um die Flexibilität im energetischen Gebäudedesign zu trainieren, betrachtet jedes Projektteam einen individuellen Klimastandort aus einem Pool von drei Klimastandorten, welche je nach Semesterthema national oder sogar weltweit verteilt sind und teilweise in extrem unterschiedlichen Klimazonen liegen.

Der Beitrag beschreibt sowohl die didaktische Konzeption des Seminars als auch die Erfahrungen, welche die Autoren beim langjährigen Einsatz der genannten Simulationswerkzeuge mit den Studierenden machen konnten.

Abstract

At the UdK Berlin, the obligatory seminar "Climate Design and Energy Efficiency" has been held in the Master's degree course in Architecture for around 10 years with around 20 students per semester. The content of the course is an architectural design on changing topics, which focuses on optimizing the indoor climate and energy efficiency. To this end, participants learn the method of energy-related building and system simulation and its application in the design process.

The students work in teams of four on a project relating to the respective semester topic, e.g. the design of a plus-energy school. They use the Simulation tools IDA ICE for modelling the architectural design and the Polysun Designer for the energy system technology described in the energy concept. The students use these simulation tools to create analyses of thermal comfort for their designs as well as energy balances for the building envelope and the system technology specified in the energy concept. The simulation analyses are carried out repeatedly during the design process in order to identify the best possible compromises for good thermal comfort while minimizing the use of non-renewable energies. In order to train flexibility in energy-efficient building design, each project team considers an individual climate location from a pool of three climate locations, which are distributed nationally or even worldwide depending on the semester topic and are sometimes located in extremely different climate zones.

The article describes both the didactic concept of the seminar and the experiences that the authors have had with the students over many years of using the simulation tools mentioned.

Einführung

Die Bedeutung der energetischen Gebäudesimulation in der Lehre innerhalb von Architekturstudiengängen nimmt als wichtiger

Teil der Berufsqualifizierung seit Jahren stetig zu. Gründe hierfür sind zum einen, dass die Berufspraxis den sicheren Umgang mit Simulationswerkzeugen erfordert, um die Wirksamkeit von Varianten zur energetischen Sanierung von Bestandsgebäuden vorab abschätzen zu können. Zum anderen werden heute Werkzeuge zur energetischen Gebäudesimulation innerhalb des architektonischen Entwurfsprozesses immer häufiger genutzt, um auch im Neubau die Anforderungen eines behaglichen Raumklimas mit einem möglichst geringen Aufwand an Betriebsenergie, grauer Energie und CO_2-Emissionen zu realisieren.

Ein weiterer Grund für die zunehmende Rolle der energetischen Gebäudesimulation in der Ausbildung und Berufspraxis von Achitekt:innen ist der heute mögliche Datenexport von Softwarewerkzeugen zum Gebäudeentwurf (CAAD-Programme) zu Werkzeugen zur energetischen Gebäudesimulation über BIM-Datenaustauschformate (Freudenberg et al., 2022). Weiterhin sorgt die Integration von Rechenkernen zur thermischen Gebäudesimulation in parametrische Entwurfswerkzeuge, welche von Architekturstudierenden im Entwurfskontext regelmäßig genutzt werden, dass der Zugang zur Anwendung der energetischen Gebäudesimulation erheblich vereinfacht wurde. Ein Beispiel hierfür sind die die Plugins Ladybug und Honeybee (Ladybug Tools, 2024) oder ClimateStudio (ClimateStudio, 2024) für Rhino/Grashoppers, welche erfolgreich in der Architekturlehre eingesetzt werden (Rizaoglu und Voss, 2022).

Hopfe et al., 2017 haben mittels einer Umfrage an 60 internationalen Architekturschulen untersucht, mit welchen didaktischen Schwerpunkten die energetische Gebäude- und Anlagensimulation in den Architekturstudiengängen vermittelt wird (Theorie, Anwendung, Analyse), in welcher Form sie gelehrt wird (Präsens, Online, Online-Tutorien), welche Simulationsarten (thermische, hygrothermische, akustische, Tageslicht- oder Strömungssimulation) in der Lehre den Schwerpunkt bilden und welche Simulationstools hierfür am häufigsten zum Einsatz kommen.

Didaktisches Konzept

Im Masterstudiengang Architektur an der UdK Berlin wird die energetische Gebäude- und Anlagensimulation seit ca. 10 Jahren in einem Master-Pflichtseminar gelehrt (UdK Berlin, 2024). Die Grundidee des Seminars besteht darin, an einem architektonischen Entwurfsthema mittels Simulationstools herauszufinden, wie sich ein behagliches Raumklima für einen vorgegebenen Klimastandort mit einem Minimum an nichterneuerbaren Energieressourcen erreichen lässt. Hierzu erlernen die Studierenden zunächst Grundfertigkeiten zur energetischen Gebäudesimulation, bevor sie diese auf die komplexe Fragestellung ihres Entwurfs anwenden.

Auswahl der Simulationswerkzeuge

Eine wichtige Überlegung bei der Konzeption des Seminars war die Auswahl der Simulationswerkzeuge, die im Seminar zum Einsatz kommen sollen. Ziel hierbei es, sich für leistungsfähige Simulationstools zu entscheiden, die trotzdem eine einfache Bedienung und flexible Modellierung bieten und zudem in den begrenzten Zeiträumen des Seminars von der Studierenden zu erlernen sind. Es wurde sich für eine Kombination der Werkzeuge IDA ICE (IDA ICE, 2024) für die Modellierung und thermische Analyse der Baukörper und Polysun Designer (Polysun Designer, 2024) für die Abbildung und Analyse der Gebäudeenergietechnik entschieden. Bei beiden Simulationswerkzeugen handelt es sich um kommerzielle Produkte, welche vergleichsweise attraktive Lizenzmodelle für den Einsatz in der Lehre bieten. IDA ICE unterstützt eine direkte 3D-Modellierung von Gebäudemodellen, was dem üblichen Arbeitsprozess der Architekturstudierenden entgegenkommt und verfügt darüber hinaus über eine IFC-Schnittstelle zum Import von BIM-Modellen aus CAAD-Programmen. Prinzipiell könnte die Gebäudeenergietechnik auch in IDA ICE mit modelliert werden, was sich aber für Studierende der Architektur als schwer verständlich und sehr komplex darstellt. Aus didaktischen Gründen wurde daher Polysun Designer für die energetische Anlagensimulation gewählt, da dieses Simulationswerkzeug über 1000 vorkonfigurierte und leicht modifizierbare Templates an Anlagensystemen verfügt. Diese können mittels umfangreicher Datenbanken für technische Komponenten der Heizungs- und Klimatechnik sowie der Solartechnik an die abzubildenden Zielstellungen der jeweils betrachteten Energiekonzepte angepasst werden. Sowohl IDA ICE als auch Polysun Designer können in Kombination mit von Meteonorm (Meteonorm, 2024) generierten Wetterdatenfiles verwendet werden, wodurch für die Semesteraufgabe weltweit verteilte Klimastandorte berücksichtigt werden können.

Neben IDA ICE und Polysun Designer werden im Seminar nach Bedarf noch ergänzende Softwaretools von den Studierenden genutzt, wie etwa OPTIVENT (OPTIVENT 2.1, 2024) für die Berechnung natürlicher Lüftungsvorgänge oder die Online-Tools von Marsh (2024) zur Sonnenstand- und Verschattungsanalyse.

Strukturierung des Seminars

Der Ablauf des Seminars ist in seinen Einzelschritten in Abbildung 1 dargestellt.

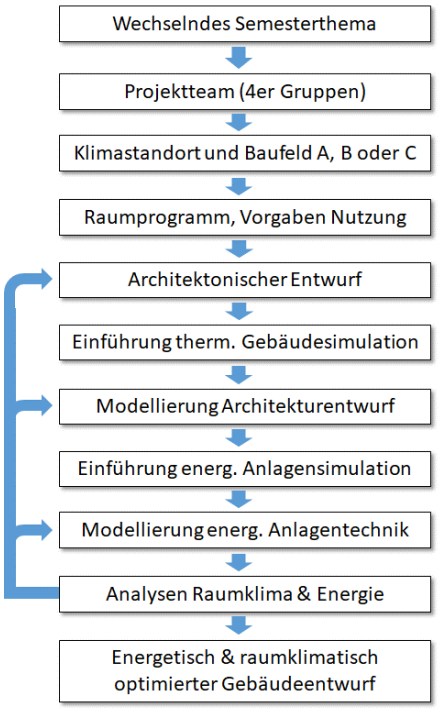

Abbildung 1: Ablauf des Seminars

Semesterthemen

Ausgangspunkt ist ein wechselndes Semesterthema, welches die Studierenden in einen architektonischen Entwurf übersetzen müssen. Das Themenspektrum, welches seit dem Wintersemester 2013/2014 bis heute behandelt wurde, ist sehr breit angelegt und schließt sowohl Gebäudetypen unterschiedlicher Größe und Komplexität (z.B. Tiny-Houses, Einfamilienhäuser, Schulen) als auch verschiedenster Gebäudenutzungen (z.B. Plusenergie-Schule, Elektrotankstelle mit Fotovoltaik, Wohngebäude, Forschungsstation, solar angetriebenes Wohnmobil, Restaurant mit integrierter Lebensmittelproduktion, Wellness-zentren) ein (vgl. Abbildung 2).

Das gemeinsame aller Semesterthemen besteht darin, dass die Studierenden mit Hilfe von architektonischen Entwurfsprinzipien, bau-konstruktiven Lösungen und verbundenen Simulationsanalysen Baukörper und Räume mit einer hohen thermischen Behaglichkeit entwerfen und diese konzeptionell mit Gebäudetechnologien verbinden, welche ein hohes Maß an Nutzung erneuerbarer Energien (Solar- und Windenergie, Umweltenergie, Biomasse etc.) ermöglichen.

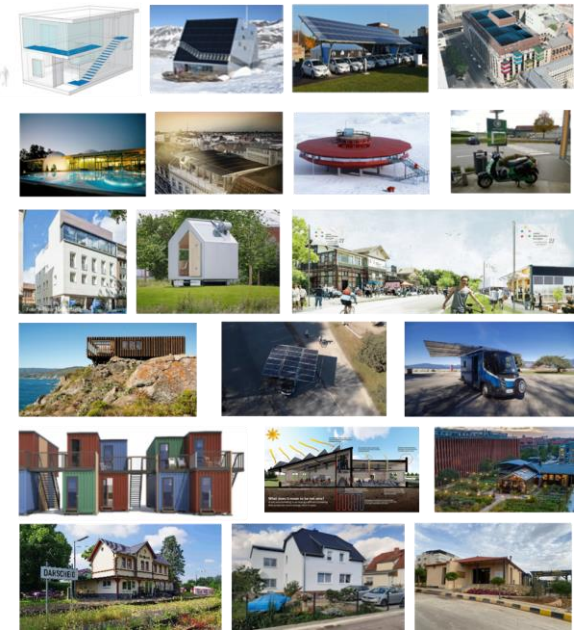

Abbildung 2: Wechselnde Semesterthemen im Seminar in den letzten 10 Jahren

Klimastandort

Nach Vorstellung der Semesteraufgabe bilden dann die Studierenden i.d.R. 5 Projektteams (4er-Gruppen) und wählen für ihren Entwurf einen von drei vorgegebenen konkreten Klimastandorten. Diese sind häufig global verteilt und stammen i.d.R. aus drei sehr unterschiedlichen Klimazonen (z.B. gemäßigter, subtropischer und tropischer Standort). Wenn das Semesterthema es erfordert, werden aber auch enger zusammenliegende Standorte mit geringeren, aber noch spürbaren Unterschieden im Lokalklima vorgegeben (z.B. Hamburg, Berlin und Freiburg). Mit den Vorgaben unterschiedlicher Klimastandorte sollen die Studierenden eine ausgeprägte Flexibilität im energetischen Gebäudeentwurf erlernen, in dem sie die jahreszeitlichen und tageszeitlichen Unterschiede bei den Standorten bzgl. des Sonnenstands, der Intensität der Solarstrahlung, der Außenlufttemperatur und -feuchte sowie der Windgeschwindigkeit und -richtung bei ihrem Entwurfsansatz differenziert berücksichtigen. Die Klimadatensätze werden hierfür über die Software Meteonorm generiert, welche auf Basis einer umfangreichen Datenbank weltweiter Wetterstationen und Interpolationsalgorithmen stündlich aufgelöste Wetterdatensätze für beliebige Standorte erzeugen kann. Abbildung 3 zeigt exemplarisch die für den energetischen Gebäudeentwurf wichtigsten Klimaparameter Außenlufttemperatur und Solarstrahlung für drei weltweit verteilten Standorte.

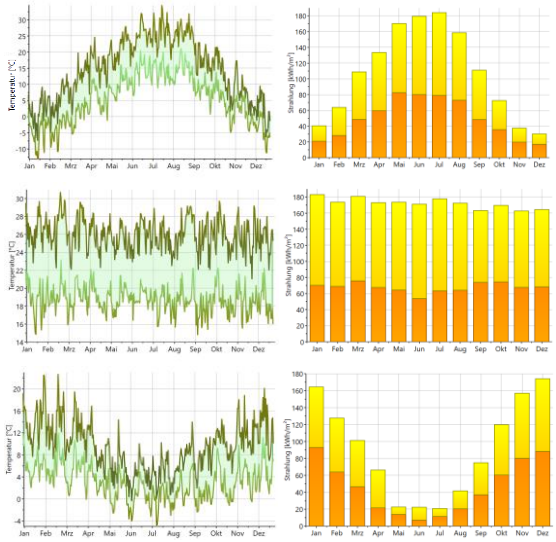

Abbildung 3: Klimaparameter minimale und maximale Außenlufttemperatur (links) und Monatssummen der diffusen und direkten Solarstrahlung (rechts) für Klimastandorte in Österreich (gemäßigtes, sonniges Klima) auf der Nordhalbkugel, in Tanzania in Äquatornähe (tropisch warmes, sehr sonniges Klima) und in Chile auf der Südhalbkugel (kaltes Klima mit sehr sonnenarmen Monaten), Klimadaten aus Meteonorm

Virtuelles Baufeld

Für die Erstellung des architektonischen Entwurfs wird den Projektteams passend zum gewählten Klimastandort ein virtuelles georeferenziertes Baufeld vorgegeben, welches vorab über Informationen der üblichen Kartendienste (Google Maps, Apple Karten oder Microsoft Bing) definiert wurde und auch Informationen zur umgebenden Bestandsbebauung miteinschließt (vgl. Abbildung 4).

Abbildung 4: Virtuelles Baufeld in Puerto Williams (Längengrad 54.934054 S, Breitengrad 67.606583 W), Quelle (GoogleMaps)

Raumprogramm und Gebäudenutzung

Die Beschreibung der Semesteraufgabe umfasst detaillierte Angaben zum Raumprogramm sowie zur Nutzung der einzelnen Gebäudezonen, welche durch gewünschte Komfortbereiche für das Raumklima, differenzierte Nutzungszeiten, Luftwechselraten sowie interne Wärmegewinne definiert werden. Weiterhin enthält die Aufgabenbeschreibung Annahmen zum Warmwasserbedarf und zum sonstigen Strombedarf des Gebäudes, welcher unabhängig von der Gebäudeklimatisierung anfällt.

Gebäudeentwurf und zugehöriges thermisches Gebäudemodell

Ausgehend von diesen Informationen erstellen die Studierenden einen Entwurf, welcher im Laufe des Semesters durch zwei Rücksprachen mit den Dozierenden begleitet wird. Abbildung 5 zeigt exemplarisch den Entwurf für eine Plus-Energieschule für den Standort Puerto Williams.

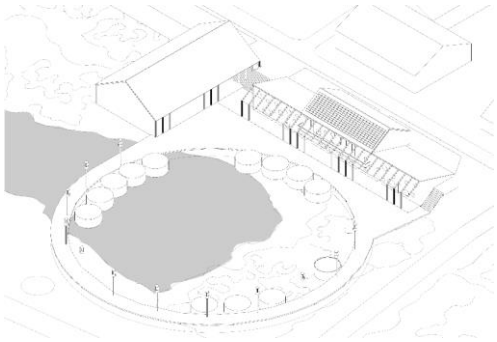

Abbildung 5: Axonometrie des Entwurfs einer Plus-Energieschule in Puerto Williams, Entwurf der Gruppe Colemann, Köchert, Mulligan Ogakova im Wintersemester 2021/2022

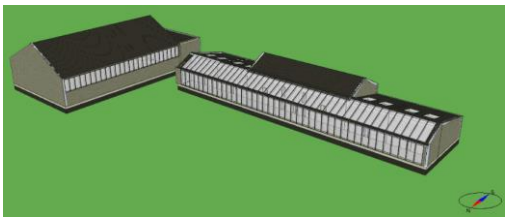

Abbildung 6: Vereinfachtes IDA ICE-Modell des Entwurfs

Der Entwurf wird danach mit dem Simulationsprogramms IDA ICE als mehrzoniges Gebäudemodell modelliert (Abbildung 6), wobei in jeder Zone die gegebenen Randbedingungen der Aufgabenstellung berücksichtigt werden. Bei diesem Modellierungsprozess lernen die Teilnehmer des Seminars den detaillierten Architekturentwurf bzgl. der Geometrie und Zonierung angepasst zu vereinfachen, um die Rechenzeiten des Simulationsmodells zu reduzieren (vgl. Abbildung 5 mit Abbildung 6).

Analyse des Innenraumklimas

Nach Fertigstellung des thermischen Gebäudemodells nehmen die Studierenden zunächst eine Analyse des frei schwingenden Innenraumklimas vor, in dem sie die Heiz- und

Kühlfunktion von IDA ICE für alle Zonen deaktivieren. Durch diese vorgeschaltete Analyse der alleinigen Reaktion der thermischen Hülle ihrer Gebäudeentwürfe auf das Außenklima können sie schon zu Beginn kritische Gebäudebereiche und Zeiträume des Innenraumklimas im Jahresverlauf identifizieren und durch geeignete architektonische Maßnahmen, wie z.B. das Anpassen der Fenstergrößen und –positionen, die Verschattung transparenter Flächen oder die Erhöhung der thermischen Gebäudemassen, entschärfen.

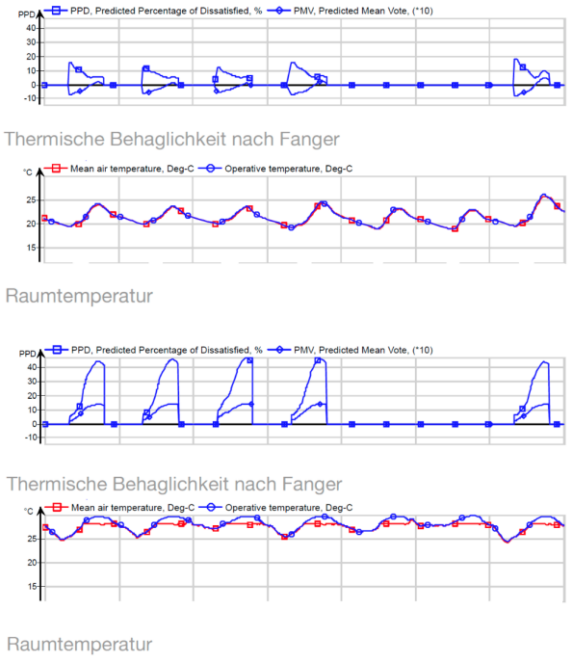

Abbildung 7: Zeitreihen der Raumtemperaturen (Luft- und operative Temperatur) und der zugehörigen Behaglichkeitsindizes PMW und PPD nach Fanger für eine ausgewählte Zone für eine Winterwoche (oben) und eine Sommerwoche (unten)

Zur Bewertung des Innenraumklimas führen die Studierenden mit IDA ICE für alle Zonen eine Behaglichkeitsanalyse nach Fanger durch, was sowohl eine übergeordnete Betrachtung des gesamten Jahres als auch vertiefende Analysen unterschiedlicher Jahreszeiten einschließt (vgl. Abbildung 7). Erst danach erfolgt im thermischen Gebäudemodell für jede modellierte Zone die Festlegung der Raumnutzung (Zeitreihen für die Nutzer-Anwesenheiten, das Lüftungsverhalten und die inneren Wärmequellen) und die Festlegung der gewünschten Behaglichkeitsbereiche, woraufhin die erste Referenzsimulation zur Bestimmung der zeitabhängigen Heiz- und Kühlenergiebedarfe durchgeführt wird.

Energiebilanzierung des Baukörpers

Abbildung 8 zeigt eine exemplarische Darstellung der in der Simulationsanalyse für das Gebäudemodell berechneten monatlichen thermischen Nutzenergiebedarfe für die Gebäudeheizung, -kühlung und die Warmwasserbereitung.

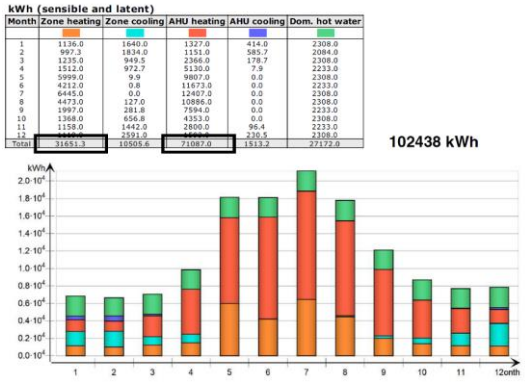

Abbildung 8: Monatliche von IDA ICE berechnete thermische Nutzenergien

Neben der monatlichen Energiebilanzierung analysieren die Studierenden auch die zeitlich hochaufgelösten Energiebilanzen der einzelnen Zonen, um z.B. die tageszeitlichen thermischen Energiegewinne und -verluste eine der Sonnenstrahlung ausgesetzten Fassade mit hohem Glasanteil zu quantifizieren.

Modellierung des Energiekonzeptes

Die von den Projektteams erstellten Energiekonzepte inkl. zugehöriger Anlagentechnik (siehe Abbildung 9) werden im nächsten Schritt von den Studierenden mittels Polysun Designer modelliert (vgl. Abbildung 9 mit Abbildung 10).

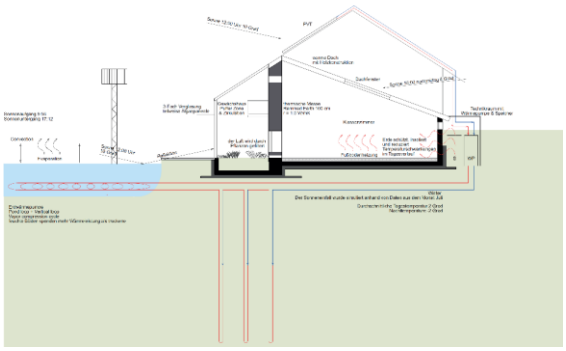

Abbildung 9: von den Teilnehmern erstelltes Energiekonzept (Plus-Energieschule Puerto Williams)

Hierfür werden die von IDA ICE berechneten monatlichen thermischen Heiz- und Kühlenergiebedarfe in das Gebäudemodell von Polysun Designer übertragen und müssen dann über die dort modellierte Gebäudeenergietechnik bereitgestellt werden.

Die hydraulischen Schemata und Regelungslogiken der für diesen Zweck gewählten Polysun-Vorlage werden nur selten verändert, da sich dies für Architekturstudierende schwierig darstellt.

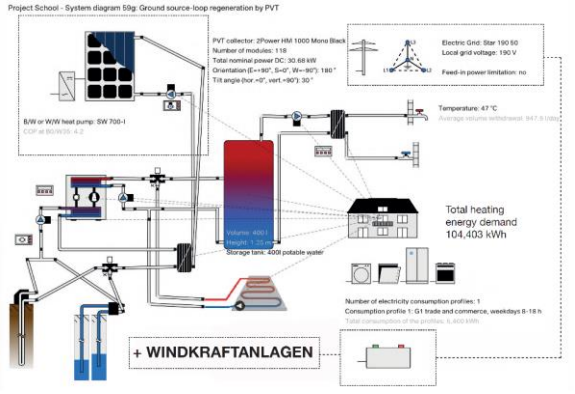

Abbildung 10: Abbildung des Energiekonzepts in Polysun Designer (Plus-Energieschule am Standort Puerto Williams)

Die Komponentenmodelle der jeweiligen Polysun-Vorlage werden dann entsprechend des Energiekonzeptes neu parametrisiert und mit weiteren elektrischen Komponenten ergänzt (z.B. Fotovoltaik-Generatoren und Solarthermie-felder mit unterschiedlicher Ausrichtung, Batteriespeicher, elektrische Verbraucher- und Netze sowie Ladestationen für die E-Mobility), was über die grafische Oberfläche inkl. der umfangreichen Produktdatenbanken von Polysun Designer sehr einfach möglich ist.

Weiterentwicklung des Lehrformats

Das Seminar wurde und wird bzgl. des didaktischen Ansatzes, der Art der genutzten Simulationswerkzeuge und der gewählten Semesterthemen kontinuierlich weiterentwickelt.

Didaktischer Ansatz

Da das Erlernen von IDA ICE im Master-Seminar einen erheblichen Zeitaufwand beansprucht, wurde im vergangenen Jahr begonnen, diese Software bereits im Bachelor-Studiengang Architektur einzuführen. Hierbei wurden einfache vordefinierte Gebäudemodelle zur Analyse der dynamischen Heiz- und Kühllasten genutzt, wodurch schon sehr viel früher der Umgang mit dem Simulationswerkzeug IDA ICE geübt wird. Polysun Designer wird schon seit Jahren in der ersten Hälfte des Bachelor-Studienganges Architektur im Fach Gebäudetechnik verwendet.

Seit mehreren Semestern werden im Seminar im letzten Semesterdrittel zusätzliche gruppen-spezifische Online-Einzeltermine angeboten, in welchen die Studierenden mit den Dozierenden Fragen zur Modellierung ihre projektspezifischen architektonischen, baukonstruktiven und gebäudetechnischen Konzepte mit IDA ICE und Polysun Designer im Detail besprechen können.

Im Wintersemester 2023/2024 wurde erstmals mit einem anderen Architektur-studiengang (Mutah University, Jordanien) ein gemeinsam definiertes Semesterthema bearbeitet. Die Studierenden in Deutschland und in Jordanien entwarfen und diskutierten gemeinsam Varianten für ein studentisches Kommunikationszentrum auf dem Campus der Mutah University, wofür sie auf beiden Seiten IDA ICE zur thermischen Gebäudesimulation ihrer Architekturentwürfe nutzen.

Verwendete Simulationswerkzeuge

Bisher wurde für das Seminar die beiden Simulationswerkzeuge IDA ICE zur thermischen Gebäudesimulation und Polysun Designer zur energetischen Anlagensimulation verwendet. Es ist angedacht, zukünftig zur räumlich aufgelösten Analyse des Innenraumklimas auch Simulations-tools zur Strömungssimulation mit zu nutzen, die durch eine einfache Handhabung für die Ausbildung von Architekt:innen geeignet sind, wie z.B. das OpenFoam-Plugin in IDA ICE.

Semesterthema

Im Sommersemester 2023 wurde erstmals ein Semesterthema gewählt, welches über die Betrachtung von Einzelgebäuden hinausgeht. Es sollten Sanierungskonzepte für Einfamilienhaus-Siedlungen des Bestands entwickelt werden, wozu neben der energetischen Ertüchtigung der Einzelgebäude auch die Analyse von Varianten einer quartiersübergreifenden Strom- und Wärmeversorgung aus erneuerbaren Energie-quellen mit Polysun Designer gehörte.

Herausforderungen im Seminar

Im Rückblick auf die vergangenen Jahre lassen sich bei der Durchführung des Seminars wiederkehrende Herausforderungen feststellen, mit denen die Studierenden konfrontiert waren.

Grundlegend muss festgestellt werden, das die Inhalte des Master-Seminars sehr anspruchsvoll konzipiert sind. Hierfür müssen die 4er-Projektteams einen hohen Arbeitsaufwand leisten und dabei intensiv innerhalb der Teams und mit den Dozierenden kommunizieren. Weiterhin besteht durch das Erlernen des sicheren Umgangs von zwei leistungsfähigen Simulationswerkzeugen und ihrer Anwendung auf eine komplexe Fragestellung innerhalb eines Semesters immer wieder die Gefahr einer Überforderung der Studierenden.

Es ist häufig nicht einfach, die von den Architekturstudierenden angedachten, teilweise sehr kreativen Energiekonzepte in der zur Verfügung stehenden Zeit angemessen mit IDA ICE und Polysun Designer zu modellieren. Bespiele hierfür sind teilweise lichtdurchlässige Vorhänge zur Verschattung, natürliche Lüftungskonzepte mit nicht trivialen Mustern

einer Gebäudedurchströmung oder die Modellierung des Wärme- und Feuchtetransports innerhalb der verschiedenen Bereiche einer Wellnesseinrichtung.

Eine weitere Herausforderung liegt immer wieder in den Möglichkeiten und Grenzen des 3D-Geometrieimports aus den üblichen Modellierungswerkzeugen des Architekturentwurfs (Archicad, Revit, Rhino, Sketchup) nach IDA ICE. Vergleichsweise gut funktioniert die externe Modellierung spezieller Geometrien (z.B. komplexe oder gebogene Gebäudeteile sowie Freiformflächen), die dann über den Geometrieimport als thermische Zonen oder Verschattungselemente nach IDA ICE importiert werden. Der Import kompletter Architekturentwürfe über die IFC-Schnittstelle nach IDA ICE wird von den Studierenden immer wieder versucht, was aber auf Grund von Modellierungsfehlern im CAAD-Werkzeug der Studierenden und noch bestehenden Schwächen der IFC-Schnittstelle von IDA ICE bisher nur selten zum Ziel geführt hat.

Es hat sich als sehr positiv herausgestellt, dass die Studierenden die Simulationswerkzeuge auf ihren eigenen Computern, i.d.R. mobile Rechner, durchführen können. IDA ICE wird ihnen hierfür als Einzelplatz- und Polysun Designer als Netzwerklizenz zur Verfügung gestellt. Im Gegensatz zu Polysun Designer ist IDA ICE auf die Windows-Plattform beschränkt, was für Architekturstudierende als Einschränkung empfunden wird, da diese häufig MacOS als einziges Betriebssystem nutzen.

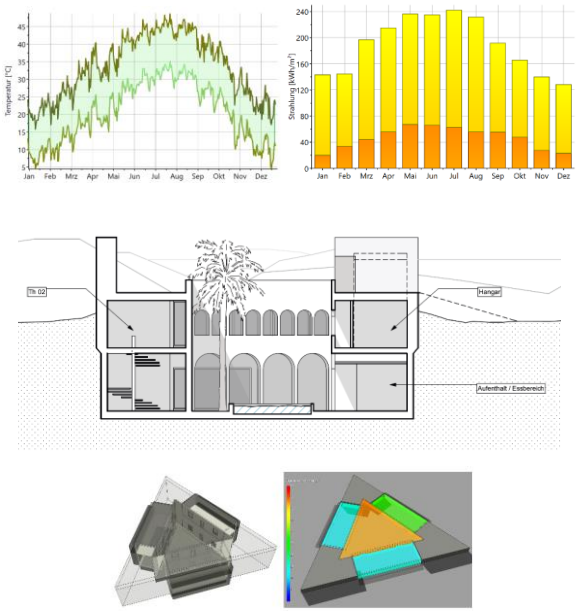

Abbildung 11: Forschungsstation für einen Wüstenstandort in der Sahara. oben: Außenlufttemperatur und Solarstrahlung, Mitte: Architekturentwurf, unten: thermische Analyse mit IDA ICE

Seminarbeispiel

Abschließend sollen exemplarisch die Ergebnisse des Seminars aus dem Wintersemester 2017/2018 vorgestellt werden, in welchem die Studierenden eine energieautarke Forschungsstation für drei extrem unterschiedliche Klimastandorte konzipierten.

Klimastandort Wüste

Für einen der wärmsten Standorte der Erde in Algerien in der Nähe der Wüstenstadt Salah mit sommerlichen Außenlufttemperaturen über 45 °C wurde von den Studierenden ein Atrium-förmiger Baukörper entwickelt, welcher sich teilweise unterhalb der Erdoberfläche befindet, um so die deutliche geringere Mitteltemperatur des Erdreichs gegenüber der Außenluft während des Sommers als äußere Randbedingungen für einen Teil der thermischen Hülle zu nutzen (Abbildung 11).

Klimastandort Südpol

Für einen der kältesten Standorte der Erde am Südpol in der Nähe der bestehenden Forschungsstation Amundsen Scott mit winterlichen Außenlufttemperaturen bis -60 °C wurde von den Studierenden ein Zylinder förmiger Baukörper entwickelt (Abbildung 12).

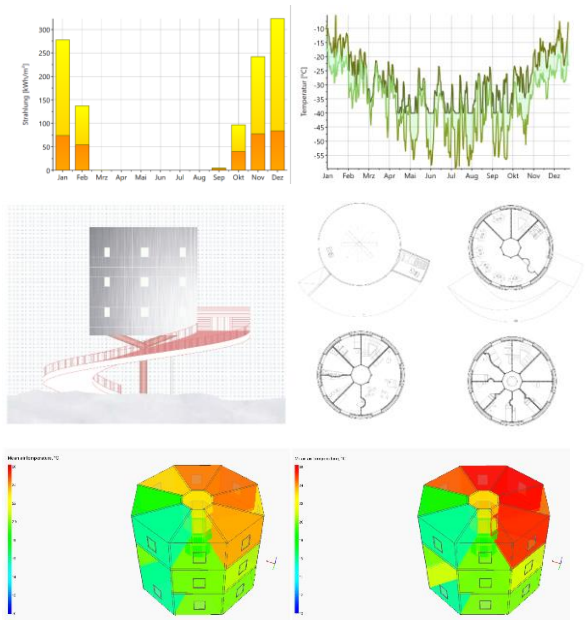

Abbildung 12: Forschungsstation am Südpol. oben: Außentemperatur und Solarstrahlung, Mitte: Architekturentwurf, unten: thermische Analyse mit IDA ICE

Die Fassade der Forschungsstation wurde allseitig mit Fotovoltaikmodulen belegt, die am Südpol in den Monaten Oktober bis Februar ganztägig von der Sonne bestrahlt werden, da dann die Sonnenbahn tiefstehend über den Horizont kreisförmig um das Gebäude verläuft.

Klimastandort Mars

Als Extremwetterstandort mit Außentemperaturen bis weit unter -80 °C für ein Klimastandort auf dem Planeten Mars wurden von den Studierenden eine Forschungsstation konzipiert, welche aus mehreren kugelförmigen Elementen besteht, die flexibel modular miteinander verbunden werden können (Abbildung 13). Zur Minimierung der Wärmeverluste in dieser Extremumgebung wurden kugelförmige Baukörper gewählt, deren Oberfläche mit verstellbaren Fotovoltaik-Modulen zur Stromversorgung belegt sind.

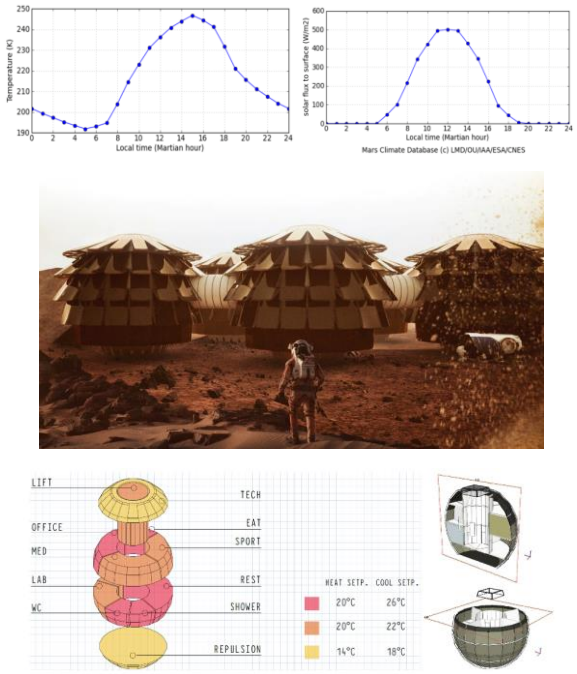

Abbildung 13: Forschungsstation für einen Standort auf der Nordhalbkugel des Mars. oben: Tagesgang der Außentemperatur und Solarstrahlung, Mitte: Architekturentwurf, unten: thermische Zonierung und zugehöriges IDA ICE-Gebäudemodell

Zusammenfassung

An der UdK Berlin wird im Masterstudiengang Architektur ein Pflichtseminar durchgeführt, in welchem in kleinen Projektteams zu einem wechselnden Semesterthema ein raumklimatisch und energetisch optimierter Gebäudeentwurf von den Studierenden erstellt wird. Hierbei wird der Baukörper mit dem Simulationswerkzeug IDA ICE modelliert, die im Energiekonzept beschriebene energetische Anlagentechnik mit dem Simulationswerkzeug Polysun Designer. Jedes Projektteam bearbeitet hierbei einen individuellen Klimastandort, um einerseits die Flexibilität beim energetischen Gebäudeentwurf zu üben. Der didaktische Ansatz des Seminars wird von den Dozenten kontinuierlich weiterentwickelt, was vor allem die Art der Betreuung und die Auswahl der Simulationswerkzeuge betrifft.

Danksagung

Wir möchten an dieser Stelle den Firmen Equa AB und Velasolaris danken, welche unser Seminar seit vielen Jahren mit Hochschullizenzen unterstützen und sich Fragen der Studierenden und Dozenten immer sehr offen und hilfsbereit gezeigt haben.

Literatur

ClimateStudio, 2024. Webseite https://www.solemma.com/climatestudio.

Freudenberg, P., Weis, D., Funcke, B. 2022. Gebäudesimulation und BIM in der Architektenausbildung an der TU Dresden – Serie: Gebäudesimulation und Berechnungstools in der Lehre. Bauphysik 44(6):344-350.

Hopfe, C., Beckman, Soebarto, V., Crawley, D., Rawal, R. 2017. Understanding the differences of Integrating Building Performance Simulation in the architectural education system. Proceedings Building Simulation 2017, 7.-9. August, San Francisco, USA.

IDA ICE, 2024. Webseite https://www.equa.se/en/ida-ice.

Ladybug Tools, 2024. Webseite https://www.food4rhino.com/en/app/ladybug-tools.

Marsh, A. 2024. Online-Softwaretools zum energetischen Gebäudedesign: https://andrewmarsh.com/software.

Meteonorm, 2024. Webseite https://meteonorm.com.

OPTIVENT 2.1, 2024. A Natural Ventilation Steady-State Calculation Tool for the Early Design Stage of Buildings, Webseite http://optivent.tools.

Polysun Designer, 2024. Webseite https://www.velasolaris.com/software/polysun-designer.

Rizaoglu, I.K., Voss, Karsten 2022. Building Perfomance Simulation in design eduction: Design-integrated versus additive use. Proceedings BAUSIM 2022, 20.-22. September, Weimar.

VPT 2024. Lehre am Fachgebiet Versorgungsplanung und Versorgungstechnik der UdK Berlin, Webseite: https://www.udk-berlin.de/studium/architektur/fachgebiete/versorgungsplanung-und-versorgungstechnik/lehre

BauSIM 2024 in Wien
23. September – 26. September

Enhancing Efficiency and Feasibility of Large-Scale Thermal Energy Storage in District Heating

Abdulrahman Dahash, Fabrizia Giordano, Ahmed Serageldin
AIT Austrian Institute of Technology GmbH, Center for Energy, Giefinggasse 2, 1210 Vienna, Austria, E-Mail: abdulrahman.dahash@ait.ac.at

Abstract

A key lever to overcome the challenges in the buildings sector related to today's extensive utilization of fossil fuels is the introduction of renewables-based district energy systems. Herein, large-scale seasonal thermal energy storage (STES) systems found its place favorably in these systems. Yet, STES systems require a thorough planning to avoid the high investment cost. Consequently, numerical models gain importance as an alternative to real-life experiments. This work investigates the role of insulation distribution within storage envelope on performance and capital cost. It further conducts a techno-economic assessment of large-scale, underground, seasonal thermal energy storage to reveal the role of insulation.

Introduction

The building stock accounts for approximately 40% of the total energy consumption in European Union (EU), half of which goes for heating and cooling demands that are predominantly reliant on conventional fossil fuels (e.g. natural gas) (Maduta et al., 2022). The combustion of these fuels significantly contributes to CO_2 emissions, contradicting emission reduction goals (D'Agostino et al., 2024) by 2050. Consequently, decarbonizing the building sector becomes crucial, aligning with the integration of renewable energy sources (RESs). District heating (DH) emerges as an efficient solution to fulfill heating demand (K. Johansen and S. Werner, 2022). Despite its effectiveness, many DH systems still rely on natural gas, posing challenges impaired EU (Jodeiri et al., 2022).

The substitution of fossil fuels with RESs presents a viable solution, although it introduces challenges, including intermittent availability and storage difficulties. Thermal energy storage (TES) systems address these challenges, offering both short and long-term storage capabilities, thereby enhancing energy system robustness and facilitating sector coupling. Consequently, the integration of TES systems becomes pivotal for efficient energy management and increasing the share of RES.

Large-scale seasonal thermal energy storage (STES) has recently gained an increasing awareness for its capacity to mitigate mismatches between heat supply and demand (Dahash et al., 2020). Among STES methods, tank TES (TTES) and pit TES (PTES) stand out for their ability to achieve higher storage temperatures, primarily using water as a storage medium. This characteristic enables them to offer higher charging/discharging rates, reducing response time and reliance on backup heaters compared to other STES methods such as aquifer TES (ATES), and borehole TES (BTES) (Yuan et al., 2021). While BTES and ATES manage to store thermal energy at relatively lower temperatures and, hence, lower capital costs compared, TTES and PTES have higher capital costs.

Therefore, this study focuses primarily on TTES systems due to their relevance in addressing planning challenges in underground TES systems. By exploring these challenges, the work aims to contribute to the comprehension and optimization of TTES implementations in the context of energy system transitions.

Literature review

Previous studies highlighted the complex nature of designing, planning and constructing large-scale TES systems. For instance, (Dahash et al., 2021) highlighted the interaction of various variables e.g. location, size, TES geometry, and hydrogeological conditions in the planning of STES systems. They concluded that planning such technologies necessitates a holistic approach, recognizing that individual variables can exert significant influence on the overall planning process (see Figure 1). Consequently, simulation-driven planning has emerged as a valuable strategy to assess the impact of different boundary conditions on STES planning. Thus,

calibrated numerical TES models serve as essential tools in such investigations.

Using numerical simulations, (Tosatto et al., 2022) investigated the role of STES type and volume in two types of district heating (DH) systems. The study revealed that increasing the STES volume results in a notable reduction in specific heat losses. Additionally, it emphasized the importance of insulation in enhancing STES performance, particularly a significant performance improvement in PTES systems with insulation. The study also provided estimates of the capital costs associated with implementing TTES and PTES across a volume range of 100,000 m^3 to 2,000,000 m^3. Yet, the investigation considered two cases for TES insulation: fully insulated or non-insulated (only top-insulated).

(Huang et al., 2020) conducted a technical analysis (e.g., solar fraction, TES performance) to reveal the impact of TES insulation levels on system operation considering five configurations ranging from full insulation to no insulation. While the work demonstrated an increase in TES capacity with upper-half insulation, it did not include a cost-to-benefit analysis of insulation installation.

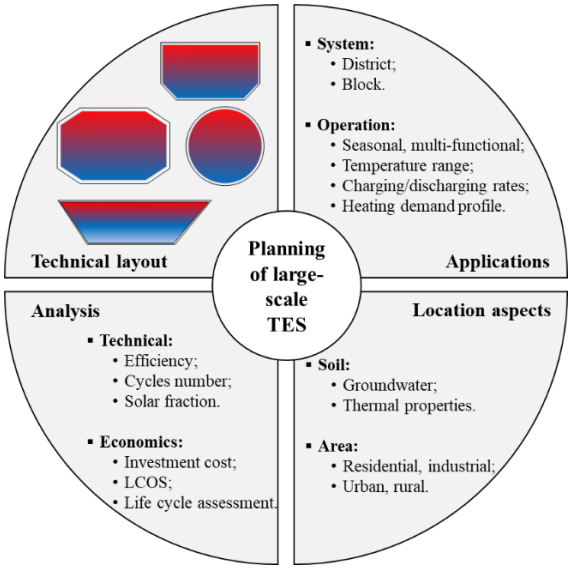

Figure 1: Several influencing parameters on the planning of underground TES and its economic feasibility (reproduced from (Dahash et al., 2021)).

Contribution of this work

This work explores the role of insulation distribution and installation within the storage envelope on the technical viability and economic feasibility of large-scale, underground, seasonal thermal energy storage. The work briefly reports the development of the numerical model used for the investigation. Next, the work presents the boundary conditions and the application case. Then, the study lists down the key performance indicators used in the techno-economic assessment for such storage systems. Yet, the work is limited to consideration of tank thermal energy storage with a total volume of 100,000 m^3 and a height of 50 m in the subsurface. Besides, the study presumes investigations under favorable hydro-geological conditions (i.e. no groundwater existence or flowing).

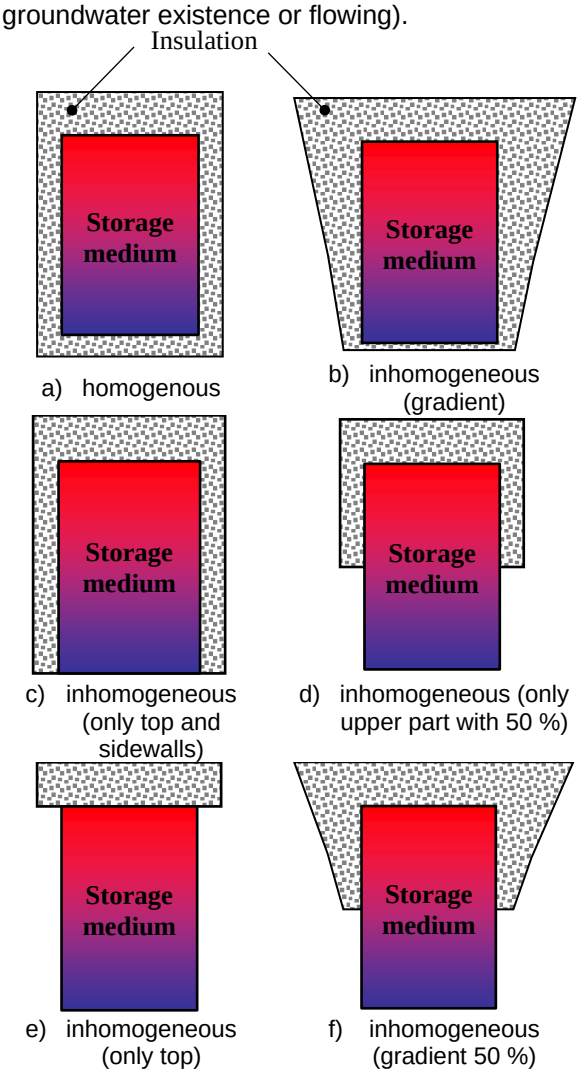

Figure 2: Homogenous and inhomogeneous insulation distribution for large-scale STES systems.

Methodology

Numerical modeling

To properly address the multi-physical aspects (i.e. conductive and convective heat transfer, and flow dynamics) in planning of large-scale STES, it is necessary to develop a numerical model with versatile capabilities such as the representation of different STES geometries, various STES envelopes and others (Dahash et al., 2021). Therefore, this work briefly reports the development of such a numerical model. The

developed model simulates a stratified TES, whereby the fluid domain can be discretized into (*n*) vertical nodes each with uniform temperature (T_i) and equal volume. Further information on the model development, calibration, validation and use can be found in (Dahash et al., 2021), (Tosatto et al., 2022) and (Dahash et al., 2020). Figure 3 elaborates a 2-D sketch for a buried TTES with a layer of aquifer zone (i.e. groundwater flow).

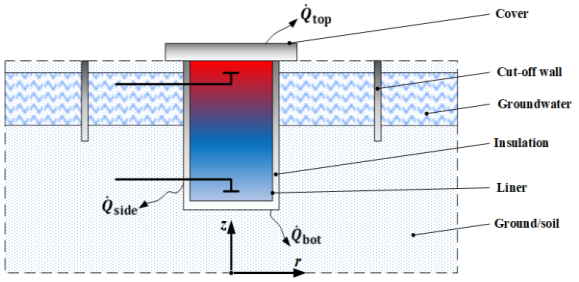

Figure 3: 2-D representation of a buried TES with: 1) cover, 2) cut-off wall, 3) groundwater, 4) insulation, 5) liner and 6) Ground domain.

The model obeys mass conservation and energy balance and, therefore, the time-dependent temperature distribution for each TES segment (i) can be described by the following expression:

$$\frac{\partial T_i(t)}{\partial t} = -\left(\frac{\dot{V}_w}{A_i}\right)\cdot\frac{\partial T_i}{\partial z_i} + \alpha\cdot\frac{\partial 2T_i}{\partial {z_i}^2} - \frac{\dot{q}_{loss,i}}{\rho A_i c_p} \quad (1)$$

Where ρ, c_p and α represent the set of thermo-physical properties for the storage medium (i.e. water) and they are: the density, specific heat capacity and thermal diffusivity, respectively. The injected/extracted flowrate of each segment is denoted as ($\dot{V}_w$), whilst A_i denotes the cross-section area of the corresponding segment (i). Each TES segment has an interface to the surrounding soil and, accordingly, any slight temperature difference between the TES fluid segment and the neighboring soil node triggers a heat transfer rate that is often accounted as heat losses form the TES. Thus:

$$\dot{q}_{loss,i} = U_{side}\cdot P_i\cdot(T_i(t) - T_{g,i}(t)) \quad (2)$$

Furthermore, it is noteworthy to highlight that the TES diffusers are assumed to be ideal due to the large TES volumes and, accordingly, low flowrates. Yet, the diffusers should be properly designed to ensure higher quality of stratification. Thus, CFD simulations are essential for this sort of investigations.

$$\rho_g c_{p,g}\frac{dT_g}{dt} = \lambda_g\left[\frac{\partial^2 T_g}{\partial z^2} + \frac{1}{r}\frac{\partial}{\partial r}\left(r\frac{\partial T_g}{\partial r}\right)\right] \quad (3)$$

Where ρ_g, $c_{p,g}$ and λ_g define the density, specific heat capacity and thermal conductivity of the ground (i.e. subsurface soil). It is important to highlight that the work assumes the subsurface as a homogenous soil with same thermos-physical properties along depth of the subsurface. Moreover, the presence of groundwater is an important factor that needs to be considered in the planning of underground, large-scale TES. Yet, this work assumes favorable geological conditions in which no groundwater is present.

Boundary conditions and assumptions

This work assumes seasonal operation of TTES whereby the charging phase starts early May and stops end of July with a constant injection temperature of 90°C. This phase is followed by a storage phase that starts early August and lasts 3 months. Once the heat is needed by beginning of November, TTES starts the discharging phase and the injection temperature into the TTES is 60°C. As TTES has no more useful energy for the DH needs, it operates in an idle phase. The injection volumetric flowrate is 0,01286 m^3/s during both dynamic phases (i.e. charging and discharging). The ambient temperature is expressed as follows:

$$T_{amb} = 10 + sin\left(\frac{2\pi t}{365}\right) \quad (4)$$

Moreover, Table 1 reports the thermo-physical properties of the different domains (i.e. TES water, TES envelope, soil and groundwater) considered in this work.

Table 1: Thermo-physical properties of the materials and heat transfer coefficients (HTC) of the different components in TES and solid ground.

Parameter	Value
Water thermal conductivity, λ_w	0.6 W/(m.K)
Water density, ρ	1000 kg/m^3
Water specific heat capacity, c_p	4200 J/(kg.K)
Overall HTC of the cover, U_{top}	0.15 W/(m^2.K)
Overall HTC of the sidewalls, U_{side}	No insulation, 90 W/(m^2.K)
Overall HTC of the bottom, U_{side}	No insulation, 90 W/(m^2.K)
Ground thermal conductivity, λ_g	1.5 W/(m.K)
Ground volumetric heat capacity, $c_{p,g}$	MJ/(m^3.K)
Ground density, ρ_g	1000 kg/m^3

Key performance indicators

In this work, three key performance indicators (KPIs) are used in order to estimate the technical performance of the considered TES system. These KPIs are energy efficiency and energy capacity efficiency used to evaluate the quantity of energy for the TES, while exergy efficiency arises as a promising tool for the optimization of TES design.

For the techno-economic analysis, the levelized cost of stored heat (LCOS) emerges as a key measure as it measures the average net present cost of stored heat across the lifecycle of the TES system under consideration. This indicator only accounts for the annualized investment cost (CAPEX) and the operation and maintenance cost (OPEX) that is 10 % of the CAPEX. LCOS does not account for additional cost for the TES decommissioning after the planned service lifetime. In this context, the service lifetime and the interest rate are 50 years and 3 %, respectively. Furthermore, the denominator ($\sum_{i=0}^{t} Q_{\mathrm{dis}}(t) \cdot \mathrm{d}t$) expresses the total amount of discharged heat for the examined year. Table 2 summarizes a list of KPIs used in this work and briefly reports the description of each metric considered. The reader is referred to (Dahash et al., 2021) if further information on the key performance indicators is needed.

Moreover, Table 3 reports a rough estimate of costs for several items in the construction of STES based on experience gained through previous projects and literature. Yet, these costs can be used to elaborate trends, but are still subject to high uncertainty. Yet, it is noteworthy to mention that these estimations represent the current state-of-the-art of the presented geotechnical solutions and not the technological improvement.

Table 2: List of the key performance indicators used in the techno-economic analysis framework adopted in this work (Dahash et al., 2021).

KPI	Equation
Energy efficiency	$\eta_{\mathrm{I}} = \frac{Q_{\mathrm{dis}}}{Q_{\mathrm{ch}}}$
Energy capacity efficiency	$\eta_{\mathrm{II}} = 1 - \frac{Q_{\mathrm{loss}}}{Q_{\mathrm{TES}}}$
Exergy efficiency	$\psi = \frac{EX_{\mathrm{dis}}}{EX_{\mathrm{ch}}}$
Levelized cost of stored heat (LCOS)	$\mathrm{LCOS} = \frac{(C_{\mathrm{inv}} \cdot ANF) + C_{\mathrm{O\&M}}}{\sum_{i=0}^{\tau} Q_{\mathrm{dis}}(t) \cdot \mathrm{d}t}$

Table 3: Breakdown of the specific costs for the construction of seasonal TES (Dahash et al., 2021).

Contribution	Specific Costs	Remark
Excavation	20 €/m³	Partly wet excavation
Diaphragm wall	550 €/m²	50 m deep
Sidewall	375 €/m³ 100 €/m²	Insulation cost Insulation installation
Bottom	100 €/m³	Insulation cost and installation (pressure resistant)
Liner	150 €/m²	VA, Stainless steel
Cover	200 €/m²	Floating cover (53 cm ins.)
Plant construction	40,000 €	Independent TES construction
Site facilities	50,000 €	Fixed

Results and discussion – Impact of insulation

The following section compares the different variants for the insulation distribution over the TES geometry. Herein, the common characteristics are: a fully buried tank with a total height of 50 m and a volume of 100,000 m^3. All insulation variants consider a top insulation thickness of 53 cm in order to produce U_{top} = 0.1 W/(m^2.K). Besides, the insulation material has a thermal conductivity of λ_{ins} = 0.08 W/(m.K). Moreover, Table 4 reports the different options for the insulation distribution that are considered in this investigation. Both configurations C and E feature insulation covering the upper 50% of the TES volume, while the remaining sidewalls remain uninsulated. Similarly, configurations B, C, E, and F are left uninsulated at the bottom of the TES, based on the assumption that lukewarm water accumulates at the TES bottom. Notably, the volume of insulation varies across configurations, with configuration D possessing the largest insulation volume and configuration F the smallest.

Table 4: A summary of the insulation variants considered in this work.

	X_{top} [cm]	X_{side} [cm]	X_{bot} [cm]	
A	53	26	26	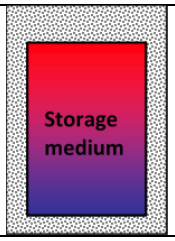

B	53	26	0	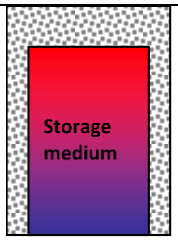
C	53	50 %: 26 50%: 0	0	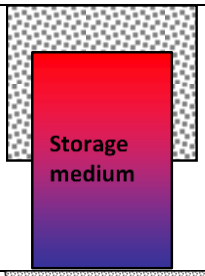
D	53	*f(r,z)*	12	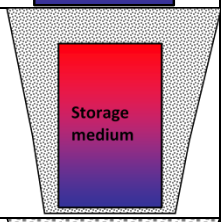
E	53	*f(r,z)*	0	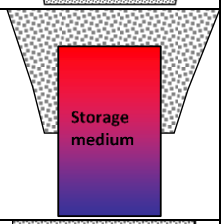
F	53	0	0	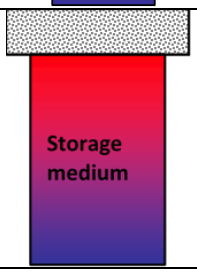

Figure 4 illustrates the specific cost for each configuration, showing that configuration D incurs the highest specific cost due to insulation installation on the sidewalls and bottom. Conversely, configuration F exhibits the lowest specific cost as no insulation is applied to the sidewalls or bottom. Compared to D, configuration A has a slightly lower specific cost due to its smaller insulation volume on the sidewalls and bottom. Further, configurations C and E have lower specific costs compared to A, despite only 50% of TES volume being insulated.

These variations in insulation distribution and volume significantly impact TES performance. Fully insulated TES (configuration A) experiences lower thermal losses, allowing more heat to be discharged. However, configuration D emerges as a more promising insulation option, boasting higher performance (e.g., energy efficiency and energy capacity efficiency) by 2.5% compared to configuration A as revealed in Figure 5, attributed to its greater insulation volume. Nonetheless, configuration A exhibits the highest exergy efficiency, indicating superior heat stratification compared to other options (Dahash et al., 2021). In other words, configuration A delivers higher-quality energy for discharged heat. Conversely, configuration D may experience more losses from TES bottom, resulting in colder temperatures and increased mixing, thereby reducing exergy efficiency.

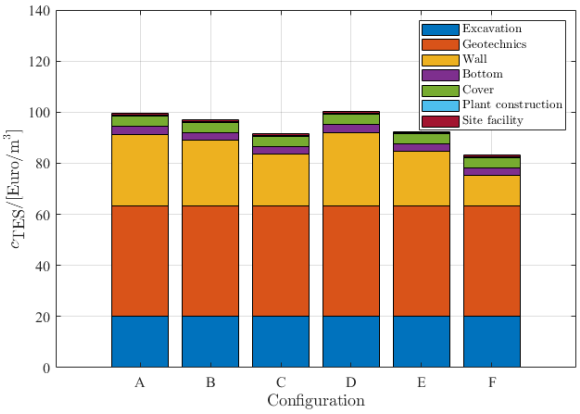

Figure 4: Breakdown of the specific investment cost for a 100,000 m^3 fully buried tank installed in HT-DH with several insulation configurations according to the costs reported in Table 3. (Geotechnics cost item refers to diaphragm wall installation, wall cost item refers to insulation cost and liner installations and bottom refers to the installation and cost of insulation and liner).

Figure 6 depicts the LCOS for various tank configurations discussed earlier. Surprisingly, the fully insulated tank exhibits the highest LCOS despite its notable efficiency of 80%. In contrast, the tank in configuration D, featuring gradient insulation, demonstrates a comparatively lower LCOS by 4 €/MWh. Meanwhile, configurations C and E exhibit similar LCOS values. Notably, configurations C and E have only 50% of the buried tank volume insulated in different patterns.

However, this comparison may yield misleading planning decisions due to variations in insulation volume and specific costs across configurations. Thus, the following discussion will compare configurations under two main constraints: 1) maintaining a top insulation thickness of 53 cm and 2) ensuring an insulation volume of 3,616 m^3 for all configurations except option F, corresponding to the insulation volume used for configuration D. Additionally, configurations B and E may have greater thickness on the TES sidewalls than on the top due to insulation distribution, necessitating modification. Thus, configurations B and E are assumed to have 80% insulation of the TES volume instead of the previous 50%.

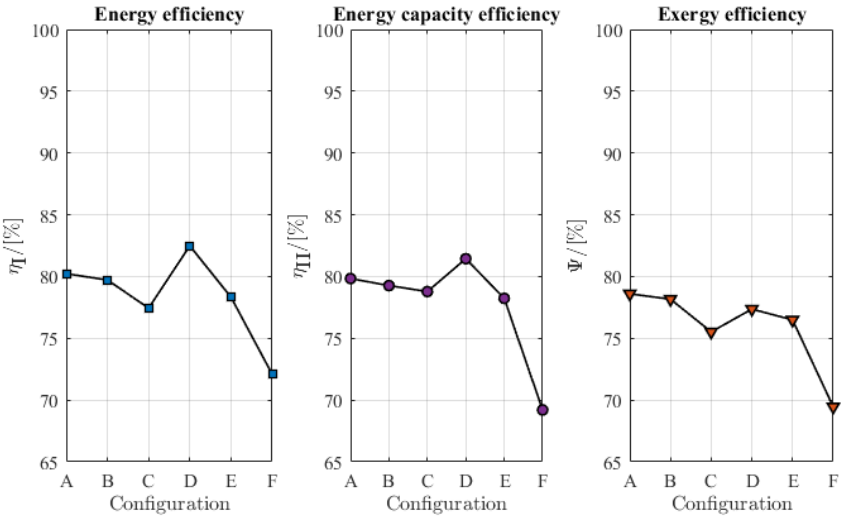

Figure 5: Energetic and exergetic efficiency for the different configurations considered for the insulation distribution for a 100,000 m^3 fully buried tank installed in HT-DH.

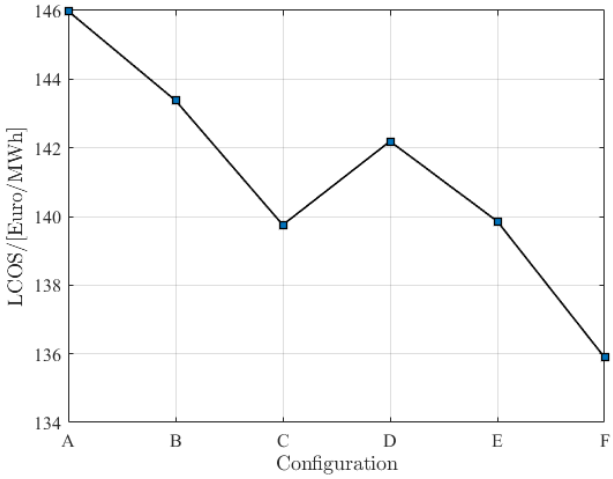

Figure 6: The levelized cost of stored heat for a 100,000 m^3 fully buried tank with different insulation configurations reported in Table 4.

Thus, Table 5 reports the adjustments made to configurations to achieve a consistent insulation volume of 3,616 m^3. Notably, configuration E represents a buried tank with 80% insulation in a gradient distribution (e.g., truncated cone), with an upper insulation thickness of 53 cm and a lower thickness of 17 cm.

Table 5: A summary of the adjustments for the insulation distribution configuration with an insulation volume of 3,616 m^3.

	X_{top} [cm]	X_{side} [cm]	X_{bot} [cm]
A	53	29	29
B	53	35	0
C	53	80 %: 26 20 %: 0	0
D	53	*f(r,z)*	12
E	53	*f(r,z)*	0
F	53	0	0

Figure 7 presents the breakdown of the specific investment cost for various configurations with a constant insulation volume of 3,616 m^3. A minor difference (< 0.5 €/m^3) is observed between configurations A, B and D, which slightly increases to 1 €/m^3 when considering configurations C and E. Notably, this difference translates to a total of €100,000 for a TES volume of 100,000 m^3. While apparently insignificant, this cost disparity could significantly influence decision-making processes, particularly for larger TES volumes exceeding 1,000,000 m^3.

Figure 8 displays the energetic and exergetic efficiency for a buried tank with a total insulation volume of 3,616 m^3 across different configurations, excluding F. Results indicate the superior performance of D (gradient insulation) compared to its counterparts, demonstrating its ability to recover the highest amount of heat for discharge into the DH. This outcome is attributed to its lower thermal losses, as evidenced by the energy capacity efficiency.

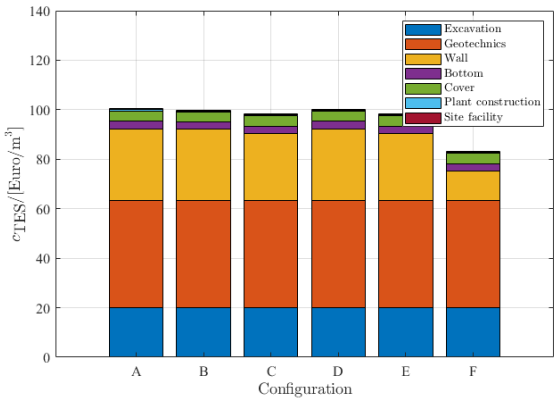

Figure 7: Breakdown of the specific investment cost for a 100,000 m^3 fully buried tank installed in HT-DH with several insulation configurations having constant volume of 3616 m^3 except configuration F. The costs calculated according to the costs reported in Table 3. (Geotechnics cost item refers to diaphragm wall installation, wall cost item refers to insulation cost and liner installations and bottom refers to the installation and cost of insulation and liner).

Figure 8 reveals another noteworthy finding – the superior performance of B, where TES remains uninsulated at the bottom compared to A, which features full insulation. This highlights the effectiveness of having greater insulation thickness on the sidewalls compared to insulating the bottom under same boundary conditions and constant insulation volume.

Configurations C and E continue to demonstrate comparable performance, consistent with previous findings (compare Figure 5). Additionally, analysis of exergy efficiency reveals superiority of B possessing the highest exergetic efficiency across all configurations – including A and D, where the TES is fully insulated. This result emphasizes the effectiveness of the insulation configuration in configuration B. However, it is important to note that these findings are dependent upon the specified boundary conditions.

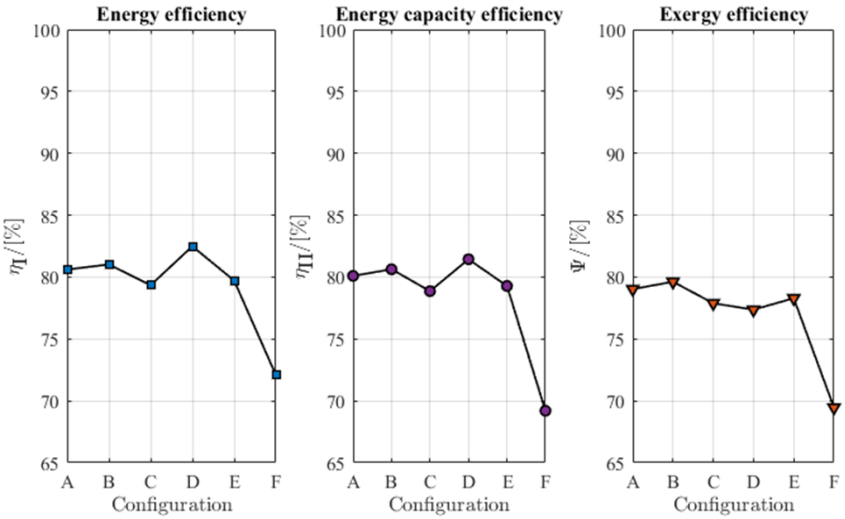

Figure 8: Energetic and exergetic efficiency for the different configurations considered for the insulation distribution for a 100,000 m^3 fully buried tank installed in HT-DH.

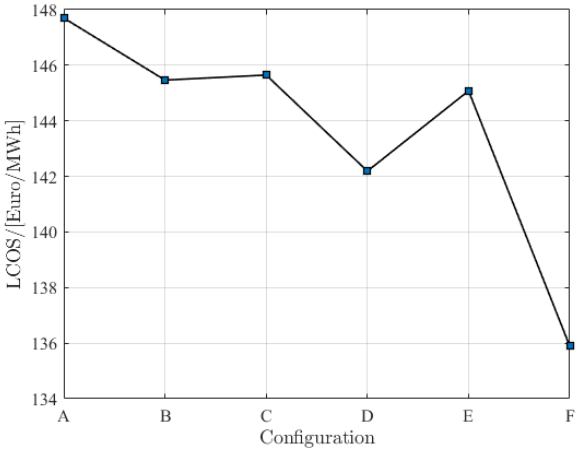

Figure 9: The levelized cost of stored heat for a 100,000 m^3 fully buried tank with different insulation configurations with a constant insulation of 3616 m^3 except F as reported in Table 5.

Given the high energetic performance of configuration D, Figure 9 shows D yielding the lowest LCOS across the set of insulated TES configurations. Conversely, configurations B and C exhibit comparable LCOS values. Therefore, configuration B may be preferable to C, as it offers higher performance in terms of both energy and exergy.

Despite having a similar specific cost to configurations B and D, moderate performance of configuration A results in the highest LCOS. This emphasizes the importance of proper insulation distribution in the TES envelope to achieve optimal performance and lower LCOS. However, the results also underline the challenge of competing against a non-insulated TES. Insulation may be essential for the TES envelope in environments where groundwater is present as emphasized in (Dahash et al., 2021).

Conclusions

Large-scale TES offers a great potential to enhance the flexibility and maximize the use of RESs and, thus, TES contributes to the decarbonization. Yet, planning of such large-scale TES systems is challenging due to number of variables that must be iteratively evaluated. One of the critical factors is the insulation level of TES as it has an impact on the techno-economic positioning of large-scale, underground TES.

Via numerical simulations, this work investigated the role of several configurations of insulation in STES pinpointing its critical role in techno-economic feasibility of large-scale TES. The findings suggested that implementing gradient insulation (D) yields optimal energetic performance and moderate LCOS when insulation volume varies. Conversely, maintaining constant insulation volume for insulated options results in the lowest LCOS with optimal energetic performance.

Future research works shall examine the influence of groundwater in the vicinity of STES, exploring prerequisite measures to mitigate its twofold impact. Additionally, our forthcoming work aims to broaden analysis by incorporating an environmental dimension for further explaining the feasibility and sustainability of large-scale TES deployments.

Acknowledgement

The present study is financially supported by the EU Horizon Europe project INTERSTORES (project no. 101136100). Views and opinions expressed are however those of the author(s) only and do not necessarily reflect those of the European Union or Research Executive Agency.

References

D'Agostino et al. (2024). Impact of climate change on the energy performance of building envelopes and implications on energy regulations across Europe. *Energy, 288*. doi:10.1016/j.energy.2023.129886.

Dahash et al. (2020). Toward Efficient Numerical Modeling and Analysis of Large-Scale Thermal Energy Storage for Renewable District Heating Systems. *Applied Energy, 279*. doi:DOI: 10.1016/j.apenergy.2020.115840

Dahash et al. (2021). Techno-economic and exergy analysis of tank and pit thermal energy storage for renewables district heating systems. *Renewable Energy, 180*, 1358-1379. doi:10.1016/j.renene.2021.08.106

Dahash et al. (2021). Understanding the interaction between groundwater and large-scale underground hot-water tanks and pits. *Sustainable Cities and Society*. doi:10.1016/j.scs.2021.102928

Huang et al. (2020). Thermal characteristics of a seasonal solar assisted heat pump heating system with an underground tank. *Sustainable Cities and Society, 53*. doi:10.1016/j.scs.2019.101910

Jodeiri et al. (2022). Role of sustainable heat sources in transition towards fourth generation district heating – A review. *Renewable and Sustainable Energy Reviews, 158*. doi:10.1016/j.rser.2022.112156.

K. Johansen and S. Werner. (2022). Something is sustainable in the state of Denmark: A review of the Danish district heating sector. *Renewable and Sustainable Energy Reviews, 158*. doi:10.1016/j.rser.2022.112117.

Maduta et al. (2022). Towards a decarbonised building stock by 2050: The meaning and the role of zero emission buildings (ZEBs) in Europe. *Energy Strategy Reviews, 44*. doi:10.1016/j.esr.2022.101009.

Tosatto et al. (2022). The challenge of planning and constructing large-scale hot water TES for district heating system: A techno-economic analysis. *Proceedings of the International Renewable Energy Storage Conference 2021 (IRES 2021)* (S. 52-66). Atlantis Press. doi:10.2991/ahe.k.220301.006

Yuan et al. (2021). District heating in 100% renewable energy systems: Combining industrial excess heat and heat pumps. *Energy Conversion and Management, 244*. doi:10.1016/j.enconman.2021.114527.

BauSIM 2024 in Wien
23. September – 26. September

Enhancing Grid Stability and Economic Operation through Heuristic Control: A Simulation Case Study

Tuğçin Kırant-Mitić[1], Karsten Voss[1]
University Wuppertal, Germany, E-Mail: kirantmitic@uni-wuppertal.de

Abstract

A positive interaction between buildings and power grids can enhance green power utilization. Notwithstanding these advancements, the unforeseen voltage stability challenges, leading to critical grid states, remains a salient concern. In this research, the power demand optimization of a case building is accomplished through the application of rule-based predictive heuristic control, with a primary focus on achieving economical operation while considering the requests from the smart grid system. As part of the Solar Decathlon Europe 21/22 competition, one of the competition buildings is exploited as case building. Cost optimized operation of the building is driven by historical electricity spot prices from the power grid of Germany. The critical grid state measurements of smart grid system are undertaken by the local utility company. During critical status, the building is expected to respond to the smart grid system by decreasing the power demand. To conduct the analysis, a co-simulation environment is developed between IDA-ICE and MATLAB. The power demand profiles of subcomponents — namely, heat pump, photovoltaic, electrical energy storage, and user-related loads— are simulated by IDA-ICE, while cost and power optimization is run in MATLAB. In conclusion, this research demonstrates an approach to support grid stability challenges through building-grid interaction.

Introduction

A positive interaction between buildings and power grid can increase green energy usage by introducing dynamic electricity prices within energy market (Zhao et al. 2015). However, despite this advancement, challenges such as unexpected voltage stability issues remain significant. In such scenarios, it becomes necessary to respond to signals from the smart grid system (SGS) by adjusting building operations to support the SGS operation. The integration of smart grid technology into building operations is referred to as building-grid interaction.

In case of voltage instability in the SGS operation, the buildings are informed by SGS technologies to adapt their operation to ensure the resilient SG operation. To achieve this, the building operation should be optimized by control algorithms. Building energy management systems are capable to receive the signal from SGS and apply demand optimization using model predictive control (MPC), rule-based control, reinforcement learning control (Zhou et al. 2023), heuristic control (Dengiz et al. 2019) and more.

Heuristics-based controls exploit the simple rules derived from experimental and practical experiences (Sánchez et al. 2019). Executing control algorithms such as MPC can be computationally expensive, but this can be mitigated by using a heuristic approach. For building energy optimization, RPHC enables the definition of selected operation setpoints to be evaluated for the solution. Therefore, control algorithms evaluate the given values rather than all possible values within a setpoint range, thus finding the solution faster. On the other hand, the RPHC approach may not provide the optimal solution since it evaluates only predefined values, not all possible values. As a result, it provides an applicable solution, though a better solution may exist. To adopt a simplified approach, (Gudi et al. 2012) evaluated household appliance scheduling for cost optimization using heuristic control with a set of defined rules, resulting in a 20% cost reduction. (Dengiz et al. 2019) applied rule-based heuristic control to minimize the heating cost of a residential area. (Cano-Tirado et al. 2024) applied a heuristic genetic algorithm to schedule a charging infrastructure operation to support SGS operation.

Novelty

In this research, the power demand optimization of a case building is accomplished through the application of RPHC, with a primary focus on achieving economical operation while

considering the requests from the SGS. In this paper, the authors discuss: 1) development and application of RPHC, 2) building a co-simulation environment, and 3) finally optimizing building operations based on the multiple signals from SGS.

Cost optimized operation of the building is driven by electricity spot prices from the German power grid for the year 2023. The critical grid state measurements of a transformer station for the same year are undertaken by the local utility Wuppertaler Stadtwerke. On critical status, the buildings are expected to decrease the power demand at the exact amount SGS needs.

As part of the Solar Decathlon Europe 21/22 competition (SDE 21/22 2022), one of the competition buildings “MIMO” (MIMO 2023) is exploited as case building in this research. More information about the building is given in Simulation section.

The co-simulation environment has been developed to ensure communication between a building energy simulation tool IDA-ICE (IDA-ICE 2023) and numeric computing program MATLAB (MATLAB 2015). Within this framework, RPHC is applied in MATLAB by employing cost optimization. The power demand profiles of distinct subcomponents - namely, the heat pump, photovoltaic array (PV), electrical storage system (ESS), and user-related loads such as lighting and plug-in devices - are simulated by IDA-ICE. These simulated profiles are then stored in MATLAB, serving as input for the calculation. The manipulated variables are the supply temperature of the thermal buffer tank (TBT) and charging/discharging value from ESS, which drives the heuristic strategy. In Co-simulation environment section, this framework is described in detail. This research is conducted only in the simulation environment and has not been applied to the real-existing building.

Simulation

The case building, MIMO, is an all-electric demonstration building equipped with an air-water heat pump (for heating purposes only) that has a thermal capacity of 5.28 kW. It is modelled with a constant coefficient of performance of 4.41. The building comprises three zones (such as community room, residential unit 1 and residential unit 2) and has a net conditioned area of 85 m^2. Utilizing TBT to fulfill both space heating and domestic hot water requirements, the efficient distribution of heat is achieved through the integration of underfloor and wall heating units. Aiming for self-sufficiency, a PV with a rated capacity of 2.8 kWp, adding to this power generation is a lithium-ion ESS with a capacity of 2.5 kWh are installed in the building. These systems are integrated into the building's energy model (Figure 1) using the building energy simulation tool IDA-ICE.

A

B

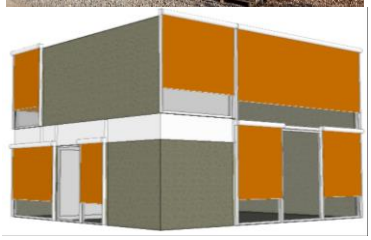

Figure 1: The picture of the case building (Sigurd Steinprinz, University of Wuppertal) (A) and the energy model view (B)

The building energy model is calibrated by monitored data during the competition period when there is a test phase for co-heating (mid-June 2022) to assess the thermal performance of the building. The results from the test period and the IDA-ICE simulation are compared as given in Figure 2, leading to accurate outcomes.

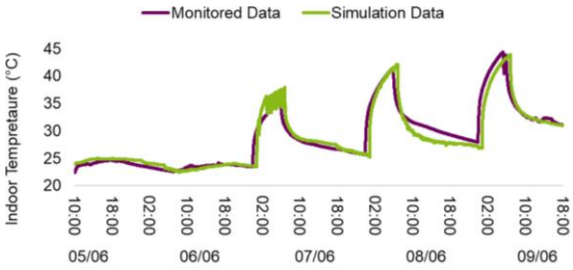

Figure 2: The indoor temperature profile of the case building for the calibration process

This paper presents a comprehensive analysis of a representative one-day heating period (18 January 2023) in response to the SGS signals within the developed co-simulation environment. The assessment is conducted between the building's business-as-usual case (BAU) and building-grid interaction case. These comparisons are performed for both before and after grid critical states, presenting optimized building operation in response to the dynamic grid environment. In this context, following cases are analyzed:

1-BAU case: In this reference case, MIMO operates under a signal-unaware condition, meaning it does not engage in active building-grid interaction. The building operates independently, with indoor temperature setpoints remaining

constant (16°C for community room and 20°C for residential units). The ESS is charged by the installed PV and discharges to cover the building's energy demand, thus operating on a self-sufficiency basis. Consequently, there are no additional measures implemented to minimize costs, unlike in scenarios involving active building-grid engagement, which is discussed in the following section.

2- Building-grid interaction case: In this scenario, the building receives signals from SGS to manage two types of operational statuses: grid-oriented and market-oriented operations (Figure 3). When the building participates in building-grid interaction, it becomes eligible to take part in the flexibility market, allowing it to consume power at more favorable prices. In response, the building assumes the responsibility of supporting the SGS in the event of critical voltage instability in the power grid, thus creating a win-win situation.

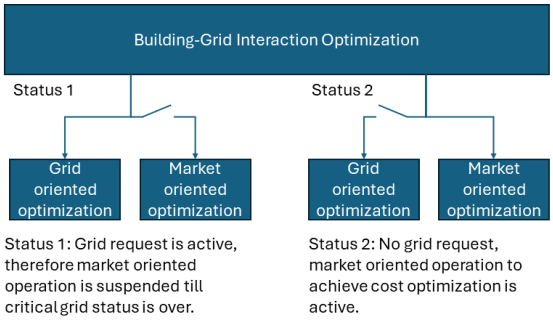

Figure 3: The two types of status occur in building-gird interaction case

In this context, the operational priority is to ensure grid stability. Therefore, the building continually monitors grid request signals. If no such signal is detected, the building then operates under a market-oriented approach to optimize operational costs by taking advantage of the flexibility market prices. To actualize the building-grid interaction case, there are several steps to be followed:

Step 1: The grid-oriented status occurs rarely, as it represents a critical situation that arises unexpectedly. The flexibility market are announced one day in advance, allowing buildings use this time to optimize their operations (e.g., temperature setpoints, EES discharging/charging actions) for the most cost-effective overall operation (referred to as Status 2 in Figure 3). For this purpose, control algorithms, such as RPHC, are applied. This is the first step executed in the co-simulation environment so that the best economical solution is found for the case building. The use of control algorithm in this research is discussed in Rule-Based Predictive Heuristic Controlsection.

Step 2: When RPHC decides the building´s setpoints and actions for market-oriented operation, they are scheduled to be applied the following day. However, if the SGS issues a request for grid support during a day when market-oriented operation is active (referred to as Status 1-Figure 3), it requires the execution of a separate optimization algorithm. This algorithm is tasked with identifying the solution to assist the grid, which involves calculating the precise setpoints and actions needed to achieve the specific reduction in power demand requested by the SGS. The effectiveness of these adjustments is assessed using the load matching index (LMI) mentioned in the Results section. This step is executed by another RPHC script in MATLAB, which is distinct from script applied in Step 1.

Step 3: Upon fulfilling the SGS's power reduction request, the building resumes market-oriented operation. However, due to the adjustments made during the grid-oriented optimization phase, the initial setpoints/actions determined in Step 1 no longer apply. Consequently, new market-oriented setpoints/actions need to be recalculated for the remainder of the day, based on the adjustments implemented in Step 2. To accomplish this, a separate RPHC script is executed in MATLAB, aimed at optimizing operational costs under the new conditions. This ensures that the building operates in the most economically advantageous manner for the rest of the day. If there is no grid request from SGS on a specific day, the building's operation continues according to the market-oriented setpoints, and actions determined in Step 1.

Co-simulation environment

In this research, two separate calculations are carried out, each requiring different programs designed to meet specific needs. These include: (1) determining building energy performance results, including HVAC operation values and thermal comfort values, and (2) implementing advanced control algorithms for demand optimization based on SGS requests and optimal cost results. Importantly, these calculations must be performed concurrently, as the results for the next time step depend on the outcomes of the previous time step in this dynamic calculation environment. To address this challenge, a co-simulation framework is established, enabling an analysis of building-grid interaction. Specifically, this research utilizes a co-simulation environment that integrates IDA-ICE (for building energy simulation) and MATLAB (for RPHC implementation).

The initial connection between IDA-ICE and MATLAB is established using a given MATLAB

script from the IDA-ICE developers. Following this, the script is improved by implementing RPHC. The initial script enables the channel connection to IDA-ICE to send and receive data using import and export modules. To avoid data loss between these programs, high resolution time steps such as one to five minutes are favorable. However, the computational burden during the co-simulation limits this process, causing the simulation to collapse before completing the defined simulation time (such as 24 hours). After testing several time steps, the time step for continuous simulation is set to 15 minutes. The determination of the proper time step involved conducting several runs and evaluating indicators such as simulation stability, data transmission stability, and the completeness of IDA-ICE simulation outputs in local directory. However, as mentioned above, data loss is a critical problem since the exported data from IDA-ICE is an input for the cost optimization calculation in MATLAB and if there is a mismatch between calculated final values and exported values. RPHC receives incorrect values, leading to performance gap between the simulated case and real case practice. To avoid this problem, another approach is applied: IDA-ICE saves the simulation results in ".prn" format in a local directory. In MATLAB, an additional section is written as part of the RPHC script to call and read the .prn files. These read data are accurate and provide reliable inputs for RPHC. Therefore, the data transferred by the export module are neglected. It should be noted that this problem is not observed during the data import process from MATLAB to IDA-ICE, but vice versa.

Another challenge in the co-simulation environment is long calculation times. For an accurate energy performance calculation, as much as different setpoints sent by MATLAB, more building performance cases are simulated in IDA-ICE allowing to the calculation of the most cost-effective result in RPHC among many different scenarios. Each simulation case means additional simulation time. Also, how long the control horizon should be (6 hours, 12 hours etc.) is another factor to consider. Therefore, some simplifications are applied to reduce the computational burden. These simplifications are explained in the Rule-Based Predictive Heuristic Control section.

The co-simulation framework is controlled mainly by MATLAB which provides the commands to set up a channel connection, create storage for transferred data and finally launches IDA-ICE. In other words, after setting up the co-simulation environment, the user doesn't use IDA-ICE anymore directly, since everything is controlled by MATLAB. After launching IDA-ICE, the simulation time "from when to when" is assigned by MATLAB script, following, the setpoints/actions values are sent to IDA-ICE. During the simulation time span, the data transfer between two programs continues. At each time step, the data "sent to" and "received from" are stored in MATLAB for post-processing, in addition to the IDA-ICE storage. Once the simulation period concludes, MATLAB issues a command for IDA-ICE to terminate its operation. MATLAB then pauses momentarily to ensure all IDA-ICE data storages are properly closed, preventing any data overlap that could be caused by the upcoming simulation. This process outlines just one simulation scenario for RPHC. However, this workflow will be repeated from the beginning for each existing RPHC scenario. The development methodology of the simulation scenarios is explained in section Rule-Based Predictive Heuristic Control.

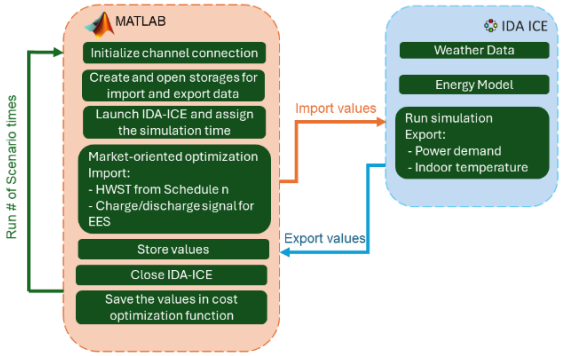

Figure 4: The co-simulation environment workflow for the market- oriented optimization (Step 1)

As mentioned in the Novelty section, the manipulated variables are the supply temperature of TBT and charging/discharging value of ESS. The explained co-simulation workflow is illustrated in Figure 4 for market-oriented optimization. In grid-oriented optimization, the primary objective is to reduce power demand by the amount requested by the SGS. The initial strategy involves exploiting the ESS to initiate discharge. In this context, the request signal (binary 0/1) and the specific amount of demand reduction required are transmitted to IDA-ICE (Figure 5). If the discharged power amount from ESS does not meet the SGS's request (which is captured from return values by IDA-ICE), various TBT setpoints are then simulated until a value close to the requested demand reduction is achieved.

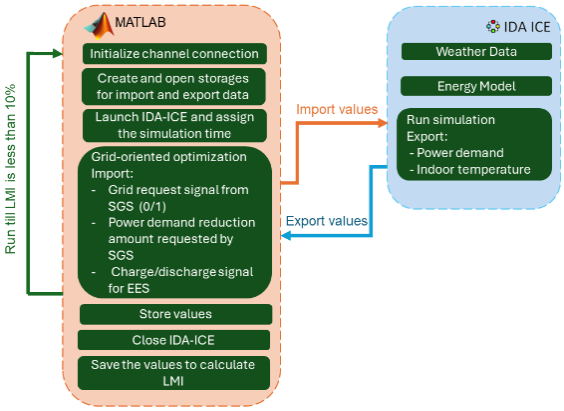

Figure 5: The co-simulation environment workflow for the grid-oriented optimization (Step 2)

SGS Signals

In this research, hourly day-ahead energy unit prices (before tax) are used for the optimization of a representative heating day - the 8th of January 2023 - which is sourced from the ENTSO-E Transparency Platform (ENTSO-E Transparency Platform Jan-2024).

In the BAU case, the TBT setpoints are determined by a heating curve that depends on the outdoor temperature. However, for the building-grid interaction scenario, the setpoints are adjusted in response to electricity price signals. To facilitate this, the hourly price signal is categorized into three levels: cheap, normal, and expensive, using a quartile analysis (25th percentile) for the simulation day. During periods identified as having the lowest electricity costs (falling within the lower quartile of day-ahead prices), the building's control system can adjust the TBT setpoints for zone heating (domestic hot water temperatures are not influenced by this operation) to be either 2.5°C or 5.0°C higher than the reference setpoint established in the BAU scenario. For durations categorized under the normal price level, two options are provided for the TBT setpoint temperatures: either 2.5°C or 5.0°C lower than the BAU reference setpoint. During periods with high electricity prices, the heat pump is turned off. If the indoor temperature is jeopardized during this period, the TBT setpoints are reverted to the standard operating temperatures defined for the BAU scenario. The motivation for limiting setpoint temperatures is to reduce the computational burden by decreasing the number of possible simulation scenarios, generating combinations only with the predefined values in RPHC. This method allows the RPHC to test specific provided setpoints, rather than attempting every possible setpoint within a given range, which could be extensive.

Secondly, as mentioned earlier, an SGS signal is triggered in cases of critical voltage instability. In this case study, we utilize real monitored data provided by the local utility. This data, collected from a transformer in Wuppertal, reflects the power demand of a neighborhood, reaching up to 100 kW. On average, a demand exceeding 50 kW triggers a yellow status, indicating slight stress on the local transformer. If the demand exceeds approximately 65 kW, it signifies a critical situation requiring buildings to support power grid stability. These thresholds are considerably higher than the peak demand observed for the case study building from the SDE 21/22 competition, which is designed for efficient energy consumption and has a peak power demand of approximately 3.0 kW during the heating period. Consequently, the building's contribution to transformer support would be minimal. To address this discrepancy, we normalize the monitored data to a scale ranging from 2 kW to 10 kW, where the yellow and red statuses are triggered after 5 kW and 6.5 kW, respectively.

Rule-Based Predictive Heuristic Control

RPHC runs various scenarios to optimize the overall operating costs of the case building by aligning them with a market-oriented operation. Here the main concern is to decrease the computation time as RPHC running with a white-box model results in long simulation times, e.g., 15 hours for a day optimization. In this context, two simplifications are conducted limiting the possible setpoints to develop the RPHC scenarios and dividing the prediction horizon (24 hours) into four control horizons.

In the SGS Signals section, the approach to limit the possible setpoints are explained. For each time step, there are two possible TBT setpoints based on the price category: During cheap price periods, either 2.5°C or 5°C above than BAU case, and during normal price period either 2.5°C or 5°C below than BAU case. Using these values, a set of simulation scenarios is developed by combining all the possible setpoints throughout a day. For example, if one hour has a cheap price with two temperature options, and the next hour has a normal price with two different temperature options, we combine these options to form four unique scenarios. When we apply this method over six continuous hours, the number of possible scenario combinations increases greatly.

Alongside the prediction horizon (24 hours), the co-simulation process includes a six-hour control horizon (Figure 6). Each control horizon comprises a series of #n simulation scenarios, categorized according to the price signal category over the control horizon. The initial control horizon predicts the optimal demand

profile from 00:00 to 06:00. The inputs for the next control horizon are the setpoint values determined and saved from the previous control horizon. During the second control horizon, simulations run from 00:00 to 12:00. For the interval from 00:00 to 06:00, the setpoint values established in the first control horizon are used, and new setpoint values for the period from 06:00 to 12:00 are projected using the RPHC. Once the final setpoint values are obtained, they are saved and employed in the following control horizon. This approach is maintained throughout the prediction horizon. Following each control horizon, the power demand outcomes for each scenario, as computed by IDA-ICE, are stored in MATLAB. These results are then utilized for the cost calculation. The scenario yielding the most favorable cost outcome is selected as the final decision.

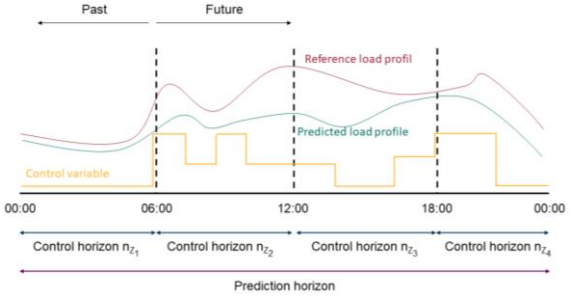

Figure 6: Prediction and control horizons in RPHC application

In the case study, an SGS signal occurs before 19:00 indicating that the predicted power demand from market-oriented optimization between 19:00-20:00 should be reduced by 1300 W due to an impending critical situation. In the Results section, the capability of the building´s energy system to respond this demand is analyzed and the outcomes are presented for each optimization as described in the Simulation section in addition to the LMI. LMI serves as an indicator to show the effectiveness of the response ratio to the power grid's demand. LMI is formulated as following:

$$LMI = \frac{P_{Market-oriented\ opt.} - P_{Grid-oriented\ opt.}}{P_{SGS\ request}} \quad (1)$$

P=Power demand from grid (Watt)

Results

This case study requires an analysis of cost optimization and demand reduction optimization in response to SGS signals, as well as a reevaluation of cost optimization for the remainder of the day after adjusting the operational setpoints to support the SGS. In this analysis, various optimization scenarios are compared on an hourly basis to the BAU case, with a focus on key performance metrics: the power demand of the heat pump, the state of charge of the ESS, the power demand from the grid, the temperature of the TBT, the indoor temperature of residential unit-1, LMI and total operational cost calculation.

In Figure 7, the ESS state of charge shows the storage utilization under different operational strategies. The BAU approach demonstrates a relatively uniform state of charge, suggesting an absence of strategic charging actions from the power grid, attributed to a strategy focused on self-sufficiency. Given that solar irradiance is typically weak during a standard heating period day, the EES cannot be charged, preventing the building from utilizing the EES's potential. On the other hand, market-oriented operation suggests an adaptive charging/discharging strategy to use lower electricity prices to charge, presented by significant charging levels, specifically during overnight.

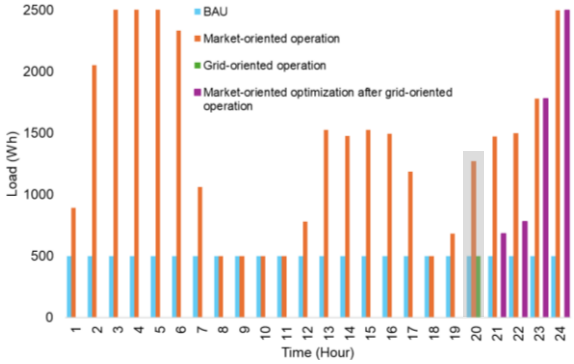

Figure 7: EES state of charge for different operation cases

In market-oriented optimization, the amount of stored energy increases between 19:00-20:00 due to a plan to charge up (using 800 W for charging). However, when it comes to supporting the grid, this charging plan isn't used. Instead, the stored energy decreases, showing that the EES is discharged by 250 W. This discharging phase is necessary to minimize the power demand from grid as requested by SGS. By changing the planned actions for the EES, power demand from grid is decreased by 1050 W in total. This action underlines the ESS's role in providing flexibility and its ability to manage between market-driven objectives and grid-supportive actions. However, since this amount is not sufficient, further action, such as, changing the heat pump power demand, is considered in the next step.

Heat pump power demand is given in Figure 8. In the BAU scenario, demand reflects a non-responsive system to price signals or grid requests. It operates only based on the thermal needs of the building. Reversely, the market-

oriented operation presents a dynamic adjustment to the fluctuating prices throughout the day.

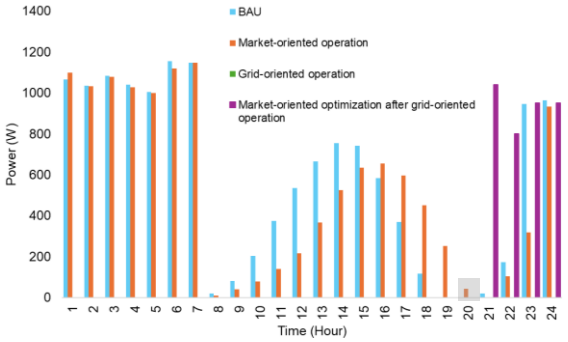

Figure 8: Heat pump power demand for different operation cases

During grid-oriented operation, to closely match the power demand reduction requested by SGS and considering that the EES strategy alone cannot fully achieve this, it becomes necessary to reduce heat pump operation, if possible, without jeopardizing thermal comfort. In this context, the heat pump operation is suspended, and the power demand of 50 W is avoided. Following the grid-oriented response, the market-oriented optimization after grid-optimization case shows an increment in demand.

Fehler! Verweisquelle konnte nicht gefunden werden. illustrates the building's total power demand from the grid under various operational strategies. In the BAU scenario, power demand remains steady at approximately 2000 W throughout the day, indicating a non-adaptive energy strategy since it doesn't take part in the energy flexibility market, however, market-oriented operation is characterized by fluctuating demand, reflecting active participation.

During grid-oriented operation, there's a notable decline in demand at 20:00, when the building has decreased its grid energy use, to match load reduction as requested from SGS. With EES and heat pump power reduction strategy, 1100 W of decrement is achieved. Following this, the market-oriented optimization after grid-responsive action shows a rise in demand, that considers both the previous support provided to the grid and current market pricing. This presents the building's role as a proactive consumer that maintains cost-effective energy habits. As previously stated, SGS requested a reduction in demand of 1300 W. Through the implementation of the applied measure, a reduction of 1100 W in demand is achieved. Based on the given formula (1), LMI is calculated to be 85%.

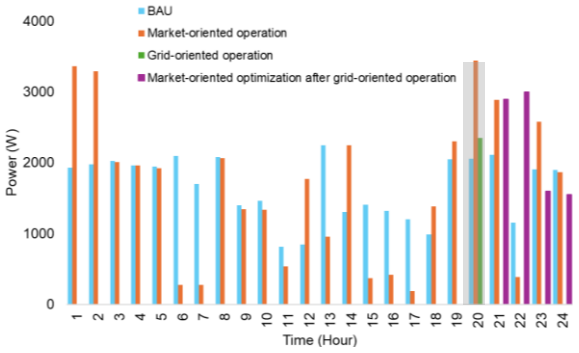

Figure 9: Final power demand for different operation cases

Figure 10 shows the upper layer temperature of TBT over a 24-hour period for different optimization cases. Due to stratification, the water is supplied to the heating units from the upper layer, ensuring the highest temperature water is used for heating purposes. The tank is designed with 8 layers, which helps maintain distinct temperature gradients and enhances the efficiency of the thermal storage system. The BAU line presents the temperature based on the heating curve. For market-oriented optimization, the temperature fluctuates more, adjusting to cost variations and showing a more responsive approach to energy pricing. During the grid optimization, the temperatures go down since the heat pump operation is suspended. However, on the following hour, the temperature rises again.

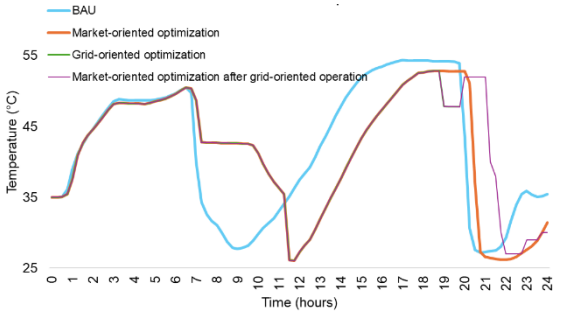

Figure 10: Thermal buffer tank upper layer temperature for different operation cases

Figure 11 tracks the indoor temperature under different scenarios, indicating how the thermal comfort is influenced by each strategy. The temperature under the BAU approach is quite stable, suggesting that the heating system maintains a consistent setting since it doesn't interact with dynamic pricing. The market-oriented result also presents similar behavior to the BAU case, since the manipulated RPHC variable is not indoor temperature profile, but TBT temperature. In this research, the motivation was to keep the indoor temperature stable as possible so that the occupants do not sense the interaction measures between the building and SGS. However, due to changes in the heat pump

operation plan during the grid-oriented operation case, we observed a slight increase in indoor temperature, approximately by 1°C, in the post-operation scenario.

In addition to the power reduction, another crucial aspect to consider is the potential economic benefit. In the BAU scenario, the total operational cost for the analyzed day is 5.64 €. Participation in the flexibility market reduced this cost to 5.45 €. Following market optimization and subsequent grid optimization, the final operational cost is determined to be 5.5 €.

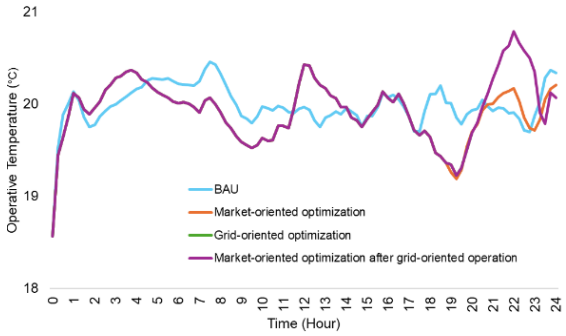

Figure 11: Indoor temperature of the residential unit-1 for different operation cases

Conclusion

The positive interaction between buildings and the power grid is incentivized by participation in the energy flexibility market to support SGS operations. Nevertheless, the practical analysis of this issue highlights the challenges of implementing load optimization simulation modelling using control strategies. The complexity of these problems surpasses the capabilities of a single program, introducing computational complications and necessitating a co-simulation environment.

In this research, a co-simulation environment between a building performance simulation program and numerical program is presented with a case study. It showcases a win-win situation to enhance grid stability and pursue cost reductions. The results are evaluated with several metrics. It is found that, with control algorithms, multiple signal optimization such as load and cost, can be achieved. However, in a highly energy-efficient experimental building like MIMO, achieving high LMI values and significant cost reductions is constrained. This limitation arises because such buildings are designed to operate at a high level of energy efficiency in BAU scenario. Consequently, the potential for realizing higher cost benefits is also limited.

References

Cano-Tirado, D.; Forchheim, M.; Asman, M.; Zdrallek, M.; Palmer, S. (Eds.) (2024): Potential Grid-Oriented and Market-Oriented Optimisation of a Local Charging Infrastructure Through a Genetic Algorithm. 18. Symposium Energieinnovation. Graz/Austria, 14.-16.02.2024.

Dengiz, Thomas; Jochem, Patrick; Fichtner, Wolf (2019): Demand response with heuristic control strategies for modulating heat pumps. In *Applied Energy* 238, pp. 1346–1360. DOI: 10.1016/j.apenergy.2018.12.008.

ENTSO-E Transparency Platform (Jan-2024): Day-ahead Prices. Available online at https://transparency.entsoe.eu/dashboard/show, updated on Jan-2024, checked on Jan-2024.

Gudi, Nikhil; Wang, Lingfeng; Devabhaktuni, Vijay (2012): A demand side management based simulation platform incorporating heuristic optimization for management of household appliances. In *International Journal of Electrical Power & Energy Systems* 43 (1), pp. 185–193. DOI: 10.1016/j.ijepes.2012.05.023.

IDA-ICE (2023): Equa Simulation AB - IDA indoor climate and energy 4.8 - Simulation Software | EQUA. Available online at https://www.equa.se/en, checked on 15-Aug-23.

MATLAB (2015): (R2015b). Natick, Massachusetts: The MathWorks Inc.

MIMO (2023): MIMO - Minimal Impact Maximum Output - Solar Decathlon Europe 21. Available online at https://mimo-hsd.de/de/, checked on 15-Aug-23.

Sánchez, Cristian; Bloch, Lionel; Holweger, Jordan; Ballif, Christophe; Wyrsch, Nicolas (2019): Optimised Heat Pump Management for Increasing Photovoltaic Penetration into the Electricity Grid. In *Energies* 12 (8), p. 1571. DOI: 10.3390/en12081571.

SDE 21/22 (2022): Solar Decathlon Europe. Available online at https://sdeurope.uni-wuppertal.de/de/, checked on 15-Aug-23.

Zhao, Yang; Lu, Yuehong; Yan, Chengchu; Wang, Shengwei (2015): MPC-based optimal scheduling of grid-connected low energy buildings with thermal energy storages. In *Energy and Buildings* 86, pp. 415–426. DOI: 10.1016/j.enbuild.2014.10.019.

Zhou, Xinlei; Xue, Shan; Du, Han; Ma, Zhenjun (2023): Optimization of building demand flexibility using reinforcement learning and rule-based expert systems. In *Applied Energy* 350, p. 121792. DOI: 10.1016/j.apenergy.2023.121792.

BauSIM 2024 in Wien
23. September – 26. September

Explainable AI for cooling load prediction and heat flow estimation using SHAP values

Alexander Neubauer[1], Stefan Brandt[1] und Martin Kriegel[1]

[1]*Hermann-Rietschel-Institut, Technische Universität Berlin, 10587 Berlin, Germany*

Abstract

Effective load management for cooling energy can be realised through accurate cooling load predictions. This can reduce peak loads and ease the burden on the power grid. Accurate load prediction can be achieved using machine learning, which are black-box models. Explainable AI can be used to make machine learning models explainable. SHAP values are employed for this purpose. Currently, there is a research gap as no comprehensive and systematic investigation of the influence of building characteristic on the SHAP values of hourly cooling load predictions has been carried out. Moreover, it has not yet been investigated whether the heat flows in a room can be represented by the local SHAP values. This study investigates the influence of individual features on the cooling load predictions. The feature importance was examined both local, for a single point in time, and global, for the entire dataset, using SHAP values for a large number of various buildings with different characteristics. The results show a correlation between building characteristics and the importance of features for the cooling load prediction. Therefore, the building characteristics are implicit in the SHAP values. This enables an purely data-driven interpretation of the building characteristics. Additionally, the study demonstrated that the local SHAP values provide a satisfactory description of the heat flows in a room. This provides a purely data-driven insight into the heat flows of the building, which can reveal optimisation potential for the building.

Introduction

The increasing demand for cooling energy in newer buildings, driven by rising outdoor temperatures and improved insulation, underscores the need for effective load management strategies. Moreover, the global space cooled in buildings is projected to increase from 105×10^9 m^2 in 2022 to 250×10^9 m^2 in 2050. The share of space cooling in final electricity consumption is expected to be 9 % in 2022, falling to 5 % in 2050 (IEA 2023*b*). Cooling plays a significant role in achieving the energy transition, despite its decreasing share of total electricity consumption. To meet the *Net Zero Roadmap*, the share of solar PV and wind in total global electricity generation will increase from 12 % to 71 % in 2050 (IEA 2023*a*).

Integrating load management for cooling systems is crucial due to the fluctuating power generation of these energy sources. The objective is to generate electricity and cooling energy simultaneously to the greatest extent possible. Load shifting of cooling energy is a viable option as thermal energy storage is more cost effective than electrical energy storage Odukomaiya et al. (2021). To ensure successful load shifting, accurate prediction of cooling load is required. Using machine learning (ML) to predict the cooling load has the advantage that no information about the building is required and the prediction can be entirely data driven. This means there is no need for a complex modelling of the building, as is the case with grey box modelling. ML models are black boxes, lacking transparency and explainability. Through the use of Explainable Artificial Intelligence (XAI), it is possible to understand how ML models arrive at their results. XAI provides insight by transforming the black box model into a kind of grey box model. This study confidently investigates the use of XAI for explaining cooling load predictions. In this study, SHapley Additive exPlanations (SHAP) values are used as the method for XAI. SHAP values explain how individual features affect a model's output, making the model more explainable.

Moon et al. (2022) investigated the explainability of electrical forecasting in a university building using SHAP values, specifically the Tree SHAP algorithm. Various machine learning models were used for the prediction, including Random Forest

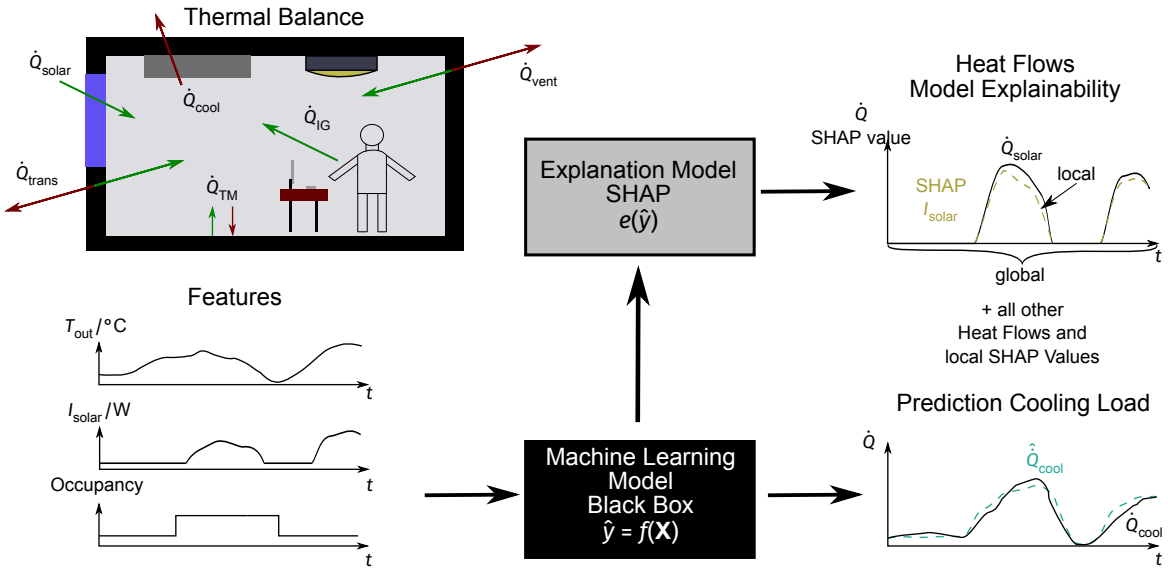

Figure 1: Overview of the work

(RF), Extreme Gradient Boosting (XGBoost) and Light Gradient-Boosting Machine (LightGBM). Among these models, LightGBM achieved the highest prediction quality. The weekly average electricity consumption and the previous day's electricity consumption had the greatest influence on the prediction. In Kuzlu et al. (2020), the XAI models LIME, SHAP and ELI5 were used to investigate which parameters have the greatest influence on solar photovoltaic power generation prediction. The sum of the SHAP values was compared with the prediction for selected time stamps. The influence of each feature could be visualised for single time steps. Neubauer et al. (2024) analysed the influence of individual features on the prediction of the heating load, based on the building characteristics. The study has conclusively shown that the building characteristics are implicitly included in the local and global SHAP values for heating load prediction.

There is still a research gap for investigating the model explainability for the cooling load prediction as a function of the building characteristics. Furthermore, the capability of the local SHAP values to represent the heat flows in a building has not been investigated. Figure 1 presents an overview of the study. The machine learning model, which is a black box model, solely learns the mapping between the features and the prediction. The explanation model, which utilises SHAP values, is used to present an explanation of the relationship between the features and the prediction. The SHAP values are examined to see whether the building characteristics are represented in the SHAP values and whether the thermal balance and associated heat flows can be represented by the local SHAP values. The objective is to enhance the transparency of the model and obtain insights based solely on data driven analysis of the building. The main contributions of this paper are:

- Predict the cooling load using LR, RF, XGBoost and LightGBM
- Show the relationship between the SHAP value for cooling load as a function of building characteristics
- Comparison of the local model explainability using SHAP values with the heat flows in a room model

Simulation

Machine Learning Regression Models

Several models were evaluated to determine the most appropriate one for this study. Four supervised learning models are cosiderd Linear Regression (LR), RF, XGBoost, and LightGBM. LR is a statistical model, while RF, XGBoost, and LightGBM are decision trees. According to Wang et al. (2020), RF and XGBoost had the highest prediction accuracy for the hourly cooling load prediction of the shallow machine learning models.

In the work of Moon et al. (2022), the LightGBM was able to deliver good results in electrical load prediction. The most appropriate model for this prediction is determined by considering multiple models.

Evaluation Metrics

The evaluation of the model accuracy uses the *root mean squared error* RMSE (Equation 1) and the *coefficient of determination* R^2 (Equation 2).

$$\mathrm{RMSE} = \sqrt{\frac{1}{n}\sum_{i=1}^{n}(y_i - \hat{y})^2} \tag{1}$$

$$R^2 = 1 - \frac{\sum_{i=1}^{n}(y_i - \hat{y})^2}{\sum_{i=1}^{n}(y_i - \bar{y})^2} \tag{2}$$

The RMSE is the root mean square error between the actual y and the predicted value $\hat{y}$. The unit of the RMSE is equal to the variable y and thus is dimensionally related. In order to compare between different time spans, dimensionless parameters such the R^2 are used. The R^2 can be between 0–1, with higher values indicating a better prediction accuracy.

Explainable AI Models

SHAP values can be used to determine the influence of features on a prediction. They are a game-theoretic approach introduced by Lundberg & Lee (2017). SHAP values are used to justify the output of machine learning models, increasing the transparency, explainability and interpretability of machine learning models. Model Explanations can be created either locally, for a single prediction, or globally, for all predictions in the dataset. The SHAP values are based on the Shapley values ϕ_i (Equation 3), which determine a fair share of the payout for a cooperative game. The Shapley value is calculated by summing the weighted marginal contributions of all possible coalitions. This is done by determining the influence of each player $1, \ldots, |N|$ in the coalition of all players N. Every possible coalition of players is S. The size of the coalition is $|S|$, the value function $v()$ contains all possible combinations of all players. The payout for all players in the coalition is $v(N)$. The marginal contribution $(v(S \cup \{j\}) - v(S))$ indicates the increase in payout if the player j joins the game. This is the core of the calculation. Therefore, the Shapley value is the sum of all weighted marginal contributions across all possible coalitions without player j.

$$\phi_j = \sum_{S \subseteq N \setminus \{j\}}^{1} \underbrace{\frac{|S|!(N - |S| - 1)!}{N!}}_{\text{weight of marginal contribution}} \cdot \underbrace{(v(S \cup \{j\}) - v(S))}_{\text{marginal contribution}} \tag{3}$$

The Shapley values fulfil the following properties:

1. Efficiency: The sum of all contributions is the payout
2. Symmetry: Two equal players receive the same payout
3. Dummy: If all marginal contributions are zero, the Shapley value is also zero
4. Additivity: For a game with two value functions $v1$ and $v2$, the Shapley values for the sum of the games can be expressed as the sum of the Shapley values

The naming convention for SHAP values differs from that of Shapley values. In the case of SHAP values, it is features instead of players and predictions instead of payouts. The calculation of the SHAP value function v is not shown in this paper, a detailed description can be found in Molnar (2023). There are several methods for calculating the SHAP value, including the *Kernel SHAP* algorithm and the *Tree SHAP* algorithm, which are compared in this work.

The Kernel SHAP (KS) is a kernel-based estimation approach for Shapley values, inspired by Local Interpretable Model-agnostic Explanations (LIME). It is a model-agnostic method that estimates SHAP values by taking samples of coalitions and performing a weighted linear regression. The linear model is trained and the estimated coefficients of the model are the SHAP values. The Tree SHAP (TS) method is for tree based models such as RF, XGBoost or LightGBM. It is therefore a model-specific method. One advantage of TS is that they require less computing time compared to KS. In addition, it is an exact method, i.e. you get the correct SHAP values and not just estimates, at least as far as the coalitions are concerned. This work considers only the Interventional Tree Estimator, which uses the tree structure to calculate SHAP values. In this case, the estimation is performed by recursively traversing the tree(s) (Molnar 2023).

Building Description

The cooling load prediction data set is generated by simulating a simplified dynamic room model. The room is modelled using two RC elements. All exterior and interior components are combined

into one equivalent element each. The area of the room is 17.5 m^2 and the room has a south facing exterior wall with a window. The exact room model is described in Lauster et al. (2014). The room is modelled using the modelling language *Modelica*. The room model used is the thermal zone with two elements for exterior and interior walls model of the Buildings library version 8.0.0 (Wetter et al. 2014). A full factorial design of the simplified room model, comprising different room surfaces (Table 1) and building characteristics (Table 2), was employed to determine the annual hourly cooling load for 15 552 various room variants. The dataset can be accessed via the GitHub repository.

The outer wall area A_{wall} and the window area A_{win} were varied to generate different room types. The surface properties of the room types are shown in Table 1. The window to wall ratio A_{win}/A_{wall} and the wall area to room volume ratio A_{wall}/V_{room} are varied by adjusting the A_{wall} and A_{win}. The ratio A_{win}/A_{wall} has a major influence on the solar gains and the transmission.

Table 1: Investigated room surfaces

Room type	A_{win}	A_{wall}	A_{win} / A_{wall}	A_{wall} / V_{room}
	m^2	m^2	1	m^{-1}
1	7	3.5	0.67	0.2
2	3.5	7	0.33	0.2
3	7	18.5	0.27	0.49

By varying the building characteristics (see Table 2) and the room surfaces in a full factorial design, the thermal balance in the different room variants changes, in some cases considerably. Due to the wide range of building characteristics, a large number of different building ages and room characteristics can be represented. Figure 1 shows the heat flow in the room, the transmission $\dot{Q}_{trans}$, the ventilation $\dot{Q}_{vent}$, the internal gains $\dot{Q}_{IG}$, the solar gains $\dot{Q}_{solar}$ and the heat storage and release in the thermal mass $\dot{Q}_{TM}$. The required cooling load $\dot{Q}_{cool}$ results from these heat flows.

The internal gains $\dot{Q}_{IG}$ act as convective and radiant heat in the space. They are simplified to the specific internal gains $\dot{q}_{IG}$. The air exchange rate (AER) and $\dot{q}_{IG}$ correspond to the values in Table 2 during the periods of use Monday to Friday from 7 am - 5 pm. Outside of the usage times, AER and $\dot{q}_{IG}$ are 0. The International Weather for Energy Calculations (IWEC) is used for the German cities of Berlin and Stuttgart, which allows different climate zones to be taken into account.

Table 2: Investigated building characteristics

Nr.	U_{wall}	U_{win}	g-value	AER	$\dot{q}_{IG}$
	W/m^2K	W/m^2K	1	h^{-1}	W/m^2
1	0.15	0.8	0.15	0.25	5.1
2	0.25	1.1	0.3	0.5	10.3
3	0.5	1.4	0.45	0.75	15.4
4	0.75	1.7	0.6	1	20.6
5	1	2.1	0.75	2	25.7
6	1.5	2.7	0.9	4	30.9

Results Analysis and Discussion

Thermal Balance

The data set for the cooling load prediction is from 1 June to 15 September (90 days). The training set is from 1 June to 5 August 2023 (72 %) and the test set is from 6 August to 31 August (28 %). Figure 2 shows the cooling energy demand Q_{cooler} for the test set depending on the building characteristics. The cooling energy demand values range from 5.1 to 552.5 kWh with a median of 182.2 kWh. The median values are represented by the olive-coloured line.

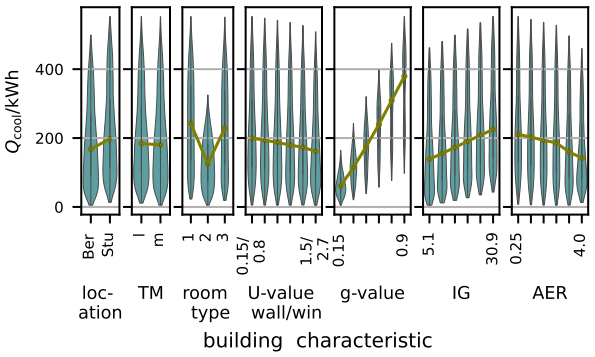

Figure 2: Thermal balance of the various room variants

The combination of a low g-value, low internal gains (IG) and room type 2 (small window area) results in low cooling energy demand values. In terms of solar radiation, the Stuttgart location has a higher $\bar{I}_{sol,so}$ of 86.8 $W\,m^{-2}$ compared to Berlin 77.54 $W\,m^{-2}$. The $\bar{T}_{out}$ are similar, with Stuttgart at 18.84 °C and Berlin 18.58 °C. Due to the higher irradiation, the cooling energy demand Q_{cool} is higher in Stuttgart. The larger window area in room type 1 (7 m^2) compared to room 2 (3.5 m^2) results in a higher Q_{cool}.

An ANOVA is used to determine which building

characteristic has the greatest influence on the cooling load. The F-values are shown in Table 4. All building characteristics have a significant influence on the cooling load ($p < 0.05$). The F-value is the ratio of the variation between sample means to the variation within the samples. The g-value has the largest F-value. Therefore, the variability of the cooling load is most influenced by this factor. The thermal mass has the lowest F-value.

SHAP Values

For the calculation of the SHAP values, we compare the KS and TS algorithm. KS uses a weighted linear regression, while TS uses tree models to determine the SHAP values. In order to select a suitable tree model, the LightGBM, XGBoost and RF variants are compared with each other. The 1 h ahead cooling load prediction uses the three features outside temperature T_{out}, solar irradiance on south-facing vertical surfaces $I_{sol,so}$ and occupancy (occu). Only these three features have a relevant feature importance (FI). Lagged or averaged features were not taken into account in this study. A hyperparameter search was conducted in advance for the models, and the most suitable hyperparameters were selected. Table 3 shows the RMSE and R^2 of the different prediction models for the selected standard room: location Berlin, thermal mass m, room type 2, U-values (wall: 0.75 W m^{-2} K, window: 1.7 W m^{-2} K), g-value 0.45, $\dot{q}_{IG}$ 10.3 W m^{-2} and AER 0.5 h^{-1}.

Table 3: Prediction accuracy for different ML models

Model Type	Train Set RMSE/W	Train Set R^2	Test Set RMSE/W	Test Set R^2
LR	114.4	0.7415	129.3	0.7886
LightGBM	51.4	0.9478	89.2	0.8992
XGBoost	53.3	0.9440	100.2	0.8729
RF	53.0	0.9446	95.8	0.8839

The LightGBM model has the lowest RMSE and the highest R^2 for the test and training set. Therefore, its prediction accuracy is the best. The high R^2 value and the low RMSE value indicate a good prediction quality. Figure 5 shows a section of the time course of the prediction and the actual value. The XGBoost and RF models also achieve similarly good values, while linear regression delivers the worst prediction accuracy. Due to its best prediction accuracy, the TS algorithm uses the LightGBM model.

The LightGBM and TS algorithm were used to calculate the relative proportion of the three SHAP values for each of the 15552 room variants. Figure 3 shows the relative SHAP values as a function of the building characteristics. The median values are represented by the olive-coloured line. For example, higher U-values lead on average to an increasing SHAP value of T_{out} and a decreasing SHAP value of $I_{sol,so}$, whereas an increasing g-value leads on average to a smaller SHAP value of T_{out} and occu and a larger SHAP value of $I_{sol,so}$. The building characteristics are therefore implicitly included in the SHAP values of the cooling load. $I_{sol,so}$ has the highest mean relative SHAP value, followed by T_{out} and occupancy.

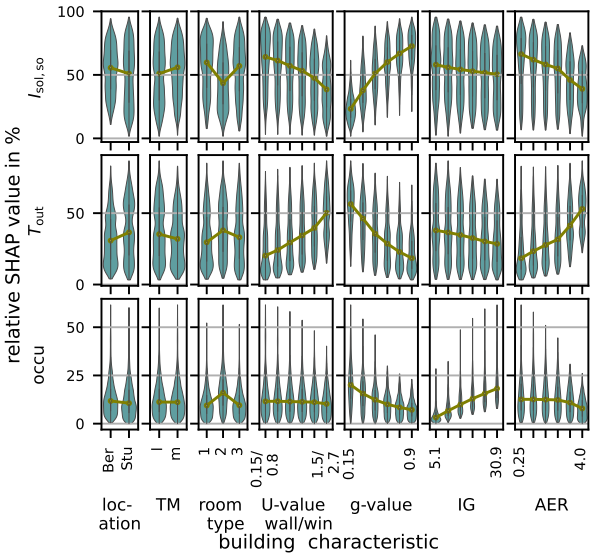

Figure 3: SHAP values depending on the building characteristic

A MANOVA was used to analyse the influence of the building characteristics (independent variables) on the SHAP values (dependent variables). The Wilks Lambda (WL) values of the building characteristics for the individual SHAP values have a similar ranking order as the F-values of the cooling energy demand (refer to Table 4).

A large or small variability of the building characteristics on the cooling energy demand therefore leads to a large or small influence of the relative SHAP values of the features on the cooling load. The building characteristics are therefore implicitly included in the SHAP values. A correlation between global model explainability based on SHAP values and building characteristics has been shown. In addition to

the global consideration (whole dataset), the model explainability can also be performed on a local level. For this purpose, the SHAP values are analysed for each time step.

Table 4: ANOVA and MANOVA of the building characteristics on cooling energy demand and SHAP values

Building Characteristic	Thermal Balance F-value	Thermal Balance Rank	SHAP values WL	SHAP values Rank
location	1152	4	0.8508	3
thermal mass	22	1	0.9280	2
room type	106	2	0.9774	1
U-value	588	3	0.4420	4
g-value	38414	7	0.2707	7
IG	3083	6	0.4072	5
AER	1818	5	0.3460	6

Figure 4 shows the local SHAP values determined with the TS as a function of the feature values for the standard room. The SHAP values increase with the feature values T_{out}, $I_{sol,so}$, and occu. The highest Pearson correlation coefficient r is observed between the occupancy value and the SHAP value of occupancy. There is also a strong correlation between the SHAP value T_{out} and the feature value T_{out}, as well as between the SHAP values $I_{sol,so}$ and the feature values of $I_{sol,so}$. Hence, there is a strong correlation between the three features and the corresponding SHAP values.

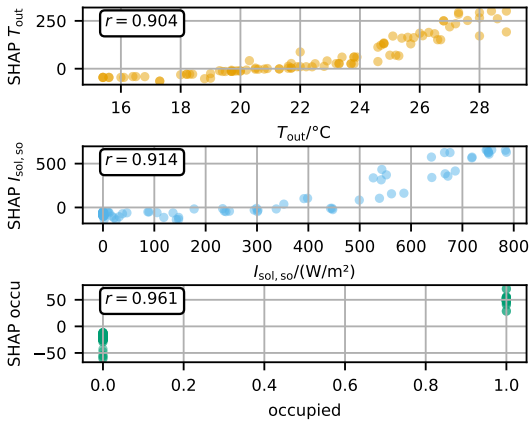

Figure 4: SHAP values depending on the feature values

Figure 5 shows the cooling load $\dot{Q}_{cool}$, local SHAP values and scaled features for two rooms from 6 to 12 August. This makes it possible to visualise the interaction between the individual variables. The LightGBM model with TS algorithm was used. The first room is the standard room 1. Room 2 has the same characteristics as room 1, but has a higher U-value (wall: 1.5 $W m^{-2} K$, window: 2.7 $W m^{-2} K$), a lower g-value (0.15) and a higher internal occupancy (30.9 $W m^{-2}$).

The first subplot shows the cooling load and the predicted cooling load $\hat{\dot{Q}}_{cool}$ for rooms 1 and 2. The predicted value of the cooling load from the LightGBM model is equal to the sum of all SHAP values and the base value, which is the mean value of the prediction over the train set. Subplots 2 and 3 show the local SHAP values of the three features (T_{out}, $I_{sol,so}$ and occu). A negative SHAP value will decrease $\hat{\dot{Q}}_{cool}$ and a positive value will increase it. The absolute sum of the SHAP values for the period from 8 to 12 August is shown under the feature names. A higher value means a greater importance of the feature.

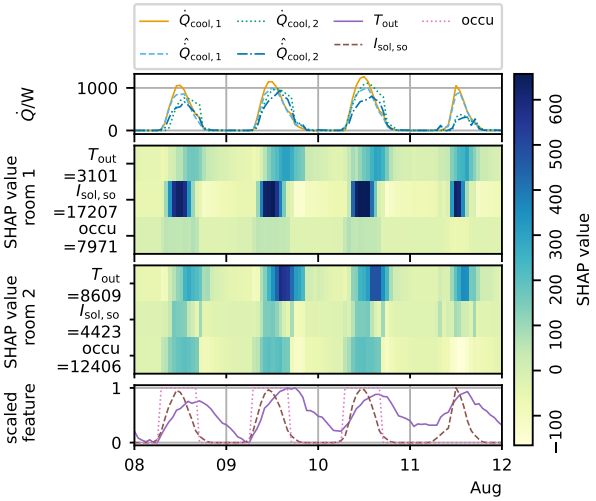

Figure 5: $\dot{Q}_{cool}$ and local SHAP values for two rooms depending on the feature values

The SHAP values are affected by the building characteristics (see Figure 3) and the feature value (subplot 4). Room 1 has a lower U-value, resulting in lower T_{out} SHAP values. The T_{out} SHAP values for room 2 (subplot 3) show a clear difference between the night hours with low T_{out} and the day hours with higher T_{out} values (subplot 4). The g-value of the windows is higher for room 1 at 0.45 than for room 2 at 0.15. This results in significantly higher sums of the absolute SHAP values of $I_{sol,so}$ for room 1. These higher SHAP values can also be seen in the temporal patterns of the local SHAP values of $I_{sol,so}$ (compare subplot 2 and 3). The influence of occupancy can be seen clearly on 11 August. In room 2, with very high internal loads, the cooling load differs significantly between the

days with occupancy (8-10 August) and without occupancy (11 August), while in room 1 the cooling load decreases only slightly on 11 August (subplot 1). The higher differences are also reflected in the SHAP values for occu between room 1 and room 2. There is therefore a correlation between the feature values and the local SHAP values over the course of time.

Comparison SHAP Values with Heat Flows

The following analysis examines whether the local SHAP values can also be used to describe the heat flows in the building. To achieve this, the SHAP values are determined using the TS and the KS algorithm. Figure 6 shows a comparison of the heat flows with the local SHAP values for room 1 during the period from the 8th to the 12th of August (part of the test set). The first subplot shows the cooling load $\dot{Q}_{cool}$ and the predicted cooling load $\hat{\dot{Q}}_{cool}$, which is equal to the sum of all SHAP values and the base value. The second subplot shows the SHAP value of $I_{sol,so}$ and the heat flow of solar radiation $\dot{Q}_{solar}$. The graph of the two variables is similar and the R_2 between $\dot{Q}_{solar}$ and $I_{sol,so}$ value is 0.754 for the TS and 0.602 for the KS.

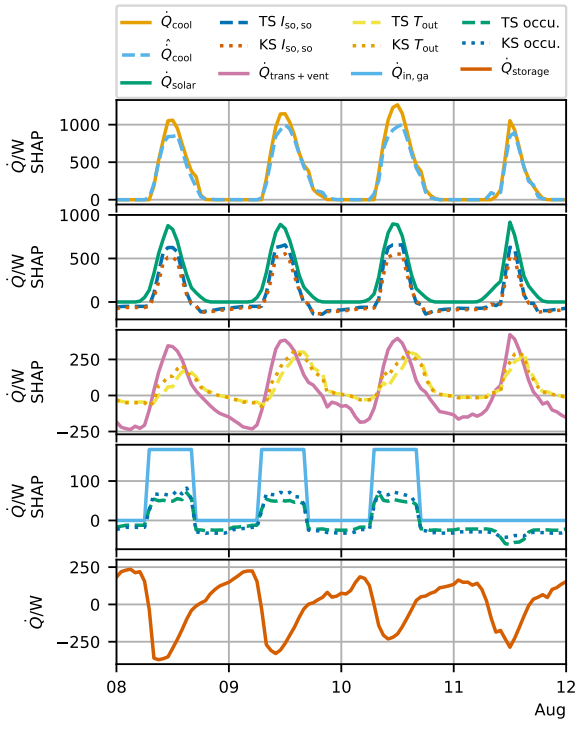

Figure 6: Comparison of SHAP values (Tree SHAP and Kernel SHAP) and the thermal balance

The comparison between the SHAP value of T_{out} and the heat flow of transmission and ventilation $\dot{Q}_{trans+vent}$ (subplot 3) shows a R_2 of 0.444 (TS) and 0.603 (KS). It is important to note that the SHAP values do not represent negative heat flows for $\dot{Q}_{trans+vent}$ at night ($T_{out} < T_{room}$). This is due to the storage and release of energy in the thermal mass $\dot{Q}_{TM}$ (subplot 5), which is not explicitly considered by the selected features and therefore by the SHAP values. This issue is also evident in the internal heat gains $\dot{Q}_{IG}$ (subplot 4), which are poorly represented by the SHAP values of occu, as indicated by the low R_2 values of 0.278 (TS) and 0.169 (KS).

Table 5 presents the R^2 values for the heat flows and the SHAP values for the KS and TS. To investigate the influence of the model prediction accuracy on the prediction accuracy of the SHAP values on the heat flows, the R^2 for the time period (TP) 1 (08-12 Aug) and the TP 2 one week later (15-22 Aug) are examined.

Table 5: Evaluation of the mapping between the heat flows and the courses of the local SHAP values

Energy	SHAP value	Kernel SHAP (KS) TP 1 R^2	Kernel SHAP (KS) TP 2 R^2	Tree SHAP (TS) TP 1 R^2	Tree SHAP (TS) TP 2 R^2
$\dot{Q}_{cool}$	$\hat{\dot{Q}}_{cool}$	0.959	0.898	0.959	0.898
$\dot{Q}_{solar}$	I_{sol}	0.602	0.385	0.754	0.598
$\dot{Q}_{trans+vent}$	T_{out}	0.603	0.309	0.444	0.126
$\dot{Q}_{IG}$	occu	0.278	0.210	0.169	0.141

Notably, in TP2, the R^2 between $\hat{\dot{Q}}_{TM}$ and $\dot{Q}_{stor}$ is lower, resulting in significantly lower R^2 between the heat flows and local SHAP values. Therefore, a good description of the heat flows by the local SHAP values is only achieved if the prediction quality of the ML model reaches good values. The KS has a higher R^2 than the TS in two out of three cases for TP 1 and TP 2. A more accurate description of the heat flows is therefore achieved with the KS, which estimates the SHAP values by using a special weighted linear regression. The calculation time for the KS is 20.960 s, many times longer than that of the TS, which is only 0.012 s.

In general, it can be stated that local SHAP values provide a limited representation of the heat flows. A more accurate representation would require information about the thermal mass properties. A feature that provides information on the temperature of the thermal mass is only realistic in simulations and is therefore

unsuitable. However, it is possible to represent the thermal behaviour of the building using lagged features or sequence-to-sequence models. These models take into account a number of past features to provide multiple step ahead predictions. Furthermore, the validation of the presented method on real buildings is challenging due to the unavailability of heat flow information and the difficulty in determining it. In addition, the simplified occupancy patterns and the consideration of only one room result in a significant simplification. Nevertheless, it has been shown that the local SHAP values can predict the heat flows of a room with satisfactory accuracy using a purely data-driven approach. This provides additional information and insights that can be used to identify optimisation potential for the building.

Summary

Accurate load prediction is crucial for cooling load management, and this can be achieved using ML models, which are black-box models. By using XAI, these models can be made explainable. In this study, SHAP values were used to analyse XAI for the cooling load of 15552 different simulated room variants. Accurate load prediction is crucial for cooling load management, and this can be achieved using ML models, which are black-box models. The SHAP values implicitly contain information about the building characteristics, and the g-values have the greatest discriminatory power on the SHAP values. The influence of features on the room the local SHAP values can satisfactorily represent the heat flows in the room. This provides data-driven insights into the building and can help to identify optimisation potential for the building. However, the selected features did not adequately map the effect of the thermal mass. In further studies, lagged features or sequence-to-sequence models should be used to map the thermal inertia of the building. Based on this, it should be verified whether one of these methods leads to a better mapping of the heat flows by the local SHAP values.

Acknowledgment

This work is funded by the German Federal Ministry for Economic Affairs and Climate Action (BMWK) in the framework of the research program EnOB:ML-EBESR 03EN1076B. The support is gratefully acknowledged.

References

IEA (2023*a*), 'Low-emissions sources of electricity', https://www.iea.org/reports/low-emissions-sources-of-electricity.

IEA (2023*b*), 'Space cooling', https://www.iea.org/reports/space-cooling-2.

Kuzlu, M., Cali, U., Sharma, V. & Güler, Ö. (2020), 'Gaining insight into solar photovoltaic power generation forecasting utilizing explainable artificial intelligence tools', *IEEE Access* **8**, 187814–187823.

Lauster, M., Teichmann, J., Fuchs, M., Streblow, R. & Mueller, D. (2014), 'Low order thermal network models for dynamic simulations of buildings on city district scale', *Building and Environment* **73**, 223–231.

Lundberg, S. M. & Lee, S.-I. (2017), A unified approach to interpreting model predictions, *in* 'Proceedings of the 31st International Conference on Neural Information Processing Systems', NIPS'17, Curran Associates Inc., Red Hook, NY, USA, p. 4768–4777.

Molnar, C. (2023), *Interpreting machine learning models with SAP: a guide with Python examples and theory on shapley values*, first edition edn, Chistoph Molnar c/o MUCBOOK, Heidi Seibold.

Moon, J., Rho, S. & Baik, S. W. (2022), 'Toward explainable electrical load forecasting of buildings: A comparative study of tree-based ensemble methods with shapley values', *Sustainable Energy Technologies and Assessments* **54**, 102888.

Neubauer, A., Brandt, S. & Kriegel, M. (2024), 'Relationship between feature importance and building characteristics for heating load predictions', *Applied Energy* **359**, 122668.

Odukomaiya, A., Woods, J., James, N., Kaur, S., Gluesenkamp, K. R., Kumar, N., Mumme, S., Jackson, R. & Prasher, R. (2021), 'Addressing energy storage needs at lower cost via on-site thermal energy storage in buildings', *Energy Environ. Sci.* **14**, 5315–5329.

Wang, Z., Hong, T. & Piette, M. A. (2020), 'Building thermal load prediction through shallow machine learning and deep learning', *Applied Energy* **263**, 114683.

Wetter, M., Zuo, W., Nouidui, T. S. & Pang, X. (2014), 'Modelica Buildings library', *Journal of Building Performance Simulation* **7**(4), 253–270.

BauSIM 2024 in Wien
23. September – 26. September

From building load profile to district load profile - a comparison of up-scaling methods

Tobias Blanke[1,3], Joachim Göttsche[1], Veronika Richter[2], Jérôme Frisch[2], Bernd Döring[3] und Christoph van Treeck[2]

[1] *Solar-Institute Jülich (SIJ), FH Aachen, Deutschland*
[2] *Institute of Energy Efficiency and Sustainable Building (E3D), RWTH Aachen, Deutschland*
[3] *Institute of Smart Building Engineering (ISBE), FH Aachen, Deutschland*

Abstract

Combining buildings into districts aggregates the diverse peak loads from individual buildings to improve the sizing of new energy supply systems. The non-simultaneity of peak loads (both electric and thermal) is evaluated using simultaneity factors. The simultaneity factor is the maximum of the district load profile divided by the maximum of the individual load profile. As the simulation of individual buildings works very well, this publication aims to present algorithms that calculate the combined load profile of district buildings from individual building load profiles using the simultaneity factor.

Four different methods are presented for this purpose: (Mean) linear scaling of the load profile to a constant mean value, (Ref. P.) scaling to a reference load profile, (N. D.) normal distribution of the load profile to the neighboring time steps and (N. D. Ref.) normal distribution of the difference between the individual building load profiles and a reference profile to the neighboring time steps. All methods take a predetermined simultaneity factor into account to smooth the maximum load peak until this simultaneity factor is met. All methods are applied to measured electrical and thermal load profiles, and the calculation accuracy is compared.

The results show that linear scaling to a reference profile model has the lowest errors. The normal distribution models lead to the lowest fluctuations.

Introduction

Different approaches apply for generating load profiles for buildings and districts of many similar buildings. Figure 1 visualizes four of these approaches. One option (A) can be the generation of synthetic profiles for the district load profile according to BDEW (2017, 2018), or VDI (2021). Afterwards, the district load profile can be down-scaled to the building load profile. This downscaling leads to low fluctuations in the load profiles on the building level.

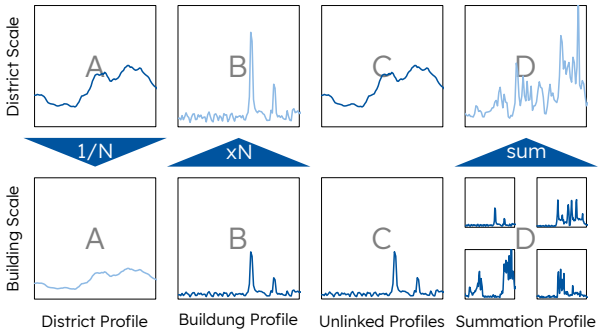

Figure 1: Common Scaling methods

Another option (B) is the use of synthetic load profiles on a building scale using load profile generators such as ISE (2024), Bucher & Andersson (2012), Pflugradt (2023), Uhrig & Müller (2017), Jordan & Vajen (2001), or Koschwitz (2020). In addition to synthetic load profiles, profiles from building energy simulations can be used as well (Stock et al. 2021, Gros et al. 2016, Braas et al. 2020). Subsequently, the building load profile can be upscaled to the district load profile. This simple upscaling of a single profile can lead to high fluctuations on the district-level load profile.

Furthermore (Option C), two synthetic or individually calculated profiles for the building and the district load profile can be used, leading to unlinked profiles.

The last option (D) is to calculate a profile for each building using a dynamic hourly building energy simulation with stochastic components or realistic variability and then sum these up to the district

load profile (Weissmann et al. 2017, Streicher et al. 2020, Delmastro et al. 2017, Kazas et al. 2015, Braas et al. 2020). This approach requires much computational power because every building profile needs to be calculated. Besides, every building needs individual assumptions. Nevertheless, this approach might be the most accurate.

Synthetic profiles like BDEW (2017, 2018), VDI (2021) have the issue of working with averaged data and are hard to individualize at district use cases. The presented literature lacks an approach to scale a building load profile to a district load profile that considers simultaneity.

An option to consider simultaneity is by introducing a factor. The simultaneity factor aims to define the simultaneity of multiple buildings and is defined as the maximum of the district load profile divided by the maximum of the individual load profile (see Eq. 1) (Winter et al. 2001).

$$SF = \frac{\max(P_{district})}{n \cdot \max(P_{building})} \quad (1)$$

Amongst others, this factor can be defined and has been published for electric vehicle charging infrastructure (Stahleder et al. 2021), electrical power systems (Xiaoming et al. 2002), the renewable energy output (Zhu et al. 2022), low voltage distribution grids (De Groot et al. 2012), district heating grids (Winter et al. 2001), and domestic hot water preparation (Braas et al. 2020).

There is a lack of research on models that can combine simultaneity factors with the up-scaling of individual load profiles to district load profiles. This publication introduces four models that can help fill this gap in research. The presented approaches are evaluated on electrical and heating test cases with different time steps. These test cases are based on measured data and include electrical as well as heat profiles.

Methodology

The methodology, the developed approaches and the test cases are visualized in Figure 2. All four models will be tested for all four test cases. Each of the four presented models are evaluated on each of the four test cases, which are further described at the end of the methodology section. The test cases are based on two datasets. The first one is taken from HTW Berlin (HTW) and the second of the Wind-Solar-Heat Pump District (WPuQ)-project (Tjaden et al. 2015, Schlemminger et al. 2022). These models are programmed and validated in a Python package (Blanke 2024). With this validated code the models will be tested using the four test cases including different time resolutions and electrical as well as heating load profiles. The results of the test cases are used to calculate the root mean squared (RMSE) and the mean absolute errors (MAE) as accuracy indicators based on Chai & Draxler (2014). They indicate the error between the scaled and summed-up test data profiles for different number of buildings using all profiles of the test data sets.

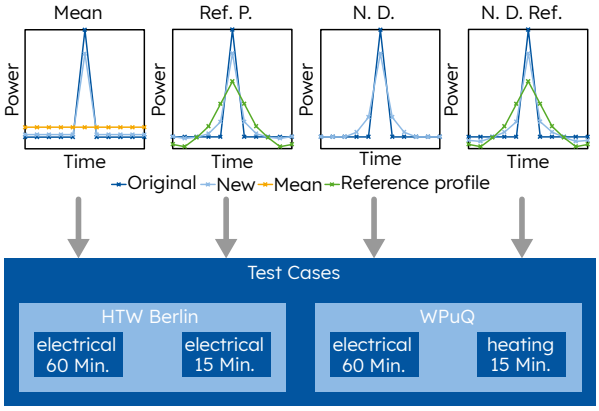

Figure 2: Method visualization

The scaling models presented in this section are expected to fulfill the following requirements. Firstly, the sum and mean values of the scaled profile should remain unchanged during scaling (see Eq. 2). This means that the sum or mean of a scaled profile (P_{new}) representing n buildings should be n times the sum or mean of the original profile. Secondly, the original profile (P_{org}) should be taken as input and then scaled. Lastly, the new profile should satisfy the simultaneity factor (SF) (see Eq. 3) condition. This requirement implies that for all time steps in the new profile, the maximum value should not exceed the maximum value of the original load profile multiplied by the simultaneity factor and the number of buildings.

$$\sum(P_{new}) = n \cdot \sum(P_{org}) \quad (2)$$

$$\max_{\forall t}(P_{new}) = n \cdot SF \cdot \max_{\forall t}(P_{org}) \quad (3)$$

(1) Mean (Mean)

The mean model scales the original load profile (P_{org}) towards mean values of the original load profile (P_{mean}), like the yearly mean or daily mean load. Equation 4 shows the basic equation using scaling factors (S) for the scaling of the new load

profile between the original load profile (P_{org}) and the mean values (P_{mean}). The scaling factor and the mean values vectors do not have the same dimensions as the original load profile vector. Therefore, a function (f) links the original load profile time step to the mean data and scaling factor time step. For example, if daily mean values are used, the first 24 time steps of the hourly resolution original load profile are linked to the first mean value. This daily mean leads to simultaneity factor and mean values vectors of a length of 365 while the original data has a length of 8760 considering hourly data.

$$P_{new}(t) = n \cdot [P_{org}(t) \cdot S(f(t)) + P_{mean}(f(t)) \cdot (1 - S(f(t)))] \quad (4)$$

The scaling factor is calculated based on the maximum value during the mean time frame (i) times the simultaneity factor (SF) minus the mean load divided by the maximum value during the mean-time-steps minus the mean load.

$$S(i) = \frac{SF \cdot \max_{t \in i}(P_{org}(t)) - P_{mean}(i)}{\max_{t \in i}(P_{org}(t)) - P_{mean}(i)} \quad (5)$$

This mean model is advantageous because it is simple and quick to calculate. After determining the maximum of the original load profile, this model mostly consists of linear equations, making the calculation fast and easy. However, the model's disadvantage is the need to select the most appropriate mean time frame.

(2) Reference profile (Ref. P.)

The reference profile model involves scaling the original load profile towards a reference profile (P_{ref}) using a scaling factor (S). However, determining the scaling factor can be challenging as it must ensure that the simultaneity factor constraint remains valid (see Eq. 3). One issue is that the time step at which the maximum values occur changes during scaling. Therefore, a minimization approach is required to address this issue. The aim of this approach is to minimize the absolute error of the maximum of the scaled profile and the target maximal value based on the simultaneity factor constraint (see Eq. 3) by changing the scaling factor (S).

$$P_{new}(t) = n \cdot [S \cdot (P_{org}(t) - P_{ref}(t)) + P_{ref}(t)] \quad (6)$$

The advantages of this model are simplicity and a comprehensible approach for a cleverly chosen reference profile. Disadvantages are the correct selection of the reference profile and the complex selection of the scaling factor, so that the simultaneity factor constraint holds.

(3) Normal distribution (N. D.)

A more complex approach is the normal distribution model. This model is based on the idea of Stock et al. (2021), which shifted the building load profile to different time steps and then summed this shifted load profiles up to a district load profile. Here, the current time step will be normally distributed towards its neighbours. The power is statistically distributed over its neighboring time steps with its variance σ (Blom 1989, Ramasubramanian 1997). Equation 7 explains the normal distribution calculation (ND) for the current time step (t) within its temporally adjacent time step (x).

$$ND(x,t) = \frac{e^{-0.5\frac{(x-t)^2}{\sigma^2}}}{\sqrt{2 \cdot \pi} \cdot \sigma} \quad (7)$$

The problem is that the sum of all temporally adjacent time steps linked to the current time step does not equal the original value. This summation error would violate the summation constraint (see Eq. 2). Therefore, this equation needs to be integrated from the middle of the previous time step to the middle of the following. The integration of the previous equation (NDI) from $x - \frac{\Delta t}{2}$ until $x + \frac{\Delta t}{2}$ leads to the Gauss error function (erf) and is:

$$NDI(x,t) = \frac{\text{erf}\left(\frac{x+\frac{\Delta t}{2}-t}{\sigma \cdot \sqrt{2}}\right)}{2} - \frac{\text{erf}\left(\frac{x-\frac{\Delta t}{2}-t}{\sigma \cdot \sqrt{2}}\right)}{2} \quad (8)$$

This integrated normal distribution (NDI) can then be used to normally distribute all time steps of the original load profile using the following equation 9.

$$P_{new}(t) = n \cdot \sum_{x=t-4\cdot\lfloor\sigma+0.5\rfloor}^{t+4\cdot\lfloor\sigma+0.5\rfloor} NDI(x,t) \cdot P_{org}(x) \quad (9)$$

The summation is constrained to four times the integer part of the variance plus 0.5, as the majority of the integral is concentrated within this region (Blom 1989). The variance (σ) is a variable that needs to be chosen so that the simultaneity factor constraint holds (see Eq. 3). Since this is not trivial, a minimization algorithm is needed here as well. This minimization is performed similarly to the reference model, but it utilizes the variance in place of the scaling factor. In contrast to previous ones, this model reduces the fluctuation for lower simultaneity factor values than the other models. The disadvantage is the complex calculation since the error function (erf) needs to be calculated quite often, which

is a computationally intensive task (Lister & Stone 1995).

(4) Normal distribution and reference profile (N. D. Ref.)

The normal distribution and reference profile model are combined to create a new model in which the difference between the original load profile and the reference profile is normally distributed. This model is shown in the following equation:

$$P_{new}(t) = n \cdot [P_{ref}(t) + \sum_{x=t-4\cdot\lfloor\sigma+0.5\rfloor}^{t+4\cdot\lfloor\sigma+0.5\rfloor} \{NDI(x,t) \cdot (P_{org}(x) - P_{ref}(x))\}] \quad (10)$$

This model combines the low fluctuations of the normal distribution model with the potentially high accuracy of the reference profile model, given a suitable reference profile. However, there is a risk of selecting a suboptimal reference profile, resulting in high computational time and low accuracy. The good news is that this model ensures that the generated profile will converge towards the reference profile for many buildings.

Test cases

Four test cases are defined for the different explained models to determine the accuracy. The Mean approach is performed using hourly and monthly mean values (H & M), resulting in an hourly mean value for each month. This method yields a total of 24 values per day multiplied by 12 months, resulting in 288 values. The first two data sets are 74 representative electrical household load profiles of the HTW Berlin with an hourly and a 15-minute resolution (Tjaden et al. 2015). These data sets contain solely electrical profiles. As heat profiles should also be evaluated, 27 of 38 single family houses of the WPuQ data set are used (Schlemminger et al. 2022). The heating load includes domestic hot water and space heating. These 27 datasets were selected because they have a complete year of measured data for 2019. This test data set uses the electrical household and heat load profiles.

All profiles in this study are adjusted to represent an annual demand of 1 MWh, since this is done for the reference profiles of BDEW (2017) as well. The Ref. P. and N. D. Ref. model require a reference profile. For the electrical profiles, we used the dynamic household (H0) profile of BDEW (2017) as the reference profile. This standard electrical load profile serves as profile for electrical grid suppliers as data basis. The dynamic profile is used since it includes seasonality. The heating test case uses the heat load profile of Hellwig (2003). This profile can be calculated considering different ambient temperatures, the wind influence and the building's insulation level. The used profile is specific for a single-family house with a high insulation building class and does not consider a wind impact. This load profile calculation needs temperature data which is already available in the WPuQ data set. We have used different numbers of buildings/load profiles to display possible changes with the decreasing simultaneity factor for higher numbers of buildings. The numbers of buildings used are 5, 10, 20, 40, 50, and 74 for the HTW data set and 5, 10, 20, and 27 for the WPuQ data set. Additionally, the models presented in this study require a simultaneity factor as input. This factor is calculated by dividing the maximum of the summed-up data for the different numbers of buildings by the maximum of the various profiles in the data set (see Eq. 1).

Results analysis and discussion

Figure 3 shows the results for the test data set of HTW Berlin with an hourly time step resolution. The figure comprises three subfigures, each containing the results of all four models. Figure 3a demonstrates 24-hour electricity load profiles for the four different models, for all buildings of the data set (n=72) with the annually highest value in the middle. Besides the summed up profile of the data basis (Sum), the original profile which is used as basis for the up-scaling times the number of buildings, and the reference BDEW profile are visualized. All new profiles based on the four models remain under the simultaneity factor limit (see Eq. 3) (SF-Limit). The normal distribution model is the only one that cannot accurately approximate the drop at around 16:00. This inability is due to the need for the model to reschedule too much load from the peak hour. The mean and reference profile models exhibit more fluctuations than the normal distribution models.

Figure 3b shows boxplots of the MAE and Figure 3c of the RMSE between the models an the correct summed up value for an annual load of 1 MW h and the four models over a varying number of buildings. Both errors follow the same pattern, with differences only in their magnitude. As the number of

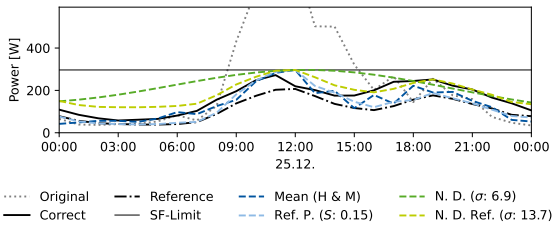

(a) Example load profiles for the annual maximal value

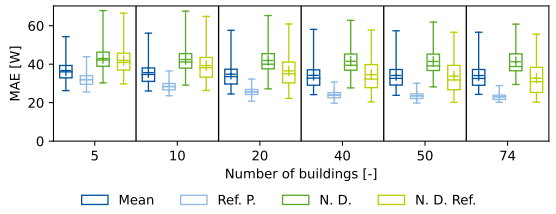

(b) Mean absolute error (MAE)

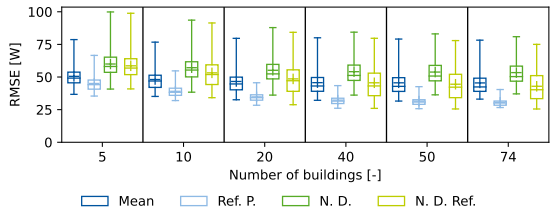

(c) Root mean squared error (RMSE)

Figure 3: Results for the electricity test data set of HTW Berlin with hourly time step resolution

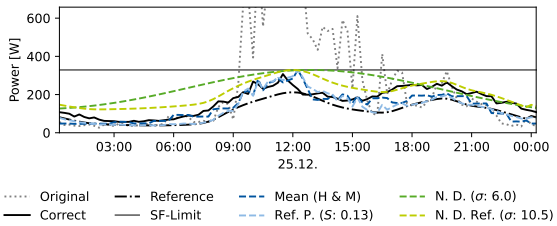

(a) Example load profiles for the annual maximal value

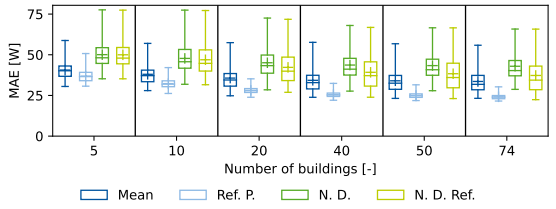

(b) Mean absolute error (MAE)

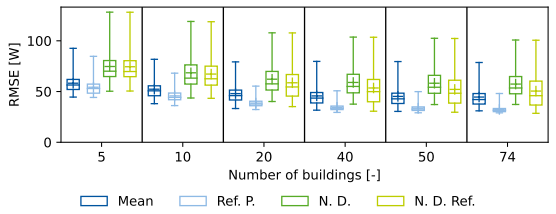

(c) Root mean squared error (RMSE)

Figure 4: Results for the electricity test data set of HTW Berlin with 15 minutes time step resolution

buildings increases, the error decreases. The reference profile model results in the smallest errors. The error reduction rate is lower for the mean and normal distribution model than for the other models. The MAE is between 20 W for the reference profile model and 70 W for the normal distribution model. The RMSE is between 30 W for the reference profile model and 100 W for the normal distribution model.

Figure 4 has the same structure as Figure 3, but for the HTW data with a 15-minute time-step resolution. The example load profiles in the figure display much higher fluctuations than the hourly time step resolution. The normal distribution model is the only model that cannot approximate the load drop at 16:00. However, the mean and reference profile models can approximate the fluctuations better than the normal distribution models. This higher performance is due to the normal distribution models attempting to reschedule the load to the neighboring time steps.

Looking at the errors, the reference model leads to the smallest errors, and both errors have the same shape. Similarly to the hourly resolution, the reference profile model's error decrease faster with the number of buildings than the other models. The MAE is between 30 W for the reference profile model and 80 W for the normal distribution model. The RMSE is between 40 W for the reference profile model and 125 W for the normal distribution model. These errors are slightly higher (3-15 W) than for the hourly resolution data, which leads to the conclusion, that the models perform equivalently for the 15 Minute resolution since this is small compared to the average hourly load of 115 W. The normal distribution with the reference profile model does not lead to significantly smaller errors than the normal distribution model for a number of buildings below 20.

Figure 5 has the same structure as Figure 3 but for the WPuQ electricity data set. The example load profiles figure shows higher fluctuations than the HTW data. Only some new profiles achieve the shape of the summed-up profile (Sum) because the shape of the original profile (Original) is too different.

After examining the MAE and RMSE, it can be found that the reference model had the smallest er-

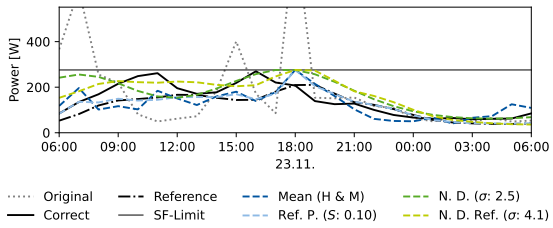

(a) Example load profiles for the annual maximal value

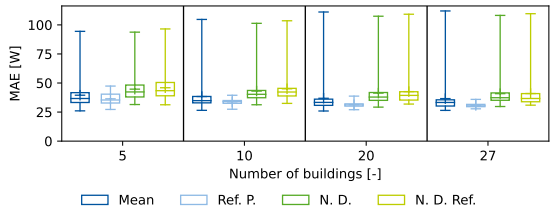

(b) Mean absolute error (MAE)

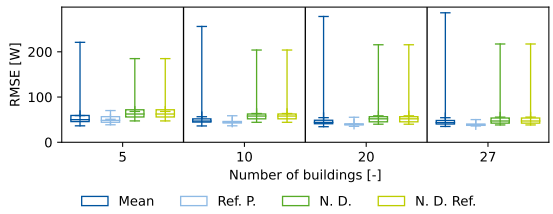

(c) Root mean squared error (RMSE)

Figure 5: Results for the test data set of WPuQ electricity profiles with hourly time step resolution

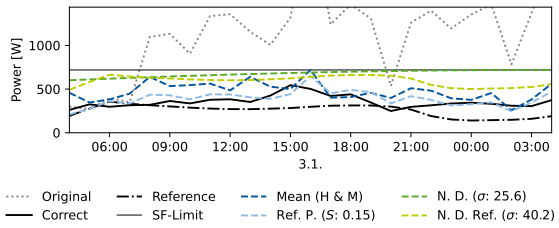

(a) Example load profiles for the annual maximal value

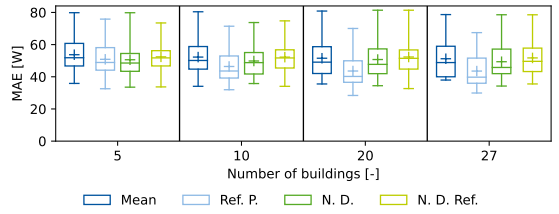

(b) Mean absolute error (MAE)

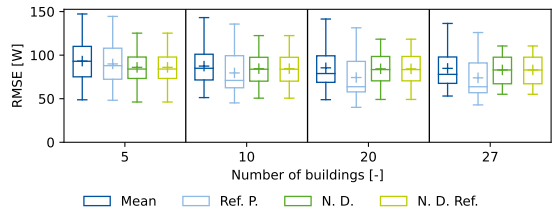

(c) Root mean squared error (RMSE)

Figure 6: Results for the test data set of WPuQ heating profiles with hourly time step resolution

rors, and both errors have the same pattern. Moreover, it can be observed that the normal distribution model with the reference profile did not lead to significantly smaller errors than the normal distribution model. The maximum error was higher than the maximum RMSE and MAEs of the previously shown HTW data calculations. The box (representing the interquartile range between Q1 and Q3) is smaller but in the same range as the HTW data. This smaller box means that most of the data set leads to the same errors.

Figure 6 has the same structure as Figure 5 but for the WPuQ heating profile data set. The example load profiles figure shows lower fluctuation during the day for the day of the maximal load. These low fluctuations are reasonable for heating profiles. The mean and reference profile models can approximate the fluctuations better than the normal distribution models. This better performance is explainable since the normal distribution models try rescheduling the load to the neighboring time steps.

Looking at the errors, the reference model leads to the smallest errors only for a number of buildings higher than 10, and MAE as well as RMSE have the same shape. Like the other data sets, the reference model error decreases with the number of buildings. For a number of buildings below 10 the normal distribution models lead to the lowest errors. In general, the errors are higher than those of the test with the other data sets, which is caused by the shape of the data set profiles.

Conclusion

Studies have demonstrated the availability of various reference profiles for districts, as well as models that can generate load profiles for a certain number of buildings from scratch. However, there is a lack of literature on models that can calculate a load profile for multiple buildings by utilizing an original profile and a simultaneity factor. This factor can be derived from existing literature and restricts the maximum power of the newly generated district load profile.

Three requirements have been established for models capable of up-scaling an original single-building load profile to a district profile. These re-

quirements dictate that the sum and mean should remain unchanged, and the model must accept the original profile as input and limit maximum power to the simultaneity factor multiplied by the maximum value of the original load profile. Four models have been presented that meet these requirements.

The mean model scales the original load profile towards a mean value, such as the yearly mean or daily mean load. The reference profile model scales the original profile towards a reference profile. The normal distribution utilizes a normal distribution to distribute each time step of the original load profile to its neighboring time steps. The normal distribution combined with the reference profile model shifts not the original load profile but the difference between the original load profile and a reference profile to the neighboring time steps, and adds this difference to the reference profile. Four test data sets based on measured data have been defined and evaluated for different numbers of buildings for all four models.

According to the results, the reference profile model exhibited the lowest errors for the electricity data sets. The reference profile model performs better than the other models, particularly for a large number of buildings. The normal distribution model leads to lower error for the heating load data set for a small number of buildings. We recommend using the normal distribution model for heating loads for a low number of same buildings and the reference profile model if a reference profile is available. The normal distribution models result in lower fluctuations, whereas the other models have high fluctuations of the original load profile, particularly for a low number of buildings.

In future research, different test data can be used to validate whether the reference model still performs best for electricity loads and the normal distribution model for heating loads. Furthermore, other models can be developed to scale up load profiles.

Acknowledgement

The project is partly funded by the German Federal Ministry of Education and Research under the funding code 13FH555IX6. The responsibility for the content of this publication lies with the authors.

Abbreviations

f Function link the current time step to the mean time step (-)

HTW Testdatensatz der HTW Berlin (Tjaden et al. 2015)

i All time step in the selected mean time frame (-)

MAE Mean Absolute Error

n number of buildings (-)

ND Normal distribution (-)

NDI Integrated normal distribution (-)

P_{mean} Mean time series of the load profile (W)

$P_{building}$ Building load profile (W)

$P_{district}$ District load profile (W)

P_{new} New time series of the load profile (W)

P_{org} Original time series of the load profile (W)

P_{ref} Reference time series (W)

RMSE Root Mean Squared Error

S Scaling Factor (-)

SF Simultaneity Factor (-)

t Current time step (s)

σ Variance (-)

WPuQ Testdatensatz von Schlemminger et al. (2022)

x Time step within the normal distribution summation (s)

References

BDEW (2017), 'Standardlastprofile Strom'. Accessed on: 16.02.2024.
URL: *https://www.bdew.de/energie/standardlastprofile-strom/*

BDEW (2018), 'Standardlastprofile Gas'. Accessed on: 16.02.2024.
URL: *https://www.bdew.de/energie/standardlastprofile-gas/*

Blanke, T. (2024), 'Time Series Scaling Module'. Accessed on: 16.02.2024.
URL: *https://git.fh-aachen.de/tb5152e/tssm*

Blom, G. (1989), *The Normal Distribution*, Springer New York, pp. 131–146. ISBN: 9781461235668.

Braas, H., Jordan, U., Best, I., Orozaliev, J. & Vajen, K. (2020), 'District heating load profiles for domestic hot water preparation with realistic simultaneity using DHWcalc and TRNSYS', *Energy* **201**, 117552. DOI: 10.1016/j.energy.2020.117552.

Bucher, C. & Andersson, G. (2012), Generation of Domestic Load Profiles-an Adaptive Top-Down Approach, *in* 'PMAPS 2012, Istanbul, Turkey'.

Chai, T. & Draxler, R. R. (2014), 'Root mean square error (RMSE) or mean absolute error (MAE)?', *Geoscientific Model Development (GMD)* **7**(3), 1247–1250. DOI: 10.5194/gmd-7-1247-2014.

De Groot, R. J. W., Morren, J. & Slootweg, J. G. (2012), 'Investigation of simultaneity in distribution networks for the assessment of DA feasibility', *International Universities Power Engineering Conference (UPEC)* . DOI: 10.1109/UPEC.2012.6398428.

Delmastro, C., Martinsson, F., Mutani, G. & Corgnati, S. P. (2017), 'Modeling Building Energy Demand Profiles and District Heating Networks for Low Carbon Urban Areas', *Procedia Engineering* **198**, 386–397. DOI: 10.1016/J.PROENG.2017.07.094.

Gros, A., Bozonnet, E., Inard, C. & Musy, M. (2016), 'Simulation tools to assess microclimate and building energy – A case study on the design of a new district', *Energy and Buildings* **114**, 112–122. DOI: 10.1016/j.enbuild.2015.06.032.

Hellwig, M. (2003), Entwicklung und Anwendung parametrisierter Standard-Lastprofile, PhD thesis, Technischen Universität München.
URL: *https://mediatum.ub.tum.de/doc/601557/601557.pdf*

ISE, F. (2024), 'Individuell, hochaufgelöst und valide. Synthetische Leistungsprofilefür Wohnen und Gewerbe.'. Accessed on: 16.02.2024.
URL: *https://synpro-lastprofile.de/*

Jordan, U. & Vajen, K. (2001), 'Influence Of The DHW Load Profile On The Fractional Energy Savings: A Case Study Of A Solar Combi-System With TRNSYS Simulations', *Solar Energy* **69**, 197–208. DOI: 10.1016/S0038-092X(00)00154-7.

Kazas, G., Fabrizio, E. & Perino, M. (2015), 'Energy Demand Profiles Assessment at District Scale: A Stochastic Approach for a Block of Buildings Demand Profiles Generation', *Energy Procedia* **78**, 3410–3415. DOI: 10.1016/J.EGYPRO.2015.11.610.

Koschwitz, D. (2020), Autoadaptives prädiktives Modell zur Quantifizierung von Gleichzeitigkeitseffekten in Lastverteilungen urbaner Energiesysteme, PhD thesis, Fakultät für Bauingenieurwesen der RWTH Aachen. DOI: 10.18154/RWTH-2020-01982.

Lister, R. & Stone, J. V. (1995), An empirical study of the time complexity of various error functions with conjugate gradient backpropagation, *in* 'Proceedings of ICNN'95 - International Conference on Neural Networks', ICNN-95, IEEE. DOI: 10.1109/ICNN.1995.488101.

Pflugradt, N. (2023), 'LoadProfileGenerator'. Accessed on: 16.02.2024.
URL: *https://www.loadprofilegenerator.de/*

Ramasubramanian, S. (1997), 'The normal distribution: 2. some roles of normality', *Resonance* **2**(7), 27–37. DOI: 10.1007/BF02838588.

Schlemminger, M., Ohrdes, T., Schneider, E. & Knoop, M. (2022), 'Dataset on electrical single-family house and heat pump load profiles in Germany', *Scientific Data* **9**(1). DOI: 10.1038/s41597-022-01156-1.

Stahleder, D., Übermasser, S., Reihs, D., Ledinger, S. & Lehfuss, S. (2021), 'ELECTRIC VEHICLE CAR PARK CHARGING SIMULTANEITY AND GRID CONNECTION POWER REQUIREMENT ANALYSIS', *CIRED 2021 - The 26th International Conference and Exhibition on Electricity Distribution* . DOI: 10.1049/icp.2021.1565.

Stock, J., Hering, D., Xhonneux, A. & Müller, D. (2021), Ecological and economic analysis of low-temperature district heating in typical residential areas, *in* 'Proceedings of Building Simulation 2021: 17th Conference of IBPSA', BS 2021, KU Leuven. DOI: 10.26868/25222708.2021.30154.

Streicher, K. N., Schneider, S. & Patel, M. K. (2020), 'Estimation of load curves for large-scale district heating networks', *IOP Conference Series: Earth and Environmental Science* **588**(5), 052032. DOI: 10.1088/1755-1315/588/5/052032.

Tjaden, T., Bergner, J., Weniger, J. & Quaschning, V. (2015), 'Repräsentative elektrische Lastprofile für Wohngebäude in Deutschland auf 1-sekündiger Datenbasis'. DOI: 10.13140/RG.2.1.5112.0080/1.

Uhrig, M. & Müller, F. R. (2017), 'Lastprofilgenerator zur Modellierung von Wirkleistungsprofilen privater Haushalte'. DOI: 10.5281/ZENODO.803260.

VDI (2021), 'Referenzlastprofile von Wohngebäuden für Strom, Heizung und Trinkwarmwasser sowie Referenzerzeugungsprofile für Fotovoltaikanlagen', *VDI 4655* .

Weissmann, C., Hong, T. & Graubner, C.-A. (2017), 'Analysis of heating load diversity in german residential districts and implications for the application in district heating systems', *Energy and Buildings* **139**, 302–313. DOI: 10.1016/J.ENBUILD.2016.12.096.

Winter, W., Haslauer, T. & Obernberger, I. (2001), 'Untersuchungen der Gleichzeitigkeit and in kleinen und and mittleren Nahwärmenetzen', *Euroheat & Power* .

Xiaoming, L., Weihua, S., Xianggen, Y., Shiqi, L. & Lianmei, Z. (2002), 'The statistical algorithm of simultaneity coefficient based on real-time data of typical consumers from power measurement system', *International Conference on Power System Technology (POWERCON)* . DOI: 10.1109/ICPST.2002.1047183.

Zhu, S., Su, X., Jiang, S., Xie, Y. & He, S. (2022), 'Analysis and Calculation Method of Simultaneity Rate of Renewable Energy Output', *IEEE Advanced Information Technology, Electronic and Automation Control Conference (IAEAC)* . DOI: 10.1109/iaeac54830.2022.9930094.

BauSIM 2024 in Wien
23. September – 26. September

From Building to District: Accelerating Urban Building Energy Modeling with an Open-Source Database for Germany

Amedeo Ceruti[1x], Mara Geske[2x*], Ulla Hartmann[3x], Hartmut Spliethoff[1], Conrad Voelker[2]

1 Technical University of Munich, Germany, E-Mail: amedeo.ceruti@tum.de

2 Bauhaus-University Weimar, Germany, E-Mail: mara.geske@uni-weimar.de

3 Fraunhofer Institute for Systems and Innovation Research, Germany, E-Mail: ullahartmann95@gmail.com

x The labeled authors declare equal authorship. Listed in alphabetical order.

**Corresponding*

Abstract

The ongoing energy transition requires Urban Building Energy Modelling (UBEM) that can analyze energy demand at different spatial scales from individual buildings to entire districts. In this paper, we introduce an open-source, customizable database tailored to the German building stock for the City Energy Analyst (CEA) software. By collecting standard data from different data sources, the authors can speed up the data collection process on an urban scale. As a proof of concept, the database is applied to three use cases of different magnitudes, ranging from individual buildings to districts with hundreds of buildings, by applying a decision tree for UBEM practitioners. All three models are validated with measured heating consumption data and deviate below 25 % in all cases. The proposed decision criteria can help practitioners navigate the modeling process transparently and reproducibly. Although tested in a German context, the proposed database and decision framework warrant broader validation by the UBEM community to validate their applicability in diverse regional contexts.

Introduction

In order to achieve the ambitious EU climate change mitigation goals, the building sector must reduce its greenhouse gas emissions by over 60% by 2030 (Fetting, 2020). This reduction must be achieved in terms of the actual demands and an increasing need for cooling and shifting energy demands due to climate change (Larsen et al., 2020). Accurately modeling and predicting the impact of occupant behavior, the local (micro) climate, and the building envelope on energy demands is instrumental to efficiently plan urban districts to accelerate the rapid transformation of the built environment.

Urban building energy models can simulate the energy demand of city districts and are an invaluable tool for analyzing complex energy systems, ranging from building refurbishments to district cooling network planning. The UBEM process can be divided into three distinct phases within the context of a building energy simulation workflow: data input, thermal modeling, and validation, as depicted in Figure 1. (Reinhart & Cerezo Davila, 2016)

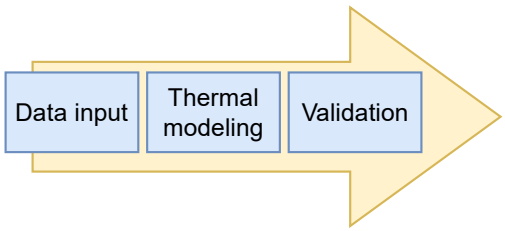

Figure 1: Schematic representation of the UBEM process.

First, the building geometries, envelope properties, use types, energy supply systems, and occupancy profiles are collected in the data input phase. Then, these parameters are used alongside meteorological data to perform the thermal modeling of the district for the investigated time frame. Lastly, the model must be validated against measured data to test its accuracy, where the error interval has been reported between 5 % and 99 % for individual buildings in urban models (Reinhart & Cerezo Davila, 2016).

UBEM tools can be classified into top-down or bottom-up approaches. Top-down approaches estimate the final building energy demand from its relationship with other parameters, such as socio-economic indicators. In contrast, bottom-up models calculate the energy consumption of each individual building, either with statistical, physics-based, or hybrid models. Physics-based

models can be further broken down into heat-balanced physics or reduced-order resistance-capacitance (RC) models. (Ferrando et al., 2020)

The open-source software CEA is classified as a bottom-up, physics-based UBEM. It can calculate energy balances of incoming radiation, external environment interaction, occupancy effects, supply, and HVAC systems of any given building. Accordingly, the specific energy demands and boundary conditions, such as domestic hot water consumption, setpoint room temperatures, or electricity demand of appliances, must defined for each building with so-called use types. (Fonseca & Schlueter, 2015)

A large amount of input data and assumptions are required because of CEA's complex model calculations. This characteristic is challenging for model reproducibility, as Malhotra and colleagues found that 67 % of reviewed UBEM simulations were based on custom "data enrichment" in combination with building archetypes (Malhotra et al., 2022). It is essential to collect the available data and assumptions transparently during the workflow for complete reproducibility.

To address the challenge of lacking or non-standardized input data, we want to introduce an open-source, customizable database tailored to the German building stock for the City Energy Analyst software. The database is designed to be integrated in a fully reproducible process, starting from information collection until energy demand simulation. An accompanying decision tree is developed to help practitioners adapt the German database to their simulation needs.

This work follows the three-step UBEM model structure by Reinhart and Cerezo Davila. In the first data input step, the developed database and decision tree for practitioners are presented. Then, the thermal modeling process of three representative case studies at different spatial scales is described and applied in step two. In the final third step, the models are validated with monitored heating consumption data. The paper concludes with a discussion of the study's results and an outlook on the presented research.

Step 1: Data Input

Three sets of input data are needed to determine the energy requirements of a building with CEA: information regarding the building's archetypes, the assemblies, and the components, depicted in Figure 2. Additionally, geometrical data of the buildings containing building height, stories, and archetype category mapping, the surrounding built environment, and weather data need to be imported. A comprehensive database of the additional data is outside of the scope of the present paper and can be acquired through various open-source tools, such as Open Street Map (OSM) or the German Weather Service (DWD).

The database structure used in this study corresponds to the structure for the software CEA. The Swiss (CH) database was used as a template, which can be used as a first approximation for areas with moderate climate according to the CEA developers (Mosteiro-Romero et al., 2017). For the customization, some specific subcategories as the HVAC systems were adopted directly as default valuese (Figure 2). Other categories were partially modified, and one subcategory was customized as a new database.

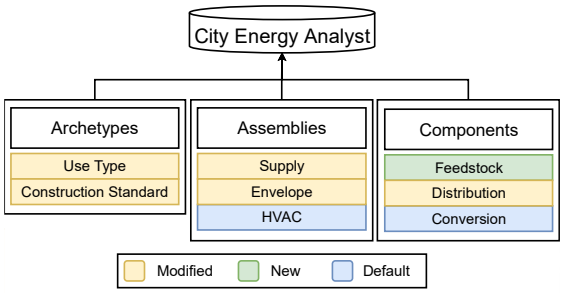

Figure 2: Summary of collected parameters in the Open-Source database.

All assumptions are openly accessible on the City Energy Analyst GitHub page, where the German database can be downloaded and is continuously developed. The overall structure consists of three main datasets. First, the archetypes dataset describes all necessary information on the following two categories:

- **Use type**: Use types cover aspects such as indoor environmental quality, building usage, and occupancy profiles. Ten use types were adapted from the default CEA types to German use by the authors. While standards such as DIN EN 18599 and DIN EN 16789-1:2019 provide valuable parameters for energy performance assessments, it is necessary to develop these norms further to increase their applicability in the German database, because the number of available use types is currently very limited and tailored to multi-zone thermal models.
- **Construction standard:** Construction standards assign envelope, HVAC, and energy supply components. Two broad categories of construction standards are available in the German database: residential buildings based on TABULA and EPISCOPE typologies (Loga et al., 2016) and non-residential buildings based on the recently published IWU typology (Hörner &

Bischof, 2022). Any given archetype is subdivided into three features: building type, age, and refurbishment status (the latter is not available in the IWU dataset). An overview of all available archetypes is presented in Figure 3.

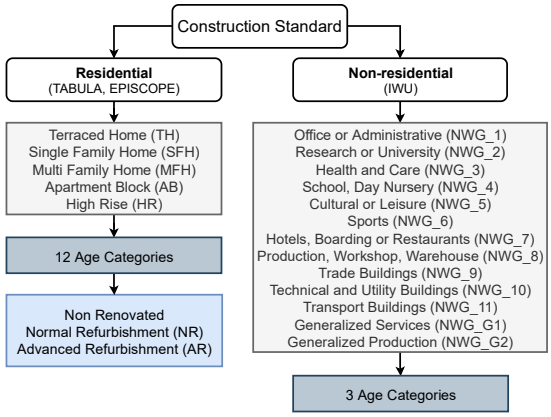

Figure 3: Overview of collected construction standards.

The second dataset, assemblies, defines the technical components of all envelopes, supply, and HVAC systems of any construction standard:

- **Supply systems:** The KEA catalog is used for the supply assemblies due to higher data availability compared to other technology cost databases (KEA-BW, 2023). This data is contrasted and completed with Steinbach et al., 2021. Six key decentral supply technologies: oil, natural gas, and biomass-fired boilers, air/water, and sole/water heat pumps, are available in several sizes.
- **Envelope:** The envelope parameters define the thermal characteristics of the structural building elements, allowing the computation of its energy balance. Archetypes, such as those developed during the TABULA project in Germany (Loga et al., 2016), provide synthesized representations of typical buildings within a specific region. However, existing TABULA archetypes often lack required data categories, including archetypes for non-residential properties and solar radiation-related envelope parameters, and must be completed with assumptions.
- **HVAC:** The information on the HVAC systems is kept as in the Swiss database since available HVAC technologies are largely equivalent to Germany.

The third dataset, components, includes the parameters of the technical subcomponents used for the building energy supply assemblies:

- **Feedstock:** The primary source for the Feedstock subcategory is data on national energy price trends (Statistisches Bundesamt [Destatis], 2023). It is a collection of statistical import, export, producer, and consumer prices for diverse primary and secondary energy types required for the available Supply technologies. Default values from CEA were adopted for the Distribution portfolio for the year 2023 by using a USD inflation rate of 24.9 %.
- **Distribution:** Because no updated values, other than those in the CEA database, were found, the 2015 values were adjusted to the year 2023 using the USD inflation rate of 24.9 %.
- **Conversion:** The information on the conversion technologies is kept as in the Swiss database.

Additionally to the three datasets, a **Decision Tree** is developed including all enrichment steps that need to be documented for reproducibility (see Figure 4). Practitioners are often faced with the challenge of limited information on the necessary parameters for UBEM simulations (Wang et al., 2022), which poses a significant constraint on the modeling process. Furthermore, it is important to consider the relationship between the accuracy of the input data and the resulting simulation results, especially when the simulation requires high-quality outcomes. Additionally, the size of the district can

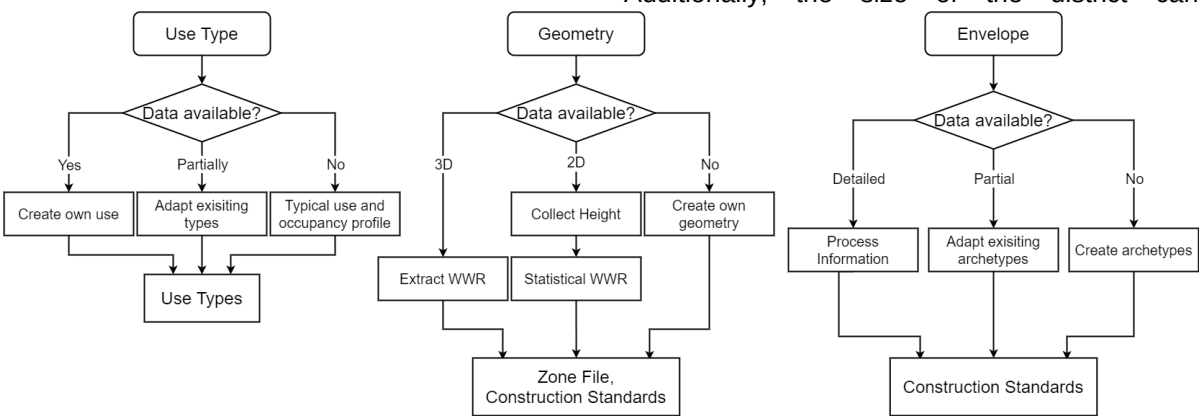

Figure 4: Decision tree to adapt the archetype components of the German database to a UBEM study depending on data availability. Abbreviation: window-to-wall ratio (WWR).

significantly impact the modeler's ability to customize and calibrate building-specific information.

Therefore, a decision tree is proposed to support UBEM practitioners during the essential data acquisition step alongside the German database application. The decision tree illustrated in Figure 4 can be applied to adapt the archetype definition with specific use type information, building geometry information, or envelope information, all of which are defined in the construction standard and use type files.

Use type information can be included by creating custom use types if detailed occupancy and usage data, such as room usage logs, is available. In cases of partially obtainable information, the existing types can be adapted to the known data. In cases of complete absence of data, prototypical uses can be used via existing profiles.

CEA defines building geometries in each district with an enriched shapefile containing the footprints and parameters, including the building heights and stories, as well as construction standard parameters, including window-to-wall ratios. The modeler must collect and assess available data, enriching the raw geometrical features with known information. In the most information-rich case, a detailed 3D geometry is available from which the footprints' shapefile and all necessary descriptive properties can be extracted to define all construction standards and the zone shapefile in detail. Alternatively, 2D geometry is available, e.g., a map, which can be used to define the required information. If no geometric information is available, geometry files must be created manually, and the available German archetypes can be used with no alterations for available building types.

The third and final element of the input files is the building envelope dataset, which contains information about the thermal properties of the building structure. These properties can be defined either with national, local, or individual building stock data. The first case is available in the German database and can be used if there is no detailed information on the district. If some additional information is available, the existing typologies can be combined with known building use type information and refurbishment status, to allow for a customized, archetype-based simulation. In the most data-rich case, data of individual buildings is known, and the parameters can be defined for each individual building. Users should be aware of the presence of special cases, such as special construction types within a given district, that are not contained in the German database by default.

Step 2: Thermal Modeling

The German database can be applied to diverse districts with data availability by following the proposed decision tree. Three UBEM application cases at different urban scales based on the categorization of public energy and urban planning by (Cajot et al., 2017), starting with a use case with a small <10 buildings district scale up to a city with hundreds of dwellings, are presented in this subsection. The case studies are described in the following subsections and summarized in Table 1.

Case Study 1: Building-scale Evaluation of the Heat Supply Transformation for a Residential District

Potential new heat supply alternatives are being evaluated for the modernization of a residential district. Therefore, the energy demand of the residential area was analyzed at different renovation levels (ranging from window replacement to facade insulation) in this study.

The district consists of nine multi-story residential buildings and two garages. These buildings share similar architectural features, an identical, conventional heat supply system, and were built and renovated within a comparable time frame. For all buildings 2D construction plans, type of heat supply, construction year, renovation status, and, partially, the characteristics (windows,

Table 1: Overview of the three analyzed use cases of the open-source German building stock database.

Case study	Building	District	City
Total Buildings	11	299	6,500
Aim	Evaluate heat supply scenarios	Analyze the effects of various input parameters	Municipal energy planning for renewable heating
Data Availability	Detailed	Limited	Statistical, Aggregated
Validation	Aggregated heating consumption (1-3 buildings)	Aggregated consumption data for electricity and gas (4-10 buildings)	Primary-side district heating power demands in 5 min resolution (130 buildings total)

exterior wall) of the building envelope were available.

The required input parameters in CEA were customized based on the aforementioned available 2D geometry data and the information provided by the building owners. Standard values based on the construction year were used for the unknown building envelope components (mostly thermal conductivity) of the roof, floor, and internal walls. The thermal modeling results of CEA were compared with the known consumption-based energy certificates of the buildings for validation. In addition a demand-based energy certificate was created for further validation, following established methodologies for energy performance certification in Germany.

Potential heat supply scenarios of the calculated thermal energy demand were assessed by simulating them with the default supply dataset of German building stock database in CEA. This allows the comparison of factors such as energy efficiency, costs, and CO_2-emissions of heat supply options. The results provide a comprehensive evaluation, enabling a recommendation for a heat supply system for the residential district.

Case Study 2: District-scale Study on the Impact of Parameter Uncertainties

This case study (Geske et al., 2023) aimed to analyze the effect of different input parameters on UBEM simulations. The urban area consists of a town center with 299 buildings in a rural area of Thuringia, Germany. The building stock consists mainly of low-rise residential buildings and is analyzed through a successive data enrichment. Based on the LoD2 geometry available for the whole state of Thuringia, building age and standard data from the German database, the data was enriched in 5 steps:

- Statistical information on the use of rural dwellings, in particular the density of occupancy and the proportion of heated space in the total area
- Vacancy information affecting about 10% of the buildings
- Usage information for a school, a hotel, a restaurant, a city hall and 71 mixed-use buildings (residential + office/retail/shop), covering about 25% of the buildings
- Refurbishment states captured through an energy audit using building archive data, covering approx. 60% of the buildings
- Geometrical adjustment to correct outdated and incorrect information in the open access data of the federal state, affecting about 56% of the buildings

The simulated data was validated using 4 years of aggregated annual heating and electricity consumption data (aggregation of 4-10 buildings). This data was climate corrected and averaged to eliminate possible fluctuations.

Case Study 3: City-scale Decision-making Support for Heating Supply Planning

The heating supply to a city in Bavaria was planned within a research project in collaboration with local stakeholders in this case study. To that end, the heating demand of the whole building stock was calculated with CEA and input into an optimization algorithm to select a cost-optimal renewable energy supply. Complete data unavailability was assumed. Therefore, all used datasets were either open-access or free to use. LoD2 geometry is freely available for the whole federal state in addition to georeferenced addresses, zoning information, and census data from 2011. However, no detailed building-specific information, such as non-residential use category, renovation status, vacant buildings, and building age, was accessible to the modelers. A detailed method to merge and process available information and calculate required parameters in PostgreSQL was used. The CEA archetypes database then maps the relevant archetype to every building to calculate energy balances in hourly resolution for the year 2022.

To validate the model, a project partner supplied primary-side heat exchanger heating power time series for 130 residential buildings in sub-hourly resolution. This information was processed, cleaned, and used as a proxy for the final heating energy demand to validate the heating demand time series.

Step 3: Validation

The German building stock database is validated with available heating consumption or demand data at all three scales, as depicted in Figure 5.

The results obtained at the **building** scale have been compared with the provided consumption-based energy certificates, which aggregate the specific end-use energy of one to three buildings. The CEA model significantly overestimated the validation data, with differences ranging from 0.06% to 35.32%. Overall, an aggregated deviation of 18 % was found. Some apartments have been unoccupied for a certain period, which may have influenced the energy certification process. Therefore, a demand-based energy certificate was created for one of the buildings as an example and compared with the CEA values. The comparison shows a deviation of -1.77 % for

the end-use energy demand and 1.97 % for the primary energy demand. CEA's monthly consumption multiplier was used to calibrate the model for user behavior.

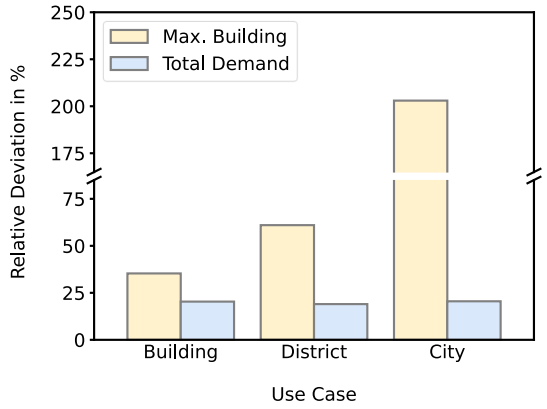

Figure 5: Absolute relative deviation between model output and measured data.

At the **district** scale, the customized scenario simulation results were 19 % higher than the climate-corrected consumption data averaged over three years. The data at this scale was available in aggregated form for small groups of neighboring buildings. For this reason, the maximum deviation shown in Figure 5 is also based on these aggregated values. Notably, most of the comparative values were less than 25 %, with an outlier at 61 % deviation.

The heat demand at the **city** scale was validated for of 130 residential buildings during the year 2022 at an hourly resolution. The measured heat power at the house station heat exchanger does not include possible thermal storage and distribution losses in the buildings. Despite this shortcoming, the model performed reasonably well in the aggregated categories, under-estimating the total yearly consumption by 20.5 % and overestimating the peak demand by approx. 50 %. The total time series accuracy shows a mean squared error of approx. 623 kW, representing 13.4 % of the measured peak demand. The accuracy decreases for individual buildings, where relative deviation from the measured data ranges from 203 % to under 30 %. The largest outlier is caused by overestimating space heating consumption of a small consumer, possibly due to an unknown energy refurbishment status of the building.

Discussion

The proposed open source, customizable database for the German building stock offers great potential for the analyzed district scales of UBEM studies. Four main challenges, encountered across the three case studies' scales, are highlighted in Figure 6.

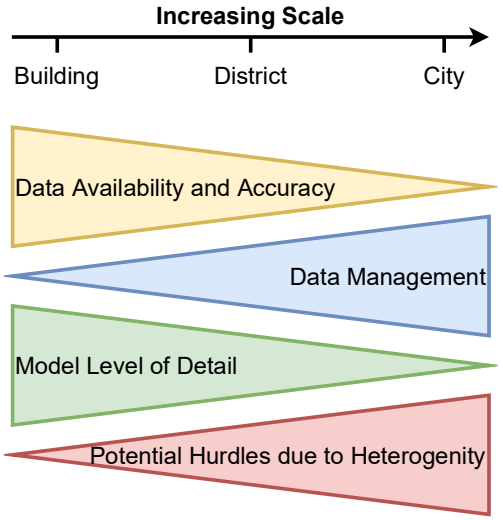

Figure 6: Overview of hurdles for UBEM at different district scales, ranging from building to city.

A high data availability can be expected at the **building** scale, resulting in less unknown building parameters. Inherently detailed and time-consuming survey requirements limit the applicability of the precise data collection method to a few buildings. All the same, a large amount of data is required, since errors do not cancel out due to the aggregation of only a small number of dwellings. Still, a small scale enables a precise calibration of the models to each case, significantly reducing the potential risk of large errors in individual buildings.

At the **district** scale, the access to data and individual building accuracy decrease. As the number of objects increases, effective data management rises in importance because of growing data size. Consequently, the level of detail may need to be reduced, which can increase the exposure to unidentified heterogeneities in the building stock.

Data on the **city** scale is generally scarce, leading to less detailed models. Therefore, a workflow with no data prerequisites and large data management needs must be used and completed with additional, possibly commercial datasets, such as listed addresses. A survey and manual correction of the biggest consumers within the modeled city districts can improve the simulation quality further. Additionally, municipal stakeholders must get involved in reviewing the modeling outcomes providing feedback and helping to navigate the heterogeneous building stock. Data scarcity is especially acute for non-residential buildings, specifically for use type and occupancy profile information, where there is either only low-quality or no information at all for most relevant use categories.

The error potential for any building is higher than the aggregated results regardless of scale due to various factors, including inherently variable user behavior. The simulation process should be regarded as iterative with active stakeholder participation to obtain improved modeling outcomes. This process scales poorly with increasing district size. Therefore, it is essential to have a representative data basis to obtain high-quality results and enable them to reach informed decisions for the studied district energy infrastructure. A workflow with minimum data requisites should be used and incrementally completed with additional information. To that end, a decision tree can be used to navigate this decision-making process with the open-source German building stock database regardless of district size.

Future Research

Using UBEM for the energy transition presents stakeholders and researchers with numerous challenges, opportunities, and open research questions outlined below.

One of the foremost challenges lies in the variability of input data availability across different German regions. This variability was also apparent in the three application examples, spanning various scales, ownership structures, and federal states. There is a need to create methods and strategies to handle incomplete data, which affects more than 67 % of UBEM case studies (Malhotra et al., 2022). Input data collection and management pose additional hurdles, increasing with district scale.

Regardless of their source, input data often exhibit errors, inaccuracies, and anomalies. Unfortunately, descriptions of data quality are often insufficient. Incomplete or outdated data further exacerbate data input complexity, requiring objective strategies to calibrate existing datasets, as demonstrated in the study by (Geske et al., 2024). Model validation, as reported by Reinhart & Cerezo Davila (2016), reveal an agreement within a 7 to 21 % range in aggregated heating loads. All three cases in this study agree with the reported errors. However, individual buildings exhibit substantially higher deviations than aggregated values, highlighting the complexity of accurately modeling energy usage at a micro level.

Addressing these challenges is crucial for the effective application of UBEM within the ongoing energy transition. Continued research and collaboration are essential to develop robust data collection, validation, and privacy protection strategies. There is a great need for additional research and data collection for non-residential buildings in Germany. This includes the development of refurbishment scenarios for the IWU typology, but most importantly, the publication of category-specific use type information and occupancy profiles for almost all relevant non-residential building types, such as hotels and warehouses. The small number of available norms are incomplete and generally aimed at multi-zone models. Additionally, significantly more detailed statistical data on the use type of buildings, as well as their age and refurbishment status are needed. Finally, industrial energy demand cannot be modeled with the currently available data basis in Germany.

Conclusion

The ongoing energy transition requires UBEM frameworks to analyze the energy demand of not only individual buildings, but also districts and cities. This work proposes an open-source, easily customizable database for the German building stock, to accelerate the data collection process. Several data sources were collected and published with the UBEM software City Energy Analyst, enabling practitioners to simulate buildings and districts quickly. In addition, this study compares three different perspectives by examining spatial scales ranging from less than ten buildings up to districts with hundreds of buildings.

The database is validated with measured data. The case studies' workflows were used to propose a set of decision criteria for practitioners to navigate the decision-making process before and during the data input process. Following this workflow, the database and the open-source software might speed up the modeling process and enhance the simulation workflow. The findings need to be further validated to assess their applicability to all regions of Germany.

Acknowledgments

TU München's authors gratefully acknowledge the Federal Ministry for Economic Affairs and Climate Action (Germany) for their funding through the project *Heat2Q* [project no.: 03EN3055A].

Bauhaus-Universität Weimar's authors gratefully acknowledge the Federal Ministry for Education and Research for their funding through the project *smood: smart neighborhood* [project no.: 03WKDH01B].

Availability of Data and Code

The database is open-source and freely available at https://github.com/architecture-building-systems/CityEnergyAnalyst. The UBEM

community at large is invited to validate and develop it further.

References

Cajot, S., Peter, M., Bahu, J.-M., Guignet, F., Koch, A., & Maréchal, F. (2017). Obstacles in energy planning at the urban scale. *Sustainable Cities and Society*, *30*, 223–236. doi.org/10.1016/j.scs.2017.02.003

Ferrando, M., Causone, F., Hong, T., & Chen, Y. (2020). Urban building energy modeling (UBEM) tools: A state-of-the-art review of bottom-up physics-based approaches. *Sustainable Cities and Society*, *62*, 102408. doi.org/10.1016/j.scs.2020.102408

Fetting, C. (2020). *The European green deal* (ESDN report No. 53). https://www.esdn.eu/fileadmin/ESDN_Reports/ESDN_Report_2_2020.pdf

Fonseca, J. A., & Schlueter, A. (2015). Integrated model for characterization of spatiotemporal building energy consumption patterns in neighborhoods and city districts. *Applied Energy*, *142*, 247–265. doi.org/10.1016/j.apenergy.2014.12.068

Geske, M., Benz, A., & Voelker, C. (2024). U-value data on an urban scale: Outlier detection using comparative thermography to improve data quality. *Energy and Buildings,* doi.org/10.1016/j.enbuild.2024.114026.

Geske, M., Engels, M., Benz, A., & Voelker, C. (2023). Impact of different input data on urban building energy modelling for the german building stock. In *Proceedings of Building Simulation: 18th Conference of the IBPSA. Shanghai, China, 04.-06.09.2023, doi.org/*10.26868/25222708.2023.1253

Hörner, M., & Bischof, J. (2022). Building typology of the non-residential building stock in Germany—Methodology and first results. *ECEEE Summer Study Proceedings; European Council for an Energy Efficient Economy (ECEEE): Hyères, France*, 935–944.

KEA-BW. (2023, January 6). *Technikkatalog zur Kommunalen Wärmeplanung*. https://www.kea-bw.de/fileadmin/user_upload/Waermewende/Wissensportal/Technikkatalog_Tabellen_v1.1.zip

Larsen, M., Petrović, S., Radoszynski, A. M., McKenna, R., & Balyk, O. (2020). Climate change impacts on trends and extremes in future heating and cooling demands over Europe. *Energy and Buildings*, *226*, 110397. doi.org/10.1016/j.enbuild.2020.110397

Loga, T., Stein, B., & Diefenbach, N. (2016). TABULA building typologies in 20 European countries—Making energy-related features of residential building stocks comparable. *Energy and Buildings*, *132*, 4–12. doi.org/10.1016/j.enbuild.2016.06.094

Malhotra, A., Bischof, J., Nichersu, A., Häfele, K.-H., Exenberger, J., Sood, D., Allan, J., Frisch, J., van Treeck, C., O'Donnell, J., & Schweiger, G. (2022). Information modelling for urban building energy simulation—A taxonomic review. *Building and Environment*, *208*, 108552. doi.org/10.1016/j.buildenv.2021.108552

Mosteiro-Romero, M., Fonseca, J. A., & Schlueter, A. (2017). Seasonal effects of input parameters in urban-scale building energy simulation. *Energy Procedia*, *122*, 433–438. doi.org/10.1016/j.egypro.2017.07.459

Reinhart, C. F., & Cerezo Davila, C. (2016). Urban building energy modeling – A review of a nascent field. *Building and Environment*, *97*, 196–202. doi.org/10.1016/j.buildenv.2015.12.001

Statistisches Bundesamt. (2023). *Prices: Data on energy price trends*. https://www.destatis.de/EN/Themes/Economy/Prices/Publications/Downloads-Energy-Price-Trends/energy-price-trends-pdf-5619002

Steinbach, J., Popovski, E., Henrich, J., Christ, C., Ortner, S., Pehnt, M., Blömer, S., Auberger, A., Fritz, M., Billerbeck, A., & et al. (2021). *Umfassende Bewertung des Potenzials für eine effiziente Wärme- und Kältenutzung für Deutschland*. https://publica.fraunhofer.de/handle/publica/301057

Wang, C., Ferrando, M., Causone, F., Jin, X., Zhou, X., & Shi, X. (2022). Data acquisition for urban building energy modeling: A review. *Building and Environment*, *217*, 109056, doi.org/10.1016/j.buildenv.2022.109056

BauSIM 2024 in Wien
23. September – 26. September

GreenPV: Untersuchung von Fassadengestaltungsmöglichkeiten mit Photovoltaik und Begrünung

Livio Keiser[1], Gianrico Settembrini[1], Sina Büttner[1], Silvia Domingo Irigoyen[1], Artem Sotnikov[1], Kilian Arnold[1]

1 Hochschule Luzern HSLU, Schweiz, E-Mail: livio.keiser@hslu.ch

Kurzfassung

Durch den Klimawandel werden Hitzewellen häufiger und extremer (NCCS, 2018), dadurch steigt auch die Hitzebelastung in Städten. Begrünungen können den Wärmeinseleffekt mindern, aufgrund des knappen Platzangebots in urbanen Gebieten werden Fassadenbegrünungen immer wichtiger. Auch erneuerbare Energien sollen ausgebaut werden, wodurch sich Fassaden als Standorte für PV-Anlagen anbieten. Das vom Bundesamt für Energie (BFE) unterstützte, zweijährige Forschungsprojekt GreenPV untersucht die Integration von Photovoltaik und Begrünungen an Fassaden. Es wurde der Einfluss von boden- und wandgebundenen Fassadenbegrünungen sowie von opaken und transparenten PV-Fassaden in Bezug auf diverse Aspekte wie Luftqualität, Lärm, Biodiversität, Regenwasserrückhalt, Aussenraumattraktivität, Gebäudebetrieb, Stromproduktion, Ökobilanz (LCA) und Lebenszykluskosten (LCC) analysiert. Mittels IDA-ICE wurden thermische Gebäudesimulationen durchgeführt und mit der an der Hochschule Luzern (HSLU) entwickelten Simulationssoftware Quartierklimamodellierung (QKM) sowie anhand von Messungen der Einfluss der Systeme auf den Aussenraum untersucht. Die Untersuchungen zeigten, dass Fassadenbegrünungen einen positiven Effekt auf das Mikroklima haben, die Schallausbreitung mindern, die Luftqualität verbessern, die Biodiversität fördern und zur Regenwasserretention beitragen. PV-Fassaden erzeugen Strom und weisen dadurch bei einer sinnvollen Anordnung eine positive Ökobilanz und Rentabilität auf. Durch eine Platzierung der PV-Module in verschiedene Orientierungen kann eine Stromproduktion über den gesamten Tag sichergestellt werden. Im Winter kann zudem mit einer südorientierten PV-Fassade mehr Strom produziert werden als mit einer PV-Dachanlage. Aus den Resultaten zeigt sich, dass Fassadenbegrünungen am besten nah am Menschen und dadurch in den unteren Stockwerken wirken. PV-Fassaden hingegen sollten an unbeschatteten Flächen mit einem hohen Stromerzeugungspotential angeordnet werden, was eher in höheren Stockwerken der Fall ist. Somit lassen sich Fassadenbegrünungen und PV-Fassaden gut kombinieren.

Abstract

Climate change leads to more frequent and more extreme heatwaves (NCCS, 2018), which also increases heat stress in cities. Greenery can reduce the heat island effect, and green façades are becoming increasingly important due to the limited space available in urban areas. Renewable energies are also to be expanded, making façades possible locations for PV systems. The two-year GreenPV research project supported by the Swiss Federal Office of Energy (SFOE) is investigating the integration of photovoltaics and greenery on façades. The impact of ground- and wall-mounted green façades as well as opaque and transparent PV façades was analysed in relation to various aspects such as air quality, noise, biodiversity, rainwater retention, outdoor space attractiveness, building operation, electricity production, life cycle assessment (LCA) and life cycle costs (LCC). Thermal building simulations were carried out using IDA-ICE and the influence of the systems on the outdoor space was investigated using the neighbourhood climate modelling (QKM) simulation software developed at Lucerne University of Applied Sciences and Arts (HSLU) as well as measurements. The investigations showed that façade greening has a positive effect on the microclimate, reduces sound propagation, improves air quality, promotes biodiversity and contributes to rainwater retention. PV façades generate electricity and therefore have a positive eco-balance and profitability when arranged appropriately. By placing the PV modules in different orientations, electricity production can be ensured throughout the day. In winter, more electricity can be produced with a south-facing PV façade than with a PV roof system. The results show that green façades work best close to people and therefore on the lower floors. PV façades should be located on unshaded surfaces with a high electricity generation

potential, which is more likely to be the case on higher floors. Green façades and PV façades can therefore be combined well.

Einführung

Mit dem Klimawandel erwarten uns trockene Sommer und mehr Hitzetage (NCCS, 2018). Das zukünftige Klima stellt uns besonders in den Sommermonaten vor grosse Herausforderungen bezüglich der thermischen Behaglichkeit in Innenräumen. Ohne eine massive Reduktion der Treibhausgasemissionen ist in der Schweiz mit einem Anstieg der jahreszeitlichen mittleren Temperatur von 3.3 – 5.4 °C bis zum Ende des 21. Jahrhunderts zu rechnen. Der Klimakältebedarf wird in Wohnbauten so stark ansteigen, dass er in der Bedeutung dem Heizwärmebedarf gleichziehen könnte (Settembrini et al., 2017). Die aktive Kühlung könnte im Gebäudepark Schweiz Einzug halten.

Der Kältebedarf wird vorwiegend dann anfallen, wenn die Solarstrahlung am intensivsten sein wird. Diese zeitliche Koinzidenz spricht dafür, dass der Energiebedarf für die Kühlung durch Stromerzeugung mit PV-Anlagen gedeckt werden kann. In Anbetracht der Energiestrategie 2050 ist ein deutlicher Ausbau der solaren Stromproduktion vorgesehen (von heute 2 TWh auf 34 TWh). PV-Anlagen an Fassaden werden voraussichtlich 10 % bis 20 % dieser Stromproduktion ausmachen.

Klimageräte produzieren Kälte für die Innenräume, führen dabei aber die entzogene Wärme nach aussen. Dieser Wärmeübertrag auf die Aussenluft ist nicht vernachlässigbar und wird den städtischen Wärmeinseleffekt zusätzlich verstärken. Grünflächen sind deshalb zur Hitzeminderung im urbanen Gebiet äusserst wichtig.

Die Gebäudehülle bietet Einsatzmöglichkeiten sowohl für PV-Anlagen als auch für Begrünungen. Es bestehen auch Synergien zwischen den zwei Systemen. Die höhere Effizienz von PV-Modulen aufgrund der Verdunstungskühlung der Pflanzen wurde verschiedentlich bestätigt (Hui & Chan, 2011; Lamnatou & Chemisana, 2015; Köhler et al., 2007; Shafique et al., 2020). PV-Dachanlagen, in Kombination mit einer Dachbegrünung, werden heute bereits oft realisiert.

An Gebäudefassaden sind Zielkonflikte und Trade-Offs vielfältiger. Aus verschiedenen Gründen haben sowohl Begrünungen als auch PV-Elemente bisher keine breite Anwendung gefunden. Der bewusste Umgang mit Fassadenoberflächen als Potential im Hinblick auf den Klimawandel kommt in der heutigen Architektursprache nicht genügend zum Ausdruck.

Hier setzt die Projektidee an. In GreenPV werden die Hemmnisse und die Akzeptanz hinsichtlich des Einsatzes von Begrünungen und PV an Gebäudefassaden untersucht. Es sollen Hinweise zum Einfluss von verschiedenen Fassadensystemen auf das Mikroklima am Gebäude sowie die Energiebilanz im Gebäude geben und diesen dem Potential der Energieerzeugung gegenübergestellt sowie Synergien aufgezeigt werden. Bei der Abwägung der Systeme bzw. bei der Bestimmung der optimalen Fassadengestaltung spielen finanzielle, energetische, gestalterische, soziale und Umweltaspekte eine Rolle. Im partizipativen Diskurs mit und zwischen den relevanten Playern und basierend auf bestehenden sowie laufenden Forschungsprojekten und -erkenntnissen sollen deshalb unter anderem Antworten auf folgende Fragestellungen erarbeitet werden:

- Welches sind die entscheidenden Faktoren, die bei der gesamtheitlichen Optimierung der Gebäudefassade im Hinblick auf den Klimawandel zu berücksichtigen sind?
- Wie kann die Fassade mit PV und begrünten Flächen gestaltet werden, damit ein maximaler Nutzen für Mensch, Energie und Umwelt entsteht?
- Wie kann die ermittelte, multifunktionale Fassade in das Gebäude integriert und wie kann deren Anwendung im Gebäudepark gefördert werden?

Systemgrenzen und Annahmen

Betrachtete Fassadensysteme

Folgende Fassadensysteme wurden in der Studie GreenPV untersucht:

- Bodengebundene Fassadenbegrünung *Hedera helix* (Efeu), Wuchshöhe 12 m
- Wandgebundene Fassadenbegrünung Vliessystem mit Mischpflanzung aus heimischen Stauden
- PV-Fassade mit opaken Modulen (Wirkungsgrad 20 %)
- PV-Fassade mit transparenten Modulen (30 % Transparenz, Wirkungsgrad 11 %)

Klimadaten und Szenarien

Als Klimadaten in dieser Studie wurde die Periode 2060 und das Szenario RCP 8.5 verwendet, was einem extremen Treibhausgasszenario entspricht. Dadurch kann die Bedeutung und das Potential von Begrünungsmassnahmen und PV-Systemen verdeutlicht werden.

Standort

Für die Betrachtung wurde ein städtischer Raum gewählt, da dieser Kontext vom Klimawandel künftig besonders stark betroffen sein wird

(Settembrini et al., 2017). Als Referenzstandort dient die Stadt Zürich (Station Zürich Kaserne). Der Standort ist für das Schweizer Mittelland repräsentativ. Die in den Simulationen verwendeten Klimadaten berücksichtigen den städtischen Wärmeinseleffekt.

Quartier und Gebäude

Es wurde ein fiktives Quartier in einem städtischen Kontext betrachtet. Dabei wurden drei Referenzgebäude (Neubau, sanierter Altbau, Altbau) untersucht, wobei der Neubau doppelt so hoch ist wie der Altbau und der sanierte Altbau (Abbildung 1). Dies widerspiegelt den in urbanen Räumen vorhandenen Unterschied der Gebäudehöhe von Alt- und Neubauten.

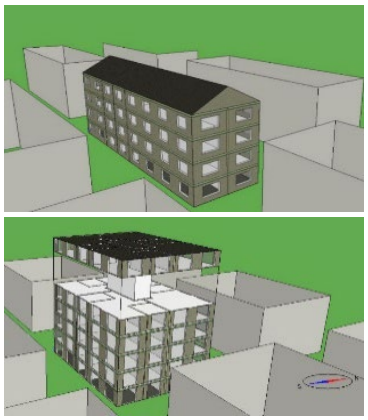

Abbildung 1: Die verwendeten Referenzgebäude, oben der Altbau / sanierter Altbau, unten der Neubau

Methoden

Die Untersuchungen der Studie wurden mittels qualitativer und quantitativer Analyse durchgeführt, wobei in diesem Paper der Fokus auf die quantitativen Untersuchungen gelegt wird.

Bei der qualitativen Analyse wurde eine umfangreiche Literaturrecherche durchgeführt, bei welcher folgende Aspekte untersucht wurden:

- Lärm in Städten
- Luftqualität
- Biodiversität
- Regenwasserrückhalt
- Attraktivität der Aussenräume

Für die quantitative Analyse wurden Gebäudesimulationen und verschiedene Berechnungen durchgeführt.

Thermische Gebäudesimulationen (IDA-ICE)

Die Evaluierung des energetischen und thermischen Potentials von Begrünungs- und PV-Systemen erfolgte primär anhand der Software IDA-ICE 4.8. Dieses Programm erlaubt die Quantifizierung von wesentlichen Kenngrössen der Betriebsenergie von Gebäuden auf Stufe Nutz- und Endenergie sowie der thermischen Behaglichkeit der verschiedenen Modellzonen. Zudem konnten damit Aussagen zur Stromproduktion durch die Installation von PV-Modulen an der Fassade gemacht werden. Die Stromerzeugung der PV-Fassade wurde in zwei Schritten berechnet. Zunächst wurde die einfallende Sonnenstrahlung mit IDA ICE berechnet. Dies wurde sowohl unter Berücksichtigung der Beschattung durch die umliegenden Gebäude als auch ohne Beschattung durchgeführt. In einem zweiten Schritt wurde mit Modelica die Stromerzeugung pro Geschoss und Orientierung berechnet.

Die folgenden Bewertungskriterien wurden mit Hilfe der Simulationen berechnet:

- Thermisches Wohlbefinden im Innenraum: Temperatur und Überhitzungsstunden
- Betrieb des Gebäudes: Wärme-, Kälte- und Stromverbrauch
- Solarpotential und Stromproduktion der PV-Fassade

Bei den verschiedenen Kriterien wurden immer nur die jeweils relevanten Fassadensysteme (PV oder Begrünung) betrachtet.

Berechnung Ökobilanz (LCA)

Die Ökobilanzierung erfolgte gemäss Merkblatt SIA 2032 «Graue Energie – Ökobilanzierung für die Erstellung von Gebäuden» (SIA, 2020). Die Berechnungen wurden anhand der KBOB-Liste «Ökobilanzdaten im Baubereich» (KBOB, ecobau und IPB, 2022) durchgeführt und beinhalten die nicht erneuerbare Primärenergie (Pene), die Treibhausgasemissionen (THGE) und Umweltbelastungspunkte (UBP).

In einem ersten Schritt wurde die Ökobilanzierung für alle Fassadensysteme sowie für die PV-Anlage durchgeführt. In einem zweiten Schritt wurde die Betriebsphase der Referenzgebäude mitberücksichtigt. In dieser Betrachtung ist vor allem die Stromproduktion über die PV-Anlagen von Bedeutung. Durch den Stromertrag reduziert sich einerseits der Verbrauch von Netzstrom, andererseits wirkt sich der ins Netz eingespeiste Strom positiv auf die Bilanz aus (die Umweltbelastung wird von der Gesamtbelastung des Gebäudes abgezogen).

Berechnung Lebenszykluskosten (LCC)

Ziel der Wirtschaftlichkeitsrechnung ist es, Kosten und Rentabilität der analysierten Fassadensysteme zu vergleichen. Die Analyse wurde anhand der dynamischen Methode der Norm SIA 480 «Wirtschaftlichkeitsrechnung für Investitionen im Hochbau» (SIA, 2016) durchgeführt. Diese Methode berücksichtigt, dass die jährlichen Ausgaben und die Einnahmen während der Betrachtungsperiode variieren können. Der Zeitwert des Geldes wurde dazu miteinbezogen. Diese Methode ermöglicht es, Zahlungsströme mit unterschiedlichen Laufzeiten und Zinssätzen vergleichbar zu machen. Die Wirtschaftlichkeit der untersuchten Fassadensysteme wurde durch die Berechnung der Lebenszykluskosten über eine Betrachtungsperiode von 30 Jahren ermittelt. Die Wirtschaftlichkeitsrechnung berücksichtigt nicht nur die Investitionskosten, sondern auch die mit dem Investitionsprojekt zusammenhängenden quantifizierbaren Ausgaben (Instandsetzung, Unterhalt und Energiekosten) und Einnahmen (Einspeisevergütung). Monetär nicht erfassbare Werte, wie bspw. Komfort, Ästhetik, Sicherheit oder weitere qualitative Aspekte, werden hier nicht behandelt und müssen ausserhalb der Wirtschaftlichkeitsrechnung in den Investitionsentscheid einbezogen werden.

Quartierklimamodellierung QKM

Die Auswirkungen der Fassadensysteme auf den Aussenbereich wurden mit der Simulationssoftware Quartierklimamodellierung untersucht. Das Tool Quartierklimamodellierung (QKM) wurde vom Institut für Gebäudetechnik und Energie (IGE) der Hochschule Luzern (HSLU) entwickelt. Mit der Software können relevante Parameter wie die PET (physiological equivalent temperature, Deutsch: physiologisch äquivalente Temperatur), die Luft- und Oberflächentemperatur, die Luftgeschwindigkeit, die Solarstrahlung und die Verdunstungsleistung berechnet werden. Dabei werden Verschattung, kurz- und langwelliger Strahlungsaustausch, Luftströmungen, Wärme- und Feuchtetransport durch Wand- und Bodenelemente und der Feuchtehaushalt der Bepflanzung berücksichtigt und mit Klimadaten im Raum und über längere Zeitperioden berechnet.

Die Simulation wurde mit Klimadaten für den Standort Zürich Fluntern im Jahr 2020 an einem Hitzetag durchgeführt. Als Simulationsmodell wurde ein fiktives, urbanes Quartier definiert (Abbildung 2). Das Gebäude in der Mitte wurde mit den verschiedenen Fassadensystemen ausgestattet, deren Einfluss auf den Aussenraum untersucht wurde. Die Details zu den verwendeten Eigenschaften der Fassadensysteme sind im Schlussbericht von GreenPV ersichtlich.

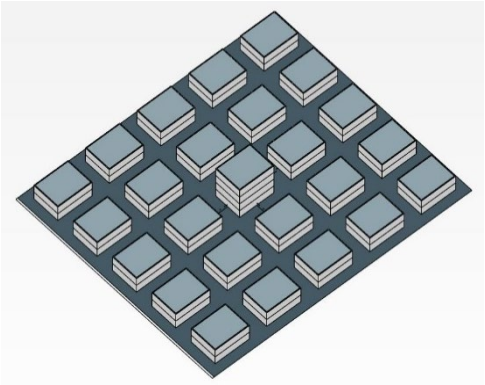

Abbildung 2: Simulationsmodell QKM

Messungen

Im Rahmen des Projekts wurden neben Literaturrecherchen und Simulationen ebenso Messungen an realen Fassadenprototypen durchgeführt (Abbildung 3). Dabei wurde der Einfluss der verschiedenen Systeme auf die Oberflächentemperatur untersucht. Die Messungen wurden auf dem HSLU-Campus in Horw an einer Südfassade durchgeführt.

Abbildung 3: Messstände mit unterschiedlichen Fassadenprototypen

Ergebnisse

Qualitative Resultate

Begrünungen können die Schallausbreitung im Strassenraum mindern (Wong et al., 2010), die Luftqualität positiv beeinflussen (Manso et al., 2021), die Biodiversität fördern (Pfoser, 2016) und führen zu Regenwasserretention (Melzer & Herfort, 2020). Die Attraktivität des Aussenraums kann durch Begrünungen und PV positiv beeinflusst werden, da beide Systeme als architektonisches Gestaltungsmittel eingesetzt werden können. Durch Begrünungen wird zudem auch die Aufenthaltsqualität verbessert, was die Attraktivität des Aussenraums zusätzlich steigert (Classen & Bunz, 2018).

Quantitative Resultate

Fassadenbegrünungen können im Sommerhalbjahr einen positiven Einfluss auf die Innenraumtemperatur und die Anzahl Überhitzungsstunden nehmen, was auch den Klimakälte- und den Klimakälteleistungsbedarf senkt. Dieser Effekt ist bei einem Altbau grösser als bei einem Neubau oder sanierten Altbau, da die Fassade weniger gut gedämmt ist. Im Winter kann durch Fassadenbegrünungen der Heizwärme- und Heizwärmeleistungsbedarf eines schlecht gedämmten Altbaus wegen der zusätzlichen Dämmung gesenkt werden. Bei einem Neubau mit einer gut gedämmten Hülle und einem hohen Fensterflächenanteil führt die Begrünung aufgrund der Beschattung und der dadurch verminderten solaren Einstrahlung zu einem leichten Anstieg des Heizwärme- bzw. des Heizwärmeleistungsbedarfs.

Die Höhe des Stromertrags der PV-Fassade hängt von dem Wirkungsgrad der Module, der Orientierung und einer möglichen Verschattung ab. PV-Fassaden können vor allem an Flächen ohne Verschattung und in den Orientierungen Süd, Ost und West (in dieser Reihenfolge) einen hohen Stromertrag erzielen. Eine Südfassade produziert zwar über ein Jahr gesehen weniger Strom als eine Dachanlage, im Winterhalbjahr (Oktober bis Februar) liefert eine PV-Anlage ohne Verschattung an der Südfassade jedoch mehr Strom als auf dem Dach. Im Tagesverlauf betrachtet liefert eine PV-Fassade ostexponiert am Morgen und westexponiert am Nachmittag am meisten Strom. Eine Südfassade erzeugt über den ganzen Tag hinweg Strom, mit dem Peak am Mittag.

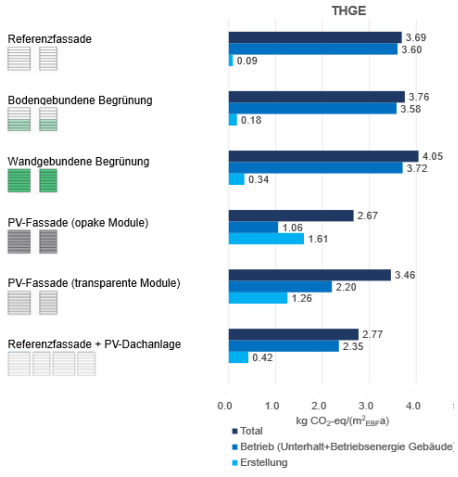

Abbildung 4: Treibhausgasemissionen der Referenzfassade, der verschiedenen Fassadensysteme sowie der PV-Dachanlage (inkl. Referenzfassade). Dargestellt sind die Ergebnisse für das Referenzgebäude «Neubau». Die Ergebnisse bezüglich der nicht erneuerbaren Primärenergie und der Umweltbelastungspunkte verhalten sich ähnlich.

Werden die Umweltbelastungen (THGE, PEne und UBP'21) betrachtet, welche bei der Erstellung, dem Unterhalt und im Betrieb der Fassadensystem anfallen, schneiden die PV-Systeme aufgrund der hohen Gewinne im Betrieb am besten ab. Die Fassadenbegrünungen (bodengebunden und wandgebunden) weisen über den Lebenszyklus gesehen nur geringfügig höhere Umweltbelastungen auf als die Referenzfassade (Abbildung 4).

Bezüglich den Initial- und den Lebenszykluskosten (LCC) erweist sich die wandgebundene Fassadenbegrünung als das klar teuerste System. Die bodengebundene Fassadenbegrünung weist im Vergleich tiefere Kosten auf, ebenso wie die Referenzfassade, welche die niedrigsten Investitions- und Unterhaltskosten aufweist. Die PV-Fassade weist hingegen deutlich höhere Investitions- und Unterhaltskosten auf als die Referenzfassade und die bodengebundene Fassadenbegrünung, jedoch kann die PV-Fassade mit opaken Modulen die anfänglichen Kosten durch Einsparungen im Betrieb und die Vergütung der Einspeisung von Strom ins Netz wieder amortisieren. Somit sind von den Fassadensystemen aus wirtschaftlicher Sicht opake PV-Module mit einem hohen Wirkungsgrad zu bevorzugen (Abbildung 5). Einzig eine PV-Anlage auf einem Flachdach ist noch rentabler.

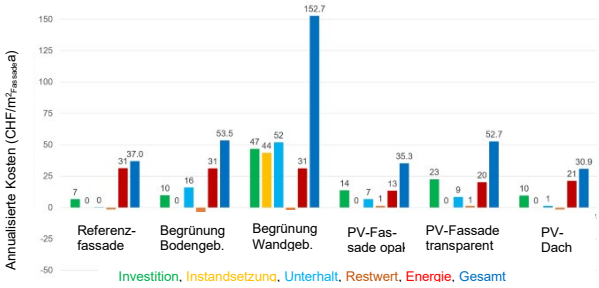

Abbildung 5: Annualisierte Kosten (Barwert) der Referenzfassade, der verschiedenen Fassadensysteme und der PV-Dachanlage (inkl. Referenzfassade) über einen Betrachtungszeitraum von 30 Jahren, dargestellt sind die Ergebnisse für das Referenzgebäude «Neubau».

Messergebnisse

An einem milden Sommertag weist die opake wie auch die transparente PV-Fassade höhere Oberflächentemperaturen auf als die Messreferenzfassade. Die Begrünungen hingegen senken die Oberflächentemperatur im Vergleich zur Messreferenzfassade um 13.9 °C (bodengebundene Begrünung) und 14.9 °C (wandgebundene Begrünung). Die Temperaturen an der Gebäudefassade hinter den Fassadensystemen werden dabei von allen Fassadensystemen durch die Beschattung gesenkt. Bei der bodengebundenen

Begrünung ist der Effekt von der Blattdichte abhängig.

Im Winter verhalten sich die PV-Fassaden bezüglich den Oberflächentemperaturen ähnlich wie die Messreferenzfassade, während die Fassadenbegrünungen die Temperaturschwankungen durch tiefere Tageswerte und höhere Nachtwerte minimieren. Die Gebäudefassade hinter den Fassadensystemen ist im Winter bei allen Systemen durch die Verschattung tagsüber und die zusätzliche Dämmung in der Nacht weniger Temperaturschwankungen ausgesetzt.

Einfluss auf das Mikroklima (QKM)

Fassadenbegrünungen beeinflussen auch die PET in der näheren Umgebung positiv. Die wandgebundene Begrünung hat im Vergleich zu den anderen untersuchten Fassadensystemen den grössten Effekt auf die PET (Abbildung 6) und den grössten Einflussbereich auf Arealebene.

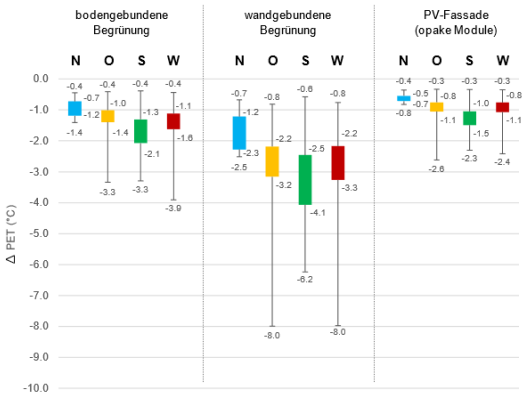

Abbildung 6: Einfluss der verschiedenen Fassadensysteme auf die PET an einem Messpunkt in 1 m Abstand zur Fassade, dargestellt ist die PET-Differenz im Vergleich zur Referenzfassade an einem Hitzetag.

Der kühlende Effekt ist dabei direkt an der Fassade am stärksten spürbar und nimmt mit zunehmendem Abstand zur Fassade ab (Abbildung 7). Die Wirkung der Fassadenbegrünung wird durch verschiedene Faktoren beeinflusst, so ist der Effekt unter direkter Sonneneinstrahlung grösser, während Wind den Kühleffekt der Begrünung mindert. Im Vergleich zu anderen Begrünungselementen wie Bäumen ist der Effekt einer Fassadenbegrünung jedoch geringer. Dies liegt insbesondere daran, dass ein Baum neben dem kühlenden Effekt (Verdunstungskühlung) ebenso Schatten spendet, wodurch die PET zusätzlich gesenkt wird. Im Gegensatz zu Fassadenbegrünungen benötigen Bäume jedoch viel Platz, welcher in einer Stadt oft nicht vorhanden ist.

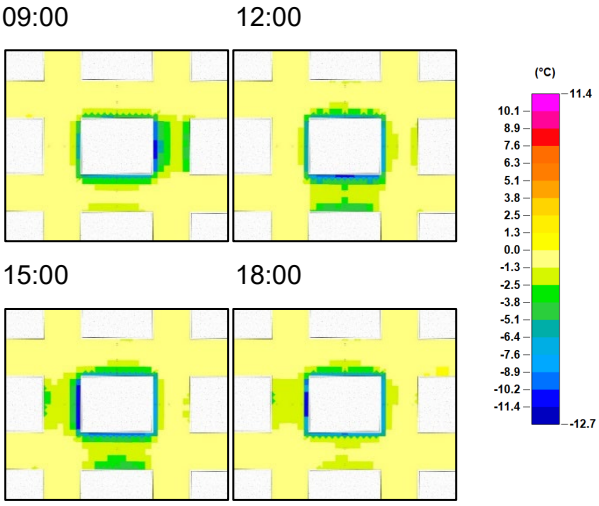

Abbildung 7: Einfluss der wandgebundenen Begrünung auf die PET im Areal. Dargestellt ist die PET-Differenz im Vergleich zur Referenzfassade zu verschiedenen Tageszeiten an einem sonnigen Sommertag (Hitzetag). Annahme: kein Wind, Abstand zwischen den Gebäuden: 11.60 m.

Die Messungen zeigten, dass PV-Module zwar höhere Oberflächentemperaturen aufweisen, jedoch hat dies keinen negativen Einfluss auf das Mikroklima. Die PET in der Umgebung wird durch PV-Module sogar leicht gesenkt.

Diskussion

Systemkombinationen

Begrünungen können insbesondere einen qualitativen Mehrwert im Aussenraum leisten, hinzu kommt das Potential zur Hitzeminderung, welches insbesondere in Städten mit Blick auf den Klimawandel immer mehr an Bedeutung gewinnen wird. Aber auch die Stromerzeugung über PV-Fassaden wird in Zukunft immer wichtiger werden und eine wertvolle Massnahme zur nachhaltigen Energieversorgung der Schweiz darstellen. Durch eine Kombination von PV und Begrünung an der Fassade könnten die Vorteile beider Systeme miteinander vereint werden.

Fassadenbegrünungen erzielen nahe am Menschen angeordnet den grössten Effekt, was in den meisten Fällen in den unteren Geschossen des Gebäudes der Fall ist. PV-Module sollten hingegen an Fassadenflächen mit hohem Stromerzeugungspotential angeordnet werden, also an Süd-, Ost- und Westfassaden ohne Verschattung. Dies betrifft meist die oberen Geschosse des Gebäudes, da insbesondere in städtischen Gebieten die unteren Geschosse oft durch Nachbargebäude verschattet werden. Dies zeigt, dass sich die Systeme in der Regel nicht konkurrenzieren und sich Systemkombinationen aus Begrünungen in den unteren Stockwerken und PV-Anlagen in den oberen Stockwerken anbieten.

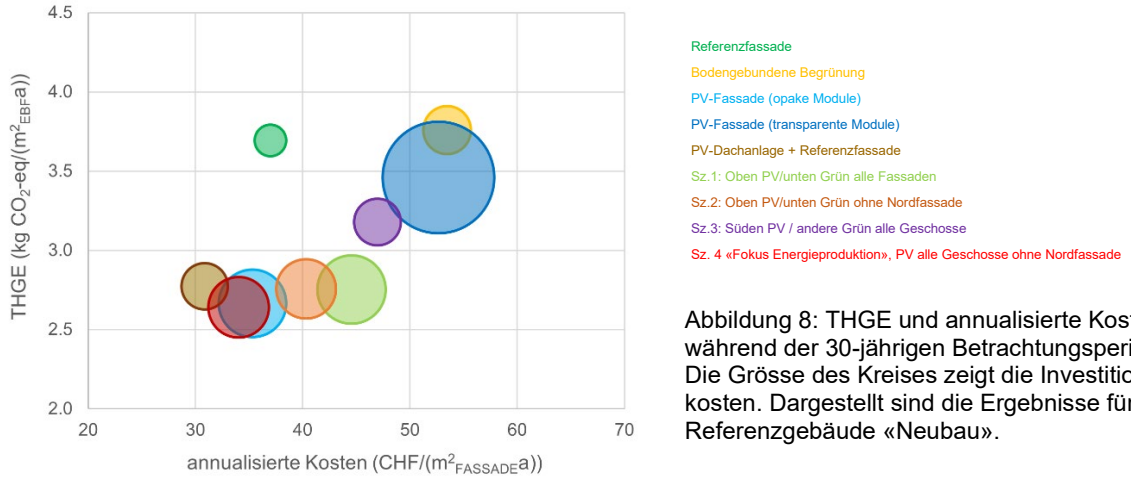

Abbildung 8: THGE und annualisierte Kosten während der 30-jährigen Betrachtungsperiode. Die Grösse des Kreises zeigt die Investitionskosten. Dargestellt sind die Ergebnisse für das Referenzgebäude «Neubau».

Aus diesem Grund wurden mehrere Szenarien mit beiden Fassadensysteme kombiniert im Hinblick auf Ökobilanz und LCC untersucht. Die Ergebnisse zeigen, dass es bezüglich der Ökobilanz vorteilhafter ist, sämtliche Fassaden mit PV-Modulen zu belegen. Dies aufgrund der Stromproduktion, welche zu hohen Einsparungen im Betrieb führt. Die Kombinationen aus Begrünungen und PV weisen zwar eine schlechtere Ökobilanz auf als nur PV, im Vergleich zur Referenzfassade weisen sie jedoch eine niedrigere Umweltbelastung auf. Eine Betrachtung der annualisierten Kosten (Barwert) der untersuchten Kombinationen über 30 Jahre zeigte, dass eine Ausstattung der Ost-, Süd-, und Westfassade mit PV zu niedrigeren Gesamtkosten führt, als wenn die gesamte Fassade (auch Nordfassade) mit PV ausgekleidet wird. Die tiefsten annualisierten Gesamtkosten weist jedoch ein Szenario mit einer PV-Dachanlage und einer Referenzfassade auf. Die Kombinationen mit bodengebundenen Fassadenbegrünungen und PV-Fassaden verursachen höhere annualisierte Gesamtkosten als die Referenzfassade.

Vergleicht man die Resultate der Ökobilanz und der annualisierten Kosten (Abbildung 8), kann gesagt werden, dass durch eine gezielte Anordnung von PV bzw. durch die Kombination von PV und Begrünung an der Fassade die THGE über den Lebenszyklus im Vergleich zur Referenzfassade gesenkt werden können (ökologische Vorteile). Gleichzeitig führt eine Kombination von PV und Begrünung über den Lebenszyklus nur zu geringen Mehrkosten.

Einfluss der PV-Module auf das Mikroklima

Wie in den Resultaten aufgezeigt, haben PV-Module einen positiven Einfluss auf das Mikroklima, trotz der höheren Oberflächentemperaturen. Der Grund dafür ist, dass ein Teil der einfallenden Solarstrahlung in Strom umgewandelt wird und die Oberfläche über einen geringen Albedo-Wert verfügt.

Hemmnisse und Massnahmen zur Steigerung der Akzeptanz von Begrünungen und PV im Fassadenbereich

Bei den Begrünungen stellen die hohen Initialkosten sowie die zusätzlichen Pflege- und Instandhaltungskosten ein Hemmnis dar. Bei den PV-Fassaden sind die grössten Hemmnisse neben den Investitionskosten der erhöhte Planungsaufwand und die geringere Produktion als auf dem Dach. Mit einer guten Planung, einer langfristigen Betrachtung (Berücksichtigung der Amortisierung) und mit finanziellen Anreizen durch Fördergefässe können die anfänglichen Kosten jedoch gemindert werden. Bezüglich der Planung kann die in diesem Projekt erstellte und öffentlich zugängliche Broschüre eine gute Orientierungshilfe bilden, welche aufzeigt, was bei PV und Begrünungen im Fassadenbereich in den verschiedenen Phasen zu beachten ist. Auch durch den Denkmalschutz sind Begrünungen und PV-Module an gewissen Fassaden nicht möglich. Es bietet sich bei solchen Gebäuden jedoch an, Begrünungen an nicht sichtbaren Bereichen, wie z.B. Innenhöfen, zu platzieren. Sowohl bei Brandschutz als auch beim Denkmalschutz lohnt sich die frühe Kontaktaufnahme mit den zuständigen Behörden.

Zusammenfassung

Fassadenbegrünungen mindern die Schallausbreitung im Strassenraum, verbessern die Luftqualität, fördern die Biodiversität und tragen zur Regenwasserretention bei. Ebenso tragen Gebäudebegrünungen zur Aufenthaltsqualität und zur Attraktivität der Aussenräume bei. PV-Fassaden erzeugen Strom und weisen bei einer sinnvollen Anordnung eine positive Ökobilanz wie auch positive Lebenszykluskosten auf. Bezüglich der Kosten und der Umweltauswirkungen ist bei den Begrünungen ein bodengebundenes System einem wandgebundenen vorzuziehen. Begrünungen wie auch PV-Fassaden haben einen positiven Effekt auf die PET in der Umgebung,

wobei die wandgebundene Begrünung den deutlich grösseren Effekt hat als die bodengebundene Fassadenbegrünung und die PV-Fassade. Verglichen mit horizontalen Grünflächen und Bäumen verfügen Fassadenbegrünungen zwar über eine kleinere Kühlleistung, können jedoch an Orten mit knappen Platzverhältnissen angewandt werden.

Um die Stromproduktion über den gesamten Tag sicherzustellen und dadurch den Eigenverbrauch zu erhöhen, ist es sinnvoll, PV-Module an Süd-, Ost- und Westfassaden an nicht beschatteten Flächen zu platzieren. Im Winter kann mit einer südorientierten PV-Fassade mehr Strom produziert werden als mit einer PV-Dachanlage. Je höher die Stromproduktion im Betrieb, desto schneller können die anfänglichen Umweltauswirkungen amortisiert werden und desto grösser ist der ökonomische Vorteil über den gesamten Lebenszyklus betrachtet. Sowohl eine PV-Fassade als auch eine PV-Dachanlage kann die anfängliche Umweltbelastung durch die Erstellung amortisieren und führt über den Lebenszyklus zu geringeren Umweltbelastungen als die reine Referenzfassade.

PV-Fassaden sollten aus ökologischen und ökonomischen Gründen an Flächen mit dem grössten Stromerzeugungspotential platziert werden. Dies sind Süd-, Ost- und Westfassaden ohne Verschattung, was in Städten in den höheren Geschossen der Fall ist. Begrünungen leisten nahe am Menschen den grössten Mehrwert, wodurch eine Platzierung in den unteren, in Städten oft beschatteten Geschossen Sinn macht. Daher lassen sich Begrünungen und PV-Anlagen bei sorgfältiger Planung an Fassaden gut kombinieren.

Danksagung

Das Projekt GreenPV mit der BFE-Vertragsnummer SI/502400-01 wurde durch das Bundesamt für Energie BFE subventioniert und durch die Steiner Lab Foundation, das Amt für Hochbauten der Stadt Zürich und durch die Dienststelle Umwelt und Energie der Stadt St. Gallen ko-finanziert.

Für den Inhalt und die Schlussfolgerungen sind ausschliesslich die Autoren des Berichts verantwortlich.

Literatur

Classen, T., & Bunz, M. (2018). Einfluss von Naturräumen auf die Gesundheit – Evidenzlage und Konsequenzen für Wissenschaft und Praxis.

Hui, S. C., & Chan, S. C. (2011). Integration of green roof and solar photovoltaic systems. Proceedings of Joint Symposium 2011: Integrated Building Design in the New Era of Sustainability.

KBOB, eco-bau und IPB. (2022). Ökobilanzdaten im Baubereich 2009/1:2022. Abgerufen am 22. Mai 2023 von https://www.kbob.admin.ch/kbob/de/home/themen-leistungen/nachhaltiges-bauen/oekobilanzdaten_baubereich.html

Köhler, M., Wiartalla, W., & Feige, R. (2007). Interaction between PV-systems and extensive green roofs. Proceedings of the 5. annual international greening rooftops for sustainable communities conference.

Lamnatou, C., & Chemisana, D. (2015). A critical analysis of factors affecting photovoltaic-green. Renewable and Sustainable Energy Reviews.

Manso, M., Teotonio, I., Silva, C., & Cruz, C. (2021). Green roof and green wall benefits and costs: A review of the quantitative evidence.

Melzer, D., & Herfort, S. (2020). Der Biotopflächenfaktor 2020 - Abschluss- und Gesamtbericht zweier Studien zur Anpassung des Berliner Planungsinstrumentes an den aktuellen Stand der Wissenschaft und Technik.

NCCS, N. C. (2018). CH2018 - Klimaszenarien für die Schweiz. Zürich.

Pfoser, N. (2016). Fassade und Pflanze. Potenziale einer neuen Fassadengestaltung.

Settembrini, G., Domingo-Irigoyen, S., Heim, T., Jurt, D., Zakovorotnyi, A., Seerig, A., . . . Menti, U.-P. (2017). ClimaBau – Planen angesichts des Klimawandels: Energiebedarf und Behaglichkeit heutiger Wohnbauten bis ins Jahr 2100. Bundesamt für Energie (BFE No. SI/501318-01).

Shafique, M., Luo, X., & Zuo, J. (2020). Photovoltaic-green roofs: A review of benefits, limitations, and trends. Solar Energy.

SIA. (2016). Norm SIA 480. Wirtschaftlichkeitsrechnung für Investitionen im Hochbau. Zürich: Schweizerischer Ingenieur- und Architektenverein.

SIA. (2020). SIA Merkblatt 2032. Graue Energie – Ökobilanzierung für die Erstellung von Gebäuden. Zürich: Schweizer Ingenieur- und Architektenverein.

Wong, N. H., Kwang Tan, A. Y., Tan, P. Y., Kelly, C., & Wong, N. (2010). Acoustics evaluation of vertical greenery systems for building walls.

BauSIM 2024 in Wien
23. September – 26. September

IEA HPT Annex 61 – Simulation von Wärmepumpen in Plusenergiequartieren

Carsten Wemhöner[1], Fabian Ochs[2], Christina Betzold[3], Franziska Bockelmann[4], Joris Zimmermann[4]

1 Institut für Energietechnik, OST Ostschweizer Fachhochschule, Schweiz, E-Mail: carsten.wemhoener@ost.ch

2 Arbeitsbereich für Energieeffizientes Bauen, UIBK Universität Innsbruck Baukonstruktion, Österreich, E-Mail: fabian.ochs@uibk.ac.at

3 Energie Campus Nürnberg, Technische Hochschule Nürnberg, Deutschland, E-Mail: Christina.Betzold@th-nuernberg.de

4 siz energieplus, Deutschland, E-Mail: franziska.bockelmann@siz-energieplus.de

Kurzfassung

Annex 61 mit dem Titel "Wärmepumpen in Plusenergiequartieren (PEQ)" im Wärmepumpenprogramm der IEA (IEA HPT Annex 61) untersucht den Einsatz von Wärmepumpen (WP) in hocheffizienten Gebäuden und Quartieren, was auch die Transformation bestehender Quartiere zu PEQ einschließt. Die Untersuchungen werden durch Simulationen für verschiedene Phasen des Planungsprozesses unterstützt. Für eine Bewertung im frühen Planungsstadium wird ein vereinfachtes Simulationswerkzeug für Laststrukturen von Ein- und Mehrfamilienhäusern sowie Bürogebäuden entwickelt. Damit können archetypische PEQ hinsichtlich Integration unterschiedlicher Gebäudelasten mit der WP, erneuerbarer Energieerzeugung und Wärmequellen analysiert werden und Varianten hinsichtlich der Potentiale bzw. der Lücke zur Erreichung eines PEQ bewertet werden. Darüber hinaus werden generische WP-Konzepte vom Einzelgebäude bis zur Quartiersebene entwickelt, die in die Kategorien (1) vollständig dezentrale WP-Einbindung auf Einzelgebäudeebene, (2) rein elektrische WP-Integration, z.B. zur Erhöhung des Eigenverbrauchs, (3) Integration auf Wärmequellenseite, z.B. gemeinsame Wärmequelle oder Mehrquellensysteme, (4) Kombination von zentraler und dezentraler (Booster-)WP und (5) vollständig zentrale WP-Einbindung gruppiert wurden. Aus Simulationen und Monitoring im realen Betrieb dieser WP-Konfigurationen werden Leitlinien für die Integrationsmöglichkeiten der WP sowie für Auslegung und Regelung, auch im Hinblick auf energetische Flexibilitätspotenziale, abgeleitet. Im Beitrag werden ein Überblick und Ergebnisse aus den Teilnehmerländern des Annex 61, die bereits vorliegen, sowie ein Ausblick präsentiert.

Einleitung

Der Klimaschutz ist eine der größten Herausforderung für die Menschheit. Das globale Kohlenstoffbudget zur Einhaltung des im Pariser Abkommen festgelegten 1.5 °C-Ziels wird bei derzeitigen CO_2-eq.-Emissionen je nach Berechnung in weniger als 5-10 Jahren erreicht. Daher sind dringend Anstrengungen in allen Bereichen zur Reduktion der Treibhausgasemissionen erforderlich, und viele Städte haben bereits den Klimanotstand ausgerufen. In vielen Ländern weltweit spielt der Gebäudepark eine Schlüsselrolle bei der Reduktion der CO_2-eq.-Emissionen, da insbesondere der Gebäudebestand eine schlechte energetische Qualität aufweist. Andererseits können Gebäude dadurch auch zu einer schnellen Emissionsreduktion beitragen. Die EU hat mit der Neufassung der EPBD-Richtlinie (2018) zur Gesamtenergieeffizienz von Gebäuden seit dem 1. Januar 2021 auf Einzelgebäudeebene Nahe-Nullenergie-Gebäude (nZEB) für Neubauten vorgeschrieben. Das Konzept von Plusenergiequartieren (PEQ) markiert eine Verlagerung vom Einzelgebäude auf die Quartiersebene, um die Anstrengungen zu verstärken und das Tempo der Energiewende zu beschleunigen. Es wird als eine der zentralen Säulen für die städtischen Energiewende in Europa entwickelt. Die Europäische Kommission hat die SET-Plan-Action 3.2 "Smart Cities and Communities" lanciert. Das Hauptziel der Action 3.2 ist die Entwicklung integrierter und innovativer Lösungen für die Planung, den Einsatz und die Vervielfältigung von PEQ. Laut der Aktion sollen bis 2025 100 PEQ in konkreter Planung, im Bau oder im Betrieb sein, die synergetisch mit dem Energiesystem in Europa verbunden sind. Die Joint Programming Initiative Urban Europe JPI UE hat ein Booklet zu 61 dieser PEQs veröffentlicht (JPI UE, 2020a).

Durch Pilotprojekte, die im Rahmen des Programms Horizont 2020 finanziert werden, unterstützt die Europäische Kommission eine breite Einführung von PEQs. Seit der Umsetzung der SET-Plan Aktion 3.2 gibt es eine wachsende Zahl von Positive Energy Districts (PED)-orientierten Initiativen und Projekten sowohl auf EU- als auch auf nationaler Ebene. Die JPI UE veröffentlichte ein ebenfalls ein White Paper zu PED (2020b), das einen Definitionsrahmen von PED enthält. Der Rahmen zielt darauf ab, eine gemeinsame Vision in ganz Europa hinsichtlich PEDs zu schaffen.

Überblick zum Annex 61

Vor diesem Hintergrund untersucht der Annex 61 im IEA Wärmepumpenprogramm die Anwendung von Wärmepumpen (WP) für Gebäudecluster und PEQ. Der Schwerpunkt liegt dabei auf kleineren Gebäudeclustern und Quartieren, hauptsächlich mit Wohn- und Büronutzung. Während sich die Mehrzahl der Projektbeiträge auf neu gebaute Cluster konzentriert, befassen sich einige Projekte auch mit Strategien zur Verbesserung der Energieeffizienz bestehender Quartiere, um sie näher an eine Null-Energie-/Emissions-Bilanz zu bringen. Neben der einzigartigen Effizienz von WP und der Fähigkeit, verschiedenen Gebäudedienstleistungen Raumheizung (RH)/ Warmwasserheizung (TWW) und Raumkühlung (RK) inkl. Entfeuchtung sogar gleichzeitig bereitzustellen, sind WP auch eine Schlüsseltechnologie zur Verknüpfung von PV-Strom vor Ort und des Heiz-/ Kühlbedarfs in Quartieren. Die Vorteile der WP-Integration in Quartieren sind also vielfältig. Um die Potenziale von WP zu bewerten, sind vier Arbeitspakete (AP) geplant:

- Auf der Grundlage der Analyse des Stands der Technik im AP1 zur Nutzung von WP in bereits bestehenden Gebäudeclustern oder PEQ werden die Konzepte zusammengestellt. Als wesentliche Einschränkungen für Cluster/PEQ ergeben sich die Gebäudelast, die Wärmequellensituation und das PV-Elektrizitätserzeugungspotenzial. Als Key Performance Indicators (KPI) und Designoptionen dienen der Gebäudeenergiebedarf (neu, renoviert, TWW), der Haushaltsstrom (Geräteauswahl), Typ der Wärmequelle (Luft. Erdreich, Wasser) und das PV-Potenzial für Eigennutzung und Netzbezug/-einspeisung. Als KPI dienen zusätzlich die CO_2-Emissionen und optional die Primärenergie auf Basis monatlicher Faktoren, die Netzinteraktion als Spitzenlast/ -einspeisung und die wirtschaftliche Bewertung durch Investitions- und Lebenszykluskosten. Die Auswertung von Lastprofilen wird über Simulationen unterstützt, wie im nächsten Abschnitt dargestellt.
- In AP2 werden aus der Konzeptanalyse generische WP-Konzepte vom Einzelgebäude bis zur Quartiersebene entwickelt, die in die Kategorien (1) vollständig dezentrale Einbindung auf Einzelgebäudeebene, (2) rein elektrische WP-Integration, z.B. zur Erhöhung des Eigenverbrauchs, (3) Wärmequellenintegration, z.B. gemeinsame Wärmequelle oder Mehrquellensysteme, (4) Kombination von zentraler mit dezentraler (Booster-)WP und (5) vollständig zentrale WP-Einbindung gruppiert wurden.
- Für vielversprechende Konzepte wird in AP 3 eine detaillierte technisch-ökonomische Analyse mittels Simulationen durchgeführt. Daraus werden Planungshinweise zur Auslegung und Regelung der WP abgeleitet sowie die Speicherintegration und der PV-Eigenverbrauch ausgewertet.
- In AP 4 wird die Effizienz des realen Einsatzes von WP in Gebäudeclustern und Quartieren charakterisiert. Dies dient zum einen zur Auswertung von Optimierungspotenzialen für die konkrete Anlage, zum anderen aber auch zur Modellvalidierung. Aus den Simulationen können dann ebenfalls Varianten und Optimierungen ausgewertet werden. Abbildung 1 zeigt die 5 generischen Konzepte zur Integration der WP in PEQ und Beispiele zugehöriger Monitoringprojekte im Annex 61.

Abbildung 1: Klassifizierung von WP-Systemlösungen in PEQ und Monitoringprojekte

Insgesamt wird für 14 Gebäudecluster und Quartiere ein Monitoring durchgeführt und von den Teilnehmerländern zum Annex 61 beigesteuert. Für viele der dargestellten Monitoring-Anlagen werden ebenfalls Simulationen durchgeführt, wie oben als Wechselspiel zwischen AP 3 und AP 4 ausgeführt.

Simulationen AP1 (PEQ-Bewertung)

Simulationen werden vor allem in den AP1 und AP3 auf unterschiedlicher Ebene durchgeführt. In AP1 dienen die Simulationen zur Auswertung von Lastprofilen und daraus synthetisierten Archetypen für PEQ, um Kombinationen unterschiedlicher Lasten auszuwerten und Aussagen zur Erreichbarkeit einer Plusenergiebilanz zu treffen bzw. die Differenz zu einer Plusenergiebilanz zu quantifizieren. Im AP3 ist das Ziel, detailliertere techno-ökonomische Auswertungen von günstigen Systemkonfigurationen bzw. Vergleiche der generischen Systemlösungen vorzunehmen. Entsprechend werden detailliertere Modelle benötigt. Dabei werden auch vielfach die Monitoring-Anlagen simuliert, womit direkt Validierungsdaten zur Verfügung stehen. Im Folgenden wird zunächst auf den Lastgenerator für vereinfachte Simulationen in AP1 eingegangen und anschließend Beispiele der detaillierten Simulationen dargestellt.

Lastkurvengenerator

Ziel des an der Uni Innsbruck entwickelten Lastgenerators ist es, anhand von Lastprofilen Aussagen zu treffen, ob das Erreichen einer Plusenergiebilanz möglich ist bzw. wie groß die Lücke zur Plusenergiebilanz ist. Dazu werden vereinfachte dynamische Simulationen in Matlab mit Einzonen („lumped mass“)-Gebäudemodellen und einem WP-Modell auf Grundlage des Gütegrades inkl. Verteil-/Speicherverlusten durchgeführt. Die elektrische Bilanz für Raumheizung (RH), Trinkwarmwasser (TWW), Haushaltsstrom und Hilfsenergie mit PV wird auf Substundenbasis ausgewertet. Die Modellparameter entsprechen der Datenlage in frühen Planungsphasen. Neben den Gebäudelasten (RH und TWW für Neubau und verschiedene Renovierungsniveaus) und dem Haushaltsstrom wird auch die Gebäudetechnik (Kombinationen aus WP mit unterschiedlichen Quellen (z.B. Grundwasser/ Außenluft), Fernwärme, Biomasse und direktelektrische Heizung) und die PV-Produktion an Dach und optional Fassade berücksichtigt. Weiterhin können sowohl elektrische als auch thermische Speicherkomponenten eingesetzt werden. Dies entspricht den oben erwähnten Einschränkungen bzw. Designoptionen. Aus den Lastprofilen kann ein Vergleich eines Defizits bzw. eines Überschusses bei unterschiedlichen Gebäudelasten kombiniert mit verschiedenen Systemkonfigurationen ausgewertet werden. Dies kann zunächst für die Gebäudekategorien Einfamilienhaus (EFH) kleines oder großes Mehrfamilienhaus (s-MFH, l-MFH), Büro oder Hotel ausgewertet werden. Die Parametrierung der Gebäude geht auf andere Forschungsprojekte mit realen Messergebnissen bzw. Tabula-Daten (IWU, 2012) zurück. Abbildung 2 zeigt die bisher implementierten Gebäudekategorien.

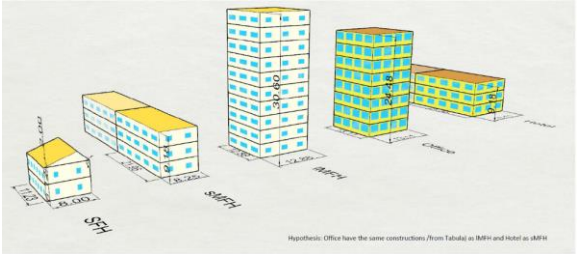

Abbildung 2: Gebäudetypen für den Lastgenerator

Zur Simulation eines Quartiers werden die relativen Anteile der dargestellten Gebäude mit der jeweiligen Gebäudehüllenqualität und der betrachteten Haustechnik und PV-Installation kombiniert. Diese Lastprofile sind vorsimuliert und werden über Vorgabe der Anteile zu Quartieren synthetisiert. Dafür wurden im Annex 61 Archetyp-PED definiert, z.B. reine Wohnnutzung EFH-Neubau mit Luft-WP und mittlere PV-Belegung. Tabelle 1 zeigt die definierten Archetyp PED als Kombination unterschiedlicher Gebäudetypen/-hüllenqualität, Gebäudetechnik und Abstufung hinsichtlich PV-Installation (klein, mittel, groß).

Tabelle 1: Archetype PEQ
L – Luft, GW – Grundwasser, DE – Direktelektrisch

PEQ	Gebäude	Technik	PV
#1	Neubau EFH 100% EFH	L-WP	Mittel
#2	Neubau MFH 70% sMFH/30% lMFH	GW-WP	Mittel
#3	Renovierter Wohnbau MFH 70% sMFH/30% lMFH	GW-WP	Mittel
#4	Renovierter Wohnbau gemischt 50% EFH/30% sMFH 20% lMFH	10% DE 60% L-WP 30% GW-WP	Mittel
#5	Gemischt 50% Büro/30% sMFH 20% lMFH	GW-WP	Mittel

Ergebnisse Lastkurvengenerator

Abbildung 3 zeigt einen beispielhaften Vergleich eines Quartiers ohne und mit PV in Kombination ohne und mit unterschiedlichen Batteriegrößen. Ohne PV-Produktion kann kein Lastausgleich durch erneuerbare Produktion stattfinden, daher zeigt die schwarze Kurve keine negativen Werte.

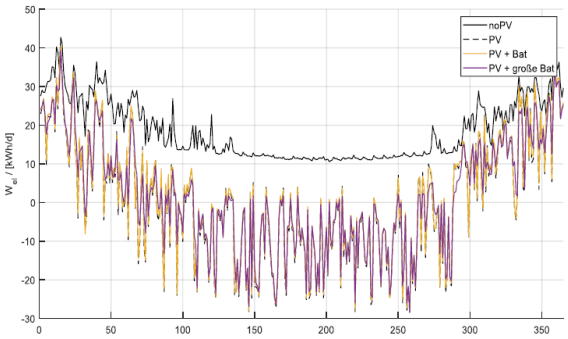

Abbildung 3: Lastprofile mit und ohne PV/Batterie

Mit PV-Produktion ergeben sich bis weit in die Übergangszeit hinein einzelne negative Werte. Dies deutet darauf hin, dass eine positive Bilanz erzielt werden kann. Ungefähr ab Anfang April bis Ende Oktober dominieren die negativen Werte, also der PV-Überschuss. Durch die Batterien können die Last- bzw. PV-Ertragsspitzen abgemindert werden. Dies wird besonders in der Jahresdauerlinie in Abbildung 4 sichtbar. Mit der PV-Produktion werden negative Werte erreicht, so dass die positive und negative Fläche sich entsprechen. Mit den unterschiedlichen Batteriegrößen laufen die Jahresdauerlinien flacher, was anzeigt, dass Last und Ertrag besser in Übereinstimmung gebracht werden können. Aufgrund des geringeren PV-Ertrags im Winter und geringeren Lasten im Sommer kann aber durch die Batterie die Last-/Ertragsspitze im Winter bzw. Sommer nicht gesenkt werden, da die Batterien nur eine Kurzzeitspeicherung erlauben.

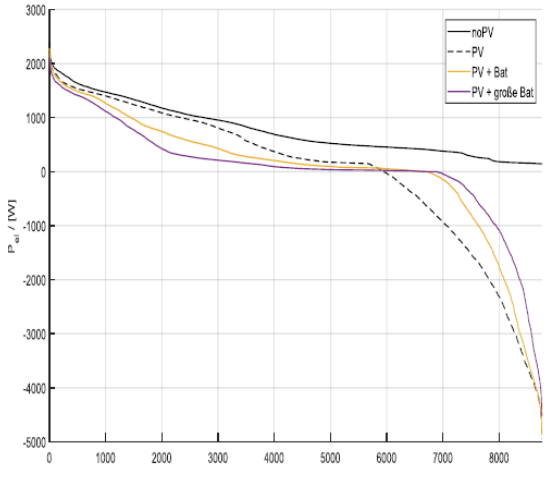

Abbildung 4: Summenhäufigkeit der Lastprofile aus Abbildung 3

Simulationen AP3 (Monitoring-Anlagen)

Wie oben beschrieben werden für viele Anlagen, für die ein Monitoring ausgewertet wird, parallel auch Simulationen durchgeführt. Im Folgenden werden einige bereits vorliegenden Ergebnisse diskutiert.

Auslegung Mehrquellen WP-Anlage

Ein Schweizer Beitrag zum Annex 61 bezieht sich auf Mehrquellen-WP, da in Quartieren mit dichter Bebauung die Quellensituation für Einzelquellen eingeschränkt sein kann. Zu dieser Problematik, die auch häufig beim Ersatz von Heizkesseln durch WP in dicht bebautem Gebiet auftritt, wurde eine Simulationsstudie (Wemhöner et al., 2023) durchgeführt, die als Ergebnis hatte, dass die Einschränkungen der Einzelquellen überwunden werden und durch Synergien bei Mehrquellen-Anlagen Effizienz- und sogar wirtschaftliche Vorteile gegenüber den Einzelquellen Außenluft oder Erdreich bestehen können. Als Pilotanlage wird eine Anlage mit einem Kesselersatz in zwei Mehrfamilienhäusern gemessen, bei der genau die Einschränkungen auftraten, die in den Simulationen untersucht wurden. Abbildung 5 zeigt die Mehrfamilienhäuser und das umgebende Gelände.

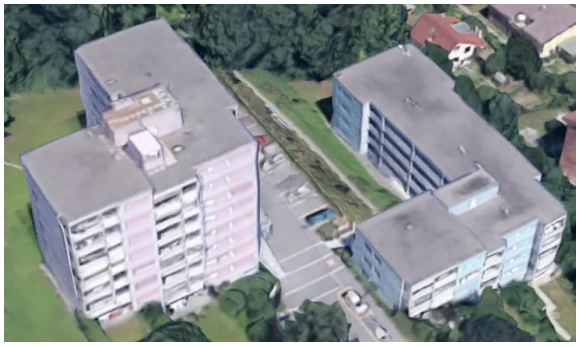

Abbildung 5: Mehrfamilienhäuser mit Mehrquellen-WP für den Kesselersatz

Für die Erdwärmesonden steht wegen der steilen Umgebung nur der begrenzte Platz des Parkplatzes zwischen den Häusern zur Verfügung. Das ursprüngliche Konzept sah 300 m tiefe Erdsonden vor, die über einen Luftwärmetauscher im Sommer regeneriert werden. Allerdings wurde bei den ersten Bohrungen ein Arteser getroffen, so dass von den Behörden eine zusätzliche Bohrbeschränkung auf 120 m erlassen wurde. Damit reichen die Erdsonden allein nicht aus. Als alternatives Konzept wurde eine Spitzenlastdeckung über die Erdsonden und die Grundlastdeckung über einen erweiterten Luftwärmetauscher untersucht. Die Simulationen werden unter Matlab-Simulink mit der Carnot-Toolbox durchgeführt, die Modellierung der Erdwärmesonden erfolgt nach einem Modell von Huber (1997) auf Grundlage der g-function von Eskilson (1987). Abbildung 6 zeigt die Resultate der Untersuchungen. Die ursprüngliche Lösung (blau) kann das Auslegungskriterium nach der Schweizer Norm SIA 384/6 (2021) einhalten, dass die mittlere Fluidtemperatur nach 50 Jahren nicht unter –1.5 °C sinkt. Eine tiefere Sonde auf 400 m

ohne Regeneration (schwarz) liefert bessere Erdreichtemperaturen bei Auslegung nach dem SIA-Kriterium. Eine Reduktion auf 120 m hingegen ist nicht mehr möglich. Ohne Regeneration (blau und rot gestrichelt) unterschreiten die Temperaturen auch mit erweiterter Luftquelle das Auslegungskriterium deutlich.

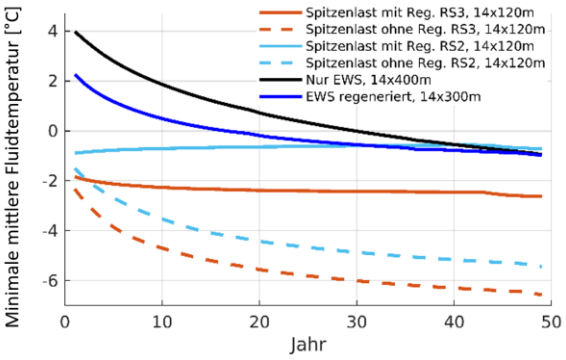

Abbildung 6: Ergebnisse Auslegung des Quellensystems

Mit Regeneration kann für eine konservative Regelstrategie (RS2), die das Erdreich nur zur Spitzenlastdeckung einsetzt, das Kriterium eingehalten werden, während die progressive Strategie (RS3) mit mehr Erdreicheinsatz das Kriterium verfehlt.

Klimaneutrale Sanierung eines MFH

In einem deutschen Beitrag der TH Nürnberg wird ein Sanierungskonzept für ein MFH im Bereich des genossenschaftlichen Wohnungsbaus entwickelt, das mittels Simulationen optimiert und die Machbarkeit des Konzepts durch Simulationen auf ein Quartier erweitert wird.

Das Verbundvorhaben EnOB „sEnSys“ (FKZ 03EN1053A) fokussiert auf die Demonstration einer Mustersanierung eines mehrgeschossigen MFH mit den Schwerpunkten einer energieeffizienten, wirtschaftlichen und netzdienlichen Anlagentechnik sowie einer hohen Nutzerakzeptanz der Bestandssanierung.

Der technische Schwerpunkt des Konzeptes liegt auf einer energieeffizienten und intelligenten Gebäudetechnik sowie der bilanziell energetischen Deckung durch regenerative Energien. Die Mehrkosten für die Komponenten und Regelungsfunktionen sollen durch eine erhöhte Systemeffizienz und der Möglichkeit des Mieterstroms und somit niedrigeren Energieverbrauchskosten kompensiert werden. Abbildung 7 zeigt ein Schema der geplanten Gebäudetechnik.

Das in den 1970er Jahren errichtete Gebäude besteht aus 32 Wohneinheiten auf einer beheizten Bruttofläche von 2600 m^2.

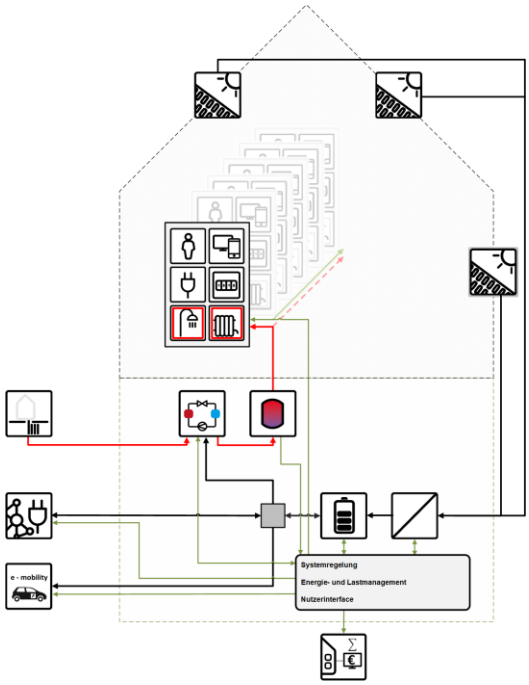

Abbildung 7: Anlagenkonzept der klimaneutralen Mustersanierung im Projekt sEnSys.

Für die Simulation des Gebäudes und der Optimierung der Anlagentechnik in TRNSYS wurde ein SketchUp-Gebäudemodell erstellt, welches das MFH in 38 thermische Raumzonen aufteilt (32 Wohneinheiten, 4 Treppenhäuser, Keller, Dachboden, siehe Abbildung 8).

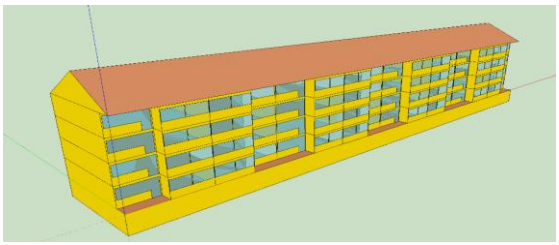

Abbildung 8: SketchUp-Modell des MFH für die Mustersanierung im Projekt sEnSys.

Das im MFH einzusetzende Energiekonzept muss möglichst verlustarm und kosteneffizient arbeiten, um die Klimaneutralität des Gebäudes erreichen zu können. In einer Simulationsstudie wurden daher drei grundlegende Hydraulikvarianten untersucht, welche sich in der Art der Trinkwarmwasserbereitung (TWWB) und der Leitungsführung im Gebäude unterscheiden:

- Variante 1: zentrale TWWB, 4-Leitersystem mit Zirkulation
- Variante 2: dezentrale TWWB, 2-Leitersystem mit Übergabestation
- Variante 3: Variante 2 mit zusätzlicher elektrischer TWW-Nacherhitzung

Als Wärmequelle diente (bedingt durch die örtlichen Gegebenheiten) bei jeder Variante eine erdgekoppelte Sole-Wasser-WP und ein Parallel-Pufferspeicher. Die Anlagentechnik der Variante 3 ist schematisch in Abbildung 9 ersichtlich.

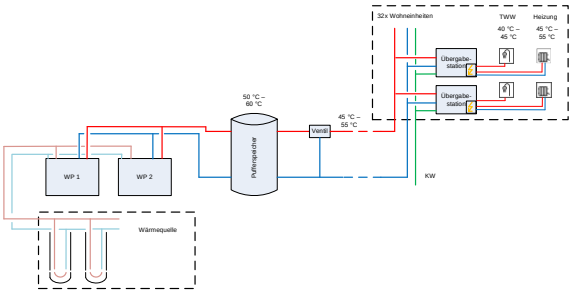

Abbildung 9: Hydraulikschema der Variante 3.

Die Komponenten und Rohrleitungen wurden entsprechend der Varianten dimensioniert und in die Simulationsumgebung integriert. Für die TWWB wurden vier unterschiedliche und für das Gebäude repräsentative Zapfprofile auf Basis des realen Gesamtverbrauchs mit DHWCalc (Jordan et al., 2017) erstellt und belaufen sich auf rund 40 Liter pro Person und Tag. Mit einer Warmwasseranforderung von 10 Liter je Woche auf 50 °C wird eine Heißwasserzapfung (z .B. für Putzen) je Wohneinheit simuliert.

In Abbildung 10 sind die relativen Verteilungen der Endenergiebedarfe der drei Varianten aufgetragen.

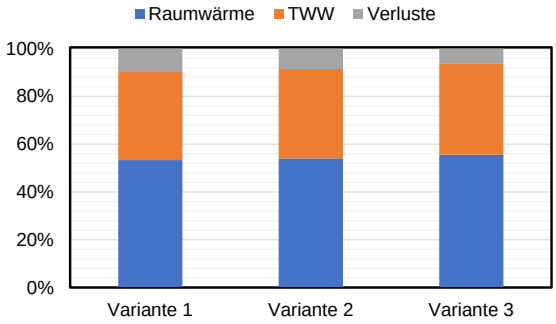

Abbildung 10: Vergleich des relativen Energiebedarfs der drei untersuchten Hydraulikvarianten.

Der Heizenergiebedarf beträgt bei allen Varianten 48.5 MWh und hat mit 57 % den größten Anteil am Gesamtenergiebedarf. Der Trinkwarmwasserbedarf beträgt im Mittel 33.3 MWh. Mit den Varianten geht eine Reduzierung der maximalen Vorlauftemperaturen im Heizkreislauf von ca. 60 °C (V1) bis auf 45 °C (V3) einher, wodurch Verteilverluste reduziert werden. Zusätzlich reduzieren sich die maximalen Systemtemperaturen im thermischen Energiespeicher. Daher reduzieren sich die Gesamtwärmeverluste um mehr als 39 % von 8.9 MWh (V1) auf 5.5 MWh (V3).

Prozentual haben die Wärmeverluste einen Anteil von 3…5 % am Gesamtenergieverbrauch.

Abbildung 11 zeigt den Vergleich der Verbrauchskosten der drei Hydraulikvarianten unter Berücksichtigung des Betreibermodells der PV-Anlage (Eigennutzung oder Mieterstrom). In allen drei Varianten sind die monetären Vorteile der Eigennutzung deutlich im Vergleich zur Volleinspeisung sichtbar. So sind diese im Mittel um rund 60 % geringer. Ebenso sind geringfügige ökonomische Vorteile im Vergleich der Varianten untereinander erkennbar. So sind die Verbrauchskosten der Varianten 2 und 3 bei Eigennutzung um 6.1 % und 13.8 % geringer als Variante 1. Bei einer Volleinspeisung können Preisvorteile in Höhe von bis zu 7.2 % (Variante 3 zu Variante 1) erzielt werden.

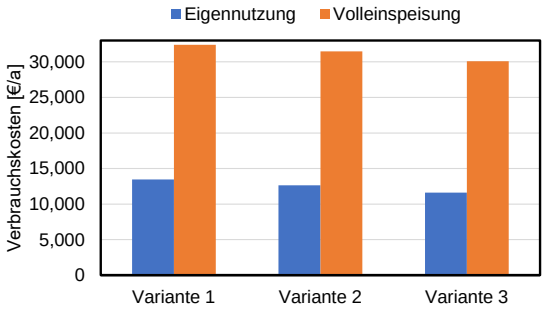

Abbildung 11: Vergleich der Verbrauchskosten der drei untersuchten Hydraulikvarianten.

Diese und weitere Simulationsstudien können das Auswahlverfahren eines geeigneten Energieversorgungskonzeptes für das MFH unterstützen, indem sie die Vor- und Nachteile unterschiedlicher Hydraulikvarianten innerhalb der definierten Randbedingungen gegenüberstellen. So geht Variante 3 als favorisiertes Energieversorgungskonzept aus den Simulationsstudien hervor. In aktuell laufenden Untersuchungen werden Sub-Typen dieser Variante erstellt, hydraulisch dimensioniert und simulativ bewertet.

Bestandsquartier mit neuem Wärmenetz

«Quarree100» ist ein in der deutschen Förderinitiative Solares Bauen / Energieeffiziente Stadt gefördertes Projekt mit einem breit aufgestellten Projektkonsortium. Ein zentrales Ziel des Projekts ist die Entwicklung und Umsetzung eines klimaneutralen und resilienten Energiekonzepts für das Quartier «Rüsdorfer Kamp» in Heide, Schleswig-Holstein in Abbildung 12. Die thermische Energieversorgung der Gebäude soll von den Energieträgern Gas, Öl und Strom auf erneuerbare Nahwärme umgestellt werden (Zimmermann, Gehlert, 2023).

Abbildung 12: Rüsdorfer Kamp im Projekt Quarree100

Die zentralen Bearbeitungsschritte sind:

- Erstellung eines Gebäudekatasters, u.a. Gebäudeart, Baujahr, Wärmebedarf
- Erstellung eines Solarkatasters, u.a. Dachorientierung, Solarertrag
- Erstellung von Lastprofilen des thermischen Bedarfs der Gebäude
- Auslegung eines Wärmenetzes für das Quartier (Röder et al. 2021)
- Modellierung und Simulation von potenziellen Energiekonzepten in TRNSYS
- Energetische, ökologische und ökonomische Bewertung der Ergebnisse

Das Energiekonzept hat im Projektverlauf diverse Iterationen durchlaufen, in Abbildung 13 ist eine der ökologisch präferierten Varianten dargestellt.

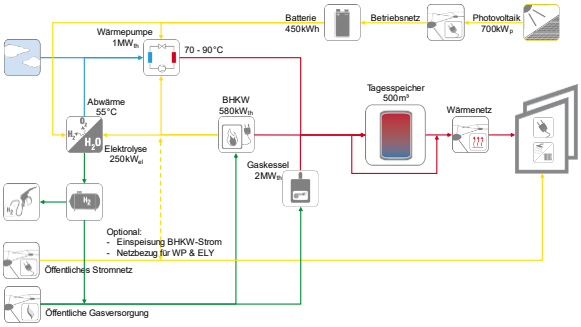

Abbildung 13: Energiekonzept zur Wärmeversorgung des neuen Wärmenetzes im Projekt Quarree100

Unter Annahme einer konservativen Anschlussquote werden 134 Gebäude an das Wärmenetz angeschlossen. Dies entspricht 58% der Gebäude (nach Berücksichtigung von zukünftiger Nachverdichtung), wovon 47% Altbauten sind. Der gesamte Wärmebedarf beträgt 6'562 MWh/a. Im präferierten Energiesystem wird Photovoltaik (PV) auf den Quartiersgebäuden installiert. Über ein Betriebsnetz wird der Strom zur Energiezentrale geleitet (nach rechtlicher Prüfung ist eine Nutzung des lokalen PV-Stroms zur Deckung des Strombedarfs der Gebäude aktuell nicht möglich, auch wenn dies ökologisch zu bevorzugen wäre).

Der lokale PV-Strom wird primär in der Luft-Wasser-WP eingesetzt. Überschüsse können in einem Elektrolyseur zur Wasserstoffproduktion verwendet werden.

Dieser ist in erster Linie für den wissenschaftlichen Betrieb ausgelegt mit dem Ziel, verschiedene Wasserstoffnutzungen wie Mobilität sowie Einspeisung in ein Erdgasnetz zu erproben. Zusätzlich zum PV-Strom kann die WP mit Netzstrom betrieben werden, wenn dies ökologisch und wirtschaftlich vorteilhaft ist. Daneben steht zur Optimierung der Wirtschaftlichkeit ein Blockheizkraftwerk (BHKW) bereit, dessen produzierter Strom in der WP nutzbar ist. Als Redundanz ist ein Gaskessel eingeplant. Die produzierte Wärme kann tagesweise gespeichert werden, um Wärmebedarf und -angebot zu entkoppeln und einen flexibleren Anlagenbetrieb zu ermöglichen.

Die Jahressimulation des Konzepts erfolgt in der Software TRNSYS mit einer Zeitschrittweite von 15 Minuten. Die einzelnen Komponenten werden dabei weitestgehend über die vorhandenen Standardtypes abgebildet. Für die Simulation des PV-Ertrags werden die individuellen Dachflächen der Gebäude entsprechend des Solarkatasters herangezogen. In der thermischen Simulation liegt das Hauptaugenmerk auf dem Zusammenspiel von WP und Wärmespeicher. Da es sich bei der WP durch die hohen Temperaturen und Leistung um kein Standardfabrikat handelt, wurden WP-Kennfelder von Herstellern angefragt und für die Simulation aufbereitet. Der Speicher ist als erdvergrabener Behälter mit thermischer Schichtung modelliert, Elektrolyseur und BHKW bilden über Equations vereinfacht die Wirkungsgradvorgaben der Hersteller ab. Das Wärmenetz mit seinen Wärmeverlusten wird in Form einer repräsentativen Rohrgeometrie simuliert.

Das erarbeitete Modell erlaubt die Abbildung diverser Betriebsstrategien, z.B. bezüglich der Präferenz von Erdgas oder Netzstrom bei Mangel an erneuerbaren Energien. Abbildung 14 zeigt ein Ergebnis der jährlichen Energieflüsse von den Quellen PV, WP, BHKW und Gaskessel (Nachheizung NH) über Wärmespeicher und Wärmenetz hin zu den Verbrauchern.

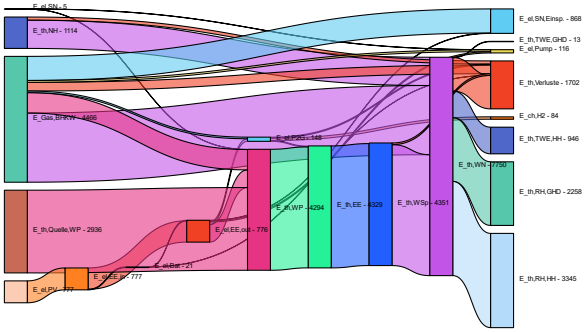

Abbildung 14: Flussdiagramm der jährlichen Energiemengen in MWh laut Simulation

Auch ohne Nutzung von Netzstrom kann über 50% der Wärmenetzeinspeisung aus der WP gedeckt werden. Das System bietet die Flexibilität, diesen Anteil durch Nutzung von Netzstrom zukünftig deutlich zu steigern. Damit handelt es sich um ein zukunftsfähiges, erneuerbares und resilientes Energiekonzept für die Energiewende. Die Umsetzung hängt aktuell noch von der Wirtschaftlichkeit des Projekts ab.

Zusammenfassung

Annex 61 untersucht den Einsatz von WP in Gebäudeclustern und Plusenergiequartieren. WP stellen nach unterschiedlichen Szenarien eine Schlüsseltechnologie für die Energiewende dar. Allerdings ergeben sich Fragestellungen nach der besten Integration auf Gebäude- oder Quartiersebene sowie zum Zusammenspiel mit anderen Wärmeerzeugern. Im Annex 61 werden dazu Simulationen in unterschiedlichen AP eingesetzt, die zu unterschiedlichen Phasen des Entwurfs- und Auslegungsprozesses korrespondieren, wobei sich die Modellierung an den verfügbaren Informationen und interessierenden Aussagen der jeweiligen Projektphase orientiert. Für die Konzeptauswertung eines PEQ wurde ein Lastkurvengenerator entwickelt, mit dem anhand einer einfachen Modellierung die Erreichbarkeit bzw. die Lücke zum Erreichen von PEQ ausgewertet werden kann. Durch Kombination von anteiligen Lastprofilen unterschiedlicher Gebäudekategorien und Kombinationen mit Technikvarianten, PV-Installationsgrössen und Speicherintegration können komplexere Quartiere vereinfacht modelliert werden. Damit werden Gleichzeitigkeiten nicht vollständig abgebildet, aber generelle Aussagen zum Verhalten von PEQ können abgeleitet werden.

Zur Modellierung der Monitoringanlagen werden detailliertere Modelle eingesetzt, wobei die Simulationsplattformen der Teilnehmerländer variieren. Die Monitoringanlagen erlauben eine Modellvalidierung, während die Modelle detaillierte Variantenrechnungen zu Auslegungs- und Regelungsfragestellungen erlauben und den realen Anlagenbetrieb dadurch optimieren können. Daraus sollen Auslegungshinweise und Regelstrategien abgeleitet werden. Eine durchgängige Modellierung von der Konzept- bis zur Betriebsphase könnte damit ein mächtiges Hilfsmittel zur Unterstützung des gesamten Bauprozesses sein.

Danksagung

Der IEA HPT Annex 61 ist ein kollaboratives Forschungsprojekt und die Autoren danken allen Teilnehmern für die konstruktive Zusammenarbeit mit offenen Diskussionen.

Die finanzielle Unterstützung auf Ebene der Teilnehmerländer und des Schweizerischen Bundesamts für Energie BFE wird herzlich verdankt.

Literatur

Eskilson, P. 1987. Thermal Analysis of Heat Extraction Boreholes. Department of Mathematical Physics, Lund Institute of Technology, Lund, Sweden

EU. 2018. European Parliament. 2018. Directive (EU) 2018/844 of the European Parliament and of the Council of 30 May 2018 amending Directive 2010/31/EU on the energy performance of buildings and Directive 2012/27/EU on energy efficiency, Journal of the European Union, L 156/75, 19.6.2018, Brussels, EU

Huber, A. und Schuler, O. 1997. Berechnungsmodul für Erdwärmesonden, BFE-Schlussbericht, Zürich, Schweiz

IWU. 2012. Typology Approach for Building Stock Energy Assessment. Main Results of the TABULA project. Darmstadt, Germany

Jordan, U., Vajen, K., 2017. DHWcalc – Werkzeug zur Generierung von Trinkwasser-Zapfprofilen auf statistischer Basis. Version 2.02b. Universität Kassel, Germany

JPI Urban Europe. 2020a. Europe towards Positive Energy Districts, Vienna, Austria

JPI Urban Europe/SET Plan Action 3.2. 2020b. White Paper on PED Reference Framework for Positive Energy Districts and Neighbourhoods, Vienna, Austria

Röder, J., Meyer, B., Krien, U., Zimmermann, J., Stührmann, T., Zondervan, E. 2021. Optimal Design of District Heating Networks with Distributed Thermal Energy Storages – Method and Case Study. IJSEPM **31**, S. 5–22

Schweizerischer Ingenieur und Architektenverband. 2021. SIA 384/6 Erdwärmesonden, Zürich, Schweiz

Wemhöner, C., Meier, Ch. 2023. HP source-Integrationsmöglichkeiten für Wärmequellen, BFE Schlussbericht, Rapperswil, Schweiz

Zimmermann, J., Gehlert, G. 2024. Design and Integration of Large Heat Pumps for District Heating with heterogeneous building structures, in: Leonhardt, S. (Ed.) Innovations and challenges of the energy transition in smart city districts, DE GRUYTER, S. 453–464.

BauSIM 2024 in Wien
23. September – 26. September

Integration of a latent heat storage in the refrigeration cycle of an air source heat pump for energy-efficient heating, cooling and DHW operations

Abdulrahman Dahash[1], Georg Klein[1], Michael Lauermann[1], Raimund Zitzenbacher[2], Stephan Preisinger[2], Bernd Windholz[1]

1 AIT Austrian Institute of Technology GmbH, Center for Energy, Giefinggasse 2, 1210 Vienna, Austria, E-Mail: abdulrahman.dahash@ait.ac.at

2 OCHSNER Wärmepumpen GmbH, 3350 Haag, Austria

Abstract

A key solution to the buildings sector's fossil fuel challenges lies in renewables and efficient technologies. This study proposes a novel concept aimed at enhancing the coefficient of performance (COP) of air-source heat pumps (ASHPs) for both heating and domestic hot water (DHW) generation. Herein, the integration of a refrigerant-PCM-water heat exchanger (RPW-HEX) into the refrigeration circuit is crucial. The RPW-HEX serves a dual purpose, acting as a desuperheater/storage for DHW during winter and as a condenser/storage during summer. Comprehensive simulations are carried out to assess the performance of the entire system. The findings reveal promising results maintaining thermal comfort for occupants with reduced ASHP operation during DHW demand.

Introduction

The residential heating and cooling sector in Europe heavily relies on fossil fuels (e.g. natural gas), which significantly contributes to CO_2 emissions and impairs climate change. To tackle this, there is a need to phase out natural gas and transition to renewable energy sources (RES) and efficient technologies (e.g. heat pumps).

Heat pump technology presents an efficient solution by utilizing low-temperature heat sources for space heating, often through floor heating systems. However, meeting the demand for domestic hot water (DHW) poses challenges due to its higher temperature requirements.

One effective strategy to enhance efficiency is through the installation of desuperheaters in heat pump systems. These components extract thermal energy from the refrigerant after compression, thereby improving performance and contributing to energy savings, especially in DHW generation for residential buildings.

Studies have explored other innovative approaches to enhance ASHP performance. For instance, (Kim et al., 2018) investigated multi-split ASHPs with thermal energy storage (TES), optimizing operation modes based on electricity availability. (D'Ettorre et al., 2019), on their part, examined energy flexibility in ASHP-equipped building energy systems (BESs), highlighting the role of TES in reducing operational costs.

(Heinz et al., 2022) studied the role of desuperheaters in ASHPs, emphasizing their role in reducing backup boiler usage. (Emhofer et al., 2019) proposed replacing desuperheaters with heat exchangers filled with PCMs, enhancing energy storage and recovery during DHW generation. A subsequent study by (Emhofer et al.) demonstrated the use of latent heat storage as a desuperheater, enabling DHW supply while cooling apartments.

This work explores the role of latent heat storage integrated within the refrigeration cycle of an air-source heat pump. This storage helps in meeting the DHW demand via charging decentralized hot-water tanks. The charging approach for these tanks can be time-dependent and temperature-dependent. The work further explores the impact of these two approaches on the performance of the proposed ASHP.

Methodology

To assess the feasibility of the proposed ASHP system, dynamic thermo-hydraulic simulations are crucial. Therefore, a comprehensive simulation model is developed in Modelica/Dymola, which includes several sub-system models:

- ASHP including components e.g. evaporator, compressor, condenser and expansion valve. Additionally, the system integrates latent heat storage modules (introduced later as RPW-HEX),

- Building distribution system: A hydronic circuit to connect the ASHP water side along with the circulation pump. Each apartment within the multi-family house is equipped with individual components like decentralized DHW tanks, pipes, valves, and electrical heating elements,
- Building model: A multi-family house is represented in the simulation, considering a specific number of apartments, their respective space heating and cooling loads, DHW demands, and heat terminals such as floor heating or radiators,
- Control system: A comprehensive control system is implemented to ensure optimal operation of the entire system.

Heat pump – refrigeration cycle

The ASHP herein analyzed consists of outdoor and indoor heat exchanger units, compressor, expansion valve and additional elements like an oil separator and hydraulic components including valves and tubes. It has a nominal capacity of 10 kW. To optimize performance and address operational constraints, a refrigeration cycle control strategy incorporates an injection valve. To ensure the refrigerant remains liquid at the expansion valve inlet, an internal heat exchanger (IHX) is included to cool the refrigerant in advance. Additionally, outdoor air circulation is enhanced with a fan component to improve heat transfer.

Expanding the ASHP system, two refrigerant-PCM-water heat exchangers (RPW-HEX) and a four-way valve (4-WV) are integrated. One RPW-HEX provides temperatures below 54°C for pre-heating and basic-charging phases, while the other handles temperatures exceeding 55°C for top-charging. Operating analogous to a desuperheater, RPW-HEXs potentially enhance ASHP's coefficient of performance (COP).

Distinguishing between the condenser outlet temperature (relevant for SH) and the ASHP outlet temperature (dedicated to DHW generation) is crucial. A 4-WV facilitates the reversal between heating and defrost/cooling operations within the refrigeration cycle.

Heating operation

During the heating operation, ASHP functions as a heat generation system, with the indoor heat exchanger acting as a condenser and the outdoor unit as an evaporator. The ASHP employs R32 refrigerant compressed by a rotary compressor (P), resulting in a hot gas state at the compressor outlet.

When the RPW-HEX modules (D) are charged, the hot gas bypasses them via valve (B3) if fully charged or charges them via manual valves (B1 and B2) if not. In the RPW-HEX, the hot gas transfers its sensible energy, storing it as sensible and latent heat. The refrigerant then leaves the RPW-HEX at a lower temperature, entering the 4-WV before flowing to the condenser (C). Here, it transfers its remaining sensible and latent energy to the counter-current flowing water, causing condensation.

To maintain the refrigerant in a liquid state at the expansion valve (X) inlet, it is cooled by the outlet flow of the expansion valve using an internal heat exchanger (IHX). After passing through the expansion valve, the refrigerant is slightly heated by the IHX before reaching the outdoor unit (evaporator, E), where it becomes superheated before returning to the compressor through the 4-WV (depicted in Figure 1 (a-b)).

To ensure a safe operation with a compressor outlet temperature below 110°C, a liquid injection valve (Z) controlled by a PI is used. If the temperature exceeds 110°C, the injection valve (Z) opens, allowing colder gas to bypass from the high-pressure side to the low-pressure side (compressor inlet), ensuring safe and efficient ASHP operation.

Cooling operation

In the reverse operation of ASHP, facilitated by 4-WV, the refrigeration cycle is adjusted. Initially, the refrigerant R32 is compressed into a hot gas state by the compressor (P). If the RPW-HEX modules are charged, the hot gas bypasses the modules via the bypass valve (B3) and 4-WV, proceeding to the outdoor unit – now functioning as a condenser. Here, the refrigerant undergoes further cooling with the aid of the IHX to ensure it remains in a liquid state upon entering the expansion valve (X). As the refrigerant expands, it enters the indoor unit – now an evaporator – where it absorbs heat from flowing water, causing the water to cool down as the refrigerant evaporates. The gas then returns to the compressor, completing the reversed refrigeration cycle (depicted in Figure 1 (c)).

If the RPW-HEX modules are not fully charged, the hot gas is directed to them after leaving the compressor to charge them. Herein, the hot gas transfers its sensible energy to the RPW-HEX modules. Afterwards, the refrigerant continues flowing to the outdoor unit, which acts as a sub-cooler. Only a small part of the unit is utilized for this purpose, as shown in Figure 1(d). From this point on, the operation is similar to Figure 1(c), where the cooling operation proceeds. During the cooling operation, the liquid injection valve (Z) remains closed.

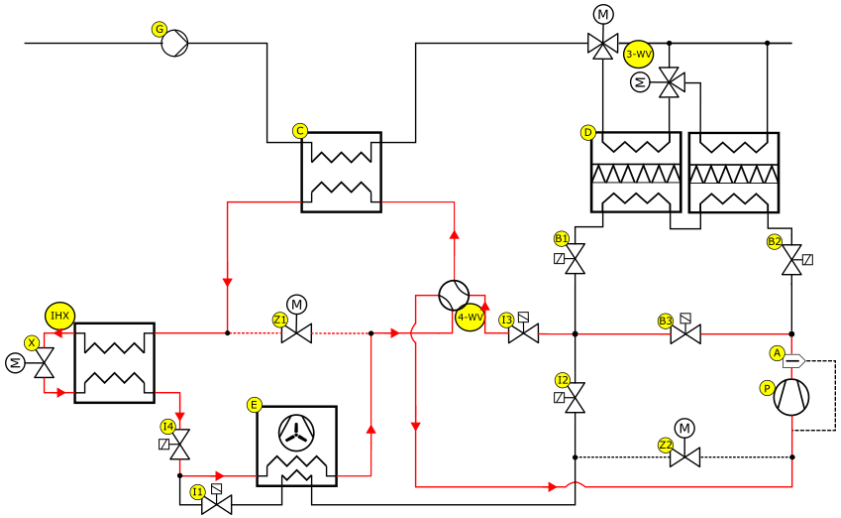

(a) Heating operation without charging of RPW-HEX modules.

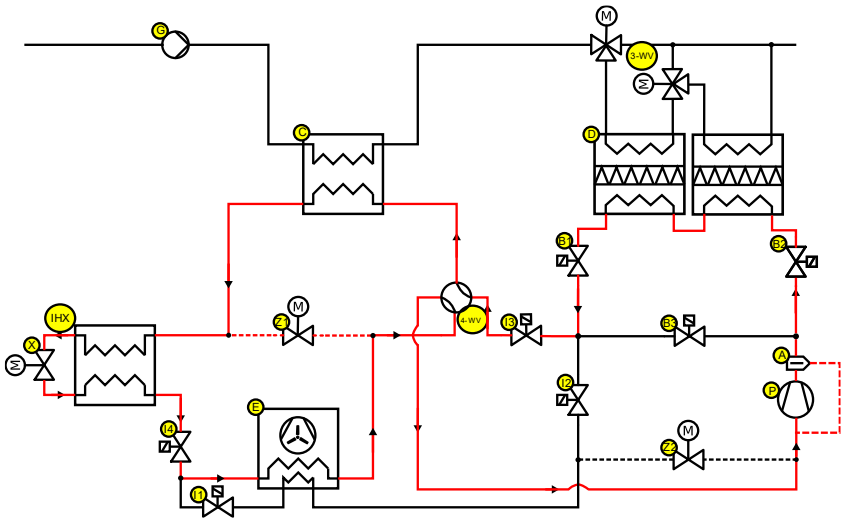

(b) Heating operation with charging of RPW-HEX modules for DHW.

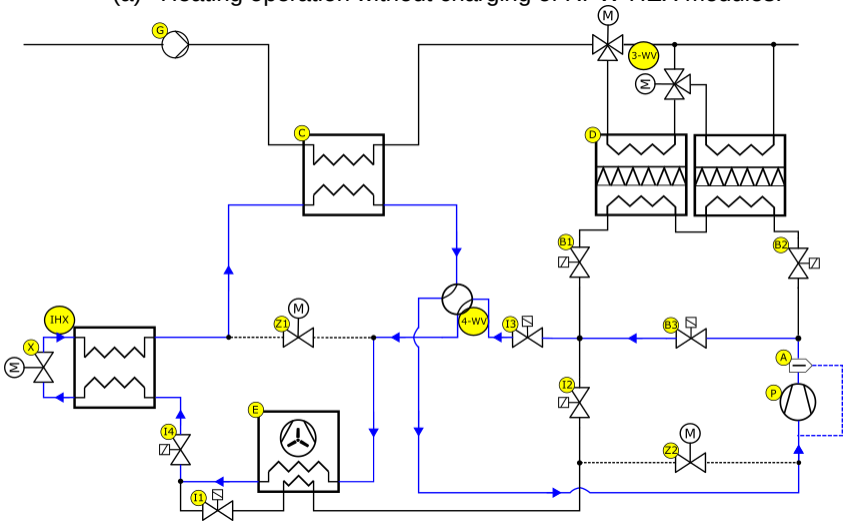

(c) Cooling operation without charging of RPW-HEX modules.

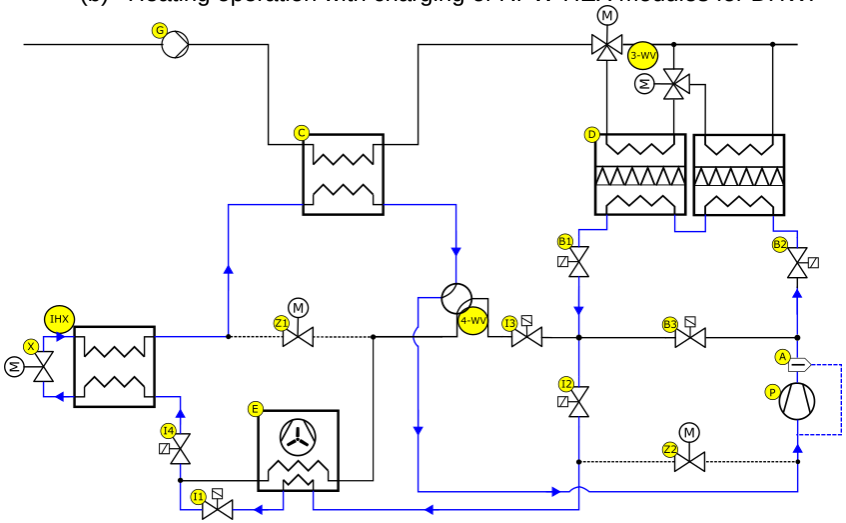

(d) Cooling operation with charging of RPW-HEX modules for DHW.

Figure 1: ASHP layout and refrigeration cycle during heating and cooling operations. P: Compressor, A: Oil separator, B1-3: Manual valves, 3-WV: three-way valve, D: Refrigerant-PCM-Water heat exchangers, C: indoor heat exchanger, G: Circulation pump, IHX: Internal heat exchanger, x: expansion valve, E: Outdoor heat exchanger, I1-4:, Z1-2: Injection valve and 4-WV: Four-way valve.

Building distribution system – water cycle

It is essential to explore the hydronic circuit, which interfaces with the ASHP refrigeration cycle through the condenser (C) and the RPW-HEX modules. The DHW generation takes priority over operations such as SH and SC.

Heating operation

Herein, water flows through the condenser (C) via a circulation pump (G, Figure 1), then to the building if SH is active, regulated by 3-WVs. Thus, no heat is extracted from RPW-HEX modules for SH. Later, the 3-WVs guide water through RPW-HEX modules to extract heat for DHW generation. Heated water charges decentralized DHW tanks (Enerboxxes) or preheats the distribution system to reduce thermal losses.

Cooling operation

The cool water is circulated using the circulation pump (G) to meet SC demand. Like in heating, water bypasses the RPW-HEX modules during cooling. Meanwhile, hot gas on the ASHP refrigeration side charges the RPW-HEX modules for later use. If DHW generation is active, water flows through the RPW-HEX modules to extract heat, proceeding similarly to heating operation.

Control strategies

Heat pump refrigeration cycle

The constraints and setpoints for the ASHP refrigeration cycle are as follows:

- Heating operation:
  - Superheating temperature ($T_{\text{heating,SH}}$) of 5K post to the outdoor unit and is regulated via an expansion valve,
  - Condenser outlet temperature on the water side is adjusted following a heating curve. This is controlled by the compressor frequency (variable-speed),
  - Maximum compressor outlet temperature ($\vartheta_{\text{COMP,out}}$) of 110°C controlled by the liquid injection valve,
  - RPW-HEX modules can be charged.
- DHW generation:
  - Similar to the heating and, thus, some constraints are kept (i.e. $T_{\text{comp,out}}$ and $T_{\text{heating,SH}}$) with some distinctions,
  - Condenser outlet temperature on the water side ($\vartheta_{\text{COND,out}}$) is set to 35°C, whereas the ASHP outlet temperature is set either to 50°C/61°C for basic charging and top charging, respectively,
  - RPW-HEX modules can be discharged.
- Cooling operation:
  - Refrigerant superheating ($T_{\text{cooling,SH}}$) of 11.1K post to the indoor unit and controlled by the expansion valve,
  - RPW-HEX modules can be charged,
  - Condenser outlet temperature on the water side is set to 18°C and controlled by the compressor frequency,
  - Liquid injection valve is always closed.

Building and building distribution system

Figure 2 illustrates the control strategy for SH, SC and DHW generation. Space heating and cooling signals are managed by a PI controller comparing indoor temperature to an indoor setpoint with a defined bandwidth (ΔT) of 1.5 K. Thus:

$$y_{\text{heating}} \quad \text{If:} \quad T_{\text{heating,ST}} - \left(\frac{\Delta T}{2}\right) < \vartheta_{\text{indoor}} < T_{\text{heating,ST}} + \left(\frac{\Delta T}{2}\right) \qquad (1)$$

$$y_{\text{cooling}} \quad \text{If:} \quad T_{\text{cooling,ST}} - \left(\frac{\Delta T}{2}\right) < \vartheta_{\text{indoor}} < T_{\text{cooling,ST}} + \left(\frac{\Delta T}{2}\right) \qquad (2)$$

Initially, the ASHP enters heating mode if (y_{heating} = true). The water supply temperature is set according to the heating curve. Thus, the ASHP focuses on SH exclusively.

For DHW generation, three phases are distinguished: pre-heating, basic charging and top charging. The Enerboxxes' mid temperature determines the phase. If the minimum temperature of any Enerboxx ($\vartheta_{\text{EB}} \geq 52$°C), indicating sufficient energy for DHW, the pre-heating phase begins to warm the circuit and minimize thermal losses. If an Enerboxx falls below this threshold but remains within a range (42°C<ϑ_{EB}<48°C), basic charging starts with a supply temperature of 50°C.

If the temperature is between 48°C and 52°C, top charging starts with a setpoint of 61°C. Charging terminates if Enerboxxes surpass 52°C. Individual Enerboxxes can be electrically heated if their temperature drops below 40°C, with terminating condition at 44°C.

Charging of RPW-HEX modules

The RPW-HEX are charged based on the ASHP's operation mode. Each module's temperature is monitored to ensure it stays above a set threshold, typically around 54°C. If the temperature drops below this threshold, charging begins, supplying hot gas until the module is charged. Charging may pause if other operational phases are activated.

Discharging of RPW-HEX modules

The discharging process of the RPW-HEX modules on the water side begins when DHW

generation is prioritized, signaled by active heating and cooling signals along with an active DHW signal.

If the basic charging is indicated and the LT-RPW-HEX module temperature exceeds 53°C, discharging initiates, setting the water temperature leaving the ASHP system to a minimum of 48°C.

Alternatively, if the basic charging phase is inactive and the top charging phase is active, the ASHP regulates the water leaving the system to 61°C. Discharging begins with the LT-RPW-HEX module, followed by the HT-RPW-HEX module if necessary. Throughout discharging, the water temperature leaving the heat pump condenser is maintained at 35°C. If the RPW-HEX modules lack sufficient energy for discharging, the water setpoint temperature leaving the heat pump condenser is set to 61°C.

Additionally, if the condenser inlet temperature surpasses the setpoint supply temperature during active ASHP operation, the compressor adjusts to the minimum rotational speed (20 Hz). A pre-heating phase of the water distribution system starts at 50°C to minimize thermal losses during discharging. During the basic charging phase, the supply temperature remains at 50°C for an efficient discharge. However, a higher temperature of 61°C is required for the top charging phase.

Numerical modelling and simulations

In this study, dynamic simulations of the entire ASHP system, including the multi-family house, building distribution system, and control units, are conducted using the Modelica language. Modelica is chosen for its object-oriented, equation-based nature, facilitating comprehensive thermo-hydraulic investigations. The simulations are performed in Dymola 2022x, a simulation environment compatible with Modelica.

To model the ASHP components, such as heat exchangers, expansion valves, separators, and compressors, the TIL 3.10.0 commercial library developed by TLK Thermo GmbH is utilized. This library is supplemented by the "TILMedia" library, providing thermophysical properties for various working media, including refrigerants. Specifically, the RPW-HEX modules are developed based on previous research and validated accordingly.

Furthermore, models for other components, e.g. building, decentralized DHW tanks (Enerboxxes), circulation pumps, valves, and electrical heaters, are integrated from the Modelica Buildings library.

Case study, boundary conditions and components dimensions

To assess the viability of the ASHP with RPW-HEX modules, a case study is conducted on a multi-family building comprising four apartments located in Vienna (AT). The outdoor temperature data for the year 2022 is considered.

Each apartment has a floor area of 125 m^2 and a height of 3 m, totaling 500 m^2. The heat load for each apartment is 25 W/m^2. Water serves as the heat transfer fluid in the building distribution system, with nominal supply and return temperatures of 35°C and 25°C, respectively. Floor heating terminals are installed in each apartment, with indoor setpoint temperatures of 21°C in winter and 25°C in summer.

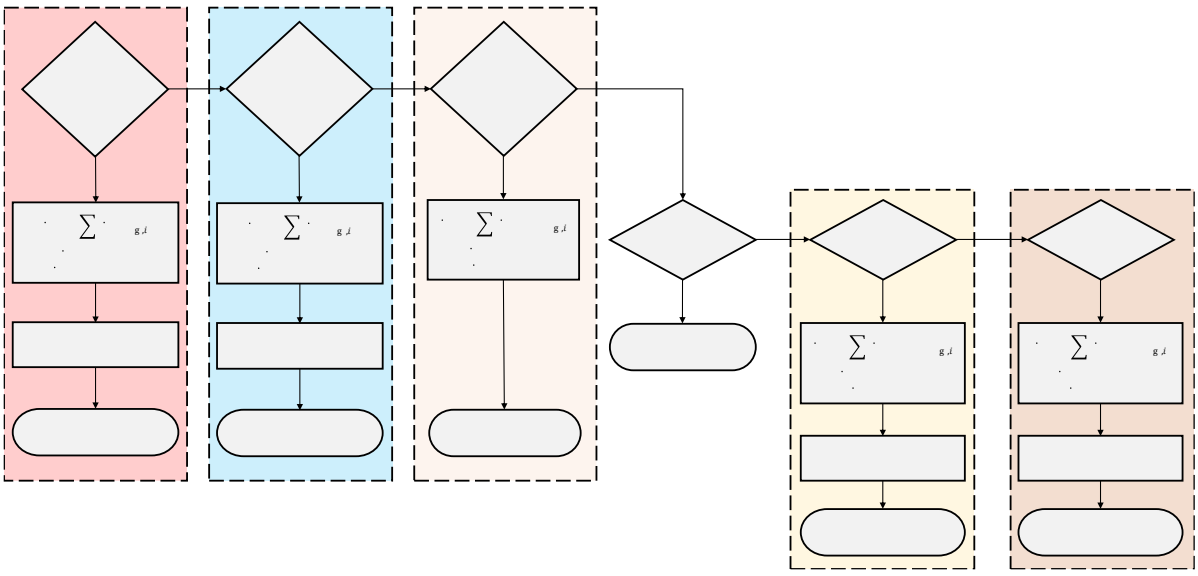

Figure 2: Top-level control strategy for the heat pump system operation.

The heating curve, defining ASHP supply temperatures for space heating based on outdoor temperature, is shown in Figure 3.

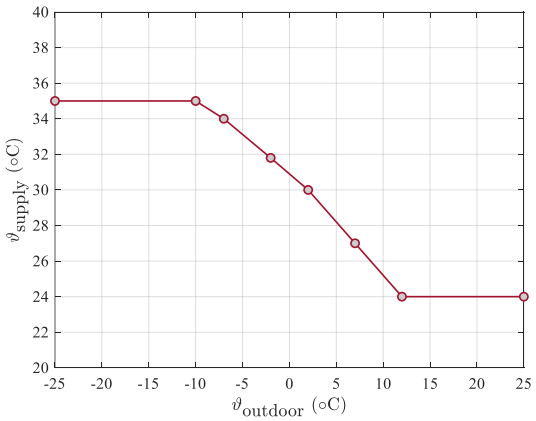

Figure 3: Typical evolution of the heat curve of an ASHP as a function of the outdoor temperature following the recommendations given in Austrian standards.

For DHW, each apartment has a min. demand of 4 kWh/day, addressed by a dedicated 140-liter decentralized DHW tank – Enerboxx – with an internal helical heat exchanger for charging. Figure 4 illustrates the conceptual layout of the BES, encompassing the ASHP, water distribution system, and heat terminals, alongside the multi-family building layout.

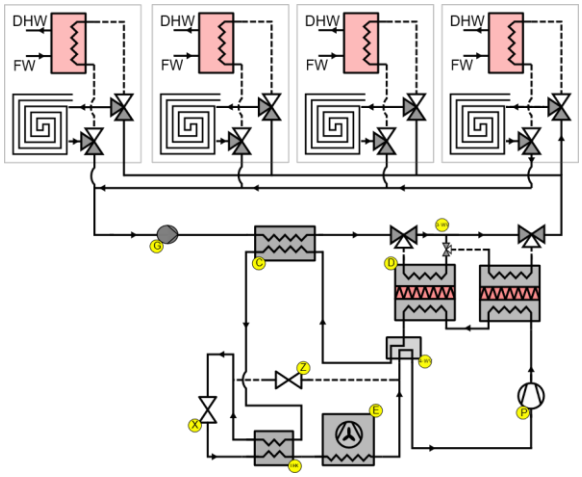

Figure 4: Conceptual layout of the building energy system (i.e. ASHP, building distribution system, heat terminals) and the layout of the multi-family building examined in this work.

Additionally, Table 5 presents typical component values and simulation boundary conditions.

Results and discussion

Enerboxxes are vital for meeting DHW demand, which remains throughout the year compared to SH. Therefore, managing their charging process is crucial. Two approaches are proposed: time-dependent and temperature-dependent. In the time-dependent method, charging occurs at predefined intervals, while in the temperature-dependent approach, charging is triggered when Enerboxxes' temperature drops below a threshold. This study will explore Enerboxxes charging management and its impact on ASHP performance.

Time-dependent approach

Herein, Enerboxxes are charged based on a predetermined schedule, with charging occurring at specific intervals during the day. Two charging periods are designated – one in the morning and one in the evening, each lasting for 130 minutes. During these periods, the ASHP prioritizes DHW operation over SH. This differs from the temperature-dependent approach illustrated in Figure 2, where charging decisions are based on temperature. The manufacturer of the Enerboxxes implements this time-dependent charging strategy. This strategy might impact space heating operations.

Figure 5 shows the indoor temperatures of the four apartments over an 11-day period. All apartments maintain temperatures within the specified range, with none experiencing thermal discomfort. However, Apartment 3, facing south, occasionally exceeds the upper temperature limit due to its orientation.

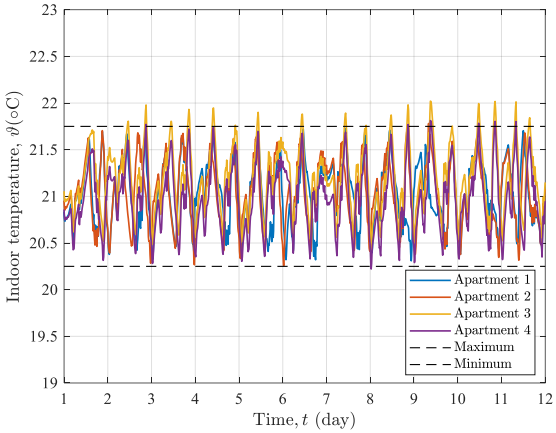

Figure 5: Evolution of indoor temperature for each apartment in the investigated case study under time-dependent charging.

Table 1 presents the SH demand for each apartment in the building under examination, along with the heat supplied by the ASHP to each apartment. Apartments (1) and (2) experience a supply shortfall, with SH demands of approximately 563 kWh and 481 kWh, respectively. The ASHP supplies 516 kWh and 451 kWh to these apartments, leaving a shortage of approximately 76 kWh over the investigation period. These higher heating demands in apartments (1) and (2) are due to their north and east orientations, respectively.

Overall, the ASHP requires 573.6 kWh of electrical input to provide a total heat amount of 1746.8 kWh to the apartments, resulting in a COP of 3.04.

Table 1: Summary on the space heating demand, and the heat supply for each apartment in the investigated case study.

	Space heating demand (kWh)	Space heating supply by ASHP (kWh)	Shortage (-), excess (+) (kWh)
AP 1	562.9	516.1	-46.8
AP 2	480.7	451.3	-29.4
AP 3	387.8	387.8	0
AP 4	391.5	391.5	0
Total	1822.9	1746.8	-76.2

Table 2 summarizes the DHW demand for each apartment covered by the corresponding Enerboxx, along with the associated thermal losses. Apartment 4 demonstrates the highest DHW demand, followed by apartment 1, while the remaining apartments show moderate demand. It is worth noting that the investigation period falls within the winter season, typically associated with higher DHW demand. The total demand for the Enerboxxes, including both DHW demand and thermal losses, amounts to 327.6 kWh over the investigation period.

Table 2: Summary on the DHW demand and thermal losses of each Enerboxx in the investigated scenario.

	DHW demand (kWh)	Thermal losses (kWh)
Enerboxx 1	86.5	6.8
Enerboxx 2	57.9	8.1
Enerboxx 3	51.1	7.9
Enerboxx 4	101.5	7.8
Total	297.0	30.6

During the basic charging phase, the LT-RPW-HEX contributes 173.3 kWh, and the HT-RPW-HEX provides 88 kWh for the top charging phase, with the ASHP supplying the remaining 66.9 kWh. Throughout this period, the ASHP consumes 21.8 kWh of electrical input, achieving a COP of 3.1 for DHW generation. It is important to note that the electrical heating elements remain inactive, indicating that the Enerboxxes' temperature never < 40°C.

Temperature-dependent approach

Here, the Enerboxxes are managed using a hysteresis-based criterion with upper and lower temperature limits set at 52°C and 51°C, respectively, as shown in Figure 4. This approach aims to maintain Enerboxx temperatures above a specific threshold, preventing the need for electrical heating activation. By dynamically monitoring and controlling tank temperatures, this strategy offers more responsive charging compared to fixed-time scheduling.

Figure 6 displays the simulated indoor temperatures of four apartments over an 11-day period. Indoor temperatures fluctuate within a bandwidth of 20.25°C to 21.75°C. Notably, temperatures occasionally dip below 20.25°C more frequently than with the time-dependent strategy. Additionally, indoor temperatures exhibit fewer oscillations compared to the time-dependent pattern. This is due to the longer duration of Enerboxxes charging in the temperature-dependent approach, but with fewer charging periods. Specifically, the time-dependent charging lasts 47.5 hours with 22 periods, while the temperature-dependent approach requires 58.3 hours and 16 periods.

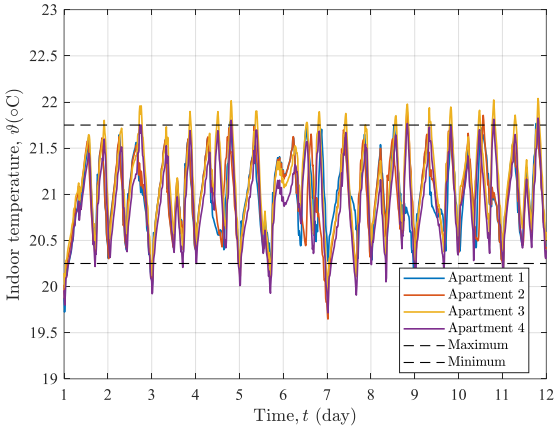

Figure 6: Evolution of indoor temeprature for each apartment in the investigated case study under temperature-dependent charging.

Table 3 reports SH demand for each apartment in the building under the temperature-dependent charging strategy. Both Apartments 1 and 2 experience a reduced supply shortage compared to the time-dependent approach, with supplies of 545 kWh and 474 kWh, respectively.

Table 3: Summary on the space heating demand, and the heat supply for each apartment in the investigated case study.

	Space heating demand (kWh)	Space heating supply by ASHP (kWh)	Shortage (-), excess (+) (kWh)
AP 1	562.9	545.1	-17.8
AP 2	480.7	474.0	-6.7
AP 3	387.8	387.8	0
AP 4	391.5	391.5	0
Total	1822.9	1798.3	-24.5

The remaining apartments have their SH demands fully met. This results in a decreased shortage of 24.5 kWh, marking a 68% improvement in SH coverage. Herein, ASHP electrical consumption increases to 588 kWh to supply a total heat amount of 1823 kWh on the condenser, resulting in a minor rise in COP to 3.06 compared to the time-dependent approach.

Table 4 documents the DHW demand for each apartment covered by the corresponding Enerboxx, along with the associated thermal losses of each Enerboxx, under the temperature-dependent charging strategy. The total demand, including DHW demand and thermal losses, is estimated at 329 kWh over the investigation period. Compared to the time-dependent charging approach, slightly higher thermal losses are observed, likely due to variations in storage temperatures and charging duration, affecting both charging phases.

Table 4: Summary on the DHW demand and thermal losses of each Enerboxx in the investigated scenario.

	DHW demand (kWh)	Thermal losses (kWh)
Enerboxx 1	86.5	7.9
Enerboxx 2	57.9	8.0
Enerboxx 3	51.1	8.1
Enerboxx 4	101.5	8.0
Total	297.0	32.1

Under this strategy, the LT-RPW-HEX share for the basic charging phase decreases to 169 kWh, while the HT-RPW-HEX share for the top charging phase increases to 93 kWh, with the remaining 68 kWh supplied by the ASHP.

These findings indicate that Enerboxxes store hot water at higher temperatures compared to the time-dependent strategy, leading to greater energy allocation to the top-charging phase. The electrical input during the considered period is estimated at 22 kWh, slightly higher than that of the time-dependent charging approach during DHW generation mode. Consequently, a similar COP of 3.25 is achieved for the DHW mode. Furthermore, the temperature of the Enerboxxes never falls below 40°C, ensuring the inactivity of the electrical heating elements.

Conclusions

This study proposed a novel concept aimed at enhancing COP of ASHPs for both heating and DHW generation. Central to this concept is the development of a redesigned refrigeration circuit incorporating an innovative refrigerant-PCM-water heat exchanger (RPW-HEX). This RPW-HEX serves a dual purpose: acting as a desuperheater/storage for DHW during winter and as a condenser/storage during summer. The efficient storage of thermal energy within the RPW-HEX allows for its discharge to Enerboxxes in residential units during DHW.

To ensure optimized operation, comprehensive simulations of the entire system were carried out in Dymola. The work explored the role of the RPW-HEX in meeting DHW demand, and the impact of the charging strategy for Enerboxxes.

The findings revealed that both approaches (time-dependent and temperature-dependent) did not violate the thermal comfort for the occupants under the set boundary conditions. The outcomes exhibited that temperature-dependent approach leads to a margin increase in the COP of the ASHP and higher share of LT-RPW-HEX leading to a reduction in ASHP operation during DHW operation.

Further work will consider the combination of both strategies leading to a “time-temperature-dependent” approach.

Acknowledgement

This research was funded by the Austrian Research Promotion Agency (FFG) under grant no. 879449 (program line “Stadt der Zukunft”, project “CHALLENGE”). The authors wish to acknowledge the financial support for this work.

References

D’Ettorre et al. (2019). Mapping the energy flexibility potential of single buildings equipped with optimally-controlled heat pump, gas boilers and thermal storage. *Sustainable Cities and Society, 50*. doi:10.1016/j.scs.2019.101689.

Emhofer et al. (2019). Integration of a compact two fluid PCM heat exchanger into the hot superheated section of an air source heat pump cycle for optimized DHW generation. *25th IIR International Congress of Refrigeration.* Montreal, Canada. doi:10.18462/iir.icr.2019.645

Emhofer et al. (kein Datum). Experimental demonstration of an air-source heat pump application using an integrated phase change material storage as a desuperheater for domestic hot water generation.

Heinz et al. (2022). The effect of using a desuperheater in an air-to-water heat pump system supplying a multi-family building. *Journal of Building Engineering, 49*. doi:10.1016/j.jobe.2022.104002.

Kim et al. (2018). Experimental study on the performance of multi-split heat pump system with thermal energy storage. *International Journal of Refrigeration, 88*, 523-537. doi:10.1016/j.ijrefrig.2018.01.021.

Table 5: Typical values and boundary conditions for the simulated components.

Symbol	Value	Description
Heat pump system		
A_{EVAP}	45.78 m^2	Evaporator heat transfer area (fins side)
A_{COND}	3.6 m^2	Condenser heat transfer area
η_{vol}	87%	Compressor volumetric efficiency
η_{isen}	60%	Compressor isentropic efficiency
d_{COMP}	0.022 l	Compressor displacement
$T_{heating,SH}$	5 K	Evaporator superheating in heating mode
$T_{cooling,SH}$	11 K	Evaporator superheating in cooling mode
$\vartheta_{comp,\ out}$	110°C	Maximum compressor outlet temperature
$f_{COMP,min}$	20 Hz	Minimum compressor frequency
$f_{COMP,max}$	120 Hz	Maximum compressor frequency
Building and distribution system		
n_{ap}	4	Number of apartments
A_{ap}	125 m^2	Apartment floor area
$\dot{q}$	25 W/m^2	Nominal specific heat load
$A_{building}$	500 m^2	Building total living area
$\dot{Q}$	12.5 kW	Building nominal heat load
ϑ_{Supply}	35°C	Nominal supply temperature
ϑ_{Return}	25°C	Nominal return temperature
$\vartheta_{heating,ST}$	21°C	Heating setpoint temperature
$\vartheta_{cooling,ST}$	25°C	Cooling setpoint temperature
V_{EB}	140 l	Volume of Enerboxx
H_{EB}	1.5 m	Height of Enerboxx
H_{HEX-EB}	1.3 m	Height of internal coil HEX in Enerboxx
RPW-HEX modules		
$x_{RPW-HEX}$	0.1 m	Thickness of RPW-HEX modules insulation
$\lambda_{RPW-HEX}$	0.04 W/(m.K)	Thermal conductivity of RPW-HEX insulation
$Q_{LT-RPW-HEX}$	4.05 kWh	Capacity of LT-RPW-HEX with RT54HC
$Q_{HT-RPW-HEX}$	1.62 kWh	Capacity of HT-RPW-HEX with RT64HC

BauSIM 2024 in Wien
23. September – 26. September

Integration verschiedener Simulationsmethoden zur energieeffizienten Sanierung am Beispiel eines Innenhofes im Welterbe Speicherstadt Hamburg

Zaher Ramadan[1], Lena Teichmann[1], Laura Fernandez Resta[2], Güren Tan Dinga[2], Lukas Boy[2], Harald Garrecht[1], Annette Bögle[2], Daniel Mondino[2], Jochen Schiewe[2]

1 Institut für Werkstoffe im Bauwesen, Universität Stuttgart, Deutschland, E-Mail: zaher.ramadan@iwb.uni-stuttgart.de

2 HafenCity Universität Hamburg, Deutschland, E-Mail: laura.resta@hcu-hamburg.de

Kurzfassung

Sowohl in der Forschung als auch in der Bauindustrie gibt es verschiedene Simulationsmethoden und -programme für thermische und energetische Analysen und Bewertungen im Bauwesen. Oft wird nur eine Methode genutzt, ohne die sinnvolle Ergänzung durch andere Methoden zu berücksichtigen. Dies liegt auch an der mangelnden Kompatibilität der Programme untereinander.

Das Forschungsprojekt „CO2-neutrales Welterbe Speicherstadt Hamburg“ untersucht unter anderem verschiedene Sanierungsmöglichkeiten sowohl in der Bau- als auch Anlagentechnik im Bereich des Denkmalschutzes. Die einzelnen Sanierungskomponenten werden durch die Umsetzung an Klein- und Großdemonstratoren anhand von Messungen und voran- wie nachgehenden verschiedenen Simulationsmethoden untersucht. Alle Informationen, welche im Projekt gesammelt werden, werden über ein IFC-basiertes Dashboard in einem BIM-Modell Bauteil- bzw. raumorientiert erfasst. Dies soll einen schnellen Austausch von Informationen und Ergebnissen sowohl für die verschiedenen Simulationsmethoden als auch für alle anderen Projektbeteiligten ermöglichen.

Ein Teilziel ist es, die passende Simulationsmethode zur passenden Fragestellung zu bestimmen und die Ergänzungen der Methoden und die optimale Nutzung von Synergien zu erforschen. Insbesondere wird auf die thermische Gebäudesimulation mit IDA ICE und die CFD-Simulation mit StarCCM+ eingegangen.

Abstract

Both in research and in the construction industry, there are various simulation methods and programmes for thermal and energy analysis and assessment in the building industry. Often only one method is used without considering the useful addition of other methods. This is also due to the lack of compatibility between programmes.

The research project "CO2-neutrales Welterbe Speicherstadt Hamburg" is investigating, among other things, various renovation options in the field of building services and plant engineering in the area of monument protection. The individual refurbishment components are analysed by implementing them in small and large demonstrators using measurements and various simulation methods, both upstream and downstream. All the information gathered in the project will be recorded on a BIM-model through an IFC-based dashboard, either by component or by room. This will enable the rapid exchange of information and results for both the different simulation methods and all other project participants.

A sub-target is to determine the most appropriate simulation method for each problem and to investigate the complementarity of the methods and the optimal use of synergies. In particular, thermal building simulation with IDA ICE and CFD simulation with StarCCM+ will be analysed.

Einleitung

In der heutigen Zeit verfügen wir über eine Vielzahl von Simulationsmethoden, die es ermöglichen, verschiedene Aspekte von Ingenieur- und Planungsaufgaben zu analysieren und zu verstehen. Von Computational Fluid Dynamics (CFD) über thermische

Gebäudesimulationen bis hin zur Lebenszyklusanalyse (LCA) bieten diese Methoden Einblicke und unterstützen die Entscheidungsfindung in zahlreichen Bereichen. Jedoch erfordert meist jeder dieser Ansätze die Entwicklung eines spezifischen Modells, was Zeit, Ressourcen und Fachkenntnisse erfordert.

Ein zentraler Aspekt, der bei der Anwendung verschiedener Simulationsmethoden oft vernachlässigt wird, ist die Vergleichbarkeit und Integration der Ergebnisse. Oftmals sind die Modelle nicht direkt vergleichbar, was die Interpretation und Integration der Ergebnisse erschwert. Darüber hinaus kann keine einzelne Simulationsmethode alle relevanten Fragen umfassend beantworten, was eine umfassende Herangehensweise erfordert (Nouri et al. 2020).

Building Information Management (BIM) bietet eine vielversprechende Lösung für diese Herausforderungen. Durch die Verwendung von BIM als Grundlage können Modelle nicht nur effizienter erstellt, sondern auch kontinuierlich aktualisiert und erweitert werden. Ein zentrales Dashboard kann als Schnittstelle dienen, von der aus Ergebnisse und Daten aus verschiedenen Simulationsmethoden angewendet und integriert werden können, ohne jedes Mal von Grund auf neu beginnen zu müssen (van Treeck et al. 2021).

Im Rahmen des Projektes 0-CO2-WSHH geht es unter anderem um die Reduzierung der Transmissionswärmeverluste über die Außenwandflächen des Innenhofes im Speicherblock H. Zusätzlich wird angestrebt, bessere klimatische Bedingungen im Innenhof zu schaffen Der gegenwärtige Zustand des Innenhofs, der eng und langgestreckt ist, erzeugt ein ungemütliches und unbehagliches Klima, das nicht zum Verweilen einlädt. Eine mögliche Maßnahme ist die Errichtung einer Überdachung für den Innenhof, um den freien Luftzugang zu beschränken und während der Heizperiode eine gezielte Temperaturregulierung zu ermöglichen. Die Nutzung der Abwärme aus den Nutzereinheiten könnte die Innenhoftemperaturen erhöhen, was wiederum die Transmissionswärmeverluste der Außenwände verringern würde. Des Weiteren soll untersucht werden, ob der Innenhof als Energiegarten fungieren kann, um die Transmissionswärmeverluste der angrenzenden Außenflächen (Wände und Fenster) zu reduzieren. Dies erfordert eine umfassende Analyse mittels numerischer Simulationen, einschließlich CFD und thermischer Gebäudesimulationen. Ein weiterer Untersuchungsschwerpunkt liegt auf der Beurteilung der Auswirkungen einer Überdachung auf das Innenhofklima unter Berücksichtigung verschiedener Witterungsbedingungen. Dabei ist es von Bedeutung, dass die Fenster weiterhin für die nächtliche Kühlung der vermieteten Nutzungseinheiten genutzt werden können.

Zur Verwaltung des im Projekt verwendeten Gebäudeinformationsmodells wurde im Zuge des Projektes eine Web-App entwickelt, die BIM-Modelle im IFC-Format darstellen und verwalten kann. Die Web-App fungiert als zentrales Dashboard zur Zusammenführung und Visualisierung relevanter Daten, einschließlich der bauphysikalischen Eigenschaften der Konstruktionen sowie verschiedener Simulationsergebnisse. Sowohl für CFD als auch für die thermischen Simulationen wurde das Dashboard genutzt. Dabei wurden die Modelle im Anschluss weiter angepasst und teilweise vereinfacht, um die Kompatibilität mit der Simulationssoftware sicherzustellen. Zusätzliche Informationen wie Klimadateien werden im Dashboard abgelegt, um eine ganzheitliche Analyse zu ermöglichen. Diese integrierte Plattform bietet einen effizienten Zugang zu den benötigten Informationen und unterstützt somit die Entscheidungsfindung und Optimierung im Projektverlauf.

CFD Simulationen

Das 3D-Fluid-Solid-Modell

Um die potenziellen Verbesserungen angemessen zu bewerten, wird der Innenhof zusammen mit verschiedenen Ausführungsvarianten einer möglichen Überdachung mittels CFD-Simulationen analysiert. Hierbei werden die Wände (Wandbauteil und Fenster), Böden sowie die nach außen offenen Durchgänge zum Innenhof hin und die Dachkonstruktion im 3D-Modell detailliert abgebildet. Um die Wärmespeicherung der opaken Bauteile zu berücksichtigen, fließen die bauphysikalischen Eigenschaften der Wandaufbauten aller zum Innenhof gerichteten Außenwände in die Berechnungen ein. Des Weiteren wird das Solarstrahlungsangebot des Testreferenzjahres verwendet, um die solaren Einträge über eine transparente Überdachung des Innenhofs zu analysieren und zu bewerten. Die Modellbildung basiert auf dem ersten Konstruktionsentwurf zur Innenhofüberdachung von Demirag Architekten. Zwei verschiedene Entwürfe wurden vorgelegt, die sich in der Höhe der Überdachung unterscheiden. Beide Entwürfe wurden mittels CFD-Analyse untersucht, um die optimale Positionierung der Überdachung aus bauphysikalischer und energetischer Sicht zu ermitteln. Eine tiefergelegene Anordnung der

Überdachung erzielt keinen energetisch oder wirtschaftlich interessanten Effekt, da die oberen Geschosse weiterhin einen hohen Verlust an Transmissionswärme und Lüftungswärmeverlust aufgrund der höheren Anströmung der zum Innenhof gelegenen Fenster an windigen Tagen erfahren.

Abbildung 1Abbildung 1 zeigt die beiden verschiedenen Höhenlagen der im Erstentwurf projektierten Überdachung.

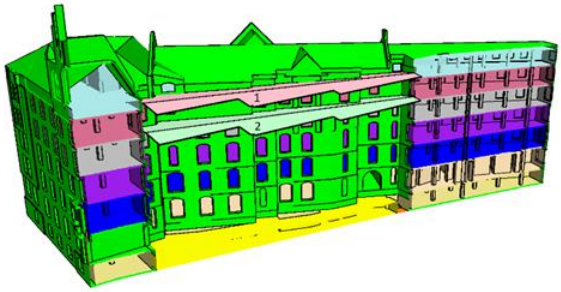

Abbildung 1: Längsschnitt durch den Block H mit den zwei Varianten der Überdachung

Für die ersten Vorsimulationen zur möglichen Integration einer Überdachung wurde das Modell in Abbildung 2Abbildung 2 erstellt. Diese Vorsimulationen dienen dazu, die Effizienz der Überdachung zu untersuchen und zu berechnen. Bei positiven Ergebnissen sind weitere Schritte geplant, darunter die Forschung zur denkmalgerechten Konstruktion der Überdachung, zum optischen Erscheinungsbild, Brandschutzmaßnahmen und zur Integration von PV-Modulen.

Abbildung 2: 3D-Modell von Block H

Um die Zellenanzahl des Modells zu reduzieren und die Berechnungszeit zu verkürzen, wurden räumliche Bereiche, die für die Innenhofsimulation weniger relevant sind, ausgelassen (Ramadan et al. 2019), wodurch ca. 1,7 Millionen Zellen bzw. Elemente entstanden. Die resultierenden Flächen wurden als Symmetrieebenen definiert.

Die unmittelbare Umgebung spielt eine entscheidende Rolle bei den Transmissionswärmeverlusten, daher wurde das Modell um eine weitere Region erweitert, wie in Abbildung 3Abbildung 3 dargestellt. Hier sind auch die Erweiterungen bei den Zugängen zu sehen, da der Einfluss der Strömung in der Umgebung berücksichtigt werden muss. Nach der Erstellung des Modells wurden die physikalischen Eigenschaften der einzelnen Bauteile sowie der Stoffe, wie Dichte, Wärmespeicherkapazität und Wärmeleitfähigkeit, als Eingabeparameter festgelegt. Die Strahlungswerte wie Emissions- und Transmissionsgrade wurden ebenfalls bestimmt, wobei die Überdachung als semitransparent betrachtet wurde.

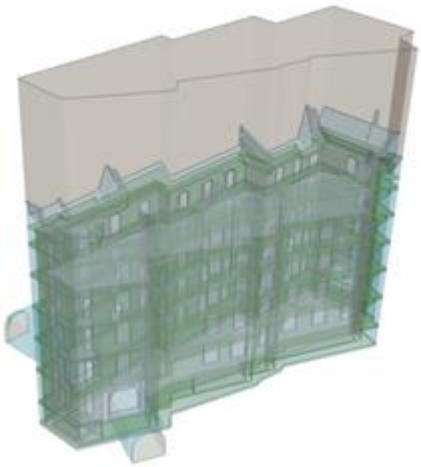

Abbildung 3: Das geschnittene 3D-Modell mit den Erweiterungen

Stationäre Betrachtung

Für die stationäre Betrachtung eines Winterfalls wurde der 15.01.2022 um 13:30 Uhr mit klarem Himmel als Stichtag ausgewählt. Zu diesem Zeitpunkt betrug die Außentemperatur 7 °C, die Windgeschwindigkeit lag bei 6,5 km/h aus südwestlicher Richtung, und es herrschte ein Überdruck von 14,75 mbar. Die Simulationen wurden unter der Annahme beheizter Räume mit einer Solltemperatur von 21 °C durchgeführt. Dabei wurde das Szenario sowohl mit als auch ohne Überdachung betrachtet, um den Einfluss der Überdachung in einer stationären Betrachtung zu untersuchen. Die Höhe der Überdachung wurde vorläufig zwischen dem dritten und dem vierten Obergeschoss festgelegt.

Die ersten Ergebnisse zeigen, dass die Transmissionswärmeverluste durch die Etagenwände zum Innenhof mit dem Einsatz der Überdachung kaum sinken. Dies liegt an den großen Zugängen zum Innenhof, die zu einer Durchmischung der Luft zwischen Umgebung und überdachtem Innenhof führen und somit die Luft im Innenhof abkühlen (Flieger et al. 2014). Daher wurden weitere Simulationen durchgeführt, bei denen diese Zugänge als geschlossen angenommen wurden, um die Abkühlung des Innenhofs durch die

Luftdurchmischung mit der Außenluft zu verhindern. Hierbei wurde die Luft im Innenhof von der Außenluft "getrennt", was zu einer deutlichen Verringerung der Luftgeschwindigkeiten im Innenhof führte. Abbildung 4 und Abbildung 5 zeigen die Strömungslinien mit der Luftgeschwindigkeit in den Quer- und Längsschnitten des Innenhofs sowohl bei geöffneten als auch bei geschlossenen Zugängen.

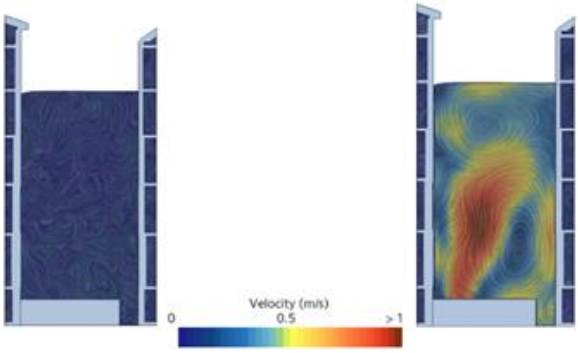

Abbildung 4: Strömungslinien und Luftgeschwindigkeiten im Innenhofquerschnitt (rechts: Zugänge offen, links: Zugänge zu)

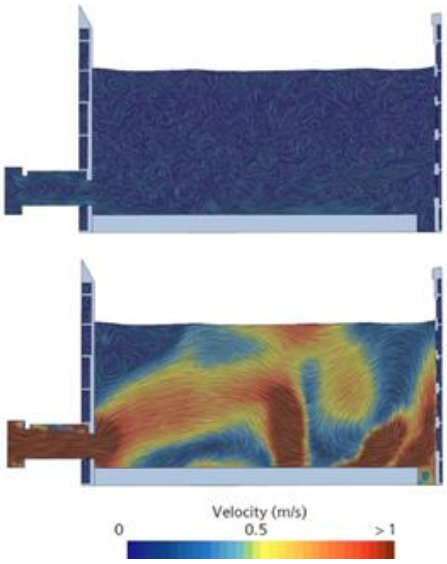

Abbildung 5: Strömungslinien und Luftgeschwindigkeiten im Innenhofquerschnitt (oben: Zugänge zu, unten: Zugänge offen)

Abbildung 6Abbildung 3 illustriert die Verringerung der Transmissionswärmeverluste in den Etagen durch die Wände zum Innenhof. In jeder Etage unter der Überdachung verringerten sich die Wärmeverluste um ca. 1,8 kW, wenn die Zugänge zum Innenhof geschlossen waren. Im Gegensatz dazu verringerten sich diese Wärmeverluste kaum, wenn die Zugänge weiterhin offen waren. Bei beiden Fällen stiegen die Wärmeverluste durch die Wände des fünften Obergeschosses um ca. 500 W an. Dies ist auf den Luftauftrieb nahe den Außenwänden zum Innenhof zurückzuführen, der die Wärme mit sich nach oben nimmt und die Lufttemperatur nahe der Wand leicht ansteigen lässt, was wiederum die Transmissionswärmeverluste in den oberen Etagen leicht verringert. Dieser Luftauftrieb wird durch die Überdachung unterbrochen, was zu einer leichten Abkühlung im Nahbereich des fünften Obergeschosses führt. Im Nahbereich des vierten Obergeschosses bleibt die Temperatur dank der Wärmekonvektion über der Überdachung jedoch unverändert. Abbildung 7Abbildung 4 stellt die Temperaturverteilung im Querschnitt des Innenhofs dar.

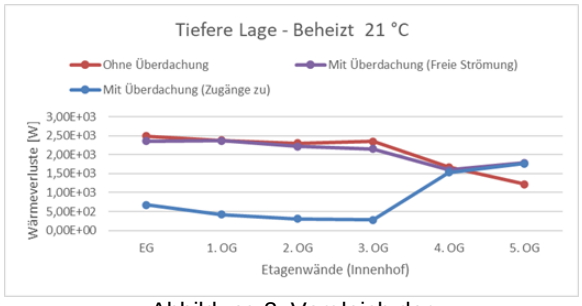

Abbildung 3: Vergleich der Transmissionswärmeverluste durch die Etagenwände zum Innenhof bei einer Überdachung zwischen dem dritten und dem vierten Obergeschoss

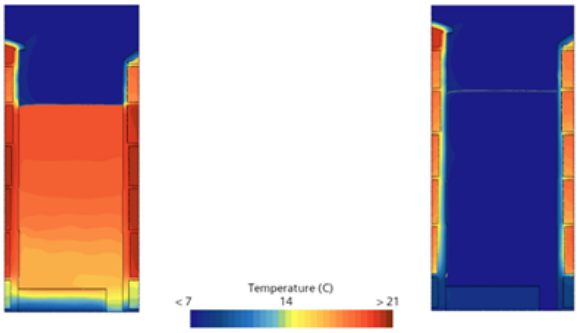

Abbildung 4: Temperaturverteilung im Innenhofquerschnitt (rechts: Zugänge offen, links: Zugänge zu)

Um die optimale Höhe der Überdachung festzustellen, wurden weitere Simulationen mit den gleichen Randbedingungen durchgeführt, jedoch mit einer Überdachung zwischen dem vierten und dem fünften Obergeschoss. Abbildung 8Abbildung 5 zeigt eine Verringerung der Wärmeverluste von bis zu 2 kW in jeder Etage unter der Überdachung. Trotz der Überdachung bleiben die Wärmeverluste beim fünften Obergeschoss im Vergleich zur tieferen Lage der Überdachung unverändert, da die Luft nahe der Überdachung aufgrund der Wärmekonvektion wärmer ist als die Luft im Fernbereich.

Abbildung 9Abbildung 6 bietet einen umfassenden Überblick über die Wärmeverluste in den drei verschiedenen Szenarien - ohne Überdachung, mit Überdachung (höherer und

tieferer Lage). Dabei beschreibt die Linie "Ohne Überdachung" die aktuelle Situation des Innenhofs, bei der die Zugänge noch offen sind. Der Hauptunterschied zwischen der höheren und der tieferen Lage der Überdachung liegt im vierten und fünften Obergeschoss. Basierend auf diesen Ergebnissen wurde die Höhe der Überdachung zwischen dem vierten und dem fünften Obergeschoss festgelegt, und es wird eine denkmalgerechte Konstruktion der Überdachung entworfen.

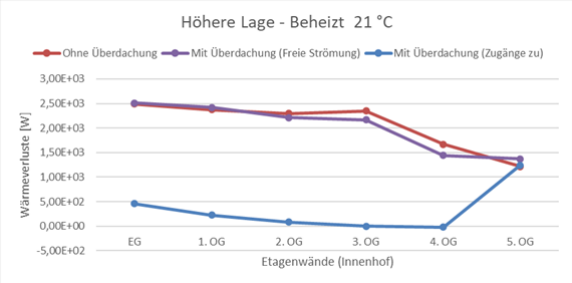

Abbildung 5: Vergleich der Transmissionswärmeverluste durch die Etagenwände zum Innenhof bei einer Überdachung zwischen dem vierten und dem fünften Obergeschoss

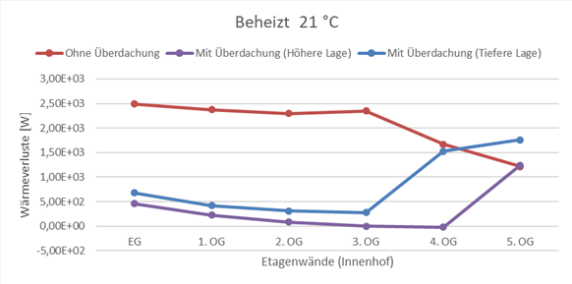

Abbildung 6: Vergleich der Transmissionswärmeverluste durch die Etagenwände zum Innenhof

Als nächster Schritt soll die eingesparte Energie durch die Überdachung und das Verschließen der Zugänge zum Innenhof für den gesamten Block mittels Gebäudesimulationen ermittelt werden. Diese Simulationen berücksichtigen den Block instationär über das gesamte Jahr, da eine derartige Betrachtung mit CFD-Simulationen aufgrund der Rechenzeit nicht durchführbar ist.

Thermische Gebäudesimulationen

Für die instationäre Betrachtungen über ein Jahr wurde ein gesondertes Grundmodell in IDA ICE erstellt. Auch hier dient das Dashboard als zentraler Punkt zum Datenaustausch zwischen den Simulationen und dem BIM-Modell und führt somit zu einer gleichbleibenden, dezentralen Datenbasis (Zucker et al. 2022).

Um den Simulationsaufwand zu reduzieren, wurde das Grundmodell vereinfacht aufgebaut. Die Geschosse wurden stark vereinfacht dargestellt und werden in der Simulation auf konstant 21°C temperiert. Dadurch können die internen Wärmegewinne, das Nutzerverhalten und die Raumnutzung vernachlässigt werden und müssen nicht simuliert werden. Die Fensterflächen wurden ausrichtungs-, geschoss- und zonenweise zusammengefasst. Die Überdachung wird zunächst vereinfacht und als eben und verglast angenommen, da die Dachkonstruktion noch nicht festgelegt wurde. Auch hier werden Varianten mit unterschiedlichem Gesamtenergiedurchlassgrad betrachtet. Durch die Vereinfachungen lassen sich keine absoluten, sondern nur relative Aussagen über die Energiebedarfsveränderung durch die verschiedenen Überdachungsversionen treffen. Folglich müssen die Betrachtungen auf Relativwerte begrenzt werden. Zur Unterstützung der Entscheidungsfindung sind diese Werte jedoch ausreichend. Zusätzlich wurden verschiedene Oberflächentemperaturen der Wände des Innenhofes simuliert und können dann für einzelne Zeiträume mit der CFD-Simulation verglichen werden.

Der Hauptunterschied, die Höhenlage der Überdachung, unterteilt die verschiedenen Varianten in zwei Hauptgruppen. Aus dem vereinfachten Grundmodell wurden zwei weitere Basismodelle entwickelt, dabei unterscheidet sich die Höhe der Überdachung in 16,8 und 20,3 m. In beiden Hauptgruppen wurden dann analog weitere Anpassungen durchgeführt. Anschließend wurden noch Untersuchungen zur Überdachungshöhe von 21,3m durchgeführt.

Des Weiteren wurde untersucht, wie sich eine Schließung der Durchgänge im Innenhof auf die thermische Situation im Innenhof auswirkt. Dabei wurde zusätzlich darauf geachtet, dass die Türen in den Durchgängen vermutlich nicht ständig geschlossen sind, sondern zu Hauptverkehrszeiten auch längere Zeit offenstehen können. Für die Darstellung dieser Problematik wurde ein Zeitplan in IDA ICE erstellt und in den Simulationsvarianten bedacht. Dabei wurde auch untersucht, ob überhaupt eine Schließung der Durchgänge zu erfolgen hat, und welchen Einfluss eine zeitweise Öffnung der Durchgänge hat.

Durch den Vergleich des Heizwärmebedarfs der verschiedenen Varianten konnte, wie auch schon in den CFD Simulationen, festgestellt werden, dass eine höhere Lage der Innenhofüberdachung den Heizwärmebedarf senkt. Die Anbringung der Überdachung ein Stockwerk höher führt zu einer Reduktion um ca. 5%. Zudem wurde festgestellt, dass eine Schließung der Durchgänge einen starken Einfluss auf die Reduzierung des

Heizwärmebedarfs hat (7-9%). Diese Ergebnisse wurden für die weitere Entwurfsentwicklung der Innenhofüberdachung beachtet. Dies führte zum Entschluss, dass der Anschluss der Innenhofüberdachung in etwa an der Traufkante entlangführen soll. Zusätzlich wurde beschlossen, dass eine feste Verglasung mit integrierten Glastüren in allen drei Durchgängen angebracht werden sollen, falls die Innenhofüberdachung umgesetzt werden soll.

Während der Entwurfsentwicklung ergab sich zusätzlich die Frage, wie groß der Einfluss der Wärmeleitfähigkeit der Überdachung ist. Daher wurden auch hier unterschiedliche Varianten erstellt und die Ergebnisse miteinander verglichen. Die Ergebnisse lassen sich dabei wie folgt zusammenfassen. Der Unterschied beim Wärmedurchgangskoeffizient der Überdachung ist rein auf die Reduktion des Heizenergiebedarfs gering. Im Vergleich von einer Überdachungslösung mit einem U-Wert von 5,8 W/m2K und einem U-Wert von 2,0 W/m2K erfolgt eine Reduktion von ca. 3%, Punkte wie Tauwasserbildung oder ähnliches sollten dann aber in einem weiteren Schritt genauer betrachtet werden.

Da eine komplett geschlossene Innenhofüberdachung im Sommer zu einer Erhöhung des Kühlbedarfs führen würde (Morbitzer et al., 2015), sollen die Durchgänge mit steuerbaren Glaslamellen ausgestattet werden, um einen Durchzug zu ermöglichen. Zudem soll die Innenhofüberdachung so gestaltet werden, dass in der Dachstruktur öffenbare Flächen integriert sind. Diese Flächen können im Sommer geöffnet werden, um eine weitere Entlüftung zu ermöglichen, wenn die Durchgänge zur Frischluftzufuhr bereits geöffnet sind.

Um dieses Szenario zu überprüfen und mögliche Zugerscheinungen zu vermeiden, wird eine CFD-Simulation durchgeführt, sobald die abschließende Dachstruktur konstruiert ist. Diese Belüftungstechnik nutzt die Kaminwirkung des Innenhofs, um hohe Temperaturen im Sommer zu vermeiden, die nach einer stationären CFD-Simulation im Innenhof unter der Überdachung im "Worst-Case"-Szenario bis zu 60 °C erreichen können. Mit der geplanten Belüftungstechnik soll eine Luftqualität im Innenhof geschaffen werden, die sowohl zum Lüften der angrenzenden Räume als auch zum Verweilen im Innenhof geeignet ist.

Des Weiteren dienen die öffenbaren Flächen im Brandfall zum Entrauchen. Auch hierfür wird eine CFD-Simulation durchgeführt, sobald die Dachkonstruktion festgelegt wurde. Zusätzlich kann der komplett überdachte Innenhof in der Übergangszeit und im Sommer bei schlechtem Wetter genutzt werden, da er sowohl wind- als auch niederschlagsgeschützt ist (van Treeck et al., 2008).

Zusammenfassung und Ausblick

Die Integration verschiedener Simulationsmethoden trägt zur Effizienz der Analyse bei. In dieser Arbeit wurden CFD-Simulationen für die stationäre Betrachtung und die Strömungsanalyse genutzt, um die optimale Höhe der untersuchten Überdachung zu bestimmen und die Bedeutung des Verschließens der Eingänge hervorzuheben. Auf der anderen Seite wurden thermische Gebäudesimulationen für die dynamischen Betrachtungen eingesetzt, um das Potenzial der Energieeinsparung durch die Überdachungsmaßnahme zu berechnen und den Einfluss der Mehrschichtigkeit der Überdachung zu untersuchen.

Zusätzlich zu den energetischen Betrachtungen müssen in die Überlegungen zur Innenhofüberdachung auch weitere Punkte der Ökologie wie auch der Ökonomie mit einfließen. Die energetische Betrachtung ist nur ein Punkt von vielen, der in der Entscheidungsfindung unterstützen kann (Vollmer et al. 2023).

Danksagung

Diese Arbeit ist Teil des Forschungsprojektes 0-CO2-WSHH „CO2-neutrale Welterbe Speicherstadt Hamburg“ (Förderkennzeichen 03EN3027), das vom Bundesministerium für Wirtschaft und Klimaschutz (BMWK) im Rahmen des "7. Energieforschungsprogramms" gefördert und mit Hilfe des Projektträgers Jülich (PtJ) durchgeführt wird.

Das Forschungsprojekt ist als Verbundprojekt angelegt und umfasst folgende Partner: Die HHLA 1. Speicherstadt Immobilien GmbH & Co. KG als gemeinsamer Koordinator, das Institut für Wekstoffe im Bauwesen der Universität Stuttgart, das BIMLab der HafenCity Universität Hamburg und der Lehrstuhl für Gebäude- und Raumklimatechnik der RWTH Aachen. Darüber hinaus sind die Behörde für Umwelt, Klima, Energie und Agrarwirtschaft sowie die Behörde für Kultur und Medien mit dem Denkmalschutzamt der Freien und Hansestadt Hamburg als assoziierte Partner beteiligt.

Literatur

van Treeck, C., Fichter, E., Weck-Ponten, S., Siwiecki, J., & Nouri, A. (2021). BIM für die Energiebedarfsermittlung und Gebäudesimulation. Building Information

Modeling: Technologische Grundlagen und industrielle Praxis, 427-441.

Nouri, A., Nicolai, A., Krämer, B., Hirth, S., Agudelo, J., Seifert, C., Malhotra A., Madjidi M., Frisch J. & van Treeck, C. (2020). Entwicklung von Qualitätsstandards für die energetische Gebäude-und Anlagensimulation als Planungswerkzeug. Proceedings of BauSIM 2020, 23-25.

van Treeck, C., Pfaffinger, M., Wenisch, P., Frisch, J., Yue, Z., Egger, M., & Rank, E. (2008). Numerische Simulation des thermischen Behaglichkeitsempfindens in Innenräumen. Konferenzbeitrag. Bausim.

Ramadan, Z., & Garrecht, H. (2019, October). Thermal flow simulation for an energy garden building block. In IOP Conference Series: Materials Science and Engineering (Vol. 615, No. 1, p. 012066). IOP Publishing.

Flieger, B., Jin, M., Steinhoff, P., Schmidt, M., Müller, D., & Chen, Q. (2014). Modellierung von Innenraumströmungen in der Gebaudesimulation. In 5th German-Austrian IBPSA Conf. RWTH Aachen Univ., Aachen.

Vollmer, M. (2023). Methode zur Ermittlung und Optimierung des ökologischen Flächenbedarfs von Gebäuden basierend auf Lebenszyklusanalysen (LCA) und thermischen Gebäudesimulationen (Doctoral dissertation, Technische Universität München).

Morbitzer, C., von der Weide, P., & Schröter, A. (2015). Simulationsbasierte Bewertung sommerlicher Bedingungen in Gebäuden. Bauphysik Kalender 2015: Simulations-und Berechnungsverfahren, 377-414.

Zucker, G., Sporr, A., Blank-Landeshammer, B., Ruhsam, C., Gutierrez, A., Kogler, K., ... & Puregger, F. (2022) BIM-basierte Planungsmethoden zur Sicherstellung von Energieeffizienz im Bauprozess.

Deutscher Wetterdienst. (2024). Offene Daten des Deutschen Wetterdienstes. Abgerufen am [10.01.2023], von [https://kunden.dwd.de/obt/index.jsp]

BauSIM 2024 in Wien
23. September – 26. September

Investigation of optimal hybrid energy systems for detached single family house districts under different boundary conditions

Maximilian Friebe[1], Arda Karasu[2] und Martin Kriegel[1]

[1]*Chair of Energy, Comfort & Health in Buildings (Hermann-Rietschel-Institut), Technische Universität Berlin, Marchstr. 4, 10587 Berlin, Germany*

[2]*Chair of Building Technology and Architectural Design, Technische Universität Berlin, Str. des 17. Juni 152, 10623 Berlin, Germany*

Abstract

Energy planning at the municipality level has come into focus in Germany with the introduction of the "Act for heat planning and the decarbonization of heating networks". A primary challenge in this process is identifying optimal energy sources and producers.

This investigation delves into the optimal design of hybrid energy systems for districts comprising detached single-family houses, considering three different building ages and varying energy costs. The optimal hybrid energy system is identified for 4158 scenarios using multi-objective optimization, considering both total annual costs and carbon dioxide emissions.

The results show, that biomass boilers present the highest capacity in the optimized hybrid energy system in all investigated scenarios. The optimal capacity of heat pumps depends on the building class and the corresponding supply temperature. In the oldest building age class they are not selected as part of the hybrid energy system, whereas they cover up to 28.2% in the newest building age class. Additionally the results reveal a strong positive correlation with the capacity of the Photovoltaics showing a correlation coefficient of 95.39% for the newest building age class. The findings underscore the advantage of hybrid energy systems for detached single family house districts, as in 99% of the scenarios the optimal system comprises of three or more different heat producers.

Introduction

Implementing the "Federal Climate Protection Act" Germany has set itself the target to reach a 65% reduction of greenhouse gas emissions by 2030, compared to 1990 (Bundestag (2019)). The building sector, which accounts for approx. 30% of Germany's greenhouse gas emissions (Umweltbundesamt (2023)) is a key component to achieve this goal. An efficient decarbonization of the building stock can only be reached with energy planning on a municipal level (Pasimeni et al. (2014)). Consequently Germany introduced the "Act for heat planning and the decarbonization of heating networks", which obliges all municipalities in Germany to create a municipal heat plan until 2028 (Bundestag (2023)).

A central issue in heat planning is the transformation of the heating sector to meet the emission reduction targets. Due to the wide range of different heat production systems, such as heat pumps, boilers and solar thermal collectors various combinations are possible. In order to identify the optimal solution, researchers apply different optimization methods. In this context, it can be distinguished between single and multi-objective optimization approaches. The majority of studies about energy system optimization adhere to multi-objective optimization methods.

Majidi et al. (2017) utilized the weighted sum method, which weighs different objectives depending on their importance in a single objective function, to optimize a hybrid energy system. In contrast Falke et al. (2016) identify so-called "Pareto-Optima", meaning optimal solutions where no feasible solution exists that could improve one objective without deteriorating at least one other objective. Another common method is the ε-constraint method, which converts a multi-objective problem into a single objective problem, defining the other objectives as constraints. Kersten et al. (2021) used the Open Energy Modelling Framework (oemof) applying a ε-constraint method, to optimize heat supply of a sub-urban region in northern Ger-

many. The same framework is applied by Friebe et al. (2023) presenting a method to compare district heating network supply with individual heating systems for each building.

In the present study parts of this methodology are used to conduct a parametric study on the optimal hybrid energy system for districts comprising detached single-family houses. The study considers different building ages and varying energy costs. The goal is to investigate the impact of these parameters on the selection of the producers and their capacity.

Methodology

The following sections explain the methodology that was applied in this study. First, the structure of the optimization model and all central assumptions are explained. This is followed by a description of the boundary conditions of the parametric study that was conducted.

Optimization model

To create the model of an average district of a detached single-family housing, the district typology developed in the research project "UrbanReNet" by Drebes et al. (2012) is utilized. The most suitable district type from this typology is type 1a, which is characterised by "small, detached residential buildings, predominantly low and medium storeys". A typical plot ratio for this district type of 0.23 and a footprint area of $200\,000\,\mathrm{m}^2$ is assumed. The building stock is modelled, using an archetype-approach. Table 1 shows the TABULA-archetypes, that are used for this purpose.

Table 1: Archetypes from the TABULA database

Building age	TABULA archetype
1958 - 1968	DE.N.SFH.05.Gen
1995 - 2001	DE.N.SFH.09.Gen
2016	DE.N.SFH.12.Gen

The weather data for a Test Reference Year for climate zone 4 serves as an input file to calculate load profiles for space heating and domestic hot water, renewable energy generation profiles and heating supply temperatures in an hourly resolution. Further details can be obtained from Friebe et al. (2023). The optimization model of the district is created using the python-framework oemof developed by Krien et al. (2020). The model utilizes an ε-constraint method, with the emission reduction target acting as a constraint and the annual costs as the objective function to be minimized. The emission reduction constraint is set at 65%, aligning with Germany's climate target for 2030. Gas-based heat generation is set as the reference for calculating emission savings.

Figure 2 shows a visualization of the optimization model. A detailed description of the model can be obtained from Friebe et al. (2023).

The model assumes a central heat supply via district heating network. To optimize the use of renewable energies, a 3-Level-district heating network with a constant temperature level for domestic hot water and a gliding temperature level for space heating is considered. For this purpose a temperature difference between district heating network supply temperature and building design temperature of 10 K is assumed (see Figure 1).

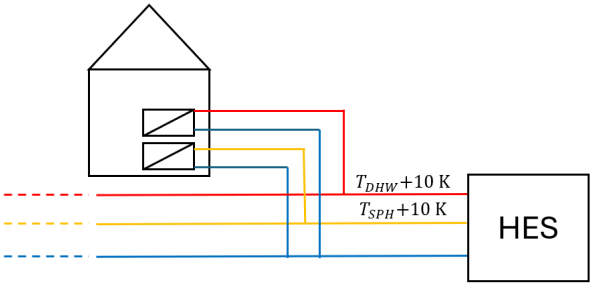

Figure 1: Schematic of the 3-Level-district heating network (HES: Hybrid energy system)

Heat losses of the DHN are taken into account using data from Dötsch et al. (1998).For a district comprising single-family houses, the reported heat loss ranges from 12 to 17% of heat losses. Therefore, the mean value of this range, 14.5%, is adopted The subsequent energy producers are then taken into consideration.

The following energy producers are taken into account:

- Combined heat and power, natural gas (CHP)
- Gas boiler (Condensing boiler, natural gas)
- Biomass boiler
- Air source heat pump
- Ground source heat pump
- Solar thermal collectors
- Photovoltaics

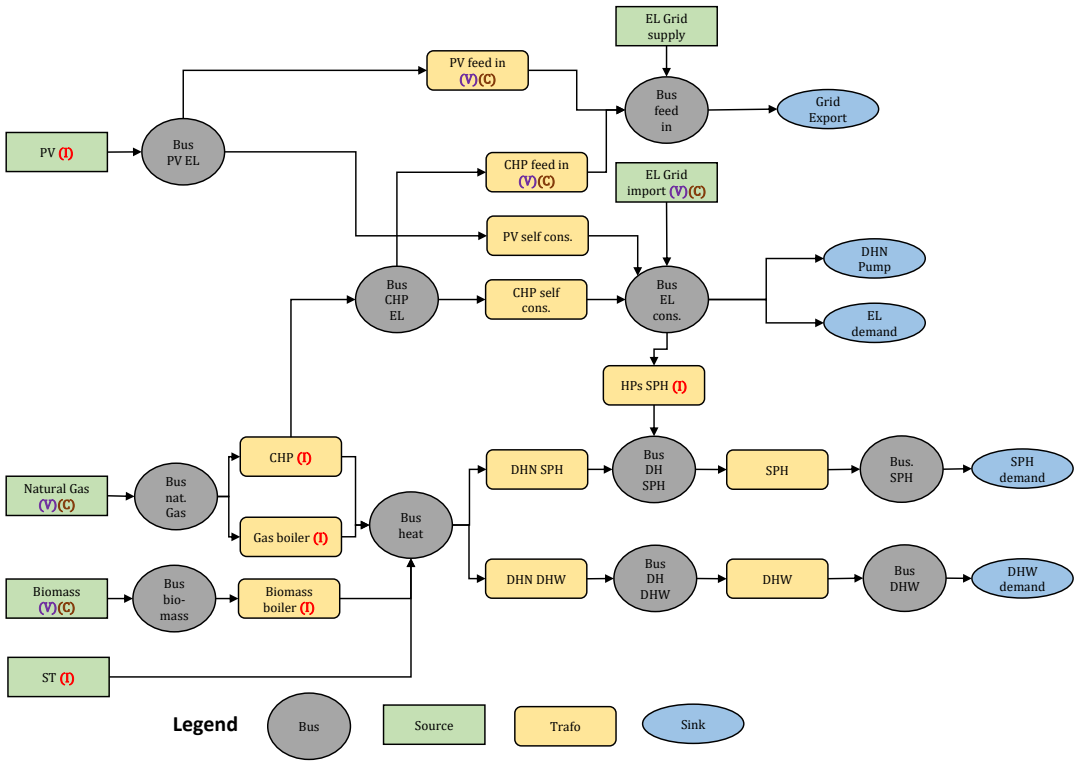

Figure 2: Schematic of the components of the oemof model. (I): components with investment costs, (V): components with variable costs, (C): components with CO_2 emissions (based on Friebe et al. (2023)).

Table 2 displays the specific annual costs for all energy producers examined in this study. These costs include investment, replacement, and operational costs. An interest rate of 4.4% is assumed. Further information about the cost calculation can be found in Dunkelberg et al. (2020*b*) and Dunkelberg et al. (2020*a*).

Table 2: Specific annual costs of energy producers (adapted from Dunkelberg et al. (2020*b*) and Dunkelberg et al. (2020*a*) adjustet to current price index).

	Specific annual costs
CHP	$93.59\,€\,kW^{-1}\,a^{-1}$
Gas boiler	$15.98\,€\,kW^{-1}\,a^{-1}$
Biomass boiler	$97.19\,€\,kW^{-1}\,a^{-1}$
Air source heat pump	$79.72\,€\,kW^{-1}\,a^{-1}$
Ground source heat pump	$173.72\,€\,kW^{-1}\,a^{-1}$
Photovoltaics	$38.27\,€\,m^{-2}\,a^{-1}$
Solar thermal collectors	$103.26\,€\,m^{-2}\,a^{-1}$

The CO_2-emissions are calculated, based on the emission factors, that are shown in Table 3.

Table 3: Emission factors of energy carriers (Umweltbundesamt (2021) and Deutsches Institut für Normung e.V. (2010))

Energy carrier	Emission factor in $kg\,kWh^{-1}$
Electricity	0.401
Natural gas	0.24
Biomass	0.04

Parametric Study

In order to account for different boundary conditions a parametric study is conducted. This study consideres the age class of the districts' buildings and the costs for different energy carriers. Three different building age classes, according to the TABULA database (Loga et al. (2016)) were investigated. Table 4 provides an overview of these age classes. The building age classes will be refered to as BA1-BA3 in the the rest of the paper. The annual heating demand was determined using the typical measured consumption data from TABULA. The corresponding system temperatures are based on typical heating systems for buildings of different ages. For domestic hot water a constant supply temper-

Table 4: Building age classes and corresponding design temperatures and heat demand (space heating: SPH and domestic hot water: DHW), that were investigated in the parametric study

Building age	T_{Sup}/T_{Ret} in °C	$Q_{SPH+DHW}$ in GWh a^{-1}
1958 - 1968 (BA1)	90/70	11.73
1995 - 2001 (BA2)	70/50	6.89
2016 (BA3)	45/35	3.78

Table 5: Investigated range of energy costs for the considered energy carriers (Strom Report (2024), Pawlik (2024), Statistisches Bundesamt (2023))

	Natural gas	Electricity	Biomass
Min. [€/kWh]	0.05	0.30	0.05
Max. [€/kWh]	0.15	0.50	0.10

ature of $60\,°C$ is assumed.

In addition to the age of the buildings, this study also investigates energy costs. Three different energy carriers are considered in the scope of the investigated energy system: electricity, natural gas and biomass.

A cost range is defined for all energy carriers using statistical data from the past ten years for energy costs in Germany.

These cost ranges are shown in Table 5. For the parametric study a resolution of 0.01€/kWh of the given range is choosen. Data from Forest Research (n.d.) is used to convert biomass prices from €/t to €/kWh.

The feed in compensation for photovoltaic plants with a peak load below 10 kW in Germany is 0.086€/kWh (Bundesministerium der Justiz (2022)). It is assumed, that electricity generated by CHP can be sold at the electricity price shown in Table 5. In order to avoid unrealistically high feed-in quantities, the feed-in quantity is capped at the amount of electricity required by the neighbourhood.

Results and Discussion

Figure 3 - 5 displays the distribution of relative capacities for the producers of the optimal hybrid energy system for the different building age classes. Each figure represents the output of 1386 simulation scenarios.

The results highlight the significance of energy costs, as the optimal capacities of the producers provide wide ranges of up to 30%.

In all scenarios, the biomass boiler covers at least 54% of the total capacity. This indicates that the low emission factor of biomass compensates for the high investment costs, when attempting to reach the emission reduction goal. BA1 has the highest mean capacity of the biomass boiler, with a percentage of 69.3%. In contrast, the air source heat pump is not selected in any of the investigated cases due to the high heating supply temperatures. CHP is used for the baseload with a maximum relative capacity of 9.3%. The ground source heat pump has not been selected for any of the scenarios in BA1.

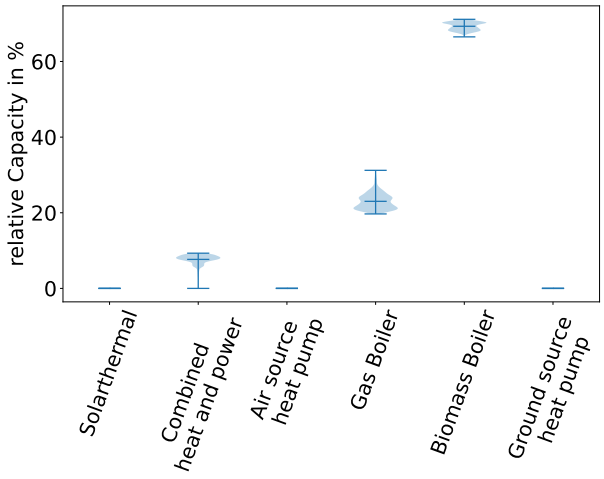

Figure 3: Distribution of optimal Producer Capacities for all scenarios with building age class BA 1 (the three horizontal lines in each violin plot represent the max-, mean- and min. values)

.

The results for BA2 show a similar picture. The only significant difference is the air source heat pump capacity, which covers up to 12.1% of the heat load.

In the case of BA3 the capacity reaches share of up to 26.55%, highlighting the impact of the low space heating supply temperatures. In contrast, the mean capacity of the gas boilers is much lower at 8.03% compared to BA1 and BA2, which have values of 23.0% and 24.50%, respectively. Only in BA3 a ground source heat pump is selected for the hybrid energy system.

In none of the investigated scenarios solarthermal collectors are selected.

Figure 6 illustrates the relationship between the relative photovoltaic area and the relative capacity of air source heat pump for BA3. The relative photovoltaic area is the ratio of the optimized pho-

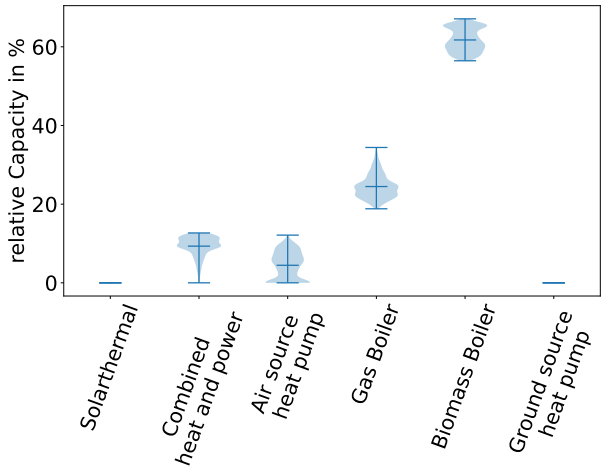

Figure 4: Distribution of optimal Producer Capacities for all scenarios with building age class BA2 (the three horizontal lines in each violin plot represent the max-, mean- and min. values)

.

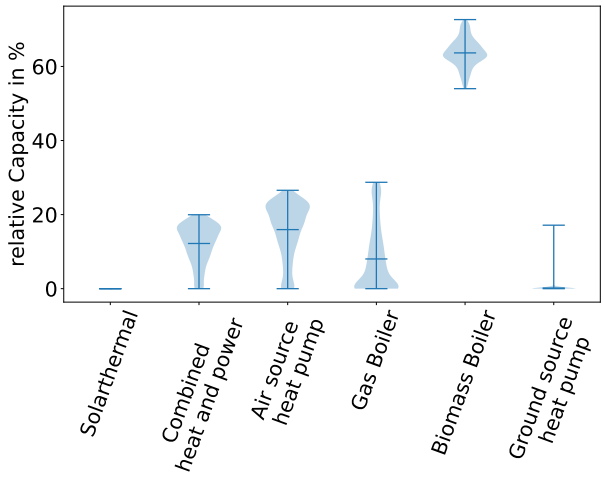

Figure 5: Distribution of optimal Producer Capacities for all scenarios with building age class BA3 (the three horizontal lines in each violin plot represent the max-, mean- and min. values)

.

tovoltaic area to the maximum available area for photovoltaics.

Each data point represents a single scenario. It can be determined that a minimum of 30% of the roof area should be utilized for photovoltaics. Additionally, there is a strong positive correlation between the capacity of the heat pumps and the photovoltaic area. This is underlined by a correlation coefficient of 95.39%. For BA1 and BA2 this correlation is weaker.

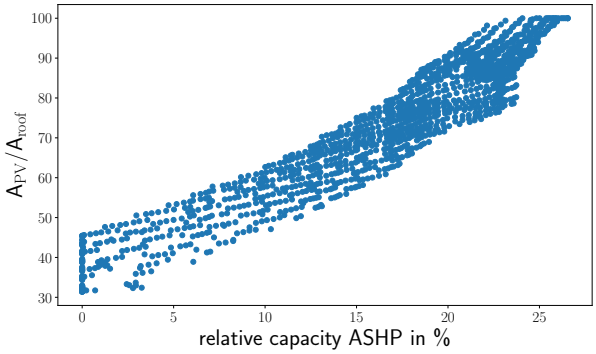

Figure 6: Correlation between optimal air source heat pump (ASHP) capacity and photovoltaic area for BA3

.

The results shown only apply to a 3-level district heating network and unlimited availability of biomass. Furthermore, the parameter study only examines some of the influencing factors. Variable feed-in tariffs and emission factors of electricity are not considered and must be investigated in further research.

Conclusion

This paper presents a parametric study for the optimal hybrid energy system for detached single family house districts under different boundary conditions. The results demonstrate the effiency of biomass boiler, as they cover at least 47.2% of the heat load in all scenarios. Additionally solar thermal collectors were not selected for any of the scenarios, because of low effiency and competition for roof area with photovoltaics. The optimal capacity of heat pumps strongly dependend on the building age class and the corresponding space heating supply temperature. The ground source heat pump is only selected in BA3 due to high investment cost. Analysing the optimal capacity of photovoltaics and air source heat pump reveals a positive correlation between both factors. This correlation is especially strong in the case of BA3.

Acknowledgment

The Technische Universität Berlin is funded for this research by the German Federal Ministry of Economic Affairs and Energy (BMWi) in the project “EnEff: HCBC” (Funding code: 03ET1632). We would also like to thank our project partner, Vatten-

fall Wärme Berlin AG for their technical and financial contribution to this project.

References

Bundesministerium der Justiz (2022), 'Gesetz zur änderung des energiewirtschaftsrechts im zusammenhang mit dem klimaschutz-sofortprogramm und zu anpassungen im recht der endkundenbelieferung'.

Bundestag (2023), 'Gesetz für die wärmeplanung und zur bundestag dekarbonisierung der wärmenetzebundestag'.

Bundestag, D. (2019), 'Bundes-klimaschutzgesetz: Ksg'.

Deutsches Institut für Normung e.V. (2010), 'Energy efficiency of buildings - calculation of the net, final and primary energy demand for heating, cooling, ventilation, domestic hot water and lighting - supplement 1: Balancing of demand and consumptio'.

Dötsch, C., Taschenberger, J. & Schönberg, I. (1998), *Leitfaden Nahwärme*, Vol. 6 of *UMSICHT-Schriftenreihe*, Fraunhofer-IRB-Verl., Stuttgart.

Drebes, C., Boczek, B., Greiner, M., Hesse, U., Kern, T., Mahlke, D., Najjar, A., Schoch, C., Schulze, J., Sieber, S., Stute, V., Ousmane, S., Wurzbacher, S., Zelmer, A., Meinberg, T., Hegger, P., Dettmar, J. & Martin, A. (2012), *UrbanReNet I - Vernetzte regenerative Energiekonzepte im Siedlungs- und Landschaftsraum*.

Dunkelberg, E., Deisböck, A., Hirschl, B., Mitzinger, T., Röder, J., Salecki, S., Thier, P. & Wassermann T. (2020*a*), 'Fernwärme klimaneutral transformieren: Eine bewertung der handlungsoptionen am beispiel berlin nord-neukölln'.

Dunkelberg, E., Deisböck, A., Hirschl, B., Mitzinger, T., Röder, J., Salecki, S., Thier, P. & Wassermann T. (2020*b*), 'Keimzellen für eine quartierswärmeversorgung: Abwasserwärmenutzung durch gebäude einer städtischen wohnungsbaugesellschaft in einem berliner bestandsquartier'.

Falke, T., Krengel, S., Meinerzhagen, A.-K. & Schnettler, A. (2016), 'Multi-objective optimization and simulation model for the design of distributed energy systems', *Applied Energy* **184**, 1508–1516.

Forest Research (n.d.), 'Typical calorific values of fuels'.
URL: *https://www.forestresearch.gov.uk/tools-and-resources/fthr/biomass-energy-resources/reference-biomass/facts-figures/typical-calorific-values-of-fuels/*

Friebe, M., Karasu, A. & Kriegel, M. (2023), 'Methodology to compare and optimize district heating and decentralized heat supply for energy transformation on a municipality level', *Energy* **282**, 128987.
URL: *https://www.sciencedirect.com/science/article/pii/S0360544223023812*

Kersten, M., Bachmann, M., Guo, T. & Kriegel, M. (2021), 'Methodology to design district heating systems with respect to local energy potentials, co2-emission restrictions, and federal subsidies using oemof: 39-58 pages / international journal of sustainable energy planning and management, vol. 31 (2021)'.

Krien, U., Schönfeldt, P., Launer, J., Hilpert, S., Kaldemeyer, C. & Pleßmann, G. (2020), 'oemof.solph—a model generator for linear and mixed-integer linear optimisation of energy systems', *Software Impacts* **6**, 100028.

Loga, T., Stein, B. & Diefenbach, N. (2016), 'Tabula building typologies in 20 european countries—making energy-related features of residential building stocks comparable', *Energy and Buildings* **132**, 4–12.

Majidi, M., Nojavan, S., Nourani Esfetanaj, N., Najafi-Ghalelou, A. & Zare, K. (2017), 'A multi-objective model for optimal operation of a battery/pv/fuel cell/grid hybrid energy system using weighted sum technique and fuzzy satisfying approach considering responsible load management', *Solar Energy* **144**, 79–89.
URL: *https://www.sciencedirect.com/science/article/pii/S0038092X1730018X*

Pasimeni, M. R., Petrosillo, I., Aretano, R., Semeraro, T., De Marco, A., Zaccarelli, N. & Zurlini, G. (2014), 'Scales, strategies and actions for effective energy planning: A review', *Energy Policy* **65**, 165–174.
URL: *https://www.sciencedirect.com/science/article/pii/S0301421513010495*

Pawlik, V. (2024), 'Preisentwicklung für holzpellets in deutschland in den jahren 2013 bis 2023'.

URL: *https://de.statista.com/statistik/daten/studie/214738/umfrage/preisentwicklung-fuer-holzpellets-in-deutschland/*

Statistisches Bundesamt (2023), ‘Daten zur energiepreisentwicklung september 2023’.

Strom Report (2024), ‘Strompreisentwicklung in deutschland’.
URL: *https://strom-report.com/strompreise/strompreisentwicklung/*

Umweltbundesamt (2021), ‘Entwicklung der spezifischen kohlendioxid-emissionen des deutschen strommix in den jahren 1990 - 2020’.

Umweltbundesamt (2023), ‘Energiesparende gebäude’.

BauSIM 2024 in Wien
23. September – 26. September

Level of Detail in Dynamic Simulation Models – a Comparison for Multi-Family Houses

Larissa Kühn[1], Benani Zoumba[1], Tobias Spratte[1], Laura Maier[1] und Dirk Müller[1]

[1]*RWTH Aachen University, E.ON Energy Research Center, Institute for Energy Efficient Buildings and Indoor Climate*

Abstract

To achieve the set climate goals, renovations and operational optimizations in the residential sector are necessary. In this context, building performance simulations have proven to help estimate the CO_2 saving potential of different renovation measures. Various modeling approaches exist that differ in their level of detail ranging from comprehensive physical descriptions to simplified representations. While literature covers comparisons of dynamic simulation models for single-family houses and non-residential buildings, a comprehensive analysis for multi-family houses is missing. Besides a different architecture, one distinct characteristic is their high diversity in occupancy patterns. Especially due to diverse user behavior and different resulting temperature set points, heat exchange between floors and flats in multi-family houses are of particular interest. This study compares models with different levels of detail in open-source tools (EnergyPlus and Modelica) for predicting heat demand in multi-family houses, taking into account inter-zonal heat exchange. Detailed building models in EnergyPlus and Modelica perform similarly in terms of accuracy, but EnergyPlus outperforms Modelica regarding the simulation time. For models with different levels of detail in Modelica, the results highlight trade-offs between accuracy and computational efficiency. Reduced-order models outperform high-order models in terms of simulation time (up to 98 %-99 %) but at the expense of accuracy in estimating the annual heat demand on flat level (13 %-46 %).

Introduction

The European Union's building sector is responsible for 36 % of total greenhouse gas emissions (European Commission 2020). To achieve the climate target of climate-neutral buildings by 2045, there is a need to increase renovation rates and accelerate the transition to zero-emission technologies. In Germany, residential buildings account for over 70 % of emissions in the building sector (Wilke 2013). Although multi-family houses (MFH) only account for 17 % of all residential buildings, they comprise 40 % of the total living space and contribute to almost 40 % of the emissions in the residential sector (Becker et al. 2022). This underlines the role of MFHs in achieving the climate targets: effective measures on a low number of buildings can lead to a significant reduction of emissions.
Building performance simulations support the optimization of energy systems and the estimation of emission savings of different renovation measures (Hensen & Lamberts 2019, Albers 2017). There are two main model paradigms: physical and empirical. Physical models are useful when data is incomplete or for analyzing possible changes to the current system (Nageler et al. 2018). For the physical representation of buildings, static and dynamic methods exist. Static methods often rely on simplified paradigms and expert-based rule-of-thumbs (e.g., methods of guideline DIN EN 12831 or DIN V 18599), while dynamic models can represent the performance of the building more realistically in terms of operational behavior (Jansen et al. 2022). Dynamic, physical modeling methods can further be divided into high-order models (HOM) or reduced-order models (ROM) regarding their level of detail in modeling. There are mainly two strategies to reduce model complexity and thus reducing the effort required for parameterization, modeling and calculation: (1) zone level aggregation and (2) simplifications in the thermodynamic behavior (e.g., neglecting dynamics or interdependence).

This study aims to find a suitable level of detail for a dynamic, physical building model of MFHs. The purpose is to identify a trade-off between model accuracy and the effort required for modeling, parameterization, and simulation. Table 1 gives an overview of current literature, which analyzes

Table 1: Literature overview

Publication	Building type	Reference	Comparison	Main findings
Lauster et al. (2014)	SFH	HOM (3 zones, IDA-ICE)	ROM (1 zone, Modelica (AixLib))	Difference in annual heating demand up to 2.52 % (RMSE:79.73 W, R^2: 0.9898) and cooling demand up to -5.49 % (RMSE: 90.25 W, R^2: 0.9261)
Jansen et al. (2022)	NRB	HOM (183 zones, Modelica (AixLib))	ROM (173/10 zones, Modelica (AixLib)), ROM (10 zones, Python)	ROM with 10 zones from AixLib meets heat demand per month best with CVRMSE up to 15 % and 97 % reduced simulation time
Jansen et al. (2021a)	NRB	HOM (82 zones, EnergyPlus)	ROM (2-82 zones, Modelica (AixLib))	Annual heating/cooling demand in ROM 10 % higher/ 10 % lower compared to HOM; Low number of zones (zoning according to usage), combining south- and north-oriented rooms, yields most realistic results
Nageler et al. (2018)	NRB	Measurement data	HOM (IDA-ICE) ROM (1 zone, IDA-ICE))	HOM: 0.96 R^2 18.5 % CVRMSE ROM: 0.92 R^2, 24.9 % CVRMSE
Kim & Braun (2015)	NRB	HOM (59 zones) TRNSYS	ROM (59 zones) Matlab	Maximum deviation of 0.235 °C; Average deviation 0.05 °C
Mourkos et al. (2020)	MFH	Measurment data	HOM (EnergyPlus)	RMSE is 1.5/1.4 °C for investigated corridors
Nageler et al. (2018)	MFH	Measurement data	HOM (IDA-ICE) ROM (1 zone, IDA-ICE)	HOM: 0.83 R^2, 29.7 % CVRMSE ROM: 0.68 R^2, 40.2 % CVRMSE
Bres et al. (2017)	MFH floors	HOM (27/32 zones) EnergyPlus	HOM (3-18 zones) HOM (7-23 zones) EnergyPlus	Results improve (2 to 12 % CVRMSE) with increasing number of zones, but greatest deviation not necessarily with lowest number of zones

modeling approaches for dynamic and physical building models regarding the level of detail for different building types and in different modeling tools. While the tools TRNSYS and IDA-ICE are commercially available, EnergyPlus and Modelica are open-source tools and will therefore be the focus of this study. EnergyPlus is well suited for detailed and very efficient simulation of buildings, but its imperative language makes dynamic modeling of coupled systems and modeling of controllers, especially feedback controllers, difficult (Wetter 2009). Modelica, an object-oriented, equation-based language, offers the flexibility for modeling multi-domain systems, including feedback controller, but is less efficient for building-specific simulations compared to EnergyPlus (Wetter et al. 2021). For completeness, however, the literature review contains all available tools. Lauster et al. (2014) analyze different modeling approaches for single-family houses (SFHs). Compared to SFHs, the modeling of MFHs differs because the buildings are larger and have different architecture (e.g., greater ratio of building volume to external surface (Loga et al. 2015)) and usage patterns (e.g., individual temperature requirements of different occupants).

However, most publications exist for non-residential buildings (NRBs) (Jansen et al. 2022, 2021a, Nageler et al. 2018, Kim & Braun 2015). Compared to NRBs, MFHs require a different approach for zone aggregation. While Jansen et al. (2021a) found that for NRBs the aggregation of zones by usage provides the best results, for MFHs this finding is not applicable. Nevertheless, the heat exchange between floors and flats should be taken into account due to the different occupancy behavior, which leads to a zone aggregation per flat. For MFHs, studies can be found by Mourkos et al. (2020), Nageler et al. (2018) and Bres et al. (2017). Nageler et al. (2018) compare measurement data to a 1-zone ROM and a detailed HOM. They use the commercial tool IDA-ICE instead of applying open-source tools and further, do not analyze different zone-level aggregations. Mourkos et al. (2020) and Bres et al. (2017) partly close this gap by using the open-source modeling tool EnergyPlus. Mourkos et al. (2020) analyze the influence of input data assumptions on simulation results and compare it to measurement data. Bres et al. (2017) further compare different level of detail regarding the number of representative zones. But still, both paper do not consider any simplifications in the physical modeling approach and only consider the modeling of three flats resp. two floors of an MFH instead of a whole building. Therefore, a comprehensive comparison of different levels of detail in open-source building modeling is still missing for MFHs. We contribute to the literature by answering the following research question:

Which open-source modeling approach (EnergyPlus or Modelica) and zone-level aggregation (roomwise, flatwise, housewise) to choose for building performance simulations of MFHs?

Use case: Typical multi-family house

This study compares simulation models of a typical German MFH. The building age class with the highest number of MFHs in Germany is 1958-1968 (Loga et al. 2015). As the building envelopes of two thirds of the MFHs built before 1978 in Germany have already been retrofitted (Walberg et al. 2022), we assume a retrofitting standard according to Loga et al. (Loga et al. 2015) (see Table 2). The study of Nikolowski (2015) presents a typical building geometry for the ages between 1945 and

1970 as shown in Figure 1. The MFH includes four floors, an unheated attic, and an unheated basement. As typical for this building age class, there are two identical flats on each floor as depicted in Figure 2. Table 3 presents additional building information. For the modeling, we further assume that the staircase is north-oriented and the building is free-standing.

Table 2: U-vales for building elements according to (Loga et al. 2015).

U values in	Wall	Roof	Floor	Window
W/(m^{2}K)	0.23	0.19	0.31	1.3

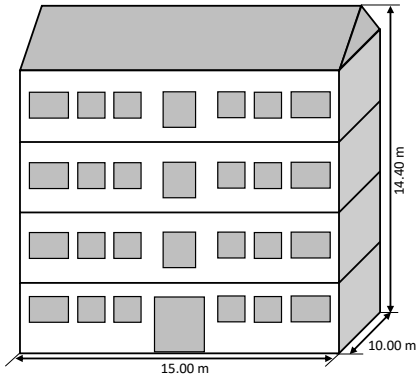

Figure 1: Typical German MFH for building age 1945-1970 according to (Nikolowski 2015).

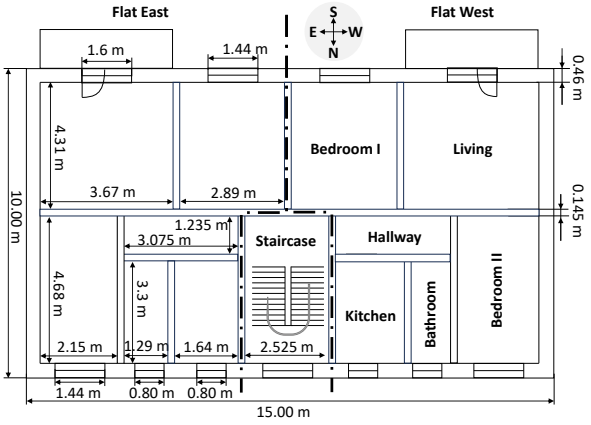

Figure 2: Floor plan of the typical MFH according to (Nikolowski 2015).

Simulation models

In this study, we compare five simulation models with four different levels of detail (see Figure 3). Two different HOMs with similar characteristics provide the highest level of detail. The HOMs capture each room, the corresponding walls, and their thermal properties individually. Furthermore, adjacent rooms can exchange heat through inner walls. However, the high level of detail is linked

Table 3: Geometric characteristics of the typical MFH according to (Nikolowski 2015).

Areas	Total heated area	413.06 m^2
	Total window area	73.44 m^2
Heights	Height rooms/basement	2.54 m
	Height attic	4.28 m

to an increased effort for modeling, parameterization, and simulation. The ROMs reduce this effort by simplifying the physical modeling and aggregating zones either to the number of flats (8 zones) or the whole building volume (1 zone). As ROM with the highest level of detail, an extended 8-zone model (8ZE) considers the heat exchange between adjacent zones, which is neglected by the other two ROMs. This heat exchange, however, gains relevance for MFHs in comparison with SFHs due to the higher proportion of building volume to exterior surface (Loga et al. 2015) and individual behavior of occupants. Influences like varying internal gains or air exchange rates further increase potential deviations. Table 4 provides information about the different simulation models and their respective approaches to model the thermal behavior of buildings, and, in particular, the MFH of this study.

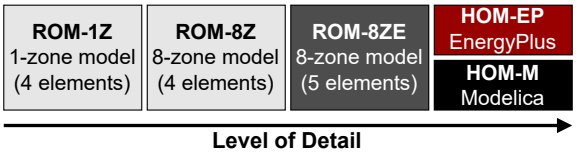

Figure 3: Overview of different simulation models and their level of detail.

High-order model: Energy Plus

EnergyPlus is an established simulation tool developed by the U.S. Department of Energy (2022) and serves as the reference for this study. Zones, components, and boundary conditions are introduced as objects with their corresponding properties. For the HOM for this study (HOM-EP), we focus on the basic configuration of EnergyPlus with detailed building surface information, internal gains by people, lights, and devices, as well as zone infiltration and ventilation on room level. Solar distribution is configured in *FullExterior* mode, which fully considers exterior surfaces, while simplifying beam solar radiation entering the zone. For further information on the underlying assumptions, we refer to U.S. Department of Energy (2022). We generate the HOM-EP from 3D building data using the Python Tool BIM2SIM (*BIM2SIM* 2024, Jansen et al. 2021b). While the conversion is automated, the creation of the 3D building model is time-consuming and requires manual input.

Table 4: Differences between modeling approaches.

Modeling object	ROM (4 elements) (1Z/8Z)	ROM (5 elements) (8ZE)	HOM Modelica (HOM-M)	HOM EnergyPlus (HOM-EP)
Zoning	1/8 zone(s)	8 zones	51 zones	51 zones
Unheated volumes	Neglected	Neglected	Fully modeled	Fully modeled
Component aggregation	Aggregated	Aggregated	Individual components	Individual components
Exterior convection coeff.	Constant	Constant	Wind speed dependent	Wind speed dependent
Interior convection coeff.	Constant	Constant	Temperature dependent	Temperature dependent
Interior radiation coeff.	Constant	Constant	Surface temp. dependent	Surface temp. dependent
Interzonal heat exchange	Neglected	Considered	Considered	Considered
Infiltration	Constant	Constant	Constant	Exterior pressure dependent

High-order model: Modelica

The Modelica HOM (HOM-M) is based on the high-order approach from the AixLib library (Maier et al. 2022), which was validated by Constantin et al. (2014) and Xanthopoulou et al. (2021). Each room contains an air volume and all corresponding building elements (exterior/interior walls, ceilings, floors, and windows) to account for energy and mass balances. Heatports connect adjacent rooms to form an entire floor, and floors to form an entire building. Through this structure, we connect four identical floors with the unheated zones (attic, staircase, and basement) to obtain the entire building. In contrast to the original model from the library, we model windows with a capacity as in EnergyPlus. Weather conditions, internal gains, and air exchange rates are applied to each room individually from external modeling components. The building and all its components have to be assembled manually, which makes modeling time-consuming.

Reduced-order models: Modelica

The ROMs are based on the German guideline VDI 6007 and created using the open-source Python tool TEASER (Remmen et al. 2018). This approach aggregates rooms with similar usage or thermal conditions to a reduced number of zones, which decreases modeling effort. Further, the corresponding building elements of each zone (walls, ceilings, floors, windows) are aggregated and represented by resistances and capacities to describe the transfer and storage of heat based on an analogy with electric circuits. The 1-zone model (1Z) considers all heated rooms as a single zone with uniform properties and, therefore, is the model with the lowest level of detail. An increased accuracy is reached by the 8-zone model (8Z), which models each apartment as an individual zone. This modeling approach can estimate the individual demand for flats resulting from different ratios of exterior surfaces to air volumes and varying numbers of occupants with different temperature requirements. However, the 8Z model neglects heat exchange between adjacent zones. This inter-zonal heat exchange is considered in an extended version (8ZE), which includes an additional wall element for each zone according to Groesdonk et al. (2023). An additional simplification in all ROMs is the neglect of unheated zones. While the staircase is not considered at all, the attic and the basement are simplified. The upper floor is connected to the roof with a constant heat transfer coefficient, and the lower floor to a constant basement temperature, equivalent to the HOM's average temperature during heating season.

Boundary conditions

We use weather data for Potsdam (DWD 2017) as this location provides an average climate for Germany (Bewersdorff 2021). As the usage patterns in individual flats can have a great influence on the heat demand, we included detailed profiles for occupancy, devices, and lighting from the tool LoadProfileGenerator (Pflugradt et al. 2022). Based on characteristics of the occupancy structure (number of adults/children, employers/pensioners per flat), Markov chains allow for a precise indication of the occupancy and activity of these occupants. By using statistical data of the housing situations in German MFHs (Destatis 2023) as input for the tool, we generate room accurate hourly load profiles for each household. Furthermore, we assume an effective volume flow of 30 m³/h per person present and an infiltration rate of 0.3 1/h as provided by the Swiss guideline (SIA 2015).

Simulation results

To compare and evaluate the different modeling approaches in this study, we run heat load calculations (steady state under standard conditions), followed by dynamic annual simulations to estimate annual heat demands and load curves. For the latter, we first assume identical temperatures in all flats, and second, apply individual temperature set points to all flats to make inter-zonal heat exchange visible. To meet the temperature requirements, we use ideal heaters in all models.

Heat load

For the heat load calculation, we apply constant boundary conditions in accordance with DIN EN 12831. We specifically set the outdoor temperature to -12.1 °C for Potsdam, neglect wind effects and internal gains from solar radiation, people, lighting, and devices. Indoor temperatures are individually defined for each room within the HOMs, ranging from 24°C for bathrooms to 15°C for hallways, and an average temperature is considered for ROMs. Figure 4 shows the results of the heat load calculation. All simulation models show similar results. While the two HOMs and the 8Z also show the same trend for the different floors, the 1Z does not. Discrepancies between the HOMs can be explained by variations in the treatment of inner convection coefficients. While external convection coefficients in the HOMs depend on the wind speed, exhibiting minimal values at 0 m/s, the ROMs maintain a constant and higher convection coefficient. However, the resulting higher heat losses in the ROMs are compensated by reduced exterior surface and window areas because of the neglect of the unheated staircase. In contrast to the normative calculation, the simulation results are up to 23 % lower. The main reason for this discrepancy is that within the normative approach the net areas of inner walls are greater, as they include the thickness of adjacent walls, and thermal bridge surcharges are taken into account.

Energy demand: Uniform temperatures

In this section, we compare the results of annual heat demand simulations with uniform indoor temperatures in all flats of 20 °C. Figure 5 depicts the annual heat demands of the building and the floors. The corresponding curves over the year are shown in Figure 6. While the two HOMs perform similarly, the three ROMs show deviations in the annual heat demand of up to 15.3 % on building level (1Z) and 31.0 % on floor level (1Z, floor 4) compared to the HOM-EP. Similar to the heat load calculation results, neglecting the staircase and additionally zoning primary cause for the deviations. Zoning means that internal gains are added to the whole building or flat rather than causing local effects. For example, the small kitchens have comparatively large internal gains, which leads to overheating of single rooms in the HOMs and lower total heat demands in the ROMs. Of the three ROMs, the 8ZE performs best with an average deviation per floor of 12.9 %, as the modeling of 8 zones and inter-zonal heat exchange mitigates the effect slightly.

Energy demand: Individual temperatures

While standards indicate constant temperature set points for residential buildings, measurements show variations between 19 and 22 °C dependent on the comfort requirements of occupants (Bewersdorff 2021). Therefore, we vary temperature set points for the different flats between 19 and 22 °C. For the 1Z the temperature is set to the mean value of 20.38 °C. Figure 7 depicts the results of the annual simulation for each flat. Furthermore, Table 5 shows the coefficient of determination (R^2) for the different models and flats compared to the HOM-EP. The results for both HOMs on building and on flat level are similar and the minimum R^2 of the HOM-M compared to HOM-EP is 0.97 for daily and 0.94 for hourly values. While the results underline the inability of the 1Z to estimate annual demands at flat level (average deviation of 46.2 %), the 8Z and 8ZE follow the trends of the HOMs with average deviations of 21.4 % and 16.6 %, respectively. For the 8Z and 8ZE, average deviation in annual heat demands on flat level are 21.4 % and 16.6 %. When considering the R^2, it also becomes obvious that the 8ZE performs best among all ROMs. In case of the 8ZE, the average hourly R^2 is only 0.84, but the daily R^2 performs comparatively well with an average of 0.94. Table 6 depicts the simulation times for the different modeling approaches. While the HOM-M performs worst with around 220 minutes for an annual simulation, EnergyPlus and the ROMs perform similar with only a few seconds to minutes.

Table 5: R^2 with individual indoor temperatures for flats (hourly/daily).

R^2	HOM-M	8ZE	8Z
F1-W	0.97 / 0.98	0.87 / 0.92	0.85 / 0.92
F1-E	0.97 / 0.99	0.82 / 0.96	0.74 / 0.90
F2-W	0.95 / 0.97	0.90 / 0.98	0.80 / 0.86
F2-E	0.94 / 0.98	0.86 / 0.94	0.86 / 0.97
F3-W	0.97 / 0.99	0.85 / 0.98	0.62 / 0.69
F3-E	0.94 / 0.99	0.71 / 0.87	0.65 / 0.82
F4-W	0.97 / 0.98	0.88 / 0.94	0.64 / 0.77
F4-E	0.97 / 0.99	0.85 / 0.95	0.79 / 0.88

Table 6: Computing times for simulations with individual temperature set points for flats (CPU: i9-10900K, 3.7 GHz; RAM: 32 GB).

Time	HOM-EP	HOM-M	8ZE	8Z	1Z
in min	0.58	220.3	4.0	3.7	0.5

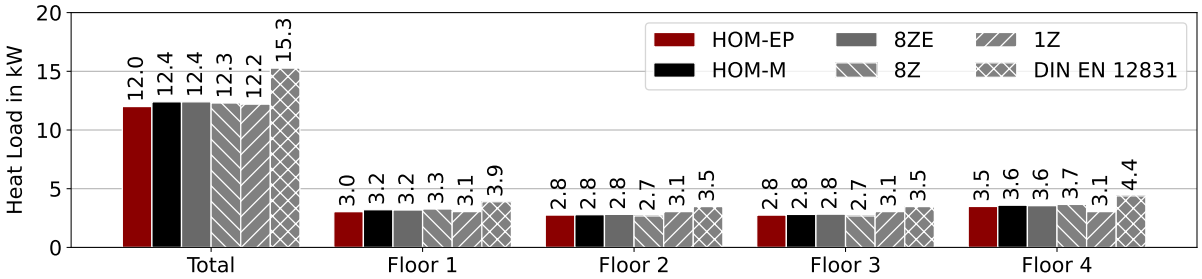

Figure 4: Heat load of the modeling approaches compared to a calculation following DIN EN 12831.

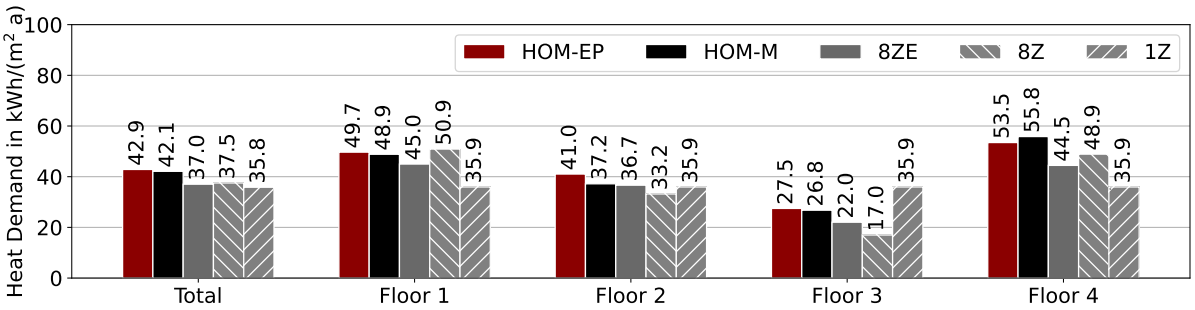

Figure 5: Annual heat demand with identical room set temperatures.

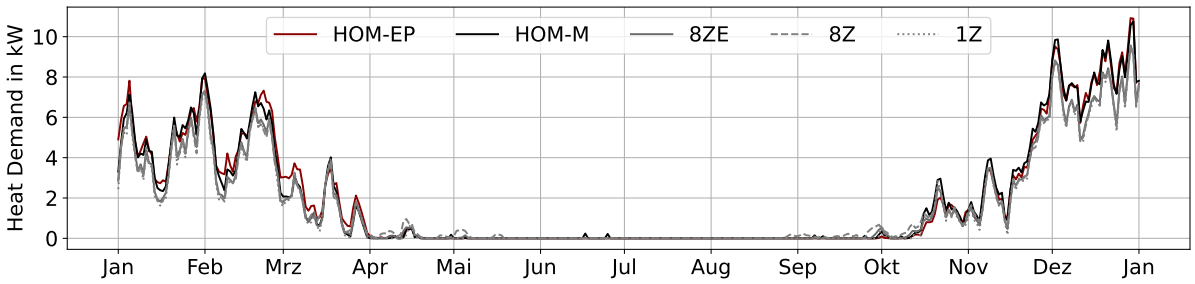

Figure 6: Annual heat demand curve with identical room set temperatures.

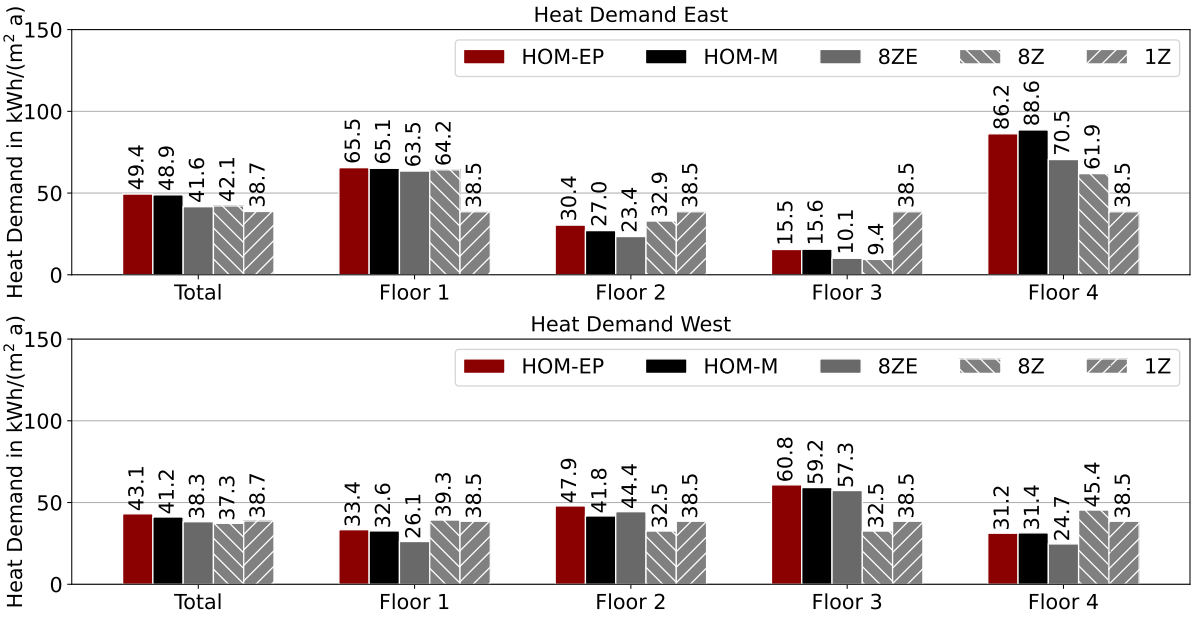

Figure 7: Annual heat demand with individual temperature set points for flats.

Discussion: Recommendations

HOMs outperform ROMs in terms of accuracy, but they require high manual modeling and parameterization effort, which also leads to an increased level of uncertainty. Considering this, Figure 8 summarizes recommendations regarding the modeling approaches. In case of the HOMs, the simulation results are similar, but the simulation times greatly differ showing great advantages of the HOM-EP. On the other hand, when it comes to the simulation of complete buildings, including the energy system and their control, Modelica is more suitable. For this reason, Spawn was developed, which enables the integration of EnergyPlus models in Modelica (Wetter et al. 2022). Further studies should extend the model comparison by a combined model in order to exploit all the advantages.

		Complexity		
		Low Building with uniform temperatures	**Medium** Flats with uniform temperatures	**High** Flats with individual temperatures
Time resolution	**Low** Yearly	ROM 1Z	ROM 8ZE	ROM 8ZE
	Medium Daily	ROM 8Z	ROM 8ZE	ROM 8ZE
	High Hourly	HOM (ROM 8Z)	HOM (ROM 8ZE)	HOM

Figure 8: Recommendations regarding the modeling scheme based on the study.

Discussion: Limitations of the study

The results of the model comparison are highly dependent on the assumptions and algorithms chosen within the different models. In the case of the ROM, different approaches to modeling unheated zones and applying internal gains at the zone level should be exploited. This could improve the results of the ROMs and shift the recommended applications more towards the ROM approach. In the case of the HOMs, both models perform similarly, but future work should compare different approaches within the models in more detail (e.g., applied algorithms for convection). In addition, detailed measurement data is needed for a final conclusion on which model performs best.

Conclusion

In this study, we compared different simulation models of a typical German MFH. Unlike other building types, MFHs are characterized by a different architecture (e.g., large ratio of building volume to external surfaces) and user behavior, which requires alternative approaches for zoning. Additionally, the heat exchange between flats/ zones becomes crucial due to varying user preferences. To investigate this, our study initially considered uniform and subsequently individual temperature settings per flat. The two HOMs compute similar results. The ROMs underestimate the heat demand given the assumptions of this study, with the ROM accounting for inter-zone heat exchange (8ZE) performing the best. In this case, heat demands at flat level are underestimated by approximately 12.9 % with constant temperatures and 16.9 % with individual temperatures compared to the HOM-EP. We also found that the HOM in EnergyPlus and the ROMs in Modelica require only a few seconds to minutes for annual simulations, while the HOM in Modelica required a simulation time of 220 minutes. Based on these findings, we recommend the different modeling schemes depending on the complexity of the use case, starting from annual energy demands at building level to hourly values at flat level.

Acknowledgment

We gratefully acknowledge the financial support by German Federal Ministry for Economic Affairs and Climate Action (BMWK, reference 01255249/1).

References

Albers, K.-J., ed. (2017), *Taschenbuch für Heizung und Klimatechnik*, 78. aufl edn, Dt. Industrieverlag, München.

Becker, S., Exner, A., Hagen, J. & Krüger, R. (2022), DENA - Gebäudereport 2023. Zahlen, Daten, Fakten zum Klimaschutz im Gebäudebestand., Technical report, Deutsche Energie-Agentur (dena).

Bewersdorff, D. (2021), Energetische Historie und Maßgaben für zu sanierende Gebäude, *in* 'HYGiency - Raumhygiene und Behaglichkeit durch energetische Sanierung im Quartier', Vol. 61, Springer Fachmedien, Wiesbaden, pp. 7–55.

BIM2SIM (2024), https://github.com/BIM2SIM/bim2sim.

Bres, A., Judex, F., Suter, G. & de Wilde, P. (2017), 'Impact of zoning strategies for building performance simulation'.

Constantin, A., Streblow, R. & Müller, D. (2014), The Modelica HouseModels Library: Presentation and Evaluation of a Room Model with the ASHRAE Standard 140, *in* 'The 10th International Modelica Conference, March 10-12, 2014, Lund, Sweden', pp. 293–299.

Destatis, S. B. (2023), Statistischer Bericht -

Mikrozensus - Haushalte und Familien - Endergebnisse 2021, Technical report.

DWD (2017), 'Ortsgenaue Testreferenzjahre'.

European Commission (2020), In focus: Energy efficiency in buildings, Technical report, Brussels.

Groesdonk, P., Jansen, D., Schmiedt, J. E. & Hoffschmidt, B. (2023), 'Integration of Heat Flow through Borders between Adjacent Zones in AixLib's Reduced-Order Model'.

Hensen, J. & Lamberts, R., eds (2019), *Building Performance Simulation for Design and Operation*, 2. edition edn, Routledge, Abingdon, Oxon; New York, NY.

Jansen, D., Mehrfeld, P., Müller, D., Fichter, E., Richter, V., Barz, A., Brunkhorst, J., Dahncke, M., Jahangiri, P., Warnecke, C., Mehrfeld, P., Frisch, J., van Treeck, C. & Lüdemann, B. (2021b), BIM2SIM - Development of semi-automated methods for the generation of simulation models using Building Information Modeling, *in* 'Building Simulation 2021', Vol. 17 of *Building Simulation*, IBPSA, pp. 1244–1245.

Jansen, D., Richarz, J., Vaeßen, D., Hering, D. & Müller, D. (2022), Comparision of Thermal Simulation Models with Different Level of Detail for Non-Residential Buildings, *in* 'BauSim Conference 2022'.

Jansen, D., Richter, V., Lopez, D. C., Mehrfeld, P., Frisch, J., Müller, D. & Treeck, C. V. (2021a), Examination of Reduced Order Building Models with Different Zoning Strategies to Simulate Larger Non-Residential Buildings Based on BIM as Single Source of Truth, pp. 665–672.

Kim, D. & Braun, J. E. (2015), 'A general approach for generating reduced-order models for large multi-zone buildings', *Journal of Building Performance Simulation* **8**(6), 435–448.

Lauster, M., Müller, D. & Leppmann (2014), 'Improving a Low Order Building Model For Urban Scale Applications'.

Loga, T., Stein, B., Diefenbach, N. & Born, R., eds (2015), *Deutsche Wohngebäudetypologie: beispielhafte Maßnahmen zur Verbesserung der Energieeffizienz von typischen Wohngebäuden*, 2. aufl. edn, IWU, Darmstadt.

Maier, L., Jansen, D., Wüllhorst, F., Kremer, M., Kümpel, A., Blacha, T., Müller, D. & University, R. A. (2022), 'AixLib: An open-source Modelica library for compound building energy systems from component to district level with automated quality management'.

Mourkos, K., Hopfe, C. J., McLeod, R. S., Goodier, C. & Swainson, M. (2020), 'The impact of accurately modelling corridor thermodynamics in the overheating risk assessment of multi-residential dwellings', *Energy and Buildings* **224**, 110302.

Nageler, P., Koch, A., Mauthner, F., Leusbrock, I., Mach, T., Hochenauer, C. & Heimrath, R. (2018), 'Comparison of dynamic urban building energy models (UBEM): Sigmoid energy signature and physical modelling approach', *Energy and Buildings* **179**, 333–343.

Nikolowski, J. N. (2015), 'Wohngebäude im Klimawandel'.

Pflugradt, N., Stenzel, P., Kotzur, L. & Stolten, D. (2022), 'LoadProfileGenerator: An Agent-Based Behavior Simulation for Generating Residential Load Profiles', *Journal of Open Source Software* **7**(71), 3574.

Remmen, P., Lauster, M., Mans, M., Fuchs, M., Osterhage, T. & Müller, D. (2018), 'TEASER: An open tool for urban energy modelling of building stocks', *Journal of Building Performance Simulation* **11**(1), 84–98.

SIA (2015), Schweizerischer Ingenieur- und Architektenverein, Raumnutzungsdaten für Energie- und Gebäudetechnik, Technical report.

U.S. Department of Energy (2022), EnergyPlus Version 22.2.0 Documentation: Getting Started, Technical report.

Walberg, D., Gniechwitz, T., Paare, K. & Schulze, T. (2022), *Wohnungsbau: Die Zukunft des Bestandes*, number Nr. 82 *in* 'Bauforschungsbericht', Arbeitsgemeinschaft für zeitgemäßes Bauen e.V, Kiel.

Wetter, M. (2009), 'Modelica-based modelling and simulation to support research and development in building energy and control systems', *Journal of Building Performance Simulation* **2**, 143–161.

Wetter, M., Benne, K., Gautier, A., Nouidui, T. S., Ramle, A., Roth, A., Tummescheit, H., Mentzer, S. & Winther, C. (2022), 'Lifting the Garage Door on Spwan, an Open-Source BEM-Controls Engine'.

Wetter, M., Benne, K. & Ravache, B. (2021), 'Software Architecture and Implementation of Modelica Buildings Library Coupling for Spawn of EnergyPlus', *Modelica Conferences* pp. 325–334.

Wilke, S. (2013), Treibhausgas-Emissionen in Deutschland, Text, Umweltbundesamt.

Xanthopoulou, K., Mehrfeld, P., Kangowski, P., Lanzerath, F. & Müller, D. (2021), 'Validation of a building model as part of the AixLib Modelica library for dynamic plant and building performance simulations', *Energy and Buildings* **250**, 111248.

BauSIM 2024 in Wien
23. September – 26. September

Modelling Approaches for Decentral Domestic Hot Water Heat Exchangers in Hydronic Simulations

Elisa Venturi, Fabian Ochs, Mara Magni, Georgios Dermentzis, Samuel Breuss
University of Innsbruck, AT, E-Mail: elisa.venturi@uibk.ac.at

Abstract

To assess the building hydronic system performance, dynamic simulations are necessary to examine factors such as return temperature and controls. Extensive simulation effort might be required, especially with complex distribution systems and multiple apartment heat exchangers (HXs). This study investigates modelling approaches to simplify the simulation models by implementing lumped HXs. The first part of the paper suggests approaches to lump hydronic systems with one and two rising pipes. The second part involves developing and optimizing lumped models and comparing them against detailed physical models. Results indicate that the modelling of the HX bypass has a great influence on the lumped HX optimization. The HX heat loss coefficient (UA) and the HX capacity influence the return temperature and the energy consumption between lumped and detailed models, suggesting the adoption of low values both for the heat loss coefficient and the capacity. The runtime-saving benefits of lumped models become evident when dealing with more than four HXs; for example, with 10 HXs, the simulation time is about one-tenth of that necessary for detailed models. Additionally, the modelling effort is significantly reduced and is independent from the number of considered (lumped) HXs. The lumped models offer a promising way to evaluate building energy performance efficiently, which is crucial for projects with multiple-apartment buildings.

Introduction and motivation

Many multi-family houses (MFHs) in Europe have the need to replace their heating systems that are based on fossil fuels. Heat pumps (HPs) present one of the dominant alternatives, both for renovations and new constructions. An example is the new building district “Campagne” in Innsbruck, Austria. The first part of the district, which was finished in 2022, includes four buildings with 307 apartments. During the design phase, various combinations of heat generation and distribution systems were investigated (Dermentzis et al., 2021). Finally, a centralized heating system with a ground-water source HP for space heating (SH), and district heating connection for the domestic hot water (DHW) preparation are installed. The hydronic system is a so-called 2+2 pipe system i.e. two pipes for SH and two pipes for DHW including a fresh-water station (FWS) (i.e. a plate heat exchanger) in each apartment.

To optimize the overall building energy performance, there is a need of dynamic simulations of building and system to investigate different control strategies and the dynamic behaviour of key properties, such as the flow and return temperatures of the system. Especially, the return temperature has an impact on the storage stratification and the HP performance. However, modelling and simulating the complete system can be challenging, especially in case of MFHs and building districts like in the Campagne, which would require the parallel simulation of 307 FWSs. Even simulating the smallest building, with 52 apartments, poses a considerable challenge in terms of modelling, computational effort and time. This creates the need for simplified simulation models, incorporating lumped components to collectively represent the behaviour of multiple components (Ochs et al., 2020).

This study focuses on deriving a method to model and simulate the apartment fresh-water stations i.e. the heat exchangers (HXs). The aim is to effectively model one lumped DHW HX for the building, rather than having a separate DHW HX for each apartment. The innovation lies in developing a methodology for modelling a lumped HX to reduce computational time and effort. To achieve this, a physical model of a sample of ten DHW HXs is simulated in MATLAB Simulink using the CARNOT Toolbox (Solar-Institut Juelich, 2024). The physical model serves as a benchmark for evaluating the performance of the developed lumped model. Thus, the goal is to quantify the effectiveness of the lumped model in terms of the trade-off between the simulation time and accuracy. Subsequently, the derived lumped model could be used to simulate the 52 DHW HXs of the smallest building of the Campagne district, where monitoring data on apartment-level are available.

The integration of lumped DHW HX models significantly contribute to the development of reliable simplified models that are crucial for evaluating building energy performance in extensive simulations, such as the one required for the project “Campagne Innsbruck Monitoring”. Moreover, the outcome of the study can contribute to the integration of building simulations into building energy standards.

Methodology

Domestic hot water HXs can be found in the literature with different names: fresh-water station (FWS, in 2+2-pipe system), heat transfer station (HTS, in 2-pipe system), apartment station, apartment supply station, apartment transfer station, and apartment satellite station. It is essential to note that these terms refer to the same item. For the sake of simplicity, we will use only the term "heat exchanger" (HX) in this study.

The study is divided into two main parts. The first part explores potential approaches to simplify the simulation model (section “Theoretical approach”). The second part focuses on the parameter optimization of the lumped model (section “Parameter optimization”).

Theoretical approach

The focus of this study is on a system with 10 HXs (see Figure 1). The system includes one HP, one thermal storage (TS), and several distribution pipes connecting the central heating system to the apartment HXs (flow and return). The system has two rising pipes (each connected to five apartments) and utilizes the Tichelmann configuration for the return (Recknagel, 2009). Several distribution systems could be considered (for the same study of 10 HXs connected to a central heating system), which would increase the complexity level. The boundaries of the current study are set after the HP and the TS. Therefore, these two components are not simulated and not considered in the possible model simplifications.

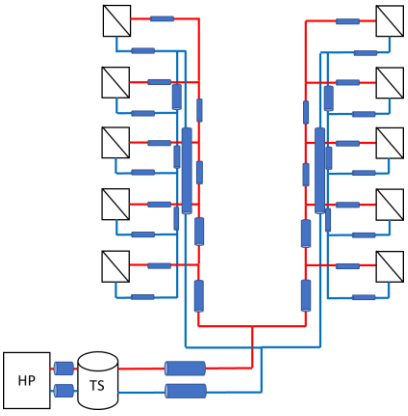

Figure 1: Scheme of the detailed case with 10 HXs

The lumped model can be thought as the simplification of all components (HX and pipes), or solely of the HXs, with the pipe lumping issue addressed as a separate part of the simplification process.

As a preliminary step, only one rising pipe is considered (figure 2a) and four possible lumped models are suggested (figure 2b). In these figures, the size of the circle corresponds to the pipe diameter.

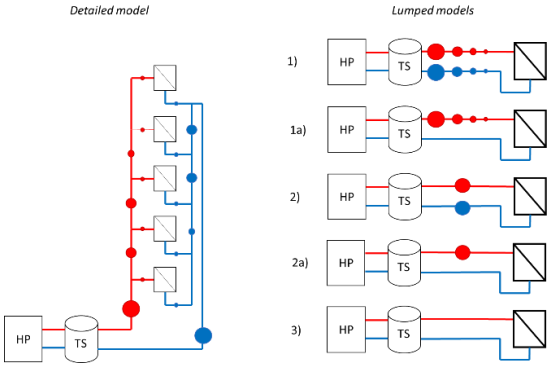

Figure 2: Detailed model with one rising pipe (left) and potential approaches for the lumped model (right). The different sizes of the circles represent the different pipe diameters

The approach 1) collects all the flow pipes of the distribution system before the lumped HX and all the return pipes of the distribution system after the lumped HX. Each pipe has a unique diameter (one pipe for each different diameter in the reality) and the length is the sum of the lengths of the pipes with the same diameter. This approach tends to overestimate distribution losses and underestimate the flow temperature to the HX (creating a false positive effect on the HP performance). Approach 1a) is a sub-variant of 1) and disregards the return pipes to further simplify the model. This approach conservatively predicts the return temperature (i.e. overestimating the return temperature and therefore staying on the safe side for the HP). Despite the further simplification, approach 1.a) maintains considerable accuracy in the estimation of the distribution losses, primarily occurring in the flow distribution rather than in the return distribution.

The approaches 2 and 2a) consider a lumped flow pipe, with approach 2) also a lumped return pipe is implemented. A calibration of the diameter and length is necessary to achieve either the same energy losses or the desired temperature at the entrance of the HX. The desired inlet temperature may be the average temperature of the five entries at the five HXs or the minimum temperature (the most disadvantaged case).

The approach 3) considers the pipe simplification in the lumped HX. Consequently, the lumped HX

becomes dependent on the characteristics of the pipes (e.g. pipe length, pipe insulation, different configurations of rising pipes, etc.). This approach is therefore useful only in cases of model calibration, i.e. the detailed model is already available and a simplified model is required for multiple simulations. However, the calibrated parameters are not applicable in different system configurations.

Similarly, the system with 10 HXs (with 2 rising pipes) can be simplified in the same way.

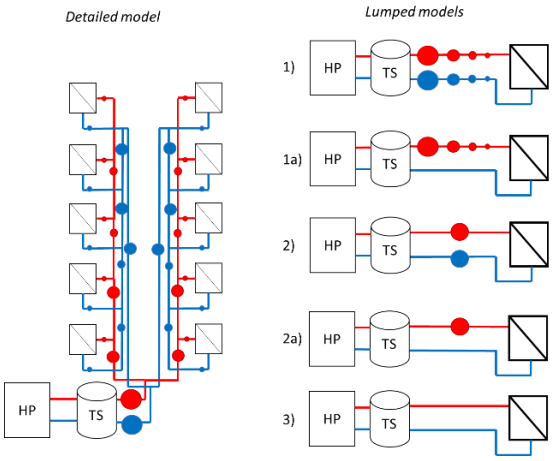

Figure 3: Detailed model with two rising pipes (left) and potential approaches for the lumped model (right). The different sizes of the circles represent the different pipe diameters

The advantages and disadvantages of each configuration remain consistent with those observed in the case with 5 HXs.

Parameters optimization

The second part of the study focuses on the optimization of the HX parameters. The goal is to optimize a lumped HX, which can be integrated into the approaches 1), 1a), 2), and 2a) (see Figure 3) of the previous section “Theoretical approach”. Only one lumped HX is modelled. The parameters to be optimized are:

- UA: Heat loss coefficient between the primary and the secondary side of the HX [W/K]
- UAloss: Heat loss coefficient between the HX and the surrounding ambient [W/K]
- cap: capacity of the HX [J/(m*K)]

The key performance indicators (KPIs) of the optimization are:

- Hourly average return temperature to the central heating system (T_{ret} in Figure 4)
- Hourly mass flow-average return temperature to the central heating system (T_{ret} in Figure 4)
- Daily energy consumption on the central heating system (E_{centr} in Figure 4)

The prerequisite for accepting the results is the fulfillment of the energy on the secondary side (user side) of the HX (E_{useful} in Figure 4). The energy is counted only when the setpoint temperature on the secondary (45°C) is reached (see “Control strategy of the HX” section).

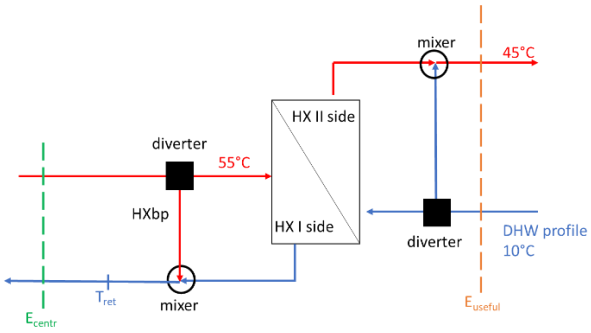

Figure 4: Model of the HX implemented in all the models

The optimization process involves comparing a detailed model with a lumped model. The analysis of the return temperature to the central heating system (T_{ret}) of the lumped model is conducted using the root mean square error (RMSE) based on the T_{ret} of the detailed models. To study the energy consumption on the central heating system (E_{centr}), the relative difference between daily energy consumption of the detailed and lumped model is examined according to (1):

$$\frac{|E_{centr,d} - E_{centr,l}|}{E_{centr,d}} \% \quad (1)$$

$E_{centr,d}$ = daily E_{centr} obtained from the detailed model; $E_{centr,l}$ = daily E_{centr} obtained from the lumped model.

In the detailed model, multiple HXs work simultaneously, whereas the lumped model has only one HX.

Several detailed models are created to simulate the contemporary presence of an increasing number of HXs, ranging from 2 to 10 HXs. Consequently, nine detailed models are generated, each corresponding to a different number of HXs (e.g. the first one with 2HXs, the second one with 3 HXs etc.).

The lumped model has two variants of the HX bypass (see “HX bypass” section).

In all the models, pipes, HP and TS are not simulated. The mass flow from the central heating system has a constant temperature of 55°C. The room temperature is assumed

constant at 20°C and the cold tapping water is assumed at a constant temperature of 10°C.

The properties of the single HX (used in the detailed model) are presented in Table 1:

Table 1: Properties of the heat exchanger in the detailed model

Description	Symbol	Value
Heat loss coefficient (primary and secondary side of the HX)	UA(1)	3818.4 W/K
Heat loss coefficient to the ambient	UAloss(1)	0.81 W/K
Capacity	cap(1)	2905 J/K

DHW profiles

For both the detailed and lumped model, several DHW profiles can be assumed.

For the detailed model, the possibilities are among:

- DHWcalc on apartment level (Jodan et al., 2005) generated on a 1-minute basis
- Profiles from the norm EN 16147-M (later shortened as EN profiles) on apartment level, different profiles available (e.g. XS, S, M, etc.)
- Monitoring data

For the lumped model, the possibilities are among:

- DHWcalc on building level
- Sum of the profiles on apartment level (not feasible with EN profiles)
- Sum of the profiles on apartment level multiplied by a simultaneity factor
- Sum of the same profile on apartment level delayed in time (feasible even with the same profile, such as the EN profile on apartment level)

In the current study, the DHWcalc and EN profiles are simulated in the detailed model. The DHWcalc profiles are randomly generated to match the annual DHW demand in the design conditions (i.e., 21.7 kWh/(m^{2}a)). With the DHWcalc profiles, the energy required from every apartment varies daily. The EN profiles are modified to match the annual DHW demand in the design conditions (as described in (Ochs et al., 2020)). Using EN profiles, the DHW profile of each apartment is delayed by 10 minutes from the previous one.

In the lumped model, the DHW profile is assumed as the sum of the single profiles (sum of DHWcalc profiles or sum of the delayed EN profiles).

Control strategy of the HX

The mass flow to the primary side of the HX is modelled as an ideal proportional control on the secondary side (i.e. mass flow on the primary side of the HX is the same as the mass flow on the secondary side of the HX). On the secondary side, an energy-balance control is implemented to fulfil the useful energy to the user with temperature of 45°C. During the waiting times (i.e. when the mass flow to the user has a temperature lower than 45°C) the energy is counted as delivered energy, but not as useful energy. A bypass is implemented to mix the outlet of the secondary side of the HX with cold water to deliver water at 45°C to the user (Figure 4). When the temperature on the secondary side of the HX is higher than 45°C, a portion of the mass flow is directed to the user to ensure 45°C (using a diverter with PI control) and less mass flow goes to the HX (both primary and secondary side).

HX bypass

In all the real FWSs, a HX bypass (HXbp) is implemented on the primary side of the HX to ensure the user's thermal comfort (i.e. to avoid long waiting times).

In the detailed model (i.e. in each apartment HX), a mass flow of 0.375 kg/min (Fink et al. 2010) is modelled to pass through the HXbp whenever no mass flow is required on the primary side of the HX. For simplicity, we refer to this mass flow as HXbp(1), meaning the mass flow flowing to the HXbp in one apartment.

The properties of the HXbp pipe (apartment level, detailed model) are outlined in Table 2.

Table 2: Properties of the HXbp pipe (apartment level, detailed model)

Diameter	0.01 m (Fink et al. 2010)
Length	0.3 m
Heat loss coefficient per length	15 W(m*K)
Effective conductivity in the axial direction	0.6 W/(m*K)
Capacity	1000 J/(m*K)
Number of nodes	10

For the lumped model, two variants of the HXbp are implemented:

1. On/off HXbp: When no mass flow is required from the lumped HX (i.e. the sum of the apartment mass flows is 0, meaning no apartment requires hot water), a mass flow of

3.75 kg/min (i.e. HXbp(1)*10) is sent to the lumped HXbp.
2. Controlled HXbp: the HXbp receives a mass flow equivalent to HXbp(1) multiplied by the number of apartments not requiring hot water.

The approach 2. is applicable only if the single DHW profiles are known. Otherwise, if only the lumped DHW profile is known, assumptions must be made to derive the number of apartments with no DHW demand in each time step.

In both variants of the HXbp for the lumped model, the properties of the HXbp pipe remain the same as in the detailed model (see Table 2), except for the heat loss coefficient. The heat loss coefficient per length has been optimized so that the mass flow after the HXbp has the same temperature as the average outlet temperature of the many HXs in the detailed model (averaged only during periods with mass flow to the HXbp > 0). The value of the heat loss coefficient changes with the increasing number of HXs represented in the lumped HX and changes with the different model of the HXbp. In total 18 values of heat loss coefficient have been found.

Dynamic simulations

The simulations are performed in MATLAB Simulink using the CARNOT Toolbox (Solar-Institut Juelich, 2024). A variable timestep is used, and the results are saved at intervals of 1 minute. Simulations are performed for 2 days. Results are analysed for 1 day (specifically, the second day, considering the first day as pre-simulation).

The simulations are performed by varying the value of UA, UAloss and cap of the lumped HX. These parameters are adjusted discretely by multiplying the values of the individual HX (UA(1), UAloss(1), and cap(1), as listed in Table 1) by factors of 1, 2, and so forth until 10. For instance, doubling the value of UA will be denoted as 2UA(1).

As a first step, the HXs are assumed adiabatic (UAloss = 0) in both detailed and lumped models. The assumption reduces the number of cases to be considered. Nine cases of simultaneous HXs (i.e. simultaneous DHW profiles) are considered, i.e. from 2 to 10 HXs. Calling *n* the number of HXs in the detailed model, *n*n* simulations are performed in the lumped model, varying the values of UA and cap of the lumped model. The *nxn* simulations are repeated 4 times (2 DHW profiles and 2 variants of the HXbp).

As second step, the non-adiabatic cases (UAloss >0) are simulated. As for UA and cap, UAloss parameter is increased discretely (1UAloss(1), 2UAloss(1), and so on, until 10UAloss(1)). The non-adiabatic cases are evaluated only for 10 HXs with DHWcalc profiles (only with the “Controlled HXbp”). Therefore, 1000 cases are simulated (combinations of 10 UA, 10 cap, 10 UAloss (*nxnxn*)).

The computational effort of the detailed and the lumped models is assessed by comparing their simulation times. To accurately measure the simulation times, each simulation is repeated 5 times, and the resulting times are averaged. The simulation time includes the compiling time.

Results

Adiabatic cases

The choice of DHW profile (EN or DHWcalc) has a minimal impact on the findings. Therefore, for sake of simplicity, only results with the DHWcalc are shown.

Optimization on T_{ret} as the compared KPI

Figure 5 shows the RMSE of the hourly average return temperature obtained with the lumped model (case of 10 HXs) with different values of UA and capacity compared to the return temperature obtained with the detailed model. The colour scale, ranging from green to red, signifies smaller to larger numbers. Results are shown for the adiabatic cases with both variants of HXbp. Results for UA values bigger than 6UA(1) and for capacity values bigger than 6cap(1) are not color-coded because they are not significant for the optimization (i.e. higher values of RMSE).

UA = UA(1) * \ cap = cap(1) *	1	2	3	4	5	6	7	8	9	10
1	1.79	1.29	0.89	0.77	0.92	1.06	1.19	1.32	1.44	1.53
2	1.88	1.37	0.94	0.78	0.88	1.03	1.16	1.29	1.40	1.51
3	1.93	1.41	0.98	0.80	0.88	1.02	1.14	1.28	1.40	1.51
4	1.97	1.37	0.98	0.82	0.89	1.02	1.14	1.27	1.39	1.50
5	1.98	1.40	0.99	0.82	0.89	1.01	1.14	1.28	1.38	1.50
6	2.00	1.40	1.00	0.83	0.89	1.01	1.13	1.28	1.39	1.49
7	2.00	1.43	1.00	0.83	0.89	1.01	1.13	1.28	1.39	1.49
8	2.02	1.42	1.01	0.84	0.89	1.01	1.13	1.26	1.38	1.49
9	2.02	1.43	1.01	0.84	0.88	1.01	1.13	1.27	1.38	1.49
10	2.02	1.43	1.03	0.86	0.89	1.02	1.13	1.27	1.38	1.49

KPI: Hourly average return temperature. Variant HXbp: On/Off HXbp

UA = UA(1) * \ cap = cap(1) *	1	2	3	4	5	6	7	8	9	10
1	0.13	0.19	0.25	0.33	0.42	0.48	0.56	0.63	0.73	0.79
2	0.14	0.20	0.26	0.34	0.39	0.44	0.52	0.58	0.65	0.71
3	0.18	0.23	0.28	0.35	0.42	0.48	0.53	0.58	0.64	0.71
4	0.20	0.25	0.30	0.36	0.42	0.48	0.54	0.59	0.65	0.71
5	0.21	0.26	0.31	0.36	0.43	0.48	0.54	0.59	0.65	0.71
6	0.22	0.26	0.31	0.37	0.44	0.48	0.54	0.59	0.65	0.71
7	0.23	0.27	0.32	0.37	0.44	0.48	0.54	0.60	0.65	0.71
8	0.23	0.27	0.32	0.37	0.44	0.48	0.54	0.60	0.65	0.71
9	0.23	0.28	0.32	0.38	0.44	0.49	0.54	0.60	0.65	0.72
10	0.23	0.28	0.33	0.38	0.44	0.49	0.54	0.60	0.65	0.71

KPI: Hourly average return temperature. Variant HXbp: controlled HXbp

Figure 5: RMSE of the hourly average T_{ret} obtained with the lumped model (top: variant on/off HXp, bottom: variant controlled HXbp) compared to the hourly average T_{ret} obtained with the detailed model, varying the UA and cap values of the lumped HX. Case of 10 HXs

In terms of capacity, an opposite trend is observed depending on whether the HXbp

variant is the on/off HXbp or the controlled HXbp. With the former, a capacity of 4cap(1) should be implemented. When the controlled HXbp is selected, a smaller capacity is recommended, e.g. 1cap(1) or 2cap(1). For both variants of HXbp, the optimal UA value is either 1UA(1) or 2UA(1). These observations regarding UA and capacity are consistent across all numbers of HXs, although they are presented here specifically for 10 HXs for the sake of simplicity.

It's evident that the choice of HXbp model significantly influences the results. When using the controlled HXbp model, the RMSE values are consistently lower, ranging between 0.13 and 0.79 K. In contrast, with the on/off HXbp model, the RMSE values are notably higher, ranging between 0.77 and 2.02 K. It's worth noting that the RMSE represents the cumulative temperature difference across all 1440 timesteps (minutes) in a day. This difference arises because when the lumped DHW profile (i.e. the sum of the 10 DHW profiles) comprises only a few DHW profiles (e.g. 8 apartments out of 10 do not require DHW), the return temperature is heavily influenced by the HXbp temperature. In the case of on/off HXbp, where there is no HXbp mass flow in such instances, the RMSE values are significantly higher compared to the HXbp model.

Similar results are shown from the analysis of the RMSE of the hourly mass-flow average return temperature, as shown in Figure 6.

UA = UA(1) * \ cap = cap(1) *	1	2	3	4	5	6	7	8	9	10
1	1.85	1.61	1.46	1.46	1.48	1.55	1.60	1.71	1.81	1.90
2	1.92	1.68	1.51	1.49	1.48	1.55	1.56	1.66	1.78	1.86
3	2.01	1.76	1.58	1.56	1.52	1.60	1.59	1.68	1.78	1.89
4	2.06	1.83	1.61	1.59	1.55	1.63	1.59	1.69	1.78	1.89
5	2.08	1.84	1.65	1.58	1.56	1.62	1.59	1.70	1.79	1.89
6	2.09	1.86	1.66	1.59	1.57	1.59	1.58	1.68	1.80	1.89
7	2.10	1.86	1.66	1.62	1.56	1.59	1.58	1.67	1.77	1.90
8	2.10	1.88	1.69	1.63	1.59	1.59	1.59	1.68	1.78	1.89
9	2.12	1.87	1.69	1.63	1.61	1.60	1.60	1.69	1.79	1.89
10	2.10	1.90	1.68	1.62	1.60	1.66	1.60	1.70	1.80	1.89

KPI: Hourly mass flow-average return temperature. Variant HXbp: On/Off HXbp

UA = UA(1) * \ cap = cap(1) *	1	2	3	4	5	6	7	8	9	10
1	0.13	0.21	0.30	0.41	0.54	0.62	0.73	0.83	0.95	1.03
2	0.15	0.22	0.30	0.41	0.48	0.55	0.66	0.73	0.83	0.90
3	0.20	0.25	0.32	0.41	0.50	0.57	0.65	0.72	0.80	0.88
4	0.23	0.27	0.34	0.41	0.50	0.58	0.66	0.72	0.79	0.87
5	0.24	0.29	0.35	0.42	0.50	0.57	0.65	0.72	0.80	0.88
6	0.25	0.29	0.35	0.42	0.51	0.57	0.65	0.72	0.80	0.87
7	0.26	0.30	0.36	0.42	0.52	0.57	0.64	0.72	0.80	0.87
8	0.26	0.31	0.36	0.43	0.51	0.57	0.64	0.72	0.79	0.86
9	0.27	0.31	0.36	0.43	0.51	0.57	0.64	0.72	0.79	0.87
10	0.27	0.31	0.37	0.43	0.51	0.57	0.64	0.72	0.79	0.86

KPI: Hourly mass flow-average return temperature. Variant HXbp: controlled HXbp

Figure 6: RMSE of the hourly mass flow-average T_{ret} obtained with the lumped model (top: variant on/off HXp, bottom: variant controlled HXbp) compared to the hourly mass flow-average T_{ret} obtained with the detailed model, varying the UA and cap values of the lumped HX. Case of 10 HXs

The influence of HXbp modelling is evident when examining the dynamic plots of T_{ret} in Figure 7. For simplicity, the results are shown only for 5 HXs (Figures 7a and 7b) and 10 HXs (Figures 7c and 7d). For both variants of the lumped model, the T_{ret} values are shown varying only UA (Figures 7a and 7c) and only cap (Figures 7b and 7d). This approach enables the observation of the distinct effects of UA and cap on T_{ret}. The depicted period is 35 minutes during the second day.

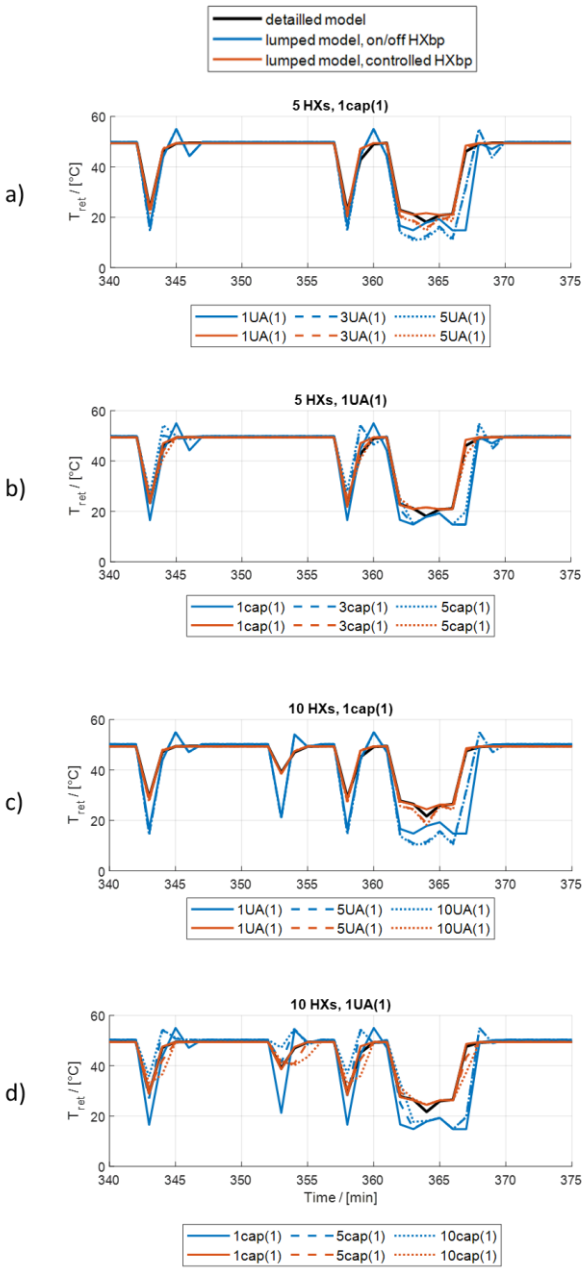

Figure 7: Dynamic T_{ret} obtained with the detailed model (black) and lumped models (on/off HXbp in blue, controlled HXbp in orange). Comparison for 5 HXs (a and b) and 10 HXs (c and d), varying the UA value of the lumped models (a and c) and the capacity value of the lumped models (b and d)

In all cases, it's evident that the lumped model with controlled HXbp (orange lines) performs

notably better in replicating the detailed model (black line) compared to the lumped model with on/off HXbp (blue line). In the short tappings, the capacity plays a more significant role in aligning the behaviour of the lumped model with that of the detailed model (Figures 7b and 7d). In the longer tappings, also the effect of the UA on the lumped model is visible (Figures 7a and 7c). This holds true for both cases involving 5 HXs and 10 HXs.

Optimization on E_{centr} as the compared KPI

Figure 8 shows the relative difference of E_{centr} obtained with lumped models (Figure 8 top: on/off HXbp and Figure 8 bottom: controlled HXbp) varying UA and cap values compared to the detailed model. For simplicity, results are shown only for the case with 10 HXs. Results for capacity values bigger than 5cap(1) are not colour-coded because they are not significant for the optimization (i.e. higher values of energy relative difference).

UA = UA(1) * \ cap = cap(1) *	1	2	3	4	5	6	7	8	9	10
1	13%	16%	20%	23%	26%	27%	29%	31%	32%	33%
2	15%	18%	22%	24%	27%	29%	31%	32%	33%	34%
3	15%	18%	22%	24%	27%	29%	31%	32%	33%	35%
4	15%	18%	22%	24%	27%	29%	31%	32%	34%	35%
5	15%	18%	22%	24%	27%	29%	31%	33%	34%	35%
6	15%	18%	22%	24%	27%	29%	31%	33%	34%	35%
7	15%	18%	22%	24%	27%	29%	31%	33%	34%	35%
8	15%	18%	22%	24%	27%	29%	31%	33%	34%	35%
9	15%	18%	21%	24%	27%	29%	31%	33%	34%	35%
10	15%	18%	22%	24%	27%	29%	31%	33%	34%	35%

KPI: Daily energy consumption on E_{centr}. Variant HXbp: On/Off HXbp

UA = UA(1) * \ cap = cap(1) *	1	2	3	4	5	6	7	8	9	10
1	2%	4%	6%	7%	9%	11%	12%	14%	16%	18%
2	1%	2%	4%	5%	7%	8%	10%	11%	12%	14%
3	1%	2%	3%	5%	7%	8%	9%	10%	11%	13%
4	1%	2%	3%	5%	6%	7%	9%	10%	11%	13%
5	1%	2%	3%	5%	6%	7%	9%	10%	11%	12%
6	0%	2%	3%	5%	6%	7%	9%	10%	11%	12%
7	0%	2%	3%	4%	6%	7%	8%	10%	11%	12%
8	0%	2%	3%	4%	6%	7%	8%	10%	11%	12%
9	0%	2%	3%	4%	6%	7%	8%	10%	11%	12%
10	0%	2%	3%	4%	6%	7%	8%	10%	11%	12%

KPI: Daily energy consumption on Ecentr. Variant HXbp: controlled HXbp

Figure 8: Relative difference of E_{centr} obtained with the lumped model (top: variant on/off HXp, bottom: variant controlled HXbp) compared to the E_{centr} obtained with the detailed model, varying the UA and cap values of the lumped HX. Case of 10 HXs

In the results of E_{centr} there is a negligible sensitivity to UA, i.e. no clear colour change is observed along the columns. However, there's a clear sensitivity to capacity, with a preference for small capacity (1cap(1) for both variants of HXbp). This holds true also for the other cases with different numbers of HXs. Similarly to the results of T_{ret}, the relative difference with the controlled HXbp (ranging from 0% to 18%) is significantly smaller than the relative difference achieved with the on/off HXbp (ranging from 13% to 35%). Interestingly, the optimization of the central energy leads to different values of UA and capacity achieved from the optimization of the return temperature.

Non-adiabatic cases

The results obtained from the non-adiabatic models are consistent with those obtained in the adiabatic simulations. Even in the detailed model, the differences in the return temperature between the adiabatic HX and the non-adiabatic HX are negligible, with differences ranging from -0.2°C to 0°C. However, it is important to note that these findings may be influenced by the assumption of well-insulated HX (UAloss of 0.81 W/K for the single HX).

Simulation times

The average simulation times for the detailed model for the increasing number of HXs (and DHW profiles) is shown in Table 3 (first row ("D.")). The second row ("L.") shows the simulation times for the lumped model for the increasing number of DHW profiles (lumped model with controlled HXbp). On average, the lumped model with on/off HXbp requires 63% more simulation time than the model with controlled HXbp.

Table 3: Average simulation time (in seconds) for the increasing number of HXs and number of DHW profiles (detailed model) and the increasing number of DHW profiles (lumped model) from 2 to 10

	2	3	4	5	6	7	8	9	10
D.	0.6	0.9	1.6	2.6	4.0	5.7	7.6	10.5	14.2
L.	0.9	0.8	0.8	0.9	1.0	1.1	1.2	1.3	1.3

The time advantage of the lumped model becomes evident when dealing with more than four HXs. For instance, with 10 HXs, the simulation time of the lumped model is approximately one-tenth that of the detailed model. The slight increase in simulation time in the lumped model with the growing number of DHW profiles can be attributed to the greater complexity of the DHW profiles, resulting in more computational steps needed to process the data.

Moreover, also the modelling time of the detailed model increases with the increasing number of HXs, as more elements are required (e.g. HXs, controls, flow diverters and flow mixers). On the contrary, in the lumped model, the modelling time is independent of the number of simulated (lumped) HXs. Therefore, the time advantage of the lumped model compared to the detailed model is always guaranteed.

Conclusions

The study aims to explore modelling approaches to lump several apartment heat exchangers (HXs) into single components to simplify the simulation model and reduce the modelling effort and the simulation runtime. The first part of the

study investigates possible approaches in the case of 1 or 2 rising pipes. The advantages and disadvantages of each approach are explained, indicating that the optimal approach may vary based on the goal of the specific study. The second part of the paper investigates the optimal combination of heat loss coefficient (UA), capacity (cap) and heat loss coefficient to the ambient (UAloss) for the lumped HX. The lumped models aim to represent an increasing number of HXs (ranging from 2 to 10). Adiabatic cases and non-adiabatic cases are studied. Two variants of heat exchanger bypass (HXbp) for the lumped model are investigated. The KPIs are the return temperature and the energy consumption. The goal is to minimise the RMSE on the return temperature (hourly average and hourly mass flow-average) and the daily relative energy difference between the lumped model and the detailed model.

The results highlight the significant impact of modelling the lumped HX bypass (HXbp). The model including the controlled HXbp leads to better results than the on/off HXbp (e.g. minimum relative energy difference of 0% in the controlled HXbp vs. 13% in the on/off HXbp). The optimal UA and capacity in the lumped model should have low values (e.g. 1UA(1) and 1cap(1)). The optimization of the central energy shows sensibility mainly on the capacity. Non-adiabatic cases confirm the findings of the adiabatic cases and they indicate a minor role of the UAloss value in terms of return temperature and energy consumption, for a specific combination of UA and cap. The minor role of UAloss is confirmed by the comparison of adiabatic and non-adiabatic detailed models.

The advantages in terms of computational time of the lumped model become evident when simulating more than 4 HXs. For example, with 10 HXs, the simulation time is about one-tenth of that of the detailed model. Additionally, the modelling effort is significantly reduced and in the lumped model becomes independent of the number of considered HXs. Considering the potential application of this model to even larger and more complex scenarios, such as 52 apartments in a single building within the Campagne project or even the entire district in Campagne comprising 307 apartments, the significance of these time savings becomes even more pronounced and crucial.

Outlook

Considering the interconnected nature of the pipe-lumping and HX-lumping approaches, it's crucial to tackle their complexities together. This requires comprehensive approaches that take into account how these lumped components interact and depend on each other.

In future work, the number of simulated HXs can be increased, potentially from 10 to 50 or more units and different DHW profiles can be applied. Moreover, the correlation between the optimal values of UA and capacity value based on the simultaneity of DHW profiles could be investigated. The findings of the current study will be applied to the Campagne project, with 52 HXs in one building and 307 HXs in the entire district. Besides, simulation results can be compared with monitoring data.

Acknowledgement

The project “Monitoring Innsbruck Campagne“ is supported by Klima- und Energiefonds (FFG Österreichische Forschungförderungsgesellschaft Nr. 899823, 'IBK_Campagne'), Leuchttürme für resiliente Städte 2040 - Ausschreibung 2022.

With the project “Monitoring Innsbruck Campagne” we contribute to the international projects IEA EBC A83 Positive Energy Districts, IEA HPT A61 Heat Pumps in Positive Energy Districts and IEA SHC T66 Solar Energy Buildings.

References

Dermentzis, G., Ochs, F., Thuer, A., Streicher, W. 2021. Supporting decision-making for heating and distribution systems in a new residential district - An Austrian case study. Energy. DOI: https://doi.org/10.1016/j.energy.2021.120141

Fink C., Kaiser A., Wagner W. 2010. Qualitätsstandards von Wohnungsstationen in Zwei-Leiter-Netzen. Ein Beircht zu messtechnischen Untersuchung.

Jordan, U., Vajen, K., 2005. DHWcalc: Program to generate domestic hot water profiles with statistical means for user defined conditions.

Ochs, F., Breuss, S., Venturi, E., Magni, M., Dermentzis, G., Fisco, S., 2020. Modelling and simulation of innovative decentral domestic hot water systems with heat pumps for multi-family buildings. BauSim 2020. DOI: https://doi.org/10.3217/978-3-85125-786-1-15

Recknagel, H., Sprenger, E., & Schramek, E.-R. (2009). Taschenbuch für Heizung und Klimatechnik.

Solar-Institut Juelich. CARNOT Toolbox Ver. 6.3, 10/2018 for Matlab/Simulink R2018b. 2018. https://fh-aachen.sciebo.de/index.php/s/0hxub0iIJrui3ED, visited in March 2024

BauSIM 2024 in Wien
23. September – 26. September

Modularity in water-water heat pumps with integrated latent heat storage for energy-efficient residential applications

Abdulrahman Dahash[1], Carlos Salvador Collado[1], Michael Lauermann[1], Raimund Zitzenbacher[2], Stephan Preisinger[2], Christoph Reichl[1]

1 AIT Austrian Institute of Technology GmbH, Center for Energy, Giefinggasse 2, 1210 Vienna, Austria, E-Mail: abdulrahman.dahash@ait.ac.at

2 OCHSNER Wärmepumpen GmbH, 3350 Haag, Austria

Abstract

The decarbonization of European buildings is crucial and addresses the necessity to promote energy efficiency measures and employ effective technologies. Exploiting the modular approach, the work integrates water-source heat pumps (WSHPs) with latent heat storage to address diverse thermal demands in a renovated multi-family house apartment. Annual simulations, executed using Modelica/Dymola, explore both serial and parallel hydraulic system connections for WSHP blocks. Results underscore the superiority of the parallel configuration across varying climates, primarily due to reduced electricity consumption. However, in colder climates, a serial connection proves essential to attain higher supply temperatures, particularly for WSHPs and WPW-HEX charging. The approach yields significant reductions in CO2 emissions, compared to conventional systems.

Introduction

The residential heating and cooling sector in European Union (EU) relies profoundly on conventional energy sources (e.g. natural gas), leading to high energy consumption and CO_2-emissions (Wei, W. and Skye, H. M., 2021). Thus, there is a growing need to transition to cleaner energy sources and decarbonize the building sector. Heat pumps and district heating are frequently identified as key technologies to accelerate this energy transition and promote sustainability (Lämmle, M. et al., 2022).

Heat pump technology, using low-temperature heat sources (e.g. ambient air, groundwater), efficiently satisfies the heating demand in buildings via electricity input (E. Osterman and U. Stritih, 2021). Compared to its conventional sensible counterparts, latent heat storage also gains significance due to its high energy density compared to hot water tanks (Maghrabie, H. M. et al., 2023).

In modern residential buildings, low-temperature thresholds for hydronic systems are crucial for energy-efficient operations. Floor heating arises as a prominent terminal to achieve energy efficiency and sustainability (Lämmle, M. et al., 2022). Domestic hot water (DHW) demands, however, require higher temperatures than space heating (SH) between 45°C and 65°C, necessitating an effective hydronic system and control strategy to meet building demands while maintaining efficiency (Emhofer, J. et al., 2020). Hence, this study investigates an 8-modular heat pump system coupled with a latent heat storage to provide space heating, cooling, and DHW for buildings in three different climates.

This work explores various hydronic system configurations for connecting water-source heat pumps (WSHPs) with each other and with a latent heat storage in order to offer the guidance for optimal operation scenarios under different configurations to satisfy both SH and DHW demands. It further examines the possibility to satisfy the space cooling (SC) demand through the connection of WSHPs' evaporators to the building hydronic system.

Literature review

Heat pumps can operate thermally or electrically and classified as absorption/adsorption or compression technologies (E. Osterman and U. Stritih, 2021). In compression mode, electricity powers the compressor raising the low-exergy source temperature. However, greater temperature differences between the source and sink reduce efficiency (i.e. coefficient of performance) due to increased electricity use. Yet, HPs found their place favorably in residential applications and within building energy systems (BESs).

(Pinamonti, M. et al., 2021) numerically investigated a system of modular heat pumps, solar seasonal storage and solar thermal

collectors for satisfying the SH and DHW for a single-family house in cold climates. The outcomes revealed that the integration of a HP can help in increasing the solar fraction leading to a feasible system. Yet, the work did not consider the use of HPs for SC.

(Jung, Y. et al., 2021) comprehensively investigated WSHPs in terms of building type, water source and water intake distance. The results showed that for all building types, the energy savings can be notably high especially for cases with higher heating-to-cooling ratio due to the low energy consumption of the water intake system. Compared to conventional systems (e.g. gas-fired boilers and cooling systems), the use of WSHPs can significantly contribute to the reduction of CO_2-emissions as emissions increase with lower heating-to-cooling ratio. An important finding was the highlight of the role of water source type and temperature turning out to be more important than the building type.

Contribution of this work

This study investigates diverse configurations of hydronic systems integrating WSHPs and latent heat storage. It aims to identify optimal operation scenarios to meet both SH and DHW demands. Additionally, it explores the potential of using WSHPs' evaporators to fulfill SC requirements within the building's hydronic system. Moreover, the work will conduct a performance analysis considering three climates (cold climate, average climate and hot climate) to highlight the optimal configuration for each climate as defined in EN 14825. Furthermore, the work will carry out a brief environmental analysis to point out the saving in CO_2-emissions if a transition from conventional BES to the proposed solution takes place.

Methodology

To assess the proposed system's suitability and configurations for modular WSHPs, numerical simulations are conducted using a dynamic thermo-hydraulic model developed in Modelica/Dymola. This model integrates WSHPs into a multi-family house environment, building upon existing models from the "Buildings" library and commercial libraries "TIL" and "TIL Media". Realistic DHW consumption profiles are incorporated into the investigation. The top-level model includes sub-system models for:

- WSHPs system consisting of multiple HP units with evaporators, compressors, condensers and expansion valves.
- Detailed building representing an intermediate apartment with a nominal SH load of 25 W/m^2, SC load and DHW demand.
- Building distribution system incorporating a hydronic circuit connecting WSHPs, circulation pump, latent heat storage, pipes, valves and heat delivery units (e.g. floor heating, radiators).
- 5th generation district heating and cooling (5GDHC) simulating a simplified network with a temperature ranging from 20°C to 30°C, where 20°C represents the inlet temperature of the evaporator.
- Control system considering all constraints and conditions.

Brief on main simulation models

Building model

The building model utilized is an extension of the "MixedAir" model within the Buildings library "Buildings.ThermalZones.Detailed.MixedAir". It represents an intermediate apartment with 8 x 10 m^2 with a height of 3 m, treated as a single thermal zone (see Table 1). The model incorporates windows on all four exterior walls, each measuring 2 x 2 m^2 and composed of triple-paned glass (clear glass, gas, clear glass).

Additionally, the model integrates an occupancy profile for each day of the year at hourly intervals. For heat transfer, the model converts occupancy per person into heat gains of 35 W/m^2 for radiant heat, 70 W/m^2 for convective heat and 30 W/m^2 for latent heat**.**

Table 1: U-values of the building sidewalls.

	VALUE	DESCRIPTION
U_{ext}	0.287 W/(m^2.K)	Structural U-vale of the building sidewalls.
$U_{fl\text{-}ce}$	0.2 W/(m^2.K)	Structural U-vale of the building floor/ceiling.

Heat pump model

This study involves four blocks of WSHPs, each comprising two modules leading to a total of eight WSHPs. These units can be connected in series and/or parallel from a hydronic perspective. For dynamic thermo-hydraulic modeling of the WSHPs' components, the “TIL library” was utilized, commonly used for dynamic simulations of refrigeration cycles, enabling detailed representation and parameterization of each HP's component.

Each WSHP module has a nominal heating capacity of 1.1 kW, resulting in a total of 2.2 kW per block. Propane (R290) is used as the refrigerant, with a maximum allowable operating pressure of 31 bar$_a$ The refrigeration cycle includes a post-condenser subcooling of 3 K and post-evaporator superheating of 7 K.

Latent heat storage model

Herein, a latent heat storage system is integrated into the building energy system. This storage intrinsically is a heat exchanger filled with phase change material (PCM), facilitating heat transfer between water from the heat pumps system and tap water for DHW production. The PCM used, Rubitherm RT55, is a paraffin with a phase change temperature of 55ºC, known for its high efficiency in heat and cold storage. Table 2 reports the most relevant thermo-physical properties of RT55.

The latent heat storage operates as a water-PCM-water heat exchanger (WPW-HEX), utilizing water as the working medium on both sides. It serves as an instantaneous water heater, capable of directly heating water to the desired DHW temperature during discharge.

Two WPW-HEX units are employed in parallel, designed as plate heat exchangers with a nominal storage capacity of 1.2 kWh/unit (for sensible and latent energy within a 15 K range around the phase transition temperature), totaling 2.4 kWh. Constructed from aluminum, each WPW-HEX unit measures 0.5 m in height and consists of 28 plates.

Table 2: RT55 properties (Rubitherm).

	Typical values
Melting Area	51ºC – 57ºC (main peak 55)
Congealing Area	56ºC – 57ºC (main peak 55)
Heat storage capacity ± 7.5%.	170 kJ/kg
Combination of latent and sensible (48ºC up to 63ºC)	48 Wh/kg
Specific heat capacity	2 kJ/kg.K
Density at solid (15ºC)	0.88 kg/l
Density at liquid (80ºC)	0.77 kg/l
Heat conductivity (both phases)	0.2 W/m.K
Volume expansion	14%

Assumptions and boundary conditions

This study considers three different cities – Helsinki (FIN), Strasbourg (FR), and Athens (GR) – representing cold, average, and hot climates, respectively. Meteorological data based on a typical meteorological year (TMY) are imported into the top-level model. The BES adjusts its supply temperature according to ambient temperature, following a heating curve as depicted in Figure 1.

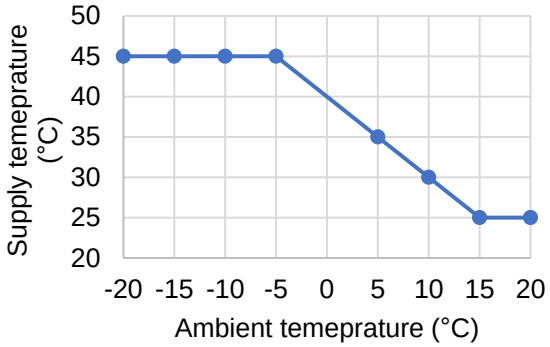

Figure 1: Setpoint Temperature calculation.

During the heating season, the supply temperature ranges from 25°C to 45°C, while in the cooling season (summer), it is fixed at 18°C.

For space heating (SH) operation, the daytime target temperature ($T_{sp,day}$) is 21ºC (from 07:00 to 19:00), with setbacks to 18°C during nighttime (from 00:00 to 07:00 and from 19:00 to 00:00). During cooling, the setpoint temperature ($T_{sp,cooling}$) is maintained at 25ºC.

Operation modes

The modes in which the system can operate are:

1. Space heating only,
2. Charging WPW-HEX only,
3. Space cooling only – WPW-HEX is full and heat is injected into 5GDHC,
4. Space cooling + charging WPW-HEX.

The proposed system cannot simultaneously fulfill SH demand and charge the WPW-HEX. In case of overlap, priority is given to WPW-HEX charging. Figure 2 depicts these modes illustrating the layout of WSHPs, WPW-HEX and other hydraulic components. Connections are adjusted based on hydraulic configuration (parallel/series) and operation mode (e.g., SH).

Space heating (SH)

Figure 2 (a) shows that the condenser side of the heat pumps is connected in series with the demand side to meet SH. The number of operating heat pumps depends on the setpoint supply temperature. The evaporator side is connected in parallel, injecting cooling energy into 5GDHC. Herein, the WPW-HEX is charged, and the DHW demand is inactive.

Charging of WPW-HEX

In this configuration, SH is neglected, and priority is given to the DHW demand. Consequently, the heat generated on the condensers side of the heat pumps is diverted via a 3-way valve to charge the WPW-HEX, which meets the DHW demand. Meanwhile, the evaporators side is connected in parallel, injecting cooling energy into the 5GDHC as illustrated in Figure 2 (b).

Space cooling (SC) and WPW-HEX charging

In this mode, the hydraulic connections are adjusted so that the evaporator side is connected to the building distribution system. This allows the cooling energy produced by the heat pumps' evaporators to be delivered directly to the building. Figure 2 (c) illustrates this configuration, clearly showing that the condenser side forms a closed loop with the WPW-HEX, while the evaporator side forms another closed loop with the building. In this setup, the cooled water from the evaporators is used to meet SC demands. It absorbs the indoor heat and is subsequently re-cooled by the evaporators. Because this mode comprises two hydraulically balanced, closed loops, interaction with the GDHC system is held unnecessary, resulting in no injection or extraction of heat from the 5GDHC system.

Space cooling (SC) only

This mode is similar to the preceding one, with the main difference being that the WPW-HEX is actively charged. Therefore, interaction with the 5GDHC becomes crucial. In this configuration, a controlled amount of fluid is extracted from the 5GDHC, heated, and then reinjected into the 5GDHC at a higher temperature.

Key performance indicators (KPIs)

The KPIs used to measure the performance of the WSHPs is the coefficient of performance (COP) for each single heating operation mode, the seasonal COP (SCOP) and the seasonal energy efficiency ratio (SEER). To demonstrate the savings potential in CO_2-emissions of the proposed system compared to its conventional counterpart, it is essential to conduct an environmental analysis on annual basis considering the amount of CO_2 produced by each system. Thus:

$$\mathrm{SCOP} = \frac{Q_{\mathrm{con}}}{P_{\mathrm{el}}} \quad (1)$$

$$\mathrm{COP}_{\mathrm{heat}} = \frac{Q_{\mathrm{con-heat}}}{P_{\mathrm{el-heat}}} \quad (2)$$

$$\mathrm{COP}_{\mathrm{DHW}} = \frac{Q_{\mathrm{con-DHW}}}{P_{\mathrm{el-DHW}}} \quad (3)$$

$$\mathrm{SEER} = \frac{Q_{\mathrm{ev}}}{P_{\mathrm{el}}} \quad (4)$$

$$M_{\mathrm{CO_2}} = f_{\mathrm{CO_2}} \cdot E \quad (5)$$

Results and discussion

Indoor temperature and thermal demands

Throughout the annual investigation, the proposed system maintains indoor setpoint temperatures within the thermal comfort range of 21°C±1.5 K during winter daylight. Same is observed during the winter nighttime. In this regard, Figure 3 shows the setpoint indoor temperatures and simulated indoor temperatures for Helsinki comparing serial and parallel configurations over a single week in winter.

In Helsinki and Strasbourg, with their cold winter climates (minimum temperatures of -21.7ºC and -9.6ºC, respectively), the system exhibits similar behavior. However, Helsinki experiences milder outdoor temperatures initially, resulting in less frequent operation of the WSHPs compared to Strasbourg. Towards the end of the study period, as outdoor temperatures change, rapid fluctuations occur due to large temperature differences between indoor and outdoor environments, imposing frequent cycling of the heat pump system due to the large temperature difference between indoor and outdoor. Besides, this highlights the role of the building's thermal mass as it losses heat fast. In Helsinki's colder nights, the WSHPs run to maintain desired temperatures, while in Strasbourg, this is rarely required.

In contrast, Athens, with its warmer climate, exhibits different behavior. Temperatures rarely fall below the target, particularly at night (rarely dropping below 18°C), resulting in significantly less operation of the heat pump system.

Despite these differences, overall system behavior remains within desired parameters, with occasional brief deviations from target temperatures. This variation is not concerning in the context of system performance but warrants consideration for further system development. Configuration differences are minimal, with similar oscillation patterns observed between target temperatures.

This study primarily focuses on three operations: space heating, space cooling, and WPW-HEX charging, it is therefore important to analyze the amount of space heating, space cooling and energy charged into WPW-HEX.

Table 3 presents relevant values for this analysis. It further reports the specific values of SH and SC together with the amount of heat injected into 5GDHC during the operation mode 3 (i.e. space cooling only).

The highest SH demand is observed in Helsinki, with Athens exhibiting the lowest demand. This trend remains consistent across both series and parallel configurations. However, the series configuration shows slightly lower SH demands resulting in a marginal increase in specific space heating values for the parallel configuration. This is attributed to smaller temperature differences in WSHPs for the series configuration.

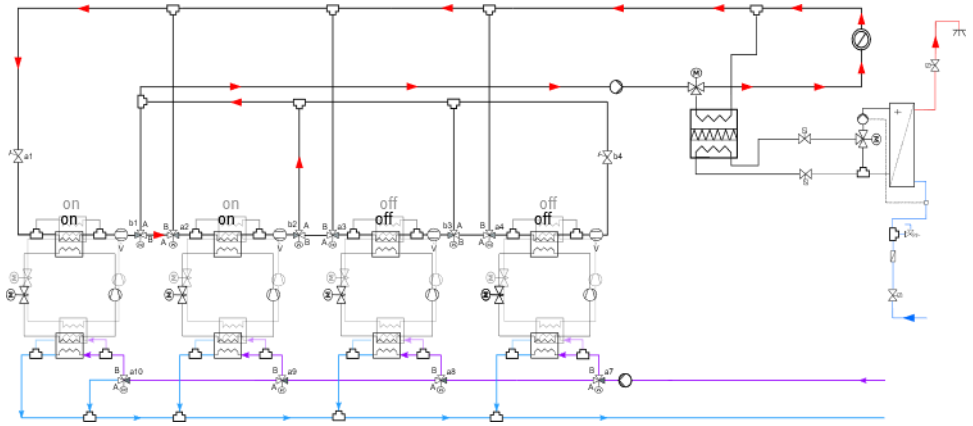

(a) Space heating operation in a serial connection (less hydraulic complexity).

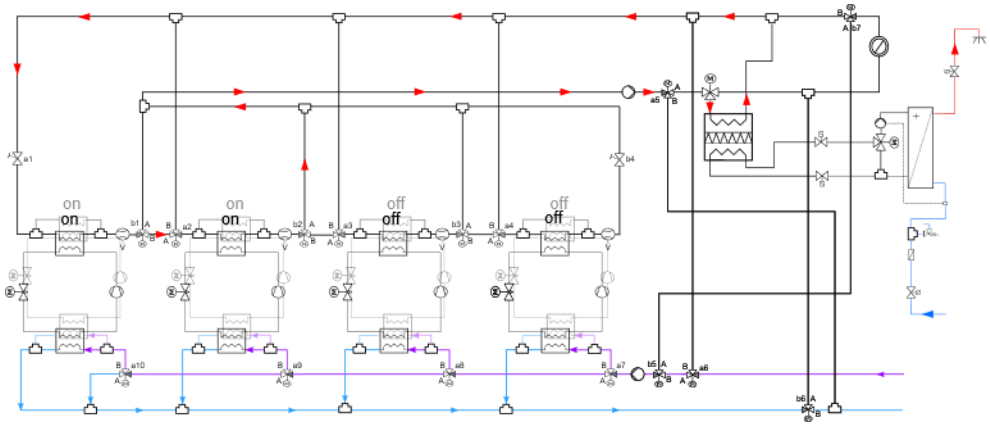

(b) WPW-HEX charging operation in a serial connection.

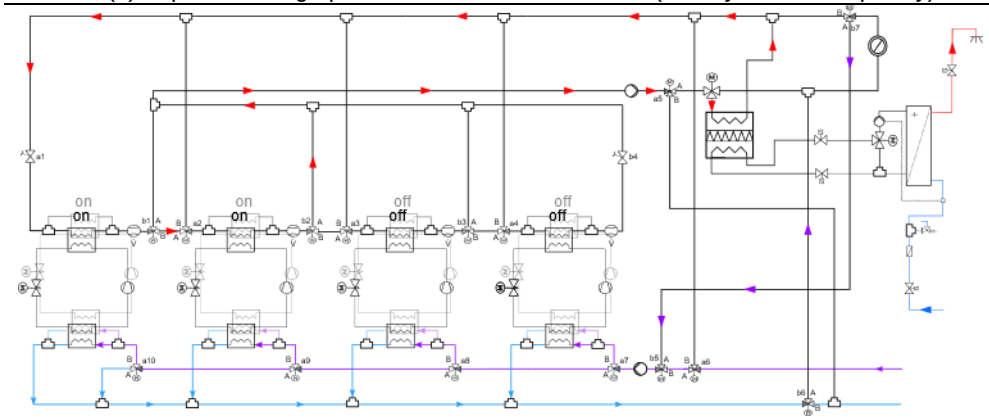

(c) Space cooling operation and WPW-HEX charging in a serial connection.

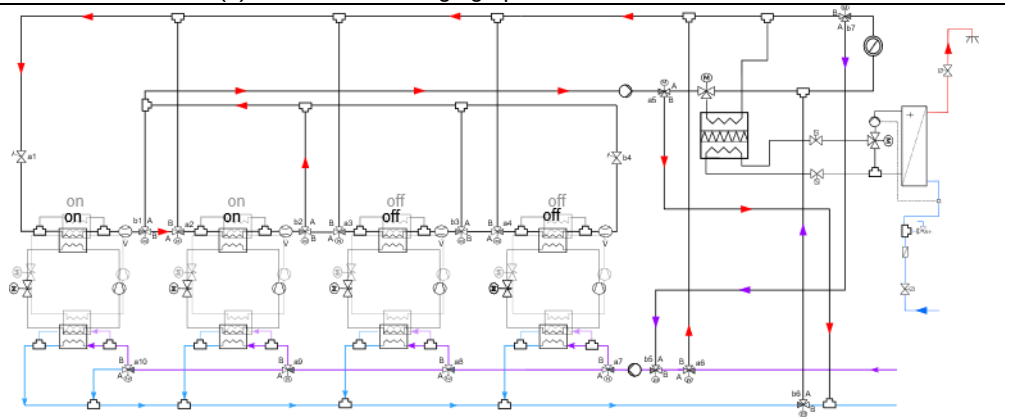

(d) Space cooling with injection of heat into 5GDHC in a serial connection.

Figure 2: The four operation modes observed in the proposed system with a serial connection. In this case, two WSHP blocks are highlighted as “on” and the other two as “off” to highlight the modularity approach of this system.

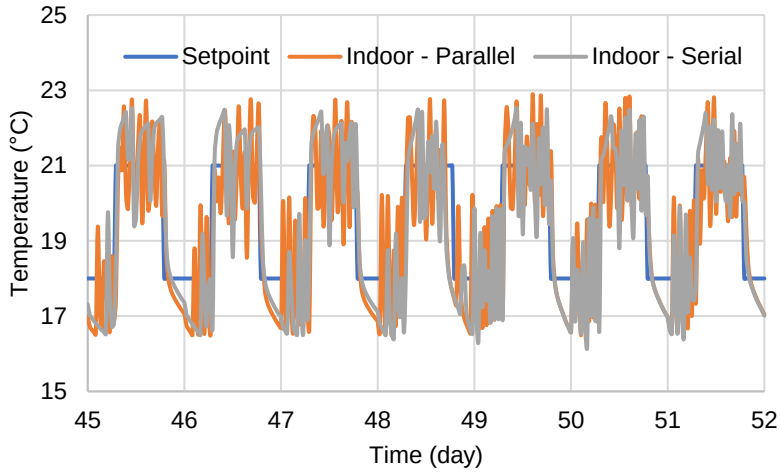

Figure 3: A single week in February for Helsinki climate with setpoint indoor temperature (blue), measured indoor temperature in parallel mode (orange), and measured indoor temperature in serial mode (grey).

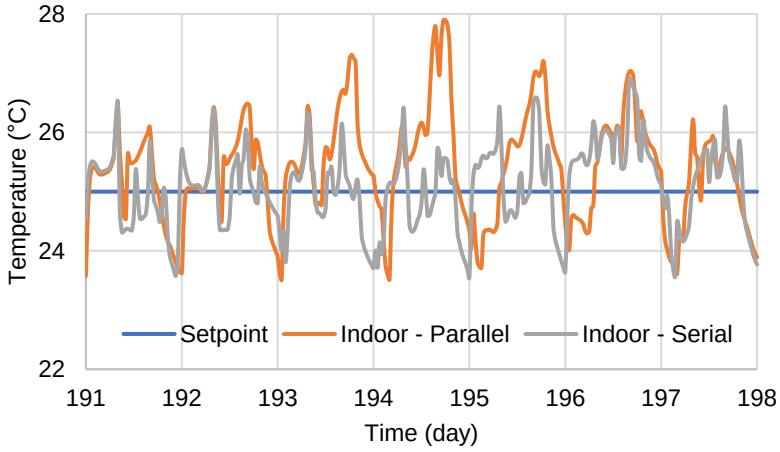

Figure 4: A single week in July for Athens climate with setpoint indoor temperature (blue), measured indoor temperature in parallel mode (orange), and measured indoor temperature in serial mode (grey).

On the contrary, for space cooling, Athens has the highest demand, while Helsinki exhibits the lowest, exposing the impact outside temperature conditions. During this operation, some heat is injected into 5GDHC (Q_{5GDHC}) since WPW-HEX is sufficiently charged. This amount is at highest in Athens due to the frequent operation of WSHPs in cooling mode.

The amount of heat injected in 5GDHC for Athens can be used to satisfy the DHW demand for another apartment with same boundary conditions. For DHW, the amount of heat charged in WPW-HEX is a good representative and it drastically decreases if a shift from a series to parallel is made. This is due to the account of heat losses from WPW-HEX that is at highest in series mode for Helsinki.

The parallel mode ensures a sufficient amount of heat is charged in WPW-HEX with moderate temperature, while the series mode charges with higher temperatures and flowrate leading to higher losses.

Table 3: Annual space heating, space cooling, charged heat in WPW-HEX and heat injected into the 5GDHC for the different locations and hydraulic configurations.

	HEL		STR		ATH	
	SER	PAR	SER	PAR	SER	PAR
Q_{SH} (kWh/a)	7069	7280	4037	4136	791	826
q_{SH} (kWh/m²)	88	91	50	52	10	10
Q_{SC} (kWh/a)	150	187	504	544	3199	3207
q_{SC} (kWh/m²)	2	2	6	7	40	40
$Q_{WPW-HEX}$ (kWh/a)	3731	3108	3665	3064	3800	3318
Q_{5GDHC} (kWh/a)	159	153	532	518	3451	3537

WSHPs Performance analysis

The highest energy consumption for heating operations is observed in Helsinki, while for cooling, Athens exhibits the highest demand as indicated in Table 4. Therein, condenser output values are slightly lower in parallel configurations than in series. This is because the temperature difference between the inlet and outlet of the heat pumps is reduced in parallel setups; hence, less heat is generated during operation. Besides, the serial operation might achieve higher temperature leading to higher thermal losses over the transmission pipes. Additionally, lower pressure losses in the parallel configuration lead to decreased electricity consumption and a marginal SCOP improvement to achieve the same heating objective, resulting in both energy and cost savings. The lowest SCOP for heating operations is approximately 3 in Helsinki, gradually increasing in Strasbourg and Athens, peaking at 3.92 in Athens. Notably, SCOP values are consistently higher in parallel mode compared to series due to the lower temperature difference.

Table 4: Performance for the different operations and configurations for each location.

		HEL		STR		ATH	
		SER	**PAR**	**SER**	**PAR**	**SER**	**PAR**
Heating	$Q_{condenser}$ **(kWh/a)**	7974	7781	4667	4490	913	875
	$P_{electric}$ **(kWh/a)**	2616	2514	1398	1335	238	223
	SCOP	**3.05**	**3.09**	**3.34**	**3.36**	**3.84**	**3.92**
Cooling	$Q_{evaporator}$ **(kWh/a)**	160	148	536	499	3334	3249
	$P_{electric}$ **(kWh/a)**	67	71	224	232	1358	1419
	SEER	**2.37**	**2.07**	**2.39**	**2.15**	**2.45**	**2.29**
Charging	$Q_{condenser}$ **(kWh/a)**	3854	3290	3818	3265	3921	3776
	$P_{electric}$ **(kWh/a)**	1716	1487	1697	1476	1728	1664
	SCOP	**2.25**	**2.21**	**2.25**	**2.21**	**2.27**	**2.27**

During cooling, energy consumption values remain similar across configurations, as the system is designed to achieve a 4K temperature decrease on the evaporator side. Consequently, differences between configurations are minimal. SEER values are slightly lower than SCOP. Lower SEER values in parallel mode can be attributed to higher indoor temperatures, particularly noticeable in Athens, resulting in slightly elevated return water temperatures.

It is important to note that there is a difference between the amount of heat generated at the condenser (Table 4) and the heat delivered to the final application (Table 3) and this is due to the account of heat losses over the hydronic network (e.g. pipes).

Environmental analysis

The benchmark for the environmental analysis is a conventional system consisting of a gas-fired boiler (4.5 kW, 90% efficiency) for space heating and DHW consumption, and an air conditioning unit (2 kW, SEER 2.6) for space cooling. In addition, a 120-liter hot water tank is included.

The HP does not generate CO_2-emissions during its operation, while electricity generation is crucial for its operation. Therefore, depending on where the electricity sources, the emission factor might vary. Therefore, this work considers the Austrian electricity mix, where energy is generated mainly from hydropower resulting in lower carbon intensity of 202 g_{CO2}/kWh_{el}. While in other European countries (e.g. Poland), fossil fuels play a critical role in the electricity mix, so a EU-27 emission factor of 265 g_{CO2}/kWh_{el} is considered.

For the conventional system, the boiler generates CO_2 due to the energy input of natural gas with an emission factor of 268 g_{CO2}/kWh_{gas}. The air conditioning unit requires electricity similar to HP.

Table 5 compares both configurations of the proposed system with the conventional system for the three climate zones. Noticeable is the biggest difference of around 2.4 t_{CO2}/a observed in Helsinki resulting from the comparison of the parallel configuration with the conventional system. This is attributed to the space heating that requires lower electricity input for the WSHPs with parallel configuration compared to the high gas input for conventional system. Meanwhile, the smallest difference is in Athens between the series configuration and the conventional system, which is where the boiler works for the least time as the AC unit almost always does. Yet, the reduction is still remarkable of 1.25 t_{CO2}/a for a single apartment.

Table 5: CO_2-emissions during the annual operation.

	Amount of CO_2 (t/year)	
	Austrian mix	**European mix**
	HELSINKI	
SER	0.89	1.21
PAR	0.82	1.12
CONV	3.23	3.24
	STRASBOURG	
SER	0.66	0.89
PAR	0.60	0.82
CONV	2.46	2.48
	ATHENS	
SER	0.58	0.79
PAR	0.57	0.78
CONV	1.93	2.03

Hence, the proposed system exhibits a great potential for decarbonization of the building stock with a range of 1.2 t_{CO2}/a up to 2.4 t_{CO2}/a per apartment under these boundary conditions. This reduction can be translated in operational cost savings since a tax of CO_2-emission will come in action. Bearing in mind a tax of around 100 €/t_{CO2} in 2022, this can yield an economic saving between 100 €/a and 240 €/a.

It is crucial to mention that such a saving of 1.2 t_{CO2}/a is not a negligible value that hinders the transformation to the proposed solution because this is only for a single apartment. Thus, this can lead to a drastic reduction in CO_2-emissions on the district scale or the city scale.

Conclusions

The decarbonization for European buildings highlights the importance to encourage energy efficiency measures and leverage effective technologies. This study adopted a modular approach, integrating water-source heat pumps (WSHPs) with latent heat storage to fulfill diverse building thermal demands. Annual simulations, conducted using Modelica/Dymola, explored serial and parallel hydraulic system connections for WSHP blocks in a renovated multi-family house apartment.

Results emphasized the advantage of the parallel configuration across various climates, attributed to reduced electricity input. However, for cold climates, a serial connection was required to achieve higher supply temperatures, particularly for WSHPs and WPW-HEX charging. The approach demonstrated substantial CO2-emissions reduction, ranging from 1 tCO2/a to 2.4 tCO2/a per apartment compared to conventional systems.

The authors recognize the incomplete presentation of results due to pages limitation. Therefore, a comprehensive analysis encompassing indoor temperature evolution, supply and return temperatures and WPW-HEX temperature demands further elaboration.

Acknowledgement

This work is part of the research project “HYPERGRYD – Hybrid Coupled Networks for Thermal-Electric Integrated Smart Energy Districts” that has received funding from the European Union’s H2020 programme under Grant Agreement No. 101036656. Therefore, the authors wish to acknowledge the financial support for this work.

References

E. Osterman and U. Stritih. (2021). Review on compression heat pump systems with thermal energy storage for heating and cooling of buildings. *Journal of Energy Storage, 39*. doi:10.1016/j.est.2021.102569

Emhofer, J. et al. (2020). Techno-economic analysis of a heat pump cycle including a three-media refrigerant/phase change material/water heat exchanger in the hot superheated section for efficient domestic hot water generation. *Applied Sciences, 10*(21). doi:10.3390/app10217873

Jung, Y. et al. (2021). Comprehensive multi-criteria evaluation of water source heat pump systems in terms of building type, water source, and water intake distance. *Energy and Buildings, 236*. doi:10.1016/j.enbuild.2021.110765.

Lämmle, M. et al. (2022). Performance of air and ground source heat pumps retrofitted to radiator heating systems and measures to reduce space heating temperatures in existing buildings. *Energy*. doi:10.1016/j.energy.2021.122952.

Maghrabie, H. M. et al. (2023). Ground-source heat pumps (GSHPs): Materials, models, applications, and sustainability. *Energy and Buildings*. doi:10.1016/j.enbuild.2023.113560

Pinamonti, M. et al. (2021). Water-to-water heat pump integration in a solar seasonal storage system for space heating and domestic hot water production of a single-family house in a cold climate. *Solar Energy, 213*, 300-311. doi:10.1016/j.solener.2020.11.052.

Rubitherm, R. . (kein Datum). *PCM RT-LINE Products.* Abgerufen am 20. February 2024 von Rubitherm Technologies GmbH: https://www.rubitherm.eu/media/products/datasheets/Techdata_-RT55_EN_09102020.PDF

Wei, W. and Skye, H. M. (2021). Residential net-zero energy buildings: Review and perspective. *Renewable and Sustainable Energy Reviews, 142*. doi:10.1016/j.rser.2021.110859

BauSIM 2024 in Wien
23. September – 26. September

Netzdienlicher Wärmepumpenbetrieb mittels erweitertem Low-Tech MPC-Algorithmus

Vukasin KLEPIC[1], Magdalena WOLF[1], Tobias PRÖLL[1]

[1]BOKU University, Department für Materialwissenschaften und Prozesstechnik, Institut für Verfahrens- und Energietechnik, Österreich, E-Mail: magdalena.wolf@boku.ac.at

Kurzfassung

Die vorliegende Arbeit präsentiert die Weiterentwicklung einer Low-Tech modell-prädiktiven Regelung (MPC) für einen netzdienlichen Betrieb von Wärmepumpen. Der zuvor entwickelte und bereits in der Literatur (Klepic et al., 2023) verfügbare, sowie in mehreren Gebäuden eingesetzte Algorithmus, optimiert vorausschauend Behaglichkeits-parameter unter Berücksichtigung von Wetter-Prognosedaten für 48 Stunden. Mit einem simplen mathematischen Gebäudemodell und einer Optimierungsfunktion wird der Heizbedarf errechnet und der optimale Heizleistungsverlauf über die Zeit bestimmt.

Aufbauend auf den ersten Ergebnissen wird der Algorithmus um eine Energiepreisprognose erweitert. Durch die Modifikation wird die gleichzeitige Optimierung der Behaglichkeit und der Wärmebereitstellungskosten möglich. Diese prognosebasierte Kosten- & Behaglichkeits-funktion ist für den Einsatz von Wärmepumpen in Gebäuden mit thermisch aktivierten Bauteilen konzipiert. Der MPC erhält durch die Erweiterung die Möglichkeit, zusätzlich zu Wetter-Prognosedaten, Day-Ahead Börsenpreise oder andere Preissignale zu verarbeiten. Dadurch kann der Betrieb von Wärmepumpen in netzdienliche Zeitabschnitte verschoben werden.

Die Analyse und Validierung des Algorithmus wird in einer Matlab/Simulink-Gebäudesimulation durchgeführt. Erste Simulationsergebnisse zeigen, dass die Wärmebereitung in Zeiten mit niedrigen Strompreisen verschoben werden kann. Dies führte zu einer signifikanten Reduktion der Wärmebereitungskosten ohne nennenswerte Komforteinbußen.

Abstract

This paper presents the further development of a low-tech model predictive control (MPC) for the grid-friendly operation of heat pumps. The previously developed algorithm, which is already available in the literature (Klepic et al., 2023) and has been implemented in several buildings, predictively optimizes comfort parameters taking into account weather forecast data for 48 hours. A simple mathematical building model and an optimization function are used to calculate the heating requirement and determine the optimum heating output curve over time.

Based on the initial results, the algorithm is extended to include an energy price forecast. This modification enables the simultaneous optimization of comfort and heat supply costs. This forecast-based cost & comfort function is designed for the use of heat pumps in buildings with thermally activated components. The extension enables the MPC to process day-ahead electricity prices or other price signals in addition to weather forecast data. This means that the operation of heat pumps can be shifted to periods that are beneficial to the grid.

The algorithm is analyzed and validated in a Matlab/Simulink building simulation. Initial simulation results show that heat generation can be shifted to times with low electricity prices. This leads to a significant reduction in heating costs without significant loss of comfort.

Einleitung

Der Energiebedarf für Heizung, Kühlung und Warmwasserbereitung ist für rund 50 % des weltweiten Endenergiebedarfs verantwortlich. Ca. 21 % dieses Bedarfs können der Industrie zugeordnet werden, der Rest entfällt auf den Gebäudesektor (Kreiner D. et al., 2021).

Der Gebäudesektor kann daher durch die Senkung des Gesamtenergiebedarfs erheblich zur Verringerung der Treibhausgasemissionen und zum Erreichen der Klimaziele beitragen. Gut wärmegedämmte Gebäude, in Kombination mit thermisch aktivierten Bauteilen (TAB) und effizienten Heiz- oder Kühlsystemen wie Wärmepumpen, schaffen die Grundlage für einen energieeffizienten Betrieb.

Durch den Einsatz von intelligenten oder prognosebasierten modellprädiktiven Regelungen kann eine effiziente Betriebsweise unterstützt werden (Schuß M., 2011).

Bestehende MPC-Regelungssysteme basieren jedoch meist auf intelligenten und komplexen Algorithmen mit hoher Rechenleistung und entsprechender Hardware (Stoffel P. et al., 2023).

Die Haustechnik für Wohngebäude verfügt in der Regel weder über Kapazitäten für umfangreiche Regelungshardware noch über die finanziellen Mittel, um solche komplexen Konzepte umzusetzen. Trotz der vielen theoretischen MPC-Konzepte ist die Zahl der realen Gebäude, die MPC-Strategien umsetzen, relativ gering (Serale G. et al., 2018).

Nachteilig ist zudem der hohe Modellierungs- und Parametrierungsaufwand für MPC und fehlende kommerzielle Werkzeuge zur einfachen Implementierung. Darüber hinaus ist die Erfahrung und das Fachwissen in der Modellierung von prädiktiven Reglerschemata eine Herausforderung (Kilian M. et al., 2016).

Wissenschaftliche Ergebnisse belegen zudem, dass die Reduzierung des Stromverbrauchs durch sehr komplexe und intelligente Wettervorhersage-Regelungen begrenzt ist. Was wiederum bedeutet, dass diese Regelungen unrentabel werden können (Thygesen R. et al., 2016).

Diese technologische Lücke eines einfachen und unkomplizierten MPC wurde durch die wissenschaftliche Arbeit von Klepic et al., 2023 adressiert. Mit der ersten Algorithmus-Entwicklung wurde ein einfaches System geschaffen, womit eine Low-Tech Wetter-prognoseabhängige Komfortoptimierung der Raumtemperatur von Gebäuden ermöglicht wird. Dieser Algorithmus kann jedoch durch einfache Erweiterungen die Möglichkeit für einen kosten-optimierten Betrieb von Wärmepumpen bieten.

Gerade der kostenoptimierte Betrieb kann durch entsprechende externe Preissignale zu einem netzdienlichen Verhalten während Heiz- und Kühlperioden führen.

Der Vergleich von aktiv gesteuerten Wärmepumpen und konventionellen Anlagen zeigt das Potenzial zur Spitzenlastreduzierung und beispielsweise zur Maximierung des Eigenverbrauchs erneuerbarer Energie. Die aktive Regelung einer Wärmepumpe führt zu einer Reduzierung des Energieaustauschs mit dem Stromnetz. Insbesondere die Einspeisung von elektrischer Energie in das Netz kann in einem Bereich von -8 bis -20% reduziert werden (Vanhoudt D. et al. 2014).

Netzdienliches Verhalten kann durch innovative Konfigurationen, bei denen Batterien, thermische Wasserspeicher und Wärmespeicher aus Phasenwechselmaterial mit herkömmlichen Wärmepumpensystemen kombiniert werden, erzielt werden. Ergebnisse zeigen, dass solche integrierten Systeme das Potenzial haben, sowohl den Spitzenstrombedarf als auch den Gesamtenergieverbrauch deutlich zu senken (Kimiaei S, et al., 2023).

Bestehende Lösungen, wie Economic Model Predictive Control (EMPC), bieten die Möglichkeit der Feinabstimmung des Wärme-verbrauchs in Abhängigkeit von den Strom-preisen. Solche EMPC sind in der Lage, den Wärmeverbrauch in Zeiten hoher Strompreise zu minimieren, während er in Zeiten niedriger Preise maximiert wird (Golmohamadi H. et al., 2021).

Komplexere Lösungsansätze, wie z. B. Algorithmen zur Partikelschwarmoptimierung, die den thermischen Komfort und die Nutzung der PV-Energieerzeugung optimieren, sind ebenfalls anwendbar (Alberizzi J. et al., 2022).

Die vorliegende Arbeit fokussiert im Unterschied zu den vorgestellten Konzepten auf den entwickelten Low-Tech Ansatz. Dieser soll sich, auch nach der Erweiterung um eine Kostenoptimierung, von den komplexen Systemlösungen abheben. Neben der einfachen Implementierung soll die netzdienliche Funktionsweise klar einen Mehrwert des MPC darstellen.

Ausgangsbasis: Low-Tech MPC mit Fokus auf Komfort

Die beiden Hauptkomponenten des ursprüng-lichen Algorithmus sind der Gebäudemodell-Algorithmus und die allgemeine Berechnungs- bzw. Optimierungsroutine.

Gebäudemodell

Generell lässt sich zusammenfassen, dass das Gebäudemodell das zentrale Element des prognosebasierten Regelungskonzepts ist. Durch die Verarbeitung von Wettervorhersage-daten ermöglicht der Algorithmus die Berechnung der zukünftigen Raumtemperatur und des nötigen Wärmeeintrags über thermisch aktivierte Bauteile, um Verluste durch die Außenwände zu kompensieren und eine Zieltemperatur zu halten. Der vereinfachte Regelalgorithmus ist darauf ausgelegt, bestehende Gebäude auf eine Zone zu simplifizieren und folgt dem gewählten Low-Tech-Ansatz des MPC.

Das Gebäudemodell arbeitet mit einer vereinfachten Energiebilanz, mit positiven und negativen Energieflüssen. Der gewählte methodische Ansatz berücksichtigt die thermische Speichermasse des Gebäudes, die

thermisch aktivierten Bauteile, die Konvektions- und Lüftungsverluste sowie die solaren Strahlungsgewinne durch Fensterflächen. Das Ergebnis der Gebäudemodellrechnung ist ein prognostiziertes Temperaturprofil für die nächsten 48 Stunden in Abhängigkeit von den vorherrschenden Umgebungsparametern.

Optimierungsroutine

Die zweite Komponente des Algorithmus ist die Optimierungsschleife. Mit dieser Schleife wird die erforderliche Heizleistung berechnet, welche notwendig ist, um die Solltemperatur T_{SP} mit der vorhergesagten Raumtemperatur T_R in Übereinstimmung zu bringen. Als Zielfunktion ist die Minimierung der Fehlerquadratsumme zwischen Raumtemperatur und Solltemperatur definiert, wie in Gleichung 1 (Klepic et al., 2023) dargestellt.

$$Min \sum_{i=0}^{47} (T_{R,i}(\vec{x}) - T_{SP})^2 \quad (1)$$

Die Ermittlung der optimalen Heizleistung erfolgt zyklisch (z.B.: jede volle Stunde) in einer Schleifenfunktion, wobei die notwendigen Daten (Raumtemperatur, Temperatur des thermisch aktivierten Bauteils, Wettervorhersagedaten) geladen werden und die Fehlerquadratsumme zwischen prognostizierter Raumtemperatur und Solltemperatur bezogen auf das Gebäudemodell berechnet wird.

Die notwendige Heizleistung wird iterativ mit positiver, negativer oder keiner Perturbation mit einer vordefinierten Heizleistungsschrittweite (Delta) berechnet. Der Algorithmus wählt den Weg mit der geringsten Summe der Fehlerquadrate, um die Solltemperatur am besten zu erreichen. So nähert er sich schrittweise der idealen Heizleistungsvorgabe an, bis die maximal mögliche Heizleistung erreicht ist. Bei dieser Methode werden alle 48 Stunden der Funktion perturbiert und gespeichert, um als Ausgangswerte für den nächsten Zyklus zu dienen. Der gesamte Zyklus wird mehrmals wiederholt, bis das beste Heizprofil für 48 Stunden erreicht ist und der Unterschied zwischen den Ergebnissen der letzten Zyklen vernachlässigbar ist. Das Ergebnis dieser letzten Optimierungsrunde dient als Heizleistungsvektor für die nächste Stunde, der erforderlich ist, um die festgelegte Zieltemperatur zu erreichen.

Simulationsumgebung

Abbildung 1 zeigt vereinfacht die vorhandene Simulationsumgebung, in der ein Beispiel-Gebäude mit spezifischem thermischen Verhalten und thermisch aktivierten Komponenten in Matlab/Simulink programmiert ist und durch reale Wetterdaten beeinflusst wird.

Ein zusätzlicher Matlab-Code berechnet die solaren Gewinne entsprechend der Wetterdaten. Der entwickelte Low-Tech MPC-Algorithmus, mit entsprechend simplifiziertem Gebäudemodell und Optimierungsroutine, ist in einem separaten Matlab-Code definiert.

Alle angeführten Simulationskomponenten sind in eine Matlab-Umgebung eingebettet, in der alle erforderlichen Eingangsdaten für den gewählten Simulationszeitraum bereitgestellt werden.

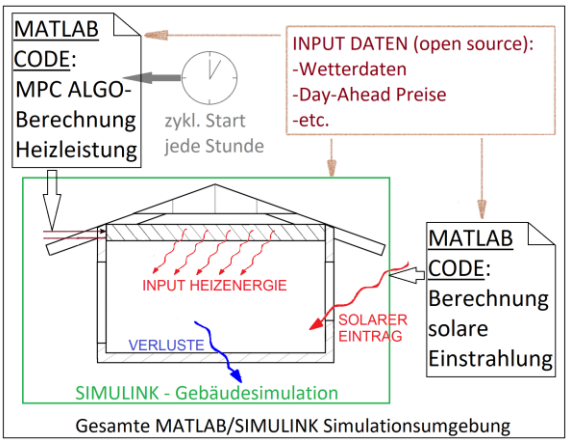

Abbildung 1: MATLAB/Simulink Simulationsumgebung

Im Vergleich zu konventionellen Regelsystemen führt dieser bestehende Low-Tech MPC Ansatz zu einer deutlichen Komfortverbesserung mit geringfügigen Kosteneinsparungen.

Erweiterung der Kostenfunktion

Um dem bestehenden Algorithmus die Berücksichtigung von Strompreisen oder anderen Preissignalen zu ermöglichen, muss die bisherige MPC Modell-Struktur erweitert werden (siehe Abb. 2). Dies führt in weiterer Folge zu einer Erweiterung der Kostenfunktion um prognostizierte, zeitabhängige Energiekosten.

Die ursprüngliche Optimierungsfunktion (Gl. 1) wurde entwickelt, um lediglich die Fehlerquadratsumme zwischen Raumtemperatur und Solltemperatur zu minimieren. Diese Zielfunktion legt den Schwerpunkt auf die Optimierung der Behaglichkeit bzw. der Raumtemperatur. Mit der Erweiterung der Kostenfunktion um die prognostizierten, zeitabhängigen Energiekosten, entsteht eine allgemeine Zielfunktion mit dem Fokus auf Komfort und Kosten.

Da der Schwerpunkt dieser Arbeit auf der Anpassung des Algorithmus für Wärmepumpen-anwendungen liegt, wird in einem ersten Schritt ein Kostenfaktor für diese Technologie eingeführt.

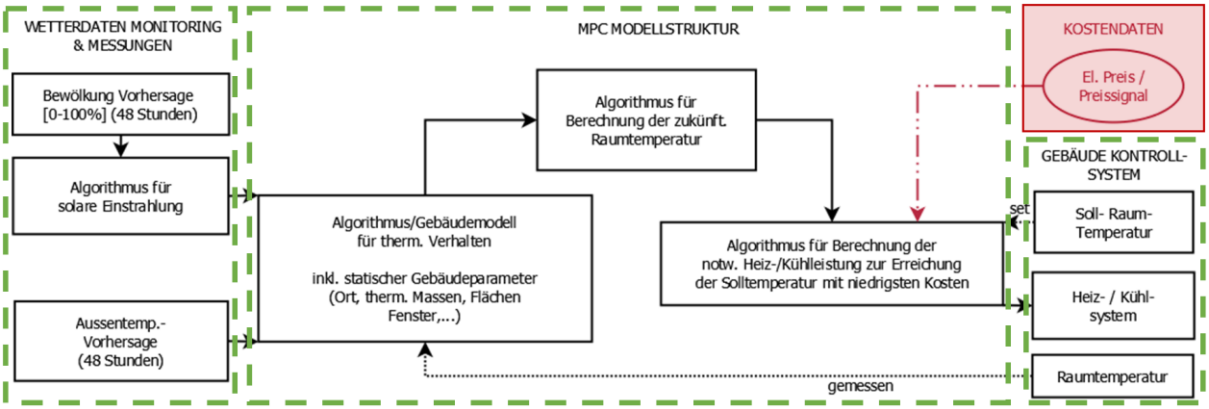

Abbildung 2: Erweiterung der bestehenden Modell-Struktur (Klepic et al., 2023) um Preissignale

Gleichung 2 berechnet die Kosten C_{Heiz} für die Heizleistung für den Zeitschritt i. Grundlage für die Berechnung ist die erforderliche Heizleistung Q_{Heiz} [kW] geteilt durch die Leistungszahl COP einer Wärmepumpe. Dieses Ergebnis wird mit der Zeitdauer Δt und den prognostizierten Stromkosten C_{Strom} [€/kWh] für diesen Zeitraum multipliziert.

$$C_{Heiz,i} = \frac{\dot{Q}_{Heiz,i}}{COP} * \Delta t_i * C_{Strom,i} \quad (2)$$

Im nächsten Schritt wird die bestehende Optimierungsfunktion um die Heizkosten (Gl. 2) erweitert, was zu der neuen Kostenfunktion führt. Darüber hinaus wird diese Gleichung um den Abweichungsfaktor α und die Potenzen β & γ erweitert.

$$f_{Kost,i}(\vec{x}) =$$

$$\begin{cases} \alpha_{pos} * \left|T_{R,i}(\vec{x}) - T_{Soll}\right|^{\beta} + \left|C_{Heiz,i}(\vec{x})\right|^{\gamma} \\ \quad if\ \ T_{R,i}(\vec{x}) > T_{Soll} \\ \alpha_{neg} * \left|T_{R,i}(\vec{x}) - T_{Soll}\right|^{\beta} + \left|C_{Heiz,i}(\vec{x})\right|^{\gamma} \\ \quad if\ \ T_{R,i}(\vec{x}) < T_{Soll} \end{cases} \quad (3)$$

Für den Fall, dass die Raumtemperatur höher oder niedriger als die Solltemperatur ist, können unterschiedliche α-Faktoren definiert werden. Mit entsprechenden Faktoren kann somit der Überhitzung oder Unterkühlung des Raumes mit unterschiedlicher Stärke und Geschwindigkeit entgegengewirkt werden. Die Potenzen β und γ verstärken die Gewichtung der Komfort- bzw. Kostenkomponente in der Gleichung.

Wie in der ursprünglichen Algorithmus-Logik, wird in der Erweiterung die Minimierung der Fehlerquadratsumme als Zielfunktion definiert (siehe Gl. 4).

$$Min \sum_{i=0}^{47} f_{Kost,i}(\vec{x}) \quad (4)$$

Die gesamte Berechnungslogik wird zyklisch wiederholt, bis das Abbruchkriterium, die minimale Änderung der Fehlersummen zwischen dem letzten und dem vorhergehenden Zyklus, erreicht ist (siehe Gl. 5)

$$\left(f_{Kost,47(n)}(\vec{x}) - f_{Kost,47(n-1)}(\vec{x})\right) < 5 * 10^{-6}(€/h) \quad (5)$$

Mit dieser Anpassung der Zielfunktion erhält der Algorithmus neue Mechanismen, die eine komplexere Nutzung der MPC ermöglichen. Zusammengefasst bedeutet dies eine genauere Kontrolle positiver oder negativer Temperaturabweichung und eine einfachere Gewichtung des Komforts im Verhältnis zu den Kosten.

Validierung der neuen Kostenfunktion

Um die Vergleichbarkeit zwischen ursprünglicher und neuer Kostenfunktion zu ermöglichen, wird die Validierung der erweiterten Kostenfunktion bewusst in der Simulationsumgebung des ersten Low-Tech MPC Papers mit den Wetter-Prognosedaten von Dez. 2022 durchgeführt. Dabei werden primär die Auswirkungen der Potenzen β und γ evaluiert.

Die gewählten Parameter für drei Simulationsszenarien sind in Tabelle 1 angeführt. Das Basisszenario beschränkt sich auf die ursprüngliche Kostenfunktion und optimiert somit lediglich den Komfort, während die anderen zwei Szenarien mit der neuen Kostenfunktion unter Berücksichtigung der Strompreise berechnet werden.

Szenarien 2 und 3 analysieren explizit die Gewichtung des Komforts durch unterschiedliche β-Faktoren im Vergleich zur Kostenkomponente.

Tabelle 1: Faktoren und Potenzen für die Validierung der neuen Kostenfunktion

Szenario	α_{pos}	α_{neg}	β	γ
Szenario 1	-	-	4	-
Szenario 2	1	1	4	1.5
Szenario 3	1	1	2	1.5

Um die Validierung so simpel wie möglich zu gestalten, wurde eine fiktive 48h Strompreisprognose hinterlegt. Für Perioden mit einer Sonneneinstrahlung >10 W/m^2 gilt dadurch ein Strompreis von 0 €/kWh, während darunter ein Preis von 0,2 €/kWh angesetzt wird.

Abbildung 3 zeigt in der Farbe blau das fiktive Preissignal und in rot die durch die Kostenfunktion berechnete und simulierte Heizleistung des Matlab-Modells.

Die erste Grafik zeigt das Ergebnis für die ursprüngliche Kostenfunktion mit Fokus auf Komfort. Die Heizleistung tritt primär in den Perioden auf, wo das Preissignal am höchsten ist. Die zweite Grafik zeigt das Ergebnis für die neue Kostenfunktion und erzielt eine gewisse Balance zwischen Komfort und Kosten. Während die dritte Grafik bzw. die dritte Simulation durch die kleinere Potenz β weniger den Komfort und mehr die Gewichtung der Kosten anstrebt.

Entsprechend der implementierten Logik verschiebt sich somit die Heizleistung in jene Perioden mit niedrigeren Energiekosten.

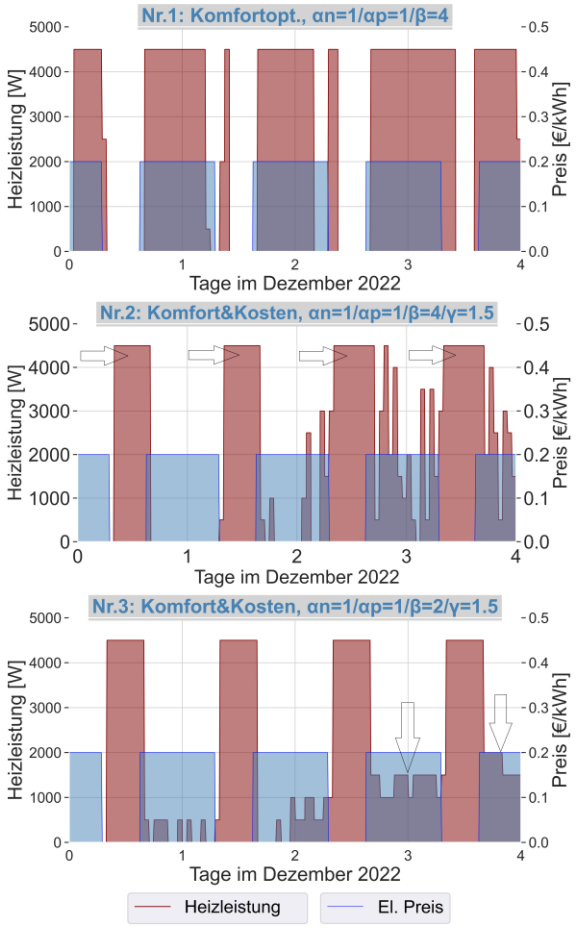

Abbildung 3: Heizleistung für die Kostenfunktion mit versch. Faktoren/Potenzen

Nachdem die Abweichungsfaktoren α_{pos} und α_{neg} in dieser Validierung nicht variiert wurden, wirkt sich die Verschiebung der Heizleistung unmittelbar auf die Raumtemperatur aus.

Während das Baseline-Szenario mit dem klaren Komfortfokus die beste Annäherung an den Temperatursollwert erzielt, wird mit zunehmender Gewichtung der Kostenkomponente der Komfort vernachlässigt, was zu einer größeren Abweichung vom Sollwert führt.

Das Baseline-Szenario hat im Betrachtungszeitraum eine 0,5% Abweichung der gemittelten Raumtemperatur vom Sollwert. Das dritte Szenario, mit starkem Fokus auf Kostenoptimierung, hat eine Temperaturabweichung von 3,7% bzw. 0,8°C absolut.

Simulation mit Day-Ahead Preisen für die Heizperiode Dezember 2023

Anschließend an die Validierung, wurde die Simulation der neuen Kostenfunktion mit gemessenen Wetterdaten und Strompreisen für Dezember 2023 durchgeführt. Dieser Monat ist von großen Temperatur- und Preisunterschieden gekennzeichnet und repräsentiert somit eine dynamische Heizperiode mit unterschiedlichen Anwendungsfällen.

Für die Simulation wurden börslich gehandelte Day-Ahead Preise der Market Coupling Auktion für den Lieferort der österreichischen Regelzone herangezogen. In der Auktion werden alle 24 Einzelstunden für den Folgetag gehandelt und bis 13 Uhr veröffentlicht. Somit ist der Preis-Forecast ab 13 Uhr bekannt und liefert einen maximalen Forecast für 35 Stunden. Die 35 Stunden sind ein Resultat der verbleibenden 11 Stunden zum Zeitpunkt der Veröffentlichung des Auktionsergebnisses, zuzüglich der 24 Stunden für den Folgetag.

Mit dieser Einschränkung muss der bisherige Algorithmus von 48 Stunden Forecast bzw. Simulationsdauer auf 35 Stunden reduziert werden. Eine zweite Herausforderung bei der Day-Ahead Preisgestaltung ist die Tatsache, dass man während einer Simulationsperiode zwar maximal 35 Stunden, jedoch minimal 12 Stunden Preis-Forecast hat. Abbildung 4 verdeutlicht die Preisverfügbarkeit für die Simulation bzw. Kostenfunktion. Um 00 Uhr sind 24 Stunden Forecast vorhanden mit einer elfstündigen Preislücke. Im schlechtesten Fall sind um 12 Uhr lediglich 12 Stunden Forecast bekannt und 23 Stunden unbekannt. Im günstigsten Fall sind 35 Stunden Forecast vorhanden.

Stunden	Uhrzeit 0	1	2	3	4	5	6	7	8	9	10	11	12	13	14	15	16	17	18	19	20	21	22	23
1	x	x	x	x	x	x	x	x	x	x	x	x	x	x	x	x	x	x	x	x	x	x	x	x
2	x	x	x	x	x	x	x	x	x	x	x	x	x	x	x	x	x	x	x	x	x	x	x	x
3	x	x	x	x	x	x	x	x	x	x	x	x	x	x	x	x	x	x	x	x	x	x	x	x
4	x	x	x	x	x	x	x	x	x	x	x	x	x	x	x	x	x	x	x	x	x	x	x	x
5	x	x	x	x	x	x	x	x	x	x	x	x	x	x	x	x	x	x	x	x	x	x	x	x
6	x	x	x	x	x	x	x	x	x	x	x	x	x	x	x	x	x	x	x	x	x	x	x	x
7	x	x	x	x	x	x	x	x	x	x	x	x	x	x	x	x	x	x	x	x	x	x	x	x
8	x	x	x	x	x	x	x	x	x	x	x	x	x	x	x	x	x	x	x	x	x	x	x	x
9	x	x	x	x	x	x	x	x	x	x	x	x	x	x	x	x	x	x	x	x	x	x	x	x
10	x	x	x	x	x	x	x	x	x	x	x	x	x	x	x	x	x	x	x	x	x	x	x	x
11	x	x	x	x	x	x	x	x	x	x	x	x	x	x	x	x	x	x	x	x	x	x	x	x
12	x	x	x	x	x	x	x	x	x	x	x	x	x	x	x	x	x	x	x	x	x	x	x	x
13	x	x	x	x	x	x	x	x	x	x	x	x		x	x	x	x	x	x	x	x	x	x	x
14	x	x	x	x	x	x	x	x	x	x	x			x	x	x	x	x	x	x	x	x	x	x
15	x	x	x	x	x	x	x	x	x	x				x	x	x	x	x	x	x	x	x	x	x
16	x	x	x	x	x	x	x	x	x					x	x	x	x	x	x	x	x	x	x	x
17	x	x	x	x	x	x	x	x						x	x	x	x	x	x	x	x	x	x	x
18	x	x	x	x	x	x	x							x	x	x	x	x	x	x	x	x	x	x
19	x	x	x	x	x	x								x	x	x	x	x	x	x	x	x	x	x
20	x	x	x	x	x									x	x	x	x	x	x	x	x	x	x	x
21	x	x	x	x										x	x	x	x	x	x	x	x	x	x	x
22	x	x	x											x	x	x	x	x	x	x	x	x	x	x
23	x	x												x	x	x	x	x	x	x	x	x	x	x
24	x													x	x	x	x	x	x	x	x	x	x	x
25														x	x	x	x	x	x	x	x	x	x	x
26														x	x	x	x	x	x	x	x	x		
27														x	x	x	x	x	x	x	x			
28														x	x	x	x	x	x	x	x			
29														x	x	x	x	x	x	x				
30														x	x	x	x	x	x					
31														x	x	x	x	x						
32														x	x	x	x							
33														x	x	x								
34														x	x									
35														x										

Abbildung 4: Day-Ahead Preisverfügbarkeit je Stunde

Auswirkung der Day-Ahead Lücke

Im ersten Schritt wurden Möglichkeiten analysiert die Lücke im Forecast zu schließen. Drei Möglichkeiten wurden simuliert und vergleichen:

1) Vortageswert für die gleiche Zeit/Periode übernehmen
2) Letztbekannten Festwert fortschreiben, bis die neuen Werte bekannt sind
3) Lücken mit Null-Werten füllen

Die Analysen haben ergeben, dass die Ergebnisse zwischen übertragenem Vortageswert und fortgeschriebenem letztbekanntem Festwert keine aussagekräftigen Unterschiede aufweisen. Sogar die Lösung, in der die Lücken mit Null gefüllt werden, lieferte akzeptable und ähnliche Ergebnisse, wie die zuvor genannten Varianten.

Dieser Umstand ist auf den stündlichen bzw. zyklischen Start des MPC-Algorithmus zurückzuführen. Durch die stündliche Optimierung werden alle Prognosedaten eingespielt und ein optimales Heizleistungsprofil für 35 Stunden erstellt. Die bekannten Forecast-Preise von 12 Stunden reichen in diesem Fall aus, um das erste Drittel des Heizprofils ausreichend gut zu berechnen und eine komplette Abweichung des MPC zu vermeiden.

Um dem Low-Tech Ansatz weiterhin zu entsprechen, wurde die Lösung des fortgeschriebenen letztbekannten Festwerts gewählt.

Ergebnisanalyse und Diskussion

Abbildung 5 zeigt die Börsenpreise inklusive der durchschnittlichen Netzkosten und Abgaben (e-Control, 2023). Basis für die Simulation sind veröffentlichte Day-Ahead Strompreise für den Monat Dezember 2023 (APG, 2023).

Zusätzlich wurde dieses Preissignal um 20% verstärkt bzw. abgeschwächt, um eine größere Preisschwankung analysieren zu können (rote Linie). Für die Matlab-Simulation wurden die Faktoren und Potenzen aus Tabelle 3 herangezogen.

Tabelle 2: Faktoren und Potenzen für die Simulationsszenarien

Szenario	α_{pos}	α_{neg}	β	γ
Nr.1: Kostenfunk. für Komfort	-	-	2	-
Nr.2: Neue Kostenfunk. (Day-Ahead)	1	5	4	1.3
Nr.3: Neue Kostenfunk. (Day-Ahead +/-20%)	1	5	4	1.3

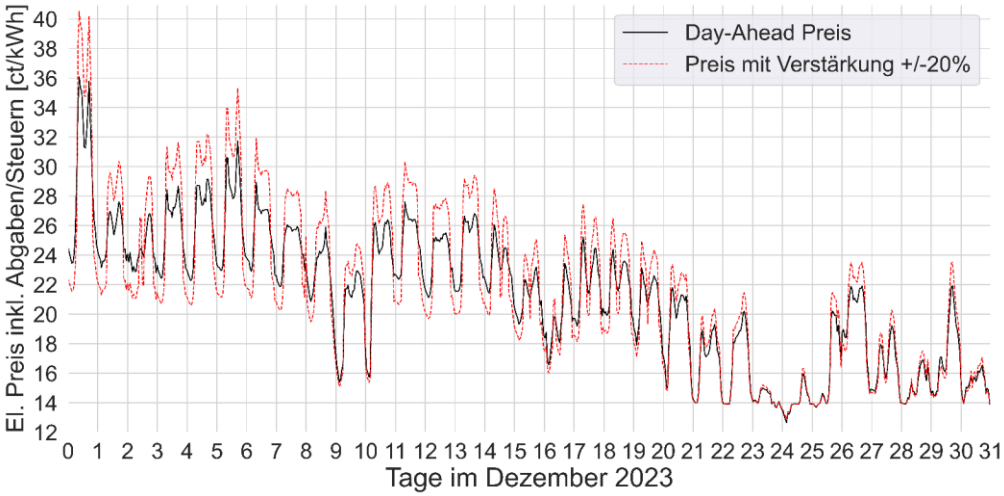

Abbildung 5: Day-Ahead Preise für Dezember 2023 (inkl. Verstärkung +/- 20%)

Im simulierten Betrachtungszeitraum Dezember 2023 sind Außentemperaturen zwischen -8°C und +15°C aufgetreten. Zudem hat es in diesem Monat mehrere Tage mit unterschiedlicher solarer Einstrahlung gegeben (20 – 400 W/m^2). Diese Wetterschwankungen sind aus dem Day-Ahead Preisverlauf ebenfalls ableitbar. Beispielsweise sind die tiefsten Strompreise zwischen 23.12. und 25.12.2023 aufgetreten, wo die wärmsten Außentemperaturen aufgetreten sind und gute Einstrahlungswerte erfasst wurden. Zu Beginn des betrachteten Monats waren die tiefsten Temperaturen und somit die höchsten Strompreise.

Abbildung 6 zeigt eine detaillierte Wochenansicht der simulierten Raumtemperaturen der drei Szenarien mit dem angestrebten Sollwert von 22°C. Die erste Simulation mit dem MPC-Algorithmus zeigt die Ergebnisse für die ursprüngliche Kostenfunktion mit Fokus auf Komfort (graue Linie). Die durchschnittliche simulierte Raumtemperatur über den Analyse-zeitraum beträgt 22,14°C.

Die zweite und dritte Simulation wurden mit der neuen Kostenfunktion durchgeführt. Der einzige Unterschied betrifft die Schwankungsbreite der Day-Ahead-Preise. Während die Simulation mit realen Strompreisen zu einer durchschnittlichen Raumtemperatur von 21,74°C führt, wirken sich größere Schwankungen des Preises stärker auf die Komforttemperatur aus.

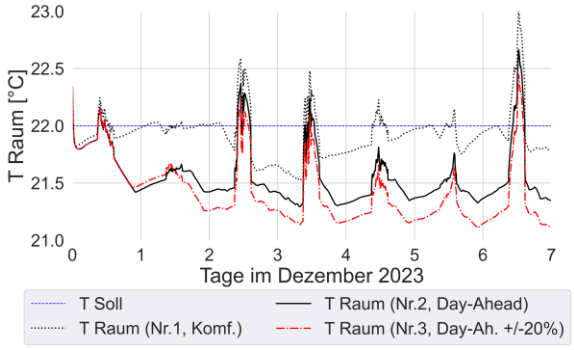

Abbildung 6: Exemplarische Wochenansicht der simul. Raumtemperatur für Preisszenarien

Dieser Temperatureffekt ist auf die Gewichtung der Kostenkomponente in der Kostenfunktion zurückzuführen. Bei größerer Schwankung der Strompreise versucht der MPC die Perioden mit niedrigerem Preis zu favorisieren. Dieser Umstand wird in Abbildung 7 deutlich.

Gerade bei höherer Preisschwankung ist der MPC in der Lage die durchschnittliche Raumtemperatur minimal zu reduzieren, die Energiekosten jedoch deutlicher zu reduzieren.

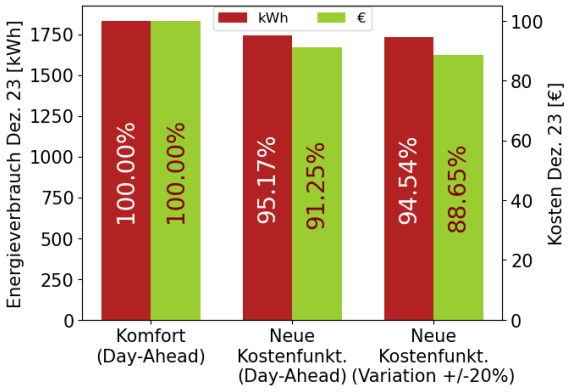

Abbildung 7: Energieverbrauch und Kosten für die gesamte Monatssimulation Dez. 2023

Im Vergleich zur reinen Komfortoptimierung beträgt die Kostenreduktion für die neue Kostenfunktion mit realen Day-Ahead Preisen 8,75%. Die Simulation mit einer +/- 20%-Schwankung des Preises führt sogar zu einer Kostenreduktion von 11,35%.

Zusammenfassung

Die Analyse der erweiterten Kostenfunktion zeigt, dass durch diese simple Erweiterung der Low-Tech MPC gewahrt bleibt, jedoch die Möglichkeit der Preissignalverarbeitung geschaffen wird. Letztendlich kann somit mit kleinen Abweichungen vom Temperatur- Sollwert bzw. Komfort eine signifikante Kosteneinsparung ermöglicht werden.

Betrachtet man die zukünftige Strommarkt-Entwicklung, ist davon auszugehen, dass die vermehrte Einspeisung von erneuerbaren Energien zu höheren Schwankungen des Strompreises führen wird. Perioden mit ausreichend Einspeisung und einem Überangebot an Energie im Netz werden niedrigere Strompreise zur Folge haben, während Perioden mit wenig regenerativer Stromerzeugung tendenziell teurer werden.

Durch diesen Umstand gewinnt der entwickelte Low-Tech MPC an Bedeutung, da durch geeignete Preissignale ein netzdienlicher Betrieb von Heiz- und Kühlsystem forciert werden kann. Zudem ist der Algorithmus in seiner Logik simpel ausgeführt und relativ einfach in Gebäuden einsetzbar. Die Implementierung des ursprünglichen MPC ist bereits in mehreren Gebäuden durchgeführt und positiv bewertet worden.

Limitiert ist der gewählte Low-Tech Ansatz bei der Betrachtung von Multi-Zonen-Objekten. In solchen Fällen muss für jede Zone ein individueller MPC-Algorithmus implementiert werden. Zudem vernachlässigt der gewählte Ansatz mögliche Einflüsse durch Personen (z.B.:

Lüften, Kochen, usw.). Abschließend ist die Abhängigkeit von akkuraten und zuverlässigen Wetterprognosedaten zu nennen. Schlechte Prognosedaten wirken sich unmittelbar auf das Ergebnis des MPC aus.

Ausblick

Detaillierte und umfangreiche Analysen der erweiterten Kostenfunktion, inklusive der Validierung aller neuen Faktoren, werden in wissenschaftlichen Journalen präsentiert.

Zudem soll weitere Forschung rund um die zusätzliche Erweiterung der Kostenfunktion betrieben werden. Beispielsweise könnte ein weiterer Erweiterungsschritt des MPC Algorithmus die Einbindung und Berücksichtigung von lokal produzierender Photovoltaik umfassen. Damit könnte abhängig vom Strommarkt und Wetterdaten der ideale Zeitpunkt für den Eigenverbrauch von Strom ermittelt werden.

Literatur

Alberizzi at al., 'Optimal Day-ahead Scheduling of Heat Pump Heating Systems Partially Fed by Renewable Generation', IEEE 11th Conference on Power Science and Engineering, 2022.

APG Austrian Power Grid, Day-Ahead Preise, https://markttransparenz.apg.at/de/markt/Markttransparenz/Uebertragung/EXAA-Spotmarkt, Zugriff am 07.02.2024

E-Control, Marktstatistik zu Strompreisentwicklung, https://www.e-control.at/statistik/e-statistik/archiv/marktstatistik/preisentwicklungen, Zugriff am 07.02.2024

Golmohamadi et al., 'Optimization of power-to-heat flexibility for residential buildings in response to day-ahead electricity price', Energy & Buildings, v. 232, p. 110665, 2021.

Keiner et al., 'Global-Local Heat Demand Development for the Energy Transition Time Frame Up to 2050', Energies, vol. 14, no. 13, p. 3814, 2021.

Killian M. & Kozek M., 'Ten questions concerning model predictive control for energy efficient buildings', Building and Environment, vol. 105, pp. 403–412, 2016.

Kimiaei et al., 'Grid-friendly ground source heat pump configurations to reduce the peak power demand of conventional electric-based heating systems', Energy & Buildings, vol. 290, p. 113084, 2023.

Klepic et al., 'Development of a low-tech MPC-algorithm for versatile applications in buildings with thermal activated components', Energy & Buildings, vol. 301, p. 113674, 2023.

Schuß M., Doctoral dissertation – 'Implementation of a predictive simulation-based controller for environmental systems in buildings', TU Wien, 2011.

Stoffel et al., 'Evaluation of advanced control strategies for building energy systems', Energy & Buildings, v. 280, p. 112709, 2023.

Serale et al., 'Model Predictive Control (MPC) for Enhancing Building and HVAC System Energy Efficiency: Problem Formulation, Applications and Opportunities', Energies, vol. 11, no. 3, p. 631, 2018.

Thygesen R. & Karlsson B., 'Simulation of a proposed novel weather forecast control for ground source heat pumps as a mean to evaluate the feasibility of forecast controls' influence on the photovoltaic electricity self-consumption', Applied Energy, vol. 164, p. 579-589, 2016.

Vanhoudt et al., 'An actively controlled residential heat pump: Potential on peak shaving and maximization of self-consumption of renewable energy', Renewable Energy, v. 63, p. 531-543, 2014.

BauSIM 2024 in Wien
23. September – 26. September

Performative Evidence of Smart and Urban Trees - Assessing the thermal and visual impact of large scale urban shading structures via simulation

Ulrich Pont[1], Magdalena Wölzl[1], Vera Stiegler[2], Rupert Wolffhardt[2], Peter Schober[2], Sigrun Swoboda[1], Peter Bauer[1]

1 TU Wien, Inst. of. Architectural Sciences, Austria, E-Mail: {ulrich.pont|magdalena.woelzl|sigrun.swoboda|peter.bauer}@tuwien.ac.at

2 Holzforschung Austria, Wien, Österreich, E-Mail: v.stiegler@holzforschung.at, r.wolffhard@holzforschung.at, peter.schober@outlook.at

Abstract

This contribution presents specific results from a project pertaining to large scale urban shading structures. These structures were named as "smart and urban trees". Thereby, we understand artificial structures that should be implemented in urban agglomerations at places and locations, where no other green-blue infrastructures can be deployed. As such Smart and Urban Trees do not pose a competition for real trees, but a supplement whenever real trees cannot be integrated in the cityscape (e.g., due to underground installations or means of transport). Whereas the project per se did address a large number of aspects of such Smart and Urban Trees (e.g., aesthetics, construction, organizational aspects, end-user acceptance, etc.), this contribution reports on the impact of such Smart and Urban Trees on thermal (physiological equivalent temperature, indoor temperatures in adjacent buildings) and visual surroundings (impact on daylight availability in the surrounding buildings), both in the public space and in the surrounding buildings. Toward this end, a case study district / neighborhood was chosen as virtual test bed for different Smart and Urban Tree designs. It could be proven that the envisioned structures can significantly contribute to mitigation of overheating phenomena, also in comparison to real, living trees.

Introduction

Cities worldwide increasingly experience the so-called Urban Heat Island effect. This phenomenon, which is interlinked with the Climate Change, has been matter to observation and scientific research for already a long time (e.g. Landsberg 1981), and is widely, prominently and intensively published since about 20 years (amongst others: Crutzen 2004, Alcoforado and Andrade 2008, Roth 2013). Roth (2013, P143) defines it as "*a phenomenon whereby urban regions experience warmer temperatures than their rural, undeveloped surroundings. The UHI is the most obvious atmospheric modification attributable to urbanization,8 the most studied of climate effects of cities and an iconic phenomenon of urban climate*". In the City of Vienna, Austria, the issue of Summer Overheating has been considered a serious issue for some years now. In 2018 the Vienna Environmental Protection Department published an Urban Heat Island Strategy Plan for the City of Vienna (MA22 2018), which suggests several strategic actions for climate-sensitive urban planning, such as protecting urban air flow and open space networks, adaptation of the urban structure and development, increasing surface permeability and adapting building styles, protecting and expansion of green and open spaces, and conservation and expansion of the stock of (street) trees. In other words, this strategy plan identifies green-blue infrastructure as key element into cooling the city in summer times. In 2019, the Urban Heat Vulnerability Map of Vienna, Austria was published (Hitzekarte 2019), which identified the densely populated central districts allocated from Northwest to Southwest around the Vienna Ringstraße as well as the city center as being most vulnerable regarding summer overheating. These districts are characterized by a comparably old building stock, very little public greenery, and little possibility to add regular green-blue infrastructure. In the street canyons of these regions there is a high degree of competition for public space usage, and we find a dense net of subsoil-installations, pipes, and even metro stations and metro lines. Therefore, trees are often not really an option in such situations. Fig. 1 shows the requirement of substrate space for differently sized trees as well as a section through a typical street in densely populated areas. Needless to say, wherever possible trees are by far the first choice in climate change and Urban Heat Island Mitigation, given their functions such

as cooling in summertime by providing shadow and evaporative cooling, dust binding, CO2-binding, noise dampening, O2-generation, positive impacting onto the human psyche, and many more. Moreover, most trees are perfectly adapted to the seasonal needs of people in the city: During summertime there is a lot of shading and cooling effect, in Wintertime there is only very little obstacle to the desired sunlight due to the seasonal drop of leaves. The well renowned climatologist Hans-Joachim Schellnhuber just recently suggested that planting and growing of 100 billion trees might allow to mitigate the climate change and help in restauration of the climatic balance (DerStandard 2023) However, there might be parts in the historic urban city centers and core districts where the planting of (reasonably sized trees) cannot be realized in a feasible way.

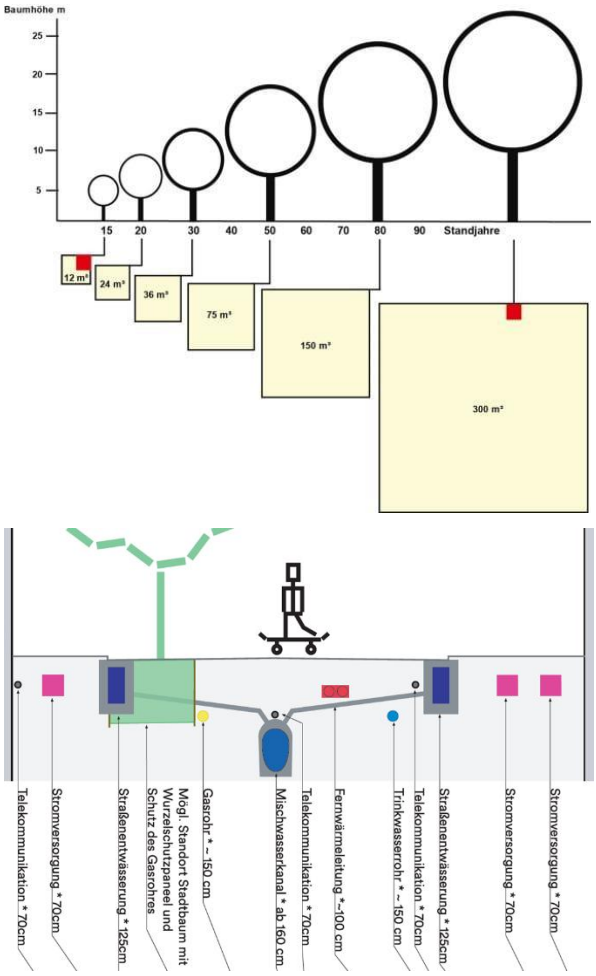

Fig 1: Typical substrate space needs of trees dependent on their height and lifeage (Top; Futurezone 2021); Typical pipes and lines below the street surface (Bottom; kommraus 2019)

Toward this end, the present contribution illustrates approach, effort, and results of a recently conducted R&D-project named Smart and Urban Tree. In this project, artificial structures have been envisioned, designed, and multiperspectivally evaluated as an alternative for urban situations not suitable for classical blue-green infrastructures.

Case Study Site & Trees versus Smart and Urban Trees?

As already reckoned, we **do not** understand our suggestion of Smart and Urban Trees as a general alternative to other means of green-blue infrastructure, but rather as a supplementary alternative for difficult or impossible urban situations. While trees require certain substrate volume, as well as water bodies require tight surfaces, the Smart and Urban Tree idea is to bridge the lack of availability of either by technical means, e.g. in form of an situation-adapted foundation of the artificial structure foreseen for shading. To fundamentally proof the concept, a street canyon of the 7th district in Vienna has been chosen. This case study location is in the most vulnerable parts for heat stress in the city. Furthermore, a surface reconstruction has to be planned and executed soon, as a new metro line is currently constructed and major parts of tunnels and station outlines will be positioned below the case study location (Kirchengasse, 7th district of Vienna). Fig. 2 illustrates the case study situation prior to the metro building site. Fig. 3 shows a map of the demonstration site. In a very first attempt to compare – in detail for the demonstration site – the performance of natural trees, artificial structures, and no measures at all, we generated a comparison based on subjective experiences, illustrating advantages (+), disadvantages (-) and potential ambiguous impacts and aspects (+/-), see Fig. 4. While the “no intervention at all” variant does not really feature a lot of positive effects, it can be clearly seen that trees have advantages as well as Smart and Urban Trees have, however, in different aspects. Vice versa, there are negative aspects in both intervention concepts that are required to be considered prior to any planning and intervention.

Fig.2: View of Kirchengasse, 1070 Vienna, prior to the metro construction works (im7ten 2022)

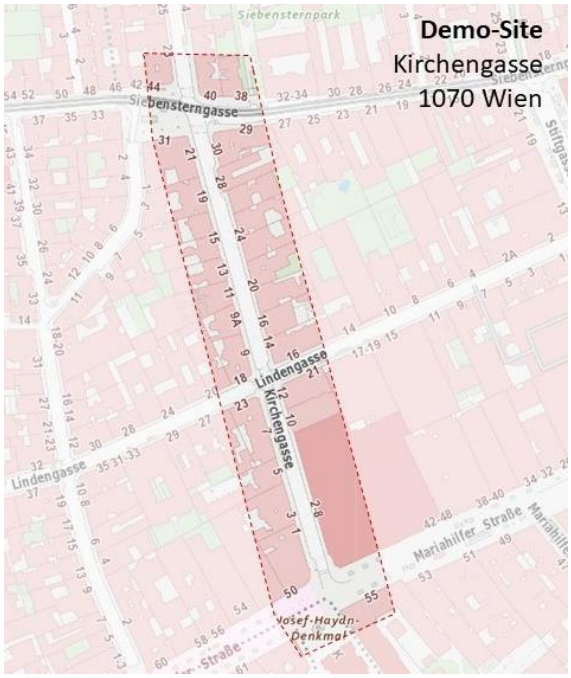

Fig 3: Map of the Case study site (ViennaGIS 2022, adapted by the authors)

Comparable structures and efforts

There is a number of comparable projects that address artificial shading or tree structures for cities. The famous *Metropol Parasol* in Sevilla, Spain (Fig. 5a) acts as an urban identifier on a large public space and provides some urban shading. The Supertree Grove (Fig. 5b) in Singapore does provide some small-scale urban shading, but also acts as landmark and touristic highlight. The University of Natural Resources and Life Sciences in Vienna proposed mobile "Climate Islands" that should increase the urban microclimate in selected squares of the city (Fig. 5c). In some German cities, urban furniture was equipped with moss plants and other greenery to provide some dust-binding and air cleaning as well as some microclimatic effects for people passing by or waiting for the public transport (Fig. 5d). In a previous attempt to provide some improvement for the microclimatic situation in courtyards, the authors conducted a design studio with graduate students adressing green artificial structures (Fig. 6a), which can be compared to the shared garden tower in the second district of Vienna (Zirkusgasse 40/42, Fig. 6b)

Fig. 5.5aMetropol Parasol (top left, Mayer 2024), 5b. Supertree Grove (top right, Supertree 2024), 5c. Climate islands (bottom left, Climate Islands 2023), 5d. moss filter furniture (bottom right, Baunetzwissen n.d.)

Aspect	Natural Tree	Smart & Urban Tree	No inter-vention
Greenary (Integration of greenery)	+	+/-	-
Shadow casting	+	+	-
Seasonal shading	+	+/-	-
cooling effect by shading and evaporation/mist	+	+	-
(Day)Light / (Day)Light control	+/-	+	-
Inhibition of free air movement	-	-	+
„Rain protection" / roofing effect	+/-	+/-	-
Additional functions can be integrated (light, spray, E-charge, ...)	-	+	-
Active electricity/Energy production (PV)	-	+	-
(Neigbor/Occupant)Acceptance	+	?	
Improvement of the street space	+	+	-
Seasonal use/usages of the street space	+/-	+	+
Implementation is simple and proven	+	-	n.a.
Can be implemented quickly and immediate	-	+	n.a.
Root space / foundation freely configurable	-	+	n.a.
Water not required for "maintenance"	-	+/-	n.a.
Costs (construction and maintenance)	+/-	-	n.a.
Care / maintenance	+/-	+/-	n.a.
Pollution of the soil	+/-	+/-	n.a.
Pollution of the construction (e.g. birds)	+	-	n.a.
Not-affected / affected building regulations	+	-	n.a.
Fire brigade access	+/-	+/-	+
Parking lot displacement	+/-	+/-	+
Unsealing	+	+	-
CO_2 binding with a metal construction SUT	+	-	-
CO_2 binding with a wooden construction SUT	+	+/-	-
O2 generation	+	-	-
Noise cancellaton	+	+	-
Dust binding	+	+	-
"Residue-free" / simple dismantling	+	+/-	
Impact on cultural heritage	+	+/-	+

Fig. 4: Comparison of Aspects/Interventions: trees, Smart & Urban Trees and no intervention at all (authors)

Fig. 6.6a Design Studio result for a courtyard tower garden (left, Fig. by the authors); 6b. existing courtyard tower garden in 2nd district of Vienna (right 2pos 2024

Many recent and past studies address the impact of urban shades for exterior spaces and adjacent buildings: Tola et al. (2023) assessed the impact of natural and artificial shades along Mediterranean coast promenades and found that without shading these spaces can be considered as “dead” during day. Razzaghmanesh et al. (2021) proofed that urban tree canopies provide significant temperature drops in densely populated urban areas. El-Sokaily (2022) could proof that large-scale shading design is an effective mean for reducing unhealthy values in the most commonly used thermal indices such as mean radiant temperature MRT, Universal Temperature Climate Index UTCI and Physiological Equivalent Temperature PET. Needless to say, there are many other publications in-depthly describing aspects of material and dimensions of shading devices, as well as impact of green-blue infrastructure, but a literature review is neither goal nor possible in this presentation. Rather, our own approach and case study is shown.

Design & Evaluation Methodology

We deployed a multi-perspective working mode to be able to fundamentally assess all aspects of the envisioned Smart and Urban Trees. Fig. 7 illustrates the principal project workflow. While the work packages addressing requirement basis (what is expected by such Smart and Urban Tree structures) and fundamentals of execution (how to generally construct/design such structures) can be considered as empirical work, the work packages pertaining to construction, functions, and modelling and simulation have been considered as “proof work” of concepts that iteratively interact and optimize outcomes. During the project it became clear that – given the exploratory structure of the project – many workflows would have to be conducted parallelly. Thus, Fig. 8 illustrates the reality of the project by far better than the original workplan.

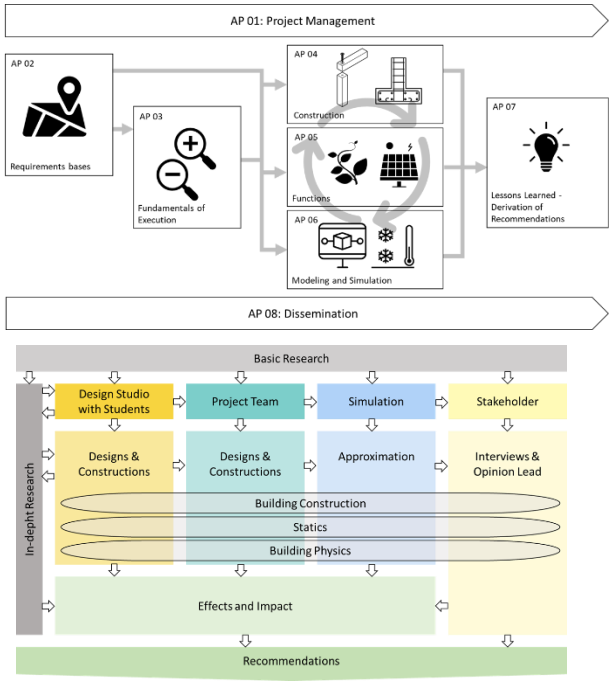

Figure 7 (top). Envisioned Workflow of the Project Smart and Urban Tree (Figure by the authors); Figure 8. Real workflow matrix as designed during the project (Figure by the authors)

While the fundamental research can be considered to have acted as basis for all other working steps, we in parallel deepened and widened the fundamental research throughout the whole project duration. That had to do with the fact that for each component, e.g. the envisioned functionalities of the smart and urban tree (power generation via PV, power fuel station for E-Bikes, social hub, artificial light carrying structure, water misting devices, …) as well as for constructions, and organizational aspects (e.g. involved governmental bodies for a realization in the public street areas) a whole rat tail of standards, laws, application guidelines, etc. had to be studied and adapted for purposes of the envisioned structure. Based on the basic research, we conducted a graduate students design studio for designing and testing Smart and Urban (SUT) tree variants, we ourselves designed some SUT-variants, we discussed simulation domains that later should be utilized for evaluation of the finalized designs, and we started to conduct qualitative interviews with interested and/or involved stakeholders. These stakeholders included the Viennese building authorities, the different magistrate bodies dealing with city illumination, public transport, street surfaces, parking lot distribution, fire safety, and heritage protection, dwellers of surrounding buildings, owners of adjacent shops, scientists from different departments such as sociology, traffic planning, urban space use and utilization, law, and public finance/economics, as

well as the local ICOMOS officials. For these interviews a guideline was designed in the early stages of the project. Regarding the simulation efforts, we primarily decided to look at the impact on the street level in view of thermal impact, and the effect our artificial structures would have onto adjacent buildings in view of temperature drops and impact on natural lighting inside of the buildings (not discussed in this paper). Given the extensive structure of the demo site and the multitude of impacting factors, it was clear that simulation efforts in these domains had to be started by strongly simplified models to reach any results. This, however, can be considered as a weak spot of the study, but given the multi-perspective approach, we were happy to reach some general statements about the performance of the proposed Smart and Urban Tree structures. In this contribution we will focus on the thermal performance domain. Toward this end, the operative (indoor) temperatures of different variants have been derived via Designbuilder (Designbuilder 2022), while the PET (physiological equivalent temperature) was chosen as indicator for the outdoor / street level evaluations. Thereby, the tool envimet (Envimet 2022) was deployed. For the Designbuilder simulations, we chose a timestep of 15 minutes. Shading elements were modeled based on single-surface library elements, utilizing standard surface qualities regarding reflectance and transmission. The building envelope properties were assumed to correspond to the most common building typology (which were 19th century Gründerzeit-buildings, featuring casement windows (U_{Win} = 2.7 W.m^{-2},K^{-1}, Total solar transmission / SHGC = 0.74, direct solar transmission = 0.67, light transmission = 0,801) and plastered brick-walls (U = 1.05 W.m^{-2}.K^{-1})

Results

Overview about designed SUTs

During the design studio 10 different designs for smart and urban trees had been generated. While all these designs feature certain strengths and weaknesses, two categories could be clearly distinguished: (i) Solitary & hybrid constructions consist of individual, self-bearing structures that would allow positioning in different suitable spots in streets. They might be combined with each other but work also as solitaire structures. Fig. 9 showcases some of these designs. (ii) Composite structures react on the linearity of the demonstration site street and work with fewer supporting columns, as they have a “body” that is situated above the streetlevel which is supported by a small number of supporting structures. Such structures require an in-depth planning process and need to consider different aspects, such as the possibility for fire brigades to use ladders onto adjacent building facades. Fi. 10 illustrates some of the composite structure designs derived from the design studio.

Setup and results of simulation-based impact assessment

As already indicated, we did simplify the SUT designs for the purposes of performance simulation. To assess the indoor conditions in adjacent buildings we used a generic floor plan that closely resembles typical *Gründerzeit* Floor Plans and put this floor plan once on a 1st floor height (about 4 m above the ground) and a 4th floor height (about 15 m above ground) in different positions in the road. Fig. 11 illustrates this set-up exemplarily. Additionally, the shading effect by the smart and urban trees was also approximated. Instead of a detailed model of each of the architectural designs, the effective shading area was calculated and added to the model to ensure reasonable calculation times. Variants of the calculation included different settings for HVAC in the building (unconditioned/passive vs. conditioned), different climate data sets (2022, 2050 – RCP 8.5), shading element material (void/no material, wooden elements, PV-elements), the seasonality (all year versus cooling period) and the height of the applied shading above ground (8m above ground, 18 m above ground). Fig. 12 highlights the setup of the simulation model for an 18m high model including sunposition and shades of 15th April, 03:00 pm.

Figure 9. Examples for solitary and hybrid structures (Figure by the authors)

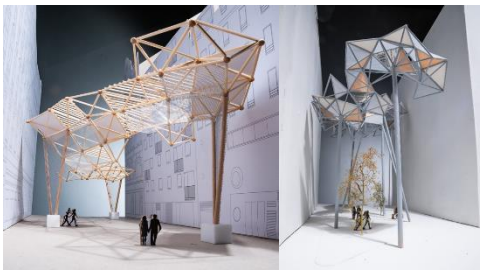

Figure 10. Examples for composite structures (Figure by the authors)

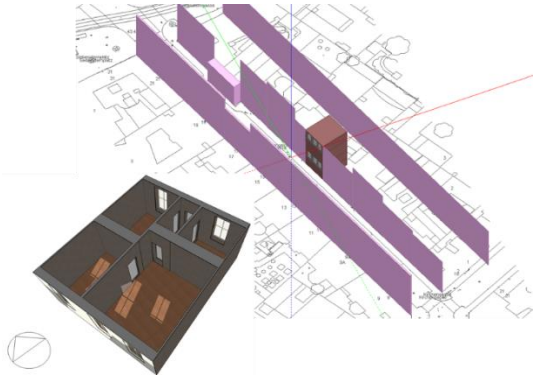

Figure 11. Exemplary setup for indoor temperature assessment via simulation (generic floorplan) (Illustration: The Authors)

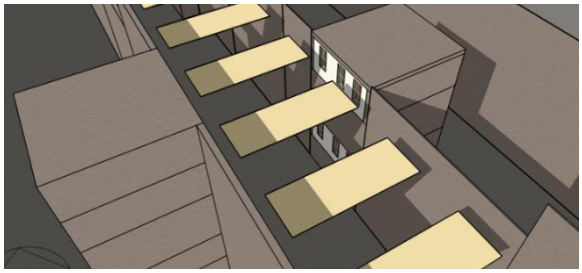

Fig. 12. Simulation model for indoor thermal conditions (18m high shading elements, 15th April 03:00 pm; Illustration: The Authors)

To provide an insight into the derived results for indoor thermal conditions, we compare the operative temperature for one of the rooms of the floor plan (living room) in the 1st floor and in the 4th floor, with a limited set of variables (Fig. 13). What can be seen is that SUTs obviously in the analysed case only make sense in 18m height, as the impact of the lower variant (8m) is neglectable (1st floor) or unfavourable (4th floor due to reflection effects). Fig. 14 does show resulting temperature differences for the living room and a children's room for different orientation of the main façade (west/east – resembling the north-south orientation of the street) for the 18m application for both climate data sets. For the street temperatures, different scenarios for different positions within a large grid (about 900.000 grid points, 2x2 m grid) were evaluated. The scenarios included no intervention, classical (few) trees setups and small-scale greenery, 8m or 18m high wooden elements, and 8m or 18m high PV elements (Fig. 15.). Exemplarily, the results for the PET for an assumed hot summer day (10.07.) should be shown for position D in the Case study road (Figure 16). Assumptions/Settings include that PET is derived on 1.8m above ground, 2m/s wind from southeast is blowing, and that the summer day is free of clouds. What can be seen is that the no intervention scenario performs worst, while the cooling effect is larger at 18 m element height (PV slightly better than wooden elements). During the day the classical tree setup, due to the adjacency to the next tree, performs best. However, what should not be forgotten is that the tree model includes evaporative cooling, while the SUTs just shade.

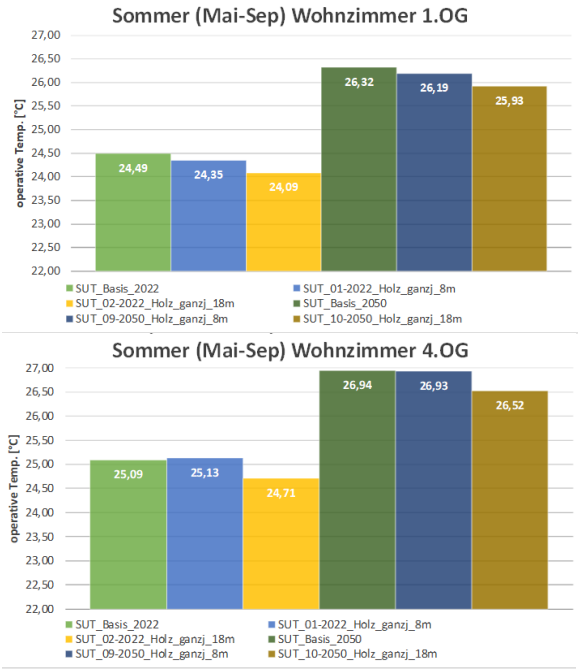

Fig. 13. Results for the application case as illustrated in Fig. 11 and 12; Top: 1st Floor, bottom: 4th floor; SUT_BASIS_2022/2050 – operative temperature (ot) without shading, climate data of 2022/50; SUT_xx_2022/205_Holz_ganzj_8m/18m – ot with wooden shading on 8/18 for climate data of 2022/2050 (illustration by the authors).

Stakeholder interviews

The interview partners in general had a benevolent attitude toward the idea and in part called it "a good idea". Moreover, the feasibility from perspective of technological realization was confirmed. However, especially the district governing politicians were not convinced about the suggested case study location and instead suggested roads with tram lines that literally make any tree plantation impossible but would allow for technically advanced SUTs. Some of the stakeholders emphasized that a participatory process and holistic planning in case of realization is of crucial importance. Especially the shop owners identified the importance of an unique, iconic appearance of SUT structures for purposes of branding/identification with a location, but in general considered the idea as very good as customers want shaded, cool spaces in front of their shops during summertime. Generally speaking, most stakeholders were convinced that legal adaptations to building regulations (e.g. to utilize adjacent facades for mounting / structural purposes) might not be

allowed yet, but are just a matter of adaptation and “suffering pressure” in view of increased climate change impact.

Temperaturdifferenz Sommer (1.Mai- 15.Sep)					
Ausrichtung	Klimadaten	Geschoß	Zimmer	Mittelwert	Maximum
West	2022	1.Obergeschoß	Wohnzimmer	0,41	1,48
			Kinderzimmer	0,4	1,23
		4.Obergeschoß	Wohnzimmer	0,36	1,13
			Kinderzimmer	0,51	1,67
	2050	1.Obergeschoß	Wohnzimmer	0,41	1,46
			Kinderzimmer	0,4	1,06
		4.Obergeschoß	Wohnzimmer	0,42	1,73
			Kinderzimmer	0,6	2,01
Ost	2022	1.Obergeschoß	Wohnzimmer	0,3	0,94
			Kinderzimmer	0,44	1,29
		4.Obergeschoß	Wohnzimmer	0,53	1,62
			Kinderzimmer	0,57	1,7
	2050	1.Obergeschoß	Wohnzimmer	0,29	0,91
			Kinderzimmer	0,46	1,33
		4.Obergeschoß	Wohnzimmer	0,57	1,91
			Kinderzimmer	0,62	1,87

Figure 14. Temperature differences achievable for east and west oriented rooms in different climate sets on different floors with an 18m SUT shading applied. (Illustration by the authors)

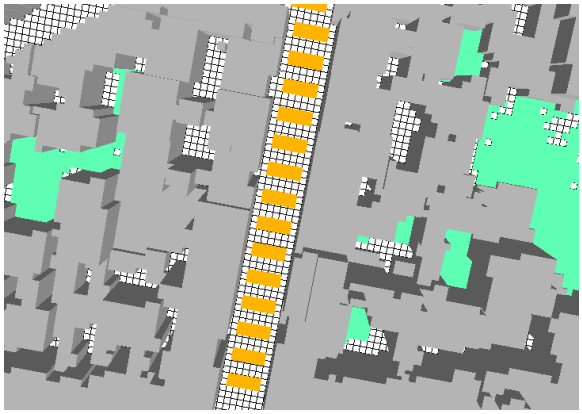

Figure 15. Envi-Met Modell of the case study area with applied shading elements, 34%/784m² roof coverage (illustration by the authors)

Conclusion

The present contribution highlighted the R&D efforts pertaining to the generation of artificial structures for urban summer shading and cooling. Thereby, we once again want to emphasize that the study does not suggest replacing natural greenery by our SUTs, but rather consider SUTs as an alternative for locations where there is no possibility for other green-blue infrastructure. In such locations, a SUT could even house (small-scale) plants to at least try to mimicry some of the tree effects. However, the study in general showed that SUTs can have a positive impact on the urban microclimate on street levels and in adjacent buildings. Needless to say, this was just an exploratory study with several shortcomings and large potentials for more in-depth studies. Politicians we talked to, all agreed that full-scale mock-ups based on the designs developed by students and project team would facilitate the assessment of the impact, not only on the urban climate, but also pertaining to acceptance of adjacent dwellers and shop owners. As such, we believe that the next step is to set up a project to realize such a Smart and Urban Tree at a critical spot in the city (not necessarily in the demonstration area that was used in this study, but rather at large scale places, or complex situations, e.g. street with tram lines). Moreover, as SUTs currently were examined on their shading impact, but not on additional technical implementation of water vaporization as mean of cooling, this should be integrated as topic in future studies.

Acknowledgement

The R&D efforts described in this project had been generously funded by the Austrian Research Promotion Agency FFG (City of the Future-Program, Proj.No.: 886959).

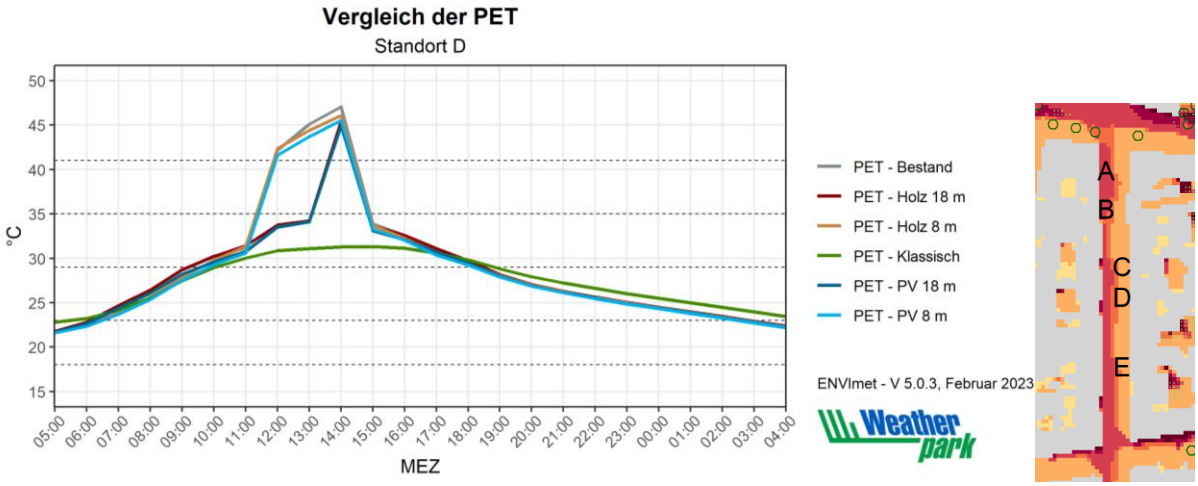

Figure 16. PET-Performance time row on standpoint D (hot summer day) (illustration by the authors)

References

2pos. 2024: Image of a tower garden in Vienna's snd district. Available via: https://lh3.googleusercontent.com/p/AF1QipP4PyM22opFqXP4b04-_hLtoC9s3p5rVfhS5oU=w600-k (accessed Feb 2024)

Alcoforado, M.-J., Andrade, H. 2008. Global Warming and the Urban Heat Island. In Urban Ecology – An International Perspective on the Interaction Between Humans and Nature (ed.: J.M. Marzluff, E. Shulenberger, W. Endlicher, M. Alberti, G. Bradley, C. Ryan, U. Simon, C. ZumBrunnen), Springer, P249-262

Baunetzwissen, n.d. Moosfiler als Stadtmöbel uind Fassadenelement – Feinstaubabsoprtion und Luftkühlung. Available via: https://www.baunetzwissen.de/stadt--und-dachbegruenung/tipps/news-produkte/moosfilter-als-stadtmoebel-und-fassadenelement-8226032 (Accessed Feb 2024)

Climate Islands. 2023. Image from https://oekastatic.orf.at/mims/2023/30/12/crops/w=1280,q=70,r=1/1875485_bigpicture_702712_kli2.jpg?s=cb6d1aa33c81861a9f6d19ad4f948ab4ff32d9ba (accessed Feb 2024)

Crutzen, P.J. 2004. New Directions: The growing urban heat and pollution "island" effect – impact on chemistry and climate. Atmospheric Environment 38 (2004) 3539–3540

DerStandard. 2023. Strobl. G. Klimaforscher: 100 Milliarden Bäume pflanzen gegen den Treibhauseffekt. Published on 30th September 2023, available via: https://www.derstandard.at/story/3000000189195/milliarden-b228ume-gegen-den-treibhauseffekt (accessed Feb 2024).

Designbuilder. 2022. Graphical User Interface for EnergyPlus and Radiance, available via www.designbuilder.co.uk (accessed Feb. 2024)

El-Sokaily, H. 2022. Large-scale shading impact on outdoor thermal comfort and overheating in dense areas. Master-Thesis at TU Wien, Vienna, Austria.

Envimet. 2022. Evaluation Software for MicroClimates; available via www.envi-met.com (accessed Feb. 2024)

Futurezone. 2021. Kotrba, D. Ein besseres Leben für Stadtbäume. Published on 22.01.2021, available via https://futurezone.at/science/ein-besseres-leben-fuer-stadtbaeume/401163708 (accessed Feb. 2024)

Hitzekarte. 2019. Urban Heat Vulnerability Map of Vienna, Austria, edited by Ecoten-urban comfort, available via: https://www.wien.gv.at/stadtentwicklung/energie/pdf/hitzekarte.pdf (accessed Feb. 2024).

Im7ten. 2022. Image of the Kirchengasse, available via https://www.im7ten.com/wp-content/uploads/2022/03/31-Siebensternviertel-CHST-03-2531-300x200.jpg (accessed Feb. 2024)

Kommraus. 2021. Wir röntgen die Straße. Public Event in the Zollergasse 18.05.2019; available via: https://www.kommraus.wien/2019/wir-roentgen-die-strasse (accessed Feb 2024).

Landsberg, H.E. 1981. The Urban Climate. New York, Academic Press.

MA22 (ed.). 2018. Urban Heat Island Strategy. Available via https://www.digital.wienbibliothek.at/wbrup/download/pdf/3559581?originalFilename=true (accessed Feb 2024)

Mayer, J.H. 2024: Website of Architect J.H. Mayer presenting Metropol Parasol. Available via: https://jmayerh.de/metropol-parasol/ (accessed Feb 2024)

Razzaghmanesh, M., Borst, M., Liu, J., Farzana, A., O'Connor, T., Selvakumar, A. 2021 Aur Temperature Reductions at the Base of Tree Canopies. J. Sustainable Water Built Environ, 2021, /(3), 04021010.

Roth, M. 2013. Urban Heat Islands. In *Handbook of Environmental Fluid Dynamics, Volume 2* (ed.: J.S.F.Harindra). CRC Press/Taylor & Francis, P143-159

Supertree. 2024. Gardens by the Bay, Sigapore. Available via: https://www.gardensbythebay.com.sg/en/things-to-do/attractions/supertree-grove.html (accessed Feb 2024).

Tola, A. Veleshnja, J., Meunier, P.L., Bisha, G. 2023. Impact of shade on outdoor thermal comfort, in the case of a Mediterranean Promenade. Journal of Physics, 2600 (2023) 092023, doi: 10.1088/1742-6596/2600/9/092023

ViennaGIS. 2022, City of Vienna GIS System. https://www.wien.gv.at/viennagis (accessed Feb 2024)

BauSIM 2024 in Wien
23. September – 26. September

Reduced complexity building and heat pump model to facilitate large scale deployment evaluations

David Reihs[1,2], Aurelien Bres[3], Karim Rezk[1], Jerik Catal[1] und Yannick Wimmer[1]

[1]*AIT - Austrian Institute of Technology*

[2]*University of Passau*

[3]*Siemens AG Österreich*

Abstract

To achieve carbon neutrality by 2050, the heating sector will need to be decarbonized quickly. Heat pumps are an ideal technology for the electrification of distributed heating demand. To study the effects of large-scale introduction of heat pumps in electric energy distribution grids, it is imperative to use detailed heat pump models. At the same time, the controllability of the heat pump needs to be reflected by the simulation model.

We propose a modeling paradigm, that uses thermal demand output from a detailed building model to build a simplified building and heat pump model that can be employed in time-discrete simulations with dynamic controls. The model enables large scale deployment evaluations for heat-pumps due to the low computational effort needed at simulation runtime. The complex building dynamics are decoupled from the simulation through the determination of the building thermal demand curves.

The Building temperature is determined using simple thermodynamic assumptions for every simulation time step. The approach is demonstrated for heating as well as cooling systems. Results are validated by evaluating building temperature in the detailed building simulation using thermal output of the simplified heat pump simulation model as heating and cooling system.

Introduction

Space heating and cooling is responsible for a significant share of final energy consumption. To tackle climate change it is critical that the heating and cooling sector will become largely decarbonized. The European Union has included heat pump technology as part of their pathways to fully renewable heating and cooling European Commission et al. (2023). The heat pump market has been growing for the last decades, with significant increases in Austria over the last years Bundesministerium Klimaschutz, Umwelt, Energie, Mobilität, Innovation und Technologie (2023). A continuing sharp increase in numbers of heat pumps will affect electricity transmission and distribution systems. Different control and pooling methods can help decrease the strain on electricity grids, but simulation models are needed that are able to evaluate large amounts of controllable heat pumps to be able to quantify the resulting effects. To analyse different control methods it is vital to create dynamic building and heat pump models that can react to changes in temperature, electric power availability, include climatic differences as well as focus on regional characteristics. Especially when investigating effects of extreme weather events on local energy infrastructure.

Related Work

Several different heat pump modelling and simulation approaches can be found in the literature. As for other building heating and air-conditioning systems, the modeling of heat pumps can be done at different levels of abstraction, from conceptual modeling (ideal loads) to system-based, component-based and equation-based modeling Trčka & Hensen (2010). The increasing level of detail and flexibility along this spectrum usually comes with an increase in data requirements and modeling effort. In the heat pump context, focus on very detailed models of the heat pump components requires component-based or even equation-based modeling, while other approaches focusing on effects large scale heat pump deployment can have on energy systems will typically follow a conceptual modeling approach. Bler-

vaque et al. (2012) present a review of methods for joint simulation of heat pumps and building models. The authors differentiate between approaches focusing on simulating quasi-static situations for particular time steps, and dynamic simulations that integrate detailed models of parts of the heat pump system. As well as that, the authors differentiate between thermodynamic models, grey box and black box models. Thermodynamic models are very detailed on a component model, while grey box and black box models integrate increasing levels of abstraction for the heat pump and building system. We present a grey box model of the heat pump system, deriving some information from data and other from basic thermodynamic considerations. The modelling approach we follow is quasi-static, considering discrete steps of operation, but not the dynamic processes in between. Fischer et al. (2017) present a methodology for modelling and simulating large amounts of heat pumps in a pool, to determine the flexibility demand-shifting heat pumps can provide. In contrast to their approach of creating generic heat pump pools, with a large number of heat pumps, we focus on modelling particular types of buildings and heat pumps situated in a particular region. Creating generic building models and simulating them using weather profiles, allows us to recreate specific communities together with local climatic conditions. Ruhnau et al. (2019) show a method for determining country specific heat demand profiles for several European countries. They provide coefficient of performance (COP) data as well, so the dataset can be used for the modelling and simulation of heat pumps. This approach presents the average heating need of a nation, but is not able to provide detailed demand profiles depending on a particular weather profile and for certain types of buildings. Another building thermal demand modelling approach is presented by Good et al. (2015). The authors suggest modelling the building as using an equivalent circuit model. This offers full controllability but does not include the integration of a complex thermal building model.

Our work contributes to the literature on modelling and simulation of heat pump systems by providing a novel methodology for employing heat demand data to develop a dynamic simulation model for building and heat pump. The resulting model can react to external control signals, such as demand response signals, as well as take into account inhabitant comfort. The bottom up approach will provide a novel way of creating large scale simulations to evaluate heat pump roll-out effects on other parts of the energy system.

Methodology

We propose a three step process for the preparation, calibration and consecutive simulation of building and heat pump models. First several sizes of the building models are set up, representing several building types and sizes. The creation of building models is done in *Autodesk Revit* ®, a program for building information model design. The building models are consequently calibrated to represent several building energy certificate classes for every building size. The thermal energy demand profiles are consequently calculated through yearly simulation in *EnergyPlus*, a building energy simulation program Crawley et al. (2001). The demand profiles are used to set up a dynamic but simplified building and heat pump model implemented in the Julia programming language, and is decoupled from the actual building simulation in *EnergyPlus* at runtime. The methodology steps are shown in Figure 1.

Building Modelling

To create generic building models for single family houses, multi family houses and offices several different form factors were defined. The form factors and key data on the implemented building models can be found in Table 1. As far as building sizes are concerned, there are three for each category: A medium-sized building, a particularly small building and a particularly large one. Working with similar parameters for each size should allow to approximate different building sizes in between by simple interpolation. Such an approach using interpolation is, however, not used in the present work. The values for m^2 per inhabitants are based on statistical data from *Wohnen 2022: Zahlen, Daten und Indikatoren der Wohnstatistik* (2023). As can be seen in the statistics of building types in Austria, the single family homes and multi family homes are by far the most common building types *Zensus Gebäude- und Wohnungszählung 2021: Ergebnisse zu Gebäuden und Wohnungen aus der Registerzählung* (2023). As far as office buildings are concerned, the variability in electric and heat loads can be assumed to vary considerably dependent on the business. For the present work no special demand (such as production lines etc.) were assumed. The value of 21.3 m^2 is used with reference to Hainoun & Loibl (2022).

The modelling procedure is based on defining a modular design for each category of buildings, which is based on a single rectangular shaped ther-

Table 1: Implemented generic building models.

	Single family house			Multi family house			Office		
Area in m^2	50	150	300	300	1500	7500	300	5000	25000
Levels	1	2	2	2	4	5	1	5	25
Zones per level	2	3	6	2	5	20	6	20	20
Zone area	25	25	25	75	75	75	50	50	50
m^2 per occupant	25	42.9	66.7	36.9	36.9	36.9	21.3	21.3	21.3

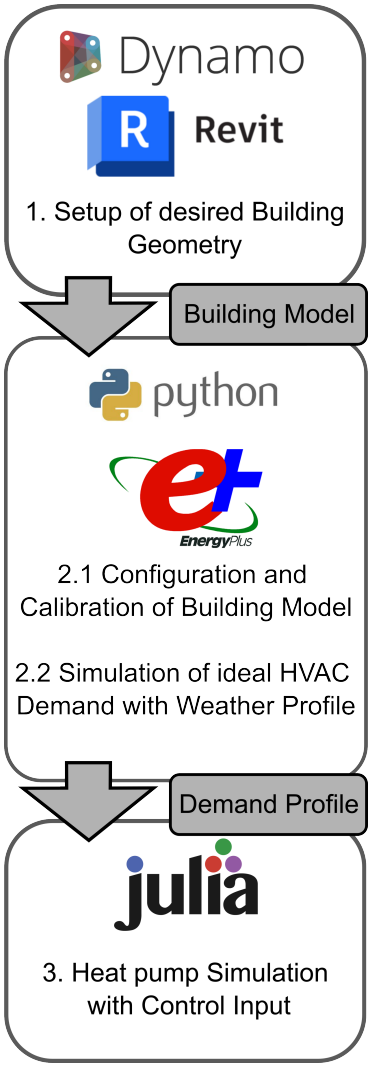

Figure 1: Proposed methodology for building and heat pump simulation

mal zone that could be repeated in X and Y directions to expand the surface area of the building level as well as in Z direction to multiply the number of levels. Once the following parameters are defined, a building information model (BIM) is automatically generated based on code created in the Dynamo Autodesk Inc. (2024) programming language for *Autodesk Revit* ®.

- Dimensions of the thermal zone
- Number of zones in X-direction
- Number of zones in Y-direction
- Number of building levels
- Number of windows per external wall

Through the *eppy* Python package Santosh (2023), the BIM models created using Dynamo are transferred into thermal models in the appropriate format to be simulated using *EnergyPlus*. Figures 2 and 3 show the 3D model of the 150 m^2 single family house and the 1500 m^2 multi family house.

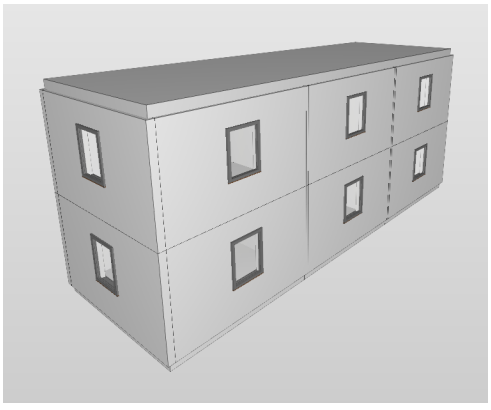

Figure 2: 3D Model of single family house with 150 m^2 floor area.

For residential and office spaces different occupancy schedules are integrated in the *EnergyPlus* thermal model. Figure 4 shows the different occupancy schedules that are implemented. Each thermal zone will receive an input of 100 Watt per person present.

Figure 3: 3D Model of multi family house with 1500 m^2 floor area.

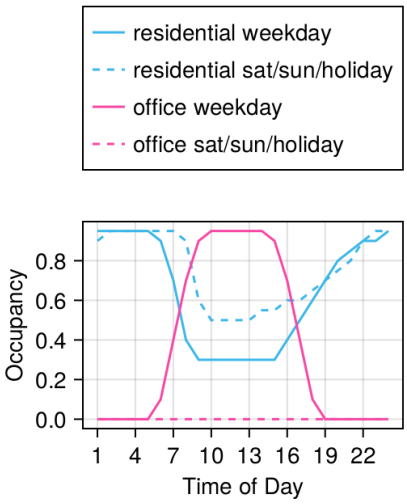

Figure 4: Occupancy in residential and office spaces.

Calibration of Buildings

The goal of this work is to provide a complexity-reduced model of numerous different types of buildings. We chose to represent the different thermal standards of buildings through different building classes according to the building energy certificates presented by Österreichisches Institut für Bautechnik (2023). The calibration of the building models for different building classes is conducted using the Python scripting language for *EnergyPlus eppy* Santosh (2023), and using the scipy package Virtanen et al. (2020) for optimization of heating demands. The optimization function is given a parameter to increase or decrease the thickness of insulation material in the building. The thickness is varied until the required thermal demand is reached. For the largest multi family house and office building, the highest heating demand levels are not possible to achieve due to heat exchange between thermal zones. The overall heat demand per building area never reaches a building class D or below. The weather data used for calibration of the building models had a significant impact on the resulting energy certificate building classes. Figure 5 shows the resulting heating demand from two buildings calibrated with different weather data. The first was calibrated using 2019 weather data, which is also used for the simulation. The second is using a typical meteorological year from the same location from 2010, which included months from years in the 1980ies and 1990ies. That climate change has taken effect since the turn of the century is clearly visible in the large discrepancy in result thermal energy demand per m^2. For the rest of this work, the building models are calibrated using the 2019 weather data and also executed using this weather data.

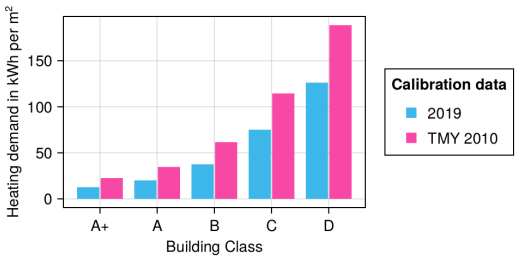

Figure 5: Comparison of heating demand for the 150 m^2 single family house for different building energy certificate classes when using different weather data used for building model calibration.

When sorting the heating energy demand over the whole year, it is clearly visible that while the

slope of the heating demand rises, the amount of hours when heating is needed throughout the year also rises for worsening energy certificate building classes. Figure 6 shows the demand curves for the 150 m^2 single family house. It can be seen that better insulated houses (building class A+ and A) require less heating energy and the time when heating is needed is reduced as well.

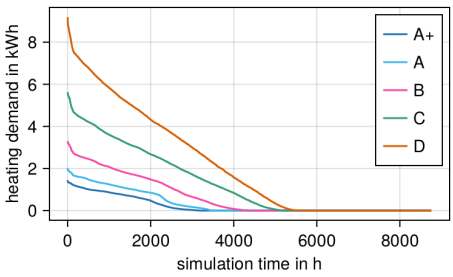

Figure 6: Sorted heating demand over the yearly simulation for the 150 m^2 single family house

Building and Heat Pump Simulation

The simplified building and heat pump simulation model is implemented in the Julia programming language, a language well suited for numeric and scientific programming Bezanson et al. (2017). This enables us to integrate well with other software written in Julia. However, the simulation model could also be implemented in other dynamic programming languages such as Python.

The simulation model is quasi-static and works on discrete simulation time steps. The input for the model is a temperature profile for environment temperature as well as the heat energy demand profile calculated using *EnergyPlus* with an ideal HVAC system.

For every simulated time step at first the COP (Coefficient of performance) of the heat pump system is determined, depending on sink and source temperature of the heat pump. The condensation temperature T_{cond} is set to be 3K above the sink temperature for the heat pump system and the evaporation temperature T_{evap} is 3K below the source temperature of the heat pump. This offset is chosen, as there is always a temperature difference between the immediate surrounding of the inlet and outlet of the HP and the average temperature of the heat sink and source.

$$COP = \frac{T_{cond}}{T_{cond} - T_{evap}} \cdot \eta_{carnot} \cdot \nu_{heatpump} \quad (1)$$

The calculation of the COP is presented in equation 1. η_{carnot} is the efficiency of the ideal Carnot process and $\nu_{heatpump}$ is the efficiency of the heat pump system, depending on the type of system that is being simulated. For air-to-air (ATA) heat pump systems, like air conditioning units, lower $\nu_{heatpump}$ are selected than for water-to-water heat pumps, such as ground water heat pumps used for heating. This reflects the lower COP that are seen for ATA systems. Source temperature T_{source} and sink temperature T_{sink} also depend on the type of heat pump that is being simulated. Heat pumps that supply radiators usually have a higher output temperature than heat pumps that supply under floor heating. The simulated heat pumps have a constant nominal electrical power $p_{nom,el}$, but the thermal power output p_{th} depends on several environmental factors that influence the COP as well as the binary thermostat switch s. The thermal energy $dQ_{\Delta T}$ responsible for a change in building temperature is given by the difference of the current thermal output power $p_{th,t}$ of the heat pump system and the thermal demand $p_{th,demand,t}$ for the time step that is acquired from the *EnergyPlus* simulation with the ideal HVAC system.

$$dQ_{\Delta T,t} = (p_{th,t} - p_{th,demand,t}) \cdot \Delta t \quad (2)$$

The simulated building is given two temperatures that control the thermostat setting for both heating and cooling system respectively, $T_{heating}$ and $T_{cooling}$. The temperature change Δ_{T,p_t} for the time step is calculated using Equations 3 and 4. $C_{p,air}$ is the heat capacity of air, γ_{air} is the specific weight of air, $V_{building}$ is the volume of the building and $C_{additional}$ is a factor representing the heat capacity of building internals such as walls and furniture. $C_{additional}$ has been experimentally determined to give the best results when it is selected to be around 7.

$$\Delta T_{p_{th,t}} = \frac{dQ_{\Delta T,t}}{V_{building} \cdot C_{p,air} \cdot \gamma_{air} \cdot C_{additional}} \quad (3)$$

$$T_t = T_{t-1} + \Delta T_{p_{th,t}} \quad (4)$$

A pseudo code example of the implemented thermostat algorithm implemented for heating and cooling systems are presented in Algorithm 1 and Algorithm 2 respectively. The thermostat control can be combined with a thermal buffer storage where excess thermal energy can be stored and withdrawn from at a later simulation step. This allows the system to offer a higher flexibility in operation.

Algorithm 1 Thermostatic control for building temperature in heating mode

$s_t = s_{t-1}$
$COP_t = COP_{T_{sink,t-1},T_{source,t}}$
$p_{el,nochange,t} = p_{nom} \cdot s_t$
$p_{th,nochange,t} = p_{el,nochange,t} \cdot COP_t$
$T_{nochange} = T_{t-1} + \Delta T_{p_{th,nochange,t}}$
if $T_{nochange} < T_{comfort,low}$ **then**
  $s_t = 1$
else if $T_{nochange} > T_{comfort,high}$ **then**
  $s_t = 0$
end if
$p_{el,t} = p_{nom} \cdot s_t$
$p_{th,t} = p_{el,t} \cdot COP_t$
$T_t = T_{t-1} + \Delta T_{p_{th,t}}$

Algorithm 2 Thermostatic control for building temperature in cooling mode

$s_t = s_{t-1}$
$COP_t = COP_{T_{sink,t},T_{source,t-1}}$
$p_{el,nochange,t} = p_{nom} \cdot s_t$
$p_{th,nochange,t} = p_{el,nochange,t} \cdot COP_t$
$T_{nochange} = T_{t-1} + \Delta T_{p_{th,nochange,t}}$
if $T_{nochange} > T_{comfort,high}$ **then**
  $s_t = 1$
else if $T_{nochange} < T_{comfort,low}$ **then**
  $s_t = 0$
end if
$p_{el,t} = p_{nom} \cdot s_t$
$p_{th,t} = p_{el,t} \cdot COP_t$
$T_t = T_{t-1} + \Delta T_{p_{th,t}}$

System sizing

The sizing of the heat pump system is done using statistical evaluations of the employed thermal demand profile. For ground source heating systems the maximum thermal energy demand divided by a factor of three is used as a value for the nominal electrical power. Using this value, a heat pump could provide the maximum required heat, even in a low COP-setting. For air source cooling systems the maximum thermal energy demand is divided by a factor of 2.5 to determine the nominal electrical power. The size of the buffer storage for heating systems is selected to be able to supply to the maximum energy demand of the heat demand profile for 2 hours.

Validation

To validate the complexity reduced building and heat pump simulation model, the resulting heating and cooling thermal energy curves are introduced to the building model in *EnergyPlus* and a yearly simulation is conducted.

Figure 7 shows the results of the thermal power output of both heating and cooling system of the building and heat pump simulation model being introduced to the building thermal model in *EnergyPlus* as a limiting power profile for the ideal HVAC system. In the lower graph, the temperature comfort limits are marked as well as the mean room temperature in the house throughout the simulation. The simplified simulation model temperature without the thermal storage keeps on dipping below the comfort limits, but does not deviate from the target temperature continuously. The cooling system tends to the upper comfort limit, but generally keeps within the comfort zone well. The simulated thermal heating output is relatively constant over the simulated year, as the simulated heating system is a ground water heat pump supplying an under floor heating system, therefore both source and sink temperature are varying only by a small margin. The simulated thermal cooling output is subject to a lot more variations, as the system is an air-to-air system where the COP depends on the outdoor temperature. The heating system that also includes a thermal buffer storage follows the thermal demand of the ideal HVAC system exactly, therefore the curve is hardly visible on the top part of Figure 7. This exact following of the ideal HVAC system power leads to a temperature that is almost equivalent to the original temperature profile, with minor deviations. The presented Figure 7 shows that our building and heat pump modelling method-

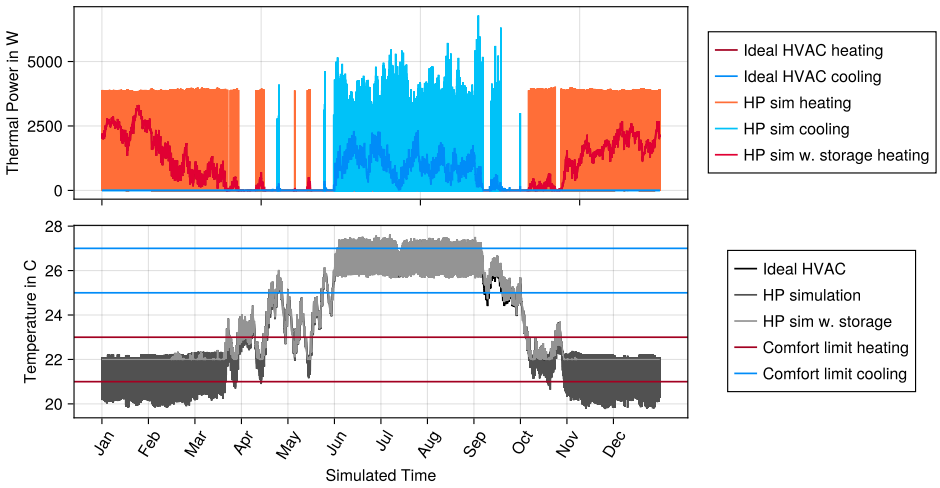

Figure 7: Comparison of energy+ ideal building model output and simulation model output. Data for the 150 m^2 single family home in building energy certificate class B is shown.

ology creates feasible heating and cooling patterns.

Figure 8 shows a comparison of the total thermal demand during the simulation of a building compared with the mean absolute deviation of the temperature profile during times with heating and cooling demand. It can be seen, that the thermal demand is portrayed very closely by the simulation model. When a thermal storage is included in the simulation, the temperature profile follows the temperature profile of the ideal HVAC system more closely, which is to be expected. Table 2 shows the mean absolute deviation of the temperature profile that is observed for the simulated heat pump when compared to the ideal HVAC system. It can be seen that the presented approach works better for well insulated houses, as the temperature deviation is lower for better building insulation classes. This could be because of the simplified approach to heat pump system sizing, and because the heat pump systems were modelled as on/off systems which cannot modulate between different output powers. The effect is reduced by simulating the heating system with a thermal buffer storage. Future work will focus on better calibration methods for different building sizes as well as building insulation classes.

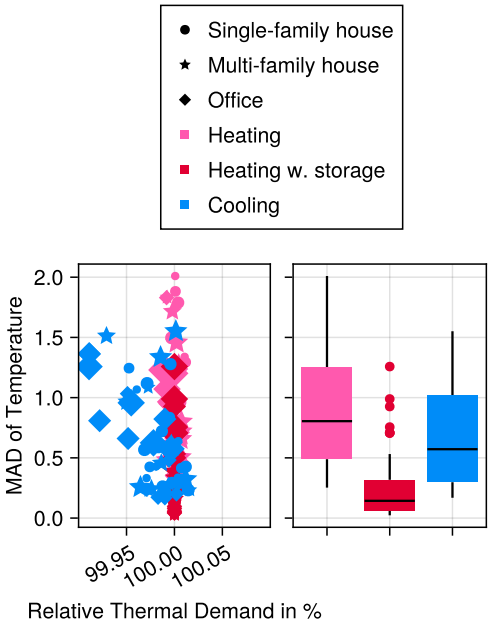

Figure 8: Statistic evaluation of temperature deviation from Energy+ with ideal HVAC system. Size of the marker corresponds to the logarithm of the size of the building.

Discussion

The validation results show that our simplified model for building and heat pump is able to create feasible heating and cooling powers for buildings. This makes it well suited for applying the approach to a large amount of buildings and evaluating inter-

Table 2: Statistical evaluation of mean absolute deviation of the validation temperature profile to the ideal HVAC system in Energy+ for all simulated building classes.

	Heating			Heating w. storage			Cooling		
	Mean	Max.	Min.	Mean	Max.	Min.	Mean	Max.	Min.
A+	0.479	1.071	0.253	0.372	1.258	0.036	0.356	0.809	0.173
A	0.518	0.950	0.331	0.291	0.989	0.051	0.353	0.661	0.169
B	0.739	0.965	0.499	0.207	0.756	0.030	0.507	0.957	0.201
C	1.220	1.339	0.963	0.191	0.707	0.027	0.873	1.362	0.482
D	1.649	2.010	1.230	0.218	0.707	0.023	1.251	1.551	1.033

actions with other parts of the energy system such as electric distribution and transmission networks. While our model outputs a combined electrical and thermal power for every simulated time step, *EnergyPlus* provides a heating demand for every zone of the building. Especially for larger buildings there can be a large deviation of heating demand between thermal zones. This leads to deviations in temperature in certain zones, consequently leading to a deviation in mean temperature. Therefore, the provided validation is not feasible for every building size. However, the overall thermal demand of the ideal HVAC system is reflected in the output of the building and heat pump simulation model and can even be adapted slightly using loss factors. The calibration of loss factors and heat pump system sizing was largely handled experimentally throughout this work, but it would be and interesting area to explore in further studies. The performance of the simplified simulation model is magnitudes higher than the complex building model. The reduced complexity building and heat pump model is able to run a yearly simulation in 203.9 ms on an Intel®Core i7-1185G7 3.00Ghz with four cores and eight logical processors and 32 GB of RAM. The same building model takes 12.4s to simulate in *EnergyPlus* on the same system. Control algorithms for heat pumps will be studied in future work, using the presented building and heat pump simulation methodology. By shifting the comfort temperature used in the thermostat, a reduction or increase of heat pump demand could be achieved. How such a shift in comfort temperature would affect the building temperature of the more sophisticated building model will be looked at in future work. Our work was focused on residential and office buildings, but the same approach could be easily extended to other types of building types, as long as typical occupation patterns and geometries can be defined. It is planned to include domestic hot water (DHW) preparation in future work using a similar heat pump modelling approach.

Conclusion

We present a methodology for creating reduced complexity building and heat pump simulation models for custom building sizes using particular climate and weather profiles. This approach allows for decoupling the building model from the control of the heat pump, making it possible to implement custom controls for heat pumps and to analyze the effects of an increased share of heat pump systems on other parts of the energy system. We have shown that a simplified building and heat pump model only based on a demand profile is able to provide reasonable room temperatures in a detailed thermal building simulation. A large variety of building models is proposed to enable the creation sets of buildings that can be evaluated together in an energy community setting. Interpolation between different sizes of buildings will enable the creation of custom model sizes. Future work will explore the effect of large scale roll-out of heat pump systems on different energy markets as well as electrical distribution and transmission grids.

Nomenclature

γ	Density
C	Thermal capacity
COP	Coefficient of Performance
dQ	Change in thermal energy
p_{el}	Electric power
p_{th}	Thermal power
s	On/Off State
T	Temperature
t	Time step
V	Volume

References

Autodesk Inc. (2024), 'Dynamo github page'.
URL: *https://github.com/DynamoDS/Dynamo*

Bezanson, J., Edelman, A., Karpinski, S. & Shah, V. B. (2017), 'Julia: A fresh approach to numerical computing', *SIAM Review* **59**(1), 65–98.

Blervaque, H., Stabat, P., Filfli, S., Muresan, C. & Marchio, D. (2012), Comparative Analysis of Air-to-Air Heat Pump Models for Building Energy Simulation, *in* 'SimBuild', Vol. 5, IBPSA-USA, Madison, Wisconsin.

Bundesministerium Klimaschutz, Umwelt, Energie, Mobilität, Innovation und Technologie (2023), Energie in österreich - zahlen, daten, fakten, Technical report, Bundesministerium Klimaschutz, Umwelt, Energie, Mobilität, Innovation und Technologie.

Crawley, D. B., Lawrie, L. K., Winkelmann, F. C., Buhl, W. F., Huang, Y. J., Pedersen, C. O., Strand, R. K., Liesen, R. J., Fisher, D. E., Witte, M. J. et al. (2001), 'Energyplus: creating a new-generation building energy simulation program', *Energy and buildings* **33**(4), 319–331.

European Commission, Directorate-General for Energy, Braungardt, S., Bürger, V., Fleiter, T., Bagheri, M., Manz, P., Billerbeck, A., Al-Dabbas, K., Breitschopf, B., Winkler, J., Fallahnejad, M., Harringer, D., Hasani, J., Kök, A., Kranzl, L., Mascherbauer, P., Hummel, M., Müller, A., Habiger, J., Persson, U. & Sánchez-García, L. (2023), *Renewable heating and cooling pathways – Towards full decarbonisation by 2050 – Final report*, Publications Office of the European Union.

Fischer, D., Wolf, T., Wapler, J., Hollinger, R. & Madani, H. (2017), 'Model-based flexibility assessment of a residential heat pump pool', *Energy* **118**, 853–864.
URL: *10.1016/j.energy.2016.10.111*

Good, N., Zhang, L., Navarro-Espinosa, A. & Mancarella, P. (2015), 'High resolution modelling of multi-energy domestic demand profiles', *Applied Energy* **137**, 193–210.
URL: *https://doi.org/10.1016/j.apenergy.2014.10.028*

Hainoun, A. & Loibl, W. (2022), Analyses of the Long-Term Energy Demand of Vienna City and Modelling Related-Key Food-Water-Energy Nexus Effects, *in* E. Heggy, V. Bermudez & M. Vermeersch, eds, 'Sustainable Energy-Water-Environment Nexus in Deserts', Advances in Science, Technology & Innovation, Springer International Publishing, Cham, pp. 457–462.

Österreichisches Institut für Bautechnik (2023), Oib richtlinie 6 - energieeinsparung und wärmeschutz, Technical report, Österreichisches Institut für Bautechnik.

Ruhnau, O., Hirth, L. & Praktiknjo, A. (2019), 'Time series of heat demand and heat pump efficiency for energy system modeling', *Scientific Data* **6**(1), 189. Number: 1 Publisher: Nature Publishing Group.
URL: *https://www.nature.com/articles/s41597-019-0199-y*

Santosh, P. (2023), 'eppy documentation'.
URL: *https://eppy.readthedocs.io/en/master/*

Trčka, M. & Hensen, J. L. (2010), 'Overview of hvac system simulation', *Automation in Construction* **19**(2), 93–99.
URL: *https://doi.org/10.1016/j.autcon.2009.11.019*

Virtanen, P., Gommers, R., Oliphant, T. E., Haberland, M., Reddy, T., Cournapeau, D., Burovski, E., Peterson, P., Weckesser, W., Bright, J., van der Walt, S. J., Brett, M., Wilson, J., Millman, K. J., Mayorov, N., Nelson, A. R. J., Jones, E., Kern, R., Larson, E., Carey, C. J., Polat, İ., Feng, Y., Moore, E. W., VanderPlas, J., Laxalde, D., Perktold, J., Cimrman, R., Henriksen, I., Quintero, E. A., Harris, C. R., Archibald, A. M., Ribeiro, A. H., Pedregosa, F., van Mulbregt, P. & SciPy 1.0 Contributors (2020), 'SciPy 1.0: Fundamental Algorithms for Scientific Computing in Python', *Nature Methods* **17**, 261–272.

Wohnen 2022: Zahlen, Daten und Indikatoren der Wohnstatistik (2023), Technical report, Statistik Austria.

Zensus Gebäude- und Wohnungszählung 2021: Ergebnisse zu Gebäuden und Wohnungen aus der Registerzählung (2023), Technical report, Statistik Austria.

BauSIM 2024 in Wien
23. September – 26. September

Revolutionizing Heating Planning: A Data-Driven Approach for Accurate and Scalable Energy Consumption Predictions

Stefanie Segbers, Alexander Küster-Inderfurth, Christoph Nytsch-Geusen
Universität der Künste Berlin, Deutschland, E-Mail: s.segbers@udk-berlin.de

Abstract

Accurately predicting heating energy consumption for buildings is crucial for optimizing communal heating planning. However, the lack of detailed building information hinders precise estimations necessary for city decarbonization and efficient use of local renewable or waste energy. To address this challenge, this study utilizes 3D geometries and open data of Berlin's half a million buildings to perform building-specific simulations and trains AI-models to predict heating consumption.

A physics library was developed using statistical data from 16 building types and 6 refurbishment scenarios, providing building model components with physical properties. Additionally, a usage library comprising 24 different usage types and a weather database spanning 13 recent years, and 3 future climate scenarios for the next 8 decades were created. Simulations on a subset of Berlin's buildings were conducted using these libraries.

To extend results city-wide, an Artificial Neural Network (ANN) was trained using input data and simulation outcomes. This approach replaces traditional simulation software, offering a more efficient alternative. An intuitive web-application with a fast AI surrogate model at its core allows individuals to access and modify results for their buildings as well as correcting values to reflect actual demands. Corrected data is incorporated into neural network training, improving accuracy for various climate scenarios and potential refurbishments.

This iterative process not only streamlines communal heating planning in Berlin but also establishes a flexible framework for continuous improvement. This emphasizes the adaptability and scalability of our proposed methodology, contributing to enhanced predictions and a more efficient approach to city-wide heating planning.

Introduction

For decarbonization concepts of cities, communities and neighborhoods, a building-specific database of the building's properties and energy demands is essential. Since German legislators have passed a law on communal heat planning (Bundesregierung, 2023), concerns on how to approach the obligations of the law are growing. A first step must be a thorough compilation of building data that represents the status quo. Often however, energy cadastres provide only block-level or 100m x 100m grid consumption data (Paardekooper, S. et al., 2018), (Dochev, I. et al., 2019), (Behörde für Stadtentwicklung und Wohnen, Stadt Hamburg, 2019). Yet, to undertake precise planning and to locally utilize renewable energies or waste heat from sources such as industry, data centers, or wastewater, building-specific data is indispensable.

In addition to the current heating consumption of buildings, future scenarios for refurbishments and the impacts of climate change (Kahlenborn, W. et al., 2021), such as increasingly mild winters or warmer summers, are crucial for long-term heat planning. Unfortunately, there is a scarcity of comprehensive and freely available information on buildings for those scenarios and in general in Germany.

Consequently, in practice energy concepts for neighborhoods, districts, communities, or cities often rely on rough assumptions regarding heating and domestic hot water consumption. Typically, the demands are extrapolated based on the building's area and educated guesses of specific values. However, more accurate predictions are imperative for long-term and precise heat planning.

Drawing from insights gained in a previous project, Open eQuarter (Nytsch-Geusen, C. et al., 2016) which utilized a GIS-based statistical approach to assess the specific energy demands of buildings in Berlin, this new method aims to further enhance accuracy and efficiency. To generate precise forecasts of the heating energy consumption for tens of thousands of buildings and

different refurbishment and climate scenarios in a short amount of time, a workflow has been developed that replaces physical-based building-specific simulations with a prognosis model based on a neural network. This workflow has been applied to the city of Berlin. To enhance the energy demand prognosis of the neural network, users are provided with the opportunity to adjust building parameters in an iterative process.

Simulations as training data

To carry out simulations with the software SimStadt (Coors, V. et al., 2021) for most of Berlin's buildings at building level, several building-specific datasets such as the cubature, the age and the type of use were compiled first. These attributes serve as key to merge further information from large statistical libraries for each individual building in the building-specific simulations: The 3D building models in CityGML format and the usage type of the building, which can be identified through ALKIS function numbers (Arbeitsgemeinschaft der Vermessungsverwaltungen der Länder der Bundesrepublik Deutschland (AdV), 2018), were merged. This information is provided by the State of Berlin through its Geoportal (Senatsverwaltung für Stadtentwicklung, Bauen und Wohnen Berlin, 2024). Some of the 3D building models contain parts of buildings such as underground garages or driveways. These were removed from the building data sets with specially designed filters to keep only data that is most relevant to heating consumption. In addition to the type of use, each individual building model was enriched with information on the age of the building. The building ages from a 1992/93 building age map and a monument map were used for this purpose. For all buildings whose building age was not covered by these maps, the mean building age of the city block from German census data was used for simplification. In many other cities in Germany, there is building-specific information on building ages, which means that applying the workflow to other areas may even eliminate the need for time-consuming evaluations of building age maps and data.

Statistical data from IWU surveys were also used to describe the physical parameters of the envelope surfaces. One survey (IWU Institut für Wohnen und Umwelt, 2016) was carried out for residential buildings and published in 2011. Here, the residential buildings were divided into five different residential building types and up to nine different construction age classes per residential building type. A second survey (IWU Institut für Wohnen und Umwelt, 2021) on non-residential buildings was recently completed and published in 2021. The non-residential buildings were divided into eleven different usage types, each containing three different building age classes. The data surveys of residential and non-residential buildings refer to buildings throughout Germany and, although only statistical data is provided, the data is currently the best source for physical parameters as it is classifying non-residential buildings into 33 categories and was deducted from data of up to 800 buildings per category.

The data collection and categorization were carried out in different ways for residential and non-residential buildings. For residential buildings, SimStadt provides a library in which the refurbishment categories were unrefurbished, so-called "original" buildings; data collected by IWU from moderately refurbished buildings, labelled “medium” by SimStadt; as well as the data from advanced refurbished buildings which were labelled “advanced” by SimStadt, see Figure 1. There were also refurbishment scenarios where a building either only had a refurbished roof, refurbished windows, or walls. For all other parts of the building, it was assumed that they were still in their original or unrenovated condition.

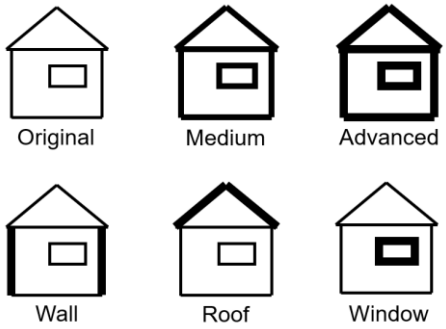

Figure 1 The six refurbishment scenarios used for building simulations in SimStadt with the highlighted refurbished components.

These refurbishment labels for residential buildings were then also used for the non-residential buildings. However, the data collected by IWU for the non-residential buildings was sorted differently in their survey: For every building category the mean average value and the standard deviations were determined. For simplification the category “medium” refurbishment was used for the mean average value. Furthermore, deviation indicating a worse refurbishment state was used for the “original” refurbishment category. The deviation indicating a better refurbishment state was used for the “advanced” category. In the example of a heat transfer coefficient this would be the lower value. For parameters such as the average storey height, the mean average value was used,

as it is assumed that a refurbishment will not change the storey height in most cases.

In addition to the library of physical parameters, a usage library was created with 24 different building usage types. These 24 types of usage are made up of 22 different non-residential and only 2 residential building use profiles. The profiles for residential buildings are very similar, with only a distinction being made between apartment buildings and smaller houses, e.g. single-family houses. For each usage profile, data from usage profiles from DIN 18599 (Deutsche Institut für Normung e.V., 2018) were used as a basis. The internal gains as well as occupancy conditions were derived from the DIN 18599 profiles. Furthermore, for every building category there is an indirectly heated area ratio set so that an assumption is made for every building. Storeys that are underground are counted as cellars and those that are not high enough for living purposes are thus considered unheated areas. Unfortunately, no assumptions could be made regarding the zoning of non-residential buildings, as the interior of the buildings is completely unknown due to the available LoD2 3D geometries. All buildings are therefore treated as single-zone models. The assignment of buildings to a usage profile in the library was done via the ALKIS building function number of each building.

The building simulations were carried out with weather data for the past 13 years. Past years were simulated as these can be compared with real consumption values. Additionally, weather data was also generated via Meteonorm (Meteotest, 2020) for the next eight decades, i.e. 2030, 2040 etc. up to 2100. The three RCP climate scenarios 2.6, 4.5 and 8.5 (IPCC, 2014) per decade were used for the simulations.

To initiate these simulations, a Python script was written that automatically simulates six refurbishment scenarios and a total of 37 weather scenarios for 408,000 buildings of Berlin using SimStadt. After the simulation, the data was processed and stored automatically in a PostGIS database.

The simulations can be repeated for other cities and municipalities in Germany. The libraries created can be used, only the 3D building models would need to be enriched with the information mentioned at the beginning and the climate data for the specific locations used in the simulation.

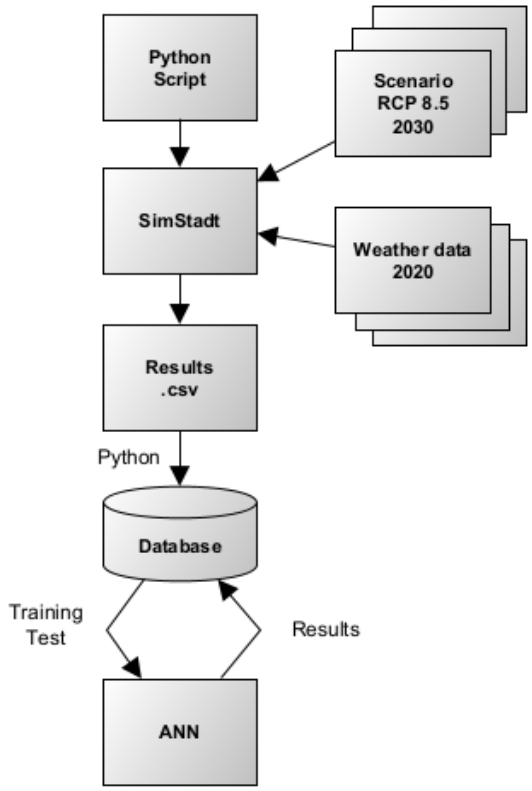

Figure 2 Training strategy for artificial neural networks (ANN) with synthetic training data derived from simulations.

Neural network as a surrogate model

In order to determine the heating and domestic hot water demands for further buildings, the extent to which ANNs can serve as surrogate models for traditional simulations is being investigated. ANN are already used in various domains to efficiently substitute complex and time-consuming simulations (Sun & Wang, 2019), (Donnelly, J. et al., 2023). Due to the enormous amount of data generated by the simulations, ANNs can achieve good forecast quality and provide quick and effective predictions for heating and hot water demands for additional buildings.

Trials with the data have shown that the prediction accuracy is higher when two different ANNs are trained for domestic hot water (DHW) and heating demands (HD). For this purpose, another Python script has been written, which accesses the simulation inputs and outputs in the database and chooses the relevant inputs and outputs for the training of the respective ANN. For the prediction of domestic hot water (DHW) far less input parameters are relevant than for the heating demand (HD). Table 1 shows the different parameters significant for the training of the prediction models.

Table 1: Input features for the distinct ANNs

Input features for ANNs	**HD**	**DHW**
Year of construction	x	x
ALKIS code	x	x
Primary and secondary usage zone areas	x	x
Heated area	x	x
Building type	x	x
Footprint area	x	
Window area	x	
Total wall above ground outwall/ shared wall/roof area	x	
Heat transfer coefficients for walls/ windows/ground/ roof/ceiling	x	
Gross volume and heated volume	x	
Storey number	x	
Average storey height	x	
Basement and/or attic heating	x	
Basement ceiling height above ground	x	
Surface area to volume ratio	x	
Climate year and scenario	x	

First, the data is prepared for the ANNs, and an exploratory data analysis is conducted. The script converts several non-numeric columns into a "category" data type. It also includes functions for displaying histograms and checking the normal distribution of the data. It analyses both numeric and categorical columns to provide insights into the distribution of the data.

Moreover, a correlation map is created to provide insights into data relationships to choose the most relevant features to feed into the network models. However, more methods, such as regularization need to be explored as the analysis of correlation between categorical features cannot be assessed by computing correlation coefficients. Moreover, a method for splitting the data into training and test sets and for detecting and handling outliers in the dataset are provided. Together, these functions ensure that the data is ready for model fitting and further analysis.

In the Python script two artificial neural network models are created using Keras (Google LLC, 2024), a high-level API for the implementation of neural networks. It enables model creation with customizable architecture and optimization settings. The script provides functions to build and train the neural network as well as functions for visualizing the training history and making predictions on unseen test data. These functions are crucial for the development and fine-tuning of neural network models for various prediction tasks.

When implementing the neural network model, various hyperparameters concerning the model's architecture and training need to be optimized. A grid search was performed using 5-fold cross-validation with GridSearchCV from scikit-learn (Scikit-learn, 2024) to optimize hyperparameters such as batch size, epochs, neurons in the hidden layers, and learning rate. The optimal parameters found were a learning rate of 0.001 and a batch size of 2048. The train/validation/test split was 0.7/0.15/0.15.

A sequential model with two fully connected (dense) hidden layers was implemented, each with 128 neurons, which is effective for regression problems. The activation functions used were ReLU (rectified linear unit) for the hidden layers and a linear function for the output layer.

The training objective was to predict hot water demand and heating demand accurately. The Mean Squared Error (MSE) was chosen as the loss function, minimized using the Adam optimizer. Training was terminated early if the validation loss plateaued, with a maximum of 256 epochs and early stopping set at 16 epochs. The model achieved the following performance metrics:

- Loss: Train 0.0350, Validation 0.0464, Test 0.0323
- Mean Absolute Error (MAE): Train 0.0385, Validation 0.0323, Test 0.0294
- Mean Absolute Percentage Error (MAPE): 11.96%

Figure 3 is a scatter plot illustrating the relationship between simulated and predicted yearly heating demands. The blue dots, which represent data points, are primarily clustered close to a straight line, indicating a strong correlation and suggesting that the model's predictions are highly accurate. However, there are a few outliers further away from this ideal fit line, highlighting areas where the model's predictions deviate from actual values. This indicates some level of uncertainty and inaccuracy in the model's predictions, which must be critically evaluated to improve the overall quality and reliability of the results.

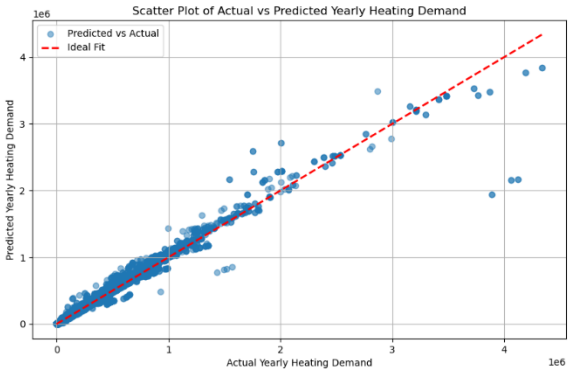

Figure 3 Scatter Plot of Actual (Simulated) vs Predicted Yearly Heating Demand

The training of the model takes about 0.0002% of the time of the simulations. Once the surrogate model is trained it can generate results in 0.000003% compared to the simulations. The Mean Absolute Percentage Error (MAPE) of 12% is not an outstanding prediction accuracy but it is considered good when compared with other calculation methods used for existing buildings.

The trained model can be saved and reloaded for further training or predictions on new datasets. For new data, input parameters need to be collected or calculated, with the outputs predicted by the model. The 3D geometry models, enriched with information from ALKIS, along with the gathered heat transfer coefficients and geometry parameters, support this process. Predictions for new data are stored georeferenced in the database.

Website for new data

Predicted heating and hot water demands will be published through a dedicated web application. All interested stakeholders will be able to access building specific prognosis data as well as underlying input data. Furthermore, users will have the ability to get data not only for single buildings but also use selection tools to extract data for the entirety of the buildings they are interested in. This will be useful e.g. for project developers who need to get an overview of the consumption in a development area. In the final implementation of the proposed web application users will even be able to submit their own building and consumption data for the already mentioned iterative refinement of the artificial neural networks.

To achieve this a complete stack of web technologies needs to be implemented, see Figure 4. As a base a PostgreSQL (The PostgreSQL Global Development Group, 2024) database management system with PostGIS (PostGIS PSC & OSGeo, 2024) extension is setup. This can be achieved in several ways, one of which is to use a Docker Container of the 3DCityDB (Yao, Z. et al., 2018) developed by TU Munich. While not being the core of the database system, the 3DCityDB and its dependencies correlate strongly with the requirements for this project. These requirements include a robust relational database management system with the capability to work with GIS based data. By starting with an instance of the 3DCityDB it is also immediately possible to import 3D geometries of entire cities into the database using the Importer/Exporter tool by the same institution.

The city of Berlin provides a 3D geometry model of the entire city in the CityGML format, that is freely available and is imported into the project database. Also imported were building input parameters from the feature list of the building database which originally comes from the ALKIS system and the mentioned libraries.

Within the project's GIS database all available building information is combined and an enriched CityGML model is exported. Only buildings and building parts that are considered to have heat energy consumption are exported.

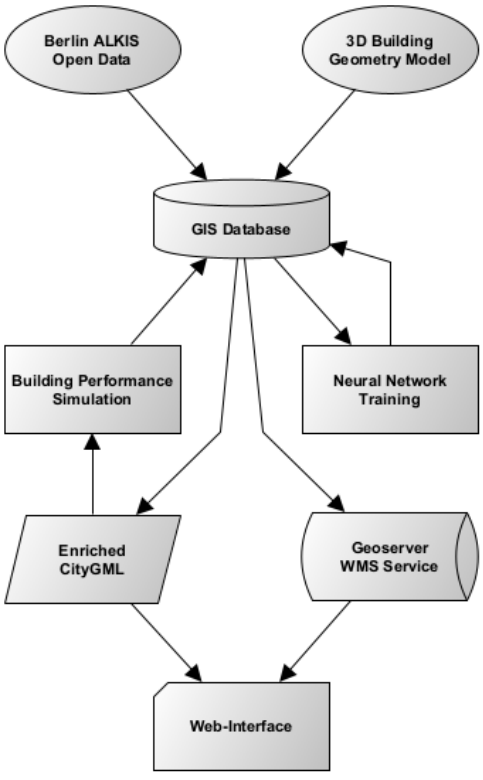

Figure 4 Data flow from source data to publication.

The same CityGML model is used for the afore mentioned simulation and training as well as for the visualization of 3D buildings within the web interface. For this the CityGML format is

converted into Cesium 3D tiles, a proprietary data format that is supported by the freely available CesiumJS (Cesium GS, Inc., 2024) JavaScript library which is used as an engine for the map part of the web interface. While 3D models can be displayed it is also possible to get a 2D map. This map is hosted by Geoserver (Open Source Geospatial Foundation, 2024) instance which serves a table of the central database with geometry information as a web map service (WMS). WMS can not only contain the 2D geometry information but also other attributes. Finally, a third way to access data is supplied with routes that are defined in the node.js backend of the described web application which can also query the central database and use predefined database functions to aggregate building information based on user requests and send them to the client's web browser for displaying.

The clients are running the presented web application by accessing the project website through a web browser, see Figure 5. When accessing they can view single building data by simply clicking individual building shapes on the 2D default view. When users choose to use one of several selection tools, they can select building groups by giving a point and a radius, by drawing a polyline with a specified distance or by drawing a polygon. The displayed data switches then to an aggregated summary of all buildings selected. Interested users can download the detailed data of all buildings by downloading a csv file.

The web interface gives stakeholders the opportunity to explore the results of our research for all buildings of Berlin. The predicted heat energy consumption is displayed together with the building energy efficiency class derived from these values. In addition, users can get aggregated results for city areas of their choice and use this data in their own projects.

Depending on how much knowledge the user has, they will be able to choose between an "expert mode" for people with domain knowledge and a simplified "citizen mode". Expert users are encouraged to also use provided APIs to get to the data more efficiently. It is possible to use the aforementioned URL routes to access data. The development of a Python API has been started, which will provide a more intuitive interface to the web API. The Python API will be published.

Figure 5 Web-interface including 3D building view.

Conclusion

In conclusion, the integration of 3D geometries, open data, and artificial intelligence (AI) has enabled significant progress in predicting heating and hot water demands for buildings in Berlin. By developing sophisticated physics and usage libraries, coupled with extensive simulations and the implementation of artificial neural networks (ANNs), this study has established a robust framework for building-specific estimations.

The iterative process undertaken facilitates faster predictions and establishes a scalable methodology applicable to city-wide or even nation-wide heating planning. Incorporating user-centric features, such as a web interface for adjustments and corrections based on actual demands, ensures continuous improvement and adaptability to diverse climate scenarios and refurbishment plans.

However, while the utilization of ANNs as surrogate models offers a high-speed alternative to traditional simulations, it does not achieve the highest accuracy, with a Mean Absolute Percentage Error (MAPE) of about 12%. This indicates that while the ANNs provide quick results, there is room for improvement in terms of accuracy. Future research should explore methods to enhance the precision of these models, such as by splitting the data into different building types or incorporating additional relevant features.

The comprehensive Python scripts developed for data preparation, model creation, and evaluation contribute to the transparency and reproducibility of the methodology. The implementation of a dedicated web application further democratizes access to prognosis data, empowering stakeholders to explore and utilize building-specific information for informed decision-making. With features allowing for selection tools, data extraction, and APIs for expert users, the platform promotes collaboration and engagement among various stakeholders involved in city planning and development.

Overall, this study emphasizes the importance of leveraging advanced technologies and open data initiatives to address challenges in communal heating planning. While the current approach provides a solid foundation, ongoing efforts to refine and enhance model accuracy will be crucial for maximizing the benefits of AI in energy optimization and climate mitigation. As cities worldwide strive towards decarbonization and resilience, the methodologies and tools developed in this research serve as valuable assets in shaping future strategies for sustainable and efficient energy practices in urban environments.

Acknowledgement

The project outcomes were only made possible through the comprehensive data acquisition efforts conducted by the Institut für Wohnen und Umwelt, in conjunction with the utilization of the sophisticated simulation tool, SimStadt, developed by the HFT Stuttgart. The statistical data as well as the simulation tool played a pivotal role in the successful attainment of the objectives.

This research is funded by the German Federal Ministry of Economic Affairs and Climate Action (FKZ 03EN3051A). We would like to express our sincere gratitude for their support.

References

Arbeitsgemeinschaft der Vermessungsverwaltungen der Länder der Bundesrepublik Deutschland (AdV). (2018). *Dokumentation zur Modellierung der Geoinformationen des amtlichen Vermessungswesens - ALKIS-Objektartenkatalog DLKM.* ALKIS-Katalogwerk.

Behörde für Stadtentwicklung und Wohnen, Stadt Hamburg. (2019). *Wärmekataster Handbuch.* Stadt Hamburg.

Bundesregierung. (2023). *Gesetz für die Wärmeplanung und zur Dekarbonisierung der Wärmenetze (Wärmeplanungsgesetz - WPG)*. Retrieved from https://www.gesetze-im-internet.de/wpg/WPG.pdf

Cesium GS, Inc. (2024). *CesiumJS - 3D geospatial visualization for the web*. Retrieved from https://cesium.com/platform/cesiumjs

Coors, V. et al. (2021). *EnEff:Stadt- SimStadt 2.0 - Schlussbericht.* Hochschule für Technik Stuttgart.

Deutsche Institut für Normung e.V. (2018). DIN V 18599-10 | 2018-09. *Energetische Bewertung von Gebäuden - Berechnung des Nutz-, End- und Primärenergiebedarfs für Heizung, Kühlung, Lüftung, Trinkwarmwasser und Beleuchtung - Teil 10: Nutzungsrandbedingungen, Klimadaten*.

Dochev, I. et al. (2019). *Aggregating and visualizing urban heat demand using graph theory. A case study from Hamburg, Germany.* preprint version.

Donnelly, J. et al. (2023). A Physics-informed Neural Network Surrogate Model for

Tidal Simulations. *5th International Conference on Uncertainty Quantification in Computational Sciences and Engineering*, (pp. 836-844).

Google LLC. (2024). *Keras*. Retrieved from https://keras.io

IPCC. (2014). *Representative Concentration Pathways*. Retrieved from https://sedac.ciesin.columbia.edu/ddc/ar5_scenario_process/RCPs.html

IWU Institut für Wohnen und Umwelt. (2016). *Datenerhebung Wohngebäudebestand 2016*. Retrieved from https://wohngebaeudedaten2016.iwu.de

IWU Institut für Wohnen und Umwelt. (2021). *ENOB DataNWG: Forschungsdatenbank*. Retrieved from https://www.datanwg.de/forschungsdatenbank

Kahlenborn, W. et al. (2021). *Climate Impact and Risk Assessment 2021 for Germany - Summary.* Umwelt Bundesamt.

Meteotest. (2020). *Meteonorm Version 8*. Retrieved from https://meteonorm.meteotest.ch/meteonorm-version-8

Nytsch-Geusen, C. et al. (2016). *Nachhaltige und energieeffiziente Bestandsentwicklung von Stadtquartieren – Entwicklung eines Analyse- und Planungstools zur energetischen Bewertung und Sanierung von Stadtquartieren (Open eQuarter).* Stuttgart: Fraunhofer IRB Verlag.

Open Source Geospatial Foundation. (2024). *GeoServer is an open source server for sharing geospatial data*. Retrieved from https://geoserver.org

Paardekooper, S. et al. (2018). *Heat Roadmap Europe 4.* Aalborg University Denmark.

PostGIS PSC & OSGeo. (2024). *PostGIS*. Retrieved from PostGIS: https://postgis.net

Scikit-learn. (2024). *Scikit-learn Machine Learning in Python*. Retrieved from https://scikit-learn.org/stable

Senatsverwaltung für Stadtentwicklung, Bauen und Wohnen Berlin. (2024). *Geoportal Berlin / ALKIS Berlin (Amtliches Liegenschaftskatasterinformationssystem)*. Retrieved from https://fbinter.stadt-berlin.de/fb/wfs/data/senstadt/s_wfs_alkis?REQUEST=GetCapabilities&SERVICE=wfs

Sun, G., & Wang, S. (2019). A review of the artificial neural network surrogate modeling in aerodynamic design. *Proceedings of the Institution of Mechanical Engineers, Part G: Journal of Aerospace EngineeringVolume 233, Issue 16*, 5863-5872.

The PostgreSQL Global Development Group. (2024). *PostgreSQL: The World's Most Advanced Open Source Relational Database*. Retrieved from https://www.postgresql.org

Yao, Z. et al. (2018). 3DCityDB - a 3D geodatabase solution for the management, analysis, and visualization of semantic 3D city models based on CityGML. *Open Geospatial Data, Software and Standards*.

BauSIM 2024 in Wien
23. September – 26. September

Simulation, Realisierung und Monitoring einer nachträglichen Bauteilaktivierung als minimalinvasives Wärmeabgabesystem in der Sanierung

Tobias Hatt[1], Thomas Ramschak[2]

[1] *Energieinstitut Vorarlberg, Österreich, tobias.hatt@energieinstitut.at*
[2] *AEE - Institut für Nachhaltige Technologien, Österreich, t.ramschak@aee.at*

Kurzfassung

Die in den 50er Jahren errichteten Mehrfamilienhäuser einer erhaltenswerten Siedlung in Bludenz, sind baulich und bezüglich ihrer Wärmeversorgung weitestgehend im Originalzustand. Die Wohnungen werden mit Einzelraumlösungen beheizt, weisen hohe Energieverbräuche und deutliche Komfortdefizite auf. Im Jahr 2023 wurden zwei Pilotgebäude in hoher thermischer Qualität saniert (FFG Projekt SüdSan).

Da kein hydraulisches Wärmeabgabesystem vorhanden ist, werden hierfür verschiedene Wärmepumpengeeignete Lösungen mit Hilfe dynamischer Gebäude- und Anlagensimulation untersucht. Varianten sind Niedertemperaturheizkörper (NT-HK) sowie die thermische Aktivierung der Außenwände. Zweites erfolgt durch ein Flächenheizsystem auf der Außenseite der Bestandswände, welches dann mit einer Dämmfassade (U_{Wand}=0,13 W/(m²K)) überdeckt wird.

Damit der Wärmeübergang vom Heizmedium in den Raum korrekt abgebildet wird, wurde das eindimensionale Wandmodell der Gebäudesimulation mit Co-Berechnungen des zweidimensionalen Wärmeflusses kalibriert. Des Weiteren wurden in Parameterstudien verschiedene Regelstrategien und Konfigurationen untersucht.

Hauptvorteile der aktivierten Außenwand sind die minimalinvasive Installation im bewohnten Zustand und die Möglichkeit zu kühlen. Nachteile sind ein, gemäß Simulation 5 kWh/(m²a) höherer Endenergiebedarf für die Beheizung, die anspruchsvollere Regelbarkeit aufgrund der Trägheit des Systems und höhere Angebotskosten. Durch die niedrigen Vorlauftemperaturen haben NT-HK wiederum nicht gewohnt hohe Oberflächentemperaturen, was zu niedrigerer Nutzerakzeptanz führen kann. NT-HK sind allerdings bekannte Lösungen, was Bauablauf und Koordination vereinfacht.

In den zwei Gebäuden wurde je ein System umgesetzt und ab Spätwinter 2024 messtechnisch begleitet.

Abstract

The multi-family houses in a settlement worthy of preservation in Bludenz built in the 1950s are largely in their original condition both structurally and in terms of their heating supply. The apartments are heated with single-room solutions, had high energy consumption and significant comfort deficits. In 2023, two pilot buildings were renovated to a high thermal quality (FFG SüdSan project).

As no hydraulic heat delivery system is available, various solutions suitable for heat pumps are investigated with the use of dynamic building and plant simulation. Variants include low-temperature radiators (LT-R) and thermal activation of the exterior walls. The second is a surface heating system on the outside of the existing walls, which is then covered with an insulating (U_{Wall}=0,13 W/(m²K)) façade.

To ensure that the heat transfer from the heating medium into the room is correctly modelled, the one-dimensional wall model of the building simulation was calibrated with co-calculations of the two-dimensional heat flux. Furthermore, various control strategies and configurations were investigated in parameter studies.

The main advantages of the activated external wall are the minimally invasive installation when the building is occupied and the possibility of cooling. The disadvantages are a 5 kWh/(m²a) higher final energy demand for heating according to the simulation, poorer controllability due to the inertia of the system and higher costs. Due to the low flow temperatures, LT-R in turn do not have the usual high surface temperatures of radiators, which can lead to lower user acceptance. However, LT-R are familiar solutions, which simplifies the construction process and coordination.

One system was implemented in each of the two buildings and are now being monitored.

Einleitung/Ausgangslage

Die erhaltenswerte Südtiroler Siedlung in Bludenz/Vorarlberg wurde zwischen 1940 und 1962 errichtet und umfasst 397 Wohnungen in kleinen Mehrfamilienhäusern (MFH) mit durchschnittlich 6-9 Parteien.

Vor allem die in den Nachkriegsjahren errichteten Gebäude wurden in einem materialsparenden Niveau errichtet und sind baulich und bezüglich ihrer Wärmeversorgung weitestgehend im Originalzustand. Alle Wohnungen wurden mit Einzelraumlösungen beheizt, sei es mit Holz/Ölöfen oder direktelektrisch; sie wiesen hohe Energieverbräuche (180-200 kWh/(m^2_{WNF}a)) und deutliche Komfortdefizite auf. In Abbildung 1 sind gemessene Temperaturen vor der Sanierung dargestellt. Man kann die Unterschiede zwischen den einzelnen Wohnungen abhängig von der Beheizungsart erkennen. Grün beispielsweise ein ungeregelter Stückholzofen (19-29°C), blau ein geregeltes direkt elektrisches Heizsystem (22-23°C). Rot ein nicht beheizter Raum (14°C).

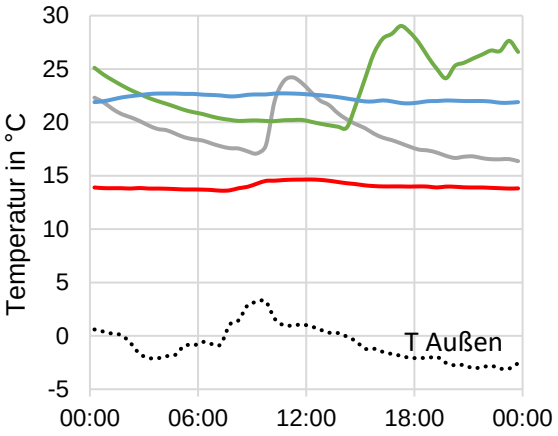

Abbildung 1: Gemessene Temperaturen vor der Sanierung (6.12.2022 in 4 Wohnräumen) Grün und grau: ungeregelt z.B. Stückholzofen, blau geregelt z.B. direkt elektrisch, rot nicht beheizt.

Im Jahr 2023 wurden zwei Pilotgebäude der Siedlung im Rahmen des österreichischen von der FFG geförderten Forschungsprojekts SüdSan in hoher thermischer Qualität saniert. Hierzu wurde neben Dämmung ($U_{Dach+Wand}$=0,13 W/(m²K)), Fenstern (U_g=0,6 W/(m²K)), Wärmepumpe (1xLuft, 1xSole) und Komfortlüftung mit Wärmerückgewinnung (WRG) das Dach jeweils südseitig vollflächig mit Photovoltaik (PV) belegt.

Hauptteil/Simulationsstudie zur nachträglichen Bauteilaktivierung

Da die Gebäude momentan kein hydraulisches Wärmeabgabesystem besitzen, werden verschiedene Wärmeabgabesysteme im Niedertemperaturbereich, die wärmepumpenoptimiert betrieben werden können, mit Hilfe dynamischer Gebäude- und Anlagensimulation in IDA ICE (EQUA, 2024) untersucht. Die Gebäude werden im bewohnten Zustand saniert, deshalb soll die Installation der Wärmeabgabesysteme minimalinvasiv erfolgen. Varianten sind Niedertemperaturheizkörper (NT-HK), Deckenheizung sowie die nachträgliche thermische Aktivierung der Außenwände. Zweites erfolgt durch ein wassergeführtes Flächenheizsystem (ähnlich Fußbodenheizung im Trockenbau) auf der Außenseite der Bestands-Außenwände, welche dann mit einer Dämmfassade (30 cm Dämmung, U_{Wand}=0,13 W/(m²K)) überdeckt werden (Abbildung 2).

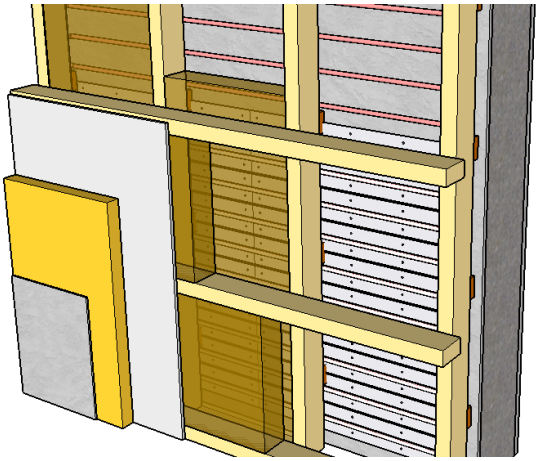

Abbildung 2: Schematischer Wandaufbau mit Bauteilaktivierung. Der Übergang vom Heizmedium an die Wand wird mit Wärmeleitblechen verbessert.

Solche Ansätze wurden zuvor in einigen Forschungsvorhaben untersucht und teilweise auch schon in der Praxis umgesetzt (Altgeld et al., 2010; Hackl et al., 2022; Hengel et al., 2020; Schmidt, 2019; Schweizer, 2021).

In den meisten Vorhaben wurde die aktivierte Wand zur Grundtemperierung eingesetzt und zur individuellen Regelung und zum Erreichen der gewünschten Temperaturen ein Zusatzheizsystem. Die Temperaturen der aktiven Schicht können so niedrig gewählt werden, dass die Wand die Transmissionswärmeverluste verringert bzw. kompensiert oder so hoch, dass die Verluste überkompensiert werden, so dass eine aktive Beheizung des Raumes stattfindet. Wie hoch die Auslegungstemperatur für den überkompensatorischen Betrieb sein muss, hängt unter anderem von der Heizlast, der Wärmeleitfähigkeit der Bestandswand, dem Wärmeübergang vom Fluid in die Wand, dem Wärmedurchlass der Dämmebene außerhalb der beheizten Schicht, der Regelung und dem Vorhandensein einer Zusatzheizung ab.

Simulationsmodell

Das Gebäude, ein MFH mit 9 Bestandswohnungen und zwei neuen im Dachgeschoß weist eine Energiebezugsfläche$_{PHPP}$ von 648 m² auf.

Zur Beurteilung der Funktionalität, Behaglichkeit und Energieeffizienz wurden Simulationsstudien mit der Software IDA ICE V5 durchgeführt. Das Gebäude wurde raumweise zoniert, die Belegung und interne Wärmequellen in Anlehnung an PHPP V10.5 (2023) angesetzt und die stündliche Auflösung nach SIA 2024 (2015) modelliert. Für die Jahressimulationen wurde ein Klimadatensatz in stündlicher Auflösung für den Standort mit der Software Meteonorm V8 (2021) generiert.

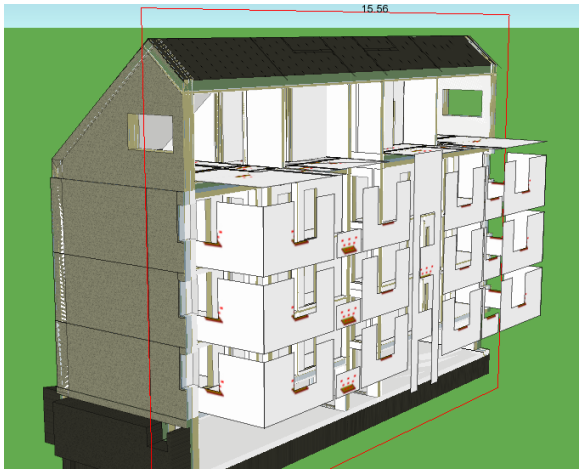

Abbildung 3: Darstellung der Geometrie der beheizten Layer (weiß) im Simulationsmodell. EG bis 2OG als aktivierte Außenwand, DG als Fußbodenheizung.

Das Wärmeabgabesystem wird als Flächenheizsystem im Modell abgebildet. Hierzu wird eine hydraulisch angebundene aktive Schicht im Wandmodell eingebracht. Das Wandmodell ist in 17 Teile diskretisiert, der aktive Layer liegt nach Teil 10 von innen. In Abbildung 3 ist der Layer der aktivierten Außenwand dargestellt. Für diesen Teil der Studie, mit Fokus auf das Wärmeabgabesystem, wurde die Wärmeerzeugung als vereinfachtes Modell einer Außenluft Wärmepumpe (COP: 4,0 bei 7/45) abgebildet. Im Modell wurde eine Komfortlüftung mit WRG implementiert. Warmwasseranwendung, Haushaltsstrom und PV-Stromerzeugung wurde für diesen Teil der Studie nicht berücksichtigt.

Die Wärmeabgabeleistung der aktivierten Außenwand hängt von verschiedenen Parametern ab. Diese sind unter anderem die Größe der aktivierten Fläche, der U-Wert der Bestandswand, der Wärmeübergang vom Fluid in die Wand, Vorlauftemperatur, Durchfluss und Regelung. Damit diese Parameter bestimmt werden können, wurde eine Parameterstudie mit 2310 Varianten durchgeführt.

Modellimitationen und Vereinfachungen: 1.) Das verwendete Wandmodell in IDA ICE ist ein eindimensionales Modell, welches keine Querverteilung (2D und 3D) abbildet. Dadurch können Verluste der aktivierten Außenwand z.B. über die Wand in den Keller/Erdreich mit dem Wandmodell nicht berechnet werden. Damit diese Verluste aber im Modell vereinfacht integriert sind, wird die Überdämmung der Heizfläche um 10% verschlechtert. 2.) Spülkästen, Badewannen und Vorsatzschalen in den Bädern werden als 1 cm EPS Dämmung angenähert. Annahme 1.) und 2.) wurden anhand dynamischer Wärmebrückenberechnungen des Projektpartners UIBK (Universität Innsbruck, Institut für Konstruktion und Materialwissenschaften, Arbeitsbereich für Energieeffizientes Bauen, (Magni, Ochs)) getroffen. 3.) Die Geometrie der Flächenheizelemente wird in der Software mit Innenmaßen modelliert. Somit ist die Fläche der Heizelemente in Realität um Wand- und Deckendicken größer. In der Umsetzung wurden Sperrbereiche um die Fenster und Wandecken zur Befestigung der Holzkonstruktion definiert. Die beiden Effekte gleichen sich geometrisch in etwa aus.

Wärmeübergang Heizfluid zur Wand

Damit der Wärmeübergang vom Heizmedium in den Raum korrekt abgebildet wird, wurde das eindimensionale Wandmodell der Gebäudesimulation mit einer zweidimensionalen Wärmeflussberechnung kalibriert. Diese Methodik ist ausführlich in (Hengel et al., 2020) beschrieben.

Der Wandaufbau der Bestandswand hat bei der thermischen Aktivierung einen Einfluss auf die Heizleistung, da hierdurch die Wärmeleitung vom Heizmedium an den Innenraum beeinflusst wird. Die Heizleistung und der U-Wert weisen einen annähernd linearen Zusammenhang auf. Der U-Wert wurde mit in situ Messungen und 2D Wärmestromberechnungen bestimmt. Der gemessene U-Wert in Steinmitte (ohne Mörtelfuge) beträgt 1,58 W/(m²K). Die Messungen korrelieren mit den Rechenwerten und es wird von einem U-Wert von 1,7-1,8 W/(m²K) ausgegangen.

Nicht nur die Wärmeleitfähigkeit der Bestandswand beeinflusst die Wärmeabgabeleistung, sondern auch der Wärmeübergang vom Heizmedium zur Wand. Ein formschlüssig eingefasstes Rohr z.B. in einer Putzschicht weist analog zur Fußbodenheizung im Estrich einen guten Übergang auf. Lose aufgelegte Rohre mit Luftspalt zur Bestandswand einen schlechten. Dieser Übergang wird in dem verwendeten eindimensionalen Wandmodell in der Simulation in IDA ICE nicht detailliert mit den verschiedenen Einflussgrößen abgebildet, sondern vereinfacht als heat transfer

coefficient (HTC) beschrieben. Dieser beinhaltet folgendes:

- Verlegeabstand der Rohrleitungen
- Wärmeübergang vom Fluid zum Rohr
- Wärmedurchlasswiederstand des Rohres
- Wärmeübergangswiederstand vom Rohr zur nächsten Wandschicht.

Die Fassade sollte ursprünglich als fertiges Element inklusive der Wärmeabgabefläche installiert werden. Deshalb und wegen des Risikos des nachträglichen Anbohrens der Leitungen sowie höheren abgeschätzten Kosten wurden diese nicht eingeputzt. Beim Pilotgebäude ist die Bestandswand mit einem groben Putz versehen, deshalb das Problem, dass die Heizungsrohre nicht formschlüssig aufgebracht werden können wie z.B. bei einer glatten Stahlbetonwand. In den vorhergenannten Studien wurden nur glatte Wände mit kleinen Luftholräumen untersucht (Hengel et al., 2020). Deshalb wird in einer Co-Berechnung für die grob verputzte Bestandswand der HTC Wert ermittelt und nicht aus der Literatur übernommen. Mit 2D Wärmestrombe-rechnungen (HTflux) für verschiedene Varianten wird die Wärmeabgabe an der Wandinnenseite ermittelt. Ziel ist es, den HTC Wert für die Simulationen in IDA ICE zu ermitteln und die Notwendigkeit von Wärmeleitblechen zu untersuchen. In einer Parameterstudie mit 100 Varianten in IDA ICE wurde für das Wandmodell der HTC-Wert von 0,5-35,0 W/(m²K) variiert und Wärmeabgabe an der Wandinnenseite ermittelt. Diese Wärmeabgabe kann dann mit den 2D Wärmebrückenberechnungen abgeglichen und der HTC Wert der jeweiligen Lösung ermittelt werden.

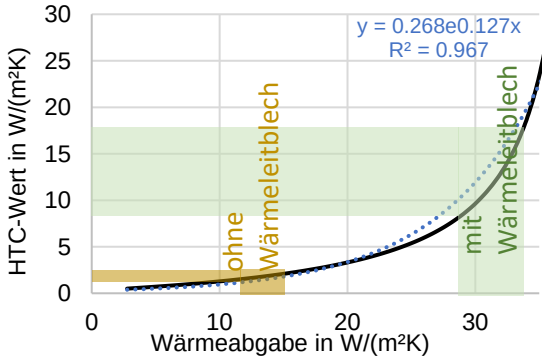

Abbildung 4: Zusammenhang zwischen HTC-Wert und Wärmestrom an der Innenoberfläche der Außenwand. Grüner Bereich mit Wärmeleitblechen, Orange ohne. (Ti=22°C, Ta= -10°C, Mittlere Fluidtemperatur: 37,5°C $U_{Bestandswand}$=1,35 W/(m²K)).

Abbildung 4 zeigt den Zusammenhang zwischen HTC-Wert und Wärmestrom an der Innenoberfläche der Außenwand. Der Zusammenhang lässt sich mit einer Exponentialfunktion annähern. Durch diesen exponentiellen Zusammenhang erkennt man, dass bei niedrigen HTC-Werten dieser Wert einen hohen Einfluss auf die Wärmeabgabeleistung des Systems hat. Bei einem HTC-Wert von 0,5-5 W/(m²K) nimmt die Abgabeleistung von 3 auf 25 W/(m²K) zu. Im Intervall des HTC von 5-10 W/(m²K) nimmt die Abgabeleistung nur noch von 25 auf 30 W/(m²K) zu. Bei dem weiteren HTC Bereich von 10-25 W/(m²K), also 15 W/(m²K) Unterschied statt vorher 5 W/(m²K), nimmt die Abgabeleistung nur noch von 30 auf 36 W/(m²K) zu. Dies zeigt, dass die Abgabeleistung mit Wärmeleitblechen nur unwesentlich geringer sein wird, als eine formschlüssige Lösung im Putzbett (HTC ca. 30 W/(m²K)). Diese Werte ordnen sich auch von der Größenordnung in die publizierten Werte aus (Hengel et al., 2020) ein.

Es zeigt sich, dass bei einer Montage ohne zusätzliche Wärmeleitbleche die Wärmeabgabe um den Faktor 2,5 niedriger liegt. Für die umgesetzte Lösung, bei der eine formschlüssige Anbringung der Wärmeleitbleche vorausgesetzt werden kann, wird mit einem HTC Wert von 18,7 W/(m²K) in den weiteren Simulationen gerechnet.

Wie hoch die benötigte Wärmeabgabeleistung der Wand sein muss, hängt von der Heizlast des Raumes und der zur Verfügung stehenden Wärmeabgabefläche (nächster Unterpunkt) ab.

Wärmeabgabe an Raum

Bei einer Fußbodenheizung nimmt die Wärmeabgabefläche linear zur Raumgröße zu. Bei der Wandheizung hängt das Verhältnis Wärmeabgabefläche (Außenwand) zur Raumgröße von verschiedenen Faktoren ab:

- Anzahl Außenwänden (z.B. Eckräume)
- Raumgeometrie (z.B. schmal und lang)
- Raumhöhe
- Fensterflächenanteil

Bei Zwischengeschoßen ist die Größe der Wärmeabgabeflächen weniger kritisch, da Heizlast und Außenwandfläche meist korrelieren. Dachgeschoß und EG sind oft kritischer, da sie höhere Transmissionswärmeverluste aufweisen.

Im Fall des Eckraums (Abbildung 5 links) können somit unter den gegebenen Randbedingungen bei fast gleicher Außenwandfläche zu Fußbodenfläche etwa 25 W/m^2_{Boden} eingebracht werden. Dieser Wert entspricht der Heizlast eines thermisch gut sanierten Gebäudes. Im Falle des schmalen Mittelraums (rechts) ist das Verhältnis Außenwandfläche/Fußbodenfläche nur etwa 0,4 wodurch nur etwa 10 W/m^2_{Boden} eingebracht werden können. Dieser niedrige Wert entspricht einem Neubau in Passivhausstandard.

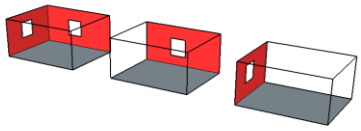

Heizflächen [m²]:	19,6	11,0	8,6
Heizfläche/ Fußboden :	1,0	0,6	0,4
Heizleistung: [W/m²Boden]	25	15	10

Abbildung 5: Wärmeabgabefläche der Wandheizung im Verhältnis zur Fußbodenfläche verschiedener Räume (4 x 5 m = 20 m²; Höhe 2.4 m, Abgabeleistung Wandheizung 25 W/m²Wand).

Das bedeutet, dass Eckzimmer mit niedrigen Heizlasten (Zwischengeschoße) ohne Wärmeleitbleche oder mit größeren Verlegeabständen ausgeführt werden könnten, alle anderen Zimmer, welche nur eine Außenwand haben, aber mit Wärmeleitblechen. In der Praxis wurden zur Vereinfachung des Bauablaufes alle Wände mit 12,5 cm Verlegeabstand und Wärmeleitblechen ausgeführt.

Ein weiterer Punkt, welcher die Wärmeabgabe der aktivierten Außenwand an den Innenraum beeinflusst, ist die Innenoberfläche bzw. bauliche Maßnahmen oder Möblierung. Am Beispiel der Badezimmer in dem Pilotgebäude ist der sichtbare, bzw. zugängliche Teil der Außenwand, welcher ungehindert Wärme an den Innenraum abgeben kann, durch Spülkasten (Kaltwasser), Badewanne und Vormauerung stark eingeschränkt. Auch große Einbauschränke behindern die Wärmeabgabe wesentlich. Die Transmissionswärmeverluste durch die Wand werden aber dennoch kompensiert und somit beispielsweise die Schimmelbildung an vorher kalten Wände hinter Schränken reduziert.

Regelung

Es wurden im Vorfeld verschiedene Regelstrategien mit Hilfe der Gebäude und Anlagensimulationen untersucht, wobei der Fokus dieser Arbeit nicht auf der Regelung liegt. Die Strategien sind nachfolgend aufgelistet, sortiert nach zunehmender Komplexität und damit assortiert zunehmenden Kosten:

1. Gesamtes Gebäude als ein Regelkreis, außentemperaturgeführt, Raumdifferenzierung über raumweise fix eingestellten Durchfluss und raumweise differenziertem Verlegeabstand.
2. Gebäude in 4 Regelkreise unterteilt, OGsNord-, OGsSüd, EGNord, EGSüd, außentemperaturgeführt, Raumdifferenzierung über raumweise fix eingestellten Durchfluss und raumweise differenziertem Verlegeabstand.
3. Einzelraumregelung mit jeweils einem eigenen Heizkreis pro Raum (37 Heizkreise)
4. In einer Masterarbeit an der Fachhochschule Vorarlberg werden derzeit prädiktive Regelstrategien untersucht (Roman Hörner, 2024). Ergebnisse liegen noch nicht vor.

Die nötige Vorlauftemperatur wird nahezu unabhängig der Regelungsart von den kritischen Räumen bestimmt und so ausgelegt, dass diese in der Heizphase konstant beheizt werden. Diese liegen nordseitig im EG neben dem Treppenhaus. Damit die Vorlauftemperatur gesenkt werden kann, werden in den zwei kritischen Räumen zur Spitzenlastabdeckung zusätzlich direkt elektrische Heizelemente vorgesehen, ebenfalls in den Bädern (24°C Solltemperatur, geringe Außenwandfläche).

Die Ergebnisse der Simulationen der einzelnen Regelstrategien sind wie folgt:

zu 1. Südräume und Zwischengeschoße weisen tendenziell höhere Temperaturen auf, da dort zwar weniger Leistung installiert ist, aber trotzdem oft keine Wärme benötigt wird, während die Nordräume noch beheizt werden müssen. Diese können bei dieser Regelungsart aber nicht getrennt geschalten werden.

zu 2. Temperaturunterschiede zwischen den Räumen (Nord-Süd) nehmen ab. Einzelne Räume wie Schlafzimmer können aber im Vergleich zur Einzelraumregelung nicht abgeschaltet werden.

zu 3. Die Temperaturverteilung über das Gebäude vereinheitlicht sich. Einzelne Räume können abgeschaltet werden. Eine schwach schwankende Temperaturkurve wie bei Heizkörpern kann trotz Einzelraumreglern durch die Trägheit nicht erreicht werden. Robuster gegen Änderungen in der Nutzung (höhere oder niedrigere Solltemperaturen) als vorherige. Technisch aufwendiger, damit auch teurer.

Wie beschrieben, liegt der Fokus dieses Projekts nicht auf den verschiedenen Regelstrategien. Es sollte aber eine Regelung umgesetzt werden, welche den bestmöglichen Nutzerkomfort bei diesem trägen System ermöglicht und auch flexibel angepasst werden kann. Deshalb wird eine Einzelraumregelung umgesetzt, die in die zentrale Gebäudeleittechnik eingebunden ist. Durch

diese hardwaremäßige Einbindung kann zu einem späteren Zeitpunkt auch eine prädiktive Regelung in der Software umgesetzt werden.

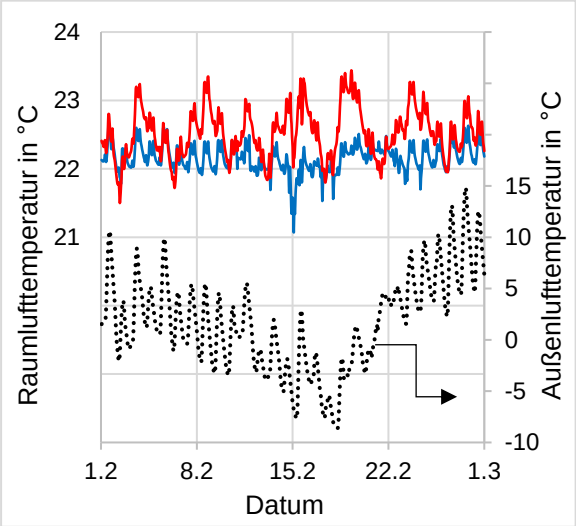

Abbildung 6: Raumlufttemperaturen mit Einzelraumregelung im Februar in Blau für einen Nordraum und Rot für einen Südraum. Schwarz gepunktet auf der Sekundärachse die Außenlufttemperatur.

In Abbildung 6 sind die Raumlufttemperaturen mit Einzelraumregelung im Monat Februar dargestellt. Schwarz gepunktet ist auf der Sekundärachse die Außenlufttemperatur dargestellt. Man erkennt, dass die operative Temperatur im Nordraum (blau) relativ konstant bei Sollwert von 22,5°C liegt. Die Einzelraumregelung ist hier konstant „An“ und die Vorlauftemperatur variiert mit der Außentemperatur. Im Südraum (rot) schwankt die operative Temperatur bei Einzelraumregelung zwar stärker, aber immer innerhalb des Komfortbereich Klasse I nach EN 16798-1. Die Regelung wechselt bei Unterschreitung von 22°C auf „An“ und bei Überschreitung von 23°C auf „Aus“. Durch die Trägheit des Systems dauert dieser Aufheizzyklus ca. 25-30 Std. Dann überschwingt die Temperatur etwa 10-15 Std. und fällt dann in 24-36 Std. wieder unter die Heizgrenze ab.

Die Ergebnisse zeigen, dass die aktivierte Außenwand mit Einzelraumregelung den Komfortbereich einhält, aber eine schnelle Änderung der Raumtemperatur, z.B. bei kälteempfinden im Krankheitsfall, nicht realisierbar ist.

Die Vorlauftemperatur (Heizkurve) wurde in einer Parameterstudie ermittelt und liegt in der Heizperiode im Mittel bei etwa 32-33°C. Bei -10°/46°C, und bei +10°/28°C).

Vergleich mit Niedertemperaturheizkörpern (NT-HK)

Eines der beiden Pilotgebäude wird mit aktivierter Außenwand beheizt, das andere mit Niedertemperaturheizkörpern. Damit beide Systeme, vor allem in Hinblick auf die Energieeffizienz, verglichen werden können, werden beide Systeme am größeren Gebäude mit Hilfe von Gebäude und Anlagensimulation untersucht. Jeder NT-HK hat ein eigenes Thermostat, also eine Einzelraumregelung. Bei der aktivierten Außenwand wird ebenfalls die Einzelraumregelung zum Vergleich herangezogen. In der Variante „aktivierte Außenwand“ werden in den zwei kritischen Räumen zur Spitzenlastabdeckung zusätzlich direkt elektrische Heizelemente vorgesehen, ebenfalls in den Bädern, da in diesen die 24°C Solltemperatur (2x30 Minuten) wegen der geringen Außenwandfläche nicht erreicht werden (siehe auch Punkt Ergebnisanalyse und Diskussion).

Die Heizkurve für die NT-HK wurde in der Simulation mit -10°/40° und 0°/35° ermittelt und liegt damit etwas niedriger als bei der Wandheizung. In Tabelle 1 sind die Energie- und Strombedarfe beider Systeme gegenübergestellt.

Tabelle 1: Vergleich der Beheizung über aktivierte Außenwände mit Niedertemperaturheizkörpern. Alle Werte in kWh/(m²a), Raumsolltemperatur 22.5°C, Bäder 24°C (2x30 Minuten), EBF: 648 m².

	Aktivierung Außenwand (+ el.direkt)	Nieder-temperatur Heizkörper
Wärme an Raum/Nutzenergie	39,0	37,1
Verteil- und Speicherverluste	7,3	6,3
Strom Wärmepumpe	13,3	13,3
Strom IR Paneele	4,5	0.0
Strom Pumpen	1,5	1,0
Summe Strom	**19,3**	**14,3**

Beide Systeme weisen in Kombination mit der guten Hüllqualität für ein saniertes Bestandsgebäude niedrige Endenergiebedarfe auf (Strombedarf: 14,3 – 19,3 kWh/(m²a)). Zusammengefasst ergibt der Vergleich folgende Ergebnisse:

- Die Tendenz, dass Räume im Winter wärmer werden als die Solltemperatur (höhere mittlere Raumtemperatur), ist bei den flinken NT-HK geringer als bei der trägen Außenwandaktivierung. Dadurch ist die Nutzenergie, welche an

den Raum abgegeben wird, ebenfalls um 1,9 kWh/(m²a) geringer.
- Durch zusätzliche Verluste der wärmeren Außenwand, höhere Verteilverluste durch mehr Anbindeleitungen, höherem Pumpenstrombedarf und die zusätzlichen elektrischen Heizelemente, ist der gesamte Strombedarf bei der aktivierten Außenwand um 5 kWh/(m²a) höher (siehe auch Kapitel Diskussion).
- Die Angebotskosten sind bei der aktivierten Außenwand mit 163 €/m²$_{WNF}$ höher als bei den NT-HK mit 133 €/m²$_{WNF}$ (inkl. Verteilung; bei Wandheizung inkl. Fußbodenheizung im Dachgeschoß und inkl. Infrarotpaneele).

Umsetzung und Diskussion

Bei vorhergenanntem Vergleich liegt die aktivierte Außenwand im Punkt Energieeffizienz 5 kWh/(m²a) höher, wobei 4,5 kWh/(m²a) auf die direkt elektrischen Zusatzheizelemente vor allem in den Bädern entfallen. Würde man diese hydraulisch ausführen, wäre der Unterschied etwa 2 kWh/(m²a). Die Zusatzheizungen sind bei Übertragung auf anderen Gebäude eventuell nicht immer notwendig, bei innenliegenden Bädern und 24°C Solltemperatur aber wahrscheinlich. Hydraulische Lösungen sind teurer und nicht minimalinvasiv, deshalb wurden hier direkt elektrische Elemente geplant. Aufgrund der Rückmeldungen der Bewohner im Januar 2024 über ausreichend hohe Temperaturen in den Bädern (22-24°C) wurde vorerst darauf verzichtet die zusätzlichen direkt elektrischen Heizelemente einzubauen.

Bis Mitte Februar 2024 wurden beide Gebäude provisorisch mit konstanter Vorlauftemperatur, ohne Einzelraumregler und teilweise mit Elektro-Heizpatronen betrieben, da die Wärmepumpen und Gebäudeleittechnik baulich noch nicht umgesetzt waren. Seit Februar 2024 sind beide Systeme mit den vordefinierten Einstellungen und Reglern in Betrieb genommen worden. Deshalb gibt es keine belastbaren Messergebnisse zu Energieverbräuchen aus dem ersten Winter.

In Abbildung 7 sind die gemessenen Temperaturen vom 14.-21.2.2024 in zwei Wohnräumen in dem Gebäude mit aktivierter Außenwand dargestellt. Da noch kein längerer Zeitraum mit aktiver Regelung vorhanden ist, können diese Werte noch nicht direkt mit den Aussagen aus Abbildung 6 verglichen werden. Es kann aber festgestellt werden, dass sich die einzelnen Räume im Bereich von etwa 20-22°C befinden, vermutlich während des Lüften auch kälter. Die Raumthermostateinstellung (Solltemperatur) ist hierbei aber nicht bekannt. In Rot ist ein Südraum dargestellt, welcher die Regelcharakteristik mit der hohen Trägheit des Systems aus der Simulation qualitativ bestätigt. Die Ausschläge nach unten (18°C) sind vermutlich durch Fensterlüftung bedingt und unabhängig vom Wärmeabgabesystem. In Blau ein Nordraum bei dem die Regelung konstant „An“ ist. Die vollständige messtechnische Auswertung erfolgt ab dem Winter 2024/2025. Im Vergleich zu den stark schwankenden Temperaturen vor der Sanierung aus Abbildung 1 sind die gemessenen Temperaturen nach der Sanierung in Abbildung 7 deutlich uniformer und gleichmäßiger über die zwei Wohnungen verteilt.

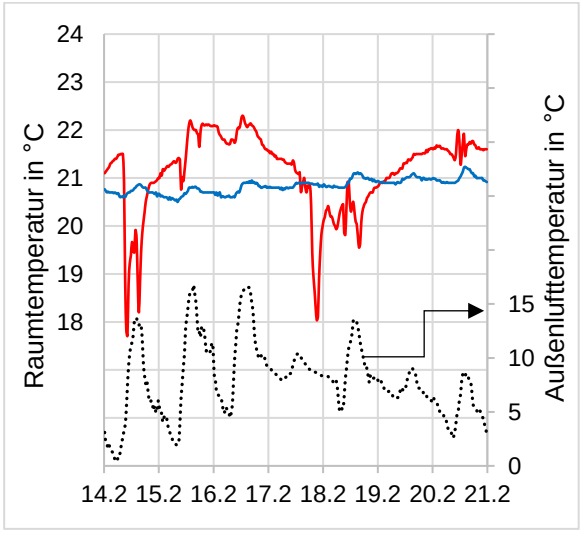

Abbildung 7: Gemessene Temperaturen vom 14.-21.2.2024 in 7 Wohnräumen in dem Gebäude mit aktivierter Außenwand.

Zusammenfassung und Ausblick

Beide Systeme lassen in Kombination mit einer thermisch hohen Hüllqualität niedrige Energiebedarfe und komfortable Temperaturen erwarten. Eine gute Überdämmung (U_{Wand} 0,13 W/(m²K)) ist für die Effizienz der aktivierten Außenwand essentiell. Hauptvorteil im Vergleich zu NT-HK ist, dass in den bewohnten Wohnungen kein Eingriff stattfindet. Auch eine Kühlung ist mit dem System möglich und es kann, wie in anderen Arbeiten untersucht, die Energieflexibilität des Gebäudes erhöht werden (Gumhalter et al., 2022). Nachteil sind der höhere Energiebedarf für die Beheizung, die schlechtere Regelbarkeit aufgrund der Trägheit des Systems und höhere Kosten. Durch die niedrigen Vorlauftemperaturen haben die NT-Heizkörper als Nachteil niedrige Oberflächentemperaturen, was zu niedrigerer Nutzerakzeptanz führen kann.

Damit sich eine hohe Nutzerakzeptanz beider Systeme einstellt, werden die Mieter auf die Be-

sonderheiten wie Trägheit bei der aktivierten Außenwand oder niedrige Oberflächentemperaturen bei den NT-HK hingewiesen.

Solange es für die aktivierte Außenwand noch keine ausreichende Praxiserfahrung gibt, ist es sinnvoll, solche Systeme zu simulieren und im Vorfeld eine Analyse der Bestandswand durchführen, da der Bestands-U-Wert einen hohen Einfluss auf die Wirksamkeit und Effizienz hat. Ebenfalls als Nachteil wurde im Projekt die Komplexität in der Ausführung gesehen, was am Prototypcharakter liegen kann. Es gibt Schnittstellen zwischen den Gewerken HLS und Fassadenbau, auch in den Verantwortlichkeiten, welche gut koordiniert sein müssen und es wird empfohlen dies frühzeitig im Projekt abzuklären. NT-Heizkörper hingegen sind in der Umsetzung ein Standardvorgehen.

Abbildung 8: Aufgebrachte Flächenheizung (System CEPA) mit Wärmeleitblechen auf der Bestandswand mit darüberlegender Dämmung.

Es wird in den beiden Mustergebäuden je ein Wärmeabgabesystem umgesetzt und messtechnisch untersucht. Dieses System der Bauteilaktivierung mit Wärmeleitblechen (System CEPA), zu sehen in Abbildung 8, wird in einem der Mustergebäude erstmals in der Sanierung als alleiniges Wärmeabgabesystem eingesetzt.

Danksagung

Das Projekt SüdSan (Sanierung Südtiroler Siedlung) wird unter der Nr. 889527 gefördert durch: FFG Österreich, Nachhaltige Sanierung, Demonstrationsprojekt (2022-2024) Energie der Zukunft, SdZ 8. Ausschreibung KP 2021. Die Inhalte liegen in der alleinigen Verantwortung der Autoren und spiegeln nicht notwendigerweise die Ansichten des Fördergebers wieder.

Literatur

Altgeld, H., Mahler, M., Cavelius, R., Horst, J., Dürnhofer, A., & Boettcher, J. (2010). Energieeinspar-und Kostensekungspotenziale durch den Einsatz von außen liegenden Wandheizungssystemen (aWH) für Niedertemperaturanwendungen. *Endbericht Projekt LEXU, Fkz*, *327370*.

EQUA. (2024). *IDA Indoor Climate and Energy (IDA ICE)* (5.0) [Software]. EQUA Simulation AB. https://www.equa.se

Gumhalter, M., Ramschak, T., & Hengel, F. (2022, April). Flexibility potentials of prefabricated facade elements with integrated active layer. *ISEC Conference proceedings*. ISEC 2022, 2nd International Sustainable Energy Conference, Graz. https://doi.org/10.32638/isec2022

Hackl, L.-M., Deralla, A., & Holzer, P. (2022). *Große Neugasse; Sanierung und Heizungsumstellung mit fassadenintegrierter Bauteilaktivierung* (S. 16). Bundesministerium für Klimaschutz, Umwelt, Energie, Mobilität, Innovation und Technologie (BMK). https://www.klimaaktiv.at/dam/jcr:6185a3ac-4e50-47bc-800f-9da8b49ad6d2/37_Grosse-Neugasse_2022-10-28.pdf

Hengel, F., Ramschak, T., Gumhalter, M., & Venus, D. (2020, September 23). Showing new concepts with thermal activated prefabricated Façades for retrofitting residential buildings. *BauSIM 2020*. BauSIM 2020.

Meteotest. (2021). *Meteonorm* (Version 8) [Software]. Meteotest. www.meteotest.ch

Passivhaus Institut. (2023). *PHPP 10.5 Passivhausprojektierungspaket* (10.5) [Software]. Passivhaus Institut. http://www.passiv.de

Roman Hörner. (2024). *Auswirkung der Regelstrategie auf die Energieeffizienz eines Bestandsgebäudes mit nachträglicher Bauteilaktivierung der Bestandswand* [Masterarbeit Fachhochschule Vorarlberg].

Schmidt, C. W. (2019). *Feldtest und dynamische Simulation der außenliegenden Wandtemperierung* [PhD Thesis]. University of Luxembourg, Luxembourg.

Schweizer, P. (2021). *Wohnen findet Stadt! - Smarte Modernisierung und Umsetzung am Beispiel der Burgfriedsiedlung Hallein* (S. 111) [Publizierbarer Endbericht]. Paul Schweizer Architekt. https://smartcities.at/wp-content/uploads/sites/3/BGR5_2021_Wohnen-findet-Stadt_Endbericht.pdf

SIA 2024:2015 (Hrsg.). (2015). *Raumnutzungsdaten für die Energie-und Gebäudetechnik*. Schweizerischer Ingenieur- und Architektenverein.

BauSIM 2024 in Wien
23. September – 26. September

Simulativer Vergleich der thermischen Bedarfsabschätzung eines Einfamilienhauses: Unterschiede zwischen der AixLib und EnergyPlus für ein High-Order-Modell

Tobias Spratte[1], David Jansen[1], Laura Maier[1] und Dirk Müller[1]

[1]*RWTH Aachen University, E.ON Energy Research Center, Institute for Energy Efficient Buildings and Indoor Climate*

Kurzfassung

Im IBPSA Project 1 wurde neben der Kernbibliothek Modelica-IBPSA auch die Bibliothek AixLib zur quelloffenen Modellierung von Gebäudeenergiesystemen mit Modelica entwickelt. Verglichen mit dem speziell für die energetische Gebäudesimulation entwickelten quelloffenen Programm EnergyPlus ermöglichen die Modelica-Bibliotheken eine physikalisch realistischere Modellierung der Regelung moderner Anlagentechnik. In EnergyPlus hingegen ist die Wärmeübertragung durch die Gebäudehülle mit einem höheren Detailgrad modelliert. Fraglich ist, in welchem Ausmaß die in der AixLib getätigten Vereinfachungen die Ergebnisse einer energetischen Gebäudesimulation beeinflussen.
In dieser Studie werden die erforderliche Heizleistung und der Heizbedarf eines Einfamilienhauses mittels Jahressimulationen des in der AixLib enthaltenen High-Order-Gebäudemodells des Einfamilienhauses und eines EnergyPlus-Gebäudemodells des Einfamilienhauses ermittelt und verglichen. Die Ergebnisse des AixLib-Gebäudemodells zeigen einen nach oben verschobenen Verlauf der erforderlichen Heizleistung gegenüber den Ergebnissen des EnergyPlus-Gebäudemodells. In der kalten Jahreshälfte wird mit dem AixLib-Gebäudemodell ein etwa 1 %, in der warmen Jahreshälfte ein etwa 31 % und im gesamten Jahr ein etwa 2 % höherer Heizbedarf berechnet. Einen großen Einfluss auf die hohe prozentuale Abweichung in der warmen Jahreshälfte hat die in EnergyPlus umgesetzte zusätzliche Diskretisierung der einzelnen Wandschichten, die im Sommer zu höheren Oberflächentemperaturen der Außenwände führt. Aufgrund des geringen Heizbedarfs in der warmen Jahreshälfte ist der Einfluss der hohen prozentualen Abweichung in dieser Periode auf die prozentuale Abweichung im Jahresheizbedarf gering.

Abstract

In the IBPSA Project 1, the core library Modelica-IBPSA as well as the AixLib library were developed for open source modeling of building energy systems using Modelica. Compared to the open source tool EnergyPlus which was developed specifically for building performance simulation, the Modelica libraries allow for a more physically realistic modeling of the control of modern HVAC systems. However, the heat transfer through the building envelope is modeled with a higher level of detail in EnergyPlus. It is unclear to what extent the simplifications made in the AixLib influence the results of a building performance simulation.
In this study, the heat load and the heat demand of a single-family house are computed and compared using annual simulations of the high-order building model of the single-family house contained in the AixLib and an EnergyPlus building model of the single-family house. The results of the AixLib building model show an upward shift in the heat load compared to the results of the EnergyPlus building model. In the cold period of the year, the heat demand is calculated to be about 1 % higher, in the warm period about 31 % higher and in the whole year about 2 % higher. A major influence on the high percentage deviation in the warm period of the year is the additional discretization of the individual wall layers implemented in EnergyPlus leading to higher surface temperatures of the exterior walls in summer. Due to the low heat demand in the warm period of the year, the high percentage deviation occurring during this period has little influence on the annual percentage deviation.

Einführung

In der Europäischen Union entfallen etwa 36 % der jährlichen Treibhausgasemissionen auf den Gebäudesektor (European Commission 2020). Um das Ziel der Klimaneutralität im Gebäudesektor bis 2045 zu erreichen, ist eine Modernisierung dieses Sektors erforderlich. Maßnahmen an der Gebäudehülle, wie die Dämmung der Fassade oder der Austausch von Fenstern, können die Heizlast eines Gebäudes reduzieren. Eine Reduzierung der Heizlast ermöglicht eine gegenüber dem bestehenden Energiesystem kleinere Auslegung eines modernisierten Energiesystems. Zur Abschätzung der Heizlast sowie des Heizbedarfs eines Gebäudes können statische Berechnungsmethoden nach DIN EN 12831 (Deutsches Institut für Normung e. V. 2017) oder DIN V 18599 (Deutsches Institut für Normung e. V. 2018) verwendet werden. Durch die Standardisierung der Berechnung wird eine hohe Vergleichbarkeit der Ergebnisse gewährleistet (Jansen et al. 2022). In der Realität sind Gebäude schwankenden Einflüssen wie Wetterrandbedingungen ausgesetzt, die die erforderliche Heizleistung des Gebäudes und deren zeitliche Änderung beeinflussen. Zur Maximierung der Energieeffizienz eines Gebäudes muss ein Energiesystem gewählt werden, das die erforderliche Heizleistung ganzjährlich mit möglichst hoher Effizienz bereitstellt. Dynamische energetische Gebäudesimulationen können im Gegensatz zu den statischen Berechnungsmethoden die zeitlich variierenden Randbedingungen berücksichtigen und somit die erforderliche Heizleistung des Gebäudes ganzjährlich abschätzen. Damit ist die dynamische energetische Gebäudesimulation ein wertvolles Werkzeug für die ökonomische und ökologische Bewertung verschiedener Modernisierungsmaßnahmen und für die Optimierung von Gebäudeenergiesystemen (Hensen & Lamberts 2011, Albers 2017).

Die Gebäudemodellierung kann nach dem physikalischen und nach dem datenbasierten Ansatz erfolgen. Beim datenbasierten Ansatz wird eine Beziehung zwischen Eingabegrößen und Ausgabegrößen mittels Messdaten erlernt. Beim physikalischen Ansatz wird diese Beziehung nach den Grundsätzen der Physik, beispielsweise mittels Massen- und Energiebilanzen, modelliert. Zudem wird das Gebäude umfassend parametriert. Der physikalische Ansatz benötigt keine Realdaten und bietet den Vorteil einer besseren Nachvollziehbarkeit zwischen Eingabegrößen und Ausgabegrößen (Chen et al. 2022). Die physikalische Gebäudemodellierung kann mit unterschiedlichem Detailgrad umgesetzt werden. Bei einer Modellierung mit geringem Detailgrad (ROM: Reduced Order Model) werden typischerweise thermische Zonen und Gebäudeelemente (Außenwände, Innenwände, Fenster, etc.) zu Kapazitäten aggregiert. Dieser Ansatz ist sinnvoll, wenn die Rechenleistung, die Rechenzeit oder die verfügbare Zeit zur Implementierung des Modells begrenzt sind (Jansen et al. 2022). Bei einer Modellierung mit hohem Detailgrad (HOM: High Order Model) werden üblicherweise keine Aggregationen der genannten Komponenten vorgenommen. Die dynamische energetische Simulation eines HOMs ermöglicht eine höhere Genauigkeit der Ergebnisse.

Zwei häufig verwendete Programme für die dynamische energetische Simulation physikalischer Gebäudemodelle sind EnergyPlus und Dymola. Das quelloffene Programm EnergyPlus (https://energyplus.net/) wurde 2001 erstveröffentlicht (Crawley et al. 2001) und wird seitdem weiterentwickelt. Im imperativen Code von EnergyPlus sind Algorithmen zur detaillierten Berechnung von Konvektion, Wärmeleitung sowie langwelliger und kurzwelliger Strahlung enthalten (U.S. Department of Energy 2023). Die Grenzen von EnergyPlus liegen in der Modellierung realitätsnaher Regelung moderner, komplexer Anlagentechnik (Wetter et al. 2022). Dymola basiert auf der quelloffenen Modellierungssprache Modelica, welche durch den akausalen, gleichungsbasierten und objektorientierten Ansatz für die Modellierung verschiedenster physikalischer Komponenten und Systeme geeignet ist. Mehrere Komponenten- und Systemmodelle können in Modelica-Bibliotheken gespeichert werden. Zur Modellierung von Gebäudeenergiesystemen mittels Modelica wurden im IBPSA Project 1 (https://ibpsa.github.io/project1/) neben der Kernbibliothek Modelica-IBPSA (https://github.com/ibpsa) auch die Bibliotheken AixLib (https://github.com/RWTH-EBC/AixLib) und Modelica-Buildings (https://github.com/lbl-srg/modelica-buildings) entwickelt. Diese quelloffenen Bibliotheken enthalten Modelle von Anlagentechnik, Regelung und Gebäuden unterschiedlicher Komplexität. Nachteilig an der Modellierungssprache Modelica ist die überlinear ansteigende Rechenzeit mit zunehmender Anzahl an Variablen. Ein detailliertes Gebäudemodell beinhaltet viele Zustandsgrößen und beeinflusst somit maßgeblich die Variablenanzahl eines Gebäudeenergiesystemmodells (Wetter et al. 2021). Eine zu EnergyPlus ähnlich detaillierte Berechnung in Modelica von Konvektion, Leitung,

kurzwelliger und langwelliger Strahlung und eine ähnlich detaillierte Modellierung aller Elemente eines Gebäudes resultieren in einem hohen Implementierungsaufwand und in einer hohen Rechenzeit (Wetter et al. 2021). Daher werden bei der Modellierung eines Gebäudes in Modelica häufig gängige Vereinfachungen getroffen.
Im in der AixLib enthaltenen HOM eines Einfamilienhauses werden Böden, Decken und Wände einzeln und mehrschichtig abgebildet. Detaillierte Algorithmen zur Berechnung der Wärmeströme sind implementiert. Die konvektiven Wärmeübergangskoeffizienten können beispielsweise unter anderem abhängig von dem Aufstellwinkel des Elements, dessen Oberflächenrauhigkeit, der Windgeschwindigkeit sowie der Temperaturdifferenz zwischen der Oberfläche des Elements und der umgebenden Luft ermittelt werden. Die Modellierung der Fenster und Türen ist hingegen vereinfacht umgesetzt. Kapazitäten dieser Elemente werden vernachlässigt und U-/g-Werte werden als konstant angenommen. Daraus ergeben sich folgende Forschungsfragen, die in dieser Studie beantwortet werden:

1) Wie hoch ist die Abweichung in den Simulationsergebnissen hinsichtlich der erforderlichen Heizleistung und des Heizbedarfs, wenn die Tür- und Fenstermodelle aus dem AixLib-HOM sowie dem EnergyPlus-Gebäudemodell entfernt und die so entstandenen Gebäudemodelle für ein Jahr simuliert werden?

2) Welchen Einfluss hat die vereinfachte Modellierung von Türen und Fenstern im AixLib-HOM auf die erforderliche Heizleistung und den Heizbedarf des Einfamilienhauses verglichen mit einem einfachen Modellierungsansatz dieser Elemente in EnergyPlus?

Methodik

Anwendungsfall: Einfamilienhaus

Das in dieser Studie untersuchte Einfamilienhaus besteht aus einem Erdgeschoss (EG) und einem Obergeschoss (OG) mit jeweils fünf Räumen sowie einem unbeheizten Dachboden. Die Grundrisse der beiden Etagen sowie die Ostansicht des Gebäudes sind in Abbildung 1 dargestellt. Das fiktive Gebäude besitzt weder Treppenhaus noch Innentüren. Geometrische Eigenschaften des Einfamilienhauses sind in Tabelle 1 gelistet.

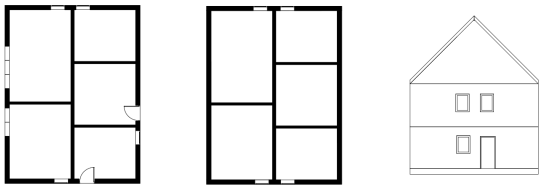

Abbildung 1: Grundriss EG (a) und OG (b), Ostansicht des Gebäudes (c)

Tabelle 1: Geometrische Eigenschaften des Gebäudes

Maße	Länge	11,37 m
	Breite	8,63 m
	Höhe	10,63 m
	Raumhöhe EG	2,6 m
	Raumhöhe OG	2,6 m
Flächen	Nettogrundfläche (NGR)	249,02 m^2
	beheizte NGR	166,01 m^2
	Bruttowandfläche	228,67 m^2
	Fensterfläche	14,04 m^2
	Außentürfläche	3,86 m^2

Modellierung der Gebäudeenergiesysteme

Für den Vergleich mit EnergyPlus wird ein EnergyPlus-HOM des Einfamilienhauses benötigt. Zunächst wird ein 3D-Gebäudemodell des Einfamilienhauses im IFC4-Format erstellt. Dazu wird das quelloffene Programm Blender (https://www.blender.org/) inklusive Add-on BlenderBIM (https://blenderbim.org/) verwendet. Das quelloffene Programm bim2sim (https://github.com/BIM2SIM/bim2sim) importiert die IFC-Datei und exportiert eine entsprechende IDF-Datei. Für die Simulation der IDF-Datei wird die in der Modelica-Buildings enthaltene Simulationsengine Spawn of EnergyPlus (Spawn) verwendet (Wetter et al. 2022). Spawn kombiniert die Stärken von Modelica und EnergyPlus durch Kopplung der Modelica-Modelle von Anlagentechnik und Regelung mit dem EnergyPlus-Modell der Gebäudehülle unter Verwendung des Functional Mock-up Interface Standards. Spawn bietet somit die Möglichkeit einer besseren Vergleichbarkeit der Simulationsergebnisse von AixLib-HOM und EnergyPlus-HOM, da Anlagentechnik und Regelung übereinstimmend in Modelica modelliert werden. Für die Anwendung von Spawn wird ein zusätzliches Modelica-Gebäudemodell benötigt, das die gekop-

Tabelle 2: Modellierung der Wärmeübertragungsmechanismen: EnergyPlus-HOM und AixLib-HOM

Elemente	Wärmeübertragungs-mechanismus	EnergyPlus-HOM	AixLib-HOM
Wände Fußböden Dach	Leitung	1D mittels Conduction Transfer Function (CTF)	1D mittels Wärmeleitfähigkeit λ
	Konvektion außen	Algorithmus: SimpleCombined	Algorithmus: ASHRAE Fundamentals (identisch zu SimpleCombined)
	Konvektion innen	Algorithmus: TARP	Algorithmus: Bernd Glueck
	langwellige Strahlung außen	in Konvektion außen berücksichtigt	in Konvektion außen berücksichtigt
	langwellige Strahlung innen	abhängig von Oberflächentemperatur und ε	abhängig von Oberflächentemperatur und ε
	kurzwellige Strahlung	α = 0,7 (konstant)	α = 0,7 (konstant)
Türen	Konvektion, Leitung	analog Wände	U-Wert = konst.
	langwellige Strahlung	analog Wände	Außen vernachlässigt, innen analog Wände
	kurzwellige Strahlung	analog Wände	vernachlässigt
Fenster	Konvektion	temperaturabhängig	U-Wert = konst.
	Leitung	λ wird aus U-Wert ermittelt	
	langwellige Strahlung	außen und innen	vernachlässigt
	kurzwellige Strahlung	Transmissionsgrad abhängig vom Strahlungswinkel	g-Wert = konst.

pelte Simulation ermöglicht. Dieses wird mittels der Modelica-Buildings-Bibliothek erstellt (Buildings-HOM). Das Spawn-HOM besteht somit aus dem eigentlichen Gebäudemodell (EnergyPlus-HOM) und einem Modelica-Gebäudemodell für die gekoppelte Simulation (Buildings-HOM).
Sowohl im EnergyPlus-HOM als auch im AixLib-HOM bildet jeder Raum eine thermische Zone. Interzonale Wärmeübertragung zwischen angrenzenden Zonen wird in beiden HOMs modelliert. Zudem werden in beiden HOMs die Böden/Decken und Außenwände vierschichtig, die Dachschrägen einschichtig und die Innenwände dreischichtig modelliert. Im AixLib-HOM werden Innenwände und Böden/Decken jeweils zur Hälfte den angrenzenden Zonen zugeordnet. Fenster und Türen werden im AixLib-HOM vereinfacht mit konstantem U-Wert und ohne Kapazität modelliert. Eine Reduktion der Außenwandfläche um die Türfläche wird vernachlässigt. Für einen fairen Vergleich der Simulationsergebnisse werden die Fenster und Türen im EnergyPlus-HOM mit dem in EnergyPlus geringstmöglichen Detailgrad modelliert. Die Außentüren werden einschichtig abgebildet. Für die Modellierung der Fenster wird das Objekt „WindowMaterial:SimpleGlazingSystem“ verwendet. Über den in diesem Objekt angegebenen U-Wert ermittelt EnergyPlus ein einglasiges Fenster mit zum U-Wert passender Dicke und Wärmeleitfähigkeit.
Tabelle 2 gibt eine Übersicht über die Modellierung der Wärmeübertragungsmechanismen, die im AixLib-HOM und im EnergyPlus-HOM für die Elemente des Gebäudes gewählt wurden. Als Raumsolltemperatur der beheizten Zonen wird 20 °C gewählt. Die an das Erdreich grenzende Oberflächentemperatur des Fußbodens wird mit konstanten 18 °C parametriert. Interne Wärmegewinne werden vernachlässigt. Zudem wird eine konstante zonenspezifische Luftwechselrate modelliert. Die Luftwechselrate der beheizten Zonen beträgt maximal 0,5 h^{-1}. Für den Dachboden wird eine Luftwechselrate von 1 h^{-1} angenommen.
Sowohl das AixLib-HOM als auch das Buildings-HOM werden in ein Modelica-Modell der quelloffenen Bibliothek BESMod (Wüllhorst et al. 2022) eingesetzt, das zur simulativen Ermittlung der erforderlichen Heizleistung des Einfamilienhauses verwendet werden kann. Die Anlagentechnik und die Regelung werden über einen idealen Heizer modelliert, der jederzeit die Heizleistung bereitstellt, die zur Erreichung der geforderten Raumsolltemperatur benötigt wird.

Simulationsszenarien

Zur Beantwortung der beiden Forschungsfragen werden die beiden HOMs ohne Türen und Fenster (HOM-red), mit Türen und ohne Fenster (HOM-T), ohne Türen und mit Fenstern (HOM-F) sowie vollständig (HOM) modelliert. Ähnlichkeiten und Unterschiede in den Simulationsergebnissen des AixLib-HOM gegenüber dem EnergyPlus-HOM werden hinsichtlich des Einflusses und der Modellierung der verschiedenen Wärmeübertragungsmechanismen analysiert. Dafür werden mehrere Simulationen mit unterschiedlichen Wetterdaten durchgeführt. Den eigentlichen Wetterdatensatz bildet das Testreferenzjahr 2015 des Deutschen Wetterdiensts vom Standort Potsdam (Deutscher Wetterdienst 2017). Dieser Datensatz wird mithilfe des quelloffenen Programms AixWeather (https://github.com/RWTH-EBC/AixWeather) wie folgt verändert:

1) „Alles konstant“: Konstante Wetterandbedingungen mit -7 °C, ohne Wind und ohne Strahlung zur Analyse der maximal erforderlichen Heizleistung

2) „T,v variabel“: Variation der Umgebungstem-

peratur, der Windgeschwindigkeit und der Windrichtung und ohne Berücksichtigung von Strahlung zur Analyse von natürlicher Konvektion, Wärmeleitung und erzwungener Konvektion

3) „Q variabel“: Variation der Solarstrahlung mit konstanter Umgebungstemperatur (-7 °C) und ohne Berücksichtigung von Wind zur Analyse der kurz- und langwelligen Strahlung

4) „Alles variabel“: Verwendung des ursprünglichen Wetterdatensatzes zur Analyse des Zusammenspiels der Effekte

Simulationsergebnisse

In diesem Kapitel werden die Simulationsergebnisse einer Jahressimulation der verschiedenen Gebäudemodelle (HOM-red, HOM-T, HOM-F, HOM) unter den definierten Wetterszenarien („Alles konstant“, „T,v variabel“, „Q variabel“, „Alles variabel“) hinsichtlich der erforderlichen Heizleistung sowie des Heizbedarfs in der Winterperiode (W: 07.01 - 31.03 & 01.10 - 31.12), in der Sommerperiode (S: 01.04 - 30.09) und in der Jahresperiode (J: 07.01 - 31.12) vorgestellt und analysiert. Die Simulationsergebnisse der ersten Woche des Jahres fließen nicht in die Analyse ein, um die Einflüsse möglicher Unterschiede in den Startbedingungen zwischen den AixLib- und den EnergyPlus-Gebäudemodellen zu reduzieren. Tabelle 3 zeigt die prozentuale Abweichung im Heizbedarf in den Perioden für jede durchgeführte Simulation.

HOM-red: Ohne Fenster & Türen

Wie Tabelle 3 zu entnehmen ist, schätzt das AixLib-HOM-red in allen Perioden und bei allen Variationen des Wetterdatensatzes den Heizbedarf höher ab als das EnergyPlus-HOM-red. Die sich bei konstanten Wetterrandbedingungen („Alles konstant“) einstellende erforderliche Heizleistung stimmt mit einer Abweichung von 0,6 % (Modelica: 4,25 kW, EnergyPlus: 4,22 kW) nahezu überein. Eine Variation der Strahlungsdaten („Q variabel“) führt zu einer leichten Erhöhung der prozentualen Abweichung auf 0,8 % in der Sommerperiode. Abbildung 3 zeigt, dass die erforderliche Heizleistung des AixLib-HOM-red gegenüber EnergyPlus in diesem Wetterszenario leicht nach oben verschoben ist. Ähnliches ist in Abbildung 2 beim Wetterszenario „T,v variabel“ erkennbar. In diesem Wetterszenario kommt es in der Sommerperiode gemäß Tabelle 3 zu einer um 7,6 % höheren Einschätzung des Heizbedarfs. Dies ist insbesondere darauf zurückzuführen, dass eine über das Jahr nahezu konstante absolute Abweichung die prozentuale Abweichung bei niedrigeren Heizleistungen erhöht. Bei Verwendung des vollständigen Wetterdatensatzes wird die erforderliche Heizleistung des AixLib-HOM-red im gesamten Jahr erkennbar höher berechnet, was gemäß Tabelle 3 zu einem um 9 % höheren Jahresheizbedarf führt. Je höher die Umgebungstemperatur und die Solarstrahlung sind, desto höher werden die prozentuale und die absolute Abweichung der erforderlichen Heizleistung. In Abbildung 4 sind die Unterschiede insbesondere in der Sommerperiode deutlich erkennbar. Während EnergyPlus eine Wandschicht in sechs bis 18 Knoten unterteilt (U.S. Department of Energy 2023), wird im AixLib-HOM jede Wandschicht über genau eine Kapazität abgebildet. Bei hoher Außentemperatur und hoher Solarstrahlung stellt sich in EnergyPlus außen an einer nach Süden orientierten Außenwand eine Oberflächentemperatur bis zu 63 °C ein, während das AixLib-HOM-red eine Oberflächentemperatur von 53 °C nicht überschreitet. Dies führt zu einer um bis zu 2 K höheren Oberflächentemperatur an der Innenseite der Außenwand in EnergyPlus, was geringere Wärmeverluste und damit eine geringere erforderliche Heizleistung in EnergyPlus zur Folge hat.

HOM-T: Einfluss der Türen

Die Simulation des HOM-T mit dem Wetterszenario „Alles konstant“ führt zu einer erforderlichen Heizleistung des AixLib-HOM-T von 4,54 kW und des EnergyPlus-HOM-T von 4,67 kW. Die Berücksichtigung der beiden Außentüren sorgt somit in EnergyPlus zu einem stärkeren Anstieg der erforderlichen Heizleistung als in Modelica. Gleiches gilt für das Wetterszenario „T,v variabel“, was in Tabelle 3 an der gesunkenen prozentualen Abweichung erkennbar ist. Im AixLib-HOM-T werden die Türen mit konstantem U-Wert modelliert, der zu jeder Zeit den in EnergyPlus mittels der Algorithmen berechneten U-Wert übersteigt. Zudem wird im AixLib-HOM-T die Türfläche nicht von der Wandfläche abgezogen. Diese beiden Unterschiede lassen einen höheren Heizbedarf des AixLib-HOM-T gegenüber EnergyPlus erwarten. In beiden Gebäudemodellen ist die Oberfläche der Türinnenseite am langwelligen Strahlungsaustausch mit den umliegenden Wänden beteiligt. Im AixLib-Gebäudemodell wird die Oberflächentemperatur der Türinnenseite mit der Raumtemperatur gleichgesetzt (20 °C). In EnergyPlus wird die Tür wie eine Wandschicht mo-

Tabelle 3: Prozentuale Abweichung im Heizbedarf - AixLib ggü. EnergyPlus

	Alles konstant			T,v variabel			Q variabel			Alles variabel		
	W	S	J	W	S	J	W	S	J	W	S	J
HOM-red	0,6	0,6	0,6	1,9	7,6	3,1	0,6	0,8	0,7	4,6	40,1	9,0
HOM-T	−2,6	−2,6	−2,6	−1,9	4,4	−0,6	−1,9	0,2	−0,9	1,4	48,0	7,0
HOM-F	2,3	2,3	2,3	3,1	7,4	4,0	2,0	0,8	1,5	4,2	26,3	5,2
HOM	−0,7	−0,7	−0,7	−0,4	4,6	0,7	−0,7	0,0	−0,3	0,9	31,0	2,3

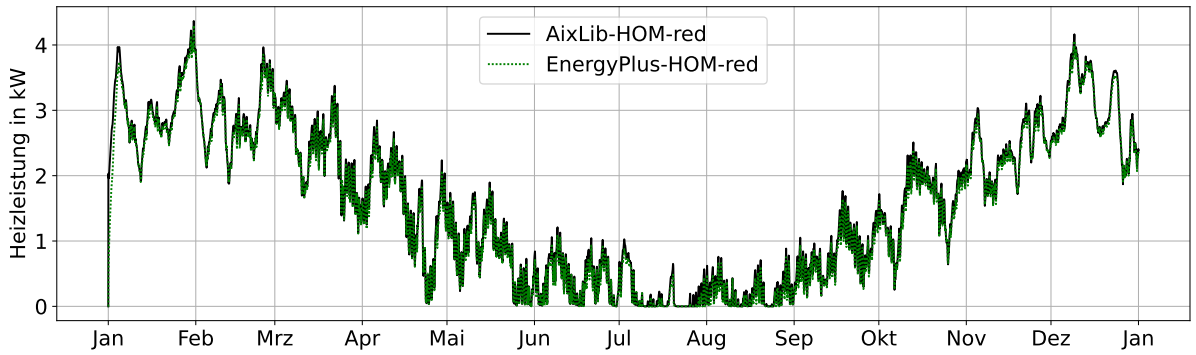

Abbildung 2: Jahressimulation des HOM-red mit Wetterszenario „T,v variabel“

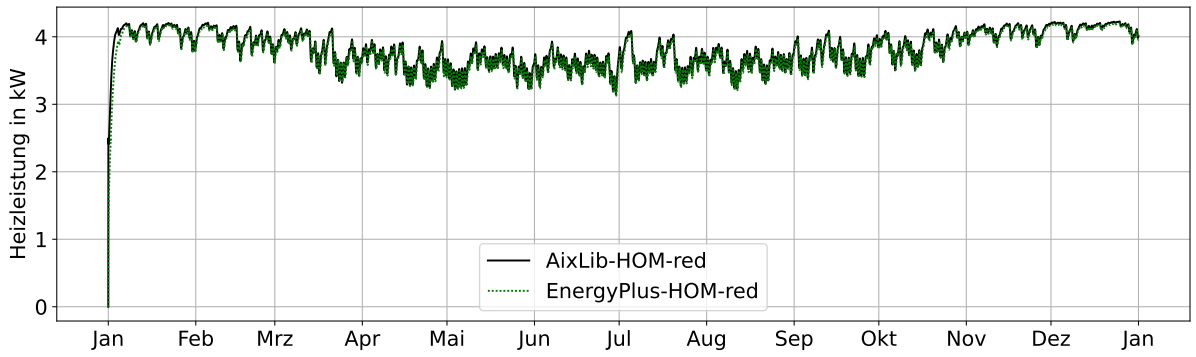

Abbildung 3: Jahressimulation des HOM-red mit Wetterszenario „Q variabel“

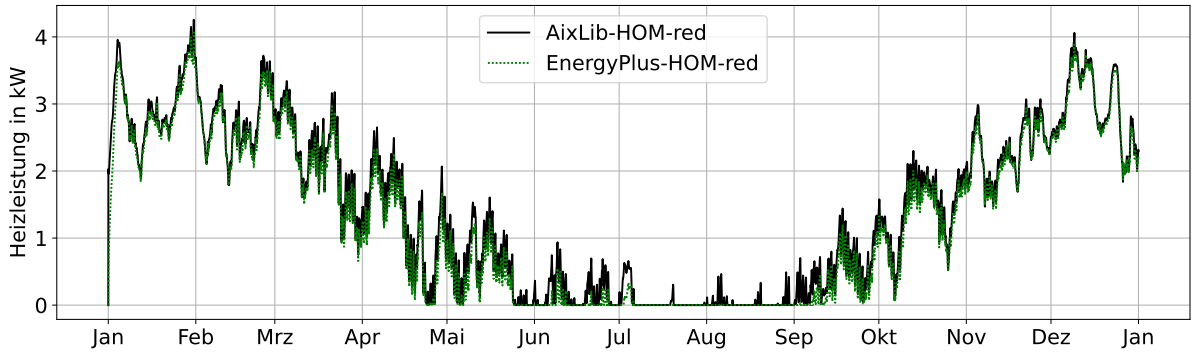

Abbildung 4: Jahressimulation des HOM-red mit Wetterszenario „Alles variabel“

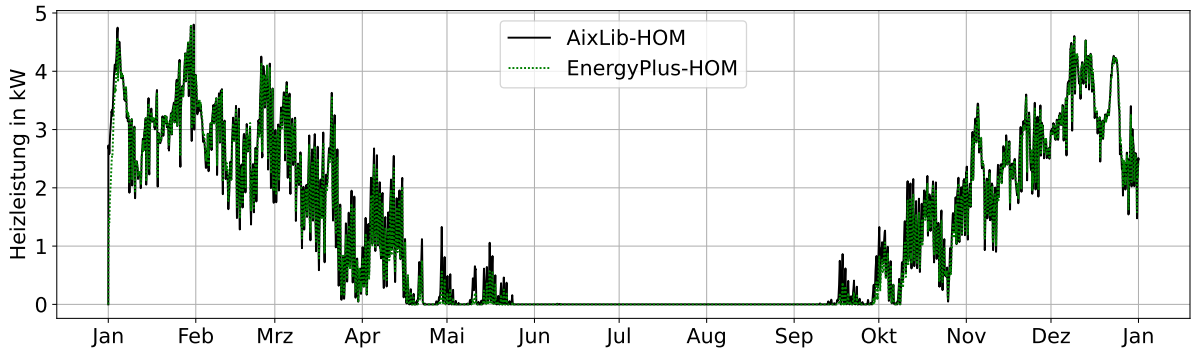

Abbildung 5: Jahressimulation des HOM mit Wetterszenario „Alles variabel“

delliert. Die Oberflächentemperatur der Türinnenseite sinkt insbesondere im Winter deutlich auf bis zu 4 °C, was die Wärmeverluste über die Tür erhöht und gleichzeitig zu einer Reduktion der umliegenden Wandoberflächentemperatur führt. Dadurch übersteigt die erforderliche Heizleistung in EnergyPlus diejenige in Modelica.
Lediglich im Wetterzenario „Alles variabel“ wird in der Sommerperiode eine Erhöhung der prozentualen Abweichung des Heizbedarfs durch die Modellierung der Türen festgestellt. Im AixLib-Modell wird die einfallende Strahlung auf die Tür vernachlässigt. Da die Tür nicht von der Wandfläche abgezogen wird, sind die Strahlungsgewinne indirekt im Wandmodell berücksichtigt. In EnergyPlus wird in dieser Periode auf der Türinnenseite eine Oberflächentemperatur bis zu 49 °C erreicht. Die Tür erwärmt damit die umliegenden Wände und die Raumluft, was den Heizbedarf in EnergyPlus reduziert.

HOM-F: Einfluss der Fenster

Die Simulation des HOM-F mit dem Wetterszenario „Alles konstant“ führt zu einer erforderlichen Heizleistung des AixLib-HOM-F von 4,75 kW und des EnergyPlus-HOM-F von 4,64 kW. Die Berücksichtigung der Fenster führt somit in Modelica zu einem stärkeren Anstieg der erforderlichen Heizleistung als in EnergyPlus. Ursächlich ist der konstante U-Wert der Fenster im AixLib-HOM-F, der den in EnergyPlus mittels der Algorithmen berechneten U-Wert übersteigt. In der Sommerperiode des Wetterszenarios „T,v variabel“ führt der höhere U-Wert im AixLib-Gebäudemodell zeitweise zu höheren Wärmegewinnen, wodurch gemäß Tabelle 3 die prozentuale Abweichung in dieser Periode durch Berücksichtigung der Fenster nahezu unverändert bleibt.
Der Vergleich der in Tabelle 3 dargestellten Simulationsergebnisse für die Wetterszenarien „Q variabel“ und „Alles konstant“ zeigt, dass solare Wärmegewinne durch die Fenster mit dem AixLib-HOM-F zu einer stärkeren Reduktion des Heizbedarfs als mit dem EnergyPlus-HOM-F führen. Dieser Effekt ist im Sommer größer als im Winter, da in EnergyPlus eine Berechnung des Transmissionsgrads abhängig vom Einfallswinkel der Solarstrahlung erfolgt, wohingegen der g-Wert im AixLib-Gebäudemodell konstant modelliert wird.

HOM: Mit Türen und Fenstern

Tabelle 3 zeigt, dass bei Simulation des Einfamilienhauses mit Türen und Fenstern (HOM) die prozentuale Abweichung des Heizbedarfs in allen Wetterszenarien gegenüber dem Ergebnis des HOM-red sinkt. Ursächlich sind insbesondere die Annahme einer konstanten Oberflächentemperatur auf der Türinnenseite von 20 °C im AixLib-Gebäudemodell und die gegenüber EnergyPlus höheren solaren Wärmegewinne durch die Fenster. Gemäß Tabelle 3 resultieren im Wetterszenario „Alles variabel“ eine prozentuale Abweichung von 0,9 % in der Winterperiode und eine prozentuale Abweichung von 2,3 % im gesamten Jahr. Abbildung 5 zeigt einen deutlich geringeren Heizbedarf in der Sommerperiode als in der Winterperiode, wodurch der Einfluss der in der Sommerperiode hohen prozentualen Abweichung von 31 % auf die Jahresbetrachtung gering ist.

Zusammenfassung

Die Simulation des um Fenster und Türen reduzierten Gebäudemodells AixLib-HOM-red führt zu einem gegenüber EnergyPlus nach oben verschobenen Verlauf der erforderlichen Heizleistung. Der jährliche Heizbedarf wird um 9 % höher kalkuliert.

Mit einem um 4,6 % höheren Heizbedarf in der Winterperiode ist das AixLib-HOM-red in der Lage, die erforderliche Heizleistung in dieser Periode mit ähnlicher Genauigkeit zu ermitteln wie EnergyPlus. Infolge der in EnergyPlus durchgeführten weiteren Diskretisierung der einzelnen Wandschichten werden in der Sommerperiode in EnergyPlus höhere Oberflächentemperaturen der Außenwände erreicht, wodurch der Heizbedarf deutlich reduziert wird. In der Sommerperiode steigt dadurch die Abweichung des Heizbedarfs auf 40,1 % an.
Die vereinfachte Modellierung der Außentüren im AixLib-HOM führt zur Berechnung geringerer Wärmeverluste in der Winterperiode und geringerer Wärmegewinne in der Sommerperiode. Trotz des geringen Verhältnisses von Türfläche zu Wandfläche ist ein deutlicher Einfluss auf die Simulationsergebnisse erkennbar. Die vereinfachte Modellierung der Fenster im AixLib-HOM führt zur Berechnung höherer Wärmeverluste in der Winterperiode und höherer Wärmegewinne in der Sommerperiode infolge von Konvektion und Wärmeleitung. Zudem werden mit dem AixLib-HOM in der Winterperiode und insbesondere in der Sommerperiode verglichen mit dem EnergyPlus-HOM höhere solare Wärmegewinne durch die Fenster berechnet. Insgesamt führt die vereinfachte Modellierung der Türen und Fenster zur Reduktion der prozentualen Abweichung des Jahresheizbedarfs von 9 % bei Simulation des HOM-red auf 2,3 % bei Simulation des HOM mit dem vollständigen Wetterdatensatz.

Limitationen und Ausblick

Da insgesamt mit dem EnergyPlus- gegenüber dem AixLib-Gebäudemodell die Wärmegewinne im Sommer höher abgeschätzt werden, können zukünftig Abweichungen hinsichtlich der erforderlichen Kühlleistung und des Kühlbedarfs untersucht werden. Reale Messdaten sollten zur Validierung der Gebäudemodelle herangezogen werden.

Danksagung

Wir bedanken uns für die finanzielle Unterstützung durch das deutsche Bundesministerium für Wirtschaft und Klimaschutz (BMWK, Förderkennzeichen 03EN6018A).

Literatur

Albers, K.-J. (2017), *Taschenbuch für Heizung und Klimatechnik*, 78 edn, Dt. Industrieverlag, München.

Chen, Y., Guo, M., Chen, Z., Chen, Z. & Ji, Y. (2022), 'Physical energy and data-driven models in building energy prediction: A review', *Energy Reports* **8**, 2656–2671.

Crawley, D. B., Lawrie, L. K., Winkelmann, F. C., Buhl, W., Huang, Y. J., Pedersen, C. O., Strand, R. K., Liesen, R. J., Fisher, D. E., Witte, M. J. & Glazer, J. (2001), 'EnergyPlus: creating a new-generation building energy simulation program', *Energy and Buidlings* **33**, 319–331.

Deutscher Wetterdienst (2017), *Ortsgenaue Testreferenzjahre von Deutschland für mittlere, extreme und zukünftige Witterungsverhältnisse*.

Deutsches Institut für Normung e. V. (2017), 'DIN EN 12831'.

Deutsches Institut für Normung e. V. (2018), 'DIN V 18599'.

European Commission (2020), In focus: Energy efficiency in buildings, Technical report, Brussels.

Hensen, J. & Lamberts, R., eds (2011), *Building Performance Simulationfor Design and Operation*, Spon Press.

Jansen, D., Richarz, J., Vaeßen, D., Hering, D. & Müller, D. (2022), 'Comparision of Thermal Simulation Models with Different Level of Detail for Non-Residential Buildings', *BauSim Conference 2022* .

U.S. Department of Energy (2023), 'EnergyPlus™ Version 23.2.0 Documentation: Engineering Reference'.

Wetter, M., Benne, K., Gautier, A., Nouidui, T. S., Ramle, A., Roth, A., Tummescheit, H., Mentzer, S. & Winther, C. (2022), 'LIFTING THE GARAGE DOOR ON SPAWN, AN OPEN-SOURCE BEM-CONTROLS ENGINE', *Building Performance Modeling Conference and SimBuild* .

Wetter, M., Benne, K. & Ravache, B. (2021), 'Software Architecture and Implementation of Modelica Buildings Library Coupling for Spawn of EnergyPlus', *14th International Modelica Conference* .

Wüllhorst, F., Maier, L., Jansen, D., Kühn, L., Hering, D. & Müller, D. (2022), 'BESMod - A Modelica Library providing Building Energy System Modules', *American Modelica Conference 2022* .

BauSIM 2024 in Wien
23. September – 26. September

Trends in energy performance certificates: A comparative study of building stock characteristics

Daniel Heidenthaler[1,2], Markus Leeb[1]

1 Salzburg University of Applied Sciences, Department Green Engineering and Circular Design, Campus Kuchl, Markt 136a, 5431 Kuchl, Austria

2 TU Wien, Institute of Material Technology, Building Physics, and Building Ecology, Karlsplatz 13/207, 1040 Vienna, Austria

E-Mail: daniel.heidenthaler@fh-salzburg.ac.at

Abstract

Energy performance certificates contain a lot of valuable information for a vast number of buildings across the globe. The increasing number, quality and accessibility of EPC-data enables promising and manifold opportunities for the utilization in urban building energy modelling approaches. This paper presents an update of a representative building approach using archetypes based on new EPC-data. For this, the building stock is divided according to categories, namely the building condition (renovated, not-renovated), construction period and building type (single-family house, multi-family house). The data analysis indicates a shift towards the renovation of buildings, with an almost exponential increase of EPCs in general, and of EPCs for renovated buildings in particular. Regarding the energy carrier, a clear trend away from fossil fuels towards renewable energy can be observed, with electricity (heat pumps) being accountable for the highest share in single-family houses and district heating in multi-family houses. A comparison of U-values for different building elements in relation to the upload year suggests that buildings may have undergone (partly) renovations without issuing a renovation EPC. In this regard, further investigations are necessary to rule out statistical uncertainties. The results of this analysis can serve as an input for urban building energy modelling approaches.

Introduction

In the European Union, residential buildings are accountable for a large share of the total energy consumption. For reaching the set climate targets, the building stock needs to be decarbonised and buildings must meet minimum energy performance requirements. For this purpose, all member states are obliged to establish energy performance certificates (EPC). EPCs are a useful tool for assessing and comparing the energy performance of buildings, enable the implementation of policies and requirements and contain a lot of valuable information. Although not initially intended, EPCs nowadays serve a variety of different applications. Pasichnyi et al. (2019) systematically reviewed 79 papers utilising EPC data and identified 13 application domains. Most studies focused on analysing and mapping the building energy performance, followed by evaluations of building energy renovation.

The authors further mention the possibility of using EPC data for automated building simulation workflows and urban building energy modelling (UBEM) (Pasichnyi et al. 2019). UBEM enables the simulation and evaluation not only of single buildings, but whole districts or countries and therefore allows for a comprehensive and widespread analysis of the building stock and future scenarios. Such UBEM approaches necessitate a vast amount of detailed data often not available or of sufficient quality. Therefore, data availability, data quality and data acquisition are named amongst others as the greatest challenges regarding UBEM in literature (Kamel 2022).

In this context, EPCs can remedy those challenges and shortcomings. EPC-data contains a lot of valuable and detailed information of individual buildings and are updated on an ongoing basis. The number of available EPCs is continuously growing. Although the implementation of certification schemes and data filing differs between member states of the EU (Semple & Jenkins 2020) and the data often lacks quality and accuracy (Iribar et al. 2021), an improvement of data availability, quality and transparency is foreseeable due to the fact that the EU accelerates the implementation of publicly available, obligatory databases and enhanced quality of EPC's (European Comission 2021).

Recent studies demonstrated the viability of EPC-based UBEM approaches. Heidenthaler et al. (2023) developed an EPC-based UBEM approach and compared the results with measurements of buildings connected to district heating. The authors conclude that results of sufficient quality can be reached even with an archetypical approach based on EPC-data. If detailed data of sufficient quality for single buildings as well as enough computational power is available, that approach may also be used for simulating individual buildings on district or country scale. Johari et al. (2023) developed an UBEM framework based on GIS (Geographic Information System) and EPC data, creating simple building-level simulation models using EnergyPlus. The model was calibrated and validated using EPC data and measurements. Beltrán-Velamazán et al. (Beltrán-Velamazán et al. 2024) followed a similar approach by developing an automated national-scale UBEM approach based on EPC data. Contrary to Heidenthaler et al. (2023), the authors do not use the EPC for setting up detailed, physical building simulation models but use the results from the EPC calculation method instead. Therefore, that framework does not allow for analysing buildings and corresponding energy consumption with high temporal resolution on an hourly basis and of innovative technologies and future scenarios.

This paper aims at providing a solid basis for detailed, physical, bottom-up urban building energy models by analysing EPC data using a representative building approach and developing archetypes. These archetypes can serve as input for urban building energy models. The paper represents an update of an already conducted analysis of EPC data (Heidenthaler et al. 2022). Since then, the number of EPCs in the database increased from 82.709 (effective date 03.2021) to 127.856 (effective date 29.01.2024) and the number of variables contained in the submitted dataset grew from 422 to 475. Therefore, trends in EPC data are identified especially regarding renovation, including variables such as energy carrier and U-values (overall heat transfer coefficients) for different building elements, accompanied by the development of archetypes. The utility of such an analysis for UBEM has been successfully demonstrated (Heidenthaler et al. 2023).

Method

This paper conducts a statistical analysis of EPC data, aiming to describe the characteristics of the building stock for the use case of Salzburg, Austria. The statistical analysis involves a clustering approach identifying several archetypes based on a few decisive categories. These archetypes are representative for the building stock regarding energy related characteristics. For this, a number of sequential steps are necessary. Partially faulty and non-processable data requires data preparation, pre-processing and data filtering, followed by a classification of the data according to the archetypes. Figure 1 contains an overview of the applied filter process.

The available dataset is composed of 475 variables, although not every EPC contains values for each variable. The database comprises EPCs for the design stage as well as completion and furthermore differentiates between building stock (if the EPC is issued for already existing buildings), new buildings (if the EPC is issued immediately after completion of a newly constructed building) and renovated buildings. For this analysis, only EPCs of actually constructed buildings are relevant (hence excluding design EPCs). Furthermore, EPCs of type building stock and newly constructed buildings are treated as one category, thus only differentiating existing/new buildings and renovated buildings.

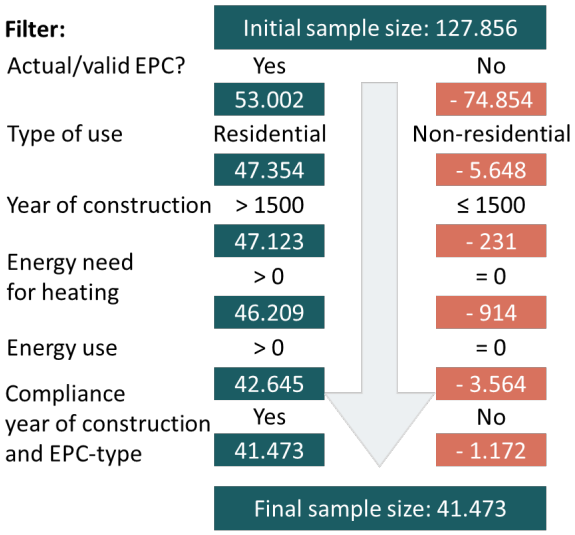

Figure 1: Overview of the filter process applied to the EPC-database

Proceeding from this filtered dataset, a statistical analysis of archetypes is conducted for several selected variables, including the energy carrier and U-values for different building elements. The archetypes are classified based on three categories (see Table 1), namely the condition (2 classes), construction period (9 classes) and type of residential building (2 classes). This classification of the dataset results in 36 archetypes. The chosen categories and classes are representative for the Austrian residential building stock and constitute widely-used classifications.

The results are representative for Salzburg, Austria, although transferability to the other federal states is expectable owing to the similarity of the building stock in Austria according to literature. If data availability is given, this approach can also be adopted for other countries, although there might be some barriers as a consequence of diverging calculation methods and naming conventions for EPCs in different countries. Nevertheless, efforts by the EU as mentioned in the introduction facilitate the standardisation of EPCs and consequently the transferability of such methods in the near future.

Table 1: Categories and corresponding classes for defining the archetypes

Category	Class	Description
COND	Renovated	Renovated buildings
	Not-renovated	Building stock and new buildings
AGE	< 1919	
	1919-1944	
	1945-1960	
	1961-1970	
	1971-1980	
	1981-1990	
	1991-2000	
	2001-2010	
	> 2010	
TYPE	SFH	Single-family house (1-2 dwelling units)
	MFH	Multi-family house (3 or more dwelling units)

Results and discussion

Figure 2 depicts the sample size of valid EPCs per archetype for the new as well as the old dataset (2021). It is evident that the sample size has increased significantly, especially for renovated buildings. Whereas the old dataset contained 4812 valid EPCs for renovated buildings, this number more than doubled in the new dataset. The number of EPCs for existing and new buildings increased from 20.048 to 29.993. Hence, the share of EPCs for renovated buildings increased from 19 % to 28 %.

According to experts, prior to the rise of issued EPCs, the number of energy consultations has risen sharply, suggesting that the energy crisis and the associated rise in energy prices recently led to a change in public awareness. Further interesting is the increase of EPCs for renovated buildings of the last two construction periods compared to the old dataset with hardly any renovations in these periods. This could be a result of the increasing subsidization of individual measures in recent years such as photovoltaic, solar thermal or heating systems, leading to an increase of EPCs of class renovation without any further thermal improvements of the building envelope.

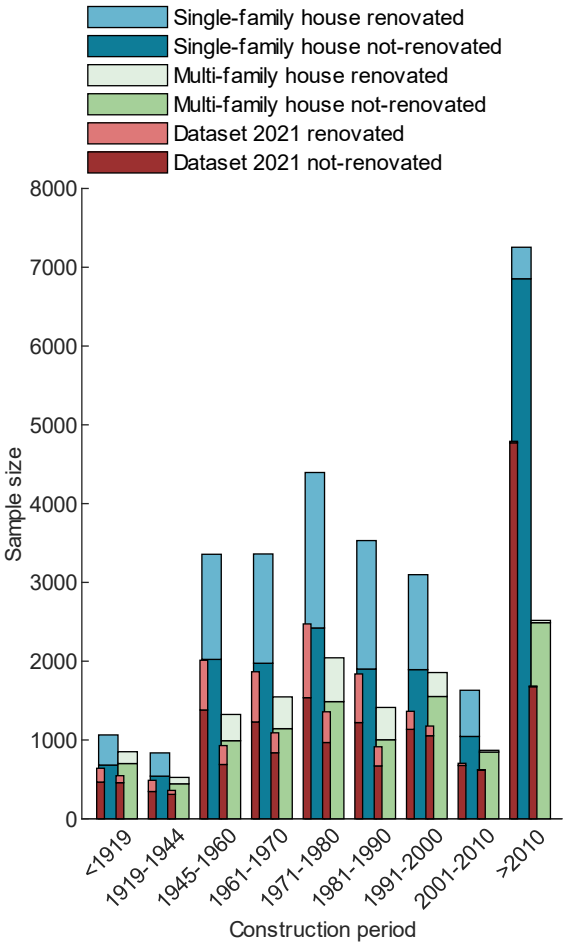

Figure 2: Sample size of valid EPCs per category and class (archetypes), comparison of new and old (dataset from 2021) sample size

In the first few years after the introduction of the EPC database, there was a steady increase in the number of new entries till 2013 (see fig. 3). While there was hardly any increase of new EPCs in the subsequent years between 2013 and 2020 (in some years, the number of new EPCs even declined), an almost exponential increase in new EPCs can be observed for the last three years.

Although EPCs for renovated and not-renovated buildings increased, the rising share of EPCs for renovated buildings is conspicuous. For the first time since the introduction of the database the number of EPCs for renovated single-family buildings exceeded the number of EPCs for not-renovated single-family buildings in 2023, indicating a shift towards renovating buildings.

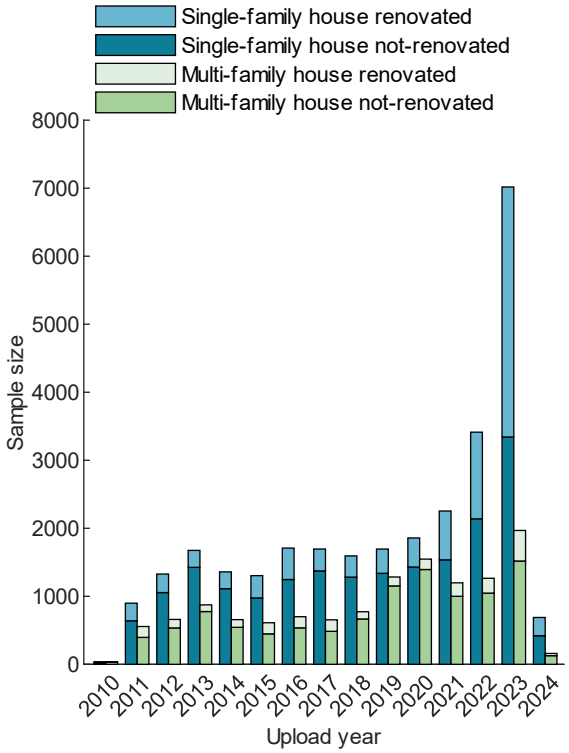

Figure 3: Number of newly issued EPCs by condition, type of building and year of upload

Figure 4 shows the distribution of different energy carriers for single-family houses and multi-family houses of all construction periods. Electricity (heat pumps) accounts for the largest share in single-family houses (28 % for not-renovated buildings and 34 % for renovated buildings) and district heating in multi-family houses (33 % for not-renovated buildings and 27 % for renovated buildings). The largest increase is observable for biomass in renovated single-family houses compared to not-renovated single-family houses, where the share has risen from 15 % to 25 %. Equally noteworthy is the high proportion of electricity (direct electric heating) in multi-family houses, even increasing in renovated buildings by 5 %. Fossil energy carriers account for 26 % to 40 %.

A closer look at the distribution of energy carriers shows the development both regarding different construction periods as well as in comparison for renovated and not-renovated buildings (fig. 5). Within the most recent construction period, electricity (heat pump) is the most commonly used energy carrier in single-family houses, followed by district heating. For multi-family houses it is vice versa. Interestingly, energy carriers in renovated multi-family houses of older construction periods are more commonly replaced by heat pumps than in more recent construction periods (prior to 2001-2010).

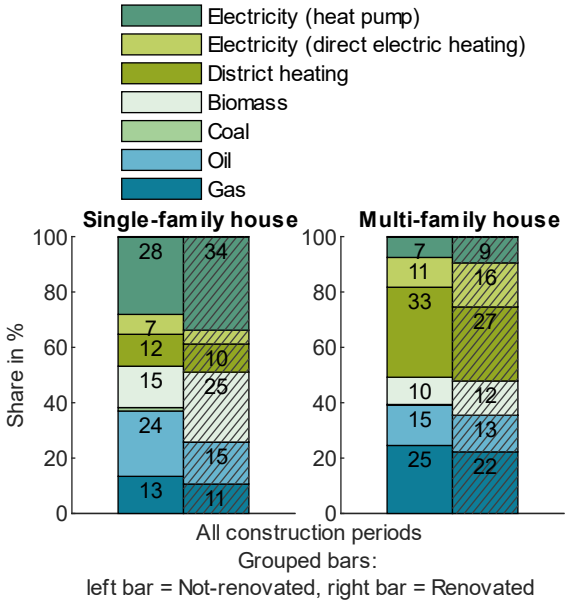

Figure 4: Share of energy carriers for single-family houses and multi-family houses (all construction periods)

For renovated single-family houses, the share of heat pumps ranges between 19 % in the oldest construction period and 70 % for buildings of the most recent construction period. Fossil fuels are more frequently replaced by other, renewable energy carriers in renovated single-family houses than in renovated multi-family houses. Overall, fossil energy carriers still make up a large proportion, with a minimum of 11 % and 37 % and a maximum of 51 % and 64 % for renovated and not-renovated buildings respectively, depending on the archetype (excluding the latest construction period, where the share of fossil fuels is significantly lower for both, single-family and multi-family houses). In general, a trend towards renewable energy carriers for renovated buildings can be observed, although this tendency is less evident for multi-family houses.

Figure 6 and figure 7 depict the median U-values of building elements (floor, ceiling/roof, window, wall) and corresponding confidence intervals for archetypes of class single-family and multi-family house respectively. Due to the fact that each EPC can contain several elements of the same category (e.g. several walls with diverging U-values), the depicted median U-values are based on an area-weighted mean U-value per building element and EPC. In general, a steady decline (with some exceptions) of U-values for all building elements of not-renovated buildings can be observed over the various construction periods. This is not true for renovated buildings, where U-values of different construction periods are similar and no general trend can be observed. In some cases, U-values of older buildings reach

lower values compared to U-values of newer buildings (e.g. renovated ceilings reach their maximum in the construction period 1981-1990 for both single and multi-family houses).

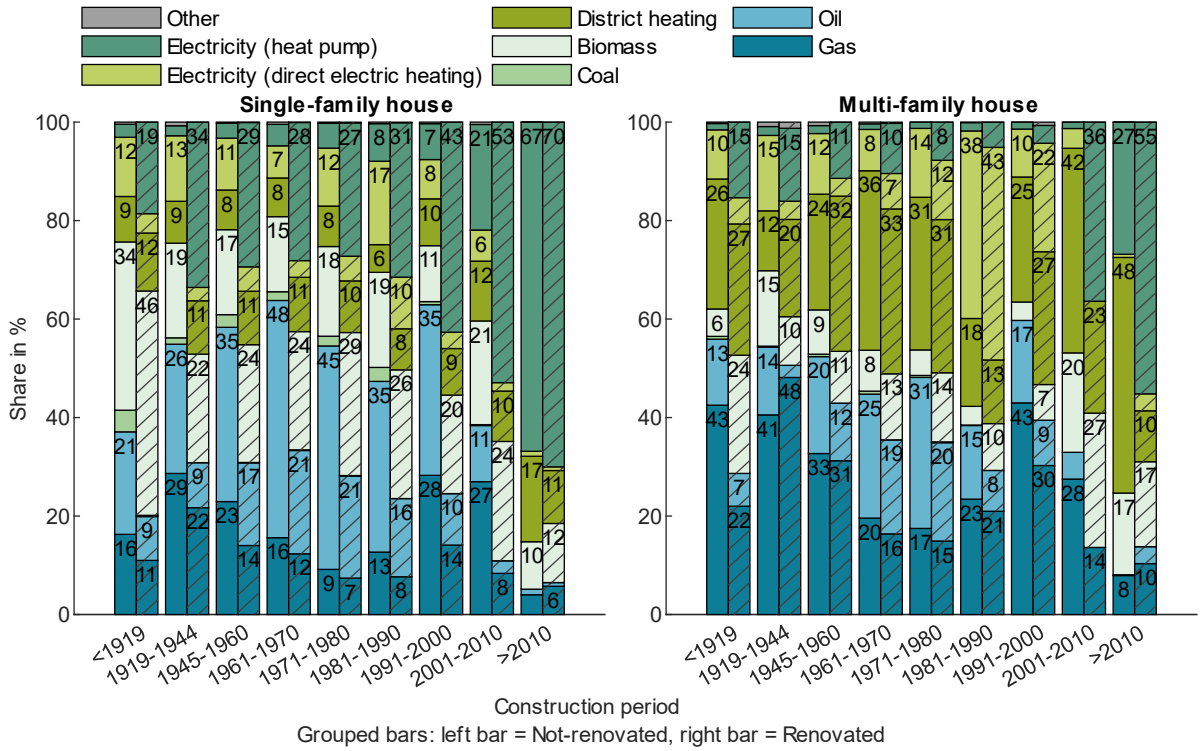

Figure 5: Share of energy carriers by archetype

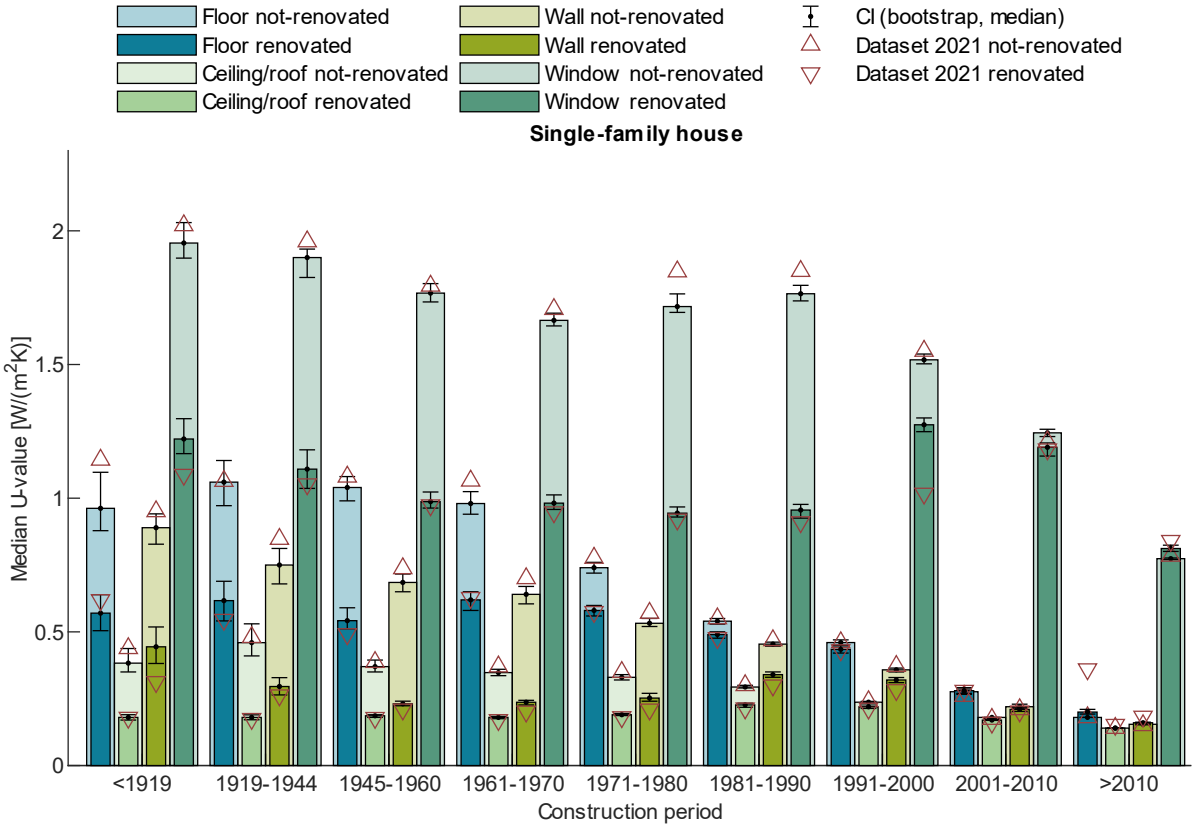

Figure 6: Median U-value and 95% confidence interval by archetype of class SFH, compared with old dataset (2021)

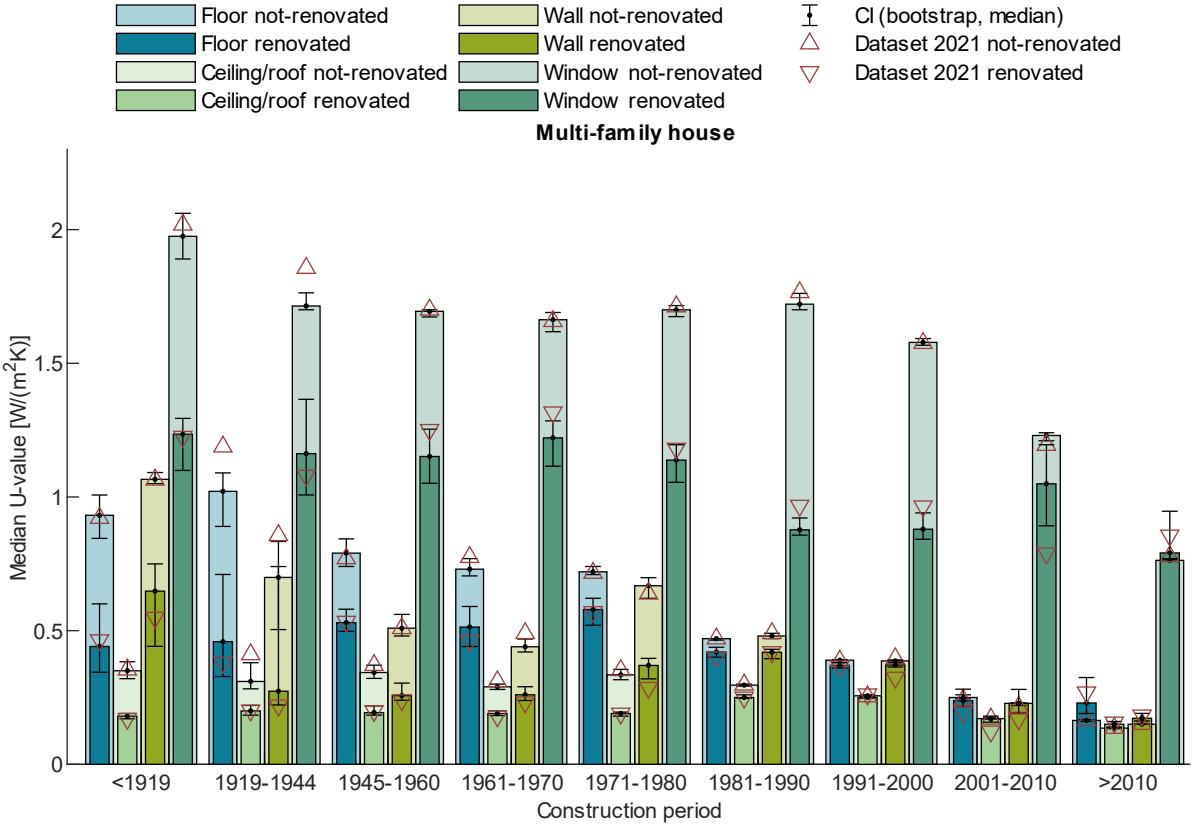

Figure 7: Median U-value and 95% confidence interval by archetype of class MFH, compared with old dataset (2021)

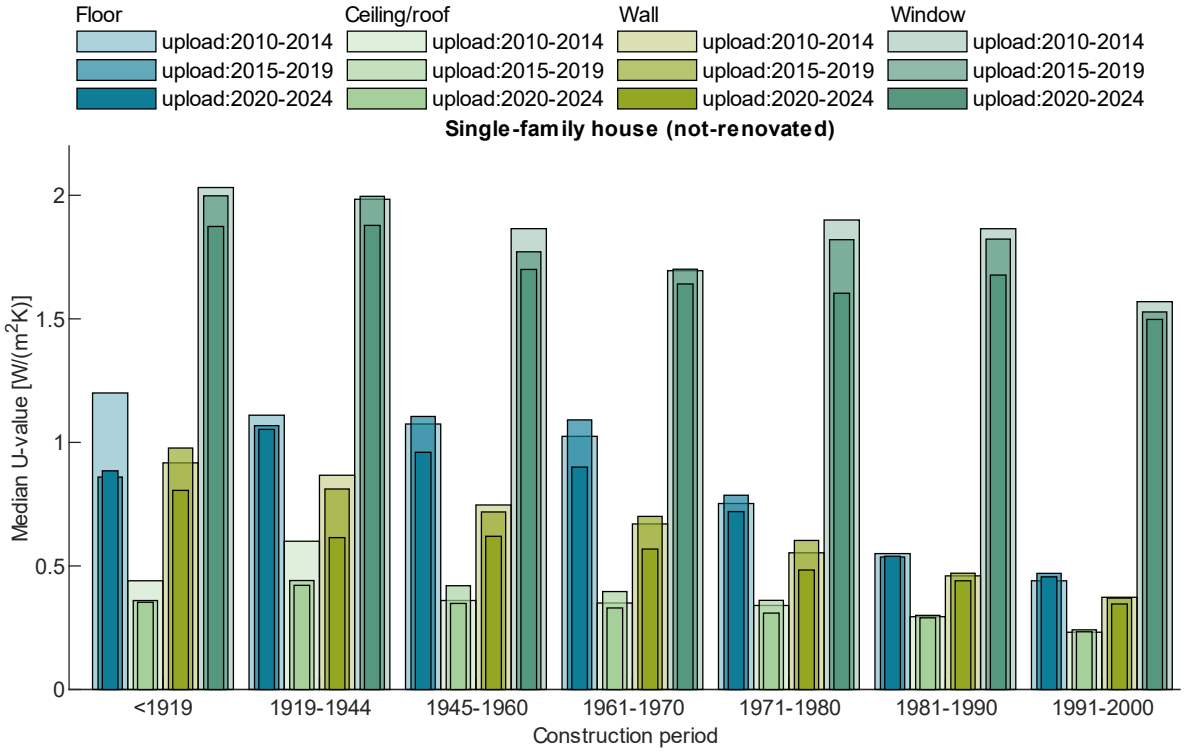

Figure 8: Median U-value of not-renovated single-family houses by construction period and upload period

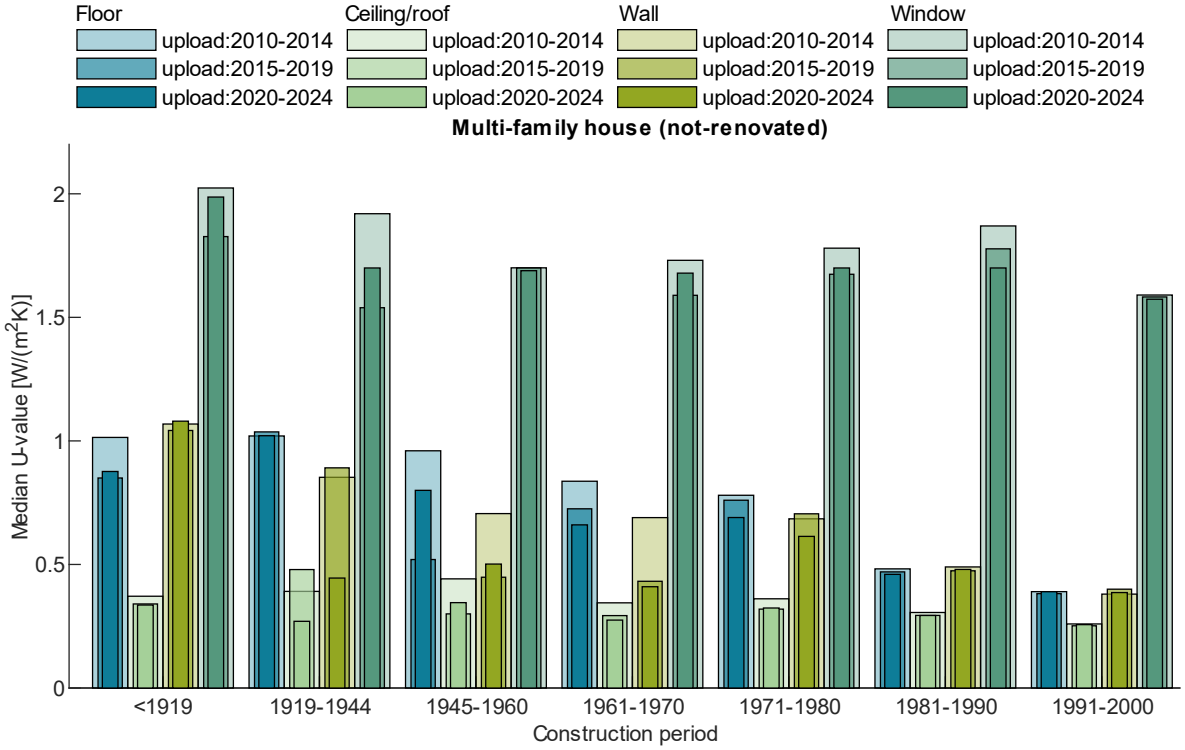

Figure 9:Median U-value of not-renovated multi-family houses by construction period and upload period

The highest reduction in absolute numbers for renovated compared to not-renovated buildings can be achieved for windows. Whilst renovated ceilings/roofs nearly reach the U-values of new buildings for all construction periods, renovated floors and walls clearly remain above the values for new buildings. This may indicate that ceilings/roofs are comparably easy to renovate. Compared to the analysis from 2021 in (Heidenthaler et al. 2022), confidence intervals decreased, as one would expect for a larger sample size. Especially for the last two construction periods, the confidence intervals are quite narrow for both, SFH and MFH.

For some construction periods and building elements, U-values for not-renovated buildings decreased significantly compared to the dataset from 2021. This suggests that some buildings may undergo a (partly) renovation without issuing a new EPC of type renovation. Hence, the number of renovated buildings may even be higher than initially apparent. This can be observed e.g. for floors of single-family houses from the oldest construction period, where median U-value decreased from 1.14 W/(m²K) in the old dataset to 0.96 W/(m²K) in the new dataset. The following analysis of U-values of not-renovated buildings in relation to the year of upload provides further insights in this regard.

Figure 8 and figure 9 depict the median U-values of not-renovated buildings in relation to the year of upload for single-family houses and multi-family houses. For this purpose, the data is subdivided according to three five-year periods concerning the year of upload, namely 2010-2014, 2015-2019 and 2020-2024. A decrease of the median U-value of a building element over the different upload periods may indicate, that a building element has undergone renovation, although no renovation EPC has been issued. For some building elements, this is clearly the case.

Almost all building elements show a decrease in U-values for the most recent upload period compared to the oldest period for both, single-family and multi-family houses, even though this decline is not significant in all cases. In general, this is more obvious for older buildings compared to buildings constructed more recently. Median U-values of floors from the oldest construction period for example decreased from 1.2 W/(m²K) (2010-2014) to 0.89 W/(m²K) (2020-2024) for single-family houses and from 1.0 W/(m²K) (2010-2014) to 0.88 W/(m²K) (2020-2024) for multi-family houses. The median U-values do not decrease steadily over the different upload periods. Instead, they might even increase, as in the previous example, where U-values increased from the second (2015-2019) to the third (2020-2024) period. This could suggest that in recent years, although some buildings may have undergone a partly renovation, EPCs have been issued for older buildings as well, for which no EPC previously existed.

Nevertheless, these conclusions must be viewed with caution, as such fluctuations of U-values could also be due to statistical uncertainties. To be able to make reliable statements about the development of renovations and associated U-values, further investigations are required.

Conclusion

Energy performance certificates contain a vast amount of valuable information. The number of EPCs grew rapidly over the last years with a particularly significant increase of EPCs of class renovation. For the first time, the number of EPCs for renovated single-family buildings exceeded the number of unrenovated single-family buildings in 2023, indicating a change in public awareness regarding the renovation of buildings.

An analysis of energy carriers shows a clear shift away from fossil fuels towards renewable energy. For single-family houses, electricity (heat pumps) account for the largest share in both, renovated and not-renovated buildings, whereas district heating is more common in multi-family houses.

A close look at the median U-values of different building elements demonstrate a steady reduction for more recent construction periods and U-values comparable to new buildings for renovated buildings. Comparing the U-values in relation to the upload year reveals that a decrease can be observed not only for renovated buildings, but for not-renovated buildings as well, indicating that some buildings may have undergone a partly renovation although no EPC of type renovation has been issued. These findings pave the way for further interesting investigations regarding renovation rates and in general the renovation status of the building stock. Due to statistical uncertainties, further investigations in this regard are necessary for robust conclusions. Such investigations could include inferential statistics for assessing confidence intervals for different upload periods or more detailed observations of individual buildings by comparing consecutive EPCs for one building.

The analysed EPC data can serve as a basis and input for simulation models on both building level (if sufficient and qualitative data on building level is available) and city or country level. Based on the analysed data such as U-values, detailed physical building models may be created and complemented with data from literature where necessary (the authors refer to Heidenthaler et al. 2023 as an example for using EPC-data in automated UBEM). The increasing number of EPCs, efforts towards public accessible databases and standardization of calculation methods further facilitate the broad application of such modelling approaches based on EPC-data and their transferability in the near future.

References

Beltrán-Velamazán C, Monzón-Chavarrías M, López-Mesa B (2024). A new approach for national-scale Building Energy Models based on Energy Performance Certificates in European countries: The case of Spain. *Heliyon*, doi:10.1016/j.heliyon.2024.e25473.

European Comission (2021). Proposal for a DIRECTIVE OF THE EUROPEAN PARLIAMENT AND OF THE COUNCIL on the energy performance of buildings (recast). Brussels. Available at https://ec.europa.eu/energy/sites/default/files/proposal-recast-energy-performance-buildings-directive.pdf.

Heidenthaler D, Deng Y, Leeb M, Grobbauer M, Kranzl L, Seiwald L, Mascherbauer P, Reindl P, Bednar T (2023). Automated energy performance certificate based urban building energy modelling approach for predicting heat load profiles of districts. *Energy*, doi:10.1016/j.energy.2023.128024.

Heidenthaler D, Leeb M, Reindl P, Kranzl L, Bednar T, Moltinger M (2022). Building stock characteristics of residential buildings in Salzburg, Austria based on a structured analysis of energy performance certificates. *Energy and Buildings*, doi:10.1016/j.enbuild.2022.112401.

Iribar E, Sellens I, Angulo L, Hidalgo JM, Sala JM (2021). Nonconformities, Deviation and Improvements in the Quality Control of Energy Performance Certificates in the Basque Country. *Sustainable Cities and Society*, doi:10.1016/j.scs.2021.103286.

Johari F, Shadram F, Widén J (2023). Urban building energy modeling from geo-referenced energy performance certificate data: Development, calibration, and validation. *Sustainable Cities and Society*, doi:10.1016/j.scs.2023.104664.

Kamel E (2022). A Systematic Literature Review of Physics-Based Urban Building Energy Modeling (UBEM) Tools, Data Sources, and Challenges for Energy Conservation. *Energies*, doi:10.3390/en15228649.

Pasichnyi O, Wallin J, Levihn F, Shahrokni H, Kordas O (2019). Energy performance certificates — New opportunities for data-enabled urban energy policy instruments? *Energy Policy*, doi:10.1016/j.enpol.2018.11.051.

Semple S, Jenkins D (2020). Variation of energy performance certificate assessments in the European Union. *Energy Policy*, doi:10.1016/j.enpol.2019.111127.

BauSIM 2024 in Wien
23. September – 26. September

Exploring Urban Typology Impacts on Trade-Offs between Global Warming Potential, Costs, and Outdoor Thermal Comfort

Roland Reitberger[1], Herbert Palm[2] and Werner Lang[1]

[1] *Technical University of Munich, Energy Efficient and Sustainable Design and Building*

[2] *Munich University of Applied Sciences, Institute for Sustainable Energy Systems*

Abstract

Trade-offs between climate change mitigation, adaptation, and costs are challenging the sustainable transformation of urban neighborhoods. Guiding urban planners in dealing with this multi-objective problem promotes balanced decision-making in the early planning phases. We use a highly interconnected neighborhood simulation model to quantify trade-offs between the three aspects and investigate case study areas in Munich, Germany. Following the concept of Urban Systems Exploration, a multi-objective optimization (MOO) algorithm is utilized to search for Pareto-optimal solutions with specific characteristics. Thereby, the Pareto fronts for the best possible trade-off in row, block, and detached typologies are identified. Comparing the results indicates strongly pronounced trade-offs between global warming potential and outdoor thermal comfort for detached typologies. The MOO analysis sensitizes urban planners to such interdisciplinary considerations and provides decision-making support in the early design phases.

Background

Climate change is challenging the current state of urban areas. On the one hand, up to 76 % of greenhouse gas emissions from final energy use stem from cities, making them one of the major mitigation potentials (Seto et al. 2014). On the other hand, urban areas are highly affected by climate change impacts like urban heat or stormwater. Thus, urban planners must progress quickly and implement climate change mitigation and adaptation simultaneously. However, although these two are highly interconnected, they are often considered separately in research and practice (Daniel et al. 2023). In addition, the evidence-based urban planning process is not always fully integrated into departmental structures and is often a matter of experience (Abd Elrahman & Asaad 2021).

Urban planning takes place within an interdisciplinary framework. Each discipline brings specific aspects, objectives, and constraints to the planning process. This results in the need for compromise solutions, the aim of which must be to achieve Pareto optimality. During the inherent decision-making process, trade-offs must be explicitly identified, quantified, and included in the discussion to meet the context-specific needs of urban areas. However, urban planners are hardly provided with guidance to handle such trade-offs (Xu et al. 2019). In particular, neighborhood development is characterized by many interactions (Jenkin & Pedersen 2009), and the resulting trade-offs can vary in severity. Research has shown examples where lifecycle-based global warming potential (GWP) and outdoor thermal comfort form trade-offs, e.g. by the contradiction that low density and high green area are good for adaptation, but mitigation improves with higher urban density (Xu et al. 2019). Furthermore, economic efficiency and the energy demand of buildings, which are highly relevant to GWP, also represent a multi-objective problem (Hillebrand et al. 2014). Our paper enhances these findings by investigating the Pareto-optimal trade-offs between lifecycle-based GWP, outdoor thermal comfort, and lifecycle costs and shows how they differ for three generic urban typologies. The results allow us to identify typologies where the trade-off must be handled with particular care. Therewith, we aim to reveal urban planners' steering options in early design phases.

State of Research

Urban environment trade-off dependencies

In urban development, multiple factors interact dynamically, requiring a thorough trade-off assessment for decision-making. One pivotal aspect is the role of green elements, which amplify the interaction between climate change mitigation and adaptation (Daniel et al. 2023). The intricate trade-offs

extend to seemingly subtle choices, such as the selection of tree species. Sharifi (2020) emphasizes the significant impact that this decision can have on urban trade-offs. McLeod et al. (2013) highlight the trade-off between building energy demand and indoor thermal comfort. They show that high energy standards may cause a worsening in the thermal performance of buildings. Furthermore, urban trees have been shown to influence this energy-comfort trade-off (Reitberger et al. 2023). Taking a broader perspective, Natanian et al. (2019) investigate trade-offs across diverse urban typologies. Their exploration of the trade-off between load-match and spatial daylight autonomy utilizes a parametric simulation model that captures essential metrics and represents various typologies. Their study shows significant variations among typologies, highlighting the nuanced nature of urban trade-offs. These studies underline the importance of considering environmental concerns and architectural decisions when developing balanced urban development strategies.

Trade-off exploration in urban systems

Research emphasizes the need for a multi-objective evaluation of trade-offs rather than optimizing for individual target dimensions (Li et al. 2022). While numerous studies have investigated specific multi-objective problems for various typologies (Natanian et al. 2019, Abdollahzadeh & Biloria 2022), the focus has often been more on the specific characteristics and simulation outcomes of neighborhoods rather than the behavior of trade-offs themselves. To address this behavior in the urban context, it is imperative to fully explore the trade-offs' extent. Making trade-offs assessable requires structured processes and methods. The Hyper Space Exploration provides a framework for this task. It distinguishes between modifiable variables (Design Space), target aspects (Target Space), and examined scenarios (Use Space) (Palm & Holzmann 2018). This principle was transferred to Urban Systems Exploration for investigating trade-offs in the urban context (Reitberger et al. 2024). By constructing a simulation model and performing multi-objective optimization (MOO), a comprehensive understanding of the target range and steering variables can be achieved. This approach provides a holistic perspective, moving beyond specific neighborhood characteristics to consider the range of trade-offs in urban planning. Thereby, it improves multi-objective decision-making in early design phases, where major impact on the results of urban designs is possible (Basbagill et al. 2013).

Methodology

The newly proposed methodology aims to quantify the trade-offs between GWP, lifecycle costs, and outdoor thermal comfort for different typologies. It combines the current state of research on neighborhood simulation with design exploration to investigate trade-off characteristics, providing decision support to urban planners in early design phases. A particular focus is on including complex target variables and the complete representation of Pareto fronts. This section describes its two main components: the simulation model and the MOO tool-chain, which follows the concept of Urban Systems Exploration (Reitberger et al. 2024).

Urban typology simulation model

In order to quantify the trade-offs, an urban simulation model that considers interactions between the aspects of lifecycle GWP, lifecycle costs, and outdoor thermal comfort is introduced. This model can simulate urban design scenarios and determine quantitative Key Performance Indicators for the three optimization targets. Figure 1 shows a schematic representation of the integrated interactions. The model is set up in the Grasshopper environment, where several components are combined: the Urban Weather Generator for considering the Urban Heat Island Effect (Bueno et al. 2013), Fast-Fluid-Dynamics for wind simulation (Waibel et al. 2017), building energy simulation with photovoltaics (PV) (Roudsari & Pak 2013), and a Python implementation of ecological Lifecycle Assessment (LCA) and Lifecycle Costing (LCC). Data exchange and common inputs are emphasized while setting up the model. For instance, PV areas lead to changing albedos of the respective surfaces, which serve as inputs for the Urban Weather Generator and thus influence the climatic conditions in the energy and outdoor thermal comfort assessment. Three typological Use Cases define the buildings' geometry: row, block, and detached. These typologies represent the most common in German cities and are therefore highly transferable (ZSK 2017). All case study areas are located in Munich and weather data is retrieved from Meteotest AG (2023). Table 1 summarizes the overarching boundary conditions. Refurbishment is considered for all typologies. Streets and trees in the outdoor space and building-related design variables, such as PV on roof and façades, are part of the MOO. Table 2 shows their respective design ranges.

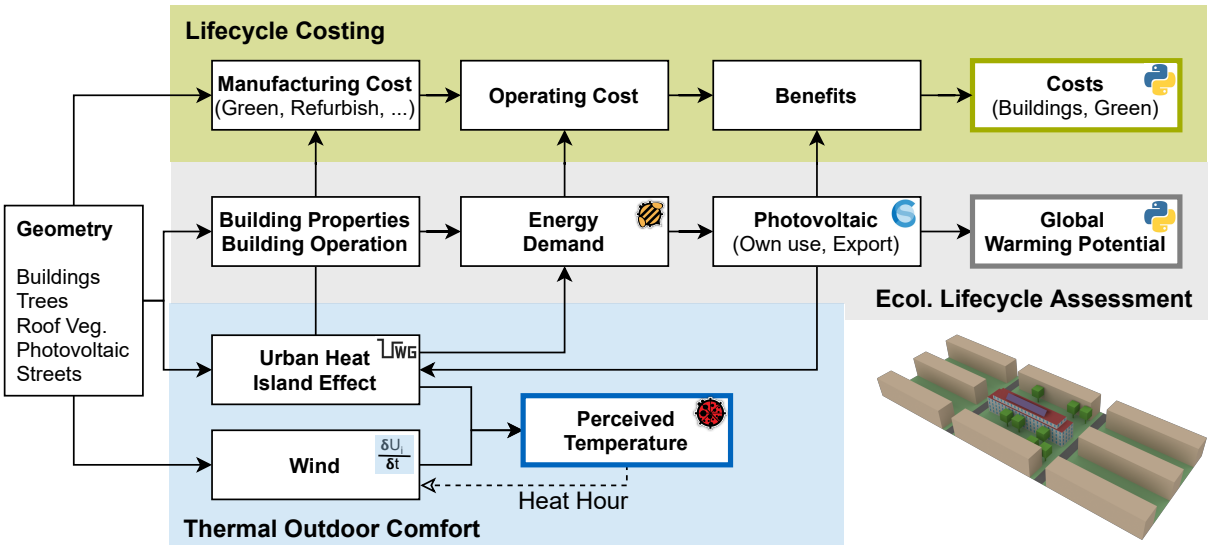

Figure 1: Simplified representation of information flow to the target variables in the simulation model.

The LCC values were compiled from sources related to the German context (BKI 2022, f:data 2022). Missing values for vegetation were obtained by literature search (Saha et al. 2019, Eschenbruch 2012). All scenarios are run with an air-heat pump (coefficient of performance = 3.0), and the cost of electricity is set at the average household price of 0.4229 € per kWh in the first half of 2023 (Statistisches Bundesamt 2023). Exported PV electricity is credited with 0.082 € to 0.058 € per kWh depending on the size of the system in accordance with the Renewable Energy Sources Act in Germany. In addition, price increases of 5 % per year on energy prices, 2 % per year for construction services, and a discount rate of 1.5 % are applied (BMI 2021). For the LCA, the phases of production (A1-A3), operation (B4, B6), and end-of-life (C3-C4) are considered. The German LCA database Ökobaudat (2020-II) is used (BBSR 2023). LCA and LCC are both conducted for a 50-year period and are related to one square meter of gross floor area. GWP and monetary benefits from electricity production are linearly reduced to zero until the assessment year 25, as by then Germany intends to be climate neutral in its electricity mix (Bundesnetzagentur 2022). The Universal Thermal Climate Index (UTCI) quantifies outdoor thermal comfort during the most uncomfortable hour of the year (Błażejczyk et al. 2013). Therefore, a point grid in the neighborhood is used, and the simulated UTCI results for the points are averaged into one value.

Multi-objective optimization

The simulation models for the three typologies are subjected to an MOO. All three targets form minimization problems for which the Pareto front (PF) needs to be identified. Focusing on Pareto points (PPs) is imperative because, for solutions that lie behind the PF, a solution that performs better in all three target aspects can be found. Hence, solutions that are not Pareto-optimal should not be pursued. Since the simulation model is computationally expensive, with one evaluation taking up to 30 minutes, an MOO environment needs to be capable of identifying many PPs with a small number of model evaluations. The tool-chain described by Reitberger et al. (2024) is used to couple the simulation models with the optimization environment. For the MOO itself, the Paref algorithm is utilized (Palm & Palm 2023). This algorithm mathematically guarantees the identification of PPs and allows to search for PPs with specific properties. Therewith, the PF edges can be identified effectively and efficiently, enabling a complete impression of the trade-off extent. The identified edge points are utilized to search for a regular grid of PPs between them. This reveals the rough shape of the PF for each of the three typologies.

Results and discussion

The presented workflow identified 28 PPs for the row housing, 36 PPs for the block housing, and 58 PPs for the detached housing. Figure 2 illus-

Table 1: Fixed simulation boundary conditions. BAC = Building Age Class according to Loga et al. (2015).

Parameter	Input	Source
Building dimensions [m]	row: 60x12x18; detached: 16x10x9; block: 70x85x25 with courtyard 40x55	(bayernatlas.de 2023)
U-value sets (BAC, constr. year) Wall, Roof, Base, Window [W/m^2· K]	row: C 1946 block: D 1956 det.: E 1962 refurbished: 0.15, 0.15, 0.15, 0.7	(Loga et al. 2015) (Passivhaus Institut 2022)
Heating setpoint [°C]	20	(DIN 2018)
Internal heatgain [people / m^2]	0.025	(DIN 2018)
Occupancy schedules	Mo-Fr: 17 - 7h; Sa-Su: 0 - 24h	-
Infiltration [m^3/s per m^2 façade]	after refurbishment: 0.0001	(Roudsari & Pak 2013)
PV efficiency [%]	modules: 22; battery: 70	(NREL 2023)
LCA insulation [-]	eco standard	(Banihashemi et al. 2022)

Table 2: Design Space for the simulation.

Nb	Input	Range
1	Tree percentage [%]	[0, 100]
2	Tree crown diameter [m]	[2, 10]
3	Tree height from ground [m]	[6, 10]
4	Crown transpar. summer [%]	[10, 30]
5	Crown transpar. winter [%]	[45, 80]
6	PV roof [%]	[0, 100]
7	PV south façade [%]	[0, 100]
8	PV east-west façade [%]	[0, 100]
9	PV battery capacity [kWh]	[0, 80]
10	Green roof soil thickness [m]	[0, 0.25]
11	Window-to-Wall Ratio [%]	[10, 50]
12	Solar heat gain coefficient [-]	[0.4, 0.85]
13	Albedo façade [-]	[0.1, 0.7]
14	Street width [m]	[3, 9]

trates the PF for the row housing typology in the three-dimensional Target Space. Each optimum in one target can only be achieved by accepting trade-offs with one or both of the other targets. The ranges of the respective target dimensions are: 29.2 to 33.9 °C for outdoor thermal comfort; -2.5 to 6.5 kgCO_2-eq./m^2·yr for lifecycle GWP; 1,780 to 2,162 €/m^2 for lifecycle costs.

For outdoor thermal comfort, the results show that a change of one heat stress level on the UTCI scale can be achieved within the Pareto solutions since the threshold between moderate and strong heat stress is 32 °C (Błażejczyk et al. 2013). The lifecycle GWP varies widely between the PPs and sometimes even becomes negative. This has been shown in other studies dealing with zero-carbon buildings, especially when PV systems are taken into account (Stephan & Stephan 2020). However, there is also contradictory research where case studies do not reach zero-carbon results. For instance, the study of Passer et al. (2016) shows no lifecycle GWP values below zero for building refurbishment in the Austrian context. These deviations may be due to differences in assessment boundaries and assumptions, such as the consideration of embodied impacts of heating systems. Our study did not include these as we only compared heat pump scenarios. Furthermore, we used the German electricity mix with the assumption of a transformation to renewables within the first 25 assessment years, while Passer et al. (2016) include a share of fossil fuels in their study. Therefore, we do not interpret our results as achieving a holistic net zero-carbon building. However, they indicate a certain range of GWP in the Pareto-optimal set.

Figure 3 shows the significant difference between the three urban typologies regarding their PF characteristics. The range of LCA results narrows from detached to row to block typology. The block typology exhibits less variation and a sharp increase in GWP in the minimal UTCI zone (green points in Figure 3). This implies that significant increases in GWP are only necessary to achieve the best possible outdoor thermal comfort. A slight reduction of outdoor thermal comfort targets opens the possibility of decreasing GWP by up to 54 % in our block case study. The detached typology shows a more even trade-off progression. Accordingly, the trade-off between GWP and outdoor thermal comfort offers a broader range of optimal solutions

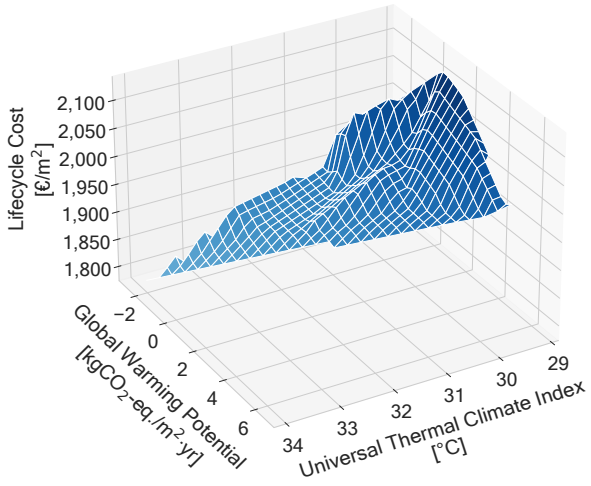

Figure 2: Pareto front of the row housing typology case study. All dimensions should be minimized.

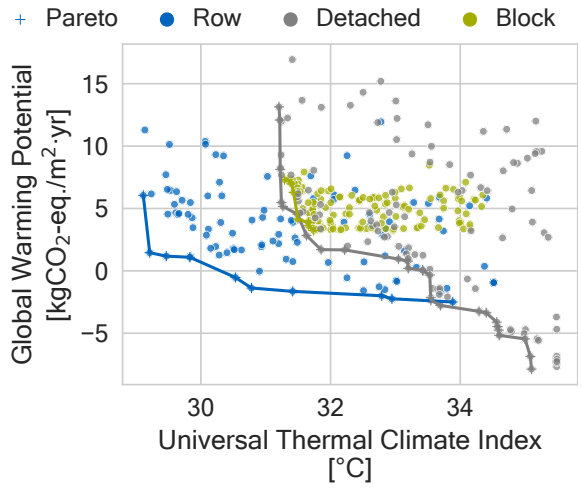

Figure 3: Pareto fronts of the considered urban typologies for the trade-off between GWP and UTCI.

in the detached typology. The trade-off extent of the row typology is located between block and detached typologies. Continuous areas can be identified where outdoor thermal comfort can be improved without a significant increase in GWP. However, completely minimizing UTCI substantially increases GWP for the row housing typology. In our study, it is possible to improve outdoor thermal comfort while keeping a small GWP trade-off up to a certain point, approximately 31 °C. One of the reasons for this trade-off is the shading effect from trees on buildings, which causes an increase in heating energy demand. Further, PV surfaces get shaded by dense tree placement, which reduces their productivity and thus increases GWP.

Figure 4 shows the Design Space associated with the identified PPs. For comparability, we normalized them according to the input ranges in Table 2. For row and block typologies, Pareto solutions behave similarly for tree percentage and crown diameter, but the values of the detached typology deviate. This shows the varying influence of vegetation on the typologies' trade-offs. While a few trees heavily shade façades and roofs of detached houses, this effect is less pronounced for the much bigger row and block typologies. Daniel et al. (2023) argue that vegetation is among the best measures for climate change adaptation. They find that interventions in outdoor spaces often have a more significant impact on climate change mitigation and adaptation than building interventions. In our study, the effect on outdoor thermal comfort is comparable for all typologies. However, the span of LCA results and therewith the balancing options of Pareto solutions are higher for the detached typology than for row and block typologies. This may explain why there are different optimal input configurations of Pareto solutions. The tree height variable is in the lower third for all typologies. Accordingly, there are still some common behaviors between the typologies when it comes to steering trade-offs.

In terms of PV surfaces, there is only a significant deviation for roof PV, which is in the medium to high range for detached and row developments and low for block developments. This may be related to the high proportion of north-facing roof surfaces in the block case study. In the simulation model, north-facing roofs are also equipped with PV systems. The row and detached typology case studies are north-south oriented, resulting in fewer low-performing north-facing roof surfaces. This makes the variable more significant for achieving optimal solutions. All typologies show high values for façade PV. Thus, the parameter has only a minor influence on the differences between the typologies in terms of trade-offs. This might change with varying densities within the typologies, as density affects the shading of façades. The PV battery capacity is determined low for smaller individual buildings since they have low own consumption. For row and block typologies, the Pareto solutions have capacities of around 40 kWh. From the remaining inputs, green roofs with low to medium thickness are beneficial for all typologies. Window-related inputs are also in comparable ranges for all typologies. The street width is in the medium to low range for all typologies, indicating optimal solutions, especially for low-traffic areas with more space for trees.

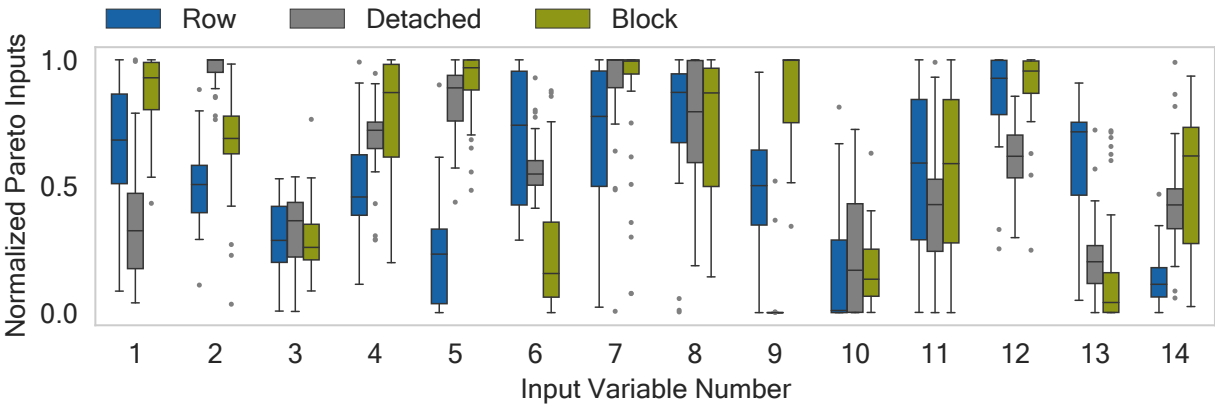

Figure 4: Boxplots of inputs leading to Pareto solutions. Input variable numbers refer to Table 2.

Limitations

In this study, we considered only one type of building arrangement per urban typology. Although these arrangements refer to a real area, they do not represent all possible configurations. Furthermore, the Use Cases define important boundary variables, such as the primary energy supply. This limits the transferability, as the multitude of types and forms within each typology introduces complexity that may give rise to distortions in the findings (Shi et al. 2021). The assumptions regarding the credits for generated electricity by PV systems significantly influence the outcomes of LCA and LCC. Additionally, volatile construction prices lead to uncertainties in the LCC results. The simulation model only offers a simplified representation of trees and their seasonal foliage dynamics. The complexity of tree behavior and the nuances of foliage throughout the seasons cannot be fully captured in the simulation, potentially limiting simulation accuracy. All case studies conducted herein are geographically constrained to Munich and rely on local weather data. Consequently, the results and conclusions drawn apply to this context.

Figure 4 compares the distribution of inputs leading to Pareto solutions. It does not allow the derivation of a certain input combination, as in MOO, optimal solutions are frequently found at the edges of the search space. However, it helps to understand which typologies are comparable regarding their trade-off behavior. Finally, there is a risk that the full range of Pareto solutions has not been discovered. Although a mathematically proven algorithm has been used, there may be solutions close to the Pareto property that were not identified within the MOO process of this study. However, such solutions could also inform urban decision-making.

Conclusion and outlook

This paper investigates how the extent of multi-objective trade-offs relates to urban typology. Neighborhood simulation models are examined for their Pareto fronts using multi-objective optimization and the associated inputs are compared. The results show that the trade-offs between lifecycle GWP, lifecycle costs, and outdoor thermal comfort differ significantly for the row, block, and detached typologies. In addition, the inputs can be used to conclude general typology constraints that support the achievement of Pareto-optimal solutions.

This holds several implications for urban planning practice and the utilization of interactions between the three aspects. Our study shows that each typology's unique characteristics significantly influence the optimal solution space. Hence, tailoring urban planning strategies to specific contexts is necessary. For instance, the block typology exhibits a narrower range of trade-offs, suggesting a more rigid relationship between thermal comfort and GWP. On the other hand, the row housing typology offers a more flexible trade-off space, emphasizing the need for balancing approaches during decision-making. The different input ranges of optimal solutions further underline the importance of typology-specific considerations. Tree and PV configurations differ significantly regarding trade-offs among GWP, costs, and outdoor thermal comfort. This contradicts one-fits-all approaches in urban planning, urging planners to strengthen their interdisciplinary and adaptable mindset. It is important to acknowledge the limitations of this study when generalizing the results. These include using simplified building geometries, assumptions about energy supply and construction costs, and the geographical constraints of the case studies.

In conclusion, this research advocates for an evidence-based and balanced approach to urban planning. Planners can design sustainable and resilient neighborhoods by recognizing and navigating the inherent trade-offs among environmental, economic, and social dimensions. To allow this, they need complete insights into the existing trade-offs, which is only possible when targets are shown next to each other and not aggregated into single values.

Future work should extend the idea of Urban Systems Exploration by incorporating typology properties into the Design Space. This would allow an in-depth understanding of the trade-off behavior, and new Use Cases could be introduced. For instance, building density could be parameterized to identify optimal configurations for the typologies and investigate the influence of density on the trade-offs. More detailed simulation models can be explored as computational power increases and simulation components improve, allowing a more detailed differentiation of design variables. Furthermore, sufficient visualizations for multi-objective decision-making should be investigated to make the findings easily accessible to urban planning practice.

Acknowledgment

This work was carried out within the research training group Urban Green Infrastructure (German Research Foundation, 437788427 - RTG 2679).

References

Abd Elrahman, A. S. & Asaad, M. (2021), 'Urban design & urban planning: A critical analysis to the theoretical relationship gap', *Ain Shams Engineering Journal* **12**(1), 1163–1173.

Abdollahzadeh, N. & Biloria, N. (2022), 'Urban microclimate and energy consumption: A multi-objective parametric urban design approach for dense subtropical cities', *Frontiers of Architectural Research* **11**(3), 453–465.

Banihashemi, F., Erlwein, S., Fellner, J., Meister, J., Reitberger, R., Schade, C., Lang, W., Pauleit, S. & Petzold, F. (2022), 'Nachverdichtung im Kontext des Klimawandels - Schlussbericht'.

Basbagill, J., Flager, F., Lepech, M. & Fischer, M. (2013), 'Application of life-cycle assessment to early stage building design for reduced embodied environmental impacts', *Building and Environment* **60**, 81–92.

bayernatlas.de (2023), 'Bayern atlas'.
URL: *https://geoportal.bayern.de/bayernatlas/*

BBSR (2023), *Ökobaudat: Informationsportal Nachhaltiges Bauen*, Bundesministerium für Wohnen, Stadtentwicklung und Bauwesen.
URL: *https://www.oekobaudat.de/*

BKI (2022), *BKI Baupreise kompakt 2023 Altbau: Statistische Baupreise für Positionen mit Kurztexten*, BKI Kostenplanung, Verlagsgesellschaft Rudolf Müller, Stuttgart.

Błażejczyk, K., Jendritzky, G., Bröde, P., Fiala, D., Havenith, G., Epstein, Y., Psikuta, A. & Kampmann, B. (2013), 'An introduction to the universal thermal climate index (utci)', *Geographia Polonica* **86**(1), 5–10.

BMI (2021), *Neubau Büro- und Verwaltungsgebäude: Gebäudebezogene Kosten im Lebenszyklus V 2015*, Bundesministerium des Innern, für Bau und Heimat.

Bueno, B., Norford, L., Hidalgo, J. & Pigeon, G. (2013), 'The urban weather generator', *Journal of Building Performance Simulation* **6**(4), 269–281.

Bundesnetzagentur (2022), 'Genehmigung des Szenariorahmens 2023-2037/2045'.

Daniel, R., Cortesão, J., Steeneveld, G.-J., Stremke, S. & Lenzholzer, S. (2023), 'Performance of urban climate-responsive design interventions in combining climate adaptation and mitigation', *Building and Environment* **236**(110227).

DIN (2018), 'DIN V 18599-10: Energetische Bewertung von Gebäuden – Berechnung des Nutz-, End- und Primärenergiebedarfs für Heizung, Kühlung, Lüftung, Trinkwarmwasser und Beleuchtung – Teil 10: Nutzungsrandbedingungen, Klimadaten'.

Eschenbruch, H. (2012), 'Daten für die Erstellung und Unterhaltung von Grünanlagen überarbeitet: Neue Kennzahlen'.

f:data (2022), 'Baupreislexikon'.
URL: *https://www.baupreislexikon.de/*

Hillebrand, G., Arends, G., Streblow, R., Madlener, R. & Müller, D. (2014), 'Development and design of a retrofit matrix for office buildings', *Energy and Buildings* **70**, 516–522.

Jenkin, S. & Pedersen, M. (2009), 'Rethinking our

built environment', *New Zealand - Ministry for the Environment* .

Li, P., Xu, T., Wei, S. & Wang, Z.-H. (2022), 'Multi-objective optimization of urban environmental system design using machine learning', *Computers, Environment and Urban Systems* **94**(101796).

Loga, T., Stein, B., Diefenbach, N. & Born, R. (2015), 'Deutsche Wohngebäudetypologie: Beispielhafte Maßnahmen zur Verbesserung der Energieeffizienz von typischen Wohngebäuden'.

McLeod, R. S., Hopfe, C. J. & Kwan, A. (2013), 'An investigation into future performance and overheating risks in passivhaus dwellings', *Building and Environment* **70**, 189–209.

Meteotest AG (2023), 'Meteonorm'.
URL: *https://meteonorm.com/*

Natanian, J., Aleksandrowicz, O. & Auer, T. (2019), 'A parametric approach to optimizing urban form, energy balance and environmental quality: The case of mediterranean districts', *Applied Energy* **254**(113637).

NREL (2023), *Best Research-Cell Efficiency Chart*, National Renewable Energy Laboratory.

Palm, H. & Holzmann, J. (2018), 'Hyper space exploration a multicriterial quantitative trade-off analysis for system design in complex environment', *International Systems Engineering Symposium (ISSE)* pp. 1–6.

Palm, N. & Palm, H. (2023), 'Multi-objective optimization algorithm classification by composing black box with pareto-reflecting functions', *Preprint on SSRN* .
URL: *https://pypi.org/project/paref/*

Passer, A., Ouellet-Plamondon, C., Kenneally, P., John, V. & Habert, G. (2016), 'The impact of future scenarios on building refurbishment strategies towards plus energy buildings', *Energy and Buildings* **124**, 153–163.

Passivhaus Institut (2022), 'Kriterien für den Passivhaus-, EnerPHit- und PHI-Energiesparhaus-Standard: Version 10b'.

Reitberger, R., Palm, N., Palm, H. & Lang, W. (2024), 'Urban systems exploration: A generic process for multi-objective urban planning to support decision making in early design phases', *Building and Environment* **254**(111360).

Reitberger, R., Theilig, K., Vollmer, M., Takser, I. & Lang, W. (2023), 'Connecting building density and vegetation to investigate synergies and trade-offs between thermal comfort and energy demand', *IOP Conference Series: Earth and Environmental Science* **1196**(012034).

Roudsari, M. S. & Pak, M. (2013), 'Ladybug: a parametric environmental plugin for grasshopper to help designers create an environmentally-conscious design', *13th IBPSA Conference* pp. 3128–3135.

Saha, S., Kandarr, J. & Jorzik, O. (2019), 'Stadtbäume im Stress. Interview [Teil 1]'.

Seto et al. (2014), *Human settlements, infrastructure and spatial planning*, IPCC Working Group III Contribution to AR5, Cambridge University Press.

Sharifi, A. (2020), 'Trade-offs and conflicts between urban climate change mitigation and adaptation measures: A literature review', *Journal of Cleaner Production* **276**(122813).

Shi, Z., Fonseca, J. A. & Schlueter, A. (2021), 'A parametric method using vernacular urban block typologies for investigating interactions between solar energy use and urban design', *Renewable Energy* **165**, 823–841.

Statistisches Bundesamt (2023), 'Pressemitteilung Nr. 388 vom 29. September 2023'.

Stephan, A. & Stephan, L. (2020), 'Achieving net zero life cycle primary energy and greenhouse gas emissions apartment buildings in a mediterranean climate', *Applied Energy* **280**, 115932.

Waibel, C., Bystricka, L., Kubilay, A., Evins, R., Carmeliet, J., Bystricky, L. & Kubilay, A. (2017), 'Validation of grasshopper-based fast fluid dynamics for air flow around buildings in early design stage', *15th IBPSA Conference* .

Xu, L., Wang, X., Liu, J., He, Y., Tang, J., Nguyen, M. & Cui, S. (2019), 'Identifying the trade-offs between climate change mitigation and adaptation in urban land use planning: An empirical study in a coastal city', *Environment international* **133**(105162).

ZSK (2017), 'Zentrum für Stadtnatur und Klimaanpassung: Klimaschutz und grüne Infrastruktur in der Stadt: Abschlussbericht'.

BauSIM 2024 in Wien
23. September – 26. September

Gebäudetypen für Nicht-Wohngebäude zur vereinfachten Durchführung von Lebenszyklusanalysen auf Stadtquartiersebene

Antonia Beltinger[1], Nico Ehlers[2], Chujun Zong[3], Werner Lang[4]
1 TU München, Deutschland, E-Mail: a.beltinger@tum.de
2 TU München, Deutschland, E-Mail: nico.ehlers@tum.de
3 TU München, Deutschland, E-Mail: chujun.zong@tum.de
4 TU München, Deutschland, E-Mail: w.lang@tum.de

Kurzfassung

Zur Erreichung der deutschen Klimaziele ist eine emissionsarme und ressourceneffiziente Weiterentwicklung des Gebäudebestandes unerlässlich. Mögliche Szenarien können in lebenszyklusbasierten Analysen großer Gebäudebestände auf Basis von semantischen 3D-Stadtmodellen simuliert werden. Als Grundlage hierfür wurde eine Typologie entwickelt, die energetisch relevante baukonstruktive Elemente von Gewerbe- und Industriegebäuden als Datenmodell abbildet.

Die Attribuierung der Typen beruht auf einer Auswertung der repräsentativen Stichprobe der deutschen Gewerbe- und Industriegebäude in der Forschungsdatenbank ENOB:dataNWG. Die darüber nicht zu generierenden Informationen wurden auf Basis einschlägiger, v.a. bauzeitlicher, Literatur gewonnen.

So konnten insgesamt 16 Typen durch jeweils ein synthetisches Gebäude inkl. Aufbauten ihrer Hüllbauteile beschrieben werden. Für diese wurden Abschätzungen des energetischen Ist-Zustandes in Form von U-Werten getroffen und darauf aufbauend zwei mögliche Szenarien energetischer Sanierung definiert.

Ferner wurden den Typen über die definierten synthetischen Gebäude ökologische Kenndaten der Umweltwirkung (GWP) und des Ressourceneinsatzes (PERT, PENRT) entsprechend DIN EN 15978 zugewiesen. Sie werden nach Lebenszyklusphasen (A1-3, B4, C3-4 und D) und Bauteilschichten getrennt ausgewiesen, um in der Anwendung der Typologie unterschiedliche Szenario-Berechnungen zur zukünftigen Entwicklung des Gebäudebestandes zu ermöglichen und die Ergebnisse vergleichen zu können.

Abstract

Emission and resource efficient development of the building stock is essential for achieving national climate targets. Development scenarios of large building stock should therefore be simulated and compared across all life cycle stages to identify sustainable solutions. This requires a data model, developed in form of a typology enriching 3D city models by depicting building envelope components.

The attribution of the building types is primarily based on the results of analyses of a representative sample of german commercial and industrial buildings in the ENOB:dataNWG research database, enhanced by relevant literature, particularly from the construction periods. Thusly 16 types were created for commercial and industrial buildings, each described by a synthetic building and its envelope components. Corresponding U-values were estimated to allow the calculation of scenarios for energetic refurbishment of varying levels of ambition.

The 16 synthetic buildings were used to assign characteristics of environmental impact (GWP) and resource usage (PERT, PENRT) conforming to DIN EN 15978. The data is shown separately, according to life cycle phases (A1-3, B4, C3-4 and D) and building component layers, to enable various alternative scenario simulations of building stock development.

Einführung

Die Bundesrepublik Deutschland hat sich das Ziel gesetzt bis 2045 klimaneutral zu sein. Um es zu erreichen, müssen im Gebäudesektor jährlich 5 Mt Co_2 Äq. eingespart werden (ERK, 2022). Es gibt unterschiedlichste Ansätze und Ideen wie dies zu erreichen sei. Um jedoch zu überprüfen welche Maßnahmen tatsächlich effektiv und

zugleich effizient sind, sind lebenszyklusbasierte Analysen großer Gebäudebestände nötig.

Zielsetzung

Diese Analysen können unter anderem mit dem von Harter entwickelten Tool Urbi+ durchgeführt werden (Harter, 2021). Momentan bildet dieses nur die technische Gebäudeausrüstung von Wohngebäuden ab, soll aber im Rahmen des Forschungsprojektes CircularGreenSimCity (HFT, o.J.; ENPB, o.J.) sowohl um baukonstruktive Elemente wie um Nichtwohngebäude (NWG) erweitert werden. Da empirische Daten über die Materialität und ökologischen Kennwerte von Bestandsgebäuden nicht systematisch erfasst sind, muss als Grundlage für Berechnungen zunächst ein Datenmodell erstellt werden. Dieses in Form einer Gebäudetypologie der baukonstruktiven Elemente einer Gruppe von NWG zu entwickeln, ist Zielsetzung der vorliegenden Arbeit.

Stand der Forschung zu NWG Typologien

Es wurden für NWG bereits einige Typologien entwickelt. Auffällig ist dabei, dass sie stark auf die Erfordernisse ihrer jeweiligen Anwendung zugeschnitten sind und sich deshalb nur schwer auf andere Anwendungen übertragen lassen. Sie lassen sich in zwei Gruppen unterteilen: Typologien für die energetische Betrachtung des Gebäudebetriebs (Deilmann et al., 2013; Dirlich et al., 2011; Klaus et al., 2010; Tiel & Riedel, 2011; Hörner & Bischof, 2022) und Typologien für die Erfassung der Materialität der baukonstruktiven Elemente (Ortlepp et al., 2016; Gruhler & Deilmann, 2015; Schiller et al., 2015; Schebek et al., 2017; Buschka, 2018; Buschka 2021). In letzterer Gruppe sticht besonders die Arbeit von Buschka hervor, da sie der Zielsetzung der vorliegenden Arbeit am nächsten kommt. Er entwickelte auf Basis der Forschungsdatenbank Nichtwohngebäude ENOB:dataNWG eine Methodik für eine die Materialität abbildende Typologie der Bürogebäude. Was Buschkas Arbeit nicht leistet, ist die Verknüpfbarkeit der Typologie mit 3D Stadtmodellen, wie dem amtlichen Level of Detail 2 (LoD2) Modell, das auf dem amtlichen Liegenschaftskatasterinformationssystem (ALKIS) aufbaut. Da die von Buschka verwendeten Klassifikationskriterien dort nicht erfasst sind, ist keine Zuordnung von Einzelgebäuden aus dem 3D Modell zu einem Typus der Typologie möglich. Außerdem ist die Typologie nicht mit ökologischen Kenndaten versehen.

Es fehlt bisher eine Typologie, die den deutschen NWG-Bestand durch Gebäudetypen abbildet, welche für lebenszyklusbasierte Analysen großer Gebäudebestände auf Basis semantischer 3D Stadtmodelle nutzbar sind.

Methodik

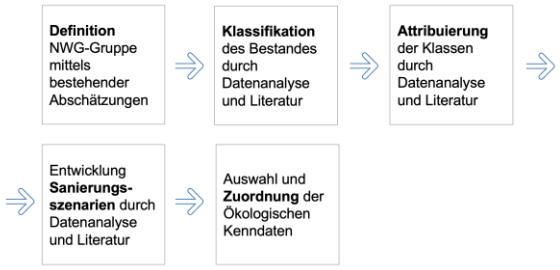

Abbildung 1: Übersicht der Methodik der Arbeit

Zur Typologisierung werden zunächst Gewerbe- und Industriegebäude als die, nach bestehenden Abschätzungen (Deilmann et al., 2013; Ortlepp, 2016), energetisch relevanteste Gruppe der NWG herangezogen.

Klassifikation

Der Gebäudetypus trägt die gemeinsamen Merkmale einer Gruppe ähnlicher Gebäude, ist dabei aber kein realer Teil dieser. Dem Typus zugrunde liegt eine Klassifikation; sie teilt den Gesamtbestand nach definierten Klassifikationskriterien in Klassen mit jeweilig verwandten Merkmalen ein und ist damit rein kategorisierend.

Bei der Klassifikation ist besonders darauf zu achten, dass die Klassifikationskriterien eine Zuordnung von Einzelgebäuden aus den Quelldaten des auf ALKIS aufbauenden amtlichen LoD2 Modells erlauben. Nur Attribute, die dort hinterlegt sind, können genutzt werden um ein jeweiliges Einzelgebäude einer Klasse und damit einem Typus zuzuordnen. Für die vorliegenden Arbeit wurden deshalb Gebäudefunktion und Baualter gewählt.

Als Datengrundlage für den Aufbau der Typologie wurde die Forschungsdatenbank ENOB:dataNWG, als einzig repräsentative Stichprobe der deutschen NWG herangezogen (IWU, 2023). Zur Nutzung ihrer Informationen wurden für die Klassifikationskriterien Baualter und Gebäudefunktion jeweils die Klasseneinteilungen der Datenbank übernommen (Cischinsky, 2022). Der Klassifikationsprozess wird dabei nur mit den Klassen fortgeführt, die mehr als 4% der Observationsanzahlen enthalten um die Validität zu gewährleisten.

Anschließend wurden die einzelnen Klassen der Gebäudefunktion und des Baualters zu einer Klassifikationsmatrix verschnitten.

Attribuierung

In einem zweiten Schritt wird für jeden Klassenschnitt durch Attribuierung von gemeinsamen Merkmalen ein charakteristischer synthetischer Vertreter, der Sub-Typus gebildet. Im Fall der Arbeit ist dies ein synthetisches Gebäude mit typischen Bauteilaufbauten.

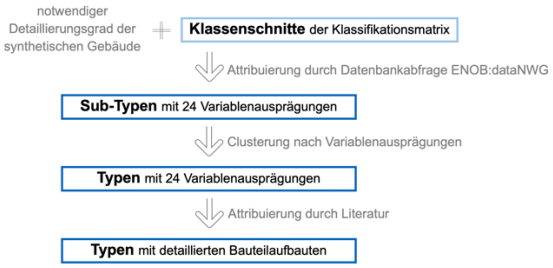

Abbildung 2: Methodische Schritte der Attribuierung

Der Detaillierungsgrad für die Attribuierung der Klassenschnitte wurde mit Hilfe des Bewertungssystems Nachhaltiges Bauen bestimmt (BMUB, o.J.). Ausgewählt wurden die Bauteile Dach, Außenwand, Verglasung, innenliegendes Tragwerk, Bodenplatte und Gründung, für die anschließend die 24 korrespondierenden Variablen in ENOB:dataNWG für alle Klassenschnitte abgefragt werden (Cischinsky, 2022). Nach Häufigkeit der Ausprägung unter den enthaltenen Observationen bzw. dem arithmetischen Mittel für numerische Variablen wird jeweils die den Klassenschnitt vertretende Variablenausprägung und somit Eigenschaft des Sub-Typus bestimmt.

Da die 24 aus ENOB:dataNWG abfragbaren Variablen nicht ausreichend sind um eine vollständige Beschreibung der Bauteilaufbauten für die Typen ableiten zu können, müssen diese unter Verwendung einschlägiger Literatur weiter ausformuliert werden. Um die Anzahl der Sub-Typen zu reduzieren, wird ein Clustering vorgenommen, bei dem über die vorhandenen Variablenausprägungen ähnliche Sub-Typen zu einem sie repräsentierenden Typus zusammengefasst werden.

Danach werden die Bauteilaufbauten der synthetischen Gebäude der geclusterten Typen mit Hilfe einschlägiger Literatur, wie bauzeitlichen Konstruktions- bzw. Industrie- und Gewerbebauatlanten oder aktueller Darstellungen historischer Baukonstruktionen, weiter ausformuliert.

Entwicklung von Sanierungsszenarien

Das energetische Niveau der für die Typen definierten Bauteilaufbauten kann in Form von U-Werten mit Hilfe des Tools Ubakus abgeschätzt werden (u-wert.net GmbH, 2023). Darauf aufbauend werden zwei exemplarische Szenarien energetischer Sanierung der baukonstruktiven Elemente definiert. Als konventionelles Szenario werden die aktuell gültigen gesetzlichen Mindestanforderungen an sanierte NWG-Bauteile aus dem Gebäudeenergiegesetz (GEG) vom 08.08.2020 in der Fassung vom 20.07.2022 definiert. Das Effizienzgebäude 40 (EG 40) gemäß der Richtlinie für die Bundesförderung für effiziente Gebäude – Nichtwohngebäude (BEG NWG) vom 09.12.2022 wird als zukunftsweisenderes Szenario herangezogen. Über die Differenz der U-Werte könnten Ein- und Ausbauschichten im Falle einer energetischen Sanierung definiert werden.

Ökologische Kenndaten

Die definierten Bauteilaufbauten und Sanierungsszenarien können in ökologischen Kenndaten gem. DIN EN 15978 abgebildet werden. Dazu wird ein Zeitraum von 50 Jahren gewählt, in dem die Lebenszyklusphasen Herstellung (A1-3), Austausch (B4), Produktion (C3,C4) und das Potential für Wiederverwertung und Recycling (Modul D) betrachtet werden. Als ökologische Indikatoren werden das Globale Erwärmungspotential (GWP), die totale erneuerbare Primärenergie (PERT) und die totale nicht erneuerbare Primärenergie (PENRT) herangezogen. Die Datengrundlage bildet die Datenbank ÖKOBAUDAT gemäß DIN EN 15804+A2 (BMWSB, 2023).

Ergebnisse

Klassifikation

In der Klassifikation verbleiben nach Ausschluss aller Klassen mit weniger als 4% der Observationsanzahlen 6 von 12 Klassen der Gebäudefunktion und 9 von 12 Klassen des Baualters. Zu einer Klassifikationsmatrix verschnitten ergeben sich somit 54 Klassenschnitte, für die jeweils unterschiedlich hohe Observationsanzahlen zur Verfügung stehen (Abb. 3).

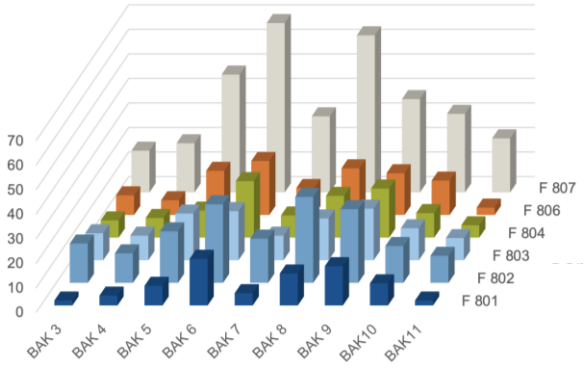

Abbildung 3: Observationsanzahlen der 54 Klassenschnitte (Baualter BAK, Gebäudefunktion F)

Einige Klassenschnitte, besonders diejenigen sehr früher und später Baualter, sind in ihrer Repräsentativität sicherlich immer noch eingeschränkt. Sie werden aber zugunsten von Konsistenz und Anwendbarkeit in der Klassifikation belassen. Insgesamt sind somit 89 % der für Gewerbe- und Industriebauten vorhandenen Observationen in den weiteren Typologisierungsprozess einbezogen.

Attribuierung

Anschließend werden für alle 54 Klassenschnitte die Ausprägungen der 24 Variablen aus ENOB:dataNWG abgefragt. Dabei fällt auf, dass für fast alle 54 Klassenschnitte die häufigste Ausprägung der Variable „Bauweise der Fassade“ die „massive Bauweise“ ist (Abb. 4). Nur 6 Klassenschnitte zeigen als häufigste Ausprägung die „Leichtbauweise“.

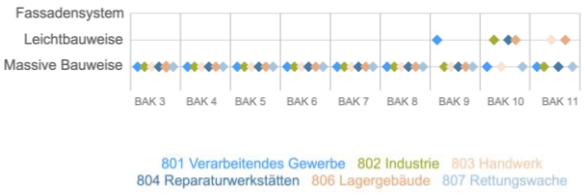

Abbildung 4: Ausprägung der häufigsten Bauweise je Typ

Unter den Sub-Typen mit vorrangig „massiver Bauweise“ ergibt sich in der Datenbankabfrage für die meisten eine „einschalige Konstruktion mit schwerem Baustoff (Kalksandstein, Vollziegel oder Beton)“ als häufigste Ausprägung der Variable „Konstruktion der massiven Bauweise“ (Abb. 5).

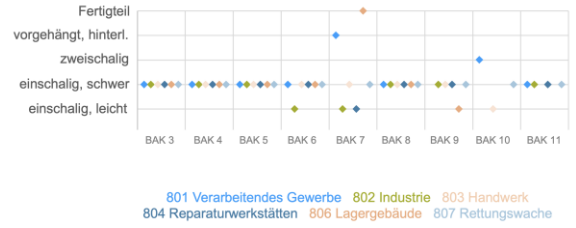

Abbildung 5: Ausprägungen der häufigsten Konstruktionsart der Typen mit Massiver Bauweise

Die Streubreite der für die Typen definierten Außenwandaufbauten ist damit auffallend gering.

Am Beispiel des Sub-Typus 802_08, welcher Industriegebäude der Baujahre 1984 - 1994 vertritt, zeigt sich jedoch, dass die Anzahl der Observationen im Klassenschnitt mit massiver und leichter Bauweise nah beieinander liegen kann (Abb. 6; qb1). Noch deutlicher wird es beim Vergleich der am häufigsten vorkommenden Massivbaukonstruktion (einschalig mit schwerem Baustoff) und der am häufigsten vorkommenden Leichtbaukonstruktion (Sandwichpaneele) (Abb. 6; qb2, qb3). Letztere liegt numerisch bei diesem Sub-Typus nur wenig hinter ersterer zurück, verschwindet aber durch die weitere Typologisierung.

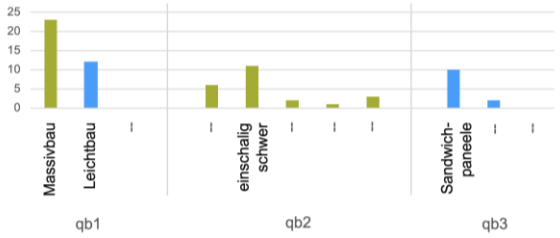

Abbildung 6: Variablenausprägungen Typ 802_08

Das Attribuierungs-Verfahren, jeweils die häufigste Variablenausprägung als stellvertretend für den Klassenschnitt anzunehmen, führt somit zu einem Variantenverlust, der bei einer Modellbildung dieser Art aber kaum zu vermeiden ist.

Clustering

Durch das Clustering wurden die 54 Sub-Typen zu 16 finalen Typen A - P zusammengefasst. Abbildung 7 zeigt wie sich die Cluster über Baualtersklassen und Gebäudefunktionsklassen hinweg erstrecken, dabei aber i.d.R. dennoch eine relative räumliche Nähe aufweisen und somit als plausibel angenommen werden können.

	F 801 Verarbeitendes Gewerbe	F 802 Industrie	F 803 Handwerk	F 804 Reparatur-Werkstätten	F 806 Lagergebäude	F 807 Rettungswache
BAK 3 1919 - 1948	Typ K	Typ H	Typ K	Typ H	Typ K	Typ H
BAK 4 1949 - 1957	Typ F	Typ I	Typ H	Typ H	Typ H	Typ K
BAK 5 1958 - 1968	Typ F	Typ F	Typ J	Typ K	Typ J	Typ H
BAK 6 1969 - 1978	Typ F	Typ C	Typ I	Typ J	Typ J	Typ K
BAK 7 1979 - 1983	Typ M	Typ C	Typ P	Typ C	Typ L	Typ K
BAK 8 1984 - 1994	Typ G	Typ G	Typ P	Typ O	Typ D	Typ O
BAK 9 1995 - 2001	TYP A	Typ G	Typ D	Typ G	Typ B	Typ D
BAK 10 2002 - 2009	Typ N	TYP A	Typ B	TYP A	TYP A	Typ E
BAK 11 2010 - 2014	Typ E	Typ E	TYP A	Typ E	TYP A	Typ E

Abbildung 7: Clusterung zu 16 Typen

Attribuierung

Nach dem Clustering werden die synthetischen Gebäude der 16 Typen mit Hilfe einschlägiger Literatur weiter ausformuliert. Exemplarisch soll dies an der Außenwand von Typ F nachvollziehbar gemacht werden. Er vertritt Gebäude industrieller und gewerblicher Produktion der Baujahre 1949 – 1978. Die Abfrage aus ENOB:dataNWG charakterisiert die Außenwand als in einschalig massiver Bauweise aus schwerem Baustoff (Kalksandstein, Vollziegel, Stahlbeton, Beton) errichtet mit einer außenliegenden Dämmung von 7 cm. Alle weiteren Informationen müssen über Literatur generiert werden. Die bauzeitliche Literatur für Ost- und Westdeutschland geht überwiegend von Stahlbeton als Baustoff aus mit einer Stärke von ca. 25 cm gem. DIN4108:1952. Da Heraklith

bis 1973 den größten Marktanteil an Dämmmaterialien hatte, wird eine Dämmung aus Holzwolleleichtbauplatte angenommen.

Insgesamt zeigt sich, dass nach abgeschlossener Attribuierung, 12 der 14 Typen eine Außenwand aus Stahlbeton haben. Dies beruht letztlich auf den aus ENOB:dataNWG gewonnenen Stichprobendaten, von denen eine Mehrheit der Observationen eine Außenwand aus schwerem Baustoff vermerkt.

Ökologische Kenndaten

Nachdem für alle 16 Typen alle Bauteileaufbauten und zugehörigen Sanierungsszenarien definiert sind, können diese in ökologischen Kenndaten abgebildet werden.

Im Vergleich der Ergebnisse der GWP pro m² Außenwand der 16 Typen zeigt sich, dass für einige Außenwände der Typen das GWP höher ausfällt als der Durchschnitt der übrigen (Abb. 8). Für Typ M liegt das z.B. an der angenommenen Außenwandbekleidung aus hinterlüftetem Aluminiumwellblech. Durch die Datenbankabfrage ließ sich die Konstruktionsart (hinterlüftete Fassadenbekleidung) ermitteln, die Materialität musste auf Basis der Literatur ergänzt werden.

Es zeigt sich, dass die nicht auf empirischer Datengrundlage beruhenden Attribute der Typen, wie die Aluminiumbekleidung, eine starke Auswirkung auf die ökologischen Kenndaten haben können.

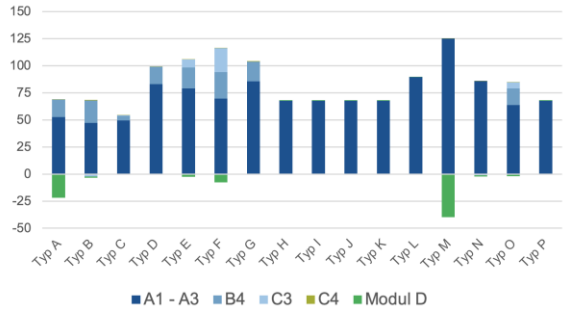

Abbildung 8: GWP in kg CO_2-Äq. pro m² Außenwand der Typen A - P im Vergleich

Gesamtergebnis

Die 16 Typen der Typologie bilden sich Anwender*innen in insgesamt 64 Steckbriefen ab. Diese weisen Bauteileigenschaften der Typen und dazugehörige ökologische Kenndaten nach Lebenszyklusphasen, ökologischen Indikatoren, Bauteilschichten sowie Ist-Zustand und Sanierungsszenarien getrennt aus. Dies ermöglicht flexible Szenarienberechnungen zu zukünftigen Entwicklungen des Gebäudebestandes. Durch eine Multiplikation der ökologischen Kenndaten der Typen (pro m² Bauteil ausgewiesen) mit den Geometrien der Einzelgebäude aus dem LoD2-Modell, können überschlägige Bilanzen der Umweltwirkung und Ressourceneinsätze berechnet werden und eine automatisierte Szenario-Analyse erfolgen.

Der Aufbau der Steckbriefe wird in Abbildung 9 beispielhaft anhand der Außenwand von Typ A erläutert.

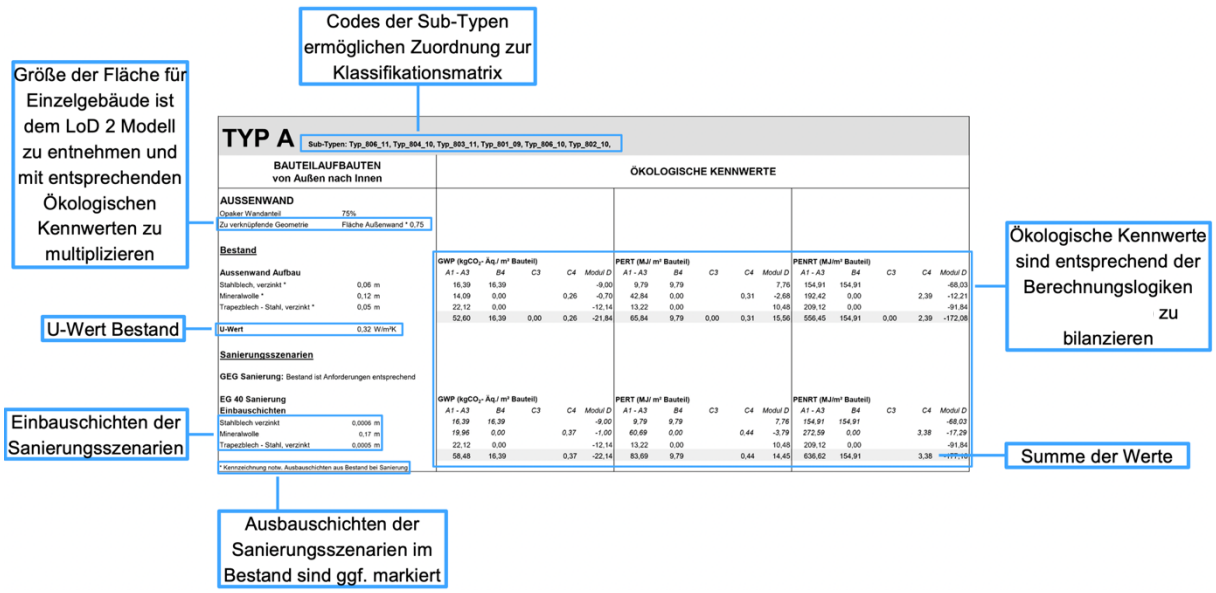

Abbildung 9: Erläuterung der Steckbriefe der synthetischen Gebäude der finalen Typen A bis P, am Beispiel der Außenwand von Typ A

Diskussion

Das Ergebnis der Typologisierung ist insofern kritisch zu betrachten, als dass nur eingeschränkt empirische Daten zur Verfügung stehen, auf Basis derer eine Typologie gebildet werden kann.

Die Datenbank ENOB:dataNWG enthält die einzig repräsentative Stichprobe des deutschen NWG Bestandes. Die über die Observationen erfassten Informationen sind jedoch nicht umfangreich genug erfasst, um die verbauten Materialien der baukonstruktiven Elemente in ökologischen Kenndaten abbilden zu können. In der vorliegenden Arbeit wird daher auf eine Ergänzung durch Annahmen auf Basis einschlägiger Literatur zurückgegriffen.

Wie am Beispiel von Typ M gezeigt können sich diese nicht empirisch belegbaren Materialdefinitionen, erheblich auf Werte ökologischer Kenndaten auswirken. Aufgrund dessen ist die Typologie nicht uneingeschränkt belastbar und nur für überschlägige Berechnungen geeignet.

Auf Basis der aktuellen Datenlage ist eine präzisere Abbildung der baukonstruktiven Elemente und Sanierungsszenarien in ökologischen Kenndaten, die für lebenszyklusbasierte Analysen großer Gebäudebestände nutzbar sind, nur schwer möglich. Es fehlt eine umfassende empirische Dokumentation des Gebäudebestandes und der Materialität seiner Bauteilaufbauten um detailliertere Aussagen treffen zu können.

Darüber hinaus haben die gewählten Klassifikationskriterien einen Einfluss darauf, welche Observationen zu Typen vereinheitlicht werden und damit auch auf die Variablenausprägungen, die die Typen zeigen. Durch die gewählte Art der Modellbildung wird die Streubreite der Variablenausprägungen innerhalb eines Klassenschnittes eingeschränkt.

Hätte man anstatt der für die vorliegende Arbeit gewählten Klassifikationskriterien Baualter und Gebäudefunktion zusätzlich oder ersatzweise die Außenwandbauweise als Kriterium mit herangezogen, wären die Observationen jedes Klassenschnittes in sich homogener ausgefallen. Infolgedessen wäre die Streuung der observierten Werte im Zuge der Attribuierung weniger stark reduziert worden, weil sie ursprünglich schon geringer gewesen wäre. Jedoch ist hiervon angesichts der Anwendungsabsicht der Arbeit abzuraten, da aus den LoD2 Daten keine Informationen zur Bauweise hervorgehen, sodass die Typologie nicht anwendbar wäre. Eine Abstraktion mit weniger Variantenverlust ist bei der vorgesehenen Anwendung der Typologie und aktuellen Datengrundlagen also nicht möglich.

Dieser Zusammenhang ist insbesondere deshalb interessant, da sich bezüglich der Konstruktionsart stellenweise ein Widerspruch der Typologisierungs-Ergebnisse zu den in der Literatur als prävalent beschriebenen Baukonstruktionen ergibt. Wie in den Ergebnissen aufgezeigt hat sich für fast 90% der Klassenschnitte eine massive Bauweise ergeben. Sonstige Literatur geht zumeist von einer Prävalenz der Skelettbauweise bei Gewerbe- und Industriebauten aus.

Fazit und Ausblick

Durch die vorliegende Arbeit wird eine aus 16 Typen bestehende Typologie der Gewerbe- und Industriegebäude entwickelt, die zur Verwendung in lebenszyklusbasierten Analysen großer Gebäudebestände auf Basis von 3D-Stadtmodellen vorgesehen ist.

Trotz einiger Einschränkungen hinsichtlich ihrer Belastbarkeit kann die Typologie als Datenmodell für überschlägige lebenszyklusbasierte Betrachtungen genutzt werden. Sie ist aufgrund der geschaffenen Schnittstellen (Klassifikationskriterien und Ausweisung ökologischer Kennwerte je m2 Bauteilfläche) für die Verwendung in lebenszyklusbasierten Analysen auf Basis von semantischen 3D-Stadtmodellen wie dem amtlichen LoD2-Modell geeignet und erweitert damit bestehende Typologien der NWGs, welche für diese Nutzung unbrauchbar sind.

Solange keine umfassende statistische Erfassung der Eigenschaften des Gebäudebestandes, z.B. durch ein Gebäuderegister, vorliegt, ist die Typologisierung eine wichtige Methode, um lebenszyklusbasierte Analysen für große Gebäudebestände durchführen zu können. Mit einer umfassenden Typologie aller Gebäude können Szenarien für die Entwicklung großer Gebäudebestände und deren Umweltwirkungen sowie Ressourceneinsätze in Tools wie Urbi+ gut modelliert werden. Für die WGs liegt eine umfängliche Typologisierung bereits vor. Im Bereich der NWGs erschließt die vorliegende Arbeit durch die Typologisierung der Gewerbe- und Industriegebäude einen Teil des Bestandes. Für die notwendige Typologisierung von weiterer NWG-Gruppen zur die Nutzung in vergleichbaren Analysen kann die Methodik dieser Arbeit gut als Vorlage genutzt werden.

Gelingt diese Vervollständigung der Typologisierung, so können – durch die Evaluierung unterschiedlicher Szenarien der

möglichen Entwicklung des Gebäudebestandes – präzise Handlungsempfehlungen für die Zukunft ausgesprochen werden, um Emissions- und Energieeinsparpotentiale effizient zu erschließen und das Ziel eines klimaneutralen Gebäudesektors zu erreichen.

Danksagung

Diese Publikation entstand im Rahmen des Forschungsprojekts EnEff:Stadt: CircularGreenSimCity (03EN3050), das vom Bundesministerium für Wirtschaft und Klimaschutz gefördert wird. Die Autor*innen bedanken sich beim Projektträger Jülich für die wissenschaftliche und technische Unterstützung dieser Studie.

Literatur

Bundesministerium für Umwelt, Naturschutz, Bau und Reaktorsicherheit (BMUB) o.J. Ersatzverfahren bei sinngemäßer BNB-Anwendung SGA_01 (LCA).

Bundesministerium für Wirtschaft und Klimaschutz (BMWi) 2022. Richtlinie für die Bundesförderung für effiziente Gebäude – Nichtwohngebäude (BEG NWG), BAnz AT 30.12.2022 B3.

Bundesministerium für Wohnen Stadtentwicklung und Bauwesen (BMWSB) o.J. ÖKOBAUDAT 2023-I. www.oekobaudat.de.

Buschka, M. 2018. Methodik zur Typologisierung von Nichtwohngebäuden für die Anwendung von Ökobilanzen – am Beispiel deutscher Büro-, Verwaltungs- und Amtsgebäude, Masterthesis, Lehrstuhl für energieeffizientes und nachhaltiges Planen und Bauen, Technische Universität München, München.

Buschka, M., Bischof, J., Meier-Dotzler, C, Lang, W 2021. Developing non- residential building stock archetypes for LCI - a German case study of office and administration buildings, The International Journal of Life Cycle Assessment, Bd. 26, 09/01 2021.

Cischinsky, H., Hörner, M., Nuss, G. 2022. Forschungsdatenbank Nichtwohngebäude ENOB: dataNWG. Variablendokumenatation Fernrechnen, Institut Wohnen und Umwelt.

Deilmann, C., Behnisch, M., Dirlich, S., Gruhler, K,, Hagemann, U, Petereit, R., Kunz, C, Petereit, K 2013. Systematische Datenanalyse im Bereich der Nichtwohngebäude - Erfassung und Quantifizierung von Energieeinspar- und CO2-Minderungspotenzialen, Bundesministerium für Verkehr Bau und Stadtentwicklung (BMVBS) Online-Publikation 27/2013.

Dirlich, S,, Gruhler, K , Deilmann C. 2011. Typologie und Bestand beheizter Nichtwohngebäude in Deutschland, BMVBS-Online-Publikation 16/2011.

Expertenrat für Klimafragen (ERK) 2022. Zweijahresgutachten 2022. Gutachten zu bisherigen Entwicklungen der Treibhausgasemissionen, Trends der Jahresemissionsmengen und Wirksamkeit von Maßnahmen (gemäß § 12 Abs. 4 Bundes-Klimaschutzgesetz).

Gesetz zur Einsparung von Energie und zur Nutzung erneuerbarer Energien zur Wärme- und Kälteerzeugung in Gebäuden (Gebäudeenergiegesetz - GEG) 2020. Artikel 1 G. v. 08.08.2020 BGBl. I S. 1728 (Nr. 37); zuletzt geändert durch Artikel 1 G. v. 16.10.2023 BGBl. 2023 I Nr. 280.

Gruhler, K., Deilmann, C. 2015. Materialaufwand von Nichtwohngebäuden. Verfahrensschritte zur Abbildung der Ressourceninanspruchnahme des Nichtwohnbau-Bestandes, Fraunhofer IRB Verlag, Stuttgart, 2015.

Harter H.M. 2021. Lebenszyklusanalyse der Technischen Gebäudeausrüstung großer Wohngebäudebestände auf der Basis semantischer 3D-Stadtmodelle, Dissertation, School of Engineering and Design, Technische Universität München.

Hochschule für Technik Stuttgart (HFT) o.J. CircularGreenSimCity. https://www.hft-stuttgart.de/forschung/projekte/aktuell/circulargreensimcity.

Hörner, M., Bischof, J. 2022. Typologie der Nichtwohngebäude in Deutschland. Methodik, Anwendung und Ausblick.

Insitut Wohnen und Umwelt (IWU), 2023. Sonderauswertung der Forschungsdatenbank des Projekts „Forschungsdatenbank Nichtwohngebäude (ENOB: dataNWG)“ (gefördert durch das Bundesministerium für Wirtschaft und Energie; Förderkennzeichen: 03ET1315).

Klauß, S, Kirchhof, W. und Maaß, A. 2010. Entwicklung einer Datenbank mit Modellgebäuden für energiebezogene Untersuchungen, insbesondere der Wirtschaftlichkeit", Bundesinstitut für Bau-, Stadt- und Raumforschung (BBSR), Bonn.

Lehrstuhl für energieeffizientes und nachhaltiges Planen und Bauen (ENPB), TU München o.J. CircularGreenSimCity. https://www.cee.ed.tum.de/enpb/forschung/laufende-forschungsprojekte/circulargreensimcity/.

Ortlepp, R,, Gruhler, K., Schiller, G. 2016. Material stocks in Germany's non- domestic buildings: a new quantification method, in: Building Research & Information, Bd. 44, S. 840 - 862, 2016.

Schebek, L., Schnitzer, B., Blesinger, D., Köhn, A., Miekley, B., Linke, H.J., Lohmann, A., Motzko, C., Seemann, A. 2017. Material stocks of the non-residential building sector: the case of the Rhine-Main area, in Resources, Conservation and Recycling, Bd. 123, S. 24-36, 2017.

Schiller, G., Ortlepp, R., Krauß, N., Steger, S., Schütz, H., Acosta Fernández, J., Reichenbach, J., Wagner, J., Baumann, J. 2015. Kartierung des anthropogenen Lagers in Deutschland zur Optimierung der Sekundärrohstoffwirtschaft, Umweltbundesamt, Dessau-Roßlau, 2015.

Thiel, D., Riedel, D. 2011. Typisierte Bauteilaufbauten – Präzisierung der Pauschalwerte für Wärmedurchgangskoeffizienten aus der Bekanntmachung der Regeln der Datenaufnahme im Nichtwohngebäudebestand, Fraunhofer IRB Verlag, Stuttgart, 2011.

u-wert.net GmbH, o.J. Ubakus.de. www.ubakus.de.

BauSIM 2024 in Wien
23. September – 26. September

Optimierung von Dämmstärke und Wärmeversorgung von vier verschiedenen Gebäudetypen unter Berücksichtigung der Dynamik und der prognostizierten Entwicklung der Emissionsfaktoren der Stromerzeugung in Deutschland

Tobias Blanke[1,3], Joachim Göttsche[1], Jérôme Frisch[2], Bernd Döring[3] und Christoph van Treeck[2]

[1]*Solar-Institut Jülich (SIJ), FH Aachen, Deutschland*

[2]*Lehrstuhl für Energieeffizientes Bauen (E3D), RWTH Aachen, Deutschland*

[3]*Institute of Smart Building Engineering (ISBE), FH Aachen, Deutschland*

Kurzfassung

Ökobilanzen, die alle Phasen im Lebenszyklus eines Gebäudes berücksichtigen, gewinnen zunehmend an Bedeutung. Aufgrund ihrer langen Lebensdauer kommt bei Gebäuden mit strombasierten Wärmeversorgungssystemen, wie Wärmepumpen, der Interaktion mit dem Stromnetz eine herausragende Bedeutung zu, insbesondere im Zusammenhang mit der Dekarbonisierung der Stromerzeugung. Der Einfluss der Dekarbonisierung über die kommenden Jahrzehnte sowie die kurzfristige Variabilität der Emissionsfaktoren auf der Basis von stundenbasierten Werten für den Strommix auf die Ökobilanz von vier verschiedenen Gebäudetypen soll hier aufgezeigt werden.

Die betrachteten Gebäudetypen umfassen ein Einfamilienhaus, ein Bürogebäude, ein Bildungsgebäude und eine Industriehalle. Ziel ist es den Einfluss der Dekarbonisierung und der Stundenauflösung auf die Auswahl der optimalen Dämmstärke für ein Wärmepumpen-basiertes System aufzuzeigen. Hierzu werden thermische und elektrische Lastprofile für die verschiedenen Gebäudetypen erzeugt. Dabei werden verschiedene Nutzungsprofile, Standorte, Dämmstärken, Fensteranteile, Ausrichtungen, Fensterverglasungen, Lüftungsvarianten und Sonnenschutzvarianten betrachtet. Für all diese Varianten werden verschiedene Szenarien in Bezug auf die Gebäudetechnik untersucht und hinsichtlich ihrer Dämmstärke sowie der Größe der gebäudetechnischen Komponenten mit GWP-Auswirkungen optimiert.

Die Ergebnisse zeigen, dass die Berücksichtigung der Dekarbonisierung der Stromerzeugung die ökobilanziell optimale Dämmstärke im Vergleich zum statischen Ansatz mit heutigen Werten halbieren kann. Auch die Berücksichtigung stundenbasierter Stromemissionswerte führt zu einer Reduzierung der optimalen Dämmstärke um nahezu 5 %.

Einführung

Wärmepumpen als Heizsysteme gewinnen in Deutschland an Bedeutung (Weinhold 2024). Dementsprechend spielt die Berücksichtigung der Emissionen während des Betriebes eines Gebäudes für die Interaktion mit dem Strommarkt eine immer wichtigere Bedeutung. Gerade bei Gebäuden mit ihrer langen Lebensdauer ist hier die Betrachtung der Dekarbonisierung des Strommarktes von entscheidender Bedeutung (Su et al. 2021, Negishi et al. 2019). Solche zeitlich veränderlichen Effekte sollten bei der Erstellung von Ökobilanzen und CO_2-Fußabdrücken realistischerweise berücksichtigt werden (Sohn et al. 2020, Su et al. 2021). Unter anderem Negishi et al. (2019) hat bereits untersucht, welchen Einfluss die Dekarbonisierung des Strommarktes hat. Dies geschah allerdings auch mit jährlich konstanten Emissionsfaktoren (Su et al. 2021). Dabei ist deren mindestens stündlich aufgelöste Betrachtung für die Bewertung von elektrischen Speichern äußert wichtig (Blanke, Hagenkamp, Göttsche, Döring, Reger & Kuhnhenne 2021).

Das Ziel dieser Veröffentlichung ist es den Einfluss der Dekarbonisierung und der Stundenauflösung der Emissionswerte für die Interaktion mit dem Strommarkt für strombasierte Gebäudetechniksysteme aufzuzeigen. Der Fokus liegt hierbei

auf der Auswahl der Dämmstärke und den Gesamtemissionen des Systems. Dazu werden die Annahmen zur Optimierung der Dämmstärke erläutert. Zuerst werden vier Beispielgebäude definiert sowie Varianten, um deren Sensitivitäten abzubilden. Für die Gebäude werden für mindestens 256 verschiedene Varianten sowie für 51 verschiedene Dämmstärken die Heiz-/ und Kühllast berechnet. Danach wird erläutert wie der potenzielle Ertrag der Photovoltaikanlagen berechnet wird. Im Anschluss werden fünf Varianten für die Berücksichtigung der Strommarktemissionen eingeführt. Als letztes wird die Optimierung der Dämmstärke sowie der damit verbundenen Gebäudetechnik erläutert. Ziel hier ist es mittels der Optimierung eine Kohlenstoffdioxid-optimierte Betriebsweise zu erhalten und somit den Einfluss der Stundenauflösung am besten herausstellen zu können.

Simulation

Für den Vergleich der verschiedenen Verfahren wurden die thermischen Gebäudelasten für verschiedene Gebäudetypen berechnet. Die betrachteten Gebäudetypen sind ein Einfamilienhaus, ein Bürogebäude, eine Gewerbehalle und ein Bildungsgebäude. Für alle Gebäudetypen werden verschiedene Szenarien durchgerechnet. Die variierten Parameter können der Tabelle 1 entnommen werden. Neben den in der Tabelle vorgestellten Varianten wird auch die Dämmstärke variiert. Die Dämmdicke wird im Vergleich zum Standardszenario von 0 m bis 0.5 m in 0.01 m Schritten als zusätzliche Dämmung erhöht. Diese wird bei Wänden, Decken und Böden gleicher maßen erhöht. Für das Wetter wird der Klimapfad RCP 2.6 verwendet, da dieser dem in Paris erklärten Klimapfad am nächsten kommt. Die Gebäudelasten können Blanke (2024) entnommen werden.

PV-Simulation

Zur Berechnung des Ertrags der PV-Module pro Quadratmeter wird die Bibliothek pvlib verwendet (Holmgren et al. 2018). Der Ertrag wird für alle vier Standorte und fünf Ausrichtungen berechnet. Die Module sind entweder mit einer Neigung von 5° nach Süden ausgerichtet für alle Gebäude mit Flachdach oder mit einer Neigung von 30° in alle Himmelsrichtungen, je nach Ausrichtung des Wohngebäudes. Für die Berechnung des PV-Ertrags wurde über alle Module der Firma Solar Fabrik gemittelt, da die Firma einer der größten deutschen Hersteller von Solarmodulen ist und die Daten in der pvlib enthalten sind (Solar 2023, Holmgren et al. 2018, Burkhardt 2023, Fonseca 2023).

Tabelle 1: Gebäudevarianten

Komponente	Standard	Varianten
Fensterverglasung (ISO 2018)	U=1.4 W/(m^2 K) g=0.67	U=0.7 W/(m^2 K) g=0.53
Fensterfläche	x1	x2
Effizienz für Lüftungswärmerückgewinnung	0 %	80 % (Klingenburg 2023, Brücken 2012)
Automatische Verschattung (ISO 2018)	keine	0.1 bei I > 200 W/m^2 und T > 16 °C
Nutzungsprofil	geringe th. Last	hohe th. Last
Ausrichtung / Form	lange Seite Richtung Süd / 5 Etagen	lange Seite Richtung West / 1 Etage
Wetter (RCP2.6) (Meteotest 2023)	Potsdam	Hamburg, München, Köln

Emissionsfaktoren der Stromerzeugung

Es werden fünf Szenarien für die Betrachtung der ökobilanz-basierten CO_2-Emissionsfaktoren für die Interaktion mit dem Strommarkt betrachtet. Das Szenario J-N betrachtet einen über das Jahr und die Lebensdauer konstanten Faktor von 395 g/(kW h). Damit der Einfluss von stündlich aufgelösten untersucht werden können werden im Szenario S-N stündlich aufgelösten Emissionswerte für das Jahr 2020 betrachtet, welche über die Lebensdauer der Gebäude konstant bleiben. Das Szenario J-D dient dazu den Einfluss der Dekarbonisierung von Strommarkt zu berücksichtigen. Deshalb wird hier der Emissionsfaktor über die Lebensdauer integriert und als über die Stunden des Jahres konstanten Faktor von 142 g/(kW h) betrachtet. Um zu überprüfen welchen Einfluss stündlich aufgelöste Emissionswerte des Strommarkts im Dekarbonisierungsprozess haben, werden im Szenario S-D die stündlich aufgelösten Daten über jede Stunde des Jahres integriert und somit für jede Stunde im Jahr über die Lebensdauer des Gebäudes gemittelte Werte betrachtet. Im Szenario O-D werden in einem 10 Jahres Raster die stündlichen Emissionswerte über die 10 Jahre integriert, um der nachfolgenden Betriebsoptimierung zu erlauben den Betrieb besser im Hinblick auf minimale Gesamtemissionen zu optimieren. Die zugrundeliegenden Datenreihen können dem Szenario S45-RCP2.6 aus Blanke, Göttsche, Döring, Frisch & van Treeck (2024) entnommen werden.

Optimierung

In dieser Veröffentlichung werden verschiedene Versorgungskonzepte untersucht. Diese sind in Tabelle 2 aufgeführt.

Tabelle 2: Energiesysteme

Bedarf / Technologie / Variante	nur Heizen				Heizen & Kühlen			
	Heizstab	L-W-WP	L-W-WP+PV	L-W-WP+PV+Sp	L-W-WP	L-W-WP+PV	L-W-WP+PV+Sp	S-W-WP+PV+Sp
Strombedarf	x	x	x	x	x	x	x	x
Wärmebedarf	x	x	x	x	x	x	x	x
Kältebedarf					x	x	x	x
Heizstab	x	x	x	x	x	x	x	x
L-W-WP		x	x	x	x	x	x	
S-W-WP								x
Geothermie								x
PV			x	x		x	x	x
Wärmespeicher				x			x	x
Kältespeicher							x	x
Stromspeicher				x			x	x

Zur Optimierung werden Typtage aus den Datenreihen gebildet, die aus der Außentemperatur (entnommen aus den Wetterdaten (Meteotest 2023)), den Photovoltaikleistungsprofilen, den Emissionsdaten für den Strommarkt und dem Heiz-/Kühlbedarf bestehen. Es werden 40 Typtage für jede Datenreihe erstellt, da diese Anzahl zu guten Ergebnissen führt (Kotzur et al. 2018a, Hoffmann et al. 2021). Zur Erzeugung der Typtage wird die Bibliothek TSAM verwendet (IER 2024, Hoffmann et al. 2020). Für das Clustern der Typtage wird die hierarchische Clusterung gewählt, da sie gute Ergebnisse für Zeitreihen dieser Art liefert (Kotzur et al. 2018a). Um auch Extrema zu berücksichtigen, werden diese als zusätzliche Clusterzentren angelegt (Kotzur et al. 2018a). Die Maximalwerte im Heiz-/Kühlbedarf, der Außenlufttemperatur und den Emissionswerten werden als Maxima betrachtet. Für die Außenlufttemperatur und die Emissionswerte werden auch ihre Minimalwerte in die Typtage aufgenommen.

Die Optimierung hat das Ziel die jährlichen Emissionen für die Konstruktion der Gebäudetechnik und Gebäudehülle (I) sowie die für den Betrieb zu minimieren. Für den Betrieb werden lediglich die zeitlich variablen Emissionen $i(t)$ für den Verkauf (P_v) und Einkauf vom Strom (P_k) berücksichtigt und mit dem Gewichtungsfaktor des jeweiligen Typtages (w) multipliziert.

$$\min \left(I + \sum_{t=1}^{t_{end}} i(t) \cdot w(t) \cdot (P_k(t) - P_v(t)) \cdot \delta t \right) \tag{1}$$

Emissionen für Konstruktion der Gebäudetechnik und Gebäudehülle (I) ergeben sich aus der Summe der Emissionen für die verschiedenen gebäudetechnischen Komponenten T und der Summe der Emissionen für die 51 verschiedenen Dämmstärken k. Die Emissionen für die Gebäudetechnik werden mit einer Steigung (m) relativ zur maximalen Größe der Komponente (P_{max}) sowie einer konstanten Komponente (d) implementiert. Es wird für alle Komponenten der Gebäudetechnik pauschal eine Lebensdauer von 20 Jahren angenommen und dementsprechend werden die Emissionen durch 20 Jahre geteilt, um einen jährlichen Wert zu erhalten. Im Gegensatz dazu hält die Dämmung den gesamten Betrachtungszeitraum von 50 Jahren. Dementsprechend werden die ausgewählte Dämmstärke (n) mit dessen Emissionen multipliziert (I_i) und durch den Betrachtungszeitraum geteilt. Die Emissionswerte für die Gebäudetechnik und der Dämmung können der Tabelle 3 entnommen werden und basieren auf Werten aus der Ökobaudat (BBSR 2023). Die Emissionswerte für die Dämmung basieren auf PIR Hartschaum und den Gebäudeoberflächen. Sie sind bezogen auf die Nutzfläche und die Dämmdicke angegeben.

$$I = \sum_{T} \left(\frac{m_T \cdot P_{max,T} + d \cdot b_T}{20} \right) + \sum_{k=1}^{51} \left(\frac{n(k) \cdot I_i(k)}{50} \right) \tag{2}$$

Die Leistung der verschiedenen gebäudetechnischen Komponenten ist limitiert zur maximalen Leistung (P_{max}) multipliziert mit einem komponentenspezifischem und ggf. zeitabhängigen Faktor (f). Ein Beispiel hierfür ist der Ertrag der PV-Anlage pro Quadratmeter, der zeitabhängig ist. Die maximale Leistung ist in dem Fall die Fläche der Anlage begrenzt. Dieser Faktor ist eins für die Limitierung der elektrischen Wärmepumpenleistung, des Heizstabes und der Speicherkapazität der Speicher.

$$P_T(t) \leq f_T(t) \cdot P_{max,T} \qquad \forall t, T \tag{3}$$

Die nachfolgende Gleichung koppelt die binäre Variable b mit der maximalen Komponentenleistung (P_{max}) über eine maximale Komponentengröße (F) und die konstanten Emissionen für die reine Anschaffung der Komponente (d).

Tabelle 3: Emissionsfaktoren (BBSR 2023)

Komponente	Steigung (m)	Achsenabschnitt (d)
Heizstab	0 kg_{CO_2}/kW	0 kg_{CO_2}
Wärmepumpen	50 kg_{CO_2}/kW	0 kg_{CO_2}
Batterie	300 kg_{CO_2}/kWh	0 kg_{CO_2}
Thermische Speicher	44 kg_{CO_2}/kWh	185 kg_{CO_2}
Photovoltaik	309 kg_{CO_2}/m^2	0 kg_{CO_2}
Gebäude	**Faktor normal**	**Faktor max Fenster**
Wohngebäude	810.4 kg_{CO_2}/m^2_{NGF}/m	774.2 kg_{CO_2}/m^2_{NGF}/m
Bürogebäude 1 Etage	437.3 kg_{CO_2}/m^2_{NGF}/m	401.9 kg_{CO_2}/m^2_{NGF}/m
Bürogebäude 5 Etagen	154.2 kg_{CO_2}/m^2_{NGF}/m	118.8 kg_{CO_2}/m^2_{NGF}/m
Bildungsgebäude	236.6 kg_{CO_2}/m^2_{NGF}/m	201.3 kg_{CO_2}/m^2_{NGF}/m
Industriehalle	532.6 kg_{CO_2}/m^2_{NGF}/m	499 kg_{CO_2}/m^2_{NGF}/m

$$P_{max,T} \leq F_T \cdot b_T \qquad \forall T \tag{4}$$

Die folgenden beiden Gleichungen verbinden den Heiz-/ ($\dot{Q}_h$) und Kühlbedarf ($\dot{Q}_c$) mit der aus den 51 verschiedenen ausgewählten Dämmstärke (n) zu dem damit verbundenen Lastprofil ($\dot{Q}_{h,i}$, $\dot{Q}_{c,i}$).

$$\dot{Q}_h(t) = \sum_{k=1}^{51} \dot{Q}_{h,i}(k,t) \cdot n(k) \qquad \forall t \tag{5}$$

$$\dot{Q}_c(t) = \sum_{k=1}^{51} \dot{Q}_{c,i}(k,t) \cdot n(k) \qquad \forall t \tag{6}$$

Zur Deckung des Heizbedarfes ($\dot{Q}_h$) kann entweder der Heizstab ($\dot{Q}_{HS}$), die Luft-Wasser-Wärmepumpe ($\dot{Q}_{L-WP,H}$) oder die Sole-Wasser-Wärmepumpe ($\dot{Q}_{S-WP,H}$) genutzt werden. Außerdem kann dem Warmwasserspeicher Wärme entzogen ($\dot{Q}_{H,E}$) und den System hinzugefügt werden oder aus dem Heizsystem entzogen und in den Speicher übertragen ($\dot{Q}_{H,L}$) werden.

$$\begin{aligned}\dot{Q}_{L-WP,H}(t) + \dot{Q}_{S-WP,H}(t) + \dot{Q}_{HS}(t) \\ + \dot{Q}_{H,E}(t) - \dot{Q}_{H,L}(t) = \dot{Q}_h(t)\end{aligned} \tag{7}$$

Zur Deckung des Kühlbedarfes ($\dot{Q}_c$) kann entweder die Luft-Wasser-Wärmepumpe ($\dot{Q}_{L-WP,K}$) oder die Sole-Wasser-Wärmepumpe ($\dot{Q}_{S-WP,K}$) genutzt werden. Außerdem kann dem Kaltwasserspeicher Kälte entzogen ($\dot{Q}_{K,E}$) und den System hinzugefügt werden oder aus dem Kühlsystem entzogen und in den Speicher übertragen ($\dot{Q}_{K,L}$) werden. Des Weiteren besteht die Möglichkeit, wenn eine Geothermieanlage vorhanden ist, diese zu nutzen um dem System Kälte hinzuzufügen ($\dot{Q}_{G,K}$) oder zu entziehen ($\dot{Q}_{G,H}$).

$$\begin{aligned}\dot{Q}_{L-WP,K}(t) + \dot{Q}_{S-WP,K}(t) + \dot{Q}_{G,K}(t) \\ -\dot{Q}_{G,H}(t) + \dot{Q}_{K,E}(t) - \dot{Q}_{K,L}(t) = \dot{Q}_c(t)\end{aligned} \tag{8}$$

Um den Bedarf an elektrischer Energie zu decken kann Strom eingekauft (P_k), die Batterie entladen ($P_{B,E}$) oder der Strom der Photovoltaikanlage (P_{pv}) verwendet werden. Der Bedarf setzt sich zusammen aus dem Strombedarf des Gebäudes (P_b), der Wärmepumpen (P_{L-WP}, P_{S-WP}) und des Heizstabes ($\frac{\dot{Q}_{HS}(t)}{0.96}$) sowie der Menge an verkaufter elektrischer Energie (P_v) und der Leistung, die genutzt wird um die Batterie zu laden ($P_{B,L}$). Es kann lediglich soviel elektrische Energie verkauft werden wie zu dem Zeitpunkt an elektrischer Energie von der Photovoltaikanlage erzeugt wird.

$$\begin{aligned}P_{pv}(t) + P_k(t) - P_v(t) - P_{L-WP}(t) - P_{S-WP}(t) \\ -\frac{\dot{Q}_{HS}(t)}{0.96} + P_{B,E}(t) - P_{B,L}(t) = P_b(t)\end{aligned} \tag{9}$$

Die Heizleistung der Sole-Wasser-Wärmepumpe ($\dot{Q}_{S-WP,H}$) setzt sich aus der elektrischen Leistung (P_{S-WP}) und der Kühlleistung ($\dot{Q}_{S-WP,K}$) der Wärmepumpe zusammen.

$$\dot{Q}_{S-WP,H}(t) = \dot{Q}_{S-WP,K}(t) + P_{S-WP}(t) \tag{10}$$

Außerdem ist die elektrische Leistung der Wärmepumpen (P_{WP}) über den COP mit der Heizleistung ($\dot{Q}_{WP}$) verbunden. Der COP beträgt für die Sole-Wasser-Wärmepumpe konstant 5.15 und für die Luft-Wasser-Wärmepumpe wird der außentemperaturabhängiger Ansatz von Hoops et al. (2022) gewählt. Der COP oder auch EER für den Kühlfall der Luft-Wasser-Wärmepumpe beträgt den des Heizfalles um eins reduziert.

$$\dot{Q}_{WP}(t) = P_{WP}(t) \cdot COP(t) \tag{11}$$

Für die Speicher wird das Model von Blanke et al. (2022) verwendet. Die Selbstentladung sowie die Lade- und Entladeeffizienzen sind Kotzur et al. (2018*b*) entnommen und betragen 0.1 %/h für die Selbstentladung sowie 99 % für die Lade- und Entladeeffizienzen des Warmwasserspeichers. Für die Batterie beträgt die Selbstentladung 0.05 %/h und die Lade- und Entladeeffizienzen 96 %. Der

Kaltwasserspeicher wird aus numerischen Gründen ohne Verluste simuliert.

Für die Geothermieanlage wird das Erdsondenmodell aus Blanke, Born, Göttsche, Herrmann, Döring, Frisch & van Treeck (2024) verwendet, wobei eine Bohrfeldkonfiguration vorgegeben werden muss. Das Wohngebäude wird mit einem Bohrfeld von zwei Sonden betrachtet, das Bürogebäude von fünf mal fünf Sonden, das Industriegebäude von elf mal vier Sonden und das Bildungsgebäude von neun mal drei Sonden. Der Abstand zwischen den Sonden beträgt 6 m. Mit diesen Konfigurationen können die Sondenfelder ungefähr unter den Gebäuden platziert werden. Das Erdreich wird mit einer Wärmeleitfähigkeit von 2.1 W/(m K) und einer Wärmekapazität von 2100 kJ/(m^3 K) angenommen. Die Erdsonden haben einen Radius von 0.075 m und einen thermischen Widerstand von 0.05 m K/W (Blanke, Hagenkamp, Döring, Göttsche, Reger & Kuhnhenne 2021, Blanke, Reger, Döring, Göttsche & Kuhnhenne 2021). Die Erdreichtemperatur sowie der Wärmefluss im Erdreich wurden aus Xing (2014) für die vier Standorte entnommen. Die minimale Fluidtemperatur wird auf 0 °C und die maximale auf 17 °C angenommen.

Für die Optimierung wird ein Python Skript erstellt und die mind. 256 Varianten werden automatisiert nacheinander durchoptimiert.

Limitierungen

Im Rahmen dieser Veröffentlichung werden die Emissionen für den Austausch der Gebäudetechnik mit dem Emissionen für den Neubau nach heutigen Emissionswerten gleichgesetzt. Dies vernachlässigt die technologischen Fortschritt und die ggf. in Zukunft anderen Emissionswerte für die Herstellung der gebäudetechnischen Komponenten. Außerdem wird nur eine begrenzte Anzahl an Nutzungsprofilen betrachtet. Somit fehlen beispielsweise Mehrfamiliengebäude. Außerdem werden lediglich CO_2-Emissionen betrachtet und keine anderen LCA-Faktoren oder Kosten.

Ergebnisanalyse und Diskussion

Abbildung 1 zeigt die Ergebnisse der Optimierung in Form von Boxplots für das Einfamilienhaus. Dabei teilt sich die Abbildung in vier Grafiken auf. Die ersten beiden Grafiken 1a und 1b zeigen die vom Optimierer ausgewählte zusätzliche Dämmdicke. Die Grafiken 1c und 1d zeigen die Ergebnisse für die betrachteten Emissionen. Weiterhin wird zwischen den Energiesystemen, welche lediglich Heizen (1a, 1c) und den Systemen, welche ebenfalls Kühlen (1b, 1d) unterschieden. Alle vier Grafiken sind für vier verschiedene Energiesysteme dargestellt und für die fünf betrachteten Emissionswerte.

Die Grafiken zeigen, dass ein Wechsel vom Heizstab auf eine Wärmepumpe zur Wärmeversorgung die zusätzliche Dämmdicke sowie die Emissionen halbiert. Dahingegen haben die anderen Energiesysteme nur einen geringen Einfluss auf die zusätzliche Dämmdicke. Auch die Einbindung der Kühlung führt zu keiner großen Veränderung bei der Auswahl der zusätzlichen Dämmdicke, erhöht allerdings die Emissionen um über 10 %. Die Einbindung einer Photovoltaikanlage reduziert die Emissionen deutlich, hat aber kaum einen Einfluss auf die zusätzliche Dämmstärke. Die Reduzierung der Dämmstärke fällt bei den Fällen mit jährlich konstanten Werten stärker aus als bei der Betrachtung mit stündlichen Werten, was sinnvoll erscheint, da bei der stündlichen Auflösung die Emissionen für die Einspeisezeiträume aufgrund der Gleichzeitigkeit mit der PV im Stromnetz gering ausfallen. Dieser Effekt kann durch die Nutzung von Speichern kompensiert und mehr als ausgeglichen werden, da die Speicher nur einen geringen Einfluss auf die Fälle mit konstanten Emissionsfaktoren haben. Die Emissionsbilanz der Speicher kann im Fall der zeitvariablen Emissionen durch geschicktes Be- und Entladen verbessert werden. Die Nutzung einer Sole-Wasser-Wärmepumpe mit Erdsonde führt zu leicht geringeren Werten als die Luft-Wasser-Wärmepumpe. Die Dämmstärke fällt für die meisten Fälle geringer aus, da die Sole-Wasser-Wärmepumpe effizienter ist.

Die Berücksichtigung der Dekarbonisierung führt in den meisten Fällen zu einer Halbierung der optimalen zusätzlichen Dämmstärke. Aus dem Vergleich von Szenario S-D im Vergleich zum Szenario O-D wird ersichtlich, dass sich kaum etwas unterscheidet und sich der Mehraufwand für die Betrachtung der 10 Jahresauflösung nicht lohnt.

Abbildung 2 zeigt die Ergebnisse für das Bildungsgebäude im selben Format, wie die Abbildung vom Einfamilienhaus. Die meisten Punkte, welche beim Einfamilienhaus gelten, gelten hier auch. Im Vergleich zu Einfamilienhaus fällt hier die zusätzliche Dämmstärke nahezu doppelt so groß aus. Auch die Emissionen fallen aufgrund der größeren thermischen Lasten deutlich höher aus und schwanken aufgrund der unterschiedlichen Lüftungsverluste für die Schul- und Hochschulnutzung. Mit der Nutzung der Photovolatik können aufgrund des geringeren Strombedarf negative Werte erreicht werden. Es wird also in einigen Fällen mehr Strom verkauft als eingekauft wer-

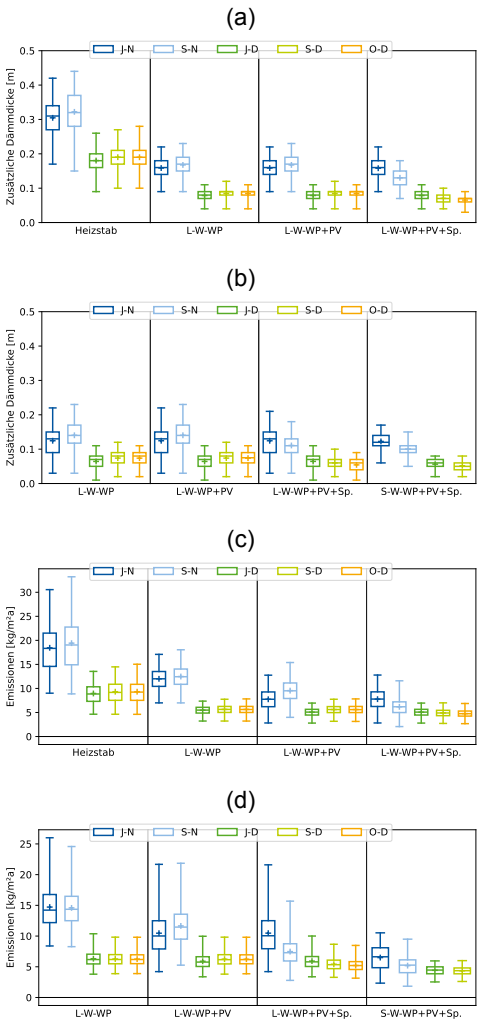

Abbildung 1: Ergebnisse für die zusätzliche Dämmdicke (a & b) sowie der Gesamtemissionen (c & d) für die reinen Heizsysteme (a & c) und die Systeme inklusive Kühlung (b & d) des Einfamiliengebäudes

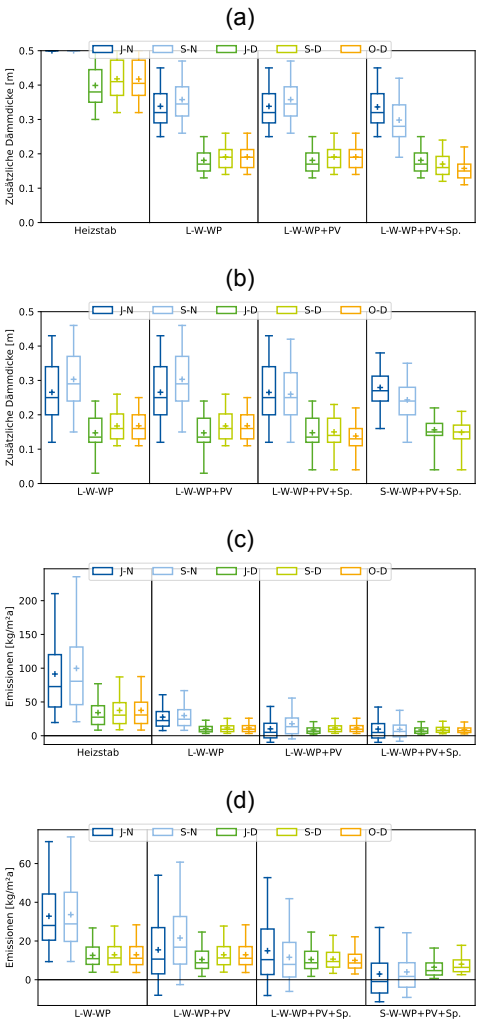

Abbildung 2: Ergebnisse für die zusätzliche Dämmdicke (a & b) sowie der Gesamtemissionen (c & d) für die reinen Heizsysteme (a & c) und die Systeme inklusive Kühlung (b & d) des Bildungsgebäudes

den muss und damit können sogar die konstruktionsbedingten Emissionen ausgeglichen werden. Dies gelingt allerdings nur in den Fällen, welche den heutigen Strommix berücksichtigen, da hier die Gutschrift für den verkauften Strom größer ist.

Abbildung 3 zeigt die Ergebnisse für das Bürogebäude im selben Format, wie die Abbildung von Einfamilienhaus. Das meiste, was für die Nutzung als Bildungsgebäude gilt, gilt auch für die Nutzung als Bürogebäude. Aufgrund des geringeren Strombedarfes ergeben sich hier negativere Emissionswerte, als beim Bildungsgebäude, für die Fälle mit einer Photovoltaikanlage.

Abbildung 4 zeigt die Ergebnisse für die Gewerbehalle im selben Format, wie die Abbildung von Einfamilienhaus. Das meiste, was für die Nutzung als Bildungsgebäude gilt, gilt auch für die Nutzung als Gewerbehalle. Die Emissionswerte werden aufgrund der höheren elektrischen Last nicht so negativ, wie die Bildungsgebäude. Hier ist der Emissionsunterschied zwischen dem Heizfall und dem Fall inkl. Kühlung mit über 100 % Unterschied aufgrund der höheren Kühllast deutlich größer. Dies begünstigt die Sole-Wasser-Wärmepumpe und diese schneidet deutlich besser als die Luft-Wasser-Wärmepumpe ab.

Zusammenfassung

Aus den Ergebnissen wird ersichtlich, dass die Art der CO_2-Bilanzierung einen signifikanten Einfluss

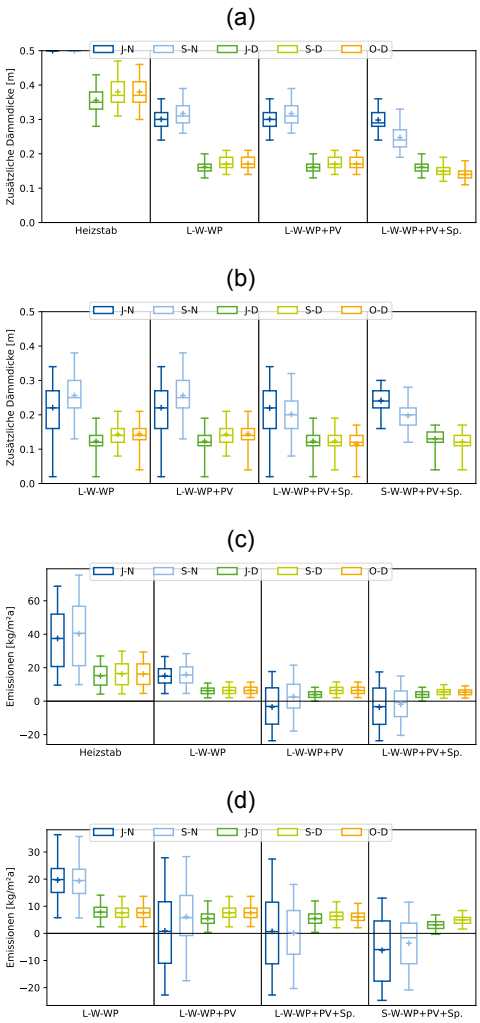

Abbildung 3: Ergebnisse für die zusätzliche Dämmdicke (a & b) sowie der Gesamtemissionen (c & d) für die reinen Heizsysteme (a & c) und die Systeme inklusive Kühlung (b & d) des Bürogebäudes

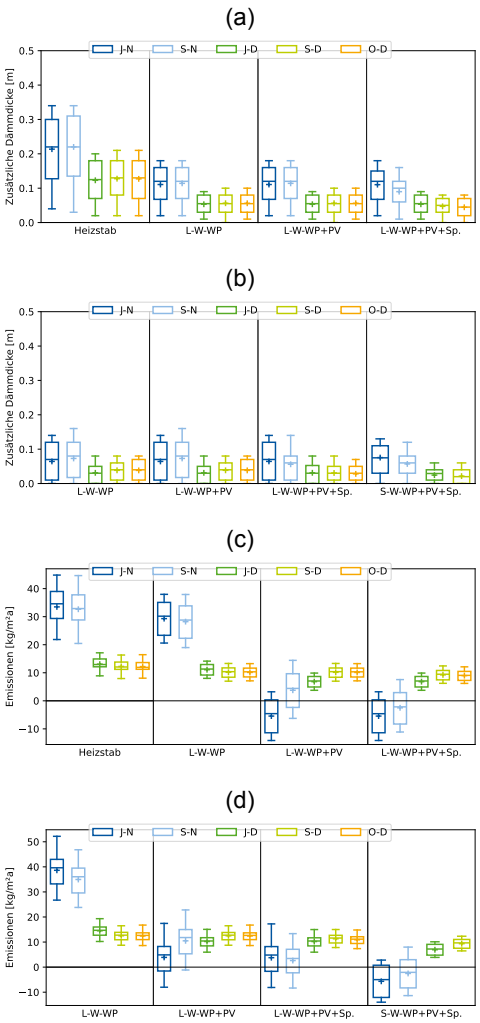

Abbildung 4: Ergebnisse für die zusätzliche Dämmdicke (a & b) sowie der Gesamtemissionen (c & d) für die reinen Heizsysteme (a & c) und die Systeme inklusive Kühlung (b & d) e der Gewerbehalle

auf die optimierte Dämmstärke und die Emissionen hat. So werden die Emissionen und die zusätzliche Dämmstärke teilweise halbiert. Dies ist ein deutlich stärkerer Einfluss als der der stündlichen Auflösung. Dieser ist mit unter 5 % bei der Dämmstärke und den Emissionen (für Fälle ohne Speicher und PV) sehr gering. Die Analyse inklusive der Stundenwerte ermöglicht die Bewertung von Speichern und hat einen erheblichen Einfluss. Bei deren Nutzung kann der Photovoltaikstrom gespeichert und später genutzt werden, welches dazu führt, das eine anfängliche Erhöhung der Emissionen durch die Betrachtung der stündlich aufgelösten Emissionswerte umgekehrt werden kann. Es wird empfohlen die Dekarbonisierung des Strommarktes mit in die Bilanzierung der Betriebsphase des Gebäudes aufzunehmen, da diese einen signifikanten Einfluss hat. Die Betrachtung von stündlich aufgelösten Werten ist primär sinnvoll, wenn elektrische Speicher betrachtet und bewertet werden sollen. Die Optimierung des Betriebes in einem 10 Jahres Raster bringt nur geringe Änderungen mit sich. Deswegen wird hier empfohlen bei der normalen 50 Jahresauflösung zu bleiben.

Für zukünftige Untersuchungen wird empfohlen die hier vorgestellten Verfahren auf andere LCA Faktoren und andere Gebäudetypen und -nutzungen auszuweiten. Außerdem kann eine Anwendung auf Quartiere und deren Energieversorgung untersucht werden.

Danksagung

Das in dieser Veröffentlichung zugrunde liegende Vorhaben wurde mit Mitteln des Bundesministeriums für Bildung und Forschung unter dem Förderkennzeichen 13FH555IX6 gefördert. Die Verantwortung für den Inhalt dieser Veröffentlichung liegt bei den Autorinnen und Autoren.

Literatur

BBSR, B. (2023), 'ÖKOBAUDAT'. Besucht am: 17.01.2024.
URL: *https://www.oekobaudat.de/*

Blanke, T. (2024), 'Supply Material for dynamic Life Cycle Assessment', *OSF* .
URL: *https://doi.org/10.17605/OSF.IO/734PB*

Blanke, T., Born, H., Göttsche, J., Herrmann, U., Döring, B., Frisch, J. & van Treeck, C. (2024), 'Model For Dimensioning Borehole Heat Exchanger Applied To Mixed-Integer-Linear-Problem (MILP) Energy System Optimization'. Wird noch veröffentlicht.

Blanke, T., Göttsche, J., Döring, B., Frisch, J. & van Treeck, C. (2024), 'Dynamic Prospective Average and Marginal Impact Factors from a Scenario-Based Method for the German Power System until 2070', *Energy, Sustainability and Society* . Wird noch veröffentlicht.

Blanke, T., Hagenkamp, M., Döring, B., Göttsche, J., Reger, V. & Kuhnhenne, M. (2021), 'Net-exergetic, hydraulic and thermal optimization of coaxial heat exchangers using fixed flow conditions instead of fixed flow rates', *Geothermal Energy* **9**(1).

Blanke, T., Hagenkamp, M., Göttsche, J., Döring, B., Reger, V. & Kuhnhenne, M. (2021), LCA optimal sizing of smart buildings' energy system components considering flexible grid-footprints, *in* 'Proceedings of Building Simulation 2021: 17th Conference of IBPSA', BS 2021, KU Leuven.

Blanke, T., Reger, V., Döring, B., Göttsche, J. & Kuhnhenne, M. (2021), 'Koaxiale Stahlenergiepfähle', *Stahlbau* **90**(6), 417–424.

Blanke, T., Schmidt, K. S., Göttsche, J., Döring, B., Frisch, J. & van Treeck, C. (2022), 'Time series aggregation for energy system design: review and extension of modelling seasonal storages', *Energy Informatics* **5**(17).

Brücken, C. K. (2012), 'Wirtschaftliche Bewertung und Optimierung von Wärmerückgewinnungssystemen'. Besucht am: 14.01.2024.
URL: *https://www.howatherm.de/download/72_optimierungwrgsystemehlh0612_2/*

Burkhardt, J. (2023), '15 Deutsche Solarhersteller und PV-Module aus Deutschland (2023)'.
URL: *https://echtsolar.de/deutsche-solarmodule-hersteller/*

Fonseca, S. (2023), 'Die 15 größten Solarhersteller aus Deutschland'.
URL: *https://gruenes.haus/photovoltaik-hersteller-deutschland/*

Hoffmann, M., Kotzur, L., Stolten, D. & Robinius, M. (2020), 'A Review on Time Series Aggregation Methods for Energy System Models', *Energies* **13**(3), 641.

Hoffmann, M., Priesmann, J., Nolting, L., Praktiknjo, A., Kotzur, L. & Stolten, D. (2021), 'Typical periods or typical time steps? A multi-model analysis to determine the optimal temporal aggregation for energy system models', *Applied Energy* **304**, 117825.

Holmgren, W. F., Hansen, C. W. & Mikofski, M. A. (2018), 'pvlib python: a python package for modeling solar energy systems', *Journal of Open Source Software* **3**(29), 884.

Hoops, H., Tjaden, T. & Rösken, K. (2022), 'RE-Lab-Projectshplib: v1.9'.
URL: *https://doi.org/10.5281/zenodo.5521597*

IER, I. (2024), 'tsam - Time Series Aggregation Module'.
URL: *https://github.com/FZJ-IEK3-VSA/tsam*

ISO (2018), 'DIN EN ISO 52016 - Energetische Bewertung von Gebäuden –Energiebedarf für Heizung und Kühlung, Innentemperaturen sowiefühlbare und latente Heizlasten –Teil 1: Berechnungsverfahren'. Besucht am: 16.01.2024.

Klingenburg (2023), 'Gegenstrom-Plattenwärmetauscher Typ GS: Hocheffizient – aus Aluminium, PET oder mit Epoxy Beschichtung'. Besucht am: 22.10.2023.
URL: *http://www.klingenburg.de/fileadmin/user_upload/germany/Downloads/GS/klingenburg_gs_de.pdf*

Kotzur, L., Markewitz, P., Robinius, M. & Stolten, D. (2018*a*), 'Impact of different time series aggregation methods on optimal energy system design', *Renewable Energy* **117**, 474–487.

Kotzur, L., Markewitz, P., Robinius, M. & Stolten, D. (2018*b*), 'Time series aggregation for energy system design: Modeling seasonal storage', *Applied Energy* **213**, 123–135.

Meteotest (2023), 'Meteonorm Software'.
URL: *https://meteonorm.com/*

Negishi, K., Lebert, A., Almeida, D., Chevalier, J. & Tiruta-Barna, L. (2019), 'Evaluating climate change pathways through a building's lifecycle based on Dynamic Life Cycle Assessment', *Building and Environment* **164**, 106377.

Sohn, J., Kalbar, P., Goldstein, B. & Birkved, M. (2020), 'Defining Temporally Dynamic Life Cycle Assessment: A Review', *Integrated Environmental Assessment and Management* **16**(3), 314–323.

Solar, F. (2023), 'Willkommen bei der Solar Fabrik'.
URL: *https://www.solar-fabrik.de/*

Su, S., Zhang, H., Zuo, J., Li, X. & Yuan, J. (2021), 'Assessment models and dynamic variables for dynamic life cycle assessment of buildings: a review', *Environmental Science and Pollution Research* **28**(21), 26199–26214. Besucht am: 16.01.2024.

Weinhold, K. (2024), 'Rekordabsatz: Wärmepumpenbranche beweist Leistungsfähigkeit trotz unsicherer Aussichten', *Bundesverband Wärmepumpe - Pressemitteilungen* .

Xing, L. (2014), ESTIMATIONS OF UNDISTURBED GROUND-TEMPERATURES USING NUMERICAL ANDANALYTICAL MODELING, PhD thesis, Oklahoma State University.

BauSIM 2024 in Wien
23. September – 26. September

Simulation-based determination of system size and energy savings for a life cycle assessment of a facade-integrated adsorption system for solar cooling of buildings

Olaf Boeckmann[1], David Borschewski[2], Simon Weber[2], Micha Schaefer[1]

1 Institute for Buildings Energetics, Thermotechnology and Energy Storage, University of Stuttgart, Germany, boeckmann@igte.uni-stuttgart.de

2 Institute for Acoustics and Building Physics, University of Stuttgart, Germany

Abstract

Reductions of CO_2 emissions from the building sector are mandatory for climate protection, while the cooling demand in this sector is increasing. This calls for the reduction of the operational energy. Against this background, a novel façade-integrated adsorption system for solar cooling is investigated. In this work, the required system sizes for different buildings are determined and a life cycle assessment is conducted to prove the savings in CO_2 emissions. The results reveal that the adsorption system can cover the cooling demand of buildings with an AV-ratio of 0.3 1/m or higher, but a share of 40 % and more of the façade towards East has to be replaced with panels of the cooling system. The façade area demand is much lower for the other compass orientations of the buildings with being zero for the façade towards South. Finally, the life cycle assessment shows that the use of the adsorption cooling system is beneficial regarding the global warming potential compared to conventional compression chillers by significantly reducing the electricity demand in the usage phase.

Introduction

The building sector accounts for almost 40% of the global CO_2 emissions due to its high demand for resources and energy (United Nations Environment Programme 2020). Therefore, with respect to the global climate protection goals, it is essential to reduce the required amount of building material in the construction of future buildings as well as to operate these lightweight buildings more energy efficiently or, if possible, energy self-sufficiently. Against this background, a novel facade-integrated adsorption system for solar cooling of buildings (Boeckmann et al. 2024) being developed and investigated within the Collaborative Research Centre 1244 at the University of Stuttgart. The proposed system combines the functionality of energy storage and cold production, with minimum occupation of inner building space.

The adsorption system consists of the three components adsorber, condenser and evaporator, see Figure 1. The adsorber and the condenser are integrated as panel-shaped façade elements into the building and the evaporator is installed as a cooling ceiling in the building. An additional adsorber is integrated into the opposite facade and an alternating operation mode is deployed to provide cooling power throughout the whole day. Furthermore, active shading of the adsorber is implemented to achieve high cooling rates at noon and to match the cold production with the demand.

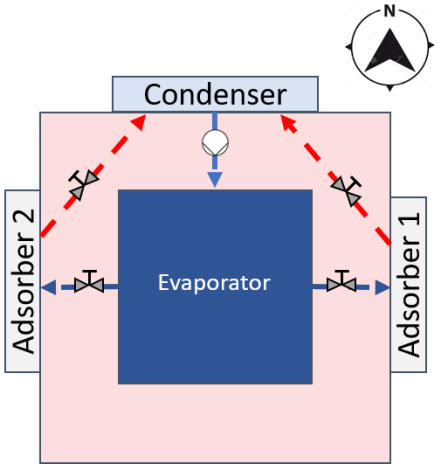

Figure 1: Top cross-section view of the façade-integrated adsorption system in the demonstration high-rise building of the CRC1244.

Adsorption cooling systems belong to the group of thermally driven cooling technologies, which are studied widely and have many applications in operation (Settino et al. 2018; Ghafoor und Munir 2015). Their positive impact on the environmental footprint of HVAC systems is proven and results mainly from large reductions in electricity consumption compared to conventional

compression chillers (Roumpedakis et al. 2020; Beccali et al. 2012). In contrast to the thermally driven solar cooling systems presented in the literature, the system in this work does not require separate solar thermal collectors, but combines the adsorber and solar thermal collector into one façade element. This is favorable due to the high potential of solar energy harvesting in this area.

The main objective of this work is the determination of the required system size, which is needed to cover the cooling power demand of different buildings, as well as the saved cooling energy. For this purpose, a building model is set up to calculate the required cooling power levels of reference buildings with a conventional HVAC system. A previously developed model of adsorption solar cooling system (Heidingsfeld et al.) is extended by a second adsorber to allow for continuous cooling and to perform system analyses. Furthermore, a life cycle assessment (LCA) is conducted to confirm that the proposed system saves CO_2 emissions.

Modeling and Simulation

This section explains the models of the investigated building, of the adsorption cooling system as well as of the conducted Life-Cycle-Assessment (LCA).

Building model

For the simulation of the building a zonal model from the IBPSA library was used and implemented in Dymola using the modeling language Modelica as presented in (Weber et al. 2022). The building model was created for different AV-ratios of squared stories with a height of $h = 2.85\ \mathrm{m}$. The AV-ratio describes the relation between volume and façade area of a building

$$AV = \frac{A_{\mathrm{F,B}}}{V_{\mathrm{B}}} = \frac{4xh}{x^2 h} = \frac{4}{x} \qquad (1)$$

where x is the length of the floor side, $A_{\mathrm{F,B}}$ the facade area and V_{B} the volume. The applied weather data (ambient temperature and solar irradiation) are generated for the location of the demonstrator building of the CRC 1244 in the university campus (N 48.749°, E 9.122°) using the Meteonorm software. This is done for all facades for the different investigated orientations of the building (South, 20° West and 40° West).

The building zone is surrounded by walls, the floor and the roof. For the walls a lightweight concrete of 25 cm with an insulation layer of 8 cm expanded polystyrene is used. Furthermore, the window share for each façade is 25 % ($U_{\mathrm{W}} = 0.6\ \frac{\mathrm{W}}{\mathrm{m^2K}}$; $g_{\mathrm{W}} = 0.32$). The floor and the ceiling are modeled as 13cm steel-concrete layers. The properties of the elements are shown in Table 1.

Table 1: Properties of walls, floor and ceiling.

Element	Material	$c_p\ [\frac{\mathrm{J}}{\mathrm{kgK}}]$	$\lambda\ [\frac{W}{mK}]$	$\rho\ [kg\{m^3]$
Outer wall - inner layer	Lightweight concrete	1000	0.21	900
Outer wall - outer layer	EPS	1450	0.035	20
Floor/ Ceiling	Steel-concrete	1000	2.5	2500

The temperature inside the building is influenced by heat flows due to the ambient conditions, the solar as well as the internal gains and the cooling or heating by the HVAC system. The internal gains are modeled to be active only during the workings hours from 7 - 18 h and are set to heat output of $11.4\ \mathrm{W/m^2}$ floor area, which results from the radiative and convective heat flows of 1 person per 14 m² floor area and the convective heat flow of 1 PC per person (DIN V 18599-10, Table A.2).

A control concept is created for the building to model to ensure that the building temperature is between 21 °C and 24 °C during working hours person (DIN V 18599-10, Table A.2). Each window is equipped with a blind, which has a constant F_c factor of 0.1. Once the solar irradiation on a window is higher than $\dot{q}_{\mathrm{sol,blind}}$, the blind is activated to limit to solar gains.

The COP of the compression chiller, which is part of the HVAC system, is set to 3.

System model

The main components are two adsorbers (A1 and A2), a condenser (C) and an evaporator (E). For both adsorber the same adsorption pair with the adsorptive water is used. As it is shown in (Dubies et al. 2023), the choice of the adsorbent has a significant influence on the system performance. For this reason, two difference adsorbents are compared in this work. On one hand Zeolith 13-X due to its well-documented properties (Mette et al. 2014) and one the other hand silica gel RD2506 (Yang et al. 2021).

For efficient absorption of solar irradiation, the outermost part of the adsorber is equipped with a selective PVD coating. A glass pane is mounted in front of the adsorber to minimize thermal losses, but with a small gap, which can be

opened to enable natural convection to cool the adsorber if required. The adsorber as well as the condenser are insulated with vacuum insulation panels to the interior to avoid undesired heat exchange. All components are manufactured in aluminum, which was found to be beneficial due to its low density and thermal mass. The further details on the structure of the components can be found in (Boeckmann et al. 2024).

The system switches between different operational phases:

1. Regeneration phase: In this phase, the adsorber is heated up by solar irradiation and connected to the condenser, so that the released water can flow to the condenser and condense. An efficient cooling of the condenser is required to effectively reduce the water uptake of the adsorber. This phase takes place while the adsorber is facing the sun, which is in the morning for A1 and in the afternoon for A2.
2. Inter-cooling phase: At the end of the regeneration phase, the pressure inside the adsorber is much higher than the pressure inside the evaporator due to the higher temperature. Therefore, an immediate connection between the adsorber and the evaporator is not possible. Therefore, the adsorber has to cool down and re-adsorb the remaining vapor. This reduces the pressure. When the pressure in the adsorber is lower than the pressure in the evaporator, the system can enter the cooling phase.
3. Cooling phase: In this phase, the room is cooled by evaporating water in the evaporator. The connection to the adsorber is opened, so that the vapor can be adsorbed, which leads to continuous evaporation. The adsorption rate strongly depends on the temperature of the adsorber with low temperatures being beneficial. Thus, the sun should not directly shine on the adsorber, which takes place for A1 in the afternoon and for A2 in the morning.
4. Inter-heating phase: Conversely to the inter-cooling phase, the adsorber has to heat up before the connection to the condenser can be opened. Once the pressure inside the adsorber is higher than the one inside the condenser, the system can switch to the regeneration phase.

To close the internal water cycle, liquid water is pumped from the condenser into the evaporator in the early morning hours. A more detailed description of the operational phases and the switching strategy is given in (Boeckmann et al. 2024; Heidingsfeld et al. 2022)

To be able to provide continuous cooling power over the day, the adsorber can be actively shaded. This allows to extend the cooling phase of A2 to the noon hours and start the cooling phase of A1 before the solar irradiation on A1 is too high.

For each component, the system model determines the evolution of temperatures, pressures as well as water masses/uptake over time. The governing equations, which describe the system model, are presented in detail (Heidingsfeld et al.).

The total cooling power, which is provided by the evaporator is

$$\dot{Q}_{\mathrm{E,total}} = A_{\mathrm{E}} \cdot \alpha_{\mathrm{R}} \cdot (T_{\mathrm{R}} - T_{\mathrm{E}}), \qquad (2)$$

where A_{E} denotes the total area of the evaporator, α_{R} the heat transfer coefficient between evaporator and room, which is assumed to a constant value of $7\ \frac{\mathrm{W}}{\mathrm{m^2K}}$ and T_{R} the room temperature. The latter is set to the upper comfort limit temperature of 24 °C.

In order to avoid temperatures in the evaporator below 15 °C to prevent condensation of the air moisture at the cooling ceiling inside the room, the evaporation rate is controlled. This is done by reducing the mass flow between evaporator and adsorber.

Therefore, the maximum cooling power per square meter of installed evaporator area yields:

$$\dot{q}_{\mathrm{E,max}} = \alpha_{\mathrm{R}}\left(T_{\mathrm{R}} - T_{\mathrm{E,min}}\right) = 7\,\frac{\mathrm{W}}{\mathrm{m^2K}}(24\ ^{\circ}\mathrm{C} - 15\ ^{\circ}\mathrm{C}) = 63\,\frac{\mathrm{W}}{\mathrm{m^2}}.$$

This is in the same magnitude as conventional cooling ceilings.

Life cycle assessment

Life cycle assessment (LCA) enables the systematic evaluation of new approaches and the derivation of important findings for the planning, construction, operation and dismantling of resource-saving, energy-efficient and sustainable buildings as well as technologies.

The standardized LCA method (product-independent according to (DIN EN ISO 14040) and (DIN EN ISO 14040), building-specific according to (EN 15804) and (DIN EN 15978)) combines a life cycle perspective, technical process chain analysis and environmental impact analysis and represents an optimal tool for analyzing and evaluation of resource efficiency and the environmental impact of either building components or entire buildings. Consequently, it

provides results and can reveal potential areas for optimizations. These can be described using common impact categories, often represented by the global warming potential (GWP), i.e. the respective contribution to climate change as well as the need for primary energetic renewable and non-renewable resources.

In this work, an LCA screening is performed to assess the CO_2 emissions of the proposed adsorption system. To classify the results, a reference system is modeled as well, utilizing a compression chiller to provide the required cooling energy. This chiller is driven by electricity from the grid (Germany), considering decreasing emissions over the lifecycle due to increasing share of renewable energies (based on the EU Reference Scenario (European Commission et al., 2021). Furthermore, the adsorption and condenser panels replace conventional façade elements, as described in Section Building model.

For the comparison, a life cycle of 25 years is assumed and only the differences between the reference case and the case with adsorption system are considered. These are:

- Production of the adsorption system (Modul A1-A3)
- Production of the replaced conventional façade elements (Modul A1-A3)
- Electricity consumption of the compression chiller (Modul B6)
- Electricity consumption of the adsorption system (Modul B6)

For the end of life (Module C3 and C4), the following scenarios are applied:

- Metal parts: Recycling
- Concrete: Landfill
- Plastics (insulation): Incineration with energy recovery
- VIP panel: Disposal
- Zeolite: Disposal

Credits for avoided burdens are considered (Modul D). LCA models were created in LCA for Experts (Version 10.7.1.28; Content version 2023.2) (Sphera Solutions GmbH 2023) and evaluated with Environmental Footprint 3.0 (European Commission et al., 2018).

Results analysis and discussion

In this section the determined results for the required cooling demand, the system size as well as for the conducted LCA are presented and discussed.

Cooling demand

The required cooling demand of the reference building is calculated using the building model and the according weather data. In Figure 2 the annual electrical energy demand by the compression chiller of the HVAC system is shown over the AV-ratio for the different cases regarding building orientation and switching factor $\dot{q}_{\mathrm{sol,blind}}$ for the blind of the windows. The energy demand is given per square meter of floor area to allow for easier comparison.

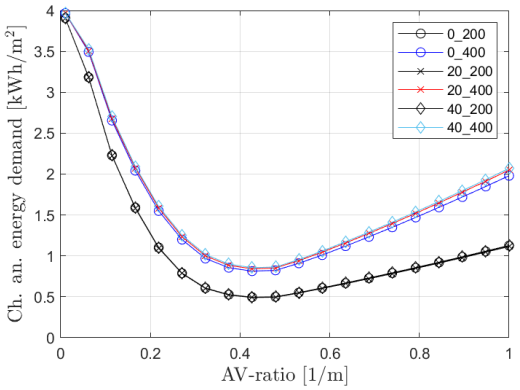

Figure 2: Annual electrical energy demanded by the compression chiller for different orientations as well as set-points for the shadings of the windows over the AV-ratio. The energy demand is given per square meter of floor area. The first number in the legend denotes the orientation and the second the switching factor of the blinds in $\frac{\mathrm{W}}{\mathrm{m}^2}$.

It is found that energy demand of the compression chiller, which is proportional to the required cooling energy, mainly depends on the AV-ratio and on the switching factor $\dot{q}_{\mathrm{sol,blind}}$. The lower the latter is, the lower is the energy demand due to less solar gains. For very small AV-ratios the heat exchange over the facades areas is rather small compared to the internal gains, which increases the cooling demand. For the very large AV-ratios the solar gains are rather large with respect to the floor area, which also increases the cooling demand per m² of floor area. The orientation of the building has a negligible influence on the cooling demand as the solar gains are distributed quite equally.

For the further analyses, five AV-ratios are chosen: 0.1, 0.2, 0.3, 0.5 and 1.0. With these values, the whole range of the required cooling range is covered. The buildings dimensions as well as the determined annual electrical energy demands of the compression chiller are given in Table 2.

Table 2: Dimensions and total electrical demand of cooling chiller for chosen AV-cases.

AV [1/m]	Floor side x [m]	Floor area [m²]	Area per façade [m²]	Annual electrical demand [kWh]
0.1	40	1600	114	3941.6
0.2	20	400	57	503.66
0.3	13.3	178	38	119.25
0.5	8	64	2.8	33.25
1	4	16	11.4	18

In Figure 3 the determined cooling power, which has to be provided by the adsorption cooling system, is plotted over the cooling period. It is found that the maximum required cooling power equals around 1120 W and occurs on day 190 of the year, which is in the beginning of July.

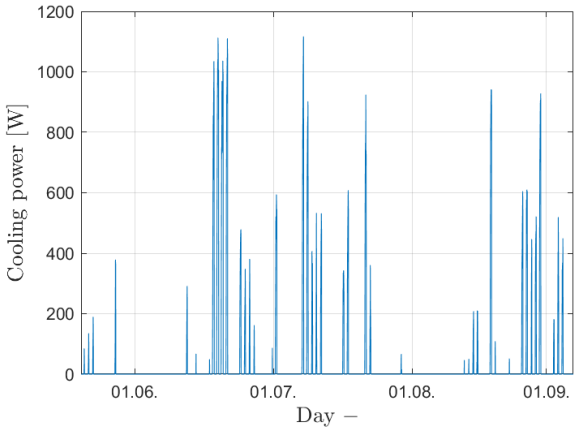

Figure 3: Evolution of the required cooling power over the cooling period for an AV-ratio of 0.5.

System size determination

In the following the determination of the adsorption cooling system size is shown exemplarily for an AV-ratio of 0.5 1/m and the adsorption pair Zeolith 13-X and water. The system is scaled to cover the total required cooling power on day 190 of the year. The evolution of cooling power demand for that day can be seen in Figure 4.

At first, the required evaporator area is calculated from the maximum total cooling power, which is 1120 W in this case, and the maximum cooling power per square meter of installed evaporator area:

$$A_E = \frac{1120\ \mathrm{W}}{63\ \frac{\mathrm{W}}{\mathrm{m}^2}} = 17.8\ \mathrm{m}^2.$$

The respective area ratio f_{E} yields 0.28.

In the second step, the required adsorber area is estimated from the maximum total cooling power. As this is required during the afternoon, the adsorber A1, which is placed on the East-façade, has to provide this maximum value. The maximum cooling power for A1 is around 100 W per installed square meter of adsorber using Zeolith 13-X as adsorbent. Thus, the required area is

$$A_{A1} = \frac{1120\ \mathrm{W}}{100\ \frac{\mathrm{W}}{\mathrm{m}^2}} = 11.2\ \mathrm{m}^2,$$

which corresponds to an area ratio f_{A1} of 0.5. Finally, the area ratios of the second adsorber and the condenser are determined running simulations with different ratios. Furthermore, simulations with f_{A1} beeing set to 0.4 are conducted, to prove that this is not sufficient.

The different combinations are compared by the coverage ratio, which is the cooling energy provided divided by the cooling energy required during the working hours and the results are summarized in Table 3. It is found that an area ratio f_{A1} of 0.4 is too low to cover the full cooling demand since the peak cooling power levels are not reached. Furthermore, it can be seen that area ratios f_{A2} of 0.125 and f_{C} are sufficient, compare Case 10. The resulting cooling power of the adsorption cooling system is shown in Figure 4.

Table 3: Coverage ratios for the solar cooling system for different system sizes with adsorption pair Zeolith 13-X and water.

Case	Area ratio f_{A1}	Area ratio f_{A2}	Area ratio f_{C}	Coverage ratio [%]
1	0.4	0.1	0.1	82.9
2	0.4	0.1	0.15	91.0
3	0.4	0.125	0.1	88.3
4	0.4	0.125	0.15	94.9
5	0.4	0.15	0.1	93.3
6	0.4	0.15	0.15	95.4
7	0.5	0.1	0.1	89.0
8	0.5	0.1	0.15	97.6
9	0.5	0.125	0.1	95.1
10	0.5	0.125	0.15	99.7
11	0.5	0.15	0.1	98.9
12	0.5	0.15	0.15	99.9

If the condenser is too small, the temperature of the water inside the condenser becomes very hot due to the heat of condensation of the condensing vapor from the adsorber. This affects the regeneration process of both, adsorber A1 and A2, which limits the maximum cooling rate, which can be provided by A1 in the afternoon, compare Case 9 in Figure 4.

If the adsorber A2 towards West is too small, the provided cooling power cannot meet the demand in the noon hours as the cooling phase of A2 stops before the adsorber A1 can begin its cooling phase, see Case 8 in Figure 4.

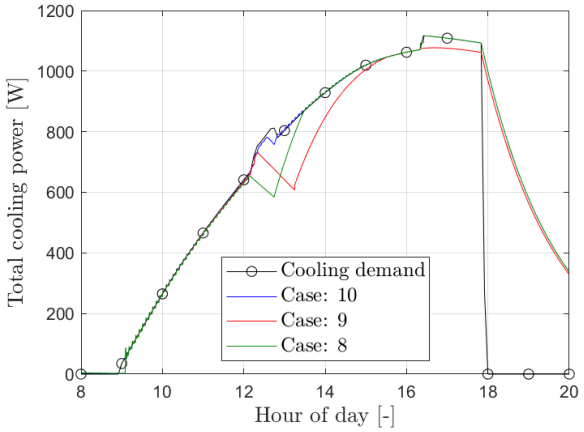

Figure 4: Evolution of cooling power over time for the day 190 of the year for a building with an AV-ratio of 0.5 1/m. The power demand to be covered is shown in black. The cooling powers provided by the adsorption cooling system is pictured in blue for the obtained maximum case, in red for the case with too little condenser and in green for a too small A2.

Furthermore, the system sizes are determined for the other chosen AV-ratios as well as for the adsorption pair silica gel RD2506 and water. For the very small ratios of 0.1 1/m and 0.2 1/m, the façade area is too small to install an adsorption system, which is able to provide to required cooling power, compared to the high internal gains.

It is found that the obtained area ratios for the façade integrated components decrease with increasing AV-ratio, refer to Figure 5. A high AV-ratio means more available façade area per floor area. Thus, the internal gains, which depend solely on the floor area, seem to have the biggest impact on the required cooling rate. For the obtained area ratio of the evaporator the opposite is the case. The lower the AV-ratio, the lower area ration.

The adsorber A2 towards the West can be smaller than A1 since the high cooling power levels occur during the afternoon and have to be covered by A1. The quotient f_{A1} / f_{A2} is found to be constant value of around 0.25 for the adsorption pair Zeolith 13-X and water.

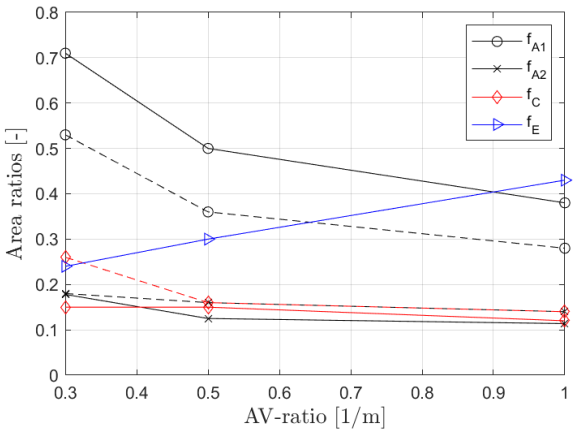

Figure 5: Determined system sizes for the four components adsorber towards East (A1), adsorber towards West (A2), condenser (C) and evaporator (E) over the AV-ratio. The full lines relate to adsorbent Zeolith 13-X and the dashed lines to adsorbent silica gel RD2506.

The results for the adsorbent silica gel RD2506 are shown in dashed lines in Figure 5. It is found that the adsorber A1 can be way smaller due to improved system performance. Nevertheless, the adsorber A2 and the condenser need to be slightly larger. For the evaporator, there is no difference depending on the adsorbent.

Life cycle assessment

The results of the life cycle assessment are presented for all three considered AV-ratios for the adsorption pair Zeolith 13-X and water in Figure 6 and for the adsorption pair silica gel RD2506 and water in Figure 7. For all cases, the global warming potential (GWP) of the respective reference systems in also shown. Please note that the reference system using RD2506 is smaller since the required façade area is smaller. As the adsorption system is thermally driven and thus has only a very limited electricity demand, the CO_2 emissions during the operational phase are negligibly. Thus, the GWP of the adsorption system results from the embodied masses. Nevertheless, it is also found that the main share of the GWP of the reference systems is also due to the embodied masses.

The results of the LCA show that the use of the adsorption cooling system applying the adsorbent Zeolith 13-X is only beneficial for the AV-ratio of 1.0. For the other AV-ratios the required system sizes are too large.

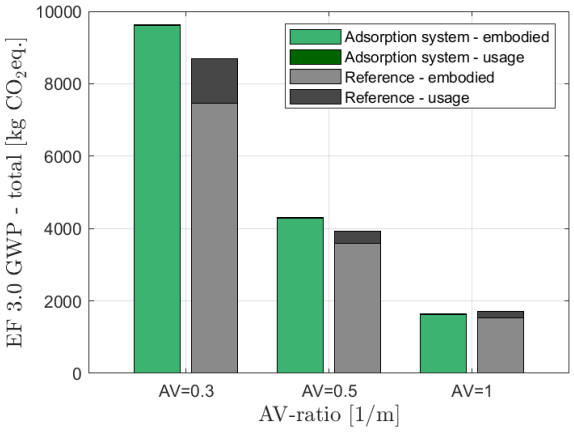

Figure 6: Global warming potential (GWP) of the adsorption system with Zeolith 13-X as adsorbent and the reference system for different AV-ratios. The GWP is split into the embodied emissions and those during the 25-year lifecycle.

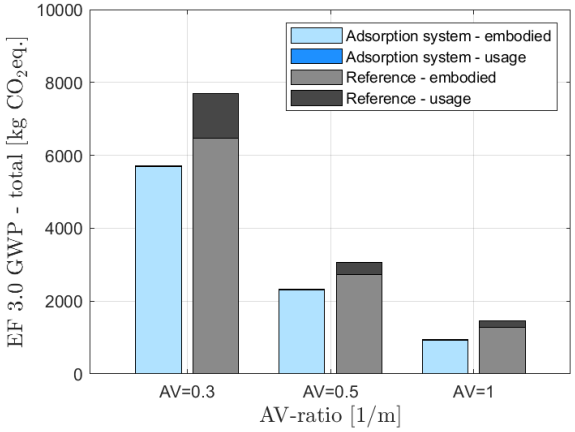

Figure 7: Global warming potential (GWP) of the adsorption system with silica gel RD2506 as adsorbent and the reference system for different AV-ratios. The GWP is split into the embodied emissions and those during the 25-year lifecycle.

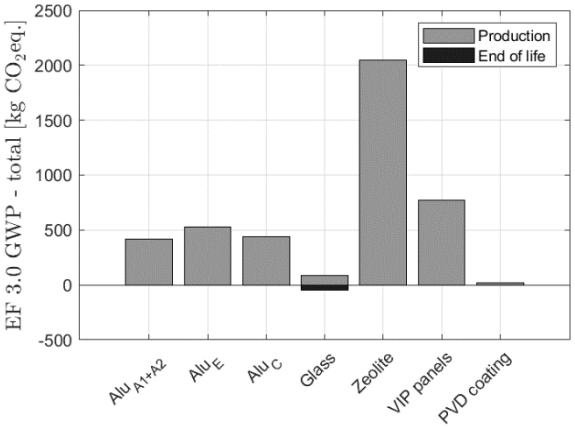

Figure 8: Global warming potential of the different components of the adsorption cooling system for an AV-ratio of 0.5 1/m and Zeolith 13-X as adsorbent. The GWP is split into the production and the end of life phase.

Using silical gel RD2506 as adsorbent, does not only reduce the required system sizes, but also decreases the GWP significantly since the mass-related GWP of silical gel RD2506 is almost three times smaller than that of Zeolith 13-X.

The GWP of the different components of the adsorption cooling system is displayed in detail in Figure 8. The biggest share is the high mass of zeolite, which is required for the adsorption process in the two adsorber, as well as the vacuum insulation panels, which are placed between the adsorber or condenser and the interior of the building.
The amount of zeolite depends strongly on the variation of water uptake during operation. This is rather low at 2.35 % for A1 and 5.05 % for A2, with a maximum of 33 % possible, see Figure 9. Therefore, one focus of future work will be to increase this variation. This could be done by optimizing the process or by using a different material. Nevertheless, the variation of water uptake of the tested adsorbent silica gel RD2506 is not much larger than that of zeolite 13-X.

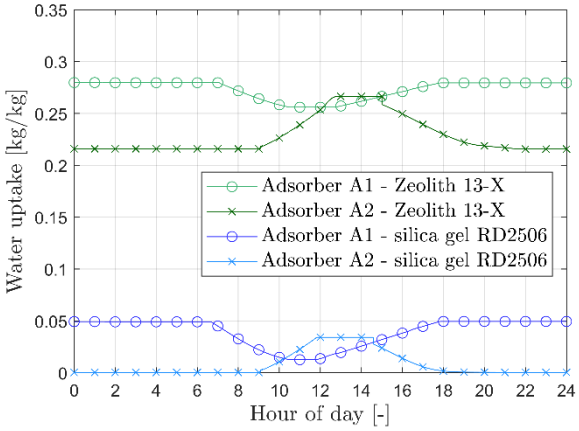

Figure 9: Water uptake of the two adsorber over one day for an AV-ratio of 0.5 1/m. The maximum value for the applied materials is 0.33.

Conclusion

In this work, the required system sizes of an adsorption solar cooling system are determined for buildings with different AV-ratios and the two adsorptions pairs Zeolith 13-X/silica gel RD2506 with water. It is found that the adsorption system can cover the cooling demand of buildings with an AV-ratio of 0.3 1/m or higher, but a share of 30 % and more of the façade towards East has to be replaced with panels of the cooling system. On the façade towards West and to the North this share is reduced by up to 75 %. The required façade area ratios decrease with increasing AV-ratios. Furthermore, a life cycle assessment is conducted, which proves that the adsorption system is able to reduce to global warming

potential of buildings due to covering the cooling demand.

In future works, the efficiency of the cooling system, especially the amplitude of the water uptake variation in the adsorber, has to be improved. Moreover, the system should be applied to other façade systems such as glass facades or lightweight curtain wall systems.

Acknowledgement

The authors thank the Deutsche Forschungsgemeinschaft (DFG, German Research Foundation) for funding under SFB1244-279064222.

References

Beccali, Marco; Cellura, Maurizio; Longo, Sonia; Nocke, Bettina; Finocchiaro, Pietro (2012): LCA of a solar heating and cooling system equipped with a small water–ammonia absorption chiller. In: *Solar Energy* 86 (5), S. 1491–1503. DOI: 10.1016/j.solener.2012.02.010.

Boeckmann, Olaf; Marmullaku, Drin; Schaefer, Micha (2024): Dyanmic modeling and simulation of a facade-integrated adsorption system for solar cooling of lightweight buildings. In: *Energies*.

DIN EN 15804:2022-03, Nachhaltigkeit von Bauwerken_- Umweltproduktdeklarationen_- Grundregeln für die Produktkategorie Bauprodukte; Deutsche Fassung EN_15804:2012+A2:2019_+ AC:2021.

DIN EN ISO 14040:2021-02, Umweltmanagement_- Ökobilanz_- Grundsätze und Rahmenbedingungen (ISO_14040:2006_+ Amd_1:2020); Deutsche Fassung EN_ISO_14040:2006_+ A1:2020.

DIN V 18599-10:2018-09, Energetische Bewertung von Gebäuden_- Berechnung des Nutz-, End- und Primärenergiebedarfs für Heizung, Kühlung, Lüftung, Trinkwarmwasser und Beleuchtung_- Teil_10: Nutzungsrandbedingungen, Klimadaten.

Dubies, Tim; Boeckmann, Olaf; Schaefer, Micha (2023): Material study of a facade-integrated adsorption system for solar cooling of buildings. In: *IRES Conference*.

European Commission; Directorate-General for Climate Action; Directorate-General for Energy; Directorate-General for Mobility; Transport; Vita, A. de et al. (2021): EU reference scenario 2020 – Energy, transport and GHG emissions – Trends to 2050: Publications Office.

European Commission; Joint Research Centre; Sala, S.; Laurentiis, V. de; Zampori, L.; Diaconu, E. et al. (2018): Supporting information to the characterisation factors of recommended EF Life Cycle Impact Assessment methods – Version 2, from ILCD to EF 3.0: Publications Office.

Ghafoor, Abdul; Munir, Anjum (2015): Worldwide overview of solar thermal cooling technologies. In: *Renewable and Sustainable Energy Reviews* 43, S. 763–774. DOI: 10.1016/j.rser.2014.11.073.

Heidingsfeld, Julia L.; Boeckmann, Olaf; Schaefer, Micha; Boehm, Michael; Sawodny, Oliver (2022): Low Order Hybrid Model for Control Design of an Adsorption Facade System for Solar Cooling. In: 2022 IEEE Conference on Control, S. 425–432.

Mette, Barbara; Kerskes, Henner; Drück, Harald; Müller-Steinhagen, Hans (2014): Experimental and numerical investigations on the water vapor adsorption isotherms and kinetics of binderless zeolite 13X. In: *International Journal of Heat and Mass Transfer* 71, S. 555–561. DOI: 10.1016/j.ijheatmasstransfer.2013.12.061.

Roumpedakis, Tryfon C.; Kallis, George; Magiri-Skouloudi, Despina; Grimekis, Dimitrios; Karellas, Sotirios (2020): Life cycle analysis of ZEOSOL solar cooling and heating system. In: *Renewable Energy* 154, S. 82–98. DOI: 10.1016/j.renene.2020.02.114.

Settino, Jessica; Sant, Tonio; Micallef, Christopher; Farrugia, Mario; Spiteri Staines, Cyril; Licari, John; Micallef, Alexander (2018): Overview of solar technologies for electricity, heating and cooling production. In: *Renewable and Sustainable Energy Reviews* 90, S. 892–909. DOI: 10.1016/j.rser.2018.03.112.

Sphera Solutions GmbH (2023): LCA for Experts Software System and Database for Life Cycle Engineering.

United Nations Environment Programme (2020): 2020 Global Status Report for Buildings and Construction.

Weber, Simon; Boeckmann, Olaf; Greiner, Andreas; Park, Sumee; Schäfer, Micha; Ostermann, Martin (2022): Optimal operation and conceptual design of a novel facade-integrated adsorption cooling system. In: *EuroSun 2022, Kassel*, S. 425–432.

Yang, Zhiyao; Gluesenkamp, Kyle R.; Frazzica, Andrea (2021): Equilibrium vapor pressure properties for absorbent and adsorbent materials. In: *International Journal of Refrigeration* 124, S. 134–166. DOI: 10.1016/j.ijrefrig.2020.12.013.

BauSIM 2024 in Wien
23. September – 26. September

Supporting the mainstreamed implementation of life cycle assessment in the established German building funding ecosystem

Muriel Lauschke[1], Sebastian Ebertshäuser[1], Rafael Horn[1]
1 Fraunhofer-Institut für Bauphysik, Deutschland, E-Mail: muriel.lauschke@ibp.fraunhofer.de

Abstract

With increasing requirements of funding criteria for buildings, Germany tries to meet its ambitious climate goals. In this context the consideration of environmental impacts, using a life cycle assessment (LCA), extends the previous focus on CO_2-emissions within the operating phase. By introducing a mandatory simplified LCA for all funding applications on new buildings, the authorities aim to achieve a broad implementation of LCA as standard component in the planning process through the established group of energy auditors. Still the energy auditors' workflows were not adequately represented during the development of the simplified LCA procedures. Resulting practical challenges that arise for this group from their new LCA task are in the focus of this work. The main challenge is how to reduce the effort to gather LCA input data. In addition, methodological improvements based on detailed information, such as that on technical services, are compared against flat-rate aggregates as applied within the current LCA approach. Characteristic parameters used in the standard-based energy balance are analyzed against those on side of LCA. Finally, the influence of the identified aspects regarding the LCA-input data on the LCA-results will be shown in an overview.

Introduction

The holistic consideration of environmental impacts through a broad implementation of life cycle assessment (LCA) requires integrating the application of this method into the existing planning processes for buildings. Therefore, Germany has introduced the "Qualitätssiegel Nachhaltiges Gebäude" (QNG, en.: "Quality seal sustainable building") as a mandatory simplified LCA procedure for new buildings in the funding system which previously has been focused on energy efficiency. Since funding applications are created before the building permit in early design phases, the approach requires to also include environmental aspects based on the available information at that time in addition to energy efficiency.

With these new regulations energy auditors - representing the main group creating the funding applications - are compelled to integrate the simplified LCA in their existing scope of work. Initial experiences show that challenges arise for them collecting the new required data, especially concerning material information on all relevant building elements, also requiring new data exchanges with other planners than before.

In contrast other parts like the technical services are considered more detailed in the energy assessment than in the QNG approach. This contribution addresses the potential synergies regarding the input data for both assessments and how strengthening them, can improve the quality and accuracy of the LCA results. This, in turn, supports energy auditors in consulting their customers with a robust and practical LCA without high expenditure.

Background

The German funding system for efficient buildings (BEG) has so far only been focused on the energy efficiency of buildings. The extension of funding applications in 2023 with the LCA approach according to QNG leads to new tasks for energy auditors. To identify the different perspectives of energy assessment and the current QNG method in the funding ecosystem, they are described in the following with the focus on technical services.

Energy assessment

The "Energy Performance of Buildings Directive" (EPBD) determines the overall framework of regulations for EU-countries to evaluate the energy efficiency of building operations. In Germany the EPBD is transposed in the "Gebäudeenergiegesetz" (GEG) (Deutscher Bundestag, 2024) and the standard DIN V 18599 representing the methodology for the obligatory energy performance certificate (EPC). In addition, these national methods are part of BEG funding and thus also of QNG.

The energy balance evaluates the energy efficiency along the primary energy demand of buildings in the operating phase. Therefore, the

procedure of DIN V 18599 considers the thermal quality of the building envelope and the technical building services like heating, drinking hot water, ventilation, air-conditioning, cooling, (HVAC), renewable energies and for non-residential buildings also lighting.

In general, for technical services four sections – generation, distribution, emission and storage – are taken into account, each requiring specific data. Default values are provided in case the input data for detailed calculation are not available which is often the case when applying for funding. As the default values give proven assumptions auditors can rely on, the calculations are ensured to be as comparable as possible. The question arises, if these default values could potentially give an added value for LCA in QNG.

Quality seal sustainable building (QNG)

QNG provides an approach to evaluate the environmental impacts during the whole life cycle of a building. The energy assessment is considered in the LCA of use phase and is evaluated along with the other phases like production, replacement and end-of-life based on regulations that consider the broader context of the LCA method. Nevertheless, the implementation of QNG contains several simplifications compared to complete LCA approaches building on EN 15978 and EN 15643. These followingly described simplifications aim for a broad implementation.

Primarily, the scope does not contain all possible modules (describing life cycle phases). In addition, it only regards two impact indicators - the Global Warming Potential (GWP) and the primary energy non-renewable total (PENRT).

Secondly, the data base for the QNG assessment is very limited. The mandatorily used “Rechenwerttabelle” (table of calculation values) only provides an extract of different versions of the more extensive ÖKOBAUDAT (Bundesministerium für Wohnen, Stadtentwicklung und Bauwesen, 2020) data base. Other sources such as EPDs are not allowed. Additionally, all life cycle stages and technical lifetimes are fixed and may not be changed. Due to missing data sets concerning HVAC in ÖKOBAUDAT also the “Rechenwerttabelle” includes only very limited data sets like generators, PV-modules and storage tanks.

Furthermore, other HVAC components like pipes for distribution, heating surfaces for emission or specific storages etc. are considered in a flat-rate aggregate related to the net floor area of the building and its primary energy demand. Although flat-rate considerations are easy to calculate, they come with a high inaccuracy and they reduce the possibility to optimize and guide the developments towards sustainable buildings (Dorn-Pfahler & Lützkendorf, 2023). Compared to the energy assessment, it occurs that the already existing data in the energy auditors’ workflows has only been taken partially into account, especially regarding HVAC.

Methodology

Studies show that HVAC causes about 25% of the buildings’ total greenhouse gas emissions (Chuchra et al., 2020). Therefore, a more detailed calculation compared to the flat-rate aggregates in QNG for early design phases should be investigated. To strengthen potential synergies between the energy assessment and QNG regarding HVAC, the following examination addresses how already utilized data in the energy balance can be also used in LCA. Thereby the influence regarding the accuracy of LCA results within QNG will be identified. The overall goal is to show how the data collection for LCA can be better connected to the established processes as well as how to leverage potentials in existing workflows to improve consistency, robustness and practicability at the same time. Figure 1 shows the considered steps to achieve this objective.

First, the sections of HVAC in the energy balance according to DIN V 18599 will be pointed out to distinguish the existing structure of information and to identify on this base which components could possibly be evaluated in detail in LCA.

In the next step it will be identified which ÖKOBAUDAT data sets for the considered sections are available. In this study the version 2020-II is used. Furthermore, it needs to be determined which functional unit is required for the environmental evaluation and which further information the data sets provide. If these information are already sufficient no further enrichment is required. Otherwise, the provided data from DIN V 18599 – especially the established default values – will be investigated concerning their usefulness. If necessary, more data of DIN V 18599 and further available data at that time in the planning process could be enriched for the conversion to the functional unit.

To show the variance and the significance of evaluating the HVAC components being only considered in flat-rate aggregates in QNG so far, their influences on LCA will be shown in simple examples. If different options for the calculation of the amount required for LCA are possible, the variants will be compared and evaluated

regarding their transparency, accuracy and the resulting expenditure for planners.

In the end, a general approach will show the required data for a LCA based on available data from energy assessment and it will be figured out which additional data eventually is required.

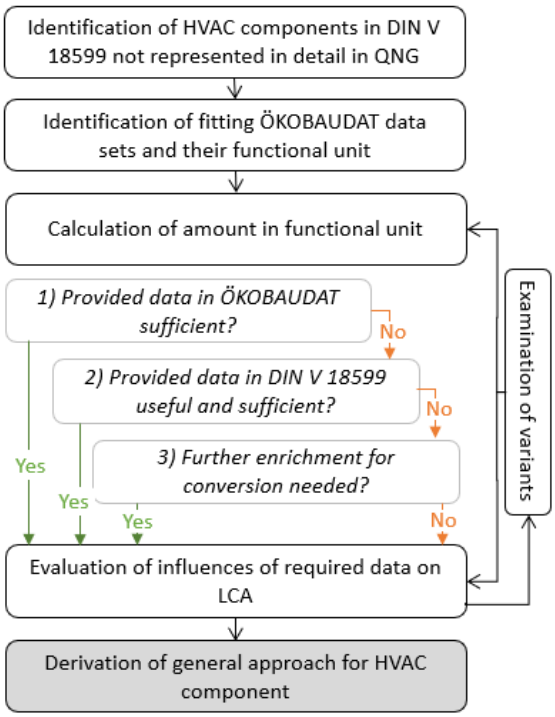

Figure 1: Methodology

Investigation of data requirements for heating distribution systems

The methodology will be applied to the heating distribution system for which the energy balance provides detailed information. It is only considered in the flat-rate aggregate in LCA according to QNG, even if studies show its high environmental relevance with about 22 % of the impacts of an exemplary whole HVAC system (Lambertz et al., 2019). For this reason, the distribution of heating systems consisting of pipes and pipe insulations will be investigated in detail in the following.

Heating pipes

1) Required and provided data in ÖKOBAUDAT

To calculate the environmental impacts of heating pipes, suitable datasets from the ÖKOBAUDAT need to be identified. For the heating pipes there are data sets for different materials, e.g. copper, PE and steal. All datasets require the functional unit “mass” in kilogram.

Therefore, most data sets provide a table for the weight per meter depending on the inside and outside diameter of the specific pipe, supporting the identification of the weight. Still the inside diameter and the pipe lengths need to be determined to use this table for calculating the mass.

2) Provided data in energy assessment

Regarding the pipe lengths first, DIN V 18599 provides a parametric model to calculate default pipe lengths for heating when no detailed calculation exists. The pipe lengths are divided in those for risers, connecting and branch pipes. The model to calculate the default lengths includes the following parameters:

- Building group (e.g. residential building, offices, logistic, etc.)
- Five different distribution network types defined in the standard
- Net floor area
- Number of storeys
- Average storey height
- Characteristic length of the supplied area (only for some non-residential buildings)
- Single- or twin-tube system
- Unheated basement or only heated storeys

This method for calculating the pipe lengths is based on statistics considering 76 buildings in 551 variations (Jagnow et al., 2010). Jagnow et al. (2010) show that the calculated pipe lengths are quite accurate comparing the values to the pipe lengths built.

The second required parameter is the inside diameter which is not directly given in DIN V 18599 and therefore needs to be enriched.

3) Further enrichment and conversion

The inside diameter varies for the different parts of the network (risers, connecting and branch pipes). In this contribution three options are proposed to determine the inside diameters in an early design phase and they will be evaluated in the following:

(1) Assuming typical inside diameters depending on the different network parts and potentially other parameters.
(2) Calculating the inside diameters based on the heating load which is already approximately calculated in DIN V 18599. With the required heating power and the used system temperatures the mass flow can be calculated. Based on this, the inside diameter can be determined with a limited flow velocity

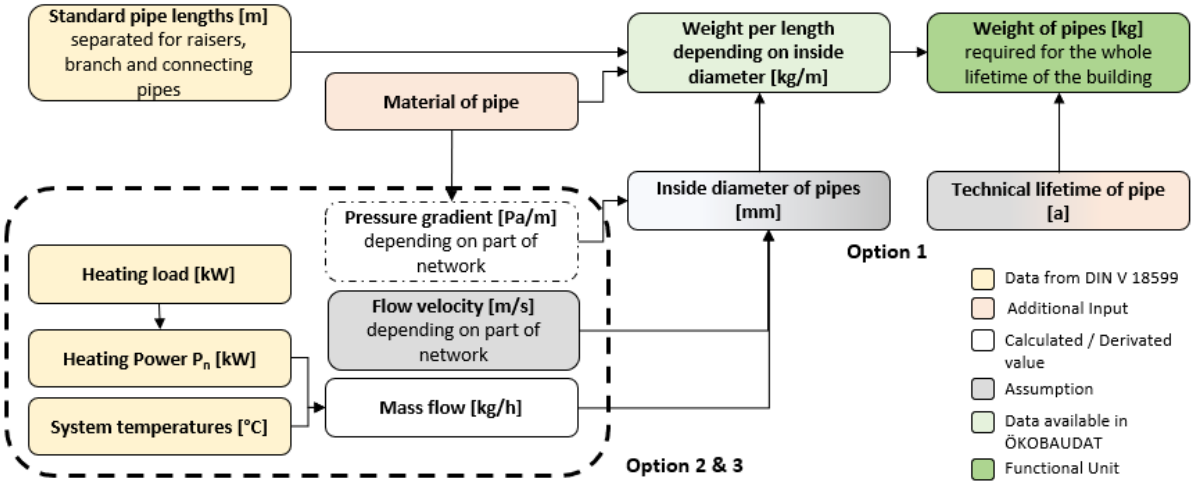

Figure 2: Workflow for evaluating heating pipes environmentally based on the energy assessment

depending on the part of the network (riser, connecting or branch pipes). While this approach still includes assumptions, it estimates the pipe dimensioning more accurately than option (1).

(3) Using tables with typical diameters depending on the same parameters as option (2) but the tables provide only specific limited results whereas option (2) offers the flexibility to calculate all possible variations (Bader et al., 2021).

Figure 2 shows the workflows of calculating the amount of pipes in the functional unit (mass) considering the three proposed options. For options (2) and (3) the flow velocity needs to be enriched. It differs for risers, branch and connecting pipes because of flow noises which should be limited depending on the location of the pipe. According to VDI 2073 Sheet 1 the connecting and branch pipes are located near users and thus the flow velocity is supposed to be lower than 0.7m/s. For main distribution pipes and the risers being farther away from users the flow velocity is assumed as 1m/s (VDI 2073 Sheet 1).

For option (3) alternatively to the assumed flow velocity the pressure gradient could be determined depending also on the three different networks parts and additionally on the roughness of the material. VDI 2073 Sheet 1 gives default values for the different network parts and an opportunity to calculate the inside diameter depending on a detailed value.

Besides the data concerning the functional unit, another required information is the technical lifetime of the material influencing how often a product must be changed during the lifetime of the whole building. In this contribution the data from VDI 2067 Sheet 1 will be used which provides service life estimations in context of economical considerations.

Heating pipe insulation

1) Required and provided data in ÖKOBAUDAT

There are several data sets in the ÖKOBAUDAT which can be used for the assessment of pipe insulations. The functional unit of them is the volume in cubic meters. Therefore, the outside diameter of the pipe is needed as inside diameter of the insulation as well as the pipe length and the insulation thickness. As described before, the ÖKOBAUDAT data sets for pipes provide their outside diameter, so this data is already given with the selection of the heating pipe data set. The length and the thickness of the insulation need to be determined differently.

2) Provided data in energy assessment

The length of the insulation can also be determined with the default pipe lengths from DIN V 18599 like described before. Regarding the insulation thickness GEG (referencing DIN V 18599) provides a minimum thickness of pipe insulations for a specific thermal conductivity (0,035 W/(mK)) and an U-value of the insulation. The minimum insulation thickness differs whether the pipes are in heated or unheated areas, but this is also an input parameter given in the energy assessment.

3) Further enrichment and conversion

Besides the given data from the ÖKOBAUDAT and the energy assessment only the material of the pipe is required as input data due to the different data sets considering several materials. In addition to the different environmental impacts of the materials, another relevant property of the material in this case is its thermal conductivity, because the minimum thicknesses according to GEG is determined for a specific thermal

conductivity of 0,035 W/(mK). If the used material has a lower thermal conductivity, less insulation thickness is needed. The required material thickness could be converted using the given thermal conductivity in energy assessment (U-value from DIN V 18599) with established rules, but apparently, the ÖKOBAUDAT data sets do not provide information about the thermal conductivity of the considered materials. That is why the standard minimum thickness is selected independent of the thermal conductivity. Figure 3 shows the workflow for calculating the amount of pipe insulation in the required functional unit (volume) and the therefore required data.

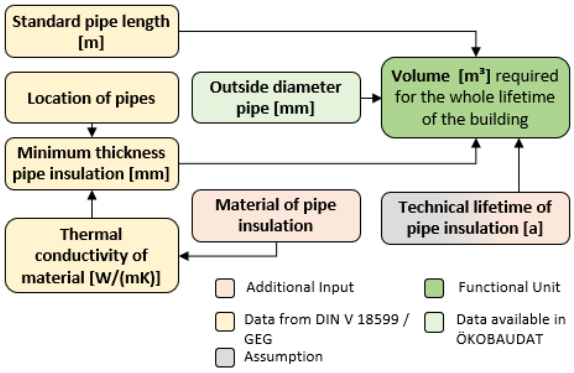

Figure 3: Workflow for evaluating heating pipe insulations based on the energy assessment

As for the technical lifetime of heating pipes VDI 2067 Sheet 1 provides values for pipe insulations as well.

Results

To identify the best option for estimating the environmental impacts of heating pipes and pipe insulations in an early design phase, the before described parameters will be investigated regarding their variance and the resulting influence on the assessed environmental impact. Therefore, exemplary input parameters of a sample building (200m² net floor area and 4 storeys of 2.8m height) are used.

As a result, the parameters that are independent of the established default values of energy assessment will be summarized in tables (Table 1 and Table 2) and evaluated additionally regarding their transparency, accuracy and the expenditure planners have determining them.

Heating pipes

Influence of data from energy assessment on LCA

All options for calculating the amount in the functional unit of pipes (mass) for LCA require the pipe lengths which are provided as default values according to DIN V 18599. As described, the default values depend on building groups and five network types as well as the geometrical input parameters being fixed in this example. Figure 4 shows the pipe lengths for building group 1 including residential and office buildings.

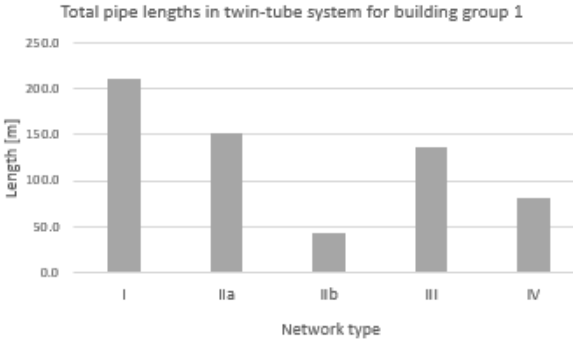

Figure 4: Total pipe lengths for different network types (building group 1)

The biggest difference is between network type I and IIb. Pipe lengths for network type I exceed those of type IIb by factor 4.9. The differences to other building groups in this example are about 20 to 30%, but the exact values vary when using different parameters, because in some cases different formulas are used for the different building groups. These significant differences between the pipe lengths already indicate that the amount of used pipes will also create varying environmental impacts in a detailed LCA, because the lengths linearly influence the used mass and thus the environmental impacts (Lambertz et al., 2019).

Influence of additional data on LCA

The first additional required data for the LCA is the used material. Figure 5 shows for similar diameters the GWP for PP, steel and copper pipes for the different network types as absolute values for this example.

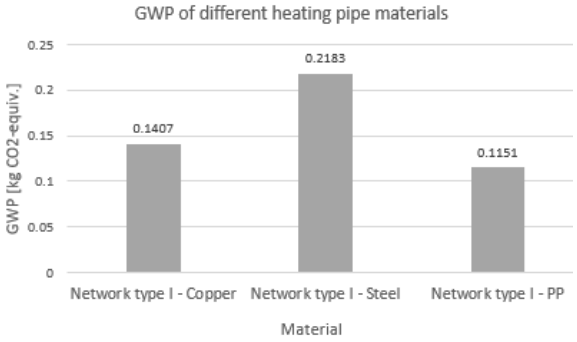

Figure 5: Differences between GWP of pipe materials

It is remarkable that the GWP for network type I made of steel is about twice as high as the one for PP pipes. Beside this environmental influence of the material, its properties also influence the required inside diameter of the pipe in two of the

three presented options for determining the inside diameter.

Before investigating these three options in detail, in general the influence of different diameters are determined. Considering typical diameters of 16, 25 and 32mm, it occurs that the weight of a 1m PP pipe with a diameter of 32mm is almost about four times as high as one for a diameter of 16mm according to the values from ÖKOBAUDAT. For steel the factor between the weight of 32 and 16mm pipes is almost three and for copper pipes it is about two. These differences are also caused by the increasing material thickness for larger diameters. Therefore, the influence of the inside diameter in general on the functional unit (mass) required for LCA is evaluated as “high”.

Regarding options (2) and (3) for determining the inside diameters for the three network parts, the flow velocity is required as first parameter. A lower flow velocity leads to a higher inside diameter. For residential buildings the flow velocity should be between 0.2 and 0.5m/s and according to VDI 2073 Sheet 1 the maximum flow velocity in branch and connecting pipes should be 0.7m/s. The difference between these flow velocities usually leads to a different inside diameter, so the influence is high. To calculate the amount of pipes on the safe side, this approach proposes for option (2) to determine 0.2m/s as constant value which leads to the highest inside diameters. For risers the flow velocity is constantly assumed as 1m/s which also contains an inaccuracy compared to the detailed planning at a later point in the planning. The tables in option (3) provide more detailed values, but only for limited variants (Bader et al., 2021).

Alternatively, for option (3) the pressure gradient could be assumed depending on the material. The variation of this parameter is for typical smooth pipes (of copper, soft steel or plastic) zero (VDI 2073 Sheet 1). Only for rougher pipes it is slightly higher (Bader et al., 2021), but also in this case the pressure gradient can be assumed as for smooth pipes (VDI 2073 Sheet 1). Therefore, the influence is considered as “low - middle”.

In the calculation of the mass flow - also required to calculate the inside diameters according to options (2) and (3) - the heating power and the delta between the system temperatures are considered. To investigate the influence of the heating power on the required inside diameter, all parameters are set constant and only the heating power is varied. As a result, Figure 6 shows that a change in the range of low heating powers has a high influence on the inside diameter. Conversely, for greater heating powers the step to the next size of the diameter gets bigger and therefore also the influence falls. Since the lower influence starts for heating powers at about 10kW, which is also the common size for heaters in residential buildings, its influence is considered as “middle” on the inside diameter.

The delta of the system temperatures usually is 15 or 10 Kelvin regarding the default values from DIN V 18599. The difference of 5 Kelvin often leads to different inside diameters. For this reason, the influence is ascertained as “high”.

Data required for LCA	**Additional information**	**Transparency**	**Accuracy**	**Influence on LCA** of heating pipe	**Expenditure**
Material of pipe	Planned material for pipes	High *input according to ÖBD data sets*	Middle *restricted data sets in ÖBD*	High	Small one extra input parameter
Inside diameter **option (1)**	Inside diameter	Middle - low	Middle – low *could be improved with statistic values*	High	Small or no *assumption, can be implemented in software*
Inside diameter **option (2)**	Pressure gradient	High - middle	Middle	On inside diameter: Low - middle	No *can be implemented in existing software*
	Flow velocity	Middle *fragmentary guidelines*	Low *only guidelines, no standard values*	On inside diameter: High	Small *default values can be implemented in software, detailed calculation leads to more expenditure*
	Heating power	High *calculation in DIN V 18599*	Middle – high *some approximations*	On inside diameter: Middle	No *calculation from energy assessment*
	System temp.	High *input parameter*	High *input parameter*	On inside diameter: High	No *calculation from energy assessment*
	Mass flow	High *physical equation*	High *physical equation*	On inside diameter: Middle	No *based on data given from energy assessment*
Inside diameter **option (3)**	Table for diameters	High *table depending on parameters as option (2)*	Middle – high *restricted (but accurate) values available*	High	Middle - small *available as table which could be included in software (Bader et al., 2021)*
Weight per length	---	Middle *available for specific data*	Middle	High *(functional unit)*	Middle - no *some data in ÖBD referring to standards available*

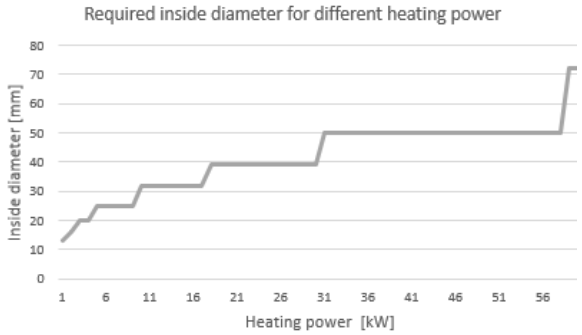

Figure 6: Dependency of heating power and inside diameter

Summarizing the results regarding the three options for determining the inside diameter, it strikes that it is the most complicated parameter to be identified in an early design phase based on the data available. For rough assumptions in early planning stages option (1) can give a general assumption with a low accuracy differentiating between the different network parts. Here more assessments are required on typical inside diameters of heating pipes in different buildings to derivate reliable statistics. Besides the general assumption, the two other options raise the accuracy of the results. For option (2) and (3) there still is an assumption for the flow velocity required, but the other values also have a significant influence on calculating the inside diameters for the three network parts and make the calculation more precise compared to a general assumption. All parameters can be determined without a high expenditure for planners because they are either already determined in energy assessment or can be implemented in software programs easily. Only a more accurate determination of the flow velocity would lead to a bit more expenditure.

Table 1 shows the overview of the additional parameters with their determined influence on LCA and additionally with their transparency and accuracy as well as the expenditure to determine them.

Heating pipe insulation

Influence of data from energy assessment on LCA

To calculate the functional unit “volume”, the length, material thickness and outside diameter of the pipe are required. The standard pipe lengths have a high influence also on the volume, as investigated before for pipes, but are directly given in DIN V 18599.

The required minimum thickness according to GEG depends on the diameter of the pipes, their location and the thermal conductivity of the insultation. Due to the missing information concerning the thermal conductivity in ÖKOBAUDAT data sets, this point is not investigated in detail and the constant value of 0,35W/mK is considered as given. Future data sets should specify this property in detail. Still, different values would also lead to different required thicknesses which is why the influence is assessed as “middle - low”.

Regarding the influence of the location of the pipes on the required volume, Figure 7 shows the differences between the volume needed for the example building with an unheated basement and without one. Pipes could also be located in other unheated zones, but the unheated basement is the most common one. In this example the unheated basement leads to 22% to 92% more volume of pipe insulation depending on the network type compared to the same building with only heated storeys. The biggest difference (92%) occurs for network type IIb, but it needs to be considered that the absolute values are here the lowest. Therefore, the influence of the pipes’ location is considered as middle.

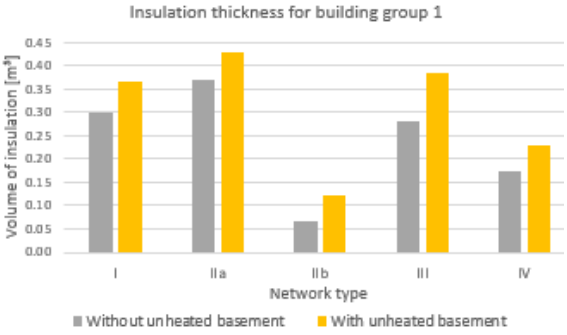

Figure 7: Differences between minimum insulation thicknesses of pipes in different locations

Influence of additional data on LCA

As additional input data for the LCA the material of pipe insulation is required. To identify differences for the GWP of common materials, three available data sets in ÖKOBAUDAT 2020-II are compared: rock wool, EPDM foam and polyurethan rigid foam. Their GWP is compared for the relevant modules in QNG related to the functional unit (m^3). The highest divergence is between EPDM foam and polyurethan rigid foam with EPDM foam causing 50% more GWP than polyurethan. The other differences are 20% and 36%. All in all, the differences for the GWP of the different materials are lower than for the material

Table 2: Overview and evaluation of additional information requirement for LCA of heating pipe insulation based on energy assessment

Data required for LCA	Additional information	Transparency	Accuracy	Influence on LCA of insulation	Expenditure
Material of insulation	Planned material of insulation	High *input can be connected directly to ÖBD data set*	Middle *because of restricted data sets in ÖBD*	Middle	Small *one extra input parameter*
Minimum pipe thickness	Thermal conductivity of material	In energy assessment high *(input)* but in LCA low *(not available in ÖBD)*	In energy assessment high *(input)* but in LCA low *information in ÖBD not available*	Middle – low	No *already given in energy assessment*
Outside diameter	Inside diameter + thickness of pipe	High *provided in ÖBD or other standards*	Middle - high	High	Small or no *given in standards and ÖBD and can be implemented in software*

of heating pipes and therefore the influence on the LCA is determined as “middle”.

As a result, Table 2 shows the overview of the investigated parameters which are needed additionally to the available data in the energy assessment and their influence on the LCA regarding their transparency, accuracy and expenditure. In general, the available data sets do not cover all pipe segments e.g. for straight and threaded pipes of the same material. More data would be required for detailed differentiation. Additionally, it would be helpful, if the data for inside and outside diameter would be all given in the same structure and in a machine-readable format in the ÖKOBAUDAT, because currently the structures differ and the data is only given in a figure.

Conclusion

The investigated large differences between possible heating distribution systems support the assumption that a detailed contemplation in LCA is appropriate and offers the possibility to guide and optimize the LCA results more accurately in contrast to the in place flat-rate aggregates in QNG. In general, a homogenous structure of the provided environmental data supports a practical implementation. Different representations like a heating pipe and its insulation in one data set lead to different approaches raising the expenditure to establish different calculations.

The examination shows that established and proven values from the energy assessment can be used to calculate a valid approximate amount of heating distribution systems’ components in early design phases supporting a more detailed but still practical LCA. Other required information can be added without high expenditure.

References

Bader, R., Baumann, I., Ihle, C. 2021. Tabellenbuch Sanitär Heizung Klima / Lüftung. Anlagenmechanik SHK Ausbildung und Praxis. 11. Auflage, westermann.

Bundesministerium für Wohnen, Stadtentwicklung und Bauwesen, 2020. ÖKOBAUDAT. Available online at https://www.oekobaudat.de/.

Chuchra, D., Di Bari, R., Jorgji, O., Albrecht, S. 2020. Die Bedeutung von Anlagentechnik für die Ökobilanz von Nichtwohngebäuden. Ergebnisse eines neuen Anlagenkonfigurators.

Deutscher Bundestag, 2024. Gebäudeenergiegesetz (GEG).

DIN V 18599. 2018. Energetische Bewertung von Gebäuden - Berechnung des Nutz-, End- und Primärenergiebedarfs für Heizung, Kühlung, Trinkwarmwasser und Beleuchtung.

Dorn-Pfahler, S., Lützkendorf, T. 2023. Ökobilanzielle Bewertung im Ordnungsrecht. Grundlagen und erste Ansätze zur vereinfachten Bewertung von Gebäuden mit angewandten Ökobilanzen. In *BBSR-Online-Publikation*.

EN 15643. 2021. Sustainability of construction works - Framework for assessment of buildings and civil engineering works.

EN 15978. 2011. Sustainability of construction works - Assessment of environmental performance of buildings - calculation method.

Jagnow, K., Oschatz, B., Wolff, D. 2010. Vereinfachung des Berechnungsverfahrens von Rohrleitungslängen für eine Fortschreibung der DIN V18599 Teil 5 und 8. In *Forschungsprogramm Zukunft Bau. Im Auftrag von BMVBS und BBR.*

Lambertz, M., Theißen, S., Höper, J., Wimmer, R. 2019. Importance of building services in ecological building assessments. In *E3S Web of Conferences*.

VDI 2067 Sheet 1. 2012. Economic efficiency of building installations.

VDI 2073 Sheet 1. 2014. Hydaulic systems in building services.

BauSIM 2024 in Wien
23. September – 26. September

Einfluss der Wettervorhersagegüte auf ein PV-unterstütztes MPC-geregeltes Wärmepumpenheizsystem

Christina Betzold, Sebastian Hummel, Arno Dentel
Technische Hochschule Nürnberg Georg Simon Ohm, Nürnberg, Deutschland,
christina.betzold@th-nuernberg.de

Kurzfassung

Dieser Beitrag beschreibt den Einfluss der Wettervorhersagegüte auf ein PV-unterstütztes und durch eine modellprädiktive Regelungsstrategie (MPC) gesteuertes Wärmepumpenheizsystem sowohl in Simulationsstudien, Laborexperimenten als auch in einem Reallabor. In einem Hardware-in-the-loop Prüfstand wird der 4-tägige Betrieb einer MPC-Regelung für eine perfekte Wettervorhersage im Vergleich zu zwei fehlerbehafteten Wettervorhersagen aus unterschiedlichen Bezugsquellen (Internet und Langwellenempfänger) durchgeführt. Der Langzeitbetrieb einer MPC-geregelten Wärmepumpenheizzentrale wird in einem Reallabor, bestehend aus einem Reihenhaus (acht Wohneinheiten) und gemeinschaftlich genutzter Wärmezentrale, untersucht und bewertet. Die MPC regelt sowohl die beiden modulierenden als auch die acht dezentralen Booster-Wärmepumpen. Über einen Zeitraum von mehreren Wochen konnte die MPC-Regelung unter realistischen Bedingungen untersucht werden. Die Ergebnisse zeigen, dass der PV-Eigenverbrauch bei fehlerbehafteten Wettervorhersagen im Vergleich zu einer perfekten MPC um bis zu 20 % niedriger ausfällt. Die Betriebskosten steigen um bis zu 48 % an. Im Reallabor zeigte der fehlerfreie Langzeitbetrieb deutlich unterschiedliche Betriebskosten bzw. Gewinne. Die positiven Einflüsse der MPC sind abhängig von Steuerbarkeit der Wärmepumpen und ebenfalls von der Wettervorhersagegüte.

Abstract

This paper describes the influence of the weather forecast quality on a PV-supported heat pump heating system controlled by a model predictive control strategy in simulation studies, laboratory experiments and under real operation. In a hardware-in-the-loop test rig, the 4-day operation of an MPC controlled heating system is carried out for a perfect, a high-quality and a low-quality weather forecast profile. The long-term operation of a MPC-controlled heat pump heating system is investigated and evaluated in a terraced house (eight residential units) with a jointly used heating system. The MPC controls both the two modulating and the eight decentralized booster heat pumps. The MPC control system was tested under realistic conditions over a period of several weeks. The results show that PV self-consumption is up to 20 % lower for faulty weather forecasts compared to a perfect MPC. The operating costs increase by up to 48 %. In the field installation, error-free long-term operation showed increased PV self-consumption by using a MPC control strategy. However, in real operation, the positive effects of a MPC are heavily dependent on the model depth and the quality of the weather forecast.

Einleitung

Eine nachfrageseitige Flexibilität von Wohngebäuden wird immer wichtiger für die Erhöhung der Resilienz des Stromnetzes. Wärmepumpen mit elektrisch angetriebenen Verdichtern bieten dieses Potential auf volatile regenerative Energieerzeuger, wie zum Beispiel Photovoltaik, bedarfsorientiert zu reagieren. So kann Überschussstrom direkt durch die Speicherung elektrischer Energie in Batteriespeichern oder über eine Wärmepumpe in thermischen Energiespeichern nutzbar gemacht und eine Lastverschiebung realisiert werden. Der Wärmebedarf eines Gebäudes kann daher als flexibel angesehen werden. Um diese Flexibilität und auch das finanzielle Potenzial bestmöglich zu nutzen, sind prädiktive Steuerungsstrategien, wie die modellprädiktive Regelung (MPC), erforderlich. Für diese sind Wettervorhersagedaten unerlässlich.

Eine MPC beruht im Wesentlichen auf der periodischen Lösung eines Optimierungsproblems, indem Wettervorhersagedaten in Kombination mit einem Anlagenmodell berücksichtigt werden, um die Betriebsführung zu optimieren. MPC-Strategien haben in der jüngsten Forschung großes Interesse geweckt (Péan et al., 2019, Thieblemont et al., 2017), da sie Vorteile in Bezug auf Betriebskosteneinsparungen, Systemleistung,

Raumkomfort und Energieflexibilität bieten. Fischer et al. (2017) ermittelten Betriebskosteneinsparungen für eine MPC-Strategie von bis zu 11 % bzw. 16 % für konstante bzw. flexible Strompreise im Vergleich zu einer regelbasierten Standardsteuerung. Für einen ähnlichen Vergleich wiesen Bechtel et al. (2020) Kosteneinsparungen von bis zu 24 % für ein Einfamilienhaus (EFH) und flexible Strompreise aus. Pichler et al. (2017) führten eine Jahressimulationsstudie für ein MPC-gesteuertes Wärmepumpenheizsystem durch. Sie ermittelten eine Steigerung des PV-Eigenverbrauchs von bis zu 30 % in einem EFH.

In der Literatur über MPC-Strategien, die sich mit der Wettervorhersage im Allgemeinen befasst, werden Schlagworte wie "perfekte", "idealisierte" oder "optimale" MPC verwendet, um auf Betriebsbedingungen zu verweisen, die eine Übereinstimmung zwischen der Wettervorhersage und den gemessenen ("realen") Wetterbedingungen aufweisen. Derartige Bedingungen können nur in Simulationen erfüllt werden, bei denen die Vorhersagedaten bekannt sind. Daher kann eine perfekte MPC als Benchmark für andere Steuerungsstrategien betrachtet werden, um die Obergrenzen des Nutzens unter optimalen Vorhersagebedingungen zu bestimmen. Sie ist im Allgemeinen nicht auf den Feldtestbetrieb übertragbar. Eine solche Benchmark-Studie wurde von Mendoza-Serrano & Chmielewski (2014) durchgeführt. Die Autoren verglichen ein MPC-gesteuertes Heizungs-, Lüftungs- und Klimasystem, das mit perfekten und keinen Prognoseinformationen ausgestattet war. Im Vergleich zu ihrer Referenzsituation wiesen sie für die perfekte und die "Null"-Prognose Kostensenkungen von bis zu 31 % bzw. 27 % auf. Die Autoren betonen den starken Einfluss der Prognoseinformationen auf die Systemleistung. Allen et al. (2018) ermittelten Kosteneinsparungen von bis zu 13,1 % bei einer perfekten Prognose und 11,1 % bei einer nicht-idealen Prognose. Löhr & Mönnigmann (2018) verglichen eine "gestrige" Vorhersage, die die Wetterdaten des Vortages als Vorhersage für den Folgetag verwendet, mit einem Regler mit perfekter Vorhersage. Beide Steuerungen schnitten gut ab. Sie kamen zu dem Schluss, dass die Systemleistung nur geringfügig abnimmt, wenn historische Wetterdaten als Vorhersage für den morgigen Tag verwendet werden. Péan et al. (2020) führten eine experimentelle Studie durch, um die Qualität der Wettervorhersage auf die Leistung einer MPC-gesteuerten Luft/Wasser-Wärmepumpe im Kühlbetrieb in einem Wohngebäude zu bewerten. Innerhalb eines dreitägigen Testprofils verglichen sie eine perfekte Wettervorhersage mit einer Vorhersage eines kommerziellen Dienstes. Der Durchgang mit ungenauer Vorhersage führte zu einem Anstieg des gesamten elektrischen Energiebedarfs und der Betriebskosten um 5,8 % bzw. 11,2 %.

Die Literaturrecherche zeigt, dass eine perfekte MPC-Strategie im Allgemeinen sowohl mit einem regelbasierten Algorithmus als auch mit einer MPC-Strategie ohne Wettervorhersagedaten verglichen wird. Heutzutage sind immer mehr Geräte und Steuerungen mit dem Internet verbunden oder können mit Empfangsantennen ausgestattet werden und haben somit Zugang zu historischen oder prognostizierten Wetterdaten. Insbesondere die Qualität der Wettervorhersagedienste, die im Wesentlichen vom Vorhersagehorizont und dem verwendeten Vorhersagemodell abhängen und deren Einfluss auf ein Wärmepumpen-Heizsystem sind zu untersuchen. Darüber hinaus basieren die meisten der rezensierten Artikel auf simulativen Untersuchungen und berücksichtigen nicht den Betrieb in einem realistischen Wärmepumpen-Heizsystem. So verglichen Betzold et al. (2020) in einer Simulationsstudie verschiedene Regelungsstrategien eines geothermischen Wärmepumpenheizsystems. Die Autoren betonten Kosteneinsparungen von 3 % bis 10 % durch den Einsatz eines MPC-Reglers anstelle einer regelbasierten Regelstrategie. Aufgrund der geringen Differenzen in den Simulationen ist eine experimentelle Verifizierung des Kosteneinsparungspotenzials in einer realistischen Betriebsumgebung von besonderer Bedeutung. Daher untersucht dieser Beitrag den Einfluss der Wettervorhersagegüte auf ein PV-unterstütztes Wärmepumpenheizsystem in Simulationsstudien, Laborexperimenten und in einem Reallabor.

Laborexperimente

Methodik

Für die Umsetzung von MPC-Strategien sind Kenntnisse über das thermische Verhalten des Gebäudes (Heizwärme- und Warmwasserbedarf), den Anteil des regenerativen Energiegewinns und das Betriebsverhalten der technischen Gebäudeausrüstung notwendig. Zusätzlich müssen für wetterbasierte MPC-Strategien Wettervorhersagedienste oder historische Wetterdaten implementiert werden.

Wetterdaten

Die Grundvoraussetzung für eine wetterabhängige MPC-Strategie sind Wettervorhersagedaten in guter Qualität, um Kosteneinsparungen oder eine Steigerung der Systemleistung zu erzielen. Für diese Studie werden drei verschiedene Quellen von Wetterdaten genutzt: gemessene („reale“) Wetterdaten und zwei Arten von Vorhersagediensten.

Alle Quellen liefern die solare Bestrahlungsstärke G und die Umgebungstemperatur T_a in 15-Minuten-Intervallen für den Standort des Stadtteils "Herzo Base" der Stadt Herzogenaurach (Deutschland) für den Zeitraum vom 7. bis zum 11. März 2021, wie in Abbildung 1 zu sehen ist. Die gemessenen Wetterdaten (Abk. und Index MEAS), die mit entsprechenden Sensoren auf dem Dach eines EFH am genannten Ort aufgezeichnet wurden, werden in den Experimenten und Simulationen als perfekte Wettervorhersage verwendet. Darüber hinaus liefern ein internetbasierter Wettervorhersagedienst (WFS) und eine fest installierte Wettervorhersagestation (WFC) Vorhersagedaten für den gegebenen Ort und Zeitraum. Letzteres stellt einen Langwellenempfänger dar, der seine Daten von einem kommerziellen Dienst empfängt.

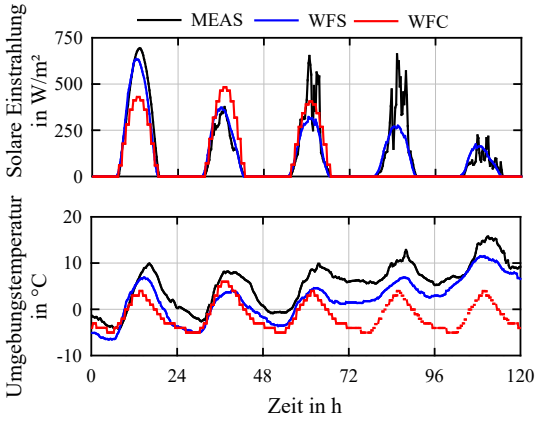

Abbildung 1 - Horizontale Bestrahlungsstärke und Umgebungstemperatur der drei verschiedenen Wetterdatenquellen für fünf aufeinanderfolgende Tage vom 7. bis 11. März 2021.

Es ist zu beachten, dass der WFC ab 1 Uhr des 4. Tages keine gültigen Wetterdaten liefert. Die empfangenen Daten zeigen konstante Werte von G = 0 W m^{-2} und keine validen Daten für T_a, was auf Kommunikationsstörungen hinweist. Eine Überprüfung der empfangenen Daten aus 2021 zeigt, dass Kommunikationsstörungen regelmäßig und häufig auftreten. In 25,6 % der Zeit wurden keine oder fehlerhafte Daten empfangen. Darüber hinaus wird die Übertragung in der Regel in längeren aufeinanderfolgenden Zeitintervallen unterbrochen. Das für diese Auswertung gewählte Zeitintervall stellt somit die typische Datenverfügbarkeit für diesen Wettervorhersagedienst dar. Eine praxisnahe Lösung der Kommunikationsstörungen wurde auch hier umgesetzt, in dem die Einstrahlung weiterhin so gesetzt wird, wie sie empfangen und die Umgebungstemperaturen auf die 24 Stunden zuvor aufgezeichneten Werte gesetzt wurden.

Qualitativ ähneln sich die drei Profile im zeitlichen Verlauf, weisen aber einige große Unterschiede in ihren absoluten oder integralen Werten auf. Die horizontale Einstrahlung für die gesamten fünf Tage summiert sich auf 13,3 kWh m^{-2}, 11,7 kWh m^{-2} und 9,3 kWh m^{-2} für das gemessene, das WFS- bzw. das WFC-Profil. Die mittlere Umgebungstemperatur kann für das gemessene, das WFS- und das WFC-Profil jeweils mit 5,4 °C, 2,2 °C und - 1,2 °C berechnet werden. Eine maximale Differenz von bis zu 10 K kann zwischen den gemessenen Werten und dem WFC-Profil festgestellt werden. Während der zeitliche Verlauf der Temperatur nur den Wärmebedarf des simulierten Gebäudes beeinflusst, wirkt sich die solare Bestrahlungsstärke sowohl auf die Gebäudesimulation als auch auf die PV-Erzeugung aus.

Da das WFC-Profil die höchste Abweichung zu den gemessenen (perfekten) Wetterdaten aufweist, wird dieser Wetterdatensatz als "(qualitativ) ausreichend" in Bezug auf die Vorhersagequalität bezeichnet. Im Gegensatz dazu ist das WFS-Profil "(qualitativ) hochwertig" und wird dementsprechend betitelt.

Gebäudesimulation

Mittels TRNSYS-Gebäudesimulationen wird der Verlauf der Gebäudeheizlast eines EFH auf Basis der drei vorgegebenen Wetterdatensätze simuliert. Als grundlegendes System- und Gebäudekonzept wird das im IEA SHC TASK32 von Heimrath & Haller (2007) beschriebene EFH und Heizsystem verwendet. Für diese Untersuchung wird der Gebäudestandard SFH60 und kein Warmwasserbedarf betrachtet. Dieser Gebäudestandard ist den Gebäuden des Stadtteils "Herzo Base" sehr ähnlich. Die beheizte Bruttowohnfläche beträgt 140 m².

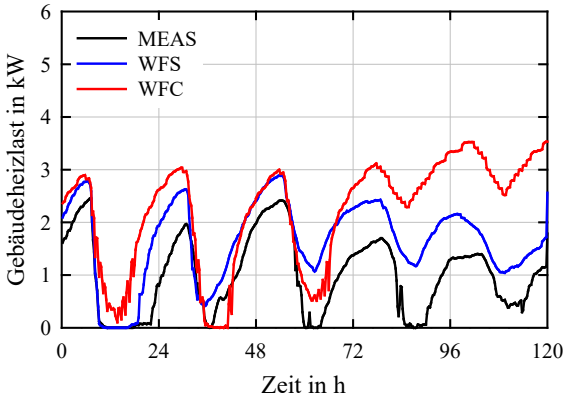

Abbildung 2 - Gebäudeheizlastprofile für den Gebäudestandard SFH60 und die drei betrachteten Wetterdatensätze.

Die Profile der Gebäudeheizlast auf Basis der drei betrachteten Wetterdatensätze sind in Abbildung 2 graphisch dargestellt. Da die gemessenen Wetterdaten die höchste Einstrahlung und

mittlere Umgebungstemperatur aufweisen, sind die Heizlasten und der Heizwärmebedarf entsprechend niedrig. Aufgrund der teilweise nicht validen Wetterdaten des WFC-Profils steigt die Gebäudeheizlast nach 72 h allmählich an und führt zu einem deutlich erhöhten Heizwärmebedarf.

Photovoltaik-Erzeugungsprofile

Für jeden Wetterdatensatz wird das photovoltaische (PV) Erzeugungsprofil im Vorfeld der experimentellen Untersuchung simuliert. Die PV-Last wird nach einem isotropen Himmelsstrahlungsmodell von Shukla et al. (2015) auf Basis der horizontalen Bestrahlungsstärke, der PV-Fläche (20 m²), des Neigungswinkels (60°) und des Wirkungsgrads der PV-Module (17,89 %) und des Wechselrichters (95 %) berechnet.

Die daraus resultierenden PV-Erzeugungsprofile sind in Abbildung 3 mit Maximalwerten von bis zu 3,8 kW zu sehen. Die Gesamtmenge der PV-Erzeugung innerhalb des Zeitraums von fünf Tagen beträgt 62,9 kWh, 51,7 kWh bzw. 46,7 kWh für das gemessene, das WFS- und das WFC-Wetterdatenprofil.

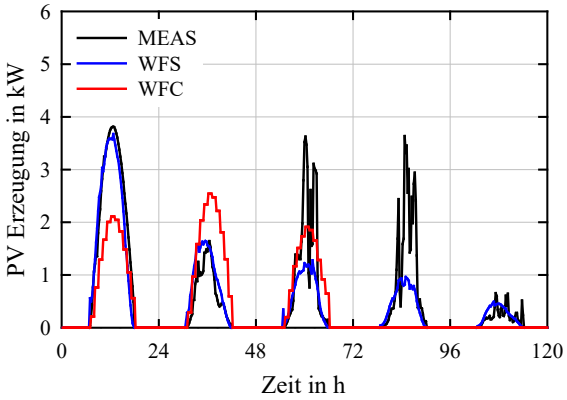

Abbildung 3 - Photovoltaik-Erzeugungsprofile für die drei betrachteten Wetterdatensätze.

Haushaltslastprofil

Sowohl für die Simulationsstudie als auch für die experimentellen Untersuchungen ist ein Haushaltslastprofil maßgebend. In Kombination mit der PV-Erzeugung kann ein Überschuss an elektrischer Energie im Gebäude entstehen. Dies ermöglicht es dem Regler, die Wärmepumpe flexibel und dynamisch zu betreiben oder den Batteriespeicher zu beladen. Das Haushaltslastprofil basiert auf Messdaten eines der Gebäude auf „Herzo Base“, an dem auch das gemessene Wetterprofil aufgenommen wurde. Die Zeitspanne ist identisch mit der des Wetterprofils. Das Haushaltslastprofil und das PV-Erzeugungsprofil für den gemessenen Wetterdatensatz sind in Abbildung 4 ersichtlich. Der Gesamtverbrauch des Haushaltes beträgt 48,1 kWh mit einer Grundlast von ca. 0,2 kW.

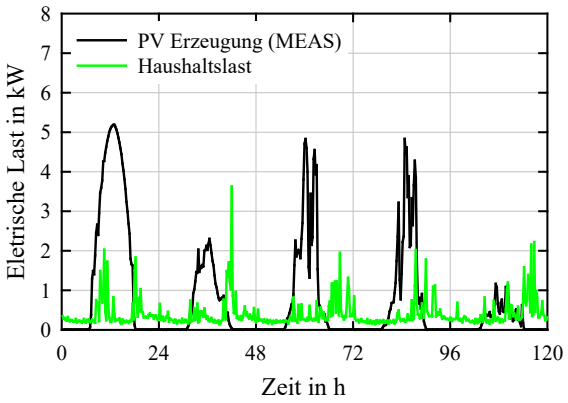

Abbildung 4 - Haushaltslast- und PV-Erzeugungsprofil.

Hardware-in-the-Loop Prüfstand

Die experimentelle Studie wird auf einem Hardware-in-the-Loop (HiL)-Prüfstand durchgeführt, der mehrere Wärmeerzeugungseinheiten mit verschiedenen thermischen Energiespeichersystemen (TES) und einem batterieelektrischen Speicher (BESS) kombiniert. Der Heizwärmebedarf und die Quelltemperatur der Wärmepumpe werden emuliert.

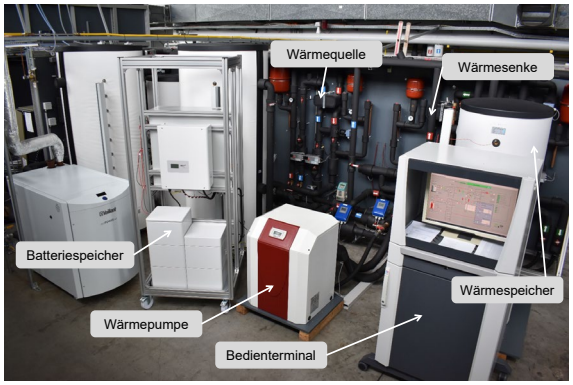

Abbildung 5 - HiL-Prüfstand für innovative Heizsysteme an der TH Nürnberg.

In dieser Studie wird eine Sole/Wasser-Wärmepumpe (WP) in Kombination mit einem 500 Liter TES eingesetzt. Die WP hat eine Standard-Heizleistung von 10,9 kW und eine elektrische Leistungsaufnahme von 2,2 kW in ihrem Betriebspunkt B0/W35. Es wird ein Coefficient Of Performance (COP) von 4,9 erreicht. Der BESS besitzt eine nutzbare Kapazität von 8,64 kWh und eine maximale Be- und Entladeleistung von 6 kW. Der Prüfstand und seine Hauptkomponenten sind in Abbildung 5 ersichtlich. Ein hydraulisches Schema und die installierten Sensoren sind in Abbildung 6 dargestellt.

Damit die externe Regelstrategie (MPC) die WP ordnungsgemäß ein- und ausschalten kann, ohne vom internen WP-Regler übergangen zu

werden, wird der Rücklauftemperatursollwert auf 55 °C gesetzt. Quellenseitig werden nahezu konstante Temperaturen $T_{evap,FL}$ von 10 °C bereit gestellt.

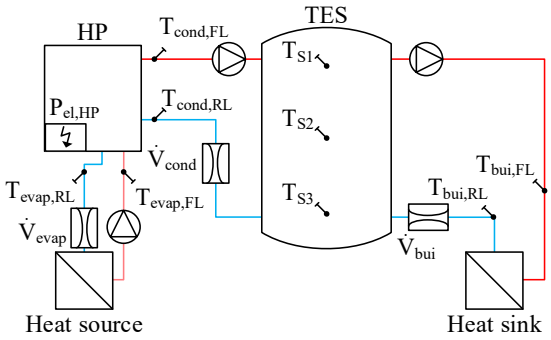

Abbildung 6 - Hydraulik- und Sensorschema des HiL-Prüfstandes.

Zur detaillierten Auswertung des thermischen Verhaltens der WP-Heizungsanlage sind im HiL-Prüfstand entsprechende Sensoren installiert (siehe Abbildung 6). Sowohl der abgehende Wärmebedarf als auch die abgegebene Wärmelast an den TES können separat bewertet werden. Die elektrische Leistung der WP als auch die Be- und Entladeleistung des BESS werden mit einem Energiezähler gemessen. Zusätzlich sind drei Temperatursensoren in gleichmäßigen Abständen über die Höhe im Inneren des TES installiert, um den Ladezustand (SoC) zu berechnen.

Systemmodell

Für die MPC ist ein Simulationsmodell des WP-Heizungssystems erforderlich, um den SoC des TES und BESS zu bewerten. Der SoC ist ein Hauptmerkmal jeder Regelungsstrategie, um den Betrieb der WP zu regulieren. Wie von Hummel et al. (2020) und Betzold & Dentel (2021) beschrieben, ist ein vereinfachtes Systemmodell bei häufigen Aktualisierungsintervallen ausreichend genau.

In Übereinstimmung mit Betzold et al. (2020) wird der TES als vollständig durchmischt angenommen. Er kann in der Systemrepräsentation des vereinfachten Systemmodells als ein einzelner Temperaturknoten dargestellt werden.

Die Heizleistung der WP wird als konstant angenommen und auf einen typischen mittleren Betriebspunkt eingestellt, der während der Voruntersuchungen und Experimente auftritt (B10/W40). Basierend auf Effizienzmessungen der Wärmepumpe am Prüfstand werden die Heizleistung und die elektrische Leistungsaufnahme im Betrieb der Wärmepumpe auf konstante Werte von 12,94 kW_{th} und 2,45 kW_{el} gesetzt.

Der BESS wird im vereinfachten Modell als ein einzelner Bilanzknoten dargestellt. Auf Grundlage von Effizienzmessungen wurden leistungsabhängige Umwandlungswirkungsgrade bestimmt, welche sich jedoch nicht linear verhalten und mit dem implementierten Optimierungsalgorithmus nicht korrespondieren. Für die Be- und Entladewirkungsgrade wurden daher jährliche Mittelwerte in Höhe von 0,897 und 0,892 angenommen.

Modellprädiktive Regelung

In dieser Untersuchung wird ein Optimierungsalgorithmus der gemischt-ganzzahligen linearen Programmierung (MILP) verwendet (siehe Betzold et al., 2020), der auf dem beschriebenen vereinfachten Systemmodell basiert. Die MPC ist in MATLAB realisiert. Die Betriebsgrenzen sind durch eine minimale und maximale Speichertemperatur von 25 °C bzw. 45 °C sowie durch die vollständige Deckung der thermischen und elektrischen Last definiert. Die Kostenfunktion basiert auf den Betriebskosten für die Haushaltslast, die elektrische Leistung der Wärmepumpe und die PV-Erzeugung aufgeteilt nach Netzeinspeisung, Netzbezug, Batteriebezug oder PV-Eigenverbrauch. Die angenommenen Preise sind in Tabelle 1 aufgeführt. Der Preis für den PV-Eigenverbrauch beinhaltet Steuern und Versicherungen. Die Batteriebezugskosten ergeben sich aus dem PV-Preis mit Aufschlag des Wirkungsgrades der Batterie von ca. 90 %.

Tabelle 1 - Für die MPC-Kostenfunktion verwendete Strompreise.

Strompreis	**Preis in € / kWh**
Netzbezug	0.291
PV-Eigenverbrauch	0.02
Batteriebezug	0.02*1.1
PV-Netzeinspeisung	-0.082

Der Optimierungshorizont wird auf 24 Stunden festgelegt, mit einem Optimierungszeitschritt und einem -intervall von jeweils 15 Minuten. Somit wird die MPC alle 15 Minuten mit aktuellen Startbedingungen neu gestartet, um einen aktualisierten Betriebsplan zu generieren. Da der Optimierungshorizont auf 24 Stunden festgelegt ist und die Wetterprofile einen Zeitraum von fünf Tagen abdecken, können die Experimente und Simulationen nur vier aufeinanderfolgende Tage (96 Stunden) andauern.

Bewertungsmetrik

Eine Bewertung der experimentellen Untersuchung findet auf Grundlage von aussagekräftigen Kennzahlen statt, welche nachfolgend erläutert werden.

PV-Eigenverbrauch: Der Anteil der PV-Erzeugung, der direkt im Gebäude verbraucht wird (Haushalts- oder Wärmepumpenstrom).

Autarkiegrad: Der Anteil des gesamten elektrischen Energiebedarfs des Gebäudes, der durch die PV-Erzeugung und elektrischer Energie aus dem BESS gedeckt werden kann.

Betriebskosten: Die Betriebskosten ergeben sich aus den Anteilen von PV-Direktverbrauch, Batterieentladung, Netzbezug und PV-Einspeisung. Die Energiepreise sind in Tabelle 1 aufgetragen.

Validierung

In einer Untersuchung von Hummel et al. (2022) wurden Messergebnisse aus Experimenten mit unterschiedlichen Regelungsstrategien zu einem simulierten Anlagenbetrieb abgeglichen, um die Methodik am Laborprüfstand zu validieren. Neben der MPC (ideal) wurden eine PV-Eigenverbrauchsoptimierte (PVC) und eine wärmegeführte Regelungsstrategie (HC) sowohl in MATLAB als auch im Laborprüfstand implementiert. Die Autoren schlussfolgerten eine qualitativ hohe Übereinstimmung zwischen den Labormessergebnissen und der Simulation, wodurch die Methodik und Funktionalität des Prüfstandes bestätigt werden konnten.

Daher wurde in diesem Beitrag die Abbildung der verschiedenen Regelungsstrategien nur simulativ bewertet. Hierfür wurde der Betrieb der MPC, PVC und HC über vier Tage mit dem Heizbedarfsprofil des Gebäudes SFH60 und des gemessenen PV-Profils abgebildet. Zusätzlich zur vorangegangenen Untersuchung von Hummel et al. (2022) wurde der BESS in die Simulation integriert. Die Ergebnisse zeigen gute Einsparpotentiale beim Einsatz einer MPC. Die Betriebskosten belaufen sich auf 4,47 €, wohingegen Kosten in Höhe von 4,73 € und 5,06 € beim Einsatz einer PVC bzw. HC entstehen. Im Vergleich zur HC sind die Betriebskosten einer PVC um 6,5 % und der MPC um 11,6 % geringer.

Experimente

Es werden drei experimentelle Messungen auf dem HiL-Prüfstand durchgeführt, um den Einfluss der Wettervorhersagequalität auf die MPC und damit auf die Leistung des WP-Heizsystems zu untersuchen. Der verwendete MPC-Algorithmus verwendet die Lastprofile, die sich entweder aus dem perfekten Wetterdatensatz (MEAS), dem hochwertigen WFS-Profil oder dem ausreichenden WFC-Profil ergeben. Die Messungen erstrecken sich über einen Zeitraum von je vier Tagen.

Im Allgemeinen können mit der idealen MPC und dem perfekten Wetterdatensatz (MEAS) die höchsten Effizienzkennzahlen in den Experimenten erreicht werden. So werden für den PV-Eigenverbrauch als auch für den Autarkiegrad Höchstwerte durch die ideale MPC von 77,5 % und 74,4 % ermittelt (siehe Abbildung 7). Mit zunehmender Verschlechterung der Wettervorhersagegüte sinken beide Metriken signifikant ab. Für den noch hochwertigen WFS-Datensatz sinkt der Eigenverbrauch um 16,4 Prozentpunkte auf 61,1 % und der Autarkiegrad um 16,7 Prozentpunkte auf 57,7 % ab. Ähnliche aber leicht erhöhte Werte können im Vergleich hierzu beim ausreichenden WFC-Datensatz berechnet werden. Betrachtet man die entstehenden Betriebskosten so ist ein klarer Verlauf hin zu steigenden Kosten bei geringerer Wettervorhersagegüte erkennbar. Die Betriebskosten für den 4-tägigen Betrieb steigen von 5,72 € bei perfekten auf bis zu 8,44 € bei ausreichenden Wettervorhersagedaten an. Dies entspricht einer Kostensteigerung um bis zu 48 %.

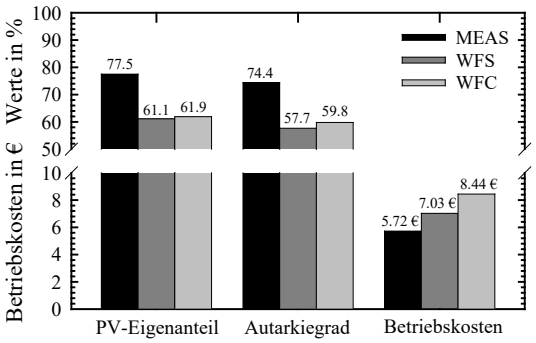

Abbildung 7 - Bewertungsmetriken der drei Wetterdatensätze im Vergleich.

Ein Bewertungskriterium des BESS sind sogenannte „Fehlladungen“, welche sich erheblich auf die Betriebskosten auswirken. Die Be- oder Entladeleistung des BESS wird durch den optimierten Fahrplan der MPC für die Zeitschrittweite von 15 Minuten festgelegt. So können sich elektrische Lasten einstellen, welche den BESS aus dem Stromnetz beladen oder in das Stromnetz entladen. In Abbildung 8 sind die kumulierten Fehlladungen des BESS für die drei Wetterdatensätze aufgetragen. Es ist eine deutliche Tendenz hin zu höheren fehlerhaften Be- oder Entladevorgängen bei minderwertigeren Wetterdatensätzen erkennbar. Die Beladung des BESS aus dem Netz beträgt bei einem perfekten Wetterdatensatz (MEAS) rund 0,5 kWh und für das qualitativ ausreichende Profil (WFC) ca. 8,7 kWh. Fehlladungen in das Stromnetz sind zwar vorhanden, fallen im Verhältnis zur Beladung aber deutlich geringer aus. So konnte eine maximale Entladung in das Stromnetz von 1,8 kWh für den ausreichenden WFC-Datensatz ermittelt werden.

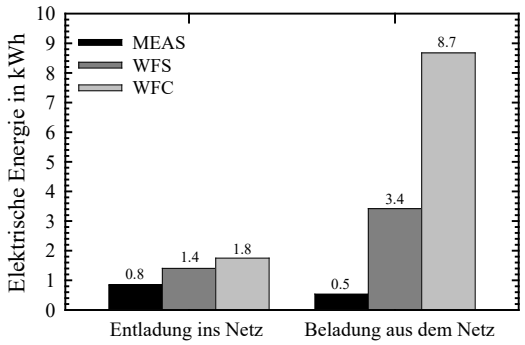

Abbildung 8 – Fehlladungen des Batteriespeichers durch Energieaustausch mit dem Netz.

Die Fehlladungen des BESS können auf zwei Hauptursachen zurückgeführt werden: die allgemeine Verringerung der Vorhersagegüte und modellbedingte Fehlerursachen. Erstere ist für mehr als 90 % der Fehlladungen verantwortlich. Die Entladung ins Netz kann weiterhin durch die Annahme einer konstanten elektrischen Leistungsaufnahme des Verdichters der Wärmepumpe erklärt werden. Da die elektrische Verdichterleistung mit steigendem Temperaturniveau während des Beladevorganges des TES zunimmt, kann der Sollwert der Batterieentladung zu Beginn höher sein, als der tatsächliche Verbrauch, was zu einer Einspeisung ins Stromnetz führt.

Realer Betrieb

Um die Regelungsstrategien im realen Betrieb zu testen, wird die MPC in einem Energiesystem von acht Reihenhäuser implementiert. Simulativ und im realen Betrieb wurden bereits verschiedene MPC-Ansätze getestet, die zu ähnlichen Ergebnissen kamen (Betzold & Dentel, 2021). Die zwei MPC-Ansätze mit Optimierungsalgorithmus MILP und GA werden in den Reihenhäusern betrieben. Sie unterscheiden sich hauptsächlich durch verschiedene Modelltiefen und Rechenzeiten.

Im realen Betrieb der prädiktiven Regelungen wird die MPC zu einem bestimmten Zeitpunkt in MATLAB gestartet. Die MPC-MILP startet stündlich, die MPC-GA nur zweimal am Tag um 12 Uhr und 0 Uhr. Der erstellte Betriebsplan wird über eine SQL-Datenbank an die Steuerung der WP weitergereicht. Gleichzeitig wird der Betrieb der Anlage auf Störungen und Abweichungen vom Betriebsplan geprüft und setzt ggf. Sollwerte zum Ein- oder Ausschalten. Dadurch wird die Betriebssicherheit im Zeitfenster der nächsten Sollwerte sichergestellt. In früheren Arbeiten von Betzold & Dentel (2022) sowie Betzold & Dentel (2021) wurde der MPC-Ablaufprozess bereits erfolgreich getestet und stellte sich als betriebssicher heraus.

Für die Auswertung wurden die MPC-MILP und MPC-GA über mehrere Wochen betrieben, sodass ein direkter Vergleich aufgrund der kurzen Zeitspanne und der unterschiedlichen Randbedingungen (z. B. Wetter oder Nutzerverhalten) nicht möglich ist. Um einen Eindruck von der Regelungsstrategie zu erhalten, werden Kennwerte aus der Sollvorgabe (Simulation) und aus Messwerten aus dem realen Betrieb der MPC gegenübergestellt.

Der MPC-MILP Betrieb erfolgte über fast sechs Wochen vom 08.03. bis 23.04.2022. Hinsichtlich der PV-Erzeugung wurde real 7,1 % mehr PV-Strom erzeugt. Gleichzeitig wurde 7,0 % mehr Energie verbraucht. Der Gewinn, der sich durch die Verbrauchskosten und Einspeisungsvergütung ergibt, ist real nur etwa halb so groß wie in der Simulation.

Der MPC-GA Betrieb erfolgte über fast neun Wochen vom 29.04. bis 06.07.2022. Die PV-Erzeugung weicht real um 1,4 % ab und der Energieverbrauch deutlich um 48,0 %. Auch hier ist der Gewinn aus Verbrauchskosten und Einspeise-vergütung nur etwa halb so hoch.

Beide MPC Betriebsphasen zeigen unterschiedliche und zum Teil sehr deutliche Abweichungen von Simulation und Messung. Dementsprechend unterscheiden sich auch deutlich die Betriebskosten / Gewinne. In beiden Fällen ist der Gewinn nur halb so hoch wie in der Simulation. Ausschlaggebend sind hierfür die Prognosegüte sowie Steuerbarkeit der WP. Die prognostizierte PV Erzeugung und Lastprognosen basieren auf einer Internetwettervorhersage, die, wie in den Laborexperimenten gezeigt, einen erheblichen Einfluss nehmen kann. Des Weiteren können die Ergebnisse aus der Simulation, die Leistungswerte darstellen, nicht direkt an die Wärmepumpen übergeben werden. Da die Sollwertvorgaben nur in Form von Sollwerttemperaturen an die reale Wärmepumpensteuerung übertragen werden können, kann der Betriebsplan nicht vollständig umgesetzt werden. In der Messung zeigt sich eine Arbeitszahl von 4.0 / 4,1 im Vergleich zur Simulation von 4.9 /5.0.

Zusammenfassung

Der Einfluss der Wettervorhersagegüte auf ein PV-unterstütztes und durch ein MPC gesteuertes WP-Heizsystem wurde sowohl in Simulationen, Laborexperimenten als auch in einem Reallabor untersucht. Es stehen hierfür gemessene und Wetterdaten von zwei unterschiedlichen Bezugsquellen zur Verfügung.

Die Ergebnisse der Labormessungen zeigen, dass der PV-Eigenverbrauch bei fehlerbehafte-

ten Wettervorhersagen im Vergleich zu einer perfekten MPC um bis zu 20 % niedriger ausfällt. Dabei steigen die Betriebskosten um bis zu 48 % an. Der Batteriespeicher hat bei nur ausreichend hoher Wettervorhersagegüte eine 17-fach höhere Fehlladung aus dem Netz und eine 2-fach höhere in das Stromnetz gezeigt. Die Labormessungen zeigten auf, dass je höher die Wettervorhersagegüte ist, desto höher ist im Allgemeinen auch die Systemeffizienz.

Im realen Betrieb der MPC in einem Reihenhauskomplex zeigen sich unterschiedliche und zum Teil sehr deutliche Abweichungen von Simulation und Messung. Dementsprechend unterscheiden sich auch deutlich die Betriebskosten bzw. der Gewinn, der nur halb so hoch ist wie in der Simulation. Ausschlaggebend sind hierfür die Prognosegüte sowie die Übertragung der Sollwerte aus der Simulation an die Wärmepumpen aufgrund von Limitierungen in der Steuerung.

Danksagung

In diesem Beitrag werden Ergebnisse aus den Projekten „sEnSys“ (FKZ 03EN1053A), "Herzo Base" (FKZ 03ET1364A) und "Herzo Opt" (FKZ 03ET1641A) vorgestellt. Diese Projekte werden / wurden gefördert durch das Bundesministerium für Wirtschaft und Klimaschutz aufgrund eines Beschlusses des Deutschen Bundestages.

Literatur

Allen J., Halberstadt A., Powers J., El-Farra N. H. Supervisory Model Predictive Control of Flexible Building Loads with On-site Solar Generation. Proceedings of the Annual American Control Conference, Milwaukee, USA. 2018;4622–4627.

Bechtel S., Rafii-Tabrizi S., Scholzen F., Hadji-Minaglou J.-R., Maas S. Influence of thermal energy storage and heat pump parametrization for demand-side-management in a nearly-zero-energy-building using model predictive control. Energy and Building. 2020;226.

Betzold C., Dentel A. Comparison and implementation of MPC and simple predictive control into a heat pump system. REHVA 14th HVAC World Congress Clima, 22nd – 25th May 2022, Rotterdam, The Netherlands. 2022.

Betzold C., Bordin S., Dentel A., Harhausen G. Control strategies for modulating heat pumps in a plus energy building. 13th IEA Heat Pump Conference, Jeju, Korea. 2020, May;11-14.

Betzold C., Dentel A. Evaluation and test operation of different model predictive control approaches for an energy system. The 17th International Conference of IBPSA - Building Simulation 2021, Bruges, Belgium. 2021.

Fischer D., Bernhardt J., Madani H., Wittwer C. Comparison of control approaches for variable speed air source heat pumps considering time variable electricity prices and PV. Applied Energy. 2017;204:93–105.

Heimrath R., Haller M. Project Report A2 of Subtask A: The Reference Heating System, the Template Solar System. Task 32, Solar Heating and Cooling Programme, International Energy Agency (IEA). 2007

Hummel S., Betzold C., Kandasamy K., Bordin S., Dentel A. Experimentelle Validierung von Simulationsmodellen an einem Hardware-in-the-loop Wärmepumpenprüfstand. The 8th Conference of IBPSA Germany and Austria, Graz, Austria. 2020.

Hummel S., Betzold C., Dentel A. Impact of the Weather Forecast Quality on a MPC-driven Heat Pump Heating System. CLIMA 2022, REHVA 14th HVAC World Congress, Rotterdam, The Netherlands. 2022.

Löhr Y., Mönnigmann M. Receding horizon heat flow control in domestic buildings- Yesterday-based disturbance predictions. Proceedings of the European Control Conference (ECC), Limassol, Cyprus. 2018;404–409.

Mendoza-Serrano D. I., Chmielewski D. J. Smart grid coordination in building HVAC systems: EMPC and the impact of forecasting. Journal of Process Control. 2014;24:1301–1310.

Péan T., Bellanco I., Salom J. Impact of the weather forecast on a predictive controller performance: experimental studies with a residential heat pump for space cooling. 13th IEA Heat Pump Conference, Jeju, Korea. 2020, May;11-14.

Péan T., Salom J., Costa-Castelló R. Review of control strategies for improving the energy flexibility provided by heat pump systems in buildings. Journal of Process Control. 2019;74:35–49.

Pichler M., Heinz A., Rieberer R. Model predictive heat pump- and building control to maximize PV-power on site use. 12th IEA Heat Pump Conference, Rotterdam, Netherlands. 2017.

Shukla K., Rangnekar S., Sudhakar K. Comparative study of isotropic and anisotropic sky models to estimate solar radiation incident on tilted surface: A case study for Bhopal, India. Energy Reports. 2015;1:96-103.

Thieblemont H., Haghighat F., Ooka F., Moreau A. Predictive control strategies based on weather forecast in buildings with energy storage system: A review of the state-of-the art. Energy and Building. 2017;153:485–500.

BauSIM 2024 in Wien
23. September – 26. September

Enhancing automated fault detection in building systems: A percentile-based scoring approach with dynamic tolerance range for residual evaluation

Sebastian Dietz[1], Frank Scholzen[2], Nicolas Réhault[3],
1 University of Luxembourg, Luxembourg, E-Mail: sebastian.dietz@uni.lu
2 University of Luxembourg, Luxembourg, E-Mail: frank.scholzen@uni.lu
3 Fraunhofer-Institut for Solar Energy Systems ISE, Germany, E-Mail: nicolas.rehault@ise.fraunhofer.de

Abstract

Fault detection and diagnostics (FDD) in heating, ventilation, and air conditioning (HVAC) systems using machine learning (ML) methods within a residual-generating approach is a promising solution to overcome obstacles in practical application. This paper proposes a residual evaluation method with a dynamic tolerance band and residual scoring for FDD processes. The score functions are automatically determined using the percentiles of the residual distribution during the training phase. The transferability of the method is demonstrated using datasets from nine different air handling units, and the performance of fault detection (FD) is evaluated based on a threshold for the total residual score. Compared to a static method based on the L_2 norm, the proposed method significantly reduces the number of false alarms, which is crucial for its acceptance in practical applications.

Introduction

The optimisation of the building energy operation with analytic tools like automated fault detection and diagnosis (FDD) can bring significant energy savings and help tackle the global greenhouse gas emissions reduction goals. Average energy savings of about 10% using FDD have been demonstrated in several pilot buildings worldwide (Kramer et al., 2020). However, due to their high parameterisation and maintenance costs, automated FDD methods are rarely implemented in practice to supervise Heating, Ventilation and Air Conditioning (HVAC) systems.

Recent research has focused on the application of ML methods in a FDD process (Mirnaghi, 2020) (Matetić, 2023). This is a promising solution since it can reduce modelling efforts, improve transferability, and increase the quality of FDD through learning the dynamic behaviour of the system from historical operating data (Kim, 2017) (Melgaard, 2022).

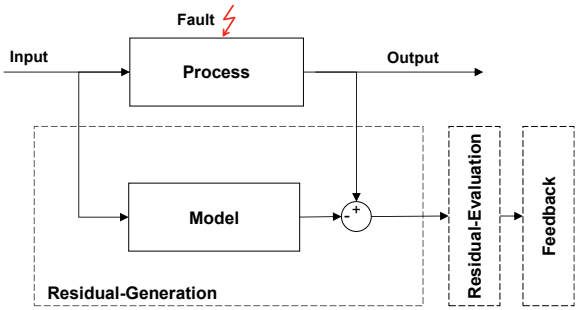

Figure 1: Scheme of a residual FDD process. Figure adapted from Ding (2013).

However, a major problem is the lack of labelled faulty building operation data, which makes it impossible to extensively learn faulty behaviours directly. An approach to address this problem is a residual generating FDD process (Figure 1) (Ding, 2013). Here, the nominal behaviour is learned and the differences between the estimates and the observed data are calculated. In the event of a fault, the residuals carry information about the fault. By evaluating the patterns in the generated residual vector, a decision can be made about the overall fault status (detection) and gather further information about the observed fault (diagnosis).

The tolerance of the overall process against false alarms and the quality of fault detection (FD) relies significantly on the residual evaluation method. A basic distinction can be made between statistical and threshold-based methods (Svärd, 2014). Statistical methods test whether the parameters of the residual distribution change due to fault effects (e.g., likelihood ratio test). However, this requires a sufficiently large amount of data in the evaluation interval, which is generally not available for HVAC systems. Threshold-based methods typically involve comparing a residual norm with a constant or adaptive threshold value (Navarro-Esbrí, 2006). While in other industrial domains a strong focus

is set on residual evaluation (Hsu, 2023), scientists dealing with HVAC systems mainly addressed residual generation. Thereby, the influence of the residual evaluation method within an automated FDD process remains insufficiently investigated (Kim, 2017). In particular, finding suitable threshold values for the FD logic is an important issue.

Therefore, in this paper, we introduce and apply an evaluation method based on operating data of air handling units (AHUs). The method employs percentile-based scoring with a dynamic tolerance band that varies according to the actual operating mode of the system. Compared to static methods, this aims to improve tolerance against false alarms without increasing the parameterisation effort. This is important for reducing implementation efforts and false alarms, while enhancing deployment and acceptance in practice. To investigate robustness and transferability issues, we have applied our method to a total of nine AHUs from three different buildings. The FD results are compared to a threshold-based FD method using the L2-Norm (Ding, 2013) of the residual vector. Although in this work only AHUs are considered, the method can also be applied to other parts of HVAC systems in buildings.

Challenges in residual evaluation

A major challenge in residual evaluation is to distinguish between model uncertainties and fault effects. Uncertainties are significantly influenced by the selected ML model and its ability to describe the dynamic behaviour of the system. Careful model selection is therefore essential. Nonetheless, the accuracy of the estimation is heavily impacted by the distribution of historical data and the range of represented operating conditions. In the context of building systems, this requires that the training data set includes all potential climatic conditions, typically spanning at least one year. Also, the implemented control strategy and the type of utilisation lead to an uneven distribution of the data corresponding to the different operating modes. For instance, AHUs may switch between heating and cooling modes based on temperature thresholds defined in the control rules. Consequently, certain operating modes might be underrepresented in the data and thus inadequately learned. Figure 2 illustrates the percentage of operating modes for an AHU data set over one year, indicating infrequent occurrences of cooling mode and heating mode with recirculated air.

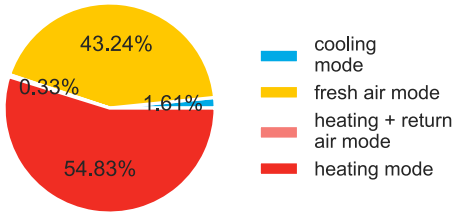

Figure 2: Percentage of operating modes over one year for case studie AHU AUD-8 of the MSA building.

HVAC systems are typically equipped with multiple sensors (state variables) and actors (control variables). In the context of residual evaluation, these variables generate a set of estimates and corresponding residuals. The ability to detect and diagnose faults improves with the number of residuals since different types of faults cause symptoms in different variables. For instance, a stuck valve in the hydraulic loop of a heating coil significantly impacts the supply air temperature in a ventilation system, while the duct pressure remains unaffected. When a fault influences multiple residuals, the overall fault state can be identified with greater certainty. Ideally, each fault creates a unique pattern in the residual vector, facilitating further fault diagnosis. However, it is essential to acknowledge that individual residuals are sensitive across different value ranges, depending on the corresponding variable (e.g., control signal versus temperature value) and the specific fault type. Even if the units are identical or normalised to a uniform value range (0-1), individual variables can respond considerably stronger to faults. This is a main challenge, as the residual magnitude cannot be used directly to assess the impact of the fault. A particular difficulty lies in dealing with discrete variables such as on/off signals that only have the values 0 or 1. An incorrect estimate leads immediately to high residuals, which can generate a high rate of false-positive alarms regarding the fault state of the system.

Residual evaluation procedure

To address the challenges in residual evaluation, we introduce a dynamic scoring method incorporating a tolerance band and a threshold-based FD. The entire procedure is illustrated in Figure 3, with the calculated residuals serving as the initial step. We apply a residual generator based on a bank of Multilayer-Perceptron models with hyperparameters tuned through Bayesian optimisation. For each observed system variable, a separate regression or classification model is trained to estimate the respective nominal behaviour. Table 1 shows the hyperparameters, while further details on the modelling procedure can be found in Dietz (2023). It should be noted that any type of ML model can be applied if the

nominal behaviour of the system is estimated with sufficient accuracy. The estimation and subsequent evaluation take place in discrete time intervals, given by the logging frequency of the Building Automation System (BAS). Periods with incomplete data records are excluded.

Table 1: Main hyperparameters of the Multilayer-Perceptron models. Range based values are selected by applying Bayesian optimisation.

Hyperparameter	**Value**
Maximum number of epochs	35
Batch-size	288
Learning rate	1e-4, 1e-5
Loss function regression	RMSE
Loss function classification	Cross-entropy
Number of hidden layers	3-6, step 1
Number of neurons in each layer	24-552, step 48
Dropout first hidden layer	0,1
Dropout 2nd to n hidden layer	0,2
Activation function	ReLu
Scaling method	Min-max scaling
Encoder (classification)	One-hot encoder

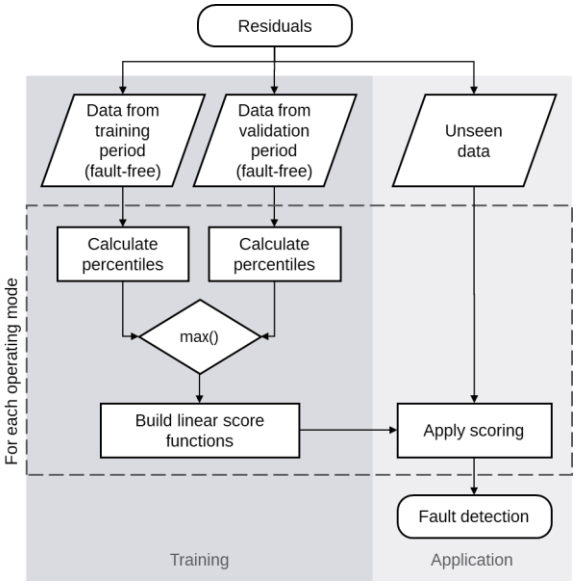

Figure 3: Flow chart of the residual evaluation procedure.

Normalising the estimates to a range from 0 to 1 result in residuals ranging between -1 and 1. A value of zero indicates the absence of faults. However, when a fault occurs, the validity range of the models may be exceeded, causing the estimates to fall outside the normalised range. In these cases, the estimates lose their physical significance, prompting us to constrain the residuals. Consequently, the residual vector for further evaluation is formulated as follows:

$$\vec{r}_t = \mathrm{MinMax}(-1,1,(\vec{y}_t - \vec{\hat{y}}_t)) \quad (1)$$

Where $\vec{r}_t$: residual vector; $\vec{y}_t$: observations and $\vec{\hat{y}}_t$: estimations at time *t*.

To model and test the residual generator, the data is divided into training, validation, and test periods. The latter represents the application scenario (unseen data). The same periods are used to fit the parameters of the residual evaluation procedure. Here it is crucial that the training and validation periods represent fault-free operation. Faulty states must be removed from the data sets as far as possible to ensure accurate parameter fitting. This can be done manually or by a set of rules. While the method demonstrates tolerance to isolated short-term faults, recurrent faults in the training data increase fault tolerance.

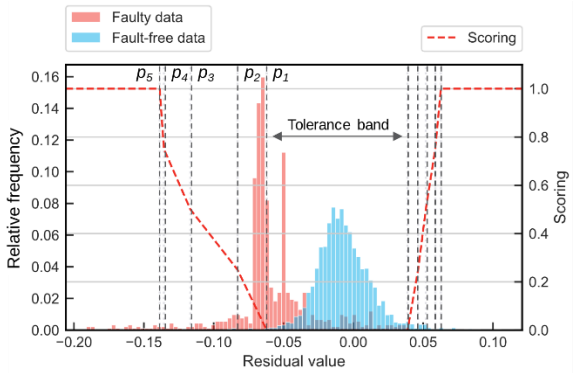

Figure 4: Histogram of supply air temperature residuals (MSA, AUD-8) for faulty (red) and fault free data (blue). The grey dashed lines show the percentiles used for linearised scoring.

Table 2: Rank of percentiles and their associated scoring values.

Percentile	Percentile Rank	Scoring Value
$p_{1,low}$ / $p_{1,high}$	1.50% / 98.5%	0.00
$p_{2,low}$ / $p_{2,high}$	0.50% / 99.5%	0.25
$p_{3,low}$ / $p_{3,high}$	0.20% / 99.8%	0.50
$p_{4,low}$ / $p_{4,high}$	0.10% / 99.9%	0.75
$p_{5,low}$ / $p_{5,high}$	0.05% / 99.95	1.00

The scoring of the residuals aims to normalise the sensitivity range of each residual, facilitating an equal assessment. The parameters to establish the scoring functions are the percentiles derived from the residual distribution of the validation period. To establish a grid for scoring, we have heuristically selected a total of ten percentile ranks, equally distributed around the median (see Table 1). Here, p_1 sets the tolerance band around the median ($Scoring = 0$), while p_5 determines the upper bound from which the maximum score value is assigned ($Scoring = 1$). Intermediate

scores are linearly interpolated between the percentiles (see Figure 4).

ML models typically provide their most accurate estimates for the training period. Consequently, residuals tend to show lower variance compared to the evaluation phase. Nonetheless, depending on the input data, it is reasonable to attain more accurate estimates during evaluation. To guarantee adequate tolerance concerning model uncertainties, it is essential to verify if the percentiles are indeed smaller for the training period (Formula 2). Finally, the linear score functions are created based on the percentiles obtained.

$$p_i = \begin{cases} p_{i,eval}; p_{i,eval} \geq p_{i,train} \\ p_{i,train}; p_{i,eval} < p_{i,train} \end{cases} \quad (2)$$

Where p_i : percentile *used for scoring*; $p_{i,eval}$: percentile *i* from the evaluation period; $p_{i,train}$: percentile *i* from the training period.

The procedure is repeated for every operating mode of the AHU to establish a dynamic tolerance band over time. For this task, the current mode is determined through a set of rules, automatically triggered based on available data points. The rules set can identify the six following distinct operating modes, corresponding to the air conditioning functions of the analysed AHUs identified: Fresh air, fresh air with activated heat recovery bypass, heating, heating with return air fraction, cooling, and cooling with return air fraction. Additional modes can be defined in scenarios involving supplementary components, like humidification or dehumidification. No evaluation is performed when the AHU is off.

Finally, the total score is calculated to evaluate the overall health status of the system. If the total score surpasses a predefined threshold level ($J_{th,s}$), a fault signal (FS) is activated (Formula 3). This threshold allows to adjust FD sensitivity in the application phase. Here, the threshold value is set at 1.5, across all case studies. However, our method can generate false positive results in the time lapse where the AHU change from one operational mode to another. Therefore, a fault detection alarm (FD_t) is only initiated if the fault signal remains true for longer than two consecutive time steps (Formula 4).

$$FS_t = \begin{cases} True; \sum_{i=1}^{n} s_{i,t} > J_{th,s} \\ False; \sum_{i=1}^{n} s_{i,t} \leq J_{th,s} \end{cases} \quad (3)$$

$$FD_t = \begin{cases} True; (FS_t \wedge FS_{t+1}) \vee (FS_t \wedge FS_{t-1}) \\ False; \ else \end{cases} \quad (4)$$

Where FD_t : fault detection alarm; FS_t : fault signal; $s_{i,t}$: score for residual i; $J_{th,s}$: threshold.

Description of the case studies

We evaluate the proposed method using data from nine AHUs located in three separate buildings. Operational data are obtained from a BAS without the installation of additional sensors. The datasets consist of status and flow variables, including temperature, pressure, humidity, and volume flows, as well as control signals for actuators such as valves, fans, and dampers. Energy or power data are not available for all AHUs and are thus excluded from the FD process. This yields in 11–22 residuals for subsequent evaluation, varying based on the AHU being observed.

Case study MSA

The Maison du Savoir (MSA) building houses the lecture halls and rectorate of the University of Luxembourg and contains three AHUs with identical topologies. Each AHU is designed to supply fresh air, heating, and cooling to a specific auditorium. and is equipped with a heating coil, an adiabatic cooling system, a heat recovery wheel, filters, and dampers which allow operation in return air mode. In cooling mode, water droplets are introduced into the extracted air stream and subsequently evaporated. This evaporation causes a reduction in temperature, enabling the transfer of cooling energy to the supply air stream through heat recovery. The AHUs vary in terms of nominal volume flow rates (AUD-4 and AUD-7 = 3150m³/h, AUD-8 = 8400m³/h), where the volume flow is controlled in two stages (60%/100%) with respect to the actual needs of the zone. Ongoing data acquisition started in May 2021 with an interval of five minutes. Due to a significant modification in the control strategy that involved variable air flow based on CO_2 measurements, only data up to mid-October 2022 is considered and divided as follows:

- Training period: 2021-05-19 to 2022-01-18
- Validation period: 2022-01-19 to 2022-07-18
- Test period: 2022-07-19 to 2022-10-18

Case study PSHN

The second case study is a primary school in Hohen Neuendorf (PSHN), Germany. Two AHUs (ZONE-A / ZONE-C) supply zones composed of eight and six classrooms respectively. The third AHU (SPO-HALL) serves a sports hall including changing rooms and showers. A hybrid ventilation system has been implemented, incorporating both mechanical ventilation and natural ventilation through motorised openings. The AHUs operate in two stages, with the second stage being activated in extreme hot or cold weather conditions when natural ventilation

openings don't open. A heating coil, a plate heat exchanger for heat recovery, outside air dampers and filters are installed. Additional radiators within the zone control room air temperature. We used data in a five-minute interval of the following periods:

- Training period: 2015-01-01 to 2015-12-31
- Validation period: 2016-01-01 to 2016-12-31
- Test period: 2017-01-01 to 2017-12-31

Case study PPPM

The third case study is a boarding school facility in Luxembourg. One of the AHUs supplies a sanitary area (SAN-1, 800 m³/h) and is equipped with a plate heat exchanger, supply and extract air fans, and filters. There is no air treatment. The second system (THEA) supplies a theatre room with a CO_2-controlled volume flow (6000 m³). The supply air is heated by a heating coil and heat recovery is facilitated through a recovery wheel. Furthermore, a residential building receives ventilation from the third system (RESI), which integrates a heat recovery wheel and heating coil. The system maintenance a minimum volume flow (2200 m³/h) that is increased depending on the humidity levels in the sanitary rooms (maximum 5000 m³). Not all data points are uniformly recorded, with some being event-based, thus posing challenges in preprocessing tasks. However, for FDD, data is aggregated at 10-minute intervals. The periods for the residual evaluation procedure are:

- Training period: 2017-01-01 to 2017-12-31
- Validation period: 2018-01-01 to 2018-07-15
- Test period: 2018-07-16 to 2018-12-31

The case studies and consequently the data sets capture a diverse range of system types, boundary conditions, available data points, time resolutions, and dynamic properties commonly encountered in practical applications. Each data set was manually analysed and labelled regarding the fault status.

Results

We applied our residual evaluation method on each AHU without specifically tuning its parameters to assess its level of automation and transferability. This furthermore enables a comprehensive comparison of the outcomes achieved.

Figure 6 presents the time series of two selected residuals from AHU AUD-8 in the MSA building over a one-day period, depicting a summertime scenario with adiabatic cooling mode. For dynamic scoring, the dotted black line and the red line represent the lower (p_1) and upper (p_5) boundaries, respectively, derived from the percentiles. Additionally, Figure 6 illustrates the sum of the individual scores and the outcome of the FD procedure.

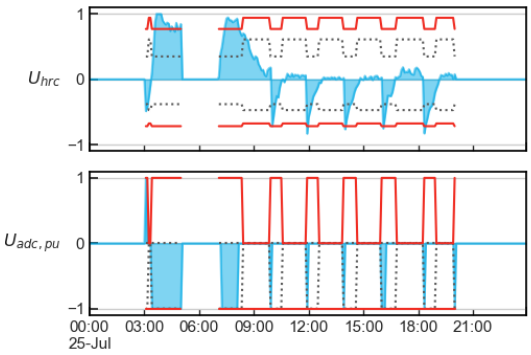

Figure 5: Time series of two exemplary residuals with the lower (p_1, black dotted line) and upper (p_5, red line) bounds for dynamic scoring.

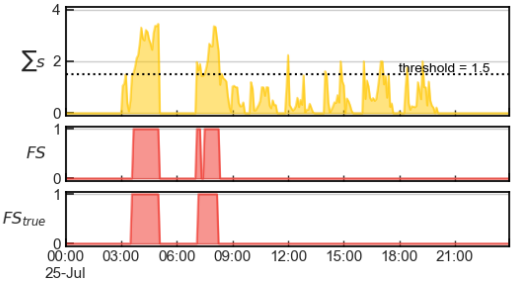

Figure 6: Example time series of the total score (top), the FD result (center) and the true fault state (bottom).

To refill the cooling system with water, the cooling function is temporarily disabled, causing the threshold values to change in steps based on the actual operating mode. The labelled fault (FS_{true}) indicates an unsuccessful attempt to refill the system due to an interrupted water supply, which results in the inability to provide cooling for the supply air. This malfunction causes high residual values, particularly in the control signal of the heat recovery wheel (U_{hrc}) and the circulation pump of the adiabatic cooling system ($U_{adc,pu}$). As a result, the overall score ($\sum s$) increases, and the fault is correctly identified. For the rest of the day, the cooling system operates without any faults. Due to the changing temperature levels during the filling process, the heat recovery temporarily switches off but gradually returns to 100%. These dynamics result in occasional spikes in the residuals and consequently in the calculated total score at regular intervals. However, the duration filter ensures that no alarms are triggered.

We assess the quality of fault using the metrics outlined in Formulas 5 to 8 (Melgaard, 2022).

$$CR = (T_p + T_n)/n \quad (5)$$

$$MisCR = (F_p + F_n)/n \quad (6)$$

$$FAR = F_p/(F_p + T_n) \quad (7)$$

$$FDR = T_p/(T_p + F_n) \quad (8)$$

CR : classification rate; $MisCR$: misclassification rate; FAR : false alarm rate; FDR : fault detection rate; T_p : number of true positive; F_p : number of false positive; T_n : number of true negative; $F_{n:}$: number of false negative; n : number of samples.

The results provided by the CR and MisCR give a comprehensive overview of the overall performance of the system. However, it is crucial to consider the frequency and the types of faults present in the time-series data, when interpreting the FAR and FDR. For instance, if only a few faults exist in the evaluation period, which is typical for real-world datasets, failing to detect even a single fault can significantly decrease FDR. Furthermore, the symptoms of a fault may become noticeable with a delay due to system dynamics, which means that the detected period does not match the fault label in terms of time. This has a negative impact on the FD metrics, although the fault is generally recognised. However, determining the true fault status for data labelling is subjective and imprecise in ambiguous situations. In addition, a binary fault state does not provide any information regarding the magnitude of the fault effects. Detecting faults without significant impacts on the state and control variables can be challenging, particularly in a residual-generating fault diagnosis process. For non-critical systems such as AHUs, this can be advantageous because it increases tolerance to no- or low-impact faults. In this context, defining the faults is also important. In technical building systems, inefficiencies often originate from design faults in control systems, such as simultaneous heating and cooling, which cannot be categorised as process faults (Isermann, 2006). However, in practical applications, it is desirable to detect such issues, which is why the definition of faults is extended in this study to include improper sequences.

Table 3 presents the resulting metrics for FD during the test period. All systems achieve high CR of over 93%, except AHU AUD4, which shows a much lower CR of 80% owing to a change in the setpoint specifications for the supply air temperature within the test period. The subsequent change in operation behaviour leads to many false alarms and requires the models to be retrained for both residual generation and evaluation.

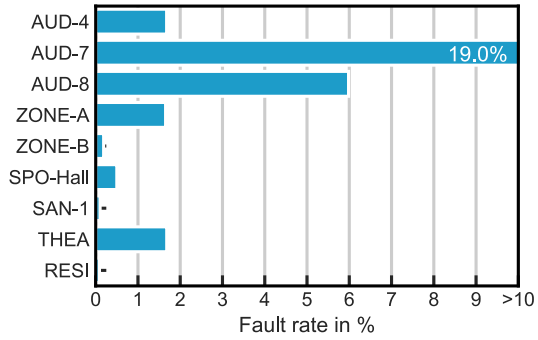

Figure 7: Fault rates (FR) of the case studies over the test period.

Table 3: Metrics of fault detection over the test period of the analysed case studies.

	System	CR	MisCR	FAR	FDR
MSA	AUD-4	80.1%	19.9%	18.9%	22.2%
	AUD-7	93.4%	6.6%	2.0%	74.0%
	AUD-8	95.8%	4.2%	3.3%	83.1%
PSHN	ZONE-A	98.7%	1.3%	0.4%	47.0%
	ZONE-B	99.8%	0.2%	0.2%	62.5%
	SPO-Hall	99.3%	0.7%	0.5%	61.5%
PPPM	SAN-1	99.7%	0.3%	0.3%	66.7%
	THEA	99.0%	1.0%	0.5%	72.1%
	RESI	99.9%	0.1%	0.1%	38.5%

Overall, the MisCR of the AHUs from the MSA building were significantly higher than those of the PPPM building, with an average of 4-6% compared to less than 1%. The individual fault rates, as shown in Figure 7, reveal that the MisCR increases as the fault rate (FR) increases. With an FR of 19%, AHU AUD-7 is characterised by the second highest (except AUD-4) MisCR at 6.6%. In addition, the AHUs of the MSA building show a comparable high FAR in the range of 2-3%, while for other systems FARs are triggered much less frequently at less than 0.5%. In terms of the FDR, AHU RESI shows the second lowest performance (except AUD-4) with a value of 39%. This can be explained by the very low FR of less than 0.1%. In general, the study shows that FD performs better for systems with lower fault rates and simpler control strategies. The control systems of the AHUs from the MSA building show switching behaviours depending on the current boundary conditions, which poses major challenges for an FDD system based on ML models.

An increasing number of residuals provides more information for FD. However, it should be noted that AHUs interact with other components of the building. Changes in boundary conditions after

model training, such as the room setpoint temperature, can lead to false alarms. As a result, it can be beneficial to ignore affected variables in the FD procedure, which are included in the control system, but represent a state variable outside the system boundary. In the MSA building, the room temperature causes temporary high score values due to overheating in summer, which was did not happen in the training phase. By disregarding the room temperature, the FAR of AUD-8 improves significantly from 3.3% to 1.0%, while FDR remains high at 81.6%.

To assess the performance of the FD method, we compare the results with a static approach. Namely, the L2 norm of the residual vector in Formula 9 has been demonstrated to be well-suited for FD (Ding, 2013). The required threshold value ($J_{th,L2}$) is obtained from the standard deviation determined in fault-free operation such as the training or validation period. The resulting detection logic show Formula 10 and 11.

$$\|\vec{r}_t\|_2 = \sqrt{\sum_{i=1}^{n}(r_{i,t})^2} \quad (9)$$

$$J_{th,L2} = \mathrm{f} * \mathrm{std}_{fault\ free}(\|\vec{r}\|_2) \quad (10)$$

$$FS_t = \begin{cases} False; & \|\vec{r}_t\|_2 \leq J_{th,L2} \\ True; & \|\vec{r}_t\|_2 > J_{th,L2} \end{cases} \quad (11)$$

FS_t : fault signal; $r_{i,t}$: residual i; f : scaling factor; $\|\vec{r}_t\|_2$: L^2 norm; $J_{th,L2}$: threshold.

As for the dynamic method, an alarm is triggered when the fault signal (FS_t) is present at two consecutive time steps (Formula 4). The sensitivity of FD for the static method is adjusted by the factor f. To compare the results with the dynamic method we tuned f manually for each AHU to achieve comparable FDRs.

Figure 8 shows the resulting FARs. While similarly high FARs of approximately 15% can be observed for AHU AUD4, other systems present larger variations. The dynamic method significantly reduces the FAR below 0.6% for the AHUs of the PPPM building and AHU SPO-Hall (PSHN), in comparison FARs of up to 15% are produced by the static method. However, the dynamic method does not always improve the FAR. For instance, the static method performs better for AUD-7 and AUD-8, as the present fault types show their symptoms in binary variables, such as the pump signal of adiabatic cooling. This leads to high residuals in the static method, allowing a large sensitive parameter f (Formula 10) to achieve comparable FDRs for the analysed datasets. Nevertheless, a larger sensitivity factor increases the tolerance to fault types that mainly affect continuous data points and may appear in further applications.

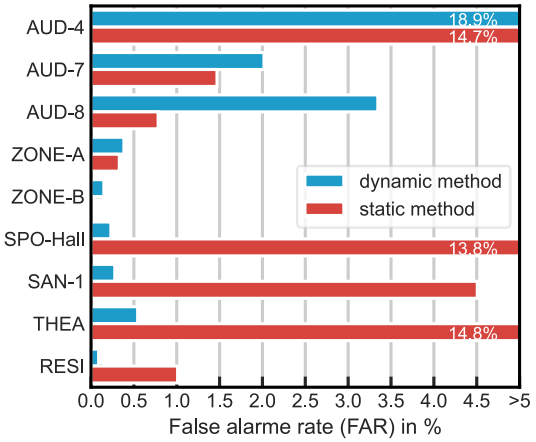

Figure 8: False alarm rates of the dynamic (blue) and the static residual evaluation method (red).

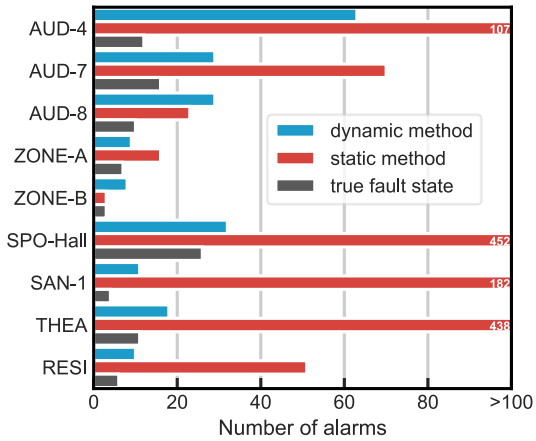

Figure 9: Number of alarms of the dynamic (blue), the static residual evaluation method (red) and the true fault state (grey).

In practical application, not only the FAR is crucial for acceptance, but also the number of triggered alarms, shown in Figure 9. It is evident that the dynamic approach is resilient against a high number of alarms, as observed for the static method (AUD-4, SPO-Hall, SAN-1, THEA). Apart from AUD8 and ZONE-B with only minor differences, the number of alarms can be significantly reduced for all systems.

Conclusion

In this study, we introduced a dynamic method for residual evaluation that utilizes a time-varying tolerance band and residual scoring. We analysed the performance of fault detection (FD) using nine different datasets from air handling units (AHU) and compared it to a static approach based on the residual L_2 norm.

Our results show that residual scoring based on the percentiles of the distributions in the training and validation periods of residual generation ensures high transferability without the need for manual parameter tuning. This presents a

significant advantage over the static method during the implementation phase, as the value range of the L_2 norm heavily relies on estimation accuracy, requiring individual sensitivity adjustments.

We achieved high classification rates, ranging from 93% to 99%, across all systems. However, the performance of our models notably declined when setpoint parameters of the AHU were changed during the application phase, requiring the models to be retrained. Nonetheless, this issue underscores a general challenge in data-driven approaches. In practical application of FDD methods in the building sector, the false alarm rate and the quantity of false alarms is crucial for acceptance. We demonstrated that dynamic scoring has enhanced residual evaluation compared to the static method and is resilient to excessive increases in false alarms even in cases with high model uncertainties in the residuals. However, good estimation quality for nominal behaviour is essential for high FDD performance. Thus, the presented residual evaluation method is not a substitute for careful model selection.

The selected percentile ranks and threshold value for the final FD decision in this study were found to be suitable but require further detailed analyses. Additionally, the individual residual scores provide valuable information on the types of faults, which should prompt further investigation into fault diagnosis.

Acknowledgement

Many thanks to Le Fonds Belval (Mr. G. Spenner) for the support of the project with operating data from the Maison du Savoir building. Special thanks to the University of Applied Sciences Berlin (Prof. F. Sick) for the data of the PSHN building and to A+P Kieffer for the operating data of the PPPM building.

References

Hsu, C. C., Frusque, G. et al. 2023. A Comparison of Residual-based Methods on Fault Detection. Proceedings of the Annual Conference of the Prognostics and Health Management Society, Vol. 15(1), 1–10. DOI: 10.36001/phmconf.2023.v15i1.3444

Dietz, S., Scholzen, F., Réhault et al. 2023. An easy to set up residual generator based on multilayer perceptron networks and Bayesian optimisation for the application in automated fault detection and diagnosis in building systems, Building Simulation Conference Proceedings Vol.18, ISSN: 2522-2708, Shanghai, China.

Ding, S. 2013. Chapter 2 Basic Ideas, Major Issues and Tools in the Observer-Based FDI Framework. In Ding, S. Model-Based Fault Diagnosis Techniques. Springer-Verlag. DOI: 10.1007/978-1-4471-4799-2.

Katipamula, S. & Brambley, M. 2005. Methods for fault detection, diagnostics, and prognostics for building systems—A review, part I. HVAC&R Research, Vol. 11(1), 3-25. DOI: 10.1080/10789669.2005.10391123

Kim, W., Katipamula, S. 2017. A Review of Fault Detection and Diagnostics Methods for Building Systems. Science and Technology for the Built Environment, Vol. 24. DOI: 10.1080/23744731.2017.1318008

Kramer, H., Lin, G., Curtin C. et al. 2020. Building analytics and monitoring-based commissioning: industry practice, costs, and savings. Energy Efficiency, Vol. 13(3), 537–549. DOI: 10.1007/s12053-019-09790-2.

Isermann, R. 2006. Fault-Diagnosis Systems – An Introduction from Fault Detection to Fault Tolerance. Springer-Verlag. ISBN: 978-3-540-24112-6.

Matetić, I., Štajduhar, I. et al.. 2023. A Review of Data-Driven Approaches and Techniques for Fault Detection and Diagnosis in HVAC Systems. Sensors, Vol. 23(1), 1–37. DOI: 10.3390/s23010001

Melgaard, S., Andersen, Kamilla H. et al. 2022. Fault Detection and Diagnosis Encyclopedia for Building Systems: A Systematic Review. Energies, Vol. 15(12). DOI: 10.3390/en15124366

Mirnaghi, M. S., Haghighat, F. 2020. Fault detection and diagnosis of large-scale HVAC systems in buildings using data-driven methods: A comprehensive review. Energy and Buildings, Vol. 229, DOI: 10.1016/J.ENBUILD.2020.110492

Navarro-Esbrí, J., Torrella et al.. 2006. A vapour compression chiller fault detection technique based on adaptative algorithms. Application to on-line refrigerant leakage detection. International Journal of Refrigeration, Vol. 29(5), 716–723. DOI: 10.1016/J.IJREFRIG.2005.12.008

Svärd, C., Nyberg, M., Frisk, E. et al.. 2014. Data-driven and adaptive statistical residual evaluation for fault detection with an automotive application. Mechanical Systems and Signal Processing, Vol. 45(1), 170–192. DOI: 10.1016/J.YMSSP.2013.11.002

BauSIM 2024 in Wien
23. September – 26. September

Monitoringkonzept für ein Demonstrationswohngebäude zur Entwicklung von netzreaktiven Betriebsführungskonzepten mit Smart Home Technologien

Pius Weidner und Andreas Gerber

Hochschule Biberach, Deutschland

Zusammenfassung

Im Rahmen des Solar Decathlon Europe 21/22 (SDE) wurde ein innovatives Demonstrationsgebäude errichtet, dessen elektrische und thermische Systeme als experimentelle Basis für die Entwicklung fortschrittlicher, netzreaktiver Betriebsführungskonzepte dienen. Zu diesem Zweck wurde ein Monitoringkonzept entwickelt und implementiert, welches heterogene Datenströme und Protokolle aus verschiedenen Teilsystemen aggregiert, verarbeitet und visualisiert. Ein zentrales Open Source Home Automatisierungstool fungiert dabei als Kommunikations- und Visualisierungsschnittstelle. Zu den Teilsystemen gehören ein netzgekoppeltes PV-Batteriesystem, die elektrischen Verbraucher und ein thermisches System mit PVT-Fassadenkollektoren, gebäudeintegriertem Speicher, Wärmepumpe und Wärmeverteilsystem. Verschiedenartige Datenquellen wie IoT-Sensoren, analoge Sensoren und frei programmierbare Steuereinheiten werden erfasst.

Die Hauptziele des Monitoring-Konzepts sind Skalierbarkeit und Flexibilität in Hinblick auf die Übertragbarkeit auf Anwendungen in der Praxis. Hierzu trägt die durchgängige Verwendung von Open-Source-Software und handelsüblicher, energieeffizienter Hardware bei. Zudem werden die gesammelten Daten lokal gespeichert. Das Gesamtkonzept erlaubt somit eine hohe Interoperabilität mit den verwendeten Geräten unterschiedlicher Hersteller. Für die Entwicklung und Programmierung von netzreaktiven Betriebsführungsalgorithmen ist die einheitliche Datenschnittstelle zu den Systemkomponenten eine Schlüsselkomponente.

Der Beitrag stellt das entwickelte Konzept, seine Implementierung sowie erste Betriebserfahrungen und Analysen vor.

Abstract

As part of the Solar Decathlon Europe 21/22 (SDE), an innovative demonstration building was build, whose integrated electrical and thermal systems serve as an experimental basis for the development of advanced, grid-responsive operational management concepts. A monitoring concept was developed and implemented for this purpose, which aggregates, processes and visualises heterogeneous data streams and protocols from several subsystems. Following the competition additional sensors and analysis tools were added. A central open source home automation tool acts as a communication and visualisation interface. The subsystems include a grid-connected PV battery system, the electrical consumers and a thermal system with PVT façade collectors, building-integrated storage, heat pump and heat distribution system. Various data sources such as IoT sensors, conventional sensors and freely programmable control units are captured.

The main objectives of the concept are scalability and flexibility in terms of transferability to applications in practice. This is aided by the consistent use of open source software and commercially available energy-efficient hardware. In addition, the collected data is stored locally. The overall concept therefore allows a high level of interoperability with devices from different manufacturers. For the development and programming of grid-reactive operational management algorithms, the standardised data interface to the system components is a key component.

This article presents the developed concept, its implementation and initial operating experience and analyses.

Einführung

Die Integration erneuerbarer Energien in Stromnetze und Gebäude ist ein entscheidender Schritt auf dem Weg zu einer CO_2-freien Zukunft. Der steigende Anteil erneuerbarer Energieträger im Energiemix schafft neue Herausforderungen: Energiequellen wie Photovoltaik und Wind sind inhärent fluktuierend. Gebäude, die ihren Energieverbrauch an das fluktuierende Angebot anpassen können, sind ein wichtiges Element, um Verteilnetze zu entlasten. Insbesondere im Bereich der Wärmeversorgung kann die thermische Speicherkapazität des Gebäudes zur Lastverschiebung und zur Spitzenlastmodulation (load shifting, peak shaving) verwendet werden. Um dieses Potential nutzen zu können, sind speziell in Gebäuden mit geringer Speichermasse - wie z.B. Gebäuden aus Holz - neuartige Speicher und ein leistungsfähiges Lastmangementsystem erforderlich. Für die Entwicklung der Speichersysteme und des Managementsystems können Simulationsmodelle durch experimentelle Untersuchungen an ausgeführten Gebäuden validiert werden. Ein Monitoringsystem, das die Energieströme für Heizung, Warmwasserbereitung, passive Kühlung und elektrische Verbraucher zeitlich hochaufgelöst bilanziert, bildet dabei die Grundlage für die Analyse und Systementwicklung.

Durch die Implementierung von Energiespeichersystemen kann die Volatilität erneuerbarer Energieträger kompensiert und die Effizienz der Energieverwendung optimiert werden. Die Forschung zeigt hier vorwiegend simulationsbasierte und einige experimentelle Ansätze um die bestmöglichen Strategien zur Energiespeicherung und -nutzung zu identifizieren. Enescu et al. (2020) zeigen die Entwicklung in großen thermischen Speichern auf Netzebene, während Hu et al. (2019) die Nutzung der Gebäudemasse als thermischen Speicher evaluieren. Nach Finck et al. (2018) konnte in Simulationen eine Speicherflexibilität bei Wasser-, PCM- (**p**hase **c**hange **m**aterials) und TCM-Speichern (**t**hermo**c**hemical **m**aterials) in Gebäuden von bis zu 24h demonstriert werden und es wird gezeigt, dass so Flexibilitäten im Netz ermöglicht werden können. Nach Li & Zheng (2016) sind insbesondere kostengünstige Speicher gesucht, um größere Flexibilitäten möglich zu machen.

Um diese Entwicklung voranzutreiben, stellt dieser Beitrag ein Demonstrationsgebäude (HDU - House Demonstration Unit) mit einem entsprechend kostengünstigen, in einen Holzbau integrierten Speichersystem vor. Der Fokus dieses Beitrags liegt auf dem implementierten Monitoringsystem, das die Evaluation und den Nutzen für das Netz dieses *Active Layer* (AL) ermöglichen soll und dessen Implementierung eine Basis für die Entwicklung von Monitoringsystemen in Wohngebäuden bietet. Die HDU ist in das Living Lab NRW in Wuppertal *Living Lab NRW* (n.d.) eingebettet, das über ein lokales Nahwärmenetz verfügt. Diese Umgebung erlaubt die praxisnahe Erprobung von netzfreundlichen Betriebskonzepten in thermischer sowie elektrischer Hinsicht. Die im Rahmen des SDE errichtete HDU und dessen Energiesystem wird in Weidner & Gerber (2023) näher beschrieben.

Ziel ist die Entwicklung von Modellen und wirksamen modell-prädiktiven Managementsystemen für den CO_2-minimalen Betrieb von Gebäuden. Die Notwendigkeit und Wirksamkeit solcher Konzepte zeigen Buttitta et al. (2021) am Beispiel simulationsbasierter Untersuchungen an elektrischen Speicheröfen in London.

Hierfür ist vorrangig die Sammlung von realen Daten durch ein Monitoringsystem unerlässlich, um damit das Gebäudeverhalten abbilden, Modelle validieren sowie Prognosen für Netzbetreiber liefern zu können. Der vorgestellte Ansatz erlaubt auch die Erweiterung der Sensorik, etwa durch die einfache Einbindung von IoT-Sensoren oder zusätzliche Softwaremodule. Dies erscheint in Anbetracht der zukünftigen Entwicklung sinnvoll, da eine zunehmende Verbreitung von IoT-Geräten nach Al-Sarawi et al. (2020) auch im Wohnungssektor wahrscheinlich ist. Somit können Synergien zu bestehenden Systemen erreicht werden. In der Konsequenz sollen damit umfassende Monitoringsysteme im Wohnungsbau möglich werden. Dies wird zudem durch die Verfügbarkeit von kostengünstigen und energieeffizienten Software- und Hardware-Lösungen unterstützt.

Das Gebäude und die technischen Anlagen

Abbildung 1 zeigt das Energieflussdiagramm der wichtigsten Komponenten des Energiesystems der HDU. Beim AL, siehe auch Abbildung 4, handelt es sich um einen thermischen Energiespeicher, der die für die Trittschalldämpfung erforderliche Masse als thermischen Speicher nutzt. Diese Beschwerung wurde in Form einer Schüttung aus Splitt oberhalb einer schall- und wärmedämmenden Trennschicht eingebracht und wie eine Fußbodenheizung thermisch aktiviert. Oberhalb der Speicherschicht ist für die Trittschalldämpfung wieder eine Dämmung erforderlich, die den Speicher auch thermisch vom Raum entkoppelt. Dadurch kann diese Speicherschicht bis zu einem gewissen Grad unabhängig von der gewünschten Temperatur im Raum be- oder entladen werden. Die Relevanz für ein sol-

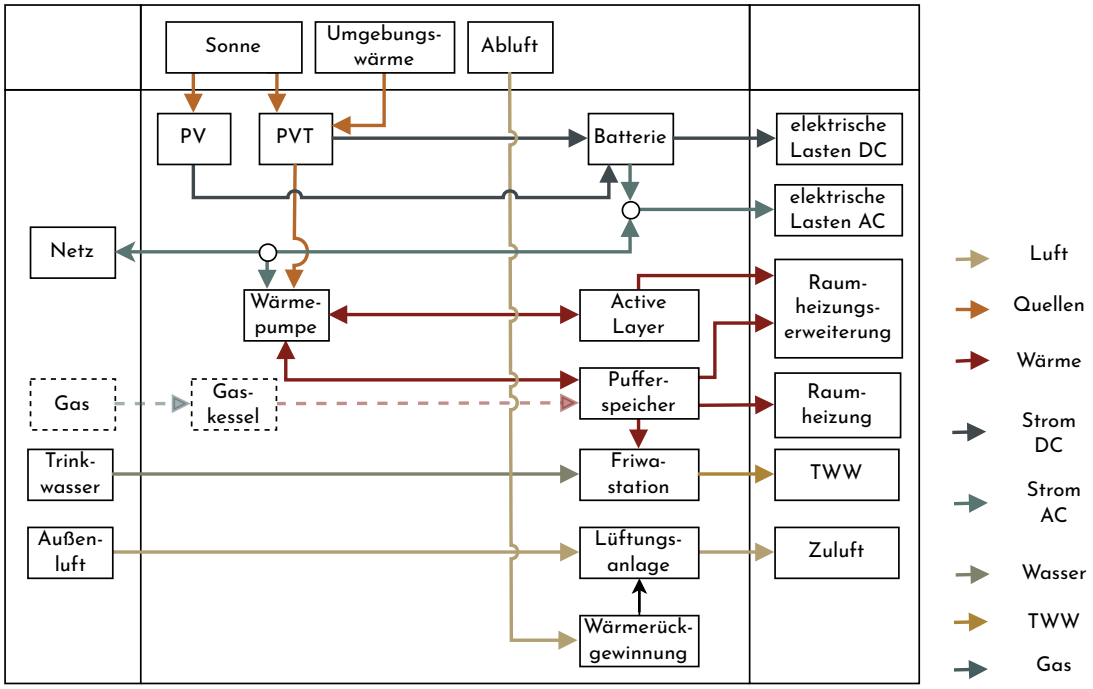

Abbildung 1: Energieflussdiagramm der HDU. Fassadenintegrierte PVT-Kollektoren mit Wärmepumpe gewinnen die erforderliche Wärme aus der Solarstrahlung und Umgebungsluft. Ein mit der Wohnfläche skalierender Speicher ermöglicht die Entkoppelung von Wärmegewinnung und Verbrauch. Photovoltaik und Batterie dienen zur Versorgung der elektrischen Verbraucher Weidner & Gerber (2023)

ches System ergibt sich vor allem aus der zunehmenden Bedeutung von Gebäuden aus Holz (Petruch & Walcher (2021)), die eine geringere thermische Speichermasse im Vergleich zu Betonbauten haben. Der Holzbau leistet einen wichtigen Beitrag zur Dekarbonisierung des Bauens (Churkina et al. (2020)).

Weitere Hauptkomponenten des Systems sind fassadenintegrierte, offene PVT-Kollektoren, die als Wärmequelle für eine leistungsmodulierende Wärmepumpe dienen. Weiterhin umfasst das System einen Pufferspeicher zur Versorgung der Raumheizung und einer Frischwasserstation (Friwa-Station) sowie eine Lüftungsanlage mit Wärmerückgewinnung.

Das Monitoringsystem

Struktur des Monitoringsystems

Abbildung 2 zeigt ein detailliertes Schema der Hardware-Komponenten des Automations- und Monitoringsystems. Auf der *Automationsebene* befinden sich frei programmierbare Regler. Sie sind für die Kontrolle der einzelnen Regelventile und Pumpen zuständig und empfangen gleichzeitig die Signale der analogen (Temperatur-)Sensoren.

Zudem gibt es ein Schnittstellengerät mit dem die Regler über eine Web-Oberfläche verwaltet, programmiert und parametriert werden können. Dieses wird über eine Ethernet-Verbindung angebunden. Das Gerät besitzt außerdem die Möglichkeit, Modbus-Geräte als Modbus-Master anzusteuern und auszulesen.

Auf der *Managementebene* befinden sich der Router und ein Mini-PC, die durch die im nächsten Abschnitt näher beschriebenen Softwarekomponenten Daten sammeln, verarbeiten und auch Regelungs- und Steuerungsfunktionen ausführen, bzw. an die Regler weiterleiten. Bei der Auswahl der Hardware wurde auf geringen elektrischen Energieverbrauch geachtet: Der Mini-PC benötigt trotz der umfangreichen Anwendungen, die er zur Verfügung stellt, weniger als 4,5 W.

Das Netzwerk kann über einen verschlüsselten Kommunikationsweg zu jeder Zeit über das Internet erreicht werden. Somit ist eine Fernsteuerung aller im lokalen Netzwerk erreichbaren Komponenten über das Internet möglich.

Die erforderlichen Softwarekomponenten des Monitoringsystems wurden auf den lokalen Router, der das System gegenüber dem Internet absichert, und den Mini-PC aufgeteilt. Die Programme mit

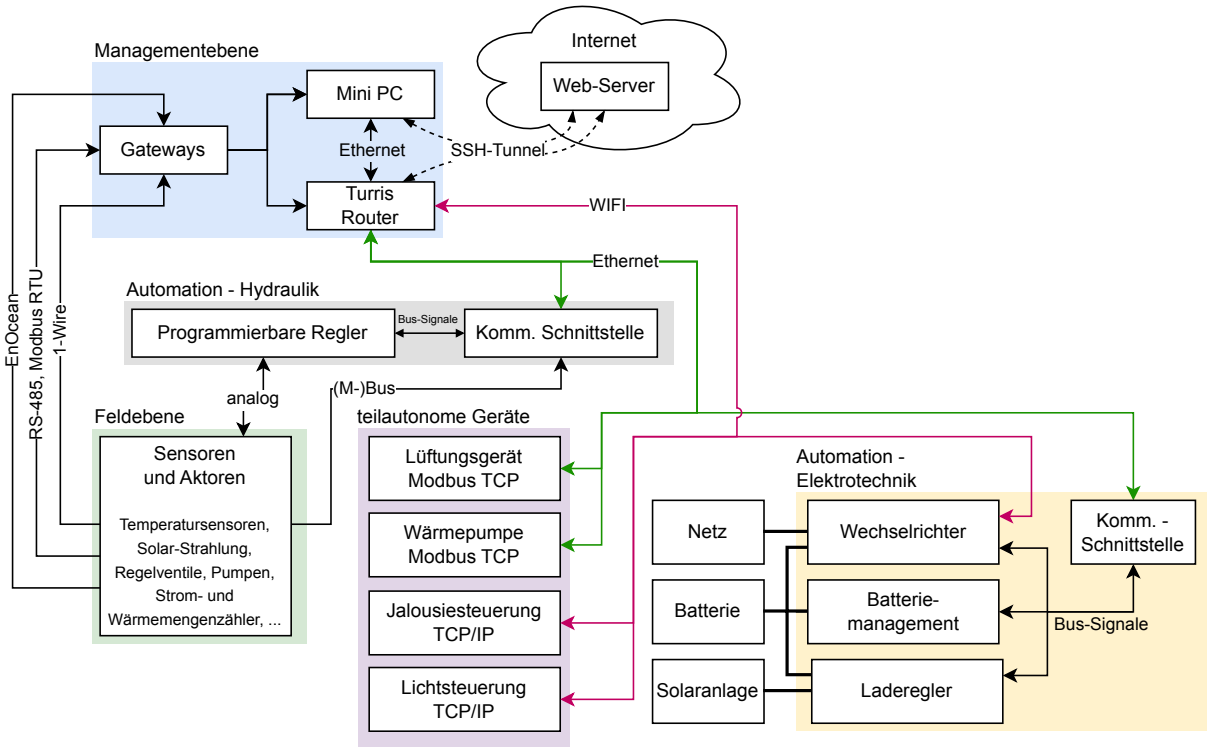

Abbildung 2: Systemkomponenten im Monitoringsystem der HDU. Aufteilung in die Managementebene, die hydraulische und elektrotechnische Automationsebenen und die Feldebene. Teilautonome Geräte haben eigene integrierte Regler oder Steuerungen

geringeren Leistungsansprüchen wurden auf dem Router installiert, während die Software mit höheren Leistungsansprüchen auf dem Mini-PC installiert wurden. Auch benötigen die Programme auf dem Mini-PC häufigere Eingriffe und Anpassungen, was deren Stabilität und Verfügbarkeit beeinträchtigen könnte. Die Komponenten, die ständig in Betrieb („always-on“) sein müssen, sollten sich auf dem Router befinden und nur in Ausnahmefällen Eingriffe erfordern. Damit soll der Einfluss auf das Gesamtsystem durch Neustarts oder Hard-Resets (Trennen vom Strom) reduziert werden.

Die Software des Monitoringsystems baut auf Open-Source-Software mit Home Assistant (HA, Home Assistant (2024)) als zentrale Kommunikations- und Sammelstelle auf. In HA ist eine einfache Integration von verschiedensten Protokollen und Zusatzfunktionen möglich. Im hier vorgestellten Monitoringsystem wurden zum Beispiel folgende Schnittstellen integriert: 1-Wire, MQTT, Modbus, EnOcean. Außerdem konnte durch die von der Community entwickelte Erweiterung ltss (siehe freol35241 (2024)) eine lokal installierte PostgreSQL Datenbank mit dem Aufsatz TimescaleDB (siehe TimescaleDB (2024)) zur Langzeit-Datenspeicherung eingebunden werden. TimescaleDB erlaubt eine effziente Speicherung der Daten durch die integrierte verlustfreie auf Zeitreihen optimierte Kompression. Mit der Erweiterung um die Visualisierungsplattform Grafana (siehe Grafana (2024)) können die Langzeitdaten neben der Visualisierung des momentanen Zustands in Home Assistant dargestellt werden.

Abbildung 3 zeigt die Softwarekomponenten und eine potenzielle Erweiterung um die Kommunikation zu Netzbetreibern oder anderen interessierten Parteien mittels Remote Zugriff.

Durch die einfache Integration von Python-Programmen in den Mini PC konnten zudem weitere Datenquellen erschlossen werden, bei denen außer einem Webinterface keine Schnittstelle verfügbar gemacht werden kann. Dazu wurden automatisierte HTTP-Anfragen implementiert. Durch Anwendung des Python-Pakets ha_mqtt_discoverable (siehe Block (2024)) konnte zudem eine schnell implementierte und strukturierte Weiterleitung der Daten via MQTT an Home Assistant erreicht werden.

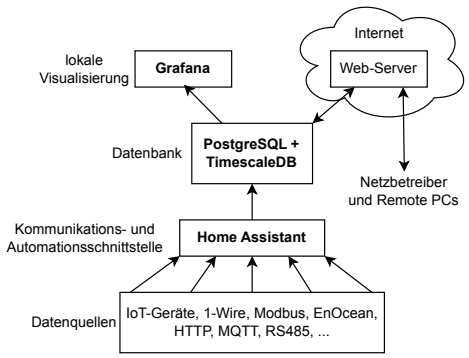

Abbildung 3: Schematisches Konzept zur Interaktion der wichtigsten Softwarekomponenten

Messkonzept

Als eine der wissenschaftlich bedeutendsten Komponenten des Energiesystems werden die Temperaturen des AL an zwei Stellen (horizontal) und in verschiedenen Schichten (vertikal, siehe Abbildung 4) gemessen. Dabei wird zum einen zwischen den Rohren gemessen und zum anderen direkt an den Rohren und den Wärmeleitblechen, die um die Rohre gelegt wurden.

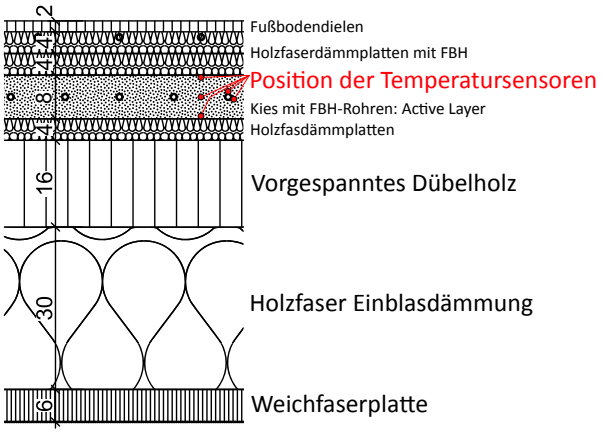

Abbildung 4: Bodenaufbau des Versuchsgebäudes mit der Position der Temperaturfühler zum Monitoring der thermisch aktivierten Splittschicht

Dies soll es möglich machen, die Temperaturverteilung innerhalb des Active Layer, also horizontale und vertikale Temperaturschichtungen zu quantifizieren. Mit Hilfe der aufgezeichneten Daten sollen Simulationsmodelle validiert werden und auf deren Grundlage zuverlässige Prognosen zur Performance des Speichersystems möglich werden.

Um Energiebilanzen und Detailanalysen für das Gebäude und seine technischen Komponenten zu erstellen wurden weitere Sensoren installiert: Wärmemengenzähler für den Active Layer, die Fußbodenheizung und die Wärmepumpe; Temperaturfühler im PVT-Kreis; Verdampfer und Verflüssigertemperaturen der Wärmepumpe wasserseitig; Fühler für Puffertemperaturen und Temperaturen der Zu- und Abflüsse des Pufferspeichers; Zu-, Fort-, Außen- und Ablufttemperaturen der Lüftungsanlage; Raum- und Außentemperaturen und das Temperaturprofil der Außenwand von innen nach außen.

Eine präzise Messung der durch die Lüftungsanlage geförderten Volumenströme steht noch aus. Bisher wird der vom Hersteller zur jeweiligen Leistungsstufe angegebene Volumenstrom aufgezeichnet.

Analyse und Diskussion

Abbildung 5 zeigt erste Ergebnisse des vorgestellten Monitoringsystems. Es zeigt sich, dass die thermische Masse des AL mit einer Vorlauftemperatur von 40 °C innerhalb von 24 Stunden von 16,5 °C auf eine Temperatur von ca. 35 °C angehoben werden kann. Außerdem zeigt das Monitoring, dass sich bei Beladung des Speichers erwartungsgemäß eine Temperaturverteilung in der Fläche ergibt, die mit zunehmender Beladungsdauer abnimmt. Eine Temperaturdifferenz von bis zu 2 K bleibt aber auch nach Durchströmung von mehreren Tagen bestehen.

Im Laufe weiterer Arbeiten sollen nähere Untersuchungen und Simulationen dazu dienen, eine Optimierung der Speicherbe- und -entladung zu ermöglichen, um z.B. ein möglichst homogene Temperaturverteilung im AL möglich zu machen.

Wie in Abbildung 6 gezeigt, gibt das Monitoring auch Aufschluss zum passiven Verhalten des Active Layer nach dem Aufheizvorgang. Die Abkühlung des Active Layer von ca. 40 °C auf annähernd Raumtemperatur dauert ca. 10 Tage. Wobei im betrachteten Zeitraum die Raumtemperatur durch die Wärmeabgabe des AL auf ca. 29 °C angehoben wurde (keine Wärmequellen waren aktiv, allerdings die Jalousie geschlossen). Durch weitere Versuche soll eine Kennlinie für die Temperatur des Active Layer ermittelt werden, bei der die Raumtemperatur nicht unnötig erhöht wird und somit möglichst viel Wärme für den netzfreundlichen oder CO_2-minimalen Betrieb gespeichert werden kann. Hiermit kann die im Active Layer gespeicherte Energie abhängig von den Umgebungsbedingungen optimiert werden.

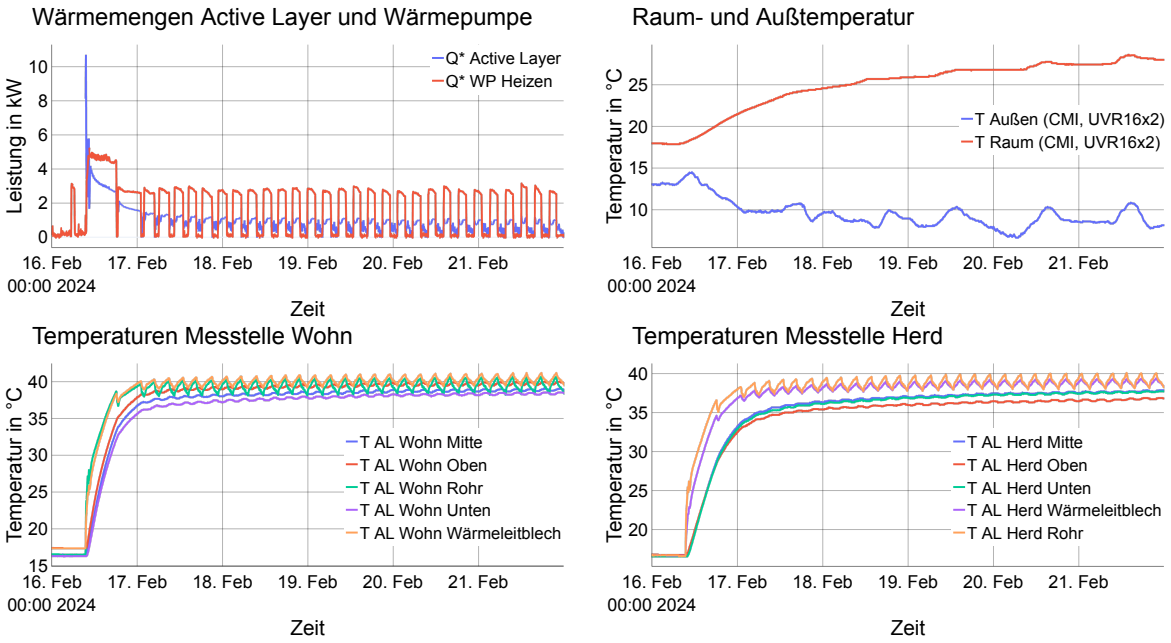

Abbildung 5: Aufheizen des AL mit ca. 40°C Vorlauftemperatur. Visualisierung durch Grafana. Die zwei unteren Diagramme zeigen deutlich die horizontale Temperaturdifferenz an den zwei gemessenen Stellen. Die Raumtemperatur steigt allein durch den beheizten AL auf über 28 °C.

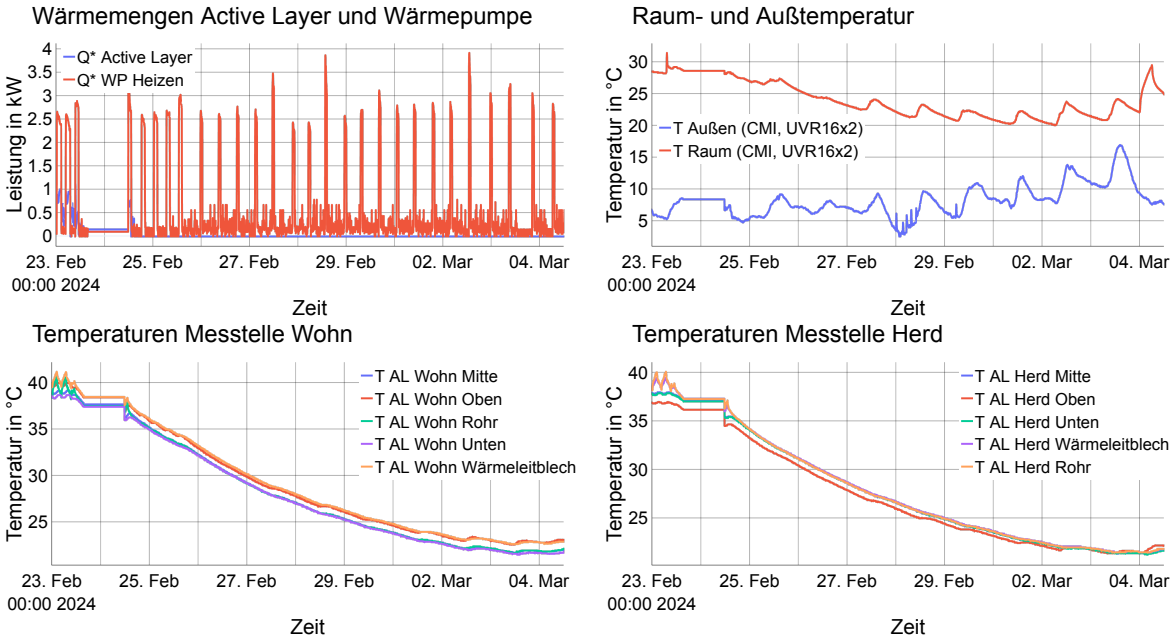

Abbildung 6: Abkühlen des AL von ca. 35 °C auf ca. 22 °C Speichertemperatur innerhalb von 10 Tagen.

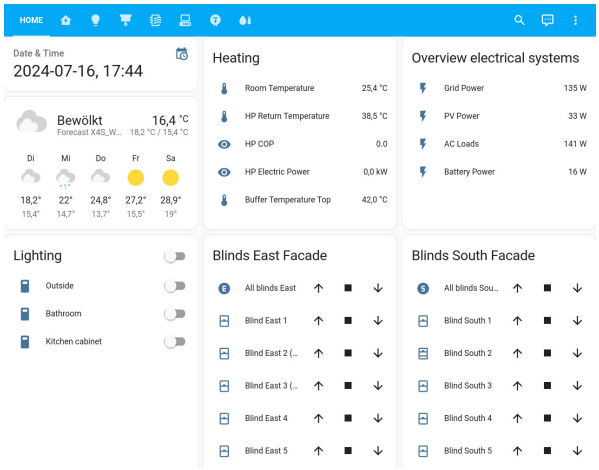

Abbildung 7: Beispiel eines Dashboards in Home Assisstant mit der Anzeige von momentanen Sensordaten und Steuerungsmöglichkeiten für Jalousien und Beleuchtung

Kommunikation

Eine grundlegende Funktion des Monitoringsystems ist die Visualisierung der Eingriff vor Ort und von außen, sowie die kontinuierliche Sicherung der Daten.

Da das Gebäude nicht direkt aus dem Internet erreichbar ist – eine typische Situation für Wohngebäude – erfolgt der Verbindungsaufbau vom Router aus über eine verschlüsselte Verbindung zu einem erreichbaren Endpunkt im Internet. Über diesen bauen autorisierte Anwendungen eine Verbindung zum Monitoringsystem auf. Diese reversen Tunnel sind leicht einzurichten und gelten als sicher (siehe z.B. Bauer (2024)). Auch die automatisierte Datensicherung nutzt diesen Kommunikationsweg. Dazu wird die Datenbank kontinuierlich mit der entfernten Datenbank synchronisiert (siehe PostgreSQL Documentation (2011)).

Durch die Integration sämtlicher Komponenten in das Smart-Home-System und die bidirektionale Kommunikation kann das Monitoringsystem übersichtliche Informationen über das Gesamtsystem für Bewohner:innen des Gebäudes aber auch detaillierte Informationen für wissenschaftliche Fragestellungen zur Verfügung stellen. Neben der Aufbereitung von Daten ist auch die Interaktion mit den Systemkomponenten möglich. Ein Beispiel für die Möglichkeiten der Nutzereingriffe zeigt das Webinterface in Abbildung 7. Die Bündelung aller Systemkomponenten in einer Plattform mit einer definierten Software-Schnittstelle ist zudem die Grundlage für geräteunabhängige Softwaremodule zur Optimierung des Gebäudeverhaltens. Weiterhin ist die Integration von Haushaltsgeräten zur Implementation von demand response möglich. Für planbare elektrische Lasten wie Waschmaschine oder Spülmaschine können zum Beispiel günstige Zeitpunkte zum Einschalten als Empfehlung für Nutzer angezeigt werden.

Fazit und Ausblick

Zusammenfassend konnte mit dem vorgestellten Monitoringsystem ein für den Wohnungsbau flexibel einsetzbares System entwickelt werden. Zum einen konnte mit Home Assistant eine einfach einzurichtende Oberfläche zur direkten Nutzerinteraktion eingerichtet werden. Zum anderen erlaubt die Datenbankanbindung mit Grafana eine umfassendes Monitoring mit Visualisierung ohne große Hardwareanforderungen innerhalb des Wohngebäudes, da die Software vollständig auf einem Mini-PC ausgeführt werden kann.

Das vorgestellte Monitoring bildet nach bisherigen Erfahrungen eine verlässliche Basis für die weiteren Arbeiten mit dem zugrundeliegenden Energiesystem des Gebäudes und dem anliegenden Living Lab. Die weiteren Untersuchungen werden sich unter anderem auf die Nutzerschnittstellen konzentrieren. Insbesondere soll aber der Active Layer einen höheren Reifegrad erlangen und seine potenzielle Integration in netzfreundliche Betriebsführungskonzepte evaluiert werden. Dazu sollen zum einen thermische Lastsimulationen durchgeführt werden. Zum Anderen soll der AL in verschiedenen Temperaturbereichen beheizt und abgekühlt werden, um dessen optimalen Temperaturbereich zu ermitteln. Weiterhin soll die Simulation eines virtuellen Netzbetreibers - z.B. durch CO_2-Preissignale Aufschluss über das Potential der thermischen Speichermassen geben.

Danksagung

Die Finanzierung erfolgte aufgrund eines Beschlusses des deutschen Bundestages durch das Bundesministerium für Wirtschaft und Klimaschutz und durch Unterstützung der Holzbauinitiative Baden Württemberg.

Gefördert durch:
Bundesministerium für Wirtschaft und Klimaschutz
aufgrund eines Beschlusses des Deutschen Bundestages

Geplant und gebaut wurde das Gebäude vom studentischen Team X4S der Hochschule Biberach.

Literatur

Al-Sarawi, S., Anbar, M., Abdullah, R. & Al Hawari, A. B. (2020), Internet of Things Market Analysis Forecasts, 2020–2030, *in* '2020 Fourth World Conference on Smart Trends in Systems, Security and Sustainability (WorldS4)', pp. 449–453.
URL: *https://ieeexplore.ieee.org/abstract/document/9210375*

Bauer, I. (2024), 'SSH-Tunnel nutzen - so geht's'.
URL: *https://www.heise.de/tipps-tricks/SSH-Tunnel-nutzen-so-geht-s-4320041.html*

Block, J. (2024), 'unixorn/ha-mqtt-discoverable'. original-date: 2022-10-25T22:49:13Z.
URL: *https://github.com/unixorn/ha-mqtt-discoverable*

Buttitta, G., Jones, C. N. & Finn, D. P. (2021), 'Evaluation of advanced control strategies of electric thermal storage systems in residential building stock', *Utilities Policy* **69**, 101178.
URL: *https://linkinghub.elsevier.com/retrieve/pii/S0957178721000126*

Churkina, G., Organschi, A., Reyer, C. P. O., Ruff, A., Vinke, K., Liu, Z., Reck, B. K., Graedel, T. E. & Schellnhuber, H. J. (2020), 'Buildings as a global carbon sink', *Nature Sustainability* **3**(4), 269–276.
URL: *https://www.nature.com/articles/s41893-019-0462-4*

Enescu, D., Chicco, G., Porumb, R. & Seritan, G. (2020), 'Thermal Energy Storage for Grid Applications: Current Status and Emerging Trends', *Energies* **13**(2), 340. Number: 2 Publisher: Multidisciplinary Digital Publishing Institute.
URL: *https://www.mdpi.com/1996-1073/13/2/340*

Finck, C., Li, R., Kramer, R. & Zeiler, W. (2018), 'Quantifying demand flexibility of power-to-heat and thermal energy storage in the control of building heating systems', *Applied Energy* **209**, 409–425.
URL: *https://linkinghub.elsevier.com/retrieve/pii/S0306261917316112*

freol35241 (2024), 'freol35241/ltss'. original-date: 2019-12-08T17:48:43Z.
URL: *https://github.com/freol35241/ltss*

Grafana (2024), 'grafana/grafana'. original-date: 2013-12-11T15:59:56Z.
URL: *https://github.com/grafana/grafana*

Home Assistant (2024), 'Home Assistant'.
URL: *https://github.com/home-assistant*

Hu, M., Xiao, F., Jørgensen, J. B. & Li, R. (2019), 'Price-responsive model predictive control of floor heating systems for demand response using building thermal mass', *Applied Thermal Engineering* **153**, 316–329.
URL: *https://linkinghub.elsevier.com/retrieve/pii/S1359431118361921*

Li, G. & Zheng, X. (2016), 'Thermal energy storage system integration forms for a sustainable future', *Renewable and Sustainable Energy Reviews* **62**, 736–757.
URL: *https://linkinghub.elsevier.com/retrieve/pii/S1364032116301095*

Living Lab NRW (n.d.). Archive Location: Wuppertal.
URL: *https://livinglabnrw.uni-wuppertal.de/de/*

Petruch, M. & Walcher, D. (2021), 'Timber for future? Attitudes towards timber construction by young millennials in Austria - Marketing implications from a representative study', *Journal of Cleaner Production* **294**, 126324.
URL: *https://linkinghub.elsevier.com/retrieve/pii/S0959652621005448*

PostgreSQL Documentation (2011), 'High Availability and Load Balancing'.
URL: *https://www.postgresql.org/docs/8.2/high-availability.html*

TimescaleDB (2024), 'timescale/timescaledb'. original-date: 2017-03-07T20:03:41Z.
URL: *https://github.com/timescale/timescaledb*

Weidner, P. & Gerber, A. (2023), 'Scalable façade-integrated PVT-systems for upward extensions in the urban context', *Journal of Physics: Conference Series* **2600**(4), 042015. Publisher: IOP Publishing.
URL: *https://dx.doi.org/10.1088/1742-6596/2600/4/042015*

BauSIM 2024 in Wien
23. September – 26. September

Neural Network-based Occupancy Detection on the Edge

Siegl Christoph[1], Hirsch Thomas[2], Kohl Theresa[1], Wotawa Franz[2] und Schweiger Gerald[2]

[1]*DiLT Analytics GmbH, Graz, Austria*

[2]*University of Technology Graz, Institute of Software Technology, Graz, Austria*

Abstract

Building occupancy information is essential to improve building performance and occupant comfort. Various non-intrusive detection methods using environmental sensors have already been explored, and ML methods have been shown to perform well in identifying occupancy patterns, but the scalability of the proposed approaches is still an open research question. Transfer learning offers a promising solution by adapting models to different targets and using shared knowledge for tasks with limited data. This study uses neural networks to detect indoor occupancy with sensor data in a real-world office setting, evaluating the performance and transferability of the models. We collected data with LoRa sensors in an office for three months and used them to train and test the Feed Forward Neural Network, Convolutional Neural Network, Long Short-Term Memory, and XGBoost models. We also explored model deployment on edge devices with TensorFlow Lite, achieving an average F1-score of 0.77 for occupancy detection and 0.62 in the transfer scenario. Our analysis identified critical features for occupancy detection.

Introduction

Occupancy data is crucial for various building energy services, such as model predictive control, demand management, or fault detection and diagnostics (Schweiger et al. 2020). Previous studies on occupancy-based control strategies have shown significant energy savings, reducing heating and cooling consumption by up to 15%, ventilation energy by up to 55%, and energy for lighting by up to 75% (Rueda et al. 2020). Occupancy detection approaches are classified into direct methods, which focus on accuracy but compromise privacy through vision or smartphone systems, and indirect methods that use environmental data (Jin et al. 2016). Indirect methods can be categorized into analytical, data-driven, and knowledge-based approaches (Rueda et al. 2020). Analytical methods mathematically model the occupant-environment interaction, knowledge-based methods use specific rules to estimate occupancy, and data-driven methods leverage machine learning (ML) on sensor data to identify occupancy patterns.

The most common features used in data-driven approaches are CO2, door/window open status (DW), energy consumption (E), light luminosity (L), motion detected by PIR sensors (M), barometric pressure (P), sound volume (S), relative humidity (RH), ambient temperature (T), desktop case temperature of computers (Tdc), and volatile organic compounds (VOC) in the air. Table 1 summarizes related work, listing the used features/sensors, underlying ML methods, survey sizes in terms of time, achieved performance, and target resolution.

While non-intrusive ML methods have proven well-suited for occupancy detection, scalability and transferability remain open. Obtaining high-quality datasets necessary for training these models is challenging and typically necessitates installing extra sensors, such as cameras, to establish a dependable ground truth. This can conflict with the non-intrusiveness target and raise privacy concerns. To mitigate these issues, we investigate the potential of transfer learning.

Edge ML aims to train and execute ML models on decentralized devices with constraint computational resources, which intends to efficiently use computational resources, to reduce network traffic and to be independent of the network connection Li et al. (2023). They divide edge ML into two main sub-categories: (i) edge inference, which covers technologies (e.g., model compression & approximation, and distributed inference) to deploy trained models. And (ii) edge learning, which covers technologies (e.g., transfer learning, and self-supervised learning) to develop and train models on edge devices.

Table 1: Related work applying data-driven algorithms to occupancy detection.

Authors	Feature Combination	Occupancy Information	Accuracy in %	Algorithm	Duration in days
Yang et al. (2014)	CO2, T, RH, L, M, S, DW	binary- and multi-class	93–97	FFNN	20
Yang et al. (2014)	CO2, T, RH, L, M, S, DW	binary- and multi-class	95–98	KNN	20
Akbar et al. (2015)	E	multi-class	94	KNN	14
Yang et al. (2014)	CO2, T, RH, L, M, S, DW	binary- and multi-class	95–98	SVM	20
Parise et al. (2019)	CO2, T, RH, M, S, P	binary-class	96	SVM	13
Candanedo et al. (2017)	CO2	binary-class	90	HMM	42
Ryu & Moon (2016)	CO2, E	prediction	93	HMM	7
Liu et al. (2016)	M	multi-class	81 - 97	HMM	-
Han et al. (2012)	CO2, RH, M	count	81	ARHMM	18
Ai et al. (2014)	CO2, T, RH	count	84	ARHMM	14
Adeogun et al. (2019)	CO2, T, RH, L, S, P, DW	multi-class	92	FFNN	4
Ekwevugbe et al. (2013)	CO2, T, RH, M, S, VOC, T_{dc}	count	75	FFNN	31
Kim et al. (2019)	T	count	84	LSTM	10
Mohammadabadi et al. (2022)	CO2, T, RH	binary-class	93	CNN-XGB	13
Sayed et al. (2023)	CO2, T, RH, L, M, S, P	binary-class	99	CNN	5

This paper contributes to the literature by:

- Comparing Feed Forward Neural Networks (FNN), Convolutional Neural Networks (CNN), Long Short Term Memory (LSTM), and XGBoost models for occupancy detection.
- Analysing the potential of transfer learning.
- Analysing the possibilities and restrictions of edge inference.
- Providing a sensor concept for occupancy detection in offices.
- Promoting open science: Open access to the data of a three-month study in two offices and to the code of the models.

Method

For our experiments, we formulate the task of occupancy detection as a multi-class classification problem. We define our occupancy classes as empty, low-occupancy (1-2), and high-occupancy (>3). We limit our model selection to ML techniques that offer native support of transfer learning. We evaluate and compare the performance of FFNN, CNN, LSTM and XGBoost models. Two types of input schemes are investigated: Tabular (1-dimensional) and sequential (2-dimensional) where each feature in the feature vector consists of a series of values in chronological order. We did not perform hyperparameter tuning and selected our model parameters, size, and architecture based on the existing literature and established rules of thumb (Heaton 2008). Table 2 and 3 provide an overview of the models used for tabular and sequential approaches.

For our transfer learning experiment, we train our models on the data from one room (learning rate $\eta_1 = 0.001$ for 20 epochs) and then transfer the model to a different room (learning rate $\eta_2 = 200^{-1} * \eta_1$ for 30 epochs). A smaller learning rate is necessary to adapt the model to the new environment while retaining the previously learned knowledge. All hidden layers are set to trainable.

We conducted a field experiment on a real-world office building in Graz, Austria. We installed sensors in two separate office rooms within the same building, differing in their size in terms of floor space and the number of contained seats (see Figure 1 and 2). Data from room A is used to develop ML models, whereas data from room B is used to evaluate the transfer learning scenario. The sensor data is recorded in five-minute intervals for room A from 12 September to 20 December 2023 and room B from 16 November 2023 to 20 December 2023.

Table 2: Model architectures and configurations used for tabular approach.

Model	#Hidden Layers	#Units Per Layer	Activation Function
[1]	[1]	[1]	[1]
FFNN_0	1	6	Sigmoid
FFNN_1	1	10	Sigmoid
FFNN_2	1	16	Sigmoid
FFNN_3	2	6:4	Sigmoid
FFNN_4	2	12:6	Sigmoid
FFNN_5	2	18:18	Sigmoid

Table 3: Model architectures and configurations used for sequential approach.

Model	#Hidden Layers	#Units Per Layer	Activation Function
[1]	[1]	[1]	[1]
FFNN_0	2	24:24	ReLu
FFNN_1	3	32:32:32	ReLu
1D-CNN	3	24:24:24	ReLu
2D-CNN	5	32:32:32:32:32	ReLu
LSTM_0	2	24:24	ReLu
LSTM_1	3	32:32:32	ReLu

Table 4: Overview of base features.

Base Features			
Name	Unit	Range	Accuracy
Date + Time	[1]	yyyy:mm:dd hh:mm	-
Motion Counter	[1]	0-255	-
Temperature	$[°C]$	0-50	± 0.2
Relative Humidity	[%]	0-85	± 2
Light	$[lux]$	4-2000	± 10
CO2 Conc.	$[ppm]$	0-2000	± 50
Average Loudness	$[dBspl]$	35-70	± 5
Peak Loudness	$[dBspl]$	65-99	± 5
#Open Windows	[1]	0-2	-
#Open Doors	[1]	0-1	-
IR-based Occupancy	[1]	0 = Unocc. 1 = Pending 2 = Occupied	-

The installed sensors capture ten variables: Open doors, open windows, motion, light, relative humidity, CO2 concentration, temperature, IR-based occupancy, peak sound level, and average sound level (Table 4). In addition, a video camera was installed to obtain a reliable ground truth.

Figure 1: Office building from the outside, highlighted room A on the right, and Room B on the left. Mounted door sensor and video camera.

Images captured by the camera, which are used to utilize occupancy ground truth, are fetched directly from the micro SD card. All other installed sensors send data via LoRa to a Kerlink Wirnet iFemtoCell LoRaWAN gateway. LoRa data frames are forwarded via MQTT over the Local Area Network to the edge device, on which the open source network server, ChirpStack (ChirpStack 2023), operates. Data is saved in an InfluxDB database, which is accessed from the server for training models in Python using TensorFlow and Scikit-learn libraries. The final ML model is then deployed with TensorFlow Lite to the edge device for inference on-premise. A Raspberry Pi 4 model B with 8GB RAM and 256GB SSD is used as edge device running on Ubuntu 22.04 LTS.

A total of 28.000 samples are collected in room A. An 80/20 static split strategy without shuffling is performed to create our training and test data sets. The training data is then used for five-fold time-series cross-validation of the tabular and sequential model set, whereas the test set is used to evaluate the final selected model. Recall, precision, F1, and accuracy are used as performance metrics for evaluation. The offices are only occupied from Monday till Friday during the day. This results in the dataset being imbalanced in terms of class distribution. Therefore, we apply a downsampling strategy, dropping a random selection of 75% percent of the empty samples within the training data to balance out the class distribution. This results in the follow-

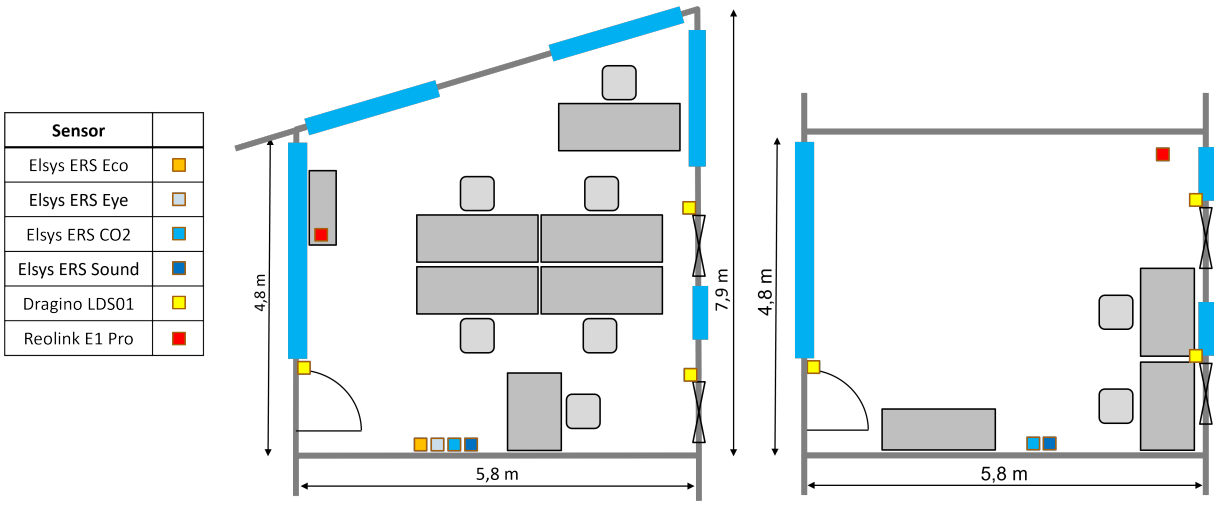

Figure 2: Sensor placement and layouts for Room A and B. North-west is up.

ing class distribution: Approximately 3.500 empty, 3.100 low and 2.300 high occupancy samples.

A total of 10.000 samples were collected in Room B. As this room only has two workplaces, the number of samples representing high occupancy is smaller than in room A. A 40-60 split is applied to separate the collected data in a fine-tuning and test set. This split ratio is chosen to have at least some high occupancy samples in both splits. No stratified split is applied to simulate a real transfer learning use case. To balance out the fine-tuning set, 70% of empty samples are randomly dropped. Trial and error showed that adding synthetic samples in the training set using SMOTE (Chawla et al. (2002) improves the ability to detect high occupancy. This increases the number of high occupancy samples from 16 to 63. Around 1200 samples are left in the training set after up- and downsampling. No samples are dropped or added to the test set, which features approximately 4000 samples in total.

Results and Discussion

Knowledge discovery

Analysing the collected data from rooms A and B (Table 5) shows that CO2 concentration, average sound level and peak sound level are distributed similarly in both rooms. Whereas, light values are significantly lower in room B. This could be due to the fact that room B has no south-west facing windows and that the data were collected in November and December. A significant difference can be seen for the motion counter. Room B shows a higher fluctuation as well as a higher maximum value. This is due to the shorter distance between the PIR sensor and the workplaces in Room B. The average number of occupants in room A and B is very similar, although room A offers six workplaces and room B two. Overall, both rooms have similar environmental conditions.

The Pearson correlation coefficients between features and the number of occupants were calculated to analyse their statistical relationships: CO2 concentration 72%, light 70%, IR-based occupancy 63%, average sound level 60%, peak sound level 56%, open doors 48%, motion 41%, open windows 37%, temperature 18% and relative humidity 13%. These findings support the assumption that CO2 concentration is the most important indicator. In addition, open doors, windows, and movement also appear to be important indicators, while humidity and temperature correlate weakly with the number of occupants.

Window lengths between 5 and 60 minutes (equal to 1 to 12 consecutive samples) are applied. We evaluate and compare the model's performance based on these different window lengths. Figure 3 shows the mean F1 cross-validation scores for varying window lengths of the sequential model set. The performance generally increases proportionally to the window length for sequential and tabular models. FFNN models outperform the others most of the time. Only at window lengths of 1 and 12, CNN1D and both LSTMs achieve better scores.

Model selection

Table 6 shows the classification performance of our tabular and sequential models. The absolute performance variance between the different sequential models is higher than the performance

Table 5: Environmental conditions and #occupants of room A and B.

		Room A				Room B			
Feature	Unit	Mean	Std	Min	Max	Mean	Std	Min	Max
CO2	$[ppm]$	543	150	380	1370	566	116	416	1361
light	$[lux]$	160	261	0	5734	73	106	0	592
average sound level	$[dBspl]$	37	5	31	63	36	5	31	66
peak sound level	$[dBspl]$	60	4	59	97	60	4	59	94
motion	[1]	0.6	2.2	0	22	1.0	3.3	0	35
humidity	[%]	36	13	14	64	24	4	16	35
temperature	$[°C]$	23.1	1.1	19.3	27.7	21.8	0.6	20.5	23.6
#occupants	[1]	0.5	1.1	0	7	0.3	0.7	0	9

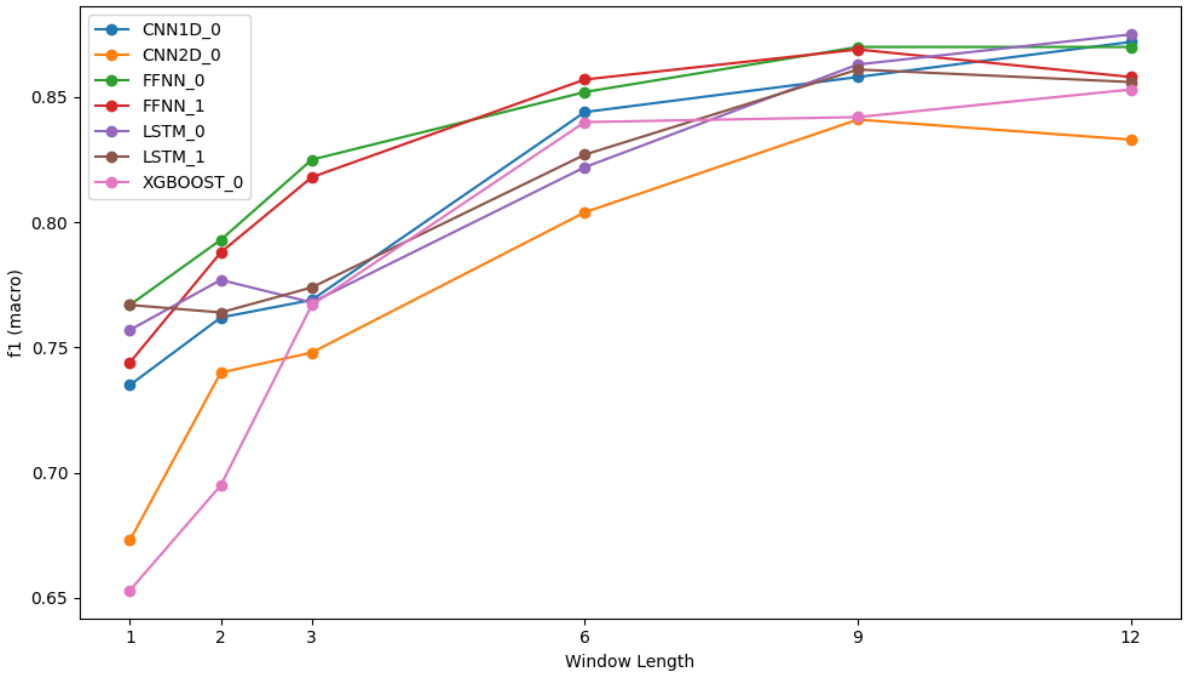

Figure 3: F1 classification performance of our models for varying window lengths.

variance of the tabular models.

The tabular FFNN models outperform the tabular XGBoost models noticeably. The best performing tabular model, FFNN_5, consists of two hidden layers with each 18 neurons, performing best at a window length of six.

The sequential models all show slightly higher recall than precision scores. The opposite can be observed for the tabular models. Generally, the sequential models reach slightly better validation scores than the tabular model.

Feature importance analysis

Next, we performed feature importance analysis using SHAP and XGBoost importance vectors. SMOTE and SHAP (Lundberg (2018)) libraries do not support three-dimensional input data per default. Therefore, the tabular approach is chosen to analyse the feature importance of FFNN_5 as the best performing tabular model.

Figure 4 shows the SHAP values of each feature, which describe the average impact on the model output. The output of the model is mainly influenced by the CO2 concentration, whether the doors are open, the average sound level and the peak sound level. Temperature, motion, relative humidity and IR-based occupancy have the least impact according to the SHAP analysis.

Analysing the feature gain values of the XGBoost model shows that temperature, relative humidity, and motion are almost irrelevant to the prediction result. IR-based occupancy is surprisingly important for the XGBoost model. CO2 concentration is

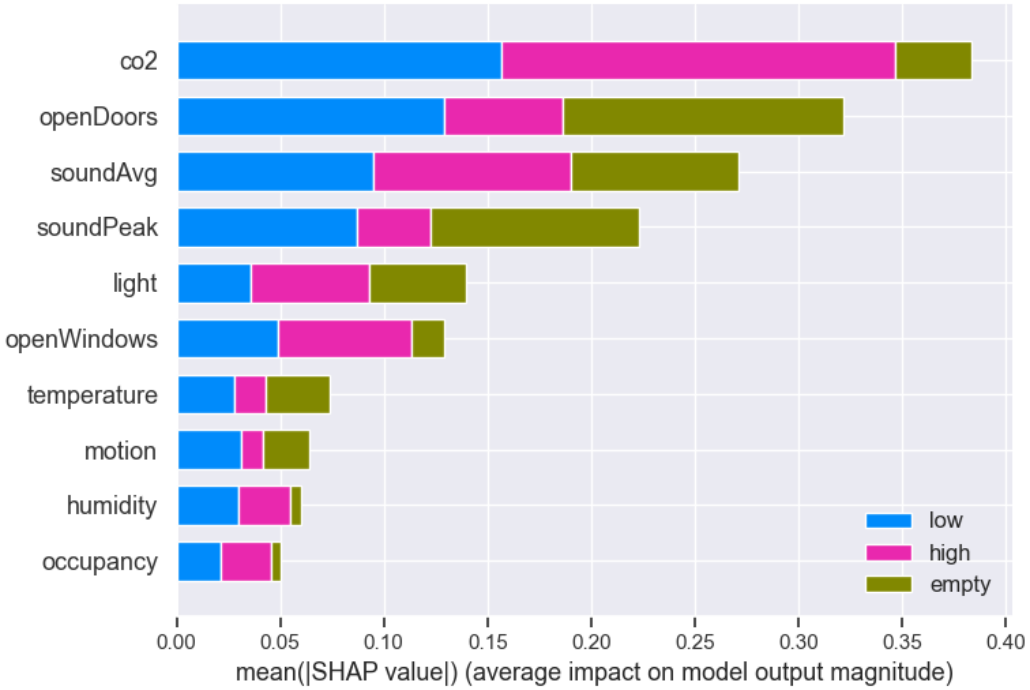

Figure 4: Mean SHAP values showing the average feature impact on FFNN_5 performance.

Table 6: Model scores from cross-validation.

Model	Accuracy	Precision	Recall	F1
Tabular Models				
FFNN_0	0.849	0.840	0.837	0.834
FFNN_1	0.847	0.839	0.838	0.831
FFNN_2	0.848	0.842	0.836	0.833
FFNN_3	0.849	0.847	0.842	0.835
FFNN_4	0.846	0.845	0.839	0.831
FFNN_5	0.855	0.848	0.843	0.841
XGBoost	0.813	0.795	0.807	0.790
Sequential Models				
CNN1D	0.858	0.848	0.849	0.844
CNN2D	0.826	0.812	0.815	0.804
FFNN_0	0.867	0.856	0.864	0.852
FFNN_1	0.873	0.860	0.875	0.857
LSTM_0	0.839	0.829	0.838	0.822
LSTM_1	0.844	0.830	0.829	0.827
XGBoost	0.856	0.847	0.855	0.840

less important to XGBoost models, whereas sound peak level is the most important feature. Based on these findings, the following reduced feature set is selected for the following experiments: CO2 concentration, light, average sound level, peak sound level and, number of open doors.

Cross-validation of the tabular models using the reduced feature set shows that FFNN_4 with twelve and six hidden units per layer delivers the best results: Accuracy 0.85, precision 0.851, recall 0.849, and F1 0.837 FFNN_4. It can be seen that the performance changes only marginally despite the elimination of half of the original features. Precision and recall scores even increased compared to FFNN_5 using all features.

Transfer learning

Before fine-tuning, FFNN_4 was able to detect high occupancy, but struggled to detect low occupancy (see Figure 5, left) in room A. After adapting the model to room B, low occupancy is detected very accurately and the model struggles to identify high occupancy5, right). This is likely due to the low number of high occupancy samples in room B. The increasing number of high occupancy samples (=minority class) through SMOTE improved the detection performance of high occupancy. Fine-tuning optimized the model more on detecting empty and low occupancy due to the sparse number of high occupancy samples. The performance improvement for detecting high occupancy by adding synthetic samples of the minority class to the fine-tuning set further demonstrates, that the initial number of high occupancy samples

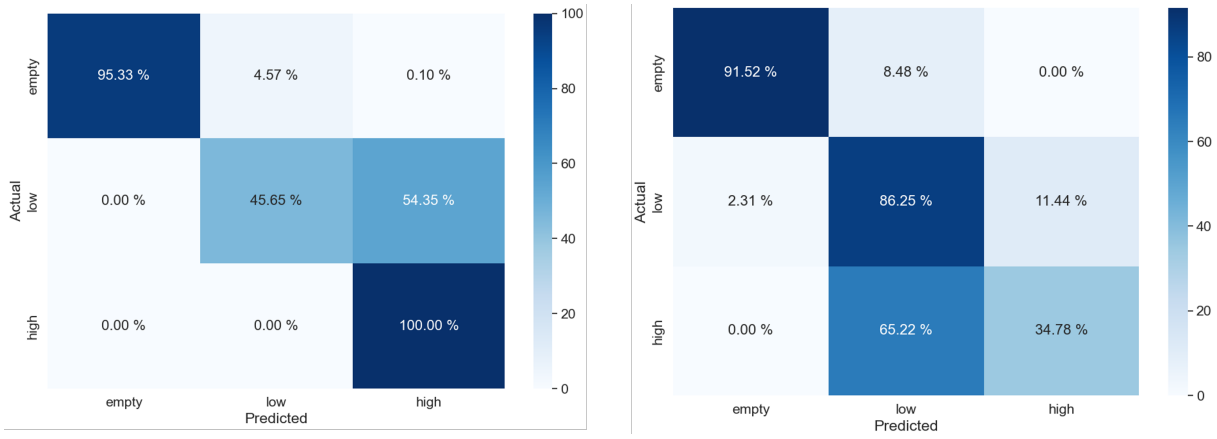

Figure 5: Confusion matrix of FFNN_4 for room A (left) and B (right).

is not sufficient.

Model deployment The models were deployed with TensorFLow Lite to the Raspberry Pi without applying any further model compression technique. This shows that edge devices with less computational resources than the Raspberry Pi 4 (ARM Cortex-A72 running at 1,5GHz and 4GB RAM) are viable options as hardware to perform edge inference.

Conclusion

This paper compares various neural network architectures and XGBoost models for occupancy detection in a real environment and evaluates the transferability of the models using two separate offices. We found that models using inputs in the form of sequences of past data perform slightly better than the corresponding tabular models utilizing only single value representations (mean) of past data. CO2 concentration, light, average sound level, peak sound level, and open door information are the most important features and are therefore proposed for a minimal solution.

For room A, empty, low, and high occupancy is detected with an accuracy of 95%, 41% and 100% by a two-layer FFNN using the tabular approach with the top features as input (window length of 30 minutes). Only a marginal performance loss occurs, caused by dropping the least relevant features. The same model can detect empty, low and high occupancy in room B with an accuracy of 92%, 86%, and 35% after adapting the model through transfer learning.

Despite our small sample size of only two rooms, our results show that transfer learning is a promising direction toward greater scalability. Furthermore, we demonstrated the viability of data processing alongside inference of neural network-based occupancy detection models on computationally weak edge devices and provide a minimal sensor concept required for occupancy detection. In future work, we will perform larger-scale studies incorporating measurements from several rooms with more diverse class distributions to allow a more detailed analysis of transfer learning and to bring the model learning procedure closer to the edge.

Data Availability

The data collected within this study and all source code of our models and evaluations are made publicly available on Zenodo Siegl et al. (2024).

Acknowledgement

The reported research has been conducted within the project OctoAI (893494) which received funding in the framework of" Stadt der Zukunft 9. Ausschreibung", a research and technology program of the Federal Ministry for Climate Action, Environment, Energy, Mobility, Innovation and Technology.

References

Adeogun, R., Rodriguez, I., Razzaghpour, M., Berardinelli, G., Christensen, P. H. & Mogensen, P. E. (2019), Indoor Occupancy Detection and Estimation using Machine Learning and Measurements from an IoT LoRa-based Monitoring System, *in* '2019 Global IoT Summit (GIoTS)', pp. 1–5.

Ai, B., Fan, Z. & Gao, R. X. (2014), Occupancy estimation for smart buildings by an auto-regressive hidden Markov model, *in* '2014 American Control Conference', pp. 2234–2239.

Akbar, A., Nati, M., Carrez, F. & Moessner, K. (2015), Contextual occupancy detection for smart office by pattern recognition of electricity consumption data, *in* '2015 IEEE International Conference on Communications (ICC)', pp. 561–566.

Candanedo, L. M., Feldheim, V. & Deramaix, D. (2017), 'A methodology based on Hidden Markov Models for occupancy detection and a case study in a low energy residential building', **148**, 327–341.

Chawla, N. V., Bowyer, K. W., Hall, L. O. & Kegelmeyer, W. P. (2002), 'SMOTE: Synthetic Minority Over-sampling Technique', **16**, 321–357.

ChirpStack (2023), 'ChirpStack open-source LoRaWAN Network Server'.
URL: *https://www.chirpstack.io/*

Ekwevugbe, T., Brown, N., Pakka, V. & Fan, D. (2013), Real-time building occupancy sensing using neural-network based sensor network, *in* '2013 7th IEEE International Conference on Digital Ecosystems and Technologies (DEST)', pp. 114–119.

Han, Z., Gao, R. X. & Fan, Z. (2012), Occupancy and indoor environment quality sensing for smart buildings, *in* '2012 IEEE International Instrumentation and Measurement Technology Conference Proceedings', pp. 882–887.

Heaton, J. (2008), *Introduction to Neural Networks for Java*, 2 edn, Heaton Research, Inc.

Jin, M., Bekiaris-Liberis, N., Weekly, K., Spanos, C. J. & Bayen, A. M. (2016), 'Occupancy detection via environmental sensing', *IEEE Transactions on Automation Science and Engineering* **15**(2), 443–455.

Kim, S., Kang, S., Ryu, K. R. & Song, G. (2019), 'Real-time occupancy prediction in a large exhibition hall using deep learning approach', **199**, 216–222.

Li, W., Hacid, H., Almazrouei, E. & Debbah, M. (2023), 'A Comprehensive Review and a Taxonomy of Edge Machine Learning: Requirements, Paradigms, and Techniques', pp. 729–786.

Liu, P., Nguang, S.-K. & Partridge, A. (2016), 'Occupancy Inference Using Pyroelectric Infrared Sensors Through Hidden Markov Models', **16**(4), 1062–1068.

Lundberg, S. (2018), 'Welcome to the SHAP Documentation — SHAP latest documentation'.
URL: *https://shap-lrjball.readthedocs.io/en/latest/index.html*

Mohammadabadi, A., Rahnama, S. & Afshari, A. (2022), 'Indoor Occupancy Detection Based on Environmental Data Using CNN-XGboost Model: Experimental Validation in a Residential Building', **14**(21), 14644.

Parise, A., Manso-Callejo, M. A., Cao, H., Mendonca, M., Kohli, H. & Wachowicz, M. (2019), Indoor Occupancy Prediction using an IoT Platform, *in* '2019 Sixth International Conference on Internet of Things: Systems, Management and Security (IOTSMS)', pp. 26–31.

Rueda, L., Agbossou, K., Cardenas, A., Henao, N. & Kelouwani, S. (2020), 'A comprehensive review of approaches to building occupancy detection', *Building and Environment* **180**, 106966.

Ryu, S. H. & Moon, H. J. (2016), 'Development of an occupancy prediction model using indoor environmental data based on machine learning techniques', **107**, 1–9.

Sayed, A. N., Bensaali, F., Himeur, Y. & Houchati, M. (2023), 'Edge-Based Real-Time Occupancy Detection System through a Non-Intrusive Sensing System', **16**(5), 2388.

Schweiger, G., Eckerstorfer, L. V., Hafner, I., Fleischhacker, A., Radl, J., Glock, B., Wastian, M., Rößler, M., Lettner, G., Popper, N. et al. (2020), 'Active consumer participation in smart energy systems', *Energy and Buildings* **227**, 110359.

Siegl, C., Hirsch, T., Kohl, T., Wotawa, F. & Schweiger, G. (2024), 'Data and Sourcecode from: Neural Network-based Occupancy Detection on the Edge', Zenodo.
URL: *https://doi.org/10.5281/zenodo.11573783*

Yang, Z., Li, N., Becerik-Gerber, B. & Orosz, M. (2014), 'A systematic approach to occupancy modeling in ambient sensor-rich buildings', **90**(8), 960–977.

BauSIM 2024 in Wien
23. September – 26. September

Performance Evaluation of Decentralized Split Unit Air-to-air Heat Pumps

Georgios Dermentzis[1], Anastasios Tsaris[1,2], William Monteleone[1], Fabian Ochs[1],

1 Unit of Energy Efficient Buildings,University of Innsbruck, Austria, E-Mail: Georgios.Dermentzis@uibk.ac.at

2 Department of Mechanical Engineering, University of Thessaly, Greece, e-mail: atsaris@uth.gr

Abstract

A holistic evaluation is performed to investigate the energy performance of air-to-air split units (also called air-conditioning units), including laboratory measurements and steady-state simulations of the refrigerant cycle. Several aspects are considered, such as indoor fan speed, varying compressor frequency, defrost and “on/off” cycles. The laboratory measurements include steady-state test points as well as dynamic operation.

The measured Coefficient of Performance (COP) varies from 1.8 to 4.9, and the maximum measured heating capacity was 2.5 kW, close to the nominal value of 2.7 kW. The measured reduction due to the defrost cycle was up to 14% in the heating capacity and 16% in the COP. It was also found that the indoor air flows were on average 40% less than the ones listed in the datasheet.

Introduction

Split air-to-air heat pumps could be a cost-effective decentralized solution for space heating (and optional cooling) in central European climates (Konrad and MacDonald 2023) in the case of renovation of multi-apartment buildings targeting low heating loads and decarbonization (Eguiarte et al. 2020),(Carroll et al. 2020). Their benefits are low costs and low space requirements. From an architectural and aesthetic point of view, the split unit might not be the best option, especially in central Europe, where people are not used to them and for example in case of many outdoor units installed in a facade. In addition, the operation in silent mode (lowest indoor fan speed) is suggested due to sound emissions (Feist 2022).

Comparing the in-situ performance of heat pumps versus design is important for quality assurance. In a case study of an installed air-to-water heat pump, the measured seasonal performance factor was 40% lower than the calculated (Hegarty et al. 2022). Although these split units are commonly used, for example in Mediterranean countries mainly for cooling, their energy performance is hard to be evaluated (Li et al. 2024), both in laboratory measurements and in real operation conditions, due to their construction and the difficulty in accurate measurement of the indoor air flow.

In this study, an air-to-air split unit heat pump is measured in the laboratory, based on a developed measuring methodology (Feist 2022). The performance of this heat pump is evaluated in detail and several steady-state operation points are derived. The measured results are used to calibrate a refrigerant cycle model, which, once validated, may expand the test points for a complete performance map. A related question is the identification of the minimum required test points for deriving the performance map with the refrigerant cycle model.

Methodology

An air-to-air split unit with a nominal heating capacity of 2.70 kW (at an outdoor temperature of 6 °C) was measured in the laboratory and evaluated concerning capacity, consumption, and performance. The results are further used to calibrate a steady-state refrigerant cycle model.

Laboratory equipment

Figure 1 presents a scheme of the test rig, including the measuring points and Figure 2 a photo of the laboratory device (Feist 2022). The inlet indoor air temperature is measured at the upper grid as the average of the grid with thermocouple sensors. Similarly, the outlet indoor air temperature is measured at the lower grid. A set of fans is operating at the lower grid to ensure that the heated air exits at atmospheric pressure (compensation for the additional pressure drop due to the box). The outlet air is directed to the calibration duct so that the volume flow of the indoor unit is measured continuously during operation. The electricity consumption of the unit as well as the outdoor inlet and outlet air temperatures are measured.

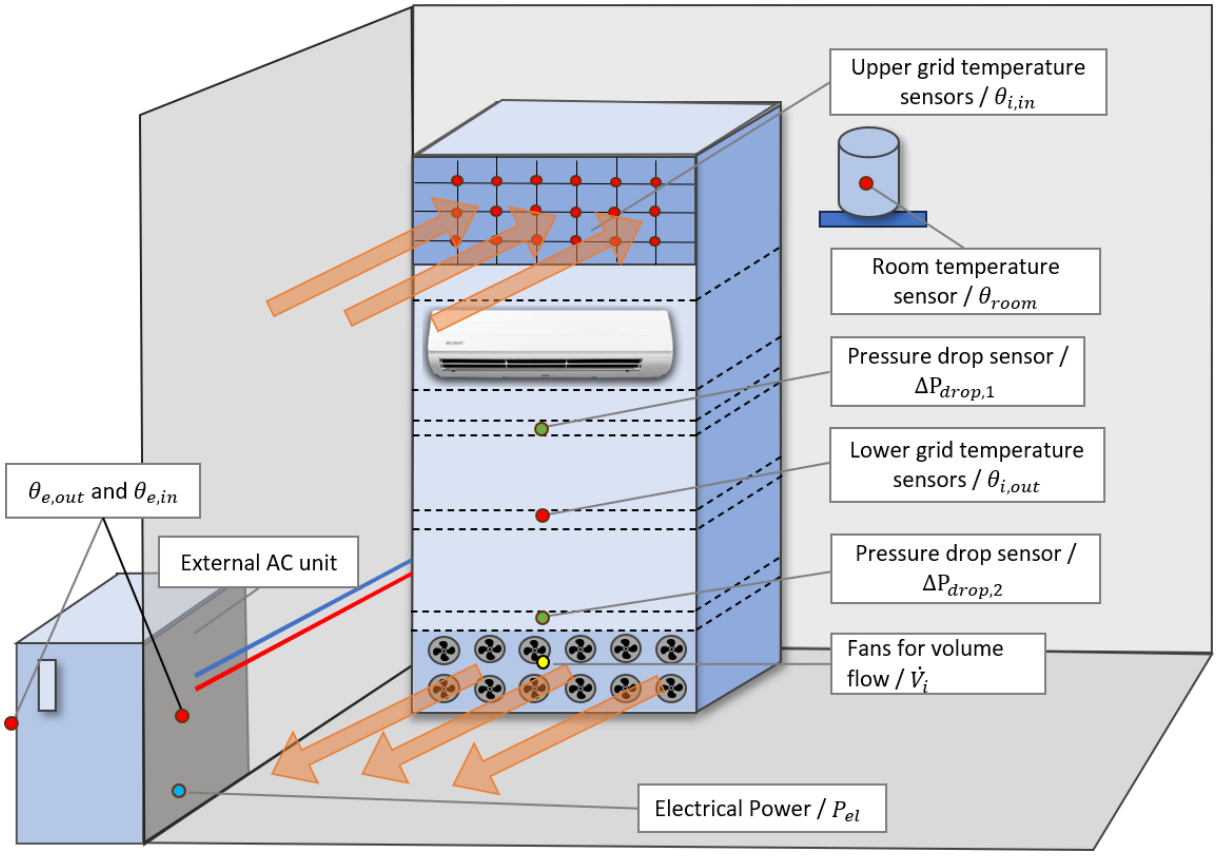

Figure 1: Scheme of the test rig and the monitoring points.

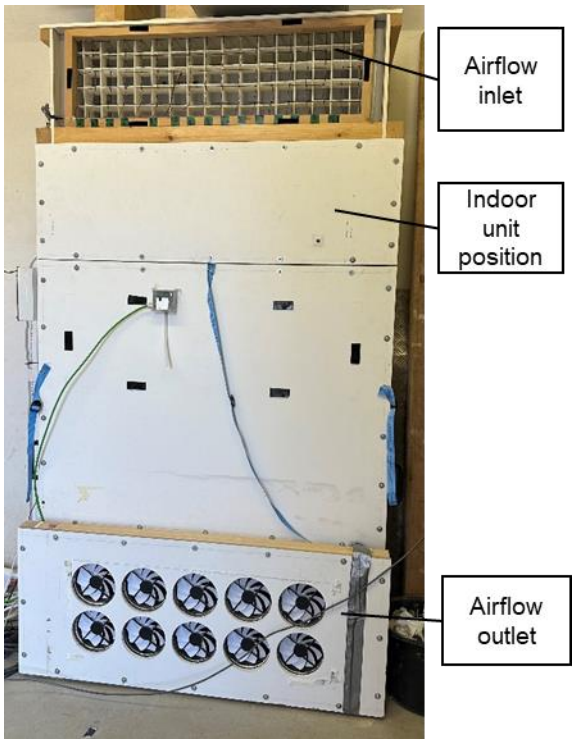

Figure 2: Photo of the measuring device.

Thus, the condenser heating capacity is calculated based on the following equation:

$$\dot{Q}_{cond} = \dot{V}_i \cdot \rho \cdot C_p \cdot (\vartheta_{i,out} - \vartheta_{i,in}) \quad (1)$$

$\dot{Q}_{cond}$: Heat Capacity of the condenser; $\dot{V}_i$: volume airflow of the indoor unit; ρ : density of air; C_p: specific heat capacity of air; $\vartheta_{i,out}$: outlet temperature of the indoor unit; $\vartheta_{i,in}$: inlet temperature of the indoor unit.

Volume flow calibration

Since the accuracy of the volume flow plays an important role in the evaluation of the thermal capacity, it was calibrated using an external (already calibrated) duct that was connected to the bottom outlet of the fans (see Figure 3), similar to Ref. (Konrad and MacDonald 2023). Figure 4 presents the volume flow results, including the values from the manufacturer's datasheet. A correlation fitting curve was introduced to calculate the indoor volume flow based on the measured pressure difference. The values from the manufacturer datasheet are significantly higher (up to 1.65 times higher) than the measured ones. Similar behaviors and differences to the datasheet are also found in literature (Williamson and Aldrich 2015).

Figure 3: Photo of the duct used for the calibration of the indoor volume flow.

$$\dot{V}_i = 107.3 \cdot \Delta P_{flow}{}^{0.5} \quad (2)$$

$\dot{V}_i$: volume airflow of the indoor unit, ΔP_{flow}: Measured pressure drop of the indoor air flow.

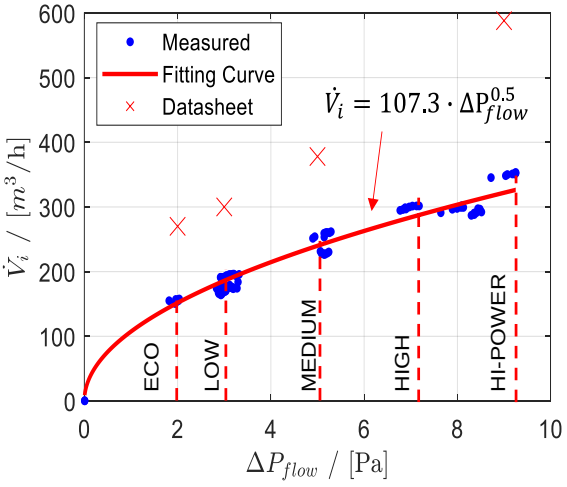

Figure 4: Calibration of the indoor volume flow – measured points and derived curve - including values from the datasheet.

Measuring method

The goal was to measure both steady-state and dynamic behavior of the unit. The first is to develop a performance map for a simulation model (both simple for design and/or detailed for dynamic simulation), and the second is to consider the dynamic effects and include them at a later stage in a dynamic simulation model. Thus, the aim was to measure many operation conditions and derive a performance map that can later be extended using the refrigerant cycle model and by that to estimate the minimum operation points that are required to construct a realistic performance map of the unit.

The source (ambient) temperature could not be fixed or controlled since the outdoor unit is located outdoors. The controller of the unit is not set to a fixed compressor speed as in standards such as EN 14825 (European Standards 2022), but it was operating as in a real environment. The unit is measured at various indoor fan speeds i.e., low, medium, high, and auto, and various operation targets, i.e., with an opened external door to force the unit to operate at maximum compressor speed or with an additional indoor heater to operate in on/off mode.

An algorithm was developed in MATLAB to automatically find steady-state periods in which the measured variables remain almost constant, and each one of these periods represents a measured test point.

Dynamic measurements are shown in Figure 5, including examples of “steady-state” periods, i.e., the electric power, heating capacity, and source and sink temperatures are on a plateau (black squares in Figure 5). To account for the steady-state test point, the measured parameters should not exceed the predefined ranges for a minimum duration of 15 minutes. The ranges are set to ±10% in the case of electric power and heating capacity and 0.5 K for the measured temperatures.

It is also noted that at the beginning of operation, the unit always operates with maximum compressor speed, so as to be heated up as fast as possible, and then the speed is controlled based on the indoor requirements, e.g. the set point temperature as shown in Figure 5. It has to be noted, that in the measurements, it seems that the setpoint temperature is not reached, however, there is a difference (or shift) between the indoor room temperature and what the unit measures itself, since what the unit measures is strongly influenced (during operation) by the heat loss of the indoor unit, and this effect is further increased by the use of the “measuring box”.

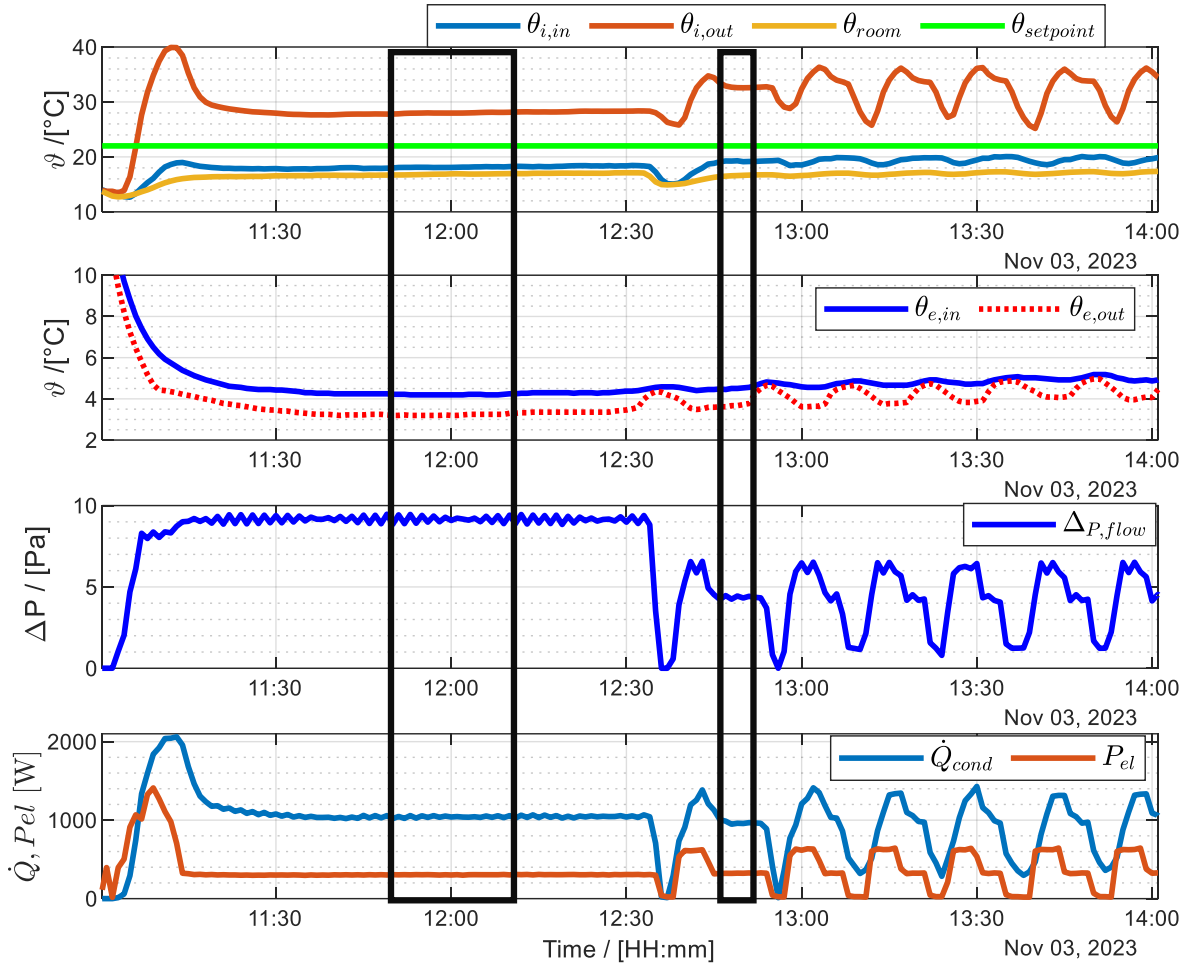

Figure 5: Operation of the split unit heat pump and identified steady-state test points.

COP evaluation

The COP is evaluated also through the Carnot cycle and compared to the measured points. The theoretical COP of the Carnot cycle is calculated for every point as follows:

$$COP_{carnot} = \frac{\vartheta_{i,out}+273.15}{\vartheta_{i,out} - \vartheta_{e,in}} \quad (3)$$

$\mathrm{COP_{carnot}}$: COP Carnot; $\vartheta_{\mathrm{i,out}}$: outlet temperature of the indoor unit; $\vartheta_{\mathrm{e,in}}$: inlet temperature of the outdoor unit.

The Carnot performance factor is then evaluated:

$$\eta_{carnot} = \frac{COP}{COP_{carnot}} \quad (4)$$

η_{carnot}: Carnot performance factor; COP: Coefficient of Performance.

Refrigerant cycle model

The steady-state refrigerant cycle model was developed in MATLAB (Monteleone et al. 2024). Inputs to the model were the inlet outdoor (source) and outlet indoor (sink) temperatures, and the air volume flows of indoor and outdoor units. The main output parameters to evaluate the model are the thermal capacity of the condenser and the electric power of the compressor. The parameters varied to calibrate the model are presented in Table 1. As expected, the speed of the compressor has the highest impact on the outputs of the model.

Table 1: Varying parameters to calibrate the model to the measured test points.

Inputs	Unit
Compressor speed	RPM
Isentropic efficiency	
Volumetric Efficiency	
Evaporator $\Delta T_{superheating}$	K
Pinch point temperature difference in the evaporator	K

Results and discussion

Heating capacity

The heating capacity of the derived measurement points is depicted in Figure 6, together with the data of the manufacturer. The heating capacity from the manufacturer's datasheet is close to the measured ones around 0 °C outdoor temperature. This is another indication that the volume flows on the datasheet are overestimated compared to the real ones, since the heating capacities between measurements and datasheet are comparable. The datasheet's values are slightly lower than the laboratory measurements around 0 °C, since defrosting is included, while in the measurements is not.

At the range from 10 °C to 12 °C, the measured points are not at maximum compressor speed, even though the set point temperature was not approached. In fact, there are measurements with an opened external door and a set point of 30 °C, in which, the compressor automatically reduced the speed after the first 18 minutes of operation without fulfilling the desired temperature needs (see also Figure 5). Thus, in the case of measurements with "locked" speed (e.g., from the datasheet), high capacity can be reached, but that is not the case in real operation. In other words, the heating capacity of the split unit during operation is less than the one reported in datasheets. This is suggested to be considered during design.

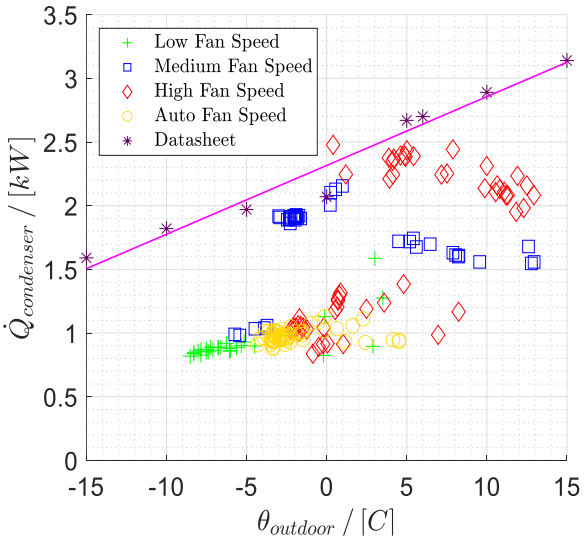

Figure 6: Heating capacity of the heat pump - measured test points and datasheet values for different indoor fan speed modes.

Figure 7 shows that, for a constant indoor fan speed, the heating capacity correlates well with the difference between the set point and the room temperature. This can be considered in the modeling of the control system of the split units in dynamic simulations.

Remark: The room temperature is different from the temperature measured by the unit as a room temperature, since it is strongly influenced by the operation of the unit due to heat losses of the unit and since it is inside the measuring box. The high temperature difference is due to the "open external door" aiming to reach maximum compressor speed.

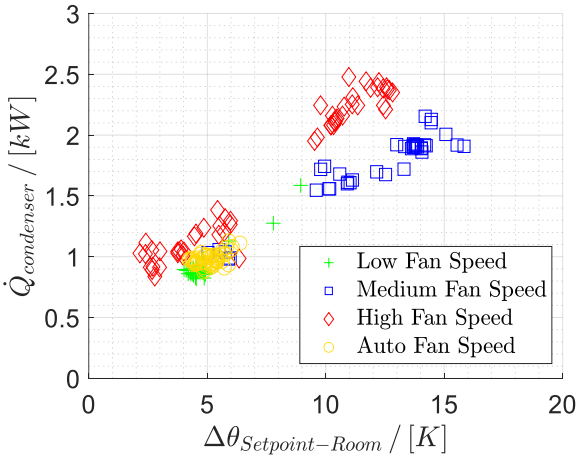

Figure 7: Heating capacity of the unit versus temperature difference between the set point and the room temperature for different indoor fan speed modes.

COP

Figure 8 shows the COP of the measured points versus the temperature difference between the sink and the source, i.e., the outlet temperature of the indoor unit and the outdoor temperature. A good correlation can be observed, with the COP varying from 1.8 up to 4.9. In the datasheet, a COP of 4.3 is mentioned, but without any temperature conditions. The largest COP is observed at low compressor speeds. Those results shows reduced performance in operation versus values in datasheet, showing the need for improved measuring/certifying methods for such systems.

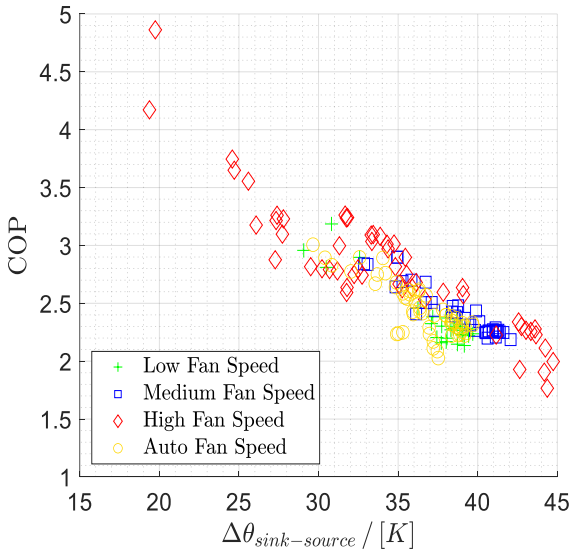

Figure 8: COP of the measured test points versus the temperature difference between sink (indoor outlet) and source (outdoor inlet) for different indoor fan speed modes.

The average Carnot performance factor (see Equation 4) of the measurement points is 0.29, with a minimum of 0.25 and a maximum of 0.32. In Figure 9, four curves are displayed calculated with the average Carnot performance factor (see Equations 3 and 4) for four different indoor outlet (sink) temperatures. Almost all the measured points lie between the curves. The minimum and maximum measured indoor outlet temperatures are 26.4 °C and 50.5 °C, respectively. From those results, it seems that to model the split unit with the Carnot performance factor method could be an acceptable simplified approximation. This can also be observed in Figure 8, since the COP is well correlated to the temperature difference between the sink (indoor outlet) and the source (outdoor inlet). However, there are still deviations. For example, at a temperature difference of 35 K, the COP varies from 2.1 up to 2.9, while with the Carnot method, between 2.3 and 2.4. Those results prove that the Carnot method can be used as a simple approach i.e., for calculation tools for engineers and planners, and that the use of source inlet and sink outlet temperatures in the Carnot method is recommended.

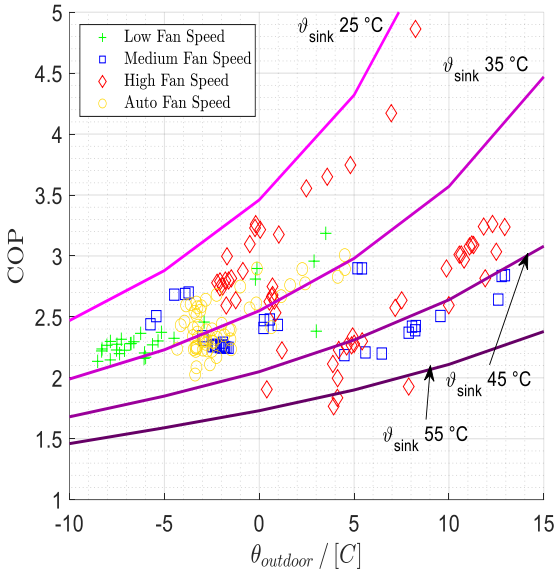

Figure 9: COP of the measured test points and curves calculated based on Carnot performance factor (Equation 4) for different sink temperature (outlet of indoor unit).

Electric power

The electric power is correlated to the outlet temperature of the indoor unit, depending also on the compressor speed, as shown in Figure 10. Similar findings are observed in Figure 11. The minimum and maximum power consumption are 240 W and 1300 W, respectively.

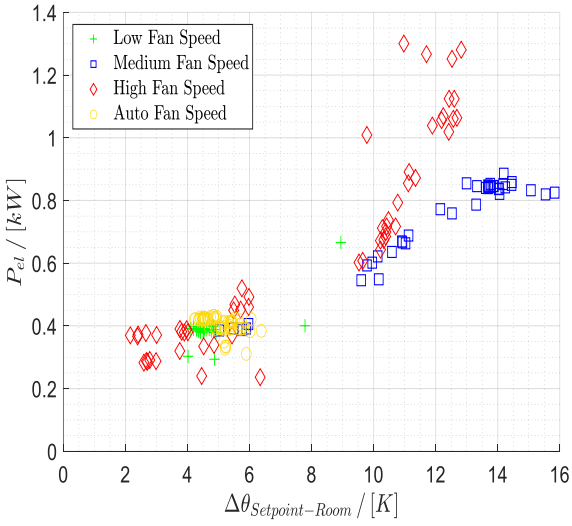

Figure 10: Measured electric total power versus temperature difference between the set point and the room temperature for different indoor fan speed modes.

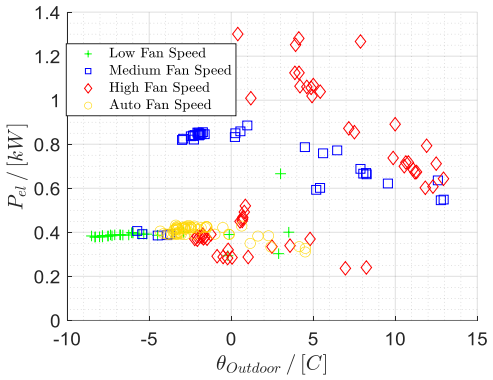

Figure 11: Measured electric total power versus outdoor temperature for different indoor fan speed modes.

Defrosting operation

Defrosting cycles are also investigated, as shown in Figure 12. The measurement point starts at 07:29 and stops at the end of the defrost cycle at 09:18. Figure 13 shows the impact of the defrost cycle on heating capacity and COP in relation to the ratio of the defrosting cycle duration and the complete test point duration, including defrosting (see Figure 12). The reduction due to defrosting varies from 2% up to 16% for the COP and from 2% up to 14% for the heating capacity. Similar to the datasheet, the peak reduction of the heating capacity due to defrosting is 14% at 0 °C (Guo et al. 2008).

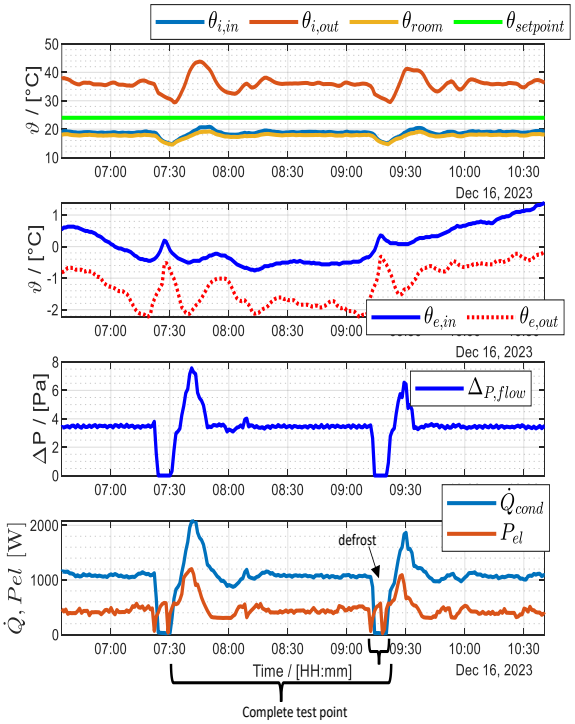

Figure 12:. Laboratory measurements including defrost cycles (at 07:22 and 09:12).

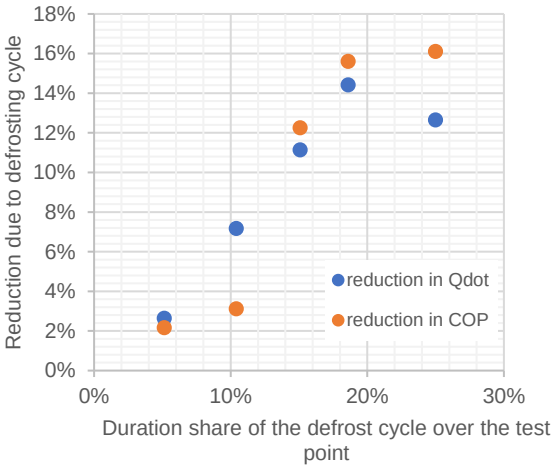

Figure 13: Reduction of heating capacity and COP due to defrost cycle depending on the ratio of defrosting duration and complete test point (see example in Figure 12)

Refrigerant cycle model calibration

Figure 14 shows the temperature – enthalpy diagram of the refrigerant cycle. The model has as output the $\vartheta_{i,in}$ of 16.4 °C, and the measured point was 15.9 °C. The electric power of the compressor (model output) is 1057 W, while the measured total electric power is 1300 W. The later value includes the consumption of the control system as well as the indoor and outdoor fan consumption. Therefore, the power difference is getting smaller and below 10% (by assuming approximately 150W for fans and control).

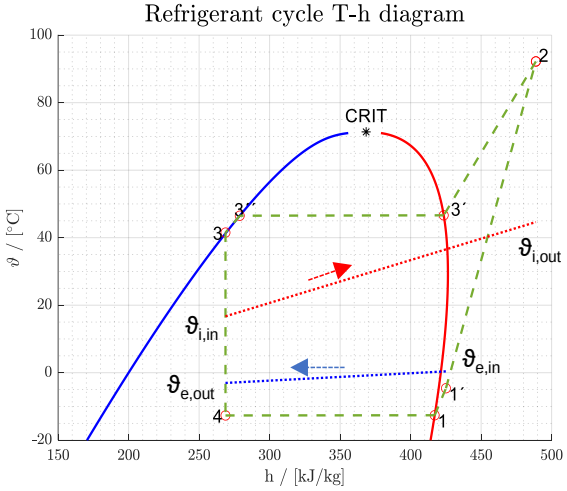

Figure 14: Temperature-enthalpy diagram of the refrigerant cycle including the indoor and outdoor air flows.

Conclusions

An air-to-air split heat pump is measured in the laboratory. Several operation conditions are measured including various ambient, indoor set point, and sink temperatures (indoor outlet), indoor fan speed modes and compressor speeds, including also defrosting and on/off cycles. The measurements are used to calibrate a steady-state refrigerant cycle model, aiming to expand the performance map and identify the minimum required measured points.

The results show that the heating capacity of the unit was in the range of the manufacturer, however, this was not true for high ambient temperatures since the controller reduces the speed even if the heating load is not covered. The indoor volume flow is 34% up to 46% less than the one found in the datasheet.

The curves derived using the Carnot cycle method have a good correlation to the measured test points, indicating that it can be used if there is limited available data. The average Carnot performance factor for that unit is 0.30. Besides, the operation of the unit seems to be controlled in such a way that for ambient temperatures higher than approximately 8 °C, the compressor speed decreases (which also means a lower indoor outlet temperature), leading to high COP values.

The measurements considering defrost cycles showed a maximum reduction of 14% in the heating capacity and 16% in the COP.

Acknowledgement

Funding from the Austrian research project (by FF) PhaseOut and the outcomes are part of international project, IEA HPT A61 Heat Pumps in Positive Energy Districts

References

Carroll, P., M. Chesser, and P. Lyons. 2020. “Air Source Heat Pumps Field Studies: A Systematic Literature Review.” *Renewable and Sustainable Energy Reviews* 134(August): 110275. https://doi.org/10.1016/j.rser.2020.110275.

Eguiarte, Olaia et al. 2020. “Energy, Environmental and Economic Analysis of Air-to-Air Heat Pumps as an Alternative to Heating Electrification in Europe.” *Energies* 13(15): 3939. https://www.mdpi.com/1996-1073/13/15/3939.

European Standards. 2022. *EN 14825: Air Conditioners, Liquid Chilling Packages and Heat Pumps, with Electrically Driven Compressors, for Space Heating and Cooling, Commercial and Process Cooling - Testing and Rating at Part Load Conditions and Calculation of Seasonal Performance*.

Feist, Wolfgang. 2022. *Heizen Mit Dem Split-Klimagerät? Experiment Zum Heizen Und Kühlen Aus Einer Räumlich Konzentrierten Quelle Im Passivhaus Darmstadt Kranichstein*. Innsbruck. www.uibk.ac.at/iup.

Guo, Xian-Min, Yi-Guang Chen, Wei-Hua Wang, and Chun-Zheng Chen. 2008. “Experimental Study on Frost Growth and Dynamic Performance of Air Source Heat Pump System.” *Applied Thermal Engineering* 28(17–18): 2267–78. https://linkinghub.elsevier.com/retrieve/pii/S1359431108000203.

Hegarty, R O, O Kinnane, D Lennon, and S Colclough. 2022. “Air-to-Water Heat Pumps : Review and Analysis of the Performance Gap between in-Use and Product Rated Performance.” *Renewable and Sustainable Energy Reviews* 155(October 2021): 111887. https://doi.org/10.1016/j.rser.2021.111887.

Konrad, Mary Elizabeth, and Brendan D. MacDonald. 2023. “Cold Climate Air Source Heat Pumps: Industry Progress and Thermodynamic Analysis of Market-Available Residential Units.” *Renewable and Sustainable Energy Reviews* 188(October): 113739. https://doi.org/10.1016/j.rser.2023.113739.

Li, Hao et al. 2024. “Efficiency Assessment of Variable Speed Air Source Heat Pump Heating Systems: A Hybrid Data-Driven and Theoretical Approach.” *Journal of Building Engineering* 87: 109018. https://doi.org/10.1016/j.buildenv.2022.109704.

Monteleone, William, Fabian Ochs, Georgios Dermentzis, and Samuel Breuss. 2024. “Simulation-Assisted Design of a Silent Façade-Integrated R290 Mini-Split Heat Pump.” *Applied Thermal Engineering* 243: 122520. https://linkinghub.elsevier.com/retrieve/pii/S1359431124001881.

Williamson, James, and Robb Aldrich. 2015. *Field Performance of Inverter-Driven Heat Pumps in Cold Climates*.

BauSIM 2024 in Wien
23. September – 26. September

Vergleichende Betrachtung von verschiedenen Konfigurationen hybrider Wärmepumpensysteme im Mehrfamilienhaus-Bestand

Michael Kropp[1], Sahil Vadadkar[1], Andreas Velte-Schäfer[1], Sebastian Herkel[2]

1 Universität Freiburg – Institut für Nachhaltige Technische Systeme INATECH, Deutschland, E-Mail: michael.kropp@inatech.uni-freiburg.de

2 Fraunhofer Institut für Solare Energiesysteme ISE, Deutschland, E-Mail: sebastian.herkel@ise.fraunhofer.de

Kurzfassung

Wärmepumpen spielen eine zentrale Rolle bei der Dekarbonisierung des Gebäudesektors. Allerdings bestehen vor allem in Mehrfamilien-Bestandsgebäuden technische und wirtschaftliche Herausforderungen. In diesem Kontext wurden Ende 2021 zwei Mehrfamilienhäuser (Baujahr 1963, Hüllsanierung 1995, 30 Wohneinheiten) mit hybriden Wärmepumpenanlagen (Wärmepumpe und Gaskessel) ausgestattet.

Um der begrenzten Wärmequellenverfügbarkeit im städtischen Umfeld zu begegnen, wurden innovative Ansätze umgesetzt: hybride photovoltaisch-thermische (PVT) Kollektoren als einzige Wärmequelle sowie ein Mehrquellen-System (MQS) bestehend aus Erdwärmesonden und einer Außenluft-Einheit.

Die messtechnische Auswertung des ersten zeitgleichen Betriebshalbjahres zeigt eine effiziente Umsetzung der MQS-Wärmepumpe mit einer Arbeitszahl von 3,2. Allerdings ist aufgrund der zu geringen maximalen Vorlauf (VL)-Temperatur von 60 - 68 °C der Betrieb des Gaskessels zur Trinkwarmwasser (TWW)-Nacherwärmung notwendig. Insgesamt deckt der Gaskessel 28 % des Wärmebedarfs. Die Analyse der Messdaten der PVT-Wärmepumpe zeigt, dass die Wärmepumpe im Sommerbetrieb (reine TWW-Bereitung) den Wärmebedarf allein decken kann (max. VL-Temperatur von 75 °C). Im gesamten Betrachtungszeitraum liegt die Arbeitszahl bei 3,0. Allerdings müssen aufgrund der Einsatzgrenzen der Wärmepumpe über 38 % des gesamten Wärmebedarfs durch den Gaskessel gedeckt werden.

Bei der Evaluation der beiden Anlagen wurden Optimierungspotentiale im Betrieb und in der Konfiguration der Wärmepumpenanlagen identifiziert. So sollte die Regelung der Wärmequelle im PVT-System und die TWW-Bereitung im MQS optimiert werden.

Abstract

Heat pumps play a central role in the decarbonization of the building sector. However, there are technical and economic challenges, especially in existing multi-family buildings. In this context, two apartment buildings (built in 1963, envelope renovation in 1995, 30 residential units) were equipped with hybrid heat pump systems (heat pump and gas boiler) at the end of 2021.

To address the limited availability of heat sources in the urban environment, innovative approaches were implemented: hybrid photovoltaic-thermal (PVT) collectors as the sole heat source and a multi-source system consisting of geothermal probes and an air unit.

The evaluation of the first half year of operation shows an efficient implementation of the multi-source heat pump with a seasonal performance factor of 3.2, although the gas boiler is necessary for DHW reheating due to the insufficient maximum supply temperature of 60 - 68 °C. Overall, the gas boiler covers 28% of the heat demand. The analysis of the measurement data of the PVT heat pump shows that the heat pump can cover the heat demand alone in summer operation (DHW heating only) with a maximum supply temperature of 75 °C. Over the entire observation period, the seasonal performance factor is 3.0. However, due to the operating limits of the heat pump, over 38% of the total heat demand must be covered by the gas boiler.

During the evaluation of the two systems, optimization potential in the operation and configuration of the heat pump systems was identified. For example, the control of the heat source in the PVT system and the DHW heating in the multi-source heat pump should be optimized.

Einleitung

Wärmepumpen (WP) können umweltfreundlich Wärme bereitstellen, indem sie möglichst erneuerbaren Strom und Umgebungswärme

nutzen. Daher wird Wärmepumpen eine zentrale Rolle im zukünftigen klimaneutralen Gebäudebestand eingeräumt. Ihre Anwendung in bestehenden Gebäuden und Quartieren ist jedoch mit technischen und wirtschaftlichen Herausforderungen verbunden, die eine breitere Anwendung verhindern (z.B. geeignete Temperaturniveaus und die Verfügbarkeit von Umgebungswärmequellen in städtischen Gebäuden) [Hess et al., 2019]. Daher spielen Wärmepumpen im bestehenden Mehrfamilienhausbestand mit einem Anteil von nur ca. 3,3 % immer noch eine untergeordnete Rolle [BDEW, 2023]. Darüber hinaus kann diese begrenzte praktische Erfahrung in Kombination mit hohen Anfangsinvestitionskosten und hohen Betriebskosten als Haupthindernis für eine breitere Einführung von Wärmepumpen in diesem Marktsegment angesehen werden. Außerdem ist die Integration von Wärmepumpen in das Stromnetz von entscheidender Bedeutung für das Energiesystem der Zukunft. Daher wird auch im Mehrfamilienhaus-Bestand lokale Stromerzeugung zukünftig eine größere Rolle einnehmen.

In diesem Zusammenhang wurde ein intelligentes und innovatives Energiekonzept für ein Cluster von fünf Bestands-Mehrfamilienhäusern mit einer beheizten Gesamtfläche von 11.243 m² entwickelt und umgesetzt, welches u.a. die Machbarkeit der Installation von Wärmepumpen in bestehenden Gebäuden demonstriert.

Der Artikel stellt die messtechnische Auswertung von zwei hybriden Wärmepumpensystemen vergleichend gegenüber. Schwerpunkte sind hierbei die Performance der Wärmepumpe und des Gesamtsystems. Daher werden die Messergebnisse aus dem ersten gemeinsamen Betriebshalbjahr im Zeitraum von Juli 2023 bis Januar 2024 ausgewertet.

Hybride Wärmepumpensysteme im smarten Quartier Karlsruhe-Durlach

Im Jahr 2021 wurde das neue Quartiers-Energiesystem (QES) für fünf Bestands-Mehrfamilienhäusern in Karlsruhe-Durlach installiert und in Betrieb genommen. Das System wurde auf der Grundlage von Simulationen und entsprechenden Energiebilanzen ausgelegt und berücksichtigt verschiedene technische, regulatorische und ökologische Faktoren [Lämmle et al., 2022]. Das QES umfasst neben den beiden hybriden Wärmepumpenanlangen, die jeweils ein Gebäude versorgen, ein Nahwärmenetz mit BHKW und Spitzenlastkessel für die restlichen drei Gebäude sowie Photovoltaik-Module, die auf allen fünf Gebäuden installiert sind. Die Dimensionierung der Anlagen erfolgte im Spannungsfeld zwischen dem Ziel niedriger CO_2-Emissionen und hoher wirtschaftlicher Rentabilität unter den in der Planungsphase angenommenen Randbedingungen (vor allem Preise für den Bezug von Erdgas und Strom, sowie Einspeisevergütung für die Rückspeisung von selbsterzeugtem Strom).

Zwei dezentrale Wärmepumpen mit einer thermischen Leistung von 55 kW_{th} bzw. 71 kW_{th}, liefern Wärme für zwei Gebäude mit jeweils 2107 m² beheizter Wohnfläche. Um die begrenzte Verfügbarkeit von Wärmequellen im städtischen Umfeld zu lösen, wurden in dem Projekt innovative Ansätze umgesetzt: hybride photovoltaisch/thermische PVT-Kollektoren als einzige Wärmequelle und ein Mehrquellen-System MQS, bestehend aus Erdwärmesonden und einer Außenluftanlage. Durch die Zusammenschaltung der Quellen kann die Größe der Erdwärmesonden im Vergleich zu einer Wärmepumpe mit nur einer Quelle um 50 % reduziert werden, während die Jahresarbeitszahl im Vergleich zu einer reinen Luft-Wasser-Wärmepumpe steigt. Die beiden vereinfachten Hydraulikschemata sind in Abbildung 1 dargestellt. Eine Übersicht über die installierten Komponenten liefert Tabelle 1. Die Wirtschaftlichkeitsbetrachtung in [Jank et al., 2023] hat ergeben, dass die Wärmepumpensysteme unter derzeitigen Rahmenbedingungen gegenüber einem System mit Gaskesseln nicht wirtschaftlich betrieben werden können. Allerdings steigt durch das integrierte QES (v.a. durch lokal erzeugten Strom) die Robustheit gegenüber Energiepreisschwankungen und steigenden CO_2-Steuern. Dadurch werden mittelfristig Wärmegestehungkosten erreicht, die unter denen konventioneller Energiesysteme liegen.

Wie in Tabelle 1 zu erkennen ist, unterscheiden sich die beiden Wärmepumpenanlagen neben der Wärmequelle und der thermischen Leistung vor allem in ihren Einsatzgrenzen (Abb. 2). Während die PVT-Wärmepumpe hohe maximale Vorlauftemperaturen von bis zu 75 °C aufweist, kann die MQS-Wärmepumpe nur Temperaturen von 60 - 68 °C bereitstellen. Dies verdeutlichen auch die Messwerte der Vorlauftemperatur der Wärmepumpen.

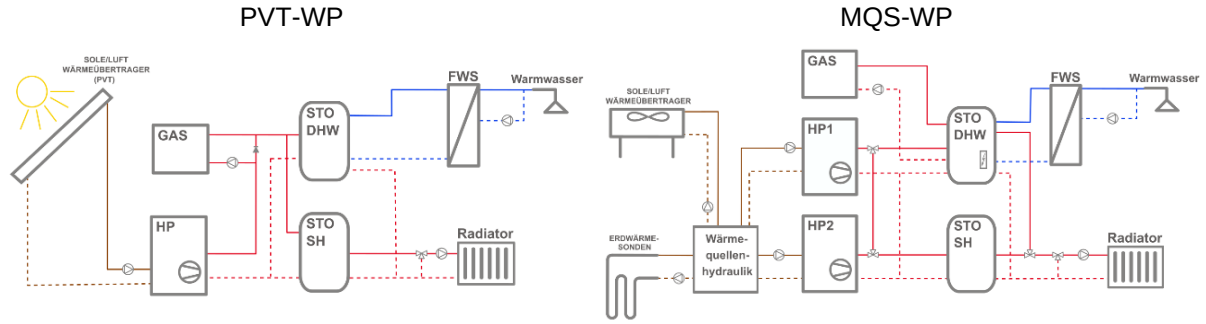

Abbildung 1: Vereinfachte Hydraulikschemata der beiden WP-Systems.

Tabelle 1: Technische Daten der beiden WP-Systeme

	PVT	MQS
Wärmepumpe	WP mit Leistungs-regelung (50 / 100 %)	2er Kaskade
Q_{th} (B0/W35)	55,4 kW	28,7 + 42,3 kW
P_{el} (B0/W35)	13 kW	5,9 + 8,7 kW
COP (B0/W35)	4,2	4,9 bzw. 4,8
Kältemittel	R134a	R410A
Einsatzgrenzen (s. Abbildung 2)	B-5/W70, B0/W75, B20/W75	B-10/W60, B0/W67, B10/W67, B25/W60
Bivalenzpunkt	0 °C (parallel) -5 °C (alternativ)	-5 °C (parallel)
Umweltwärme	PVT (202 m²) 40 kW	Mehrquellen Außen-lufteinheit: 40 kW Erdwärmesonden-feld: 30 kW
Gaskessel	92 kW	91 kW
TWW-Speicher	1,8 m³	1,7 m³
RH-Speicher	0,9 m³	0,85 m³

Die maximale Vorlauftemperatur ist vor allem bei der Trinkwassererwärmung im Mehrfamilienhaus ein limitierender Faktor: In sog. Großanlagen werden Temperaturen am TWW-Erwärmer von mindestens 60 °C vorgeschrieben. Durch die Grädigkeit des Wärmeübertragers (Frischwasserstation) sind somit Temperaturen von über 68 °C im TWW-Speicher notwendig. Wegen der Temperatur Einsatzgrenzen der Mehrquellen-Wärmepumpe (im stabilen Betrieb sind maximale Speichertemperaturen von 62 °C erreichbar) muss bei der TWW-Bereitung immer der Gasbrennwertkessel zugeschaltet werden. Dagegen kann die PVT-Wärmepumpe über den gesamten Einsatzbereich die notwendige TWW-Temperatur bereitstellen. Hier sind vor allem die minimale und maximale Soleeintrittstemperatur von -5 °C bzw. 20 °C limitierend für den Einsatz der WP. Dies kann bei hohen Soletemperaturen durch eine Rücklaufbeimischung abgemildert werden. Bei niedrigen Außentemperaturen und damit auch niedrigen Soletemperaturen muss aber das Gasbrennwertgerät die gesamte Wärme bereitstellen. Aufgrund der Einsatzgrenzen primärseitig und der Wahl der Quelle (Erdwärme) kann die Mehrquellen-Wärmepumpe ganzjährig Wärme bereitstellen.

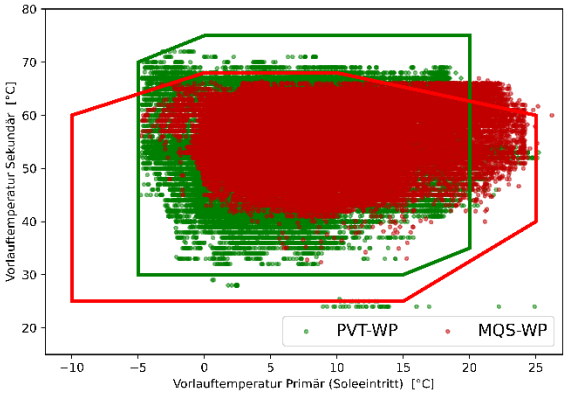

Abbildung 2: Einsatzgrenzen sowie gemessene Vorlauftemperatur (Minutenwerte) der beiden Wärmepumpen.

Während die MQS-Wärmepumpenanlage seit Anfang 2022 in Betrieb ist, konnte aufgrund von hohen Körperschallemissionen die Inbetrieb-nahme der PVT-Wärmepumpe erst im Juni 2023 erfolgen. Im Folgenden werden daher Monitoring-Ergebnisse aus dem ersten gemeinsamen Betriebshalbjahr im Zeitraum von Juli 2023 bis Januar 2024 ausgewertet.

Monitoring-Ergebnisse

Gesamtauswertung

Abbildung 3 stellt das Verhalten der beiden bivalenten Wärmepumpensysteme (links: PVT-Wärmepumpensystem, rechts: Mehrquellen-Wärmepumpensystem) anhand des gleitenden Wochenmittels der Wärmeleistungen dar. Oben

sind die Verbraucher Raumheizung (rot) und TWW (blau), in der Mitte und unten die Erzeuger Gasbrennwertgerät (grau), WP (grün) dargestellt für Raumheizung (Mitte) und TWW (unten).

Die beiden Gebäude zeigen ähnliche Verbräuche über den Auswertezeitraum. Zwischen Juli und Ende September liegt hauptsächlich TWW-Last vor. In beiden Systemen liegt die Heizgrenztemperatur bei ca. 18 °C, (z. B. geringe Heizlast Anfang August und Anfang September). Im PVT-System ist außerdem Heizbetrieb in allen Sommermonaten vorhanden, da ein ständiger Durchfluss durch eine dauerhaft laufende Pumpe im Heizkreis des Gasbrennwertkessels auftritt. Der Verbrauch im Betrachtungszeitraum bezieht sich in beiden Gebäuden insgesamt auf etwa 1/3 TWW-Bereitung und 2/3 Raumheizung.

Die Heizlast der beiden Gebäude unterscheidet sich leicht in den Übergangsmonaten Oktober und November. Hier liegt im PVT-System ein leicht höherer Verbrauch vor. In den sehr kalten Tagen im Januar stimmt der Verbrauch und auch die maximale Leistung der beiden Systeme gut überein.

Abbildung 3 links zeigt, dass die WP im PVT-Wärmepumpensystem die gesamte Last bis Mitte Oktober deckt. Aufgrund der maximalen Vorlauftemperatur der Wärmepumpe kann der gesamte Bedarf der TWW-Grundlast im Sommer durch die WP gedeckt werden. Es zeigt sich, dass der Einsatz des Gaskessels außentemperaturabhängig ist. Mit kälteren Außentemperaturen nimmt die Unterstützung des Gasbrennwertgerätes zu und bei Temperaturen unterhalb von 5 °C übernimmt das Gasbrennwertgerät sogar den Großteil der Wärmeerzeugung. Im gesamten Betrachtungszeitraum liegt der Anteil des Gasbrennwertgerätes bei über 38 %, im TWW-Betrieb bei 20 % und bei der Raumheizung etwa 47 %.

Die Messdaten des Mehrquellensystems (Abb. 3 rechts) zeigen, dass das Gasbrennwertgerät etwa die Hälfte der TWW-Grundlast trägt (52 %) und bei der Raumheizung die WP-Kaskade der Hauptwärmeerzeuger (85 %) ist. Im Dezember und im Januar zeigt sich bei sehr geringen Außentemperaturen eine Unterstützung des Heizkreises durch das Gasbrennwertgerät. Insgesamt werden durch den Gaskessel 28 % des Gesamtverbrauchs gedeckt.

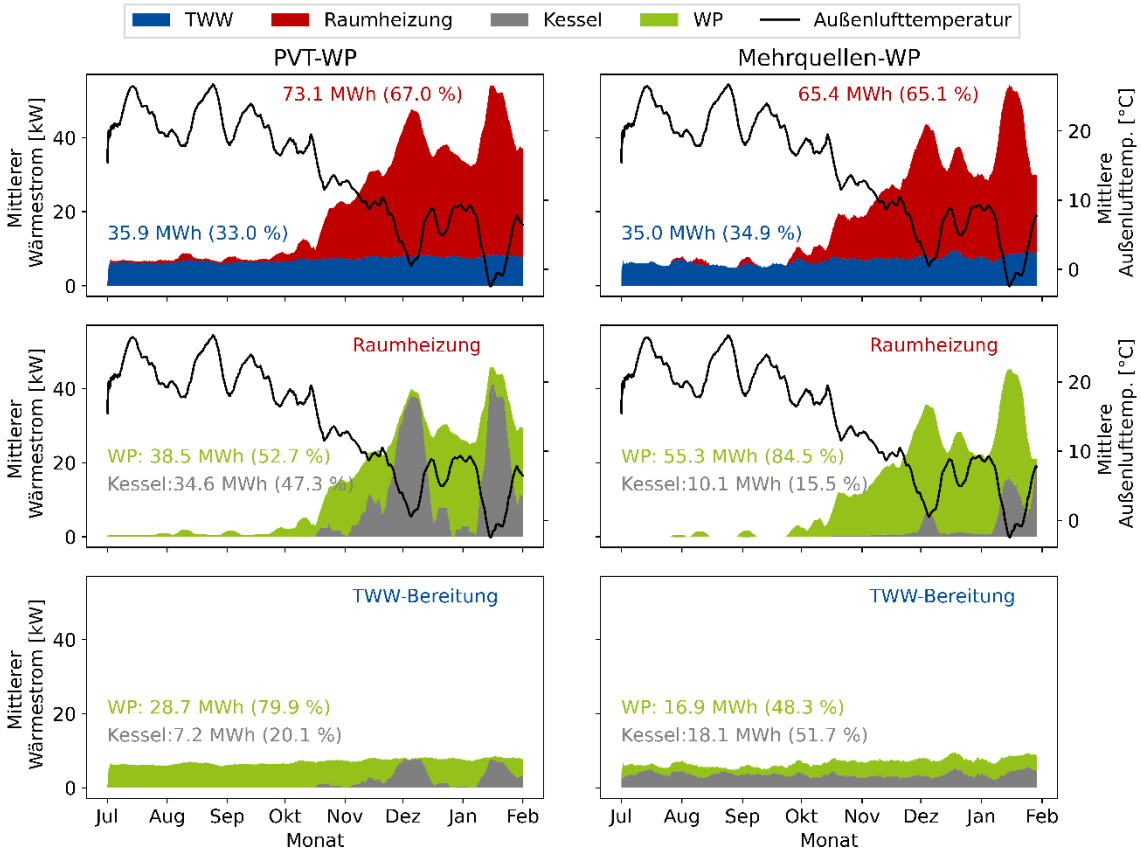

Abbildung 3: Gleitendes Wochenmittel der Wärmeleistung der Verbraucher (oben) TWW (blau) und Raumheizung (rot) sowie der Erzeuger (Mitte: Raumheizung, unten: TWW-Bereitung) Gasbrennwertgerät (grau), Wärmepumpe (grün) im Auswertungszeitraum.

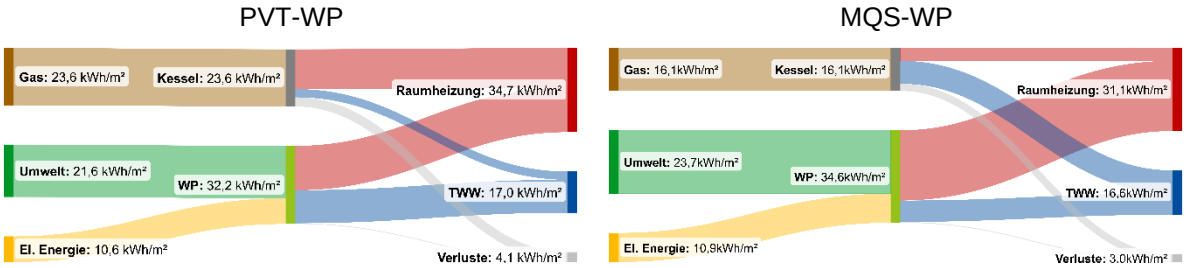

Abbildung 4: Sankey-Diagramme der Wärmebereitstellung über den gesamten Auswertungszeitraum.

Abbildung 4 zeigt die Sankey-Diagramme der Energieflüsse der beiden WP-Anlagen im Betrachtungszeitraum. Dies verdeutlicht nochmals die Anteile der Wärmeerzeuger bei der Wärmebereitstellung. Außerdem ist ein hoher Anteil an fossilen Energieträgern bei der Wärmebereitstellung zu erkennen.

Zum Vergleich der beiden Gesamtsysteme werden die Treibhausgasemissionen bei der Wärmebereitstellung im Betrachtungszeitraum ermittelt. Basierend auf [Bongs et al., 2022, Fritsche & Greß, 2019] werden die $CO_{2,äq.}$-Emissionsfaktoren f_{Strom} = 403 $g_{CO2,äq.}$/kWh und f_{Gas} = 201 $g_{CO2,äq.}$/kWh für Deutschland verwendet. Die Werte beziehen sich auf äquivalente CO_2-Emissionen, welche direkte und indirekte Emissionen von CO_2 und anderen Treibhausgasen berücksichtigen. Für das PVT-WP-System ergeben sich so CO_2-Emissionen von etwa 19,0 t und für das MQS von 16,0 t. Die Treibhausgasintensität für die gesamte Wärmebereitstellung beträgt demnach 174 g/kWh (PVT) bzw. 159 g/kWh (MQS), für die Raumheizung 176 g/kWh bzw. 139 /kWh und für die TWW-Bereitung 174 g/kWh bzw. 197 g/kWh. Beim PVT-System gibt es kaum Unterschiede in der Treibhausgasintensität der Wärmebereitstellung für Raumheizung und TWW. Der höhere Anteil der WP bei der TWW-Bereitung wird durch eine schlechtere Arbeitszahl kompensiert. Dagegen ist im MQS die Treibhausgasintensität bei der TWW-Bereitung aufgrund des hohen Gaskesselanteils am höchsten und bei der Raumheizung aufgrund des höheren WP-Anteils am geringsten.

Im Vergleich mit dem System vor der Sanierung (Wärmeversorgung durch alte Gaskessel mit dem in [Jank et al., 2020] angenommenen konstanten Wirkungsgrad von 80 %) liegen die CO_2-Emissionen im gleichen Zeitraum bei 27,4 t (PVT) bzw. 25,2 t (MQS). Für den Zeitraum können die CO_2-Emissionen also um 31 % (8,4 t) für das PVT-System und 36 % (9,2 t) für das MQS reduziert werden.

Monatsweise Analyse

Im Folgenden wird eine monatsweise Charakterisierung der beiden WP-Anlagen durchgeführt. Dafür sind nachfolgend die kumulierten Energien für Raumheizung (RH) und TWW beider Erzeuger dargestellt (Abb. 5). Außerdem ist die monatliche Arbeitszahl MAZ der WP inklusive Quellantrieb und Abtauung (AZ 3 nach [Zottl et al., 2012]) für TWW, RH und gesamt über den Betrachtungszeitraum aufgetragen.

Bei der TWW-Erwärmung im Sommer kann die PVT-WP die gesamte Energie bei einer MAZ von 3,0 bereitstellen. Aufgrund der Unterstützung durch den Gaskessel muss im Sommer die Mehrquellen-WP nur einen geringeren Temperaturhub bereitstellen, aufgrund des hohen Stromverbrauchs der Außenlufteinheit liegt die MAZ zur TWW-Bereitstellung mit 3,1 aber auf dem Niveau der PVT-WP. Mit fallenden Außenlufttemperaturen und damit auch geringeren Quellentemperaturen sinkt die MAZ zur TWW-Bereitung in beiden Anlagen.

In der Heizperiode liegt die MAZ zur Raumheizung in beiden Anlagen auf einem ähnlichen Niveau, allerdings kann die Mehrquellen-WP einen höheren Anteil decken. Hier ist das Mehrquellensystem vorteilhaft: bei niedrigen Außentemperaturen kann die Wärme aus den Erdwärmesonden mit relativ konstanten Temperaturen entzogen werden. Aufgrund hoher geforderten Temperaturen im Heizkreis bis zu 60 °C sinkt aber auch hier die MAZ ab. Die Arbeitszahl des PVT-Systems ist außentemperaturabhängig. Zum einen ist dadurch der Temperaturhub der WP größer als der des MQS (dadurch sinkt die MAZ) und zum anderen muss aufgrund der Einsatzgrenzen der WP der Gaskessel große Anteile der Wärmeerzeugung übernehmen.

Um dies detaillierter zu untersuchen, ist in Abbildung 6 ein Tagesverlauf des PVT-WP-Systems in der Übergangszeit (21. November 2023, mittlere Außentemperatur 9 °C) dargestellt.

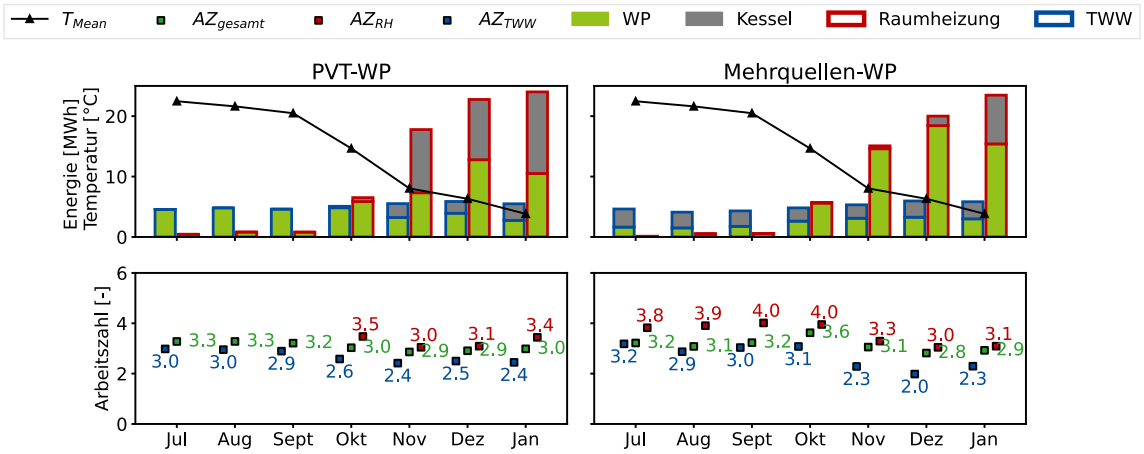

Abbildung 5: Monatlicher Wärmeverbrauch Raumheizung und TWW sowie Erzeuger (oben) und Monatsarbeitszahl des PVT-WP-Systems (grün) und differenziert nach RH (rot) und TWW (blau).

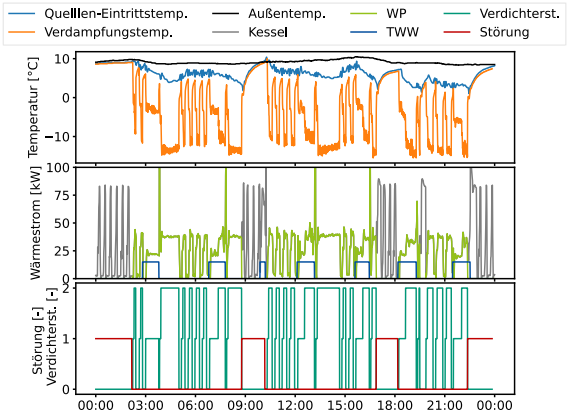

Abbildung 6: Tagesverlauf der Außen-, Quellen-Eintritts- und Verdampfungstemperatur, des Wärmestromes der PVT-WP und des Kessels sowie der Betriebspunkte und Störmeldung der WP am 21.11.2023.

Im Betrieb mit einem Verdichter und einer Wärmequellen-Eintrittstemperatur von 6 – 7 °C ergibt sich eine Verdampfungstemperatur von -4 °C bis -2 °C. Im Betrieb mit zwei Verdichtern liegt die Verdampfungstemperatur deutlich niedriger (< -12 °C). Dies führt zu Störungen und damit auch zur Abschaltung der WP (Druck- und Temperaturunterschreitung im Verdampfer). Es ist zu erkennen, dass vor Auftreten der Störung die Temperaturdifferenz zwischen Außenluft und Quelleneintrittstemperatur steigt. Es kann also nicht genügend Energie der Außenluft entzogen werden.

Es ist außerdem zu erkennen, dass im Raumheizbetrieb die Wärmeerzeuger oft takten. Dies liegt an einer relativ geringen Hysterese von 5 K. Diese soll zukünftig vergrößert werden um die Laufzeit zu erhöhen.

Abgleich mit Simulationsergebnissen

Für die Auslegung der Wärmepumpe wurden in der Planungsphase Modelle in Dymola/Modelica aufgebaut. Eine detaillierte Gegenüberstellung der Simulationsergebnisse mit dem Feldversuch des Mehrquellen-Wärmepumpensystems kann in [Metz, 2024] nachgelesen werden. Die wichtigsten Erkenntnisse sind:

- Hohe Übereinstimmung von Raumwärmeverbrauch, und Wärmepumpenanteil in Simulation und Feldtest.
- AZ im Feldversuch ist niedriger als in der Simulation aufgrund real höherer Hilfsenergiebedarfe der Wärmequelle Außenluft und Abweichungen in der Senkenregelung

Im Folgenden soll daher die Gegenüberstellung der Messdaten des PVT-WP-Systems mit Simulationsergebnissen erfolgen. Dazu wurde das vorhandene Simulationsmodell mit gemessenen Daten der Außenlufttemperatur, der solaren Einstrahlung und der TWW-Verbrauchsprofile parametriert. Abbildung 9 zeigt die Gegenüberstellung der Messdaten und der Simulationsdaten. Es ist zu erkennen, dass der Verbrauch für Raumheizung und TWW gut übereinstimmen. Der Anteil von WP und Kessel unterscheidet sich jedoch stark. Während der Gaskessel in der Simulation nur bei sehr kalten Außentemperaturen anspringt, übernimmt der Gaskessel im Feldtest bei Außenlufttemperaturen von unter 10 °C einen signifikanten Anteil der Wärmeversorgung. In der Simulation ist die Einsatzgrenze der WP und damit die primäre Vorlauftemperatur (Soleeintritt) ausschlaggebend: Sinkt die Soletemperatur unter -5 °C schaltet die WP ab und der Gaskessel übernimmt die Wärmeversorgung. In den Messdaten ist allerdings zu erkennen, dass die WP auch bei höheren Soletemperaturen bereits auf Störung geht (Temperatur- und Drucküberwachung im Verdampfer) und abschaltet. Dadurch ist der Anteil des Kessels in den Messdaten vor allem in

der Übergangszeit deutlich höher als in der Simulation. Dies zeigt aber auch das Potential der Anlage den Anteil an fossilen Energieträgern zu reduzieren, welches durch eine Anpassung der internen Wärmepumpen-Regelung erfolgen könnte. Dies gilt es im Laufe der weiteren Auswertung zu untersuchen.

Bei Betrachtung der monatsweisen Arbeitszahl der WP lässt sich feststellen, dass die MAZ im TWW-Betrieb der Simulation leicht über der des Feldtestes liegt (Abb. 7). Im RH-Betrieb teilweise (November und Dezember) sogar deutlich über dem Feldtest. Dies liegt an einer leicht höheren Quelltemperatur (PVT-Kollektor wurde in der Simulation vereinfacht als Kennlinienmodell abgebildet) und vor allem an Abweichungen in der Senkenregelung (u.a. Drehzahlreduzierung der Pumpe) und geringerer Taktung der WP. Dies wird zusätzlich im Tagesverlauf des Wärmestromes deutlich (Abb. 8). Die WP kann beinahe den gesamten Tagesbedarf decken und taktet viel weniger als im Feldtest. Der Gaskessel unterstützt nur die TWW-Bereitung kurzzeitig. Ziel des weiteren Projektverlaufs ist daher durch Optimierungsmaßnahmen einen Betrieb der PVT-WP nahe der Simulation zu ermöglichen.

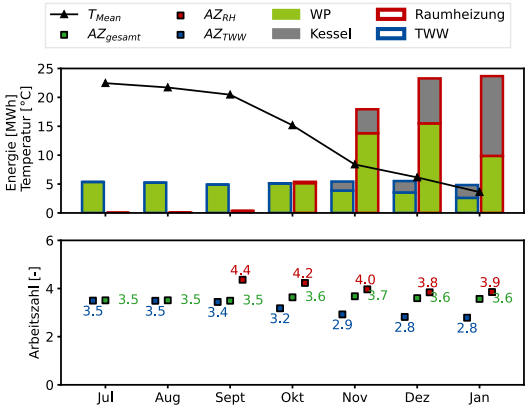

Abbildung 7: Monatlicher Wärmeverbrauch RH und TWW sowie Erzeuger (oben) und MAZ des Simulationsmodells der PVT-WP-Anlage (grün) und differenziert nach RH (rot) und TWW (blau).

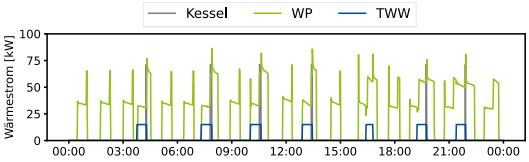

Abbildung 8: Tagesverlauf des Wärmestromes der PVT-WP und des Kessels am 21.11. (Simulation).

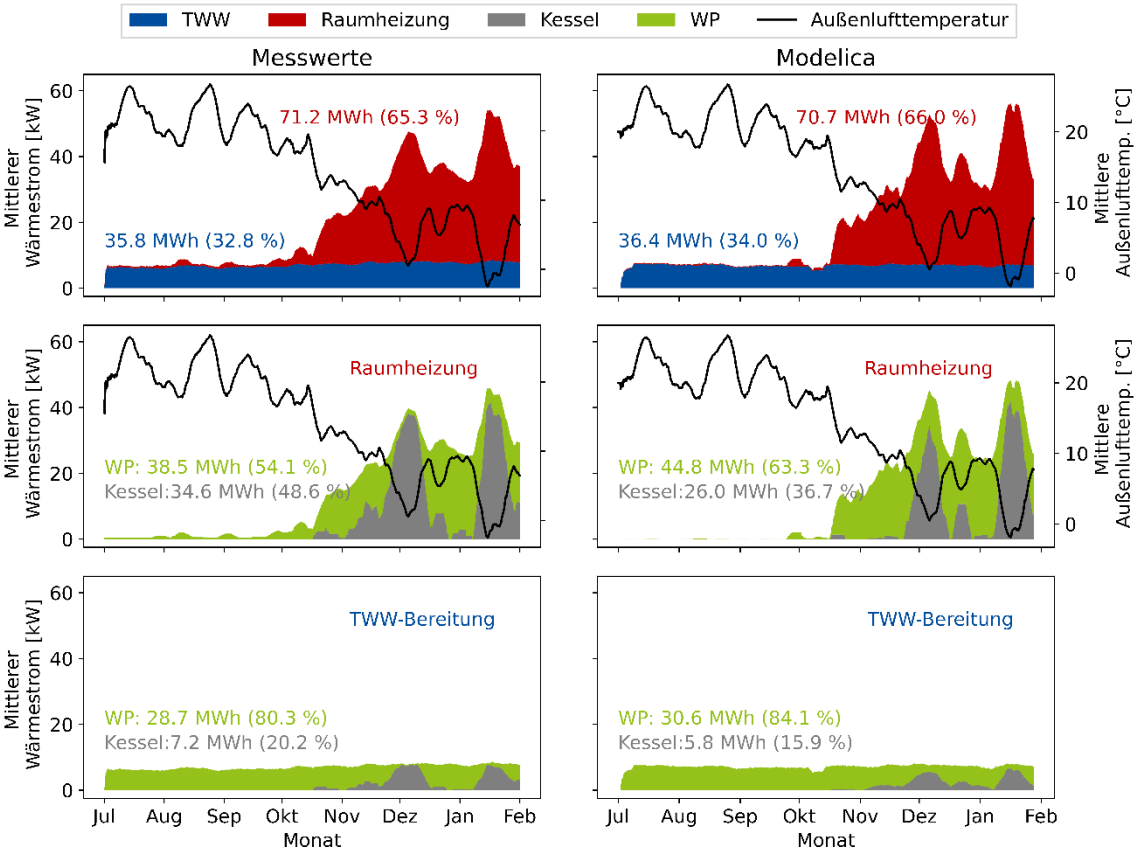

Abbildung 9: Gleitendes Wochenmittel der Wärmeleistung der Verbraucher (oben) TWW (blau) und Raumheizung (rot) sowie der Erzeuger (Mitte: Raumheizung, unten: TWW-Bereitung) Gasbrennwertgerät (grau), Wärmepumpe (grün) der PVT-WP-Anlage (links) im Vergleich Simulationsdaten.

Zusammenfassung

Die Auswertung der beiden bivalenten Wärmepumpensystemen zeigt, dass Wärmepumpen auch im Mehrfamilienhaus-Bestand die erforderliche Wärme für Raumheizung und TWW effizient bereitstellen können, jedoch weiterhin auf den Einsatz fossiler Energieträger angewiesen sind. So erreichte das MQS-Wärmepumpensystem im Betrachtungszeitraum eine Arbeitszahl von 3,2 mit einem Gaskesselanteil von 28 % und das PVT-Wärmepumpensystem eine Arbeitszahl 3,0 bei 38 % Gaskesselanteil. Im Vergleich mit den alten Gaskesseln können in beiden Anlagen über 30 % der CO_2-Emissionen eingespart werden. Die innovativen Ansätze zeigen, wie die begrenzte Verfügbarkeit von Wärmequellen im städtischen Umfeld gelöst werden kann, allerdings besteht bei beiden Anlagen auch noch Optimierungspotential.

Das PVT-WP-System bietet den Vorteil eines WP-Aggregats mit hohen VL-Temperatur von bis zu 75 °C, wodurch die TWW-Bereitung allein durch die Wärmepumpe gedeckt werden kann. Allerdings ist die verwendete WP-Quellen-Konfiguration bereits bei Außentemperaturen unter 10 °C anfällig für Störungen, was in der Übergangszeit hohe Anteile des Gaskessels bei der Wärmebereitstellung nach sich zieht.

Beim MQS-WP-System liegt die maximale VL-Temperatur zwischen 60 und 68 °C, was den ganzjährigen Einsatz eines Gaskessels für die TWW-Bereitung erfordert. Jedoch kann durch die Wahl der Quellen und des WP-Modells die WP ganzjährig betrieben werden.

Durch die Kombination der WP mit fossilen Wärmerzeuger können Quellen kleiner dimensioniert und Investitionskosten gesenkt werden. Um CO_2-Emissionen zu minimieren, ist es jedoch wichtig, den Gasanteil möglichst gering zu halten. Dazu wurden verschiedene Optimierungsmöglichkeiten identifiziert:

- Im PVT-System sollte die Regelung der Wärmequelle optimiert werden und unter bestimmten Umständen die Leistung der Wärmepumpe limitiert werden. Dadurch kann der Gasanteil in der Übergangszeit reduziert werden. Dies zeigt auch der Abgleich mit den Simulationsdaten.
- Bei der MQS-WP können Maßnahmen wie die Absenkung der Rücklauftemperatur der Frischwasserstation, das Speichermanagement und die Absenkung der Temperatur in der Trinkwasserinstallation z.B. durch einen Einsatz von Ultrafiltration den Anteil des Gaskessels an der TWW-Bereitung reduzieren.

Danksagung

Die Forschungsprojekte SQ-Durlach (03ET1590) und SQ-Durlach II (03EN3095) werden vom Bundesministerium für Wirtschaft und Klima gefördert mit Unterstützung der Karlsruhe Energie Service KES. Wir danken unseren Projektpartnern für die gute Zusammenarbeit.

Literatur

Bongs, C. et al. 2022. Abschlussbericht LowEx-Bestand Analyse: LowEx-Konzepte für die Wärmeversorgung von Mehrfamilien-Bestandsgebäuden.

BDEW (2023): Wie heizt Deutschland 2023? Berlin: Bundesverband der Energie- und Wasserwirtschaft e. V.

Fritsche, U., Greß, H,-W, 2019. Der nichterneuerbare kumulierte Energieverbrauch und THG-Emissionen des deutschen Strommix im Jahr 2018 sowie Ausblicke auf 2020 bis 2050: Bericht für die HEA - Fachgemeinschaft für effiziente Energieanwendung e.V.

Hess, S., Vollmer, R., Wapler, J., Kleinstück, M., Bongs, C., Henning, H.-M. 2019. Ambient Heat Source Availability for Low-Ex Heating of Multi-Family Buildings, ISES Solar World Congress 2019 in Santiago (Chile)

Jank, R., Lämmle, M., Hess, S., Kropp, M. 2020. Verbundprojekt Smartes Quartier Karlsruhe-Durlach (SQ-Durlach). Projektbericht Phase A: Konzeptentwicklung.

Jank, R., Lämmle, M., Rink, M. 2023. Wirtschaftlichkeitsbetrachtung eines smarten Energiekonzepts für ein Bestandsquartier in Karlsruhe. Zeitschrift für Energiewirt. 47.

Lämmle, M., Kropp, M., Metz, J., Herkel, S. 2022. Simulation and Measurement results of a smart district with connected heat pumps, PV and CHP as a model project for decarbonizing multifamily buildings, BauSIM 2022 in Weimar.

Metz, J. 2024. Entwicklung und experimentelle Analyse eines Mehrquellen-Wärmepumpensystems aus Erdreich und Außenluft. Dissertation, Albert-Ludwigs-Universität Freiburg im Breisgau.

Zottl, A., Nordmann, R., Coevoet, M., Riviere, P., Miara, M., Benou, A., Riederer, P., 2012. Sepemo Report D4.2. /D 2.4. - Concept for evaluation of SPF Version 2.2: A defined methodology for calculation of the seasonal performance factor and a definition which devices of the system have to be included in this calculation. Heat pumps with hydronic heating systems.

BauSIM 2024 in Wien
23. September – 26. September

Bauakustische Simulation einer Holzrahmenwand

Alexander Stenitzer[1], Maximilian Neusser[2], Bernd Nusser[1]
1 Holzforschung Austria, Österreich, E-Mail: a.stenitzer@holzforschung.at
2 TU Wien, Österreich, E-Mail: maximilian.neusser@tuwien.ac.at

Kurzfassung

Bauphysikalische Simulationen haben sich im Planungsalltag der Hygrothermik bereits fest etabliert. Die Simulation realer physikalischer Effekte in der Bauakustik, speziell im Leichtbau, und die Möglichkeit präzise Vorhersagen zu treffen, stellt bisher aber noch eine Herausforderung dar. Mit der zunehmenden Nachfrage im Holzbau wachsen sowohl die Ansprüche als auch der Bedarf an Planungssicherheit. Die zuverlässige frequenzabhängige Prognose des Schalldämm-Maßes von Leichtbauteilen könnte ressourcenintensive Messungen einsparen. Bisher hat sich die Finite Elemente Methode (FEM) als geeignete Methode erwiesen, um bauakustische Parameterstudien an Leichtbauteilen durchzuführen und konstruktive Veränderungen in Relation zueinander zu bewerten. In diesem Artikel wird die Simulation einer Holzrahmenwand in Fenstergröße mithilfe der FEM präsentiert. Die Simulationsergebnisse, durchgeführt mit der Software "COMSOL Multiphysics 6.1", werden mit bauakustischen Messungen verglichen. Mithilfe der Simulation wird das Schalldämm-Maß mit einer maximalen Abweichung von 5 dB pro Terzband prognostiziert. Bei der FEM ist die Qualität der Eingangsdaten entscheidend, wobei durch Modalanalysen relevante Steifigkeitswerte und Verlustfaktoren aller Materialien ermittelt werden. Dieser Ansatz gewinnt insbesondere bei mehrschichtigen Bauteilen mit anisotropen Materialien an Relevanz. Zusätzlich zur Modellvalidierung wurden anhand des Modells unterschiedliche Parametervariationen durchgeführt. Die Ergebnisse der Parameterstudie werden in dieser Arbeit ebenfalls detailliert dargelegt.

Abstract

Building physics simulations have already become firmly established in the everyday planning of hygrothermal conditions. In contrast, simulating real physical effects in building acoustics, especially in lightweight construction, to enable precise predictions is still a challenge. With the increasing demand in timber construction, both the requirements and the need for planning security are growing. Reliable frequency-dependent prediction of the sound insulation of lightweight components could save resource-consuming measurements. So far, the Finite Element Method (FEM) has proven to be a suitable method for conducting building acoustics parameter studies on lightweight components and evaluating constructive changes in relation to each other. This article presents the simulation of a timber frame wall in window size using the FEM. The simulation results, conducted with the software "COMSOL Multiphysics 6.1", are compared with building acoustic measurements. Using the simulation, the sound insulation is predicted with a maximum deviation of 5 dB per 1/3-octave band. In FEM, the quality of the input data is crucial, with relevant stiffness values and loss factors of all materials determined through modal analyses. This approach becomes particularly relevant for multi-layered anisotropic components. In addition to the validation, parameter variations were carried out based on the model. The results of these studies are also discussed in this work.

Einleitung

Die frequenzabhängige Prognose der Schalldämmung von komplexen und inhomogenen Bauteilkonstruktionen ist ein häufiges Forschungsthema in der Bauphysik. Aus planerischer Sicht können Holzrahmenwände derzeit nur aufgrund erfolgter Schallmessungen oder Abschätzungen mit hohen Unsicherheiten bauakustisch geplant werden. Aus wissenschaftlicher Sicht gibt es bereits, für die Planungspraxis allerdings zu aufwendige, Methoden, um frequenzabhängige Prognosen des Schalldämm-Maßes solcher Bauteile zu erstellen. Eine davon ist die Finite Elemente Methode (FEM) (z. B.: Bard et al., 2017).

Unterschiedliche Forschungsarbeiten haben gezeigt, dass mittels FEM valide Prognosen der Luftschalldämmung von Wänden in Holzbauweise möglich sind (vgl. Neusser, 2017). In Neusser & Bednar, 2021 wird für reine Wandbildner eine Übereinstimmung zwischen Mess- und Simulationsergebnissen von $\Delta R \leq \pm 3$ dB erreicht. Wichtige Einflussfaktoren bei der Modellierung

der Schalltransmission durch Holzleichtbauwände sind nach Neusser, 2017 beispielsweise:

- Materialeigenschaften (dynamisches E-Modul, Innerer Verlustfaktor, Querkontraktionszahl, Dichte, Strömungswiderstand, Porosität)
- Geometrie (Bauteilabmessungen, Schichtdicken, Verbindungsmittelabstände)
- Verbindungsmittel (Steifigkeiten, Position, Anzugsmoment)
- Verbindung zwischen Bauteil und Prüfstand

Die Erkenntnisse von Neusser & Bednar, 2021 dienten als Grundlage für die Modellierung des in dieser Arbeit vorgestellten Modells. Der Fokus des Modells lag auf der Ermittlung der Materialeigenschaften, um ein bestmögliches Simulationsergebnis zu erzielen. Die untersuchte Wand hatte eine Größe von 1230 × 1480 mm und war wie in Tab. 1 angeführt, aufgebaut:

Tab. 1: Aufbau der untersuchten Holzrahmenwand in der Fensteröffnung (Prüffläche = 1,8 m²). a…Schraubenabstand; e…Achsabstand

Dicke		Material
16,0	mm	MDF, geschraubt mit a = 50 mm
240,0	mm	Steher (60 × 240) mm², e = 600 mm
240,0	mm	Dämmung (MW)
15,0	mm	OSB, geschraubt mit a = 50 mm
271,0	**mm**	**Gesamtdicke**

Neben der Modellierung wurde die beschriebene Wand auch messtechnisch untersucht. Das Schalldämm-Maß wurde im Prüfstand des Akustik Center Austria nach ÖNORM EN ISO 10140-2:2021 gemessen. Die dazugehörigen Einzahlwerte wurden nach EN ISO 717-1:2020 bestimmt.

Anhand des Simulationsmodells werden nachfolgend Parameterstudien zur Netzauflösung, zum Strömungswiderstand der Gefachdämmung, zu dynamischen E-Moduli und flächenbezogenen Massen der Beplankungen diskutiert. Abschließend wird das prognostizierte Schalldämm-Maß des validierten Simulationsmodells der Messung gegenübergestellt.

Simulationsmodell

Die Grundlagen des Simulationsmodells, insbesondere die zu Neusser, 2017 abweichenden Modellierungsansätze, werden nachfolgend beschrieben. Die Modellierung und Simulation erfolgte mit der Software „COMSOL Multiphysics 6.1“. Für weitere, hier nicht näher behandelte, Details zu den Modellierungsansätzen wird auf Neusser, 2017 verwiesen. Die Geometrie des Modells ist in Abb. 1 zu sehen.

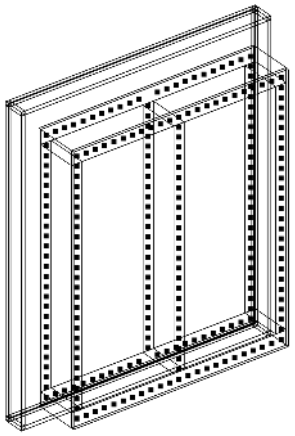

Abb. 1: Geometrie der simulierten Holzrahmenwand innerhalb der Simulationsumgebung von „COMSOL Multiphysics 6.1“.

Schalldämmmaß

Das Schalldämmmaß R (oder Schalltransmissionsverlust) einer Wand ist wie folgt definiert:

$$R = log_{10}\left(\frac{1}{\tau}\right) \quad (1)$$

Der Schalltransmissionsgrad τ ist das Verhältnis aus der durch das Schallfeld in einem Senderaum resultierenden auf die Wand einfallenden Schallintensität I_i und der von der Wand in einen Empfangsraum abgestrahlten Schallintensität I_e.

$$\tau = \frac{Re(I_i)}{Re(I_e)} \quad (2)$$

Diese Definition stellt insbesondere die numerische Simulation vor größere Herausforderungen, da neben der eigentlichen Struktur des zu untersuchenden Bauteils, auch Sende- und Empfangsraum und deren akustischen Oberflächeneigenschaften zu berücksichtigen sind. Ebenso ist in der Regel das gemessene Schalldämmmaß nach ÖNORM EN ISO 10140-2:2021 [1] gerade bei tiefen Frequenzen von der Lautsprecherposition und des resultierenden modalen Schallfeldes abhängig. Die Grenzfrequenz für den ca. 50 m³ großen Empfangsraum liegt nach Lerch et al., 2009 bei ca. 270 Hz. Für eine möglichst fehlerfreie Abbildung der Messsituation sind daher der Senderaum und dessen Eigenschaften ganzheitlich innerhalb der Simulation abzubilden. Dadurch sind in Relation zu den interessierenden Biegewellenlängen sehr große Domänen zu diskretisieren, wodurch ein hoher Berechnungsaufwand entsteht.

In dieser Arbeit werden das nicht diffuse Schallfeld im tiefen Frequenzbereich sowie der Einfluss des Raumes und der Lautsprecherposition nicht berücksichtigt. Das auf das Bauteil einfallende Schallfeld im Senderaum wird als homogenes,

isotropes und diffuses Schallfeld beschrieben. Dabei wurde der Ansatz verfolgt, dass das diffuse Schallfeld auf der Senderaumseite des Bauteils als Summe von N unkorrelierten ebenen Wellen mit gleichförmig zufällig verteilten Einfallswinkeln φ_n, θ_n beschrieben werden kann. Die Druckverteilung $p_{Raum}(x, y, z)$, als Grundbedingung in der FEM Simulation, kann also wie folgt berechnet werden:

$$p_{Bauteil} = p_{Raum} + p_{Reflexion} \quad (3)$$

Unter der Annahme, dass das Bauteil selbst schallhart ist, kann die reflektierende Komponente des Schalldruckfeldes am Bauteil wie folgt berechnet werden:

$$p_{Reflexion} = \frac{1}{\sqrt{N}} \sum_{n=1}^{N} e^{-i(k_{n,x}x + k_{n,y}y + k_{n,z}z)} e^{i\Phi_n} \quad (4)$$

mit

$$k_{n,x} = \cos(\theta_n) \quad (5)$$

$$k_{n,y} = \sin(\theta_n)\cos(\varphi_n) \quad (6)$$

$$k_{n,z} = \sin(\theta_n)\sin(\varphi_n) \quad (7)$$

Die Oberflächen des Empfangsraums werden dabei absorbierend modelliert, was bedeutet, dass keine Rückkopplung zwischen Bauteil und dem sich ausbildenden Schallfeld im Empfangsraum besteht. Damit wird der Empfangsraum als unendlicher Halbraum modelliert. Innerhalb der FEM-Umgebung erfolgt dies als Luftvolumen, das mittels PML („Perfect Matched Layer“) eingefasst ist. Dieser Rand kann als absorbierende Randbedingung für die Luftdomäne angesehen werden. Es findet somit keine Reflexion des vom Bauteil abgestrahlten Schallfeldes an dem Rand des Luftvolumens statt. Zur Implementierung in die FEM und der mathematischen Beschreibung der Eigenschaften des PML wird auf Kaltenbacher, 2015 verwiesen.

Die Diskretisierung der Raumvolumina auf der Sende- und der Empfangsraumseite wird somit fast bis zur Gänze eingespart. Abb. 2 zeigt eine schematische Darstellung der Situation, die innerhalb der FEM-Umgebung abgebildet wurde.

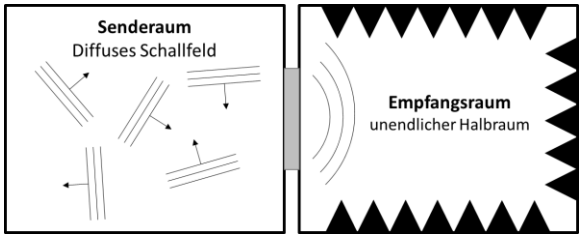

Abb. 2: Schematische Darstellung der innerhalb der FEM-Umgebung modellierten Schallfelder in Sende- und Empfangsraum.

Struktur

Für das strukturelle System wird die Struktur durch die Differentialgleichung der Bewegung für einen Kontinuumskörper beschrieben, wobei kleine Deformationen angenommen werden. Ausgehend von der Navier-Gleichung im Equilibrium kann nach Kaltenbacher, 2015 die Bewegungsgleichung mithilfe des Differenzialoperators B wie folgt in Matrizen Schreibweise dargestellt werden.

$$f_V + B^T \sigma = \rho a \quad (8)$$

mit

$$\boldsymbol{B} = \begin{pmatrix} \frac{\partial}{\partial x} & 0 & 0 & 0 & \frac{\partial}{\partial z} & \frac{\partial}{\partial x} \\ 0 & \frac{\partial}{\partial y} & 0 & \frac{\partial}{\partial z} & 0 & \frac{\partial}{\partial x} \\ 0 & 0 & \frac{\partial}{\partial z} & \frac{\partial}{\partial y} & \frac{\partial}{\partial z} & 0 \end{pmatrix}^T \quad (9)$$

$$\boldsymbol{\sigma} = \begin{pmatrix} \sigma_{11} & \sigma_{12} & \sigma_{13} \\ \sigma_{21} & \sigma_{22} & \sigma_{23} \\ \sigma_{31} & \sigma_{32} & \sigma_{33} \end{pmatrix} \quad (10)$$

$$\boldsymbol{a} = \frac{\partial^2 \boldsymbol{u}}{\partial t^2} \quad (11)$$

$$\boldsymbol{u} = \begin{pmatrix} u_1 \\ u_2 \\ u_3 \end{pmatrix} \quad (12)$$

Wobei σ den Spannungstensor nach Cauchy, a die Beschleunigung des Festkörpers und f_V die Summe der äußeren Kräfte darstellt. Die Modellierung des strukturellen Materialverhaltens beruht auf der Annahme, dass die Werkstoffe sich linear elastisch und isotrop verhalten. Für solche Materialien lässt sich der Zusammenhang zwischen Spannungen und Verzerrungen über das Hooksche Gesetz definieren. Die berücksichtigte innere Dämpfung des Materials wird über ein komplexes E-Modul beschrieben. Dieses Modell entspricht einer Strukturdämpfung mittels isotropen Verlustfaktors η. Dabei kann das komplexe E-Modul E des Materials wie folgt beschrieben werden:

$$E = E(1 + i\eta) \quad (13)$$

Kopplung Fluid – Struktur

Grundlegend erfolgt die Kopplung von Struktur und Fluid an der gemeinsamen Grenze ihrer beiden Domänen durch ein vorausgesetztes Kräftegleichgewicht und einer Kontinuitätsbedingung. Die erste Bedingung zur Kopplung von Fluid und Struktur folgt aus dem bedingten Gleichgewicht zwischen Schalldruck p_f des Fluids und der Normalkomponente σ_n der mechanischen Spannungen der Wand an der Grenzfläche.

$$\sigma_n = -n p_f \quad (14)$$

Die zweite Bedingung folgt aus der Anforderung der Kontinuität an der Grenze zwischen Struktur und Fluid und bedingt, dass die Normalkomponenten der Geschwindigkeiten der Strukturoberfläche v und die der des Fluids v_f an der Grenzschicht gleich groß sind und kann wie folgt dargestellt werden (vgl. Kaltenbacher, 2015):

$$v = \frac{\partial u}{\partial t} v_f = -\nabla\psi \quad (15)$$

$$n \cdot (v - v') = 0 \quad (16)$$

$$n \cdot \frac{\partial u}{\partial t} = -n \cdot \nabla\psi \quad (17)$$

Dämmstoff

In Neusser, 2017 wurden unterschiedliche Modelle zur Modellierung der Schallübertragung im Ständerzwischenraum untersucht. Eine Modellierung der Schallübertragung über den Hohlraum dieser Konstruktion bedarf somit einer geeigneten Modellierung der Schalltransmission und des akustischen Verhaltens solcher Dämmstoffe. Aufgrund der feingliedrigen Struktur dieser Materialien ist es in der Regel nicht möglich, diese Strukturen und die Wechselwirkung zwischen Luft und Fasern in der FEM aufzulösen. Eine Möglichkeit das Verhalten solcher Materialien in Simulationsmodellen abzubilden, ist die Darstellung als äquivalentes Fluid dessen Eigenschaften durch das Fluid in der porösen Struktur und durch die der porösen Struktur selbst bestimmt werden. Die Implementierung des äquivalenten Fluids mit dessen Eigenschaften der komplexen Schallgeschwindigkeit c_c, der äquivalenten Dichte ρ_c und des effektiven Kompressionsmoduls K_{eff} erfolgt analog zu Neusser, 2017.

$$\rho_c = \rho_{rig} \quad (18)$$

$$c_c = \sqrt{\frac{K_{eff}}{\rho_{rig}}} \quad (19)$$

Das hier verwendete Modell Johnson-Champoux-Allard (JCA) geht von einer starren porösen Struktur aus (vgl. Allard & Atalla, 2009), die durch die komplexen Kenngrößen der Dichte ρ_{rig} und des Kompressionsmoduls K_{eff} beschrieben wird.

$$\rho_{rig} = \frac{\tau_\infty \rho_f}{\varepsilon_p}\left[1 + \frac{R_f \varepsilon_p}{i\omega\rho_f\tau_\infty}\sqrt{1 + \frac{4i\omega\tau_\infty^2\mu\rho_f}{R_f^2 L_v^2 \varepsilon_p^2}}\right] \quad (20)$$

$$K_{eff} = \frac{\gamma p_A}{\varepsilon_P}\left[\gamma - (\gamma - 1)\left(1 + \frac{8\mu}{i\omega L_{th}^2 Pr\rho_f}\sqrt{1 + \frac{i\omega L_{th}^2 Pr\rho_f}{16\mu}}\right)^{-1}\right]^{-1} \quad (21)$$

$$L_v = \frac{1}{s}\sqrt{\frac{8\mu\tau_\infty}{\varepsilon_p R_f}} \quad (22)$$

τ ist der Porositätskrümmungsfaktor, L_v ist die viskose charakteristische Länge, L_{th} ist die thermisch-charakteristische Länge.

Dynamische Materialkennwerte

Als Eingangsdaten für die Simulation wurden im Zuge von Schwingungsversuchen die dynamischen Eigenschaften

- Verlustfaktoren (frequenzabhängig)
- Dynamische Biege-E-Moduli von stabförmigen Werkstoffen (frequenzabhängig)
- Dynamische Biege-E-Moduli von Plattenwerkstoffen

bestimmt.

Die hierfür verwendeten stabförmigen Probekörper (Steher) hatten eine Länge von 1800 mm. Die Plattenwerkstoffe OSB bzw. MDF hatten die Abmessungen 1500 × 1250 mm bzw. 1500 × 625 mm. Die eingesetzten Materialien wurden in einer dafür angefertigten Konstruktion elastisch gelagert (Abb. 3).

Abb. 3: Bei der Modalanalyse der Werkstoffe wurden diese elastisch aufgehangen (hier: OSB).

Verlustfaktor

Die Verlustfaktoren wurden in Anlehnung an ÖNORM EN ISO 10848-1:2017 [16] ermittelt. Die gemessene Körperschallnachhallzeit T_s pro Terzband wurde anschließend wie folgt in Verlustfaktoren η umgerechnet.

$$\eta = \frac{2{,}2}{fT_s} \quad (23)$$

Die frequenzabhängigen Verlustfaktoren der Materialien wurden im Simulationsmodell übernommen.

Dynamischer Biege-E-Modul

Für die Ermittlung der dynamischen E-Moduli wurden die Bauteile mittels elektrodynamischem Schwingungserreger und weißem Rauschen angeregt. Die Oberflächenschnelle wurde mittels Laservibrometrie bestimmt. Die dynamischen E-Moduli wurden anhand der Eigenmoden nach Blevins, 2001 berechnet. Bei der OSB mit einer Dimension von 1500 × 1250 mm waren die Eigenmoden (2, 2), (1, 3) und (3, 1) einer quadratischen, orthotropen Platte gut erkennbar. In Abb. 4 sind die gemessenen den simulierten Eigenmoden der untersuchten OSB gegenübergestellt. Im Gegensatz dazu konnte bei der MDF-Platte mit einer Dimension von 1500 × 625 mm lediglich die Mode (2, 2) eindeutig gefunden werden, anhand dessen die Steifigkeit ermittelt wurde.

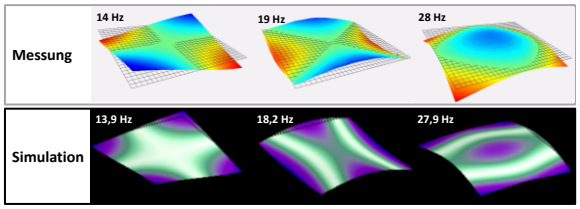

Abb. 4: Mittels Laservibrometrie (oben) und FEM (unten) ermittelte Eigenmoden der OSB.

Trotz der aufgrund des Herstellungsprozesses möglichen Anisotropie der Plattenwerkstoffe (vgl. Niemz & Sonderegger, 2017), war diese aus den Eigenmoden nicht ersichtlich. Erste Modalanalysen anhand von Streifen quer und längs zur Plattenrichtung ergaben besonders tieffrequent (< 100 Hz) eine starke Richtungsabhängigkeit. Diese verringert sich mit steigender Frequenz.

Die Frequenzabhängigkeit des E-Moduls wurde anhand der Streifen ebenfalls ersichtlich. Sowohl die Modalanalyse der OSB Streifen als auch der MDF Streifen zeigten wie in Villasante & Fernández-Serrano, 2022 tendenziell sinkende E-Moduli mit steigender Frequenz.

Es war eine starke Streuung unter den Probekörpern zu erkennen, weshalb keine schlüssige Frequenzabhängigkeit ermittelt werden konnte. Die E-Moduli der Plattenwerkstoffe (OSB und MDF) wurden deshalb als nicht frequenzabhängig im Modell angenommen.

Die Modalanalyse der stabförmigen Bauteile (Steher) ergab eine starke Frequenzabhängigkeit des dynamischen E-Moduls nach Blevins, 2001. Die frequenzabhängigen E-Moduli der Steher wurden im Simulationsmodell übernommen.

Schraubenmodell & Lagerung

Die Schraubverbindungen zwischen Bauteilen werden durch starre punktuelle Verbindungen an ihrer tatsächlichen Lage im Modell repräsentiert (vgl. schwarze Punkte in Abb. 1). In Neusser, 2017 wurde gezeigt, dass die Modellierung der Schraubverbindung als starre punktuelle Verbindung zu einem übermäßig steifen Verhalten führt. Aufgrund der Anzahl der Schraubverbindungen im Grundbauteil, stellt die Verwendung dieses Schraubenmodells jedoch einen notwendigen Kompromiss dar, um die allgemeine Reduktion der Komplexität des Simulationsmodells zu erreichen.

Die Lagerung des Probekörpers wurde an 4 Punkten als starr angenommen. Es wurden keine Untersuchungen zum Einfluss und zur genauen Einspannsituation des Bauteils im Prüfrahmen durchgeführt. Diese Randbedingung kann insbesondere im tiefen Frequenzbereich zu erheblichen Abweichungen zwischen den berechneten und gemessenen Schalldämm-Maßen führen (vgl. Neusser, 2017).

Netzauflösung

Die notwendige Netzauflösung des Modells der Holzrahmengrundwand in Fenstergröße wurde parametrisch untersucht. Die Auflösung wurde mit den in der verwendeten Software „COMSOL Multiphysics 6.1“ vorliegenden Einstellungen von „coarse“ bis „extremely fine“ stufenweise erhöht. In Tab. 2 sind die minimalen und maximalen Elementgrößen der Einstellungen dargestellt.

Tab. 2: Minimale und maximale Elementgrößen bei unterschiedlicher Netzauflösung in „COMSOL Multiphysics 6.1“.

Netzauflösung	Elementgröße in mm	
	minimal	maximal
coarse	47,6	255,0
normal	30,6	170,0
fine	17,0	136,0
finer	6,8	93,5
extra fine	2,6	59,5
extremely fine	0,3	34,0

Probleme, die sich durch zu geringe bzw. zu hohe Diskretisierung ergeben, werden in Neusser, 2017 geschildert. In den folgenden Simulationsergebnissen wird anschaulich, wie sich die Netzauflösung auf das prognostizierte Schalldämm-Maß auswirkt.

Ergebnis und Diskussion

Parametervariation

Netzauflösung

In der nachstehenden Abb. 5 ist das im hochfrequenten Bereich abfallende Schalldämm-Maß aufgrund einer zu geringen Netzauflösung dargestellt.

Die Dichte des Netzes ist bei geringer Auflösung nicht ausreichend, um die kurzen Wellenlängen korrekt abzubilden. Der Vergleich der Netzauflösungen zeigt, dass durch die geringste Auflösung („coarse“) schon bei 1200 Hz von der höchsten („extremely fine“) abweicht. Im Gegensatz dazu weicht die zweithöchste Auflösung („extra fine“) erst ab 2000 Hz von dieser ab.

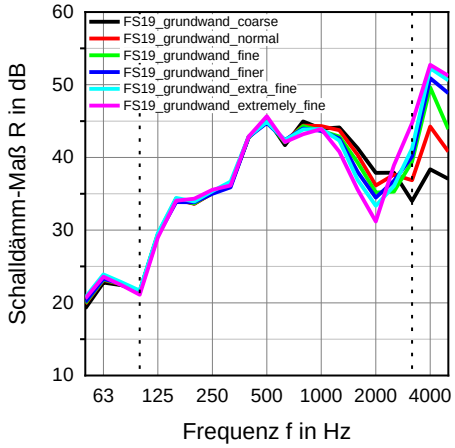

Abb. 5: Einfluss der Netzauflösung auf das prognostizierte Schalldämm-Maß.

Die Anzahl an finiten Elementen und in Folge auch die Rechenzeiten von FEM-Modellen steigen mit höherer Netzauflösung exponentiell an. Aufgrund der vorliegenden Parameterstudie wurde für die weiteren Simulationen eine Netzauflösung von „finer“ gewählt. Die gewählte Auflösung hat sich bei Gegenüberstellung mit der Messung im Prüfstand als ausreichend erwiesen. Dieser Kompromiss ermöglicht eine effiziente Simulation unter Berücksichtigung der Rechenleistung und auch der Genauigkeit der Ergebnisse bis mindestens 1000 Hz.

Strömungswiderstand

Der Strömungswiderstand des Dämmstoffs im Ständerzwischenraum wurde nicht gemessen. Mithilfe von Simulationsergebnissen wurde der Einfluss dieses Parameters auf das Prognoseergebnis überprüft. Abb. 6 zeigt das Ergebnis einer Parameterstudie, bei der der Strömungswiderstand im erwartbaren Bereich von 4 kPa s/m² bis 19 kPa s/m² variiert wurde.

Der Strömungswiderstand hat im Frequenzbereich zwischen 63 Hz und 1000 Hz einen erkennbaren Einfluss auf das berechnete Schalldämm-Maß. Mit zunehmendem Strömungswiderstand ist eine Vergrößerung des Schalldämm-Maßes zu beobachten. Für die folgenden Simulationen wurde im Abgleich mit den Messdaten ein Strömungswiderstand von 10 kPa s/m² gewählt.

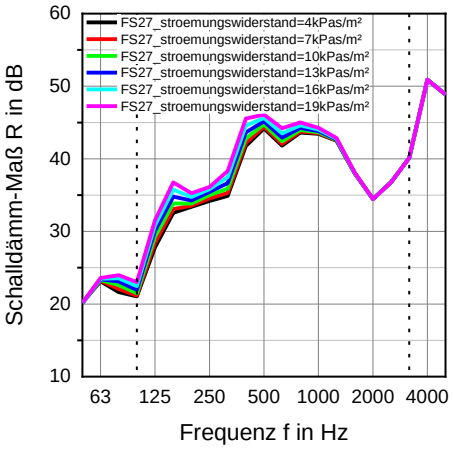

Abb. 6: Einfluss des Strömungswiderstands des Dämmstoffs auf das prognostizierte Schalldämm-Maß.

Dynamischer Biege-E-Modul der Beplankung

Im Zuge einer Variantenstudie wurde der Biege-E-Modul der empfangsraumseitigen Beplankung (OSB) um die Faktoren 0,5 und 2 verändert. Die Auswirkung dieser Variation auf das Schalldämm-Maß des gesamten Bauteils ist in nachstehender Abb. 7 zu sehen.

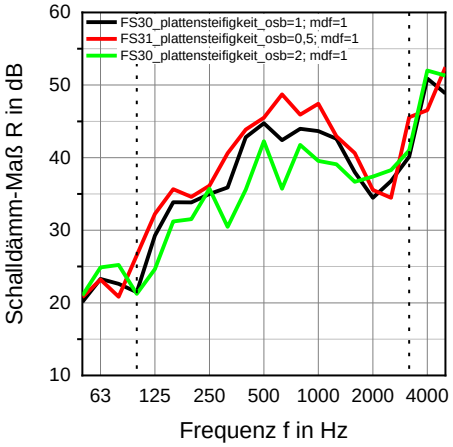

Abb. 7: Einfluss des E-Moduls der OSB auf das prognostizierte Schalldämm-Maß.

Je biegeweicher die Beplankung ist, desto höher sind die simulierten Schalldämm-Maße der Holzrahmenwand. Dies wirkt sich vor allem mittelfrequent aus, was auf eine höhere Energieübertragung zwischen Steher und Beplankung bei höherem E-Modul zurückzuführen sein könnte. Im Bereich der Koinzidenzfrequenz ist bei steiferer OSB eine Verschiebung zu tieferen Frequenzen zu beobachten.

Flächenbezogene Masse der Beplankung

Wie im vorangegangenen Beispiel wurde im Zuge der folgenden theoretischen Untersuchung die Masse der OSB um die Faktoren 2 und 3 erhöht. Die simulierten Schalldämm-Maße sind in Abb. 8 dargestellt.

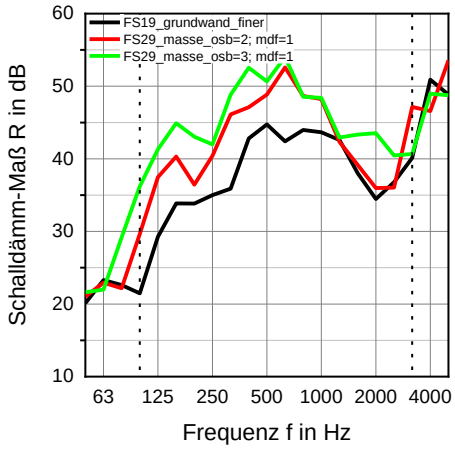

Abb. 8: Einfluss der flächenbezogenen Masse der OSB auf das prognostizierte Schalldämm-Maß.

Wie zu erwarten, führt die höhere Masse der OSB zu einer höheren Luftschalldämmung. Diese ergibt sich zum einen nach dem Berger'schen Massegesetz, zum anderen kommt bei der Leichtbaukonstruktion vor allem die Verschiebung der Masse-Feder-Masse-Resonanz zum Tragen. Die Erhöhung der Masse einer Schale sorgt für eine Verschiebung zu tieferen Frequenzen, wodurch es jeweils um ein Terzband früher (63 Hz; 80 Hz; 100 Hz) zu einem steilen Anstieg des Schalldämm-Maßes kommt.

Simulation vs. Messung

Folgende Abb. 9 zeigt den Vergleich der gemessenen Schalldämmung mit dem simulierten Ergebnis. Ergänzend ist zu dem Simulationsergebnis das Schalldämm-Maß mit 1/24-Oktav-Auflösung dargestellt (dünn schwarz durchgezogen). In der Legende können auch die Einzahlwerte R_w, C und C_{tr} abgelesen werden. Die Abweichungen der Simulation von der Messung sind ebenfalls frequenzabhängig dargestellt. Die mittlere Abweichung sowie die Standardabweichung des Vergleichs sind unten rechts eingeblendet. Abweichungen größer null bedeuten dabei eine Überschätzung des Schalldämm-Maßes in der Simulation.

Unter 100 Hz kommt es zu den insgesamt größten Abweichungen. Diese können auf durch das Modell nicht erfassbare Raummoden zurückzuführen sein. Weiters wurde die Lagerung der Bauteile, die im tieffrequenten Bereich einen Einfluss auf das Schalldämm-Maß hat, zwar berücksichtigt, aber nicht näher untersucht. Der Vergleich der gemessenen und simulierten Schalldämm-Maße zeigt eine zufriedenstellende Übereinstimmung. Im Bereich von 100 Hz bis 3150 Hz resultiert die größte Abweichung durch eine Überschätzung des Koinzidenzeinbruchs im Modell. Der Grund könnte in der nicht frequenzabhängig abgebildeten Steifigkeit der Beplankungen liegen.

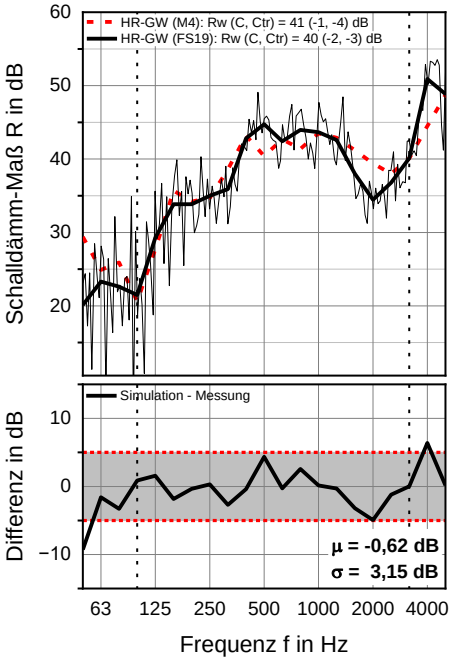

Abb. 9: Oben: Gegenüberstellung des simulierten (schwarz) und des gemessenen (rot strichliert) Schalldämm-Maßes der Holzrahmengrundwand. Das simulierte Ergebnis ist auch in 1/24-Oktavband-Auflösung dargestellt. Unten: Differenz des simulierten und gemessenen Schalldämm-Maßes der Holzrahmenwand.

Zusammenfassung

Im Zuge der Arbeit wurde ein Simulationsmodell einer Holzrahmenwand im kleinen Maßstab (1,8 m²) basierend auf den Erkenntnissen von Neusser, 2017 erstellt. Ergänzend dazu wurden dynamische Materialkennwerte der verwendeten Materialien durch Modalanalysen ermittelt. Einzig der Strömungswiderstand des Dämmstoffs wurde im Zuge einer Parametervariation im Abgleich mit der Messung festgelegt. Diese flossen in das finale Modell mit ein.

Die Parametervariationen zum Einfluss des dynamischen E-Moduls bzw. der Masse der empfangsraumseitigen Beplankung haben gezeigt, dass die simulierten Ergebnisse der Erwartung laut Theorie folgen. Während die frequenzabhängige Prognose der Schalldämmung durch FEM im Planungsalltag noch nicht angewandt wird, eignet sie sich sehr gut zur Abschätzung der Auswirkungen von Parameterveränderungen.

Der Abgleich des simulierten mit dem gemessenen Schalldämm-Maß zeigt über den Frequenzbereich von 100 Hz bis 3150 Hz Abweichungen des simulierten Schalldämm-Maßes von maximal 5 dB pro Terzband. Unter 100 Hz kommt es zur größten Abweichung. Diese kann auf im Modell nicht erfasste Raummoden, sowie die

Vereinfachung der Lagerung zurückgeführt werden. Zur Optimierung des vorliegenden Modells sollten in weiterer Folge die dynamischen Eigenschaften aller Materialien frequenzabhängig untersucht werden und in die Simulation einfließen.

Danksagung

Die Autoren bedanken sich bei der österreichischen Forschungsförderungsgesellschaft (FFG) und den Projektpartnern für die Förderung des Projekts Coole Hülle (FO999889550).

Literatur

Allard, J.F.; Atalla, N. 2009: Propagation of sound in porous media - modelling sound absorbing materials. John Wiley & Sons, Ltd, Chichester (United Kingdom).

Bard, D.; Negreira, J.; Guigou-Carter, C. et al. 2017: Modelling prerequisites – FEM/SEA – Impact and Airborne Sound. Report no STB01 WG1. RISE Research Institutes of Sweden AB, Göteborg (Sweden).

Blevins, R.D. 2001: Formulas for natural frequency and mode shape. Krieger Publishing, Malabar, Florida.

Kaltenbacher, M. 2015: Numerical simulation of mechatronic sensors and actuators – Finite elements for computational multiphysics, third edition. Springer-Verlag Berlin Heidelberg.

Lerch, R.; Sessler, G.; Wolf, D. 2009: Technische Akustik – Grundlagen und Anwendungen. Springer Bln, Berlin.

Neusser, M. 2017: Analyse des Einflusses von Verbindungsmitteln auf das Schalldämm-Maß von leichten Trennwandkonstruktionen durch realitätsnahe Modellierung von Schraub- und Klebeverbindungen. Wien, Technische Universität Wien, Dissertation.

Neusser, M.; Bednar, T. 2021: Modifikation eines Modells von Verbindungsmitteln zur Prognose des Schalldämmmaßes von Leichtbaukonstruktionen mittels Finiten Elemente Methode in dem erweiterten Frequenzbereich. In: e & i Elektrotechnik und Informationstechnik.

Niemz, P.; Sonderegger, W. 2017: Holzphysik – Physik des Holzes und der Holzwerkstoffe. Carl Hanser Verlag GmbH & Co. KG, München.

ÖNORM EN ISO 10140-2:2021: Akustik - Messung der Schalldämmung von Bauteilen im Prüfstand - Teil 2: Messung der Luftschalldämmung.

ÖNORM EN ISO 10848-1:2017: Akustik - Messung der Flankenübertragung von Luftschall, Trittschall und Schall von Gebäudetechnischen Anlagen zwischen benachbarten Räumen im Prüfstand am Bau.

ÖNORM EN ISO 717-1:2020: Akustik - Bewertung der Schalldämmung in Gebäuden und von Bauteilen - Teil1: Luftschalldämmung.

Villasante, A.; Fernández-Serrano, Á. 2022: Dynamic modulus of elasticity in flexural vibration tests of Pinus sylvestris sawn timber obtained with fundamental resonant frequency and overtones. In: Holzforschung 76, Heft 6, S. 485-492.

BauSIM 2024 in Wien
23. September – 26. September

Explainable AI for deriving predictive and trustworthy operational rules for building energy control

Lilli Frison[1], Tim Rist[1], Nicolas Réhault[1]
1 Fraunhofer Institute for Solar Energy Systems ISE, Freiburg, Germany
E-Mail corresponding author: lilli.frison@ise.fraunhofer.de

Abstract

Innovative solutions for optimizing energy use and reducing carbon emissions lead to increasing complexity of the building energy systems, influenced by varying conditions such as weather, user behavior, energy availability and grid requirements. This poses a challenge to traditional control strategies based on simple "if-then" rules. To maximize energy efficiency or control buildings with complex objectives, new intelligent strategies are needed that can use prediction and optimization calculations. Traditional expert rule systems are becoming too complex for building operators to understand, necessitating a shift to advanced model-based control (MPC) techniques. However, their demand for sophisticated building automation infrastructure and systems expertise are challenging.

Our research addresses these challenges by fostering Explainable Artificial Intelligence (XAI) techniques to extract new knowledge from existing data, such as measurements, simulations or expert knowledge, and translate it into simple, comprehensible rules. The aim is to create a method that approximates the behavior of complex optimization-based control strategy through a learning-based rule base. This results in an easily implementable, humanly understandable, and thus trustworthy rule-based control system that adapts to environmental changes and achieves a near optimal control.

To investigate the potential of the developed concept, we apply it to the use case "grid-supported heat pump control" and compare it with other control approaches such as MPC in term of control performance and trustworthiness. The testing is conducted within a hardware-in-the-loop experiment in a heat pump laboratory, ensuring a rigorous assessment of the method's effectiveness and reliability.

Introduction

By combining different technologies – such as photovoltaics, solar thermal systems, combined heat and power units, and heat pumps – integrated into smart electricity and heating networks at the building or district level, significant reductions in CO2 emissions and energy consumption can be achieved (Clauß et al., 2017). This results in complex overall systems that must operate under highly variable conditions such as weather, user behavior, energy availability and grid requirements. In building automation systems, it is standard practice to deploy control strategies by using rule-based algorithms, which dictate system responses under specified conditions. However, due to this increasing complexity of building energy systems, conventional control strategies based on simple "if-then" rules using current and past measurements show limitations for operating such systems effectively. To maximize energy efficiency or control a building with complex objectives, new intelligent strategies are required that can utilize predictions and optimization calculations. Incorporating predictions increases the number and complexity of possible rules to the point where formulating easily understandable expert rule systems for building operators becomes impossible. One promising control approach is Model Predictive Control (MPC) (Gwerder et al., 2010; Serale et al., 2018). However, MPC places high soft- and hardware demands on building automation and operator expertise due to the needs of setting-up and calibrating tedious physics-based model and then solving an optimization problem. The emergence of data-driven machine learning (ML) methods has introduced significant advancements in building automation, offering inherent advantages over traditional model-based predictive control.

For user acceptance and trust in safe operation, and consequently, widespread adoption in building automation, easily understandable control decisions are necessary. To ensure

secure and trustworthy AI deployment in building automation, it is important to consider the following two requirements: users must trust the control logic and the control system should be easily implementable into existing building automation systems. The first requirement can be achieved by providing users with a clear understanding of the control strategies to ensure transparency and explainability. The second requirement should be fulfilled without the need for additional data points unless they are readily available in the automation system. In summary, making the complex machine learning model explainable enhances model transparency, trust, ensures regulatory compliance and safety, aids in model debugging and improvement, and supports critical decision-making.

Explainable Artificial Intelligence (XAI) is a young subfield of AI research that allows human users to understand and trust the results and outputs generated by ML algorithms. The application of these methods to building energy technology has not yet been a focus of research, even though they hold great potential for increasing the robustness and acceptance of practical use in building automation. Preliminary work on this paradigm can be found in May-Ostendorp (2012) who explored the use of offline model predictive control using AI methods such as Decision Trees and Artificial Neural Networks in mixed-mode buildings to achieve near-optimal supervisory control. This work emphasizes the importance of leveraging historical and simulation data for optimizing building operations, a principle that is central to our approach in developing understandable and robust control methods through AI. Similarly, Picard et al. (2018) demonstrated the potential of using approximate MPC, facilitated by ML, to enhance building control systems. Their work underscores the relevance of AI in developing more efficient control strategies for building energy systems, aligning with the objectives of our research to make AI-generated knowledge accessible and understandable. Zhang et al. (2018) applied XAI to improve the understanding of simulation models in the context of building energy consumption. Their research highlights the potential of XAI to explain complex AI models, making them more accessible to stakeholders and end-users. A similar AI research topic is Imitation Learning, which involves AI systems learning complex tasks through the observation of human experts, and aligns closely with the goals of XAI by facilitating the development of AI models whose decisions and strategies can be easily understood and trusted by users. This learning approach not only enhances the performance of AI systems in tasks such as energy optimization and predictive control but also significantly contributes to making these systems more transparent and explainable. For instance, Hussain et al. (2021) explored the use of imitation learning in conjunction with XAI techniques to explain the decision-making process of AI in energy-efficient building design, demonstrating how AI can mimic expert-level strategies while maintaining a level of interpretability essential for user trust and acceptance.

In this research, we develop an AI-based method to learn new knowledge from existing data obtained by offline simulation and make it accessible to humans in the form of understandable rules and relationships. The intelligent operating rules generated can contribute to improve the resource efficiency of increasingly complex building heating systems. The goal of this project is to develop methods that approximate the input/output behavior of optimization-based or expert knowledge-based control through simple control schemes. The result is an understandable and robust control approach that can be easily implemented, consider predictions about environmental conditions, and mimic optimal control behavior. We specifically develop a rule-based system for building energy systems and applied it to a proactive heat pump control with varying electricity costs.

Method

A knowledge-based system represents a sophisticated form of intelligent information processing, where knowledge is meticulously structured and made accessible through advanced techniques of knowledge representation and modeling. Frequently, the term "knowledge-based system" is interchangeably used with "expert system," underscoring their capability to emulate the decision-making process of human experts in specific domains. Such systems dynamically generate new insights or knowledge by analyzing and interpreting data sourced from measurements, simulations, or other empirical methods. Within the broad spectrum of knowledge-based systems, rule-based systems stand out for their distinct approach to knowledge representation. In these systems, knowledge is encapsulated in a set of explicit rules. These rules systematically guide the system's reasoning process, enabling it to draw logical conclusions or make decisions akin to human reasoning. This rule-based architecture not only facilitates a transparent and interpretable reasoning process but also allows for the straightforward integration and modification of domain-specific knowledge.

For a successful realization of this approach for obtaining an understandable base of operational rules, the definition of an automated workflow is required, see Figure 1. First, the data set is created by means of offline simulation (1). In a rule derivation process, new knowledge in the form of rules (knowledge derivation) from the existing database is learned (2). The new knowledge forms an AI-generated but humanly understandable expert rule system (3) and can be used in controllers for the heating and cooling supply of a building. To identify optimal operating behavior and represent it in the form of rules, we developed an algorithm based on decision trees. Unlike neural networks, which are understood as black-box models, decision tree rules can be directly visualized. Interpretability ensures that the logic behind any given decision can be communicated in a manner that is accessible to individuals without specialized AI knowledge and to control infrastructure, fostering safe and easy integration in building automation systems. The decision tree is trained on the existing optimized database and generates understandable "if-then" rules. These rules are then used for an optimized and proactive control scheme. When developing decision trees, there are various possibilities to influence the number, complexity, and robustness (how well the rules perform with new data) of the rules.

In the following section, we give a brief overview about the functioning principle of decision trees.

Decision Trees

A decision tree is a data structure, an ordered, directed graph that represents decision rules. In the context of handling continuous data, the decision tree model is also referred to as a regression tree, unlike its counterpart, the classification tree, which is designed to categorize instances into discrete classes based on their attributes. A decision tree operates through a hierarchical, tree-structured model where each internal node represents a "test" on an attribute, each branch represents the outcome of the test, and each leaf node represents a class label (decision taken after computing all attributes).

Decision trees are intrinsically aligned with the principles of explainable AI due to their inherent interpretability and the transparent nature of their decision-making processes. The graphical representation as a tree diagram illustrates hierarchical, sequential decisions. They can make predictions by learning simple decision rules derived from the data features. This structure facilitates a straightforward visual and logical representation of the decision-making process, enabling users to trace the path from root to leaf, thereby understanding the rationale behind each decision. Their main advantage is that they are easy to interpret and visualize. Decision trees offer additional tools for interpretation such as feature importance analysis, which identifies which variables significantly impact the model's decisions. This analysis augments the explainability of the decision tree model itself and provides insights into the underlying data and the domain being modeled.

Despite their advantages, decision trees encounter specific challenges, particularly in contrast to artificial neural networks. A notable limitation is their occasional lack of ability to generalize to unseen data. This means that while decision trees may perform well on the training dataset, their ability to accurately predict outcomes on new, unseen data can be compromised. Moreover, decision trees are susceptible to instability; slight changes in the input data can lead to significantly different tree structures. This instability not only affects their reliability but also complicates the model's interpretability and consistency over time. To address these issues, decision trees are often utilized within ensemble methods, such as random forests or gradient boosting. Ensemble methods combine the predictions of multiple decision trees to produce a more robust and stable model, significantly improving generalization capabilities by reducing overfitting and increasing the model’s accuracy on unseen data.

We use the tree as a regression problem to predict an unknown variable based on the features which are composed of existing prediction of disturbance signals and possibly the current system state. During the learning phase, specific decision rules are learned from the training data as follows. Given training vectors $x_i \in R^n . i = 1, \dots, m$, and vector of true labels $y \in R^m$, a decision tree partitions the space

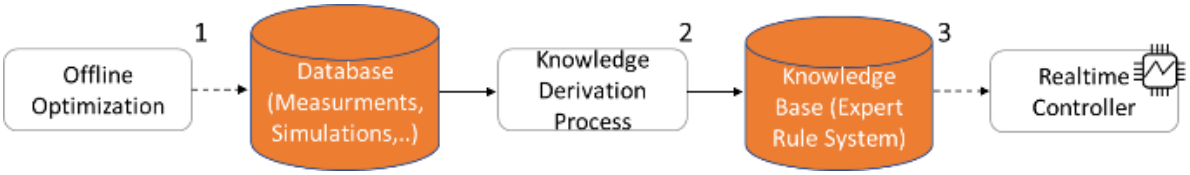

Figure 1: Rule derivation pipeline

recursively so that data with the same label are grouped together. Let the data point k be denoted by Q. For each candidate split $\theta = (j, t_k)$, consisting of a feature j and a threshold value t_k, the data is split into two subsets $Q_{left}(\theta) = \{(x,y)|x_j \leq t_k\}$ and $Q_{right}(\theta) = Q \setminus Q_{left}(\theta)$. The error value is calculated using a function $H()$, called impurity. For the regression task, $H()$ is calculated using the mean squared error:

$$\overline{y}_k = \frac{1}{N_k}\sum_{i \in N_k} y_i$$

$$H(X_k) = \frac{1}{N_k}\sum_{i \in N_k}(y_i - \overline{y}_k)^2.$$

The problem is reduced to finding a split that minimizes the error value at Q, i.e., $G(Q,\theta)$:

$$G(Q,\theta) = \frac{n_{left}}{N_k} H\big(Q_{left}(\theta)\big) + \frac{n_{right}}{N_k} H\big(Q_{right}(\theta)\big).$$

The parameters are selected that minimize the error value $\theta^* = \operatorname{argmin}_\theta G(Q,\theta)$. This step is repeated recursively for $Q_{left}(\theta^*)$ and $Q_{right}(\theta^*)$ until the maximum allowed depth is reached.

Example

In our case, we use the tree as a regression problem to predict the heat pump water supply temperature based on the existing prediction of disturbance signals such as grid electricity price and ambient temperature at the current moment and in the future. The training data for the algorithm are simulated trajectories that have been generated by an offline optimization of the system. An example of a simple decision tree for our problem is given in Figure 2.

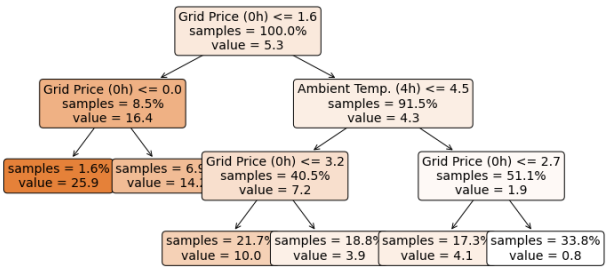

Figure 2: Example of a decision tree with 6 leaves and a depth of 4. Labels indicate the impurity function (squared error) and the percentage of data that was used for the split.

The decision tree leads to six precise rules describing the dependence of the output, which in this example is the heat pump power, on the various inputs, which are formed by various external economic and environmental factors such as electricity grid price and ambient temperature at the current time and their predicted values at future time points. The list of learned rules for optimized predictive heat pump operation inferred from the learned decision tree in Figure 2 is as follows:

1. If Grid Price at 0h > 2.7 Cent/kWh and Ambient Temp. at 4h > 4.5°C, then $P_{hp,th} = 0kW$.
2. If Grid Price at 0h between 1.6 and 3.2 Cent/kWh and Ambient Temp. at 4h <= 4.5°C, then $P_{hp,th} = 10kW$.
3. If Grid Price at 0h > 3.2 Cent/kWh and Ambient Temp. at 4h <= 4.5°C, then $P_{hp,th} = 4kW$.
4. If Grid Price at 0h between 1.6 and 2.7 Cent/kWh and Ambient Temp. at 4h > 4.0°C, then $P_{hp,th} = 4kW$.
5. If Grid Price at 0h between 0 and 1.6 Cent/kWh, then $P_{hp,th} = 14kW$.
6. If Grid Price at 0h <= 0.0 Cent/kWh, then $P_{hp,th} = 26kW$.

Test and Validation

To evaluate the effectiveness of the developed concept, it is essential to determine if proactive, rule-based strategies can be developed for practical applications using the proposed method. These strategies should perform reliably in real-world situations and offer advantages over other approaches.

Hardware-in-the-Loop Test Setup

In a Hardware-in-the-Loop (HIL) experiment, the novel method is tested for practical suitability and robustness in the secure environment of a laboratory. By combining physically existing components (heat pump) with simulation software and conditioning modules emulating the simulated components (building, ground source for heat pump), as shown in Figure 3, the test can be conducted under realistic conditions. Thus, the HIL experiment represents the final testing stage before the field test in a real (inhabited) building.

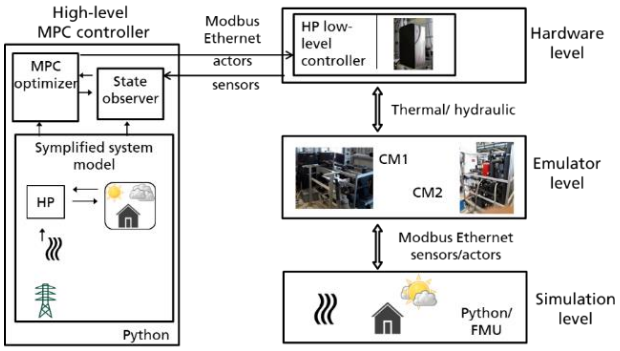

Figure 3: Hardware-in-the-Loop Test setup

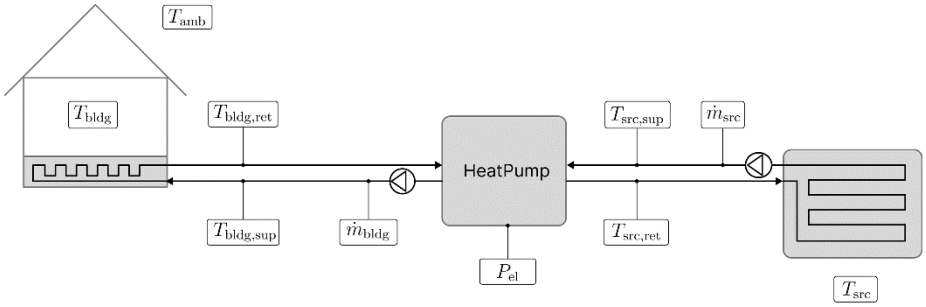

Figure 4: Diagram of the application problem consisting of an emulated building (simulation), heat pump, and emulated geothermal heat source.

Application Problem Setup

The goal is to explore, using a straightforward but realistic example, the viability and potential of the concept. This is achieved by applying the developed methodology to a practical scenario: the operation of a grid-supportive heat pump in a building. The experimental setup includes a simulated building, a heat pump, and a simulated geothermal heat source, as illustrated in Figure 4. The selected building is based on a reference building, as shown in Figure 7, from the open-access building database TABULA (TABULA, 2017). As detailed in Table 1, some of the building parameters, such as thermal mass, were adjusted from those of the original reference building to increase the load shifting potential.

The simulation utilizes a single-zone model, governed by the fundamental principles that describe thermal behavior. The heat pump in the lab is a water-to-water heat pump with a peak thermal power of 26 kW.

The aim of the control problem is to run the heat pump in a way that flexibly adapts to the grid by minimizing energy costs while maintaining the building's indoor temperature near the target value. We consider the electricity price, simplified here as the EEX (European Energy Exchange) price without any extra taxes or fees, as an indicator of grid conditions. Conversely, in operations that do not adapt to grid flexibility, the goal is to reduce electric energy consumption. A

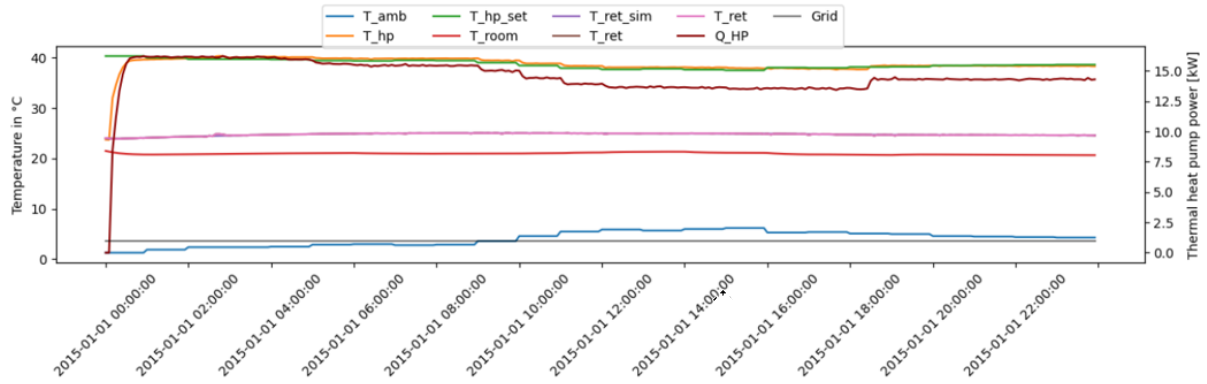

Figure 6: Heating curve regulated heat pump operation

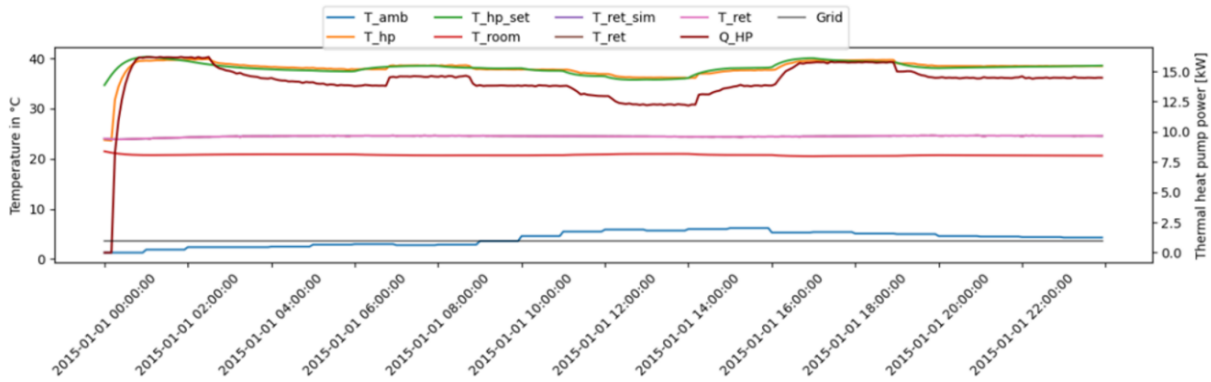

Figure 5: MPC controlled heat pump operation

specific day, January 1, 2015, has been selected as the test scenario, along with the corresponding weather data. On this day, the ambient temperature varies between 1.3°C and 6.2°C and the EEX electricity price varies between -4.7Cent/kWh and 2.6 Cent/kWh. The set point temperature is 21°C and for simplicity, we do not consider a night set-back.

Figure 7: Reference building DE.N.MHF.09.Gen (Source: TABULA Web Tool https://webtool.building-typology.eu/#bm)

For reference, we consider a heating curve controller and a MPC controller as described in (Frison et al., 2018). The heating curve controller operated the supply temperature according to the current outdoor temperature. The heating curve is tuned to the considered building and the considered test day.

Table 1: Building parameters of the simulated building (parameters were adapted from original reference building)

Floor area	A_{floor}	835 m^2
Transmission Heat transfer coefficient (adapted)	H_{tr}	540 W/K
Heat transfer coefficient for ventilation	H_{ve}	355 W/K
Specific heat capacity of a building (adapted)	c_{bldg}	100 Wh/m^{2}K

Results

In our initial series of experiments, we examined the energy efficiency of heat pump operation using both a standard heating curve controller and a MPC controller, as illustrated in Figure 6 and Figure 5, respectively. The MPC controller, which optimizes the heat pump's supply temperature based on an internal model of the system, demonstrated marginally superior energy consumption outcomes. This experiment serves on one hand as a validation of the MPC controller's effectiveness but also highlights the

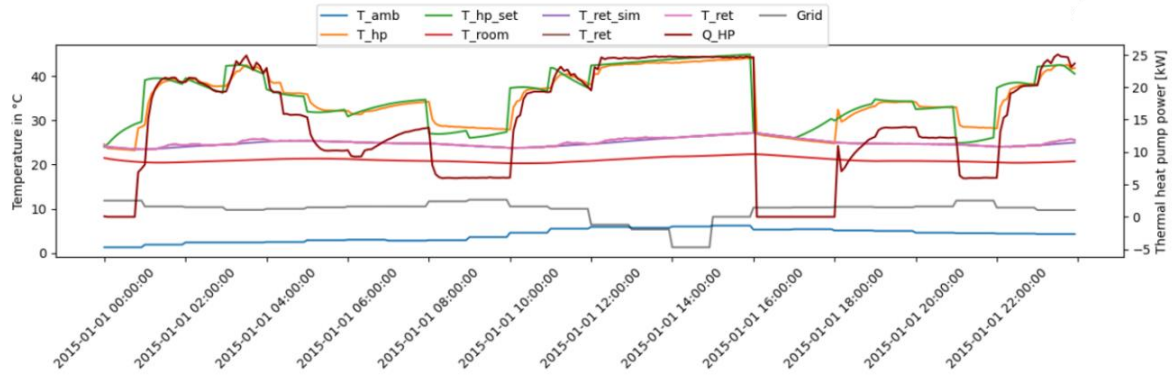

Figure 8: Price signal-optimized heat pump operation for one day, regulated with MPC.

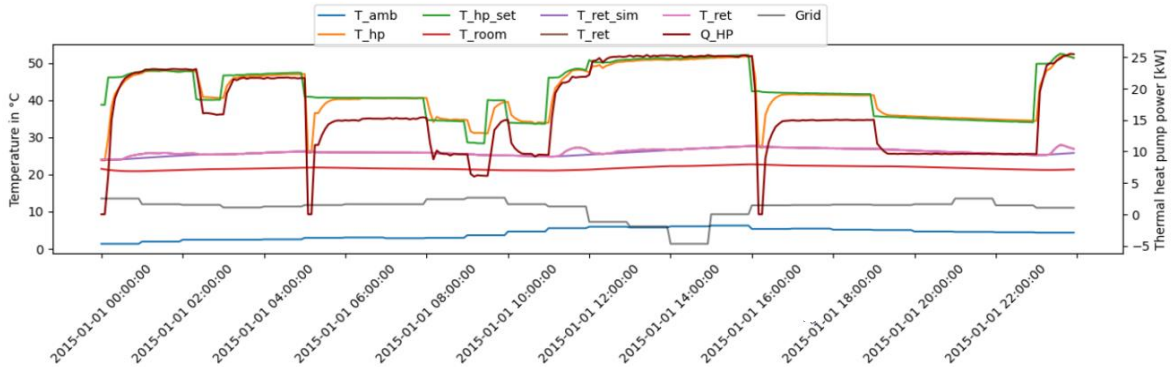

Figure 9: Price signal-optimized heat pump operation for one day, regulated with learned rules.

Table 2: Comparison of KPI results for different controllers during 24-hour test operation. Variable cost refers to the variable component of energy expenses.

	Energy consumption (th.)	Energy consumption (el.)	Variable Cost Euro	Comfort deviation (max/av.)
Heating curve control	349 kWh	56 kWh	0.56	0.37K/0.12K
MPC (min. energy consumption)	340 kWh	54 kWh	0.54	0.51K/0.26Kh
MPC (price-based)	349 kWh	66 kWh	0,2	0.74K/0.22K
Learned rules	397 kWh	79 kWh	0,38	0.17K/0.01K

challenge of surpassing a well-tuned heating curve's performance for energy efficient building operation.

In the second part of the experiment, we devised an MPC controller for grid-flexible heat pump operation minimizing the electricity cost of heat pump operation, as shown in Figure 8. Using this data, the self-learning rule-based controller was derived with the proposed approach, with results shown in Figure 9. The rule base derived through AI methods contains conditions based on various variables such as outdoor temperature and electricity price at different time points and the current moment and the predicted values for the future. Essentially, this rule base constitutes a complex decision system where temperature and grid conditions at various time points trigger specific responses. They dictate how the heat pump's power should be regulated at different electricity prices to ensure the most cost-effective operation. The electricity grid conditions at various time points play a crucial role in determining the responses, often in conjunction with the ambient temperature conditions. For example, the full power of the heat pump should be utilized when the grid signal falls more than one standard deviation below the mean, and additionally, the outdoor temperature is not significantly higher than the mean. The conditions need to be evaluated, and the correct rule applied to determine the appropriate response which leads to the minimal energy cost operation.

Table 2 compares key performance indicators for different strategies. As expected, the MPC control, based on optimization calculations, leads to the most cost-effective operation. Comparing the behavior resulting from MPC control with the schemes generated by the method presented here, it is evident that the rule schema produced can also react to the price signal and save costs compared to standard regulation.

Conclusion

The outcome of this project is a method that derives new knowledge in the form of understandable rules from an existing database, such as measurement or simulation data. This leads to a knowledge-based system for energy systems. As this work should serve as an initial feasibility analysis, we conclude that further work should be invested in generating and adapting the rules to increase quality and interpretability. Besides learning intelligent operating rules, this approach is also interesting for other objectives. An example is deriving new insights from a large measurement dataset that is not directly accessible to the human user.

Acknowledgement

The research work is supported by funds from the Federal Ministry for Economic Affairs and Energy (BMWi) under grant numbers 03SF0623A/B/C, as decided by the German Bundestag. Project management is undertaken by the Project Management Agency Jülich (PtJ). The authors express their sincere gratitude for the funding, support, and collaboration.

References

Clauß, J., Finck, C., Vogler-Finck, P., & Beagon, P. (2017). Control strategies for building energy systems to unlock demand side flexibility–A review. *IBPSA Building Simulation 2017, San Francisco*

Frison, L., Paul, S., Koller, T., Fischer, D., Frison, G., Boedecker J., Engelmann, P. (2020). Hardware-in-the-loop test of learning-based controllers for grid-supportive building heating operation. Proceedings *IFAC Automatic Control Conference Berlin 2020.*

Gwerder, M. (2010). Prädiktive Gebäuderegelung mithilfe von Wetter- und Anwesenheitsvorhersagen: Resultate des

Projekts OptiControl. *SGA-SSPA-SSAC Bulletin Nr. 57*.

Hussain, A., Nguyen, T., & Lee, J. (2021). Enhancing Explainability in Imitation Learning for Energy-Efficient Building Design. Journal of Building Performance, 12(4), 567-580.

May-Ostendorp, P.T. (2012). Offline Model Predictive Control of Mixed Mode Buildings for Near-Optimal Supervisory Control. Dissertation University of Colorado at Boulder.

Picard, D., Kvasnica, M., & Helsen, L. (2018). Approximate model predictive building control via machine learning. *Applied energy 218, 199-216*.

Serale, G., Fiorentini, M., Capozzoli, A., Bernardini, D., Bemporad, A. (2018). Model predictive control (MPC) for enhancing building and HVAC system energy efficiency: Problem formulation, applications and opportunities. *Energies*, *11*(3), 631.

TABULA WebTool. https://webtool.building-typology.eu, 2017 (accessed Feb. 2024).

Zhang, Y., Siebers, P.-O., & Aickelin, U. (2018). Using data mining to improve the performance of thermal energy storage systems. Renewable and Sustainable Energy Reviews, 82, 3356-3366.

BauSIM 2024 in Wien
23. September – 26. September

Modelling Ice Formation and De-icing for Enhanced Performance of Compact Facade-integrated Air-to-Water Heat Pumps

William Monteleone[1], Fabian Ochs[1]
1 Unit of Energy Efficient Buildings, University of Innsbruck, Austria

Abstract

To boost the renovation of multi-family buildings in densely populated areas, decentralised air-to-water heat pump solutions are one of the alternatives to replace fossil-based (e.g. gas or oil) boilers. A common issue faced by all heat pumps in alpine and sub-alpine climates is the need to defrost the outdoor heat exchanger. This study investigates the performance of a compact façade-integrated 1.5 kW R290 air-to-water heat pump, developed using a holistic component-to-system level approach. A semi-empirical frost formation model is introduced and the system's capability to meet the space heating demand of a small, renovated flat is assessed by means of dynamic system simulation. Due to the frequent defrosting cycles and to the worsening of the performance of the outdoor heat exchanger at low air temperatures, a 1 kW electric post-heater is needed to support the heat pump during the coldest months. A system performance factor of 1.95 is reached considering the whole heating season.

Introduction

To achieve a fully decarbonised building stock by 2050, a crucial step involves accelerating the rate of renovations and the replacement of apartment-wise gas boilers (European Commission, 2023; Lutsch, 2017). A promising solution for multi-family buildings in densely populated areas is seen in serial renovations with prefabricated façades (Pihelo et al., 2017; Silva et al., 2013). Enhancing the efficiency and sustainability of building infrastructure can be achieved by integrating compact and silent decentralised air-to-water heat pumps (HPs) into façade elements (Dermentzis et al., 2018; Siegele et al., 2019). This innovative approach could support the decentralised transition from conventional flat-wise gas boilers providing a solution for both domestic hot water (DHW) preparation and space heating (SH). Despite their numerous advantages, a common challenge faced by all air-to-water HPs is their performance under freezing conditions and the subsequent need for de-icing (Vocale et al., 2014). In this work, a façade-integrated 1.5 kW R290 air-to-water HP, developed following a holistic component-to-system level approach (Ochs et al., 2022) is investigated. This study addresses in particular the aspects of ice-formation and de-icing by introducing a semi-empirical model for ice formation.

Performance maps for the thermal capacity and the electric power consumption of the HP are presented and introduced in a dynamic HP system model developed within MATLAB-Simulink. Here the HP system is coupled to a 37 m^2 flat undergoing renovation and to a detailed model of the hydraulic circuit and terminals for the supply of the SH demand. The aim of this work is on one hand to assess the capability of the system to meet the SH demand of the single flat and, on the other hand, the findings of this study will underline the importance of considering the degradation of the air-side heat transfer when evaluating the applicability of compact, low-power HPs.

Concept

The developed decentralised HP concept, shown in Figure 1, consists of a façade-integrated outdoor unit, housing the evaporator and four axial fans and of an indoor unit with the compressor and the remaining hydraulic components for the delivery of the SH demand. The same concept has been implemented for DHW preparation, as also described in (Monteleone et al., 2024).

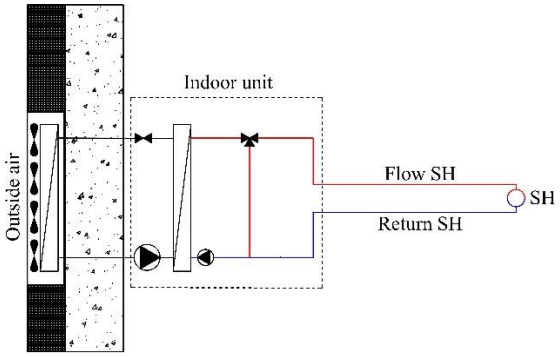

Figure 1: Conceptual design of a façade-integrated mini-split HP for the supply of the SH demand.

The refrigerant cycle is based on propane (R290) therefore the maximum refrigerant charge is constrained to 150 g for split indoor installations (IEC 60335-2-40, 2022). De-icing is provided by means of flow reversing and the refrigerant cycle does not have an accumulator.

Case study

To assess the capability of the HP to supply the SH demand for a small flat, a virtual concept demonstration was provided to investigate the applicability of the HP for a small flat depending on the quality of the building envelope and on the supply temperature of the heating system. The residential building shown in Figure 2, located in Innsbruck, Austria, subjected to renovation and for which floor plans and information about the heating system were made available, was selected for this analysis. The building has a ground floor and four floors above ground, with mainly single-room apartments with a living area of 37.3 m². The typical apartment consists of a living room, where the thermostat for the heating system is installed, a bedroom, a bathroom and an atrium. Except for the atrium, all rooms are directly heated by radiators. The simulated renovation scenario corresponds to a deep renovation with mechanical ventilation with heat recovery (MVHR) and replaced radiators, with a heating demand (HD) of 49 kWh/(m^2 y).

Figure 2: Multi-family house selected as virtual demonstration, street side view.

Theory

Ice formation on the surface of a fin-tube heat exchanger takes place if the surface temperature of the fin is lower than the dew point and the freezing temperature of water. It is a complex physical phenomenon combining fluid dynamics, heat and mass transfer. The evaluation of the frost layer growth requires therefore a complete characterisation of the airflow pattern and the solution of the continuity, momentum, heat transfer and vapour transport equations for the air-frost interface as in (Lenic et al., 2009). As the first ice crystals begin to nucleate on the surface of the heat exchanger, a porous structure slowly forms and spreads. The continuous transition from water vapour to frost causes the frost layer to increase in density and grow further away from the heat exchanger surface. This causes an increase in the thermal resistance of the frost layer, thus causing an increase in the surface temperature and generating a liquid film at the interface between air and frost. The formed liquid film will eventually diffuse inside the frost layer and freeze. The heat and mass transfer within the frost layer is described by equations (1) and (2):

$$\rho_f \frac{\partial T_f}{\partial t} = \nabla\left(\frac{\lambda_f}{c_{p,f}} \nabla T_f\right) + q_{sub} \frac{\partial \rho_f}{\partial t} \quad (1)$$

$$\frac{\partial \rho_f}{\partial t} = \nabla\left(\mathrm{D}_{eff}\, \rho_a\, \nabla\,(\rho_v/\rho_a)\right) \quad (2)$$

Where q_{sub} is the specific heat of sublimation and D_{eff} the effective diffusion coefficient of water vapour through the frost layer. As frost growth fully develops, part of the water vapour deposits on the frost layer, while the remaining part diffuses through the layer increasing its density. During this phase, the growth rate can be expressed with the equations (3) to (5). For the calculation of the overall heat transfer coefficient of the heat exchanger under frost formation conditions (for example by means of a modified ε-NTU method as suggested in (Chung et al., 2019)), the variation of the thickness of the frost layer with time must be calculated, as shown in equation (6).

$$\dot{m}_a = \dot{m}_{\Delta y} + \dot{m}_{diff} \quad (3)$$

$$\dot{m}_a = \rho_a\, D\, \nabla \mathrm{w} \quad (4)$$

$$\dot{m}_{diff} = -\rho_a\, D_{eff}\, \frac{\mathrm{d}}{\mathrm{dy}}(\rho_v/\rho_a) \quad (5)$$

$$\frac{dy_f}{dt} = \frac{1}{\rho}\left(\dot{m}_a - \dot{m}_{diff}\right) \quad (6)$$

It is immediately understandable that, when considering a system simulation involving the heat pump, the hydraulic network and the building, a detailed physical model of ice formation would be computationally demanding for the evaluation of the system performance over a whole year. Therefore, a simplified experiments-based frost formation model needs to be developed.

Methodology

Experiments

To measure the steady-state performance of the refrigerant cycle, a functional model of the HP was set up in the PASSYS test cells of the University of Innsbruck (see Figure 3). In order to reach quasi-steady heat sink conditions, a hot water storage with a volume of 200 litres was used as heat receiver. The temperature conditions on the façade are imposed by means

of a movable climate chamber, while the relative humidity cannot be controlled with the existing infrastructure. The nominal heating power of the HP at A7W50 is 1.5 kW. Table 1 summarises the boundary conditions applied during the experimental procedures. Based on the measurements, performance maps for the thermal capacity, for the cooling capacity and for the electric power consumption were generated depending on the source and sink temperatures. Each measurement starts with a completely ice-free evaporator and ends when the high-pressure failure of the HP control is triggered due to the presence of ice on the evaporator surface. To quantify the impact of ice formation on the refrigerant cycle, the variation of the condenser power as well as of the electric power consumption was observed and empirical-based functions were deduced as a function of time and of the outdoor temperature. Comparing the actual value of the condenser power or of the electric power consumption against the nominal steady-state value under frost-free conditions, a correction factor is introduced, as highlighted in equations (7) and (8).

$$f_{cond} = \frac{\dot{Q}_{cond,act}}{\dot{Q}_{cond,nom}} \quad (7)$$

$$f_{el} = \frac{P_{el,act}}{P_{el,nom}} \quad (8)$$

Table 1: Summary of the boundary conditions applied during the measurements.

BC	Value
Source (air) temperature	0...2...4 °C
Source (air) relative humidity	90 %
Air volume flow	350 m^3/h
Sink (water) temperature	35 °C
Water volume flow	4 l/min

Figure 3: Functional model of the indoor unit of a façade-integrated split air-to-water heat pump.

Simulation

Based on the measurements, performance maps of the HP were generated by means of a refrigerant cycle model developed within the MATLAB environment, as described in (Monteleone et al., 2024) and shown in Figure 4. Performance maps were thus calculated for -15, -7, 2, 7, 12, 20 °C outdoor air temperature, as well as 35, 45, 55 °C water supply temperature and given as an input to a dynamic system model in MATLAB-Simulink with the use of the Carnot Toolbox and Carnot UIBK libraries (Solar-Institut Juelich FH Aachen, 2018; Unit of Energy Efficient Building - University of Innsbruck, 2018). The model includes the flat, the hydraulic circuit and the heat terminals. A conceptual scheme of the flat, with the position of HP and radiators, is shown in Figure 5. A single circulation pump supplies heating water to the circuit with a total volume flow of 7 l/min. The considered temperature setpoint during the heating season corresponds to 22.5 °C to be on the safe side regarding the user influence. The heating season lasts from January to May and then from September to December.

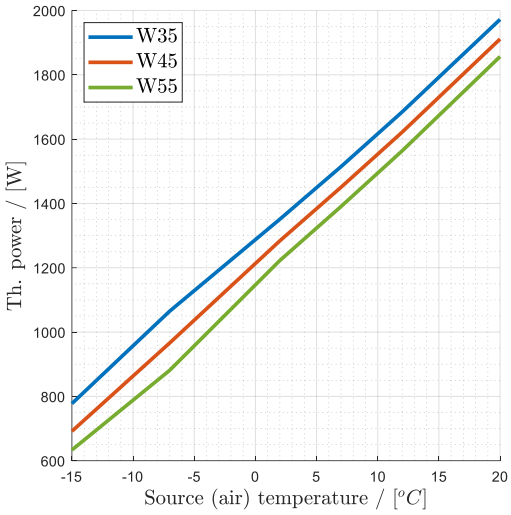

(a)

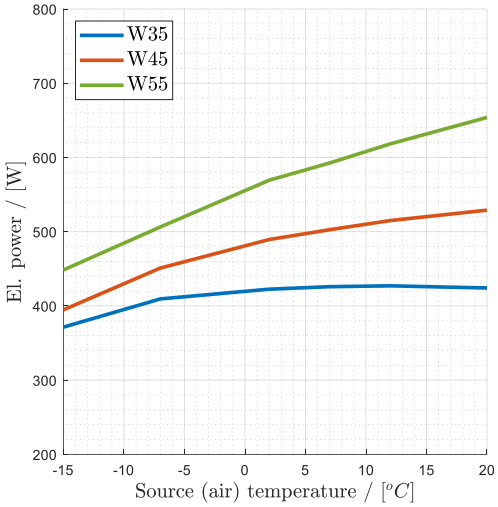

(b)

Figure 4: Simulated performance maps of (a) condenser power and (b) electric power consumption for the split-type air-to-water HP for sink temperatures between 35 and 55 °C and air temperatures between -15 and 20 °C.

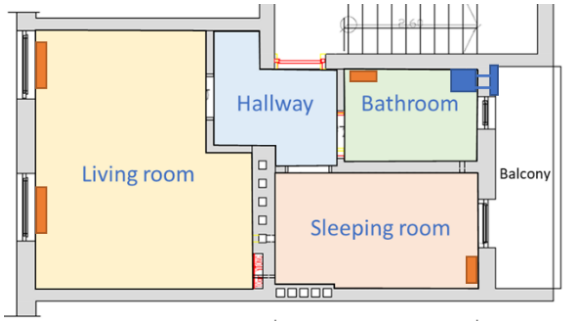

Figure 5: Conceptual drawing of the flat with position of the radiators for each room (orange) and HP (blue).

The HP is turned on and off by means of a thermostat placed in the living room with a switching differential of 1 K. Additionally, for each room, a PI-controlled diverter allows the fine tuning of the water volume flow. When the thermal capacity of the HP alone is not sufficient to supply the SH demand and the thermostat in the living room indicates a temperature that is 3 K lower than the setpoint, a 1.0 kW central electric post-heater is activated.

HP control

In addition to the thermostatic control, the HP is also equipped with an internal control aimed at minimising the number of on-off cycles and at deciding when to activate de-icing. The minimum operational interval for the HP corresponds to 2 minutes, while the maximum depends on the outdoor air temperature. If the air temperature is higher than 6 °C, the HP is allowed to run as long as the thermostatic control in the living room turns it off. Below this temperature limit, the maximum operational interval corresponds to 60 minutes. During this interval, depending on the outdoor relative humidity as in (Zhu et al., 2015), a correction factor as in (7) and (8) is applied to the condenser power and to the electric power consumption of the compressor to consider the worsening of the performance of the refrigerant cycle under frost formation. Once the 60 minutes have passed, the room thermostatic control is overridden, and the HP is shut down to start de-icing for a total of 10 minutes. This hypothesis was adopted to make sure that the entire frost layer is removed within this interval. It must be however pointed out that this might lead in the reality to unnecessary defrosting cycles, as frost growth is not constant but depends on relative humidity and temperature of the ambient air. For instance, as remarked in (Zhu et al., 2015), for temperatures between 0 and 6 °C and relative humidity between 50% and 70%, only mild frosting takes place. In those cases, the duration of the de-icing cycles could be considerably shortened or vice versa the operational interval of the HP could be extended without major performance drawbacks. De-icing takes places by means of flow reversing and the electric power consumption of the compressor during this phase is also counted.

KPIs for performance evaluation

The HP performance will be evaluated for each month of the heating season by means of the performance factors (PFs) shown in equations (9) to (10).

$$PF_{HP} = \frac{Q_{HP,th}}{Q_{HP,el}} \quad (9)$$

$$PF_{HP,sys} = \frac{Q_{HP,th}}{Q_{HP,el} + Q_{HP,el,deicing} + Q_{postH,el}} \quad (10)$$

$Q_{HP,th}$ = Heat delivered from the HP to the flat in [kWh$_{th}$]; $Q_{HP,el}$ = Electricity required by the HP to supply the flat's SH demand in [kWh$_{el}$]; $Q_{HP,el,deicing}$ = Electricity required by the compressor during de-icing in [kWh$_{el}$]; $Q_{postH,el}$ = Electricity required by the electric flow-type post-heater to support the supply of the flat's SH demand in [kWh$_{el}$].

Results and discussion - Experiments

Figure 6 (a) to (c) highlights the trend of the condenser power and of the compressor electric power consumption with time at ambient temperatures of 0, 2 and 4 °C respectively. Due to the inertia of the refrigerant cycle and to the absence of a refrigerant accumulator, the HP reaches steady state conditions approximately after 15-20 minutes of operation. This behaviour is independent from the outdoor air temperature for the actual tests. Once in steady state, the HP delivers a constant thermal capacity for a limited amount of time, then a decrease in condenser power is observed. The duration of the interval with constant condenser power, as well as the rate of decrease, are strongly depending on the outdoor air temperature as this affects how fast the surface temperature of the heat exchanger falls below the dew point and the freezing point of water. This results in a maximum operational interval of 72 minutes at 0 °C, 77 minutes at 2 °C and 79 minutes at 4 °C at a relative humidity of about 90%. Differently from the condenser power, the electric power consumption exhibits no relevant change in absolute value. Therefore, for further evaluations, this will be considered constant and independent from frost formation. Based on the measurement results, the correction factor function to be applied to the thermal capacity of the HP, depending on time and outdoor temperature is shown in the contour plot of Figure 7.

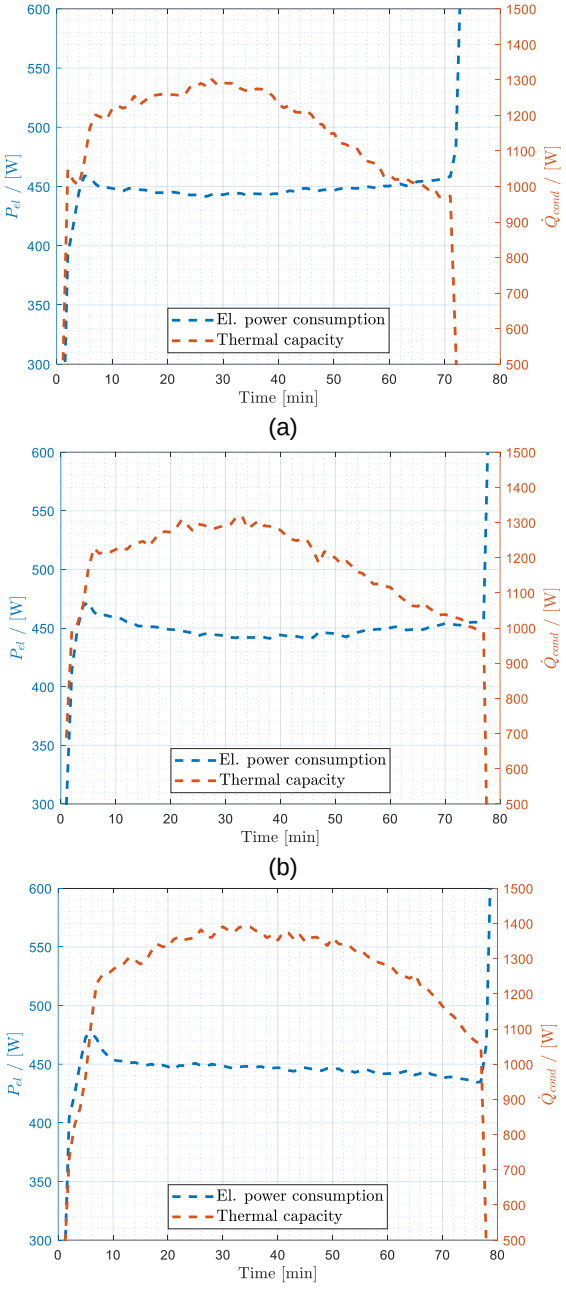

Figure 6: Measured condenser and electric power depending on time at ambient temperature of (a) 0 °C, (b) 2 °C and (c) 4 °C.

As highlighted in the graph, for air temperatures higher or equal than 6 °C, the heat exchanger is virtually frost free and no correction factor is applied. For temperatures between 0 and 4 °C, in the first 15 minutes of operation, no correction factor is applied, in accordance with the measurements shown in Figure 6. After 60 minutes of operation, a correction factor equal to 0.6 (e.g. 60% of the steady-state frost-free thermal capacity) would be applied at 0 °C, 0.75 at 2 °C and 0.85 at 4 °C. At air temperatures lower than 0 °C the decrease in the thermal capacity is much steeper and, for example, a

correction factor of 0.5 would be applied at -2 °C after 60 minutes of operation.

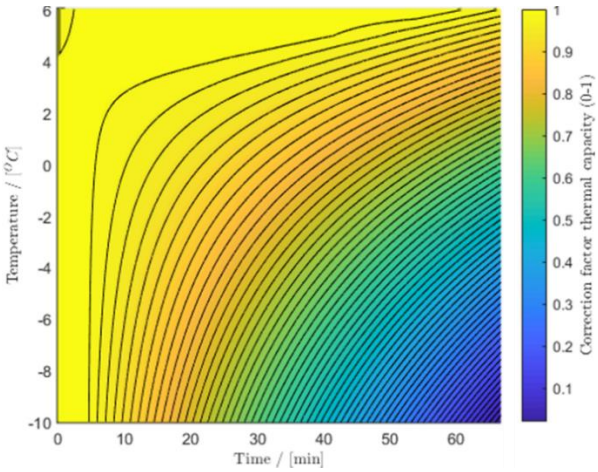

Figure 7: Contour plot of the correction factor for the thermal capacity used in the dynamic system simulations.

Results and discussion - Simulations

Considering the correction factor function shown in Figure 7, the HP system performance was analysed and the simulation results depicted in Figure 8 were obtained for a renovated 37 m^2 flat. First, the simulated daily average temperature for each thermal zone of the considered flat for each day of the year is highlighted. Due to the control of the HP, the temperature in bedroom and bathroom is, as expected, lower than the temperature in the living room. The heating setpoint can be kept by the HP system throughout the whole heating season, except for some weeks at the end of January and during December when the temperature in the living room is on average 1.0 K lower than the required setpoint. Figure 8 then summarizes the thermal energy delivered by the HP to the flat during the heating season, as well as the electric energy necessary for the HP itself, the electric post-heater (PH) and for de-icing. Electric post-heating is needed only during December and January. More specifically the electric consumption for post-heating accounts for 52 and 118 kWh$_{el}$ for December and January respectively. The electric consumption for de-icing accounts instead for 6.2 % of the total electric consumption during the heating season. Then, the PFs according to equations (9) and (10) were calculated. The PF, considering PH and de-icing, ranges from 1.33 in January to 3.14 in September. The PF over the whole heating season corresponds to 1.95.

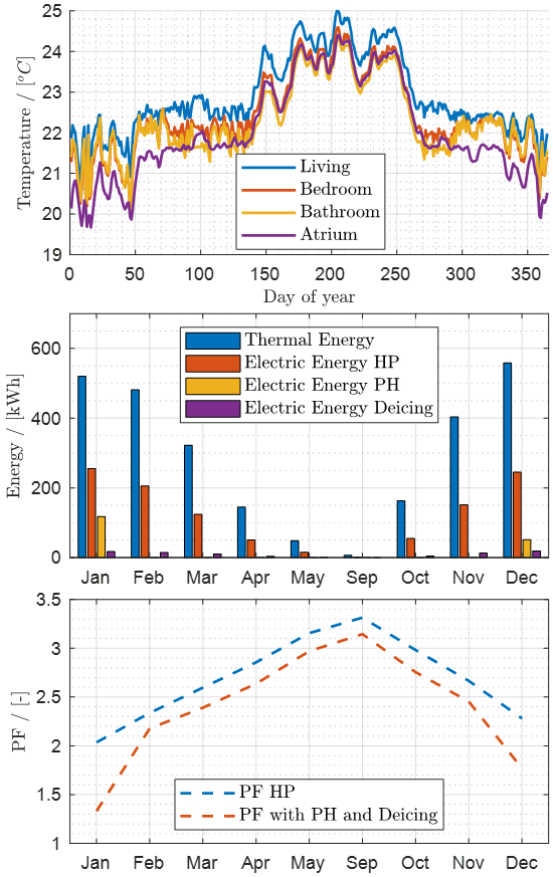

Figure 8: From top to bottom yearly simulated temperature for each thermal zone, energy balance of the HP system and PF during the heating season.

Conclusion

Within this work, a semi-empirical model for frost formation has been presented and implemented within a dynamic HP system simulation for a 37 m^2 renovated flat. Based on laboratory measurements, a correction factor for the thermal capacity, function of the outdoor air temperature and the operational interval, was calculated and adopted within the dynamic HP model. During the experiments, no substantial variation was noted instead for the electric power consumption of the compressor and therefore no factor was applied in the simulations. For the considered hypotheses, the developed split air-to-water HP can supply the SH demand for most of the heating season, while a 1 kW electric post-heater is needed during December and January to support the HP operation due to the colder outdoor air temperatures and the more frequent de-icing cycles. Therefore, a HP seasonal performance factor of 2.39 is obtained from the dynamic system simulations, 1.95 if the electric consumption for de-icing and post-heating are also considered. In the future a more accurate frost-formation model needs to be implemented by introducing the relative humidity as additional

variable during the experimental procedures. Additionally, a small buffer storage will be also introduced within the dynamic system model and its influence on the HP operation and on the use of the post-heater will be analysed.

Nomenclature

Act	Actual
BC	Boundary conditions
Cond	Condenser
DHW	Domestic hot water
El	Electric
HD	Heating demand
HP	Heat pump
MVHR	Mechanical ventilation with heat recovery
Nom	Nominal
NTU	Number of transfer units
PF	Performance factor
PostH	Post-heater
SH	Space heating
Sys	System
Th	Thermal

Acknowledgements

This work has been part of the research projects “FitNeS” (FFG-Nr. 867327) and “PhaseOut” (FFG-Nr. 999895470) funded by the FFG (Austrian Research Promotion Agency) in the “Stadt der Zukunft” program.
Our thanks go to the project partners Drexel und Weiss, Drexel Reduziert, Element Design, IIG, Winter, Rothbacher, and Kulmer Holzbau.

References

Chung, Y., Yoo, J. W., Kim, G. T., & Kim, M. S. (2019). Prediction of the frost growth and performance change of air source heat pump system under various frosting conditions. *Applied Thermal Engineering*, *147*, 410–420. https://doi.org/10.1016/j.applthermaleng.2018.10.085

Dermentzis, G., Ochs, F., Siegele, D., & Feist, W. (2018). Renovation with an innovative compact heating and ventilation system integrated into the façade – An in-situ monitoring case study. *Energy and Buildings*, *165*, 451–463. https://doi.org/10.1016/j.enbuild.2017.12.054

European Commission. (2023). *Energy Performance of Buildings Directive*. https://energy.ec.europa.eu/topics/energy-efficiency/energy-efficient-buildings/energy-performance-buildings-directive_en

IEC 60335-2-40. (2022). *Household and similar electrical appliances - Safety - Part 2-40: Particular requirements for electrical heat pumps, air-conditioners and dehumidifiers*.

Lenic, K., Trp, A., & Frankovic, B. (2009). Transient two-dimensional model of frost formation on a fin-and-tube heat exchanger. *International Journal of Heat and Mass Transfer*, *52*(1–2), 22–32. https://doi.org/10.1016/j.ijheatmasstransfer.2008.06.005

Lutsch, W. (2017). Clean energy for all Europeans. *Euroheat and Power (English Edition)*, *14*(2), 3. https://doi.org/10.2833/9937

Monteleone, W., Ochs, F., Dermentzis, G., & Breuss, S. (2024). Simulation-assisted design of a silent façade-integrated R290 mini-split heat pump. *Applied Thermal Engineering*, *243*, 122520. https://doi.org/10.1016/j.applthermaleng.2024.122520

Ochs, F., Monteleone, W., Dermentzis, G., Siegele, D., & Speer, C. (2022). Compact Decentral Façade-Integrated Air-to-Air Heat Pumps for Serial Renovation of Multi-Apartment Buildings. *Energies*, *15*(13). https://doi.org/10.3390/en15134679

Pihelo, P., Kalamees, T., & Kuusk, K. (2017). NZEB Renovation with Prefabricated Modular Panels. *Energy Procedia*, *132*, 1006–1011. https://doi.org/10.1016/j.egypro.2017.09.708

Siegele, D., Ochs, F., & Feist, W. (2019). Novel speed-controlled exhaust-air to supply-air heat pump combined with a ventilation system. *Applied Thermal Engineering*, *162*. https://doi.org/10.1016/j.applthermaleng.2019.114230

Silva, P. C. P., Almeida, M., Bragança, L., & Mesquita, V. (2013). Development of prefabricated retrofit module towards nearly zero energy buildings. *Energy and Buildings*, *56*, 115–125. https://doi.org/10.1016/j.enbuild.2012.09.034

Solar-Institut Juelich FH Aachen. (2018). *CARNOT Toolbox*. https://fh-aachen.sciebo.de/index.php/s/0hxub0iIJrui3ED

Unit of Energy Efficient Building - University of Innsbruck. (2018). *carnotUIBK Toolbox*.

Vocale, P., Morini, G. L., & Spiga, M. (2014). Influence of outdoor air conditions on the air source heat pumps performance. *Energy Procedia*, *45*, 653–662. https://doi.org/10.1016/j.egypro.2014.01.070

Zhu, J. H., Sun, Y. Y., Wang, W., Deng, S. M., Ge, Y. J., & Li, L. T. (2015). Developing a new frosting map to guide defrosting control for air-source heat pump units. *Applied Thermal Engineering*, *90*, 782–791. https://doi.org/10.1016/j.applthermaleng.2015.06.076

BauSIM 2024 in Wien
23. September – 26. September

Parameterstudie zur Optimierung der Belüftung in Kinosälen anhand eines Automatisierungstools und zonaler Strömungssimulationen

Christina Matheis[1], Gunnar Grün[12]

1 Fraunhofer Institut für Bauphysik IBP, Deutschland, E-Mail: christina.matheis@ibp.fraunhofer.de

2 Universität Stuttgart, Institut für Akustik und Bauphysik, Deutschland, E-Mail: gunnar.gruen@iabp.uni-stuttgart.de

Kurzfassung

Eine nutzerorientierte Planung gewinnt in der Baubranche immer mehr an Bedeutung. Somit sind auch Aspekte wie die Innenraumluftqualität und -hygiene vermehrt zu beachten. Um das Raumklima optimal auszulegen, wird ein Parametrierungswerkzeug vorgestellt, mit dem simulationsbasiert eine Vielzahl an Varianten hinsichtlich der Raumluftströmung untersucht und bewertet werden kann. Das dazu erstellte Tool automatisiert die Prozessabläufe von Parameterstudien und ist in der Programmiersprache Python implementiert. Die Raumluftströmung wird mit einem zonalen Simulationsansatz ermittelt und basiert auf dem VEPZO-Modell (Velocity Propagating Zonal Model) nach (Norrefeldt et al. 2012).

Als Anwendungsfall wird in dieser Studie die optimierte Belüftung in Kinosälen betrachtet. Dabei wird zum einen der Einfluss von verschiedenen Lüftungsarten, -mengen und Belegungsdichten auf die Raumluftqualität mittels CO_2 als Marker untersucht. Zum anderen sollen die Auswirkungen von Partikelquellen und der Einsatz von mobilen Luftreinigungsgeräten bewertet werden. Für die Auswertung werden die lokalen CO_2- und Partikel-Konzentrationen der Frischluftmenge gegenübergestellt.

Abstract

User-oriented planning is becoming increasingly important in the construction industry. As a result, aspects like indoor air quality and hygiene also need to be taken into account more and more. In order to optimally design the indoor climate, a method to investigate a large number of variants of indoor air flow is presented using a simulation-based parameter studies tool. The tool created for this purpose automates the process of parameter studies and is implemented in the programming language Python. The VEPZO-model (Velocity Propagating Zonal Model) (Norrefeldt et al. 2012) forms the base for the tool, which consists of a zonal simulation approach for indoor air flow patterns.

This study considers optimized ventilation in cinemas as application case. On the one hand, the influence of different ventilation types, quantity and occupancy rate on indoor air quality is investigated using CO_2 as a parameter. On the other hand, the effects of particle sources and the use of mobile air purification devices will be investigated. For the evaluation, the local CO_2 and particle concentrations are compared with the amount of fresh air.

Einleitung

Bei der Planung von Räumlichkeiten rückt – auch aufgrund der Erfahrungen mit der Corona-Pandemie – die Luftqualität in Innenräumen in den Fokus. Um ein komfortables und gesundes Raumklima zu gewährleisten, ist es immer wichtiger dies bereits in der Planung aufzugreifen und die Räume mit einer effektiven Belüftung auszustatten. Damit können die Innenluftqualität unter Hygiene- und Komfortaspekten betrachtet und nutzerfreundliche Räume mit einer hohen Qualität geschaffen werden.

Dies erfordert in der Planungsphase geeignete Tools und Möglichkeiten, die Betrachtung des Raumklimas möglichst effizient zu gestalten. In der Planungsphase sind typischerweise jedoch Informationen zur Ausbildung der Raumluftströmung und möglichen Ausbreitung von Luftbestandteilen nicht verfügbar, um schnell und mit geringem Aufwand Varianten zu vergleichen. Mit dem hier vorgestellten Parametrierungswerkzeug sollen verschiedene Belüftungssituationen unter variierten Realbedingungen simulativ getestet werden können. Als Basis dafür dient das Raumströmungsmodell VEPZO (Velocity Propagating Zonal Model) nach (Norrefeldt et al. 2012). Dessen zonaler Simulationsansatz ermöglicht durch die geringen Rechenzeiten eine Berechnung mit einer Vielzahl an Parametervariationen in der frühen

Planungsphase. Die Automatisierung des Simulations- und Auswerteprozesses soll die Planung effektiv und anwenderfreundlich gestalten.

Simulationstool und Parameterstudie

Um eine Parameterstudie mit dem Tool durchführen zu können, muss ein zonales Basismodell nach (Norrefeldt et al. 2012) vorhanden sein. Bei diesem verwendeten zonalen Ansatz wird das Raumvolumen in 100 bis 1.000 Zonen unterteilt. Die einzelnen Zonen sind über Strömungsmodelle miteinander verbunden. In diesen wird der Luftaustausch zwischen den Zonen durch ein Aufsummieren der herrschenden Kräfte unter Berücksichtigung der Verluste durch die Ausbreitung berechnet.

Das Basis-Modell kann automatisiert an die Planungsvariationen angepasst und simuliert werden. Die Simulation erfolgt in Interaktion mit der Software Dymola. Die Berechnungsdauer einer Simulation ist je nach Simulationszeitraum und Raumgeometrie auf wenige Minuten an einem handelsüblichen Rechner beschränkt.

Simulationstool

Das entwickelte „Parameter-Studies Tool“ (PST) ist in der Programmiersprache Python implementiert. Die Bedienung erfolgt über eine graphische Benutzeroberfläche (graphical user interface, GUI), um eine einfache und intuitive Bedienung zu ermöglichen. Darin sind das Modell, die Szenarien-Variationen und Randbedingungen zu der Simulation und den Ergebnissen entsprechend einzustellen (Abbildung 1).

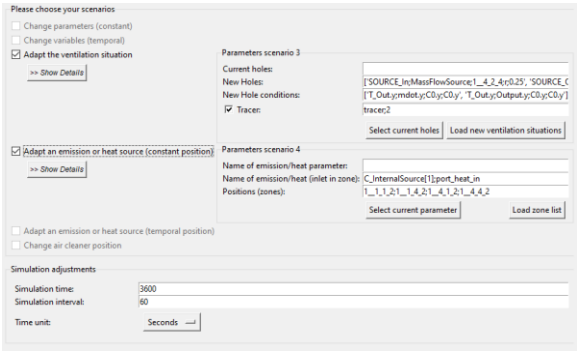

Abbildung 1: Ausschnitt der GUI des Parametrisierungstool.

Es können folgende Szenarien für eine Parameterstudie betrachtet werden:

- Konstante Parameter variieren
- Transiente Parameter variieren
- Belüftungssituationen variieren
- Emissions-/Wärmequelle variieren (konstante Position)
- Emissions-/Wärmequelle variieren (temporäre Position)
- Luftreiniger hinzufügen oder variieren

Für jede Variation wird dabei das Basis-Modell angepasst und ein neues Modell erstellt. Dieses kann entweder voll automatisiert über das PST simuliert oder die Modelle in einer Modelica Datei gespeichert und manuell in der Software Dymola geladen und simuliert werden. Zusätzlich wird bei dieser Option ein Modelica-Skript erstellt, in dem alle Modelle der erstellten Datei über eine Schleife nacheinander simuliert werden. Das ermöglicht individuelle Anpassungen und mehr Kontrollmöglichkeiten in den neuen Modellen.

Die Auswertung der Daten erfolgt ebenfalls automatisiert über die Schnittstelle zwischen Python und Microsoft-Excel©.

Mit der beispielhaften Parameterstudie zur Untersuchung der Luftqualität in Kinosälen werden die Möglichkeiten des Tools aufgezeigt.

Parameterstudie

Die Parameterstudie betrachtet ein adaptierbares Raummodell eines Kinosaals als Anwendungsfall. Es wird mit einem generischen Modell gearbeitet. Bei diesem kann die Geometrie in ihrer Länge (l, L), Breite (B) und Höhe (h, H) dem Anwendungsfall angepasst werden. Die Grundform des Kinosaals ist in Abbildung 2 dargestellt.

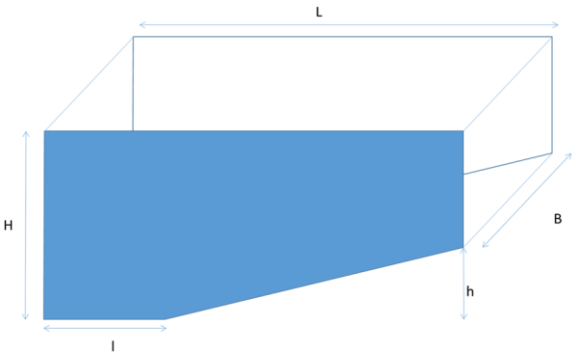

Abbildung 2: Adaptierbare Geometrie der Kinosäle.

Das Modell hat dabei immer die gleiche Anzahl Zonen und ist in der Länge (x-Richtung) in 8 Zonen, in der Breite (y-Richtung) in 5 Zonen und in der Höhe (z-Richtung) in 6 Zonen unterteilt. Somit ändern sich bei unterschiedlichen Geometrien nur die Zonengrößen und die Gesamtanzahl bleibt bei 230 Zonen.

Zudem werden ein Zuschauerbereich (Schräge in Abbildung 2), ein Bühnen- und ein Gangbereich definiert. Eine bespielhafte Darstellung ist in Abbildung 3 zu finden. Die Bestuhlung und die Geometrie (L=9,20 m,

B=5,73 m, H=5,15 m) sind dabei an einen konkret untersuchten Kinosaal in Weilheim angelehnt. Die Grundfläche des Raumes ist ca. 60 m² und der Kinosaal bietet Platz für 41 Personen.

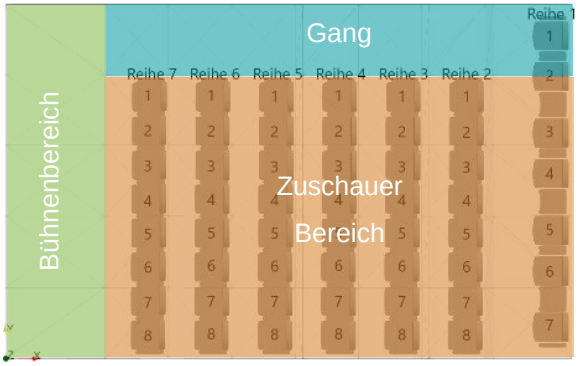

Abbildung 3: Aufteilung des Kinosaals in verschiedene Funktionsbereiche.

In der Untersuchung werden vier verschiedene Belüftungsszenarien, drei Belegungen und vier Umluftraten untersucht. Tabelle 1 zeigt die variierenden Parameter und deren Werte. Es entstehen dadurch 48 verschiedene Szenarien.

Tabelle 1: Multivariable Betrachtung der Parameterstudie.

Parameter	**Varianten**
Belüftung	Mischlüftung 1 (M1), Mischlüftung 2 (M2), Quelllüftung 1 (Q1), Quelllüftung 2 (Q2)
Belegung	30 %, 60 %, 100 %
Umluftanteil	0 %, 20 %, 50 %, 80 %

Bei der Quelllüftung wird die Luft jeweils im Zuschauerbereich von unten einbracht und im Deckenbereich wieder abgesaugt. Q1 und Q2 unterscheiden sich hinsichtlich der Position der Abluftöffnungen, die sich zum einen an den Seitenwänden (Q1) und zum anderen an der Leinwand und der Rückwand (Q2) befinden (siehe Abbildung 4 a) und b)). Die Zuluft-Düsen der Mischlüftung sind unterhalb der Decke an der Rückwand platziert. Bei Variante M1 findet die Luftabfuhr vorne unter der Leinwand und in Variante M2 in Bodennähe im vorderen Bereich der Seitenwände statt (siehe Abbildung 4 a) und b)). Der Zuluft-Volumenstrom ist je nach Belegung bedarfsgeführt und während des Simulationszeitraums konstant. Die Ausgangsbasis dabei ist ein Zuluft-Volumenstrom von 60 m³/(h*Pers.). Dies entspricht bei einem Umluftanteil von 50 % einem Außenluftvolumenstrom von 30 m³/(h*Pers.) für einen Zuschauersaal nach DIN EN 16798-1 (Kategorie II, schadstoffarmes Gebäude). Die Lüftungsszenarien bestimmen die Luftströmung im Raum und wirken sich somit auf die Schadstoffabfuhr und die Luftqualität aus. Ebenso hat die Belegung durch die Wärme- und CO_2-Emissionen der Personen Auswirkungen auf diese zwei Aspekte. Pro Person wird eine sensible Wärme von 75 W und ein typischer CO_2-Volumenstrom eines Erwachsenen von 21,6 l/h (Ostmann et al. 2023) freigegeben. Der Umluftanteil wirkt sich auf den CO_2-Gehalt der Zuluft aus.

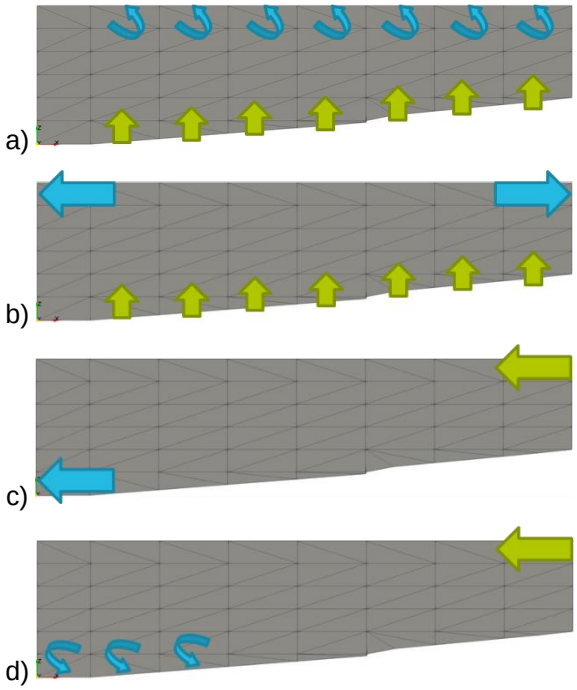

Abbildung 4: Seitenansicht des Kinosaals zur Darstellung der vier Belüftungsszenarien mit Zuluft (grün) und Abluft (blau). a) Quelllüftung Q1, b) Quelllüftung Q2, c) Mischlüftung M1, d) Mischlüftung M2.

Die Auswertung der Luftqualität basiert auf dem Tracergas CO_2, kann jedoch beliebig auf andere skalare Marker, wie luftgetragene Partikel, angewendet werden. Für die Frischluft wird eine CO_2-Konzentration von 460 ppm angenommen. Es wird jeweils die gemittelte CO_2-Konzentration im Zuschauerbereich auf Kopfhöhe ausgewertet.

Des Weiteren findet eine Untersuchung der Verbreitung von luftgetragenen Aerosolen im Raum statt. Dabei wird jeweils eine Person an verschiedenen Positionen im Zuschauerbereich als Schadstoffquelle betrachtet. Der Mensch emittiert im Sitzen $2{,}710^{-10}$ kg/s Aerosole mit einem Atemvolumenstrom von 0,54 m³/h und einer Aerosolkonzentration in der Atemluft von $1{,}8*10^{-3}$ mg/m³ (Müller et al. 2020). Für deren Reduktion werden die Auswirkungen der

Positionierung von mobilen Luftreiniger untersucht. Dabei werden vier verschiedene Standorte ausgewählt, die in der Abbildung 5 gezeigt sind. In allen Fällen wird ein Luftvolumenstrom des Reinigers von 625 m³/h angesetzt. Der Luftdurchsatz entspricht der Stufe 3 von 4 bei einem Gerät, das laut Herstellerangaben für ein Raumvolumen von 300 m³ ausgelegt ist. Bei dieser Stufe beträgt der Schallpegel in einem Meter Abstand 45 dB(A). In den Empfehlungen der meisten Hersteller sind keine Angaben zur Belegungsdichte gegeben. Die Raumluft wird jeweils im unteren Bereich des Gerätes angesaugt und die gereinigte Luft wieder nach oben ausgeblasen.

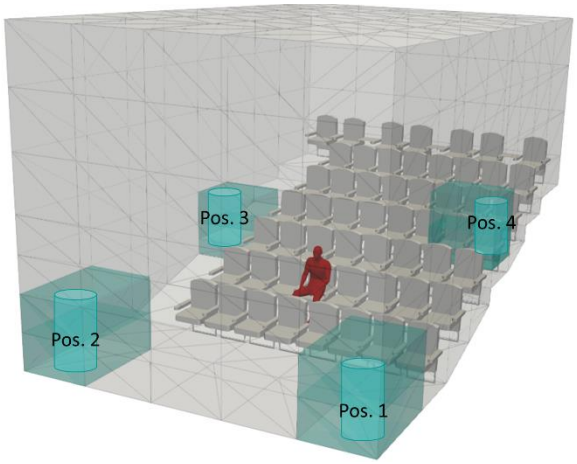

Abbildung 5: Positionierung der mobilen Luftreinigungsgeräte (LR) im Kinosaal.

Es wird die eingeatmete Dosis eines Menschen während eines 90-minütigen Kinoaufenthalts ausgewertet. Die Dosis wird aus dem Integral der Konzentrationen und dem Atemvolumenstrom berechnet (vgl. Gleichung 1).

$$Dosis = \dot{V}_{Atmen} \cdot \int_{t_{start}}^{t_{Ende}} c_i(t)dt \quad (1)$$

$\dot{V}_{Atmen}$ = Atemvolumenstrom, hier 0,54 m³/h (Müller et al. 2020); $\mathbf{c_i(t)}$ = zeitaufgelöster Konzentrationsverlauf in der ausgewerteten Zone i; t_{Ende} bzw. t_{start} = Start- und Endzeitpunkt

Ergebnisanalyse und Diskussion

Die Modelle konnten innerhalb von wenigen Sekunden per Maus-Klick an die definierten Bedingungen angepasst werden. Die Simulation erfolgte dann über die Anwendungssoftware Dymola. Die erzeugten Ergebnisdateien mit den zeitlich aufgelösten CO_2-Konzentrationen pro Zone bilden die Basis für die automatisierte Auswertung. Die Mischlüftungsvariante 1 (M1) entspricht der realen Belüftung des Beispielkinosaals. Somit kann eine Validierung des Modells für diesen Fall anhand von Messdaten durchgeführt werden. In den Messungen wurde dazu die CO_2 Abklingkurve an 12 verschiedenen Positionen im Raum gemessen. Die CO_2 Sensoren weisen eine Genauigkeit von ± 50 ppm auf. Ein Vergleich aus Messung und Simulation zeigt sich im Mittel eine Abweichung der Konzentration von Messwert von ± 90 ppm (siehe Abbildung 6).

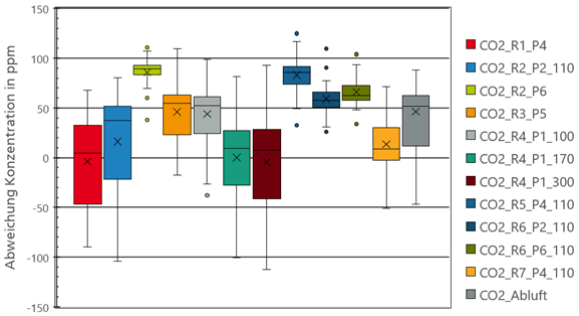

Abbildung 6: Abweichung der gemessenen und simulierten CO_2-Konzentrationen an verschiedenen Positionen im Beispielkinosaal. „R“ in der Legende entspricht der Reihe, „P“ dem Sitzplatz im Saal (vgl. Abbildung 3) und die Zahl beschreibt die Höhe der Position.

In der folgenden Untersuchung werden die CO_2-Konzentrationen der verschiedenen Belüftungsvarianten miteinander verglichen. Dabei zeigt Abbildung 7 die simulierten CO_2-Konzentrationen abhängig von der Frischluftrate bei einer vollen (41 Pers.) und einer niedrigen Belegung (12 Pers.). Die senkrechte dickere Linie bei 1.260 ppm entspricht der empfohlenen CO_2-Konzentration der Raumluft nach DIN EN 16798-1 (bei einer Frischluft-Konzentration von 460 ppm, Kategorie II). Es lässt sich feststellen, dass bei der simulierten Geometrie die Quelllüftungsvarianten niedrigere CO_2-Konzentrationen zur Folge haben. Um im Mittel 1.260 ppm zu erreichen, kann mit einer Quelllüftung im Auslegungsfall (100 % Belegung, Umluftanteil 50 %, Zuluft-Menge 60 m³/h) die Frischluftmenge im Vergleich zur Mischlüftung um ca. 140 m³/h reduziert werden. Je höher die Frischluftmenge ist, desto größer sind die Auswirkung auf die Luftqualität zwischen den Belüftungsszenarien. Dies zeigt sich unabhängig der Belegungsdichte. In den betrachteten Fällen ist eine minimale Frischluftmenge von ca. 24 m³/(h*Pers.) notwendig, um den Empfehlungen der DIN EN 16798-1 gerecht zu werden (hellblaue Linie in Abbildung 7). Dies ist für alle 3 Belegungsdichten gültig. Der minimale Frischluftvolumenstrom von 30 m³/(h*Pers.) aus der Norm ist somit für eine gute Raumluftqualität ausreichend und kann aus Sicht der Luftqualität bzgl. CO_2 bei einer genauen Planung weiter reduziert werden. Dies ist vor allem für Räume mit einem hohen Personenaufkommen relevant.

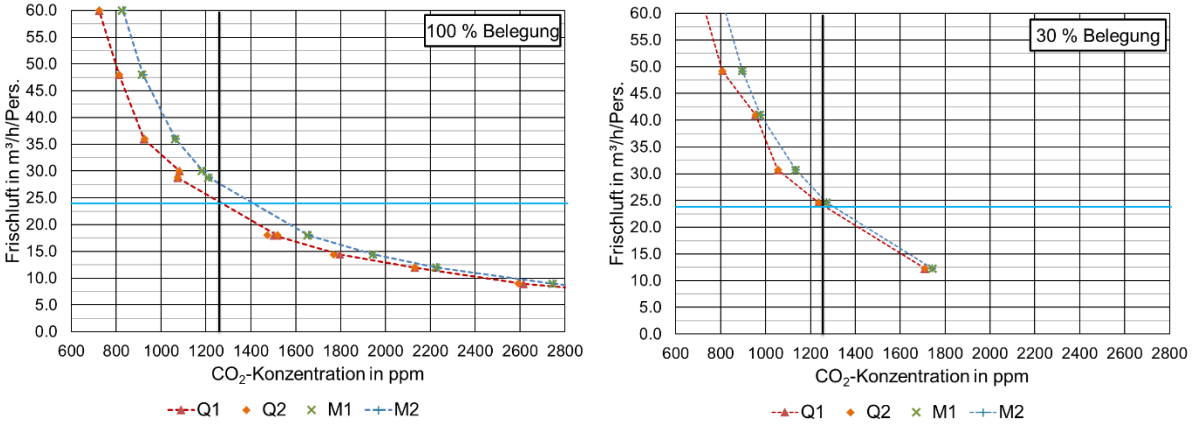

Abbildung 7: Diagramme mit dem Zusammenhang von Frischluft und CO_2-Konzentration bei a) 100 % Belegung und b) 30 % Belegung.

Für die weiteren Untersuchungen der Aerosolverteilung im Raum wird eine Form der Quelllüftung (Q1) ausgewählt. In den Simulationen wird jeweils ein Mensch als Aerosolquelle betrachtet. Da sich die emittierende Person auf allen Plätzen befinden kann, wird die Position der Quelle innerhalb des Zuschauerbereiches variiert. Es werden 28 Positionen für den Emitter betrachtet, dass zu 28 Simulationen für jede Position des Luftreinigers führt. Um daraus den Einfluss der Luftreiniger-Positionen zu ermitteln, werden die Aerosolkonzentrationen zonenweise gemittelt. Es entstehen für jede Luftreiniger-Position räumlich aufgelöste Aerosolkonzentrationen mit den Mittelwerten aus den verschiedenen Quellpositionen. Die Konzentrationen sind während des betrachteten Zeitpunktes konstant. Somit steigt die eingeatmete Dosis linear zur Aufenthaltszeit im Kinosaal.

In der Abbildung 8 ist die Reduktion der eingeatmeten Aerosole in % im Vergleich zum Fall ohne Luftreiniger aufgezeigt (100 % Belegung bei einem Frischluftvolumenstrom von 30 m³/(h*Pers.)). Die Werte stellen jeweils den Maximalwert der Dosis im Zuschauerbereich auf Kopfhöhe dar.

Die Verwendung eines mobilen Luftreinigers zeigt einen Effekt auf die eingeatmeten Aerosole. Durch die Verwendung der Geräte mit einem Luftdurchsatz von 625 m³/h wird in etwa die Hälfte der Raumluft gefiltert. Damit ist eine Reduktion von ca. 10 % bis 16 % möglich. Die Luftreiniger-Position 1 erweist sich am wirksamsten. Hier ist das Gerät vorne an der Seitenwand bei den Zuschauern aufgestellt und eine Dosisreduktion von 15,9 % erreichbar. Position 2 stellt den größten Abstand zu den Personen dar und zeigt die geringste Effizienz. Trotz der Platzierung mitten im Zuschauerbereich ergibt sich aus Position 4 eine mittlere Reduktion. Das liegt an der erhöhten Position, indem die gereinigte Luft oberhalb der Kopfhöhe eingeblasen wird. Der Reiniger an Position 3 zeigt ähnliche Ergebnisse. Es ist ersichtlich, dass ein Luftreiniger und dessen Position zur Reduzierung der Aerosole beitragen, jedoch der Reinigungseffekt beschränkt ist.

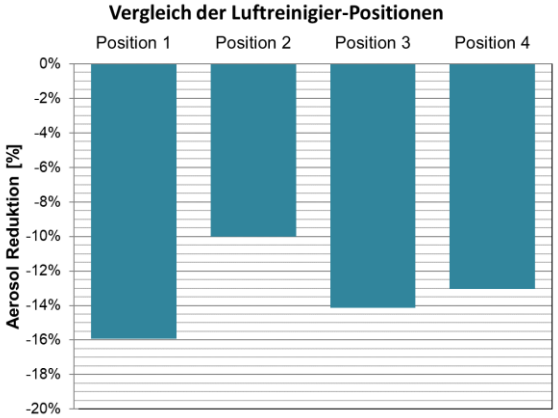

Abbildung 8: Vergleich der maximalen Dosis-Werte der unterschiedlichen Luftreingier Positionen.

Während eines Kinofilmes (90 min) steigt die eingeatmete Dosis im Bereich der Bestuhlung ohne Luftreiniger auf maximal 0,56 mg Aerosole (vgl. Abbildung 9 a)). Unter Verwendung eines Luftreinigers an Position 4 ergibt sich hingegen eine maximale Dosis von 0,47 mg Aerosole (vgl. Abbildung 9 b)). Die räumlich aufgelösten Aerosol-Dosen sind in den Schnittdarstellungen in der Abbildung 9 dargestellt. Bei den Werten handelt es sich um Mittelwerte aus den 28 Simulationen mit verschiedenen Positionen des Emitters.

Die Werte ohne Luftreiniger (a) steigen erwartungsgemäß entlang der x- und y-Achse in Richtung der hinteren Ecke im Zuschauerbereich. Hier ist die Quelldichte der

Aerosole auf die 4 Raumecken bezogen am dichtesten. Die anderen Ecken schließen an den Gang oder den Bereich vor der Bühne an, in denen keine Aerosole emittiert werden. Folglich werden in der hintersten Reihe (x-Achse: 8) die meisten Aerosole eingeatmet. Bei der Verwendung des Luftreinigers (Position 4) (b) ist in der Nähe des Reinigers eine deutliche Aerosolreduktion von über 50 % ersichtlich. Daraus folgt die naheliegende Empfehlung den Luftreiniger möglichst in Bereich mit einer hohen Belegungsdichte zu positionieren, falls der Platz dafür vorhanden ist. Mit dem entwickelten Werkzeug kann diese Positionierung abhängig von der vorliegenden Lüftungssituation optimiert und mit geringem Aufwand identifiziert werden.

a)

ohne Luftreiniger

y-Achse \ x-Achse	1	2	3	4	5	6	7	8
5	0.30	0.31	0.32	0.32	0.40	0.39	0.47	0.46
4	0.30	0.35	0.37	0.38	0.40	0.40	0.49	0.50
3	0.28	0.34	0.37	0.36	0.43	0.45	0.48	0.53
2	0.28	0.34	0.36	0.35	0.44	0.47	0.48	0.53
1	0.29	0.35	0.38	0.33	0.45	0.49	0.51	0.56

b)

Luftreiniger Position 1

y-Achse \ x-Achse	1	2	3	4	5	6	7	8
5	0.19	0.21	0.22	0.23	0.30	0.29	0.38	0.38
4	0.19	0.23	0.27	0.28	0.31	0.31	0.40	0.42
3	0.17	0.22	0.26	0.26	0.33	0.35	0.39	0.44
2	0.14	0.20	0.25	0.26	0.34	0.38	0.39	0.45
1	0.08	0.15	0.22	0.25	0.34	0.38	0.42	0.47

Abbildung 9: Schnittdarstellung auf Kopfhöhe der mittleren eingeatmeten Aerosole in mg a) ohne Luftreiniger und b) mit Luftreiniger auf der Position 4. Der blaue Rahmen markiert die genaue Position des Luftreinigers.

Zusammenfassung

Um die Luftqualität und die Positionierung von mobilen Luftreinigern in dicht belegten Räumen bewerten zu können, wurde ein Parametrierungswerkzeug entwickelt. Dieses greift auf die zonale Simulation der Luftausbreitung mit dem VEPZO-Modell in Abhängigkeit der Lüftungsart und positionierter Quellen (z. B. Personen) und Senken (z. B. Luftreiniger) zurück. Als Anwendungsfall wurde die Situation in einem Kinosaal betrachtet.

In der Parameterstudie wurden verschiedene Belüftungs- und Belegungsszenarien betrachtet und mittels der CO_2-Konzentrationen bewertet. In den Auswertungen der resultierenden CO_2-Konzentrationen zeigt sich, dass die Frischluftrate entscheidend ist. Durch die Anordnung der Lüftungsauslässe wird die Luftströmung und somit auch die CO_2-Konzentrationen beeinflusst. Die Mindest-Frischluftrate gemäß DIN EN 16798-1 könnte hierfür nach einer simulativen Betrachtung auf 24 m³/(h*Pers.) reduziert werden. Dieser Volumenstrom pro Person wäre für alle Belegungsdichten hinreichend. Als Folge davon kann vor allem bei großen Räumen mit hoher Belegungsdichte der Volumenstrom reduziert und damit unter anderem Energie eingespart werden.

Des Weiteren wurden verschiedene Aerosolquellen simuliert und der Einfluss von mobilen Luftreinigern auf die eingeatmeten Aerosole untersucht. Dabei stellt jeweils eine infektiöse Person auf verschiedenen Positionen im Zuschauerbereich eine solche Aerosolquelle dar. Die Betrachtung der eingeatmeten Aerosol-Dosis während eines Kinoaufenthalts von 90 min zeigt einen Reinigungseffekt durch die Inbetriebnahme eines gut positionierten mobilen Luftreinigers. Es können unabhängig von der Position der Schadstoffquelle einer infektiösen Person Reduktionen der maximalen Dosis um ca.16 % aufgezeigt werden. Somit ist Wirkung eines Luftreinigers einer Frischlufterhöhung des gleichen Volumenstroms unterzuordnen. Zwischen den verschiedenen Positionen der Geräte sind teilweise nur geringe Unterschiede zu erkennen.

Damit stellt sich das entwickelte Parametrierungswerkzeug (PST) als effizientes, simulationsbasiertes Werkzeug für die Bewertung und Optimierung der Raumluftqualität in Innenräumen heraus. Somit lassen sich bereits in der Planung kritische Bereiche identifizieren und abschätzende Simulationen für diverse Varianten über längere Zeiträume (hier: Dauer eines Kinofilms) durchführen. Ungünstigen Lüftungssituationen kann sodann – beispielsweise mit mobilen Luftreinigern – gezielt entgegengewirkt und somit die Raumluftqualität gesteigert werden.

Literatur

DIN EN 16798-1: Energetische Bewertung von Gebäuden – Lüftung von Gebäuden – Teil 1: Eingangsparameter für das Innenraumklima zur Auslegung und Bewertung der Energieeffizienz von Gebäuden bezüglich Raumluftqualität, Temperatur, Licht und Akustik – Modul M1-6; 07/2015; Beuth-Verlag GmbH, Berlin

Müller, D.; Rewitz, K.; Derwein, D.; Burgholz, T.M.; Schweiker, M.; Bardey, J.; Tappler, P. 2020. Abschätzung des Infektionsrisikos durch Aerosolgebundene Viren in belüfteten Räumen. RWTH Aachen Uviersity.

Norrefeldt V., Grün G., Sedlbauer K. 2012. VEPZO – Velocity propagating zonal model for the estimation of the airflow pattern and temperature distribution in a confined space. Building and Environment

Ostmann P.; Derwein, D.; Rewitz, K.; Kremer, M; Müller, D. 2023. Entwicklung eines numerischen Strömungssimulationsmodells zur Berechnung der Aerosolausbreitung in Klassenräumen. RWTH Aachen Uviersity

The Modelica Association. 2024. Modelica. https://modelica.org/. Zugegriffen: 27.06.2024

BauSIM 2024 in Wien
23. September – 26. September

Shared Memory Parallelization Strategies and Speedup Scaling of the Hygrothermal Building Component Simulation Program HAM4D_VIE

Simon Hinterseer[1], Andreas Sarkany[1] und Bernhard Steiner[1]

[1] *TU Wien, Research Unit for Building Physics*

Abstract

Hygrothermal building simulation is helpful for predicting and enhancing building performance, durability, and energy efficiency. Simulating different scenarios allows for better design, addresses concerns like mold, material decay and energy waste, which is increasingly important in light of climate challenges. Given the computational intensity of such simulations, the efficient use of computational resources like available CPU cores is paramount for manageable execution times.

The *HAM4D_VIE* simulation program, which has been developed and used in research and teaching at TU Wien for many years, does not rely on linear algebra operations or linear solvers like many other simulation algorithms, but rather implements an alternative approach iterating over cell and face objects of the construction component's mesh. Using this program as an example, this paper outlines challenges and solutions in the parallelization process of such an algorithm using multithreading with the OpenMP API. Different implementation strategies are evaluated with respect to their resulting execution time, and speedup scaling is measured on an office machine as well as on compute nodes of the VSC-4 supercomputer.

Execution time measurements on both machines reveal a speedup of several folds which shows that our implementation improves the overall performance of the simulation. However, when comparing the degree of parallelization suggested by Amdahl's Law with the one suggested by performance profiling, a significant difference was observed, which indicates substantial overhead due to thread management. This underscores the need for further optimization in both parallelization techniques and the used data structures.

Introduction

HAM4D_VIE (or just *HAM4D* for brevity) was developed at TU Wien to introduce simulation capabilities concerning heat, air flow and moisture in building components. It has been validated in Deseyve & Bednar (2006) and Bednar et al. (2010).

The inherently high computational load of simulation programs limits the possible applications of *HAM4D* by increasing computation times significantly with increasing model size or simulated time spans. Since the computational power of single CPU cores has become mostly stagnant, modern CPUs offer more and more cores to the user. In order to benefit from this development, it is however necessary to parallelize computer programs. This divides the work load of the program onto several workers (i.e. threads or processes) which occupy multiple CPU cores simultaneously. A common method for implementing multithreading is the use of OpenMP (OpenMP (2021)), an API that allows multithreaded programming for C, C++ and FORTRAN. It is especially convenient when parallelizing already existing code, which is why it was chosen for this project.

Like many forms of parallelization, the use of OpenMP can cause significant overhead due to thread management, which is detrimental to the performance of the parallelized result, as shown by Bull et al. (2012) and Fürlinger & Gerndt (2007).

HAM4D's approach, that involves iterating over cells and faces of a construction component's discretized model, causes frequent processing of many relatively small but parallelizable loops. This is not uncommon in multiphysics simulations and parallelization with OpenMP is expected to show considerable overhead here, see Bronevetsky et al. (2008).

One way of analyzing the performance of a parallelized program is to examine the speedup when comparing it to its sequential implementation. This

speedup can be computed according to Amdahl's Law, see Amdahl (1967)

$$S = \frac{T_1}{T_n} = \frac{1}{1 - p + \frac{p}{n}} \tag{1}$$

Here, the speedup S is defined as the ratio of the run time T_1 for sequential execution and the run time T_n for parallel execution with n workers (i.e. threads or processes). It can be calculated from the parallel portion of the program p which is defined as the amount of workload, that is perfectly parallelized ($0 \leq p \leq 1$).

Amdahl's Law shows that the speedup is inherently limited, no matter how much resources are dedicated to a task as long as there is a non-zero portion of the task that is not perfectly parallelized. This can be seen in Figure 1.

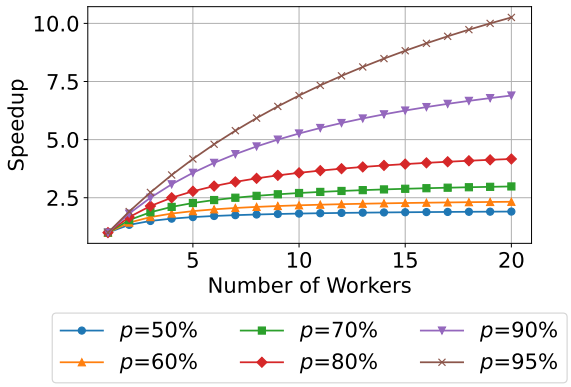

Figure 1: Amdahl's Law shows that the achievable speedup is inherently limited by the portion of sequential workload $1 - p$.

In this work, the parallelized portion, that is derived from comparing observed speedup, that is measured as $S = T_1/T_n$, with speedup according to Amdahl's Law, is compared with the parallelized portion according to performance profiling. The difference between the two will be used to quantify the overhead of the parallelization. Furthermore, several parallelization techniques are being compared and evaluated (see Section *Results and interpretation*). These techniques are explained in Section *Parallelization strategies* after giving a short overview of the program structure.

HAM4D program structure

In order to put the parallelization techniques, that were used into context, the program structure of *HAM4D* is being briefly outlined here: The program approximates the solution of an initial value problem, by using an adaptive Runge-Kutta method, see Butcher (2016). The necessary time derivatives for temperature and moisture content are approximated by using the Finite Volume Method, see Radi & El Hami (2018).

In terms of data structures, *HAM4D* uses arrays of cell and face objects. Cells and faces are modeled as composite data types (i.e. C++ `struct` objects), that are approximately 1 kB in size each, holding mostly floating point numbers that store physical properties (e.g. temperatures or capillary pressure values).

To give a general idea, Figure 2 shows an overview of a Runge-Kutta step when computing heat conduction. Moisture transport has a similar structure while air flow is outside of the scope of this work.

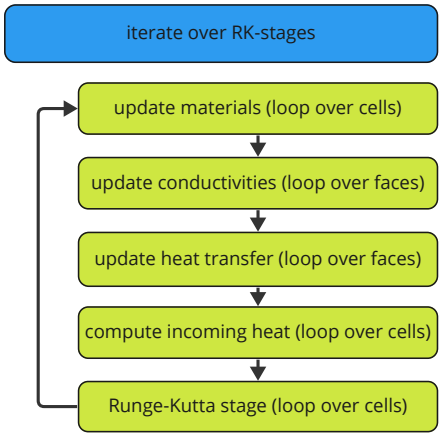

Figure 2: The way *HAM4D* performs a Runge-Kutta step using heat conduction as an example. It includes looping over all cell- and face objects several times.

The items listed in Figure 2 include the updating of the material for each cell. This implements heat and moisture dependencies of material properties. The following two items represent the computation of the transport coefficients as well as the actual heat transfer, which are stored as properties of face objects. Afterwards, the time derivative of the temperature is computed for each cell using the incoming heat from neighbouring cells, which then serves as input into the function that implements the Runge-Kutta stage.

Each of these items is realized in *HAM4D* as a function that contains a single for loop, which either iterates over the cells or the faces of the model. In the next section, the parallelization of these loops will be discussed. In the last item (Runge-Kutta

stage), the error estimate is computed for each cell. Depending on the maximum error estimate over all cells, the program will either continue with the next time step or repeat the last one with a reduced step size. When the program is executed in parallel, it necessitates a collective determination of the maximum error estimate, which is also discussed in the next section.

Parallelization strategies

In this section, the used parallelization strategies are presented. The impact of these strategies on the programs performance is discussed in the *Results and interpretation* section.

Number of parallel constructs

OpenMP allows the use of parallel constructs to indicate that the code within each is to be executed concurrently by a specified number of threads. In this work, two basic approaches are being examined: Creating one parallel construct for each of the for loops described above (see *HAM4D program structure*) or creating one parallel construct for the whole simulation. This was done in order to test whether OpenMP will always create and terminate threads upon entering and leaving parallel regions, or rather just activate threads from an implicitly managed thread pool and put them to sleep whenever they are not needed.

Using a parallel construct per for loop would cause the creation and termination of threads every time such a for loop starts, should the utilized OpenMP implementation not make use of a thread pool. This can easily happen thousands of times per simulated hour. Using one single parallel construct, on the other hand, is not expected to create and terminate threads more than once per simulation.

Collective determination of the maximum Runge-Kutta error estimate

Since the adaptive Runge-Kutta method is applied for each cell (see Section *HAM4D program structure*), it is necessary to determine the maximum error estimate over all cells of the simulation domain. In sequential execution, this maximum is one single floating point number, which can be updated for each cell as is depicted in Figure 3.

Three approaches to the parallelized determination of the maximum error estimate are examined: using a critical section, using thread-local maxima and using atomic operations. These approaches are discussed next.

The first approach ensures correct results by updating the maximum value as depicted in Figure 3 within a critical section using the `#pragma omp critical` directive. This ensures that at most one thread tries to update `max_value` at a time. In case a second thread tries to update `max_value` before the first one is finished, the second thread has to wait.

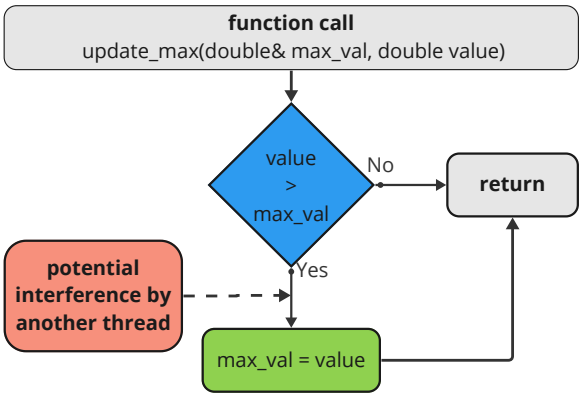

Figure 3: Updating a maximum value in this straightforward way is possible in sequential execution, but is not thread-safe since another thread might write to `max_val` between the comparison and the actual updating of the value.

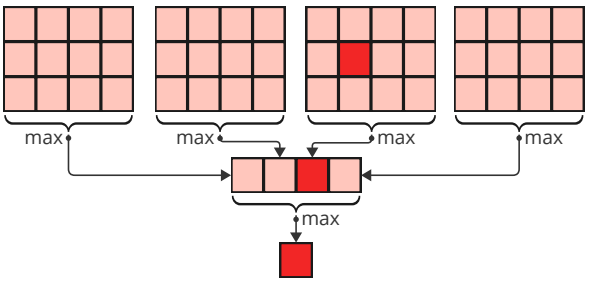

Figure 4: Determining the maximum error estimation via an array of thread-local maxima. After each thread has determined the maximum element within its assigned sub-domain, the master thread determines the maximum of the (rather few) local maxima.

The second approach uses an array of floating point numbers, where each entry is assigned to a certain thread. This thread will use its entry to store the greatest error estimate of all the sections handled by this thread (the thread-local maximum) without having to worry about interference from other threads. After the thread-local maxima have been determined, the master thread will sequentially find the maximum value inside the array. This algorithm is depicted in Figure 4.

The third approach uses a thread-safe function, that updates the maximum value using an atomic operation. This function was published by zch & Naszta (2013) and is depicted in Figure 5.

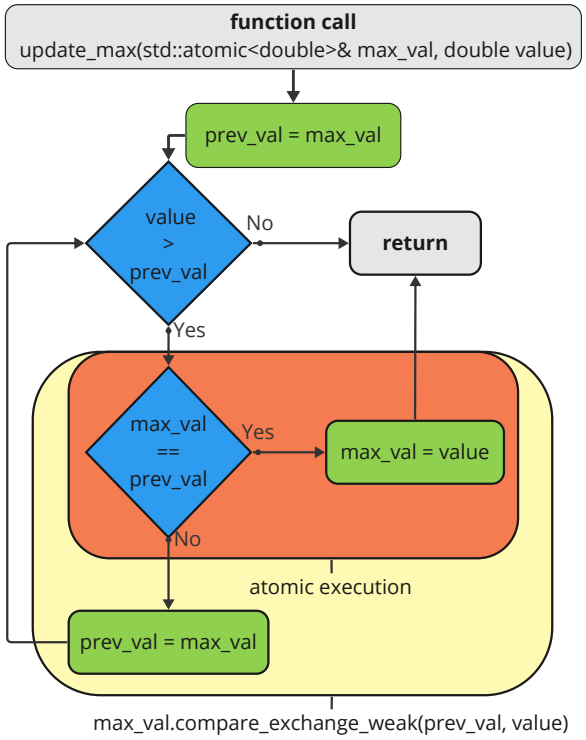

Figure 5: Flow chart of the thread-safe maximum function using atomic operations. `max_val` is being updated in case `value` is greater. The thread-local variable `prev_val` is used to register interference by other threads: If the comparison `max_val == prev_val` fails, `max_val` has been changed by another thread. Interference within the block marked as *atomic execution* is impossible.

Scheduling policy

The scheduling policy controls the distribution of the work load for certain loops including parallel for loops. The strategy can be chosen to either be `static`, `dynamic` or `guided`. Static scheduling will divide the iterations of a for loop into equally sized chunks of consecutive iterations and assign one such chunk to each thread. The dynamic scheduling strategy will assign each thread a chunk with a predefined size (default chunk size is 1) which it will work on. Once the thread is finished, it will request another chunk until there is no more work to be distributed. Guided scheduling is similar to dynamic, however, OpenMP will adjust the chunk size proportionally to the remaining number of iterations. Dynamic scheduling is advisable, if the workload is expected to be unbalanced, which would cause one thread to take considerably longer to complete its assigned work. Since Fürlinger & Gerndt (2007) suggests, that load imbalance can have a significant impact on OpenMP, different options for scheduling policy are examined here.

Wait policy

This controls the behavior of waiting threads. With `active` wait policy, threads are expected to consume processor cycles while waiting, while `passive` wait policy induces the OpenMP implementation to prevent threads from consuming processor cycles while waiting. Since a substantial amount of the OpenMP thread management overhead is expected to be caused by thread synchronization, these options are examined here.

Benchmarking methods

The program version that was defined as a baseline used static scheduling with default chunk size, active wait policy and thread-local maxima for the determination of the maximum error estimate. This version was used for the speedup scaling. When examining these parameters, only one of them was changed at a time.

When generating the results, wall clock based time measurement is used as a performance metric. Results were gathered running *HAM4D* simulations on two systems:

- A laptop PC equipped with an AMD® Ryzen® 7 5800H with 8 physical or 16 logical cores respectively, running at 3.2 GHz. The operating system is Ubuntu 20.04.3 LTS, running within WSL2 on Windows 10.

- Single compute nodes of the fourth installment of the Vienna Scientific Cluster (VSC-4) supercomputer. These dual CPU nodes are equipped with two Intel® Xeon® Platinum 8174 Processors with 24 physical or 48 logical cores each, running at 3.1 GHz base and up until 3.9 GHz maximum frequency. The operating system is AlmaLinux 8.9.

For each data point given in the figures in the next section, 30 runs of the program were executed. The displayed value in the results section is the mean value of the runs, and the error bars indicate one single standard deviation.

The construction simulated in the benchmarks describes a rising damp problem in below street level zones of a refurbishment project (see Figure

6), that was simulated in the course of another research project. Details can be found in Lewis et al. (2022). To allow 30 simulation runs with each configuration, only a time frame of 100 hours was simulated in each run.

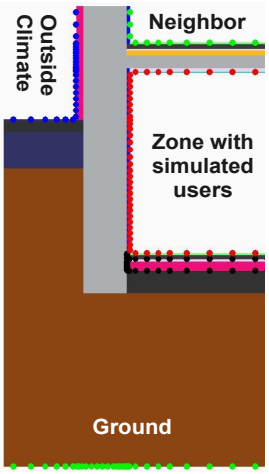

(a) materials and boundary conditions

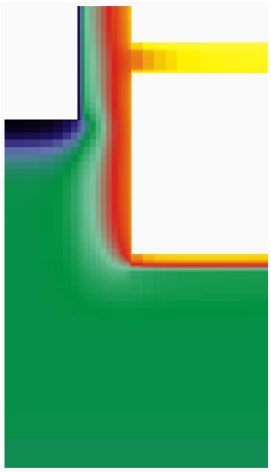

(b) temperatures after 100 hours

Figure 6: Simulated model. The dotted lines indicate boundary conditions: Blue: outside climate; green (top): neighbour climate, green (bottom): ground climate with high moisture causes rising damp; red: inside users causing heat and moisture loads. The black dotted lines depict sealing membranes, that are implemented as modifications to face objects.

Results and interpretation

While a three- to four-fold speedup was achieved through parallelization, considerable parallelization overhead is being observed.

Usage of a thread pool

The creation and termination of threads is one of the possible causes of overhead. However, Figure 7 shows that both the version that uses one single parallel construct and the one using one parallel construct per for loop, perform equally well. At least the former is expected to create threads just once during the whole simulation as explained in Section *Parallelization strategies*.

The observation, that the performance does not depend on the number of parallel constructs indicates, that the utilized OpenMP implementation does not create and terminate threads with every encounter of a parallel construct here, but manages a thread pool in the background, which is a known feature of many OpenMP implementations, see Alessandrini (2016).

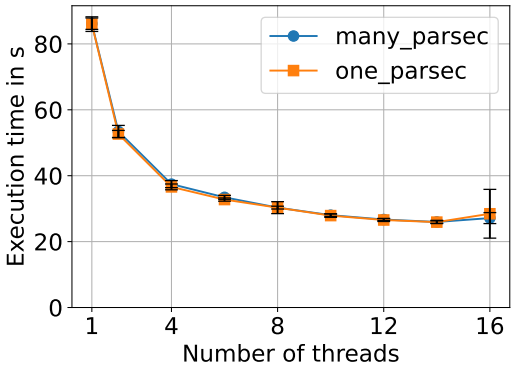

Figure 7: Execution times for different numbers of parallel constructs. No significant difference in performance between the two variants can be observed.

Collective determination of the maximum error estimate

The strategy for updating the maximum does have a substantial impact on the performance as can be seen in Figure 8. While the strategies of using thread-local maxima and using atomic operations perform equally well, the version that uses a critical section performs noticeably worse.

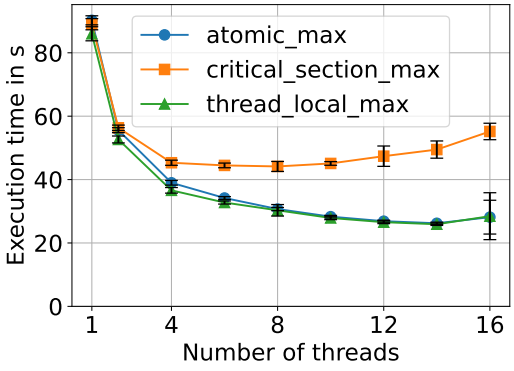

Figure 8: Execution times for different algorithms to update a maximum value. The usage of thread-local maxima or atomic operations performs equally well, while using a critical section causes almost up to a two-fold increase in computation time at 16 threads.

The detrimental effect of using a critical section

is sufficient to cause an increase in execution time, once the number of threads exceeds 8. This indicates, that creating barriers in the code contributes substantially to parallelization overhead.

Load imbalance

As already mentioned in Section *Parallelization strategies*, load imbalance has been identified as a major reason for OpenMP's overhead, which is why options for scheduling policy were examined. Figure 9 shows, however, that dynamic scheduling does not improve performance. This indicates that the parallelization overhead in our application is not due to load imbalance.

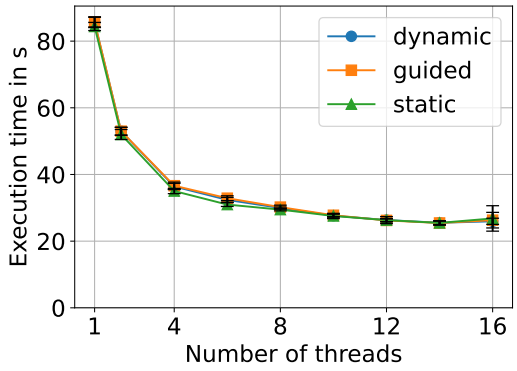

Figure 9: Execution times for different scheduling policies. No meaningful influence on the program's performance can be observed.

This hints at frequent cache misses, since processing consecutive iterations of a for loop is expected to perform better than processing scattered iterations, due to a lower spatial locality of the memory access pattern of the latter, see Rauber & Rünger (2023).

Wait policy

Whenever a thread is being forced to wait, the behavior depends on the specified wait policy, as was discussed in Section *Parallelization strategies*. Figure 10 shows that this has noticeable impact on the program's performance. When setting choosing a `passive` wait policy, increasing the number of threads beyond 6 turns out to be detrimental to the program's performance.

Speedup scaling

Performance profiling, that was done for single-threaded simulation runs in Visual Studio under Windows 10, indicates that 94.5% of the execution time is being spent in fully parallelized functions. These are functions that consist of a single parallelized for loop. However, when examining the scaling of the speedup, a much lower percentage of parallelization is being observed. Both Figure 11 and Figure 12 show a speedup scaling that suggests a degree of parallelization around 75% (also revisit Figure 1 for clarification of Amdahl's Law). This indicates significant overhead of the utilized parallelization techniques. Furthermore, it is noticeable that the speedup scaling continues at a constant degree of parallelization into the hyper-threading domain (i.e. more threads than available physical cores). This indicates that logical CPU cores will often be idle and yield the resources of the physical core. One possible explanation for this are frequent cache misses, see Rauber & Rünger (2023).

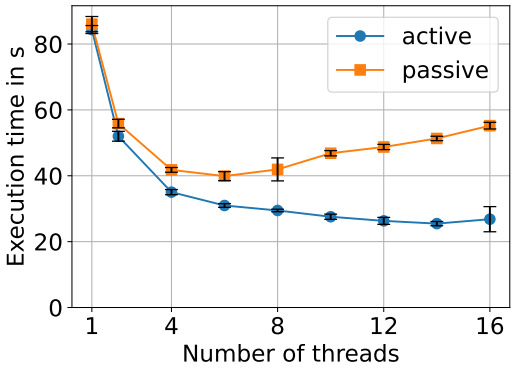

Figure 10: Execution times for different wait policies. A `passive` wait policy performs worse causing 2.06 times the computation time at 16 threads.

Figure 11 and Figure 12 show a noticeable drop off in speedup, when increasing the number of threads to the maximum number of available logical cores. This could be due to *HAM4D* threads being interrupted by activity of the operating system.

Discussion and conclusions

When simulating a real world research problem, including complex physical phenomena like rising damp, the examined parallelization strategies offer a gratifying speedup of 3 to 3.5-fold on a laptop PC and up to 4-fold on VSC-4 nodes.

However, while being a powerful parallelization API, that offers excellent scaling in many other cases, OpenMP does show significant overhead in our application. This overhead does not seem to be due to load imbalance, but rather appears to

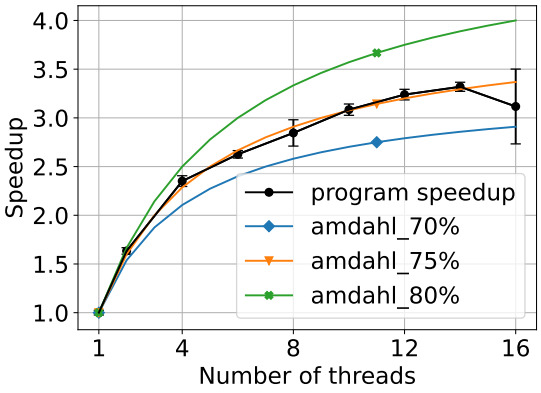

Figure 11: Speedup scaling of *HAM4D* on the laptop PC. A degree of parallelization of approximately 75% can be observed.

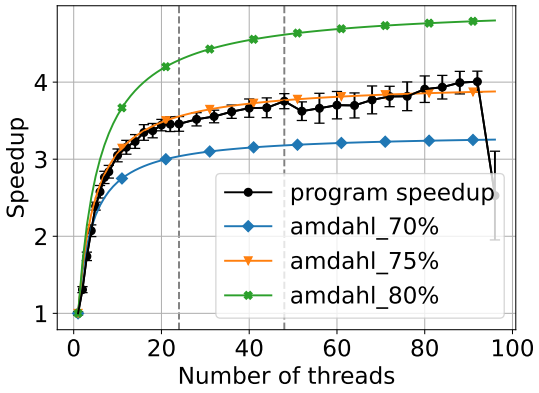

Figure 12: Speedup scaling of *HAM4D* on a node of the VSC-4. A degree of parallelization of approximately 75% can be observed. The vertical lines indicate 24 threads or 48 threads respectively - at the first mark the second CPU is starting to be utilized; at the second mark hyperthreading starts on both CPUs.

be linked to thread management and, more specifically, thread synchronization. This is hinted at both by the high impact of OpenMP's wait policy on the program's performance as well as by the poor performance when using a critical section when updating the maximum error estimate. It is also a possible explanation for the poorer than expected degree of parallelization, since each of the parallelized for loops of *HAM4D* comes with an implicit barrier at the end in order to sync up the threads at that point.

Besides the findings concerning parallel computing, there are several observations that suggest suboptimal memory access patterns of *HAM4D*. One of them is that the program scales with a constant degree of parallelization into the hyperthreading domain. This indicates that logical cores are able to yield their physical resources, which is not expected when the cores are kept busy at all times.

Furthermore, static scheduling with its large default chunk size is expected to perform better than dynamic scheduling with a default chunk size of 1, if load balancing is not an issue, because of higher spatial locality of the memory access pattern. The observation of equal performance suggests that there is no benefit in processing consecutive iterations of a for loop in *HAM4D*. Several potential reasons for this can be found in the code.

One is due to the data structures used: both cell and face objects are stored in arrays of compound data structures of about 1 kB for each cell or face. This means that the values for any given physical property of multiple objects are being stored quite far apart in RAM. For example the place where one cell's thermal conductivity is stored is 1 kB away from the next conductivity value. So, whenever a CPU core requests the floating point number representing conductivity, the cache line that is loaded in response only holds that one single conductivity and a lot of other (most likely unused) information about this or the next cell. Accessing RAM however takes hundreds of CPU cycles, which will mostly be wasted waiting for the necessary information. For this reason it is advisable to use "structs of arrays" rather than "arrays of structs", see Geshi (2019).

Another reason for low spatial locality of *HAM4D*'s memory access patterns is that there are several instances of memory access, that can be sketched as `cell[face[i].cell_left].conductivity`, which once again results in a scattered memory access, where most likely only parts of the loaded cache line hold useful information.

Future Work

In terms of data structures, the improvement of spatial locality through the transformation from an "array of structs" to a "struct of arrays" data structure as well as other measures to improve spatial locality of memory access are being anticipated. This is expected to reduce the frequency of cache misses. While not improving the speedup scaling of the parallelization, it is anticipated that this will improve the single-threaded performance of the program.

With regards to parallel computing and thread

management, some of the for loops can be fused into one. This would reduce the number of implicit barriers which seem to be a major reason for the poor speedup scaling.

Finally, while it is not uncommon for multiphysics simulations like *HAM4D* to perform the computational work within a number of for loops, theses simulations are particularly prone to a substantial overhead of OpenMP, as already mentioned. A different approach would be to perform the computational work within a linear solver or via matrix operations. While this might not be possible for all physical phenomena; that *HAM4D* simulates, it is being considered for some of the more straightforward ones like heat transport.

Author Credit Statement

All authors declare that they have no conflicts of interest.

Simon Hinterseer. Conceptualization, Implementation, Writing, Visualization, Expertise Numerical Methods and Parallel Programming

Andreas Sarkany. Reviewing, Project Supervision, Expertise Hygrothermics

Bernhard Steiner. Reviewing, Programming Supervision, Expertise Computer Science

References

Alessandrini, V. (2016), *Shared memory application programming: concepts and strategies in multicore application programming*, Elsevier.

Amdahl, G. (1967), Validity of the single processor approach to achieving large scale computing capabilities, *in* 'Proc. of the AFIPS Conference', Vol. 30, AFIPS Press, pp. 483–485.

Bednar, T., Deseyve, C., Jung, M., Nusser, B. & Teibinger, M. (2010), Impact of airflow on the risk assessmant of flat roofs, *in* 'Proc. of the 7th International Conference in Indoor Air Quality, Ventilation and Energy Conservation in Buildings'.

Bronevetsky, G., Gyllenhaal, J. & De Supinski, B. R. (2008), CLOMP: Accurately characterizing OpenMP application overheads, *in* R. Eigenmann & B. R. De Supinski, eds, 'OpenMP in a New Era of Parallelism', Vol. 5004, Springer Berlin Heidelberg, pp. 13–25. Series Title: Lecture Notes in Computer Science.

Bull, M., Reid, F. & Mcdonnell, N. (2012), A microbenchmark suite for OpenMP tasks, *in* 'OpenMP in a Heterogeneous World', Springer Berlin Heidelberg, pp. 271–274.

Butcher, J. C. (2016), *Numerical Methods for Ordinary Differential Equations*, 1 edn, Wiley.

Deseyve, C. & Bednar, T. (2006), Wind induced thermal losses through compact pitched roof constructions – test roof – measurements, simulation model and validation, *in* 'Research in Building Physics and Building Engineering (3rd International Building Physics Conference)', Taylor & Francis Group, London, pp. 459–464.

Fürlinger, K. & Gerndt, M. (2007), Analyzing overheads and scalability characteristics of OpenMP applications, *in* 'High Performance Computing for Computational Science - VECPAR 2006', Vol. 4395, Springer Berlin Heidelberg, pp. 39–51.

Geshi, M. (2019), *The Art of High Performance Computing for Computational Science, Vol. 1: Techniques of Speedup and Parallelization for General Purposes*, Springer Singapore.

Lewis, T., Wegerer, P., Hinterseer, S. & Bednar, T. (2022), 'Space4free: A feasibility study on the conversion of historic 100+ year old brick basements (type "gründerzeit") to flats in downtown vienna, 2022 CIB world building congress'.

OpenMP (2021), 'OpenMP application programming interface'.
URL: *https://www.openmp.org/*

Radi, B. & El Hami, A. (2018), *Advanced Numerical Methods with Matlab® 2: Resolution of Nonlinear, Differential and Partial Differential Equations*, 1 edn, Wiley.

Rauber, T. & Rünger, G. (2023), *Parallel Programming: for Multicore and Cluster Systems*, Springer International Publishing.

zch & Naszta (2013), 'How to atomically update a maximum value?'.
URL: *https://stackoverflow.com/a/16190791*

BauSIM 2024 in Wien
23. September – 26. September

Impact of Zoning Strategy on Heating Load, Heating Demand, Comfort and Air Quality for a Flat Equipped with Different Ventilation Systems

Mara Magni[1], Fabian Ochs[1], Elisa Venturi[1]

1 University of Innsbruck, Austria, E-Mail: mara.magni@uibk.ac.at

Abstract

Building simulation plays a pivotal role in optimizing energy performance and indoor comfort in residential structures. However, it is well known that the adoption of dynamic simulations is time-consuming in terms of the time required for modelling and for the simulation itself. This makes it particularly important to create the model as simplified as possible but detailed enough to be able to answer the design questions. In order to find the trade-off, the quality of the available data/information has to be taken into account too.

This study delves into the significance of comparing results obtained from simplified single thermal zone building simulations against their more detailed multi-thermal zone counterparts, particularly in the context of analysing flats equipped with mechanical ventilation systems.

Introduction

The definition of the thermal zone (TZ) is a key element in the building modelling process as it defines the spatial discretization of the building model. In each zone, the heat and mass balance equations will be solved and typically the air is considered fully mixed, therefore the available outputs refer to the defined TZs (Brès et al., 2017). The most accurate approach would be to model each room (or even part of it) as a single TZ. This is not possible as it would require too long modelling and computational time and the results would be difficult to interpret. The other extreme approach is to model the whole building with only one TZ. In most of the cases an intermediate solution is required and to find the trade-off is not trivial (Brès et al., 2017). A series of papers on this topic can be found in the literature. (Wu et al., 2023; Shin & Haberl 2019; 2022; Brès et al., 2017) all agree that the zoning strategy is based on the modeller's experience and is very case-specific, nevertheless has a high impact on the simulated energy balance and thermal comfort. (Shin & Haberl 2019) made a comprehensive literature review and listed the main aspects that have to be considered while zoning the building: Set-point, ventilation strategy, operation periods, schedules, occupancy and position (e.g. core-perimeter, central-top-bottom). Currently, the ASHRAE 90.1–2016 suggests a core-perimeter approach but there is a lack of comprehensive guidelines describing the most appropriate zoning approach based on the case study and simulation goals. In fact, as mentioned by (Wu et al., 2023) thermal zoning can be a dynamic process that develops through the different phases (from design to operation) where the available level of information is very different (e.g. during the design phase, information about HVAC and properties of spaces might be unknown). This also poses an additional obstacle to the automatization of BIM to BEM process. (Brès et al., 2017) compare the accuracy of different thermal and HVAC zoning approaches providing some general guidelines (e.g. the aggregation of rooms with different uses may lead to a large error) nevertheless the ventilation strategy is not described. (Shin & Haberl, 2022) suggest a procedure for automatizing the thermal zoning based on grid/cluster approach, especially for the design stage when the HVAC is not known.

The reviewed literature provides important insights into zoning strategy and related complexities, nevertheless, studies with a focus on the zoning strategy considering different ventilation concepts are missing. Within this work, the results of a “detailed” model where each room is modelled as one thermal zone are compared with the results of a simplified one thermal zone model considering four different ventilation concepts (i.e. extract air, MVHR with enthalpy and sensible heat recovery and controlled window ventilation). This analysis enables to outline the differences in terms of heating demand, heating load, and air quality for the different cases and models.

Method

Case Study

This study focuses on a multi-family building that will be built in Navis municipality in the district Innsbruck-Land in the Austrian state of Tyrol. Navis is located at about 1000 m above sea level and is characterized by a cold climate where the ambient temperature swings between -15 °C and 30°C and is 90% of the year below 18°C. The

analysed building is composed of 16 flats and has a Treated Area (TA) of 1615 m^2. The building is oriented towards the southwest and the back side of the building (northeast) leans against the terrain.
The total envelope area is ca. 2235 m^2, the net room height is 2.63 m and the average U-value of the envelope including thermal bridges is 0.24 W/(m^{2}K). The external walls are built with Porotherm and have a thickness of 82 cm (U-value: 0.146 W/(m^{2}K)), while the roof, floor and external walls leaning against the ground are made with concrete and an insulation layer and have a U-value of 0.073 W/(m^{2}K), 0.127 W/(m^{2}K) and 0.168 W/(m^{2}K) respectively. The windows are triple pane windows with a U-value of 0.78 W/(m^{2}K).

Simulation Model

The building is modelled using Matlab/Simulink with the carnotUIBK (Siegele et al., 2019) library. The equations governing the building model are described in (Magni et al. 2021). This library allows to perform multi-TZ simulations and to modify the definition of the TZs easily. Thanks to this feature it is possible to easily regroup the rooms according to different zoning strategies. For this case study, it has been decided to focus on the flat with the highest Heating Demand (HD) (ground floor, N-W oriented, Figure 1b) and use a coarser zoning for the rest of the building (as described in Figure 1). The selected flat has been modelled once defining each room as a TZ and once grouping all the rooms in one TZ.

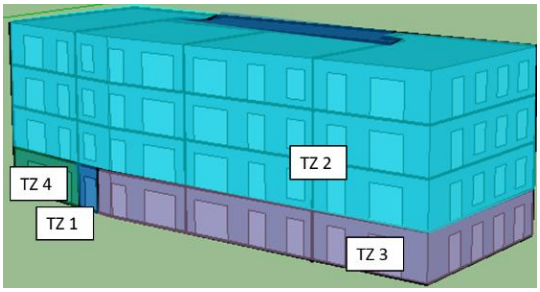

(a)

(b)

Figure 1: (a) view and (b) floor plan of the simulated building. The different colours indicate the thermal zones that have been considered in the simulation model.

The flat is characterised by a living area of 100.3 m^2 and is composed of an open living-kitchen-entrance space (TZ4), three sleeping rooms (TZ5, TZ6 and TZ7), WC (TZ8), bathroom (TZ9) and storage room (TZ10). The rest of the building is composed of the non-heated staircase (TZ1), the remaining 3 flats located on the ground floor (TZ 3) and the other three floors with 12 flats (TZ2). An underground garage is located below the ground floor of the building.
The sensible internal gains are defined for each room and the lighting and occupancy gains are considered with a seasonal variation. The total internal heat gain for the whole building is 26.6 kWh/m$^2_{TA}$a. The dynamic behaviour of the total internal gains (Occupancy, Equipment and Lighting) is reported in Figure 2 for the first week of the year for the different rooms of the flat.

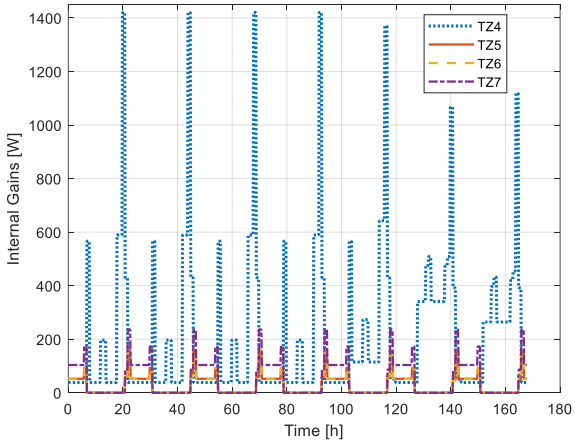

Figure 2: Total internal gains for the living room/Kitchen (TZ4), two child sleeping rooms (TZ5 and TZ6) and the parents sleeping room (TZ7).

For what concerns the humidity generation, based on the activity of the people (sleeping or relaxed) and on the operative temperature (from 22 to 26°C) the humidity generation per person can vary between 0.05 l/h and 0.07 l/h. Additional humidity sources are considered in the kitchen and bathroom (see Figure 3) for a total average humidity generation rate of 3.5 l/day for a flat with 4 people.

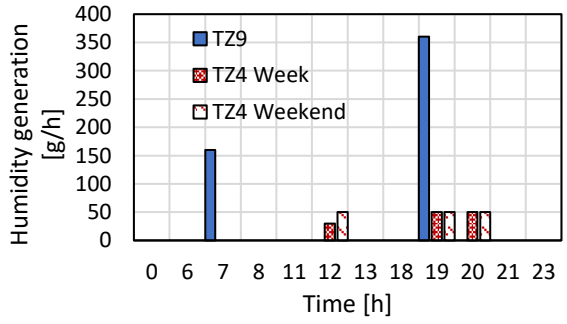

Figure 3: Humidity generation profile for Bathroom (TZ9) and Kitchen (TZ4).

A simplified humidity buffer is considered in the model by increasing the air capacity by a factor 10 (Effective Capacitance, EC approach). As highlighted by (Woods Jason et al., 2013) the EC approach is not the most accurate for moisture buffering. Considering the effective moisture penetration depth (EMPD) or modelling the walls with a hygrothermal model would theoretically relevantly increase the accuracy of moisture prediction. Nevertheless, as the materials that will be used within the flat are unknown, more complex models would considerably increase the computational time without increasing the accuracy as there is high uncertainty regarding the input. Considering also that the relative humidity is not the main focus of this work the authors decided to apply a simplified approach (EC) for moisture buffering.

A CO2 generation rate per person from 20.4 g/h to 25.5 g/h is included in the simulation depending on the activity level (i.e. sleeping and relaxed respectively) (Persily & de Jonge, 2017). In each room, a constant TVOC source of 115 µg/(m^2_{TA}·h) (as suggested by (Kopeinig, 2015) is also considered.

All the described sources (i.e. sensible and latent internal gain, humidity sources, CO2 and TVOC) for each room/TZ are summed up when the whole flat is modelled with one TZ.

The weather file is created using Meteonorm v8.1 for the specific location of the building considering the horizon profile of the mountains. Moreover, the shadings from the surrounding objects on the different parts of the building envelope are also dynamically calculated using Rhino/Ladybug (see Figure 4) and the dynamic shading factors are used as inputs in the Simulink simulation.

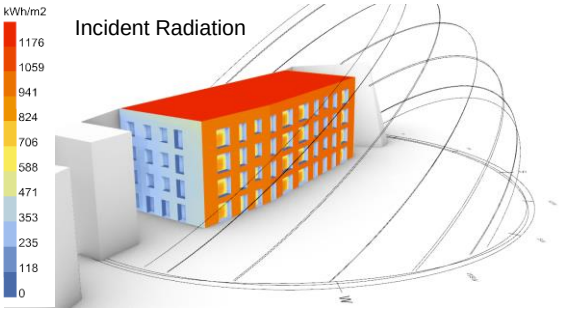

Figure 4: Rhino model used for the calculation of the shading.

Each window is equipped with external movable shadings that can be activated from the 1st of April until the 31st of October if the impinging solar irradiation is higher than 150 W/m^2 and the shading would block 70% of the incoming radiation.

Ventilation Systems

Four different ventilation systems are simulated within this study (using both the MTZ model and the 1TZ model):

- an extract air system (see Figure 56a);
- a mechanical ventilation with an enthalpy heat recovery system (see Figure 56b);
- and with a sensible heat recovery system (see Figure 56c) and;
- a controlled mechanical window opening system with an extracted air system for the WC and bathroom (see Figure 56d).

(ASHRAE Handbook, 2020)(ASHRAE Handbook, 2020)

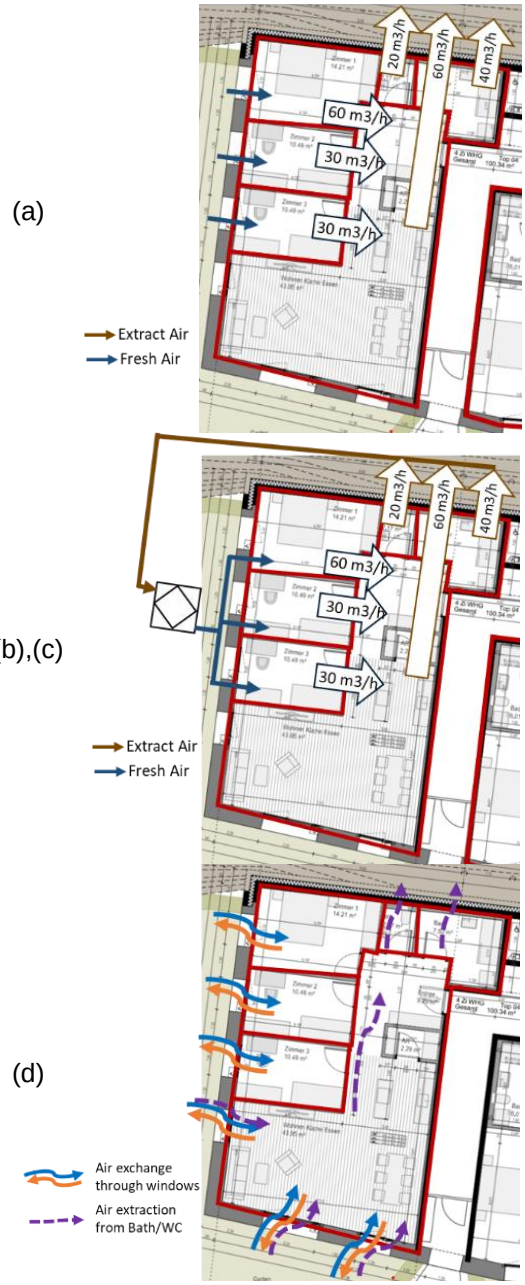

Figure 5: Sketches of the different analyzed ventilation systems.

An hourly air extraction profile from the WC and bathroom, to avoid mould risk, is modelled in each system that corresponds on average to an air change rate of 0.075 V/h for the considered flat (see Figure 6Figure 5 for the total extract volume flow, 37.5% of which is extracted from the WC and the rest from the bathroom).

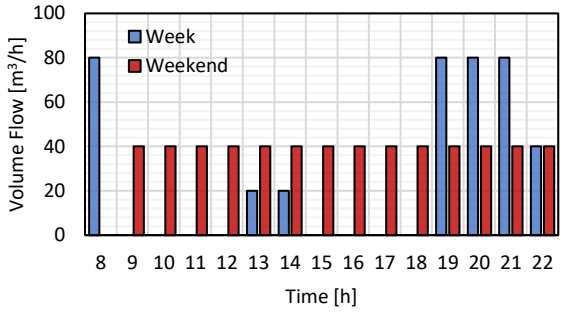

Figure 6: Extract air flow (from WC-TZ8 and Bathroom-TZ9)

The enthalpy exchanger is considered with a temperature and moisture effectiveness of 75% and 55% respectively. The preheating set point for this system depends on the temperature and humidity conditions of the extract air and varies between -25°C ($T_{extract}$ 22.2°C and RH 20%) to -7°C ($T_{extract}$ 22.2°C and RH 60%) (ASHRAE Handbook, 2020).
The sensible heat recovery system is considered with a temperature effectiveness of 85% and a preheating set point of -5°C (ASHRAE Handbook, 2020).

The systems a, b and c are simulated with a constant air volume flow of 30 m³/h/pers (as reported in Figure 56), 25 m³/h/pers, 20 m³/h/pers, 15 m³/h/pers and 10 m³/h/pers but also controlling the air volume flow based on the CO_2 level in each room to a maximum value of 2000 ppm, 1900 ppm, 1800 ppm, 1700 ppm, 1600 ppm, 1500 ppm, 1400 ppm, 1300 ppm, 1200 ppm, 1100 ppm. The controlled window ventilation system (see Figure 56d) on the contrary is only controlled based on the CO_2 level (varying from 2000 ppm to 1100 ppm).
The same ventilation systems are modelled also with the 1TZ model of the analysed flat. In this case, the thermal zone will have only one air "inlet" and "outlet" and in the case of CO_2-controlled volume flow, the CO_2 of the TZ representing the whole flat will be used. In contrast, when a constant volume flow is considered the total volume flow of each room is used as air exchange for the whole flat modelled as one TZ.
It is important to mention that the air exchange between the different thermal zones (in the detailed model) is reduced to the air volume flow moved by the mechanical ventilation system. This means an assumption of closed doors is made which represents the most extreme case for this comparison as the one thermal zone approach will approximate the case where there is a perfect mix of air between all rooms.
In addition to the hygienic ventilation, a constant infiltration rate of 0.042 1/h is considered except for the bathroom (TZ9), WC (TZ8) and storage (TZ10) as they have no access to the ambient (this corresponds to an average infiltration rate for the whole flat of 0.037 1/h).
An ideal free cooling (and bypass of the heat recovery system if present) is modelled when the room temperature exceeds 24°C.

Results

In this section, the energy demand of the whole building and the analysed flat calculated with the MTZ model are presented. Afterwards, the results of the MTZ model are compared with the one obtained with the 1TZ approach for what concerns the energy demand the heating load and the air quality and comfort prediction.

Energy demand of the analysed flat and building

Figure 7 shows the annual heating demand (HD), simulated with the MTZ model, for the analysed flat and the whole building for the different ventilation systems, included in this work, controlled based on the CO_2 level (limit to 1100 ppm) and a constant volume flow of 30 m³/h/pers. The black dashed line indicates the HD requirement to achieve the passive house (PH) level (considering a heating set point of 20°C). This comparison highlights that only the cases with MVHR can achieve the PH requirements (it has to be noticed that the simulations have been performed using a set point of 22°C while PH certification applies a set point of 20°C).

From Figure 7 it can be seen that the extract air and the CO2-controlled window ventilation systems do not present high differences in terms of HD, but their HD is considerably higher than the one required by the cases with MVHR. Furthermore, Figure 7 highlights that the analysed flat, due to its position, has a higher HD compared to the building HD.

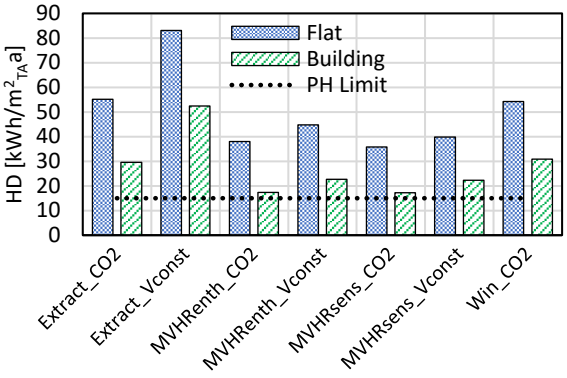

Figure 7: Annual heating demand for the analyzed flat and the whole building for the four different ventilation systems controlled based on the CO_2 (max 1100ppm) and constant volume flow (i.e. 30m^3/h/pers) (from (Magni et al., 2024) modified).

Comparison of the simplified 1TZ model and the MTZ model

Energy Demand

Figure 8 presents the HD of the 1TZ model (solid column) and the additional HD resulting from the MTZ model (dashed column) for all the analysed cases. In addition, the relative deviation between the results of the 1TZ and MTZ is reported using the markers. From Figure 8 it can be noticed that the HD simulated with the MTZ model is in all the cases higher compared with the one predicted by the 1TZ model. The deviation is especially high in the cases where the volume flow is controlled based on the CO_2 level and without a heat recovery system (up to 7%). For the cases with MVHR the deviations are always below 3.5% since here the impact of ventilation losses is lower thanks to the heat recovery. It is interesting to notice that, also in the cases where the air change rate is fixed, constant deviations in terms of HD between the 1TZ model and the MTZ model are present. This is related to the fact that during the day the living room (biggest room of the flat) might get warm due to the internal and solar gains while the sleeping rooms remain cold and still need heating (see Figure 9).

In the 1TZ model where the temperature is an average of the whole flat, in those moments the temperature exceeds the set point switching off the heating. Figure 9 depicts this difference for the extract air ventilation system with a constant air volume flow of 30 m^3/h/pers. From Figure 9 it can be noticed that during the daytime (when the living room-TZ4 gets warm) the heating power of the 1TZ model trends to 0 as the average temperature of the flat is slightly higher of the set point (i.e. 22°C).

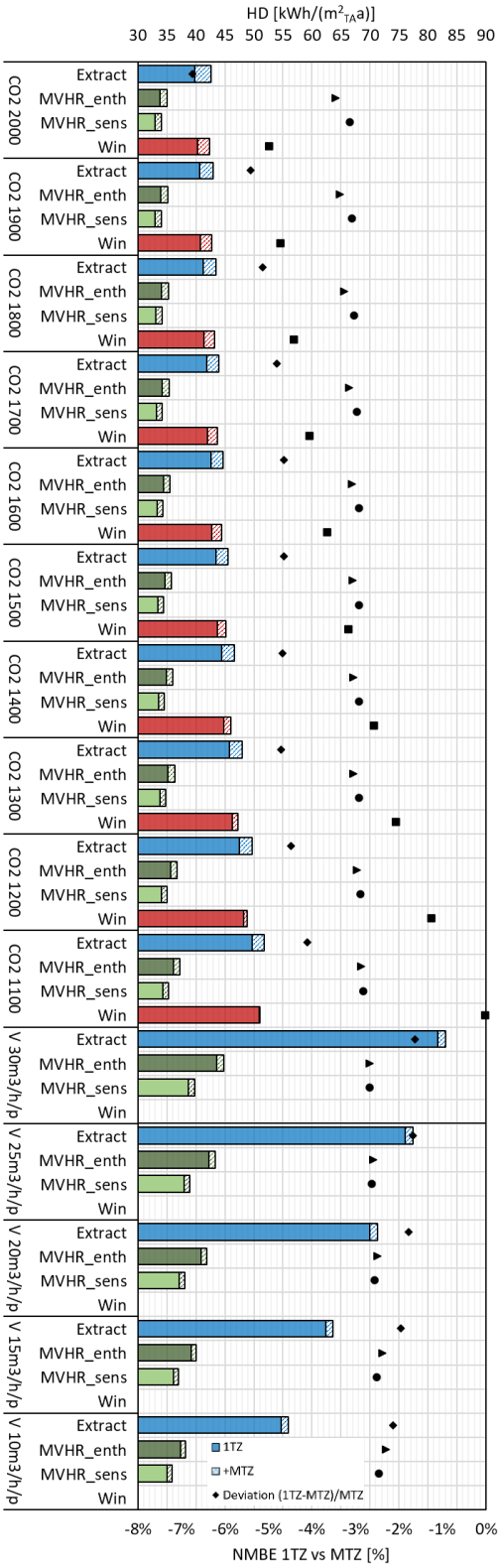

Figure 8: Annual Heating demand for all the analyzed cases simulated with the 1TZ model and MTZ model and the relative deviation.

In contrast, in the MTZ model, the sleeping rooms remain cold and still need heating (see the results of TZ7 in Figure 9).

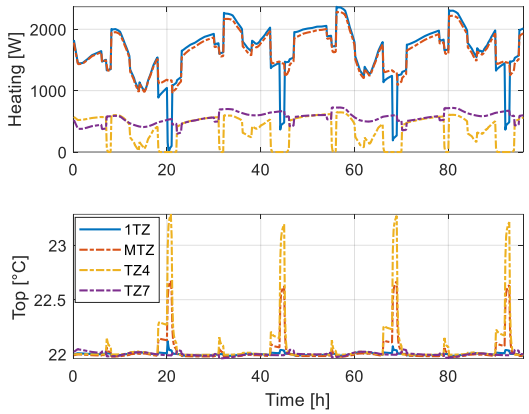

Figure 9: Dynamic behavior of heating demand and operative temperature for the case with extract air ventilation and constant volume flow (i.e. 30 m^3/h/pers).

Heating Load

Another important result of the dynamic simulation is the heating load that can be used for dimensioning the heat generation system and the emission system. The daily average heat load for the whole flat derived as a result of the 1TZ simulation presents a good match with the results of the MTZ simulation (see Figure 10) with a relative deviation below: 2% for the cases with MVHR, 3% for the case with extract air and 5% for the window ventilation cases. Nevertheless, if the flat HL calculated with the 1TZ model is used to derive information about the HL of the single rooms based on the area ratio, this can lead to very high deviations compared to the HL room-wise predicted by the MTZ model. In particular, the HL of the living room would be overestimated and the HL of the sleeping room underestimated.

Figure 10 also highlights that the ventilation systems without heat recovery (HR) lead to a much higher HL compared to the cases with HR.

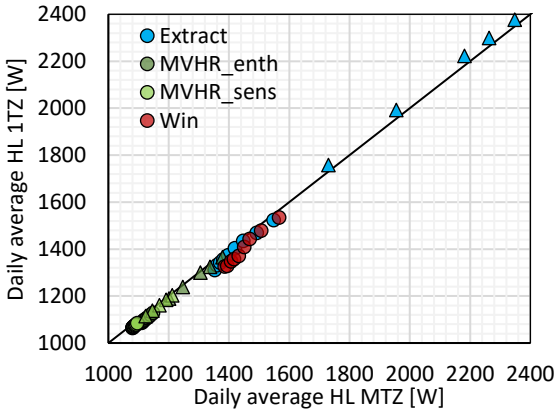

Figure 10: Daily average Heating Load (HL) for the analyzed flat as a result of the MTZ vs 1TZ simulations for all the analyzed cases. The triangles represent the cases controlled with constant air volume flow while the circles the cases controlled on different levels of max CO_2.

Air Quality and Comfort

Figure 11 shows the average CO_2 level for the analysed flat considering only the periods in which people are present in the rooms/flat. The results of the 1TZ model are represented by the y-axis while the results of the MTZ model are on the x-axis. A perfect match would be represented by points lying on the diagonal line.

From Figure 11 it can be noticed that the cases with a constant volume flow (i.e. triangle) also have the same average CO_2 level on both MTZ and 1TZ models. On the contrary, the cases in which the air volume flow is controlled on the CO_2 level (i.e. circles) present deviations between 1TZ and MTZ. In general, the 1TZ model leads to a higher average CO_2 level, compared to the MTZ, as the ventilation is activated only when the whole flat reaches the CO_2 maximum allowed value. In the MTZ model on the contrary, during the night the sleeping room will reach the CO_2 limit, enabling the ventilation system while the living room will have a lower CO_2 level (as no one is in this room overnight), leading to a lower average CO_2 level for the whole flat compared to the 1TZ model. It is also interesting to notice that the cases of controlled window ventilation and extract air lead to similar average CO_2 levels for the 1TZ model while the window ventilation system has lower average CO_2 compared to the extract air system in the MTZ model. This is due to the fact that the extract air flow (needed for the bathroom and WC) is flowing through the living room in case of window ventilation while for the cases with MVHR and extract air is flowing with the rest of the air through the sleeping rooms (see Figure 56).

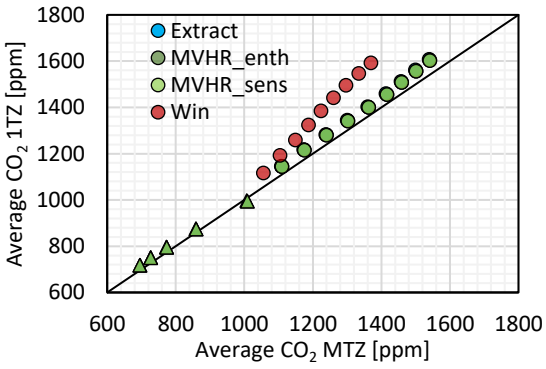

Figure 11: Average CO_2 (considering only the periods in which people are present in the different rooms) for the analyzed flat as a result of the MTZ vs 1TZ simulations for all the analyzed cases. The triangles represent the cases controlled with constant air volume flow while the circles the cases controlled on different levels of max CO_2.

The air flowing through the living room leads to an extra reduction of the CO_2 level in this room that would not be necessary when the maximum allowed CO_2 level is high, while when this air flow is passing through the sleeping rooms this would be anyway needed as the sleeping rooms are the most critical rooms.

Figure 12 shows the results in terms of flat average TVOC of the 1TZ model vs the MTZ model for the different cases. The comparison in terms of average TVOC shows relevant differences between the MTZ and the 1TZ even for the cases with constant volume flow. This is related to the ventilation paths that are considered in the MTZ model and not in the 1TZ model. In fact, in the MTZ model the sleeping rooms, for the cases with MVHR and extract air, receive a high-volume flow of fresh air therefore the TVOC level in these rooms is very low. The air moves then to the living room where the TVOC content is slightly higher due to the TVOC generation rate of the living room. The highest TVOC content is cumulated in the WC and bathroom where there are no people present. For this reason, the average TVOC content is lower in the MTZ model compared to the 1TZ model for the cases with mechanical ventilation. The case with window ventilation behaves slightly differently as each room is ventilated separately and there is no overflow.

A similar trend can be seen in Figure 13 reporting the average relative humidity. Here it is important to mention that all the systems without enthalpy recovery present a very low humidity level, especially the cases with constant air volume flow or controlled with a low maximum CO_2 level, which might lead to discomfort.

Figure 14 presents the number of hours in which the supply air temperature is below 0°C, in people's presence, as a result of the MTZ vs 1TZ model for all the analysed cases. The results for the cases with extract air and window ventilation highly differs between the 1TZ and MTZ model.

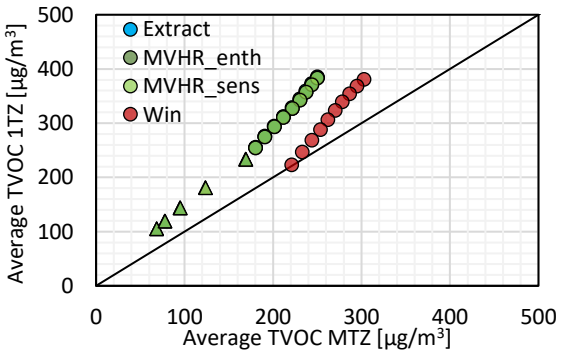

Figure 12: Average TVOC (considering only the periods in which people are present in the different rooms) for the analyzed flat as a result of the MTZ vs 1TZ simulations for all the analyzed cases. The triangles represent the cases controlled with constant air volume flow while the circles the cases controlled on different levels of max CO_2.

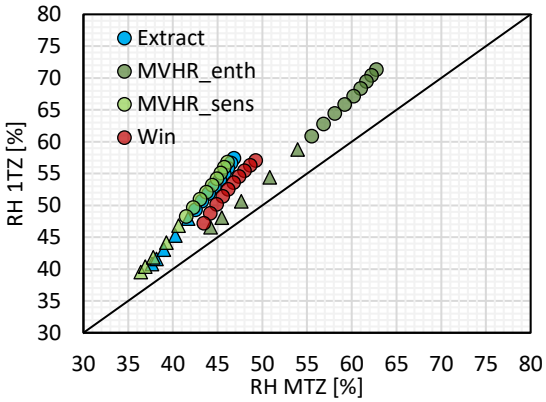

Figure 13: Average Relative Humidity (RH) (considering only the periods in which people are present in the different rooms) for the analyzed flat as a result of the MTZ vs 1TZ simulations for all the analyzed cases. The triangles represent the cases controlled with constant air volume flow while the circles the cases controlled on different levels of max CO_2.

In particular, the 1TZ model always leads to a higher number of hours in which the supply temperature is below 0°C and this is due to the fact that in the 1TZ model, there is always someone present while in the MTZ model also happens that the air is supplied, for example, to the sleeping rooms while people are in the kitchen/living room. This aspect cannot be depicted with a lumped 1TZ model.

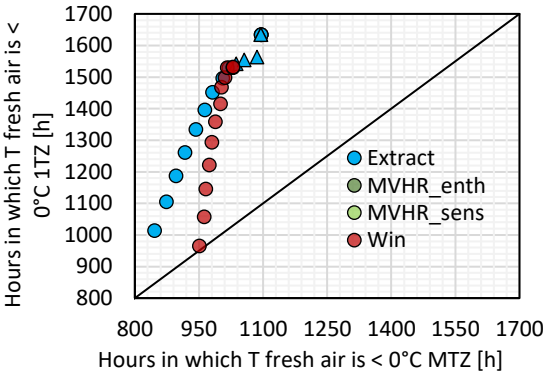

Figure 14: Number of hours in which the supply air temperature is below 0°C in people presence for the analyzed flat as a result of the MTZ vs 1TZ simulations for all the analyzed cases. The triangles represent the cases controlled with constant air volume flow while the circles the cases controlled on different levels of max CO_2.

Moreover, it is important to mention that the cases with MVHR never have a supply temperature below 0°C while the cases with extract air and window ventilation have a very high number of hours in which the supply

temperature is below 0°C. Even if the air flow is controlled on a max CO_2 level of 2000 ppm these ventilation systems will have about 900 hours in which the supply air temperature is below 0°C and the people are present in the ventilated room.

Conclusion

This work presents an in-depth comparison between two different zoning strategy (i.e. “detailed” each room as a thermal zone vs “simplified” only one thermal zone). In particular the impact of the zoning on the results (i.e. energy demand, air quality and thermal comfort) is shown considering four different ventilation system (i.e. extract air, MVHR with enthalpy and sensible heat recovery and controlled window ventilation) and two different control strategies (i.e. constant air volume flow and volume flow controlled on the CO_2 level). The results show an acceptable relative deviation in terms of heating demand (HD) between the two modelling approaches, of about 2.5%, if a constant air volume flow is applied. Nevertheless, the relative deviation in terms of HD can be as high as 7% when the volume flow is controlled based on the CO_2 level and the ventilation system has no heat recovery.
The deviations in terms of heating load of the analysed flat are in the range of 2% for the cases with MVHR, 3% for the case with extract air and 5% for the window ventilation cases. The results of air quality and comfort (i.e. average CO_2, TVOC, RH, air supply temperature) present high deviations between the two modelling approaches. The main reasons for this are that in the 1TZ model it cannot be distinguished between the position of the different persons inside the flat and the air path (in case of overflow ventilation) cannot be modelled.

Acknowledgment

The work presented in this paper was possible through the collaboration project “2226” with Neue Heimat Tirol. The authors are grateful for the financial support.

References

ASHRAE Handbook. 2020. *Air-to-Air Energy Recovery Equipment*.

Brès, Aurélien, Florian Judex, Pieter De Wilde, Aurelien Bres, and Georg Suter. 2017. ‘Impact of Zoning Strategies for Building Performance Simulation’. In . https://www.researchgate.net/publication/327057564.

Kopeinig, Gabriel Rojas. 2015. ‘Optimization Potentials for Mechanical Ventilation of Energy Efficient Housing Simulation and Evaluation Methods’.

Magni, Mara, Fabian Ochs, Elisa Venturi, Georgios Dermentzis, and Harald Konrad Malzer. 2024. ‘Simulation-Based Comparison of Energy Demand, CO2-Emissions and Life Cycle Cost of Different HVAC Systems for Passive Houses’. In *Passive House Conference*.

Magni, Mara, Fabian Ochs, Samuel de Vries, Alessandro Maccarini, and Ferdinand Sigg. 2021. ‘Detailed Cross Comparison of Building Energy Simulation Tools Results Using a Reference Office Building as a Case Study’. *Energy and Buildings* 250 (November):111260. https://doi.org/10.1016/J.ENBUILD.2021.111260.

Persily, A., and L. de Jonge. 2017. ‘Carbon Dioxide Generation Rates for Building Occupants’. *Indoor Air* 27 (5): 868–79. https://doi.org/10.1111/ina.12383.

Shin, Minjae, and Jeff S. Haberl. 2019. ‘Thermal Zoning for Building HVAC Design and Energy Simulation: A Literature Review’. *Energy and Buildings* 203 (November):109429. https://doi.org/10.1016/J.ENBUILD.2019.109429.

Shin, Minjae, and Jeff S. Haberl, 2022. ‘A Procedure for Automating Thermal Zoning for Building Energy Simulation’. In *Journal of Building Engineering*. Vol. 46. Elsevier Ltd. https://doi.org/10.1016/j.jobe.2021.103780.

Siegele, Dietmar, Eleonora Leonardi, and Fabian Ochs. 2019. ‘A New MATLAB Simulink Toolbox for Dynamic Building Simulation with B.I.M. and Hardware in the Loop Compatibility’. *Proceedings of Building Simulation 2019: 16th Conference of IBPSA*, 2651–58. https://doi.org/10.26868/25222708.2019.210641.

Woods Jason, Winkler Jon, and Christensen Dane. 2013. ‘Moisture Modeling: Effective Moisture Penetration Depth Versus Effective Capacitance’. In *Thermal Performance of the Exterior Envelopes of Whole Buildings XII International Conference*.

Wu, Zhaoji, Jack C.P. Cheng, Zhe Wang, and Helen H.L. Kwok. 2023. ‘An Ontology-Based Framework for Automatic Building Energy Modeling with Thermal Zoning’. *Energy and Buildings* 296 (October):113267. https://doi.org/10.1016/J.ENBUILD.2023.113267.

BauSIM 2024 in Wien
23. September – 26. September

Indoor climate and heat demand of surface-heated rooms considering the radiatively participating air

Lukas Schmitt[1] and Martin Kriegel[1]

[1] *Technische Universität Berlin, Hermann-Rietschel-Institut, Marchstr. 4, 10587 Berlin*

Abstract

Radiation absorption by water vapor in indoor air is already a well-known phenomenon. However, the radiative heat transfer between surfaces and air is frequently incorrectly deemed negligible in building energetics and HVAC (Heating, Ventilation, and Air Conditioning) simulations. Thus, we demonstrate a model for numerically determining the radiative heat transfer between the room envelope – containing a heated surface – and the indoor air. Considering a broad range of boundary conditions, the effect of radiative heat transfer between surface and air on the indoor climate and the heat demand of a room is analyzed in a Monte-Carlo based sensitivity analysis.

It is found that considering radiation absorption by the room air can significantly reduce the spread between the mean radiant temperature and the air temperature. Extreme deviations occur with large room sizes, high air exchange rates, high relative humidities, low thermal transmittances and low outdoor temperatures. It is found that neglecting radiation absorption by the indoor air leads to an underestimation of the heat demand if the ratio of ventilation to transmission heat losses increases. Within the cases investigated, the room heat demand increases by up to $30\,\%$ if radiation absorption of water vapor is considered in the room energy balance.

Introduction

Indoor air is mostly assumed and modeled to be transparent to thermal radiation in building energetics. As this assumption is only valid if the indoor air does not contain significant amounts of radiatively active gases, the absorption of radiation by a radiatively active gas has already been subject of numerous studies in the context of HVAC (Heating, Ventilation and Air Conditioning) and building physics applications.

Emission or absorption of infrared radiation is related to the change of rotational and/or vibrational energy levels in molecules. Since changes in the rotational energy level require a dipole moment, radiative transfer by unpolar molecules is minor to that of polar, polyatomic molecules. (Modest 2013). As a result, nitrogen, oxygen and hydrogen only provide weak absorption lines in the infrared spectrum and can be neglected in heat transfer calculations for HVAC applications. On the other hand, water vapor, carbon dioxide and methane provide strong absorption lines in the infrared spectrum (Rothman et al. 2013).

Brändli (1998) found the effect of radiation absorption by carbon dioxide being small compared to radiation absorption by water vapor. As the volume number density of methane ($\sim 10^{18}\,\mathrm{m}^{-3}$) is negligible small compared to water vapor ($\sim 10^{22}\,\mathrm{m}^{-3}$) in typical HVAC applications, methane and carbon dioxide are thus also neglected in this study. Finally, only water vapor radiation absorption is subject of the subsequent analysis.

Among others, Schenker & Keller (1995) and Glicksman & Chen (1998) already determined the heat transfer rate by radiation absorption of water vapor in the room air in exemplary use cases and compared it with other forms of heat transfer. Furthermore, e. g. Kondo et al. (2000) analyzed the effect of radiation absorption by water vapor on the temperature distribution in the air volume. Serra & Semiao (2019) additionally analyzed the effect on the velocity field.

While the influence of water vapor on the radiant heat transfer between the room envelope and indoor air is well understood, there remains a knowledge gap regarding the impact in practical HVAC applications where radiation absorption by indoor air is typically neglected. As the effect of radiation absorption in the indoor air is most crucial for radiative heating systems, this study focuses on surface-heated rooms. We aim to clarify the impact of the additional heat transfer mechanism on the mean radiant temperature, the air temperature and the en-

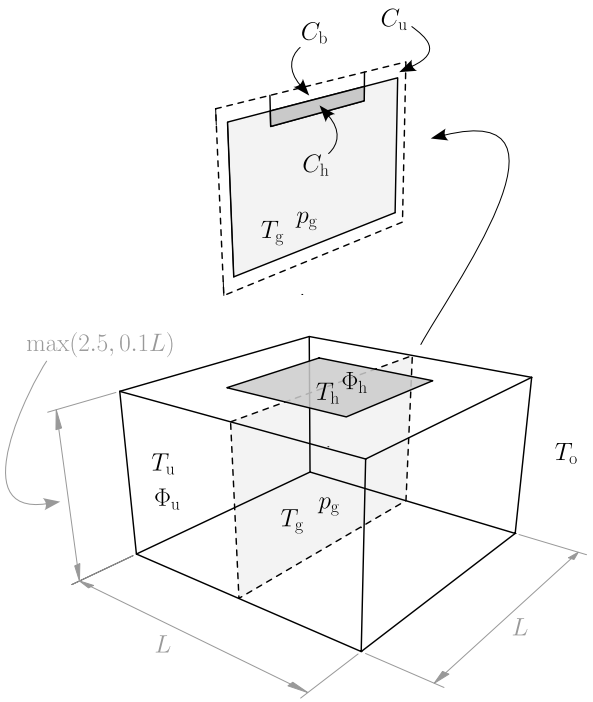

Figure 1: Exemplary representation of a box-shaped room with size L containing a heated surface (darkgray) with temperature T_h and envelope proportion Φ_h, an unheated surface (white) with temperature T_u and envelope proportion Φ_u, an air volume containing a radiatively active gas (lightgray) with partial pressure p_g and temperature T_g.

ergy required to heat a room across various boundary conditions and room geometries.

Analysis model

The effect of radiation absorption on the indoor climate and heat demand in a surface-heated room is evaluated in a simple box-shaped room (Fig. 1) considering water vapor as the only radiatively active gas. The room envelope is divided into a heated (h) and an unheated (u) surface with temperatures T_h and T_u. Thereby, the heated surface is either located on the ceiling or on the floor. The corresponding view factors $\Phi_\mathrm{h} = A_\mathrm{h}/A$ and $\Phi_\mathrm{u} = A_\mathrm{u}/A = 1 - \Phi_\mathrm{h}$ are fixed to be equivalent to the envelope proportions of the heated and unheated surface. A defines the area of the room envelope.

The gas volume is described by the temperature T_g and the partial pressure p_g of the radiatively active gas, i. e. water vapor. Additionally, the room dimension is given by the size parameter L and the outdoor temperature is defined as T_o.

The room model in Fig. 1 is transferred to the resistance-capacity (RC) model shown in Fig. 2. Herein, the heat exchange is modeled using heat transfer coefficients h, thermal transmittances U and thermal resistances R. The thermal capacities for the heated and unheated surface are given as $C_\mathrm{h} = c_{p,\mathrm{h}} A_\mathrm{h}$ and $C_\mathrm{u} = c_{p,\mathrm{u}} A_\mathrm{u}$. As the surface heating system is located on top of the unheated envelope, $C_\mathrm{b} = c_{p,\mathrm{u}} A_\mathrm{h}$ accounts for the unheated surface (as insulation) behind the heated surface. The corresponding equation system is only evaluated for steady states. Thus applies:

$$C_\mathrm{h} \frac{dT_\mathrm{h}}{dt} = C_\mathrm{u} \frac{dT_\mathrm{u}}{dt} = C_\mathrm{g} \frac{dT_\mathrm{g}}{dt} = C_\mathrm{b} \frac{dT_\mathrm{b}}{dt} = 0 \tag{1}$$

The measuring variable for comparing the heat demand $\dot{Q}_\mathrm{h}$ considering various boundary conditions is the operative temperature T_op. Following this, the heat demand

$$\dot{Q}_\mathrm{h} = f(T_\mathrm{op}, L, n, \Phi_\mathrm{h}, T_\mathrm{o}, U_\mathrm{u}, p_{\mathrm{H_2O}}) \tag{2}$$

is given as a function of the operative temperature T_op, the room size L, the air exchange rate n, the view factor of the heated surface Φ_h, the outdoor temperature T_o, the thermal transmittance U_u and the water vapor partial pressure $p_{\mathrm{H_2O}}$. The thermal transmittance U_h serves for a thermal decoupling of the heated and unheated surface and is fixed to be $0.04\,\mathrm{W\,m^{-2}\,K^{-1}}$.

Radiative heat transfer

The radiation exchange between a heat flux emitted by a surface and the air volume depends on the emissivity of the radiatively active air components. Since the evaluation of the emissivity in theory requires spectral integration over thousands of absorption lines, a total emissivity approximation by Leckner (1972) is used in this analysis and given in Eq. (3).

$$\ln \epsilon = \sum_{i=0}^{M} \sum_{j=0}^{N} c_{ij} \left(\frac{T_\mathrm{g}}{1000} \right)^j \left(\log_{10} \frac{p_\mathrm{g} x}{1000} \right)^i \tag{3}$$

Herein, the coefficients c_{ij} for water vapor are given in Eq. (19). The maximum approximation deviation from values calculated with spectral data is given by $5\,\%$ and the equation is valid for a total air pressure of $1\,\mathrm{bar}$. Following Hottel & Sarofim (1967), the absorptivity α can then be approximated by

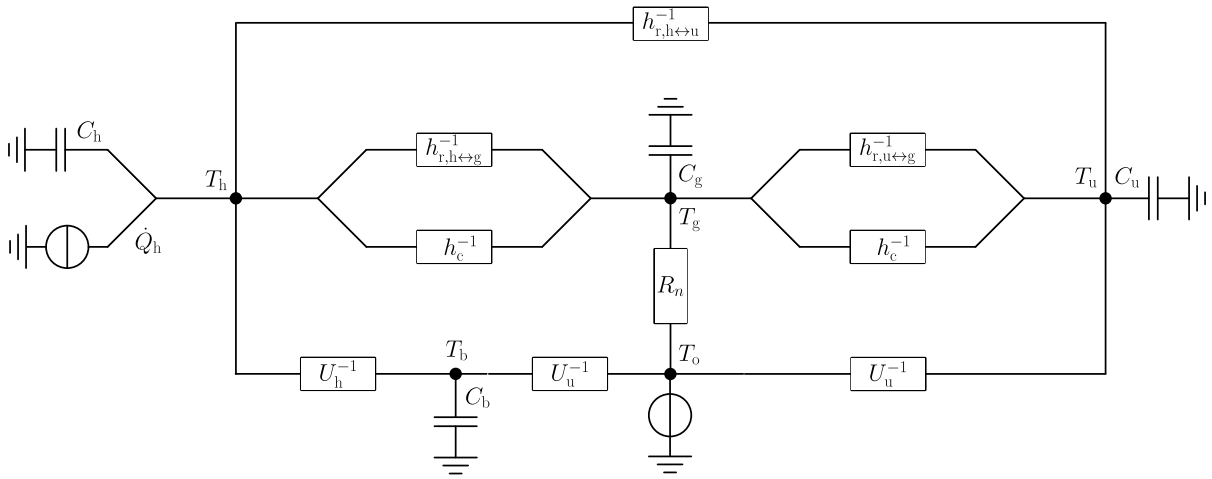

Figure 2: Resistance-capacity (RC) model corresponding to the box-shaped room in Fig. 1.

$$\alpha(T_\mathrm{s}, T_\mathrm{g}, p_\mathrm{g}x) \approx \left(\frac{T_\mathrm{g}}{T_\mathrm{s}}\right)^n \epsilon\left(p_\mathrm{g}x\frac{T_\mathrm{s}}{T_\mathrm{g}}, T_\mathrm{s}\right) \tag{4}$$

wherein n equals 0.45 for water vapor. It should be noted that the application of Eqs. (3) to (4) is limited to enclosures containing black surfaces only. Subsequently, the heat transfer coefficient for radiation exchange between the heated surface (h) and the gas volume (g) is proposed to be

$$h_{\mathrm{r,h\leftrightarrow g}} = \begin{cases} \sigma\dfrac{\alpha_\mathrm{h}T_\mathrm{h}^4 - \epsilon T_\mathrm{g}^4}{T_\mathrm{h} - T_\mathrm{g}} & , T_\mathrm{h} \neq T_\mathrm{g} \\ 0 & , T_\mathrm{h} = T_\mathrm{g} \end{cases} \tag{5}$$

$h_{\mathrm{r,u\leftrightarrow g}}$ is calculated analogously. As the heated surface is planar (either floor or ceiling), the view factor between the heated (h) and the unheated (u) surface is given as $\Phi_{\mathrm{h}\to\mathrm{u}} = 1$. Considering the reciprocity relation $\Phi_{\mathrm{h}\to\mathrm{u}}A_\mathrm{h} = \Phi_{\mathrm{u}\to\mathrm{h}}A_\mathrm{u}$, it follows $\Phi_{\mathrm{u}\to\mathrm{h}} = A_\mathrm{h}/A_\mathrm{u}$. If $T_\mathrm{h} = T_\mathrm{u}$, $h_{\mathrm{r,h\leftrightarrow u}} = 0$. For $T_\mathrm{h} \neq T_\mathrm{u}$ applies

$$h_{\mathrm{r,h\leftrightarrow u}} = \sigma\Phi_{\mathrm{h}\to\mathrm{u}}\frac{(1-\alpha_\mathrm{h})T_\mathrm{h}^4 - (1-\alpha_\mathrm{u})T_\mathrm{u}^4}{T_\mathrm{h} - T_\mathrm{u}} \tag{6}$$

The presented radiative heat transfer coefficients are to be applied on a single path connecting two surface differentials trough a gas. If a complex spatial discretization of the space is to be avoided, a spectrally averaged mean beam length x describing the room adequately can be found. Appropriate formulas are given in Hottel & Sarofim (1967) and Howell et al. (2020). Alternatively, a geometrical mean beam length x_0, considering the room volume V and the enclosing area A, can be determined by

$$x_0 = \frac{4V}{A}. \tag{7}$$

According to Modest (2013), a mean beam length x can be approximated by

$$x = 0.9x_0 \tag{8}$$

while accepting a maximum error of 5 %.

Convective heat transfer

In this analysis, convective heat transfer coefficients h_c are determined according to Glück (2008). The approximation functions represent the upper range of free convection and the lower range of mixed convection respectively. The heat transfer coefficient $h_{\mathrm{c,v}}$ for planar, vertical plates with approximately homogeneous temperature distributions are calculated as

$$h_{\mathrm{c,v}} = 1,6|T_\mathrm{s} - T_\mathrm{g}|^{0.3} \tag{9}$$

The heat transfer coefficients $h_{\mathrm{c,h,up}}$ and $h_{\mathrm{c,h,down}}$ for horizontal plates are determined as

$$h_{\mathrm{c,h,up}} = 2|T_\mathrm{s} - T_\mathrm{g}|^{0.31} \tag{10}$$

for upward heat flows and

$$h_{\mathrm{c,h,down}} = 0.54|T_\mathrm{s} - T_\mathrm{g}|^{0.31} \tag{11}$$

for downward heat flows. Subsequently, the total convective heat transfer coefficient h_c can be expressed as

$$h_\mathrm{c} = \begin{cases} y_\mathrm{w} h_\mathrm{c,v} + y_\mathrm{c} h_\mathrm{c,h,down} + y_\mathrm{f} h_\mathrm{c,h,up} & , T_\mathrm{s} > T_\mathrm{g} \\ 0 & , T_\mathrm{s} = T_\mathrm{g} \\ y_\mathrm{w} h_\mathrm{c,v} + y_\mathrm{c} h_\mathrm{c,h,up} + y_\mathrm{f} h_\mathrm{c,h,down} & , T_\mathrm{s} < T_\mathrm{g} \end{cases} \tag{12}$$

with the weighting factors y_w, y_c and y_f representing the proportion of wall, ceiling and floor areas in the heated or unheated room envelope. It applies: $y_\mathrm{w} + y_\mathrm{c} + y_\mathrm{f} = 1$. Finally, convective heat losses due to ventilation of the room are taken into account as

$$R_n = \frac{1}{n \rho_\mathrm{g} V c_{p,\mathrm{g}}} \tag{13}$$

Herein, n and V describe the air exchange rate and the volume of the room. ρ_g and $c_{p,\mathrm{g}}$ define the density and the specific heat capacity of the air.

Sensor models

The operative temperature T_op is derived from Eq. (14). Herein, the body surface temperature is modeled as T_b = 25 °C.

$$\begin{aligned} & \sigma(T_\mathrm{r}^4 - T_\mathrm{b}^4) + h_\mathrm{c,v}(T_\mathrm{b}, T_\mathrm{g}) \cdot (T_\mathrm{g} - T_\mathrm{b}) \\ = \; & \sigma(T_\mathrm{op}^4 - T_\mathrm{b}^4) + h_\mathrm{c,v}(T_\mathrm{b}, T_\mathrm{op}) \cdot (T_\mathrm{op} - T_\mathrm{b}) \end{aligned} \tag{14}$$

The mean radiant temperature T_r is determined by Eq. (15).

$$T_\mathrm{r}^4 = (1 - \alpha_\mathrm{u}) \Phi_\mathrm{u} T_\mathrm{u}^4 + (1 - \alpha_\mathrm{h}) \Phi_\mathrm{h} T_\mathrm{h}^4 + \epsilon T_\mathrm{g}^4 \tag{15}$$

T_r is evaluated in the center of the room. Thus, the absorptivities $\alpha_\mathrm{u}(T_\mathrm{u}, T_\mathrm{g}, \frac{p_\mathrm{g} x}{2})$ and $\alpha_\mathrm{h}(T_\mathrm{h}, T_\mathrm{g}, \frac{p_\mathrm{g} x}{2})$ and the emissivity $\epsilon(T_\mathrm{g}, \frac{p_\mathrm{g} x}{2})$ are evaluated at $\frac{x}{2}$.

Results and discussion

The impact of water vapor radiation absorption on the mean radiant temperature, air temperature and the energy required to heat a room is analyzed across various boundary conditions and room geometries. Therefore, the analysis model is designed in *Modelica*, exported as *FMU* and simulated with *pyfmi* (Andersson et al. 2016). The derived equation system undergoes quantitative evaluation in a Monte Carlo-based sensitivity study, involving 28,672 steady-state simulations. Thereby, heat transfer coefficients, temperatures and the heat demand are determined setting the operative temperature T_op to 20 °C and generating uniformly distributed samples using the boundary parameters in Table 1.

Table 1: Sensitivity analysis boundary parameters and value ranges

Parameter	Value range
L	4 to 100 m
n	0.1 to 2 h^{-1}
Φ_h	0.01 to 0.5
T_o	−20 to 15 °C
U_u	0.1 to 3 $\mathrm{W\,m^{-2}\,K^{-1}}$
$p_{\mathrm{H_2O}}$	0 to 2340 Pa

In case of ceiling-mounted surface heating systems, the sampling algorithm allows view factors Φ_h covering the whole range, enabling partial surface heating. If the sampled view factor is larger than the available surface proportion, i.e. the complete ceiling area, the view factor is then reduced to the highest valid value. In case of floor heatings, only full-surface heating systems are taken into account. The view factor is chosen so that it corresponds exactly to the proportion of the floor area in the room envelope.

Every sample is solved with the sampled value for $p_{\mathrm{H_2o}}$ and without considering radiation absorption by the indoor air ($p_{\mathrm{H_2o}} = 0$). Subsequently, the impact of the radiative heat transfer between the room envelope and air volume on the indoor climate is evaluated by analyzing the temperature spread

$$\Delta T = T_\mathrm{r} - T_\mathrm{g} \tag{16}$$

between the mean radiant temperature (T_r) and the gas temperature (T_g). As considering a radiatively participating gas may cause a divergent temperature spread, the corresponding error $e(\Delta T)$ for neglecting radiation emission and absorption in the indoor air is defined in Eq. (17).

$$e(\Delta T) = \Delta T(p_{\mathrm{H_2o}}) - \Delta T(p_{\mathrm{H_2o}} = 0) \tag{17}$$

Different combinations of gas and surface temperatures, enabling the same operative room temperature, affect the energy balance of the room as ventilation and transmission heat gains and losses differ. Neglecting radiation emission and absorption in the room air subsequently may lead to a deviating heat demand. The corresponding (relative) error $e(Q_\mathrm{h})$ is defined in Eq. (18).

$$e(\dot{Q}_\mathrm{h}) = \frac{\dot{Q}_\mathrm{h}(p_{\mathrm{H_2O}}) - \dot{Q}_\mathrm{h}(p_{\mathrm{H_2O}} = 0)}{\dot{Q}_\mathrm{h}(p_{\mathrm{H_2O}} = 0)}. \tag{18}$$

As sampling data from Table 1 can generate non-realistic use cases, a postprocessing is conducted. Ensuring the thermal comfort according to DIN EN ISO 7730 (2006), simulation results not fulfilling $T_\mathrm{h} < T_\mathrm{op} + 100\mathrm{K}$ for ceiling-mounted surface heating systems and $T_\mathrm{h} < 29°\mathrm{C}$ for floor heatings are not considered in the following analysis. In addition, cases with invalid water vapor partial pressures, i.e. cases in which the partial pressures are higher than the saturation pressures, are removed from the data set. This results in a final sample size of 20,475 valid simulations for floor heatings and 23,271 valid simulations for ceiling-mounted surface heating systems.

For more vivid classification, the water vapor partial pressure $p_{\mathrm{H_2O}}$ is subsequently converted into relative humidity ϕ.

Heat transfer coefficients

Fig. 3 shows the heat transfer coefficient probability density (Pr) for radiation exchange between surface and gas, surface and surface and convection using an univariate kernel density estimation. In all cases, an average heat transfer coefficient for radiation exchange between surface and gas between $1.01\,\mathrm{W\,m^{-2}\,K^{-1}}$ and $1.07\,\mathrm{W\,m^{-2}\,K^{-1}}$ can be determined. The maximum heat transfer coefficient for radiation exchange between surface and gas for floor and ceiling heating systems is given as $1.79\,\mathrm{W\,m^{-2}\,K^{-1}}$ and $2.52\,\mathrm{W\,m^{-2}\,K^{-1}}$. Within the observed cases, the heated surface at the ceiling induces the lowest convective heat transfer. Subsequently, the impact of radiation absorption is highest in this case. Except for floor heatings, heat transfer between surface and gas is of the same order of magnitude as the convective heat transfer.

Indoor climate and heat demand

Fig. 4 shows the effect of radiation absorption on the temperature spread ΔT between the mean radiant temperature (T_r) and the gas temperature (T_g). It can be observed that regarding the effect of radiation absorption reduces the average temperature spread as relatively more heat is transferred to the gas volume. In case of ceiling-mounted surface heating systems the mean temperature spread reduces from $6.8\,\mathrm{K}$ to $4.5\,\mathrm{K}$. In case of floor heatings the mean temperature spread reduces from $3\,\mathrm{K}$ to $2\,\mathrm{K}$.

Fig. 5 shows the errors $e(\dot{Q}_\mathrm{h})$ and $e(\Delta T)$ regarding the parameters in Table 1 for ceiling-mounted surface heating systems. Neglecting the effect of radiation absorption in the gas volume can result in underestimating the room heat demand $\dot{Q}_\mathrm{h}$ by $30\,\%$ in maximum. Within the $95\,\%$ confidence interval, the room heat demand $\dot{Q}_\mathrm{h}$ is underestimated by $14\,\%$ in maximum. Extreme values occur for large room sizes L, high air exchange rates n, high relative humidities ϕ and low thermal transmittances U_u. The view factor Φ_h and the outdoor temperature T_o only show a minor effect. It can be observed that the error $e(\dot{Q}_\mathrm{h})$ for neglecting radiation absorption by the gas volume increases if the ratio of ventilation to transmission losses increases. The effect is minor ($e(\dot{Q}_\mathrm{h}) < 0.05$) if rooms are getting small (L <20 m).

Determining the correct temperature spread between the mean radiant temperature and the gas temperature highly depends on the room size L, the air exchange rate n, the relative humidity ϕ and the outdoor temperature T_o. Variations in the thermal transmittance U_u show a minor impact. In this study, increasing the view factor Φ_h always comes along with an increase of the heated surface and thus a decrease of the mean surface temperature if the same operating temperature is to be maintained. As a result, the view factor Φ_h has no significant effect on the temperature spread error $e(\Delta T)$ in the observed temperature range. Maximum values for $e(\Delta T)$ occur for large rooms, high air exchange rates, low outdoor temperatures and high relative humidities.

Regarding floor heatings in Fig. 6, the probability distributions of the errors $e(\dot{Q}_\mathrm{h})$ and $e(\Delta T)$ are closer to 0 compared to ceiling-mounted surface heating systems. This is caused by lower temperature differences $T_\mathrm{h} - T_\mathrm{g}$ and $T_\mathrm{h} - T_\mathrm{u}$. However, the direction of all effects is basically maintained. As cases with floor temperatures above $29\,°\mathrm{C}$ are removed in the postprocessing, the result distributions for floor heating misses cases with low outdoor temperatures T_o, high thermal transmittances U_u and high air exchange rates n.

Limitations

In this study, the gas volume is realized as one-node model and thus implicitly assumes a spatially homogeneous temperature and water vapor distribution. As vertical air temperature spreads are high, the potential error has to be analyzed in further investigations. Additionally, the study only considers black surfaces. Since the emissivity of solid materials in buildings (except of metals) are mostly in the vicinity of 0.95, the error is assessed as minor.

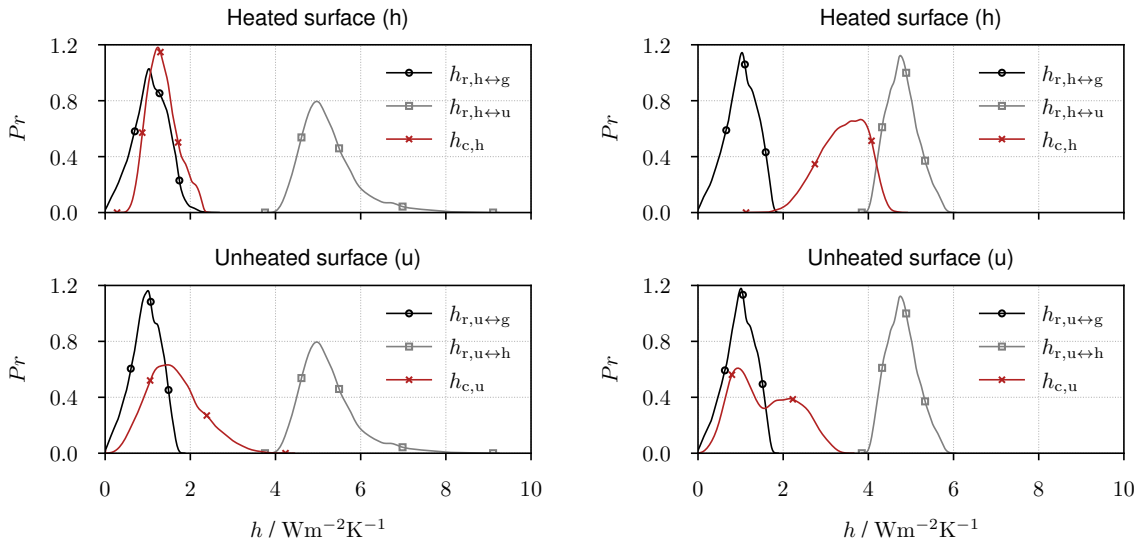

(a) Ceiling heating (b) Floor heating

Figure 3: Heat transfer coefficient probability distribution (Pr) using an univariate kernel density estimation

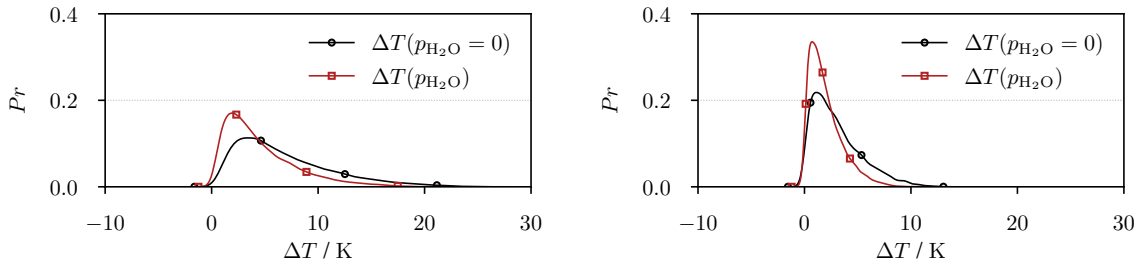

(a) Ceiling heating (b) Floor heating

Figure 4: Temperature spread probability distribution (Pr) using an univariate kernel density estimation

Convection is treated in a very simplified way. The applied heat transfer coefficients are only valid for generalized, mean cases. If forced convection dominates, the convective heat transfer coefficients for downward heat flows can deviate by up to $1.5\,\mathrm{W\,m^{-2}\,K^{-1}}$ for temperature differences of $30\,\mathrm{K}$ (Glück 2008).

The enclosing area of a box-shaped room A_{room} differs from the enclosing area A_{sphere} of an isochoric sphere. Depending on the geometry of the room and the arrangement of the heated surface, the assumed correlation between the view factor and the proportion of the heated surface may differ in practical applications.

The comparison of ceiling and floor heating systems is affected by the location for measuring the operative temperature as controlled variable. Since the measurement location is closer to the floor in practical applications, the impact of radiation absorption on $e(\dot{Q}_{\mathrm{h}})$ and $e(\Delta T)$ increases for ceiling heating systems and decreases for floor heatings as the mean beam length differs for the sensor models.

Conclusions

This study showed the effect of water vapor radiation absorption on the temperature spread between the mean radiant temperature and the air temperature as well as the effect on the heat demand of surface heated rooms. The effect is analyzed quantitatively for a broad range of typical boundary con-

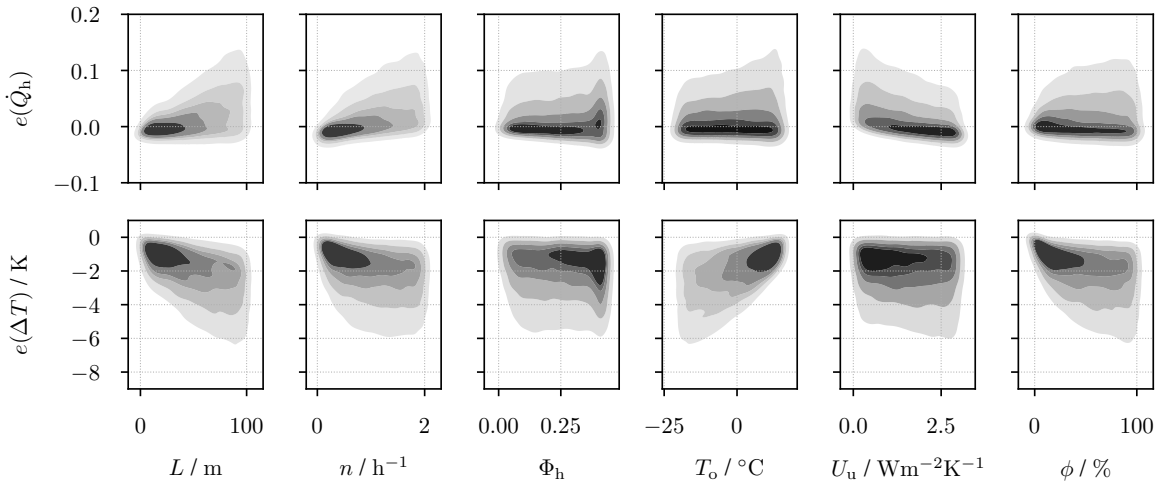

Figure 5: Parameter analysis for ceiling-mounted surface heating systems illustrated as bivariate probability distribution (Pr) using a kernel density estimation. The colors represent levels for 20 % (darkgray), 40 %, 60 %, 80 % and 95 % (lightgray) of the probability mass.

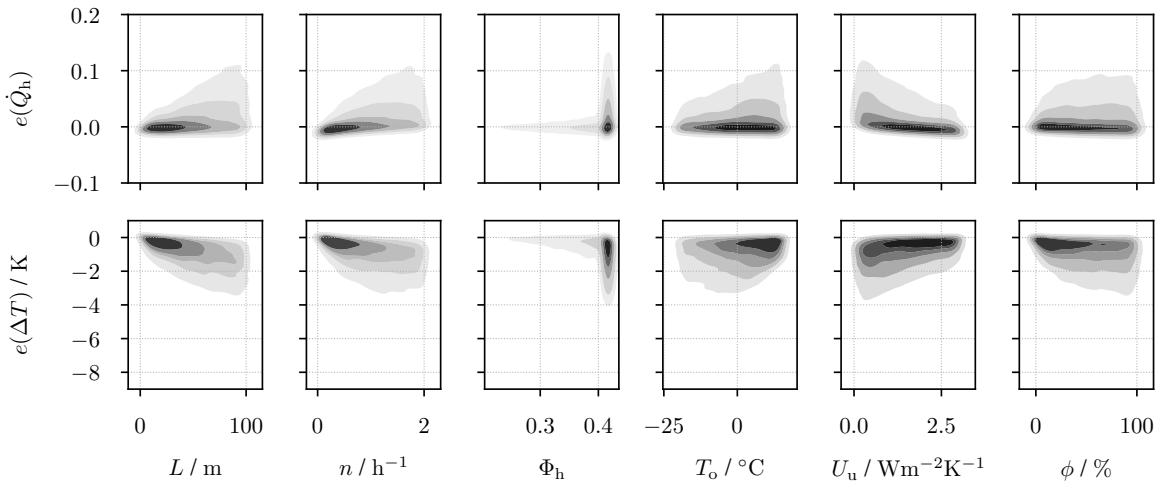

Figure 6: Parameter analysis for floor heating systems illustrated as bivariate probability distribution (Pr) using a kernel density estimation. The colors represent levels for 20 % (darkgray), 40 %, 60 %, 80 % and 95 % (lightgray) of the probability mass.

ditions.

Neglecting the effect of radiation absorption in the indoor air can result in significantly underestimating the room heat demand and overestimating the temperature spread between the mean radiant temperature and the air temperature. Extreme errors occur for large rooms sizes, high air exchange rates, high relative humidities, low thermal transmittances and low outdoor temperatures. Variations of the view factor only show a minor effect. Neglecting radiation absorption by the gas volume becomes most crucial if the ratio of ventilation to transmission losses increases.

Further analyses will address detailed 3D simulations for determining the quality of the mean beam length approximation and evaluations at deviating measurement points. Additionally, carbon dioxide is included in the model. The simulation model is also evaluated in dynamic use cases to evaluate heating-up processes considering radiation emission and absorption in the indoor air.

CRediT authorship contribution statement

Lukas Schmitt: Conceptualization, Methodology, Software, Validation, Formal analysis, Investigation, Data curation, Writing - Original Draft, Writing - Review & Editing, Visualization. **Martin Kriegel:** Supervision, Writing - Review & Editing, Resources.

Acknowledgement

This research did not receive any specific grant from funding agencies in the public, commercial, or not-for-profit sectors.

Appendix

The coefficient matrix $\mathbf{C}_{ij}$ for evaluation of water vapor in Eq. (3) with $M = N = 2$ by Leckner (1972) is given in Eq. (19).

$$\begin{aligned}\mathbf{C}_{ij} &= \begin{bmatrix} c_{00} & \cdots & c_{0N} \\ \vdots & \ddots & \vdots \\ c_{M0} & \cdots & c_{MN} \end{bmatrix} \\ &= \begin{bmatrix} -2.2118 & -1.1987 & 0.035596 \\ 0.85667 & 0.93048 & -0.14391 \\ -0.10838 & -0.17156 & 0.045915 \end{bmatrix}\end{aligned} \tag{19}$$

References

Andersson, C., Åkesson, J. & Führer, C. (2016), Pyfmi: A python package for simulation of coupled dynamic models with the functional mock-up interface, Technical report.

Brändli, M. (1998), Einfluss der IR-Absorption von Wasserdampf auf den laminar-turbulenten Uebergang in der Grenzschichtströmung der Luft an vertikalen Wänden, PhD thesis.

DIN EN ISO 7730 (2006), 'Ergonomie der thermischen umgebung – analytische bestimmung und interpretation der thermischen behaglichkeit durch berechnung des pmv- und des ppd-indexes und kriterien der lokalen thermischen behaglichkeit'.

Glicksman, L. & Chen, Q. (1998), Interaction of radiation absorbed by moisture in air with other forms of heat transfer in an enclosure, *in* 'Roomvent 98-6th International Conference on Air Distribution in Rooms', pp. 111–118.

Glück, B. (2008), Innovative wärmeübertragung und wärmespeicherung - heizen und kühlen mit niedrigexergie (lowex), Technical report.

Hottel, H. C. & Sarofim, A. F. (1967), *Radiative transfer*, McGraw-Hill Book Company.

Howell, J. R., Mengüc, M. P., Daun, K. & Siegel, R. (2020), *Thermal Radiation Heat Transfer*, Taylor & Francis Group.

Kondo, Y., Ogasawara, T. & Fujimura, J.-i. (2000), Interactive simulation of room air temperature and absorption/emission of radiative heat with room moisture, *in* 'Proceedings of ROOMVENT, Air distribution in rooms; Air distribution in rooms, ventilation for health and sustainable environment, International conference', pp. 427–432.

Leckner, B. (1972), 'Spectral and total emissivity of water vapor and carbon dioxide', *Combustion and Flame* **19**(1), 33–48.

Modest, M. F. (2013), *Radiative Heat Transfer*, Elsevier LTD, Oxford.

Rothman, L., Gordon, I., Babikov, Y., Barbe, A., Benner, D. C., Bernath, P., Birk, M., Bizzocchi, L., Boudon, V., Brown, L., Campargue, A., Chance, K., Cohen, E., Coudert, L., Devi, V., Drouin, B., Fayt, A., Flaud, J.-M., Gamache, R., Harrison, J., Hartmann, J.-M., Hill, C., Hodges, J., Jacquemart, D., Jolly, A., Lamouroux, J., Roy, R. L., Li, G., Long, D., Lyulin, O., Mackie, C., Massie, S., Mikhailenko, S., Müller, H., Naumenko, O., Nikitin, A., Orphal, J., Perevalov, V., Perrin, A., Polovtseva, E., Richard, C., Smith, M., Starikova, E., Sung, K., Tashkun, S., Tennyson, J., Toon, G., Tyuterev, V. & Wagner, G. (2013), 'The HITRAN2012 molecular spectroscopic database', *Journal of Quantitative Spectroscopy and Radiative Transfer* **130**, 4–50.

Schenker, G. N. & Keller, B. (1995), 'Line-by-line calculations of the absorption of infrared radiation by water vapor in a box-shaped enclosure filled with humid air', *International Journal of Heat and Mass Transfer* **38**(17), 3127–3134.

Serra, N. & Semiao, V. (2019), 'Is air moisture relevant on radiative heat exchange inside built environments?', *Engineering Computations* **37**(4), 1291–1316.

BauSIM 2024 in Wien
23. September – 26. September

Modeling, simulation and performance analysis of radiant cooling panels operating below the dew point

Kim Helder[1], Marion Hiller[1], Roland Koenigsdorff[2], Max Bauer[1], Felix Thumm[1]

[1]*Transsolar Energietechnik GmbH, Germany, E-Mail: helder@transsolar.com, hiller@transsolar.com, bauer@transsolar.com, thumm@transsolar.com*

[2]*Hochschule Biberach, University of Applied Sciences, Germany, E-Mail: koenigsdorff@hochschule-bc.de*

Abstract

Global energy demand for space cooling continues to steadily increase, leading to challenges in terms of energy efficiency and sustainability. Surface cooling systems offer advantages regarding energy efficiency but are constrained by an inability to operate below the dew point of room air. Innovative designs address these limitations. Condensation-free radiant cooling panels with fleece and a partially infrared-transparent membrane are one such solution and the focus of this study. This paper presents a modeling approach for these panels and investigates the performance differences compared to a conventional cooling panel.

The model accounts for the fleece, air gap, and membrane, but not the capillary tubes and cooling fluid. The thermal conductivity of the fleece was unknown and determined experimentally. The ISO 15099 thermal glazing model was adapted and implemented in TRNSYS to evaluate thermal comfort and cooling capacity. Measurements on below dew-point-panels under different conditions were compared to simulation results, showing the model accurately describes the thermal behavior. Simulations provide layer temperature data unobtainable through direct measurement. A simulation study assessed performance in various climates and development potentials. Using below-dew-point panels in warm, humid climates with natural ventilation offers great potential to reduce air conditioning energy demand. The study also suggests performance improvements by optimizing the system's structure.

Introduction

Increasing population, climate change, and growing demand for thermal comfort have heightened the need for sustainable cooling solutions in buildings. Cooling is vital for health, well-being, and productivity. Innovative technologies are essential to meet the growing cooling energy demand sustainably. (IEA, 2018)

Radiant cooling systems, in contrast to conventional air-based systems, reduce energy consumption, exhibit lower maintenance costs, and decouple fresh air supply from heating and cooling (Dorit Aviv, 2021). However, the dew point problem and the resulting limited cooling capacity of radiant cooling systems are a disadvantage, especially in the context of window ventilation and in warm and humid climates (Helene Teufl, 2021).

Innovative design concepts of cooling panels aim to extend the operating possibilities to below the dew point. One approach is to add an infrared-transparent membrane facing the room. The transparency of the membrane to infrared (IR) wavelengths allows for radiant cooling of occupants without air coming into direct contact with the cooling surface. Consequently, the cooling surface can be below room dew point temperature.

Whereas conventional chilled ceilings and panels operating above the dew point have been widely simulated, there is a lack of simulation models and analysis for innovative designs that can operate below the dew point.

This paper describes the development of a novel simulation approach for investigating radiant cooling below the dew point using infrared transparent membranes.

The object of the investigations is a commercially available panel, “Climate Panel” by Interpanel, that uses infrared-transparent membranes to enable surface cooling below the dew point. This product is described in detail in (Interpanel, 2021). Since some parameters are unknown and no simulation model is available, a simulation model is developed following the methods used by ISO 15099 for glazing systems.

Unknown system parameters are identified through steady-state measurements. The model is implemented in a dynamic thermal simulation (TRNSYS 18, 2024) of a meeting room under varying conditions to assess thermal comfort and energy demand. Dynamic measurement data from installed "Climate Panel" products in a meeting room are compared with simulation results.

Finally, the model is used in a simulation study to evaluate panel performance in warm temperate and tropical climates and identify development potentials.

This paper is based on the results of an unpublished master's thesis (Helder, 2022); further studies on radiant cooling panels operating below the dew point are published in (Eric Teitelbaum, 2019), (Ke Du, 2021).

Material and Methods

Cooling Panel design

The cooling panel used in this research is an airtight panel consisting of a cooling surface, a fleece, an air gap and a partially infrared-transparent membrane that prevents the room air from reaching the cooling surface (see Figure 1).

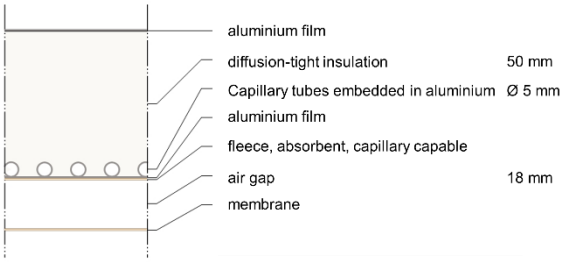

Figure 1: Sketch of Interpanel "Climate Panel" construction (based on (Buff, private communication, 2021))

The panel envelope is airtight to moisture to prevent room air from reaching the cooling surface. This is achieved using the frame, an aluminum film, diffusion-tight insulation, and a diffusion-tight polymer film.

The high-efficiency cooling surface includes an aluminum film above the air gap that absorbs heat from the room and provides a uniform surface temperature for high cooling efficiency. Capillary tubes, coated with aluminum for improved conductivity, are embedded within diffusion-tight insulation to enhance heat transfer.

An absorbent and capillary-active fleece between the cooling surface and the air gap prevents condensation inside the panel, even if the panel's airtightness decreases over prolonged use. The fleece absorbs any resulting moisture and diffuses it away from the cooling surface. According to the manufacturer, the fleece inhibits radiant heat transfer by 10 - 15% (Buff, private communication, 2021).

Between the fleece and the room-side membrane, there is an 18 mm thick air gap (Buff, private communication, 2021). The thickness of this air layer and the minimum operational temperature of the panel's room-side surface are interdependent, as the air layer acts as insulation (Eric Teitelbaum, 2019).

The membrane consists of a special polymer that is diffusion-tight, flame-retardant, UV-resistant, and antistatic (Interpanel, 2021). Its transmittance for thermal radiance is approximately 71.1% (Interpanel, 2021).

Test room

Three "Climate Panel" products were installed as suspended ceiling panels in a test room as shown in Figure 2. The test room is a typical meeting room in Stuttgart, Germany.

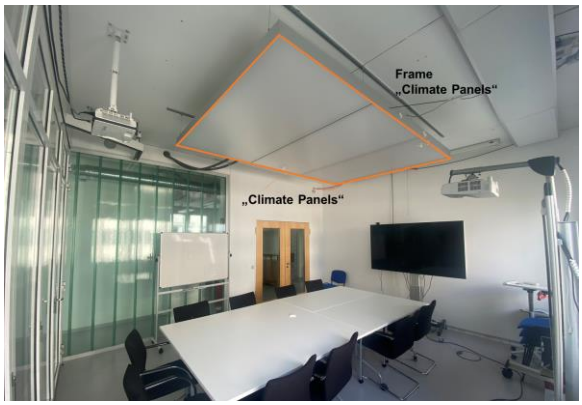

Figure 2: Photo of the Test-room with three "Climate Panels"

The test room has the following dimensions: length 5.4 m, width 4.86 m, height 3.3 m. A total of three panels with a total panel surface of 6.9 m² are installed. The influence of the windows of the room and solar gains are minimized by covering the windows with cardboards. As the windows were covered with cardboard, the temperature of these surfaces is similar to the surrounding surfaces. At the time of the measurements, the room was unoccupied and is not being ventilated.

For the "Climate Panel," the supply and return temperatures of cooling water, the surface temperature of the room-side membrane at two locations and the surface temperature of the frame are measured. The water mass flow is measured by a flowmeter. Room thermal comfort conditions are measured by globe temperature at two different heights, the air temperature and humidity (see Figure 3). The sampling rate of

these measurements is ten seconds. Additionally, surface temperatures of the interior surfaces of the room are measured using an infrared thermometer at intervals of 20 minutes.

The aim of this study and series of measurements is the application in building simulation and not the development of a precise model. For this reason, simplified measurements are carried out in a test room, not a closed chamber. Measurement inaccuracies must therefore be assumed.

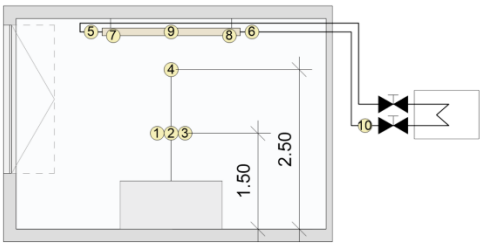

1 – globe-thermometer
2 – surface temperature measurement of room
3 – radiation-shielded room temperature & RH sensor
4 – globe-thermometer
5 – immersion sensor return temperature
6 – immersion sensor supply temperature
7 – surface temperature measurement 'Climate Panel'
8 – surface temperature measurement 'Climate Panel'
9 – surface temperature measurement frame 'Climate Panel' 02
10 –

Figure 3: Vertical section of the room including the climate panels showing the measuring equipment

Series of measurements were carried out with different boundary conditions. The following conditions form the basis for parameter identification and comparison with the simulation results:

- M1: Air temperature 30 °C, humidity > 50%, mass flow is varied
- M2: Air temperature 27.5 °C, humidity > 50%, mass flow is varied

For parameter identification and comparison of the simulation with the measurements, the test room is replicated without windows in the simulation program.

Modelling approach

Since a high thermal conductivity of the capillary tubes embedded in aluminum is expected and parameters such as the thermal conductivity of the fleece and the temperature of the air gap are unknown, a simplified simulation approach was chosen. Because the focus of this research is on comparing the performance of the "Climate Panel" to a conventional cooling panel, detailed modelling of the entire system with capillary tubes and fluid is excluded. However, the modelling of the fleece, the air gap and the membrane is included. The partially infrared-transparent membrane, the additional air gap and the fleece require different modelling capabilities than common chilled ceiling models offer.

In fact, the structure of the "Climate Panel" shows parallels to glazing systems which are available in building simulation software. In building simulation programs such as TRNSYS (TRNSYS, 2024) and EnergyPlus (EnergyPlus, 2024), for example, the detailed thermal model of ISO 15099 is available.

The ISO 15099 model is based on heat flow balances of each layer. The layers are merely differentiated by air-impermeable (e.g. glazing) and permeable (e.g. shading elements) layers. Figure 4 shows the heat flow for each layer *i*-1, *i*, *i*+1 etc. of the system. If the direction of the heat flow is a priori unknown, it is depicted from right to left.

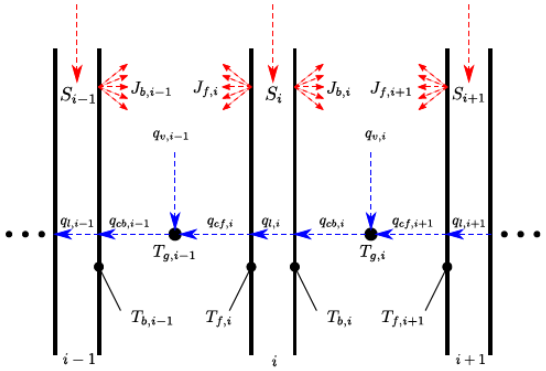

Red: short and long wave radiation
Blue: convection and conduction

Figure 4: Thermal exchanges in the ISO 15099 model of a glazing system (Schöttl, 2013)

The variables illustrated in Figure 4 are described below:

The **radiosities $J_{f,i}$ and $J_{b,i}$** include the fraction of thermal radiation emitted by the boundary surface (EM) as well as those transmitted and reflected:

$$J_{f,i} = \overbrace{\epsilon_{f,i}\sigma T_{f,i}^4}^{\text{EM}} + \tau_{I\,R,b,i}\, J_{f,i+1} + r_{I\,R,f,i}\, J_{b,i-1} \quad (1)$$

$$J_{b,i} = \epsilon_{b,i}\sigma T_{b,i}^4 + \tau_{I\,R,f,i}\, J_{b,i-1} + r_{I\,R,b,i}\, J_{f,i-1} \quad (2)$$

By means of **heat conduction,** a heat flow emerges and flows through the solid layer with the thickness d_i and thermal conductivity λ_i.

The **convective heat transfer** h_{cv} causes the flows $q_{cf,i}$ and $q_{cb,i}$. They flow from the solid layer to gas and vice versa.

The **radiation flow S_i** caused by the solar radiation absorption of each individual layer as well as the option of **heat flow due to ventilated air** gaps, $\dot{q}_{ven}$, are not needed for modelling a chilled ceiling panel.

Figure 5 illustrates how the "Climate Panel" is modeled following the methods of ISO 15099 for glazing systems. The fleece is modelled as a glass layer, the air gap is modelled as an air gap in the glazing system and the membrane as a permanently closed internal shading.

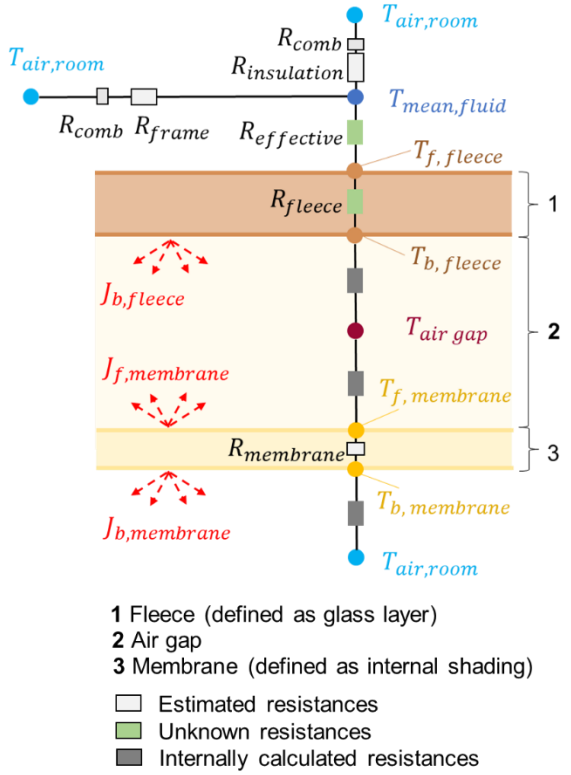

Figure 5: Modelling approach of the cooling panel

The material properties of the layers are known. However, the thermal conductivity and the effective heat transfer coefficient between the fleece and the mean cooling fluid must be determined in a parameter identification.

The cooling performance in the simulation is calculated based on the sum of the heat transport through the membrane: the heat transport through the insulation above the cooling surface of the panels, and the heat transport through the frame. The heat transfer through insulation and frame is calculated based on ordinary heat conduction.

Implementation in TRNSYS

For simulation of the test room including the "Climate Panels," the software package TRNSYS (TRNSYS 18, 2024) was used.

The ISO 15099 model is available as an AddOn of multizone building model for modelling complex fenestration systems (CFS). The implementation allows a calculation of the thermal system of equations proceeding separately from the optical calculations. The solution process is performed iteratively, due to the temperature dependency of the heat transfer coefficients.

The resistance R_{frame} shown in Figure 5 is defined as 0.73 K/W; $R_{insulation}$ is 0.14 K/W. The material properties of fleece and membrane for setting up the system are transferred to a generic input file of the CFS model (see Table 1). Solar and visible material properties as well as the effective openness fraction are set to zero. Pre-processing tools such as Berkeley Lab Window (Berkley, 2024) can be used for this purpose.

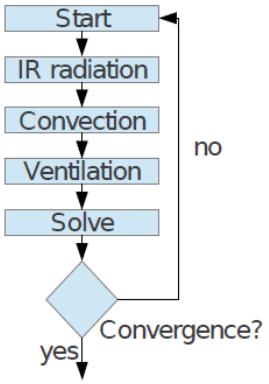

Figure 6: Flow chart of the iterative solution process of the thermal problem

Table 1: material properties of membrane and fleece input into TRNSYS (Buff, private communication, 2021)

Properties	Membrane	Fleece
IR transmittance	71.1 %	0 %
IR front emissivity	23.9 %	0%
IR back emissivity	23.9 %	90 %
conductivity	160 W/m/K	*unknown*

Results

Parameter identification for steady-state conditions

By comparing measured and simulated room-side surface temperatures of the membrane and cooling performances of the cooling panel for steady-state conditions, the unknown parameters can be adjusted: thermal conductivity of the fleece and an effective heat transfer coefficient between the fleece upper surface and the fluid. The goal of the adjustment is to make the simulated values and trends of the cooling

performance and membrane temperature behave as identically as possible to the measured values.

To compare the simulation with measurements, steady-state measurement values from each measurement point are initially imported and then input into the building model. Stationary measurements are chosen at points in time toward the end of each measurement period when the system has reached steady state. Surface temperatures are imposed on all internal surfaces such as walls, ceiling and floor using a massless component with low resistance and high external heat transfer. The convective heat transfer coefficient on the inner side is internally calculated by the simulation program and therefore depends on material properties and present temperatures (Ke Du, 2021). The room temperature is set to the measured room temperature using ideal heating and ideal cooling. The imposed temperatures are listed in the following table.

Table 2: Boundary conditions for steady-state parameter identification

Temperature Wall 1	29,00 °C
Temperature Wall 2	25,40 °C
Temperature Wall 3	26,60 °C
Temperature Wall 4	25,10 °C
Temperature Floor	24,90 °C
Temperature Ceiling	25,20 °C
Air Temperature	27,83 °C

With the steady-state analysis the following parameters are identified:

- Thermal conductivity fleece: 0.06 W/m/K
- Effective heat transfer coefficient: 27.8 W/m²/K

With a thermal conductivity and a effective heat transfer coefficient as listed above, simulation results are achieved that are in good agreement to the measured results of cooling performance and room-side membrane temperature. The thermal conductivity of the fleece is not the actual thermal conductivity of the material. It describes the sum of resistances of the heat transfer from the cooling surface to the air gap. The simulation period for comparing the simulation results with the measurements was ten seconds.

Comparison of transient simulation vs. measurements

To compare transient simulation results with the measurements, again the simulated and measured room-side surface temperatures of the membrane of the cooling panel as well as its cooling performance are considered. For the transient simulations, the parameter values identified under steady-state conditions were used (see above).

The results of the comparison of measured and simulated membrane temperature are shown in Figure 7. The solid lines depict simulation results and measurement results are shown as dashed lines.

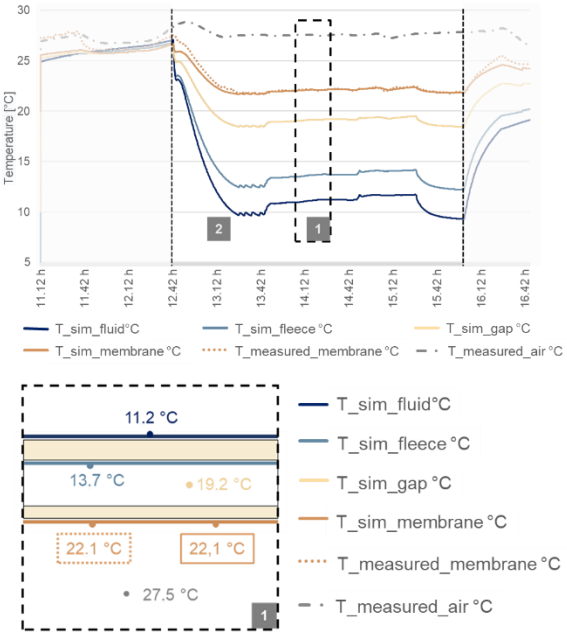

Figure 7: Simulation results for the comparison of the simulation model: comparison of membrane temperatures from simulation and measurement

The following insights can be derived, with some points referring to specific states marked in Figure 7 for better understanding:

- The difference between simulation results and measured values of the membrane temperature in steady state is small, at state 1 measured and simulated is 22.1 °C (Figure 7, state 1).
- A difference between measured values and simulation results of the membrane temperatures can be observed in the transient phase after starting the system (Figure 7, state 2).
- The surface temperature of the underside of the fleece differs from the cooling panel surface temperature by 2.5 K at state 1 (Figure 7, state 1).
- The air temperature within the air gap falls between the membrane temperature and the fleece temperature (Figure 7, state 1).
- The curve progression of the simulation results for layer temperatures is similar, with smaller amplitude changes the further away from the cooling panel.

At an average cooling water temperature of 11.8 °C and a room temperature of 27.5 °C, the temperature of the membrane in simulation and measurement is 22.1 °C. The mean air temperature in the gap is 19.2 °C and the fleece surface temperature facing the air gap is 13.7 °C. The dew point temperature is 16.2 °C.

In Figure 8, the results for the performances of the same simulation are illustrated. The simulated cooling performance is compared with the measurement. The measurement results are shown as dashed lines. Both water-side and air-side calculated performances based on the measurement results are depicted.

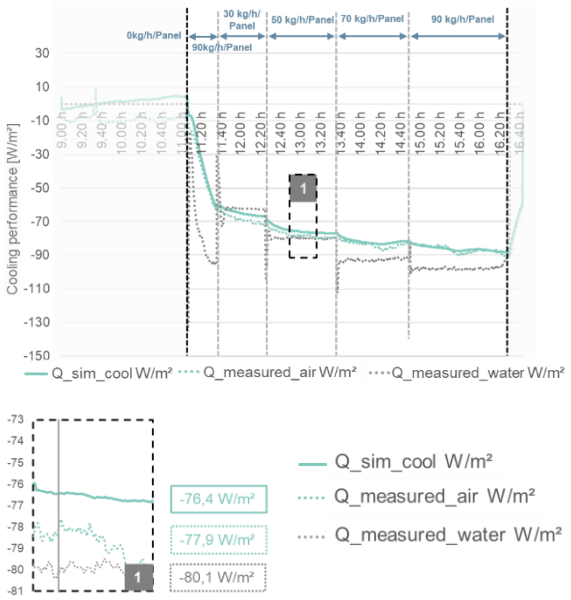

Figure 8: Simulation results for the comparison of the simulation model: Comparison of cooling performances from simulation and measurement

The following insights can be derived:

- The difference between the simulation results of the cooling performance and the water-side measured cooling performance is lowest at a mass flow rate of 30 kg/h/panel to 40 kg/h/panel (1.5 W/m²).
- The higher the mass flow rate, the larger is the difference between simulated cooling performance and water-side measured cooling performance.
- The trend of the air-side measured cooling performance is similar to the simulation results of the cooling performance.
- The air-side measured cooling performance deviates significantly from the water-side measured cooling performance.

The results indicate that modeling the thermal behavior of radiant cooling operating below the dew point using the developed simulation model is effective. At a mass flow rate of 50 kg/h/panel, the simulated cooling performance is 76.4 W/m², the measured water-side performance is 77.9 W/m² and the measured air-side performance is 80.1 W/m². The simulation therefore adequately matches the measurements, particularly the water-side measurements. The simulation results provide insight into additional layer temperatures within the panel that could not be observed in the measurement-based investigations. To improve the accuracy of the model, further investigations should focus on tracking and minimizing sources of error such as condensation, system inertia, and measurement errors in determining both water-side and air-side performance.

Simulation studies

Finally, two different simulation studies were carried out. First, the influence of design parameters on the panel performance was investigated. Subsequently, the potential of radiant cooling operating below the dew point was compared for two different climate zones with building simulation.

Impact of different parameters on panel cooling capacity

In this study, the variation of different parameters was investigated: the IR-transmission of the membrane, the influence of the fleece, and the enlargement of the panel area, see Table 3.

Table 3: Simulation series Parameter study

	Variation	Specification
V 01	enhanced membrane transmission	IR-properstes of membrane: Transmission 90 %, Emission: 5 %, Reflection: 5 %
V 02	Without fleece	Conductivity fleece 1000 W/m/K
V 03	enhanced membrane transmission + without fleece	IR-properstes see V01 + Conductivity fleece 1000 W/m/K
V 04	Enlargement of panel area	One additional panel: four panels in total

Increasing the panel area and enhancing the IR-transmission of the membrane have a comparatively minor impact on the cooling performance of the panels. If the fleece could be omitted in the construction of the panels (V02), the cooling performance would be increased by 43%, relative to the air-side cooling performance

of the base variant of the simulation model. Additionally, using a membrane with increased IR-transmission further increases the cooling performance by 50% (V03). The change in parameters mainly affects the cooling performance.

Application and comparison of the developed model in two climate zones with conventional systems

A sample room with a geometry identical to the test room used in this study is simulated with the tropical climate of Singapore and the warm-temperate climate in the summer of Stuttgart. These investigations serve as a proof of concept, an exemplary study. The most important boundary conditions are listed in the following table.

Table 4: boundary conditions

occupation	0.37 pers/m²; weekdays 8 – 18h
orientation windows	south
internal gains	80 W/pers
ventilation rate (natural ventilation)	200 m³/h; weekdays 8 – 18 h and if 12 °C < Tamb < T_{room}
shading	Movable external shading: close 200 W/m²; open 150 W/m²
construction	Heavyweight
simulation period	1 h

The following cases are investigated for both the warm-temperate climate in the summer of Stuttgart and the tropical climate of Singapore:

- radiant cooling panels operating below the dew point, medium fluid temperature: 10 °C, if the membrane temperature falls below the dew point temperature, no cooling is performed
- conventional surface cooling ("Chilled Ceiling" model in TRNSYS); supply temperature: dew point temperature +2 K, min 16 °C
- no cooling.

The simulation results highlight the advantages of the investigated panels. Radiant cooling operating below the dew point achieves higher cooling performances and lower operative temperatures in both warm-temperate and tropical climates compared to a conventional chilled ceiling panel. As expected, the difference in cooling performance between the two is significantly higher in the tropical climate of Singapore. This can be attributed to the higher dew point temperature in Singapore and consequently higher supply water temperatures in case of a conventional chilled ceiling. Although the investigated panels can achieve supply water temperatures below the dew point temperature, the supply water temperature of these panels is also limited in the tropical climate. At too low supply water temperatures, the dew point temperature is still undercut at the room-side membrane surface. Despite the increased membrane temperature, its temperature partially remains below the dew point temperature of the room air. Due to continuous window ventilation in the model, external conditions have a direct impact on the indoor environment.

Figure 9 shows an analysis of the operative temperatures of the tropical climate. The chart shows the percentage of hours during the time of use for each case, in which the simulated operative temperatures rise above 28 °C or 30 °C, respectively. The reduction in hours above 30 °C for the case without cooling compared to the variant with conventional radiative cooling is minimal. With the use of radiant cooling operating below the dew point, this can be reduced by one-third. The proportion of hours above 26 °C is even reduced by 64% and 72%, respectively.

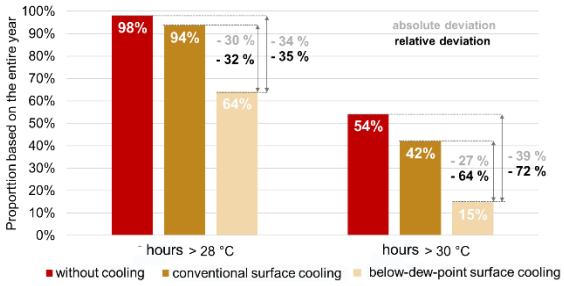

Figure 9: comparison of hours of overheating for the investigated variants in tropical climate

Since the dew point temperature in the Stuttgart climate rarely leads to significant limitations of the operation of the conventional panel, the difference between sub-dew-point radiant cooling and conventional cooling panel is smaller here. Therefore, the use of this technology is particularly beneficial in humid climates. However, despite the increased cooling performance of panels operating below the dew point, indoor temperatures in tropical environments remain high. To enhance the impact of the panels, increasing the panel's surface area is possible.

Conclusion

With the developed simulation model, it is possible to assess the thermal impact of sub-dew point radiant cooling on indoor spaces under variable conditions during the planning process. The TRNSYS add-on CFS enables the creation of a simulation model that realistically captures the thermal behavior of the investigated panels,

particularly the membrane temperature and cooling capacity. The results of the simulations provide insights into additional layer temperatures within the panel, which could not be examined in the measurements conducted.

The potential study based on the developed model demonstrates the influence of the fleece on the performance of the cooling panels. The study shows that the performance of the panels can be improved by up to a maximum of 50% by removing the fleece and improving the IR-transmission of the membrane.

The simulation studies carried out with the new modeling approach indicate that radiant cooling below the dew point offers potential for energy-efficient cooling, particularly in humid climates. The results of applying the simulation model in building simulation are interpreted as plausible based on the findings of the measurement and simulation studies. Simulations of the panels in combination with natural ventilation in the tropical climate of Singapore and the warm-temperate climate in the summer of Stuttgart demonstrate that this technology offers advantages over a conventional chilled ceiling panel in high dew point temperature conditions of Singapore. In warm-temperate climates, sub-dew point radiant cooling achieves the highest cooling performance and lowest operative temperatures compared to conventional panels or the no-cooling variant. However, the difference in performance and temperatures compared to a conventional panel in Stuttgart is smaller than in a tropical climate.

As the function of the system investigated mainly operates with thermal radiation, there is potential for the technology's application beyond buildings, such as improving outdoor thermal environments. The results of this work may serve as a basis for further investigations. Plausibility checks and comparison of cooling performance simulation indicate that the results should be interpreted deeper considering the sources of error. To improve the accuracy of the model, sources of error should be further investigated and minimized. Examinations of the panels in a climatic chamber and with calibrated sensors are also deemed valuable.

Acknowledgement

The authors would like to thank Alexander Buff and Interpanel GmbH for providing the “Climate Panel” panels for this research and Mariana LiebmanPelaez for her time and support.

References

Berkley. (2024). Retrieved from https://windows.lbl.gov/

Buff, A. (2021, 08). private communication.

Buff, A. (2021, 09 15). private communication.

Buff, A. (2021, 10 20). private communication.

Dorit Aviv, K. W. (2021, 03 22). *A fresh (air) look at ventilation for COVID-19: Estimating the global energy savings potential of coupling natural ventilation with novel radiant cooling strategies.* Retrieved from https://www.ncbi.nlm.nih.gov/pmc/articles/PMC7983460/

EnergyPlus. (2024). Retrieved from https://energyplus.net/

Eric Teitelbaum, A. R. (2019, 01). Revisiting radiant cooling: condensation-free heat rejection using infrared-transparent enclosures of chilled panels. *Architectural Science Review*.

Helder, K. (2022). *Potentialstudie zur Strahlungskühlung bei Unterschreitung des Taupunkts.* Master's thesis at Biberach University of Applied Sciences.

Helene Teufl, M. S. (2021). Potential and challenges of a user-centric radiant cooling approach. *Energy & Buildings 246 (2021)*.

IEA. (2018, 05). *The Future of Cooling.* Retrieved 01 29, 2022, from https://www.iea.org/reports/the-future-of-cooling

Interpanel. (2021). *Interpanel*. Retrieved from https://www.interpanel.com/

Ke Du, H. W. (2021). Condensation-free radiant cooling with double-skin infrared-transparent membranes. *Building and Environment*.

Schöttl, P. (2013). Integration komplexer Verglasungssysteme mit Bidirectional Scattering.

Standardisation, I. O. (2003). Thermal performance of windows, doors and shading devices - Detailed calculations (ISO 15099).

TRNSYS 18. (2024). Retrieved from https://www.trnsys.de/trnsys18

BauSIM 2024 in Wien
23. September – 26. September

Simulation-based evaluation of thermal comfort in buildings, by mitigation of heat stress through passive measures

Lukas Lauss[1], Christian Hepf[1], Thomas Schmid[1], Juan Romero Amaya[1], Thomas Auer[1]
1 Chair of Building Technology and Climate Responsive Design,
Technical University Munich, Germany, E-Mail: lukas.lauss@tum.de

Abstract

To reduce energy consumption and the associated CO_2 emissions caused by cooling buildings, conventional energy-intensive active cooling of buildings must be avoided and passive design strategies need to be given priority. This paper investigates the effectiveness of passive measures for thermal performance in summer. The introduced methodology, using building performance simulations (BPS) with representative future weather data sets is applied to explore the prospective potential for passive measures in cooling buildings without compromising the health and performance of building users. Moreover, the effects of passive measures on thermal comfort as well as energy demand are quantified based on sensitivity analyses. The main finding is that passive design strategies can ensure thermal comfort in summer and thus make a major contribution to decarbonize the building sector.

Introduction

Background and Problem Definition

The Earth's climate is currently undergoing a concerning transformation. Since record-keeping began, 2023 has had the highest temperatures, making the last nine years the warmest globally. The global average surface temperature in 2023 was 1.48 °C higher than the 1850-1900 average (C3S, 2024). Additionally, for the first time in history, every day exceeded the pre-industrial level by at least 1 °C, with two days in November exceeding 2 °C (C3S, 2024). Compared to the pre-industrial reference period, the global average temperature has already risen by over 1.1 °C on a long-term average (IPCC, 2023). This warming trend is attributed to human activities, specifically the emission of greenhouse gases. The Paris Agreement aims to limit global warming by reducing greenhouse gas emissions to well below 2 °C and preferably to 1.5 °C by 2100 compared to the pre-industrial average temperature. However, current projections indicate that the global average surface temperature will reach 1.5 °C above pre-industrial levels already by the early 2030s (IPCC, 2023). Beyond this threshold, there is a high risk of surpassing various tipping points, triggering irreversible effects in ecosystems and further accelerating climate change (Armstrong McKay, D. I. et al., 2022).

Motivation and Task

Europe is experiencing the most rapid warming due to climate change, with temperatures on the European mainland rising approximately twice as fast as the global average since the 1980s (EUA, 2024). In Germany, the average annual temperature is already 1.7 °C higher than in 1881, with further increases projected (UBA, 2023). How high this temperature rise will be and how it will progress over time depends primarily on future greenhouse gas emissions. Alongside rising temperatures, heat extremes have increased in frequency and intensity. The number of summer days with a daily maximum temperature of at least 25 °C has more than doubled since the 1950s and the number of hot days with a daily maximum temperature of at least 30 °C has almost tripled (DWD, 2024). Climate change, with increasing outdoor temperatures, significantly affects buildings, leading to indoor overheating and thermal discomfort. Elevated room temperatures induce heat stress and strain on cardiovascular health, as well as cognitive impairments and various health issues, ranging from comfort losses to heat-related fatalities. To mitigate indoor overheating, air conditioning systems are often used as a countermeasure, primarily relying on energy-intensive conventional chillers. Consequently, the operation of air conditioning systems contributes to increased electricity consumption and additional CO_2 emissions, reinforcing the cycle of climate change. Therefore, decarbonizing the building sector involves minimizing CO_2 emissions associated with building climate control. For this reason, the German Building Energy Act (GEG) advocates for increased use of passive design strategies for thermal performance in summer, mandating

compliance with minimum requirements for summer heat protection according to DIN 4108-2. Consequently, these measures aim to passively reduce cooling energy demand for air-conditioned buildings and prevent high summer room temperatures in non-mechanically cooled buildings.

Methodology

This research investigates the effectiveness of passive measures in enhancing thermal comfort and reducing energy demand. For this purpose, we conduct whole dynamic building simulations to analyze the comprehensive impact of passive measures in high-resolution granularity at a detailed room level. The effectiveness of passive measures is quantified by assessing their potential to decrease comfort violations due to overheating in terms of overtemperature hours (OTH [h/a]) as well as overtemperature degree hours (OTDH [Kh/a]) compared to a defined reference base case. Additionally, we assess whether these measures can limit indoor overheating to an acceptable level based on corresponding exceedance frequencies (EF [%]) according to the DIN EN 16798-1 adaptive comfort band.

Through these simulation-based investigations into the limits of passive measure effectiveness, *we aim to address the overarching research question of whether and how it is still feasible to construct as well as operate buildings without mechanical cooling in the future?*

The thermal comfort evaluations are based on the adaptive comfort band defined by DIN EN 16798-1. Consequently, the simulation results of OTH lead to an EF during occupancy or usage time. Moreover, we differentiate between Category II (normal level of expectations: PMV ± 0,5 & PPD < 10 % for new and renovated buildings) and Category III (acceptable, moderate level of expectations: PMV ± 0,7 & PPD < 15 % applied to existing buildings) within the adaptive comfort band. The justification for using DIN EN 16798-1 is that our building simulation model does not employ mechanical cooling. Due to the fact that the effectiveness of passive design strategies may change due to climate change, we conduct simulations using different climate datasets. In this research the current climate is represented by the German Weather Service's (DWD) location-accurate Test Reference Years (TRY) TRY-2045, while future climate scenarios are represented by the summer-focused TRY-2045x (Hutter, C. et al., 2023). Additionally, the building location varies to examine the influence of different summer climate regions according to DIN 4108-2. The annual dynamic thermal building simulations are fulfilled with the software IDA-ICE.

To implement our study, we establish an iterative simulation process consisting of three simulation levels. In the first simulation level, 30 different passive measures are simulated as individual analyses. This generates insights into their effectiveness on thermal comfort and their impact on energy demand. Subsequently, in the second simulation level, the most effective passive design strategies are combined, considering their effects on energy demand and modelled as various combinations of measures to investigate potential synergy effects. In this context, sensitivity analyses are conducted to identify passive measures that significantly influence the simulation results and those that play a subordinate role. Finally, in the third simulation level, a normative verification of summer heat protection according to DIN 4108-2 is conducted. The demonstration of measure combinations follows the simulation boundary conditions prescribed in the norm and is evaluated based on the defined target variable OTDH.

Modelling & Simulation

Building Simulation Model

The analyzed building model is based on the sample building from VDI 6009-1 and represents a typical office building in Germany. Figure 1 shows that the generic building model depicts a three-story office building. The office spaces are arranged along the east and west facades, with a standard axis spacing of 1.35 meters. With a room width of three axes and a room depth of four axes, this results in a net room area of 20.7 m², equivalent to a two-person office. In the central zone of each floor, there is an interior core containing sanitary rooms, an elevator, storage, and utility rooms. Additionally, the north facade of the central zone houses the staircase, while a break room and meeting room are located on the south facade of each floor. The respective zones define simulation boundary conditions, such as occupancy schedules, lighting, internal heat sources, etc., according to DIN V 18599-10. Furthermore, detailed occupancy profiles are modeled based on standard profiles defined in DIN V 18599-11 for office spaces. Additionally, simulation boundary conditions, such as the threshold for solar protection control of sun shading systems, are based on DIN 4108-2. The building envelope's energy quality follows the energy standard defined in the German Building Energy Act (GEG). The fictional building simulation model is located in Potsdam in the reference scenario, representing the average summer climate region B according to

DIN 4108-2. The Potsdam location is in accordance with DIN V 18599-10 also valid as the generally applicable reference climate for Germany.

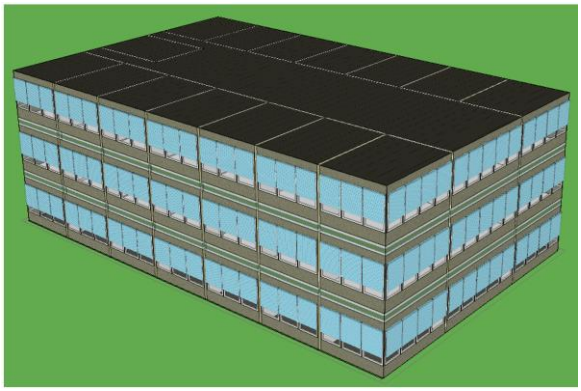

Figure 1: Building Model in IDA-ICE

The detailed investigations into thermal comfort at the room level focus on an interior office with west orientation and on the southwest-oriented corner office, both on the first floor. Based on these worst-case scenarios, it can be ensured that thermal comfort in these two types of rooms will also be maintained in all other rooms. Figure 2 depicts the six configurations of the examined office room types depending on the facade type and window-wall ratio.

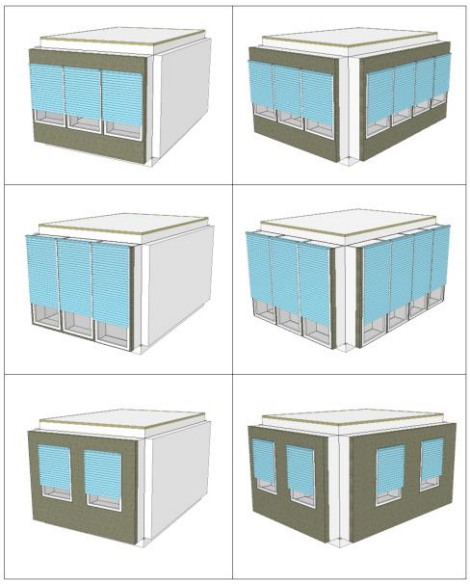

Figure 2: Room types and facade types

Parameter Groups and Passive Measures

In order to conduct meaningful simulations, an extensive selection of passive measures for summer heat protection is carried out. As a result, a simulation matrix of 30 variants is created, divided into eight parameter groups, as shown in Table 1. The reference baseline is characterized by variants indexed as "0" within each parameter group.

Table 1: Investigated Passive Measures

Par.Group	Variant
Glazing G	G0: Double-pane thermal insulation glazing Ug=1.22 W/m²K, g=0.63
	G1: Three-pane thermal insulation glazing Ug=0.61 W/m²K, g=0.53
	G2: Three-pane solar control glazing Ug=0.73 W/m²K, g=0.29
	G3: Three-pane solar control glazing+ Ug=0.71 W/m²K, g=0.11
Window-Wall Ratio (WWR) W	W0: Strip facade (WWR 60 %)
	W1: Fully glazed facade (WWR 93%)
	W2: Punctuated facade (WWR 35 %)
Sun Shading S	S0: External sun shading (Fc=0.25)
	S1: Internal sun shading (Fc=0.75)
	S2: Fixed structural shad. (1.0 m depth)
	S3: Reveal depth (0.3 m)
	S4: without sun shading
Sun Shading Control C	C0: Irradiance limit 200 W/m²
	C1: Irradiance limit 150 W/m²
	C2: Irradiance limit 100 W/m²
	C3: Irradiance limit 300 W/m²
	C4: Sun shading permanently closed
	C5: Sun shading permanently open
Room Height H	H0: Clear room height 3.00 m
	H1: Clear room height 3.50 m
	H2: Clear room height 2.50 m
Design & Construct-ion D	D0: Light construction (except ext. wall)
	D1: Heavy construction
	D2: Double-layer masonry
	D2_S3: Double-layer masonry with 0.75 m reveal depth for sun shading
Electrical Equipment E	E0: 150 W/Workplace (15 W/m²)
	E1: 100 W/Workplace (10 W/m²)
	E2: 50 W/Workplace (5 W/m²)
	E3: 200 W/Workplace (20 W/m²)
Ventilation Strategy V	V0: Natural window vent. w/o night vent.
	V1: Nat. night vent. through tilted wind.
	V2: Nat. night vent. through vent. flaps
	V3: Automatic night vent. thr. vent. flaps
	V4: Natural night ventilation as cross ventilation via office zones, corridors and staircase through tilted windows
	V5: User misbehavior: when presence permanently tilted windows (outside heating period)
	V6: User misbehavior: when presence permanently fully open windows (outside heating period)
	V7: User misbehavior: all windows permanently closed (outs. heat. period)

Results and Discussions

The results presented below are divided into three subsections of the different simulation levels: individual passive measures, combinations of passive measures, DIN 4108-2 standard verification.

Simulation Level 1 „Individual Passive Measures“

Figure 3 illustrates the percentage exceedance frequency (EF) of the adaptive comfort band according to DIN EN 16798-1, with reference to Category II, at Potsdam city center. The percentage criteria refer to the period during which the operative room temperature exceeds the upper limits of the adaptive comfort band during occupancy. The simulation results distinguish between the South-West oriented corner office (SW) and the interior West oriented office (W). It is evident that in the corner office, none of the passive measures can meet the 1 % criterion. Regarding the interior office, only variant D1 (heavy construction) fulfills the 1 % criterion. The same situation arises for the 3 % criterion, wherein variant D2 (double-skin masonry) can also achieve the threshold in the West office, thus aligning within the context of thermal mass.

	< 1 %		< 3 %		< 5 %		< 10 %		EF [%]	
	SW	W	SW	W	SW	W	SW	W	SW	W
Base	x	x	x	x	x	x	✓	✓	8.3	7.7
G1	x	x	x	x	x	x	✓	✓	8.1	7.7
G2	x	x	x	x	✓	✓	✓	✓	5.6	4.1
G3	x	x	x	x	✓	✓	✓	✓	4.9	4.5
W1	x	x	x	x	x	x	x	✓	10.9	7.7
W2	x	x	x	x	✓	✓	✓	✓	4.7	4.7
S1	x	x	x	x	x	x	x	✓	15.2	9.0
S2	x	x	x	x	x	x	x	✓	16.7	9.2
S3	x	x	x	x	x	x	x	✓	15.7	9.5
S4	x	x	x	x	x	x	x	✓	17.4	9.7
C1	x	x	x	x	x	x	✓	✓	8.6	7.7
C2	x	x	x	x	x	x	✓	✓	8.7	7.6
C3	x	x	x	x	x	x	✓	✓	8.6	7.8
C4	x	x	x	x	x	x	✓	✓	8.3	7.7
C5	x	x	x	x	x	x	x	✓	17.3	9.7

	< 1 %		< 3 %		< 5 %		< 10 %		EF [%]	
	SW	W	SW	W	SW	W	SW	W	SW	W
H1	x	x	x	x	x	x	✓	✓	8.9	7.3
H2	x	x	x	x	x	x	✓	✓	8.2	7.8
D1	x	✓	x	✓	✓	✓	✓	✓	4.5	0.9
D2	x	x	x	✓	x	✓	✓	✓	6.9	1.3
D2_S3	x	x	x	x	x	x	✓	✓	11.6	5.1
E1	x	x	x	x	x	x	✓	✓	8.4	7.4
E2	x	x	x	x	x	x	✓	✓	8.7	6.5
E3	x	x	x	x	x	x	✓	✓	8.5	7.9
V1	x	x	x	x	x	x	✓	✓	8.2	7.3
V2	x	x	x	x	x	x	✓	✓	8.3	7.5
V3	x	x	x	x	x	x	✓	✓	8.4	7.8
V4	x	x	x	x	x	x	✓	✓	7.9	7.4
V5	x	x	x	x	x	x	x	x	24.0	15.8
V6	x	x	x	x	x	x	x	x	16.7	18.7
V7	x	x	x	x	x	x	x	x	44.7	45.1

Figure 3: EF depending on room type for Category II at Potsdam city center with TRY 2045

Figure 4 presents the simulation results of passive measures concerning Category III of the adaptive comfort band. In this scenario, the result matrix, compared to Category II, shifts towards a generally greener depiction, indicating that the thresholds can be complied by several passive measures. The 1 % criterion can be met in the corner office by three passive measures: G3 (three-pane solar control glazing+), W2 (punctuated facade), and D1. Similarly, for the West office, the threshold can also be met by G2 (three-pane solar control glazing) and D2. The results for the 3 % criterion in the corner office align with the same five passive measures as those for the 1 % criterion in the West office. For the West office, the 3 % criterion can be achieved through a variety of means, with the threshold met by 16 out of 30 variants.

	< 1 %		< 3 %		< 5 %		< 10 %		EF [%]	
	SW	W	SW	W	SW	W	SW	W	SW	W
Base	x	x	x	x	✓	✓	✓	✓	4.2	3.1
G1	x	x	x	✓	✓	✓	✓	✓	3.8	2.5
G2	x	✓	✓	✓	✓	✓	✓	✓	1.2	0.3
G3	✓	✓	✓	✓	✓	✓	✓	✓	0.6	1.0
W1	x	x	x	x	✓	✓	✓	✓	5.6	3.6
W2	✓	✓	✓	✓	✓	✓	✓	✓	0.4	1.0
S1	x	x	x	x	x	x	x	✓	11.0	5.4
S2	x	x	x	x	x	x	x	✓	13.1	6.1
S3	x	x	x	x	x	x	x	✓	11.7	5.8
S4	x	x	x	x	x	x	x	✓	14.0	6.2
C1	x	x	x	✓	✓	✓	✓	✓	4.0	2.8
C2	x	x	x	✓	✓	✓	✓	✓	3.9	2.7
C3	x	x	x	x	✓	✓	✓	✓	4.7	3.2
C4	x	x	x	x	✓	✓	✓	✓	4.2	3.1
C5	x	x	x	x	x	x	x	✓	14.0	6.0

	< 1 %		< 3 %		< 5 %		< 10 %		EF [%]	
	SW	W	SW	W	SW	W	SW	W	SW	W
H1	x	x	x	✓	✓	✓	✓	✓	4.4	2.6
H2	x	x	x	x	✓	✓	✓	✓	4.2	3.3
D1	✓	✓	✓	✓	✓	✓	✓	✓	0.2	0.0
D2	x	✓	✓	✓	✓	✓	✓	✓	1.3	0.0
D2_S3	x	x	x	✓	x	✓	✓	✓	6.7	1.7
E1	x	x	x	✓	✓	✓	✓	✓	4.2	2.6
E2	x	x	x	✓	✓	✓	✓	✓	4.2	1.8
E3	x	x	x	x	✓	✓	✓	✓	4.3	3.3
V1	x	x	x	✓	✓	✓	✓	✓	3.7	2.4
V2	x	x	x	✓	✓	✓	✓	✓	3.8	2.4
V3	x	x	x	✓	✓	✓	✓	✓	3.9	2.7
V4	x	x	x	✓	✓	✓	✓	✓	3.5	2.1
V5	x	x	x	x	x	x	x	✓	16.0	8.6
V6	x	x	x	x	x	x	x	x	10.0	11.2
V7	x	x	x	x	x	x	x	x	42.6	43.3

Figure 4: EF depending on room type for Category III at Potsdam city center with TRY 2045

Figure 5 depicts the effects of changes in location, showing results of passive measures for the summer climate region C, at Mannheim city center. In this context, concerning Category III, none of the variants can achieve the 1 % criterion. However, the 3 % criterion can be met for the corner office by employing four passive measures: G3, W2, D1, and D2. When considering the West office, the possibilities expand to include passive measures G2 and E2 (low internal loads), as well as the impractical measure C4 (permanent closure sun protection).

	< 1 %		< 3 %		< 5 %		< 10 %		EF [%]	
	SW	W	SW	W	SW	W	SW	W	SW	W
Base	x	x	x	x	x	✓	✓	✓	6.5	4.3
G1	x	x	x	x	✓	✓	✓	✓	5.9	3.2
G2	x	x	x	✓	✓	✓	✓	✓	3.2	1.5
G3	x	x	✓	✓	✓	✓	✓	✓	2.4	1.5
W1	x	x	x	x	x	x	✓	✓	9.4	5.7
W2	x	x	✓	✓	✓	✓	✓	✓	1.6	1.5
S1	x	x	x	x	x	x	x	✓	15.0	7.7
S2	x	x	x	x	x	x	x	✓	17.4	8.5
S3	x	x	x	x	x	x	x	✓	15.5	8.1
S4	x	x	x	x	x	x	x	✓	18.3	8.9
C1	x	x	x	x	x	✓	✓	✓	6.2	3.7
C2	x	x	x	x	x	✓	✓	✓	6.2	3.6
C3	x	x	x	x	✓	✓	✓	✓	7.2	4.1
C4	x	x	x	✓	✓	✓	✓	✓	4.9	2.5
C5	x	x	x	x	x	x	x	✓	18.4	8.9

	< 1 %		< 3 %		< 5 %		< 10 %		EF [%]	
	SW	W	SW	W	SW	W	SW	W	SW	W
H1	x	x	x	x	x	✓	✓	✓	6.1	3.3
H2	x	x	x	x	x	✓	✓	✓	6.8	4.6
D1	x	x	✓	✓	✓	✓	✓	✓	2.0	1.2
D2	x	x	✓	✓	✓	✓	✓	✓	3.0	1.2
D2_S3	x	x	x	x	x	✓	x	✓	11.0	3.4
E1	x	x	x	x	x	✓	✓	✓	6.4	3.4
E2	x	x	x	✓	x	✓	✓	✓	6.1	2.6
E3	x	x	x	x	x	✓	✓	✓	6.4	4.3
V1	x	x	x	x	x	✓	✓	✓	5.4	3.1
V2	x	x	x	x	x	✓	✓	✓	5.6	3.9
V3	x	x	x	x	x	✓	✓	✓	5.8	5.8
V4	x	x	x	x	✓	✓	✓	✓	4.9	4.9
V5	x	x	x	x	x	x	x	x	26.7	26.7
V6	x	x	x	x	x	x	✓	✓	8.6	8.6
V7	x	x	x	x	x	x	x	x	43.4	43.4

Figure 5: EF depending on room type for Category II at Mannheim city center with TRY 2045

Building simulations are utilized to investigate energy demand in addition to thermal comfort. This enables the assessment as well as interactions between thermal comfort and energy demand. The used target variable is the net energy demand (NED), which is represented by four energy flows: heating demand, lighting energy demand, user electricity, and domestic hot water demand (see Figure 6). Domestic hot water demand provided by decentralized instantaneous water heaters remains unchanged across all variants and is included for completeness. The user electricity is solely influenced by the parameter group E "Electrical Equipment" and maintains a constant value in the remaining variants. For the comparison of variants, the base case with 37.3 kWh/m²a corresponds to 100 %, and consequently, the changes in passive measures result in either an energy-related increase or decrease in energy demand.

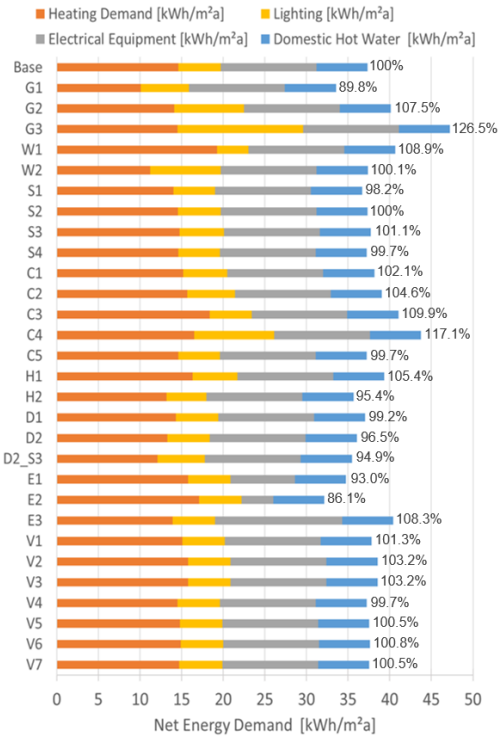

Figure 6: Net energy demand depending on the individual energy flows at Potsdam city center

The greatest increase in energy demand is caused by the variant G3 (three-pane solar control glazing+). Here, the energy demand exceeds the base case by 26.5 %, primarily due to the tripled lighting energy demand resulting from the low g-value. The second-largest increase in energy demand is caused by the permanently closed sun protection (C4), which also leads to a significant increase in lighting energy demand, resulting in an approximately 17 % higher energy demand. Replacing the two-pane thermal insulation glazing (base G0) with a three-pane thermal insulation glazing (G1) significantly reduces the heating demand, resulting in an approximately 10 % lower energy demand. Considering the different proportions of window areas reveals the interaction between heating demand and lighting energy demand. Full glazing (W1) leads to a significantly increased heating demand with lower lighting energy demand, resulting in an approximately 9 % higher energy demand. The opposite trend is observed with the punctuated facade (W2), where the heating demand decreases with increasing lighting energy demand, ultimately leading to a consistent energy demand. Minimizing the electrical power consumption of office equipment (E2) can significantly reduce user electricity, resulting in an approximately 14 % lower energy demand. Conversely, increasing the electrical power consumption (E3) of office equipment leads to an increase in energy demand of approximately 8 %.

Figure 7, summarizes the simulation results of thermal comfort or energy demand using a scatter plot. Starting from the base case, each passive measure results in a directional change. Ideally, the state point of a passive measure in the diagram would lie in the lower left quadrant. This means that the passive measure achieves a significantly lower energy demand while simultaneously improving thermal comfort in the form of less overtemperature degree hours.

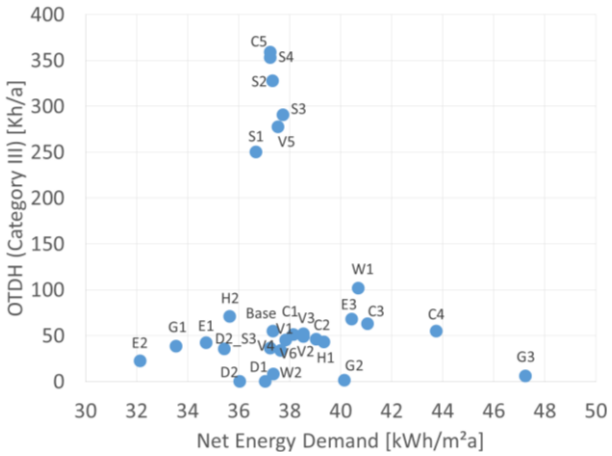

Figure 7: Comparison of simulation results for Office-West at Potsdam City Center with TRY2045

Based on the scatter diagram, the following variants can be derived, which lead to an improvement in thermal comfort by reducing overtemperature degree hours compared to the base case. In this context, it should be noted that due to the external solar shading (S0), a low number of OTDH is already achieved in the base case (55 Kh/a). Furthermore, the effects of passive measures on energy demand in the form of increased (+) or decreased (-) demand are listed in Table 2.

Table 2: Compilation of passive measures with improved thermal comfort compared to the base case

Rank	Var.	OTDH [Kh/a]	Rank	Var.	Δ Energy [%]
1	D1	0	1	E2	-13.9
2	D2	0	2	G1	-10.2
3	G3	3	3	E1	-7.0
4	G2	5	4	D2_S3	-5.1
5	W2	8	5	H2	-4.6
6	E2	22	6	D2	-3.5
7	V6	34	7	S1	-1.8
8	D2_S3	35	8	D1	-0.8
9	V4	36	9	V4	-0.3
10	G1	38	10	W2	+0.1
11	E1	42	11	V6	+0.8

12	H1	43	12	V1	+1.3
13	V1	45	13	V2 / V3	+3.2
14	C2	46	14	C2	+4.6
15	V2	49	15	H1	+5.4
16	C1	51	16	G2	+7.5
17	V3	52	17	G3	+26.5

Simulation Level 2 "Combinations of Passive Measures"

Based on Simulation Level 1, combinations of passive measures (CPM) are compiled and simulated. The selection of passive measures focuses on both improved thermal comfort and reduced energy demand. Furthermore, practical implementation and ease of application of each measure are also considered in the selection process. Consequently, among the different night ventilation strategies, the variant with free, manual night ventilation through tilted windows (V1) is chosen. Due to the fact that solar control glazing (G2, G3) leads to a significant increase in energy demand, they are not implemented in the CPMs. As a result, four different CPMs are investigated, depending on all facade types (W0, W1, W2) and the two room types (W & SW). The simulations for the combinations of measures are conducted at the Mannheim city center location using the weather dataset TRY 2045x. Due to the combination of the location for the summer climate region C with the future weather dataset as well as consideration of the urban heat island effect, the climatic boundary conditions correspond to a worst-case scenario.

In the 1st combination, an external sunshade (S0), triple-pane thermal insulation glazing (G1), heavy construction (D1), and free manual night ventilation with tilted windows (V1) are combined. As shown in Figure 8, this combination allows for all percentage criteria to be met in both Category II and Category III for the Office-West with strip facade (W0). In the corner office, all threshold values can also be met except for the 1 % criterion in Category II. Concerning energy demand, S0/G1/D1/V1 results in a 20 % energy savings compared to the base case, reducing to 29.6 kWh/m²a. When considering the fully glazed facade (W1) with the combination of measures, the same scenario is observed for the Office-West as in the corner office with a strip facade. Consequently, despite the combination, the 1 % criterion for Category II cannot be met with full glazing. The corner office with full glazing presents the most critical situation, where neither the 1 %, 3 %, nor 5 % criteria can be met for Category II. Conversely, with a fully glazed facade, only the 10 % criterion for Category II can be met despite the CPM. In Category III, with S0/G1/D1/V1, all threshold values can be met for the corner office except for the 1 % criterion. The energy demand remains nearly unchanged compared to the strip facade, and the energy savings quantify to approx. 20 % compared to the base case. For the punctuated facade (W2), the combination enables all percentage criteria to be met for both room types. Additionally, a reduction of 12 % energy use is achieved compared to the reference variant with the same facade type.

The 2nd combination of measures also consists of S0/G1/B1/L1 and is additionally extended by A2 to investigate the influence of reduced internal loads of electrical appliances through sensitivity analyses. The CPM S0/G1/D1/V1/E2 results in only minor changes in the simulation results for the percentage exceedances of the adaptive comfort band and ultimately leads to the same result as CPM 1 (see Figure 8). The energy demand decreases by approximately 35 % compared to the base case for both the strip facade and the fully glazed facade, resulting in 23.9 kWh/m²a (W0) and 24.2 kWh/m²a (W1), respectively. For the punctuated facade (W2), the reduction is 25 %, resulting in an energy demand of 27.9 kWh/m²a.

The 3rd combination of measures investigates the influence or sensitivity of a lightweight construction (D0) instead of a heavy construction (D1). As depicted in Figure 9, changing from D1 to D0 results in a significant deviation in the simulation results. For the strip facade (W0), both room types can only meet the 10 % criterion in Category II. Regarding Category III, the Office-West can meet the 3 % criterion, and the corner office can achieve the 5 % criterion. The energy demand decreases by 17 % compared to the base case for the strip facade, amounting to 31.0 kWh/m²a. When considering the fully glazed facade (W1), it becomes apparent that without

S0+G1+D1+V1	EF < 1 %		EF < 3 %		EF < 5 %		EF < 10 %		Simulation Results		
	Cat. II	Cat. III	Cat. II	Cat. III	Cat. II	Cat. III	Cat. II	Cat. III	EF Cat. II [%]	EF Cat. III [%]	NED [kWh/m²a]
W0_W	✓	✓	✓	✓	✓	✓	✓	✓	0.5	0.0	29.6
W0_SW	X	✓	✓	✓	✓	✓	✓	✓	3.0	0.1	
W1_W	X	✓	✓	✓	✓	✓	✓	✓	2.0	0.1	30.0
W1_SW	X	X	X	✓	X	✓	✓	✓	7.6	3.0	
W2_W	✓	✓	✓	✓	✓	✓	✓	✓	0.0	0.0	33.0
W2_SW	✓	✓	✓	✓	✓	✓	✓	✓	0.3	0.0	

Figure 8: Simulation results for combination CPM 1 (and combination CPM 2)

thermal mass in the corner office, only the 10 % criterion for Category III can be met. For the Office-West, the 5 % criterion for Category III and the 10 % criterion for Category II can be achieved. The energy demand for the fully glazed facade is 31.6 kWh/m²a, representing a 15 % energy savings. With the punctuated facade (W2), despite the reduced thermal mass, the 5% criterion can be met for Category II. Regarding Category III, the punctuated facade can even achieve the 1% criterion, and with 34.1 kWh/m²a, the energy demand is approximately 9 % lower than the base variant.

S0+G1+D0+V1	EF < 1 %		EF < 3 %		EF < 5 %		EF < 10 %		Simulation Results		
	Cat. II	Cat. III	Cat. II	Cat. III	Cat. II	Cat. III	Cat. II	Cat. III	EF Cat. II [%]	EF Cat. III [%]	NED [kWh/m²a]
W0_W	X	X	X	✓	X	✓	✓	✓	7.4	1.8	31.0
W0_SW	X	X	X	X	X	✓	✓	✓	8.7	4.2	
W1_W	X	X	X	X	X	✓	✓	✓	7.6	3.7	31.6
W1_SW	X	X	X	X	X	X	X	✓	10.3	6.1	
W2_W	X	✓	X	✓	✓	✓	✓	✓	4.6	0.6	34.1
W2_SW	X	✓	X	✓	✓	✓	✓	✓	3.7	0.5	

Figure 9: Simulation results for combination CPM 3 (and combination CPM 4)

With the 4th combination of measures, sensitivity analyses of construction method and glazing type are conducted. In contrast to the 1st CPM, both lightweight construction (D0) and two-pane thermal insulation glazing (G0) are employed. The CPM S0/G0/D0/V1 results in only minor changes in the simulation results for the percentage exceedances of the adaptive comfort band and ultimately leads to the same outcome as CPM 3 (see Figure 9). Therefore, the exchange from G1 to G0 only affects the energy demand. For the strip facade (W0), the energy demand is 33.8 kWh/m²a, resulting in energy savings of 9 % compared to the reference. The fully glazed facade (W1) leads to 3 % energy savings compared to the reference, with an energy demand of 36.0 kWh/m²a. The reduction for the punctuated facade (W2) is approximately 6 %, with a value of 34.9 kWh/m²a.

Simulation Level 3 „DIN 4108-2 Standard Verification“

In the third simulation level, the normative evidence is provided for the building code minimum standard according to DIN 4108-2. To comply with DIN 4108-2, non-residential buildings must not exceed the maximum value of 500 Kh/a for degree-hours above the reference temperature. The simulations are conducted for the location of Mannheim city center, corresponding to summer climate region C, thus resulting in a reference value of 27.0 °C for the operative temperature. Using the first combination of measures S0/G1/D1/V1, as shown in Figure 10, the normative threshold of 500 Kh/a can be accomplished for all facade and room types except for the fully glazed corner office (W1_SW). Due to the fact that internal heat loads are precisely defined at 144 Wh/m²d in the norm calculation according to DIN 4108-2, the second CPM with altered or reduced internal loads becomes obsolete. With the third combination of passive measures S0/G1/D0/V1, the normative requirement of 500 Kh/a can only be met for three room types. These include the west office with ribbon facade (W0_W) and both room types with punctuated facade (W2_W, W2_SW). Neither for the corner office with ribbon facade (W0_SW) nor for the two room types with full glazing (W1_W, W1_SW) can evidence be provided for compliance with summer heat protection according to DIN 4108-2. A comparison between the first and third CPM reveals the influence of thermal mass. While the corner office with ribbon facade (W0_SW) and the west office with full glazing (W1_W) significantly undercut the norm threshold with thermal mass in the first CPM, this is no longer possible without thermal mass in the third CPM, resulting in a significant increase in OTDH above the reference temperature by a factor of 5. Additionally, it becomes evident that degree hours above the reference temperature drastically increase by a factor of approximately 3 for the fully glazed corner office (W1_SW). The fourth CPM leads to a further increase in OTDH above the reference temperature for the two room types with ribbon facade (W0_W, W0_SW) and full glazing (W1_W, W1_SW). Nonetheless, compliance with the norm for summer heat protection can still be achieved without thermal mass (D1) and triple-pane thermal insulation glazing (G1) for the west office with ribbon facade (W0_W). No changes in degree hours above the reference temperature are observable for the punctuated facade (W2_W, W2_SW), and therefore, positive evidence for compliance with summer heat protection can be easily provided for this type.

	OTDH [Kh/a]					
	W0_W	W0_SW	W1_W	W1_SW	W2_W	W2_SW
CPM 1	1	140	103	644	0	1
CPM 2	-	-	-	-	-	-
CPM 3	188	670	569	1885	60	159
CPM 4	278	839	742	2063	60	159

Figure 10: Simulation results DIN 4108-2 verification

Conclusion and Outlook

The consequences of climate change, with rising outside air temperatures and increasing periods of heat, also have numerous negative effects on buildings. In the building sector, these effects range from loss of thermal comfort as well as reduced user satisfaction to serious health problems and increasing energy consumption for cooling buildings. As a result, the thermal performance of buildings in summer is becoming increasingly important due to climate change and will play an even greater role in the future. Within the scope of this study, the effectiveness of passive design strategies for summer heat protection in terms of thermal comfort was investigated. Through a multitude of extensive simulation-based analyses, evidence was provided that in the future (TRY 2045x), with the aid of passive measures, the thermal performance in summer with respect to the adaptive comfort range according to DIN EN 16798-1 can be achieved without mechanical cooling. Nevertheless, based on numerous whole building simulations, it has also been revealed that due to climate change, future summer thermal performance cannot be maintained at 100 % for all room as well as facade types throughout the entire occupancy or usage period. In this context, there is a need to define a maximum allowable frequency of exceeding comfort thresholds, as was already included in the previous standard DIN EN 15251 at 3 % (or 5 %). The implementation of a definition for an exceedance frequency is also demanded by this research, proposed at 3 % by the authors of this paper based on their research and results in this study. Achieving thermal performance in summer throughout the entire occupancy period requires the consistent implementation of combinations of measures for summer heat protection. The most effective passive measures, considering minimal energy demand, include the following planning and architectural design features: reduced window-wall ratio (avoiding full glazing!), external sun shading systems, thermal mass, and night ventilation. Moreover, the use of energy-efficient appliances should be noted, as they offer a double benefit and utility through reduced internal loads. On one hand, this can positively influence thermal comfort, and on the other hand, substantial energy savings can be achieved. The dual benefit is also evident in the use of thermal mass, as besides improved thermal comfort, energy savings can also be realized. Regarding solar control glazing, it should be noted that although they are an effective passive measure for summer thermal performance, they are associated with significant additional energy demand due to increased lighting energy requirements. Therefore, the other mentioned passive measures should be preferred. As a result, the objective should primarily focus on architectural design rather than technical solutions to maintain thermal comfort in summer, aiming to minimize resource consumption as well as CO_2 emissions in building operation while maximizing thermal performance in summer.

Future research should focus on conducting life cycle assessments of passive design strategies to analyze their climate impact across their entire life cycle. Further research is needed to quantify the greenhouse gas potential (GWP) of passive measures during all life cycle phases, from manufacturing to disposal. Building upon the promising results outlined in this paper, efforts to address remaining issues will be ongoing in forthcoming publications.

Acknowledgement

The research reported in this paper was supported by the German Federal Institute for Research on Building, Urban Affairs and Spatial Development (BBSR) as part of the research initiative "Zukunft Bau" (FWD–10.08.17.7-21.07).

References

Armstrong McKay, D. I. et al., 2022. Exceeding 1.5°C global warming could trigger multiple climate tipping points. Science. Volume 377. doi: 10.1126/science.abn795

C3S. 2024. Global Climate Highlights 2023. Copernicus Climate Change Service (C3S), European Union's Earth Observation Programme.https://climate.copernicus.eu/copernicus-2023-hottest-year-record

DWD. 2024. Klimatologischer Rückblick auf 2023. Deutscher Wetterdienst, Offenbach, Germany. https://www.dwd.de/DE/leistungen/besondereereignisse/temperatur/20240201_klimarueckblick-2023.html

EUA. 2024. European climate risk assessment. European Environment Agency, Copenhagen, Denmark.https://www.eea.europa.eu/publications/european-climate-risk-assessment

Hutter, C. et al., 2023. Kühle Gebäude im Sommer. Anforderungen und Methoden des sommerlichen Wärmeschutzes. Ingenieurbüro Hausladen. Research report. Umweltbundesamt. Climate Change.https://www.umweltbundesamt.de/publikationen/kuehle-gebaeude-im-sommer-0

IPCC. 2023. Climate Change 2023: Synthesis Report. Sixth Assessment Report of the Intergovernmental Panel on Climate Change, Geneva, Switzerland. doi: 10.59327/IPCC/AR6-9789291691647

UBA. 2023. Monitoringbericht 2023 zur Deutschen Anpassungsstrategie an den Klimawandel, Umweltbundesamt, Dessau-Roßlau, Germany. https://www.umweltbundesamt.de/publikationen/monitoringbericht-2023

BauSIM 2024 in Wien
23. September – 26. September

BEYOND building physics - pilot testing of a novel virtual reality-learning environment

Christina J Hopfe[1], Matej Gustin[1], Georg Arbesser-Rastburg[2], Saeed Safikhani[2], Johanna Pirker[2], Robert S McLeod[1]

1 IBPSC, Graz University of Technology, Austria, E-Mail: c.j.hopfe@tugraz.at
2 ISDS, Graz University of Technology, Austria

Abstract

"Beyond building physics" is a newly developed virtual learning environment that was developed from a combination of three technologies: Virtual Reality, Building Performance Simulation and the Internet of Things. The integration of virtual reality in education has emerged as a pivotal focus, driving disruptive advancements in experiential learning. This paper summarizes student feedback from testing a quest (or mission) involving a task that is player controlled. The task takes place within a VR gaming room where the thermodynamic principles of construction materials, energy efficiency strategies, and building performance are conveyed to students.

Introduction

Engineering schools worldwide are facing a host of challenges including falling enrolments, poor attendance, and a lack of diversity in their recruitment profiles (Poole, 2022). Building physics is traditionally taught in classroom settings, where students learn the principles of, for example, thermodynamics, i.e. radiation, conduction and convection. Similarly, awareness of the importance of building physics in relation to sustainability (including high performance buildings, energy efficiency etc.) is a central part of the curricula and is usually taught in a conventional didactic manner. In traditional settings students typically receive instruction from a single source with little peer-to-peer or multi-sensory interaction. Unsurprisingly pedagogic theory, including specific studies focused on the teaching of building performance in higher education underscore how such approaches have often delivered exceptionally poor learning outcomes (Beausoleil and Hopfe., 2015). This means that there is an urgent need to evolve new and innovative teaching practices, that better engage students whilst yielding more robust learning outcomes (McLeod and Hopfe, 2021). Interest in Virtual Reality (VR) and Augmented Reality (AR) technologies has grown steadily in recent years, in particular as a result of increasingly affordable head-mounted displays (HMD) which provide access to various VR applications. Immersive experiences are not only interesting for leisure and entertainment but also open new perspectives in the field of education. As part of this project, a VR environment, incorporating Energy-Plus building performance simulation (BPS) has been developed to create a teaching tool capable of displaying the effects of changing the thermo-physical properties of a room. The virtual environment (VE) was created within a university building at TU Graz that can be altered in terms of its orientation, insulation levels, selection of construction materials and solar shading (amongst other elements). It has been tested with engineering students to understand the effect that such VR pedagogic tools may have in relation to their understanding and learning in the built environment. This paper presents the results of a pilot study involving stakeholder interviews with a focus group of engineering students. The aim of the research was to establish which aspects of building physics they find most challenging to learn and how VR gaming can play a role in augmenting the education of building physics students.

Pedagogical basis

How students learn

The learning pyramid, in Figure 1, illustrates that people learn best when they are actively involved in the learning process. The retention rates given in the figure are estimated by the U.S. National Training Laboratories Institute for Applied Behavioral Science (NTL). For example, people retain only about 5% of what they are taught in a lecture, and only about 10% of what they have learnt from reading. In contrast to these traditional or passive learning methods, people retain much more with teaming or participatory learning methods, such as when they are

engaged in group discussions, when they practice what they have learnt under the guidance of a coach, or, especially, when they apply their newly acquired knowledge in a realistic setting. Biggs and Tang (2007) provide an explanation for why lectures can be so ineffective. While effort is required to follow a lecture, the act of passively sitting and listening tends to lower the student's concentration level.

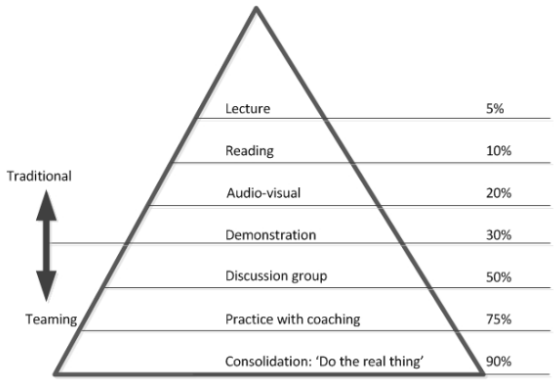

Figure 1 Learning pyramid showing average retention rates (adapted from National Training Laboratories Institute for Applied Behavioural Science)

Furthermore, a student's attention can typically be maintained for only about 10 to 15 minutes, without a change in activity. They point out that although lectures can be effective for presenting information (although not as effective as reading), they are ineffective for stimulating higher order thinking, such as hypothesizing, evaluating, and reflecting. Felder (1988) pointed out that students learn in a variety of ways. Some respond well to teaching styles that emphasize abstract concepts, whereas others respond better to teaching styles that emphasize facts. Some are more visual, while others more verbal. He put forward a conceptual framework that included 32 learning styles, and proposed that instructors adopt a range of teaching techniques to accommodate the learning styles of all students. This includes providing a balance of concrete information and abstract concepts; emphasizing both theoretical fundamentals along with practical problem solving. He also recommended the use of diverse media and modes of instruction, as opposed to relying heavily upon traditional lectures.

Biggs and Tang (2007) promote a form of outcome-based teaching and learning called constructive alignment that immerses students in an environment that requires them to use learning activities most likely to lead to the intended outcomes. This starts with an explicit statement of the intended learning outcomes (ILOs) that informs the students of what they should be able to accomplish, and how well they should be able to do it. This is followed by incorporating teaching/learning methods that engage students in activities that link directly to achieving the ILOs. The third essential feature of constructive alignment is developing methods for assessing how well the ILOs have been achieved. Throughout this entire process, it is imperative to align the teaching/learning activities and assessment tasks to the ILOs.

Virtual and augmented reality for learning

Learning can happen in various ways with different effects (see Figure 1). Virtual Reality (VR) has gained significant attention in recent years, particularly in the context of education and training (Panerai et al., 2018). It differs from augmented reality (AR), the latter being a real-time direct or indirect view of a physical real-world environment that has been enhanced by adding virtual computer-generated information to it (Carmigniani et al., 2010). In contrast, the former relies solely on the user's perception of reality and hence remains entirely virtual. VR users immerse themselves in the environment and (in contrast to AR) cannot control their presence in the real world but are rather controlled by the game. VR also requires a headset device, whilst AR might only require a smartphone. This is considered a clear advantage of the VR technology as with the help of HMDs and haptic feedback gloves it targets multiple senses (such as hearing, feeling, and seeing) which can be of great value when teaching about thermodynamic concepts in buildings, for example. The company ARtillery Intelligence studied VR and AR usage in the U.S. in 2020 and found that satisfaction towards AR and VR experiences differs, with AR reaching slightly higher satisfaction levels. However, it is notable that that VR received incredibly high interest ratings from the perspective of gaming and education applications (45% for VR in comparison to only 23% for AR) (AI, 2020). In a review article by Soto et al. (2020) a number of documents were screened on Scopus and divided depending on the area of publication in the Scopus databases. The authors showed that articles on VR in engineering rank third (with 24.64 % of the retrieved documents mentioning VR. Only social science (39.21 %) and computer science (67.27 %) were more popular. Publication outputs continue to show an exponential increase in work on the topic of VR, with the total scientific output in this field almost doubling every 10 years. This demonstrates that there is an increasing uptake of VR, in the domain of engineering. Sırakaya and Sırakaya, (2020) pointed out that the increase in the number of AR-STEM studies in

Scopus and other publications in recent years gives an indication that this topic may become even more popular in the coming years. This is in line with findings by Galati et al. (2019) on the adoption rate of VR headsets and devices that is shown to keep increasing and is projected to reach 1.73 billion in 2024 with its target user age group, ranging from 16 to 44 years (70% of all users), closely aligned with the age of college and university students.

Concerns have been raised that VR usage may be too complex, in particular for those without technological abilities like children (Galati et al, 2019). This finding could have a negative effect on educational effectiveness and increase contact time with lecturers and lead to time loss and hence frustration of students when playing VR games. Kim and Hall (2019) analysed the use of VR and its influence on motivation and concluded that the perceived enjoyment of using VR is considered rather high. A substantial number of papers have reviewed the use of VR and its advantages in relation to effectiveness, motivation and participation in fields such as plastic surgery training, training of skills for people with disabilities, elderly support and aspects of loneliness, tourism and others (Soto et al., 2020; Abi-Rafeh et al., 2019 Klippel et al., 2019 Makransky & Lilleholt, 2018). However, to date there are no studies that investigate the merits of VR in the field of teaching building physics.

Design of the educational VR game "Beyond building physics"

Simulation setup

The simulation setup to enable the VR educational environment consists of three main parts: 1. the pre-running of EnergyPlus simulations; 2. the Machine Learning (ML) model trained on the former input/outputs to provide rapid estimation in real-time; and 3. The visual simulations, incorporating these outputs, in the VR. This workflow is shown in Figure 2. Upon selecting the desired inputs, the simulation request is sent to the server via an Application Programming Interface (API) whereupon the ML simulation occurs and the results are returned to the VR via the API. Upon pressing the simulation button within the VR game, the visualized results are updated in real-time. The total heating/cooling energy consumption and energy efficiency rating, of the resultant building, are outcomes of the VR simulations.

From BIM to VR

A modern newly built office building, at the Inffeldgasse Campus of TU Graz, was used for the initial setup (Figure 3). The initial design of the Beyond Building Physics educational game focused on a single corner office (with internal dimensions 3,9 x 5,2 x 3,0 m), which is located on the first floor of the building. This office was specifically selected because it is south facing and therefore receives higher solar gains in wintertime, relative to the other orientations. Moreover, since the office is occupied by TU Graz staff this facilitated the installation of the necessary monitoring equipment. The building uses an underfloor heating and cooling system and it is equipped with two air-handling units to circulate, filter and supply fresh air to the offices. The selected office was equipped with a number of different WiFi/LoraWAN sensors to monitor the indoor environmental conditions and energy use. A WiFi environmental multi-sensor device and datalogger was installed to measure the air temperature, relative humidity, CO_2 levels, air pressure and illuminance (using an external photometric probe with a 0-200,000 lux range) equipped with a cosine correction diffuser to provide accurate measurements on flat surfaces from all angles (Gustin et al., 2022).

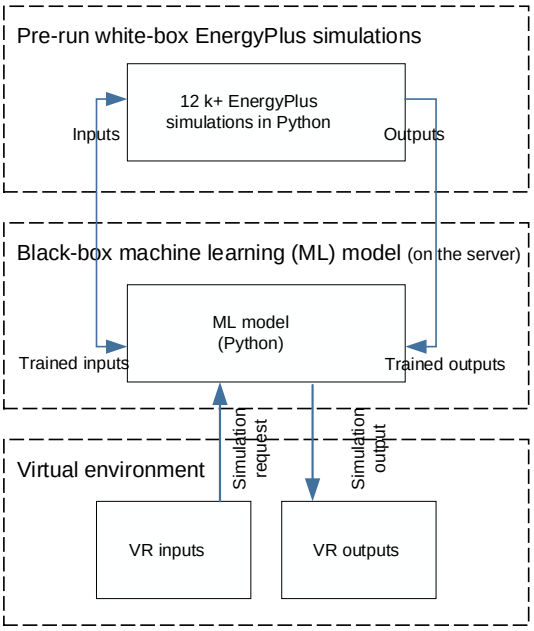

Figure 2 Simulation setup

Window/door contact sensors were installed to monitor opening states and frequency statistics regarding their use. Infrared occupant counting devices were used to monitor the occupancy patterns of the office; contact temperature probes were used to monitor the temperatures of all the different internal surfaces: i.e. walls, floor, ceiling, windows and corners of the external walls (as a proxy for thermal bridges); and plug-load electricity monitors were used to record the power consumption in the office. The virtual

replica of the room (as shown in Figure 3) was developed with the game engine Unreal Engine 5 (Unreal Engine, 2022b), assisted by two plugins DataSmith (industry CAD extensions support) (Unreal Engine, 2022a) and MegaScans (high-quality materials support) (Quixel, 2022). Following the initial setup of using the case study building model itself and providing additional computer-generated information, such as visualisations showing the building's structure and systems, an immersive escape room experience was created centred around building physics and energy simulation. An escape room is a game where users must complete a series of tasks in order to escape from a virtual room and successfully finish the task. In Beyond building physics users find themselves challenged to complete successive tasks related to the model office (described in the previous setup) in order to ultimately unlock the exit to the escape room.

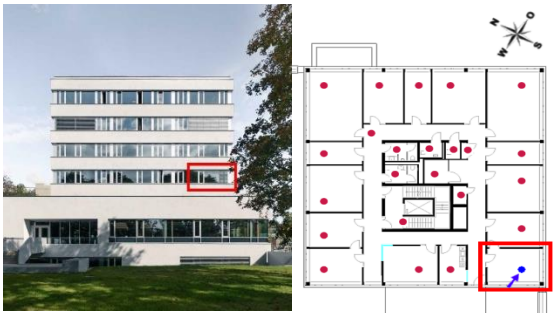

Figure 3: South-West view of the EBS Centre and of the office (marked in red)

VR game “Beyond building physics”

Visually, the “Beyond building physics” game embraces a cyberpunk[1] theme, with wood, glass, and metal dominating the architectural palette. Visual elements, object textures, and sound effects contribute to a visually rich and engaging thematic experience. The game takes place in both day and nighttime settings, with appropriate lighting schemes deployed during the night. The game comprises of two virtual spaces: a minimalistic, dark entry area and a main room housing the interactive apparatus needed for completion of the task. Upon entering the main room, the door locks, initiating the experience. A quest system, coupled with a hint system, guides players sequentially through the game, providing information about the tasks and their educational content. The VR game incorporates haptic, visual, and audio feedback. To aid navigation, a guidance system utilises lights, paper clues, and audio hints. Lights are selectively used to illuminate areas relevant to completing tasks. Paper clues, featuring sketches describing interactions, can be taken and later projected onto a canvas for reference. Audio hints, triggered by a device, visually similar to a Walkman, provide additional information about specific tasks and educational content.

Figure 4 AR image corner room with wooden window frames and shading

Figure 5 View of the main room during the daytime, when standing next to the door to the entry area

Haptic feedback/vibration occurs when interacting with objects in the VE, such as rotating a table, pressing a button, or pulling down a lever. This is complemented by audio feedback, where each physical interaction produces distinct noises, further enhancing the realism provided by haptic, auditory, and visual stimulus (as all moving parts are visible). Hence, the VR game “Beyond building physics” provides an immersive environment, which engages multiple senses (seeing, hearing, and feeling).

The quest system involves major and minor quests, ranging from picking up items to assembling walls and optimizing energy efficiency. Upon completing quests, players receive notifications, contributing to a sense of progression. The major quests involve challenges such as choosing the correct city in which the building is located (to allow for the correct climate data to be incorporated), assembling timber, masonry, and concrete walls, and achieving specific energy efficiency targets, cost and structural stability rankings. The interactive apparatus available in the game

[1] Cyberpunk is a subgenre of sci-fi in a dystopian futuristic setting that tends to focus on a "**combination of lowlife and high tech**", featuring futuristic technological and scientific achievements, such as AI and cyberware. *Sterling, Bruce (1986). "Preface". Burning Chrome by William Gibson. Harper Collins. p. xiv.*

includes a hint projector, an information centre, a layer designer, a wall assembly machine, a wall layout shelf, and a central desk. These components and tools serve distinct purposes and are instrumental in completing quests. For example, the wall assembly machine allows players to create wall layouts, while the layer scaling machine enables adjustments to the materials selected and thickness of wall layers.

The central desk, serves as a multifunctional hub, facilitating various interactions such as setting the time of day, orienting the office building correctly, and adjusting simulation parameters (such as the time step). The table also plays a crucial role in running building energy simulations and visualizing results. The VR environment includes various devices, which can be used to display information such as mould risk evaluations, U-value calculations, cost categories, structural stability grades, energy efficiency levels, together with the consumed annual energy for both heating and cooling. Achieving specific goals in each category is crucial for progress in the game. The game culminates in the completion of all quests, unlocking the final lock, and allowing players to return to the entry area, thereby signalling the end of the educational VR experience.

Task and intended learning outcomes

The task developed in Beyond building physics is targeted at university undergraduate students who wish to develop an initial knowledge of building physics. It responds to the observations made in the introduction section, emphasizing the value of learning through practical experience, whilst using activity changes to maintain motivation and engagement. The learning activity involves assembling three different wall assemblies (masonry, reinforced concrete and timber) correctly, considering factors such as costs, structural integrity, mould risks, and the provision of sufficient insulation. Also, the order the construction materials were used in was assessed, in relation to their effect on changing the location of the dew point temperature (within the external wall assembly). Procedures such as this help students to understand the physical implications of using internal versus external insulation as well as the hygrothermal characteristics of specific materials within a construction assembly. Since participating in such an intense virtual experience can be challenging for newcomers, the game was developed such that it requires minimal guidance, thereby allowing the students to immerse themselves without support (i.e. the game was designed to function without the need for additional task description, briefing notes etc.). As previously discussed, an ILO is a means of outlining what the student will be able to do at the end of the learning task in terms of the knowledge, understanding, and skills acquired. Therefore, in designing ILOs, it is necessary not only to understand what is central to the topic, but also to be able to summarize, present, and teach it to others. We have divided the ILOs for the task into knowledge and understanding, intellectual abilities, and practical skills, as outlined below.

Knowledge and understanding: On completion of the task, students should have developed knowledge and understanding of:

ILO KU-1 a buildings heat loss coefficient and its relation to materials, costs, and insulation effectiveness.

ILO KU-2 a building's typical construction materials and their main purposes (structural stability, insulation, weather resistance).

Intellectual abilities: On completion of the task students should have developed the intellectual abilities to:

ILO IA-1 Realize the implications of material choices (such as using internal versus external insulation) upon the prediction of energy efficiency targets and develop the ability to select appropriate wall construction setups for given criteria, based on costs, sustainability, energy efficiency, and structural stability.

Figure 6: Example VR setup, glasses and navigation handset

Practical skills: ILO PS-1 On completion of the task students should have developed the practical skills to handle the VR devices and move around in a gaming environment completing quests without any supervision or external guidance.

Procedure and type of feedback: Students were not provided with any written description of the exercise. They were given the VR equipment and (after completing a short tutorial on how to use VR controllers to navigate in VR) had to puzzle out the task and assignment independently during the game. Within the VR environment, there was a flyer, guiding them through the task

and providing additional information. For all but one user, in the focus group study, this was their first time using VR. The participating students had the possibility to ask questions to the instructor three times during the game. We gathered two different types of feedback from the students:

1. Formative feedback (in the classroom) immediately before and after the task

Feedback during an activity is a common method of gathering feedback from students. It takes around 10 minutes during the class to have the participants anonymously complete a feedback form. The following five questions were posed to the students:

1. What program of studies are you currently enrolled in?
2. How would you rate your current knowledge of building physics?
3. What is your preferred learning style?
4. In your opinion, which aspects of building physics do you find most challenging or believe that most students would struggle with (multiple choices allowed)?

And summative feedback after the task:

5. In your opinion, which aspects of building physics did you find the educational VR game most helpful with (multiple choices allowed)?

2. In the summative feedback gathering we tried to understand any specific issues the students faced with each of the exercises as well as documenting their newly acquired knowledge gained during the game. This was done via recorded interviews after the VR gaming experience.

Results

In-class feedback from students

Six male students from varying engineering and construction related backgrounds participated in the study, from the following degree programmes: Architecture Bachelor (n=1), Architecture Master (n=2), Civil Engineering Bachelor (n=2), Mechanical Engineering (n=1). The task took in each case around 1 h to 1.5 h (including a brief VR tutorial and participation in the VR game). The focus group questionnaires and interviews took on average about 30 min per participant to complete, 10 minutes before (5 min for pre-questionnaires and 5 minutes for a brief individual interview) and 20 minutes after the VR experience (about 15-18 min to complete the post-test questionnaires and 2 minutes for a short one-to-one interview in case of some follow-up questions). Two of the participants stated having some basic building physics knowledge; the remaining four stated having none to only very basic knowledge. In terms of the preferred learning style, they could choose between four different options (Figure 7). No one stated that their preferred learning style would be kinaesthetic (learning through hands-on activities and experiences). Two stated they would prefer auditory (i.e. learning through listening and discussions) and two reading/writing (learning through reading and writing activities). The majority stated however that active learning modes (e.g. engaging in hands-on activities, presenting, group discussions etc.) were preferred to passive modes (e.g. reading, listening to lectures and presentations, watching videos etc.).

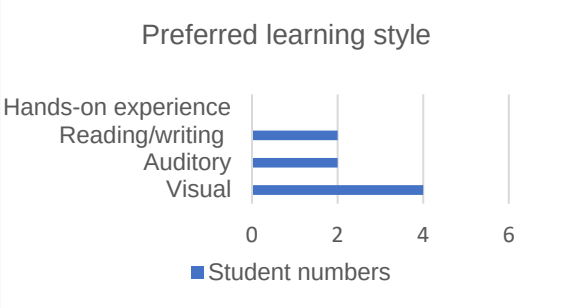

Figure 7: Students' responses on the preferred style of learning before the VR gaming experience

In terms of their opinion, regarding which aspects of building physics they would find most challenging or believe that most students would struggle with (multiple choices allowed), a list of options was provided. The participants chose the following list of options out of the entire portfolio (Figure 8):

- Daylighting design: balancing natural light levels and minimising glare while considering energy efficiency
- Acoustics: grasping the principles of sound control and its integration into building designs for occupant well-being
- Ventilation strategies: recognise the importance for indoor air quality and energy efficiency
- Functional layers in external walls (e.g. insulation etc.) for optimal thermal and structural performance
- Thermal mass and inertia: in moderating temperature fluctuations and optimising energy performance
- Air infiltration: recognising the impact of unintentional air leakage on building energy efficiency and occupant comfort
- Thermal proprieties of materials (i.e. thermal conductivity, resistance and

transmittance) as well as U-value calculations for effective insulation
- Moisture control in buildings: understanding strategies to prevent condensation and mould, considering insulation and ventilation
- Energy efficiency and Energy Performance Certificates (EPC) Ratings: what are the key factors (e.g. building envelope, HVAC systems, building design, orientation etc.)
- Building envelope insulation: recognising the significance in preventing energy losses and maintaining thermal comfort

Figure 8 summarizes aspects considered challenging in building physics from a student's perspective. Half of the respondents thought that acoustics is a challenging field in building physics, a topic that lends itself to be part of an immersive VR environment. Not selected from the sample of options were for example: mechanical heating and cooling systems as well as humidity control. After the game students were asked to comment on aspects of building physics that the educational VR game was most helpful with. The answers to this question are shown in Figure 9. They show that the topics that were incorporated as part of the ILOs within the VR game matched the responses of the students.

Analysis

All but one students rated their participation as either "an enjoyable exercise" or even "a very enjoyable experience". In relation to the question: "what they have specifically learnt from undertaking the assignments?" Students commented how they learnt to "create building materials data and assign it to a building". Based on the feedback provided after the VR experience, their knowledge on construction materials had improved. Students could name several of the insulation materials which were provided as part of the game such as EPS, XPS; cellulose, rock wool, and vacuum insulation. Two of the students could provide further information on the thermal properties and acceptable U-values for specific constructions.

What do the results mean with regard to outcomes from the state of the art?

Issues on technical difficulties with using VR were documented in the literature (Galati et al., 2019). The Beyond building physics task showed that VR has the ability to create a stimulating and engaging learning experience for students. However if difficulties are not addressed immediately, it can also cause frustration with the game and lead to an abrupt ending of the learning experience. This finding suggests that some students will need more scaffolding and support than others, particularly when engaging with VR for the first time. Costs of equipment will certainly play a role when VR is considered in large classroom teaching (the Alienware M15R4 gaming laptop cost over 2000 EUR, and the Valve Index VR Kit was over 1000 EUR). If the VR activity is well designed and integrated into the wider module delivery plan it could lead to increased participation in in-class teaching and also significant time savings for teaching staff, as it does not require the preparation of a handout brief, task description or supervision. From a health perspective one of the students mentioned general discomfort and some dizziness when using the game, so further research is needed to understand whether some students might be negatively affected by the use of VR equipment.

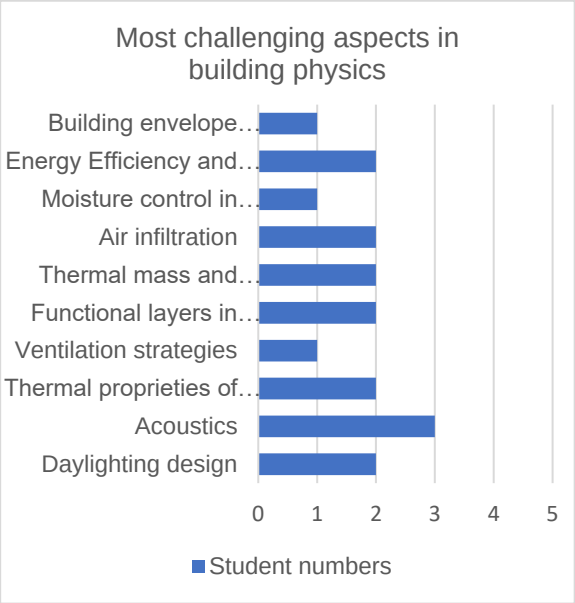

Figure 8: Students' responses on the most challenging aspects in building physics before the gaming experience

What do the results reveal for future work?

There is a need to engage engineering students in a wider variety of experiential learning activities. The recent Covid pandemic has triggered a downshift in student attendance rates, with many asking for virtual options, such as providing lectures online or offering videos instead of in-class lectures. Many of the participants, despite not choosing kinaesthetic methods in the beginning (and opting for traditional learning styles such as lectures and reading) responded differently at the end of the task. When asked to rank their preferred learning methods, following the task, 5 out of 6 chose practical methods (such as audio- visual, practical with coaching and/or a demonstration). Whilst methods such as lectures and reading

were grouped towards the lower end of the scales. This reveals that despite some initial challenges, there are many potential benefits to incorporating VR learning activities (including increased motivation, practical engagement and knowledge retention) which could transform VR into a powerful technology with which to augment future building physics and engineering education.

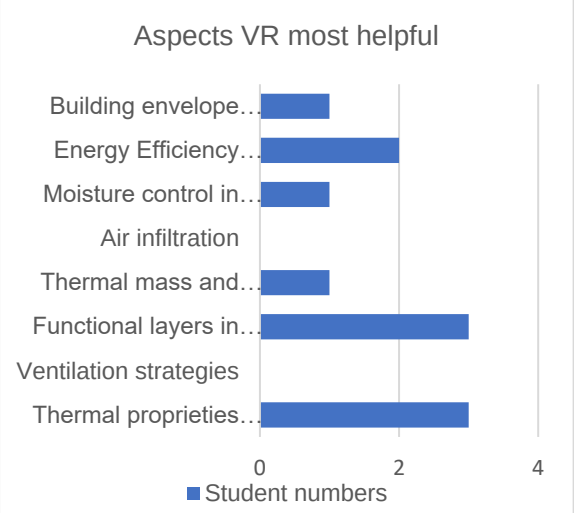

Figure 9. Students' response on aspects they found VR most helpful in understanding after the gaming experience

Conclusions

Focus group interviews with students using the newly developed VR game "Beyond building physics" demonstrate that it provided a comprehensive and engaging introduction to the fundamentals of building physics. Feedback showed that the use of VR positively changed students' attitudes towards the benefit of kinaesthetic learning methods. Moreover, the VR game allowed students to develop proficiency in aspects of building physics that they considered challenging prior to the task. Further research is warranted to understand whether the positive results of this initial focus group study are generalisable to a wider audience.

Acknowledgement

This research was funded by the Austrian Research Promotion Agency (FFG) under the 8th call City of the Future (Stadt der Zukunft), FFG Project Number FO999887002.

References

J Abi-Rafeh et al.. (2019). Nonbiological Microsurgery Simulators in Plastic Surgery Training: A Systematic Review. Plastic and Reconstructive Surgery, 144(3), 496-507.

G Arbesser-Rastburg et al (2024) Project Beyond: An Escape Room Game in Virtual Reality to Teach Building Energy Simulations, IEE conference, Milan, 5th-8th August

I Beausoleil-Morrison, C J Hopfe (2015) Teaching building performance simulation through a continuous learning cycle, Proceedings of BS2015: 14th Conference of IBPSA, India

J Biggs and C Tang (2007). Teaching for Quality Learning at University. Open University Press, Maidenhead, UK, 3rd ed

MN Campos Soto, et al., (2020). Virtual reality and motivation in the educational context: Bibliometric study of the last twenty years from Scopus, January-june 2020 Vol. 15, No. 1, 44-56,

J Carmigniani et al. (2011). "Augmented reality technologies, systems and applications". Multimedia Tools and Applications. 51 (1): 341–377.

R.M Felder, L Silverman (1988). Learning and teaching styles in engineering education. Journal of Engineering Education, 78(7):674–681

F Galati, et al. (2019). Pros and Cons of augmented reality in education. Proceedings of EDULEARN19 Conference, 1st-3rd July 2019, Palma, Mallorca, Spain

M Gustin et al. (2022) A Novel Concept For Virtual Reality Enhanced Building Energy Modelling, BauSIM Conference 2022 in Weimar, Germany

M Gustin, et al. (2024). Revolutionising Building Physics Education: The "Beyond" Project's Journey into Immersive Learning with VR

CJ Hopfe, et al. (2022a), Teaching data analysis for building performance simulation–Series: Building simulation and calculation tools in teaching, Bauphysik 44 (5), 285-290

CJ Hopfe et al. (2022b) Digital Erasmus–a pan-European approach to teaching building performance and resilient design, CLIMA 2022 conference

MJ Kim and CM Hall (2019). A hedonic motivation model in virtual reality tourism: Comparing visitors and non-visitors. International Journal of Information Management, 46, 236-249. https://doi.org/10.1016/j.ijinfomgt.2018.11.016

A Klippel et al. (2019). Transforming Earth Science Education Through Immersive Experiences: Delivering on a Long Held Promise. Journal of Educational Computing Research, 57(7), 1745-1771. https://doi.org/10.1177/0735633119854025

S Panerai et al. (2018). Remote Home-Based Virtual Training of Functional Living Skills for Adolescents and Young Adults with Intellectual Disability: Feasibility and Preliminary Results. Frontiers in Psychology, 9, 1-6

RS McLeod and CJ Hopfe (2021) Experiential learning in building physics: The icebox challenge, Journal of Building Physics 45 (3), 391-401

D Poole (2022). Engineering schools are riddled with issues – reinvention is required

M Sırakaya and DA Sırakaya (2020). Augmented reality in STEM education: a systematic review, Interactive Learning Environments, DOI 10.1080/10494820.2020.1722713

BauSIM 2024 in Wien
23. September – 26. September

Thermostat Control and Window Opening: Impact on Indoor Environmental Conditions and Building Performance

Ghadeer Derbas[1, 2], Eziama Ubachukwu[1], Philipp Althaus[1], Andre Xhonneux[1] and Dirk Müller[1,3]

[1]*Forschungszentrum Jülich, Institute of Climate and Energy Systems, Energy Systems Engineering (ICE-1), Jülich, Germany*

[2]*Department of Architecture, Palestine Technical University-Kadoorie, Tulkarm, Palestine*

[3]*E.ON Energy Research Center, Institute for Energy Efficient Buildings and Indoor Climate, RWTH Aachen University, Aachen, Germany*

Abstract

This paper investigates thermostat interventions and window openings across 77 offices during the heating and transition seasons of 2023. A cloud-based heating controller, that takes user preferences and anticipated presence schedules, was evaluated in two buildings of the Living Lab Energy Campus (LLEC) at Forschungszentrum Jülich, Germany. Occupants adjust the setpoint via a web-based interface or local interaction. Data on indoor and outdoor environmental parameters, occupancy and occupant behaviour, and heating consumption were collected. Additionally, a web-based survey was conducted on March 2024 for further insights. The results indicate that the heating controller effectively adapts to user preferences and occupancy patterns, significantly influencing heating consumption, alongside the impact of building construction age. Besides, an initial economic evaluation revealed that the implemented measures resulted in approximately 18.5% of energy savings. The heating controller combined with window openings maintained indoor thermal comfort, with 63.7% of occupants preferred no change in the indoor temperature, and 83.5% reported acceptance of the indoor thermal conditions. About 69% of respondents attributed their satisfaction with room control to their accessibility to different control options. Space orientation was found to be an important factor affecting temperature setpoints and window opening duration.

Introduction

The urgency to address the environmental impact of the building sector, which contributes to one-third of greenhouse gas (GHG) emissions (https://energy.ec.europa.eu), requires immediate and informed actions. Appropriate integration of building automation and advanced control systems (BACS) in buildings can enhance energy efficiency and indoor comfort by adjusting systems to meet occupants' needs and preferences (Garzia et al. 2023). While research has focused on smart technologies and control systems, understanding occupants' interactions with building interfaces and their impact on comfort and satisfaction requires further investigation (Aldakheel et al. 2023).

Window openings and thermostat adjustments have a significant impact on building energy consumption and indoor environmental conditions (Belazi et al. 2019). For example, D'Oca et al. (2014) demonstrate in their simulation analysis that the energy consumption in dwellings, where occupants control window openings and heating setpoints, can have up to 61% higher compared to deterministic approaches. This discrepancy arises because user interactions, particularly window openings, lead to increased ventilation losses. Similarly, Gunay et al. (2016) illustrated that in cold climates, manually operated windows with stochastic occupant behavior models can increase space heating requirements by up to 15%. However, few studies examined the impact of thermostat and window use on indoor environmental conditions and building performance in real-world field studies.

Previous studies have focused on window opening and thermostat use modelling behavior to study their impact on building performance. For example, Liu, Gunay & Ouf (2021) analyzed window and thermostat use patterns based on environmental measurements and occupant behaviour data collected from two buildings in Ottawa, Canada, to in-

form building control strategies. By employing discrete time Markov logistic regression and decision tree models, the researchers aimed to predict occupant actions based on indoor environmental conditions. The results provided insights into how indoor conditions impact the decisions of occupants to adjust thermostats and open/close windows. Consequently, the study recommended improvements in control sequences to optimize energy efficiency and occupant comfort.

Previous studies have focused on evaluating thermostat use in terms of thermal discomfort. For instance, Stopps & Touchie (2020) examined occupant thermal comfort and HVAC operation in high-rise condominium buildings in Toronto, Canada. This research utilized field data collection methods, including surveys and connected thermostat data, to infer occupant comfort and identify opportunities for improved energy efficiency and comfort. Despite the presence of in-suite controls, the research revealed prevalent thermal discomfort, with the Predicted Mean Vote (PMV) model and setpoint deviation not consistently aligning with occupant-reported thermal sensation. In another study, with the aim to improve perceived control in offices by addressing usability issues of thermostat interface, Brackley et al. (2021) employed a three-phase approach study in 25 offices within an institutional building in Ottawa, Canada. The authors assessed existing controls, developed new features to improve the functionality of the user interface, and gathered feedback from users. The results suggested considering human factors principles, such as clear feedback after an adjustment and communication system status, and emphasizing the need to incorporate human factors research to improve perceived control.

In response, this paper aims to evaluate the impact of thermostat use (i.e., cloud-based controller and user interventions) combined with window opening on indoor environmental conditions, occupant thermal comfort and satisfaction, and building heating consumption, to enhance room automation strategies for improved user comfort and energy efficiency.

Methods

To fulfill the objectives of this study, the following framework was employed across two buildings:

- **Data collection and processing:** raw data was extracted from a local database server. Data fetching, cleaning, resampling, and filtering was performed using Jupyter Notebook.
- **Data visualization and analysis:** Descriptive statistics and data visualization methods (i.e., boxplot, bars, stacked bars) were used to analyze the collected data. Statistical tests such as paired t-test statistical analyses were performed to find significant differences.
- **A web-based questionnaire** was conducted to provide insights into the monitored data. Statistical analysis of the questionnaire was performed using IBM SPSS (version 29.0.2.0).

Buildings description

The investigation covered 77 offices across two offices buildings, namely Building A and B, located within the Living Lab Energy Campus (LLEC) project at Forschungszentrum Jülich (FZJ), Germany. LLEC is a comprehensive living lab comprising 16 buildings equipped with sensors and actuators to test novel monitoring and model-based control approaches at room, building, and district levels (Althaus et al. 2022). Key characteristics of both buildings are summarized in Table 1. Building B is a new structure, while Building A is an older, non-retrofitted building. The evaluation was conducted using data collected from January to April and October to December, 2023. During this period, the daily average outdoor temperature ranged from -7.3 to 14.3 °C, and the relative humidity ranged from 36% to 100%. Weather data was collected from the meteorological weather station tower located at FZJ, recorded every 10 minutes.

Table 1: Buildings A and B key characteristics

	Building A	Building B
Construction year	1976	2021
No. of floors	2	3
NFA (m^2)	999	2003
Orientation	NW, SE	NE, SW
Building shape	L-shape	Rectangular
No. of offices	32	45

Thermostat control

The thermostat radiator valves (TRVs) installed in both considered buildings are controlled by a dedicated automation application, allowing the integration of user preferences in different ways. As a result, users can indicate their setpoint preferences and anticipated presence through a web-based interface, named *JuControl* (Ubachukwu et al. 2023), or manually by setting a temperature setpoint at the TRVs. During the study period, various control configurations were tested. Throughout unoc-

cupied times, a temperature-setback is applied. If no setpoint preference is provided by a user, a fallback setpoint of 19 °C during working hours and 17 °C during nighttime is applied. The current automation configuration generates a setpoint trajectory based on the input data provided by the occupants. One variant of a rule-based control approach applied to the TRVs involves shifting any increase in the temperature setpoint by a timespan Δt in advance to warm up the building before occupancy, as shown in Figure 1. Further details can be found in Ubachukwu et al. (2023), Althaus et al. (2024).

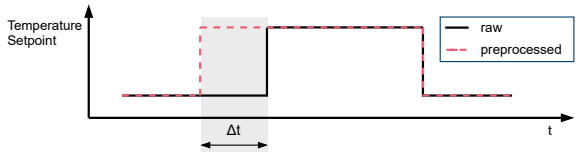

Figure 1: Schematic of setpoint trajectory preprocessing introducing pre-heating.

Questionnaire

A web-based questionnaire was conducted using *LimeSurvey*, an online survey tool (https://www.limesurvey.org/). The survey was distributed on March 5th, 2024, for one week to collect data about user behaviour and feedback. The questionnaire design was informed by previous related studies (Stopps & Touchie 2020, Brackley et al. 2021, Liu, Lee, Bilionis, Karava, Joe & Sadeghi 2021), and comprised 38 questions grouped into 6 sections: demographic data, work activity and workplace context, interaction with thermostats and windows, thermal sensation, preferences, acceptance and satisfaction. A total of 91 participants completed the survey, with 25.3% from Building A (N=23), representing 39% of building's occupants, and 74.7% from Building B (N=68), representing 54% of the occupants. Among the participants, 56% identified as male, 43% as female, and 1% as other. Main findings about thermostat and window adjustments, thermal comfort and satisfaction are presented in this paper.

Monitored offices and observed data

The study analysis was performed on 32 offices in Building A and 45 in Building B. These offices differ in terms of orientation, size, occupancy, and floor level. Offices in both buildings are equipped with Indoor Air Quality (IAQ) multi-sensors, TRVs, and "smart" window handles, with windows being manually operated. More details about the devices and communication protocols can be found in Althaus et al. (2022). During the study period, the following monitored datasets were extracted:

- Indoor environmental-related data such as indoor temperature (°C), relative humidity (%), and CO_2 concentration (ppm), measured by indoor air quality (IAQ) multi-sensor, recorded every 15 minutes.
- Occupant-related data such as window states (0: closed, 1: tilted position, 2: partially to fully open), temperature setpoint triggered by cloud-based heating controller, setpoint triggered by users, and radiator valve opening (0-100%), all recorded as event-based measurements.
- Occupancy-related data: presence (0: unoccupied, 1: occupied), are extracted from *Juracle*, a behavior evaluation engine developed by Ubachukwu et al. (2023).
- Heating consumption (kWh), measured every 60 minutes.

Results analysis and discussion

First, an overview of heating controller's impact on heating consumption daily profile in Building B and occupancy patterns in Building A are presented as an example.

Heating consumption daily profile

In 2023, Building A had a higher average heating consumption per area per hour (8.62 kW/m^2) compared to Building B (5.89 kW/m^2). This difference can be attributed to the older structure of Building A, which leads to increased thermal losses, or due to user behaviour uncertainties. Figure 2 shows an example of heating consumption daily profiles for Building B during the study period. The distinct patterns can be explained by differences in heating system's supply, which maintain the indoor temperature based on both user preferences and controller setpoints. The figure demonstrates a notable increase in the average daily profile around 6:00 am due to the controller activation to warm up the buildings before occupants arrive. In the evening, a corresponding decrease around 6:00 pm aligns with the end of typical working hours. These findings highlight the influence of the heating controller on the daily heating consumption profile, considering different occupancy levels and user preferences.

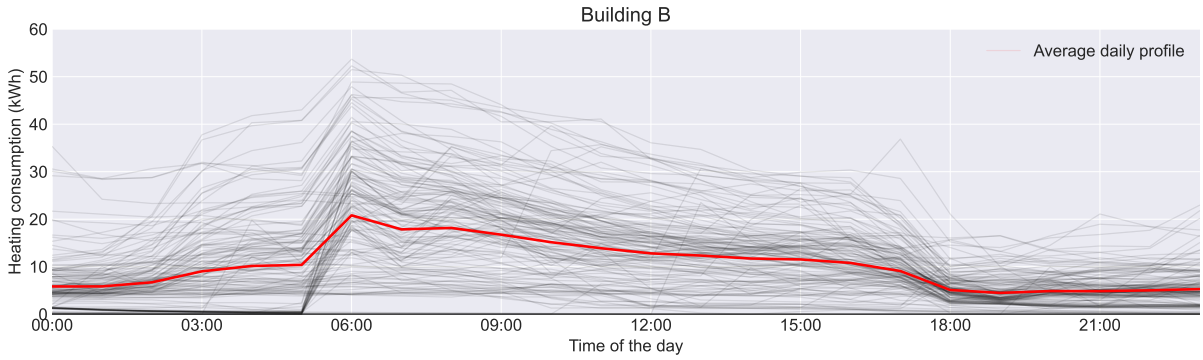

Figure 2: Heating consumption daily profiles for Building B. The red line represents the averaged daily profile over the study period.

Room occupancy patterns

Occupancy plays a crucial role in influencing building energy consumption. In this study, the average occupancy (i.e. binary presence) was analyzed across 29 offices in Building A over a typical day, averaged from January 2nd to April 18th 2023, excluding weekends. Presence was derived by *Juracle* based on CO_2 mass balance in the room. Figure 3 shows distinct occupancy patterns in each office. Some offices were occupied up to 60% of the days, while most offices were occupied for relatively fewer days, taking into account holidays within the period. Notably, the offices were most frequently occupied between 8:00 am and 5:00 pm.

Presence monitored data was not available for Building B, however, survey results indicated that 44% of respondents reported working from the office for three or more days per week. Overall, the majority of occupants (78.5%) worked typical workday hours. These findings provide valuable insights into the behavioural patterns, discussed in the following sections.

Thermostat and window operation

Temperature setpoints

The mean of daily average temperature setpoints in offices, stemming from all user input interfaces, including JuControl schedule, JuControl direct setpoint input, and TRVs, ranged between (17.4–23.2 °C) in Building A and (16.7–22.7 °C) in Building B. In Figure 4 (a), the distinction among input sources indicates that local interaction inputs cover more extreme values, slightly higher than the mean. The highest average was recorded in NE_ and SW_facing offices in Building A, and NE_offices in Building B, while the lowest was in NW_facing offices in Building A (18.9 °C). Figure 4 (b) shows the distribution of temperature setpoints derived only from online interfaces, excluding local interaction, in Buildings A and B offices, grouped by orientations. Non-significant differences were observed in the mean of controller setpoints across different orientations. Valve opening daily averages ranged from 30-53 % in Building A, and 28-56 % in Building B, as shown in Figure 4 (c).

Figure 5 shows an example of temperature setpoints deviations from the daily averaged temperature to the default setpoint during the day (19 °C) in Building B. It is noticed that the indoor temperature deviations ranged from (−0.63–3.12 K) across all offices. Offices from R33-R45, located in the 3rd floor, showed the lowest setpoint deviations compared to those on the 1st and 2nd floors, likely due to occupants' familiarity with JuControl and controller mechanism. In Building A, the mean indoor temperature deviated between (0.13–4.24 K).

Window states duration

People open windows in two positions: partially to fully open for "shock ventilation", and a tilted position for "trickle ventilation". The results indicate that the daily average window opening duration varied widely in Building A offices for trickle ventilation, ranging from 0 to 28 min with an average of 5.5 min. Figure 6 shows that occupants in SW_ and SE_facing offices of Building A tended to open windows for longer duration compared to other offices. Regarding shock ventilation, occupants in Building A tended to open windows for an average duration of 3 min, whereas those in Building B for 1 min. Within Building A, people located in SW_facing offices tended to open windows for longer daily duration, likely due to high indoor temperature and CO_2 concentration, as shown in Figure 8. Occupants in Building B located in SW_facing offices tended to open the window for shorter duration compared to Building A. This finding can be ex-

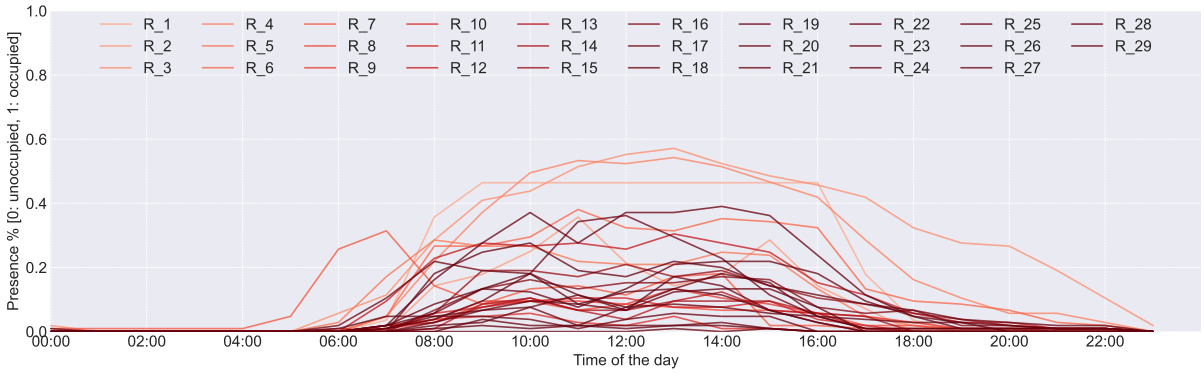

Figure 3: Daily average occupancy profile of 29 offices in Building A (2nd Jan - 18th Apr, 2023).

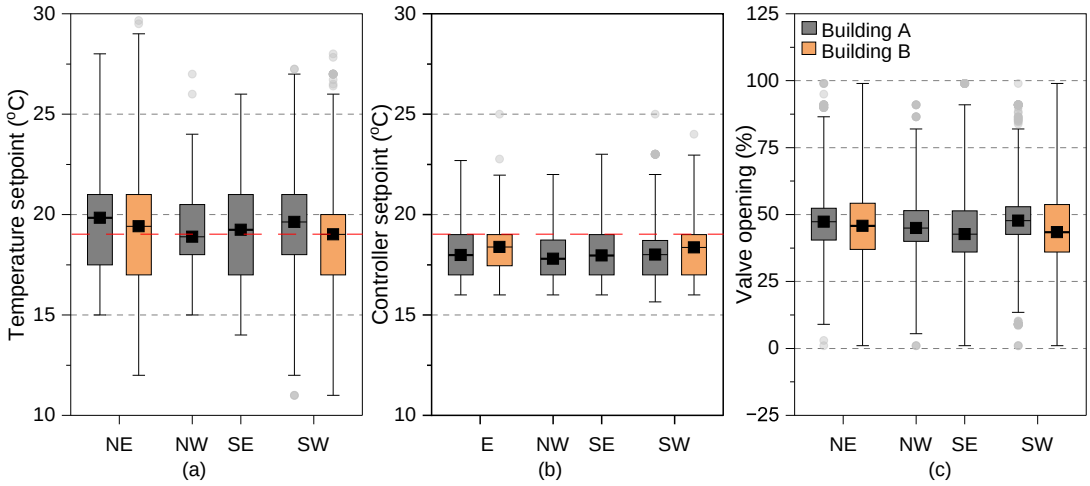

Figure 4: Distribution of daily average (a) temperature setpoints, (b) controller setpoints, and (c) radiator valve opening per office orientation in Buildings A and B during the study period. The red dashed line represents the default controller setpoint (19 °C).

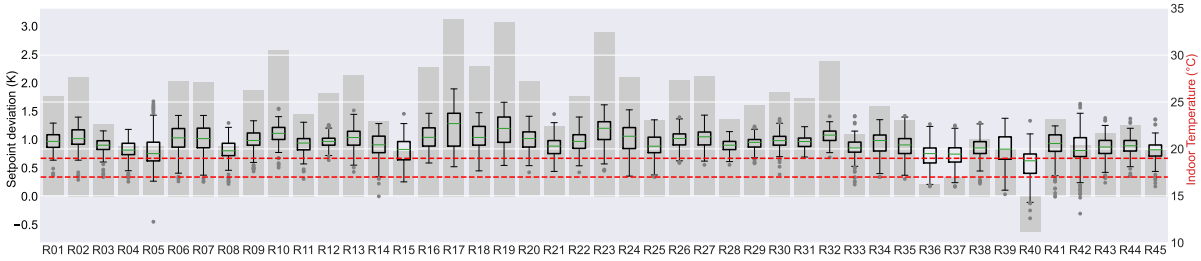

Figure 5: Gray bars represent indoor temperature deviations (K) from heating controller default setpoint in Building B offices. Boxplot represents the distribution of daily average indoor temperatures.

plained by social constraints, as 67% of the offices in Building B are open-plan offices according to questionnaire results. Office orientation can play a crucial role affecting the temperature setpoints and window opening duration. Therefore, it is recommended to consider room orientation while developing heating controller setpoints.

Thermostat and window adjustments: Questionnaire results

Currently, access to JuControl is only granted upon users' consent to the data policy agreement. In building A, 82.6% of the respondents reported having access to JuControl, compared to 75% in Building B. Among those with access, the majority in

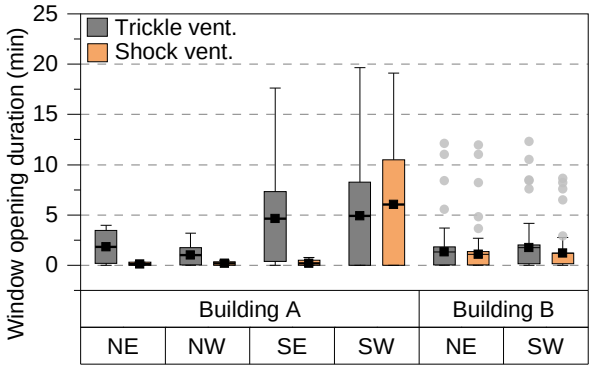

Figure 6: Window opening duration (min) daily average in Buildings A and B offices per orientation.

Building A (89%) and B (78%) did not adjust the temperature setpoint using JuControl, while only 8% of respondents tended to adjust the setpoint once or more per day, as illustrated in Figure 7. The frequency of user interventions via TRVs was higher when people did not have access to JuControl. About 75% of occupants in Building A adjusted the TRVs once per week, while 35% in Building B did that once or more per day. Moreover, 30.4% of respondents in Building A were satisfied with the heating controller's ability at maintaining the temperature setpoint to their comfort preferences, while more people reported satisfaction in Building B (41.2%). This difference was not statistically significant (p-value = 0.09) using Mann-Whitney U Test. Among those satisfied with controller performance, 69% attributed their satisfaction to the ability to control the thermostat via JuControl.

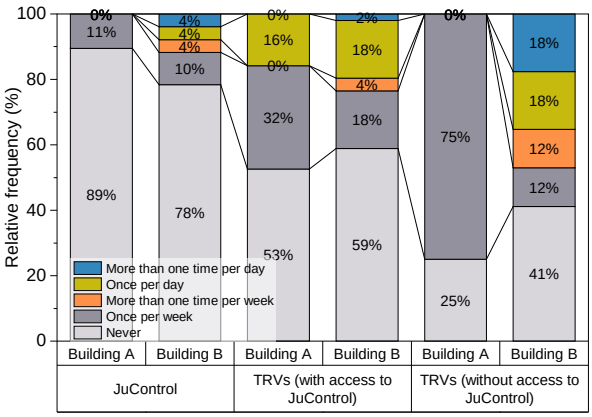

Figure 7: Frequency of thermostat adjustments using JuControl and TRVs (with and without access)

In Building A, about 62% of respondents tended to open the window at least once daily, while in Building B more people did the same (83.6%). Half of the respondents reported opening windows for 5-10 minutes daily. Shock ventilation was used by 53%, while 27% used trickle ventilation. The lowest frequency was observed in NW_facing offices, with 38% respondents open the window once or more per day. In contrast, more people in SE_ (91%), NE_ (87%) and SW_facing offices (81%) did the same. These findings align with the monitored data results as shown in Figure 6. More than 80% of respondents in both buildings reported opening their window in the morning upon arrival to the office or when the room felt stuffy to get a fresh air. However, a few people considered CO_2 concentration displayed on JuControl as indicator to open the window (4% and 7% in Building A and B, respectively).

Overall, the heating controller combined with window opening effectively maintained thermal comfort across the buildings, despite the impact of individual user preferences on temperature setpoints. Office orientation appears to influence both temperature setpoints and window opening duration due to different experiences of thermal conditions. Additionally, occupant accessibility to various control options such as TRVs and JuControl, along with their familiarity with these systems, probably increased their satisfaction with indoor environment and reduced user interventions.

Impact on indoor environmental conditions

The daily average indoor temperature in offices of Building A fluctuated between 16.8°C to 21.2°C, and in Building B between 18.3°C to 22.1°C, indicating different user preferences for thermal comfort. Figure 8 (a) shows the indoor temperature distribution by floor, revealing significantly lower temperatures on the 1st and 2nd floor of Building A compared to B ($p < 0.05$). Additionally, the average temperature was significantly lower in the 3rd floor compared to other floors in Building B. This can be a result of the lower temperature setpoints observed in this floor, as shown in Figure 4.

Figure 8 (b) illustrates that NE_ and SW_facing offices exhibited the highest average temperatures, while NW_ and SE_facing offices showed the lowest in Building A. A similar pattern was observed in NE_ and SW_facing offices in Building B. This can be explained by (1) an increase in temperature setpoints as shown in Figure 4 (a), and/or (2) lower frequency of window openings since high daily average CO_2 concentrations were observed in the same offices of both buildings, as shown in Figure 8 (c). The former figure shows that CO_2 concentration varied widely, ranging from (540-1,860) ppm in Building A and (670-1,810) ppm in Building B, reflecting differences in occupancy and

ventilation rates. Furthermore, Building B offices showed higher CO_2 levels compared to Building A offices, possibly due to (1) the prevalence of shared and open-plan offices in Building B, contrasting with mainly single offices in Building A, and (2) the significantly higher air tightness in Building B. However, daily average relative humidity levels remained within the comfort range (35-55%) in both buildings.

Notably, significant differences in indoor temperature and CO_2 concentration were observed across both buildings, varying by office orientation and floor. These factors are crucial to consider when designing room automation systems to ensure optimal user comfort and energy efficiency.

Impact on thermal comfort and satisfaction: Questionnaire results

Participants were asked about their thermal sensation using the ASHRAE 7-point scale (+3: hot, +2: warm, +1: slightly warm, 0: neutral, -1: slightly cool, -2: cool, -3: cold). About one-third of respondents felt slightly cool to cool in Buildings A (33%) and B (37%). Fewer people felt warm, with 26% in Building A and 14.7% in Building B, while the rest reported a neutral sensation. Occupants located in the NW_facing offices in Building A (μ = -1.3) and NE_offices in Building B (μ = - 0.7) felt cooler compared to other offices. Over half of respondents in Buildings A and B (56.5% and 66.2%, respectively) preferred no change in indoor temperature. However, more occupants in Building A (21.7%) preferred warmer conditions compared to those in Building B (5.9%), likely due to Building A's older structure, despite both buildings using the same heating controller.

Participants rated their thermal satisfaction with indoor temperature based on a 5-point scale (1: very unsatisfied, 5: very satisfied). Majority of respondents in Building A (82.6%) and Building B (80.9%) reported being neutral to satisfied. Besides, people were asked about their thermal acceptance on a 3-point scale (1: unacceptable, 2: neutral, 3: acceptable). The majority reported that the indoor temperature was neutral to acceptable, with 82.6% in Building A and 83.8% in Building B.

Impact on economic performance

After the initial test campaign, a preliminary economic evaluation showed that the above implemented measures lead to 18.5% energy savings in Building A. By further simplifying access to JuControl, the related-energy savings can be increased. For example, this could be achieved by making large parts of JuControl always available, regardless of the consent of office colleagues, which could be agreed on with (e.g.) the workers council after the first test campaign. By assuming the current prices for heating supply and full equipment with sensors (i.e., indoor air quality, door/window sensors) and heating valve actuators used in the LLEC, the return of investment (RoI) is about 7 years. For scientific purposes, offices were equipped with a variety of sensors such as door and window sensors, may not be necessary in larger commercial applications. By reducing the setup to the strictly required hardware, such as the actuators of the heating valves and temperature measurement, on one hand, and switching from EnOcean to LoRaWAN communications protocol (i.e., only one gateway is required instead of multiple cabled transceivers), could reduce the RoI to less than 5 years.

Conclusions

This paper presents an evaluation study of a cloud-based heating controller combined with window opening operations. Using real-world measurements and questionnaire-based data, the study assessed their impact on indoor environmental conditions, thermal comfort, and heating consumption.

These results indicate that the heating controller effectively adjusts heating supply based on user preferences and occupancy patterns, as shown by the distinct daily consumption profiles within different building construction age. Besides, the controller combined with window openings successfully maintained thermal comfort across the offices. Besides, the majority of occupants (63.7%) preferred no change in indoor temperature, and 83.5% reported their acceptance of indoor thermal conditions.

Few interventions were observed when users had access to JuControl and TRVs, and 69% attributed their satisfaction to access to JuControl. Office orientation showed a significant impact on thermostat and window use operations, making it crucial for optimizing room heating control.

Acknowledgment

The evaluation in this work was supported by the German Federal Ministry of Education and Research (BMBF: Funding number 01DH16027) within the framework of the Palestinian-German Science Bridge project. The hardware setup, Juracle and JuControl development, and related ICT infrastructure are funded by the German Federal Ministry of Industry and Climate Action (BMWK: Funding number 03ET1551A) within the LLEC project. Special thanks to Palestine Technical University.

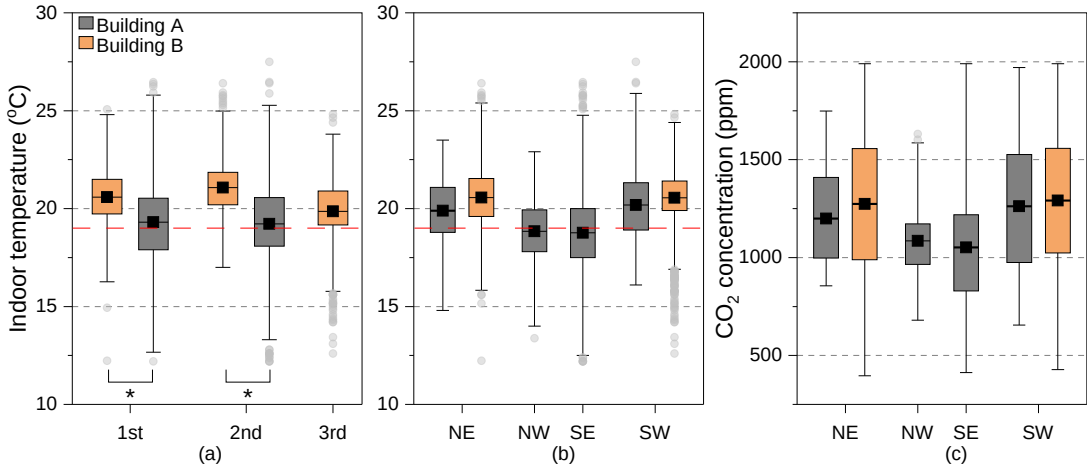

Figure 8: Daily average distribution of (a, b) indoor temperature and (c) CO_2 concentration in different orientations and floors in Buildings A and B during the study period. The red dashed line represents the default controller setpoint.

References

Aldakheel, J., Bahrar, M. & El Mankibi, M. (2023), Indoor environmental quality evaluation of smart/artificial intelligence techniques in buildings–a review, *in* 'E3S Web of Conferences', Vol. 396, EDP Sciences, p. 01101.

Althaus, P., Johnen, S., Xhonneux, A. & Müller, D. (2024), Cloud-based controller architecture for the testing of conventional and model predictive room heating controllers in a real-world environment, *in* 'CoDIT 2024 conference', Accepted.

Althaus, P., Redder, F., Ubachukwu, E., Mork, M., Xhonneux, A. & Müller, D. (2022), 'Enhancing building monitoring and control for district energy systems: Technology selection and installation within the living lab energy campus', *Applied Sciences* **12**(7), 3305.

Belazi, W., Ouldboukhitine, S. E., Chateauneuf, A. & Bouchair, A. (2019), 'Experimental and numerical study to evaluate the effect of thermostat settings on building energetic demands during the heating and transition seasons', *Applied Thermal Engineering* **152**, 35–51.

Brackley, C., O'Brien, W., Trudel, C. & Bursill, J. (2021), 'The in-situ implementation of a feature-rich thermostat: A building engineering and human factors approach to improve perceived control in offices', *Building and Environment* **199**.

D'Oca, S., Fabi, V., Corgnati, S. P. & Andersen, R. K. (2014), 'Effect of thermostat and window opening occupant behavior models on energy use in homes', *Building Simulation* **7**, 683–694.

Garzia, F., Verbeke, S., Pozza, C. & Audenaert, A. (2023), 'Meeting user needs through building automation and control systems: A review of impacts and benefits in office environments', *Buildings* **13**(10), 2530.

Gunay, H. B., O'Brien, W. & Beausoleil-Morrison, I. (2016), 'Implementation and comparison of existing occupant behaviour models in energyplus', *Journal of Building Performance Simulation* **9**(6), 567–588.

Liu, W., Gunay, H. B. & Ouf, M. M. (2021), 'Modeling window and thermostat use behavior to inform sequences of operation in mixed-mode ventilation buildings', *Science and Technology for the Built Environment* **27**(9), 1204–1220.

Liu, X., Lee, S., Bilionis, I., Karava, P., Joe, J. & Sadeghi, S. A. (2021), 'A user-interactive system for smart thermal environment control in office buildings', *Applied Energy* **298**.

Stopps, H. & Touchie, M. F. (2020), 'Managing thermal comfort in contemporary high-rise residential buildings: Using smart thermostats and surveys to identify energy efficiency and comfort opportunities', *Building and Environment* **173**.

Ubachukwu, E., Althaus, P., Xhonneux, A., Riebesel, L., Pick, J., Lieberenz, P. & Müller, D. (2023), Llec energy dashboard suite: User engagement for energy-efficient behavior using dashboards and gamification, *in* 'ECOS 36TH', Modellierung von Energiesystemen.